Applications of Diamond Films and Related Materials: Third International Conference

A. Feldman
Y. Tzeng
W. A. Yarbrough
M. Yoshikawa
M. Murakawa
(Editors)

NIST Special Publication 885

United States Department of Commerce
Technology Administration
National Institute of Standards and Technology

Proceedings of the
Applied Diamond Conference 1995

Applications of Diamond Films and Related Materials: Third International Conference

National Institute of Standards and Technology
Gaithersburg, MD
August 21-24, 1995

Edited by
Albert Feldman
National Institute of Standards
*   and Technology*
Gaithersburg, MD, USA

Yonhua Tzeng
Auburn University
Auburn, AL, USA

Walter A. Yarbrough
Pennsylvania State University
University Park, PA, USA

Masanori Yoshikawa
Tokyo Institute of Technology
Tokyo, Japan

Masao Murakawa
Nippon Institute of Technology
Saitama, Japan

NIST Special Publication 885

PREFACE

Interest in commercializing diamond technology and related materials technologies continues to grow. This can be attested to by the large number of abstracts received for this meeting, the Third International Conference on the Applications of Diamond Films and Related Materials. More than 300 abstracts were received. Of the titles chosen for presentation, 191 were submitted as papers which appear in these proceedings. Papers were received from 22 countries and nearly half of the papers are from countries other than the United States. The distribution is as follows: U.S.A–97, Russia–20, Japan–17, China–13, Germany–6, Ukraine–6, U.K.–5, South Korea–5, Switzerland–5, two each from France, Singapore, Taiwan and the Netherlands, and one each from Australia, Belarus, Brazil, Canada, India, Israel, Sweden, Thailand, and Yugoslavia.

Cutting tools coated with CVD diamond are of immediate commercial interest. Other applications, such as diamond windows and diamond heat spreaders, are developing but at a slower pace. In addition to interest in CVD diamond technology, there is a continually growing interest in commercializing diamond-like carbon. Interest in cubic boron nitride is receiving more attention because of its resistance to oxidation and because it can be used on tools to machine ferrous materials. A new category of hard materials, CN_x, is still in an exploratory stage of development. It is not yet known to what extent these materials will be commercially useful.

We thank all of the sponsors, cooperating societies, contributors, committee members, and session chairs who have made this conference a success.

Albert Feldman
Conference Chairman

Walter Yarbrough
Organizing Committee Chairman

Masanori Yoshikawa
Organizing Committee Co-Chairman

Yonhua Tzeng
Program Committee Chairman

Masao Murakawa
Program Committee Co-Chairman

APPLIED DIAMOND CONFERENCE 1995

Held at

National Institute of Standards and Technology
Gaithersburg, MD
August 21–24, 1995

Sponsor

National Institute of Standards and Technology

Cosponsors

American Physical Society
Diamond Microelectronics Company
Materials Research Society

Cooperating Societies

American Carbon Society
American Ceramic Society
ASM International
IEEE—Electron Devices Society
Japan New Diamond Forum
Optical Society of America
SPIE

ACKNOWLEDGMENT

ADC'95

EXECUTIVE COMMITTEE

Albert Feldman
National Inst. of Standards and Technology
Gaithersburg, MD, USA

Yonhua Tzeng
Auburn University
Auburn, AL, USA

Mutsukazu Kamo
National Inst. for Res. in Inorganic Materials
Tsukuba, Japan

Walter A. Yarbrough
Pennsylvania State University
University Park, PA, USA

A.H. Lettington
University of Reading
Reading, UK

Shuji Yazu
Sumitomo Electric Ind. Ltd.
Hyogo, Japan

Masao Murakawa
Nippon Institute of Technology
Siatama, Japan

Masanori Yoshikawa
Tokyo Institute of Technology
Tokyo, Japan

CONFERENCE CHAIRMAN

Albert Feldman
National Institute of Standards and Technology
Gaithersburg, MD, USA

INTERNATIONAL ADVISORS

John C. Angus
Case Western Reserve University
Cleveland, OH, USA

Osamu Saeki
Kobe Steel Company, Ltd.
Kobe, Japan

Thomas R. Anthony
GE Corporate R&D Center
Schenectady, NY, USA

Michael Seal
Sigillum, B.V.
Amsterdam, The Netherlands

Andrej R. Badzian
Pennsylvania State University
University Park, PA, USA

Boris V. Spitsyn
Institute of Physical Chemistry
Moscow, Russia

Hou Li
Beijing Institute of Synthetic Crystals
Beijing, China

Nobuo Setaka
Chiba, Japan

Benno Lux
Technische Universitat Wien
Vienna, Austria

ORGANIZING COMMITTEE

PROGRAM COMMITTEE

Hiroshi Kawarada
Waseda University
Tokyo, Japan

Noribumi Kikuchi
Mitsubishi Material Corporation
Saitama, Japan

Claus-Peter Klages
FhG-IST
Hamberg, Germany

Paul Klocek
Texas Instruments
Dallas, TX, USA

Koji Kobashi
Kobe Steel Ltd.
Kobe, Japan

Kunio Komaki
Showa Denko K.K.
Nagano, Japan

Robert R. Reeber
U.S. Army Research Office
Research Triangle Park, NC, USA

Ronald A. Rudder
Research Triangle Inst.
Research Triangle Park, NC, USA

Kunio Shibuki
Toshiba Tungaloy Co., Ltd.
Kawasaki, Japan

Staffan Söderberg
Sandvik Cormant Materials & Processes
Stockholm, Sweden

Clifford L. Spiro
GE Corporate R&D Center
Schenectedy, NY, USA

Charles B. Willingham
Raytheon Company
Lexington, MA, USA

Max Yoder
Office of Naval Research
Arlington, VA, USA

LOCAL ARRANGEMENTS

Edgar Etz, Chairman
National Inst. of Standards and Technology
Gaithersburg, MD, USA

Edward N. Farabaugh
National Inst. of Standards and Technology
Gaithersburg, MD, USA

Larry Robins
National Inst. of Standards and Technology
Gaithersburg, MD, USA

Keith Snail
Naval Research Laboratory
Washington, DC, USA

TABLE OF CONTENTS

DIAMOND—ELECTRON DEVICES AND SENSORS

DIAMOND—CUTTING TOOLS

DIAMOND PROCESSING

DIAMOND GROWTH AND GROWTH CHARACTERIZATION

DIAMOND—ADHESION, FRICTION AND WEAR

DIAMOND—LARGE AREA/HIGH RATE GROWTH

DIAMOND OPTICS

DIAMOND—THERMAL PROPERTIES AND APPLICATIONS

MODELLING

CUBIC BORON NITRIDE

CARBON-NITROGEN FILMS

MISCELLANEOUS

ADDITIONAL PAPERS

KEYNOTE

Applications of Diamond Films and Related Materials: Third International Conference, 1995
Editors: A. Feldman, Y. Tzeng, W. A. Yarbrough, M. Yoshikawa, and M. Murakawa

3

THE CURRENT STATUS OF CVD DIAMOND APPLICATIONS AND
PROSPECTS FOR THE FUTURE

Michael Seal

Sigillum BV, P.O. Box 7129, Amsterdam 1007JC, Netherlands

Key words: heat-sinks, markets, prospects, tools,
wear-resistance, windows

Abstract

This is a review of the principal present markets for CVD
diamond, and of the commercial progress made since the
first ADC in 1991.   Tools, heat-sinks, and windows are
the principal CVD diamond products currently being sold.
CVD diamond coatings are also being applied to provide
wear resistance for such products as dies, nozzles, and
bearing surfaces.   Prospects for the future for these
and possible new products are also discussed.

1. Introduction

The four years since the first Applied Diamond Conference
have seen tremendous advances in understanding the
science of CVD diamond growth and the technology of
effecting it at high rates uniformly over large areas.
Various publications at the time of the first ADC
indicate norms for 1991 for CVD diamond growth rates from
microwave plasmas of around 2 µm/h and substrate dia-
meters around 5 cm.   To-day in 1995 there is equipment
on the market which makes possible the growth of good
quality diamond at rates of over 10 µm/h over diameters
of 15 cm.   It is not my purpose here to review that
progress, but rather to ask the question what influence
it is likely to have on the development of markets for
CVD diamond?

The early work on CVD diamond deposition in the U.S.A.,
Russia, and Japan led to the realisation that here was a
product with almost unlimited potential.   For a time
almost every research paper on CVD diamond began with a
listing of the superlative physical properties of the
material as justification for the research.   The media
picked this up and some inflated the possibilities beyond
economic reason.   We were in the classic situation of

writers predicting the future, where it is not too
difficult to forecast how existing technology will
develop, but much harder to forecast the economics and
sociology.

By 1991 much research on CVD diamond had been funded.
There had been great successes, but also the realisa-
tion that there were some distinctly intractable prob-
lems to be faced.   Financial sponsors were beginning
to ask questions about the pay-back.   The founders of
the ADC conferences amongst many others realised that
some very practical questions needed to be addressed.
The early euphoria about CVD diamond was fading, to be
replaced in some circles by undue pessimism as the
pendulum swung too far the other way.   My theme now is:
where do we stand commercially to-day?

2. Survey results

To try to find some answers, I sent letters to 35 com-
panies which I knew were involved in CVD diamond resear-
ch and/or might be selling CVD diamond products.   I
received 12 replies.   Of the non-respondents 5 letters
were either returned by the Japanese post office or are
unlikely to have reached their destinations because of
the Kobe earthquake, which occurred just after I wrote
the letter.   The response was thus 40% which seems
quite good for this kind of enquiry.   Of the 12 res-
pondents, 8 stated that they were currently selling CVD
diamond products.   If I add to these the names of 5
non-respondent companies which I know to be selling such
products, I reach a total of 13 companies currently
selling CVD diamond products in Europe, Japan, and the
U.S.A.   The principal products are cutting tools (8
companies), heat-sinks (5 companies), infrared windows
(4 companies), wear resistant parts (4 companies), and
X-ray windows (2 companies).

3. Cutting tools

The first question one must ask about these or any other
product is: what is the competition?   In the case of
cutting tools, there are already major markets served by
natural and high pressure synthetic diamond tools, PCD
diamond tools, and cemented carbide and nitride tools,
in order of increasing sales volume.   Natural diamond
tools serve markets ranging from dresser tools contain-
ing unshaped diamonds of relatively low quality (used
for shaping and dressing conventional abrasive grinding
wheels), to precisely shaped single crystal diamond
tools used for the accurate generation of surfaces to

tolerances in the micrometre to nanometre range, e.g. in the turning of computer hard discs. Tools shaped from high-pressure, high-temperature synthetic diamond crystals are also used for high precision applications.

PCD (polycrystalline diamond) tools are used for the turning, milling, and drilling of a variety of non-ferrous metal, ceramic, plastic, and wood components (e.g. aluminum-silicon alloy pistons) and in mining and rock-drill bits. Cemented tungsten carbide and other hard carbide, nitride, and oxide tools are used in general metal-working applications. They may have hard coatings, especially of carbides, nitrides, or oxides to improve wear lifetimes.

CVD diamond tools are of two types, namely those where a free-standing block of diamond material is brazed to a shank and subsequently finished, and those where a thin layer of material is deposited directly on a pre-shaped tool of cemented tungsten carbide, silicon nitride, or the like. In both cases the cutting edge is poly-crystalline diamond with material properties which one might at first sight think are not too different from those of conventional PCD. It turns out, however, that there are very significant performance differences. The reasons probably lie in one or more of the following factors: absence of metal binder, different crystallite size and texture, better thermal conductivity, better thermal stability and corrosion resistance.

Published case studies from at least 5 tool manufac-turers show that in some cases much larger product runs can be obtained with CVD diamond tools than with PCD tools. The published improvements range from 25% to more than a factor of 40. Significantly the best-established improvements seem to be with highly non-uniform materials such as high-silicon aluminum casting alloys, fiber-reinforced composites, and green ceramics, though improvements have also been obtained with more uniform materials such as graphite, soft non-ferrous metals, and simple plastics.

Both thick and thin film CVD diamond tools show advan-tages, but obviously thick film tools will be the more expensive and thus in the more difficult position as regards competition with PCD. Thin film coated cut-ting tool inserts are already making substantial inroads on an established market and look like being a success story for CVD diamond in the very short term. A world-wide market for diamond-coated cutting-tool inserts in excess of $ 25 million annually seems imminent and could

grow substantially, especially as the production costs and thus competitive stance are a fairly strong function of production volume.

Thus in many applications CVD diamond gives better cutting performance than PCD. On the other hand, PCD does have one advantage against CVD diamond, namely its greater fracture toughness -- the cobalt binder seems to provide a cushioning effect reducing crack propagation. PCD will probably remain the material of choice for the heavy duty applications which use diamond, such as brazed cutter segments on oil and gas industry drill crowns. It is interesting to note though that PCD only holds a very small part of the overall heavy drilling market, the majority of which is covered by steel and cemented carbide cutters.

An advantage of CVD diamond lies in the fact that intricate shapes can be coated. Twist drills are a good example (especially small drills for fiber-reinforced circuit boards). Cutting tools with chip-breaker geometries are another. On a larger scale rotary milling cutters offer opportunities for CVD diamond coating. In the past adhesion and uniformity have been major problems for CVD diamond coatings. Though great progress has been made and these problems seem to have been solved in regard to small products, they may still restrict expansion into the markets for larger area products. Nevertheless we can probably expect a worldwide annual market for all kinds of CVD diamond tools of $ 100 million by 1997 and growing rapidly thereafter. The main restricting factor is that diamond cannot be used to machine steel or other ferrous metals.

A further and new competitor for CVD diamond is DLC. Steel tools can be coated directly with DLC and diverse new tools become possible. Depending on their performance, these may well become more significant commercially than CVD diamond tools in some applications. There is also the whole gamut of wear-resistant components, for which DLC seems ideally suited.

4. Heat-sinks

These encompass a range of substrates for electronic devices, some of which are more properly described as heat spreaders, and some of which are more truly heat sinks. They probably represent the largest current market for CVD diamond in terms of value. The strength

of CVD diamond in this application lies in its undoubted technical superiority.   The thermal conductivity of even average quality CVD diamond is at least 3 times that of copper at room temperature, and is only surpassed by the best diamond qualities such as natural type 2A or high pressure synthetic type 1B.   These are expensive with prices per unit volume which increase quite dramatically as the size increases beyond say 200 mg, whereas the price per unit volume of CVD diamond remains approximately constant or may in some circumstances even decrease with volume.

For large substrates (above 5mm square), CVD is the only form of diamond which seems economically viable.   This is not necessarily true for the smallest sizes (below 0.5mm square), but the major potential markets are going to require the larger sizes.   The competition for these will then be materials such as aluminum nitride, copper-tungsten, silicon, alumina, or beryllia with thermal conductivities an order of magnitude worse.   The design question then becomes the classic one: is it worth paying a higher price for a better product?   What will happen as prices come down further?   Obviously the market should expand rapidly, but there are technical problems which are likely to restrict market growth in the near term.

The first of these is the difficulty of polishing, closely associated in its economic effects with the difficulty of achieving uniform growth thickness.   Both become more difficult as the substrate area increases. They are related in that uniform growth reduces the need for polishing, but there is as yet no really satisfactory method of polishing large CVD diamond plates.   The conventional techniques with diamond powder on iron laps are too slow.   Applying greater pressure with more robust machinery does help, though polishing is still too slow.   For the future unconventional techniques will probably be needed.   These include laser and ion-beam machining, reactive ion etching, and chemical methods such as hot-metal polishing and the old Dawihl-Fritsch technique (hot oxygen).

For most applications pattern metallisation of the diamond substrate is needed.   Patterns include contact stripes, insulating areas, and bonding areas with different solder coatings.   There are problems of metal adhesion to the diamond and of solder flow and solder-flow restriction.   Also, since most applications involve wafer-scale processing, there are problems of dicing the patterned wafers without producing graphite

and thereby short-circuiting the device, and without
damaging the metal layers mechanically.

The current size of the CVD diamond substrate market is
difficult to determine since devices go through long
development cycles involving co-operation of diamond
supplier and electronics house at the research and
development stage, design and qualification programs,
and finally production cycles which may be short or long.
Since the diamond is a small part of a much larger
program, the demand can fluctuate wildly over quite
short time frames.   Nevertheless overall demand is
growing and current sales are likely to be in the range
of low eight figures in dollars worldwide.   Whether the
number is $ 10 million or $ 40 million is hard to judge.

Currently available advertising literature lists a num-
ber of device types as sales targets.   They include
laser diodes, power FETs, microprocessors, high power IC
modules, and two-dimensional and three-dimensional
multichip modules.   Significant success in one or more
of these fields could increase the market by an order of
magnitude or maybe more.

5. Infrared windows

Pure diamond has an intrinsic infrared optical absorp-
tion system in the wavelength range 2 - 6µm, but is
transparent beyond that effectively to infinite wave-
length, as well as in the visible and ultraviolet
regions.   As thin plates it is also partially trans-
parent in the 2 - 6µm range as the intrinsic absorption
is weak.   It therefore makes an ideal window material
for devices designed to detect thermal radiation.   In
comparison with competitive materials such as zinc
sulfide, zinc selenide, potassium bromide and other
salts, it has the advantage of great hardness and
strength and resistance to solvent attack, particularly
by water.   It is thus not surprising that much effort
has been devoted to producing good optical quality CVD
diamond.   The problems have largely been caused by the
polycrystalline nature of the material, which gives rise
to optical scattering at the grain boundaries.   Material
is now available through which one can read typescript
easily, but which nonetheless conveys a slightly hazy
appearance.   It is amply good enough for infrared
spectroscopy and non-critical imaging.

The first and probably still the major uses for CVD
diamond windows were and are most likely military.

There was a need for a strong non-water-soluble window material to cover missile-seeker sensors. Detailed military procurement figures for such window materials are not generally available, and I shall not essay any guess as to what they might be. The civilian applications cover items such as infrared windows for corrosive environments in on-line composition monitoring in the chemical process industry. Windows and prisms for laboratory infrared equipment are another market. There is potential for wider scale use in bar-code readers, for instance, but the semi-mass markets are more likely to be satisfied by DLC coatings. The optical market remains a very promising field for CVD diamond and will continue to be so as quality improves and prices come down.

6. Wear resistant parts

The companies responding to my letter listed the following as current products in this class: micrometer measuring faces, bearing surfaces, wire dies, wire guides, and abrasive jet nozzles. All are fairly obvious applications for a hard, inert, wear-resistant material, and there will doubtless be many more. There will be some niche markets and some major ones, but there is no evidence yet for any one dominant application.

7. Other products

Being a thin film application, X-ray windows were among the earliest CVD diamond products. There are two uses, namely as windows to protect soft X-ray detectors (e.g. in light element EDAX) and in high resolution X-ray lithography.

Amongst the mechanical applications, industrial knives are a "natural" for CVD diamond, and doubtless will become a major market once the price is low enough. The principal factor keeping prices high is the fact that most knives are relatively large and require either uniform growth of a diamond layer on a shaped substrate or the ability to polish large areas of CVD diamond economically. These are the same problems faced in the heat-sink applications (section 4). Slitting knives for foils, tapes, paper, fabrics, and plastic sheeting are obvious candidates for diamond. On the mass-market scale one may note that there has already been at least one patent granted for diamond-coated razor blades.

The often-quoted "diamond age" to replace the "silicon
age" in active electronics still seems quite distant.
Single crystal diamond growth and effective n-type dop-
ing form together a sine-qua-non.   The breakthrough,
when it comes, will probably impact high temperature
electronics first.   In the meantime diamond cold
cathodes look promising.

8. Summary and conclusions

My short conclusion is that the CVD diamond industry is
healthy and starting to expand rapidly.   The main pro-
ducts are cutting tool inserts, heat-sinks, and infrared
windows.   An important corollary is that sales have not
expanded as fast as the optimists of four years ago
would have had us believe.   There were forecasts then
that total worldwide sales of all CVD diamond primary
products would reach $ 500 million annually by 1995.
1995 is here and I doubt at the time of writing (March)
that total sales levels have reached even 10% of that.
This is a personal estimate based on impressions and not
exact data.   Whatever the numbers, there are certainly
significant commercial sales now.   There are well de-
fined and well tested products on the market.   New
products are being introduced.   Companies have estab-
lished marketing channels.   In short it is to-day a
commercial scenario very different from the development
and prototyping prologue of 1991.   It will surely
expand now.

9. References and acknowledgments.

There are deliberately no detailed references in this
review.   If supplied diligently the number of such
items would be in the hundreds.   Much work on CVD dia-
mond has been published in the Proceedings of Conferen-
ces in the ADC, Diamond Films, and ICNDST series, as
well as in the journal "Diamond and Related Materials".
There were also conferences reported in the Electro-
chemical Society series and a book in the same series
reviewing progress to 1994 (K.E. Spear & J.P. Dismukes,
editors, "Synthetic Diamond").   I have relied in part
on these publications for technical background and for
some of the commercial background.   I have also made
substantial use of advertising and technical literature
supplied by a number of companies.   For this I thank
especially: AEA Technology, Astex Inc., CemeCon GmbH.,
GE Superabrasives, Harris Diamond Corp., Kennametal
Inc., Norton Diamond Film, AB Sandvik Coromant, and
Valenite Inc.

DIAMOND
ELECTRON EMISSION

Applications of Diamond Films and Related Materials: Third International Conference, 1995
Editors: A. Feldman, Y. Tzeng, W. A. Yarbrough, M. Yoshikawa, and M. Murakawa

13

HIGH EMISSION CsI COATED DIAMOND DYNODES FOR AN ELECTRON MULTIPLIER

G.T. Mearini, I.L. Krainsky, and J.A. Dayton, Jr.

NASA Lewis Research Center, 21000 Brookpark Rd., Cleveland, Ohio 44135

Key Words: diamond, secondary electron emission

Abstract

High secondary electron emission (SEE) has been observed from CVD grown diamond. Values of the secondary electron coefficient (σ) have been measured between 10 and 20 from as-received (hydrogen terminated) diamond films, but the emission was unstable under continuous exposure to electrons and σ decreased with a fluence dependence due to electron induced hydrogen desorption from the diamond surface. It was observed recently, that activation of a CsI coated diamond surface by electron exposure left a thin Cs layer (1 to several monolayers) which stabilized the secondary emission to values of $\sigma = 20 - 35$ at 1500 eV, independent of the primary current density. These electron beam activated-alkali terminated (EBAAT) diamond films are being used as dynodes in an electron multiplier assembly. This assembly has been tested previously using hydrogen terminated diamond dynodes operated in a hydrogen environment.

1. Introduction

A long list of electronic applications for CVD diamond is being investigated since the acceptance of diamond as a negative electron affinity material, first proposed by Himpsel, et al.[1] Practical uses for this material has been made possible by the relative ease of fabrication and the large area coverage obtainable by many of the growth techniques. Field emission from CVD diamond films at low applied fields (~ 20 kV/cm)[2], makes diamond a potential candidate for flat panel display[3] and cold cathode applications. High, stable SEE properties observed from EBAAT diamond[4] may enable more efficient designs of devices utilizing secondary emitters such as electron multipliers and PMTs. Materials currently used in these applications display values of σ which range between 2-4[5].

2. Experimental Procedure

The dynodes used for this work were conductive CVD diamond films grown on Si,

cut into < 1 cm² approximately square pieces, and vacuum coated with ~ 2.5 nm of CsI. The samples, shown in Figure 1, were provided by General Vacuum, Inc.

The samples were activated before they were received by rastering a 20 µA electron beam with a 0.5 mm spot size over 0.5 cm X 0.5 cm. σ vs. time was measured during the activation procedure, and the targets were considered activated when σ stabilized as is seen in Figure 2. The 2.5 nm thick coating of CsI did not provide a uniform coverage as was observed initially during the activation process, where the florescent CsI coated surface contained many "dark" regions. This was also evident from the SEE

Fig.1   SEM micrograph of representative CVD diamond dynode.

measurements, since σ = 38 without rastering, and 20 during the rastering which indicated that uncoated diamond regions were exposed to the beam, where σ ≈ 2[6]. The sample designated as the first dynode was coated with 50 nm of CsI and only partially activated to allow florescence during operation which made it easier to position the electron beam.

The electron multiplier assembly, which uses 8 dynodes, has been discussed previously with diamond on Mo dynodes[6], and is shown in Figure 3. "Pre-activation" of the dynodes was performed to avoid graphitizing the surfaces due to ion sputtering from Cs^+ and I^+, which occurred previously when dynodes were activated while in use in the electron multiplier.

For this work, all measurements of the gain of the electron multiplier were made in a direct current mode at a pressure of 1.0×10^{-9} torr. An electron beam of known current was directed at the first dynode, and the output from the collector was measured with a voltmeter.
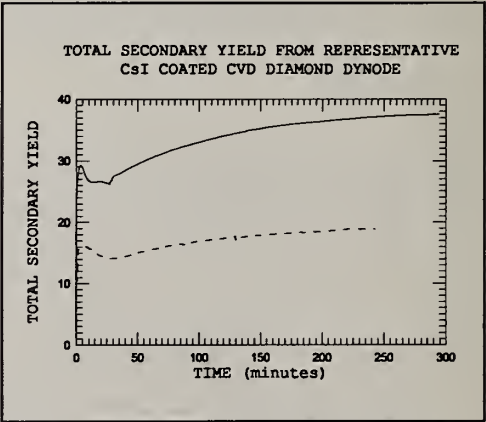
Fig. 2   Solid line: primary current density = 1.5 mA/cm² @ 1500 eV. Dashed line: 80 µA/cm² @ 1500 eV.

3. Experimental Results

The results here will be compared to results obtained previously with this same setup, from uncoated diamond dynodes while running the device in a hydrogen environment[7].

σ from the 8 EBAAT diamond dynodes ranged from 15 to 20 at 1 keV. The dynodes were cut from a 2" Si previously coated with diamond, which made cutting square samples difficult. This resulted in variations in the shape and size of the different dynodes, with most being trapezoidal rather than square, and all < 1 cm² in area.

Fig. 3 Schematic diagram of electron multiplier.

Output measurements were made with the primary current adjusted at three different levels as is seen in Table I. It is important to note that, at these values of primary beam current, commercially available electron multipliers would most likely be destroyed. In our case the limitations were saturation due to space charge and a poor geometry for collecting secondary electrons. In previous measurements we obtained gain of nearly 10^6, however the output was unstable and the device was ultimately destroyed due to sputtering from the hydrogen ions in the presence of the high voltage[7].

Table I. Gain vs. Primary Current

Primary Current	Gain
2.0 μA	1.3×10^2
2.5 nA	2.2×10^4
9.0 pA	1.3×10^5

In the case of the EBAAT dynodes, the output was stable and could be operated indefinitely. The ultimate gain obtained in the DC mode was 1.3×10^5 while using a primary current of 9.0 pA.

4. Summary and Conclusions

Eight EBAAT diamond samples were tested as dynodes in an electron multiplier assembly. The dynodes were created by vapor depositing CsI onto conductive CVD diamond on Si, and activated by electron exposure. The electron multiplier produced stable output in ultra-high vacuum, with a maximum gain of 1.3×10^5.

The lower gain obtained from the EBAAT dynodes, as compared to uncoated diamond dynodes tested previously in a hydrogen environment, may be due to the unusual shapes and smaller sizes of the dynodes, and the partial activation of the first dynode. The low gain was also due to saturation of the multiplier at the relatively high primary currents. The present setup will be tested in an electron pulse counting mode to more accurately determine the gain.

The feasibility of EBAAT diamond in secondary electron emitting applications has been demonstrated with this experiment. Future work will include coating dynodes from a commercially available electron multiplier with EBAAT diamond to determine any real improvement over the current technology.

Acknowledgements

References

[1]   F.J. Himpsel, J.A. Knapp, J.A. Van Vechten, and D.E. Eastman, Phys. Rev. B, **20(2)**, 624 (1979).
[2]   J.D. Shovlin, M.E. Kordesch, Appl. Phys. Lett., **65(7)**, 863 (1994).
[3]   K. Derbyshire, Solid State Tech., Nov., 55 (1994).
[4]   G.T. Mearini, I.L. Krainsky, J.A. Dayton, Jr., Yaxin Wang, Christian A. Zorman, John C. Angus, R.W. Hoffman, and D.F. Anderson, Appl. Phys. Lett., **66(2)**, 242 (1995).
[5]   A.S. Gilmour, Jr., *Microwave Tubes* (Artech House, Norwood, MA, 1986), p. 136.
[6]   G.T. Mearini, I.L. Krainsky, and J.A. Dayton, Jr., Surf. and Int. Anal., **21**, 138 (1994).
[7]   G.T. Mearini, I.L. Krainsky, Yaxin Wang, J.A. Dayton, Jr., R. Ramesham, and M.F. Rose, Thin Solid Films, **253**, 151 (1994).

Diamond Negative Electron Affinity Surfaces, Structures and Devices

R. J. Nemanich, P. K. Baumann, and J. van der Weide
Department of Physics and Department of Materials Science and Engineering
North Carolina State University
Raleigh, NC 27695-8202

Abstract

The electron affinity of a semiconductor relates the band structure of the semiconductor at the surface to the vacuum ground state near the surface. Wide bandgap semiconductors have the possibility of exhibiting a negative electron affinity (NEA) meaning that electrons in the conduction band are not bound by the surface. The surface conditions are shown to be of critical importance in obtaining a negative electron affinity. In this study, angle resolved UV-photoemission spectroscopy (ARUPS) is used to detect the effect. Surface terminations ranging from adsorbates, metals and insulators are shown to induce an NEA on diamond. In particular, it is demonstrated that hydrogen termination can induce a NEA on (111), (100), (110) and (311) surfaces. Theoretical studies have indicated a basis for the observed NEA effects. In contrast, as-prepared surfaces with oxygen termination often exhibit a positive electron affinity. It is shown that thin metal layers of Ti, Ni, Cu, and Co can induce a NEA on the (111) surface, and new evidence indicates NEA on the (100) surface. NEA materials could prove useful in cold cathode applications, and potential and limitations are discussed.

Introduction

The electron affinity of a semiconductor is defined as the energy required to remove an electron from the conduction band minimum to a distance macroscopically far from the semiconductor (i.e. away from image charge effects.). At the surface this energy can be shown schematically as the difference between the vacuum level and the conduction band minimum. The electron affinity is not, in general, dependent on the Fermi level of the semiconductor. Thus while doping can change the Fermi level in the semiconductor and the workfunction will change accordingly, the electron affinity is unaffected by these changes. An alternative view is that the electron affinity is a measure of the heterojunction band offset between the vacuum and a semiconductor of interest. For most semiconductors, the conduction band minimum is below the vacuum level and electrons in the conduction band are bound to the semiconductor by an energy equal to the electron affinity. In some cases, surface conditions can be obtained in which the conduction band minimum is above the vacuum level. In that case the first conduction electron would not be bound to the sample but could escape with a kinetic energy equal to the difference in energy of the conduction band minimum and the vacuum level. This situation is termed a negative electron affinity. (Note that the electron is still bound to the vicinity of the sample by coulomb forces.)

The electron affinity or work function of a material is usually ascribed to two aspects of the material (1) the origin of the atomic levels, and (2) the surface dipole due to the surface termination.[1] These effects are shown schematically in Fig. 1. The

atomic levels are more or less intrinsic to a material and cannot be changed. This is not the case for the surface dipole. The surface dipole can be substantially affected by surface reconstructions and surface adsorbates. As a simple example to illustrate the magnitude of this effect consider a surface with hydrogen termination, and assume that the average nuclear and electronic charges are point charges separated by 0.5Å. Then for a surface density of $1 \times 10^{15} cm^{-2}$ we would find a ~9eV effect due to the surface dipole. (Certainly complete charge transfer is never a reasonable possibility, but this simple calculation demonstrates the significance of the surface dipole.) Because of the large effect of the surface dipole, it is essentially impossible to determine if a material is "intrinsically NEA." Thus the surface termination is critical in describing the electron affinity (or NEA) properties of a material.

Physical Properties Affecting the Workfunction or Electron Affinity
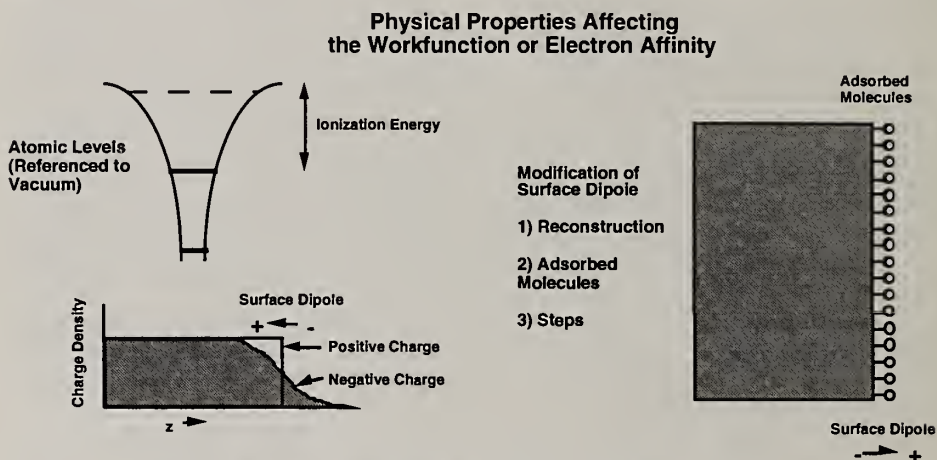
Fig. 1   A representation of the effects which contribute to the workfunction (or electron affinity) of any material. While the atomic levels are an intrinsic property of the material, changes in the surface bonding can substantially affect the workfunction or electron affinity.

One method to measure the electron affinity of a semiconductor is UV-photoemission.[2,3] The changes in the spectra due to NEA are indicated in Fig. 2.[4] The electrons from the valence band are excited into the conduction band. In transiting towards the surface, electron scattering occurs and a large number of secondary electrons accumulate at the valence band minimum. For materials with a positive electron affinity these electrons cannot escape, while for a NEA the electrons can be emitted directly and will be observed with a low kinetic energy. Thus the two effects which signify a NEA are an extension of the spectral range to lower energy and the appearance of a sharp peak at low kinetic energy. This feature will appear at the largest (negative) binding energy in typical presentations of UPS spectra.

In addition to the sharp feature that is often evident in the spectra of a NEA semiconductor, the width of the photoemission spectrum (W) is related to the bandgap E_g and the excitation energy hv. The relation is that $hv = E_g + W$. Careful measurements of the width of the spectra are helpful in distinguishing whether the effect is direct emission of the electrons from conduction band states or whether excitons are involved in the emission process. The effects of excitons have recently been reported by Pate and co-workers.[5]

E_c

Secondary
Electrons

E_v

Valence band

Energy
Gap

$h\nu$

E_{vac} for <u>Positive</u> Electron Affinity

E_{vac} for <u>Negative</u> Electron Affinity
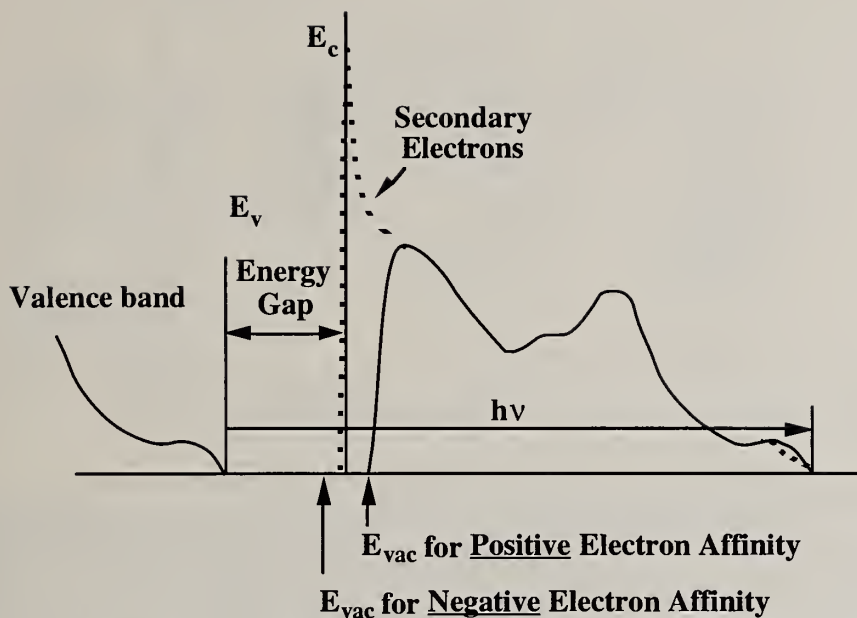
Fig. 2   A schematic of how NEA affects the photoemission spectra. For a NEA surface the spectra is broadened to lower kinetic energy and a peak due to quasi thermalized electrons is detected also at the lowest kinetic energy.

Experimental
        The experiments described in this summary paper were carried out in an integrated UHV system with surface preparation, film growth and surface characterization capabilities. The system consists of eight chambers interconnected by a linear sample transfer mechanism. The overall length of the sample transfer chamber is ~35ft. A portion of the system is shown schematically in Fig. 3. This system shows the relations of the UV photoemission system, the plasma surface processing system, the LEED/Auger systems, and the metals MBE chamber. In the experiments described here, the UV-photoemission measurements were made with HeI (21.21eV) radiation and the electrons were analyzed with a VSW HAC50 50mm mean radius hemispherical electron analyzer. The spectra were collected at normal emission with a collection angle of ~2°. The sample was biased with ~1V so that the low energy electrons can overcome the workfunction of the analyzer. While higher sample bias can be employed, the low bias used here is to minimize spectral distortions that occur due to changes in the effective collection angle for the higher sample bias.

20
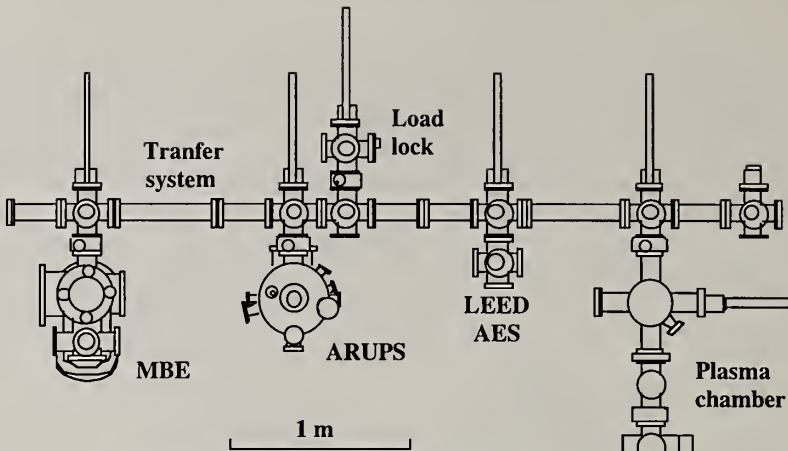
Fig. 3. A schematic of a portion of the integrated surface processing and characterization system used in the studies described here.

Surface Termination Effects

While the NEA of H-terminated diamond (111) has been established for many years,[2,3,4,6] it has only recently been shown that H-terminated (100) surfaces exhibit a NEA.[7,8,9] The UV photoemission of a diamond (100) surface versus annealing is shown in Fig. 4. The results indicate the development of a sharp feature at the lowest kinetic energy (i.e. largest negative binding energy) of the spectra and an increase in the width of the spectrum. Auger spectra obtained from the same surfaces indicated the presence of oxygen termination for the as prepared surface, and the oxygen remained until ~1000°C. Thus the presence of oxygen was correlated with a positive electron affinity. It is difficult to detect the presence of H by the techniques available in this study, but partial H termination is likely from the wet chemical surface preparation treatments employed in this study. A theoretical analysis reported in concert with the experimental study also supported the presence of H-termination in obtaining a NEA of the (100) surface.[7] The study proposed that the annealed (100) surface with a 2x1 reconstruction was monohydride terminated and exhibited a NEA.

A schematic of the changes in the band alignment with H termination is indicated in Fig. 5. The band bending indicated is consistent with that expected for p-type (B doped) diamond. The two schematics have been aligned at the vacuum level to indicate the effect of the surface dipole. The H termination changes the surface dipole which results in a shift of the semiconductor bands with respect to the vacuum level.

UV-photoemission measurments of H-terminated (110) and (311) surfaces also exhibited the characteristics of a NEA. Future studies should focus on the stability of the H-terminated surfaces and the interactions with oxygen.

An alternative surface treatment that can be employed to induce a NEA on diamond is a thin metal layer. It is now well established that low workfunction metals such as Cs can be used to induce a NEA on III-V semiconductors such as GaAs. These surfaces are commonly employed in high efficiency photocathodes. For diamond, it was initially shown that Ti on diamond (111) surfaces resulted in a NEA, [10] and Ni on diamond was also found to exhibit a NEA.[11] Recent studies have also indicated a NEA for Co or Cu on diamond (100) surfaces.[12,13] The photo-emission spectra of diamond surfaces with a few monolayers of these different metals are summarized in Fig. 6. All spectra show the sharp feature associated with a NEA.
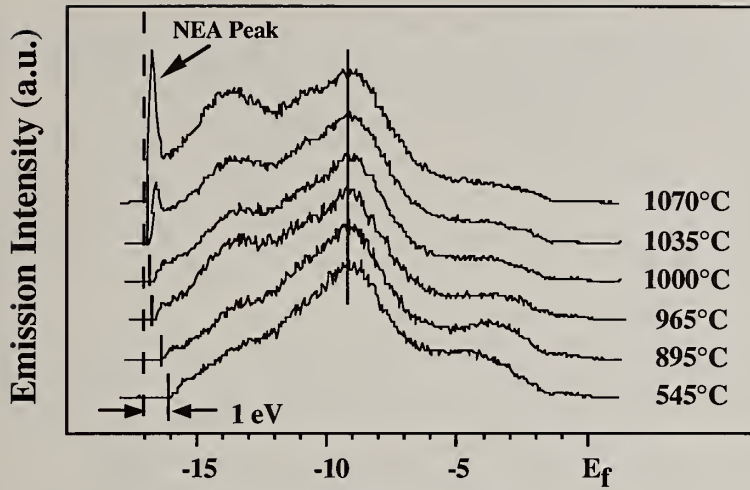
Fig. 4 The photoemission of a diamond (100) surface as a function of annealing. The broadening of the spectral width and the sharp feature at high (negative) binding energy (i.e. low kinetic energy) are indicative of a NEA.

Electronic Bands Near the Surface
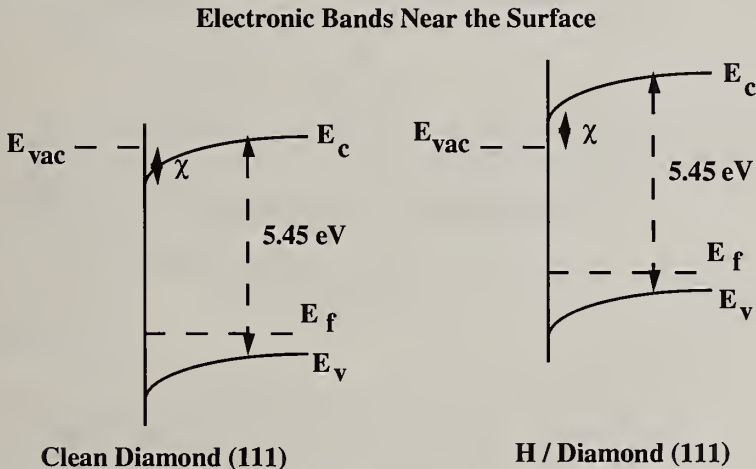
Fig. 5 The band alignments of clean diamond and H terminated diamond surfaces. Note that the figures have been aligned at the vacuum level.

As noted in the introduction a surface dipole is critical in establishing the relation between the band structure of the semiconductor and the vacuum. For the case of the metal overlayer the dipole is actually established at the metal semiconductor interface. This is the same dipole that results in the Schottky barrier. The vacuum level is referenced to the metal through the metal workfunction, and the interface dipole references the band structure of the semiconductor to the metal.

Of the results obtained to date the most significant may be the observation of a NEA of Co on diamond (100).[13] These films have been shown to be uniform with

little tendency to islanding as has been observed for Ni and Cu.[14] In addition, it has been shown Ti-oxide will also cause an NEA on the (111) surface,[15] and this surface could also prove more stable than the pure metal layers.
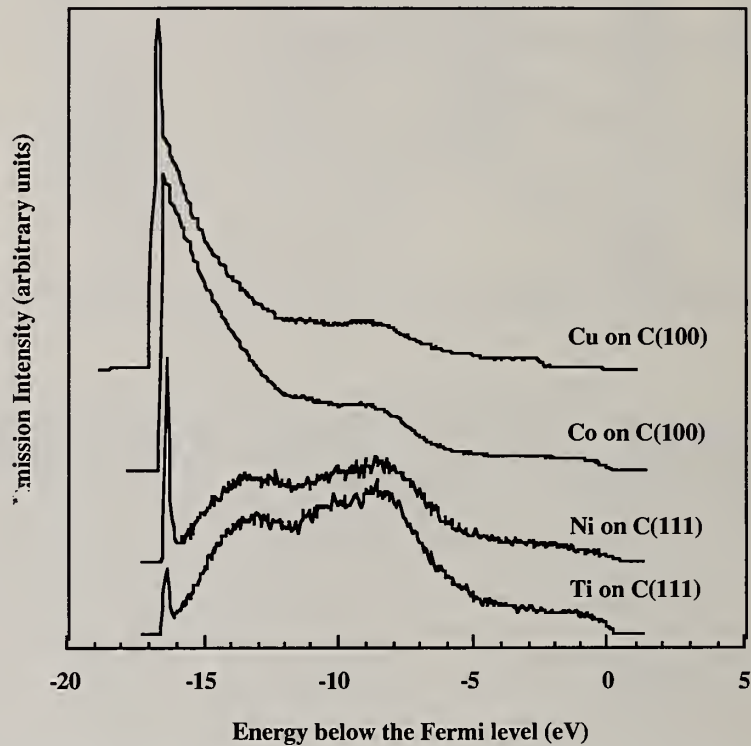
Fig. 6. UV-photoemission spectra of diamond surfaces with thin metal overlayers. The metal thicknesses correspond to several monolayers.
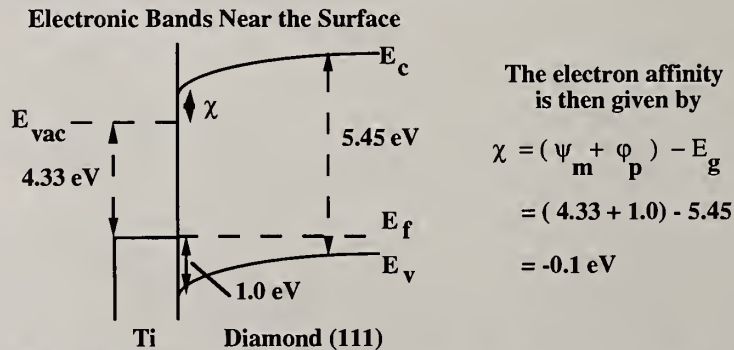
Fig. 7. The band structure at the surface of diamond with a thin metal coverage. The electron affinity can be deduced from the Schottky barrier, the metal workfunction and the diamond bandgap. The numbers for Ti on diamond (100) are illustrated.

Device Issues

In the past few years there has been significant interest in several applications that could involve vacuum electron emission. One of the most discussed applications is for displays.[16] There have been several recent demonstrations of field emission displays using arrays of point emitters. The sharp point emitters result in a field enhancement at the tip and a possible reduction in the workfunction due to the steps on the surface. The current versus voltage from a field emitter follows the Fowler-Nordheim expression. Other possible applications of field emitters is vacuum microelectronics and large area cold cathodes for high frequency or high power applications.

The advantage of vacuum over semiconductor applications is in the breakdown field and the mobility of the electrons. The breakdown field of any vacuum device would be determined by the surfaces of cathode or anode rather than the semiconductor. Of course the carriers are free from phonon scattering in the vacuum and the trajectories would be essentially ballistic paths.

The I-V dependence of an ideal NEA based emitter would exhibit emission at any (negative) voltage. At low fields the current would be limited by the space charge in the vacuum around the emitter (following Child's law) and at higher voltage the current would be limited by the resistance of the semiconductor and the contact. The energy distribution of the emitted electrons from a NEA cathode should be very narrow (~kT), and it should exhibit a noise component related to the resistance of the semiconductor and contact. This is in contrast to either thermal emitters (i.e. hot cathodes) or field emitters that exhibit fluctuations based on the statistics of the highest energy part of the electron distribution.
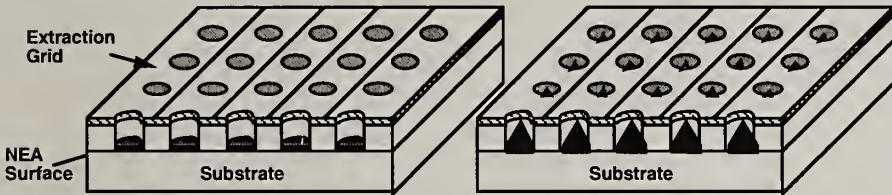
Fig. 8. Schematic of cold cathode grid structures employing either a flat NEA surface or a pointed emitter.

An electron emitter based on a negative electron affinity material would have several unique advantages over pointed field emitters. These would include low turn on voltage, high current, low erosion, and low noise. Fig. 8 compares two structures that could be employed in the applications noted above. The field emitter would require a significant field established through a potential between the tip and grid layer. In contrast, the NEA device would be controlled by a small field established by the grid to balance the anode to cathode field.

The research described here and the advances of others has established that obtaining a NEA surface is achievable. It is likely that these surfaces could be made stable for relatively high current emission. The major technological problem is supplying electrons to the conduction band of diamond. The studies described here employed above bandgap light to excite carriers. There may be some applications where light excitation can be used in cathode structures. A more desirable situation is to obtain an ohmic contact to an n-type NEA semiconductor. This involves a true

challenge for diamond, since reliable n-type doping is not readily obtainable. Furthermore, the ohmic contact to the n-type semiconductor could also be troublesome, since a very low workfunction material would be the obvious choice. This may not be necessary, though, if high levels of n-type doping are achievable.

Acknowledgment

References
1. Zangwill, A (1988), *Physics at Surface*, (Cambridge).
2. Himpsel, F.J., J.A. Knapp, J.A. van Vechten, and D.E. Eastman (1979), Phys.Rev. **B20**, 624.
3. Pate, B.B. (1986). Surf. Sci. **165**, 83.
4. van der Weide, J., and R. J. Nemanich, "Argon and Hydrogen Plasma Interactions on Diamond (111) Surfaces; Electronic States and Structure", Applied Physics Letters **62**, 1878-1880 (1993).
5. C. Bandis and B.B. Pate, "Electron Emission Due to Exciton Breakup from Negative Electron Affinity Diamond," Phys. Rev. Lett. **74**, 777(1995).
6. Nemanich, R.J. , L. Bergman, K. F. Turner, J. van der Weide and T. P. Humphreys, "Properties of Interfaces of Diamond," Trieste Semiconductor Symposium on Wide-Band-Gap Semiconductors, Physica B **185**, 528-538 (1993).
7. van der Weide, J., Z. Zhang, P. K. Baumann, M. G. Wensell, J. Bernholc and R. J. Nemanich, "Negative Electron Affinity Effects on the Diamond (100) Surface", Physical Review B **50**, 5803-5806 (1994).
8. van der Weide, J., and R. J. Nemanich,"Angle-Resolved Photoemission of Diamond (111) and (100) Surfaces; Negative Electron Affinity and Band Structure Measurements", J. Vac. Sci. Technol. **B 12**, 2475-2479 (1994).
9. P. K. Baumann and R. J. Nemanich, "Negative Electron Affinity Effects on H Plasma Exposed Diamond (100) Surfaces", J. Diamond Mat. (in press).
10. van der Weide, J., and R. J. Nemanich, "Schottky Barrier Height and Negative Electron Affinity of Titanium on (111) Diamond," J. Vac. Sci. Technol. **B 10**, 1940-1943 (1992).
11. van der Weide, J., and R. J. Nemanich,"Influence of Interfacial Hydrogen and Oxygen on the Schottky Barrier of Nickel on (111) and (100) Diamond Surfaces", Physical Review **B49**, 13629-13637 (1994).
12. P.K. Baumann, T.P. Humphreys and R.J. Nemanich, "Comparison of Surface Cleqaning Processes for Diamond (100)," Mat. Res. Soc Symp. Proc. vol **339**, 69 (1994).
13. P.K. Baumann and R.J. Nemanich, "Negative electron affinity effects and Schottky barrier height measurements of Co on diamond (100) surfaces," this proceedings.
14. P. K. Baumann, T. P. Humphreys, R. J. Nemanich, K. Ishibashi, N. R. Parikh, L. M. Porter and R. F. Davis, "Epitaxial Cu Contacts on Semiconducting Diamond", J. Diamond and Related Materials **3**, 883-886, (1994).
15. Bandis, C., D. Haggery, and B.B. Pate, "Electron emission properties of the NEA (111) 2x1 diamond -TiO interface," Mat. Res. Soc. Symp. Proc. vol. **339**, 75 (1994).
16. K. Derbyshire, "Beyond AMLCDs: Field emission displays?" Solid State Technology **37**, 55 (1994).

PHOTOELECTRIC EMISSION STUDIES OF CVD DIAMOND FILMS

C. BANDIS[1], W. CHANG[1], B.B. PATE[1], M. A. PLANO[2], M. D. MOYER[2], and M. A. MORENO[2]
[1]Physics Department, Washington State University, Pullman, WA 99164-2814 USA
[2]Crystallume, 3506 Basset Street, Santa Clara, CA   94054 USA

Key words: NEA, photoelectric, band bending, electron affinity, transport

Abstract

Near bandgap photoelectric emission properties of polycrystalline CVD diamond films are investigated. Our results find three characteristic photoelectric yield spectra. The same three characteristic photoelectric yield spectra are also found in single crystal studies. The categories correspond to differences in bulk doping and illustrate the importance of band bending at the surface to electron emission from diamond.

1. Photoelectric Emission

An indirect bandgap semiconductor, such as diamond, is characterized by very weak absorption near threshold, so that the penetration depth of bandgap radiation exceeds tens of microns. In such a case, photoelectric emission is a bulk effect and can be understood in terms of a three step model (as developed by Spicer [1]) consisting of: (a) bulk excitation, absorption of light generates photoexcited carriers, (b) transport of the carriers to the surface region, and (c) escape of electrons from the surface into the vacuum. Since the photoabsorption mechanism (i.e., carrier photo-excitation) in diamond is well understood, one can use the three step model to study both the transport and escape steps of the emission process. The escape step is strongly affected by the electron affinity, χ, which is the energy barrier for conduction band minimum electrons to be emitted into vacuum. The existence of negative electron affinity ($\chi < 0$) makes possible electron escape for carriers at energies as low as the conduction band minimum. There is both experimental [2-7] and theoretical [3, 8] evidence for the existence of true negative electron affinity at specially prepared diamond surfaces (i.e., the vacuum level lies below the conduction band minima). This characteristic offers to make NEA diamond films efficient electron emitters. For example, extremely large secondary electron yields have been achieved from NEA diamond materials [9, 10]. Diamond thin films grown by usual CVD methods are known to be hydrogenated [11]. Since hydrogenated (111) and (100) diamond surfaces [2, 3] exhibit negative electron affinity (NEA), as-grown diamond thin films should also exhibit NEA. With this in mind, CVD diamond materials were studied after air transfer from the growth reactor to the analysis chamber without further preparation.
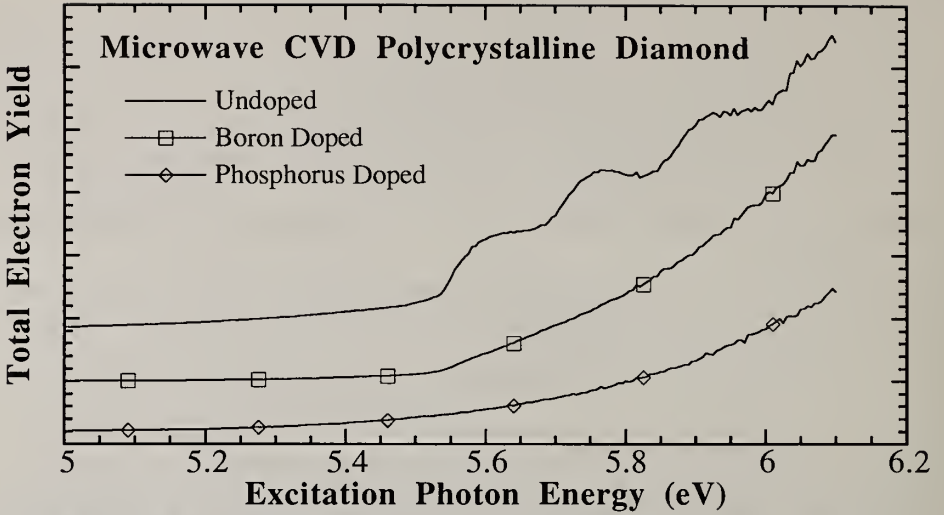
Figure 1: Photoelectric yield from microwave CVD polycrystalline diamond.

2. Experimental Techniques

The experiments were performed in an ultra high vacuum system with the samples at room temperature. A Hg-Xe arc-lamp was employed as a source for near band-gap radiation. The photon energy was selected with the use of a 1 m normal incidence monochromator and refocused at the sample position into a 1 mm x 2 mm rectangular spot at an energy resolution of 50 meV or less. The excitation spectra are normalized with respect to the photo-yield of sodium salicylate [12]. The diamond films were deposited on silicon using microwave plasma enhanced CVD. Undoped, boron-doped and phosphorous-doped diamond films were investigated.

3. Results

In Fig. 1 we show photoelectric yield measurements of the three high quality microwave CVD diamond films as a function of the excitation photon energy (normalized to the incident light intensity). In Fig. 2 we show the photoelectric yield from single crystal diamond under the conditions of nearly flat bands, downwards band bending, and (we suspect) upwards band bending. There is a strong correspondence between the form of the photoelectric yield from the three CVD polycrystalline diamond films and the three single crystal measurements. Single crystal studies [6, 13], based upon the three-step model, have understood the photoelectric yield characteristics of single crystal type IIb diamond (Fig. 2) in terms of the observed changes in band bending (built-in electric fields) at the surface. Furthermore, empirical examination has found [14] that the photoelectric yield from hydrogenated type Ib diamond material (Fig. 2) varies as the excess energy above threshold to the fourth power (threshold energy =4.3 eV).

Near the surface, the band alignment of a semiconductor to the Fermi level is usually determined by the density of surface (and near-surface) states rather than bulk doping. Hydrogenated diamond surfaces are characterized by valence band maximum (VBM) to
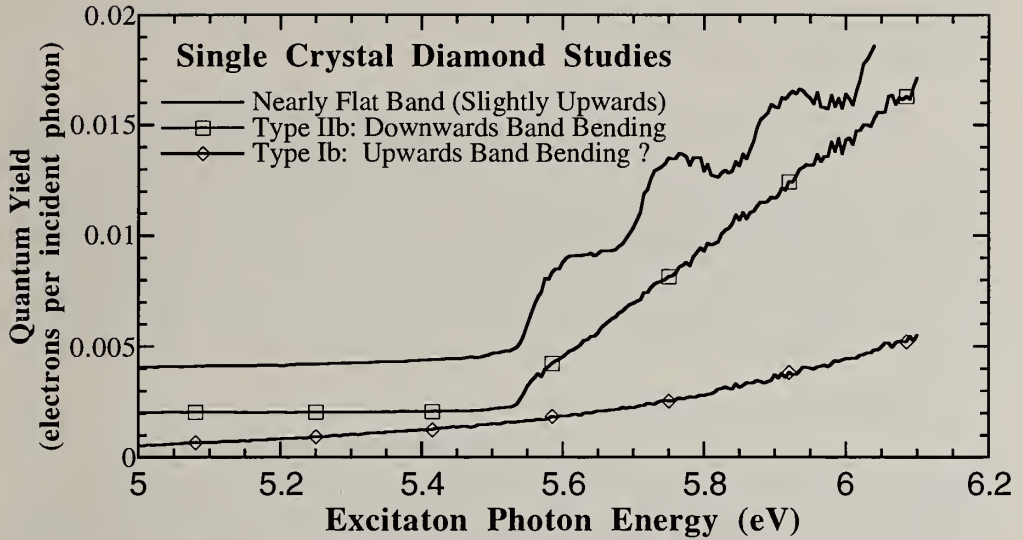
Figure 2: Photoelectric yield from single crystal diamond.

Fermi level energy separations of from 0.5 to 1.0 eV [2, 3, 5-7, 15, 16]. Doping determines the Fermi level alignment in the bulk. Therefore, band bending at the surface can depend upon both bulk doping and surface treatment. With identical surface treatments (all surfaces as grown via microwave CVD) the bulk Fermi level position will determine band bending. If the valence band maximum (VBM) lies closer to the Fermi level in the bulk (p-type doping) than at the surface, then there is downwards band bending. If the conduction band minimum (CBM) in the bulk lies closer to the Fermi level than it does at the surface, then there is upwards band bending.

Two of the films shown in Fig. 1 (undoped and boron doped) exhibit a sharp threshold at 5.53 eV which is similar to that observed (Fig. 2) from natural single crystal NEA diamond. The third CVD diamond film (phosphorus doped) bears strong similarity to the emission measured from hydrogenated type Ib, high pressure high temperature (HPHT) grown diamond (Sumitomo Sumicrystal™). Sumicrystal™ diamond contains substitutional nitrogen at concentrations of 10^{18} to 10^{19} cm^{-3}.

Truly intrinsic (undoped) material is characterized by a mid-gap Fermi level (in the bulk) and by extremely long characteristic band bending lengths. This would lead to nearly flat bands near the surface, with slight upward band bending. In fact, the observation of the oscillations in "as-polished" (111) single crystal diamond is associated with nearly flat bands (slight upwards band bending) at the surface [6]. In that case, the photoelectric emission is dominated by exciton transport and emission, since the small electric fields in the nearly flat upwards band bending region act to turn electrons away from the surface [5].

Significant boron doping in diamond drops the bulk Fermi 0.4 eV or less above the valence band maximum. This leads to downwards band bending at the surface. In this

case, photoelectric emission results from both bulk photoexcitation of excitons and electrons. The form of the emission reflects [6] the presence of emission from conduction band electrons.

Substitutional phosphorus or nitrogen, should lead to n-type bulk material (although the levels are deep). Diamond material with an n-type bulk will produce upwards band bending. One would expect that strong upwards band bending to the surface would lead to drastically reduced photoelectric emission, even with a true NEA surface. We have found that the yield of the polycrystalline diamond film varies as the excess energy above threshold to the fourth power (threshold energy = 4.8 eV). As mentioned above, this is the same dependence on photon energy (except for a different threshold value) as found for Sumitomo HPHT diamond. The fundamental mechanism responsible for this form of the photoelectric yield has not been determined.

4. Conclusions

The photoelectric emission characteristics of high quality CVD polycrystalline diamond films are very similar to emission from single crystal diamond. The photon energy dependence of the photoelectric yield from diamond materials, characterized by nearly flat bands or by downwards band bending at the surface, are well understood within the context of the three step model. The functional form of the photoelectric yield of both HPHT substitutionally nitrogen doped, and CVD phosphorus doped diamond are similar (excess energy to the fourth power dependence). This empirical similarity may be due to common upwards band bending to the surface for both materials. However the mechanism for emission is unresolved.

5. Acknowledgments

6. References

1. W. E. Spicer, Phys. Rev. **112** (1), 114 (1958).
2. F. J. Himpsel, *et al.*, Phys. Rev. B **20** (2), 624 (1979).
3. J. van der Weide, *et al.*, Phys. Rev. B **50** (8), 5803 (1994).
4. J. van der Weide and R. J. Nemanich, JVST B **10** (4), 1940 (1992).
5. C. Bandis and B. B. Pate, Phys. Rev. Lett. **74** (5), 777 (1995).
6. C. Bandis and B. B. Pate, Phys. Rev. B, submitted (1995).
7. C. Bandis and B. B. Pate, Surf. Sci., submitted (1995).
8. W. E. Pickett, Phys. Rev. Lett. **73** (12), 1664 (1994).
9. G. T. Mearini, *et al.*, Appl. Phys. Lett. **66** (2), 242 (1994).
10. D. P. Malta, *et al.*, Appl. Phys. Lett. **64** (15), 1929 (1994).
11. B. D. Thoms, *et al.*, Appl. Phys. Lett. **65** (23), 2957 (1994).
12. J. Samson, *Techniques of Vacuum UV Spectroscopy* (Wiley, New York, 1967).
13. C. Bandis, *et al.*, Mat. Res. Soc. Symp. Proc. **339**, 75 (1994).
14. C. Bandis and B. B. Pate, in preparation.
15. B. B. Pate, Surf. Sci. **165**, 83 (1986).
16. J. van der Weide and R. J. Nemanich, Appl. Phys. Lett. **62** (16), 1878 (1993).

Applications of Diamond Films and Related Materials: Third International Conference, 1995
Editors: A. Feldman, Y. Tzeng, W. A. Yarbrough, M. Yoshikawa, and M. Murakawa

29

SAW FILTERS BASED ON DIAMOND

Shinichi Shikata, Hideaki Nakahata, Kenjiro Higaki, Satoshi Fujii, Akihiro Hachigo, Hiroyuki Kitabayashi, Yuichiro Seki, KeiichiroTanabe and Naoji Fujimori

Itami Research Laboratories, Sumitomo Electric Industries Ltd.,

1-1-1 Koya-kita Itami 664 JAPAN

Abstract

The surface acoustic wave (SAW) devices using a ZnO/diamond structure was summarized in this paper including late result on high frequency filter of 3.5GHz by 0.75 μ m inter-digital transducers on diamond. This technology is applied to 1.5GHz narrow bandwidth filter by resonator type filter. Theoretical studies with new material systems were also performed. Zero temperature coeeficient filter can be expected by additional amorphous SiO_2 deposition. By $LiNbO_3$ / diamond structure, high electro-mechanical coefficient can be expected with high SAW velocity. The varieties of material systems on SAW and advanced devices based on diamond will find broad applications on high frequency devices in future communication systems.

1. Introduction

(1) Communication systems of high frequency

The increasing demands for large data volume transmissions and mobile communications have spurred the numerous plans for communication systems with world wide standardization. Recently, the radio spectra are recognized as limited and valuable natural resouces, and reallocation of spectra are under way. It was a historical epoch that the radio spectra are sold at auction by the United States Goverment in 1994. Table 1 shows the frequencies of major communication systems in world. For the mobile communication systems, high frequency of 0.9 to 1.9GHz are being used for 2nd generation digital systems. For 3rd generation systems, Future Public Land Mobile Telecommunication Systems (FPLMTS or IMT2000) is currently under delibetion. This system combine the many systems of mobile communications in over 2GHz frequency, and the system will allow international roaming. Looking for satellite communication, the global positioning system (GPS) created by U.S.Department of Defence using 1.5GHz is now provided for civilian users. Recently the navigation services are

available not only for marine and airborne, but also for terrestrial systems. In near future, new satellite communication services utilizing low earth orbit (LEO) are planned. As shown in Table 1, 1.6GHz and 2.5GHz will be used for its frequencies. For mobile communications, the high frequency surface acoustic wave (SAW) filters are used as bandpass filter of radio frequency (rf). The local communication systems such as wireless LANs and vehicular information communication systems will also be carried out in ISM band of 2.5GHz and 5.8GHz. For optical fiber communication systems, the Synchronous Digital Hierachy (SDH), well known as Synchronous Optical Network (SONET) in United States, had been adopted for high bit rate communication networks. In this system based on 155.52Mbps and its higher hierachy of 622.08Mbps and 2.48832Gbps, the SAW filters are used in retiming clock generation. 5Gbps and 10Gbps are also used for public communication infrastructure. In near future, Broardband Integrated Services Digital Network (B-ISDN) will be in service, looking for Fiber To The Home (FTTH) age. In this service, various communication bands are integrated by asynchronous transfer mode (ATM) technology.

SAW devices also have varieties of applications including conventional applications of filters, resonators, and delay lines. The convolvers for spread spectrum (SS) comunication, the identification (ID) tag for local wireless ID systems, and SAW based QPSK systems are the examples of advanced application of SAW devices.

(2) Materials for surface acoustic wave devices

For conventional SAW devices, piezoelectric bulk crystals with low phase velocity from 2,500 to 4,500m/s, such as quartz, $LiNbO_3$ and $LiTaO_3$ are used. The frequency of the device is determined by next simple equation.

$$F = V / \lambda \tag{1}$$

Here, the F,V and λ denote frequency, SAW velocity and wavelength, respectively. The wavelength is determined by the size of line and spaces of inter-digital transducers (IDT). Thus, the fine pattern lithography or the high velocity material are alternative to obtain high frequency devices. Recently, the advanced technologies of lithography are available both with stepper and processes. 0.45μ m IDT are obtained [1] by i-line stepper combined with phase shift process, and applied to retimimg filter of 2.488GHz. Reduction of the IDT size is suffered from the problems associated with reliability, power, and fabrication margin in manufacturing process. Thus, the high velocity materials are required.

For high velocity materials, new piezo-electric bulk crystal of lithium tetra borate $(Li_2B_4O_7)$ [2] has been developed and its velocity is 6,780m/s. The layered structures of piezo-electric materials on high velocity substrates are also effective for SAW devices. Recently, ZnO/Sapphire [3] and AlN/Sapphire [4] SAW devices have been developed and obtaied high velocities of 5,300m/s and 6,700m/s, respectively. Amongst all the materials, diamond is well known as super hard material and the surface acoustic velocity is very high. With piezo-electric material deposited on a diamond substrate, over 10,000 m/s can be available. For these four years, we have been studying SAW characteristics of ZnO / diamond layered structure[5)-12)] and found that this material

system is practical for high frequency SAW filters. In this paper, the results on ZnO/diamond are summarized and also the new material systems with diamond are theoretically proposed.

2. SAW filters by ZnO / diamond structure

First, the studies on SAW filters by ZnO/diamond layered structure on silicon are summarized in this section with late result.

The polycrystalline diamond preparation and SAW fabrication process flow was reported elsewhere[6] [7] [8] for the ZnO / Al / diamond / Si structure SAW, but briefly reviewed here. The silicon wafers were used as substrates. Approximately 20 μ m thick poly-crystalline diamond films were deposited by hot filament CVD with deposition conditions of CH4 / H2 = 1 ~ 2%, 80Torr pressure and using 2150℃ tungsten filaments. For the SAW fabrication process, 40nm thick pure Al was evaporated, and fine-line inter-digital transducer (IDT) was fabricated by conventional photo-lithography and etching processes. This was followed by the deposition of a ZnO thin film which was carried out by conventional radio frequency (RF) magnetron sputtering with conditions of Ar : O2 = 6 : 4 , 0.02Torr , 200℃ and 150W of RF power. After the deposition, ZnO formed on IDT pad area was removed by processes of lithography and etching. Finally, the ZnO / diamond /Si structure SAW device was fabricated.

The locus of the development of ZnO/diamond structure SAW filters are shown in Fig.1. These are the results of filters with the input and output IDTs consist of 40 pairs of single electrode of transversal type and unapodized. The thickness of ZnO was taken to be kh1=0.7 (k=2 π / λ and h1 is thickness of ZnO). The phase velocity and electro-mechanical coupling coeeficient are 8,940m/s and 1.87%, respstively. As can be seen from the figure, up to 3.5GHz high frequency filters are available with 0.75 μ m lithography on diamond. By using conventional materials, 3.5GHz is obtained by quarter micron lithography. The insertion loss of these filters at the center frequency are also given in this figure including bi-directional loss of 6dB. The loss analysis for 1.5GHz filter was studied and given elsewhere [8], and largest part of loss is propagation loss. This quite high value of the propagation loss is the combined effect of the losses by ZnO and diamond. This loss may be reduced by refinement of ZnO deposition process. It is of interest that (0001) ZnO can epitaxially grown on diamond (111) plane even with high lattice mis-match of 28.8% by epitaxial relationship of [11-20] ZnO // [-101] diamond[12]. The standard deviation of X-ray rocking curve of ZnO on (111) diamond was about 1/5 of the ZnO deposited on poly-crystalline diamond. This might be one of the technique to reduce propagation loss. In Fig.2, frequency dependence of IDT size is shown for ZnO/diamond, sapphire based SAWs, and conventional materials. As can be seen from the figure, diamond SAW have large advantage over 2GHz devices.

Above mentioned filters are fabricated for study and demonstration by IDTs without design technology. Looking for application, the narrow bandwidth filter is designed and fabricated. The composite longitudinal mode resonator (CLMR) type filter which

have reflectors outside IDT is successfully fabricated[13] with 1.5 μ m IDTs. The result is shown in Fig.3 and 8.7dB insertion loss is obtained for 1.45GHz. The 3dB down bandwidth was 0.4%.

3. Theoretical studies on new material systems

(1) Temperature stable SAW filters by SiO2 / ZnO / diamond structure

The temperature coeeficient is one of the important characteristics of SAW devices, especially for narrow bandwidth devices. The temperature coeeficient of frequency (TCF) of the ZnO/diamond structure SAW filter have practical level of about -28ppm/℃ , which is as same as LiTaO3 and much smaller than LiNbO3. In order to meet requirements on wide range of filter applications such as optical communication, lower TCF is required.

Amorphous SiO2 is well known as positive temperature coeeficient material and combined with negative materials to layered structure, zero TCF can be expected. It has already been reported that this is posible for LiTaO3 [14]. This technique is applied to ZnO/diamond strucure by theoretical calculations by Campbell's method[15] and Finite Element Method [16]. As can be seen in Fig.4, temperature coeeficient can be reduced to zero at kh2 = 0.37 and 0.72 for 0th and 1st mode Rayleigh wave, respectively. Here, h2 is the thickness of SiO2. The SAW velocities and electro-mechanical coupling coeeficients are also varied with SiO2, but practical values are expected to be obtained.

(2) SAW filters by LiNbO3 / diamond and LiTaO3 / diamond structures

In our studies of diamond SAW, only ZnO has been considered as piezo-electric thin film, because of its high orientation to c-axis regardless of the substrates. It is needless to say that various kinds of piezo-electric thin films deposited on diamond have large advantage on high SAW velocity and wide range of SAW material systems based on diamond can be considered. The typical piezo-electric materials of LiTaO3 and LiNbO3 are considered[17]. Both crystals are classified into 3m group in Hermann-Mauguin's space group. But, considering the thin film growth on diamond, c-axis oriented films are expected because of the difficulties in single crystal growth on hetero substrates. With this assumption, the elastic contant c14 and pezo-electric constant e22 can be set zero, which make calculations carried out by 6mm group. The result on LiNbO3 / diamond structure is shown in Fig.5. As can be seen from the figure, LiNbO3 / diamond structure have potential of high electro-mechanical coefficient of 9% with high SAW velocity of 11,890m/s. LiNbO3 (001) is pseudo-lattice matched to diamond (111) by 102%, thus LiNbO3 is expected to grow on diamond epitaxially. The calculated results are summarized by representative parameters in Table.2 with conventional materials as reference. Diamond based SAW devices are expected to have high potential for various types of applications with varieties of material systems.

4. Conclusion

Utilizing diamond's high SAW velocity, a SAW device using a ZnO / diamond structure was studied. Up to 3.5GHz bandpass filter was successfully demonstrated using 0.75 μ m L&S IDTs on diamond. The narrow bandwidth filter was designed and fabricated by the composite longitudinal mode resonator (CLMR) type filter, and 8.7dB insertion loss was obtained for 1.45GHz. Theoretical studies with new material systems were performed. Zero temperature coeeficient filter can be expected by additional amorphous SiO_2 deposition. New structure with piezo-electric materials of $LiNbO_3$ and $LiTaO_3$ on diamond structures were also investigated. Especially by $LiNbO_3$ / diamond structure, high electro-mechanical coefficient can be expected with high SAW velocity.

The varieties of material systems for SAW filter and advanced devices based on diamond will find broad applications on high frequency devices in future communication systems.

5. Acknowledgement

6. References

1) K.Asai, A.Isobe, T.Tada, and M.Hikita, Proc. IEICE General Conf.Japan, A-378 (1995)
2) T.Sato and H.Abe, IEEE Ultrasonics Conf. Proc. , (1994)
3) J.Koike,K.Shimoe, and H.Ieki, Jap.J.Appl.Phys.,32,2337 (1993)
4) T.Kobayashi et al.,Proc. 15th Symp. Ultrasonic and Electronics,Japan, 187 (1994)
5) H.Nakahata et al., 52nd Meeting of the Jap. Soc. of Applied Physics Ext. Abstr., 12-a-Q-8 (1991)
6) S.Shikata,H.Nakahata,A.Hachigo and N.Fujimori, Diamond and Related Materials, 2, 1197 (1993)
7) H.Nakahata, A.Hachigo, S.Shikata and N.Fujimori, IEEE Ultrasonics Conf. Proc. , 377 (1992)
8) S.Shikata,H.Nakahata,K.Higaki, A.Hachigo,N.Fujimori,Y.Yamamoto,N.Sakairi, and Y.Takahashi, IEEE Ultrasonics Conf. Proceeding , 277 (1993)
9) H.Nakahata, A.Hachigo, S.Shikata, N.Fujimori, Y.Takahashi, T.Kajiwara and Y.Yamamoto Jpn.J.Appl.Phys.,33, 324 (1994)
10) K.Higaki, H.Nakahta, S.Fujii, A.Hachigo,S.Shikata and N.Fujimori, IEICE Meeting,1-435 (1994)
11) S.Shikata, H.Nakahata, K.Higaki, S.Fujii, A.Hachigo, and N.Fujimori, Int'l Conf.New Diamond Science and Technology, Proc.697,Kobe (1994)
12) A.Hachigo,H.Nakahata,K.Higaki, S.Fujii, and S.Shikata, Appl/Phys.Lett.,65,2556 (1994)
13) Y.Takahashi, N.Sakairi, Y.Yamamoto, H.Nakahata, K.Higaki, S.Fujii, A.Hachigo, S.Shikata and N.Fujimori, Proc. IEICE Fall Conf.,Japan, A-227 (1994)
14) R.Inaba and K.Wasa, Jpn.J.Appl.Phys.,20, Suppl.20-3,153(1981)
15) H.Nakahata, K.Higaki, S.Fujii, A.Hachigo, S.Shikata and N.Fujimori, Proc. IEICE Fall Conf.,Japan, A-228 (1994)
16) K.Ohbuchi and M.Koshiba, Proc. IEICE General Conf.,Japan, A-374 (1995)
17) H.Nakahata, K.Higaki, S.Fujii, A.Hachigo, S.Shikata and N.Fujimori, IEEE Trans. Ultrasonics,Ferroelec., and Freq. Contr., to be published in May Edition (1995)

Table 1. Frequencies of major communication systems

		Frequency (GHz) 1 2 3 4 5 6 7 8 9 10
Optical		
Mobile	2nd	
	FPLMTS	
	LEO Satellite	
GSO Satellite		
ISM	Wireless LAN VICS etc	
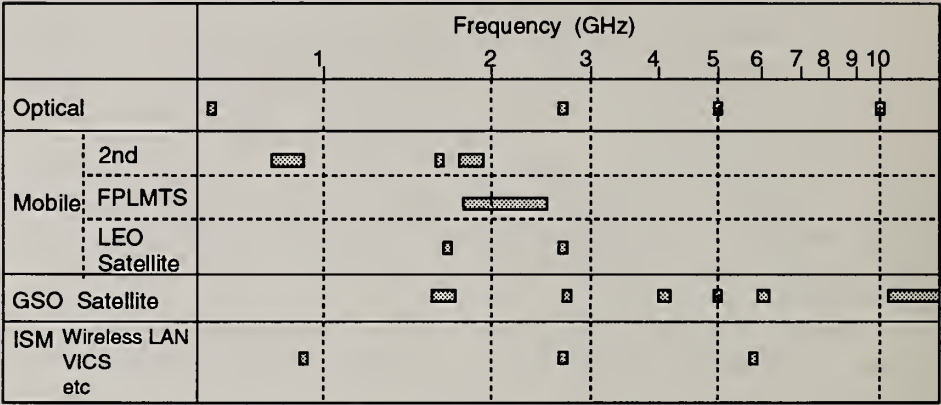
Table 2. The characteristics of diamond based SAW materials

		velocity (m/s)	electro-machanical coupling coefficient (%)	TCD (ppm/C)	relative dielectric constant
quartz	ST cut	3158	0.16	0	4.4
LiNbO3	128 Y cut X prop.	3980	5.5	75	44.3
	64Y cut X prop.	4742	11.3	70	
LiTaO3	X cut 112Y prop.	3290	0.75	18	42.6
	36Y cut X prop.	4160	5.0	32	
ZnO/glass		2600	1.9	25	ZnO 8.55 glass 3.75
ZnO/diamond/Si		10520	3.1	22	ZnO 8.55 diamond 5.7
		7180	5.0	30	
SiO2/ZnO /diamond/Si		10710	1.5	0	SiO2 3.75 ZnO 8.55 diamond 5.7
		8050	3.9	0	
LiNbO3/diamond/Si		11890	9.0	——	LiNbO3 44.3 diamond 5.7
LiTaO3/diamond/Si		10610	3.6	——	LiTaO3 42.6 diamond 5.7
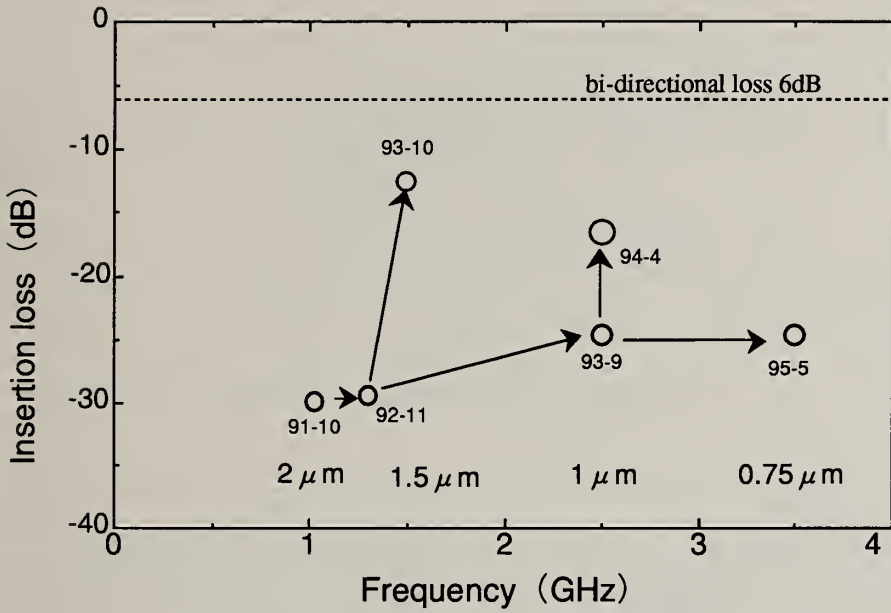
Fig.1   Locus of the developement of ZnO/Diamond SAW
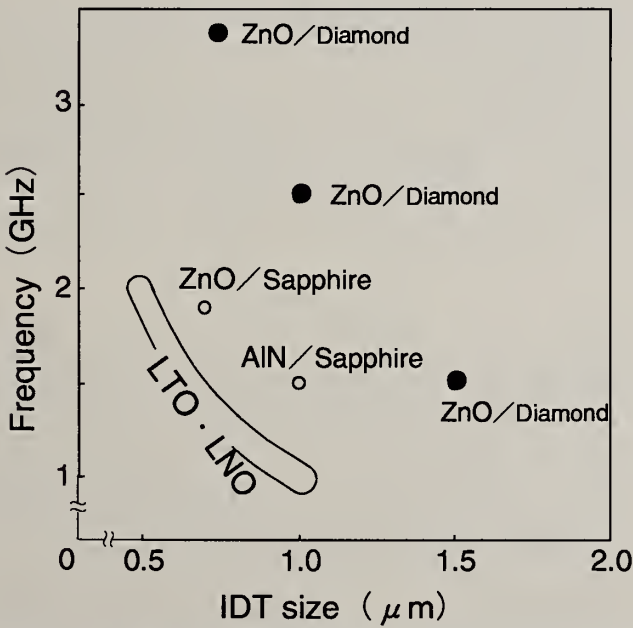
Fig.2   Frequency to IDT size relation of ZnO/Diamond SAW
with respect to the other materials
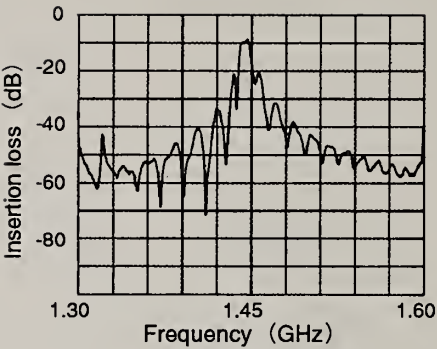
Fig.3 Characteristic of resonator type filter
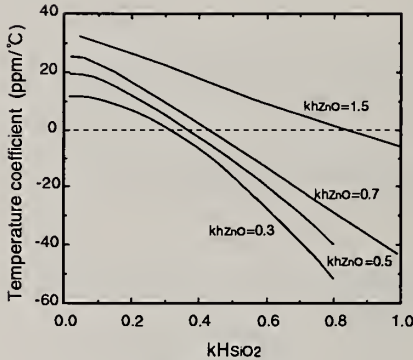
(a) 0th mode
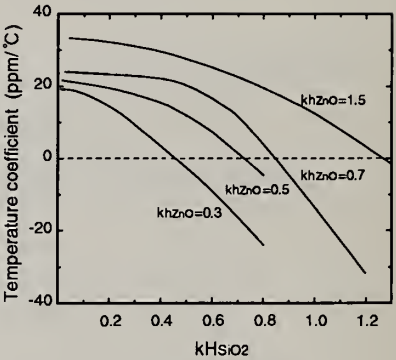
(b) 1st mode

Fig.4 Temperature coefficient of SiO2/ZnO/Diamond SAW
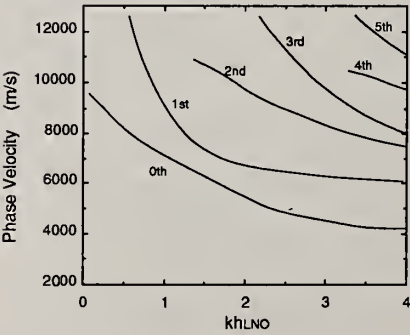
(a) Velocity
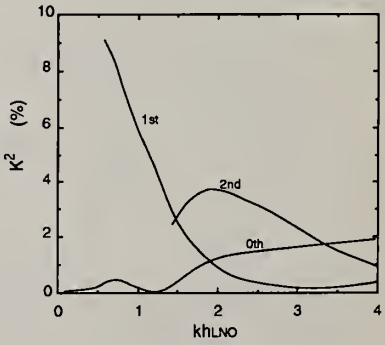
(b) Coupling coeeficient

Fig.5 Velocity and coupling coeeficient of
LiNbO3/Diamond SAW

PATTERNED POLYCRYSTALLINE DIAMOND MICROTIP VACUUM DIODE ARRAYS

W.P. Kang[1], J.L. Davidson[1], Q. Li[2], J.F Xu[2], D.L. Kinser[1], and D.V. Kerns[1]

[1]Applied and Engineering Sciences, Vanderbilt Univ., Nashville, TN 37235, U.S.A
[2]Electronic Engineering, East China Normal Univ., Shanghai, P.R. China

Key words: diamond, patterning, pyramidal arrays, vacuum diodes

Abstract

Electron field emission from an array of patterned pyramids of polycrystalline diamond for vacuum diode applications has been investigated. High current emission from the patterned diamond microtip arrays are obtained at low electric fields. A current density from the diamond microtips of $14mA/cm^2$ was observed for a field of <10 V/µm. Field emission for these diamond microtips exhibits significant enhancement both in total emission current and stability compared to pure silicon emitters. Moreover, field emission from patterned polycrystalline diamond pyramidal tip arrays is unique in that the applied field is found to be lower (2-3 order of magnitude lower) compared to that required for emission from Si, Ge, GaAs, and metal surfaces. The fabrication process utilizing silicon shaping and micromachining techniques for the fabrication of diamond diaphragms with diamond microtip arrays for vacuum microelectronic applications has been developed. The processing techniques are compatible with IC fabrication technology. The effect of temperature annealing on the current emission characteristics were also investigated.

Introduction

The advance in integrated circuit (I.C.) fabrication and silicon micromachining technology has given vacuum devices a rebirth in microelectronic form. Carrier transport in "vacuum state" microelectronic devices is not limited by velocity saturation due to scattering effects in semiconductor as in their conventional "solid state" microelectronic counterparts. Thus, vacuum microelectronic devices are capable of operating at a higher speed than presently available solid state devices. Central to the field of vacuum microelectronic is the search for a high efficiency electron emission cathode. In the past few years, many different materials, structures, and techniques have been investigated for fabrication of vacuum cold cathode devices[1-5]. The most desirable properties for an electron emission cathode are low operating gate voltage, high emission current density and uniformity, and emission stability.

The material properties of diamond, such as the low electron affinity, wide band-gap, high chemical stability, hardness and superb thermal conductivity, are unique for vacuum microelectronics applications. This paper describes a novel field emission device using sharp tips of well patterned pyramids of polycrystalline diamond for the development of vacuum field emitter diode arrays. The use of local field enhancement at sharp points constructed by micromachining techniques in diamond material as reported here is a new development in this area. We present the detailed fabrication process of a polycrystalline diamond patterned pyramidal emitter array and the electron emission characteristics of the array in diode configuration.

Experimental Method

P-type <100> silicon wafers with a resistivity of 2 to 3 ohm-cm were used as the substrate for PECVD diamond deposition. The fabrication process is started by growing a 1-1.5µm oxide layer on silicon substrate using steam thermal oxidation. Normal photolithography was then used to define the mask array. Elements of the array are defined by oxide window with square patterns. To form the inverted pyramidal structures, silicon wafers were wet etched with a etch-stopped process using potassium hydroxide : normal propanol : deionized water solution. Polycrystalline diamond film, 5-10 micron thick, were deposited on the surface of a silicon wafer with the inverted pyramidal "mold" by microwave plasma chemical vapor deposition using a mixture of 99% hydrogen and 1% methane gas, and a substrate temperature of 850°C. P-type boron doped polycrystalline diamond film was fabricated via an *in situ* boron solid source doping method. Selective etching of the silicon backside was performed to expose the patterned diamond microtip and free standing diamond diaphragm. The quality of the diamond microtips were characterized using Raman spectroscopy. The microstructure of the freestanding diamond diaphragm with patterned microtips was examined by SEM. The electrical properties of the microtip arrays were characterized for electron emission. The current emission characteristics of the emitter array in diode configuration were measured in a vacuum environment ($1x10^{-6}$ torr), in both forward and reverse bias.

Result and Discussion

Fig. 1 shows an array of 7x7 patterned polycrystalline diamond pyramidal microtips on a polycrystalline diamond membrane. Fig. 2 shows a single pyramidal microtip of base 2µm x 2µm and tip radius of about 200Å. As evident by these SEM micrographs the capability of patterning polycrystalline diamond microtips on diamond film is demonstrated. Selective deposition and molding of undoped or doped polycrystalline diamond film in silicon mold and subsequent creation of free standing polycrystalline diamond diaphragm with diamond pyramidal microtip has been achieved. The processing technique is compatible with IC technologies.

The relative change in emission current of the microtip array versus applied field (Fig.3) shows a diode characteristic. The data indicate that a high current (0.1mA) in forward

bias can be obtained under a low electric field of less than 10V/µm at pressure of 10^{-6} torr. No emission current was observed in reverse bias regime. Field emission for these diamond microtips, in forward bias, exhibits significant enhancement both in total emission current and stability compared to pure silicon emitters. Moreover, field emission from patterned polycrystalline diamond pyramidal tip arrays is unique in that the applied field is found to be lower (2-3 order of magnitude lower) compared to that required for emission from Si, Ge, GaAs, and metal surfaces.

Device operation in the field emission process is controlled by the Fowler-Nordheim tunneling process[6]. The conduction current density is given by:

$$J = K_1 (E^2 / \Phi) \exp [- (K_2 \Phi^{3/2}) / E]$$

where $E = (\beta V)/d$, K_1 and K_2 are constants, Φ is the work function of the emitting surface, V is the anode-cathode voltage, and β is the field enhancement factor controlled by the cathode radius of curvature at the point of emission, and d is the spacing between the cathode tip and the anode.

Fowler-Nordheim field emission behavior of the diamond-based pyramids was analyzed and shown in Fig. 4. The results indicate a good field emission behavior.

Conclusion

Well controlled structure of polycrystalline diamond-based pyramidal arrays on diamond membrane have been fabricated for vacuum microelectronic applications. High electron emissions under low electric field have been obtained. This electron emission behavior suggests many practical applications of such diamond-based vacuum micro diodes. The processing techniques developed are compatible with IC fabrication technology. It involves selective deposition and molding of undoped or doped polycrystalline diamond films in a silicon mold and subsequent creation of free standing polycrystalline diamond diaphragms with diamond pyramidal tip. The effect of doping, hydrogen plasma tip sharpening and high temperature annealing on the current emission characteristics are currently under investigation.

References

1. H. F. Gray, Proc. 29th Intl. Field Emission Symp., p. 111, 1982.
2. I. Brodie, IEEE Trans. on Electron Devices, **36**, p. 2641, 1989.
3. C. A. Spindt, C. E. Holland, A. Rosengreen and I. Brodie, IEEE Trans. on Electron Devices, **38**, p. 2355, 1991.
4. E. A. Adler, Z. Bardai, R. Forman, D. M. Goebel, R. T. Longo and M. Sokolich, IEEE Trans. on Electron Devices, **38**, p. 2304, 1991.
5. M. Yuan, Q. Li, W. P. Kang, S. Tang and J. F. Xu, Journal of Vacuum Science Technology B, 12(2), p. 676-679, 1994.
6. C. A. Spindt, et al., "Research into Micron-size Emission Tubes", IEEE Conf. on Tube Techniques, 1966.

Fig. 1
Array of diamond pyramids on diamond.

Fig. 2
A single pyramidal microtip on diamond.
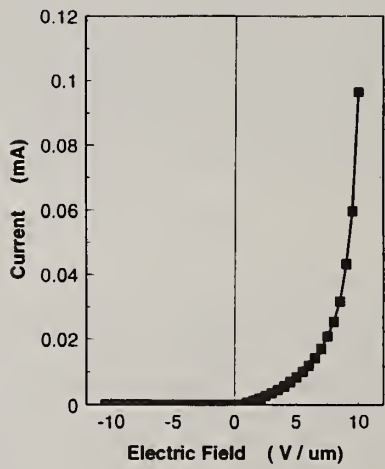
Fig. 3
Emission current vs. applied field
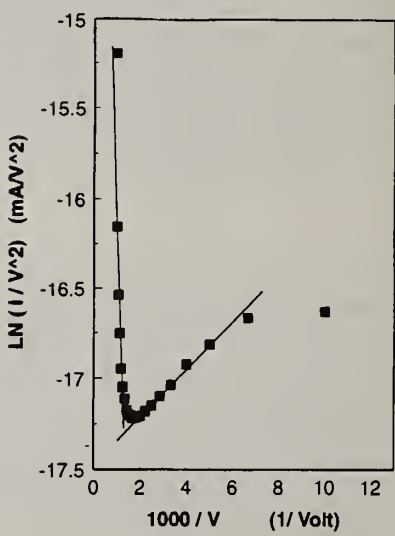
Fig. 4
Fowler-Nordheim field emission plot

Applications of Diamond Films and Related Materials: Third International Conference, 1995
Editors: A. Feldman, Y. Tzeng, W. A. Yarbrough, M. Yoshikawa, and M. Murakawa

41

NEGATIVE ELECTRON AFFINITY EFFECTS AND SCHOTTKY BARRIER HEIGHT MEASUREMENTS OF COBALT ON DIAMOND (100) SURFACES

P.K. Baumann, R.J. Nemanich

Department of Physics, North Carolina State University, Raleigh, North Carolina 27695-8202 USA

Key words: cold cathodes, metal contacts, negative electron affinity, Schottky barrier height.

Abstract

The effects of growing thin cobalt films on natural type IIb diamond (100) substrates were investigated by means of ultraviolet photoemission spectroscopy (UPS). Prior to deposition the diamond samples were annealed to 1150°C in UHV resulting in a positive electron affinity surface. Upon deposition of 2Å of Cobalt a negative electron affinity (NEA) was observed and a Schottky barrier height of 0.35 eV was measured by means of UPS. The presence of a cobalt layer was confirmed employing *in-situ* Auger electron spectroscopy (AES). As evidenced by atomic force microscopy (AFM) uniform Co films were deposited replicating the underlying diamond substrates.

1. Introduction

The electron affinity of a semiconductor is defined as the energy difference between the vacuum level and the conduction band minimum. For most materials the vacuum level lies above the conduction band minimum, corresponding to a positive electron affinity. Surfaces of wide bandgap semiconductors like diamond have the potential of exhibiting a negative electron affinity (NEA) since the conduction band minimum lies near the vacuum level. Electrons present in the conduction band have sufficient energy to overcome the workfunction of a NEA surface and can be emitted into vacuum. Indeed, different surface preparation techniques can shift the position of the vacuum level and therefore induce a NEA or remove it [1-3]. Furthermore it has been demonstrated that metals like Ti, Ni and Cu can induce a NEA on diamond surfaces [4, 5, 1]. Photoemission spectroscopy is found to be a very sensitive method to determine whether a surface exhibits a NEA or not. Secondary electrons appear as a sharp peak at the low energy end of photoemission spectra for NEA surfaces [6, 7].

2. Experimental Details

The UHV system used in this study consists of several interconnected chambers including systems used for annealing, metal deposition, UPS and AES. Natural type IIb single crystal diamond (100) substrates (3.0 x 3.0 x 0.25 mm) were used in this study. First the samples were electrochemically etched to remove non diamond carbon and metal contaminants [8]. This etch included applying a DC bias of 350V

between two Pt electrodes that were placed in deionized (DI) water as an electrolyte. The samples were suspended in water between the two electrodes. Following the electrochemical etch a HF dip was employed to remove SiO_2 from the surface [1]. Then the wafers were mounted on a Mo holder and transferred into the UHV system (base pressure ~ 1 x10^{-10} Torr). As an in vacuo cleaning step the wafers were annealed to 1150°C for 10 minutes. This caused the pressure to rise to ~ 7 x 10^{-9} Torr. Subsequent to annealing thin Co films of 2 Å of were deposited by means of a hot filament. The thickness of the Co layers was determined by means of a quartz crystal oscillator. During deposition the pressure rose to ~ 2 x 10^{-9} Torr. Following the annealing - and the growth steps, UPS and AES were employed to analyze the surface properties. HeI (21.21 eV) radiation was used to facilitate the photoemission of electrons. The 50 mm hemispherical analyzer employed to measure the emitted electrons had an energy resolution of 0.15 eV. A bias of 1V was applied to the sample to overcome the workfunction of the analyzer and thus to detect the low energy electrons emitted from the NEA surface. The position of the sharp NEA peak at the low energy end of photoemission spectra corresponds to the energy position of the conduction band minimum, E_C (Fig. 1). Emission from E_C is positioned at $E_V + E_G$ in the spectrum, where E_V is the energy of the valence band maximum and E_G that of the bandgap. Emission from the valence band maximum appears at $E_V + h\nu$ in the spectrum. The spectral width or the distance between emission from the valence band maximum and the conduction band minimum is therefore $h\nu - E_G$. With the values for He I radiation $h\nu = 21.21$ eV and the bandgap of diamond $E_G = 5.45$ eV a spectral width of ~ 15.7 eV is determined for a NEA surface. However, for the case of a positive electron affinity surface the low energy cutoff will be determined by the position of the vacuum level and the spectral width will be smaller.
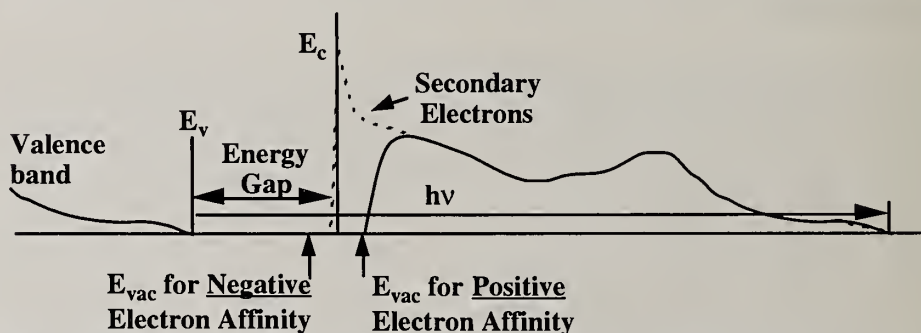
Fig. 1 Schematic diagram of photoemission spectra for a negative electron affinity surface (dotted line) and a positive electron affinity surface (solid line).

3. Results and Discussion

AES spectra of the as loaded samples exhibited features indicative of the presence of oxygen on the surface. Subsequent to the 1150°C anneal no oxygen could be detected on the surface of the diamond substrates by means of AES. As evidenced by UPS the surfaces exhibited a positive electron affinity (Fig. 2). It has been reported previously that heating diamond (100) to 1150°C results in the removal of

oxygen and a surface with a positive electron affinity [3, 9]. Upon deposition of 2Å of Cobalt a negative electron affinity (NEA) was observed and a Schottky barrier height of $\Phi_B \cong 0.35$ eV was measured by means of UPS as shown in Fig. 2. Equation (1) gives an expression for the electron affinity χ of a p-type semiconductor following the formation of a Schottky barrier [10]:

$$\chi = (\Phi_M + \Phi_B) - E_G \qquad (1)$$

With the value for the metal work function of cobalt $\Phi_M = 5.00$ eV, the bandgap of diamond $E_G = 5.45$ eV and the measured Schottky barrier height, an electron affinity of $\chi \cong -0.1$ eV can be calculated. This result is in agreement with the experimental data. Previously this simple work function model has been used to explain metal induced NEA effects for Ti and Ni deposited on diamond (111) [4, 5]. The presence of a cobalt layer was confirmed employing AES. AFM images of the diamond wafers clearly display linear groves with a depth of ~ 20 Å. These kind of features are due to the commonly applied procedure of polishing the samples with diamond grit. As evidenced by AFM Co was deposited as uniform films replicating the groves of the underlying diamond substrates (Fig. 3).

4. Conclusions

Thin cobalt films have been deposited on diamond (100) crystals. A metal induced NEA was observed and a Schottky barrier height of $\Phi_B \cong 0.35$ eV was determined by means of UPS. Furthermore, the cobalt layers were found to be uniform.

5. Acknowledgments

6. References

1   P.K. Baumann, T.P. Humphreys and R.J. Nemanich, in Diamond, SiC and Nitride Wide Bandgap Semiconductors, edited by C.H. Carter, G. Gildenblat, S. Nakamura, R.J. Nemanich, Mater. Res. Soc. Proc. **339**, Pittsburgh, PA, 69 (1994).
2   J. van der Weide and R.J. Nemanich, Appl. Phys. Lett. **62**, 1878 (1993).
3   J. van der Weide, Z. Zhang, P.K. Baumann, M.G. Wensell, J. Bernholc and R.J. Nemanich, Phys. Rev. B **50**, 5803 (1994).
4   J. van der Weide and R.J. Nemanich, J. Vac. Sci. Technol. B **10**, 1940 (1992).
5   J. van der Weide and R.J. Nemanich, Phys. Rev. B, **49**, 13629 (1994).
6   F.J. Himpsel, P. Heimann and D.E. Eastman, Sol. State Commun. **36,** 631 (1980).
7   B.B. Pate, W.E. Spicer, T. Ohta and I. Lindau, J. Vac. Sci. Technol. **17,** 1087 (1980).
8   M. Marchywka, P.E. Pehrsson, S.C. Binari and D. Moses, J. Electrochem. Soc., Vol. **140**, No. 2 (1993) L19.
9   P.K. Baumann and R.J. Nemanich, Proc. of the Fifth European Conference on Diamond, Diamond-like and Related Materials (J. Diamond Rel. Mat., 1995) in press.
10   E.H. Rhoderick and R.H. Williams, Metal-Semiconductor Contacts (Clarendon, Oxford, 1988).
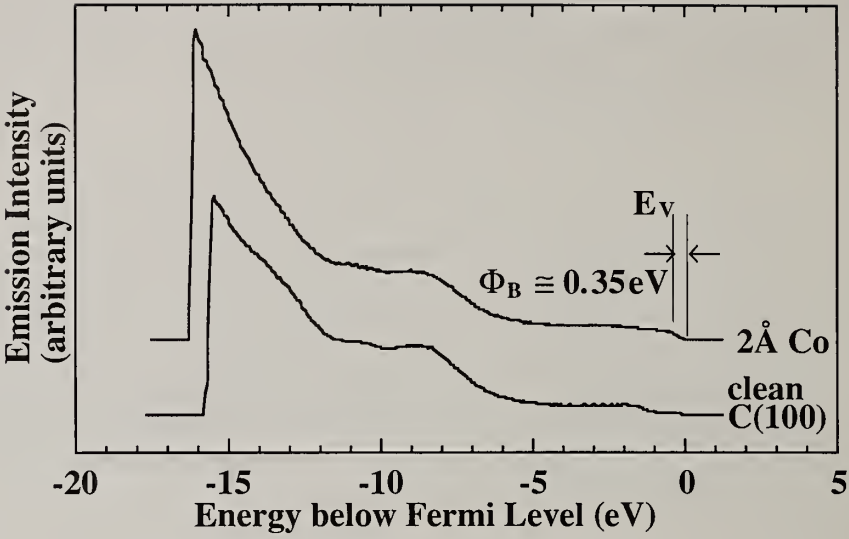
Fig. 2 UV photoemission spectra of diamond (100) following a 1150°C anneal and of Co deposited on diamond.
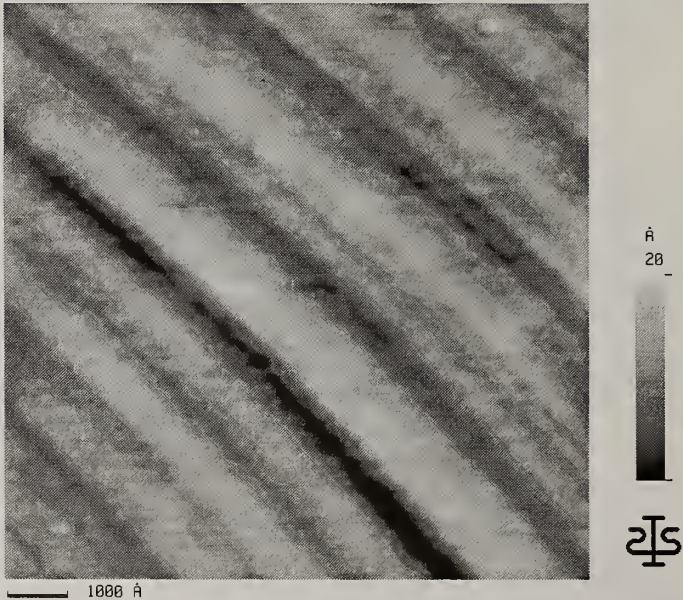
Fig. 3 AFM micrograph of 2Å of cobalt deposited on diamond (100).

Applications of Diamond Films and Related Materials: Third International Conference, 1995
Editors: A. Feldman, Y. Tzeng, W. A. Yarbrough, M. Yoshikawa, and M. Murakawa

45

GROWTH OF DIAMOND PARTICLES ON SHARPENED SILICON TIPS FOR FIELD EMISSION

<u>E.I. Givargizov</u>, L.L. Aksenova, V.G. Galstyan, A.V. Kuznetzov, V.I. Muratova, E.V. Rakova, and A.N. Stepanova

Institute of Crystallography, Russian Academy of Sciences,
Moscow 117333, Russia, FAX (095) 135-1011

Key words: diamond particles, silicon tips, overgrowth, field emission

Abstract

Diamond particles were grown on regular arrays of sharpened silicon tips. Depending on growth conditions, the particles had different shapes and different microstructures: from fine-crystalline to single-crystalline. By varying growth conditions, it was possible to obtain various extent of coating of the tips: from single particles on or close to very ends of the tips up to total overgrowing of the tips down to their roots. Field emission measurements have demonstrated different characteristics for fine- and large-grain coatings.

1. Introduction

Field emission from diamond has recently attracted a great attention for applications due a unique property of the material - namely, negative electron affinity of its (111) surface. This property has been observed in experiments with single crystals of diamond. Recently, another approach to realization of the property was proposed: deposition of diamond particles on high-aspect-ratio silicon tips. In this paper, further research in preparation of diamond-coated silicon tips is presented with an emphasis on their microstructures and characteristics.

2. Experimental Procedure

The experiments were performed under practically the same conditions as those in the paper [1], except for the temperature of the hot filament: its range was extended about 100°C at the high-temperature side.

In addition, a seeding procedure was introduced: before deposition of diamond particles, the silicon-tip arrays were inserted into a suspension of 2-5 nm diamond particles in alcohol for 1-2 min.

Some deposition experiments were made without the seeding procedure. It was found that the number of diamond particles deposited on the seeded silicon tips was far higher than that on non-seeded ones.

The samples obtained were investigated by scanning electron microscopy and an electron diffraction technique. Field-emission measurements were made in a vacuum of 10^{-8} Torr.

3. Results and Discussion

As before [1], it has been observed in these experiments that there was a strong tendency for diamond particles to deposit on the ends of the tips. This was observed for both seeded and non-seeded samples. In sufficiently long processes, all the tips were overgrown from their ends down to their roots.

This is demonstrated in fig. 1. Here, fig. 1a relates to samples obtained in relatively short, about 20 min, processes. Only separate particles are seen on the ends of the tips. In longer processes, the upper parts of the tips are rather densely overgrown by diamond particles (fig. 1b). Finally, in fig. 1c are shown tips overgrown in a long-period, about 1 hour, process. Between the tips, on plane areas on the substrate, some diamond particles are formed, too.

The phenomenon of the preferential deposition of diamond particles on the ends of the tips has been explained by enhanced local heating of the ends due to preferential recombination of atomic hydrogen, characteristic of the hot-filament CVD process used, in combination with a relatively poor thermal conductivity of the high ("long") silicon tips. The reaction of methane decomposition is endothermic, hence, it proceeds preferentially at the relatively hot tip ends having better "geometric collection factor" for atomic hydrogen that arrives from the hot filament. The same, to a lesser extent, is true for edges of the tips [1]. For this reason, there is almost no deposition of diamond at the plane areas of the substrate (see fig. 1c).

Depending on experimental conditions, either fine-crystalline (with grain sizes about 10 nm, see fig. 2a) or large-crystalline (fig. 2b) diamond particles were formed. It has been shown that single-crystalline diamond particles, deposited at the very ends of the silicon tips can be epitaxial to the silicon lattice with (111) diamond // (111) Si [2]. These changes in the microstructure of the diamond particles are mainly due to the increase of the temperature of the hot filament resulting in both an increase of the concentration of the atomic hydrogen and an increase of the stationary temperature of the tips. It is clear that both these factors improve the quality of the diamond formed: (1) the higher the concentration of the atomic hydrogen, the stronger is the etching ability of the agent (*i.e.*, the lower is the supersaturation in the vapor phase and at the growth

interface), and the higher is the quality of the diamond crystallites; (2) the higher the temperature of the tips, the more intensive is the surface diffusion of the adsorbed species at the growing diamond crystals, and the better is their quality.

The diamond nature of the particles has been confirmed by the electron-diffraction pattern taken from the ends of an irregular silicon-tip array having such particles (fig. 3). In the pattern shown in fig. 3b, the dark and bright Kikuchi-lines are a result of the diffraction from the silicon tips, while the Debye rings, indicated by arrows, have indices (111), (220) and (311), that belong to diamond particles.

Field-emission measurements of the diamond-coated tips were performed. The results obtained for the fine-crystalline samples can be explained by either NEA-affected emission or an emission from sharp nano-size points [3]. The emission from large-grain or single-crystalline particles has another character and can be interpreted as an emission of hot electrons [4].

4. References

1. E.I. Givargizov, V.V. Zhirnov, A.V. Kuznetsov, and P.S. Plekhanov, Growth of diamond particles on sharpened silicon tips, Mater. Lett. **18**, 61-63 (1993).
2. A.N. Stepanova, L.L. Aksenova, A.V. Kuznetsov, E.V. Rakova, and E.I. Givargizov, Heteroepitaxial deposition of single-crystal diamond particles on sharpened silicon tips, Mater. Lett. **22**, 285-287 (1995).
3. E.I. Givargizov, V.V. Zhirnov, A.N. Stepanova, E.V. Rakova, A.N. Kiselev, and P.S. Plekhanov, Microstructure and field emission of diamond particles on silicon tips, Appl. Surf. Sci. **87/88**, 24-30 (1995).
4. N.S. Xu, R.V. Latham, and Y. Tseng, Field-induced electron emission from CVD diamond films on planar Mo substrates, Diamond Films Technol. **4**, 249-258 (1994).

Fig. 1a

Fig. 1b

48
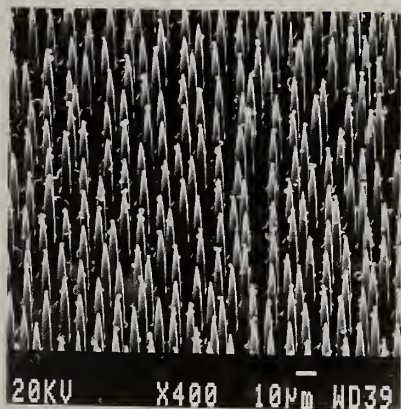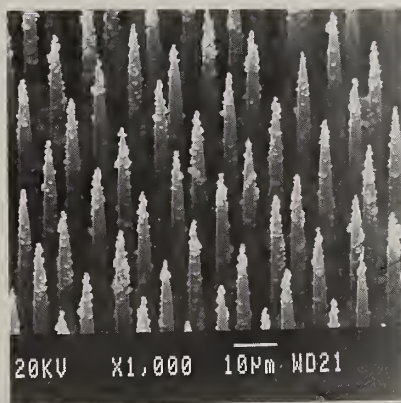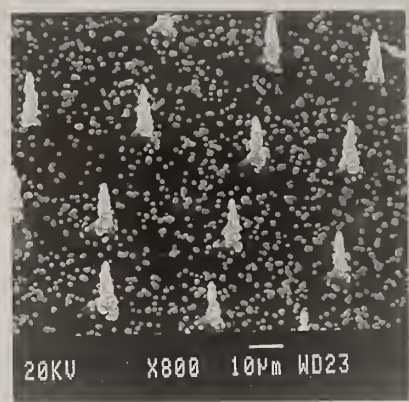
Fig. 1c

Fig. 1. Overgrowing of silicon tips by diamond particles in processes of different durations: a - 20 min; b - 40 min; c - 1 hour.
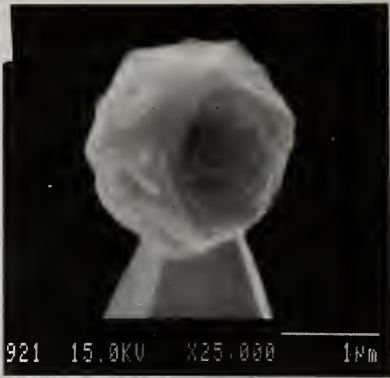
Fig. 2.   Various microstructures of particles on tip ends: a - fine-crystalline; b - large-crystalline particles.
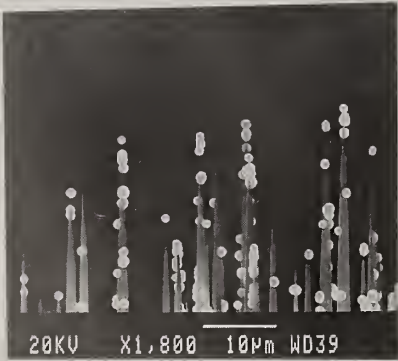
Fig. 3.   Diamond particles on ends of irregular tips (a) and corresponding electron diffraction picture (b).

Applications of Diamond Films and Related Materials: Third International Conference, 1995
Editors: A. Feldman, Y. Tzeng, W. A. Yarbrough, M. Yoshikawa, and M. Murakawa

49

FABRICATION AND CHARACTERIZATION OF DIAMOND FIELD EMITTER DIODE WITH BUILT-IN ANODE

D. Hong and M. Aslam

Department of Electrical Engineering, Michigan State University, East Lansing, MI 48824, U.S.A.

Key words: CVD Diamond, Field Emission

Abstract

Diamond field emitter diodes with built-in anode are designed, fabricated and characterized. Boron-doped p-type polycrystalline diamond film grown by hot filament chemical vapor deposition (HFCVD) is used as an emitter material. A four mask fabrication process is employed using diamond film technology compatible with Si integrated circuit (IC) processing. Photoresist is used as a sacrificial layer to produce a vacuum gap between anode and cathode. Current versus voltage (I-V) data, measured at 10^{-6} Torr, shows Fowler-Nordheim (F-N) field emission behavior. The current density measured at 0.2MV/cm is approximately $0.5A/cm^2$.

1. Introduction

The demonstration of field emission from carbon-doped diamond diode in 1991 by Geis et al. [1] has led to the study of field emission from diamond films prepared under different conditions [2,3]. The negative electron affinity (NEA) and chemical immunity of diamond permit the use of low emission fields and less stringent vacuum environment. In an earlier study, we used a metal probe, not attached to the emitter structure, to demonstrate field emission from p-type polycrystalline diamond films [2]. In this paper, we describe the design, fabrication and characterization of an application-oriented diamond field emitter diode with built-in anode. The structure is fabricated using a four-mask IC-compatible process. The I-V data of the completed structure show a typical F-N field emission behavior.

2. Experimental

The emitter fabrication process is depicted in Fig. 1. A 3-micron thick layer of SiO_2 is deposited at low temperature on a p-type (100) Si wafer. The oxide is annealed in N_2

at 1000 °C for 30 min to improve its insulating properties. Using standard IC photoli-thography, the oxide is patterned and is used as mask for Si etching (Fig. 1a). Photore-sist, mixed with diamond powder with a particle size in the range of 0.1 μm, is spin-coated and patterned. As the diamond is typically deposited at 900 °C, the photoresist evaporates leaving behind the diamond particles which act as seeds for diamond growth by CVD process [4] using HFCVD reactor. As shown in Fig. 1(b), p-type poly-crystalline diamond grows only on Si. Diamond quality is monitored by scanning elec-tron microscopy (SEM) and Raman spectroscopy. Photoresist is spin coated at a very low spin speed to make it thick enough to serve as a sacrificial layer. Sacrificial photo-resist layer is patterned and aluminum (Al) is thermally evaporated on top of the pat-terned photoresist layer. Al is patterned and part of sacrificial photoresist is now exposed to be removed (Fig. 1c). After removing the sacrificial layer, the separation between Al and diamond, computed by taking into account the thicknesses of sacrifi-cial photoresist, oxide, etched Si and diamond film, is in the range of 9~10 μm. Al is also evaporated on the backside of wafer to serve as a cathode electrode (Fig. 1d). Completed samples are annealed at 400 °C in N_2 ambient for 30 min. SEM pictures of one completed field emitter diode are shown in Fig. 2. The current voltage (I-V) data is taken by placing the wafer inside a vacuum chamber with a pressure of 10^{-6} Torr.

3. Results and Discussions

The I-V characteristic of one diode is shown in Fig. 3, the corresponding F-N plot is shown in the inset. This data is taken for a 20x20 μm^2 diamond emitter. The exponen-tial I-V curve and the straight-line F-N plot indicate that measured current is field emission current. The current density measured at 0.2MV/cm is approximately 0.5A/cm^2 as compared to reported values in the range of 0.1~10A/cm^2. A particularly inter-esting feature of our diode structure is its use in pressure microsensors and field emit-ter display cells with minor changes in original design.

Although the diode structure has been used to demonstrate field emission using built-in anode, some problems were experienced during the fabrication. As shown in Fig. 2 (a), there are a large number of diamond stray particles. These are due to remaining diamond particles, which are not washed away completely during the development process of the diamond-loaded photoresist. They can affect the yield if they form a continuous film and if their size becomes too large. A multi-step or spray development process is being considered to prevent diamond particles from reattaching to the sur-face in undesired areas. It is also noticeable that there are more stray particles near the edge of well. This may imply that diamond particles were not able to escape from deep well during the development of the resist. Due to the above mentioned problems, only a fraction of devices fabricated were found to function properly. Currently, efforts are in progress to address these problems and to improve the fabrication yield.

4. Conclusions

Diamond field emitter diodes with built-in bridge shaped anodes are designed, fabricated and characterized for possible applications to pressure sensors and field emission displays. A field emission current density of 0.5A/cm^2 is measured at an electric field strength of less than 0.2MV/cm at a pressure of 10^{-6} Torr.

5. Acknowledgment

6. References

1. M. W. Geis, N. N. Efremow, J. D. Woodhouse, M. D. Aleese, M. Marchywka, D. G. Socker, and J. F. Hochedez, IEEE Elec. Dev. Lett., 12, 456 (1991).
2. D. Hong and M. Aslam, J. of Vac. Sci. Technol. B 13(2), 427 (1995).
3. K. Okano, K. Hoshina, M. Iida, S. Koizumi, and T. Inuzuka, Appl. Phys. Lett. 64 (20), 2742 (1994).
4. A. Masood, M. Aslam, M. A. Tamor, and T. J. Potter, J. Electrochem. Soc. 138, L67 (1991).
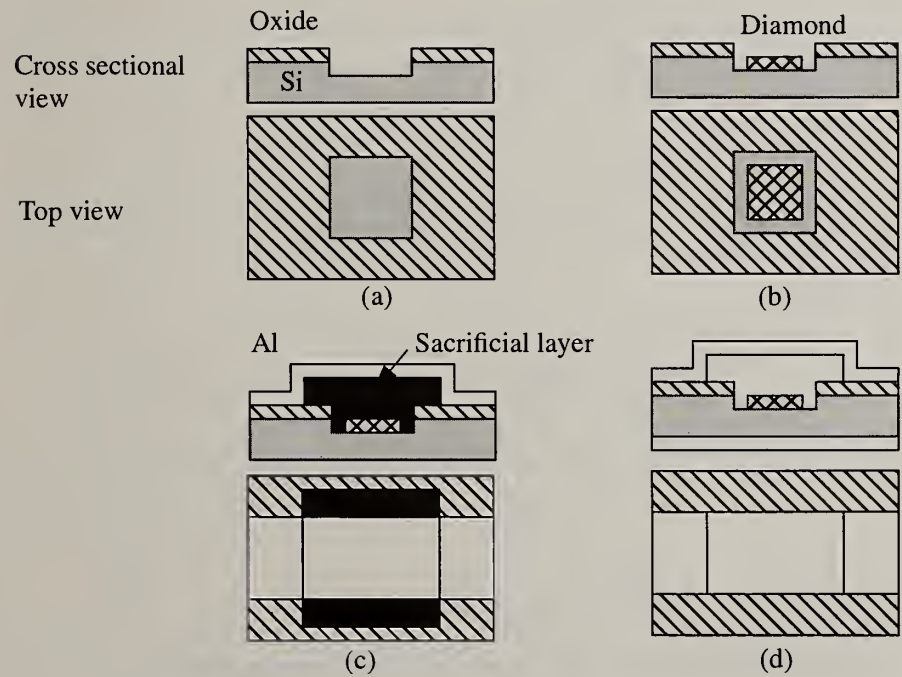
Fig. 1. Cross sectional and top views of emitter fabrication process.

(a)   (b)
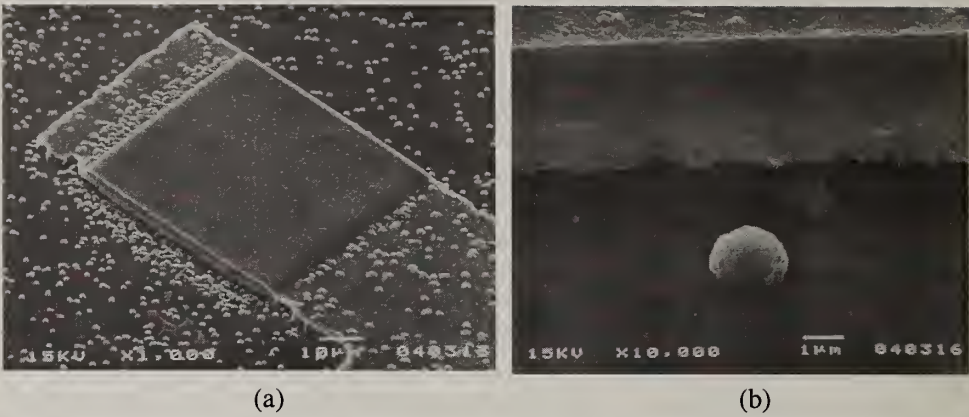
Fig 2. SEM micrographs; (a) diamond field emitter diode overview,
       (b) close-up view
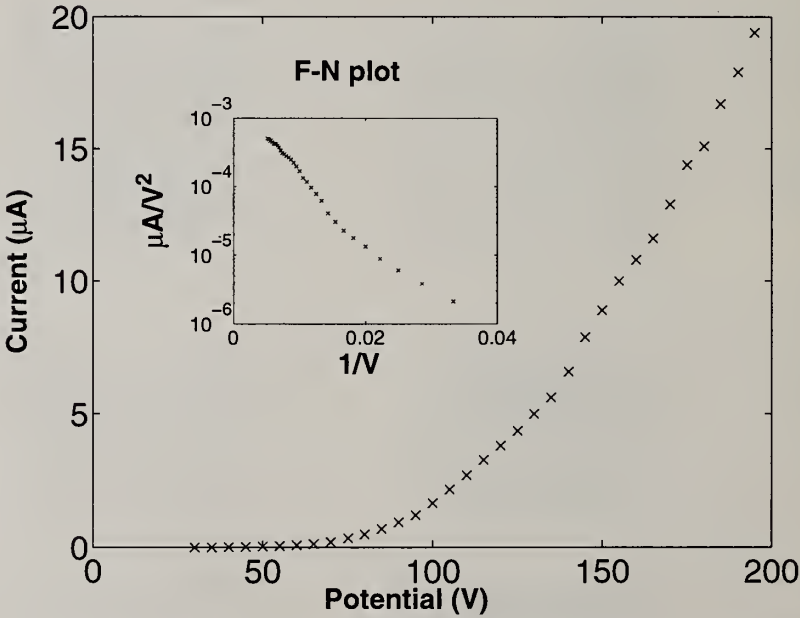
Fig. 3. I-V and Fowler-Nordheim plot of a diamond field emitter diode.

CHANGES OF WORK FUNCTION OF CVD DIAMOND WITH ULTRAVIOLET LIGHT

N. Eimori, Y. Mori, A. Hatta, T. Ito and A. Hiraki

Department of Electrical Engineering, Osaka University,
2–1 Yamadaoka, Suita, Osaka 565, Japan

Key words: diamond, electron affinity, surface, ultraviolet light

Abstract

The electron affinity of the polycrystalline chemical vapor deposited diamond surfaces was investigated using ultraviolet lights. The specimen surfaces were treated with annealing at 773K in the O_2 atmosphere and oxygen adsorbed on the specimen surface. The electron affinity of specimen surface shows positive. However, after the white light irradiate to specimen, the shift of threshold of photoyield was occurred, and the electron affinity became negative. The partial pressures of CO and O in the vacuum chamber increases with ultraviolet light irradiation. It is considered that oxygen were desorbed from specimen surface.

1. Introduction

The cold cathode made of negative electron affinity (NEA) semiconductor is expected for applications to flat displays and microvacuum tubes. Chemical vapor deposited (CVD) diamond film is the most hopeful about NEA devices.

In the case of natural diamond, it is known that the (111) surface has negative electron affinity property [1]. We have investigated the electron affinity of (111)- , (100)- and polycrystalline surfaces of CVD diamond by electron energy loss spectroscopy with low incident energy and photoelectron yield spectroscopy using ultraviolet synchrotron radiation (UVSOR) lights [2-4]. The photoelectron yield from (111)- and (100)-surface after hydrogen plasma treatment was higher than those annealed in O_2 atmosphere.

In this work, the electron affinity of oxygen adsorbed CVD diamond surface shifting with irradiating to VUV lights is described. The electron affinities of specimens were investigated by photoelectron yield spectra using UVSOR lights with energies near the band-gap of diamond (5.5 eV).

2. Experimental

Polycrystalline diamond films were synthesized using a microwave plasma CVD on (100) Si substrates. B_2H_6 diluted with H_2 (100ppm) was used for boron doping of B to prevent the specimens from charging up during spectroscopic measurements of electron emission. The specimens were annealed at 773K in O_2 atmosphere to obtain the O-adsorbed surface [5]. Oxygen atoms exist only on the surface of specimen having diamond structure, as determined from Auger electron spectroscopy and Rutherford backscattering spectrometry.

Photoelectron yield measurements were carried out at room temperature in the ultra high vacuum chamber ($< 10^{-8}$Torr) using UVSOR light at the Institute for Molecular Science (Okazaki, Japan). A 5-mm-thick quartz filter was used to eliminate light of $h\nu > 8$ eV. Photoelectron yield spectra were calibrated by the energy profile of incident light, the sensitivity for the wavelength of the grating and the storage ring current. Photoelectron yields were measured before and after irradiation to the white UVSOR light (¡ 10^6 photons/s, ¡ 8 eV). Photoelectron yield during the measurement was stable because the monochromated light for measurement was weaker by 3 order than the white UVSOR light.

3. Results and discussion

Figure 1 shows the photoelectron yield spectra of specimens before (curve a) and after (curve b) the white UVSOR light irradiation. In Fig. 1(a), the onset of photoelectron yield appears just above 5.8 eV, which is larger than the fundamental band gap of diamond. This indicates that the electron affinity of the O-adsorbed surface is positive. The electron affinity of the diamond surface without adsorption of oxygen is negative, as reported in our previous work [2,3]. The electronegativity of O atoms may play the major role in the increase of work function [6,7].

The time dependence of photoelectron yield during VUV light irradiation is shown in Fig. 2. The photoelectron yield increased gradually, and became about 5 times larger after 40 minutes irradiation. The partial pressures of CO and O in the sample chamber increased rapidly at the beginning of VUV light irradiation and decreased gradually after 10 minutes irradiation. This shows that the O atoms desorbed from the specimen surface with the C atoms due to VUV photons.

After the VUV light irradiation, the threshold of photoelectron yield curve shifts to lower-energy side by about 0.6 eV, compared to that before irradiation. The threshold energy of photoelectron yield is 5.2 eV, which is lower than the band-gap energy of diamond. This indicates that the electron affinity of this surface is negative. The reason for the electron affinity shifting to the lower energy side is considered that O atoms at the specimen surface desorbed with C atoms.
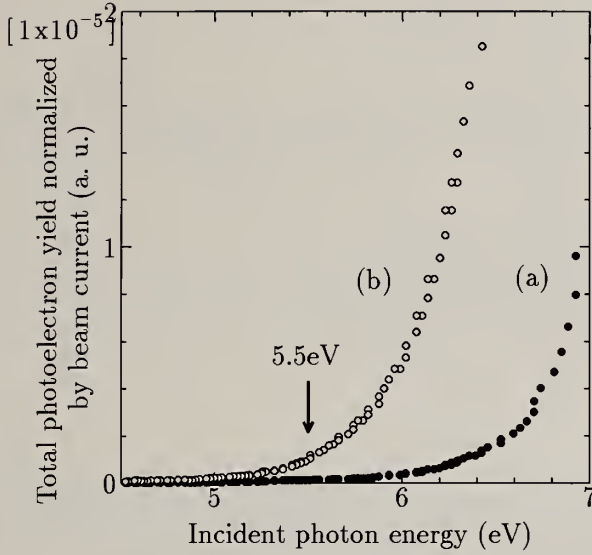
Figure 1: Photoelectron yield of CVD diamond surface annealed at 773K in O atmosphere before (curve a) and after (curve b) VUV light irradiation.

The threshold of photoelectron yield after VUV light irradiation is lower than the band-gap energy, 5.5 eV. Two possible reasons can be considered for the origin of electron emission at photon energes lower than the band-gap energy. One is that the electrons of possible surface states may be excited to conduction band. Such surface states located in the band gap near the valence band maximum may be formed by the dangling bond formed by the photodesorption or H termination of them became the pressure in the vacuum chamber could not ignored for hydrogenation of the surface. It is reported that the hole concentration formed at surface by exposing to hydrogen plasma is estimated to be $3.0 \times 10^{18} cm^{-3}$ [8]. As the other, the electrons at the acceptor level originating from doped boron are considered to be excited to the conduction band and to diffuse to the surface. In this case, the so much density of surface states is considered to be formed by oxygen desorption, so the former seems to be weighty.

4. Conclusions

The electron affinity of oxygen adsorbed surface is positive, however, it became negative after VUV light irradiation resulting in enhancement of photoemission. CO gas was observed to be emitted from the diamond surface adsorbed with oxygen during VUV light irradiation.
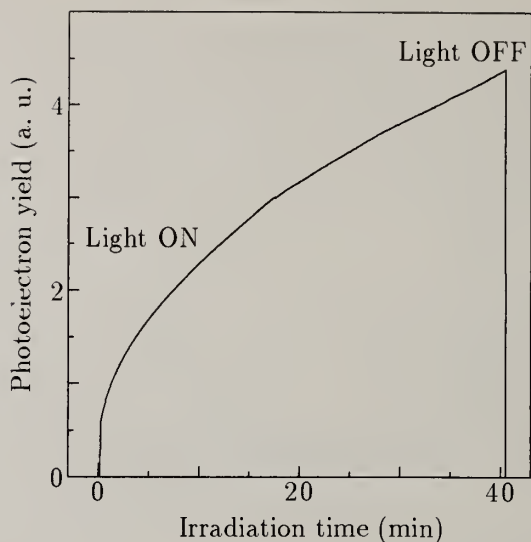
Figure 2: Time dependence of photoelectron yield with irradiating VUV lights.

5. Acknowledgements

6. References

1. F. J. Himpsel, J. A. Knapp, J. A. VanVechten and D. E. Eastman, *Phys. Rev.* **B20** (1979) 624.
2. N. Eimori, Y. Mori, A. Hatta, T. Ito, and A. Hiraki, *Proc. First International Symposium on Control of Semiconductor Interfaces, Elsevier, Amsterdam* (1994) 149.
3. N. Eimori, Y. Mori, A. Hatta, T. Ito, and A. Hiraki, Jpn. J. Appl. Phys. **33** (1994) 6312.
4. N. Eimori, Y. Mori, A. Hatta, T. Ito, and A. Hiraki, Diamond and Related Materials, in press.
5. Y. Mori, N. Eimori, A. Hatta, T. Ito and A. Hiraki, Jpn. J. Appl. Phys. **31** (1992) L1718
6. C. Silvestre and M. Shayegan, Phys. Rev. **B37** (1988) 10432.
7. M. Tikhov, G. Rangelov and L. Surnev, Surf. Sci. **231** (1990) 280.
8. T. Maki, S. Shikama, M. Komori, Y. Sakaguchi, K. Sakuta and T. Kobayashi, *Jpn. J. Appl. Phys.* **31** (1992) L1446.

CRYSTALLINE AND AMORPHOUS DIAMOND COATINGS ON SILICON FIELD EMITTERS

J. Liu, <u>A. F. Myers</u>, S. M. Camphausen, M. T. McClure, J. J. Cuomo, and J. J. Hren

Department of Materials Science and Engineering, North Carolina State University, Raleigh, NC 27695-7907, Tel: (919) 515-3568, Fax: (919) 515-7724

Key words: cathodic arc, electron microscopy, field emission, MPCVD, nano-tips

Abstract

Amorphous and crystalline diamond were deposited on Si field emitters to improve the emission characteristics of the cathodes. The coated emitters were studied by field emission and electron microscopies. Field emission results and Fowler-Nordheim analysis indicate enhanced emission from the coated emitters, as compared to uncoated Si cathodes. The diamond coating morphology and the microstructure of the coating/emitter interface were examined by electron microscopy.

I. Introduction

Intense and stable field electron emitters are essential components for a new generation of high-performance vacuum microelectronic devices and flat panel displays [1]. As common choices of the emitter cathode, silicon and other metal field emitters were usually found to have vacillating currents during operation. The emitter surface was considered to be the main reason for such instability. To improve the performance as well as to enhance the emission current density, a more stable surface coating needs to be developed to make silicon emitters retain their desirable features while minimizing their shortcomings. In the present study, we deposited crystalline and amorphous diamond on the surfaces of silicon emitters and investigated their microstructures as well as the resultant electrical properties.

Synthesized crystalline and amorphous diamond (c-D and a-D) are known to have a high percentage of tetrahedral C-C sp^3 bonds. As a result, they exhibit extreme physical hardness, high resistivity, and chemical inertness. These properties make c-D and a-D useful for a wide variety of applications, especially as a coating material for field emitters. In addition, the deposition process can be controlled to form smooth thin films on highly curved emitter surfaces. Some electrical-related properties of silicon, c-D, and a-D are listed in Table I for purpose of comparison.

II. Experimental Procedures

II.1. Preparation of Si field emitters

Single crystal Si field emitters were used in the experiments. These needle-shaped single and multiple silicon emitters were grown on 1x1 mm^2 silicon substrates and

Table I. Comparison of crystalline and amorphous diamond with pure silicon for field emission applications

Property	Silicon	Crystalline diamond	Amorphous diamond
Electron affinity	4.05 eV	NEA on some facets	unknown
Electron mobility	1.5×10^3 cm^2/V-s	2.0×10^3 cm^2/V-s	variable
Electrical breakdown field	2.5×10^5 V/cm	1×10^7 V/cm	10^6 V/cm
Thermal conductivity	1.5 W/cm-°C	20 W/cm-°C	7.5×10^{-2} W/cm-°C
Chemical stability of surface	Sensitive to adsorbates	Inert to adsorbates	Inert to adsorbates

are especially well-suited for microstructural and electrical analyses. The Si whiskers were first grown by eutectic procedures, followed by chemical sharpening [2]. Repeated oxidation and subsequent HF etching were used for further sharpening of the Si tips to a nanometer-scale radius of curvature. The emitters are nearly 100 µm high and usually have 30-nm or less tip radii of curvature. A transmission electron microscopy (TEM) image of such a Si tip is shown in Fig. 1. An oxide layer on the Si tip surface can clearly be seen. During the experiments, specimens were first cleaned using concentrated HF to remove the native oxide, and any other contaminants, before loading into the reactor chamber.

500nm

200 24KX JL0459
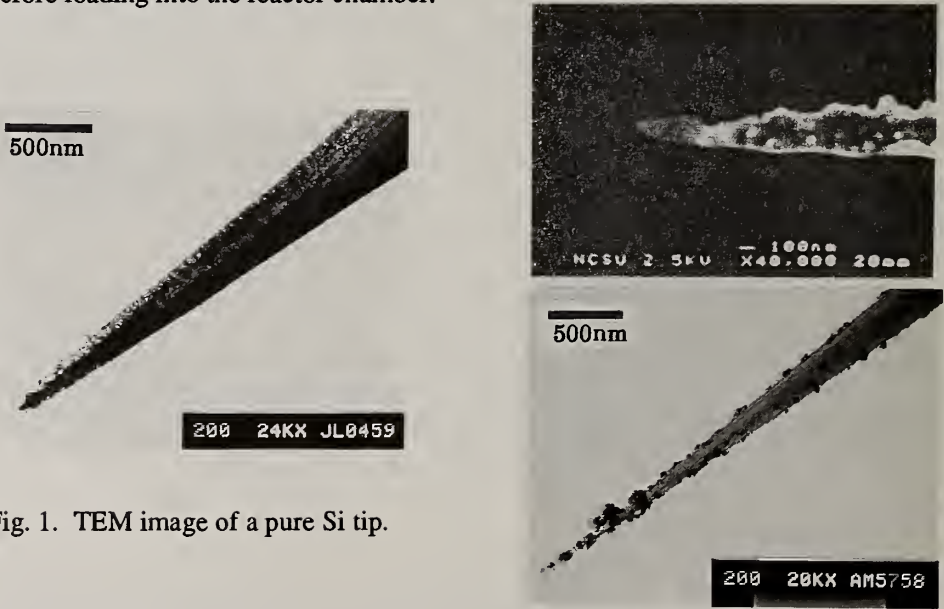
Fig. 1. TEM image of a pure Si tip.

NCSU 2 5KU X40.000 20nm

500nm

200 20KX AM5758

Fig. 2. Electron micrographs of c-D and a-D coated Si tips.

II.2. Diamond deposition

The crystalline diamond deposition process includes a H_2-plasma pretreatment, bias-enhanced nucleation, and growth. All of the processes were carried out in a high vacuum microwave plasma chemical vapor deposition (MPCVD) reactor chamber [3]. A final cleaning pretreatment for the Si emitters was carried out *in vacuo* using thermal annealing and a H_2 plasma at a pressure of 15 Torr. Bias-enhanced nucleation was performed for up to 25 minutes to nucleate diamond on the clean Si emitter surface.

Amorphous diamond was deposited on Si field emitter tip surfaces using a filtered cathodic arc described previously by Lossy et al [4]. This process can produce a-D with a 93% sp^3 content. The Si tips were held in place with a specialized copper specimen holder, which was mechanically attached to a water cooled substrate. The temperature of the cooling water during the process was maintained between 10 to 20°C. All processing runs had a duty cycle of one minute on and one minute off. Experiments were carried out with varying deposition times, ranging from 0.5 to 5 minutes. The background pressure of the system was 1×10^{-6} Torr, and the deposition pressure was 5×10^{-6} Torr.

III. Microstructural analysis and electrical characterization

After c-D and a-D depositions, the Si samples were investigated using SEM and TEM, as well as electron energy loss spectroscopy (EELS). Fig. 2 illustrates typical Si tips after c-D and a-D coating processings.

Field emission current-voltage (I-V) measurements were performed on the coated Si emitters. The results were compared to those obtained from pure Si emitters. A total emission current of a few μA per tip was usually achieved during a typical experiment. A set of I-V measurements from a pure Si tip, a c-D coated Si tip, and an a-D coated Si tip is shown in Fig. 3. Emission data from each sample was taken by computer-controlled electrometers using several consecutive measurements.
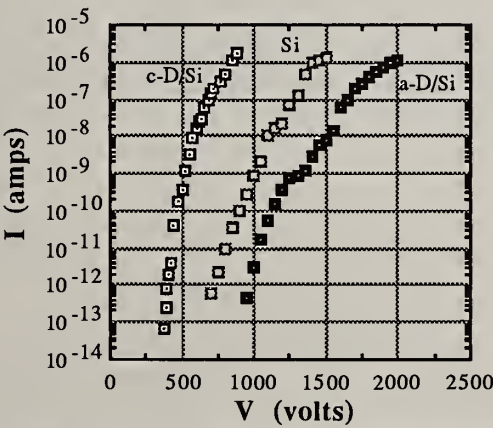
Fig. 3. Field emission current-voltage characteristics of
pure Si, and a-D and c-D coated Si emitters.

Table II. Field emission parameters obtained from a Fowler-Nordheim analysis

Specimen (single tip)	Emitting area, α (cm2)	Tip radius of curvature, r (cm)	Effective surface work function (eV)
Si	6.76×10^{-15}	3.0×10^{-6}	3.86
c-D coated Si	9.97×10^{-12}	4.0×10^{-6}	5.0
a-D coated Si	2.74×10^{-13}	3.5×10^{-6}	4.3

Field emission currents from diamond coated Si emitters, especially from crystalline diamond coated ones, exhibited exceptional stability compared to pure Si emitters. It was found that the stability of diamond coated emitters was one to two orders of magnitude higher than that of pure Si emitters. Another particularly interesting result by conventional Fowler-Nordheim analysis is that the effective emitting area, α, from c-D and a-D coated emitters appeared much larger, compared to pure metal or Si emitters. Some measured results are listed in Table II. For both c-D and a-D coated emitters, the effective emitting area was found to be between 10^{-13} to 10^{-12} cm^2 per emitter. The same procedure applied to uncoated Si tips yielded very small emitting areas in the 10^{-16} to 10^{-15} cm^2 range. This surprising result from diamond coated emitters implies that the electron emission may come from the full tip surface. This phenomenon could be an important means for obtaining higher emission currents as well as better current stability. However, it was found that electron emission from an a-D coated emitter required a higher voltage because of an increased tip radius of curvature after the deposition. The poor electrical conductivity of the undoped a-D film also contributed to the increased operating voltage and possibly to a higher effective surface work function. A suitable doping procedure should yield significantly improved performance.

IV. Summary

Crystalline and amorphous diamond coated Si emitters have demonstrated significant enhancement in field emission performance as compared to pure Si emitters. Field emission measurements and Fowler-Nordheim analysis of coated emitters have shown promising new results which imply a large emitting area as well as much better emission stability. Similar studies promise to provide complementary information for new electronic materials and should have an impact on determining the mechanism of emitter operation.

References

[1] Proceedings of the International Vacuum Microelectronics Conference, *IEEE Trans. on Electron Devices*, **36-40**, (1989-1992); *J. Vac. Sci. Technol.*, **B11** & **B12** (2) (1993-1994).
[2] E. I. Givargizov, *J. Vac. Sci. Technol.*, **B11** (2), 449 (1993).
[3] S. D. Wolter, B. R. Stoner, J. T. Glass, and et al., *Appl. Phys. Lett.*, **62** (11), 1215 (1993).
[4] R. Lossy, D. L. Pappas, R. A. Roy, and J. J. Cuomo, *Appl. Phys. Lett.*, **61** (2), 171 (1992).

Applications of Diamond Films and Related Materials: Third International Conference, 1995
Editors: A. Feldman, Y. Tzeng, W. A. Yarbrough, M. Yoshikawa, and M. Murakawa

61

ELECTRON EMISSION OBSERVATIONS FROM AS-GROWN AND VACUUM-COATED CHEMICAL VAPOR DEPOSITED DIAMOND

A. Lamouri, G.T. Mearini, Y.X. Wang and R.E. Kusner

General Vacuum, Inc., P.O. Box 605204, Cleveland, Ohio 44105

Key words: field emission.

Abstract

Field emission has been observed from CVD diamond grown on Mo and Si substrates. Emission was observed at fields as low as 20 kV/cm. The samples were tested in the as-grown form, and after coating with thin films of Au, CsI and Ni. The emission current was typically maximum at the onset of the applied field, but was unstable, and decreased rapidly with time from the as-grown films. Thin (~ 15 nm), vacuum deposited Au layers significantly improved the stability of the emission current at values approximately equal to those from uncoated samples at the onset of the applied field. Thin layers of CsI, ~ 5 nm, were also observed to improve the stability of the emission current but at values less than those from the uncoated samples at the onset of the applied field. While Au and CsI improved the stability of the emission, Ni was observed to have no effect.

1. Introduction

State of the art field emitters generally require applied fields above 5×10^7 V/cm. Unassisted field emission from chemical vapor deposited (CVD) randomly oriented polycrystalline diamond films grown on Si and Mo has been demonstrated and observed at room temperature at fields as low as 20 kV/cm. The total current densities ranged from 1 μA/cm^2 to 0.1 mA/cm^2, averaged over the entire sample.

2. Experimental setup

The CVD diamond films were made by depositing a 10-20 μm continuous film on 1x1 cm^2 Si or Mo substrates by thermal decomposition of 1% methane in hydrogen using the hot tungsten filament technique. The substrates were polished with 1/4 μm diamond paste and ultrasonically cleaned in alcohol before they were introduced into the deposition chamber. Au and Ni were evaporated on the diamond samples from Al$_2$O$_3$ crucibles and CsI was evaporated from a Ta boat in

a diffusion pumped high vacuum chamber which was operated at 3×10^{-8} Torr. The thickness of the Au, Ni and CsI layers was determined using a Quartz Crystal Microbalance (QCM) which was calibrated with a thickness interferometer. Following the deposition, the substrates were removed from the deposition chamber and immediately introduced into the test chamber.

The field emission tests were performed in an ion pumped high vacuum chamber at a base pressure of 7×10^{-7} Torr. The measurements were carried out using an anode with a diameter (~ 5 mm) slightly smaller than the dimensions of the samples which were approximately 1 cm^2. This anode was used in order to eliminate possible field emission currents emanating from the "sharp" edges of the cathode. The measurements were obtained by applying up to 12 kV across a 1 mm gap separating the anode and the emitting cathode. The high voltage was applied to the anode and the emission current was measured at the cathode as a function of applied field. The field was varied by increasing the applied voltage or by varying the cathode-anode separation.

3. Result and summary

After the diamond samples were introduced into the measurement chamber, a gradually increasing field was applied in order to induce emission. Typical "turn-on" fields for Si and Mo diamond-coated electrodes ranged from 20 to 50 kV/cm. For the uncoated samples, the field emission currents were typically maximum at the onset of the applied field, but were unstable, and decreased rapidly as a function of time. As a result, no meaningful I-V data could be recorded from the as-grown CVD diamond samples. However, when the diamond films were coated with thin layers of Au, relatively stable emission currents with values equal to or close to those from the uncoated samples at the onset of the applied field were observed. In addition to a significant improvement in stability, a substantial enhancement of the field emission currents was observed when Au films approximately 15 nm thick were present on the diamond surface. As shown in Fig. 1, the emission currents were relatively stable and increased with Au coverage between 0.5 and 15 nm. These results are in good agreement with the data of Shovlin and Kordesch[1]. In fact, they were only able to observe field emission current from their CVD diamond after they were coated with 15 nm presumably due to the enhancement of emission current at this Au coverage. For coverages greater than 15 nm, the emission currents, although relatively stable, decreased rapidly as a function of Au coverage. No emission currents were observed from CVD diamond on Mo coated with thick layers (~130 nm) of Au. The data presented in Fig. 1, were obtained from the same CVD sample which was tested in the as-grown form and with incremental cold coverages. Samples that were tested only after they were coated did not have maximum emission currents like those from the as-grown samples at the onset of the applied field. The emission currents from these samples were similar to those of Fig. 1 at comparable Au coverages.

Typical data recorded from the CVD diamond samples coated with 10 nm of Au are plotted in Fig. 2. These data indicate that, within the experimental field range, the I-V characteristics are well described by the Fowler-Nordheim regime. In addition, they show that even the Au-coated samples are unstable for high fields since stronger fields are required to obtain the same field emission currents from successive voltage ramps.

Preliminary data from thin layers of CsI (0.1 and 5 nm), vacuum deposited onto the diamond samples, significantly improved the stability of the emission current at values comparable to those from Au at the same coverage as shown in Fig. 3. These results are not surprising since CsI films 5 to 10 nm thick are known to stabilize and enhance Secondary Electron Emission (SEE) from CVD diamond after they have been activated by electron bombardment.[2] Measurement for thicker CsI films on CVD diamond-coated Mo are currently underway and it is possible that more stable and enhanced emission currents will be obtained for coverage of ~10 to 20 nm.

The mechanism responsible for the stability of the emission currents induced by CsI and the stability and enhancement induced by Au is not understood at present. It is possible that hydrogen termination of the surface, believed to be responsible for stabilizing and enhancing SEE from CVD diamond[3], is stabilized when Au or CsI is present on the surface. In fact the instability of the coated samples for long exposures is believed to be the result of sputter erosion of hydrogen due to ions formed close to the cathode presumably due to the relatively high pressures (mid 10^{-7} Torr) in our test chamber. In their measurements of secondary yields from CVD diamond, Mearini et al.[4] discovered that the total secondary yields are significantly reduced when the substrates are bombarded by high energy hydrogen ions due to graphitization of the diamond surface.

We have also tested field emission from CVD diamond films on Mo coated with Ni. Unlike Au and CsI, Ni does not appear to have any effect on the electron emission. As shown in Fig. 4, the emission currents for Ni-coated CVD diamond were observed to decrease very rapidly as a function of time although the maximum emission currents at the onset of the applied field were comparable to those from diamond samples coated with Au and CsI.

Acknowledgment

References

[1]   J.D. Shovlin and M.E. Kordesch, Appl. Phys. Lett. **65**, 863 (1994).

64

[2]   G.T. Mearini, I.L. Krainsky and J.A. Dayton, Jr., Surf. Interface Anal. **21**, 138 (1994).

[3]   G.T. Mearini, I.L. Krainsky, J.A. Dayton, Jr., Y.X. Wang, C.A. Zorman, J.C. Angus, D.F. Anderson, Appl. Phys. Lett. **66**, 242 (1995).

[4]   G.T Mearini, I.L. Krainsky, Y.X. Wang, J.A. Dayton, Jr., R. Ramesham and M.F. Rose, Thin Solid Films **253**, 151 (1994).
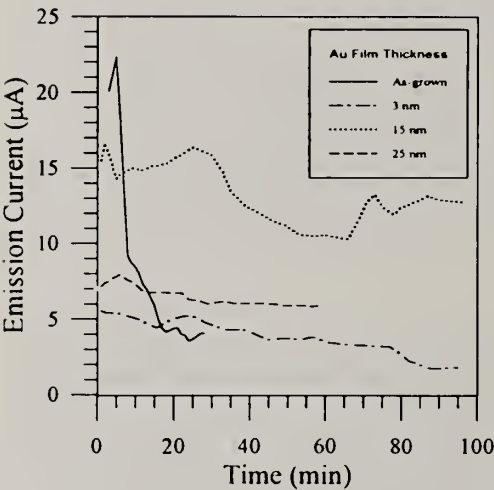
Fig. 1.   Emission current (at 100 kV/cm) as a function of time from CVD diamond on Mo for different Au film thickness.
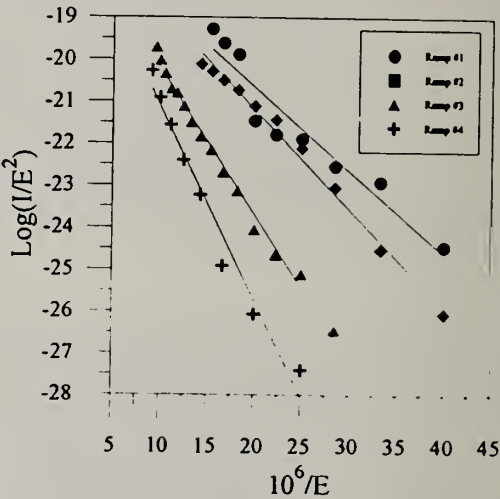
Fig. 2   Fowler-Nordheim plots of emission current from CVD diamond film on Mo coated with 10 nm of Au.
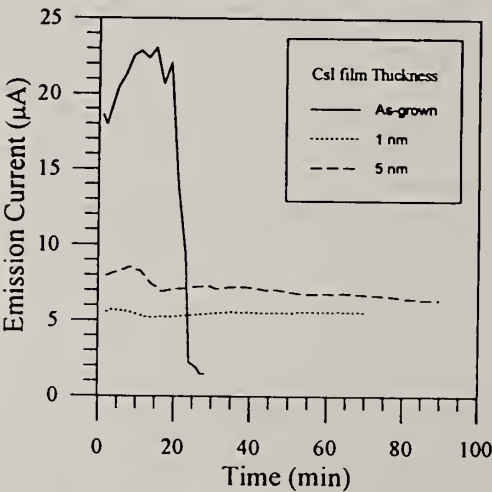
Fig. 3.   Emission current (at 100 kV/cm) as a function of time from CVD diamond on Mo for two different CsI film thickness.
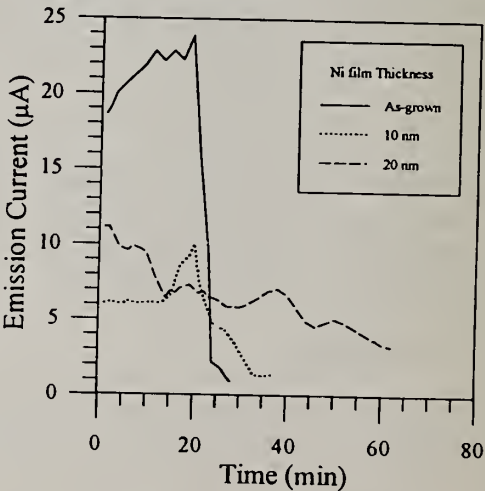
Fig. 4.   Emission current (at 100 kV/cm) as a function of time from CVD diamond on Mo for different Ni film thickness.

SELECTIVE DEPOSITION OF DIAMOND THIN FILMS ON FIELD EMITTER TIPS IN DENSE ARRAYS

O. Auciello,[1] R. Spitzl,[2] and J. Engemann[2]

[1]MCNC, Electronic Technologies Division, 3021 Cornwallis Rd., Research Triangle Park, NC 27709-2889, USA
[2]Forschungszentrum für Mikrostrukturtechnik-fmt, Bergische Universität, Gesamthochschule Wuppertal, Obere Lichtenplatzer Str. 336, 42287 Wuppertal, Germany

Key words: diamond, deposition, field emitters, selective

Abstract

First results are presented which demonstrate the feasibility of selective deposition of diamond films on dense arrays of Si tips. We are able to grow diamond films either covering the whole tip structure or the very top only, depending on the tip geometry, dimensions, and deposition conditions. The diamond films are grown using a plasma-deposition technique in conjunction with a methane-hydrogen gas mixture. It is demonstrated that the seeding process and plasma manipulation are critical to achieve the conditions necessary to produce selective diamond deposition on the tips. Scanning electron microscope (SEM) images are presented to demonstrated the different film morphological characteristics.

1. Introduction

Field emitter cathodes are being investigated for various applications such as emissive flat panel displays,[1] high-power, high-frequency devices,[1] and vacuum field emission transistors and diodes.[2] Metal[3] and semiconductor (e.g. Si [4] and GaAs [5]) field emitter arrays have been fabricated and their emission properties tested under different conditions. Field emitter cathodes with either metal or semiconductor tips are prone to catastrophic failure at high current densities.[3] Although semiconductor field emitters can yield high current densities (> 1500 A / cm^2),[6] they are easily contaminated and will not operate after being exposed to oxygen. A third approach, currently under investigation, involves using field emitters coated with wide-bandgap (> 5 eV) materials, which have their conduction bands close to the vacuum energy level, even in the presence of O_2 and H_2O background gases. A candidate material under investigation as a field emitter coating with enhanced emission properties is diamond.[7] Pure diamond is not a good candidate because is low charge-carrier concentration. However, diamond can be either n- (although not clearly demonstrated yet) or p-type doped[8] and grown with relatively low trap density and high carrier mobilities, which make it a semiconductor. The feasibility of fabricating diamond cold cathodes have recently been demonstrated.[7] These cathodes were produced by fabricating diodes in p-type diamond via carbon ion implantation into hot substrates. Emission current

densities in the range 0.1 to 1 A / cm^2 were measured when biasing the diode with voltages in the range -100 to -200 V. Based on the initial results discussed above, the possibility exist for a much higher emission current if appropriately doped diamond films can be grown on field emitters. However, before doped diamond films can be grown on field emitter tips, it is necessary to develop appropriate procedures to growth plain diamond films. In addition, it is necessary to develop a technique to selectively grow diamond films on the tips of high density field emitter arrays.

This paper is to report recent work performed in our laboratory which demonstrates the feasibility of selective deposition of diamond films on the Si tips of dense arrays of field emitters . We demonstrated that the diamond films can be selectively grown in such a way that they either cover the whole tip structure or the very top only, depending on the tip geometry, dimensions, and deposition conditions.

2 . Experimental Procedure

Silicon ungated field emitter arrays were cleaned with acetone and alcohol and introduced into a microwave plasma system. Diamond films were grown using a microwave plasma-deposition technique utilizing a methane (2%)-hydrogen (98%) gas mixture with a total pressure of about 30 mbar and a power of about 500 Watts. The deposition temperature was in the range 650 - 700 °C. It is relevant to point out that the substrate temperature was measured via a thermocouple positioned inside an inconel substrate holder plate underneath the substrate. Therefore, the temperature quoted in this paper most probably is not the real temperature on the tips. Work is in progress to determine the temperature on the tips, since this is one of the critical parameters that contribute to control the selective growth of the diamond films. A carbon seeding step was necessary prior to diamond growth. The seeding step involved exposing the Si field emitter arrays to a methane (2%)-hydrogen (98%) microwave plasma in the presence of a graphite electrode positioned in front of the substrate and applying a negative bias   (about - 200 V) to the substrate. The parameters for the seeding step have not been optimized yet. However, the initial results presented here indicate that these parameters are critical for a successful seeding step and subsequent diamond film growth.

3 . Results and Discussion

Diamond films were grown on Si field emitter arrays each containing tips with different geometry and dimensions (see Figs. 1 (a) and 2 (a)). A diamond film growth for a period of two hours, using the conditions described in section 2, yielded a selective deposition that resulted in a total coverage of the pyramidal field emitters (see Figs. 1 (b) and 1 (c)). On the other hand, one hour diamond growth on the columnar emitters shown in Fig. 2 (a), under similar conditions to those used during the growth on the pyramidal emitters, yielded the growth of a single small diamond particle on the sharp top of the emitters (Fig. 2 (b)). The diamond particle shown in Fig. 2(b) is representative of the many particles observed on different emitters.

It is important to point out that not all Si tips were covered with diamond films. Immediately identifiable factors that may affect the uniformity of the diamond growth across the whole emitter array include: (a) uniformity of emitters size and geometry, (b) temperature uniformity on all tips, (c) uniformity of the electric field and of the local plasma environment on each tip, and (d) uniformity of the seeding process. Other factors not yet identified may play a role also. Systematic experiments are underway to

determine the effect of each one of the factors mentioned above and to identify others that are not evident at this time.
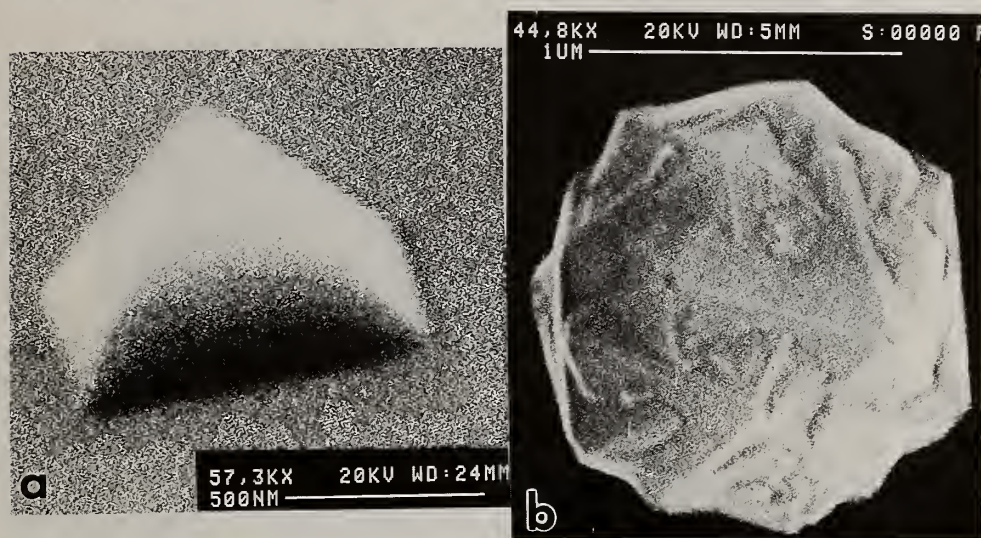
Fig. 1 (a) SEM micrograph of a Si pyramidal emitter. (b) SEM micrograph of a diamond particle selectively grown on one of the pyramidal emitters as shown in (a).
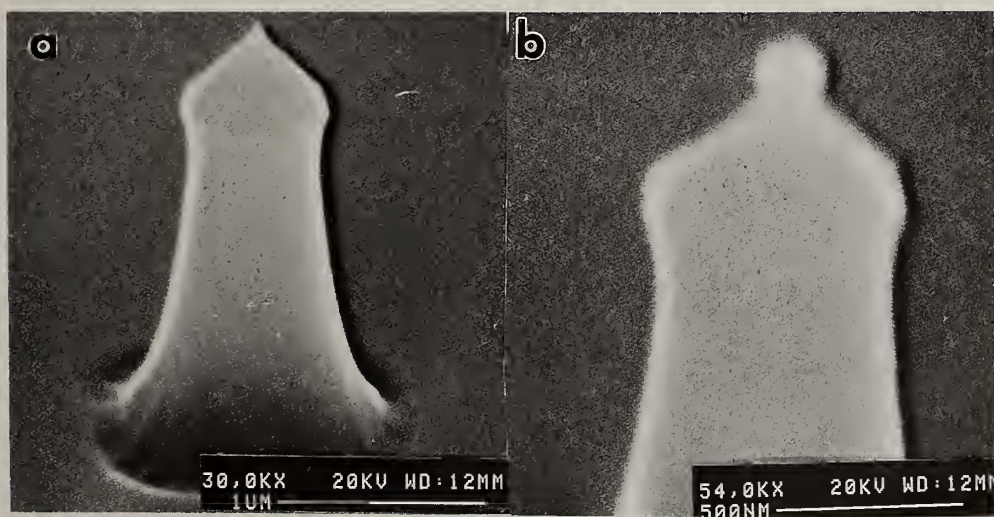
Fig. 2 (a) SEM micrograph of a columnar Si field emitter in an array. (b) diamond particle grown on the top of a columnar field emitter similar to that show in (a) in the same array.

Although not all emitters are covered with diamond particles in the arrays used in the first experiments reported here, the selectivity of the deposition process is good, as demonstrated by Fig. 3, which shows diamond particles grown on top of pyramidal

emitters similar to that shown in Fig. 1 (a). A close examination of the field emitter array shown in Fig. 3 reveals that diamond has been grown only on the tips.
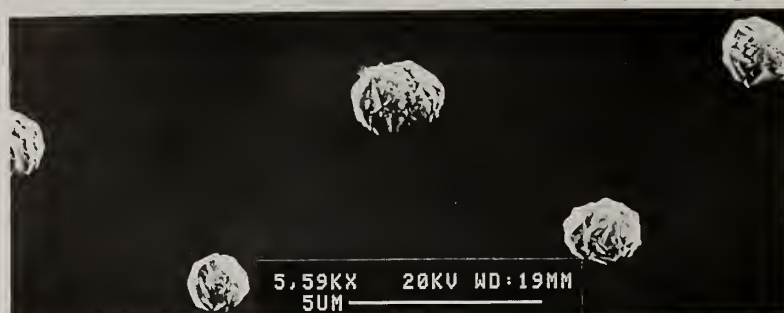
Fig. 3 SEM micrograph showing selective growth of diamond films on Si emitter arrays.

In conclusion, we have demonstrated the feasibility of producing selective growth of diamond films on tips of Si field emitter arrays. The technique may be applied to produce selective diamond deposition on field emitter materials, although this need to be demonstrated. Further work is in progress to demonstrate the feasibility of doping the selectively grown diamond particles and to measure the electron emission characteristics of the diamond coated arrays.

4. Acknowledgments

5. References

1. W. D. Palmer, J.E. Mancusi, C.A. Ball, W.T. Joines, G.E. McGuire, D.Temple, D. Vellenga, and L. Yadon, IEEE Transac. on Electron Devices, **41** (1994) 1866.
2. C.T. Sune, G.W. Jones, and D. Vellenga, J. Vac. Sci. Technol. **B10** (1992) 2984.
3. C.A. Spindt, C.E. Holland, A. Rosengreen, and I. Bodie, Proc. 3rd Int. Conf. Vacuum Microelectronics, C.A. Spindt and H.F. Gray (Eds.) IEEE, New York (1991).
4. R.U. Martinelli and D.G. Fisher, Proc IEEE **62** (1974) 1339.
5. J.J. Scheer and J. van Laar, Solid State Commun. **3** (1965) 189.
6. G.G.P. van Gorkom and A.M.E. Hoeberechts, J. Vac. Sci. Technol. **B4** (1986) 108.
7. M.W. Geis, N.N. Efremow, J.D. Woodhouse, M.D. McAleese, M. Marchywka, D.G. Socker, and J.F. Hochedez, IEEE Electron Device Letters **12** (1991) 456.
8. M.W. Geis, in Proc. Mater. Res. Soc. "Diamond, SiC, and Related Wide Bandgap Semiconductors," J.T. Glass, R. Messier, and N. Fujimori (Eds.), vol. **162** (1990) 15.

DIAMOND
ELECTRON DEVICES AND
SENSORS

Applications of Diamond Films and Related Materials: Third International Conference, 1995
Editors: A. Feldman, Y. Tzeng, W. A. Yarbrough, M. Yoshikawa, and M. Murakawa

71

DIAMOND TRANSISTORS AND CIRCUITS

D. L. Dreifus, J. S. Holmes, and B. R. Stoner

Kobe Steel USA Inc., Electronic Materials Center, 79 T.W. Alexander Drive, Research Triangle Park, North Carolina, 27709, USA.

Key words: devices, diamond, electronics, highly-oriented diamond, transistors

Abstract

Metal-oxide-semiconductor field-effect transistors (FETs) have been fabricated using B-doped diamond thin films deposited on (100) highly-oriented polycrystalline diamond (HOD) and single crystal insulating diamond substrates. The HOD material has properties superior to randomly-oriented polycrystalline diamond and offers a viable alternative to large area single crystal diamond. Concentric-ring FETs were fabricated using standard optical lithography and silicon dioxide was used as the gate dielectric. Diamond FETs exhibited well-behaved pinch-off and saturation of the channel current at temperatures up to 325°C for both HOD and single crystal diamond devices. Single crystal devices have been characterized in both enhancement and depletion-mode at elevated temperatures in excess of 500°C. Single crystal devices have been biased in common source amplifier configurations and NAND and NOR digital logic circuits. The behavior of field-effect transistors fabricated on HOD and single crystal diamond films, as well as diamond transistor circuits will be presented.

1. Introduction

There have been many publications describing the virtues of diamond's unique combination of properties such as its wide bandgap, high breakdown field, high thermal conductivity, high electron and hole mobilities, and radiation hardness.[1-6] Several theoretical analyses suggest that diamond devices could potentially exhibit performance superior to that of devices fabricated from other materials such as Si and GaAs.[3, 6] Hence, diamond has been regarded as a suitable material for electronic devices operating under hostile conditions such as high temperature, high power, high radiation, and high frequencies.[1-3] A great deal of excitement has been generated by reports of working transistors fabricated from single crystal diamond.[7] The performance of diamond transistors, however, has varied greatly, depending on device structure, starting material, doping technique, and device processing technologies.

In contrast, there have been reports that refute the optimistic outlook for diamond electronic devices.[8-10] In these latter reports, authors indicate that many unresolved issues need to be addressed, such as the lack of low activation energy dopants, the state of diamond device process technologies, the growth of high quality doped diamond layers, and the availability of a suitable large-area substrate.

The issue of the deep B acceptor level is being addressed by researchers who are theoretically examining the effects of incomplete ionization. Additional analyses of the effects of incomplete ionization on the performance of diamond FETs has shown a large variability in the device behavior with respect to changes in operating temperatures.[11, 12] Shin *et al.*[13] have re-examined the expected high frequency performance of diamond devices[3] in light of incomplete ionization. It was predicted that devices operating at temperatures in excess of 600°C are expected to exceed the performance of GaAs and SiC rf power FETs. Shiomi *et al.*[14] have presented one approach to circumventing the difficulty of obtaining complete ionization: a diamond MESFET using a δ-doping or pulse-doping structure. The authors were able to demonstrate room temperature operation of a 2 μm gate length x 39 μm gate width device that exhibited a transconductance of 388 μS/mm. Furthermore, the growth of high quality CVD diamond thin films has been demonstrated. Room temperature carrier mobilities approaching 1600 cm^2/V•s have been obtained.[15] The electronic properties of these films exceed most natural semiconducting diamonds.

Although diamond device processing technology continues to advance, one limiting factor for the previously reported devices is that they are all fabricated using single crystal diamond substrates. While this is not a problem as far as device operation itself is concerned, it is a severe limitation in terms active device area and cost. This is due to the small size and high cost of available high quality natural and synthetic diamond substrates. Ideally, large area single crystal diamond or alternate substrates on which diamond can be grown heteroepitaxially would be desirable. Although initial hetero-nucleation results on SiC[16] and Ni[17] indicate that this may be possible, true heteroepitaxy has not yet been realized except on single crystals of cubic-BN.[18, 19] Unfortunately, cubic-BN is currently as difficult to produce in large-area single crystals as diamond. Thus, natural and synthetic high-temperature, high-pressure material remain the sole sources of substrates for monocrystalline diamond films.

The economic viability and the availability of polycrystalline diamond films have many groups trying to fully characterize the electronic properties of these films.[1, 5, 20-23] Polycrystalline diamond films have been deposited over large areas using a variety of deposition techniques.[13, 23, 24] Boron-doped semiconducting diamond films can be easily obtained.[21] Promisingly, the first operation and subsequent enhanced performance of FETs fabricated using polycrystalline diamond films has been reported.[23, 25, 26] The effects of grain boundaries upon electrical properties, however, results in inferior performance by several orders of magnitude between polycrystalline and single crystal diamond devices. Recently, an engineered polycrystalline material in which the individual grains are highly-oriented with respect to the substrate and adjacent grains has been synthesized. This (100)-oriented material shows promise for becoming a potential substrate material for diamond electronic devices.[27] The individual grains in highly-oriented polycrystalline diamond are aligned such that only low-angle grain boundaries are present. The electrical properties of this material have already been shown to be superior to randomly-oriented polycrystalline diamond.[21]

In this work, depletion-mode metal-oxide-semiconductor field-effect transistors (MOSFETs) have been fabricated using single crystal and highly-oriented polycrystalline diamond materials. The devices exhibit well-behaved characteristics, including saturation and complete pinch-off of the channel current. Variable

temperature operation has been observed. Large drain-to-source currents and transconductances have also been demonstrated. These results provide experimental evidence in support of the viability of active diamond electronic devices.

2. Experimental

Natural single crystals and highly-oriented diamond thin films were used as substrates. The HOD substrates consisted of 15-40 μm of undoped diamond deposited onto several 5 mm x 5 mm Si substrates. The techniques for producing and characterizing these films have been published previously.[16, 28] Film characterization included scanning electron microscopy, profilometery, van der Pauw Hall-effect measurements, and capacitance-voltage measurements. Field-effect transistor fabrication and characterization techniques have also been published previously.[11, 29] The resultant gate length, width, and source-to-drain spacing were 2 μm, 314 μm, and 12 μm respectively. The current-voltage (I-V) behavior of diamond FETs was characterized as a function of temperature in 25°C increments as high as 550°C. Selected single crystal diamond devices were then configured into amplifier and digital logic circuits. A simple common-source amplifier circuit was constructed by connecting a discrete diamond MOSFET to an external load resistor and power supply. Similarly, simple logic gates were configured by connecting a pair of diamond MOSFETs to an external load resistor and power supply. The behavior of the various circuits was measured as a function of temperature up to 400°C.

3. Results and Discussion

Post deposition analyses of the diamond layers were performed. Scanning electron, Raman, and secondary ion mass spectroscopic techniques were used. The surface morphologies of the various diamond materials were viewed using SEM. For the case of homoepitaxial diamond layers, the surface was practically featureless. In the final stages of growth of the highly-oriented polycrystalline diamond films, the individual grains coalesced resulting in a smoothing of the surface as compared with randomly-oriented polycrystalline diamond. A micrograph of surface morphology of an HOD film is shown in Fig. 1. In both diamond materials, a well-defined peak at 1332 cm^{-1} was observed in the Raman spectra, indicating the presence of diamond. A photoluminescence background was observed in the spectra for the highly-oriented layers but was non-existent in the homoepitaxial diamond layers. Secondary ion mass spectroscopy was used to determine the impurity concentration of a randomly-oriented polycrystalline diamond layers grown at the same time as the FET active layers. Uniform atomic B concentrations in the range between 1×10^{17} cm^{-3} to 5×10^{17} cm^{-3} were routinely obtained throughout the p-type layers.

Hall-effect measurements were performed to correlate the electronic transport with the crystallographic properties. For the first set of single crystal films, room temperature carrier mobilities of 400-500 cm^2/V•s were measured for single crystal films with atomic B concentrations of 1×10^{17} cm^{-3}. Room temperature measurements on randomly-oriented polycrystalline and highly-oriented polycrystalline diamond layers grown simultaneously with the above mentioned single crystals yielded mobilities in the range of 20-50 cm^2/V•s and 125-175 cm^2/V•s respectively. The larger carrier mobilities measured in the highly-oriented diamond layers are attributed to the presence of only low-angle grain boundaries.[21, 28] Growth conditions were subsequently optimized to provide higher quality epitaxial device layers. The carrier

mobilities of the homoepitaxial samples used in the device fabrication were all above 1000 cm^2/V•s.[21, 30] Carrier mobilities in excess of 1300 cm^2/V•s for films doped with an atomic B concentration of 1.8×10^{17} cm^{-3} have since been achieved on type IIa substrates.[31] Results for films with still larger room temperature mobilities of 1580 cm2/V•s will be reported elsewhere.[15] Additionally, carrier mobilities as large as 280 cm^2/V•s have been measured for highly-oriented diamond layers.[28, 30]

25 µm
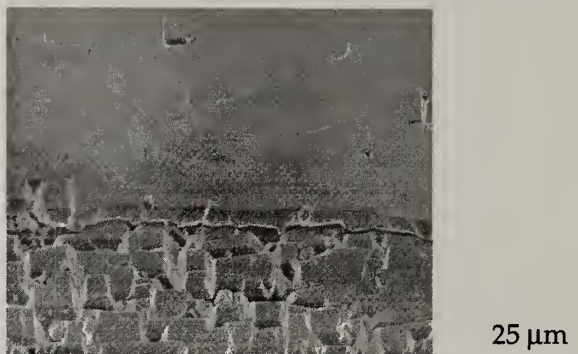
Fig. 1. A scanning electron micrograph of the surface morphology of a coalesced HOD diamond layer. The lower portion of the micrograph shows oriented diamond nuclei on the substrate which were masked during the final HOD growth.

Current-voltage measurements were made on the processed devices. The drain-to-source and gate-to-source currents between electrodes were measured to evaluate the properties of the ohmic contacts and the insulating properties of the gate dielectric. Linear I-V behavior was observed for the ohmic contacts, while the gate current was less than 1nA in all cases. Capacitance-voltage measurements were made on selected MOS gates on homoepitaxial diamond layers. From the slope of $1/C^2$ vs. V, uncompensated acceptor concentrations were determined. These results were in good agreement with the values for atomic B concentration as determined by SIMS.[32]

Devices fabricated from homoepitaxial diamond were measured from room temperature to 550°C while devices fabricated from HOD layers were characterized to 400°C. MOSFETs in both materials have been shown to exhibit operation consistent with depletion-mode devices and saturation and pinch-off of the channel current were observed at elevated temperatures. Current-voltage characteristics for a single crystal diamond and an HOD FET operating at 325°C shown in Figs. 2(a) and (b) respectively. At temperatures in excess of 500°C, a parasitic conducting channel was observed, and pinch-off of the channel current was not achieved.[11] When larger gate biases were used, the gate leakage currents approached 1nA, indicating the onset of catastrophic breakdown of the gate dielectric. The failure of the gate oxide has been reported previously.[2] Other single crystal diamond MOSFETs exhibited drain-to-source currents of 15 mA when biased in enhancement mode as shown in Fig. 3. The maximum transconductance observed for a single crystal device was 1.3 mS/mm. It is interesting to note that similar characteristics were observed for early demonstrations of SiC FETs.[33] A maximum transconductance of 76 µS/mm was determined from the measured characteristics for devices fabricated from HOD thin films. Although the drain-to-source currents are lower than the single crystal

device, the characteristics of highly-oriented polycrystalline diamond MOSFETs are significantly improved as compared to devices fabricated from randomly-oriented polycrystalline diamond.[25, 26] For the active devices fabricated using HOD films, the individual grain sizes are much larger than the gate length of the device. Thus the drain-to-source current is expected to traverse only a few grain boundaries as it flows radially in the device. In addition, the HOD material possess low-angle grain boundaries in comparison to randomly-oriented polycrystalline diamond. Transistors fabricated from the highly-oriented diamond were characterized to a temperature of 400°C before gate failure was observed.

(a)   (b)
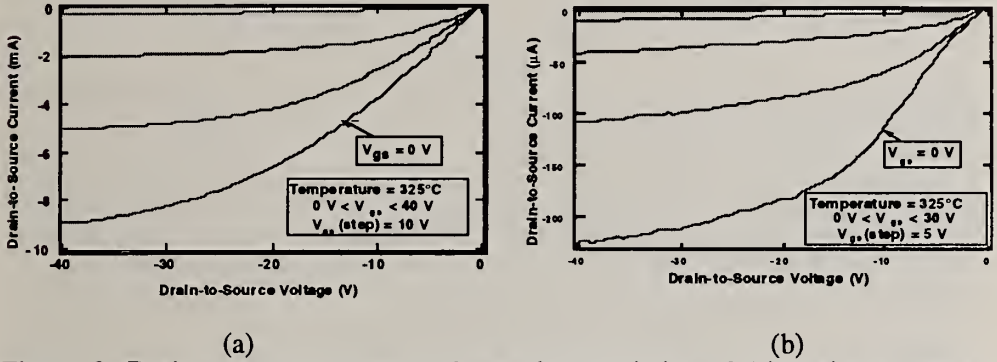
Figure 2. Drain-to-source current-voltage characteristics of (a) a single crystal diamond and (b) a highly-oriented polycrystalline diamond field-effect transistor operating 325°C.
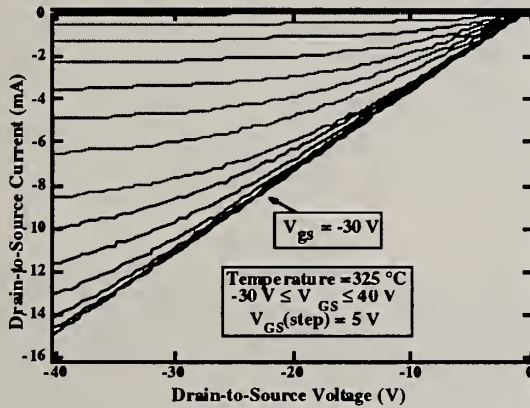
Figure 3. Drain-to-source current-voltage characteristics of a single crystal diamond field-effect transistor operating in enhancement and depletion mode at 325°C.

Individual diamond MOSFETs were biased into a simple common-source amplifier. The resultant gain versus frequency plot is shown in Fig. 4 for a diamond amplifier operating at 75°C and 250°C. As expected, amplifier performance improved as a function of temperature. A DC gain of 5 was observed at 250°C operation. The gain versus frequency data exhibited the roll-off characteristics of a circuit dominated by a
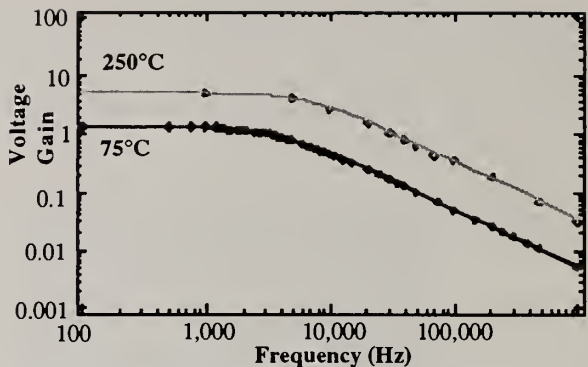
Figure 4: Frequency response for a simple common-source amplifier utilizing a diamond MOSFET. The DC voltage gain is 1.4 at 75°C and 5 at 250°C.

resistance-capacitance time constant. Unity gain resulted at an input frequency of 30 kHz. Devices were not designed specifically for this circuit application. Replacing the load resistance with an active depletion-load should improve amplifier gain. Frequency response could also be improved by decreasing the device impedance.
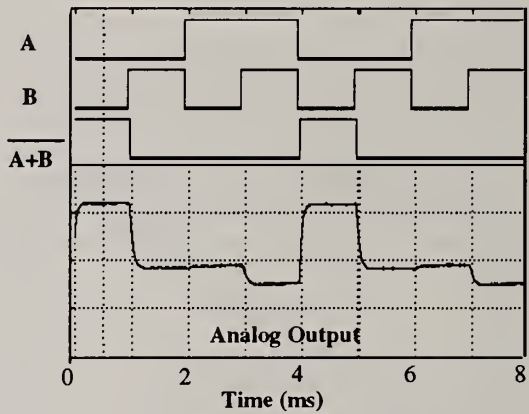
Figure 5: Plot of the input and output waveforms of a diamond NOR circuit. Signals A and B shown are the TTL input signals as viewed through a logic analyzer. The input signals are followed by the logic output of the NOR circuit. The analog output is also shown as viewed by an oscilloscope.

Diamond MOSFETs were used to construct simple digital logic gates. A NOR gate was constructed by connecting two diamond MOSFETs in series with an external load resistance and power supply. The input and output signals of the digital circuit operating at 400°C are shown in Fig. 5. Standard TTL logic signals were used to drive the NOR circuit. Utilization of TTL inputs was facilitated by the relatively low pinch-off voltage of the constituent transistors. This is the first demonstration of a digital circuit based solely on diamond transistors. Again, the devices were not optimized for digital circuit performance using 5 volt input logic levels. Lower pinch-off voltages of the component transistors would result in more ideal output

characteristics. Also, decreased device capacitances should enhance the frequency performance of the circuit.

4. Conclusions

Substantial improvements in the field of diamond electronics have been reported. Operation of diamond MOSFETs exhibiting modulation, saturation, and pinch-off of the channel current have been demonstrated using single crystal and highly-oriented polycrystalline diamond thin films. Diamond FETs exhibited well-behaved pinch-off and saturation of the channel current at temperatures up to 325°C for both HOD and single crystal diamond devices. Single crystal devices have been characterized in both enhancement and depletion-mode at elevated temperatures of 550°C. Drain-to-source currents of 229 μA and 15 mA and transconductances as large as 76 μS/mm and 1.3 mS/mm have been observed for HOD and single crystal devices respectively. These improvements in transistor performance have led to the construction of operational analog and digital circuits using diamond MOSFETs. A simple common-source amplifier utilizing a diamond MOSFET demonstrated a DC gain of 5 at 250°C. Simple NAND and NOR logic gates utilizing a pair of diamond MOSFETs proved operational at 400°C. Optimization of transistor structures and utilization of a diamond transistor as an active load should markedly improve analog and digital performance. The establishment of techniques to reproducibly fabricate functional diamond MOSFETs represents a substantial improvement in diamond electronics technology. The demonstration of active devices fabricated from HOD thin films suggests that this material may be suitable for use as a large-area substrate alternative to single crystal diamond.

5. Acknowledgments

6. References

1. M.W. Geis, *Proc. of IEEE* **79**(5), 669-677, 1991.
2. S.A. Grot, G.S. Gildenblat and A.R. Badzian, *IEEE Elec. Dev. Lett.* **13**(9), 462-464, 1992.
3. R.J. Trew, J.-B. Yan and P.M. Mock, *Proc. of IEEE* **79**(5), 598-620, 1991.
4. C.A. Hewett, C.R. Zeisse, R. Nguyen and J.R. Zeidler, in *1st International High Temperature Electronics Conference,* Albuquerque, NM, 1991.
5. K. Kobashi *et al.*, in *2nd International Conference on the Applications of Diamond Films and Related Materials,* M. Yoshikawa, M. Murakawa, Y. Tzeng and W.A. Yarbrough, **ADC '93**, 35-42, Tokyo, Japan, 1993.
6. K. Shenai, R.S. Scott and B.J. Baliga, *IEEE Trans. Elec. Dev.* **36**(9), 1811-1823, 1989.
7. S.A. Grot. "Active Diamond Electronic Devices." in *Diamond: Electronic Properties and Applications.* L.S. Pan and D.R. Kania ed., 443-461 Kluwer Academic Publishers, Boston, 1994

8. I.M. Buckley-Golder and A.T. Collins, *Dia. and Rel. Mat.* **1**, 1083-1101, 1992.
9. A.T. Collins, *Semicond. Sci. Technol.* **4**, 605-611, 1989.
10. A. Collins, *Mat. Sci. and Eng. B - Solid State Mat. for Adv. Technol.* **11**(1-4), 257-263, 1992.
11. D.L. Dreifus, A.J. Tessmer, J.S. Holmes and L.S. Plano, in *Second International High Temperature Electronics Conference*, D.B. King and F.V. Thome, **Vol. 1**, Charlotte, NC, 1994.
12. K.J. Grahn, P. Kuivalainen and S. Eranen, *Physica Scripta* **T54**, 151-154, 1994.
13. M.W. Shin, R.J. Trew and G.L. Bilbro, in *Second International High Temperature Electronics Conference*, D.B. King and F.V. Thome, **Vol. 1**, IV-15, Charlotte, NC, 1994.
14. H. Shiomi, Y. Nishibayashi, N. Toda and S. Shikata, *IEEE Elec. Dev. Lett.* **16**(1), 36-38, 1995.
15. B.A. Fox *et al.*, in *to be published, Fall Materials Research Society Meeting.*, Boston, Mass, 1995.
16. B.R. Stoner and J.T. Glass, *Appl. Phys. Lett.* **60**(6), 698-700, 1992.
17. Y. Sato, H. Fujita, T. Ando, T. Tanaka and M. Kamo, *Phil. Trans. R. Soc. Lond.* **342**, 31-37, 1993.
18. S. Koizumi, T. Murakami, T. Inuzuka and K. Suzuki, *Appl. Phys. Lett.* **57**, 563-565, 1990.
19. M. Yoshikawa, H. Ishida, A. Ishitani, S. Koizumi and T. Inuzuka, *Appl. Phys. Lett.* **58**, 1387-1389, 1991.
20. M. Werner, V. Schlichting and E. Obermeier, *Dia. and Rel. Mat.* **1**, 669-672, 1992.
21. D.M. Malta, J.A. von Windheim and B.A. Fox, *Appl. Phys. Lett.* **62**(23), 2926, 1993.
22. L.M. Edwards and J.L. Davidson, *Dia. and Rel. Mat.* **2**, 808-811, 1993.
23. K. Nishimura, K. Kumagai, R. Nakamura and K. Kobashi, *J. Appl. Phys.* **76**(12), 8142-8145, 1994.
24. J.F. Prins, *Appl. Phys. Lett.* **41**(10), 950-952, 1982.
25. A.J. Tessmer, K. Das and D. Dreifus, *Dia. and Rel. Mat.* , 89-92, 1992.
26. A.J. Tessmer, L.S. Plano and D.L. Dreifus, *IEEE Elec. Dev. Lett.* **14**(2), 66-68, 1993.
27. B.R. Stoner, S.R. Sahaida, J.P. Bade, P. Southworth and P.J. Ellis, *J. Mater. Res.* **8**(6), 1334, 1993.
28. B.R. Stoner *et al.*, in *Diamond Film Semiconductors*, **SPIE - 2151**, 2-13, Los Angeles, California, 1994.
29. D.L. Dreifus *et al.*, in *Diamond, SiC, and Nitride Wide Bandgap Semiconductors*, C.H. Carter Jr., G. Gildenblat, S. Nakamura and R.J. Nemanich, **339**, 109-120, San Francisco, California, 1994.
30. D.M. Malta, L.S. Plano, G.J. Tessmer, C.-t. Kao and B.A. Fox, in *The Second International High Temperature Electronics Conference*, D.B. King and F.V. Thome, **Vol. 2**, P-75, Charlotte, NC, 1994.
31. L.S. Plano, D.M. Malta and B.A. Fox, in *presented at Third International Symposium on Diamond Materials*, Honolulu, HI, 1993.
32. M.L. Hartsell *et al.*, in *The Second International High Temperature Electronics Conference*, D.B. King and F.V. Thome, **Vol. 2**, p-81, Charlotte, NC, 1994.
33. R.F. Davis, G. Kelner, M. Shur, J.W. Palmour and J.A. Edmond, *Proc. of IEEE* **79**(5), 677-701, 1991.

Applications of Diamond Films and Related Materials: Third International Conference, 1995
Editors: A. Feldman, Y. Tzeng, W. A. Yarbrough, M. Yoshikawa, and M. Murakawa

79

ELECTRON BEAM ACTIVATED DIAMOND DEVICES

Shiow-Hwa Lin, and Lawrence H. Sverdrup

ThermoTrex Corporation, 9550 Distribution Avenue, San Diego, CA 92121-2306

Key words: carrier generation, electron bombardment, high power diamond switch.

Abstract

Natural type IIa diamond wafers of various thicknesses and active areas were used to
construct several electron beam activated diamond devices. The electron bombard-
ment yields a current-voltage characteristic very similar to that of a bipolar transistor.
The device on-state resistance is consistent with a simple carrier drift and space
charge model. The diamond conduction to bombarding current gain ranges from
1,000 to 3,000 depending upon the target thickness and the bombarding electron
energy. Average voltage gradients in diamond targets on the order of a mega-volt per
centimeter were obtained. This enabled switch demonstration with delivery of 26kW
to a resistive load. Using short duration electron pulses, high-repetition-rate sub-
nanosecond switching speed consistent with the circuit time constant is demonstrated.

1. Introduction

The properties of high carrier mobility and saturated velocity, breakdown strength,
and thermal conductivity clearly suggest diamond's superior electronic performance
potential [1]. CVD Diamond films are attracting more attention and progress toward
improving the electronic and material properties is being steadily made. Among the
goals is to make diamond films that have properties comparable or superior to those
of natural diamonds for electronic application [2,3]. Doping of diamond to make
conventional diamond semiconductor devices has met with only limited success [4,5].
Some of diamond's unique properties derive from its large bandgap (5.5eV). Unfor-
tunately this makes photoconductive switching difficult since it requires deep UV
photons [6]. A method that sidesteps these problems is to induce conductivity in
intrinsic diamond by electron bombardment [7]. One electron-hole pair is produced
for each 16.5eV of energy dissipated by the bombarding electrons [8]. Bulk damage
to diamond is not seen until bombarding energies exceed 170keV [9]. For each high
energy bombarding electron in the tens of kilovolt range, thousands of carrier pairs
are generated resulting in a large conductivity modulation and efficient switching.

2. Results and Discussion

Description of the target fabrication, electrode construction and the electron source are
reported in other papers [7,10]. The electron bombarded diamond devices yield a current-

voltage characteristic very similar to that of a bipolar transistor. Fig. 1 shows the family of curves for a 3μm thick, 0.1mm² active area diamond target. For a given bombarding current, conduction current increases with the bias voltage until a saturated current is reached. Higher beam current corresponds to a higher saturated conduction current. Currents of up to 13.5A have been generated in this device, representing a maximum conduction current density of 14kA/cm². Comparison between the bombarding current and the diamond conduction current indicates a gain ranging from 1,000 to 3,000 depending upon the target thickness and the bombarding electron energy. The measured gain is consistent with a Monte Carlo carrier generation code for electron energy deposition [11].

When sufficient carrier densities are generated so that the diamond is operated under the space charge limited conditions as in the lower left corner of Fig. 1, the diamond voltage drop V_d and the diamond current I_d can be modeled by a simple relation

$$\frac{V_d(Volt)}{I_d(Amp)} = 1.2 \cdot 10^4 \frac{d^2}{A}(\Omega) = R_{on}, \qquad (1)$$

where d is the thickness and A is the active area of the diamond device. The model assumes carriers moving at the saturated velocities, no trapping, short transit times so that carrier recombination is negligible, and a uniform carrier generation in the active volume. The electric field profile inside diamond is then quadratic. The measured data in Fig. 1 suggests an on-state resistance of 1.7Ω, whereas the calculated on-state resistance for this diamond target is 1.4Ω. The agreement between the calculation and the measurement is rather good despite the many approximations and assumptions made.

High power diamond switching is demonstrated with a 10μm thick, 2mm² active area wafer. The experiments have been limited by the available bombarding electron beam current. The bombarding beam does not generate enough carriers in the switch volume to minimize the on-state switch resistance. The highest current switched with this device was 51A into a 10Ω load with a 60kV, 30mA electron beam (see Fig. 2). Maximum voltage applied was 750V(DC) which represented a 0.75MV/cm field gradient. More than 26kW was delivered to the load and the diamond internal dissipation was 12 kW. The electron beam power that controls the switching is less than 10% of the switched power.

The target used in a high speed switching experiment was a 12μm thick, 0.5mm diameter active area natural type IIa diamond wafer. Sub-nanosecond electron pulses are generated by a simple inductively-coupled resonant electrostatic deflection system at 56MHz. The electron beam deflection generates a one inch linear scan at the diamond target plane. Faraday cup measurement (cup aperture diameter was 0.5mm) showed that the electron pulse 10-90% risetime was 400ps. The true risetime was probably less since the measurement was instrument limited to 350ps (1GHz bandwidth). Fig. 3a shows the diamond device output for this experiment. It shows a series (112MHz pulse repetition rate) of 2ns long, 60V peak voltage pulses as expected. Risetime of these pulses was measured to be 570ps. The high speed equivalent circuit of this device consists of a current source $I_d(t)$ in parallel with the diamond capacitance as shown in Fig. 3b. The minimum risetime of the circuit (i.e. impulse response) is then

$$t_{rise} = 2.2 \cdot R_l C_d. \tag{2}$$

Since the diamond capacitance is 4.4pF, the RC-limited risetime is 490ps. The measured risetime is consistent with a convolution of the RC-limited risetime and the scope risetime.

3. Conclusion

The present work has demonstrated the potential of diamond for high power and high speed application. Electron beam activation does not require doping as is necessary in conventional three terminal diamond devices. The results show that efficient high power and high speed switching is possible. The device bombarded current-voltage characteristics are consistent with a carrier generation and a simple carrier drift and space charge model. Lower on-state resistance is possible with larger and thinner active area diamond devices. The device high speed performance also agrees with a simple circuit model. Efforts to improve the breakdown characteristics and the quality of large area diamond films are most desirable for scaling this technique to higher power and efficiency.

Acknowledgments

References

1. Proc. IEEE, May 1991 special issue on Large Bandgap Electronic Materials and Components, and K.V. Ravi, Material Science and Engineering, **B19**, 203 (1993).
2. R. Hessmer, M. Schrech, S. Geier and B. Stritzker, Diamond and Related Materials, **3**, 951 (1994).
3. M.I. Landstrass, in Diamond-Film Semiconductors, SPIE **Vol. 2151,** 52 (1994).
4. M.W. Geis, Proc. IEEE, **79**, 699 (1991).
5. J. Bernholc, S.A. Kajihara, and A. Antonelli, in Proc. 2nd Intl. Conf. on New Diamond Science and Technology, Edited by R. Messier, J.T. Glass, J.E. Butler and R. Roy, 923, 1991.
6. C.H. Lee, in Picosecond Optoelectronic Devices, C.H. Lee, Editor, p. 378, Academic Press, 1984.
7. S.H. Lin, L. Sverdrup, K. Garner, E. Korevaar, C. Cason and C. Phillips, in Optically Activated Switching III, SPIE **Vol.1873**, 97, 1993.
8. R.C. Alig and S. Bloom, Phys. Rev. Lett., **35**, 1522 (1975).
9. J. Koike, D.M. Parkin, and T.E. Mitchell, Appl. Phys. Lett., **60**, 1450 (1992).
10. S.H. Lin and L. Sverdrup, in Fourth Intl. Symp. on Diamond Materials, Reno, Navada, May 1995.
11. Tiger codes are available from Oak Ridge National Laboratory, Radiation Shielding Information Center, P.O. Box 2008, Oak Ridge TN 37831-6362.

Bombarded Current-voltage Curves For Diamond #24

- Active area diameter = 300 μm
- Active area thickness = 2.9 μm
- Bombarding beam voltage = 50 kV
- Surface NOT laser machined
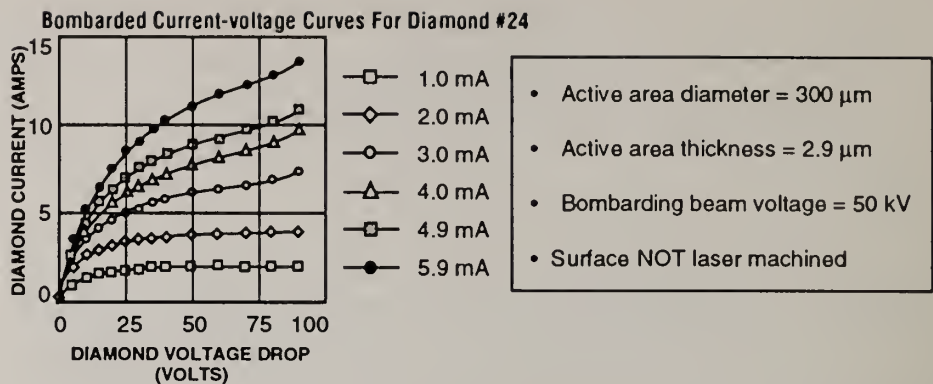
Fig. 1. The electron beam bombarded diamond target has a current-voltage characteristic very similar to that of a bipolar transistor. In this analogy, the bombarding electron beam represents the base current.

-46 dB @ 50 Ω (x 196)

(2a)

(2b)
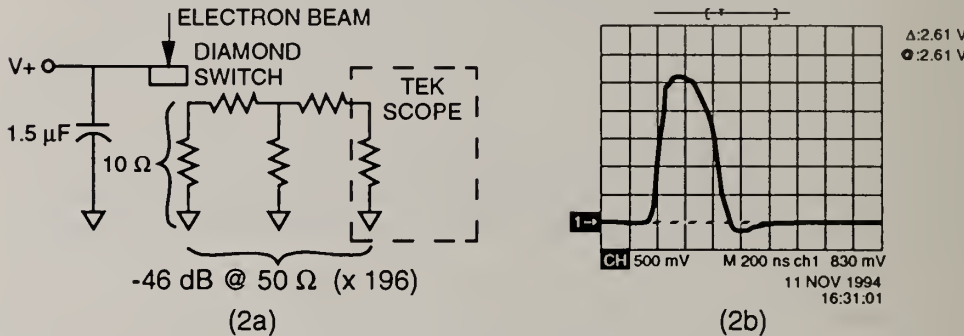
Fig. 2. High power electron beam activated switching. The diamond switch test setup is schematically shown in Fig. 2a. The diamond switch and voltage source are in series with a 10 ohm load. The voltage waveform across the load is shown in Fig. 2b attenuated by 46 dB (1 volt at scope input = 196 volts across load). The data shows that more than 50 amps of current and 26 kW of power were delivered to the load.

(3a)

(3b)
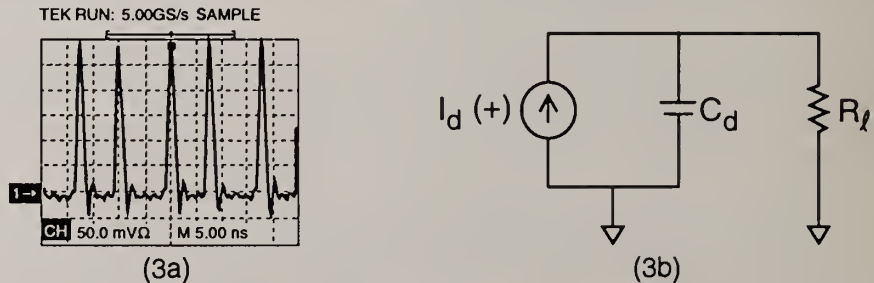
Fig. 3. a). Output from a diamond switch bombarded with a scanning electron beam. Switch active area is 12μm thick and 0.5mm diameter. Electrode area is larger and has a capacitance of 4.4pF. The scope risetime is limited to 350ps by the vertical amplifier. b). Equivalent circuit for this experiment. $R_\ell = 50\Omega$.

Applications of Diamond Films and Related Materials: Third International Conference, 1995
Editors: A. Feldman, Y. Tzeng, W. A. Yarbrough, M. Yoshikawa, and M. Murakawa

83

DESIGN AND PRODUCTION OF DIAMOND DEVICES

W. Haenni, J. P. Dan, A. Perret, J. P. Thiébaud, and P. Weiss

CSEM Swiss Center for Electronics and Microtechnology, Inc.
Rue Jaquet-Droz 1, 2007 Neuchâtel, Switzerland

Key words: diamond device manufacturing, selective area deposition, selective area
            etching

EXTENDED ABSTRACT

The outstanding properties of thin diamond films (hardness, chemical inertness, high
thermal conductivity, high transparency, etc.) make them a good candidate for sensors,
electronic or micromechanical devices, either self-standing or as part of microsystems
[1-14].

The structuring of diamond films and production of devices based on their properties
has been described several times in the literature. Intrinsic as well as p-type doped
diamond layers are now routinely deposited by different suppliers. To make full use of
these layers in microtechnical products, it is necessary to further master suitable
structuring techniques. Two methods have been developed and tested namely, selective
area deposition (SAD) [15-25] and direct etching of blanket-deposited diamond films
[26-32]. Both of these complementary approaches are described here, aiming at the
production of thin diamond film structures suitable for example, to manufacture
chemical sensors (Fig.1), cantilever beams or electrodes.

Direct dry etching of blanket deposited diamond films is an obvious method for
patterning, since this approach is standard for nearly all other deposited materials used
in microelectronics (polysilicon, silicon dioxide and nitride, aluminum, etc.). It was
found that a plasma using an oxygen/fluorine mixture provides an excellent etching of
diamond, at rates of 100 nm/min. The selectivity versus silicon dioxide is more than 50
to 1. This means that silicon dioxide may be used as a mask, giving smooth and well-
faceted diamond structures, with a line definition better than 2 m. Unfortunately,
boron-doped diamond cannot be etched under these plasma conditions. This is
presumably related to the formation of an inert boron carbide film. Other etchant
mixtures described in the literature such as oxygen/argon have been tested, but neither
the etching rate nor the selectivity against the silicon dioxide mask are satisfactory. This
limits the application of the attractive plasma technique to cases where the diamond
does not require electric conduction such as protective and insulating layers, AFM tips
(Fig.2), etc.

The SAD technique used here takes advantage of the fact that the diamond deposition
requires a "priming" operation. By depositing and structuring a photoresist layer on
silicon, silicon nitride or silicon dioxide, the "priming" treatment can be masked off
from defined areas. After photoresist removal, diamond only grows in the "primed"

areas, which were originally free of photoresist. By optimizing this lift-off process, diamond structures with linewidths down to 2,5 m and a pitch of 5 m were obtained. Another method consists of the application of a diamond containing photoresist layer [1,25]. After development of the photoresist layer, diamond grows only where the diamond containing photoresist is remaining.

Any SAD process faces two major difficulties. The first one - which has often been mentioned in the litterature - consists of random nucleation of diamond in non-selected areas, and is now almost mastered. The second one concerns the modification of the silicon nitride substrate during the diamond deposition; however not much is published on this aspect. The gases used during the diamond process deposition are chemically active, and may cause surface modification of the non-selected areas. This results in the formation of a very thin silicon carbide or carbonitride film, which is conducting and has high internal stress. The existence of this highly detrimental layer has been confirmed by electron microanalysis on silicon nitride substrates. This effect can be effectively eliminated by removing the modified silicon nitride in the non-selected areas. Such a process can be implemented in a very straightforward and self-aligned way.

The SAD technique has been applied to the manufacturing of several structures, such as electrical test devices with Van der Pauw and Kelvin patterns. The results presented have been measured on a test lot, together with chains of 18 contacts, consisting of a tungsten/titanium alloy (9:1) heat treated at 450° C. Also molybdenum contacts have been successfully applied, where an ohmic behavior could be observed even without a heat treatment. The typical sheet resistivity for a 1 μm thick layer of boron-doped diamond was 250 Ω/square. For a 10 μm x 10 μm contact, the resistance was typically 100 Ω. The corresponding resistor chains showed a yield of 95 %.

In conclusion it can be said that the mastering of these technologies allow to develop more sophisticated devices such as pressure gauges, particle detectors, flat pannel displays, etc. which could be greatly enhanced by using diamond films of high quality.

REFERENCES

1. I. Taher, M. Aslam, M. A. Tamor, T. J. Potter, R. C. Elder, Sensors and Actuators A 45 (1994) 35
2. M. Aslam, G. S. Yang, A. Masood, Sensors and Actuators A 45,2 (1994) 131
3. T. Roppel, M. Baginski, D. Jaworske, R. Ramesham, Sensors and Materials, 2, 6 (1991) 329
4. H. E. Hintermann, IEEE Colloquium on "Diamond in Electronics and Optics" 7/1
5. M. Binggeli, J. P. Dan, A. Grisel, W. Hänni, H. E. Hintermann, P. Krebs, C. Müller, Proceedings, 2nd Intern. Conf. on the Application of Diamond Films and Related Materials, Tokyo, (1993) 51
6. H. J. Boving, W. Hänni, M. Maillat, J. P. Dan, P. Niedermann, Proceedings, MRS Spring Meeting, San Francisco, (1995) to be published
7. N. Blanc, N. DeRooij, University of Neuchâtel, internal research on AFM tips
8. S. J. O'Shea, R. Atta, M. E. Welland, submitted to Review Scientific Instruments
9. D. A. Fischer, W. Phillips, J. Vac. Sci. Technol. A 10,4 (1992) 2119
10. K. Miyata, D. L. Dreifus, J. Appl. Phys. 73,9 May (1993) 4448
11. M. W. Geis, N. N. Efremow, J. D. Woodhouse, M. D. McAleese, M. Marchywka, D. G. Socker, J. F. Hochedez, IEEE Electron Device Letters, 12,8 (1991) 456

11. M. W. Geis, N. N. Efremow, J. D. Woodhouse, M. D. McAleese, M. Marchywka, D. G. Socker, J. F. Hochedez, IEEE Electron Device Letters, 12,8 (1991) 456

12. H. Nakahata, K. Higaki, A. Hachigo, S. Shikata, N. Fujimori, Y. Takahashi, T. Kajihara, Y. Yamamoto, Jpn. J. Appl. Phys. 33 (1994) 324

13. B. Löchel, H. J. Schliwinski, H. L. Huber, J. Trube, L. Schäfer, C. P. Klages, H. Lüthje, Microlectronic Engineering 17 (1992) 175

14. M. F. Ravet, A. Gicquel, E. Anger, Z. Z. Wang, Y. Chen F. Rousseaux, Proceedings, 2nd Intern. Conf. on the Application of Diamond Films and Related Materials, Tokyo, (1993) 77

15. K. Higuchi, S. Noda, Diamond and Related Materials, 1 (1992) 220

16. J. L. Valdes, J. W. Mitchel, J. A. Mucha, L. Seibles, H. Higgins, J. Electrochem. Soc. 138,2 (1991) 635

17. R. Ramasham, Thin Solid Films, 229 (1993) 44

18. R. Ramasham, T. Roppel, J. Mater. Res. 7,5 (1992) 1144

19. S. J. Lin, S. L. Lee, J. Hwang, T. S. Lin, J. Electrochem. Soc. 139,11 (1992) 3255

20. C. D. Iacovangelo, European Patent Application 0 528 592 A1, (1993)

21. S. Katsumata, S. Yugo, Diamond Films and Technology, 3,4 (1994) 199

22. X. Ning, Z. Zhihao, S. Zhuo, Z. Xiaofeng, X. Chunfang, W. Peiming, X. Peisheng, Surface and Coatings Technology, 63 (1994) 159

23. M. Y. Mao, T. P. Wang, J. F. Xie, W. Y. Wang, MEMS (1995) 392

24. X. Jiang, E. Boettger, M. Paul, C. P. Klages, Appl. Phys. Lett 65,12 (1994) 1519

25. S. Katsumata, Y. Oobuchi, T. Asanno, to be published in Diamond and Related Materials

26. B. Miller, R. Kalish, L. C. Feldman, A. Katz, N. Moriya, K.Short, A. E. White, J.Electrochem. Soc. 141,4 (1994) 141

27. B. R. Stoner, G. J. Tessmer, D. L. Dreifus, Applied Physics Letters 62,15 (1993) 1803

28. V. Y. Armeyev, NN. I. Chapliev, I. M. Chistyakov, V. I. Konov, V. G. Ralchenko, V. E. Strelnitsky, V. Ya. Volkov, Materials and Manufacturing Processes, 8,1 (1993) 9

29. C. Vivensang, G. Turbann, E. Anger, A. Gicquel, Diamond and Related Materials, 3,4-6 (1994) 645

30. N. Liu, Z. Ma, X. Chu, T. Hu Z. Xue, X. Jiang, S. Pang, J. Vac. Sci. Techno. B 12.3 (1994) 1712

31. V. I. Konov, V. G. Ralchenko, S. M. Pimennov, A. A. Smoli, T. V. Kononenko, Proceedings of the SPIE, 2045, (1994) 184

32. M. Marchyka, P. E. Pehrsson, S. C. Binari, D. Moses, J. Electrochem. Soc. 140,2 (1993) 19
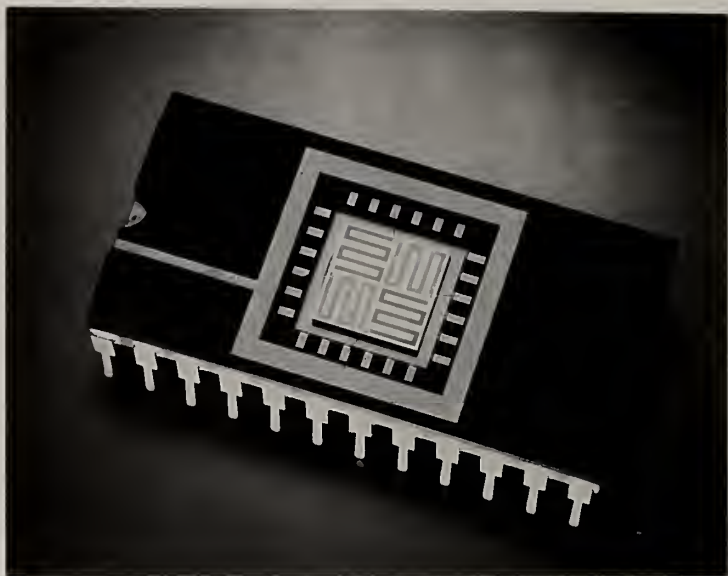
Fig. 1: Wheatstone bridge element of a gas sensor device
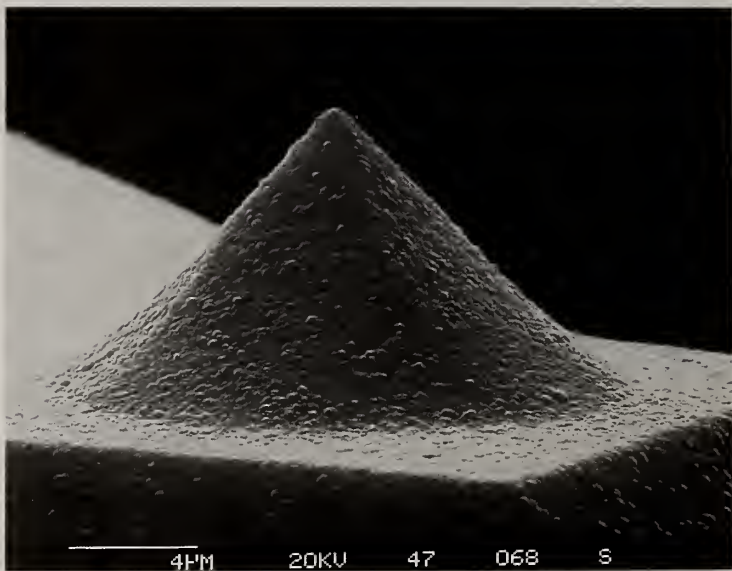
Fig. 2: Silicon AFM tip with a boron doped diamond coating

Applications of Diamond Films and Related Materials: Third International Conference, 1995
Editors: A. Feldman, Y. Tzeng, W. A. Yarbrough, M. Yoshikawa, and M. Murakawa

87

HIGH SENSITIVITY AND WIDE TEMPERATURE TOLERANCE HYDROGEN GAS SENSORS UTILIZING PECVD DIAMOND TECHNOLOGY

Y. *Gurbuz[1]*, *W. P. Kang[1]*, *J. L. Davidson[1]*, *D.V. Kerns[1]*, *and B. Henderson[2]*

[1]Dept. of Applied and Engineering Sciences, Vanderbilt University, Nashville, TN 37235, U.S.A
[2]Physitron, Inc., 3304-A Westmill Drive, Huntsville, Al 35805

Key words: diamond, hydrogen, PECVD, sensor

Abstract

A novel diamond-based hydrogen sensor using Pd/i-diamond/p-diamond metal-insulator-semiconductor structure has been developed. Hydrogen-sensing behaviors of the device have been analyzed as a function of hydrogen partial pressure and temperature by using current-voltage (I-V) and capacitance-voltage-frequency (C-V-F) methods. The effects of the hydrogen adsorption on the device parameters are investigated. The hydrogen sensitivity is high, reproducible, and repeatable over a wide temperature range including room temperature. The use of the diamond film technology opens a door for the development of wide temperature tolerance microelectronic gas sensors.

I. Introduction

Extensive research in catalytic-gate microelectronic gas sensors such as MOS capacitors [1], MOSFET's [2], Schottky diodes [3] and lately MOS system with the adsorptive oxide layer [4] have been conducted in silicon and GaAs technologies. But the limited operating temperature range of these conventional semiconductor-based gas sensors (Si-based technology less than 150°C and GaAs-based technology less than 300°C) has critically restricted their wide utilization for such applications as the detection of toxic gas from a combustion process and *in situ* emission monitoring.

Recent advances in the plasma enhanced chemical vapor deposition (PECVD) process have resulted in the realization of high quality and high temperature tolerant polycrystalline diamond films [5]. Diamond is considered to be very useful material for solid-state electronic applications due to its wide band gap(5.5eV), high breakdown

voltage(10^6-10^7 V cm^{-1}), high thermal conductivity(20 W cm^{-1} K^{-1}), electrical stability, and compatibility with hostile environments. The PECVD method allows polycrystalline diamond to be grown on many different substrates at a much lower cost than other semiconductor films.

We have developed the first reported prototype diamond-based chemical gas sensor using thin layered Pd/i-diamond/p-doped diamond structure. Hydrogen sensing characteristics of the device have been investigated as a function of hydrogen partial pressure and temperature. The hydrogen sensitivity is found to be large, repeatable and reproducible. Analysis of the device parameters confirm that the hydrogen sensitivity of the device is attributed to the adsorption of hydrogen dipoles at the Pd/i-diamond interface. The voltage drop across the hydrogen dipole layer modifies the I-V and C-V characteristics of the device.

II. Experimental

The diamond-based hydrogen sensor was fabricated in a layered Pd/i-diamond/p-diamond configuration on a tungsten substrate. P-type polycrystalline diamond films, doped *in situ* from a boron solid source, 5-10 μm thick were deposited on the surface of the tungsten substrate (2cm×2cm) using PECVD. A thin undoped diamond interfacial layer was then deposited on the p-diamond layer. Diamond films were deposited using the parameters: 99% hydrogen and 1% methane gas, microwave power of 1500 watts, pressure of 40 torr, and a substrate temperature of 850°C. Films were then annealed for one minute at 850°C in argon. Raman spectroscopy of these diamond films shows the 1332cm^{-1} peak indicating characteristic sp^3 bonding and a slight broad graphite peak at 1580 cm^{-1}. SIMs studies of the p-diamond layer indicate a boron doping concentration of 10^{18}cm^{-3}. Finally, a palladium electrode 0.1μm thick and 1mm in diameter was thermally evaporated on the i-diamond surface to complete the device.

III. Results and Discussions

Typical I-V characteristics of the diamond-based hydrogen sensor, before and after exposure to H$_2$ at the operating tempeature of 27°C, are shown in Fig. 1. The figure shows a large change in the I-V characteristics of the device, shifted from near ohmic to rectifying behavior, upon the device's exposure to 0.01 torr of H$_2$ gas. The effect is reproducible and repeatable upon adsorption/desorption of hydrogen gas. Fig. 2 shows the detection sensitivity, ΔI, versus hydrogen partial pressure for the device operating at T=55°C under a fixed (-0.4 V) forward bias voltage. The figure shows a rapid increase in ΔI upon H$_2$ adsorption at low H$_2$ partial pressures, followed by a trend to saturation at higher H$_2$ partial pressures. A typical repeatability test of the sensor for the detection of H$_2$ gas in an open air(1 atm.) background is shown in Fig. 3. The device, maintained at 85°C, was exposed to a series of H$_2$ pulses with a fixed flow rate 10ml/min. The device responds with a recovery time in seconds upon turning the H$_2$ gas

on/off, showing that the detection of H_2 is fast, sensitive, reproducible, and repeatable.

Analysis of the electrical conduction mechanisms of the sensor in air and in hydrogen environments at T=27°C is shown in Fig. 4 and 5. The results show the conduction in reverse bias region (Fig. 4) and that space charge limited current (SCLC) occurs in the forward bias region(Fig. 5). Therefore, accurate determination of the reverse saturation current, I_0, and ideality factor, n, can be extracted from the reverse I-V characteristics to the zero-voltage intercept and the gradient of the plot, respectively. The calculated values of the ideality factor, n, and barrier height, ϕ_b, are given in Fig. 4. As seen from the figure, ϕ_b changes by 0.05 eV after exposure to H_2. Ideality factors determined from the straight line sections of the plots were 1.15 for the device examined and they remain unchanged. In forward bias region, the voltage drop accross the hydrogen dipole reduces the electric field across the i-diamond layer thereby decreasing the current of the sensor in H_2 environment. Fig. 6 shows the C-V characteristics of the Pd/i-diamond/p-diamond hydrogen sensor operating at 100KHz before and after exposure to hydrogen. Open markers depict the capacitance values prior to hydrogen adsorption and solid markers after exposure to hydrogen. A large decrease in capacitance upon H_2 absorption is evident from Fig. 6. It can also be seen that for the same frequency a larger change in capacitance upon hydrogen adsorption is evident at the higher temperature.

IV. Conclusion

Performance of the new diamond-based hydrogen sensor has been demonstrated. The study shows that PECVD diamond film can be utilized in a Pd/i-diamond/p-diamond configuration for the detection of H_2. It is believed that the use of PECVD diamond film in such devices will implement microelectronic-gas sensors for a wider and higher temperature applications than those based on conventional semiconductor technology.
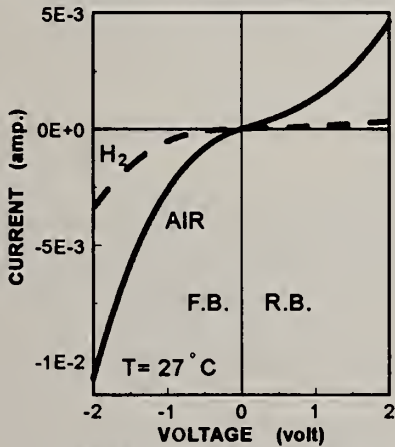
Figure 1. I-V of Pd-Diamond H2
Sensor: (a) in air, (b) in 0.01 Torr H2
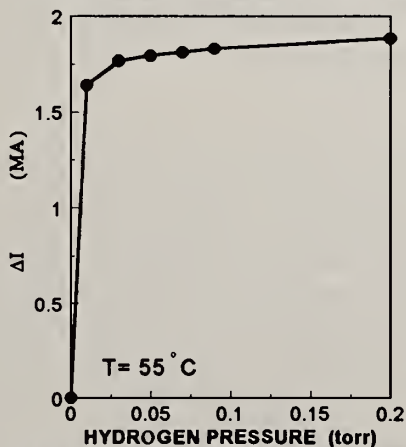
Figure 2.Change in Diode Current with
Hydrogen Partial Pressure at 55 °C

90
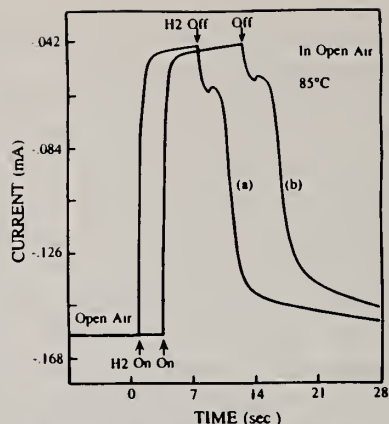
Figure 3. Repeatability Test of the Sensor for H_2 Detection in Open Air
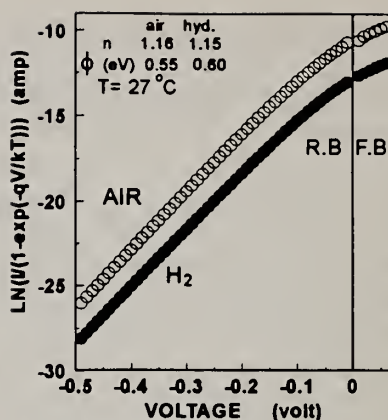
Figure 4.Plot of Ln(I/(1-exp(-qV/kT))) vs. Voltage
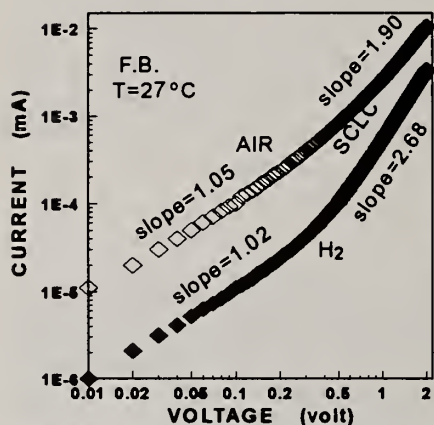
Fig. 5. I-V Characteristics of the device
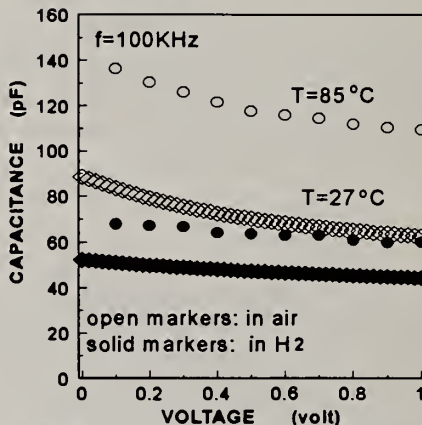
Fig. 6. C-V Characteristics of the device

References

1. I. Lundstrom, S. Shivaraman and C. Svensson, A hydrogen-sensitive Pd-gate MOS transistor *J. Appl. Phys.*, **46**, 3876-3881 (1975)
2. I. Lundstrom, A. Spetz, F. Winquist, U. Ackelid and H. Sundgren, Catalytic Metals and Field-effect Devices, *Sensors and Actuators* B, **1**, 15-20 (1990)
3. W. P. Kang and Y. Gurbuz, Comparison and Analysis of Pd- and Pt-GaAs Schottky Diodes for Hydrogen Detection, *J. Appl. Phy.* , **75**, 8175-8181 (1994)
4. W. P. Kang and C. K. Kim, Performance and detection mechanism of a new class of catalyst(Pd, Pt, or Ag)-adsorptive oxide(SnO_x or ZnO)-insulator-semiconductor gas sensors, *Sensors and Actuators*, **22**, 47-55 (1994)
5. J. L. Davidson, "Diamond Properties and Electronic Devices," Invited paper, *International Symposium on Diamond Science and Technology (Electrochemical Society Meeting)*, Hawaii, May (1993)

BORON-DOPED DIAMOND ELECTRODES FOR ELECTROCHEMICAL APPLICATIONS

Heidi B. Martin, Alberto Argoitia, <u>John C. Angus</u>, Alfred B. Anderson and Uziel Landau

Case Western Reserve University, Cleveland, OH 44106 USA

Key Words: electrodes, electrochemistry, hydrogen evolution, oxygen evolution

Abstract

The electrochemical behavior of boron-doped diamond electrodes in liberating hydrogen and oxygen from aqueous solutions was studied by voltammetry. Compared to platinum, the diamond electrodes gave a much wider potential range over which no significant water decomposition occurred. They are, therefore, suitable substrates for reactions spanning a wide potential range. Diamond electrodes have the further advantage of dimensional and chemical stability, even in very aggressive environments.

1. Introduction

There have been a few prior reports of the use of diamond electrodes in aqueous electrochemistry [1,2,3], but the field remains largely unexplored. We describe a simple technique for making boron-doped diamond electrodes and their behavior in liberating hydrogen and oxygen from aqueous electrolytes.

2. Experimental

Boron-doped diamond films were grown on 0.5 mm diameter tungsten wires using hot-filament assisted chemical vapor deposition from 1% CH_4 in H_2 at 20 torr. The filament temperature was approximately 2100C. The boron source was a compact of hexagonal boron nitride (h-BN). The tungsten wires were suspended with their axes parallel to and at a distance of 1 mm from the h-BN during diamond deposition. Continuous, well-faceted diamond films of about 10 μm in thickness and a (111) texture were grown in 24 hours. See Figs. 1 and 2. Secondary ion mass spectroscopy showed a uniform doping level of $\approx 10^{21}$ boron atoms/cm^3; no nitrogen was detected. The electrodes were unaffected by prolonged etching in HNO_3.

Prior to the electrochemical measurements, the diamond electrodes were ultrasonically cleaned in an Alconox solution and rinsed with ultrapure water. The Pt electrodes were soaked in concentrated HNO_3 and heated in a flame until red hot. The 0.5 M H_2SO_4 electrolyte was prepared using analytical grade H_2SO_4 and ultrapure water. Cyclic voltammograms were obtained at a scanning rate of 200 mV/sec. Potentials were measured with respect to a standard calomel electrode and converted to the standard hydrogen scale. IR compensation was also made. A Pt counter electrode was used for all runs. Geometric areas, not corrected for surface roughness, were used to calculate current densities from the observed currents.

Voltammograms for platinum and boron-doped diamond electrodes are shown in Figs. 3 and 4. Each scan was repeated over 20 times with essentially identical traces. The diamond electrodes gave a much broader potential range over which no significant water decomposition occurred compared to Pt. Fig. 4 shows that the potential range without water decomposition on the diamond electrodes extended from approximately -1.5 V to +2.75 V (vs. the standard hydrogen electrode). Diamond electrodes treated in a 0.1 M NaF solution gave an even wider potential range. For comparison, in Fig. 3 the potential range without water decomposition on Pt is from approximately 0 to 1.75 V, which is in agreement with literature data.

3. Summary and Conclusions

Voltammetry results show a wide potential range over which boron-doped diamond electrodes can be used to perform electrochemical reactions without hydrogen or oxygen evolution. Diamond film electrodes also provide extreme chemical and dimensional stability. These properties make diamond electrodes extremely attractive for electrolytic applications including gas evolution, electrochemical syntheses, electrochemical sensors, and redox reactions. Since these applications require only thin films of diamond, the cost should be attractive.

4. Acknowledgements

5. References

1. Yu. V. Pleskov, A.Ya. Sakharova, M.D. Krotova, L.L. Bouilov, and B.V. Spitsyn, *J. Electroanal. Chem.* **228**, 19-27 (1987).
2. R. Tenne, K. Patel, K. Hashimoto and A. Fujishima, *J. Electroanal. Chem.* **347**, 409-415 (1993).
3. Greg M. Swain, *J. Electrochem. Soc.* **141**, 3382-3393 (1994).
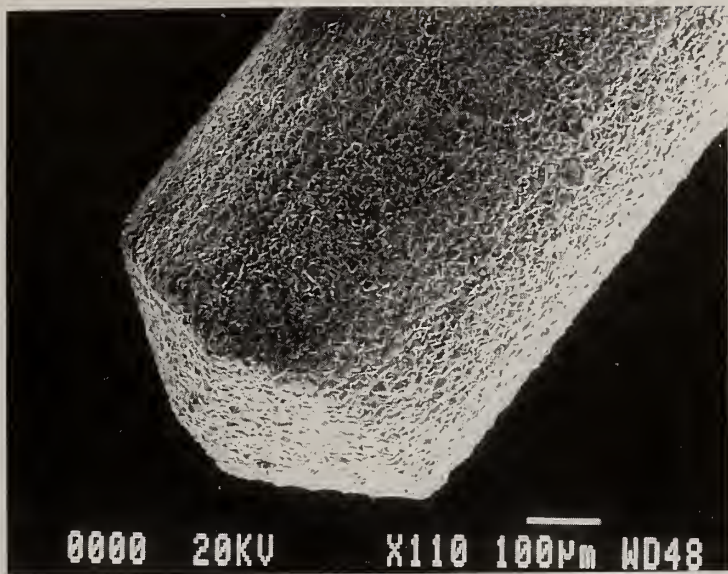
Figure 1. Scanning electron micrograph of boron-doped diamond electrode.
The mark is 100 μm.
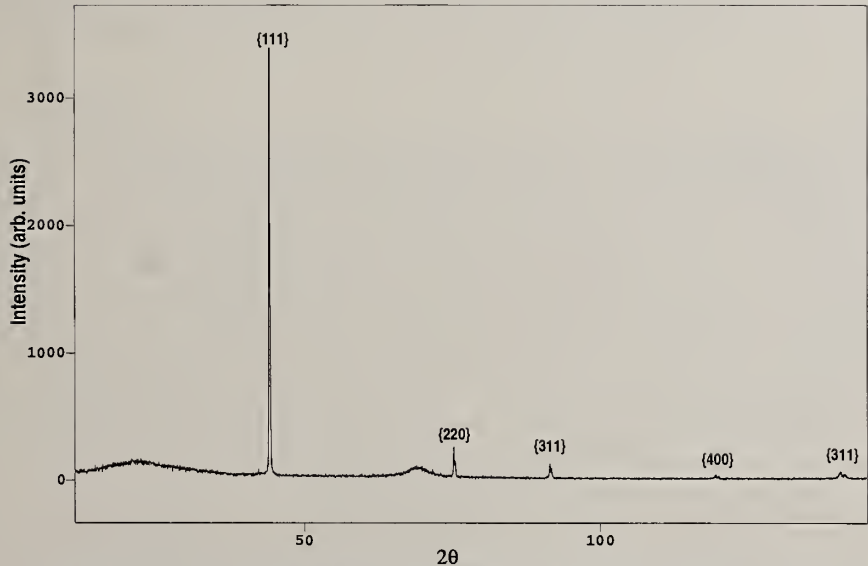
Figure 2. X-ray diffractogram of boron-doped diamond film. Note
significant (111) texture.
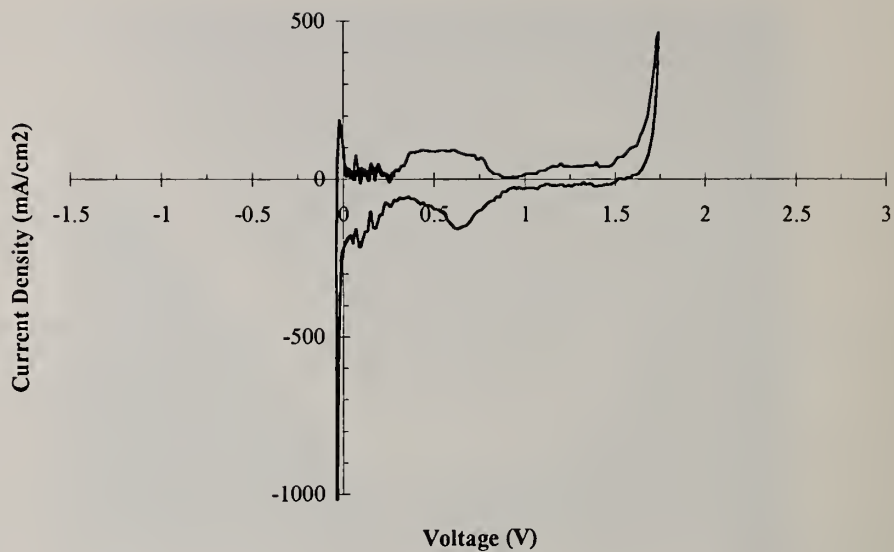
Figure 3. Cyclic voltammogram of Pt electrode in 0.5 M H_2SO_4
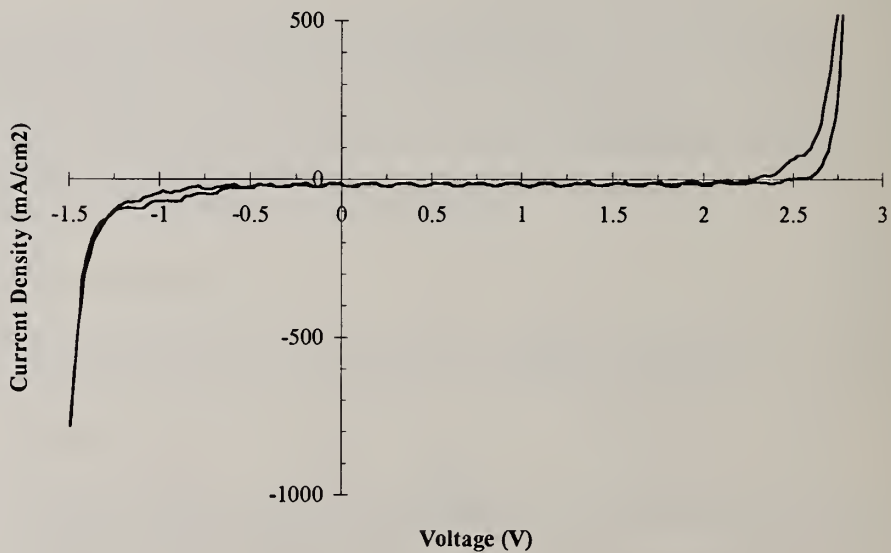
Figure 4. Cyclic voltammogram of boron-doped diamond electrode in 0.5 M H_2SO_4

Applications of Diamond Films and Related Materials: Third International Conference, 1995
Editors: A. Feldman, Y. Tzeng, W. A. Yarbrough, M. Yoshikawa, and M. Murakawa

95

PIEZORESISTIVE GAUGE FACTOR OF POLYCRYSTALLINE DIAMOND MEASURED AT DIFFERENT FIELDS AND TEMPERATURES

S. Sahli, X. Hou, and M. Aslam

Department of Electrical Engineering, Michigan State University,
East Lansing, MI 48824, U.S.A.

Abstract

The gauge factor of boron-doped diamond films grown on oxidized Si substrates by hot filament chemical vapor deposition (CVD) reactor was measured by the cantilever beam method. For an annealed film, the gauge factor increases strongly with electric field only in the range of 411-611V/cm. Interestingly, the zero-stress resistivity decreases strongly in this range. Such an increase in gauge factor is not found for an un-annealed film. The field-dependence of gauge factor is reported for the first time. The gauge factor was also measured in the temperature range of 22-80 $^{\circ}$C for two samples with different doping levels. Preliminary results suggest that the increase of gauge factor with temperature is prominent only for high resistivity.

1. Introduction

The discovery of a large piezoresistive gauge factor in p-type vapor-deposited diamond films [1] has generated a large interest for diamond piezoresistive sensors [2,3,4]. The reported gauge factor values are in the ranges of 5-100 and 200-550 for polycrystalline and monocrystalline diamond films, respectively [1,4]. As the electronic properties of polycrystalline diamond are sensitive to temperature and high electric field, it is important to carefully study the effect of field and temperature on the piezoresistive gauge factor. Although an increase of gauge factor with temperature has been measured in a limited temperature range [1], no data are available for the field dependence of gauge factor. In this paper, we study the effect of field and temperature on the piezoresistive gauge factor of polycrystalline diamond films for the field and temperature ranges of 0.02-611V/cm and 22-80 $^{\circ}$C, respectively. Initial results show that the dependence of gauge factor on electric field and temperature is related to doping density, annealing, texture and grain size.

2. Experimental

The piezoresistors used in this study were grown on oxidized Si substrates using hot filament CVD (HFCVD). Pre-deposition selective nucleation was achieved by patterning a mixture of diamond powder photoresist (DPPR) using standard photolithography [5]. In contrast to other nucleation techniques, this procedure insured that no mechanical damage was inflicted on the substrate. A layer of undoped diamond was grown to 1.3μm followed by a doped layer of 0.2-0.3μm. Pure boron powder was used for in-situ doping. This double layer insures that the active sensing film is continuous and it maximizes the vertical doping uniformity. Film annealing was carried out at $600^{o}C$ in N_2 environment for 10 min using a rapid thermal processor (RTP). Thermally evaporated Al, annealed at $400^{o}C$ in N_2 in RTP, was used for ohmic contacts to diamond. The diamond quality was monitored by Raman spectroscopy and secondary electron microscopy. The gauge factor was measured using a cantilever beam setup [1]. We assume that stress is continuous at the interface between the diamond resistors and the silicon substrate since the diamond film is much thinner than the substrate and the resistors are much smaller in size. Also, we neglect the effect of internal stress in the diamond film. Sample temperature was maintained constant to within $\pm 0.5^{o}C$ using a temperature control loop and a K-type thermocouple.

3. Results and Discussions

We first observed that the value of the resistivity of B-doped diamond films depends on the electric field applied to measure it. As the piezoresistive property, at least for semiconductors, is essentially related to resistivity we decided to investigate the effect of electric field on the measured piezoresistive gauge factor of these films. The gauge factor of an annealed sample, computed at 430 μstrain, is plotted as a function of applied electric field in Fig. 1. The results show that the gauge factor is independent of field in the range of 0.02-206V/cm but increases drastically at fields in the range of 411 - 611 V/cm. Interestingly, as shown by the inset of Fig. 1, the zero-stress resistivity decreases in this range. Similar measurements performed on an un-annealed polycrystalline resistor, as shown in Fig. 2, show that the measured piezoresistive behavior is not very stable. Due to this instability it is not clear wether the observed slight increase in gauge factor is true or an artifact of noise. The inset of Fig. 2 shows that, unlike the case of the annealed sample, the zero stress resistivity decreases over the range of 0.02-600 V/cm.

Previously, the effect of temperature on the gauge factor of diamond was reported only for one doping level and for a limited temperature range [1]. In the present work, the gauge factor of p-type CVD diamond films was measured in the temperature range of 22-80 ^{o}C for two samples with different doping levels. The results plotted in Fig. 3 along with the data from [1], seem to indicate that the effect of temperature on gauge factor is strongly related to doping density. The sample with resistivity of 5Ω-cm [1]

shows a rapid increase of gauge factor with temperature. The gauge factor of the 0.7Ω-cm sample also increases with temperature; but at a much slower rate. In contrast, the gauge factor of the 0.07Ω-cm sample slowly decreases with temperature.

4. Conclusions

The gauge factor of B-doped polycrystalline annealed diamond films shows a rapid increase for electric fields above 200V/cm. It is noteworthy that the zero-stress resistivity of the annealed film decreases rapidly above 200 V/cm. Our results suggest that the gauge factor increase with temperature is highest for samples with the lowest doping concentration.

5. Acknowledgment

6. References

[1] M. Aslam et al., "Piezoresistivity in vapor-deposited diamond films," Appl. Phys. Lett., 60(23), Jun. 1992, 2923-2925.
[2] O. Dorsch et al., "Piezoresistive effect of boron-doped diamond thin films," Diamond 92 (ICNDST-3), Heidelberg, Germany, 1992.
[3] D.R. Wur, J. L. Davidson et al., "Fabrication and Characterization of Polycrystalline Diamond Film for strain Sensing Applications," Transducers 93, Yokohama, Japan, 1993.
[4] I. Taher, M. Aslam, M. Tamor, "Piezoresistive Microsensors using p-type CVD Diamond Films", Sensors and Actuators A, vol. 45 (1), 35-43, 1994.
[5] A. Masood et al. "Techniques for Patterning of CVD Diamond Films on non-Diamond Substrate," J. Electrochem. So., Vol. 138, No. 11, Nov. 1991, L67-68
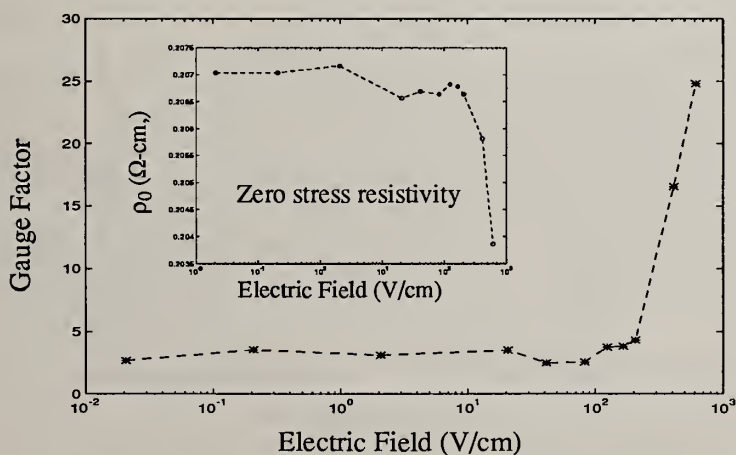
Figure 1. Effect of electric field on the gauge factor of B-doped and annealed polycrystalline diamond film.
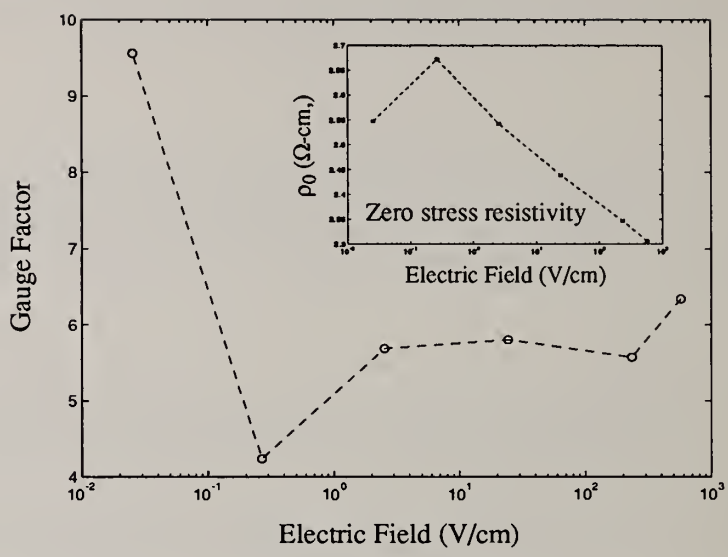
Figure 2. Effect of electric field on the gauge factor of B-doped unannealed polycrystalline diamond film.
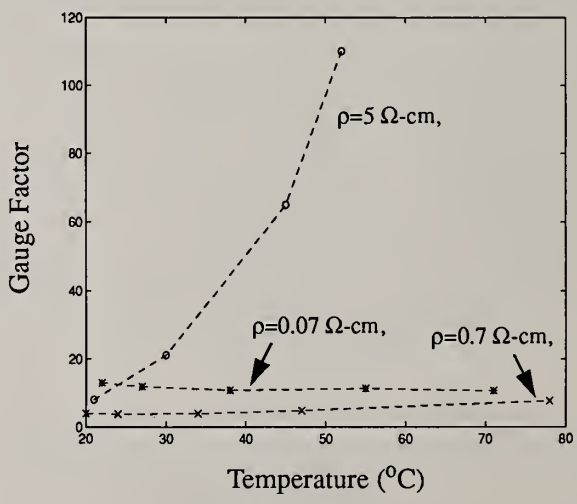
Figure 3. Effect of temperature on the gauge factor B-doped annealed polycrystalline diamond

Applications of Diamond Films and Related Materials: Third International Conference, 1995
Editors: A. Feldman, Y. Tzeng, W. A. Yarbrough, M. Yoshikawa, and M. Murakawa

99

DIAMOND PHOTOVOLTAICS: CHARACTERIZATION OF CVD DIAMOND FILM-BASED HETEROSTRUCTURES FOR LIGHT TO ELECTRICITY CONVERSION

G.Popovici[1],M.A.Prelas[2], S.Khasawinah[2], T.Sung[2],V.I.Polyakov[3], P.I.Perov[3], N.M.Rossukanyi[3], A.I.Rukovishnikov[3], A.V. Khomich[3], A.I. Krikunov[3], I.G.Termetskaya[4], and V.P.Varnin[4]

[1] Rockford Diamond Technology, 501 S. Sixth Street, Champain, IL 61820-5579.
[2] Department of Nuclear Engineering, University of Missouri Columbia, Missouri 65211.
[3] Institute of Radio Engineering & Electronics, RAS, 11 Mohovaya str., 103907 Moscow, Russia.
[4] Institute of Physical Chemistry, RAS, 31 Leninsky av, 117915 , Moscow, Russia.

Keywords : Photovoltaics, barrier junctions, boron-doped films

Abstract

Undoped and boron-doped CVD polycrystalline diamond film photovoltaic structures were prepared and their electrical, optical and photoelectric characteristics were investigated. The effect of annealing on these characteristics was studied. The diamond film heterostructures developed open circuit photovoltages greater than 1 V.

1. Introduction

Photovoltaic effects in diamond film structures are of interest for photovoltaic device applications, particularly for ultraviolet radiation conversion into electricity [1]. These structures must contain built-in electric field regions where the photogenerated carriers are separated, such as p-n junctions, unipolar barrier structures, or insulating films with electrodes of metals with different work functions on opposite sides. In this paper, we present new experimental data on photovoltaic structures with built-in electric fields based on undoped and boron-doped polycrystalline diamond films.

2. Experimental results and discussion

Boron-doped polycrystalline diamond films were grown on silicon and tungsten substrates by hot filament chemical vapor deposition as described elsewhere [2,3]. Free-standing B-doped diamond film samples were used. All the samples were

annealed in air at different temperatures ranging from 100 to 700 C, with the aim to find the fabrication regime of the structures with the best electric and photoelectric characteristics.

In this work, Ni and Ti electrodes were used. The work function values of Ni and Ti allow to get a reasonably high (more than 1 eV) barriers to diamond. Of course, interface states can influence, to a great extent, the barrier hight, as well as other electrical and photoelectric properties of the metal/diamond junctions. Semitransparent electrodes with an area about 2 mm^2 were deposited on the undoped diamond films by evaporation of Ni in vacuum and d.c. magnetron sputtering Ti, the W substrate was used as the second electrode. For free standing boron-doped diamond film, Ni electrodes were deposited onto both top and bottom surfaces. Current-voltage (I-V) and capacitance-voltage (C-V) characteristics were measured on all samples. Photoelectric characteristics were measured in open circuit conditions with flash lamp pulse illumination. It was shown [4] that this technique allows to measure the barrier heights at different interfaces in the structure under study. In this work, we used 0.2 ms flash lamp light pulses. The light intensity was high enough to get the photovoltage to about the saturation value for the given conditions, so these data could be used for estimation of the barrier heights or their difference on opposite sides of the diamond film.

a) Schottky-type barrier structures. The I-V characteristics of the Ni/Diamond/Ni structure as measured in "sandwich" configuration (between two Ni electrodes on opposite sides of the film) are shown in Fig.1*a*. Curve 1 was taken from the sample with electrodes deposited before annealing the diamond film, and curve 2 - from the sample made with the diamond film annealed at 530 C for 20 min. It is seen that I-V
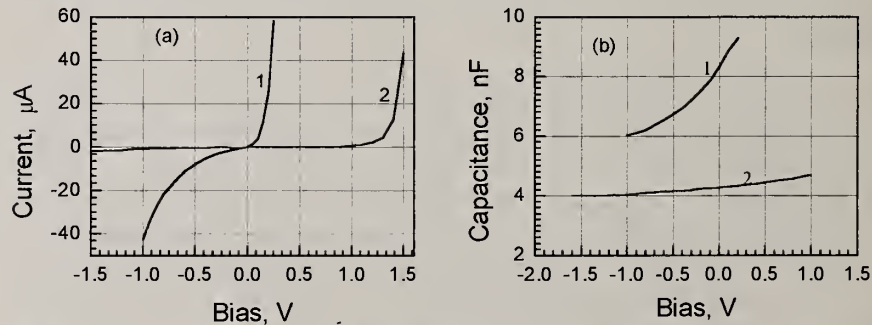
Fig.1. I-V (*a*) and C-V (*b*) characteristics of Ni/Diamond/Ni structure made of the free- standing diamond films by depositing Ni electrodes before (1) and after (2) annealing.

characteristics are of rectifying type, especially after the thermal treatment. One can conclude that the Ni electrodes are of different type on the top and bottom surfaces of the diamond film. The C-V characteristics of the Ni/Diamond/Ni structure also

changed on annealing. Smaller capacitances resulted, with a weaker voltage dependence (Fig. 1,*b*). Assuming the simplest Schottky type barrier structure, such a behavior might result from an increase of the depletion region width W. However, the real situation could be more complicated; for example, an insulating layer might to be formed on top of the film on oxidation [5], thus, decreasing the capacitance of the structure.

The photoelectric results for the Ni/Diamond/Ni sample depended drastically on annealing, too, with the open circuit photovoltage increased from 0.2 to above 0.7 V. The kinetics of the photovoltage measured at different biases showed the possibility of controlling the barrier height through biasing (Fig.2,*a*). It is seen that at certain bias voltages, the photovoltage approaches zero, and even changes its sign. A realistic
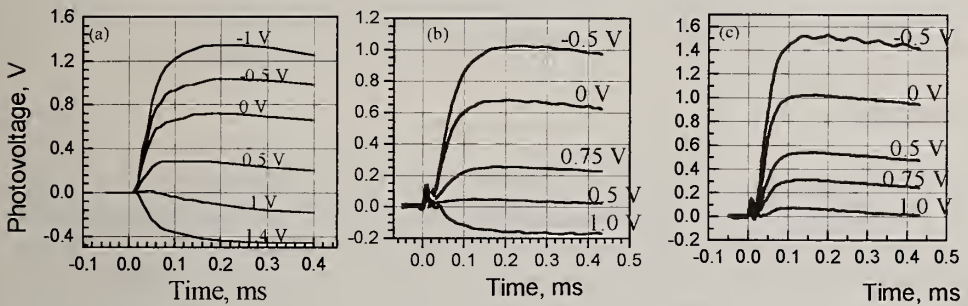
Fig. 2. The dependence of the kinetics of the photovoltage on the bias applied for barrier Ni/Diamond/Ni structure (*a*), non-doped diamond film based diodes with Ni (*b*) and Ti (*c*) top electrodes.

model for our samples, which describes qualitatively all the experimental data, includes the existence of a high resistance layer under the metal electrode (in analogy with metal-insulator-semiconductor structures). In such a model, the flat band case could be realized at definite bias voltages [6], resulting in zero photovoltage. It looks probable that the annealing modified the near surface layer to make it semiinsulating. This decreased the leakage current and helped obtaining higher photovoltage values. The thickness of this layer was estimated from the C-V characteristics as 10 nm.

b) Metal-insulator-metal structures. The I-V characteristics for the most of the annealed samples were slightly nonlinear and symmetrical at voltages less than 1-2 V, with rather low current levels, 10^{-6}-10^{-10} A. From these data, one can come to conclusion that the current is of leakage nature and the carriers flow mainly through the intergrain regions which may consist of non-diamond carbon phase. Hence, in this case there are rather high barriers at the diamond-metal interfaces which prevent in a great extent the carrier injection into the conductance or the valence bands. The C-V

characteristics taken from all the annealed samples showed no voltage dependence of the capacitance. This fact evidences in spreading the depletion region through all the thickness of the film - just the case which is expected for undoped insulating films. Fig.2, *b* and *c*, show the photovoltage results obtained for the sample consisting of the 1 μm thick undoped diamond film grown on W substrate, with two different metal electrodes on top of the film. Photovoltage values were near to the saturation, as was confirmed using neutral filters. Large saturation photovoltage values of 0.7 V for Ni electrode and in excess of 1 V for Ti electrode were obtained for the case of zero bias voltages. When applying the bias voltage to the sample, the built-in electric field can be increased or decreased, and even its sign can be changed, see Fig.2, *b* and *c*. From the diminishing the photovoltage at .7 V bias for the Ni electrode and at 1 V for the Ti one, one can come to conclusion that the barrier differences at the interfaces diamond-W and diamond-Ni or diamond-Ti are equal to .7 and 1 eV, respective. These data are consistent with the maximum photovoltages obtained at zero biases from the diodes with these two metals as semitransparent electrodes.

Conclusion

Undoped and boron-doped diamond films were grown on tungsten and silicon substrates. Two types of metal-diamond film-metal diodes were fabricated with Ni or Ti semitransparent electrodes on top of the films. The barrier height differences between bottom and top electrodes were measured using the photovoltage saturation method. It was demonstrated that photovoltaic elements with open circuit photovoltage as high as 1 V can be successfully fabricated.

<div align="center">REFERENCES</div>

1. M.A.Prelas, E.J.Charlson, E.M.Charlson, J.Meese, G.Popovici, and T.Stacy. 2nd International Conference on Application of Diamond and Related Materials, MYU, Tokyo, 1993, pp.329-334.
2. S. Khasavinah, T. Sung, B. Spitsyn, W. H. Miller, G. Popovici, M. A. Prelas, E. J. Charlson, E. M. Charlson, J. Meese, and T. Stacy, Diamond Materials, ed. J. P. Dismukes and K. V. Ravi, Electrochem. Soc. Proc. V. **93-17**, 1993, p. 1032-1035.
3. P.I.Perov, V.I.Polyakov, A.V.Khomich, N.M.Rossukanyi, A.I.Rukovishnikov, V.P.Varnin, I.G.Teremetskaya, Wide Band Gap Electronic Materials, M.Prelas and P Gielisse, Ed., Kluwer Academic Publisher, Netherland, 1995.
4. V.I.Polyakov, P.I.Perov, O.N.Ermakova, M.G.Ermakov, A.I.Rukovishnikov, V.I.Sergeev, Sov. Phys. Semiconductors **23** (1989) 75
5. P.Gonon, A.Deneuville, E.Gheeraert, F.Fontaine, F.Lenormand, J. Appl. Phys Vol.76, No.6, p.3929-3931(1994).
6. S.M.Sze, Physics of Semiconductor Devices. New York, 1981, p. 790-836.

EFFECT OF GRAIN SIZE AND TEMPERATURE ON THE FIELD-DEPENDENCE OF THE RESISTIVITY OF B-DOPED DIAMOND

S. Sahli, X. Hou, and M. Aslam

Department of Electrical Engineering, Michigan State University,
East Lansing, MI 48824, U.S.A.

Key words: Resistivity, CVD Diamond, Temperature effect.

Abstract

The field-dependence of the resistivity of boron-doped homoepitaxial, small-grain and large-grain diamond films deposited on insulating substrates is investigated as a function of grain size and temperature. The resistivity of the epitaxial film remained independent of field for the temperature and field ranges of 296 - 633K and 40 - 600 V/cm, respectively. The small grain films exhibited a change of resistivity starting at 10 V/cm for the 21Ω-cm sample but showed no change for the 4.9Ω-cm sample. The resistivity of the film with a grain size of 200-300μm starts decreasing at approximately 0.2V/cm at room temperature. The rate of resistivity reduction due to field increases in the temperature range of 296 - 510K, then starts to decrease between 510 - 633K.

1. Introduction

In order to understand the operation and improve the design of microsensors, field emitters and high-power diamond devices, it is necessary to study the electronic transport properties as a function of the applied electric field and temperature. Such a study was conducted for B-doped chemical vapor deposited (CVD) diamond epitaxial films [1] and undoped polycrystalline diamond films [2]. Both studies reported non-linear characteristics of the resistivity at high field and attributed it to excess carrier generation via impact ionization [1] and to Poole-Frenkel conduction [2]. No such data is available for B-doped polycrystalline diamond films. Moreover, the effect of temperature on this non-linearity is unknown for any type of diamond film. In this work, the field dependence of the resistivity of B-doped CVD diamond films is investigated. Initial results suggest that the non-linear behavior of the resistivity at high electric fields is strongly related to doping density and temperature, and seems to be affected by the grain size in case of polycrystalline films.

2. Experimental

Homoepitaxial, small-grain (1-2μm) and large-grain (200-300μm) p-type diamond films were used in this study. In order to ascertain that the I-V measurements reflect the electrical properties of the p-type diamond layer, all films were deposited on insulating substrates and doped in-situ with boron using hot filament CVD (HFCVD) deposition. Table I list the sample specifications.

Table I. Sample Specifications

Sample	Substrate	Grain Size	Undoped Layer	Metal Contacts
Homo-epitaxial	Type 2a[**]	NA	Type 2a	Sputtered Ti-Pt
Large grain	Polycrystalline[*]	200-300 μm	Polycrystalline	Evaporated Al
Small grain	SiO_2	1-2 μm	Polycrystalline	Evaporated Al

[*] Diamonex Company.
[**] Dubbelldee Harris Corp., Mt. Arlington, NJ.

The highest applied field during measurement was limited by the voltage limit of the equipment being used. The voltage across the sample was computer monitored. The sample temperature was maintained constant using an automatic temperature controller and a K-type thermocouple. A specially designed characterization chamber was used for temperature measurements performed at a pressure of 10 mtorr.

3. Results and Discussions

We initially observed that the resistivity of B-doped polycrystalline diamond resistors depends on the electric field being applied to measure it. As shown in Fig. 1, the resistivity of small grain samples decreased at high fields. Samples with high resistivity exhibit higher sensitivity to field. All samples tested in Fig. 1 were deposited on the same wafer in the same run. Our examination under SEM shows that the film is continuous. There exist considerable fluctuations in both the grain size and the degree of twinning in the films. We believe that the difference in the doping level is a result of the resistors not being at the same distance from the holder containing the Boron powder during in situ doping. The data in Fig. 1 suggest that the resistivity is constant for low fields and the I-V data show ohmic behavior. The resistivity starts to drop at a field level that depends on the doping density. The resistivity of samples with lower doping levels starts to decrease at lower field values and exhibits faster rate of decrease. This regime is not observed for samples with low resistivity such as $\rho=4.9\Omega$-cm. The fact that the onset of field dependence of the resistivity of our polycrystalline samples is observed at fields lower than the 10^5V/cm, reported earlier for films not intentionally doped and deposited on non-insulating substrates [2], is not well understood at this time. The resistivity of our p-type epitaxial film remained constant for applied fields in the range of 0.01-200V/cm. This result does not contradict the report of 10kV/cm as

the onset of nonlinear field effect on the resistivity of doped epitaxial films [1].

To study the effect of grain size on the field-dependence of the resistivity, two samples with a grain size of 200 - 300μm and 1 - 2μm were tested. The results, plotted in Fig. 2, show that the resistance of the large grain sample starts to decrease at 0.2V/cm. More data is needed to understand the effect of grain size on the resistivity behavior at high fields.

In order to study the effect of temperature on the observed resistance non-linearity, we tested the epitaxial and small grain samples for temperatures and fields in the ranges of 296 - 633K and 40 - 600V/cm, respectively. The resistance of the epitaxial sample remained constant. In order to present the resistivity data for different temperatures in one graph the normalized resistivity, ρ_E/ρ_{40}, where ρ_E denotes the resistivity measured at E V/cm was plotted in Fig. 3. The resistivity starts to decrease at approximately 40V/cm for all temperatures. For each temperature, we compute the percentage of resistivity decrease due to field as $\Delta\rho/\rho = (\rho_{40} - \rho_{600})/\rho_{40}$. As illustrated in the inset of Fig. 3, the resistivity dependence on field seems to be enhanced in the range of 300 - 530K but attenuated between 530-633K.

4. Conclusions

The comparison between the results of our epitaxial and polycrystalline B-doped diamond films clearly suggests that the change of resistivity in the case of polycrystalline films can be related to their polycrystalline morphology specifically to the presence of grain boundaries as is the case for polycrystalline silicon [3]. The field at which the resistivity starts to decrease is relatively low and seems to be strongly related to doping and temperature. More data is essential to further understand and quantify the dependence of the resistivity of polycrystalline diamond films on field. Such data is expected to help define the parameters to achieve polycrystalline diamond films with controllable resistivity ad hence improved electrical properties.

5. Acknowledgment

6. References

[1] Shozo Shikama et al. "Experimental Study on High-Field Transport in B-doped CVD Diamond Epitaxial Films," 2nd International Conference on the Applications of Diamond Films and Related Materials.
[2] Bohr-ran Huang and D. K. Reinhard, "Electric field-dependent conductivity of polycrystalline diamond thin films," App. Phys. Lett., 59 (12), Sep. 1991, 1494-1496.
[3] G. E. Pike and C. H. Seager, "The dc voltage dependence of semiconductor grain boundary resistance," J. App. Phys., 50 (5), May 1979, 3414-3422.
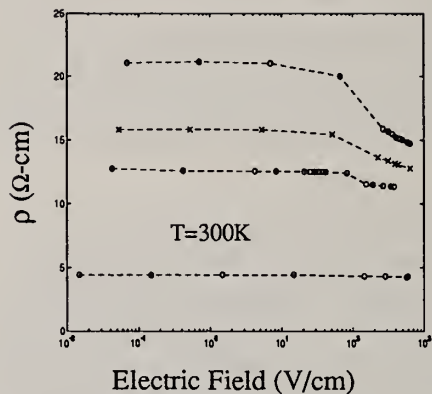
Figure 1. Effect of electric field on the resistivity of small grain samples having different doping levels
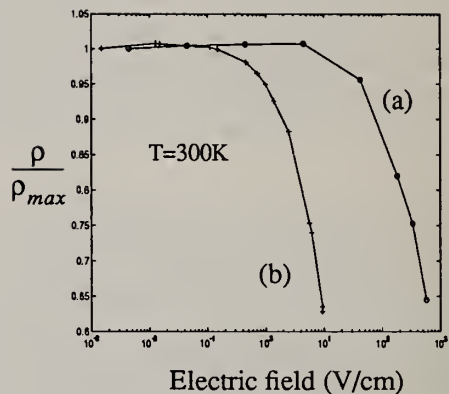
Figure 2. Normalized resistance as a function of field for (a) small and (b) large grain samples.
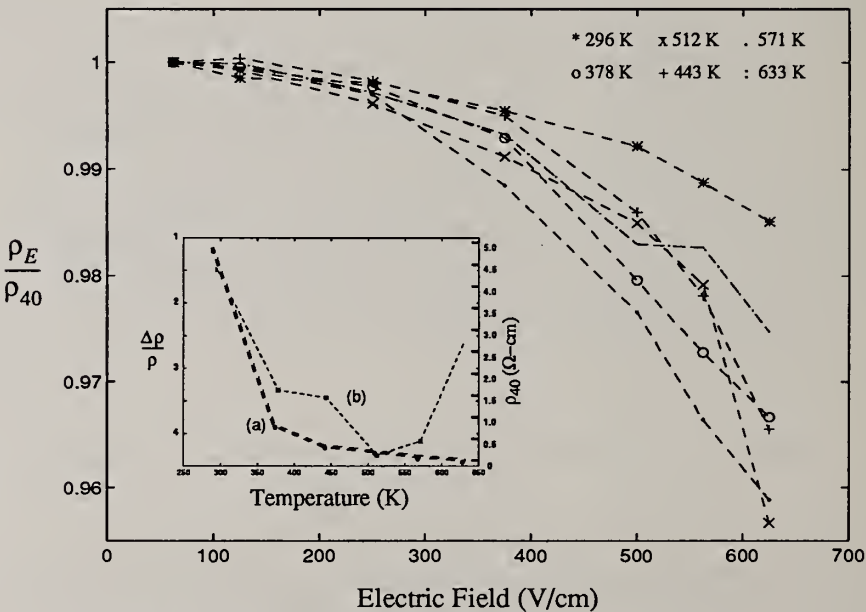
Figure 3. Normalized resistivity vs. field of small grain sample measured under different film temperature.
Inset: (a) resistivity at 40V/cm, (b) percentage of field induced resistivity decrease.

BORON DOPED POLYCRYSTALLINE DIAMOND FILMS FOR STRAIN SENSING APPLICATIONS

D. Wur, J.L. Davidson, W.P. Kang, D. L. Kinser and D. V. Kerns

Vanderbilt University, Nashville, TN 37235 USA

Abstract

It has been recently established in our work and others that boron-doped polycrystalline diamond films (PDF) have piezoresistivity (PZR) [1,2,3]. This property opens PDF to the field of sensor applications using strain sensing. Polycrystalline diamond films have been prepared with microwave plasma enhanced chemical vapor deposition (CVD) method and boron-doped to p-type semiconductors. In addition, by combining the piezoresistive effect in doped PDF and the insulating property of undoped PDF, whereby doped diamond resistors reside on a dielectric diamond substrate diaphragm, a monolithic all-diamond microstructure for examining the strain response of patterned p-doped diamond PZRs was fabricated and characterized. This work examines some critical issues of diamond for strain sensing applications such as its rupture stress and edge stress of diamond diaphragm and the high temperature responses of a diamond strain sensor.

1. Introduction

Silicon planar processing and micromachining technologies have made silicon a major sensor material. However, silicon is not a high temperature material, it will plastically deform at 600 °C [4] and current leakage limits silicon devices to operation at temperature below ~ 150 °C. Therefore, a high temperature material such as diamond for sensor applications at elevated temperature is a desirable possibility. Such applications include hypersonic inlet pressure monitoring, non-obtrusive leading edge stress monitor, in situ combustion engine pressure measurement and nuclear power proximity control.

Chemically vapor deposited (CVD) polycrystalline diamond films (PDF) have been applied in radiation detectors, photodetectors and thermistors[5,6,7]. Polycrystalline diamond films have the advantageous properties of wide bandgap (5.4 eV), low thermal coefficient of expansion(1-1.5 ppm/C)[8], high thermal conductivity (10 W/cm K)[9] and high Young's Modulus (105×10^{10} N/m^2) when compared with other semiconductor materials. Recently, the piezoresistive effect of boron-doped diamond films has been established.[1,2,3] This property extends PDF to strain sensing applications such as pressure sensors. These properties and the ability to fabricate PDF with semiconductor

processing (doping, photolithographic patterning and interconnect) indicate this potentially superior electronic material could provide advanced devices and sensors for high temperature, high power and harsh environments.

2. Experimental

Polycrystalline diamond films have been prepared by microwave plasma enhanced CVD method and boron-doped to p-type [10]. For the diamond strain sensor, the undoped diamond layer serves as an insulating diaphragm and boron-doped diamond piezoresistors are patterned on top of it. Fig. 1 shows the layout of the strain sensor. The dashed circle represents the edge of the diaphragm. Two resistors (R1 & R2) are positioned on top of the diaphragm. The other four resistors (R3 - R6) are off the diaphragm. A half bridge configuration (see Fig. 2) can be formed which utilizes R1& R2 as active arms and R3 & R4 as null arms. Two other resistors (R5 & R6) are placed off the diaphragm for reference purposes. The fabrication procedures have been described previously[10].

3. Results and Discussion

The use of PDF as the diaphragm material has three advantages; PDF is chemically inert and can serve as an etch-stop with large etching time tolerance, PDF can be deposited with control by adjusting deposition time and other growth parameters resulting in selectability of diaphragm thickness and PDF is extremely stiff and strong, adding to the mechanical ruggedness of the sensor.

The rupture stress of a diaphragm can be defined as the stress at which the diaphragm reaches the elastic strain limit where permanent damage occurs to the diaphragm. For a circular diaphragm with a clamped edge, the maximum stress σ_{max} at the circumference is [11],

$$\sigma_{max} = \frac{3}{4} P_{max} (\frac{r}{t})^2 \tag{1}$$

r and t are diaphragm's radius and thickness, P_{max} is pressure. To examine the rupture stress of diamond diaphragms, several samples have been tested. The rupture stress of the diamond diaphragms ranged from $1.84 \pm 0.42 \times 10^{11}$ to $5.20 \pm 1.2 \times 10^{11}$ dyne/cm^2 with an average of $3.40 \pm 0.79 \times 10^{11}$ dyne/cm^2. The difference in rupture stress among these samples was because of imperfections in the diamond diaphragms and differences in thickness and boundary clamping.

Compared to the rupture stress of silicon, 6.24×10^8 dyn/cm^2 [12] , diamond film has a rupture stress nominally three orders of the magnitude larger. Hence the diamond diaphragm is more rugged than silicon, can withstand much higher pressure conditions and a thinner diaphragm thickness could be achieved using diamond. For a given pressure P_{max}, the minimum thickness t_{min} of diaphragm has the relationship:

$$t_{min} = r \sqrt{\frac{3}{4} \frac{P_{max}}{\sigma_r}} \qquad (2)$$

For example, assume P_{max} to be 250 mmHg with radius r as 1 mm, a silicon diaphragm would require a minimum thickness of 20 µm while diamond diaphragm would require only 2.5 µm. A thinner diaphragm can reduce the CVD deposition time and improve sensitivity.

A diamond sensor, described previously[13] was used to examined the edge stress of diamond diaphragm. In such a configuration, two piezoresistors were located in the center and two others close to the edge of the diaphragm as seen in Fig.3. It was found that the center piezoresistors have a linear response with respect to the pressure while the edge piezoresistors do not. These edge piezoresistors were tested at a lower pressure range of 0 to 35 mmHg (nominally 7 mmHg increase per interval). Fig. 4 shows the resistance change to the pressure applied. It can be seen that the resistance of the edge piezoresistor *decreases* below 7 mmHg pressure. In fact, this is consistent with the stress profile as shown in Fig. 5 [14]where the edge stress is compression. The non-ideality in this configuration is a rather high aspect ratio, r/t, (nominally 500 to 1000) which arises primarily from the large radius used in these designs compared to smaller configurations where r/t is around 100. From the relationship describing the maximum pressure for linear strain operation [15]:

$$P_{max} \leq \frac{8E}{3(1-v^2)}(\frac{t}{r})^4 \ (N/m^2) \qquad (3)$$

the pressure for linear strain operation of these diaphragms with a large aspect ratio would fall in the range of 0.2 to 3 mmHg. This suggests the edge stress changes from compression to tension at pressure above 20 mmHg which could be a boundary condition change. In other words, a diaphragm with such a large aspect ratio r/t (500 to 1000) will behave as a case of clamped edges at low pressure and becomes a case of supported edges [16] as pressure increases. For the case of a diamond diaphragm with aspect ratio of 100, pressures to 230 mmHg could be applied in the linear strain domain.

Also in this work, the sensor shown in Fig. 1 was fabricated. The diaphragm size is nominally 8 mm with 5 ± 0.2 µm in thickness and shows no current leakage. The diamond piezoresistors have thickness of 1 ± 0.2 µm and resistivity $102 \pm 5 \ \Omega$ cm at room temperature. The temperature dependence of the film resistivity follows an Arrhenius relation

$$\rho = \text{constant} \times \exp(E_A/kT) \qquad (4)$$

with activation energy $E_A = 0.14 \pm 0.2$ eV as seen in Fig. 6. The half bridge voltage output is 12 mV/5V/200mmHg at room temperature and decreases to 5mV/5V/200mmHg at 200 °C as seen in Fig. 7. The decrease in voltage output response at higher temperature may come from release of trapped holes in the grain boundaries as the temperature increases.

4. Conclusion

A large rupture stress of CVD PDF has been observed. The dependence of stress distribution in a diamond film diaphragm on aspect ratio has been observed. A diamond strain sensor was operated and characterized to 200 °C.

5. References

1. D.R. Wur and J.L. Davidson, "Piezoresistivity of Polycrystalline Diamond Films", *MRS Fall Meeting*, 1992.
2. M. Aslam, I. Taher, A. Masood, M.A. Tamor, and T.J. Potter, "Piezoresistivity in Vapor-Deposited Diamond Films", *Appl. Phys. Lett.*, **60**(23), 2923-2925, 1992.
3. M. Werner, K. Holzner, O. Dorsch, E. Obermeier, R.E. Harper, C. Johnson, P.R. Chalker and I.M. Buckley-Golder, "Piezoresistive Effect of Boron Doped Diamond Thin Films", *Diamond and Related Materials*, **2**, 1096-1099, 1993.
4. G.L. Pearson, W.T. Read, Jr., and W.L. Feldman, "Deformation and fracture of small silicon crystal's" Acta. Met., vol5, 181-191, 1957.
5. Shun-Ichi Kanda, "Development of diamond radiation detectors", *The Vancouver Meeting, Particles & Field*, 2, 1126-1128, 1991.
6. S.C. Binari, M. Marchuwka, D.A. Koolbqaeck, H.B. Dietrich and D. Moses, "Diamond metal - Semiconductor - Metal Ultraviolet photodetectors", *Diamond and Related Materials*, 2, 1020-1023, 1992.
7. M.Wernner, E.Obermeier, "Thermistor based on doped polycrystalline diamond films", 669-672, *Diamond and related materials*, 1992.
8. R. C. Eden, "Application of Synthetic Diamond Substrates for Thermal Management of High Performance Electronic Multi-Chip Modules", *Applications of Diamond Films and Related Materials*, 259-268, 1991.
9. J.E. Graebner, S. Jin, G.W. Kammlott, J.A. Herb, C.F. Gardinier, "Large Anisotropic Thermal Conductivity in Synthetic Diamond Films", *Nature*, 359, 401-403, (1992).
10. J.L. Davidson, D.R. Wur, and W.P. Kang, "The Piezoresistance of Boron-Doped Diamond on an Undoped Diamond Membrane", *Diamond Materials*, 1048-1053, (eds. J.P. Dismukes and K.V. Ravi), The Electrochemical Society, Inc., 1993.
11. W.H. Ko, M. Bao, and Y. Hong, "A High-Sensitivity Integrated-Circuit Capacitive Pressure Transducer", *IEEE Transactions on Electron Devices*, **29**(1), 48-63, 1982.
12. Clauser et al., *The Encyclopedia of Engineering and Processing*, London, England: Reinhold, 1963, p. 616.
13. J.L. Davidson, D.R. Wur, W.P. Kang, D. Kinser, D.V. Kerns, J.P. Wang, and Y.C. Ling, "Microelectronic Pressure Sensor with Diamond Piezoresistors on Diamond Diaphragm", *Fourth International Conference on the New Diamond Science and Technology*, Kobe, Japan, July 1994.
14. Design Considerations for Diaphragm Pressure transducers, *Micro-Measurements Tech. Notes*, 129, 1968.
15. Hermann K.P. Neubert, *Strain Gauges Kinds and Uses*, p. 141, 1967, St. Martin's Press, New York.
16. S. Timoshenko and S. Woinowsky-Krieger, *Theory of Plates and Shells*, p. 56, 1959, McGraw-Hill Book Company, New York.
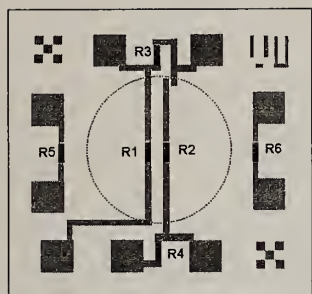
Fig. 1. Layout of strain sensor.
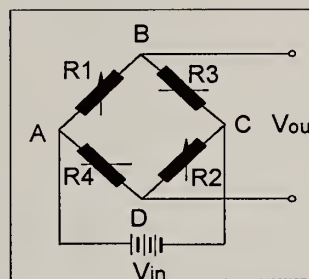
Fig. 2. Half bridge configuration.
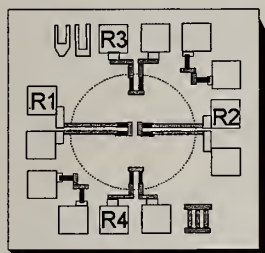
Fig. 3 Layout of sensor
from previous work[13].

Fig. 4. Resistance change of piezoresistors R1
and R3 at pressure of 0 to 35 mmHg.

Fig. 5. Stress distribution of circular diaphragm.
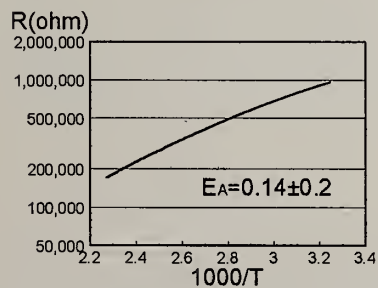
Fig. 6 Arrhenius plot of diamond resistors.
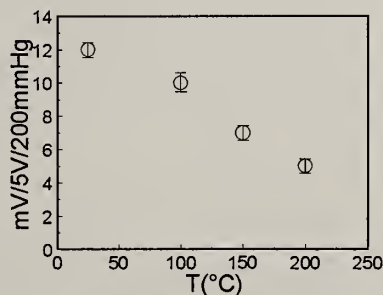
Fig.7 Voltage output vs. temperature.

A DIAMOND THIN FILM FLOW SENSOR

Sacharia Albin[1], John C. Hagwood[1], John B. Cooper[2], David L. Gray[3], Scott D. Martinson[3], and Michael A. Scott[3]

[1]Department of Electrical & Computer Engineering
[2]Department of Chemistry and Biochemistry
Old Dominion University, Norfolk, VA 23529-0246
[3]NASA Langley Research Center, Hampton VA 23665

Abstract

We present the results of theoretical modeling and experimental testing of a diamond thin film sensor for flow studies. It is shown that the high thermal conductivity of a diamond film can enhance the frequency response of the flow sensor. One-dimensional heat diffusion equation was solved using the finite difference method for determining the frequency response. Two different sensor structures were analyzed: a Ni film on a quartz substrate (Ni/Q) and an intermediate layer of diamond film between the Ni film and quartz substrate (Ni/D/Q). The theoretical model predicts a frequency response for the Ni/D/Q sensor higher than that of the Ni/Q sensor. Diamond films for the Ni/D/Q sensor were deposited onto the quartz substrate by microwave plasma-enhanced chemical vapor deposition (MPECVD). The conditions for a high nucleation density were established for obtaining a continuous diamond thin film. A subsequent nickel film patterned and deposited serves as the sensing arm in the bridge circuit of an anemometer. The measured frequency response of the Ni/D/Q sensor combination is greater than 220 kHz, as compared to the Ni/Quartz sensor response of 120 kHz.

1. Introduction

Diamond thin films possess a unique combination of properties among solid state materials including high thermal conductivity, chemical inertness, high resistivity and large breakdown field. Applications utilizing these properties have recently been

reported in hydrogen sensing [1], temperature sensing [2], and flow sensing [3]. High velocity, high temperature flow sensing capabilities are critical for detecting transitions in the hypersonic and supersonic regime. A hot-film anemometer consisting of a conducting thin film deposited on an insulating substrate detects transition regions in fluid flow. The high frequency components, a function of the Mach and Reynold's number, need to be determined for analyzing the flow characteristics. Conventional metal film sensors are limited by the properties of the thin film to measuring instabilities around 60 kHz. Researchers at NASA Langley have developed thin metal film sensors of Cr and Ni for boundary layer transitions at both ambient and cryogenic temperatures [4]. However, a need arises for identifying appropriate materials for measuring high speed flow transitions in the 200 - 400 kHz range at temperatures above 500 °C.

Frequency response analyses of thin film sensors were carried out by Vidal [5] and Lowell and Patton [6]. Decoupling the thermal effects of the film from the substrate allows the film temperature to change faster than the substrate temperature. This corresponds to maintaining a large ratio of film thermal conductivity to substrate thermal conductivity (k_f/k_s). The maximum frequency response is related to ($k_f/\rho_f c_f d_f^2$ or α_f/d_f^2) where ρ_f, c_f, α_f, and d_f are the density, heat capacity, diffusivity and thickness of the film. Therefore, achieving a high frequency response requires the combination of a thin film material with a high k_f and a substrate material with a low k_s. Table 1 lists the thermo-physical properties of the chosen thin film and substrate materials which meet the above discussed criteria. Diamond is chosen as the film material due to the following properties: highest value of thermal conductivity, large negative temperature coefficient of resistance and chemical inertness at high temperatures. Also, doping diamond has yielded resistivity values in the range 0.1-100 Ω-cm [7]. Quartz has a low value of thermal conductivity among other possible substrate materials as Si and Al_2O_3. As mentioned earlier, a low value of k_s is important for high frequency analysis. Therefore, the (D/Q) combination, which has a very high k_f/k_s ratio, should exhibit a high frequency response.

Frequency response simulations were carried out to predict the sensitivity of Ni and diamond films deposited on quartz substrates. The results of such simulations should indicate the effect the interlayer of diamond has on the frequency response. The finite difference method was used to solve the one-dimensional heat diffusion equation for determining the frequency response of the sensor. The details of the

Table I. Thermo-physical properties of materials at 300 K

Material Parameter	Ni	Diamond	Quartz
ρ (kg/m^3)	8900	3500	2650
k (W/m^{o}K)	90.7	2300	10.4
c (J/kg^{o}K)	444	509	745

analysis are explained elsewhere[8]. Fig.1 illustrates a schematic of the model used for analyzing the frequency response. The frequency response values were determined using a sinusoidal forcing function. The result is shown in Fig.2. The 3dB response of the normalized temperature amplitude variation for the Ni/D/Q sensor is around 2×10^5 Hz. The response of the Ni/Q sensor is about an order of magnitude lower. Hence, the diamond film interlayer will enhance the frequency response of the proposed flow sensor.

2. Sensor Fabrication

Two different types of sensors were fabricated for frequency responses measurement. Fabrication of the Ni/Q sensor was carried out by patterning and depositing nickel films on fused quartz substrates by electron-beam evaporation to a thickness of 0.5 μm. For the Ni/D/Q sensor, diamond films were grown on quartz substrates using a microwave plasma-enhanced chemical vapor deposition system. The deposition chamber consist of a 6" vertical cavity with a 4" diameter graphite susceptor connected to an induction heater. The temperature of the susceptor is monitored by a thermocouple inserted at the base of the susceptor. For uniform thin film growth, a considerable nucleation density is necessary. Diamond nucleation and growth processes on quartz substrates have been investigated by several researchers[9-12]. Previous investigations of diamond nucleation on various forms of silica by MPECVD has produced different results. Lauten et. al. demonstrated the formation of diamond on SiO_2 without substrate abrasion prior to deposition [9]. Instead, it is shown that a gas phase seeding process consisting of increasing the CH_4 concentration, decreasing substrate temperature and lowering microwave power is sufficient for increasing the nucleation density. For this present work, we define nucleation enhancement of diamond films on quartz substrates as a two-step mechanism. The initial step is abrasion with 1μm diamond paste prepared with a Minimet abrasion apparatus. This prescratching procedure causes an immediate means of nucleation by seeding stable fragments on which diamond growth can occur. The second step, similar to Lauten's proposal, is called carbon saturation of the substrate. Carbon species impinge on the substrate from the gas phase and

diffuse into the bulk of the substrate. When the substrate becomes incapable of being penetrated by diffusion, the surface carbon concentration increases and eventually stabilization of the nucleus is formed. Creation of a large density of these stable nuclei is imperative for assuring uniform thin film growth. The abraded samples were placed upon the graphite susceptor during deposition. The chamber is first evacuated to a desired pressure with a turbomolecular pump. Table II lists the deposition parameters used for nucleation and growth of the diamond thin films. The deposition parameters given under the nucleation step are initialized. Maintaining a 14% CH_4 in H_2 gas mixture during a two hour seeding time was found to be sufficient for enhancing the nucleation density. After gas phase seeding, modifications of the deposition parameters were necessary for uniform thin film growth. A 3% CO in H_2 was used during the growth step. This process promoted the formation of OH radicals within the gas phase species. The combination of OH radicals and atomic H should effectively promote diamond growth by preferentially etching non-diamond carbon faster than diamond.

Table II. Nucleation and Growth Process Parameters

Parameters	Nucleation Step	Growth Step
Hydrogen Flow (sccm)	430	900
Methane Flow (sccm)	70	9
CO Flow (sccm)	0	27
Substrate Temperature (^{O}C)	600	750
Total Pressure (Torr)	20	35
Microwave Power (W)	723	1000
Time (hours)	2	6

Diamond film growth was confirmed by Raman spectroscopy and SEM. The SEM pictures shown in Fig. 3 reveal a continuous thin film, and verify a high nucleation density achieved using the two step process. A nickel film was subsequently deposited upon the diamond film. Due to the surface roughness of the diamond films, a nickel film thickness of 1.6 μm was necessary. After depositing the nickel films, both the Ni/Q and Ni/D/Q sensors were connected to a testboard.

3. Frequency Response Measurement

The frequency response of each sensor was determined using a Dantec Constant Temperature Anemometer (CTA) system. The main unit of the CTA model consists

of a servo amplifier, filter decade resistance, square wave generator, and other auxiliary components. An associated CTA Standard Bridge and 5 meter Cable Compensation Unit are connected to the main unit of the CTA. Other equipment utilized for testing the sensors include: 100 MHz Yokogawa digital oscilloscope, multimeter, and 5 meter coaxial cable. A constant temperature anemometer is one method of implementing hot wire or hot-film anemometry. Hot film anemometry operates on the principle that the electrical resistance of a metallic conductor is a function of its temperature. In a constant temperature anemometer, the sensing film is placed in a variable current feedback loop which maintains a constant temperature. Any resistance change is detected as a voltage difference between the arms of a Wheatstone bridge. This voltage difference is electronically conditioned in stages and fed back as an input to the bridge. Therefore, the varying film resistance and compensating current created will be proportional to the flow velocity. However, a technique exists for determining the frequency response of a sensor using an anemometer in the absence of a flow. The "cold resistance" of the sensor, which is the resistance value without an applied signal, is measured. It is then multiplied by a constant known as the overheat ratio, to get a resistance value termed as "hot resistance." The variable resistance of the bridge circuit is initially set to the hot resistance value. A 3 kHz square wave signal is applied to the sensor input and the output is displayed on the digital oscilloscope. Fig.4 shows the frequency response of both the Ni/Q and Ni/D/Q sensors. The measured frequency response of the Ni/D/Q sensor is better than 220 kHz, as compared to the Ni/Quartz sensor response of 120 kHz. This suggest that an intermediate layer of diamond has enhanced the frequency response of the Ni/Q sensor.

4. Conclusions

The results of theoretical modeling predicted a high frequency response for a sensor which has an interlayer of diamond film. Though the theoretical values were not achieved, the experiments clearly demonstrated that the (Ni/D/Q) sensor has a significantly higher frequency response than that of the (Ni/Q) sensor. The high thermal conductivity of a diamond film is a factor for enhancing the frequency response of the Ni/D/Q flow sensor. Such sensors will be useful for high speed flow studies.

5. Acknowledgments

118

6. References

1. W. P. Kang, et. al., J. Electrochem. Soc., **141**, 2231, 1994.
2. M. Aslam, et. al., in 'Diamond Film Semiconductors', SPIE **2151**, 145, 1994.
3. S. Albin, et. al., in 'Diamond Film Semiconductors', SPIE **2151**, 152, 1994.
4. C. B. Johnson, et. al., Proc. ICAF'87 Record, 141, 1987.
5. R. J. Vidal, WADC Tech Note 56-315, **AD-97238**, 1956.
6. H. H. Lowell and N. Patton, NACA TN **3514**, 1955.
7. B. V. Spitsyn, Proc. MRS In. Conf. **1991**, 909, 1991.
8. S. Albin, et. al., 'Thermal Anemometry', ASME, FED-vol.**167**, 181, 1987.
9. F. S. Lauten, Y. Shigesato, and B. W. Stoner, Appl. Phys. Lett. **65**, 210, 1994.
10. D. J. Pickrell, et. al., J. Mater. Research, **6**, 1264, 1991.
11. S. Prawer, et. al., J. Appl. Phys. **69**, 6625, 1991.
12. J. Rankin, et. al., J. Mater. Research, **9**, 2164, 1994.
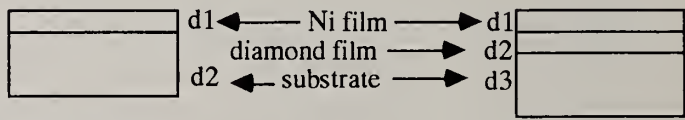
Fig.1. Two sensor structures analyzed by finite difference method.
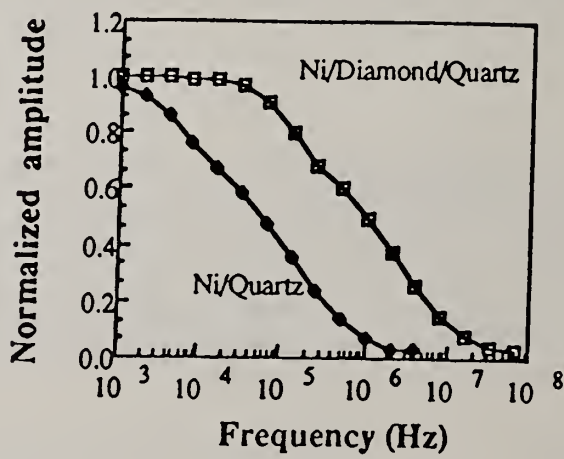
Fig. 2. Theoretical frequency response of the two sensors.

Fig. 3a. Diamond grown on an untreated quartz substrate showing a low nucleation density. Well-defined facets are clearly visible indicating the good quality of the crystals.

Fig. 3b. Continuous diamond film growth on a surface-treated quartz substrate using gas phase seeding.
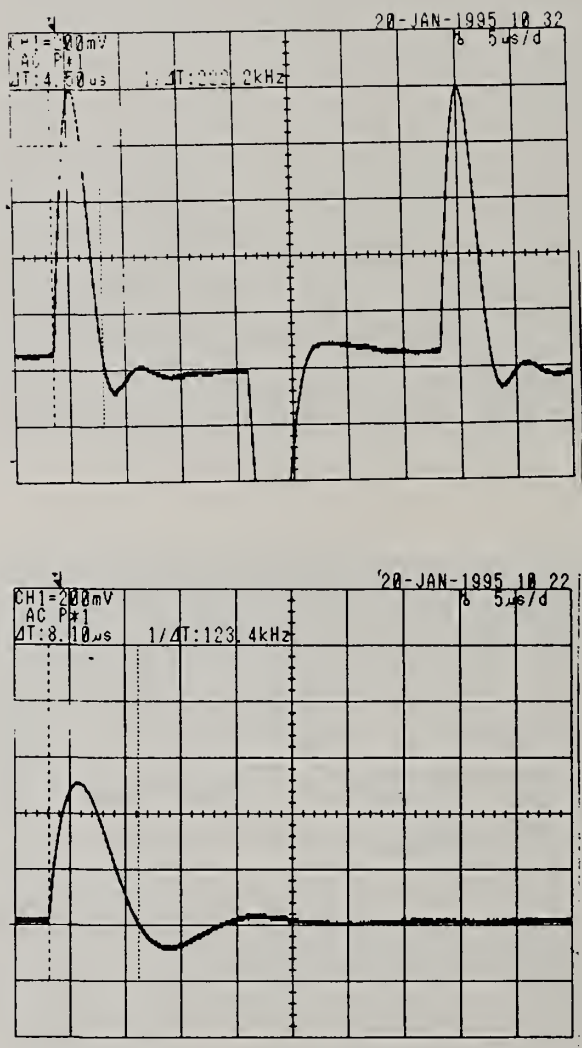
Fig.4. Frequency response of Ni/Diamond/Quartz sensor (top) and Ni/Quartz sensor (bottom), respectively. The measured frequency response of the Ni/D/Q sensor is >220 KHz, as compared to the Ni/Q sensor response of 120 KHz. This is a clear demonstration of the suitability of diamond film for flow sensing applications.

Applications of Diamond Films and Related Materials: Third International Conference, 1995
Editors: A. Feldman, Y. Tzeng, W. A. Yarbrough, M. Yoshikawa, and M. Murakawa

121

A THERMAL-SENSITIVE DEVICE FABRICATED WITH DIAMOND FILM AND A PLANAR MICROELECTRODE

Changzhi Gu, Zengsun JIn, Xianyi Lu, Guangtian Zou and Qiang Meng

The State Key Lab. of Superhard Materials
Inst. of Atomic and Molecular Physics
Jilin University, 130023 Changchun, P.R. China

Key words: diamond film, HFCVD, thermal-sensitive device,
          Microelectrode

Abstract

Polycrystalline diamond film were deposited by means of the hot filament CVD technique (HFCVD) onto a planar interdigital Ti microelectrod arrays, and forming a thermal-sensitive device. The resistor changes of diamond film caused by temperature are shown to be sensitive, reproducible, rapid and stable thermal-sensitive device. The characteristics of thermal-sensitive for this device was study. Functionalized diamond film deposited onto planar microelectrode arrays can easily detect temperature from 20℃ to 700℃.

1. Introduction

In the recent few years, the application of diamond films synthesized by using various chemical vapor deposition (CVD) methods have been achieved in some field [1]. Specially, the thermal-sensitive of diamond film is its more attractive property [2], since it can be used as a temperature sensor at high temperature, but diamond film can be described as insulators with intrinsic conductivities; thus, conductance measurements on diamond film are somewhat difficult to perform with high a accuray. The fabrication of an effective thermal-sensitive device using diamond film requires careful selection of the substrate and measurement technique.

In this paper, we designed a planar interdigital Ti microelectrode arrays, diamond films synthesized by hot filament chemical vapor deposition (HFCVD) were deposited onto this electrode arrays, and forming a thermal-sensitive device, the thermal-sensitive characteristics of this device were describe.

2. Experiments and results

Polycrystalline diamond film were deposited by means of the hot filament CVD technique. Two tungsten filament at a 15mm interval were place 10mm above a substrate to achieve uniform deposition on measurement electrode placed on a quartz substrate holder heated to 900 °C, gas mixtures of CH_4 and H_2, 2% CH_4 concentration, at a total pressyre at 5.3 KPa were used for diamond film deposition. Tungsten filament temperature was about 2000°C, and was monitored by optical pyrometer. The time of deposition was 2 hours. The Raman spectroscope of diamond film was shown as Fig. 1, the sharp peak at 1333 cm^{-1} indicated that the sample is a cubic diamond, and no obvious broad peak located at about 1550 cm^{-1}, which represented the graphite or amorphous carbon phase in the film, can be observed in the Raman spectra. This showed that the film is composed of high quality diamond crystals containing very few non-diamond phase carbon. The scanning electron microscope photograph of diamond film was shown in Fig. 2, the films were composed of micro diamond crystals with grain size ranging from 2 to 3 μm, and the orientation of grains was (100)-faced

The measurement electrode performs two vital function in the thermal-sensitive device of diamond film. First, it makes an ohmic contact to the diamond film. Second, it facilitates the measurement of very low conductances. The electrode must be microfabricatable in a planar configuration. The measurement electrode used in this work is illustrate in Fig. 3. It consists of an interdigital array of metal electrodes lithographically patterned on a quartz substrate. The quartz substrate was polished with 0.5μm diamond particles for 15 minutes, then was cleaned and coated with 0.5μm of Cr followed by 1.5μm of Ti, patterned lithographically and etched to provide 30 finger pairs of electrodes having a width of 30μm, spaced 30 μm from the adjacent electrode, the finger overlap distance was 1cm.

Ti was selected as the electrode material since it is known to form an ohmic contact with the diamond film[3]. The electrode geometry provide a very large ratio of electrode perimeter to electrode spacing which is important for measuring weakly conducting materials. the measured conductance of any material can be describe by the relationship

$$S= (P/d) * t * \sigma \qquad (1)$$

where S is the measured conductance, P is the electrode perimeter, t is the film thickness, σ is the intrinsic conductivity and d is the distance between electrodes. Since P/d is fixed by the electrode reometry and is a very large number (i.e. 19667 for this electrode) , the measured conductance S can be substantial even the film thickness t, or the conductivity σ is quite small.

In our paper, the thickness of diamond thin film is 2 μm, S can be measured by appling a DC bias of 20 Volts between the two electrodes to the interdital microelectrode and measuring the current. Both the bias and current flow were monitored by the Keithley electrometers. In Fig. 4, we give the resistor changes to various ambient temperature. As can be seen, the changes of resistor were sensitive when the temperature change from 20℃ to 700℃, and the curve was linear. Specially, the device is convenient to detect high temperature, for example, the resistor of diamond film was less than 100 MΩ when the temperature is high than 200℃. So the resistor measurement is very easy to make with high precision at high temperature. The resistor-temperature coefficient (α) can be given from Fig. 4 as .follow:

$$\alpha = (1/R) * (dR/dT) = 4.5*10^{-3}/℃ \qquad (2)$$

it is large than other thermal-sensitive resistors repoted (α is $3.85*10^{-3}/℃$ for Pt film). The intrinsic conductivity of diamond film calculated by formula (1) is $3.6810^{-10}\Omega^{-1}cm^{-1}$. the further experiment show that the response and recovery time of this device are 10 senconds and 16 senconds, and the device is stable to various temperature. the characteristics of thermal-sensitive for this device are conficent to different sample prepared in same condition, so the device is reproducible.

3. Conclusion

124

In conclusion, a thermal-sensitive device was fabricated with diamond and planar interdigital Ti microelectrode arrays. This device can easily detect temperature from 20 ℃ to 700 ℃, it exhibits high sensitivity rapidly reponse and good stablity, it is convenient to reproduct.

4. References

1. K. Baba et al., J. Appl. Phys., 69 (1991) 7313
2. N. Nakahata etal., New Diamond (Japan New Diamond Forum 1988) P. 64
3. N. D. Belton et al., Appl Phys. Lett., 54 (1989) 416
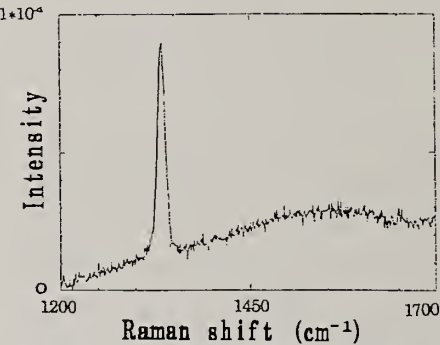
Fig. 1 The Raman spectroscope of
diamond film
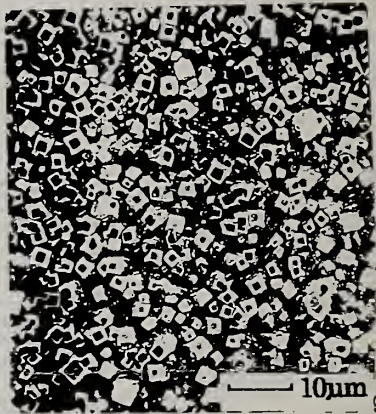
Fig. 2 The Scanning electron microscope
photograph of diamond film
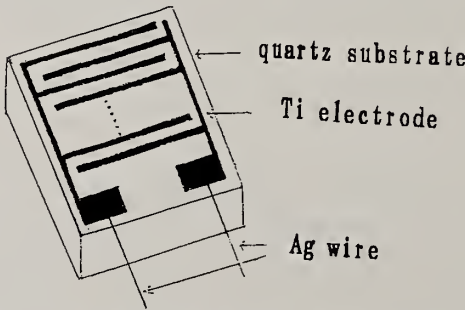
Fig. 3 The detailed view of the planar
measurement electrode
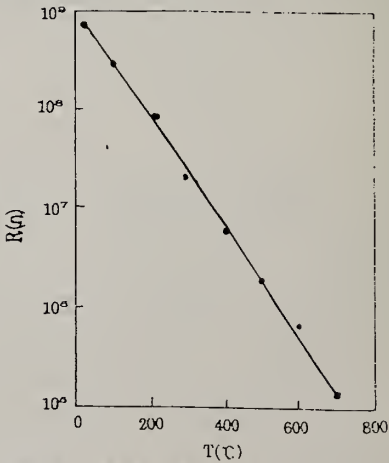
Fig. 4 The resistor-temperature
characteristic of diamond film

Applications of Diamond Films and Related Materials: Third International Conference, 1995
Editors: A. Feldman, Y. Tzeng, W. A. Yarbrough, M. Yoshikawa, and M. Murakawa

125

CVD Diamond Resistor as Heater and Temperature Sensor

G. S. Yang and M. Aslam

Department of Electrical Engineering, Michigan State University, East Lansing, MI 48824, U.S.A

Key words: CVD, diamond, heater, temperature sensor

Abstract

Heat generation and temperature control, essential for most heater applications, require different components in a conventional system. We achieve the heat generation and temperature measurement simultaneously by using a single diamond resistor. Chemical vapor deposited (CVD) p-type diamond resistors with different dimensions were fabricated on polycrystalline diamond or oxidized Si substrates using diamond film technology compatible with integrated circuit (IC) processing. The temperature response of the resistors was characterized in the temperature range of 25 - 500 °C. Power densities in access of 600 watt/in^2 were achieved.

1. Introduction

The heat generation and temperature control are essential for most heating applications. Normally, different materials are used for heat generation and temperature sensing. In such a configuration, thermal properties of different materials, if not carefully considered, may cause problems. It is also important to minimize the uncertainties in the measurement associated with the heat dissipation and the placement of sensing elements. These difficulties may be eliminated by using a single element as heater and temperature sensor simultaneously. The desired material properties for such an element include high thermal conductivity, the ability to be used as an electrical conductor and insulator, high sensitivity to temperature and mechanical stability. Diamond seems to be an excellent material for such an application. Due to its large band gap of 5.5 eV, diamond can be used as an electrical insulator (undoped) and a semiconductor (boron doped). CVD diamond thermistors with an excellent sensitivity were demonstrated over a wide temperature range of 80 - 1270 K [1]. In this paper, we report, for the first time, the use of a single diamond resistor as a thin film heater and temperature sensor.

2. Experimental

The doped and undoped diamond films used in the present study were prepared by a hot filament CVD reactor equipped with a 4.5 X 5 inch^2 tantalum filament array. Typical deposition conditions were 1% methane in hydrogen at 50 torr with a total flow rate of 404 sccm. The substrate and filament temperatures were maintained at 850 - 900 ^{o}C and 2000 - 2200 ^{o}C, as measured by thermocouple and optical pyrometer, respectively. Two stainless steel holders containing high purity boron powder were placed on substrate holder for in-situ doping.

Two different structures were designed and fabricated to characterize the temperature sensing and heating properties of diamond resistors as shown in Fig. 1. In the case of oxidized Si substrates, diamond powder loaded fluid (DPLF) was spin-coated to enhance the nucleation [2] and was patterned by photolithography [3]. A layer of undoped diamond was found to enhance the quality of doped layer even for very high doping levels. In case of the 2nd structure, a boron-doped layer with a thickness of one micrometer was deposited on a commercially available 1 cm^2 undoped-diamond substrate [4].

Using a rapid thermal processor (RTP), a ten-minute heat treatment was performed at 650 ^{o}C in nitrogen for all samples before the metal evaporation to stabilize the temperature response of the doped diamond film. A Au/Ti double layer or Al was used to provide the electrical contact. An RTP annealing at 400 and 700 ^{o}C for Al and Au/Ti contacts, respectively, was used to enhance the adhesion between metal and diamond.

3. Results and discussion

The relationship of power density and heating temperature was determined for all samples under different conditions. The temperature of resistors measured at the different points by a thermocouple is proportional to the applied power under 200 ^{o}C. Representative curves of data collected for temperature measured at the center of each resistor are shown in Fig. 2. Relatively large amount of heat loss occurring through convection and radiation at temperatures above 300 ^{o}C causes a nonlinear relationship between applied power and temperature. As expected, more efficient heating was observed in the cases of free standing and vacuum configurations. Due to the smaller and thinner substrate size of samples in structure 2, more effective heating was observed.

The Steinhart-Hart equation, defined by $\frac{1}{T} = a + b(\ln\rho) + c(\ln\rho)^2 + d(\ln\rho)^3$, was used to characterize the resistivity-temperature relationship of all thermistors in the range of 25 - 500 ^{o}C. An average error of less than 1% resulted for temperature sensing application. By monitoring the applied voltage across the resistor and

current flowing through it, the resistance can be calculated, therefore the temperature can be deduced from the Steinhart-Hart equation with predetermined coefficients during heating processes. Collected data are shown in fig. 3. The average error for self-heating temperature measurement over the temperature range of 25 - 500 °C is 4.6%. The higher percentage of error is due to an increased deviation for applied field greater than 400 Volt/cm. The field dependence of resistivity of diamond films is reported else where [5].

In the case of commercially available thick film heater based on nickel, Al, carbon steel alloy [6], the maximum operating temperature and power density are in the range of 300 - 1200 °C and 5 - 250 watt/in^2, respectively. By applying power of less than 10 watt, a heating temperature of approximative 550 °C was achieved. A higher maximum heating temperature is possible if a passivation layer is used or the heater is operated under non-oxidizing environment. A relatively high power density of 600 watt in^2 was observed for free standing sample.

The Steinhart-Hart equation has been determined to be the best mathematical expression for the resistance-temperature relationship of a negative temperature coefficient thermistor [7]. The sensitivity of temperature response of thermistor is usually characterized by the constant β [7], which is define by $\beta = \ln(R_1/R_2)/(1/T_1 - 1/T_2)$. The typical value of beta for conventional metal-oxide thermistors ranges from 2000 to 4000 over 25 to 400 °C [7]. The beta value of diamond thermistors is typically in the range of 1000 to 5500. In this article, β of all samples ranged from 940 to 1310, which is capable to provide an effective heat generation with reasonable accuracy. The higher sensitivity (β) is achieved at low doping level where the corresponding resistance values are unacceptably high for practical applications. Especially for heating applications, low resistance is desirable to provide efficient heating.

4. Conclusion

Heat generation and temperature measurement were achieved simultaneously by using a single CVD diamond resistor. It is not only capable to deliver a relative high power density (~ 600 watt/in^2) thus provide an efficiency and uniformly heating, but also able to monitor the temperature with an error less than 4.6% up to 500 °C. In addition, the diamond resistors could be direct deposited on the object to be heated with an exact and accurate custom designed pattern. Due to the negative temperature coefficient of resistance, diamond heater provides more efficiency while operating at high temperature range. The power density could be further enhanced by increasing the doping level or film thickness. The sensing properties at high field level are under study.

128

5. References

1. M. Aslam, G. S. Yang, and A. Masood, Sensors and Actuators: A., 45, 2, 131-137, (1994).
2. G. S. Yang and M. Aslam, Appl. Phys. Lett. 66(3), 311 (1995).
3. A. Masood, M. Aslam, M. A. Tamor and T. J. Potter, J. Electrochem. Soc., Vol. 138, No. 11, L67 (1991).
4. The polycrystalline diamond substrate is commercially available from Diamonex Inc.
5. S. Sahli, X. Hou and M. Aslam, "Field dependence of the resistivity of B-doped polycrystalline diamond films as a function of grain size and temperature", is presented elsewhere in this conference.
6. R. B. Tait, R. Humphries, and J. Lorenz, IEEE Transactions on Industry Applications, 30(3), 573 - 577, (1994).
7. R. Pallas-Areny and J. G. Webster, "Sensors and Signal Conditioning," Wiley, New York, 1991, 55 - 61.

6. Figures

Test structure 1(1.5 cm^2)   Test structure 2 (1 cm^2)

P-type Diamond (1μm)

Undoped Diamond
(1-1.5, 200 μm for structure 1, 2)

Metal Contact (0.5 μm)

Oxidized Silicon (500 μm)
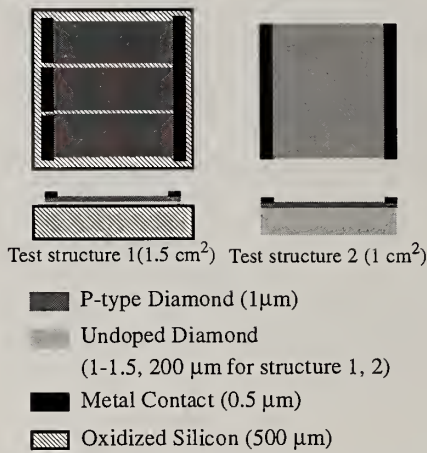
Fig. 1 Schematic diagrams of two test structures. The resistors on structure 1 are 1 x 0.3 cm^2.
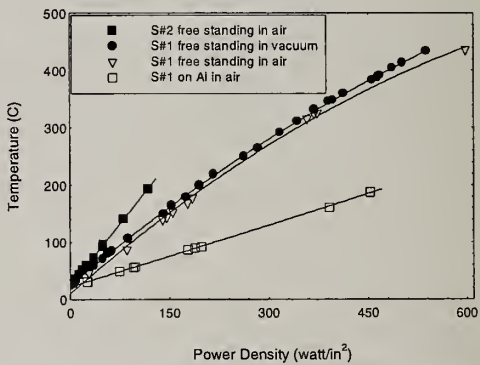
Fig. 2 Power density versus heating temperature
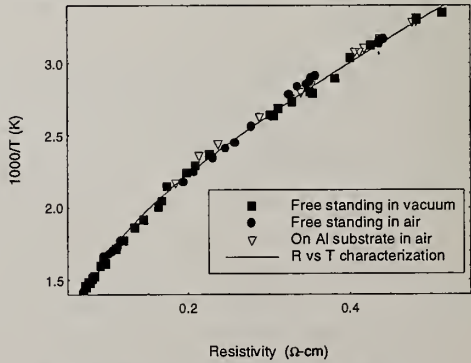
Fig. 3 Heater application characterization.
Average error over 25 - 500 °C = 4.6%

Applications of Diamond Films and Related Materials: Third International Conference, 1995
Editors: A. Feldman, Y. Tzeng, W. A. Yarbrough, M. Yoshikawa, and M. Murakawa

129

CVD DIAMOND FILMS FOR X-RAY DETECTORS

V.F. Dvoryankin, A.A. Kudryashov, Yu.Sh.Temirov,
L.L Bouilov*, G.A. Sokolina*, A.E.Alexenko*

Institute of Radio Engineering and Electronics of RAS, Fryazino, Moscow Reg.,
141120, Russia
*Institute of Phisical Chemistry of RAS, Moscow, 117915, Russia

Key words: CVD diamond films, X-ray detectors

Abstract

The diamond films produced by enhanced chemical vapor deposition (CVD) technique
have been used to fabricate the radiation detectors. The polycrystalline diamond films
have a measured resistivity $\sim 10^{15}$ Ω cm. We report the characterization of the
detectors made from CVD diamond thin (~ 20 μm) films. The response of the detectors
to a flux of X-ray photons produced by an X-ray tube was investigated. The detector
response to X-ray flux is almost linear. These results show that CVD diamond film
detectors can be used for X-ray flux and dose measurements.

1. Introduction.

In the last few years the progress was made in diamond film growth by CVD [1,2].
High resistivity (up to 10^{13} Ω cm) polycrystalline diamond films up to a few hundred
micrometers thick are deposited on large surfaces with a good reproducibility. Such
diamond films can be used for the fabrication of the radiation detectors [3,4]. Because
of the large number of variables, systematic correlation between growth parameters
and diamond quality is one of the main tasks in developing CVD diamond detectors. In
this report CVD diamond films [5] are used as room temperature X-ray
photoconductors as their dark current is low due to their fairly large bandgap.

2. Model of the detector.

The X-ray radiation detection is one step electron process: direct conversion due to the
photoeffect X-ray-electric charge. The simple model of detector does not differentiate
between the carriers, assumes zero contact resistance, uniform illumination of the
photodetector and uniform current flow within the detector [6]. According to this model
the X-ray induced detector current I_{ph} is given by

$$I_{ph} = eE\,\mu\tau nA\ , \tag{1}$$

where e -the charge of an electron, $E=V_b/t$ - the electric field within the detector, V_b- the detector bias voltage, t - the thickness of the detector, μ and τ - the carrier mobility and the lifetime, n - the density of carriers generated per second in CVD diamond film by the X-ray radiation, A - the surface area of the detector. The density of carriers is given by

$$n = \frac{\varepsilon_D \eta}{\omega A t}\ , \tag{2}$$

where ε_D - the X-ray energy absorbed within the detector; $\varepsilon_D =\varepsilon_0 - \varepsilon_t$, ε_0 - the incidence X-ray energy on the detector, ε_t- the X-ray energy passed through the detector of the thickness t, η- the quantum yield. The energy absorption coefficient for the carbon is known [7], ω - the electron-hole pair generation energy ($\sim$ 13 eV [8]). The intensity of the X-ray radiation produced by an X-ray tube depends on the anode atomic number Z, the X-ray tube high voltage U, the X-ray tube current I_A and the wavelength λ. The integral intensity of the bremsstrahlung X-ray spectrum can be expressed as

$$I_t = \int_{\lambda_{min}}^{\infty} I(\lambda)d\lambda\ , \tag{3}$$

where λ_{min} ($\overset{\circ}{A}$) = 12.345/U (kV). One of the important parameters of CVD diamond detectors is the carrier collection distance $d=\mu E\tau$. As can be seen from (1) the detector photocurrent depends on the value d. When this distance is much smaller than the diamond thickness t, the observed detector photocurrent is proportional to the ratio d/t. According to [9] at high electric field within the detector ($E > 10$ kV/cm) CVD diamond films saturate at a collection distance around 10 - 15 μm, significantly lower than that of natural diamond. The onset of this saturation is probably related to imperfections and defects in the CVD diamond films.

3. Experimental results.

The detectors were fabricated using CVD diamond films about 20 μm thick deposited on the tungsten substrates. The titanium pads 1 mm in diameter were deposited on the film surface to form the electric contacts. The X-ray tube with a copper anode was used as a source of X-rays. The X-ray tube high voltage and the X-ray tube current covered ranges 11 kV < U <50 kV and 2 mA < I_A < 14 mA, correspondingly. The excitation X-ray tube voltage of CuK_α characteristic spectrum is equal 8.86 kV. The detector parameters in this report were taken with the bias voltage V_b =10 V ($E \sim 5$ kV/cm). Fig. 1 shows the X-ray detector current (the dark current $\sim$ 2 pA was substracted from the total current) as a function of the X-ray tube flux at the X-ray tube

high voltages 11, 27 and 40 kV. The detector photocurrent increases almost linearly with the X-ray tube current in the range 6 mA $< I_A <$ 12 mA. The photoelectric activity of the detector can be characterized by $S = \Delta\sigma / \sigma_0$, where $\Delta\sigma = \sigma - \sigma_0$, σ_0 - the dark electroconductivity of the detector and σ - the electroconductivity of the detector under X-ray illumination. The detector electroactivity is shown as a function of the X-ray tube current at the X-ray tube high voltages 11, 27 and 40 kV in fig. 2. Fig. 2 shows that the CVD diamond detectors can be successfully used for X-ray flux and dose measurements.

4. Conclusion.

The calculation of the X-ray detector photocurrent is connected with the difficulties of the measurements of the lifetimes, the mobilities and the concentrations of the electron and holes excited by the X-ray radiation in the CVD diamond films. The formation of the ohm contacts on the CVD diamond film surfaces is one of the main tasks in the development of the CVD diamond detectors.

5. References.

1. M.A. Plano, S. Han, D.R. Kania, M.I. Landstrass. Diamond and Related Materials, 2 (1993), 820.
2. J.L. Kaac, P.K. Gantzel, J. Chin, W.P. West. J. Mater. Res., 5 (1990), 1480.
3. C.P. Beetz, B. Lincol, D.R. Winn, K. Segall, M. Varas and D. Wall. IEEE Trans. Nucl. Sci., 38 (1991), 107.
4. F. Foulon, T. Pochet, E. Cheeraert, A. Deneuville. IEEE Trans. Nucl. Sci., 41 (1994), 105.
5. Л.Л. Буйлов, А.Е. Алексенко, А.А. Ботев, Б.В. Спицын. Докл. АН СССР, 287 (1986), 888.
6. J.S. Blakemure. Semiconductor statistics. Pergamon Press, Oxford-London-New-York -Paris, 1962
7. О.Ф. Немец, Ю.В. Гофман. Справочник по ядерной физике. Наукова думка, Киев, 1975
8. C. Canali, E. Gatti, S.F. Kozlov, P.F. Manfredi, C. Manfredotti, F. Nova and A. Quirini. Nucl. Instr. and Meth., A160 (1979), 73.
9. M. Franklin, A. Fry, K.K. Gan, S. Han, H. Kagan, S. Kanda, D. Kania, R Kass, S.K. Kim, R. Malchow, F. Morrow, S. Olsen, W.F. Palmer, L.S. Pan, F. Sannes, S. Schnetzer, R. Stone, Y. Sugimoto, G.B. Thomson, C. White and S. Zhao. Nucl. Instr. and Meth., A315 (1992), 39.
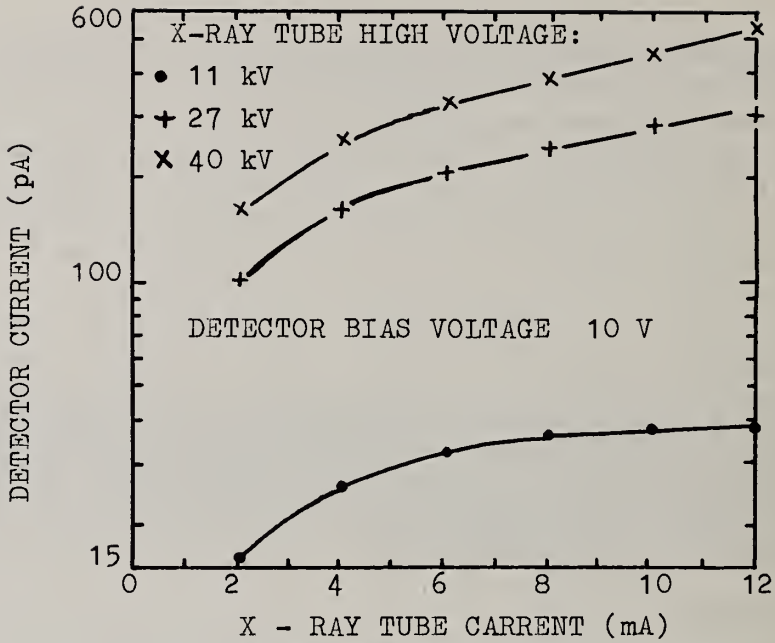
Fig.1. X - ray induced detector current versus
X - ray tube current.
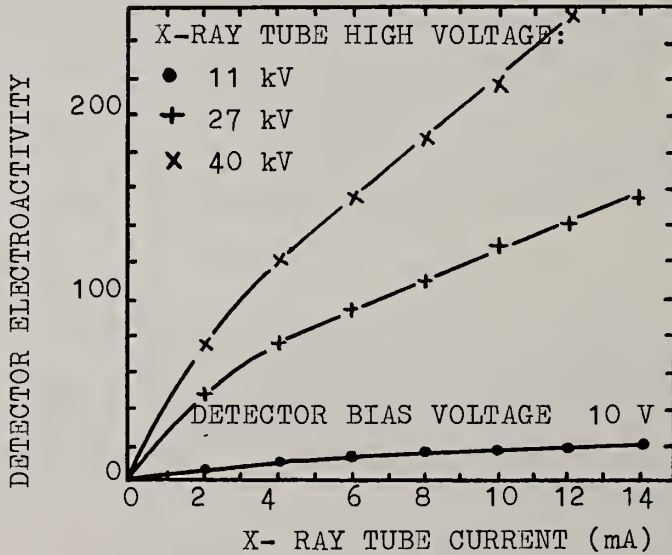
Fig.2. Detector electroactivity as a function
of X - ray tube current.

NANOCRYSTALLINE DIAMOND MEMBRANE GROWTH BY CYCLIC RENUCLEATION

L.M. Troilo,[1] M.S. Owens, J.E. Butler, L. Shirey and G.M. Wells[2]

Naval Research Laboratory, Washington, D.C. 20375
1) Geo-Centers, Inc., Fort Washington, MD 20744
2) Center for X-ray Lithography, University of Wisconsin-Madison, Stoughton, WI 53589

Key words: diamond, membrane, nanocrystalline, x-ray lithography

Abstract

Smooth, clear nanocrystalline diamond films have been grown on Si substrates to a thickness between 0.7 and 3.0 microns, and were subsequently etched into membrane structures for use as proximity mask membranes in x-ray lithography, x-ray window, and optical pellicle beamsplitter applications. The diamond deposition was by microwave plasma enhanced, chemical vapor deposition using a cyclic renucleation process. The gas mixtures of hydrogen, methane, nitrogen and oxygen were cyclically altered to control grain size and quality. Nanocrystalline grain sizes were achieved without significant introduction of amorphous carbon into the material as determined by micro-Raman analysis.

1. Introduction

Diamond membranes less than 2 microns thick are candidates for proximity mask membranes in x-ray lithography of patterns less than 0.25 microns.[1] Properties that make diamond an excellent alternative for x-ray lithography applications include: high optical transparency which would allow for through the mask alignment; high radiation hardness which would provide extended life of the membrane;[2] and high Young's modulus which would provide minimal pattern movement.[3] Important practical issues for the use of diamond films in these applications are surface smoothness, optical transparency, low light scatter, controlled tensile stress, and durability. Polycrystalline diamond films have micron sized crystallites which typically have a surface roughness on the order of hundreds of nano-meters which is unacceptable for sub 0.25 micron patterns. The well known bulk properties of hardness and low chemical reactivity make post-deposition polishing of diamond economically inefficient and technically challenging. Because of the larger thermal expansion coefficient of Si relative to diamond, compressive thermal stresses are expected when film and substrate are cooled to room temperatures from deposition temperatures above 800°C. The intrinsic stress of polycrystalline diamond films can be controlled by controlling deposition parameters such as methane concentration, deposition temperature and pressure.[4] Recently, two distinct types of stress have been measured: tensile intrinsic; and thermal compressive.[5] The direct deposition of smooth, transparent and tensile diamond membranes via plasma chemical vapor deposition has been the desired method of membrane fabrication[6] and is the focus of this study.

Our approach to the growth of smooth, controllably tensile films is to combine a high initial nucleation density with the growth of high quality, controlled nanocrystalline grain size diamond films. This approach employs the incompatibility between conditions optimal for diamond growth and nucleation. Following the initial nucleation, deposition conditions are used for high quality diamond deposition, which are then briefly altered to induce renucleation upon the growth surface. Multiple repetitions of this process of growth and renucleation leads to a limited grain size distribution and cessation of columnar grain growth. The resulting tensile membrane exhibits nanocrystalline grain size, and minimal amount of non-diamond carbon.

2. Experimental Procedure

Diamond samples presented in this study were deposited on both n and p type Si(100) wafers. These double sided, polished wafers had diameter and thickness dimensions of 75 mm and 0.38mm, respectively. The n type samples were doped with antimony to a resistivity of 0.010 ohm-cm while the p type wafers were doped with boron to a resistivity of $\geq$ 23.0 ohm-cm. The native oxide layer inherent on these wafers was removed with a 10-15 minute buffered hydrofluoric acid (15% NH_4OH, 22%HF and 63% H_2O by volume, pH of 4) treatment.[7] The substrates were subsequently rinsed with de-ionized water and air dried. Next, wafers were manually dry polished for 3-4 minutes on a 155mm polishing cloth that was impregnated with 0.1 micron diamond powder. Excess diamond powder was removed in a methanol rinse and wipe. The samples were blown dry in a stream of nitrogen and immediately placed into the reactor for deposition.

Depositions were performed in an Applied Science and Technology, Inc. (AsteX) PDS-17 Microwave Plasma Enhanced Chemical Vapor Deposition Reactor. This reactor was equipped with a 1.5kW microwave power generator and a 3.5kW RF substrate heater. The wafer was placed on to a 6mm thick, 100mm diameter TZM alloy (molybdenum) cap that sat on a graphite susceptor/sample stage. A base pressure of 60mTorr was achieved in the reactor prior to starting hydrogen flow at 500 sccm. Once the desired deposition pressure was reached (15-25Torr), the sample was heated at a rate of approximately 15°/min to the desired deposition temperature. After reaching the temperature set point, the hydrogen plasma was turned on and allowed to stabilize before initiating the flow of the other process gases into the reactor. Process gases used in fabricating these membranes were high purity: H_2; CH_4; N_2; and O_2. To avoid damage to the nucleation step that may result from hydrogen plasma etching, only 1-2 minutes were allowed before turning on the process gases. Growth rates and film thickness were monitored *in-situ* using a helium-neon laser interferometry system.

As-deposited samples were opened into membranes by etching a 25mm diameter hole in the back center of the wafer using a simple "roto-etch" technique. (Materials and Technology, Inc. Poughkeepsie, N.Y). This technique incorporates a rotating teflon stage on which the sample was placed face down and a HF:Nitric:Acetic acid solution was slowly deposited and quickly sucked away via a triple trapped vacuum pump. The large wetting angle between the acid solution and wafer allowed a controllable active etch area and a clean diamond/Si interface.

Micro-Raman spectroscopy was used to determine the crystalline nature of the material, the relative amount of non-diamond carbon and any background/fluorescence in the sample.[8] Visible transmission was measured from 400 to 900nm, the surface of the samples was analyzed for pinholes using a High Resolution Scanning Electron Microscope (Leica Cambridge 360 FE), and the surface roughness was measured via a Topometrix Explorer Atomic Force Microscope. Internal stress (σ) of the samples was measured using a resonant frequency of circular diaphragms via the equation:

$$\sigma = \rho(2.61a\nu)^2$$

where ρ is assumed to be the bulk density of diamond (3.515 g/cc), a is the sample radius, and ν is the frequency. It was assumed in this analysis that the sample had uniform stress and thickness. The thickness variation was 0.5-0.6μm from the center to the sample edge.

3. Results

Various membrane parameters as a function of growth conditions are listed in Table I. Sample A was grown without the incorporation of N_2 or O_2 in either the growth or nucleation steps. Samples B and C were selected as representing the best and much less than optimal conditions, respectively, of

membranes fabricated with N_2 and O_2 in the process. The only difference between Samples B and C is the higher deposition temperature for C. The dramatic differences in properties between these two samples indicates the strong function that temperature plays in membrane growth.

Membrane average stress was measured as a function of process conditions and Figure 1 shows that stress as a function of gas pressure, with the desired value (100-200 MPa) attained at 15 Torr. Figure 2 shows the UV-visible spectra of samples fabricated under the conditions listed in Table I, and the effect that non-diamond carbon plays in optical transmission.

4. Discussion and Conclusions

The production of tensile, nanocrystalline diamond films has usually involved a trade-off in the physical characteristics of the film/membrane. Surface smoothness and low light scatter were usually attained by increasing the carbon species concentration during growth, at the expense of decrease optical transmission, inclusion of non-diamond carbon, and sacrificed physical properties. The addition of oxygen to the hydrogen/carbon growth mixture is well known for minimizing the non-diamond carbon in the deposited material and improving the optical transparency, while the addition of nitrogen has resulted in increased step density, twinning, and renucleation on the growth surface. The critical process parameters of plasma power, gas pressure, surface temperature, and carbon species concentrations impact the quality and microstructure of the deposited diamond films. These have been used to control the stress of the deposited films while the processing chemistry was modified to achieve significant improvements in the optical transparency, surface smoothness, and light scattering characteristics.

5. References

1. H. Windischmann, G. F. Epps, *J.Appl. Phys.* **68**(1) 5665 (1990); Y. Vladimirsky, J.R. Maldonado, O.Vladimirsky, A. Starikov, R. Fuentes, D. Guarnieri, S.W. Whitehair, and J. Cuomo, *J.Vac.Sci.Technol.* **B8** (6) 1579 (1990).
2. K. Suzuki, R. Kumar, H. Windischmann, H. Sano, Y. Iimura, H. Miyashita, and N. Watanabe, *J. Vac. Sci. Technol.* B9 (6), 3266 (1991); G.M. Wells, S. Palmer, F. Cerrina, A. Purdes, and B. Gnade, *J. Vac. Sci. Technol.* **B8** (6), 1575 (1990).
3. Y. Aikawa and K. Baba, *Jpn. J. Appl. Phys.* **32** 4680 (1993); H. Windischmann, G.F. Epps, and G.P. Ceasar, *MRS Proc. of the Int'l Conf. New Diamond Sci. and Technol.*, Pittsburgh, PA, 1991 p.767-727.
4. H. Windischmann, G.F. Epps, Y. Cong, and R.W. Collins, *J. Appl. Phys.*, **69**(4) 2231 (1991); N.I. Maluf, R.F.W. Pease, and H. Windischmann, *J. Vac. Sci. Technol.* B8(6) 1584 (1990).
5. D. Schwarzbach, R. Haubner, and B. Lux, *Diamond and Related Materials*, **3** 757 (1994).
6. F.G. Celii, D. White, Jr., and A.J. Purdes, *Thin Solid Films*, **212** 140 (1992); L. Schafer, A. Bluhm, C.P. Klages, B. Lochel, L.M. Buchmann, and H.L. Huber, *Diamond and Related Materials*, **2** 1191 (1993).
7. V.A. Burrows, Y.J. Chabal, G.S. Higashi, K. Raghavachari, and S.B. Christman, *Appl. Phys. Lett.* **53** 998 (1988).
8. D.B. Oakes, J.E. Butler, K.A. Snail, W.A. Carrington, and L.M. Hanssen, J. Appl. Phys. **69**, 2602 (1991).

Table I.　Characteristic properties of diamond membranes fabricated under different conditions. Sample A is a typical of a membrane made without O_2 and N_2 in the process. Samples B and C are membranes made with O_2 and N_2 at 800°C and 900°C, respectively.

	Sample A		Sample B		Sample C
Pressure (Torr)	20		15		15
Temperature (C)	800		800		900
Percent Carbon in:					
nucleation	3.0		1.4		1.4
growth		0.5		0.7	
0.7					
Percent Oxygen in:					
nucleation	0		0.3		0.3
growth	0		0.3		0.3
Percent Nitrogen in:					
nucleation	0		0.7		0.7
growth	0		0		0
Gas flow during growth (sccm):	404		1021		1021
Deposition time (minutes)	350		330		330
Thickness (microns)	1.2		1.1		1.1
Transmittance (%):					
maximum	60		85		70
peak to peak at 633nm	4		20		6
1/2max at 633nm	38		64		53
Stress (MPa)	320		170		297
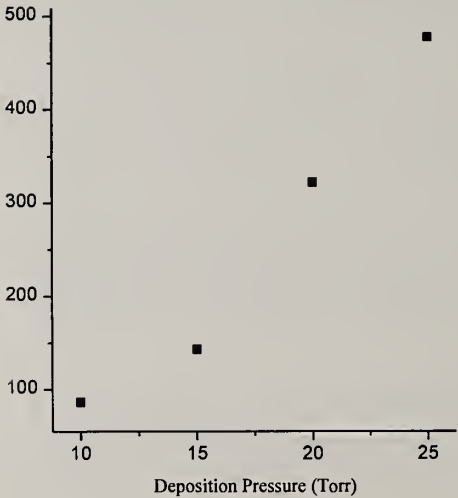
Figure 1: Membrane stress as a function of gas pressure. All other conditions are constant.
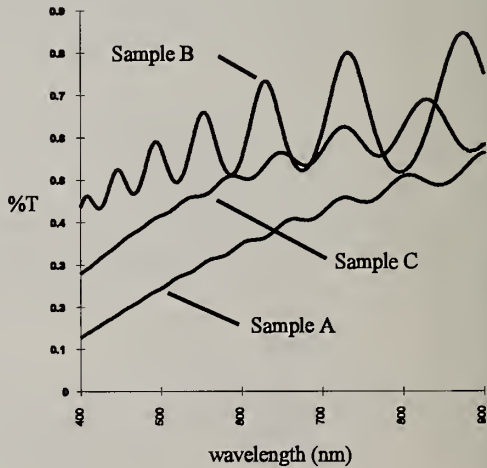
Figure 2: Membrane optical transmission for samples summarized in Table I.

Applications of Diamond Films and Related Materials: Third International Conference, 1995
Editors: A. Feldman, Y. Tzeng, W. A. Yarbrough, M. Yoshikawa, and M. Murakawa

137

Titanium Acoustic Diaphragm Coated with Polycrystal Diamond Film

Zhiwei ZHANG, Zhen YAN, Hesun ZHU, Qinghua ZHAO, Chuanbao CAO
Research Center of Materials Science, Beijing Institute of Technology, 100081
Beijing, P.R.China

Abstract

The spherical titanium diaphragm, which is widely used in high frequency loudspeaker, coat with polycrystal diamond film (DF) was prepared for the first time in China by the method of DC arc plasma jet. Its acoustic performance was remarkably upgraded, as confirmed by Raman Shift Spectrum and frequency response curve. Its sensibility was improved by 3-6 dB and frequency widened by 5×10^3Hz. The frequency range extended from 2.2×10^3Hz to 25×10^3Hz. The preparation and process of DF is discussed.

Key Words: Diamond Film, Acoustic, Titanium, Diaphragm

1 Introduction

It is well known that the audible range of sound is about 40Hz-16×10^3Hz for most people. Nowadays, the diaphragms are mainly made from titanium. Its High Resonance Frequency(HRF) is 16×10^3 to 18×10^3Hz. After coated with diamond-like carbon (DLC), titanium diaphragm got a HRF about 35×10^3Hz. The HRF value of diamond film (DF) diaphragm is 63×10^3Hz. From these data, we can deduce that if titanium diaphragm coated with DF, its HRF value must be further improved. We can also see the difference among several diaphragms from the table I according to their sound conduction velocity ($c=(E/\rho)^{1/2}$).

Table I Properties of several diaphragms

Material	Sound speed(km/s)	Yang's modules(10GPa)	Density(g/cm^3)
steel	5.1	20	7.9
Al	5.2	7.4	2.7
Ti	5.2	11	4.5
WC	6.8	72	15.6
DLC-Ti	6.8	20	4.5
B$_4$C	9.6	35	3.8
3-layer B$_4$C	9.6	35	3.6
DF-Al$_2$O$_3$	10	46	3.8
Al$_2$O$_3$	10.4	43	3.9
Be	12.3	28	1.8
DF	16.5	90	3.3
Diamond	18.5	115	3.5

2 Preparation

We use a DC arc plasma jet to prepare the diamond film. The equipment was designed by ourselves[1]. The reactive gases are methane (CH_4) and hydrogen (H_2). The working gas is argon (Ar). Their ratio are: Ar/H_2=7/1, H_2/CH_4=100/5. The flux of Ar is 0.1 m^3/h.

From experiment we known that it is difficult to separate DF diaphragm from its substrate materials such as molybdenum and silicon because of its fragility. So one way to solve the problem is to make multilayer DF-Ti diaphragm. Ti has two allotropes When its temperature is below 882°C, it has α-structure (hexagonal close-packed), the ratio of space usage is 0. 7405; When its temperature is above 882°C, it has β-structure (body-centered cubic), the ratio of space usage is 0.6801. When Ti changes phase from α-phase to β-phase, its volume will expand. So it is easy for Ti to distort in the form of 0.06-2 mm thick film. But 0.04 mm thick Ti can avoid distortion, which conducts heat quickly.

We get a Ti diaphragm coated with DF as follow process. Take a 25mm string length Ti diaphragm as the substrate. Pretreat 10 minutes by ultrasonic device in alcohol liquid containing diamond powder, The aim is to clean oil, water and to generate scratch   which is beneficial for the nucleation of diamond. Then we clean the diaphragm by absolute ethyl alcohol. After deposit DF, a new diaphragm was created.

3. Measurement of Ti Diaphragm Coated with DF
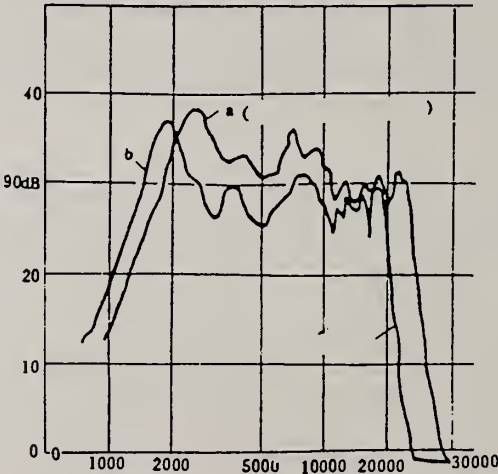
Fig. 1 Frequency response curve.   Fig. 2 Raman shift spectrum
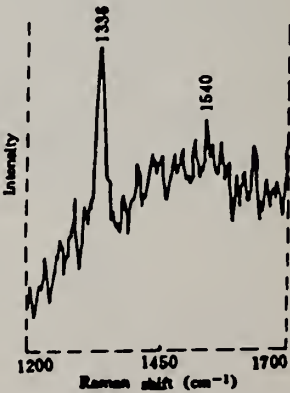
Table II   YDQG5-1 spherical top tweeter using result

Item	Ti diaphragm	DF coated Ti diaphragm
Thickness(μm)	35	37
Resonance frequency f_0(Hz)	1800	2450
Effective frequency range(Hz)	f_0-20000	f_0-25000
Characteristic sensitivity level(dB)	91	94
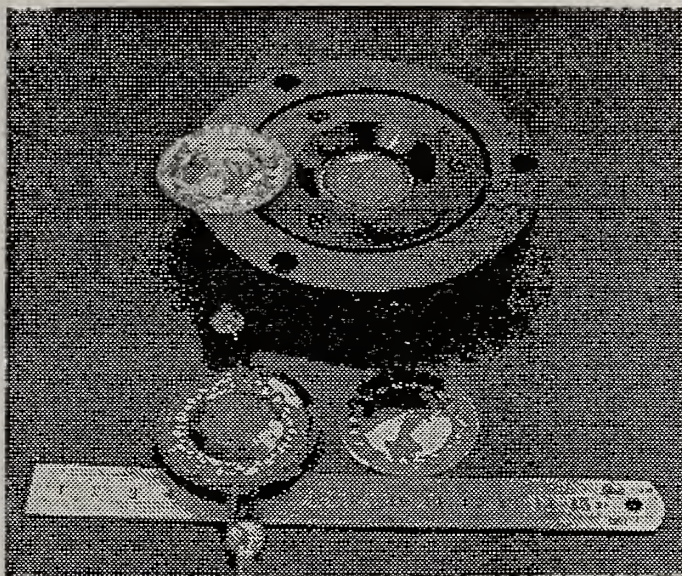
Fig.3 Samples of tweeter and the new diaphragm.

4. Conclusion

After a sequence of experiment, we can see several results. 1) DC arc plasma jet method can prepare good quality DF coating on Ti diaphragm. 2)The new diaphragm is a more sensible material. 3) The new diaphragm has a high HRF value than the old one. 4) The technique of preparation is very particle.

References

1. Yan Zhen, Li Rongzhi, High-Tech Report, 1991(5):17-19
2. Yoshioka T, Imai O, Ohara H et al. Thin Solid Films of Ceramic and Diamond and Their Application, 1988(36):311-318
3. Park S S, Lee J Y. J. App. Phys., 1991,69(4):2618-2622
4. Zhiwei Zhang, Rongzhi Li, Hesun Zhu, Minhua Mao, Titanium Film Coated with Polycrystal Diamond, High Technology Letters, 1993,3(8):12-15
5. Zhiwei Zhang, Rongzhi Li, Hesun Zhu, Review of Diamond Film and High-Fidelity Acoustic Diaphragm Materials, 1994, 8(4):330-336
6. Zhiwei Zhang, Qinghua Zho, Minhua Mao, Hao Jiang, Discussion on Physical Change of Complex Diaphragm Coated with Nitride for Tweeters, 1995(1):35-38

Applications of Diamond Films and Related Materials: Third International Conference, 1995
Editors: A. Feldman, Y. Tzeng, W. A. Yarbrough, M. Yoshikawa, and M. Murakawa

141
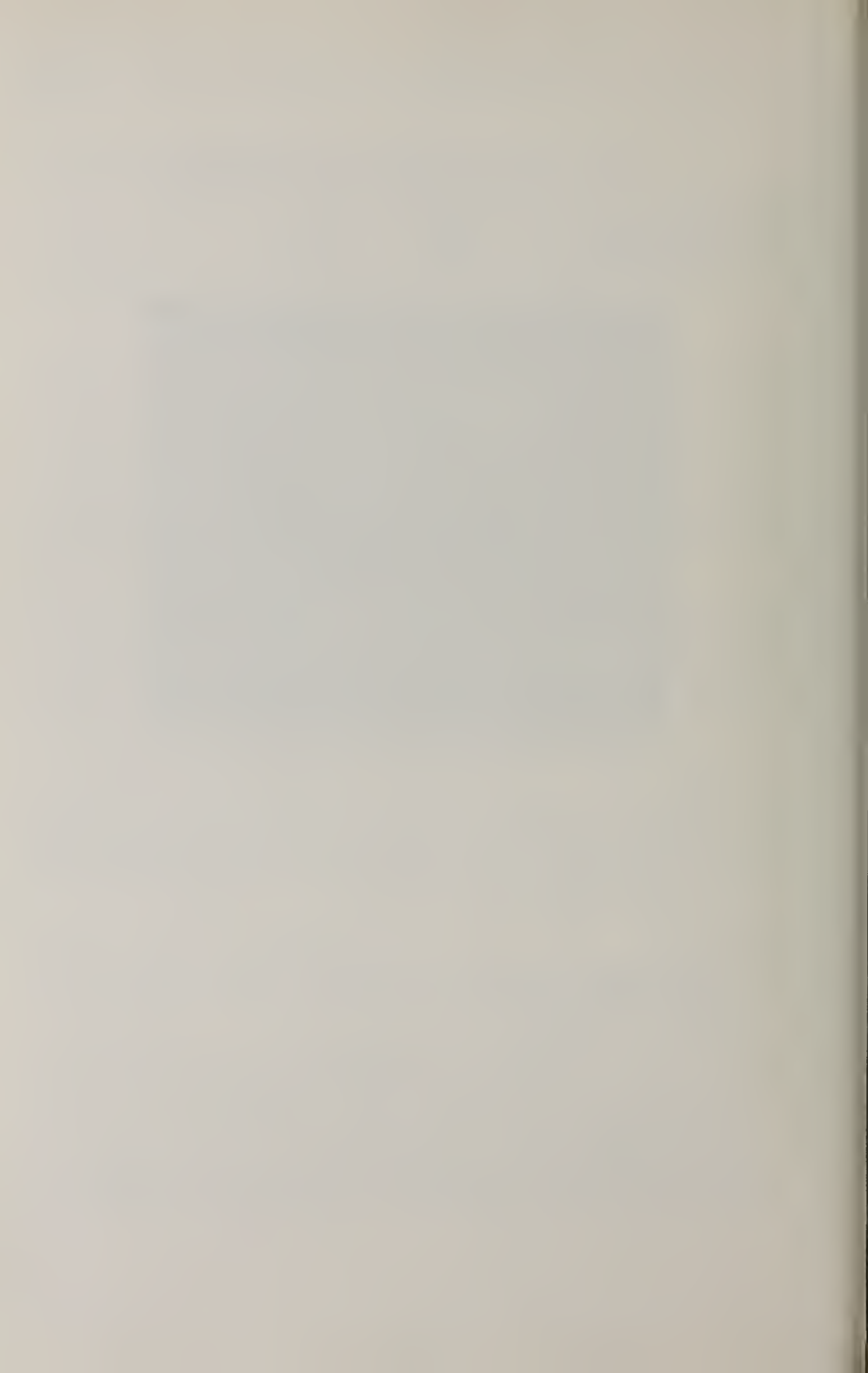
DETERMINATION OF BARRIER HEIGHT OF BORON DOPED POLYCRYSTALLINE DIAMOND THIN FILM SCHOTTKY DIODES USING A CAPACITANCE-VOLTAGE TECHNIQUE

Ganming Zhao, Elaine Charlson, Tina Stacy, E. J. Charlson

Department of Electrical & Computer Engineering
University of Missouri, Columbia, Missouri 65211, U.S.A.

Key words: barrier height, capacitance-voltage, CVD, Schottky diode, thin film

Abstract

Distinctive frequency dependent capacitance-voltage (C-V) characteristics of boron-doped chemical vapor deposited (CVD) diamond thin film Schottky diodes were observed. The results exhibited not only small signal differential capacitance dependence on both the reverse bias voltage and test frequency, but also linear inverse squared capacitance-voltage characteristics at all test frequencies, ranging from 1 kHz to 1 MKz. The Schottky barrier heights of both Al- and Au-hot filament CVD diamond Schottky diodes were determined to be 1.04 and 1.09 eV, respectively. An effective carrier concentration in the range of 0.5 to 1.5×10^{17} cm^{-3} was estimated. The distinct C-V characteristics obtained in this study are attributed to careful surface cleaning and the use of moderate boron doped diamond thin films.

1. Introduction

Since 1988, when G. Sh. Gildenblat and co-workers reported the first polycrystalline diamond thin film Schottky diode[1], much effort from many research groups has been devoted to reproducing and studying diamond thin film Schottky diodes, using a variety of diamond film synthesis approaches, characterization tools and techniques for the formation of rectifying contacts[2-4]. However, the work related to the electrical characterizations of diamond thin film Schottky diodes which has been reported so far, has concentrated on studies of current-voltage (I-V) characteristics, breakdown behavior, barrier height measurements, and temperature effects. There are few reports on studies of frequency dependent C-V characteristics of boron doped CVD diamond thin film Schottky diodes. The major problems associated with C-V study can be attributed to the deep level impurity effect of the boron dopant in diamond, and CVD diamond surface treatments. Studies show that substitutional boron dopants form deep impurity levels, lying at about 0.37 eV above the diamond valence band[1,5]. Therefore, the semiconductor shows relatively high resistivity due to few free holes being ionized to valence band from deep centers at room temperature. Schottky diodes made from such substrates could exhibit more complicated C-V characteristics than their silicon counterparts do.

In this paper, an experimental study of the frequency dependent C-V characteristics of polycrystalline diamond thin film Schottky diodes is presented. Schottky diodes used for this study were fabricated using thermally evaporated aluminum and gold contacts to boron doped polycrystalline diamond thin films grown using a multiple hot filament CVD (HFCVD) process. Both aluminum and gold contacted diodes exhibited I-V characteristics similar to those of diodes fabricated on microwave plasma assisted CVD diamond thin films[1]. However, distinctive C-V characteristics were observed, exhibiting not only small signal differential capacitance dependence on both the reverse bias voltage and test frequency, but also linear inverse squared capacitance-voltage characteristics, at all test signal frequencies, ranging from 1 kHz to 1 MKz. Furthermore, the built-in potentials found from $1/C^2$ versus bias voltage plots were test frequency independent. The Schottky barrier heights of both Al- and Au-HFCVD diamond Schottky diodes were determined to be 1.04 and 1.09 eV, respectively. These barrier heights are consistent with the results obtained using a DC photoelectric method. An effective carrier concentration in the range of 0.5 to 1.5×10^{17} cm^{-3} was estimated from the slope of the $1/C^2$ vs. reverse bias plot at a test frequency of 1 kHz. In order to get better a understanding of these characteristics, a novel theoretical capacitance-voltage-frequency analysis of single deep level boron doped thin film diamond Schottky diodes is being carried out.

2. Experimental

Boron doped polycrystalline diamond thin films used for Schottky diodes were deposited on p-type (100) silicon substrates using a modified four-hot-filament CVD method with hydrogen and methane as the reaction gases and with acetone vapor as the carrier gas for the boron dopant (trimethyl borate). X-ray diffraction, scanning electron microscopy and Raman spectroscopy studies indicated that high quality boron doped polycrystalline diamond films were obtained. Details regarding the growth technique, process parameters and material characterization were reported earlier[6]. Prior to the metal deposition, two treatments, (i.e. dehydrogenation and surface chemical cleaning), were utilized to provide a stable diamond bulk film and a clean surface, according to the procedures described in Ref. 3. Schottky diodes were then fabricated by thermal evaporation of semi-transparent aluminum contacts on boron doped diamond thin films whose thickness was about 7-8 μm. The circular Al and Au contact areas were 4.5 and 3.2 mm^2, respectively. The small signal capacitance-voltage measurements were taken using a personal computer controlled Hewlett-Parkard 4192 A LF impedance analyzer, with the frequency range varying from 1 kHz to 1 MHz.

3. Results and discussion

Figures 1 and 2 show the $1/C^2$-V-f characteristics for Al- and Au-diamond Schottky diodes. In both cases, the measured diode capacitances were reverse bias dependent at all test frequencies, which was different than what was observed on our previously reported silver-diamond diodes[2], as well as Glover's single crystal diodes[5]. This new observation of C-V-f characteristics of diamond Schottky diodes is attributed to careful diamond surface cleaning and the reduced effect of the diode's series resistance. In Glover's study, a large series resistance was observed and it could not be neglected in the analysis of the C-V-f characteristics. The significant series resistance was attributed to two sources. One is the use of a thick (a few mm) HTHP diamond substrate which has 3 orders higher bulk diamond
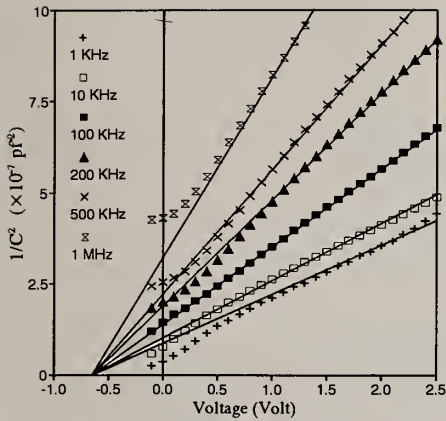
Fig.1 1/C²-V-f characteristics of Al-CVD diamond diode.
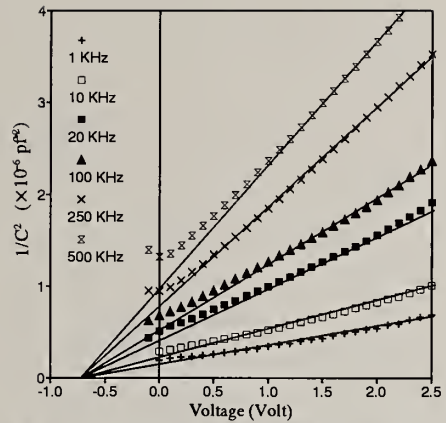
Fig.2 1/C²-V-f characteristics of Au-CVD diamond diode.

resistance compared to that of a thin film substrate (a few micrometers thick) with similar doping. The other source is the absence of proper diamond surface cleaning procedures to remove the highly resistive graphitic surface layer. Although a boron doped HFCVD diamond thin film was utilized on our silver on diamond Schottky diodes, a damaged surface layer was present near the interface due to the relatively high energy sputtering process, and hence probably resulted in the effect on the C-V-f characteristics.

Since the small signal capacitances of both kinds of diodes were controlled by the barrier capacitance of the depletion region, linear relationships between inverse squared capacitances and reverse biases were obtained for all test frequencies. Although the capacitances were frequency dependent in both cases, their intercepts on the voltage axis corresponding to the various frequencies investigated were comparable. Therefore, the barrier height ϕ_b can be determined by[5]:

$$\phi_b = V_i + \psi_a + \frac{KT}{q} \log(g) , \qquad (1)$$

where V_i is the extrapolated voltage intercept, ψ_a is Fermi level above the valence band, and g is the hole degeneracy factor (here g=2), T is the temperature, and q and K are the electronic charge and Boltzmann's constant, respectively. Apart from the last term, which is less than 0.02 V, V_i corresponds to the point where the Fermi level reaches the deep level at the surface. From Figures 1 and 2, the extrapolated voltage intercepts, V_i', was found to be 0.65 $\pm$ 0.05 V for Al-diamond diodes and 0.70 $\pm$ 0.05 V for Au-diamond diodes. Because of the small difference between the Fermi level and the deep impurity level in the deep level impurity controlled semiconductor, the well-known boron level ψ_a = 0.37 eV for lightly and moderately doped diamond was used for the calculation of Schottky barrier heights[5]. The barrier heights were found from equation (1) to be 1.04 eV and 1.09 eV for Al- and Au-diamond Schottky diodes, respectively. These results are very close to the barrier height of 1.15 eV, for both Al and Au contacts, determined using a dc photoelectric method[7]. Furthermore, corresponding to each a.c. signal frequency ω_s, the effective doping profile $N_{eff}(\omega_s, x)$ can also be extracted from the slopes in Figures 1 and 2, using equations (2) and (3):
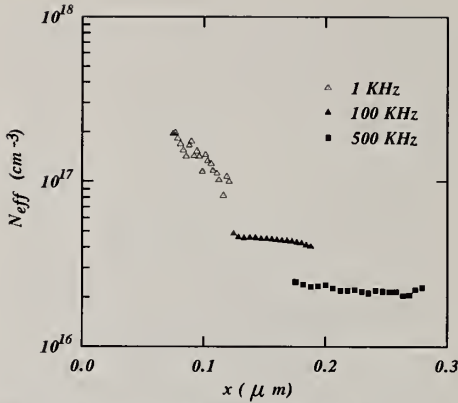
Fig.3   Effective doping profile of Al-CVD diamond diode.
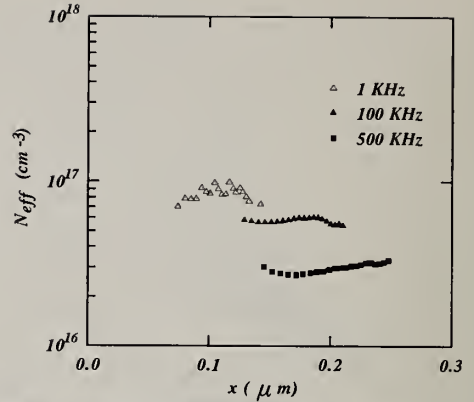
Fig.4   Effective doping profile of Au-CVD diamond diode.

$$N_{eff} (\omega_s, x) = \frac{2}{q\varepsilon} (\frac{dC^{-2}}{dV_r})^{-1} \qquad (2)$$

$$x = \frac{\varepsilon}{C} , \qquad (3)$$

where C is the measured diode capacitance per unit area, V_r is the reverse bias, ε is the dielectric constant (i.e. $5.5 \times$ free space permittivity for diamond), and x is the vertical depth from the diamond surface. Here, a simple model is used which assumes complete ionization of N_{eff} in the region of x, instead of the physical depletion region. Figures 3 and 4 show the effective doping profiles $N_{eff}(\omega_s, x)$ for Al- and Au-diamond Schottky diodes. Clearly, the effect of the deep levels is to produce an apparent effective doping decrease with an increase of the a.c. signal frequency, due to the slow response of the deep level impurities. This effect is known to occur in silicon Schottky diodes which have deep level traps[8]. Since the depth x is derived from the capacitance using equation (3), the effect of using this model is to shift the real doping profile away from the metal surface at high frequencies. Although this model does not represent the exact physical location of the doping profile, the N_{eff} profiles qualitatively show that the uniformity in the vertical direction is quite good in both samples. These results also confirm that the effective doping concentrations in both samples, which were grown in the same HFCVD run, are very similar, in the range of 0.5 to 1.5 $\times$ 10^{17} cm^{-3}.

4. References

[1] G. Sh. Gildenblat, et al, Appl. Phys. Lett., **53** 586(1988)
[2] G. Zhao, et al, Appl. Phys. Lett., **61** 1119(1992)
[3] G. Zhao, et al, J. Appl. Phys., **73** 1832(1993)
[4] T. Stacy, et al, J. Appl. Phys., **74** 763(1993)
[5] G. H. Glover, Solid-State Electronics, **16** 973(1973)
[6] G. Zhao, et al, Diamond Films and Technology (in press)
[7] G. Zhao, et al, in Proc. of MRS, **339** 191(1994)
[8] G. I. Robert and C. R. Crowell, Solid-State Electronics, **16** 29(1973)

Applications of Diamond Films and Related Materials: Third International Conference, 1995
Editors: A. Feldman, Y. Tzeng, W. A. Yarbrough, M. Yoshikawa, and M. Murakawa

145

DIAMOND FILM METAL-SEMICONDUCTOR-METAL PHOTODETECTOR

V.V.TOKIY[1], V.I.TIMCHENKO[1], V.A.SOROKA[1], N.TOKIY[1], B.V.SPITSYN[2], L.L.BOUILOV[2]

[1]Research Group of Diamond Electronic & Coatings
Donbass State Academy of Constructions and
Architecture, 339023 Makeyevka, Ukraine
[2]Institute of Physical Chemistry of Russian Academy of
Sciences, 117915 Moscow, Russia

Key words: photodetector, surface, undoped diamond film

Abstract

The polycrystalline diamond photodetector was characterized over a wavelength range of 400-2000nm. The origin of unwanted photoresponse for visible light is connected with reconstructed 2x1 and unreconstructed 1x1 parts of surface (111) of the undoped polycrystalline diamond film. It allow to propose its decrease by means of annealing and hydrogenating of diamond film at 870K.

1. Introduction

Photodetectors for ultraviolet and soft X-ray radiation in the presence of unwanted visible light could find application in areas such as solar physics research, atmospheric studies, celestial astronomy, and military systems [1-4]. In recent works, it was reported that metal-semiconductor-metal photodetectors have been fabricated in natural, synthetic, and polycrystalline insulating diamonds by [4-6]. They were characterized over a wavelength range of 130 - 700nm. In polycrystalline diamond photodetector for wavelengths from 450 nm to 700 nm authors of [4] observed unwanted increasion of response. The elucidation of the origin of this unwanted phenomenon was difficulty because of small in numbers of dicrete measuring.

In present work, the MSM structure was used to uninterrupted measure the photodetection properties of undoped polycrystalline diamond film (UPDF) for wavelengths from 400nm to 2000nm. It allow to determine the origin of diamond film photoresponse for visible light and to propose the way of its decrease.

2.Materials and methods

2.1.Preparation

UPDF was prepared on (111)-oriented p-type Si substrates by chemical vapour deposition [7]. A gas mixture consisting of 0.5 vol% CH and 99.5 vol% H was used to deposit UPDF. The total gas pressure and the deposition temperature were fixed at 112 Torr and 1170 K respectively. The film was 0.01 mm in thickness.

To avoid substrate leakage effects the sample was epoxied to a glass plate diamond side down) and the Si substrate was removed whith an HF + HNO etch.

In present work, the electrode configuration consisted of two 0.5 mm thick, 5 mm long and 3 mm wide aquadag stripes. The separation between the stripes was 1.5 mm. The electrodes were located onto the "rear" side of the film, which has been in contact with the Si wafer during the deposition process.

2.2.Measurements

The electric field was along the growth surface of UPDF and the current-voltage characteristics were symmetric for both polarities. The illumination was perpendicular to this plane. The illuminated area of the UPDF was 4.5 mm. The spectral dependence of the photocurrent was determined by using the quartz prism monochromator. A tungsten source was employed in the visible region. The photocurrent measurements were made using a "light on - light off" technique. The pulse width was 9 ms.

3.Results and discussion

The quantum efficiencie (QE) of the UPDF detector measured at difference biases in air as function of wavelengths are shown in Fig.1. Where QE is taken to be equal to the total number of electrons collected at the contacts divided by the total number of photons incident on the area between the stripes, measured in arbitrary units. The applied biases between the contacts were 400V, 600V and 800V.

The spectral characteristic indicates two the energy thresholds for carrier generation 0,6 eV and 1,4 eV.

These results are consistent with model which is shown in Fig2. Where empty surface states formed from dangling bond lie above Fermi level, E , within the bulk forbidden gap and will serve as electron traps. The tops of the reconstruction 2x1/2x2 and unreconstruction 1x1 surface(111) valence band are 1,4 eV

and 0,6 eV below Fermi level, respectively [8]. In this model photogeneration of holes can be due to the transition from the surface valence band to a empty surface level.

4.Conclusions

From these results we can conclude that changes of semiconductor properties of UPDF surface, for example by means of hydrogenation, excite the change of spectral photodetector characteristic. This proposition agree with before observing in [9] inactivation 0.6 eV and 1,4 eV trap levels after hydrogenation at 870K.

5.Acknowledgments

6.References

1. G.R.Carruthers,J.S.Morrill,B.C.Dohne and S.A.Christensen, The FP-675 far ultraviolet cameras experiment: observations of the far-UV space environment,SPIE Conf.1764, Ultraviolet Technology IV,July 1992.
2. R.Meier, Ultraviolet spectroscopy and remote sensing of the upper atmosphere,Space Sci.Rev.,58 (1991) 1.
3. K.V.Ravi, 2nd Int.Conf.on the Appl.of Diamond Films and Related Materials, ed.M.Yoshikawa, M.Murakawa, Y.Tzeng, W.A.Yarbrough, MYU, Tokyo, 993, 13.
4. S.C.Binari, M.Marchywka, D.A.Koolbec, H.B.Dietrich and D.Moses Diamond and Related Materials,2 (1993) 1020.
5. M.Marchywka,S.C.Binari and D.Moses,2nd Int.Conf.on the Appl.of Diamond Films and Related Materials, ed.M.Yoshika wa, M.Murakawa,Y.Tzeng,W.A.Yarbrough,MYU,Tokyo,1993,399
6. D.R.Kania, M.I.Landstrass, M.A.Plano, L.S.Pan, S.Han,Diamond and Related Materials,2 (1993) 1012.
7. B.V.Spitsyn,L.L.Bouilov and B.V.Derjaguin J.Cryst.Growth, 52 (1981) 19.
8. B.B.Pate, Surf.Sci.,165 (1986) 83.
9. Sugino,Y.Muto,K.Karasutani and J.Shirafuji,Diamond and Related Materials, 2 (1993) 803.
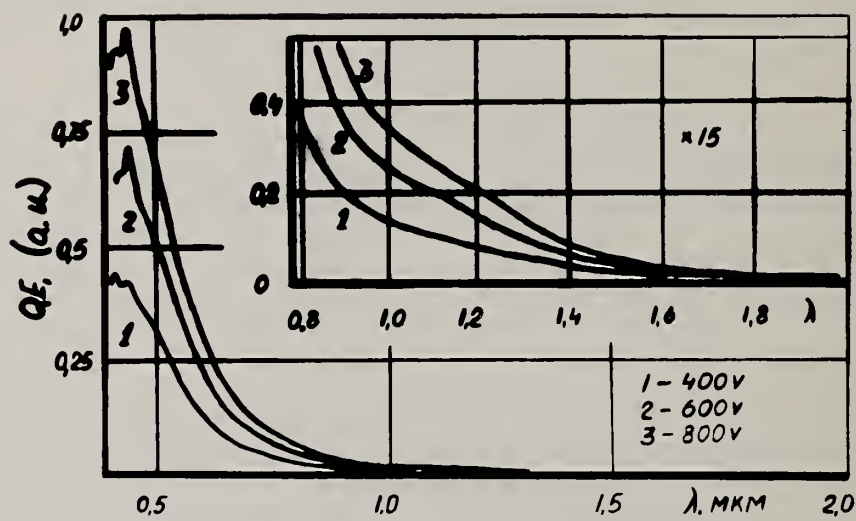
Fig.1 Quantum efficience, as function of
wave lengths
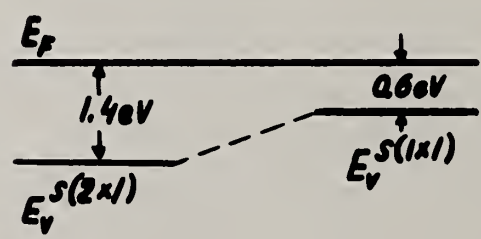
Fig.2 A Schematic of electrons energy levels
near diamond surface.

Applications of Diamond Films and Related Materials: Third International Conference, 1995
Editors: A. Feldman, Y. Tzeng, W. A. Yarbrough, M. Yoshikawa, and M. Murakawa

149

SPECTRAL CHARACTERISTIC OF DIAMOND-SILICON SANDWICH STRUCTURES OF PHOTODIODE, PHOTOCONDUCTOR AND MISFET

V.V.TOKIY[1], V.I.TIMCHENKO[1], V.A.SOROKA[1], N.TOKIY[1], B.V.SPITSYN[2], L.L.BOUILOV[2]

[1]Research Group of Diamond Electronic & Coatings
Donbass State Academy of Constructions and
Architecture, 339023 Makeyevka, Ukraine
[2]Institute of Physical Chemistry of Russian Academy of
Sciences, 117915 Moscow, Russia

Key words: photovoltaic, sandwich, undoped diamond film

Abstract

In the present work we considered the photoelectric properties of the undoped polycrystal diamond films on the (111)-oriented p-type Si substrate. The spectral characteristic of the photovoltaic structure indicates three the energy thresholds for carrier generation of 1 eV, 1.1 eV and 1.2 eV. We can connected the first two with electron emission and third with hole emission from Si to diamond.

1. Introduction

Application of amorphous and polycrystalline diamond films in such electronic device as photodiode [1], photoconductor [2], MISFET [3] has awakened a great interest in conduction phenomena in diamond-silicon sandwich structures. Information which can be obtained from the analysis of the current-voltage characteristic and temperature dependence of conductivity is effectively extended by photoelectric measurements of this structures where diamond is the "insulating" layer, and Si is the semiconducting layer. Photoelectric investigations in sandwich structures consist usually of the measurements and the analysis of the spectral characteristic.

2. Experimental details

2.1. Sample preparation

In the present work we considered the properties of the undoped polycrystal diamond films (UPDF), which were produced using the thermal gas-phase

activation method. The nucleous and growth was on the (111)-oriented p-type Si substrate with a thickness of 1 mm and a surface area of about 1 sm at the temperature of 1200 K using mixture CH and H . Substrate temperature was determined with an optical pyrometer. After growth the diamond film with substrate cool with rate of 10 K/h.

The film was 0.0135 mm in thickness. Electrodes, one of which is transparent to light rays, are placed on opposite faces of a platelike sample. The top electrode was replaced by distilled water. The advantage of using the water counterelectrode rather than the more usual metal counterelectrode is that the water is transparent in the wavelength region of interest, for photon energies less than 6 eV. The water electrode was located onto diamond side diamond-silicon sandwich structure. The silicon side of the sandwich structure was located onto the silver plate, which was served for the second electrode.

2.2.Measurements

A block diagram of the apparatus for measurements of the spectral character-istic of diamond-silicon sandwich is shown in Fig.1.

The direction of illumination was along the growth direction of UPDF from UPDF to silicon. The area of the illuminated electrode was 20 Sq.mm . The spectral dependence of the photocurrent was determined by using the quartz prism monochromator. A tungsten source was employed in the visible region. The photocurrent measurements were made - using a "light on - light off" technique. The pulse width was 9ms.

The photovoltage was determined by connecting the sample in series with the 10^{7}-W input resistor of the amplifier, with one side of the sample and resistor grounded. The nongrounded side of the sample was illuminated, and the voltage drop across the resistor was measured.

3.Results and discussion

A plot of the square root of the quantum efficiency of the diamond-silicon sandwich structure measured in air as a function energy of photon is shown in Fig.2. Where QE is taken to be equal to the total number of electrons collected at the contacts divided by the total number of photons incident on the area of the illuminated electrode, measured in arbitrary units.

Thus, the water cannot absorb energy from the light and consequently no carriers can be photoemitted from the water side [4]. The carriers photo-emitted from the Si into UPDF was then identified as electrons from the direction of the current in the external circuit.

The spectral characteristic indicates three the energy thresholds for carrier generation of 1 eV, 1.1 eV and 1.2 eV.

4.Conclusions

The current due to photoemission of carrier from silicon into diamond can be explained as a superposition of several injection processes.

The analysis of the spectral characteristic indicates the emission of electrons for low energies and of holes for higher energies. The energy thresholds found from the spectral characteristic give two barrier heights for electron emission first - 1 eV and second - 1.1 eV, and for hole emission - 1.2 eV.The observed effect is fo the interest for photovoltaice of energy conservation system,which was disccussed in [5].

5.Acknowledgments

6.References

1. Tomas Mandel, Manfred Frischholz, Reinhard Helbig and Albert Hammer-schmidt, Post-deposition-treatment of diamond-like carbon films and application for heterojunction photodiodes, 2nd International Conference on the Applications of Diamond Films and Related Materials, Editors : M.Yoshikawa, M.Murakawa, Y.Tzeng, and W.A.Yarbrough. MYU, Tokyo 1993 Printed in Japan, 405.
2. Hirokazu Nakane, Tsutomu Mitani and Hideo Kurokawa, Application of diamondlike carbon films to the protective layer of organic photoconductors, ibid. 433.
3. N.K.Annamalai, Jon Sawyel, Pramod Karulkar, ZMR SOD MISFET's, ibid. 347.
4. A.M.Goodman, J.Appl.Phys. 41 (1970) 2176.
5. M.A.Prelas, E.I.Charlson, I.M. Messe, G.Popolici, and T.Stacy,Laser and Particle Beams, 11, (1993), 65.
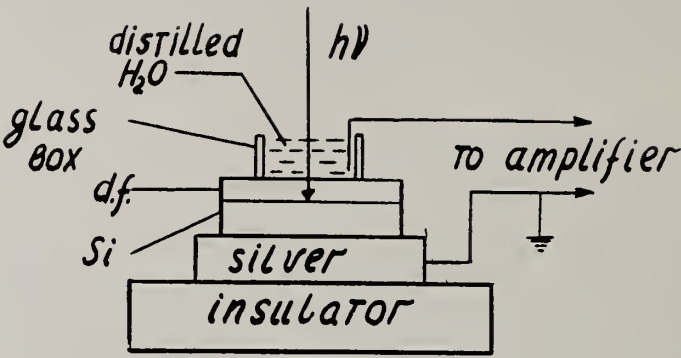
Fig.1   A Scheme observe of photovoltaic effect
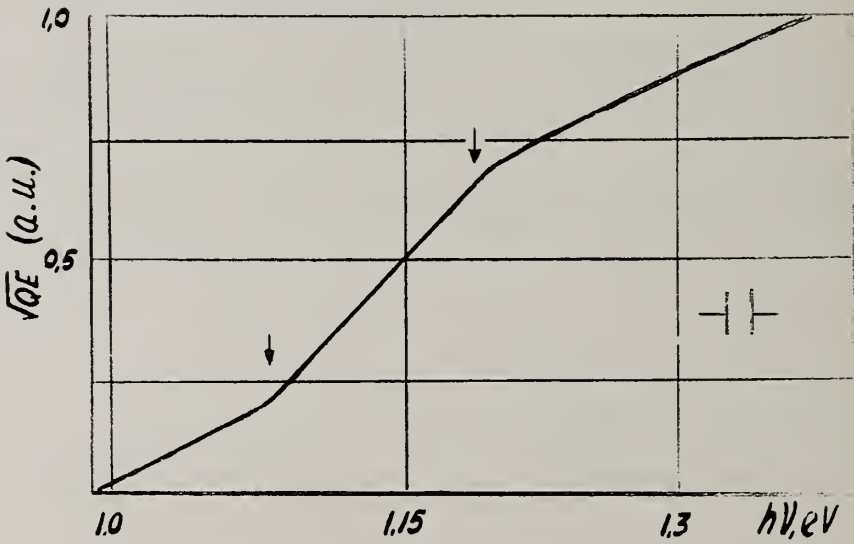
Fig.2   Qantum efficience,as function of energy photon.

Applications of Diamond Films and Related Materials: Third International Conference, 1995
Editors: A. Feldman, Y. Tzeng, W. A. Yarbrough, M. Yoshikawa, and M. Murakawa

153

ENCAPSULATION OF ELECTROLESS COPPER PATTERNS INTO DIAMOND FILMS

S. M. Pimenov[1], G. A. Shafeev[1], E. N. Loubnin[2], S. V. Lavrischev[1], and V. I. Konov[1].

[1]General Physics Institute, Russian Academy of Sciences, 38 Vavilov str., Moscow 117942, Russia
[2]Institute of Physical Chemistry, Russian Academy of Sciences, 31 Leninsky prospekt, Moscow 117915, Russia

Key words: diamond, encapsulation, laser, metallization, patterning

Abstract

The results are reported on encapsulating copper lines into diamond films grown by a DC plasma CVD. The process includes the steps of (i) laser activation of diamond for electroless metal plating, (ii) electroless copper deposition selectively onto the activated surface regions, and (iii) diamond re-growth on the Cu-patterned diamond films. The composition and electrical properties of the encapsulated copper lines were examined, revealing high purity and low electrical resistivity of the encapsulated electroless copper.

1. Introduction

Because CVD diamond is considered to be one of the most promising substrate materials for advanced packaging [1], methods for selective diamond metallization (in particular, for multilevel metallization) are to be developed. Also, for some electronic applications metal electrodes are to be encapsulated into diamond to avoid surface effects on the device performance [2]. Among metallization materials copper is characterized by high electrical conductivity and good electromigration properties, both needed for application in large-scale-integration systems [3]. In addition, copper has a lattice constant near that of diamond and does not form stable carbides, that influences the properties of diamond-copper interface at elevated temperatures [4].

In the present paper we report on encapsulation of copper lines into diamond films by a technique which is based on our previous results on selective area metallization of diamond by electroless metal plating [5, 6]. Peculiarities of diamond growth on electroless copper as well as some properties of the encapsulated copper were investigated.

2. Experimental

Diamond films of 30-40 μm thickness were grown onto Si and Mo substrates by means of a DC plasma CVD [7]. The activation of diamond surface for

electroless metallization was achieved via the surface modification during ablative etching by either a KrF excimer laser (λ=248 nm) or by a copper-vapour laser (λ=510 nm) [5, 6]. Then, the laser-etched trenches of 20-100 μm in width and several millimeters in length were electroless coated with copper. To provide high nucleation density for subsequent diamond growth onto the electroless copper, the Cu-patterned diamond films were immersed into the nanosized diamond powder suspension in alcohol, or the powder was added to the electroless copper bath. After this pretreatment, diamond growth was continued on the Cu-patterned films to encapsulate copper lines into diamond. The ends of the copper lines were preserved from diamond growth to be able to measure electrical resistance of the encapsulated copper lines.

3. Results

Figure 1 illustrates the successive steps of the metallization process: (a) laser-induced activation of the diamond surface for electroless metal plating, (b) electroless copper deposition selectively onto the activated surface regions, and (c) diamond re-growth on the Cu-patterned diamond films.

At the activation stage (Fig. 1a), the trenches of 100 μm in width, 3 mm in length and 5-10 μm in depth were produced by ablative etching with a KrF excimer laser. It is important that rough diamond film surface is smoothed during laser ablation [8]. Then, copper is deposited from electroless plating solution onto the laser-activated regions of the film surface (Fig. 1b). The thickness of the copper deposits was 2-3 μm. After immersion of the Cu-patterned film into the diamond grit suspension, continued diamond growth resulted in encapsulation of the copper lines in diamond as shown in Fig. 1c. The thickness of the diamond layer which covered the copper was 7 μm to 15 μm. The deposition temperature was 850-900°C. It is interesting that copper lines did withstand a sharp increase in temperature at the switching on of the arc discharge, whereas attempts to grow diamond on electroless nickel failed because of the nickel lines were peeled off the diamond surface just upon switching on the discharge. Such behaviour of copper is thought to be explained by its high plasticity.

Since the ends of copper lines were saved from diamond growth, measurements of electrical resistance of the lines were made after encapsulation. These measurements showed that the lines remained highly conductive, and the value of electrical resistivity was estimated to be 2.5-6 $\mu\Omega \cdot$cm. The presence of the "redundant" conductive layer (graphitized surface layer induced by laser etching [8]) may be helpful in supporting interconnect performance if the metal line uniformity would be destroyed, e.g., by formation of voids. Assuming the electroless metal deposits to be nonporous coatings, the accessibility of the graphitized diamond surface for atomic hydrogen is to be limited and, consequently, this layer is to be unchanged during diamond re-growth. To establish this fact, direct characterization of the structure of the "buried" graphitized layer is required.

Figure 2 shows SEM and X-ray (Cu-K$_\alpha$) images of the diamond film cross-section obtained by the excimer laser cutting across encapsulated copper lines (the images in SEM and X-ray modes correspond to adjacent copper lines).
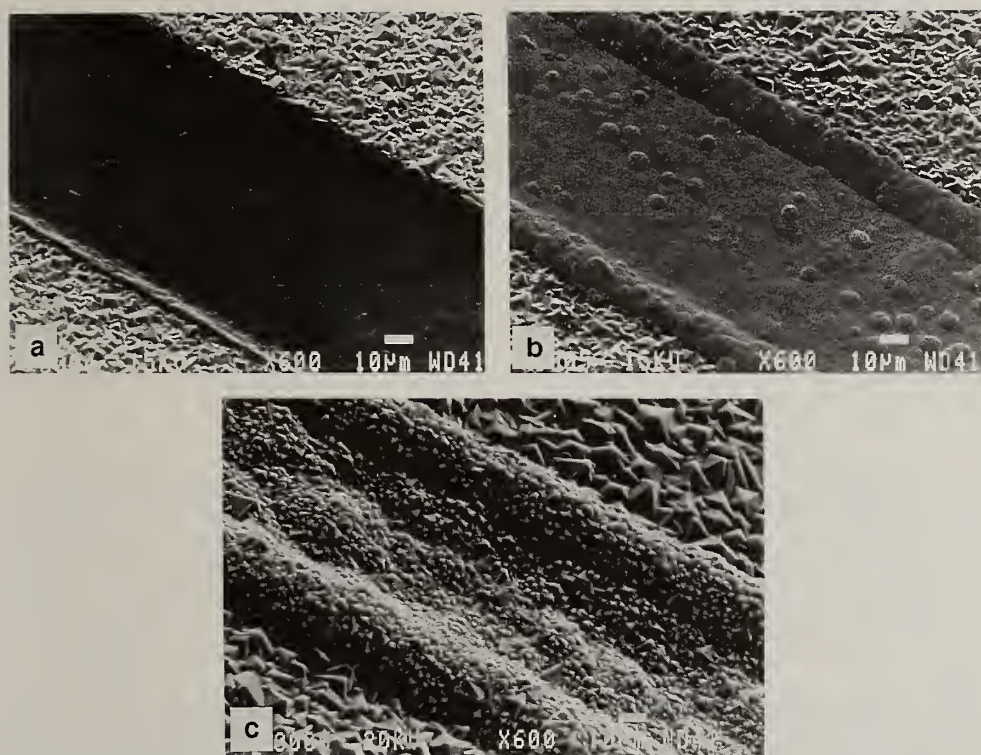
Fig. 1. Three stages of the metallization process: a) activation of diamond surface by laser etching, b) metallization of a laser-etched trench with electroless copper, c) encapsulation of a copper line into diamond film.

In this case mechanically polished diamond surface was activated by a copper-vapour laser etching [6], and seeding was performed by introducing nanosized diamond particles in copper during electroless deposition. As temperature is increased upon switching on the arc discharge, embedded diamond particles should diffuse to the copper surface and serve as nucleation sites for diamond growth. Auger electron spectrum (Fig. 3), made from the cross-section area of the copper line, showed high purity copper with very low content of carbon.

Fig. 2. SEM (a) and $Cu-K_\alpha$ (b) images of the cross-section of a diamond film with encapsulated Cu lines.

156
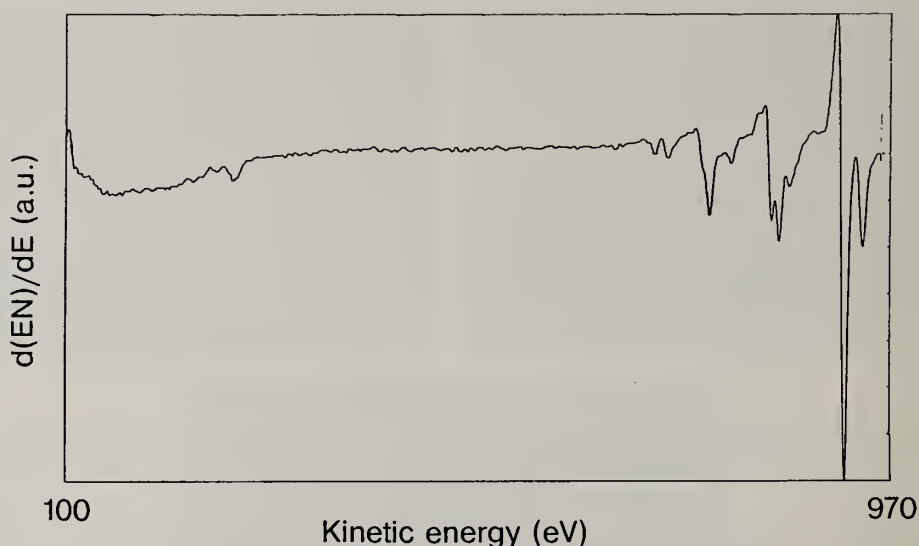
Fig. 3. The AES spectrum of the encapsulated copper. The spectrum was obtained from the cross-section area of a copper Cu line, shown in Fig. 2.

The metallization/encapsulation steps can be repeatedly performed at the same diamond substrate to form multilevel copper interconnects in the diamond film. Vertical interconnects through the diamond substrate can also be made by electroless plating onto the activated surface of laser-etched holes, orifices, etc. We conclude, therefore, that the encapsulated Cu metallization is a promising approach for 3D interconnection technology as well as for creating "in-diamond" electrodes in various diamond-based electronic and optoelectronic devices.

5. References

1. R.C. Eden, Diamond Related Mater. 2 (1993) 1051.
2. H. Yoneda, K. Ueda, Y. Aikawa, K. Baba, and N. Shohata, Appl. Phys. Lett. 66 (1995) 460.
3. J.S.H. Cho, H.-K. Kang, S.S. Wong, and Y. Shacham-Diamond, MRS Bulletin, June 1993, p. 31.
4. P.K. Baumann, T.P. Humphreys, R.J. Nemanich, K. Ishibashi, N.R. Parikh, L.M. Porter, and R.F. Davis, Diamond Related Mater. 3 (1994) 883.
5. S.M. Pimenov, G.A. Shafeev, V.A. Laptev and E.N. Loubnin, Appl. Phys. Lett. 64 (1994) 1935.
6. S.M. Pimenov, G.A. Shafeev, A.A. Smolin, V.I. Konov, V.A. Laptev and E.N. Loubnin, Diamond Films Technol., 3 (1994) 241.
7. A.A. Smolin, S.M. Pimenov, V.G. Ralchenko, T.V. Kononenko, V.I. Konov, and E.N. Loubnin, Diamond Films Technol. 3 (1993) 1.
8. S.M. Pimenov, A.A. Smolin, V.G. Ralchenko, and V.I. Konov, Diamond Films Technol. 2 (1993) 201.

Applications of Diamond Films and Related Materials: Third International Conference, 1995
Editors: A. Feldman, Y. Tzeng, W. A. Yarbrough, M. Yoshikawa, and M. Murakawa

157

A NOVEL METALLIZATION SCHEME FOR DIAMOND

A. Bächli[1], E. Kolawa[1, 2], J. W. Vandersande[2], and M-A. Nicolet[1]

[1] California Institute of Technology, 116-81, Pasadena, Ca 91125, USA
[2] Jet Propulsion Laboratory, Pasadena, Ca 91109, USA

Key words: adhesion, contact, diffusion barrier, heat sink, gold, metallization

Abstract

An adherent and metallurgically stable metallization system for diamond is presented. The big improvement in metallurgical stability is attributed to the use of a ternary, amorphous Ti-Si-N diffusion barrier. No diffusion between the layers and no delamination of the metallization was observed after annealing the schemes at 400 °C for 100 hours and at 900 °C for 30 minutes. Thermal cycling experiments in dry air from -65 to 150 °C and adhesion tests were performed.

1. Introduction

Metal-diamond contacts are needed for most applications of CVD diamond. The requirements on such contacts vary greatly from application to application. Important for many of these are metallurgical stability at elevated temperatures and good adhesion, such as for the bonding of components on CVD diamond heat sinks for multi-chip modules. These two requirements, however, are difficult to meet with a single film, since good adhesion requires a reaction between the covalently bonded diamond and the metal. The metallization schemes available today for diamond consist of a thin adhesion layer (typically Ti or Cr) that bonds a thicker metal or alloy layer (typically Au or Au-Sn) to the diamond substrate [1]. Unless the interaction is efficiently prevented, Cr from the adhesion layer will be dissolved in the thicker Au film, since the solubility of Cr in Au is substantial at elevated temperatures [2]. The same holds for Ti in Au, where compounds can form as well [2, 3]. These metallurgical interactions degrade adhesion and electrical properties at the bond, thus limiting the applicability of these metallizations. The upper
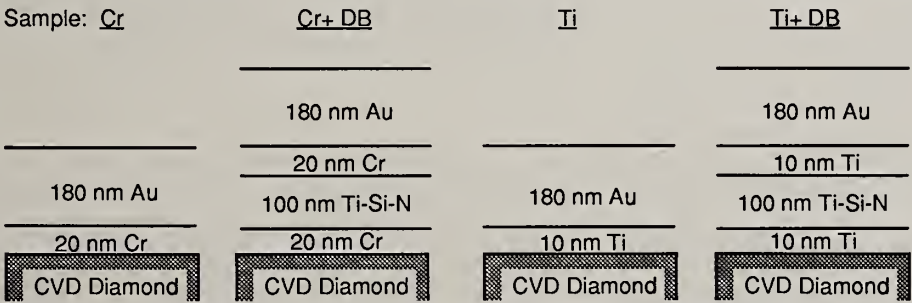
Fig. 1 Sample types used in this study: Schematic cross section of as-deposited samples.

temperature limit for metallizations that use the Ti-W/Au scheme to impede diffusion is below 400 °C [4]. A Ti/Pt/Au metallization that we deposited on diamond failed upon 30-min-vacuum annealing at 450 °C. and non of the commercially available diamond metallization schemes, which we tested for this experiment, could withstand higher temperatures than 450 °C [5].

We present a diamond/Ti/Ti-Si-N/Ti/Au metallization that has a metallurgical stability greatly superior to the currently used metallization schemes. It contains a reactively sputter-deposited amorphous Ti-Si-N film which has been developed as a diffusion barrier between silicon substrates and copper overlayers [6]. This exceptional diffusion barrier much enhances the performance of diamond metallization schemes. We discuss the stability of this metallization and compare it with a similar scheme (diamond/Cr/Ti-Si-N/Cr/Au) where Cr instead of Ti is used as an adhesion layer, and with the corresponding metallizations that do not contain the diffusion barriers (diamond/Ti/Au and diamond/Cr/Au).

2. Experimental Procedure

The diamond substrates used in this study were polished 250 µm-thick free-standing CVD-grown wafers. Prior to metal depositions the diamond wafers were annealed in a flow of forming gas at 650 °C for 3 hrs. Thin films were deposited by rf-magnetron sputtering in a vacuum chamber with $2x10^{-7}$ Torr base pressure. Four types of contact schemes were prepared by sequential deposition of thin layers onto the diamond substrates without breaking vacuum. The schematic cross sections of the as-deposited samples together with the abbreviations used to refer to these samples (Cr, Cr+DB, Ti, Ti+DB) are shown in Fig. 1. Metal targets and Ar gas were used to sputter-deposit the Cr and Ti films, while the amorphous Ti-Si-N films were reactively sputter-deposited with Ti_5Si_3-composite targets in a mixture of Ar and N_2 [6].

One sample of each type was kept as a reference. A second sample was thermally cycled 100 times between -65 °C and 150 °C in dry air according to MIL STD 883. Adhesion tests were performed on these samples after thermal cycling using a 64 ounce / inch tape. A third sample of each type was annealed in a vacuum tube furnace ($5x10^7$ Torr) at 200 °C for 30 min. Annealing for 30 min at a higher temperature was repeated with those samples until atomic interdiffusion could be detected by backscattering spectrometry. The elemental composition profiles of all thermally cycled and all furnace-annealed samples together with their respective reference samples were characterized by 3.2 MeV $^4He^{++}$ backscattering spectrometry. The cross section of the He-carbon scattering is enhanced at this energy, allowing one to also detect a change in the carbon concentration close to the diamond-metal interface [7]. The samples were tilted 7 ° against the incident He beam direction. The scattering angle of the detected particles was 170 °.

3. Results and Discussion

Comparing the backscattering spectra of annealed samples with the spectra of their reference sample, as shown in Fig. 2, allows detection of interdiffusion between the various layers. Chromium already diffuses substantially into the Au film at 300 °C (Fig. 2.a). The adhesion of this film is so poor after the 400 °C annealing that it peals off upon gentle handling with tweezers. At 300 °C interdiffusion is also observed between the Cr and the Au film above the barrier in the Cr+DB sample. The Cr adhesion layer below the barrier, however, remains unchanged, which means that the barrier is tight. Even after annealing at 600 °C no diffusion is observed in the adhesion layer below the barrier and there are no signs of delamination in the annealed Cr+DB samples.
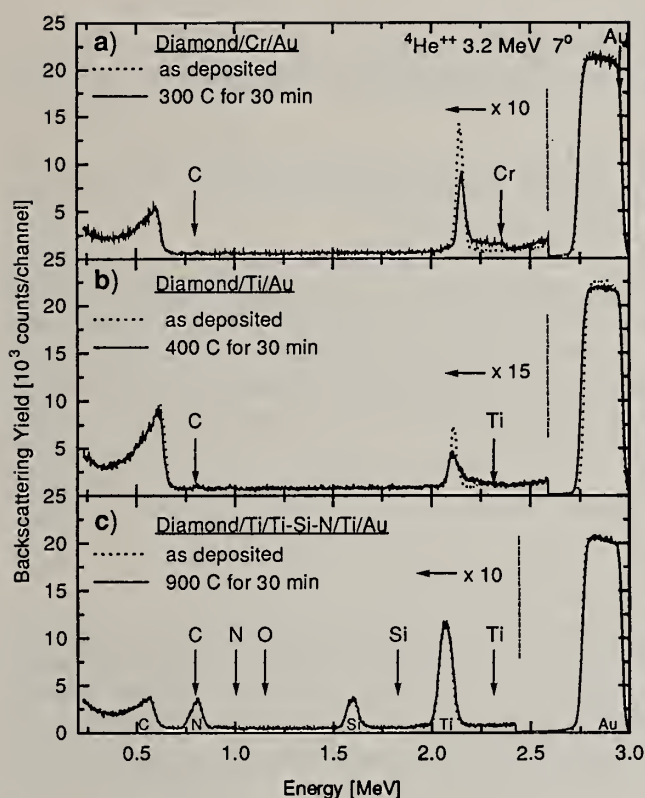
Fig. 2   3.2 MeV He backscattering spectra:
a) Cr reference sample and the sample annealed at 300°C
b) Ti reference sample and the sample annealed at 400°C
c) Ti+DB reference sample and the sample annealed at 900°C.

Table I   Interdiffusion between (Cr or Ti) and Au detected after vacuum annealing. i: interdiffusion is observed by backscattering spectrometry (b. s.) ; ni: no interdiffusion is observed by b.s.; ii: initial interdiffusion is observed by b.s.; d: delamination

	Cr	Cr+DB	Ti	Ti+DB
as deposited	ni	ni	ni	ni
200 °C / 30 min	ni	ni	ni	ni
300 °C / 30 min	ii	ii	ni	
400 °C / 30 min	i+d		ii	ni
500 °C / 30 min			i	
600 °C / 30 min		i		ni
700 °C / 30 min				ni
800 °C / 30 min				ni
900 °C / 30 min				ni
400 °C / 100 hr				ni

The onset of interdiffusion in the Ti sample between the Ti and the Au bilayer is observed after annealing at 400 °C (Fig. 2.b). In the Ti+DB sample there is no detectable interdiffusion in the annealed samples, not even after annealing at 900 °C (Fig. 2.c). No tests were performed at higher temperatures because the gold would evaporate. Discoloration and interdiffusion was not observed within the layered Ti+DB sample after vacuum annealing at 400°C for 100 hrs.

The interdiffusion of Cr into Au is observed at 300 °C for the Cr+DB as well as for the Cr sample and the interdiffusion of Ti into Au is observed at 400 °C in the Ti sample. However, no interdiffusion of Ti into Au is detected up to 900 °C in the Ti+DB sample. Nitrogen from the barrier most likely diffuses into the Ti layer to form TiN, as was observed in the W-N/Ti system [8]. The lack of similar behaviour in the Cr+DB can be attributed to the lower stability of CrN (ΔG= -60 kJ/mol) compared to TiN (ΔG= -266 kJ/mol) [9].

Table I summarizes the backscattering data on interdiffusion after 30 min vacuum annealing. It shows temperatures at which no interdiffusion (ni), initial interdiffusion (ii), interdiffusion or reaction (i), or delamination (d) has occurred. Except during the initial stages, the interdiffusion of Cr or Ti with Au was accompanied with a color change of

the Au film. Table I clearly shows that the metallization scheme with the Ti adhesion layers and the ternary diffusion barrier (Ti+DB sample) is metallurgically much more stable than the Ti, the Cr, and the Cr+DB samples.

No changes in the surface appearance (optical microscopy) and the composition profiles (back-scattering spectrometry) were observed after thermally cycling the four different sample types, as deposited, one hundred times between -65 °C and 150 °C.

Tape-adhesion tests performed on these samples show that the adhesion after thermal cycling is poorest for the Ti and the Cr samples (film pealed off completely), is better for the Cr+DB sample (50 % of the film stayed on), and is best for the Ti+DB sample (90% of the film stayed on). Although not a quantitative measurement, these tape-adhesion test results reveal that the adhesion of the Ti+DB metallization is superior to that of the three other metallization schemes discussed here. Adhesion test have not been made on the annealed samples so far. However, no delamination due to normal handling of the metal film was observed after annealing the Ti+DB sample at 900 °C and the Cr+DB sample at 600 °C.

4. Conclusion

A diamond metallization using a Ti-Si-N layer as a diffusion barrier is presented. The system diamond/Ti/Ti-Si-N/Ti/Au showed good adhesion to polished diamond after thermal cycling and no interdiffusion was detected after vacuum annealing at 400 °C for 100 hrs. This metallization was metallurgically stable to 900 °C. It's performance is thus expected to be superior compared to the currently available commercial metallization schemes. There, interdiffusion of the adhesion layer and Au, observed below 450 °C, is a limiting factor.

Diffusion barriers of the same type are expected to enhance the range of applications for metallizations on SiC and on nitride substrates as well.

References

1. H. A. Naseem, I. Meyyappan, C. S.Prasad, W. D. Brown, ICEMM Proc. '93, (1993) 62.
2. T. B. Massalski, Binary Alloy Phase Diagrams, 2nd ed. (ASM International, 1990).
3. T. C. Tisone and J. Drobeck, J. Vac. Sci. Technol. 9 (1972) 271.
4. I. Meyyappan, A. P. Malshe, H. A. Naseem, W. D. Brown, Thin Solid Films 253 (1994) 407.
5. E. Kolawa, not published results (1994).
6. J. S. Reid, X. Sun, E. Kolawa, M-A. Nicolet, IEEE Electron Device Let. 15 (1994) 298.
7. R. W. Hill, Phys. Rev. 90 (1953) 845.
8. F. C. T. So, E. Kolawa, H. P. Kattelus, X.-A. Zhao, M-A. Nicolet, C.-D. Lien, J. Vac. Sci. Technol. A 4 (1986) 3078.
9. E. A. Brandes, G.B. Brook, Smithells Metals Reference Book, 7th ed., Butterworth-Heinemann Ltd, Oxford, UK (1992) pg. 8.23-24.

Applications of Diamond Films and Related Materials: Third International Conference, 1995
Editors: A. Feldman, Y. Tzeng, W. A. Yarrough, M. Yoshikawa, and M. Murakawa

161

THERMALLY STABLE METALLIZATIONS ON POLYCRYSTALLINE DIAMOND FILMS

Sam Liu[1], Tom Lamp[2], Kitt Reinhardt[2], and Clarence Severt[2]

[1]University of Dayton Research Institute, Dayton, OH 45469-0170, USA
[2]Aerospace Power Division, Aero Propulsion and Power Directorate, Wright-Patterson Air Force Base, OH 45433-6533, USA

Key words: contact, diamond, metallization, ohmic, thermal stability

Abstract

Present work focused on the electrical properties and thermal stability of Au, Ni/W, and Al/W contacts to p-type polycrystalline diamond films, and Ni/Ti/W contact to "n-type" polycrystalline diamond films. The Au, Ni/W, and Al/W contacts to p-type diamond films illustrate perfect ohmic behavior in the as-deposited condition. The contact resistivity is in the range of 10^{-4} ohm-cm^2 determined by TLM. On the other hand, Ni/Ti/W contact to "n-type" diamond film shows very large resistance with low leakage current in the as-deposited condition. All these metallization systems exhibit good thermal stability. The contact resistance of the Al/W contact to p-type diamond decreased slightly, however, little change in I-V characteristics was observed for Ni/W and Ni/Ti/W metallizations after annealed at 650°C for 78 hours.

1. Introduction

Diamond has an unusual combination of excellent electrical and thermal properties such as high thermal conductivity, wide band gap, high hole mobility, and high breakdown voltage. Advances in the growth, doping, and processing technologies of diamond films made in the past five years have made diamond a promising candidate for semiconductor elements used in high power and high frequency electronic devices and devices to be used in high temperature, chemically harsh and high nuclear radiation flux environments.

Contact metallization is a fundamental part of semiconductor technology. Many vital semiconductor device parameters, including maximum speed and high-power performance, depend critically on metallization resistance. A number of preliminary studies on contacts to boron-doped diamond film has been conducted [1-3]. More

efforts are required to reduce the contact resistivity, and to test and improve the thermal stability of contacts. Greater understanding of the mechanism for ohmic contact formation and the carrier transport across the metal-diamond interface is also needed.

2. Experimental

The polycrystalline diamond films were obtained from Advanced Technology Materials and were fabricated by CVD on Si substrates. The p-type diamond films were boron doped to $3.0 - 8.7 \times 10^{20}/cm^3$. The thickness of the p-type diamond films is 11 microns. For the present time, the n-type diamond films are not available yet due to problems with doping. The nominal n-type diamond films used in this study were phosphorus doped with the doping level of only $5.6 \times 10^{14}/cm^3$. The thickness of the nominal n-type diamond films is 21-22 microns. The films were first degreased in trichloroethylene, acetone, and methanol at 50°C for 5 minutes, followed by etching in H_2SO_4 and HCl for 5 minutes, respectively. After the acid etching, the films were soaked in DI water and dried by flowing nitrogen.

Standard photolighthographic techniques were used to produce the transmission line measurement (TLM) patterns. The depositions were carried out in a Denton DV502 sputtering system. The system was pumped down to about 5×10^{-7} torr before deposition. An argon atmosphere was used during sputtering. Au, Ni/W, and Al/W were deposited on the p-type diamond films and Ni/Ti/W layers were deposited on the nominal n-type diamond films. The thickness of the sputtered metal layer is about 150 nm.

Current-voltage curves were measured using a Sony 370 Curve Tracer. The contact resistivity of ohmic contacts was determined by TLM. In addition to the electrical characterization, the interface reaction has been studied using Auger electron spectroscopy and x-ray diffraction.

4. Results and discussion

Fig. 1 gives the I-V curves of the Au, Ni/W, and Al/W contacts to p-type diamond films. It can be seen from Fig 1 that all these contacts illustrate ohmic behavior in the as-deposited condition. The contact resistivity is in the range of 10^{-4} ohm-cm^2 determined by TLM. On the other hand, the Ni/Ti/W contact to "n-type" diamond film shows a very large resistance with low leakage current in the as-deposited condition, as shown in Fig. 2. All these metallization systems exhibit good thermal stability. The contact resistance of the Al/W contact to p-type diamond decreased slightly, however, little change in the I-V characteristics was observed for the Ni/W and Ni/Ti/W metallizations after annealed at 650°C for 78 hours.
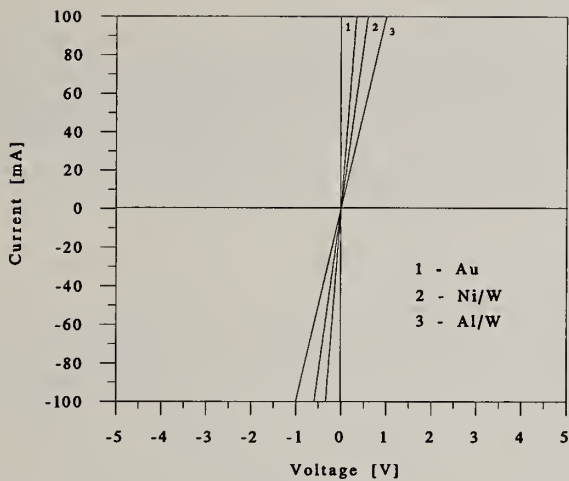
Fig. 1. I-V curves of Au, Ni/W, and Al/W contacts on p-type
diamond films in the as-deposited condition.
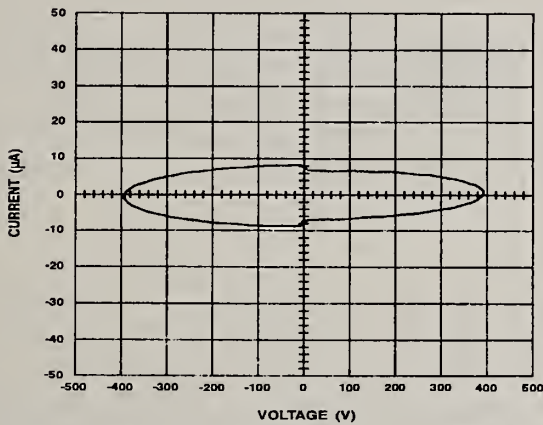
Fig. 2. I-V curves of Ni/Ti/W contact on "n-type" diamond film
in the as-deposited condition.

Auger electron spectroscopy (AES) was used to obtain chemical depth profiles of Al, W, O and C for the Al/W contact on the p-type diamond in the as-deposited condition and after annealing at 650°C for 1 hour, and the results are shown in Fig. 3 and 4. The sputter rate was about 8 nm/min., and the metal/diamond interface is at about 280 nm from the top metal (W) surface. It can be seen from Fig. 3 and Fig 4 that there is no significant difference in the chemical profiles between the specimen in the as-deposited condition and the specimen annealed at 650°C for 1 hour. Also, none of the elements shows sharp chemical profiles at the interfaces in the as-deposited

condition compared to the profiles we usually see for the metallizations on SiC. We believe that this is due to the surface roughness observed on the diamond film (the diamond films we used were not polished) but not to any interdiffutions at the interface. The only notable change after annealing is that aluminum has diffused through the tungsten layer to the surface area where it has reacted to form an aluminum oxide layer.
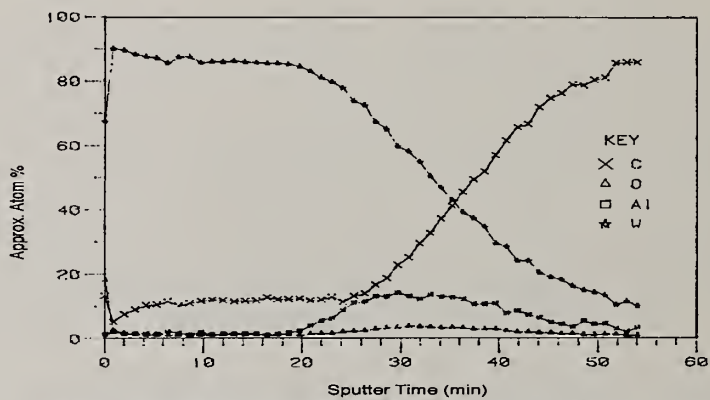
Fig. 3. AES chemical profiles of Al, W, C, and O for Al/W contact to p-type diamond in the as-deposited condition.
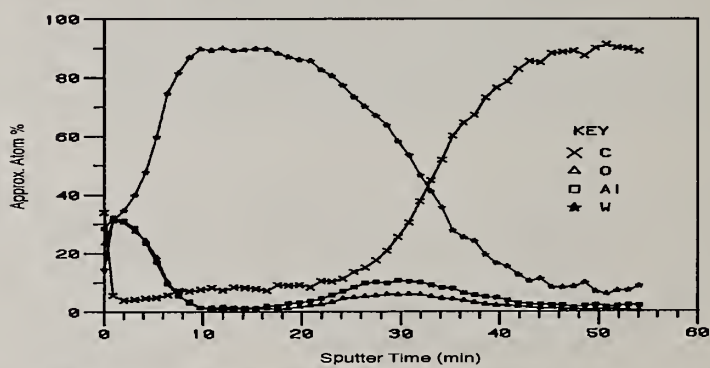
Fig. 4. AES chemical profiles of Al, W, C, and O for Al/W contact to p-type diamond after annealed at 650°C for 1 hour.

4. References

1. K.L. Moazed, R. Nguyen, and J.R. Zeidler, IEEE Electron Device Letters, **9** (1988), p. 350.
2. K.L. Moazed, J.R. Zeidler, and M.J. Taylao, J. Appl. Phys. 68 (1990), p. 2246.
3. K. Dos, V. Venkatesan, K. Miyata, D.L. Dreifus, and J.T. Glass, Proc. of the First International Conference on the Applications of Diamond Films and Related Materials - ADC '91, Auburn, Alabama, U.S.A., August 17-22, 1991, p. 301.

Applications of Diamond Films and Related Materials: Third International Conference, 1995
Editors: A. Feldman, Y. Tzeng, W. A. Yarbrough, M. Yoshikawa, and M. Murakawa

165

IRRADIATION AND ANNEALING OF [10]B DOPED CHEMICAL VAPOR DEPOSITED DIAMOND FILMS.

S.A. Khasawinah[1], Galina Popovici [1,2], J. Farmer[3], T. Sung[1], M. A. Prelas[1],

[1] Nuclear Engineering Department, University of Missouri, Columbia, Missouri 65211

[2] Rockford Diamond Technology, Professional Arts Bldg., 501 S. Sixth Street, Champaign, IL 61820-55789

[3] University of Missouri Research Reactor, Columbia, MO, 65211

Key words: neutron, irradiation, [10]B, annealing

Abstract

[10]B doped diamond films grown by hot filament chemical vapor deposition were neutron irradiated for two weeks. The as-irradiated, and annealed samples, along with an unirradiated sample, were analyzed using Raman spectroscopy and X-ray diffraction. It was found that a nondiamond amorphous phase was formed on irradiation. This phase transformed back to diamond on annealing. No graphite formation was observed.

1. Introduction

Interest for study of irradiation and annealing of boron doped diamond films is twofold. First, boron is commonly used as an acceptor dopant in diamond electronics. Natural boron contains 80.1% [11]B and 19.9% [10]B. [10]B has a large neutron capture cross section with the reaction [10]B (n, α) [7]Li. The energy of reaction is rather high (2.7 MeV), so radiation defects will be created. Therefore a study of neutron irradiated boron doped films is of interest for electronic applications in high neutron radiation environments. Second, Li-doping can be achieved by the reaction [10]B (n, α) [7]Li with isotopically enriched boron [1]. Interstitial lithium is predicted be a shallow donor [2]. This could be a useful method of n-type doping if the feasibility of healing radiation defects is demonstrated. It is known that on annealing the damaged regions can reconstitute diamond or graphitize. [3] depending on the irradiation dose. The graphitization happens at high irradiation doses when a large amount of sp^3 bonds is broken, and the lattice becomes amorphous.

There is a wealth of literature on irradiation of natural and synthetic diamonds by high energy particles [3- 6]. However, neutron irradiation studies on boron doped CVD diamond films have not yet been reported. In this paper the influence of neutron radiation on the quality of ^{10}B doped diamond films grown by CVD is reported. The possibility of healing the radiation damage by annealing was also investigated.

2. Experimental

The diamond films were grown in a hot filament reactor for eight hours. The growth conditions have been described elsewhere [7] The samples were doped in-situ using a solid source of 95% isotopically enriched ^{10}B. Secondary ion mass spectroscopy (SIMS) analysis was used to determine the boron concentration. One fragment was left unirraddiated and the other one was irradiated for two weeks, at the Missouri University Research Reactor (MURR) in Columbia, Missouri. The thermal neutron flux was 1.1×10^{14} n/cm^2 sec and the fast flux (E> 0.1 MeV) was 1.3×10^{14} n/cm^{2}sec. In addition to the radiation damage produced by fast neutrons, the ^{10}B (n, α) ^7Li reaction is expected to produce heavy damage as well. Upon removal from the reactor it was observed that the diamond samples had peeled off the silicon substrate. Each samples was divided into two pieces. One of the pieces was annealed in argon at 1000 °C for two hours. The annealed samples were boiled in a $Cr_2O_3+H_2SO_4$ mixture for 20 min to dissolve the surface graphite layer usually formed during thermal treatments. X-ray diffraction and Raman scattering were used to characterize the samples. The Raman spectra were measured using excitation by an argon ion laser operated at 514.5 nm.

3. Results and Discussions

The X-ray diffraction patterns of two samples are presented in Figures 1(a)- 1(c). Figure 1(a), unirradiated sample, has only diamond peaks. There is some (100) texture as the (400) peak (at $2\Theta=119.7°$) is higher relative to the (111) peak than for a powder without preferential orientation. For nontextured samples the intensity of the (400) peak, $I_{(400)}$, should be equal to 0.08 of $I_{(111)}$. In Figure 1 (a) $I_{(400)}$ represents approximately 0.4 of $I_{(111)}$. The irradiated sample (fluence $\phi_n=1.6\times10^{20}$ n/cm^2, E>0.1 MeV) has, in addition to the diamond peaks, a continuous amorphous-like band with a broad peak at $2\Theta \approx 24$ ° showing the presence of a disordered non-diamond carbon phase (Fig. 1b). The diamond (111) peak is reduced in height comparing with the band corresponding to nondiamond carbon phases. The preferential (100) orientation has disappeared, there is no (400) peak at $2\Theta=119.7$ °. After annealing (Fig 1c) the intensity of the nondiamond phase band relative to the diamond (111) peak became smaller. However, annealing did not remove all disordered carbon. In this regard, there is an agreement between the

results obtained by the Raman spectra and the X-ray diffraction data, as will be seen below.

The Raman spectra are presented in Figure 2 (a) - 2 (c). All spectra have the diamond peak height normalized to unity. The spectrum of the unirradiated sample (Fig. 2 a) has a peak at 1333 cm^{-1} and a broad peak around 1500 cm^{-1}. The former is the diamond line and the latter is usually observed in diamond-like carbon (DLC) [8-9]. Figure 2 b presents the Raman spectrum of the sample that was irradiated. The diamond peak shifted to the smaller wave numbers, most probably due to the radiation induced stress, as the samples were de-laminated from the substrates on irradiation. A broad band at wavenumbers below 1316cm^{-1} also appeared. This band is most probably due to scattering on the phonons caused by the breakdown of the selection rules as the lattice lost its coherence. There is a faint maximum at 990 cm^{-1}, not observed before in Raman spectra of diamond films. There is a peak at 1627 cm^{-1}. There are no peaks at 1347 and 1580 cm^{-1} due to graphite [8]. The luminescence background at wavenumbers larger than 1700 cm^{-1} became lower. The peak at 1622 cm^{-1}, observed in the irradiated samples., was observed by us in nanophase diamond obtained in explosion [9]. Therefore it is reasonable to assume that this peak is related to a carbon phase formed in highly nonequilibrium conditions like the explosion method or neutron irradiation. This carbon phase converts in diamond during annealing. The Raman spectrum of the sample that was irradiated and subsequently annealed (Fig. 2 c), is very similar to that of the unirradiated sample. The position of the diamond line is back to the original spot (1333 cm^{-1}), indicating that the radiation induced stress was removed.
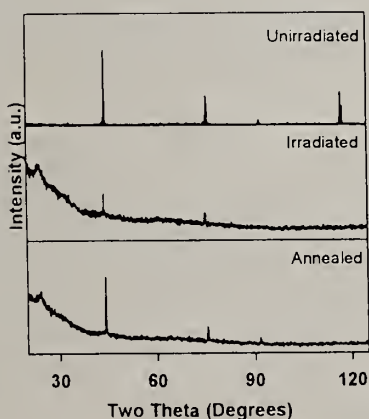
Figure 1: X-Ray Diffraction
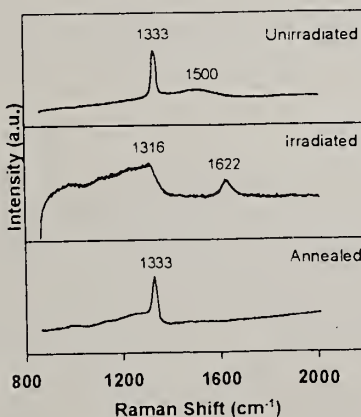
Figure 2: Raman Spectra

The luminescence background became slightly larger. However, annealing could not totally remove the band at wavenumbers below 1330 cm^{-1} indicating that the diamond lattice does not recovered totally, as it was seen in X-ray measurements. The annealing time and /or temperature were too small. Graphite formation was not observed either during irradiation or during annealing.

The energy of the reaction ^{10}B (n,α) ^{7}Li is Q=2.7 MeV and the cross section σ is 3837 barn. The boron concentration n in the films as determined by SIMS was about 10^{20} cm^{-3}. The number of reactions produced was thus $N = \sigma \phi_n n = 6 \times 10^{19}$. The number of events produced by the interaction of fast neutrons with carbon atoms was 1.4×10^{20} (neutron scattering cross section for carbon equal to 4.75 barn). The total number of events per cm^3 is of the order 2×10^{20}, that is, one event for every 1000 carbon atoms. This corresponds to the volume of a cube with an edge of 10 atoms, or 1.54 nm (the distance between two atoms in the diamond lattice is equal to 0.154 nm). It is known that defects, like vacancies, displaced carbon atoms and dangling bonds, result from neutron irradiation. These defects can aggregate, forming clusters. It is therefore reasonable to assume that due to the formation of vacancy clusters and voids, and the formation of nondiamond phases in an irradiated sample, the coherent domain mean size of diamond crystals will be small. The diamond X-ray diffraction lines should be much widened. However, experimentally obtained X-ray diffraction lines were not widened dramatically. This gives an intuitive image of the irradiated sample resembling to the Swiss cheese: there are the inclusions of the desordered phase in the bulk of the diamond lattice.

Both samples were delaminated from the substrates during irradiation. The cause of the delamination seems to be induced by irradiation stress, as well as preferential action of radiation on nondiamond carbon which is usually formed on the interface of diamond film and substrate. Therefore, the irradiation with the subsequent annealing can be used for obtaining freestanding diamond films.

References

1. B. Spitsyn, G. Popovici, M. A. Prelas, *Second International Conference on the Applications of Diamond Films and Related Materials*, ed. M. Yoshikawa, M. Murakawa, Y. Tzeng and W. A. Yarbrough, August 25-27, 1993, Tokyo, Japan p. 57-64
2. J. Bernholc, S. A. Kajihara, and A. Antonelli, (1991) *New Diamond Science and Technology*, MRS Int. Conf. Proc., editors R. Messier, J. T. Glass, J. E. Butler, R. Roy, p. 923
3. J. F. Prins, Materials Sci. Reports, **7**, 271 (1992)
4. J. P. F. Sellshop, *The Propeties of Diamond*, Edit. by J. E. Field, Acad. press, London, 1979, p. 108-159
5. A. T. Collins, Phisica B **185**, 284 (1993)
6. J. Wilks, E. Wilks, *Properties and Applications of Diamond,* Publ. Butterworth-Heinemann, Oxford, 1991, p.85-91, 285-289
7. S. Khasawinah, T. Sung, B. Spitsyn, W. H. Miller, G. Popovici, M. A. Prelas, E. J. Charlson, E. M. Charlson, J. Meese, and T. Stacy, *Diamond Materials*, edit. J. P. Dismukes and K. V. Ravi, Electrochemical Society Proc. v. 93-17, 1993, p. 1032-1035
8. D. S. Knight and W. White, J. Mater. Res. **4**, 385 (1989)
9. G. Popovici, S. Khasawinah, J. Sung and M. A. Prelas, unpublished data

OPTICALLY ENHANCED FORCED DIFFUSION OF SULFUR AND CHLORINE IN DIAMOND

Galina Popovici[1,2], T. Sung[2], M. A. Prelas[2], and R. G. Wilson[3],

[1]Rockford Diamond Technology, 501 S. Sixth Street, Champaign, Illinois 61820-5579
[2]Nuclear Engineering Department, University of Missouri, Columbia, Missouri 65211
[3]Hughes Research Laboratories, Malibu, California 90265

Key words: diffusion, diamond, chlorine, sulfur

Abstract

Diffusion of sulfur and chlorine in natural diamond was studied under electric bias with thermal and optical ionization of impurities. It was shown that the concentration of sulfur and chlorine was two orders of magnitude larger in the positively biased samples compared with negatively biased ones when optical ionization was used. Most probably these impurities diffuse through interstitial sites of the diamond lattice as negatively charged ions. The new method of optically enhanced forced diffusion of impurities may have practical interest for diamond and other wide band gap semiconductors, allowing larger concentration of diffused atoms to be obtained at lower temperatures.

1. Introduction

Diamond has a great potential for electronic and optical applications [1]. To realize this potential, controlled doping of diamond by optical and electrical active impurities should be achieved. Diffusion is widely used for semiconductor doping. However, there is a limited number of works on diffusion in diamond [2-5]. Because the diamond lattice is the most rigid lattice of all known materials, diffusion of impurities in the diamond lattice is considered difficult at temperatures lower than the graphitization temperature [6]. Diffusion of charged impurities through the semiconductor lattice at a given temperature can be forced by using dc electric field [3, 5]. Electric field forced diffusion of impurities was studied for silicon and germanium [7]. However, this method did not find practical applications, as the resistance of these semiconductors at the temperatures used for diffusion is low; therefore only low potential can be applied. Diamond and other wide band gap materials may have a large resistance to high temperatures [8], therefore a large potential can be applied during

diffusion. To be influenced by an electric field, the impurity must be charged, i. e. be ionized. To be ionized thermally, the impurity should form a shallow level in the diamond lattice. Electric field forced diffusion of boron was proved successful [5], as boron is known to be a shallow level in the diamond lattice. Optical ionization may be used to ionize deeper impurities, that cannot be ionized thermally. This method was proposed by our group [5]. To our knowledge there are no experimental papers on optically enhanced forced diffusion in diamond. The optically enhanced, forced diffusion of S, Na, , Al, Li, Cl, O, and H was studied [9]. The diffusion concentration of all impurities was enhanced by laser irradiation. In this paper the depth profiles of sulfur and chlorine only are discussed. The results on the other impurities will be published elsewhere.

Experiment

Natural diamond Ia crystals were used for diffusion. The experimental setup is shown in Fig. 1 (inset). The samples were placed on a graphite support with an embedded tungsten heater. The temperature of the support was measured using chromel-alumel thermocouple. P_2S_5 and $LiClO_4$ salts were used as a diffusion source. The diffusion source was placed between the samples. In this arrangement the doped surfaces have practically the same temperature and the same surface conditions. The only difference is the sign of the applied electric field. Diffusion was performed in an argon atmosphere.

Table I. Conditions of diffusion

Sample	T °C	Laser	V (V)	I(mA)	t(min)
1	770	off	+236	(0.3-0.4)	24
2	770	off	-236	(0.3-0.4)	24
3	730	on	+228	(0.2-0.8)	24
4	730	on	-228	(0.2-0.8)	24

A He-Ne laser was used to ionize impurities optically. Samples 1 and 2 were diffused under electric field without laser irradiating and samples 3 and 4 with laser irradiating during diffusion. Samples 1 and 3 were biased positively, and samples 2 and 4 were biased negatively. The conditions of diffusion are given in the Table I. After diffusion, the samples were boiled in a $CrO_3+H_2SO_4$ mixture for 20 min (to dissolve the graphite layer usually formed on the diamond surface during thermal treatments) and washed in deionized water. Secondary ion mass spectrometry (SIMS) was used to measure the depth profiles of impurities. Cs bombardment and negative secondary ions were used for analysis of sulphur and chlorine depth profiles. Calibration was achieved using implanted standards in crystalline diamond. The SIMS data in the first few tens of nanometer from the surface are within the SIMS equilibration distance and should be disregarded.

Results and Discussions
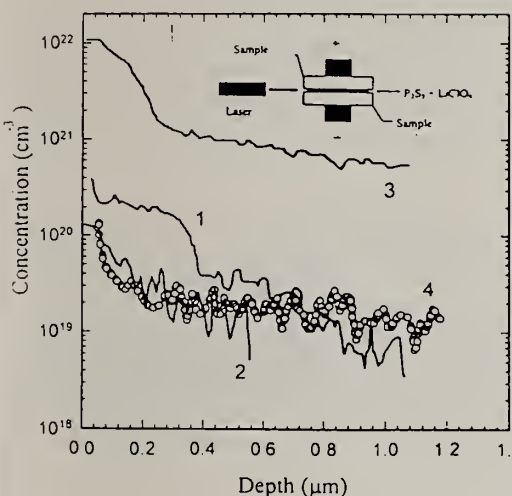
Fig. 1. SIMS profiles of sulfur
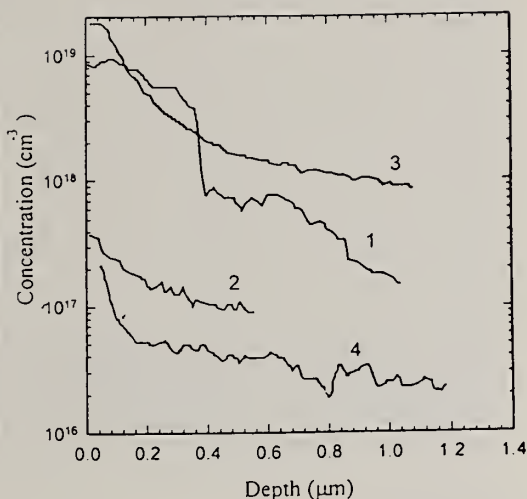
Fig. 3. SIMS profiles of chlorine.

The results on diffusion of sulfur are presented in the Fig. 1. The sulfur concentration was 2×10^{19} cm^{-3} at the depth of 0.5 μm for sample 2 biased negatively, and approximately two times larger at the same depth for sample 1 biased positively. Sample 1 had some irregularities on the diffused surface, which can explane the irregularities in the depth profile for this sample. The sulfur concentration of the positively biased sample 3 increased at least two orders of magnitude, when laser irradiation was used. The concentration of the negatively biased sample 4 remained approximately the same as the biased, but non irradiated, sample 2. The results for chlorine diffusion (Fig. 2) are similar to that of sulfur. The concentration of Cl for sample 1, which was biased negatively, is approximately 1×10^{18} cm^{-3} at the depth of 0.5 μm, and is larger by an order of magnitude at the same depth than the concentration of the negatively biased sample 2. The concentration of the positively biased laser irradiated sample 3 is 2×10^{18} cm^{-3} at the depth of 0.5 μm and is larger by two orders of magnitude than the concentration of laser irradiated negatively biased sample 4.

The difference in the diffusion curves for the positively and negatively biased samples (1 and 2, respectively) in the electric field may is due to the thermal ionization of the sulfur and chlorine atoms in the diamond lattice. That means both levels are shallow enough to be partially ionized at the diffusion temperature implying that the energy of ionization of these levels is of the order of 2kT $\approx$ 0.2 eV. The chlorine level might be shallower than the sulfur level, as the influence of the electric field is stronger for chlorine (the concentration is one order of magnitude larger in the positively biased

sample for chlorine and only twice as large for sulfur). Laser irradiation enhanced the concentration of diffused atoms of the positively biased sample 3 by two order of magnitude for both chlorine and sulfur, compared with the negatively biased sample 4. As the ionization energy of the He-Ne laser is 1.96 eV, much larger than the thermal ionization energy, one can assume that all chlorine and sulfur atoms were ionized by the laser and their movement was influenced by the electric field. The optically enhanced forced diffusion of the impurities may have practical interest for diamond and other wide band gap semiconductors, allowing larger concentration of diffused atoms to be obtained at lower temperatures.

The enhancement of diffusion due to the positive bias implies that both sulfur and chlorine diffuse as negative ions. That means these atoms might form acceptor levels in the diamond band gap. However, these impurities should be donors only in substitutional positions of the diamond lattice. In interstitial positions, both sulfur and chlorine should be acceptors. Acceptor-like diffusion of fluorine in the diamond lattice was observed earlier [3]. The diffusion of sulfur and chlorine may go through the interstitials as well as through the substitutional sites. The electric field may favor diffusion through the interstitials. More research should be done to clarify this issue.

Conclusions

The concentration of sulfur and chlorine was two orders of magnitude larger at the same temperature in positively biased samples compared with negatively biased samples when optical ionization was used. The optically enhanced forced diffusion of impurities may have practical interest for diamond and other wide band gap semiconductors, allowing larger concentration of diffused atoms to be obtained at lower temperatures..

References

[1] M. N. Yoder, Applications of Diamond Films and Related Materials, edited by Y. Tseng, M. Yoshikawa, M. Murakawa, and A. Feldman (Elsevier Science Publishers, NY 1991) p. 287-293

2. R. Kalish, Diffusion in Diamondin, in Properties and Growth of Diamond, edited by G. Davies (INSPEC, the Institute of Electrical Engineers, London, 1994) p. 215-220

3. G.Popovici, T. Sung, S. Khasawinah, M. A. Prelas, and R. G. Wilson , Diamond, SiC and Nitride Wide Bandgap Semiconductors, edited by C. H. Carter, Jr., G. Gildenblat., S. Nakamura and R. J. Nemanich, MRS v. 339 (MRS, Pittsburg, PA, 1994) p. 601-606

4. G. Popovici, R. G. Wilson, T. Sung, M. A. Prelas, and S. Khasawinah, to be published in J. Appl. Phys v. 77, 15 May.

5. G. Popovici, T. Sung, S. Khasawinah, M. A. Prelas, and R. G. Wilson, to be published in J. Appl. Phys v. 77, 1 June.

6. B. V. Spitsyn, G. Popovici, and M. A. Prelas, Second International Conference on the Applications of Diamond Films and Related Materials, edited by M. Yoshikawa, M. Murakawa, Y.Tzeng and W. A. Yarbrough (MYU, Tokio, Japan,1993) p. 57-64

7. B. I. Boltaks, Diffusion in semiconductors, edited by H. J. Goldsmidt, (Academic Press, New York, NY, 1963) p. 93-128

8. J. E. Field, Tables of Properties, in The Properties of Natural and Synthetic Diamond, edited by Field (Acad. Press, London, 1992) p. 667-699

9. G. Popovici, T. Sung, M. A. Prelas, and R. G. Wilson, unpublished data

DIAMOND CUTTING TOOLS

AGILE AND GREEN MANUFACTURING AND SUPER HARD COATED CUTTING TOOLS

Chi-Hung Shen

General Motors Technical Center, MD/A-03, Warren, MI. 48090, USA.

Key words: agile manufacturing, CBN, dry machining, adhesion, tools, wear

Abstract

The paper discusses the global movement towards an agile and green manufacturing environment and their impacts on high volume producers such as the automotive industry. In the area of machining, two major shifts are envisioned: 1) proliferation of highly flexible CNC single spindle machining centers to replace conventional dedicated transfer lines and 2) implementation of "dry" machining systems where there are no or minimal use of machining fluids. In order to migrate towards these goals and still remain competitive and profitable, economically viable high performance super hard coated cutting tools must be developed. Machining results with CVD diamond coated tools are presented to illustrate their current capabilities and limitations. Key areas for further research and development of super hard coating tools will also be discussed.

1. Introduction

The significance and the associated benefits of CVD diamond coating on cutting tools are well documented. Hence, the international fervor in overcoming the technical barriers for the successful development and commercialization of diamond coated tools is very much at a frantic pace. Numerous end products of diamond thin films or thick films deposited on silicon nitride, silicon carbide, or "modified" tungsten carbide substrates have been announced for indexable inserts using an assortment of coating methods and proprietary "recipes" and systems. It is the general consensus of the machining industry that rotating tools such as drills, end mills, reamers, and taps and other types of cutting tools that have very complex cutting edges/geometries are really the key benefactors of the CVD diamond coating. As the technology gradually matures, these coated tools will become available from the next wave of development even though there already have been some early commercial claims on drills, end mills and taps. It is also

expected that diamond coated form tools and wear parts will either be developed in parallel or in very close succession of the mainstream cutting tools.

It is well known that CBN (cubic boron nitride) is the second hardest material after diamond and its compact form is a very effective tool in the difficult-to-machine ferrous and other exotic alloy arena where diamond has a chemical compatibility problem. Because of its similar fabrication approach as PCD (polycrystalline diamond), PCBN (polycrystalline cubic boron nitride) tools encounter the same restrictions on geometries and small sizes. Thus, a viable CBN coating is as important as and may be even more so than diamond since the world has a large demand for and machines more high-valued-added ferrous superalloys. In one estimate, the total current worldwide cutting tool market is about $18 billion and may grow to $25 billion by the year 2005. If the robustness of both types of coating are well established and the prices are cost effective, these diamond and CBN coated tools may become so common for both the manufacturing sector as well as the public consumers (an example is TiN coated drills) that we may be looking at a potentially significant share of the $18-25 billion cutting tool market.

The above described briefly the commonly known reasons for the super hard coated cutting tools. We would like to highlight and discuss in this paper two major global trends that have been gaining tremendous momentum among the industrialized countries. It is hoped that the implications of which would provide additional incentives and urgency to the coating industry to accelerate the development efforts in super hard coatings for the machining community.

2. High Speed CNC Equipment Portfolio for Agile Manufacturing

Over the last two decades, the manufacturing world has gone through unprecedented changes and upheavals primarily because of the rapid advances of many new manufacturing technologies and management philosophies and also the fierce competition from overseas countries. The US automotive makers, being traditionally conservative and weighted down heavily by inefficient corporate infra-structure, were slow to respond resulting in huge financial and employment losses. It is only in more recent years that the industry has been revitalized and become more forward looking to develop realistic corporate strategies for the future.

One of the main concerns for the product and manufacturing planners is the ability to design, test, and start building new products in the shortest lead time without incurring major capital investment costs. Another is the judicious planning of the manufacturing capacity to react quickly to market demand changes, e.g., the ability to convert a passenger car line to a sport utility truck line to meet shifts in consumer tastes. Fig. 1 shows the dilemma that a manufacturing plant encounters throughout the product and equipment life cycles for a traditional dedicated transfer

line machining system wherein each machining station is designed and built to perform one specific task but no others efficiently. There is very little flexibility and it is very costly to adapt the dedicated system to new product designs or volume changes due to unplanned customer demands. The demand is never steady and when one of the stations in the transfer line goes down the whole line stops and there will be no production until the particular machine gets fixed. Hence, the planned capacity seldom matches the demand from the market. In principle, it is feasible to prepare slightly ahead for new but minor changes in product designs (variants) by having a convertible dedicated transfer line which is designed in advance with special optional features so that it can be converted to machine certain pre-planned variants of a component. However, the additional cost to prepare for this conversion is usually quite substantial (about 70% premium) and the conversion time is fairly long in terms of several months to over a year.

In contrast, the advent of higher performance CNC machining centers has broadened the planning options in the manufacturing equipment arena. The machining centers are very versatile and can perform many different machining operations through the use of tool changing magazines and easy CNC programming and the changeover can be done within a few hours. It is also noteworthy that the cost of the machining center has been decreasing steadily over the last 15 years (Fig. 2). Hence, the modern tendency is to utilize as many of these machining centers as economically feasible in clusters of manufacturing cells. The dominant manufacturing strategy for most automotive companies is to have a portfolio containing a mixture of flexible, convertible, and fixed equipment as depicted in Fig. 3. The optimal percentage of each kind of equipment in the portfolio, of course, has to depend on very specific parameters and constraints within each company. Full scale agile manufacturing can now be realized in a plant by organizing and moving these machining centers around the plant floor wherever they are needed to meet unexpected production demands, phase out old design components, or introduce new product programs.

However, in order to bring up the production capacity to cost justify the still more expensive agile system, the single spindle CNC machining center needs to be operated at a much higher machining rate especially for those precision hole making operations which were customarily done on multi-spindle machines. The currently very common usage of PCD or CBN tools in the high speed face milling is well documented but the key obstacle to attain a higher penetration rate for drills, reamers, and taps is the availability of the super hard coated tools. Hence, the quest for manufacturing agility and cost effectiveness has propelled the development and commercialization of reliable and economical super hard coated indexable inserts and small rotating tools to another level of critical importance.

3. Green Manufacturing Environmental Concerns

The current worldwide consumption of metalworking fluids is around 640 million gallons and it is estimated that 52% is used for machining purposes and 31% is applied to stamping processes. There is a very strong global trend to minimize the use of metalworking fluids which have been demonstrated to be the main sources of many industrial pollution problems. For many years, the Big Three have teamed up with UAW, federal agencies, local governments, and research institutes to carry out extensive studies to ascertain the health and safety effects of the metalworking fluids in production plants. Recently an agreement has been signed between UAW and the Big Three to progressively reduce the allowable particulate concentration level in the manufacturing plants to the very low level of 0.5 mg/m^3.

Several on-site measurements have shown that a plant can attain this level with no serious difficulty if there is no "wet" machining operations around, e.g., at the assembly area. Where there are coolant applications, the data hovered barely around 1.0 mg/m^3. The current outlook is that the lowest concentration level of 0.5 mg/m^3 will not be achieved if no new technologies are developed. An alternative approach has been proposed and is rapidly gaining momentum. It is the global technological initiative towards total elimination or disuse of coolant in various machining operations. Nevertheless, before we can shut off the coolant and perform **"dry"** machining, we need to examine the various functional roles of a machining fluid. Fig. 4 illustrates that the coolant has expanded its traditional roles many times over simply because it is convenient and readily available. Thus, it is used as a lubricant for machine slides, to control the temperature of the part and the machine, to flush out the chips from the machined parts, fixtures, clamps, and pallets, and even as a housekeeping aid for flushing the shop floor. After reviewing all the real or perceived uses depicted in Fig. 4 and estimating the relative degree of difficulty in machining various processes dry (Fig. 5), we found out that many of the coolant functions can be handled easily with other means or substitutes. However, it was concluded that three key roles (Built-Up-Edge (BUE) reduction, chip ejection, and temperature control) need the development of new technologies or approaches to alleviate or minimize the respective concerns in order to accomplish dry machining in the very space-confined deep hole manufacturing processes. It is noted that because BUE affects the chip morphology, it also has a heavy coupling effect with both chip ejection and temperature control. Due to the lack of space, we would not digress the subjects too much here but we would like to describe the BUE problem a little more in detail in the next paragraph.

First of all, BUE is defined as the quasi-stable phenomenon when some of the machined work material adheres to and wraps around the cutting edge of a tool covering both the rake and the flank faces of the tool during a metal cutting process. The accumulation of the metal can be quite sudden and, after it has reached a certain size, it may break away by itself partially or completely. The

process of the BUE formation and its break-away may appear repeatedly over the entire duration of the machining operation. Due to its unpredictable and unstable nature, the BUE will affect the production of a consistent part dimension and surface finish. Also, because the BUE is compacted under extremely high compressive stresses and its adhesion to the tool surface is so strong that, very frequently when it breaks away, a part of the tool tip is also torn away reducing the expectancy of a tool's normal useful life. Basic research over the years has unraveled its formation mechanism but there is no robust predictive models to control BUE formation. Experiences have showed that increases in the cutting speeds and the use of diamond and CBN tooling have minimized dramatically the BUE formation. This is the main reason that PCD indexable inserts have been so effective and popular in aluminum machining where BUE is prevalent with other cutting tool materials. From this brief discussion, we should realize that for dry machining to succeed in small deep holes, which constitute for over 60% of machined features in many automotive components, there is a global urgency to develop super hard coated rotating tooling such as drills, reamers, and taps.

4. CVD Diamond Tooling Tests & Performance

The majority of the coated tools were evaluated in the laboratory environment. The machining samples were hyper-eutectic 390 aluminum alloy containing 16-18% silicon. They were fabricated by the lost foam casting method into long hollow cylinders and rectangular strips (Fig. 6). O.D. traverse turning tests were performed on a horizontal lathe having a 3,000 rpm capability and drilling tests were done on a high speed (12,000 rpm) machining center. Cutting forces were monitored with Kistler's turning and drilling dynamometers. During a test, the coated tool would be removed at regular intervals and inspected under an optical microscope or a scanning electron microscope (SEM). Occasionally, the tool would be covered with aluminum and this was etched off by a sodium hydroxide solution in an ultrasonic bath prior to inspection and wear measurement.

Further details of the turning experiment and the assessment have been described in [1]. Initially, the thin film diamond coated indexable inserts were obtained from 9 sources. Inspection showed that they varied vastly in substrates, grain sizes, film thickness and roughness, and adhesion strengths. These differences were reflected in their immensely different and inconsistent levels of performance. When the coating was detached from the substrate the cutting force would increase rapidly as indicated in Fig. 7. The inconsistency and scatter in tool wear is depicted in Fig. 8. Since [1], we have tested two more coating sources and their performance is also below expectation (Fig. 9). We will not go into a full discourse of the various failure modes but it will suffice to illustrate the catastrophic failure when the film adhesion was not strong (Fig. 10) and the well defined wear scar when the coating was slowly worn through by the desirable attritious wear mechanism (Fig. 11).

More recently, we have started to test some coated end mills and drills. The end mills were used to mill the skin off the 390Al drilling strip samples. It was found that the end mills were all chipped after one or two passes over the edge of the strips. The coated drills fared a little better. They lasted for a couple of hundred holes (similar to an uncoated carbide drill) before the coating was chipped or delaminated. Fig. 12 showed that the torque had not increased too much probably because the carbide edge underneath the diamond film was still sharp when the test was terminated.

5. Conclusion

It is apparent that the current batch of CVD diamond coated tooling is still not ready for automotive applications despite many technical advances and optimistic projections [2,3,4]. Until the wide spread tool life variation has been reduced significantly the production plants will not embrace this technology readily.

The global manufacturing focus towards flexible high speed machining centers and dry coolant-free machining environment would need the unquestionable success in the development and implementation of both the diamond and CBN coated tooling. The manufacturing community welcomes the conerted and cooperative efforts among the academia, national laboratories, and tooling suppliers to face up to these challenges.

6. Acknowledgement

The author wish to thank all the coating sources for the opportunities to evaluate their prototype tools and exchange technical information. He also would like to appreciate the careful tests and inspection done by his technician, Jimmy Staten.

7. References

[1] C. H. Shen, " Machining Performance of Thin Film Diamond Coated Inserts on 390 Aluminum", Trans. of NAMRI/SME, Vol. XXII, 1994, p. 201-207.
[2] H. E. Hintermann and A. K. Chattopadhyay, "Low Pressure Synthesis of Diamond Coatings", Annals of CIRP, Vol. 42/2/1993, p. 769-783.
[3] D. G. Bhat, "Diamond-Coated Cutting Tools-A Status Report", Mat. Tech., Vol. 9, 1994, p. 253-261.
[4] E.E. Sprow, "Diamond Coatings: Ready to Rip?", Manufacturing Engineering, February 1995, p. 41-46.
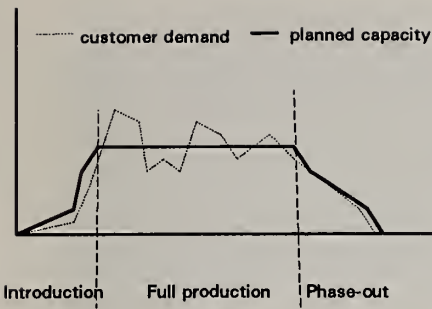
Fig. 1. Demand Fluctuation over Time
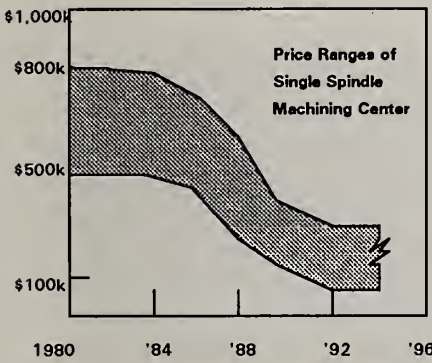
Fig. 2. Price of CNC Machining Center
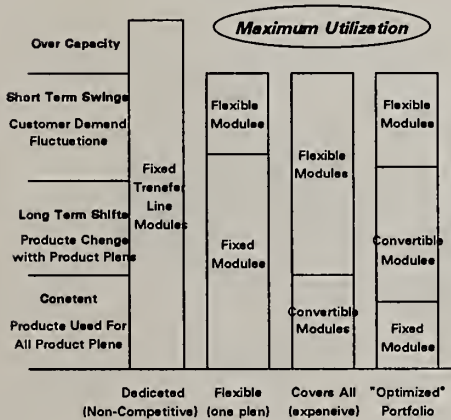
Fig. 3. Manufacturing Strategies
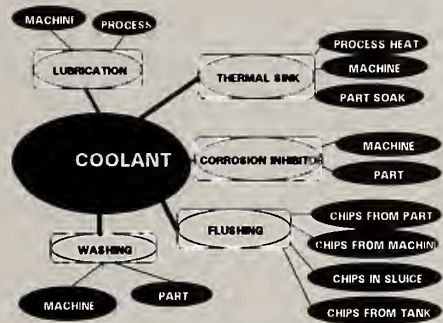
Fig. 4. Various Coolant Uses in Production
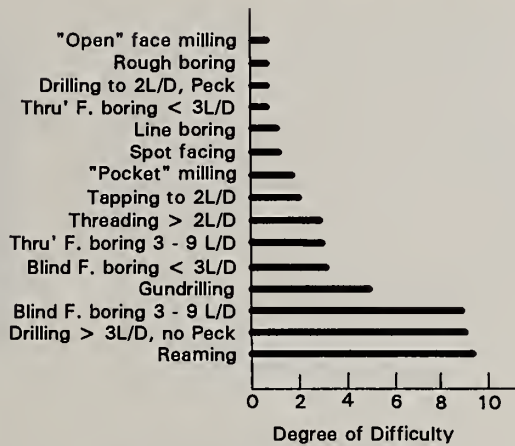
Fig. 5. "Dry" Machining Difficulties
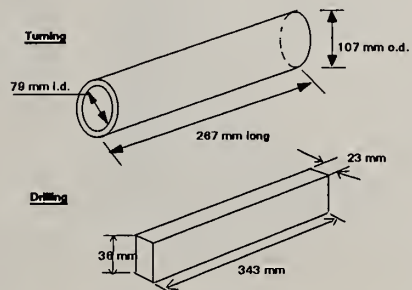
Fig. 6. 390 Al Turning & Drilling Samples
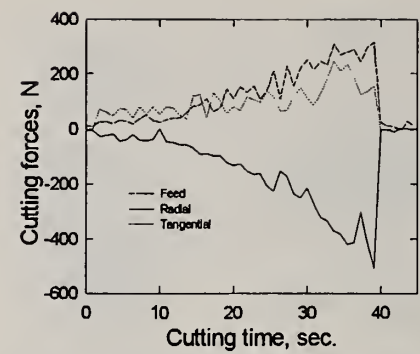
Fig. 7. Failure Signal of a Coated Insert

Fig. 10. SEM of a Spalled Insert
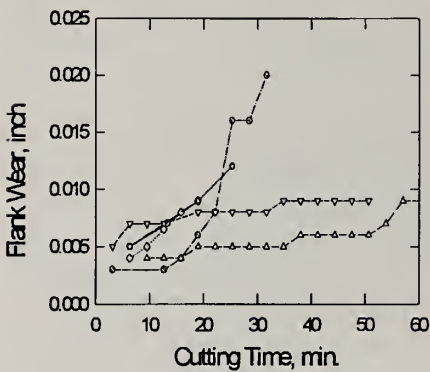
Fig. 8. Performance Scatter of Inserts

Fig. 11. SEM of a Worn Through Insert
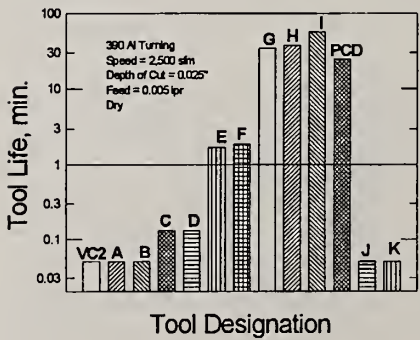
Fig. 9. Performance of Various Suppliers
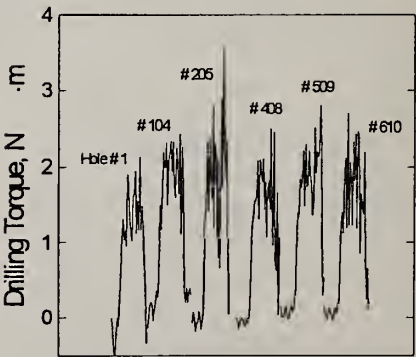
Fig. 12. Torque Variation of a Coated Drill

WEAR MECHANISM OF DIAMOND COATED CUTTING TOOLS

T. Leyendecker, O. Lemmer, S. Esser and M. Frank

CemeCon GmbH, Talbotstraße 21, D-52068 Aachen, Germany

Key words: adhesion, CVD, diamond, pretreatment, wear, tools

Abstract

Since Diamond Coatings were introduced into the market in 1989, five years experience in industrial applications of diamond coated cutting tools enables to present an overview of tool life and wear behavior of diamond coated cutting tools due to different cutting conditions and workpiece-materials. Machining reinforced plastics, presintered ceramic compacts, aluminum·alloys, metal-matrix composites and graphite, different wear behavior occurs at the cutting edges of diamond coated tools. Having a good adhesion fatigue and chemical wear of Diamond coatings determines life time of the tools. By a profound pretreatment procedure CVD-Diamond coated tools can compete with conventional PCD-tools.

1. Coating process

The diamond deposition was performed using the hot-filament-CVD method with tungsten filaments. The small-lot production unit is fully automated and able to coat up to 200 standard inserts per batch.
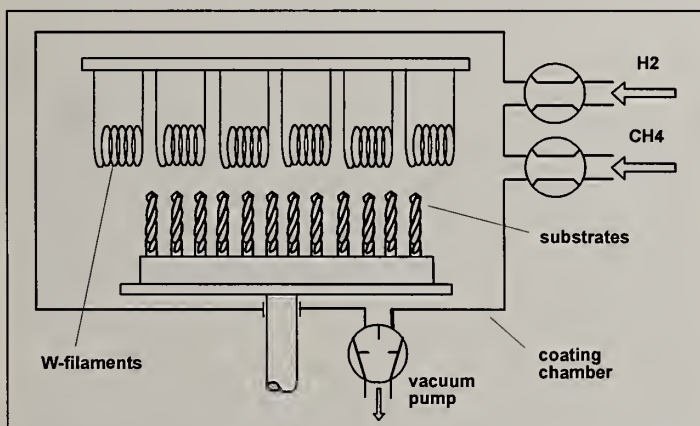
Fig. 1. Scheme of the hot filament coating unit.

Table I.   Standard coating parameters

total pressure	1500	pa
H_2-gas flow per volume	1	ml_n min^{-1} cm^{-3}
CH_4 content	1	%
filament temperature	2000	°C
substrate temperature	900	°C
filament-substrate-distance	10-20	mm
coating time	20-100	h
coating thickness	5-30	μm

2. Surface pretreatment

For the diamond coating of cemented carbides a low content of Co-binder is generally considered to be substantial, because Co catalytically promotes the formation of graphite. Moreover a reproducible surface-state without pores is essential. There should be no modification of the chemical surface composition by the sintering or grinding procedures during tool manufacturing.

The surface composition is not as easy controllable as the overall Co-content or the geometric dimensions. Particularly sintered surfaces show great differences in composition, even on different locations on the same tool. So a Co-content from 1 to 7% were measured on a 6%-cemented carbide grade by EDX-analysis.

Sintered or polished surfaces need an additional surface preparation by grinding or blasting before the pretreatment.

On the surface the Co-content must be reduced from the bulk value of at most 6% below 0,5%. Until now this is only possible by excessive chemical etching in hot $HCl:HNO_3:H_2O$ 1:1:1 solution. After removal of the etching-products a seeding procedure is performed by an ultrasonic diamond suspension.. The pretreatment can be divided into the following steps (see also Fig. 2):

- mechanical preparation depending on surface conditions
- degreasing in alkaline solution
- etching in acids (HCl/HNO_3)
- cleaning from etching products
- seeding by ultrasonic diamond suspension in ethanol
- ultrasonic removal of not adherent diamond seeds
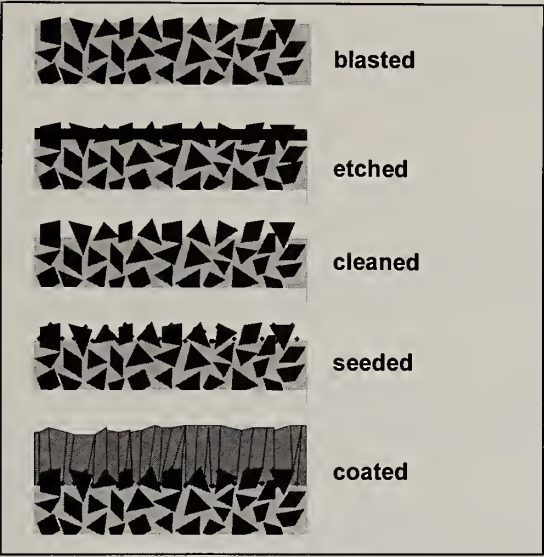
Fig. 2. Standard surface pretreatment for cemented carbides

By the pretreatment the surface becomes rougher. Between the WC grains many undercuts developed, which were filled with diamonds seeds during the seeding procedure. So the adhesion of the diamond films is improved by mechanical clamping (s. Fig. 3).
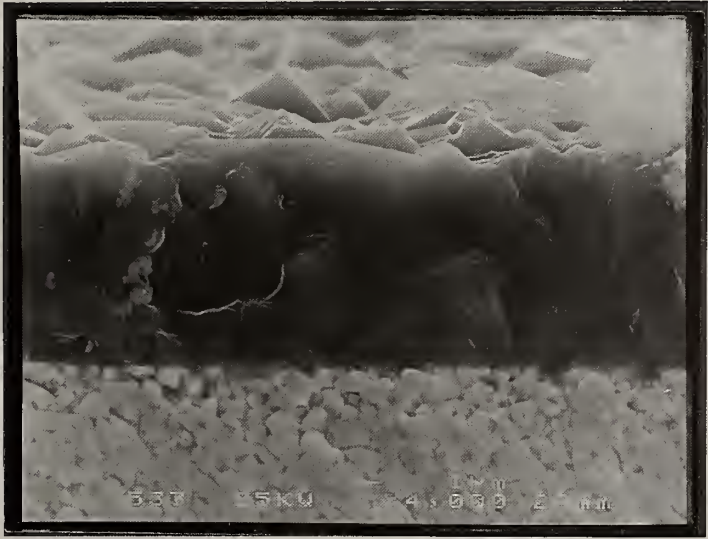
Fig. 3. Cross section of a diamond coated cemented carbide tool pretreated as above.

If the Co-content is to high the compound material is weakened by the etching procedure. So an upper limit of about 6 wt.% Co is demanded [1].

3. Wear mechanism of polycrystalline diamond tools (PCD).

Concerning the wear of conventional diamond-cutting-tools (PCD), much experience by manufacturers, users and scientists exists [2]. The cutting edges of these tools consist of synthetic manufactured diamond grains embedded in a binder phase consisting mostly of cobalt and nickel. There are different sources of wear [3]:

The wear by mechanical and chemical effects on PCD-tools is higher than on pure diamond, like the CVD-diamond coating. The mechanical wear is due to the rinsing of the soft binder phase followed by isolation and removal of the diamond grains. The chemical wear is caused by diffusion of carbon atoms into the binder phase and graphitisation by catalytic reactions with the surrounding cobalt and nickel. The chemical reactions in addition cause embrittlement of the Co-binder phase. Diffusion and graphitisation diminish the diamond. Due to the chemical wear by reactions with oxygen and the workpiece material, PCD and CVD-diamond tools are not suitable for machining materials with a high solubility of carbon like ferrous materials.

While PCD cutting edges are cut from the bulk material and soldered on cemented carbide shapes the geometry of CVD coatings is not restricted and most of conventional tools geometries are coatable. On the other hand the coating thickness of PCD is considerably thicker (max. 1 mm) than for CVD-Diamond-coated tool (5 - 40 µm). Nevertheless CVD-coating can beat PCD as shown below. This is due to the lack of a binder phase and the compressive stress in the coating caused by different thermal expansion coefficients between diamond and tool. This stress is able to compensate the cutting pressure.

4. Performance Tests

The advantage of CVD-diamond tools is obvious in machining extreme abrasive materials. Turning and milling of graphite are intense abrasive procedures and PCD tools are commonly used while conventional tools fail quickly.

Fig. 4 shows the tool life for PCD-insert versus CVD-diamond- and TiN-coated cemented carbide (ISO grade K10) during rough turning of graphite. In this case coated spherical cutters and PCD tool of equal geometry were used. The criteria for tool life was a width of wear land (WWL) of 0,1 mm.

The conventional TiN-coated tool is worn immediately. While the tool path is increased by a factor of 6,5 for the PCD tool, the factor is in fact 11 for the CVD diamond coated tool. Especially for this tool the tool life is superpropotional increased at higher cutting speeds.
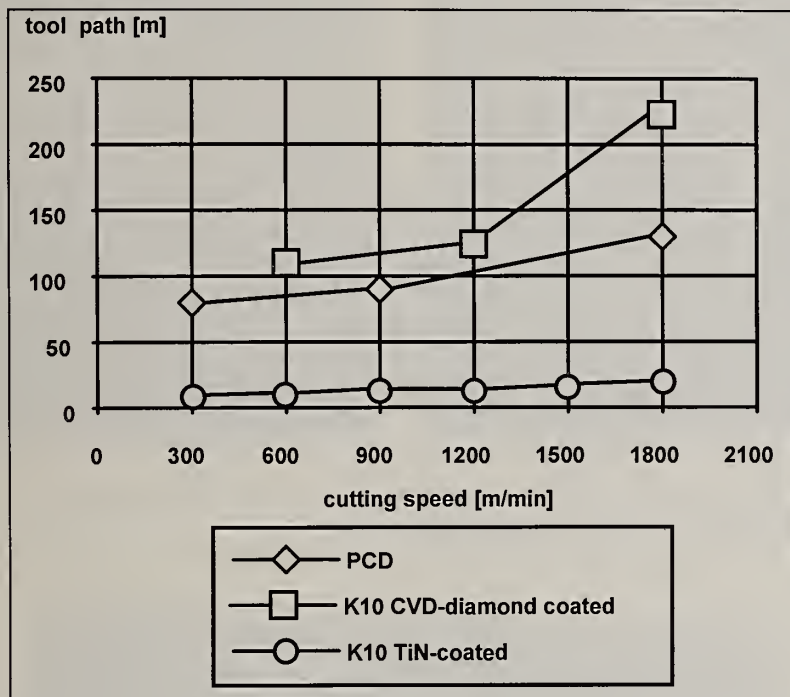
Fig. 4. Tool life of PCD in comparison to TiN and diamond-coated cemented carbides for rough turning of graphite [4].

Table II.   Cutting conditions for Fig. 4.

material	EK85			
feed per edge	f_t	=	0.05	mm
cutting width	a_e	=	12	mm
cutting depth	a_p	=	3	mm
end mill diameter	D	=	12	mm
cutting edges	n	=	2	
tool life criteria	WWL	=	0,1	mm

While in the beginning the wear is low on the rake, the diamond is worn away at the flank and the rough diamond coating is leveled completely (Fig. 5 left). In comparison the right side of Fig. 5 shows the wear of the PCD tool with cavities in the surface caused by eroded binder and due to that by removed diamond grains.

The progress of crater and flank wear is very constant. Fig. 6 shows the crater wear at the end of the test. In the crater the diamond coating is continually thinned and the substrate is reached without any step.
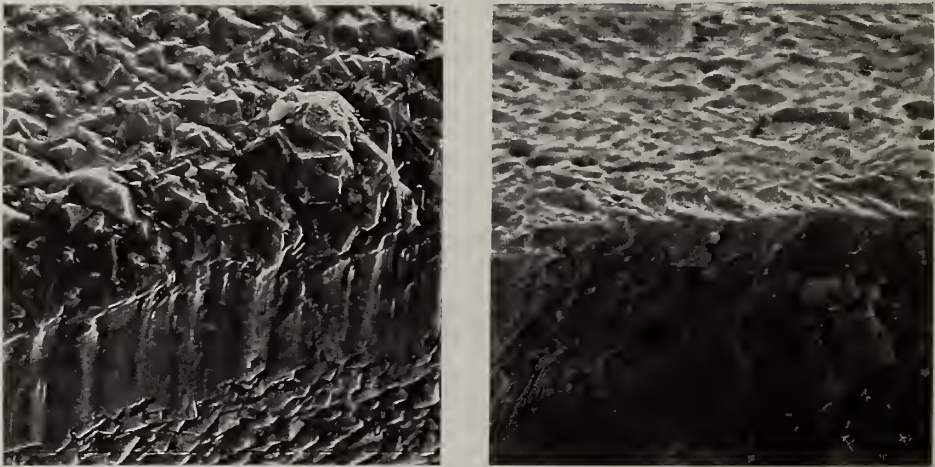
Fig. 5. Flank wear after 25 m for CVD-diamond coated cemented carbides (left and PCD (right). Magnificaton =1000:1
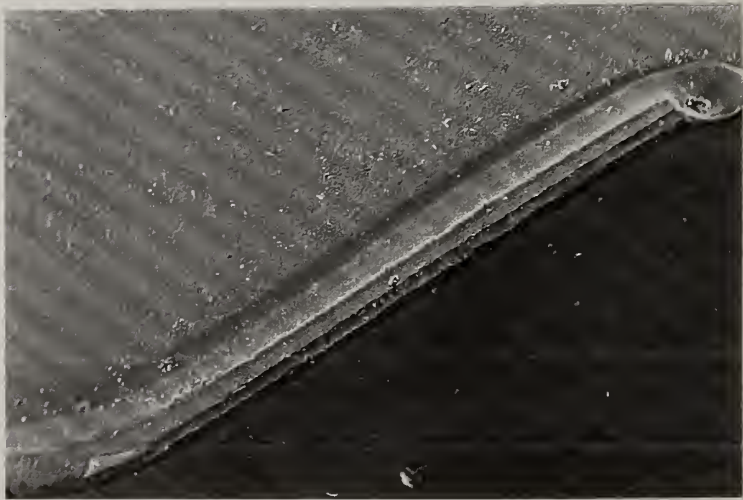
Fig. 6. Crater wear at the end of the cutting test.

Comparable results are obtained by finishing milling of graphite as shown in Fig. 7. In comparison with the PCD tool the tool-path for the CVD-diamond coated tool was increased from 250 m to 400 m. In comparison with the uncoated tool the factor was nearly 10.
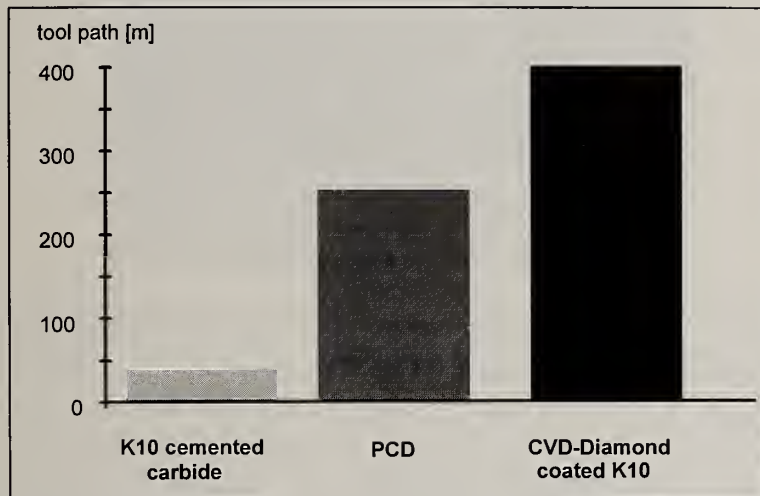
Fig. 7. Tool life for finishing milling of graphite [4].

Table III. Cutting conditions for Fig. 7.

Material	graphite V1466		
cutting speed	v_c	= 600	m/s
cutting width	a_e	= 1	mm
cutting depth	a_p	= 5	mm
end mill diameter	D	= 6	mm
cutting edges	n	= 2	
tool life criteria	WWL	= 0,1	mm

There are many successful cutting tests with CVD-diamond coated tools for other high abrasive materials, like reinforced plastics and aluminum or green compacts for cemented carbides and ceramics. In many cases the performance is better than for PCD, but in every case significantly better than uncoated. Fig. 8 for example shows the same type of wear at the cutting edge after turning AlSi-alloy with 20 vol.% Saffil (Al_2O_3-fibers). Even here the tool life was increased by a factor of about 10 in comparison to the uncoated tool [5].
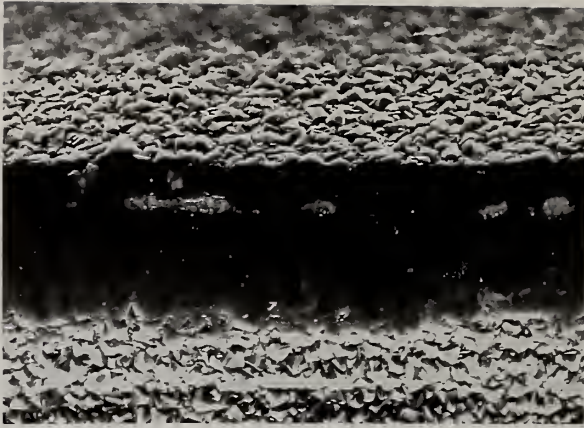
Fig. 8. CVD-diamond coated K10 after turning AlSi12CuMgNi with 20 vol.% Saffil
(magnification = 500:1) [5]

5. Conclusions

The performance of CVD-diamond coated tools can surpass common PCD-tools can be significantly higher. With a well adherent diamond coating produced by a reproducible cemented carbide surface and profound pretreatment procedures before the coating process the advantages of binder-free diamond can come into action. More improvement is expected, if the coating thickness is increased and the cemented carbide grade as well as the tool shape are optimized for CVD-coating.

References

[1] Leyendecker,T.;Lemmer,O.;Jürgens,A.;Esser,S.;Ebberink,J;
    Industrial application of crystalline diamond-coated tools
    Surface and Coating Technology, 48, 1991, p.253-260
[2] Spear, K. E: and Dismukes, J. P. (ed),
    Synthetic Diamond: Emerging CVD Science and Technology,
    Wiley, New York, 1993
[3] Lemmer, O.,
    Verschleißverhalten diamantbeschichteter Werkzeuge
    Thesis lecture, RWTH Aachen, Institut. für Werkstoffkunde, 1993
[4] König, M.
    Institute für Produktionstechnologie, Frauenhofer-Gesellschaft (IPT FhG) Aachen
    Internal report
[5] Biermann,D.; Weiner;
    Universität Dortmund, Institut für spanende Fertigung, Internal report 1993

IN SITU TEMPERATURE MEASUREMENT ON DIAMOND - COATED TOOLS: A NEW INSTRUMENT FOR OPTIMIZING CUTTING PROCESSES

Peter Müller-Hummel and Michael Lahres
Daimler-Benz AG, Production Research and Environment, P. O. Box 2360, 89013 Ulm
(Germany), e-mail: 100416.612@compuserve.com

Abstract

A new measuring technique is described in the presented paper, which can determine the absolute temperatures at the rake face of diamond - coated inserts during dry turning. Cutting temperatures, which can be measured by this infrared thermographic system, varied with the workpiece material aluminium- (AlZnMgCu1.5) and gray cast iron- (GG25) alloys and the cutting conditions. A good agreement exists between the measured temperatures and the corresponding tool wear values. To verify the repeatable calibration results, there are two methods used and described to measure the spectral directional emissivity of the chip bottom side. This temperature measuring system can be used for determining the machinability of various workpiece materials with new cutting tools. Additionally, it will be an important test equipment to better understand tool wear mechanisms.

1. Introduction

During machining processes, a considerable amount of the machining energy is transformed into heat /1/. This results in an increase of the tool and workpiece temperatures. The temperature distributions are determined by the heat conductivity and specific heat capacity of the tool and the workpiece, heat flux, capacity of the heat abduction and finally the amount of heat loss based on radiation and convection /2/. The maximum temperatures occur in the contact zone between chip and tool /3/. The tool life during the machining process is influenced especially through the temperatures at the edge /4,5/.

On diamond - coated inserts, oxidation reactions accur in oxygen atmosphere at temperatures higher than 500°C and in a vacuum of 10^{-6} torr at temperatures higher than 1400 °C /4/. These influence the wear behaviour negatively and shortens the tool life /5/. To expand the application field of diamond - coated tools for Al, Ti or Fe - based alloys, it is necessary to determine the maximum temperatures at the rake face. With this capability, it is possible, to establish the cutting conditions for a maximum material removal rate depending on an allowable tool load.

2. Temperature measurement

The new measuring technology to determine the temperatures in the cutting zone was presented in detail earlier (**Fig. 1**) /6/. The infrared - thermographic temperature measurement in the contact zone between the chip bottom and the rake face is possible by means of the infrared transmissivity of diamond in the CVD diamond - coated insert. Through a borehole of a commercially - available tool holder, an infrared path can be realized. Hence, projection (without mechanical contact and in real - time) of the infrared radiation from the chip bottom onto the scanner of a high resolution thermographic camera is possible /7/.
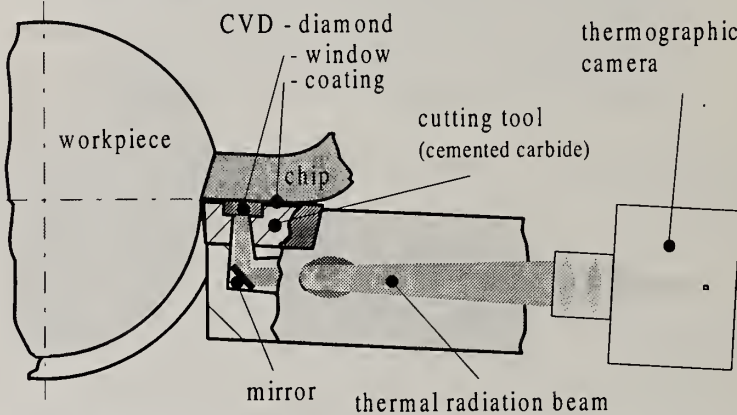
Fig. 1: Model of the temperature measuring system with a tool face borehole

For calculating the absolute temperatures, it is necessary to measure the spectral directional emissivity ε_λ of the tested workpiece material. To verify the results, there are two methods used to measure repeatable the spectral directional emissivity. First, the direct method, where the emissivity is determined from the ratio of the emitted radiance to the reference blackbody radiance, both at the same temperature. Secondly the emissivity is determined by measuring the reference temperature using a thermocouple /8/. With this setup the spectral directional emissivity of the chip bottom side of AlZnMgCu1.5 was measured to $\varepsilon_\lambda = 0.09$ and for GG25 to $\varepsilon_\lambda = 3.4$ (with $\lambda = 8$-12 μm and an uncertainty of 10% each).

3. Results

It is possible to record the absolute temperature distribution at the chip bottom and thus at the rake face of diamond - coated inserts during dry turning of an AlZnMg-Cu1.5 - malleable alloy with the measuring system described above. It is evident that in the investigated area the measured temperature values increase with the rising time-cutting volume. (**Fig. 3**). The measured temperature values range between 400 and 800°C. The temperature distribution image shows clearly, that the maximum temperatures in chip flow direction occur in the first third of the CVD window (**Fig.**

2). The window is not covered totally by the chip width, because the depth of cut chosen for this case was $a_p = 0.5$ mm.
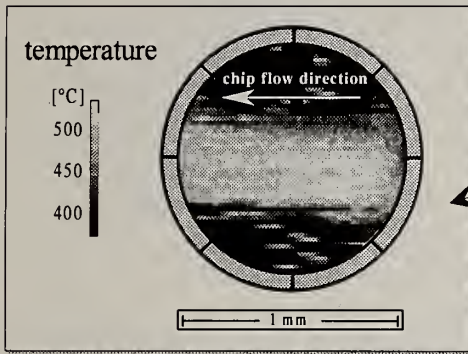
Fig. 2: Temperature distribution at the chip bottom side for $v_c = 1000$ m/min, $f = 0.1$ mm/rev. and $a_p = 0.5$ mm
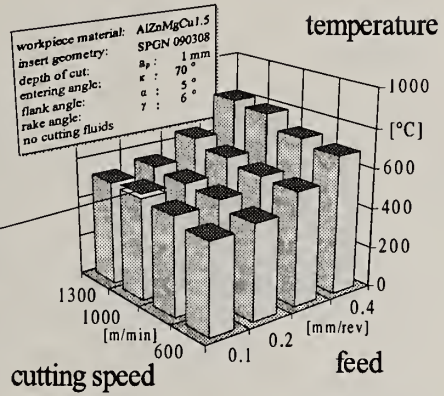
Fig. 3: Absolute temperature values as a function of the cutting speed and feed during dry turning of an AlZnMgCu1.5 - malleable alloy·

How do these measured temperatures influence the wear behaviour of the tested diamond - coated inserts?

The wear characteristic of a CVD and a polycrystalline diamond insert is presented in diagram Fig. 4. It is evident that both types of inserts exhibit relatively low flank wear values after 100 min cutting time. In comparison, after 100 min cutting time an uncoated tungsten carbide insert exhibits a flank wear of about 550 µm.
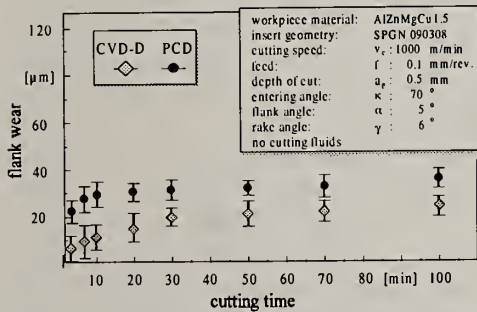
Fig. 4: Flank wear of a diamond - coated insert in comparison to a PCD - insert

Fig. 6 shows the temperature values for dry turning of the GG25 casting alloy. The absolute values range between 270 and 850°C. The belonging wear characteristic (flank wear) is plotted in **Fig. 5** additionally. Cutting speeds above 180 m/ min (constant feed of 0,2 mm/rev.) lead to a large increase of the flank wear rates for CVD - diamond inserts after 4 minutes of cutting time. In contrast to this behaviour, cutting speeds of 130 m/ min and below result in low flank wear rates for CVD - diamond, polycrystalline diamond and uncoated cemented carbide (K10) still after 30 minutes of cutting time.
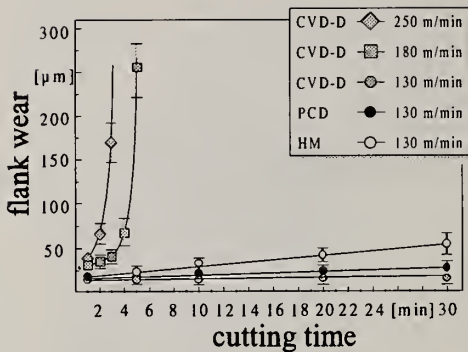
Fig. 5: Flank wear of diamond - coated inserts in comparison to a PCD - and an uncoated cemented carbide - insert

Fig. 6: Absolute temperature values as a function of the cutting speed and feed during dry turning of an GG 25 - casting alloy

4. Discussion and Conclusions

The presented infrared measuring system is applicable to determine the maximum temperature values on diamond - coated inserts. Turning the GG25 - casting alloy, the correlation between the cutting temperatures (**Fig. 6**) and the flank wear rates (**Fig. 5**) can be pointed out. Temperatures above 500°C result in high flank wear rates even after 4 min of cutting time, while the temperatures below 500°C show minor flank wear rates for CVD diamond inserts (**Fig. 7**). Therefore, it can be declared, that CVD diamond inserts are also suitable in cutting gray casting alloys in the case of preselecting optimized cutting parameters. In the case of the AlZnMgCu1.5 - malleable alloy, there was determined a low temperature range at the rake face.

Fig.7: Wear mechanisms for machining as a function of the cutting temperature (qualitatively) /9/

This temperature field has a minor influence on the wear behaviour of the diamond, because the chip flows continuously and is partly melted over the rake face and thus prevents the entering of oxygen into the contact zone. Under these conditions, cutting of AlZnMgCu1.5 - malleable alloys is also possible with diamond - coated tools above temperatures > 500°C.

References

/1/ Vieregge, G., Die Energieverteilung und die Temperaur bei der Zerspanung; *Werkstatt und Betrieb*; 86 (1953), pp. 691.

/2/ Spur, G and Ullmann, F.; Ermittlung der Temperaturen auf der Werkzeugspanfläche beim Drehen; *VDI-Zeitschrift*; 133 (1991), No. 4, pp. 81.

/3/ Trent, E. M.; Metal Cutting; *Butterworth - Heinemann Ltd.*; Oxford; 1991.

/4/ Wilks, J. and Wilks, E.; Properties and Applications of Diamond; *Butterworth-Heinemann Ltd.*; Oxford, 1991

/5/ Evans, C.J. et al.; Cryogenic Diamond Turning: Theory and Experiment; *Proceedings of the ASPE annual meeting*; 1992, pp.57

/6/ Müller-Hummel, P. and Lahres, M.; Infrared temperature measurement on diamond-coated tools during machining; *Proc. 4.th European Conf. on Diamond, Diamond-like and Rel. Coatings, Albufeira, Portugal, 1993*; Elsevier, Oxford, 1993, pp. 765.

/7/ Müller-Hummel, P.; *German Patent* DE 42 33 035, 1992.

/8/ DeWitt, D. P. and Incropera, F. P.; Physics of thermal radiation, in: "Theory and practice of radiation thermometry", *Wiley and Sons*; 1989, pp 21

/9/ König, W. and Fabry, J.; Schneidstoffe - Stand und Tendenzen; *Metallwissenschaft und Technik*; 37, (1983); pp. 709.

Applications of Diamond Films and Related Materials: Third International Conference, 1995
Editors: A. Feldman, Y. Tzeng, W. A. Yarbrough, M. Yoshikawa, and M. Murakawa

197

EFFECT OF LASER IRRADIATION ON ADHESION STRENGTH OF DIAMOND FILMS ON WC-6wt%Co HARD METAL SUBSTRATE

F.X. Lu[1], C.M. Li[1], J.J. Wang[1], X.L. Liao[1], Y.L. Zhou[2], H.B. Lu[2], and S.F. Xu[2]

[1]University of Science and Technology Beijing, Beijing 100083, P.R. China
[2]Beijing Institute of Physics Sinica Academia, Beijing, 100080, P.R. China

Abstract

Effect of laser irradiation pre-treatment on adhesion strength of diamond films on WC-6wt% Co hard metal substrate was studied. Adhesion strength of diamond films on the hard metal substrate were measured by the Scraper Test, and were compared to those deposited in identical conditions but the substrate were subjected to etching in acidic solution. It was found that at a film thickness of 2-6μm, laser pre-treatment almost doubled the adhesion strength as compared to acid etching pre-treatment. Detailed SEM examinations confirmed the mechanisms suggested by the present authors in their earlier work that the improvement in adhesion strength by laser pre-treatment was due to the surface Co depletion and surface modification by the high power density laser beam.

1. Introduction

Diamond film coated cutting tools are of particular interests for their excellent performance and relatively low cost. However, the most widely used hard metal substrate contain certain amount of Co as its binder phase, which unfortunately promote the deposition of graphite and so lead to a very poor adherence. Numerous papers and patents were published in the past few years concerning the great efforts made to improve the adherence of the diamond films with the WC-Co substrate [1,2].

Our previous results [3] have shown that a novel method of excimer laser pre-treatment, by which Co depletion and surface modification (roughening) can be realized simultaneously, could be used to enhance the diamond film adhesion to cemented carbide tool substrate. In this paper, scraper test [4] was employed to investigate the effect of laser pre-treatment on the enhancement of adhesion, and the mechanisms were discussed.

2. Experimental

Commercial WC-6wt% inserts were used as the substrate. After cleaning in a ultrasonic bath, they were irradiated by a pulsed NeCl excimer laser beam (λ=308nm, 40 ns, 10 Hz). The power density was 0.5 - 2 J/cm^2. For the purpose of comparison pre-treatment of etching in HCl:HNO$_3$:H$_2$O solution (1:1:1) was also adapted. Diamond deposition was conducted in a microwave reactor with maximum power output of 1.5 kW. A gas mixture of H$_2$ - CH$_4$ (0.5 - 2 %) was used. The substrate temperature was kept at 700 - 900°C. Co content was determined by XPS technique. The surface of the substrate before and after the diamond deposition were examined by scanning electron microscopy (SEM). Scraper test was conducted on a specially designed tester according to Murakawa et al. [4].

3. Results and discussion

XPS studies showed that after laser treatment at a power density of ~ 1.13J/cm^2, the surface Co content of the hard alloy substrate was depleted from its nominal composition of 6wt% to as low as 0.76wt%. Whilst its surface was apparent roughened (modified). These observations further confirmed the previous results of the present authors [3]. However it was found in the present investigation that there was a threshold power density level of ~ 0.5J/cm^2, below which no effect on Co depletion nor surface modification could be observed. Surface roughening was found to increase with increasing power density, but there existed a optimum value of power density level, above which Co content did not decrease, instead, it was found to increase again with increasing laser intensities due to the sputtering effect. In the present investigation etching in HCl:HNO$_3$:H$_2$O solution for 5-15 min. was found to be able to deplete the Co content from 6wt% to as low as 0.2wt%.

Fig.1 shows diamond films deposited on laser treated and etched surface of the WC-6wt%Co hard alloy tool substrate, Fig.1(a) and (b) shows the diamond films deposited at the edge of WC-6wt%Co hard alloy tool substrate, where it can be seen that film quality were equally good. Fig.2(c) and (d) are the cross section SEM photographs, one can see that the interface between diamond film and the substrate was rather smooth for the etched substrate, whilst for the laser treated substrate was irregular and uneven.

Fig.2 shows the load-distance curves of scraper tests for adhesion measurement for diamond films of a thickness of 2μm deposited on the etched and laser treated hard alloy substrate. The lower load level in the left hand side of the curves indicates the friction force of the scraper blade against the hard alloy substrate surface before cutting into the film-substrate interface. Whilst the higher load level in the right hand side represents the resistance exerted
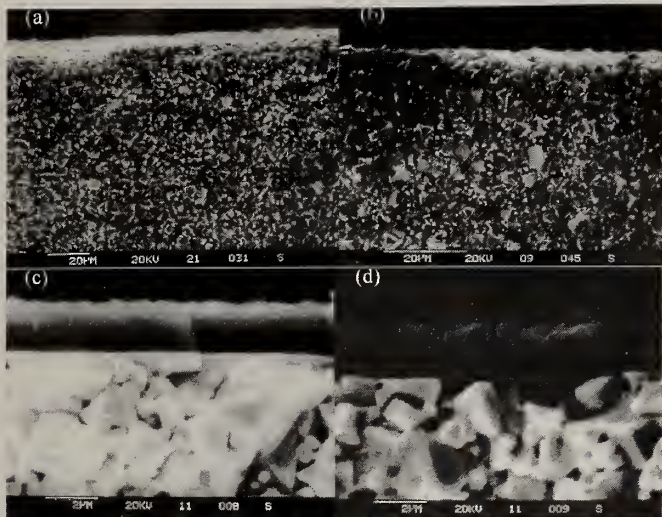
Fig.1. Diamond films deposited on the etched ((a) and (c)) and laser treated ((b) and (d)) WC-6wt%Co tool substrate.
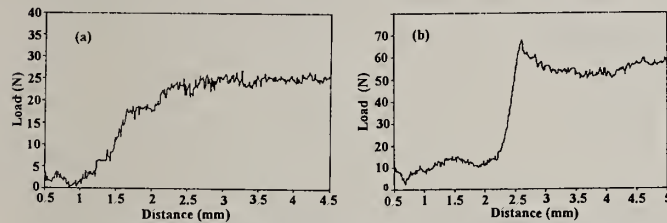
Fig.2 Typical load-distance curves of scraper test for adhesion strength measurement for diamond films deposited on (a) : etched (b) : laser treated WC-6wt% hard alloy substrate

on the scraper blade after cutting into the interface and advancing forward. From the difference adhesion strength can be calculated [4]. Adhesion strength measurement from scraper test is also depended on the film thickness. As shown in Fig.3, for film thickness of 2-6μm, adhesion strength for diamond films deposited on the laser treated hard alloy substrate was almost twice as much as that on the etched substrate.
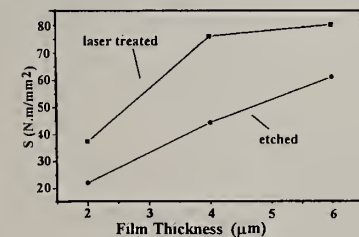
Fig.3 Adhesion strength of diamond films as measured by scraper test

Fig.4 shows the cutting tracks of the hard alloy substrate surface due to the action of the scraper blade after the test. Where it can be seen that, for the etched substrate diamond film was completely chipped off, whilst for the laser treated sample remaining diamond film debris were clearly discernible.

200
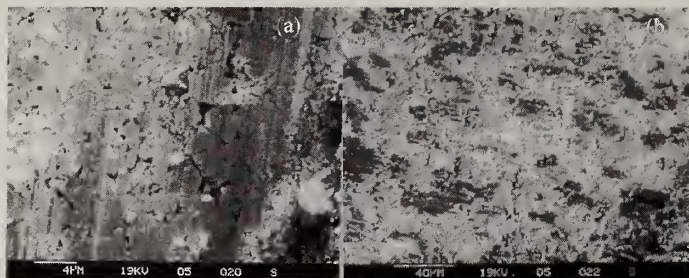
Fig.4 Cutting tracks on the hard alloy substrate surfaces after the scraper tests.
(a) etched substrate   (b) the laser treated substrate

Difference in the mechanisms in film breakage by the scraper blade was also observed. For the etched substrate diamond film was chipped off and broken into fragments in relatively big size, whilst for the laser treated sample diamond film was smashed into small pieces by the scraper blade. By comparing the photographs shown in Fig.1 and Fig.4 one can come to the conclusion that the observed enhancement of diamond film adhesion strength was due to the combination effect of surface Co depletion and surface modification of the high power density laser pre-treatment. And it may provide a novel method for preparation of high performance diamond coated cutting tools.

4. Conclusions

Excimer laser irradiation pre-treatment can greatly increase the diamond film adhesion on WC-6wt%Co hard alloy tool substrate. The mechanisms responsible for this enhancement is the combination effect of Co depletion and surface modification (roughening) due to the high power density laser beams.

5. Acknowledgment

6. References

1. N. Kikuchi and K. Yoshimura : New Diamond, 7 (1987) 26.
2. Y. Saito, K. Sato, S. Matuda and H. Koinuma: J. Mat. Sci., 26 (1991) 2937.
3. F.X.Lu, C.M. Li, J.J. Wang, Y. Tzeng, J. Wei, D.Z. Gong and G. Wang. Advances in New Diamond Science and Technology, S.Saito et al. eds., MYU, Tokyo, 1994, 795.4.
4. M.Murakawa et al., Thin Solid Films, 181(1989)443.

Applications of Diamond Films and Related Materials: Third International Conference, 1995
Editors: A. Feldman, Y. Tzeng, W. A. Yarbrough, M. Yoshikawa, and M. Murakawa

201

APPLICATIONS FOR PRECISION CUTTING OF SHARPENING CVD DIAMOND FILM

Fuminori Okuzumi and Masanori Yoshikawa

Tokyo Institute of Technology, 2-12-1 O-okayama, Meguro-ku, Tokyo 152, Japan

Key words: CVD diamond, diamond cutting tool, thermochemical polishing

Abstract

A thick CVD diamond has been expected to the applications for cutting tools. But it is difficult to sharpen thick CVD diamond films by means of a conventional sharpening method using diamond grinding wheel for forming a large chipping of scores of micrometers at the cutting edge. Accordingly, we have made a thermochemical polishing apparatus capable of polishing a sharpening for cutting tool and thick CVD diamond films were processed by this apparatus. And then the cutting test by aluminum alloy was conducted and the cutting performance of thick CVD diamond films polished by thermochemical polishing method was evaluated

1. Introduction

Although the thick CVD diamond film is an appropriate material for cutting tool, when processing the cutting edge for the cutting tool, it is not easy to sharpen with a diamond wheel. That is, in cutting edge polishing by diamond wheel, a high load is applied to the tip edge, and in the case of thick CVD diamond film, a large chipping of scores of micrometers is formed at the cutting edge. Consequently, several other methods [1] [2] for polishing CVD diamond have been proposed and examined aiming at practical use. But all of these methods have their advantages and disadvantages, no particular method have proven quite satisfactory in cutting edge processing of CVD diamond. Hence a new cutting edge polishing has been keenly demanded. Accordingly, we have attempted to process the cutting edge of thick CVD diamond film by a new polishing method [3] making use of thermochemical reaction [4] capable of polishing efficiently at light load.

Further, the features of cutting edge sharpened by using this new apparatus and the cutting performance of this tip have been evaluated. We were able to study the practicality of this new method for applications involving precision cutting.

2. Experimental methods

Figure 1 shows a sketch of the thermochemical polishing apparatus. It is a glovebox with a table to fix a CVD diamond bite and a heater. The iron plate is fixed to the heater with screws, and it can be replaced quite easily. The table can be freely moved along the X and Y axes with respect to the iron plate, and can be inclined or rotated to left and right so that the workpiece's flanks can be processed.

To prepare a sample of a thick CVD diamond film, a CVD diamond film with 150 μm thickness was synthesized on a sintered diamond substrate with 5 mm square using the MW plasma CVD method. To improve polishing efficiency, the table surface and side of the CVD diamond were polished beforehand with #1500 vitrified diamond grinding wheel. The sample was then processed to have an angle of flank of 8° and nose radius of 0.4 mm using the same grinding wheel. This prepared sample was then installed in the thermochemical polishing apparatus. After oxygen in the glovebox was substituted with argon gas until the oxygen in the box decreases to less than 1000 ppm, the inside pressure is adjusted to be larger than the atmospheric pressure by 0.5 kPa by pouring hydrogen gas at 50 cc/min and argon gas at 1000 cc/min. And then the iron plate was heated to 800°C, the flank is polished at the sliding speed of 1 mm/sec for 2 hours.
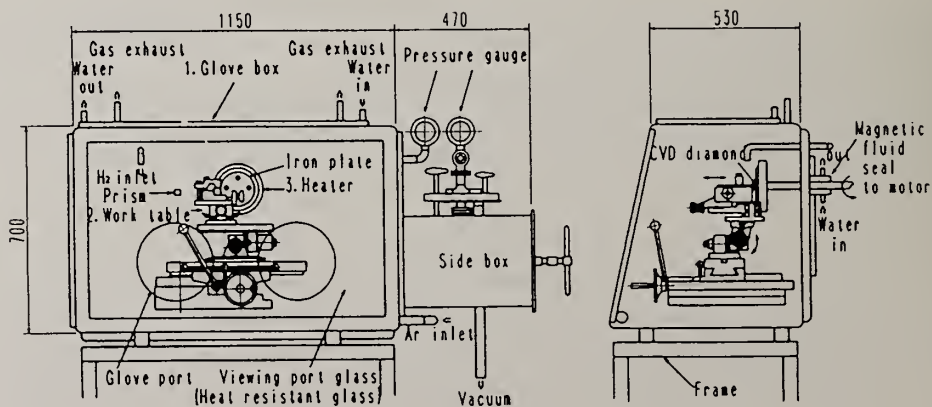
Fig. 1 A sketch of the practical thermochemical polishing apparatus

3. Experimental results and discussion

3-1 POLISHING RESULTS

Figure 2 shows SEM images of CVD diamond cutting tools at the edgetop where a face and a flank meet. In Fig. 2 (1), all over the edge was rough as a result of chipping while being processed by #1500 diamond grinding wheel. In the other, Fig. 2 (2), the edge polished by thermochemical polishing was a sharp and smooth surface. This is because the thermochemical polishing effectively removed projections caused by chipping.
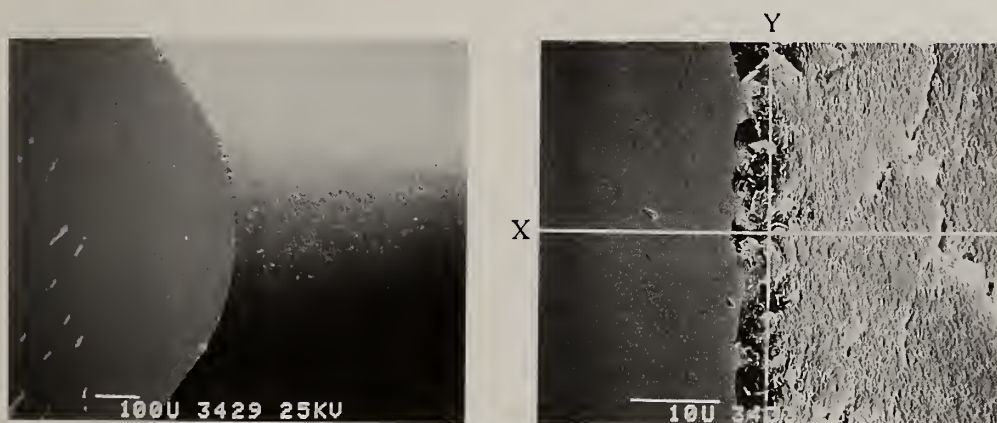
(1)Cutting edge sharpened by #1500 diamond wheel
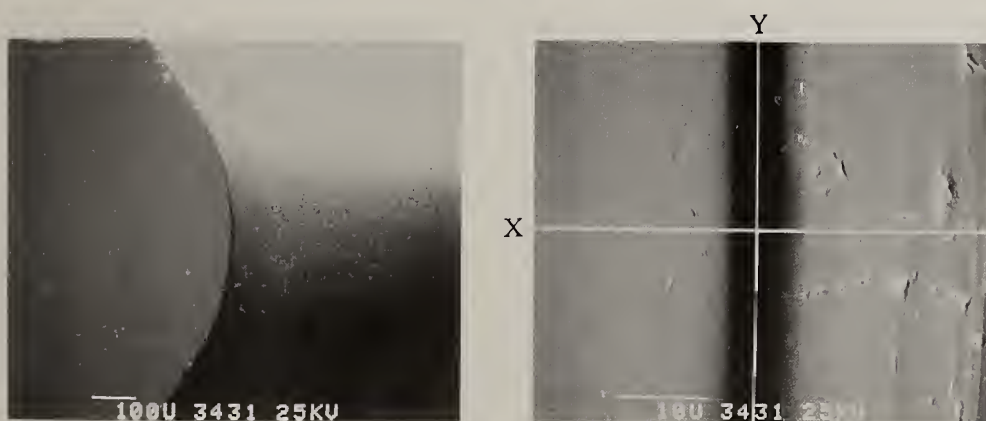
(2)Cutting edge polished by thermochemical polishing

Fig. 2 SEM images of the cutting edges sharpened by #1500 diamond wheel and polished by thermochemical polishing

204

Figure 3 shows the surface roughness of each edgetop observed by an Electron Probe Surface Shape Analyzer (EPSSA) in the X- and Y- direction given in Fig. 2. The #1500 diamond wheel processing produced a rake of 1.5 nm and a flank of 6.2 nm in surface roughness. The surface roughness of the edgetop was much larger, 20 nm in X-direction and 72 nm in Y-direction. This reveals that a #1500 diamond grinding wheel may finish the face of CVD diamond to sufficient smoothness.

X direction of cutting edge　　　　　　Y direction of cutting edge

(1)Cutting edge sharpened by #1500 diamond wheel

X direction of cutting edge　　　　　　Y direction of cutting edge

(2)Cutting edge polished by thermochemical polishing
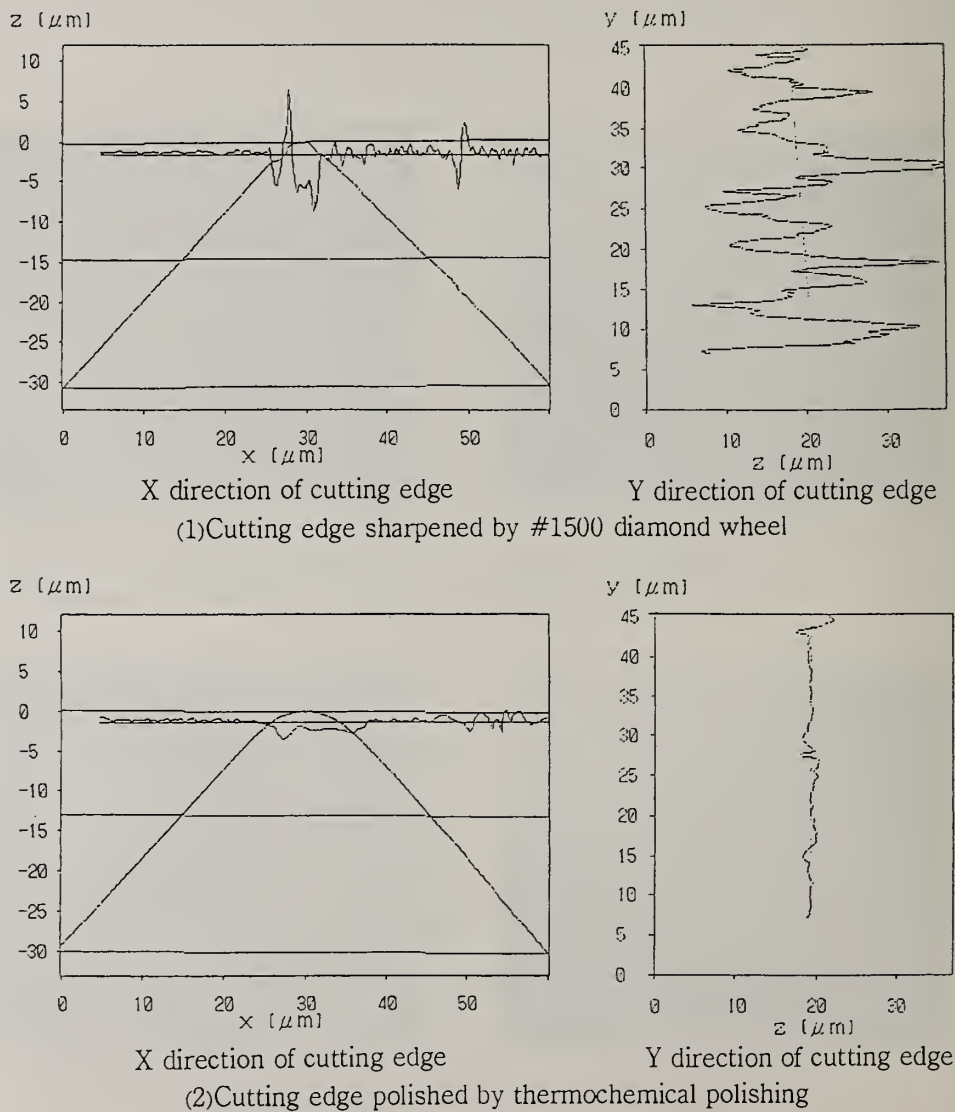
Fig. 3 Surface profiles of cutting edges sharpened by #1500 diamond wheel and polished by thermochemical polishing

However, this processing brought the edgetop at intersection of the two finished faces to larger roughness. The thermochemical polished CVD diamond tool was smooth everywhere on the face, edgetop and flank in X-direction, 1.3 to 1.7 nm in surface roughness. In Y-direction the roughness was as small as 6 nm on the face and flank and fairly smooth at the whole surface.

When processed with a #1500 diamond grinding wheel, the edgetop at intersection of the face and flank was comparatively sharp, but its cutting edge roundness was not measurable because of chipping. On the other hand, though the thermochemical polished edgetop was smooth without chipping, its cutting edge roundness was slightly round, about 10 μm in curvature. This indicates that the cutting edge was polished probably with the biting into an iron plate.

3-2 Evaluation of cutting performance
The cutting performance of sharpened CVD diamond tools was evaluated by cutting aluminum alloys. One turning test was to cut an Al-Mg alloy for use a magnetic disk substrate under the conditions, shown in Table 1. A single crystal diamond cutting tool polished by scaife to the same edge shape was examined for comparison. Figure 4 shows the change in surface roughness of the work with the cutting time. The three cutting tools showed no marked change for the first 100 minutes in surface roughness. In case of the cutting tool sharpened by #1500 diamond grinding wheel, the surface roughness was comparatively larger, Ra 1.18 μm. On the other hand, in case of the thermochemically polished CVD diamond cutting tool, the surface roughness was Ra 0.81 μm. It was close to the roughness by natural diamond, Ra 0.73 μm. It is proved that thermochemically polished CVD diamond cutting tool endures a long time use without wear and can be an acceptable substitute for single crystal diamond cutting tool.

Table I   The cutting conditions of aluminum alloy

Work Conditions	Al-4.5%Mg alloy (JISA5083)	Al-20%Si alloy (A390)
Edge shape	(0, 0, 8, 8, 45, 45, 0.4)	(0. 0, 8, 8, 45, 45, 0.4)
Cutting speed	380 m/min	400 m/min
Feed rate	10 μm/rev	0.12 mm/rev
Depth of cut	20 μm	0.1 mm
Cutting fluid	Dry	Dry
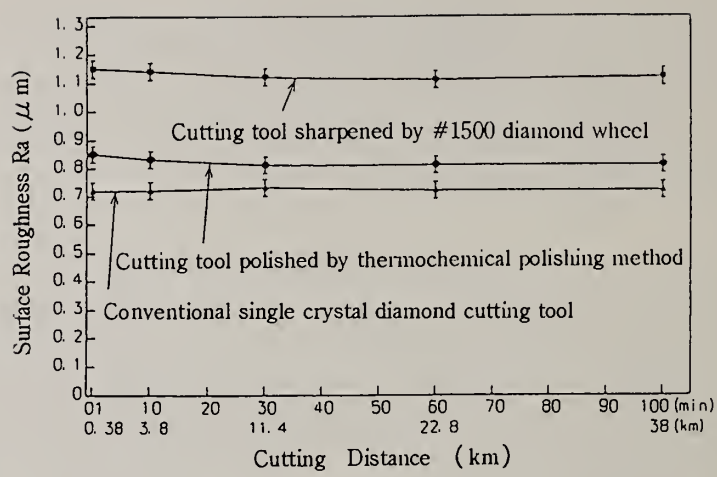
Fig. 4 Relation between surface roughness and cutting distance using CVD diamond tools and a single crystal diamond tool

Cutting tool sharpened by #1500 diamond wheel		Ra : 1.18 μm Rz : 4.40 μm Rmax : 4.77 μm
Cutting tool polished by thermochemical polishing method		Ra : 0.81 μm Rz : 3.25 μm Rmax : 3.64 μm
Single crystal diamond cutting tool		Ra : 0.73 μm Rz : 2.96 μm Rmax : 3.59 μm
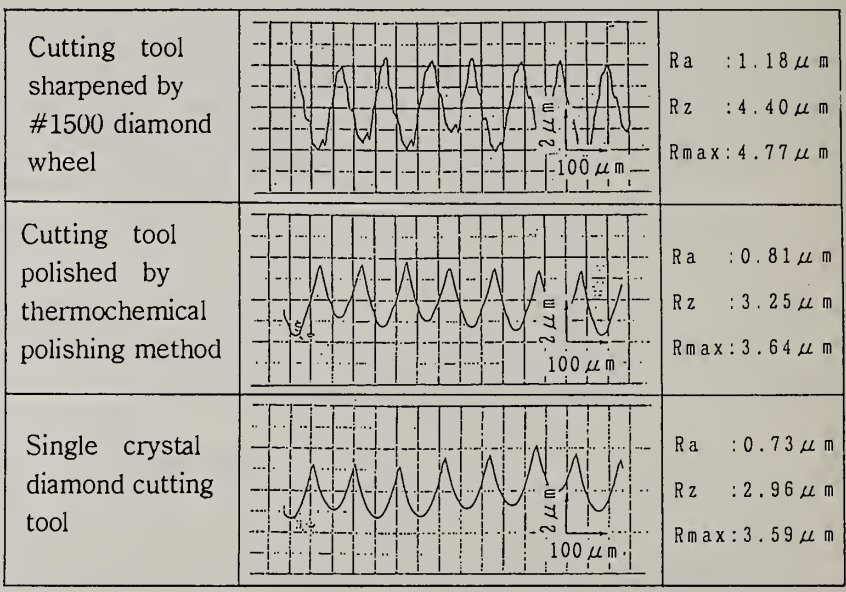
Fig. 5 Surface profiles and surface roughness of the workpieces after 100 min cutting

Figure 5 shows the surface profiles of the work, made by these three cutting tools after 100 minutes. These profiles prove to be transcripts of the each edge shape. The CVD diamond cutting tool sharpened by #1500 diamond grinding wheel produced an uneven surface with many narrow ridges and channels, indicating that the cutting edge was

uneven. This agrees well to the above-mentioned EPSSA observation of surface roughness. The thermochemically polished CVD diamond cutting tool produced as smooth a surface as the single crystal diamond cutting tool did , which means that both of them have a similarly good cutting ability. Therefore, ploy-crystalline CVD diamond may be an acceptable tip for a cutting tool when polished by thermochemical polishing.

Another turning test was to cut a high-silicon aluminum alloy under the conditions, shown in Table 1, for 40 minutes. Figure 6 and 7 show the flank wear width and surface roughness of the work in this turning test. The CVD diamond cutting tool sharpened by #1500 diamond grinding wheel began large chipping in one minute of cutting. The thermochemically polished CVD diamond cutting tool also formed very small chipping, but its flank was relatively smooth with an even distribution of scratches. This early difference in flank wear was likely to cause a difference in surface roughness of the work, Rmax 8.5 μm for the #1500 diamond grinding wheel and Rmax 5.5 μm for thermochemical polishing in one minute of cutting. Afterwards, flank wear progressed gradually, however, there was no significant change in flank wear width and surface roughness of the work up to 40 minutes.

Thus, as a good cutting tool, thermochemically polished CVD diamond has proved to have good abrasion resistance to very hard abrading alloys, such as high-silicon aluminum.
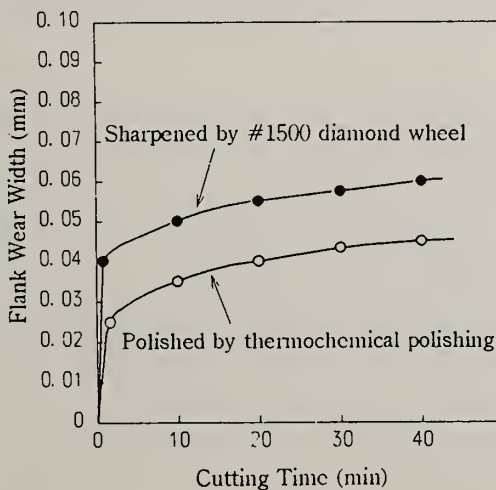
Fig. 6 Relation between cutting time and flank wear width

208
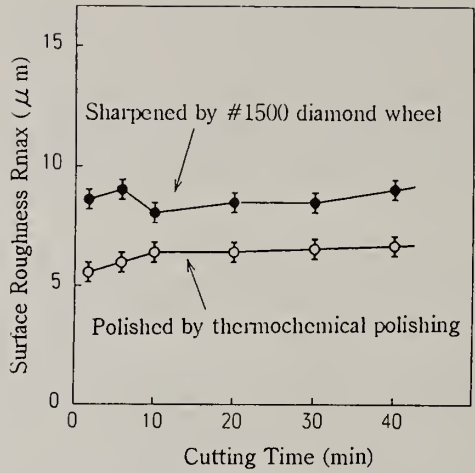
Fig. 7 Relation between cutting time and surface roughness

4. Summary

We produced experimentally a thermochemical polishing apparatus for CVD diamond as a cutting tool. Results obtained from the turning test of aluminum alloy with such cutting tools are as follows:

1) Thermochemical polishing   satisfactorily sharpened a CVD diamond cutting edge. Its edge was very smooth with Ra 1.4 nm.

2) A thermochemically polished CVD diamond cutting tool was able to cut aluminum alloy much smoother than a CVD diamond cutting tool sharpened by #1500 diamond grinding wheel.

Thermochemical polishing has proved to be effective in producing a CVD diamond tip for a precision cutting tool.

5. References

1. B. Bhushan et al., Diamond Films and Technology, 4 (1994) 71.
2. A. Hirata, H. Tokura and M. Yoshikawa, Thin Solid Films, 212 (1992) 43.
3. M. Yoshikawa, The Int. Soc. for Optical Engineering, 1325 (1990) 210.
4. H. Tokura, C. Yang and M. Yoshikawa, Thin Solid Films, 212 (1992) 49.

Applications of Diamond Films and Related Materials: Third International Conference, 1995
Editors: A. Feldman, Y. Tzeng, W. A. Yarbrough, M. Yoshikawa, and M. Murakawa

209

TECHNIQUES FOR DIAMOND THINNING AND POLISHING BY DIFFUSIONAL REACTIONS WITH METALS

S. Jin, W. Zhu, and T. E. Graebner

AT&T Bell Laboratories, Murray Hill, NJ 07974

Key words: thinning, polishing, diamond

Abstract

Control of diamond film geometry, such as thinning, patterning, shaping, and polishing processes, is essential for nearly all diamond film applications. Because of their extreme mechanical hardness, such processes are often costly and time consuming. In this paper, new efficient processing techniques for thinning and polishing of CVD diamond films using chemical reactions with molten rare earth metals will be described.

Introduction

The process of CVD diamond etching by molten rare earth metals is carried out either by multiple layer stacking of rare earth metal sheets and diamond films and heating to above the melting point of the metal or by dipping of the diamond films into a bath of molten rare earth metal. The molten-metal-etching removes both the rough growth facets on the top surface and the fine-grained bottom region of the film, the mechanism of which is believed to be the diffusional transfer of carbon atoms in diamond to the molten rare earth metal. Some orientation-dependent anisotropy in etching rate is seen. Etching kinetics as fast as 50 μm/min has been observed.

Results and Discussion

Etching of CVD diamond films by molten rare earth metals[1-4] can be accomplished either by multiple layer stacking of rare earth metal sheets and diamond films and heating to above the melting point of the metals or by dipping of the diamond films into a bath of molten rare earth metals. A schematic illustration of an exemplary, experimental diamond-etching assembly is given in Fig. 1. The Mo buffer layers are used to keep the aluminum oxide suport layers from chemical attack by the molten rare earth metal.

A substantial thinning of the film with a reduction in thickness of greater than 70 μm has been obtained by Ce-etching after only ~ 4h at 920°C. This thinning rate is more than 5 times faster than in the case of solid metal etching by Fe or Mn even with 2 to 3 orders of magnitude higher compressive stressed applied in the solid metal processing.[5,6] It has been observed that if the same level of low compressive stress (e.g. ~ 1 psi) is used for the solid metal etching, essentially no measurable thinning (<< 1 μm) is obtained.

High-speed diamond etching[7] with a rate as high as ~ 50 μm/min can be accomplished in an optimized molten rare earth processing, e.g., using low-cost mischmetal (which is a non-purified mixture of rare earth elements with Ce and La as major components). The rate of diamond etching in molten rare earth processing typically slows down with the time of etching as shown in Fig. 2, because of the gradual saturation of the molten rare earth with dissolved carbon.

It is generally desirable to lower the etch processing temperatures for the ease of processing. This is especially true for the thinning, etching, or patterning of future diamond-based semiconductor devices. Such devices will most likely contain some dopants, metallizations, and other components which may be adversely affected if the processing temperatures are much higher than ~ 500°C. Substantially lowered etch processing temperatures can be used if appropriate alloys of rare earth and transition metals are utilized.[4] For example, a Ce-22 at. % Ni eutectic alloy has a melting point of 477°C as compared to 798°C for pure Ce. A La-27 at. % Ni eutectic alloy (m.p. ~ 570°C), a Ce-19 at. % Ag eutectic (m.p. ~ 509°C), and other alloys of rare earth with Co, Cu, Au, Al, Zn, etc. also exhibit relatively low melting temperatures in the neighborhood of 400-500°C.

The molten-metal-etching removes both the rough growth facets on the top surface and the fine-grained bottom region of the film, the mechanism of which is believed to be the diffusional transfer of carbon atoms in diamond to the molten rare earth metals. The essentially complete removal of the rough growth facets by molten lanthanum and cerium processing (920°C/4h) is clearly illustrated in Fig. 3. Additional mechanical polishing may be added, if necessary, to obtain yet smoother surface finish.

Shaping of diamond into non-flat geometry has not been studied extensively because of the lack of convenient technique. The molten rare earth processing may be utilized for shaping CVD diamond films, e.g., for preparation of wires, needles, lenses, or other complicated geometry. Various masking techniques are employed to locally block or slow down the diamond film etching and obtain the desired geometry.

The molten metal etching can be locally adjusted or controlled if appropriate etch-blocking or etch-retarding mask materials (such Mo films) are deposited on the selected regions of the diamond surface. For example, the recessed valley regions of the as-grown, highly faceted CVD diamonds can be preferentially covered with the etch retarding mask materials so as to induce more etching in the unprotected, protruding facet regions, and achieve flatter surface by the molten rare earth etch process. Such a mask approach can also be utilized for diamond shaping if proper, thickness-gradient mask layers are employed.

References

1. S. Jin, J. E. Graebner, M. McCormack, T. H. Tiefel, A. Katz, and W. C. Dautremont-Smith, Nature *362*, 822 (1993).
2. S. Jin, L. H. Chen, J. E. Graebner, M. McCormack, and M. E. Reiss, Appl. Phys. Lett. *63*, 622 (1993).
3. W. Zhu and S. Jin (unpublished).
4. M. McCormack, S. Jin, J. E. Graebner, T. H. Tiefel and G. W. Kammlott, Diamond and Related Materials *3*, 254 (1994).
5. S. Jin, J. E. Graebner, G. W. Kammlott, T. H. Tiefel, S. G. Kosinski, L. H. Chen, and R. A. Fastnacht, Appl. Phys. Lett. *60*, 1948 (1992).
6. S. Jin, J. E. Graebner, T. H. Tiefel, G. W. Kammlott, and G. J. Zydzik, Diamond Films and Related Materials, *1*, 949 (1992).
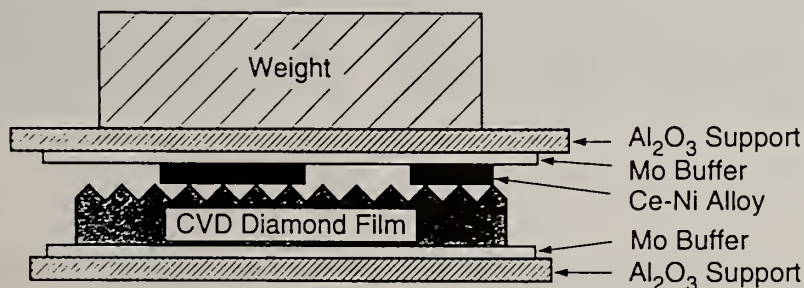
Fig. 1   Schematic illustration of the experimental diamond-etching assembly.
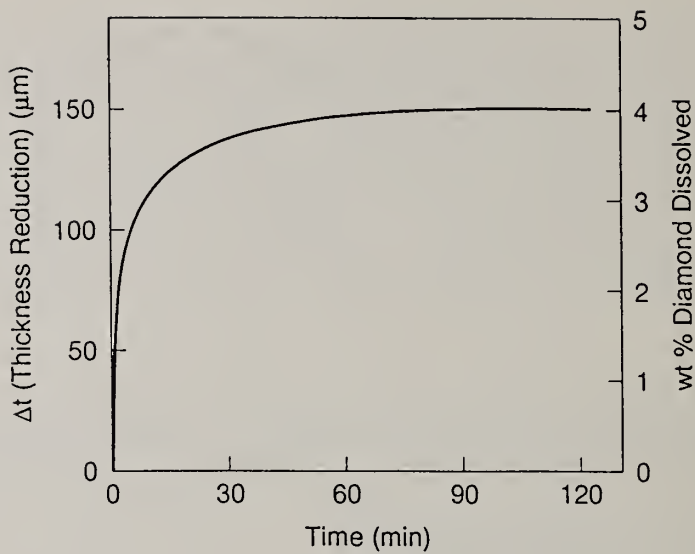
Fig. 2   The rate of thickness reduction in molten rare earth etching of CVD
diamond films.
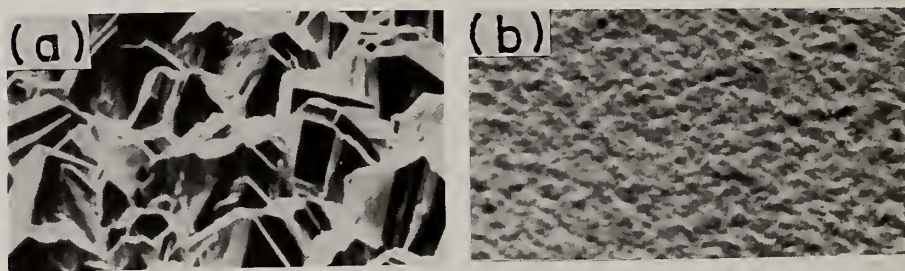
Fig. 3   Scanning electron micrographs (top view) of the CVD diamond films
before (a) and after (b) molten lanthanum etching.

MICROCUTTING CHARACTERISTICS ON THE SINGLE CRYSTAL DIAMOND TOOL WITH EDGE RADIUS USING MOLECULAR DYNAMICS

Jeong-Du Kim[1] and Chan-Hong Moon[2]

[1,2]Department of Mechanical Engineering, Korea Advanced Institute of Science and Technology, 373-1, Yusong, Taejon, 305-701, Korea

Key Words : Microcutting, Edge radius, Molecular Dynamics, Morse Potential

Abstract

Ultrprecision metal cutting(UPMC) technology which makes possible submicrometer form accuracy and nanometer roughness is devloped to reach the 1nm nominal(undeformd) thickness of cut. At this thickness level, a few of atom's layers should be considered. In this paper using the Molecuar Dynamics simulation, the phenomena of microcutting with a subnanometer chip thickness, the cutting mechanism for tool edge configuration to consider the sharp edge and round edge tool, the cut material and cutting speed are evaluated. Cutting mechanism of subnanometer depth of cut is evaluated.

1.Introduction

Recently the Ultraprecision Metal Cutting(UPMC) has been rapidly developed with the demand of optical, electrical and mechanical parts which reach the several micrometer or submicrometer at form accuracy and the several nanometer at surface roughness. Compared to technique development, the micromaching mechanism is not evaluated still and the uncountable phenomena is found, which are the effective negative rake angle for edge radius of tool at the micro depth of cut and the friction generation between flank face and the elastic recovery[1,2,3].

In this paper microcutting software is developed and the verification of cutting mechanism for the edge radius configuration, cutting characteristics at the ultra high cutting speed and the cutting phenomenon for aluminium and copper are investigated.

2. Molecular Dynamics

To apply the molecular dynamics, as the one of method to describe the

relation between atoms, the potential is suitable. Morse potential is experimental potential. Fig.1 shows the microcutting two dimensional model for the face-centered-cubic material and the force acting atom i is the resultant surrounding the atom. Because the acceleration of an atom is nonlinear due to the potential, the velocity and displacement is solved from numerical integration. Schofield algorithm can be possible to reduce integration time though large memory compared with Verlet algorithm. As the cut material copper(Cu) and aluminium(Al) are used and the single crystal diamond used as the tool. The diamond tool which has the three dimensional structure is considered rigid body with one third copper lattice size. The Cutting conditions are listed in Table I. To simulate microcutting with the limited atoms(several hundred or thousand) the boundary condition should be included and largely separated into displacement and thermal boundary condition. The boundary condition is fixed and thermal condition is the method of Woodcock.

3. Simulation and results

Fig.2 shows the cutting process for the sharp edge tool and the cutting can be observed. Fig.3 shows the magnified cutting around the edge of tool during cutting. It is seen that friction at the rake tool face causes the resistance for the upward chip flow to press the atoms under cutting line and can create the dislocation. The pressure at the flank face releases and atom's layers move upward, which seems to be namely the elastic recovery. It can be seen the damaged layer is very small for the sharp edge tool. Fig.4 is the cutting example for the round edge radius and the material can be cut like the sharp edge tool. In Fig.5, the extinct feature of the round edge tool cutting is that the shear area exists around the edge radius and beneath the cutting line. And in addition to shear the ploughing around tool round and rubbing beneath flank face can be shown. Fig.6 shows the cutting process of chip forming at the cutting speed $100m/s$ and $1000m/s$. The cutting mechanism at $100m/s$ is thicker chip than $1000m/s$ and the propagation of dislocation ahead of tool and the shear area is wider. Fig.7 and Fig.8 are cutting process for copper and aluminium with round edge tool at the $1000m/s$ cutting speed. For two cases all the dislocation is created at the front of tool for the shearing from pressure around edge round. Aluminium has propagation at the $[\bar{1}01]$ direction, for the lower yield strength than copper.(copper yield strength is 70Mpa and aluminium 35Mpa) For the copper the dislocation is created and propagated to $[0\bar{1}1]$ direction, this is due to the new shearing of atoms moving to next layer beneath flank face. The elastic-plastic recovery of aluminium is larger than copper. Fig.9 and Fig.10 are the cutting processes for copper and aluminium with sharp edge tool. The difference of sharp edge from round is that there is not the ploughing due to round edge, so that small elastic-plastic recovery and damaged layers. This shows that the surface is good for the sharper edge tool

4. Conclusions

(1)The cutting for edge radius tool is compared of shearing, ploughing around edge radius and rubbing under the flank face.

(2)With faster cutting speed the chip is thicker, shear area is narrower and the magnitude of thrust force becomes small.

(3)For the sharp edge tool the damaged layer becomes small than round edge.

References

[1]J.D. Kim and D.S Kim, "The study on the microcutting characteristics at the ultraprecision cutting", Fall conference of KSME,pp706-711,1993.

[2]N.Ikawa,S.Shimada,H.Tanaka,G.Ohmori, "An atomistic analysis of nanometric chip removal as affected by tool-work interaction in diamond turning",Annals of CIRP,Vol.40,Jan.,pp551-554.,1991

[3] T.Inamura,H.suzuki,N.Takezawa,"Cutting experiments in a computer using atomic models of a copper crystal and a diamond tool", JSPE, Vol.25, No.4, Dec.,pp259-266,1991.

Table I Cutting condition for a material and tool

	Workpiece	Tool
Material	Copper,Aluminium	Diamond
Lattice size(nm),a	0.361(Cu), 0.403(Al)	0.1203
No. of atoms	1000, 2300	78, 219
Cutting speed(m/sec)	100, 1000	
Reference position of tool(nm)	0.6	
Time step(fsec)	1.0	
Cut off length(Å)	7.5	3.0

Fig.1 Interaction Force Model between atoms

cutting speed : 100m/sec
cutting depth : 1nm
Fig.2 Cutting Process for a sharp edge tool

Fig.3 Mechanism around sharp edge tool

216

cutting speed : 100m/sec,
depth of cut : 1nm
Fig.4 Cutting Process
for a round edge tool
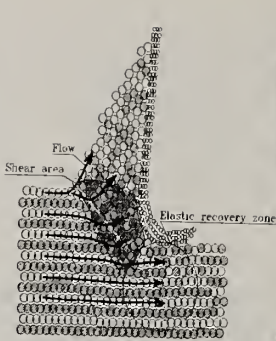
Fig.5 Mechanism around

round edge tool
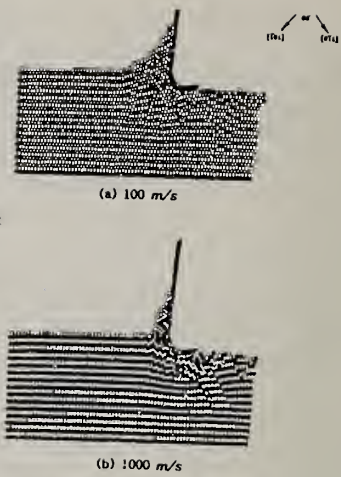
Fig.6 Chip formation for different cutting speed
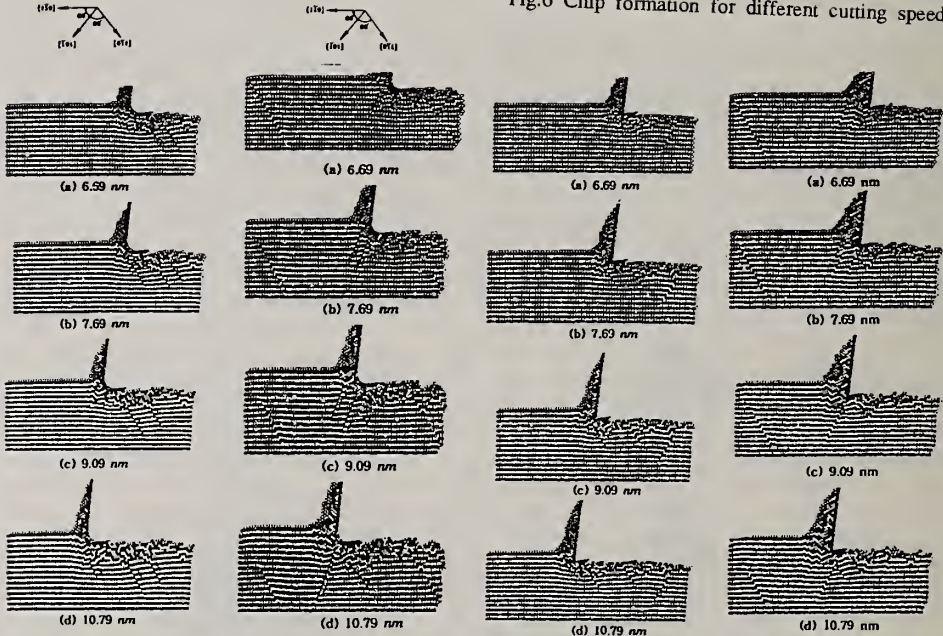
cutting speed : 100m/sec,
depth of cut : 1nm
Fig.7 Copper cutting
with a round edge tool

cutting speed : 100m/sec,
depth of cut : 1nm
Fig.8 Aluminium cutting
with a round edge tool

cutting speed : 100m/sec,
depth of cut : 1nm
Fig.9 Copper cutting
with a sharp edge tool

cutting speed : 100m/sec,
depth of cut : 1nm
Fig.10 Aluminium cutting
with a sharp edge tool

217

"PCD-TIPPED CUTTING TOOL SYSTEMS FOR BEST-IN-CLASS MANUFACTURING"

Dr. Bert P. Erdel

MAPAL, Inc.
81 Sutton Lane
Piscataway, New Jersey 08854

Key words: Aluminum, Best-in-Class Manufacturing, Hardness, Precise
            Machining, Polycrystalline Diamond

Abstract

To meet the stringent demands on today's manufacturing, cutting tool systems had
to be developed with innovative design features built-in. In nearly all applications
involving non-ferrous metals, these cutting tools are diamond tipped. They
dramatically outperform any other "conventional" or substitute cutting material.
They can be run up to 50% faster than carbide grades and simultaneously even
extend tool life up to 10-fold while improved workpiece quality, increased
productivity and reduced production costs are just a bonus.

1. Introduction

The consumers' erratic, unpredictable change in product taste and their unrelenting
demand for product quality, has manufacturing scrambling for fast and high-
precision machining systems and processes.

PCD-cutting tools are making a considerable contribution on the production floor
through increasing quality and faster machining and doing so by lowering cost per
part. To understand the design of such tooling systems is, first, to understand the
PCD's physical and chemical characteristics.

The ultrahard tool material PCD (polycrystalline diamond) is an extremely tough, inter-grown mass of randomly orientated diamond crystals, produced at very high pressures and temperatures, using carefully selected synthetic diamond particles. During the sintering process, the PCD layer is integrally bonded to a tungsten carbide substrate. The resulting composite material is characterized by a combination of the hardness, abrasion resistance and thermal conductivity of diamond and the toughness of tungsten carbide.

PCD is available in three standard grades, based on the average diamond grain size of the starting material. In general, a finer grain size provides a better edge quality, while a coarser grade offers greater wear resistance.

The application area is defined by the thermochemical resistance of PCD and is, therefore, limited to workpiece materials with a chip-forming temperature below 700^0 C. Furthermore, the workpiece material should have no affinity to carbon, so as to avoid diffusion wear on the cutting edge at elevated temperatures. Suitable materials include non-ferrous metals, such as aluminum, copper and their alloys and non-metallic materials such as glass- and fiber-reinforced plastics, ceramic, wood and composites.
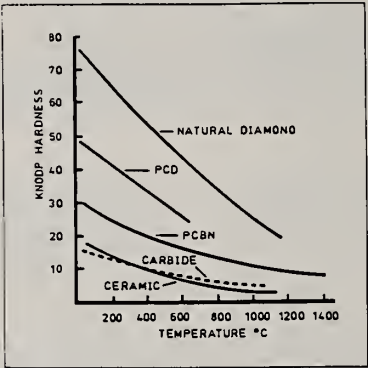
Source· GE Superabrasives

Source: De Beers Industrial Diamond LTD.

Fig. 1 Hardness of Comparative
         Cutting Materials

Fig. 2 Flank Wear

PCD-tooling is very popular in the manufacturing of light metals, especially aluminum, even abrasive high-silicon content aluminum (12% - 20% Si) can be machined with excellent surface finishes and long tool life at high speeds. Polycrystalline diamonds offer great possibilities in finish-machining parts of selected materials and all kinds of configurations. However, their use calls for a

rigid precision setup of machine tool part fixturing, tool clamping and above all well designed and engineered cutting tools.

The ongoing trend toward more use of light-weight workpiece materials and the desire to machine at ever higher speeds, virtually invites the use of PCD-tipped tooling.

* Finish-machining: Typically the last operation to give the workpiece its final geometry and appearance.
* One-pass machining: Designated as one operation from the cast piece to the final configuration.
* Precision-machining: Usually done with blueprint tolerances of a few μm.
* Combination tooling which machine several workpiece configurations at once, such as boring, facing, chamfering.

Diamond cutters come in different shapes, forms, dimensions and geometries, depending on the machining operation (boring, turning, milling, etc.), the workpiece material and the given machining parameters. They are either a brazed-in integral part of the tool body or the cutter constitutes an insert (usually indexable with two identical cutting edges.
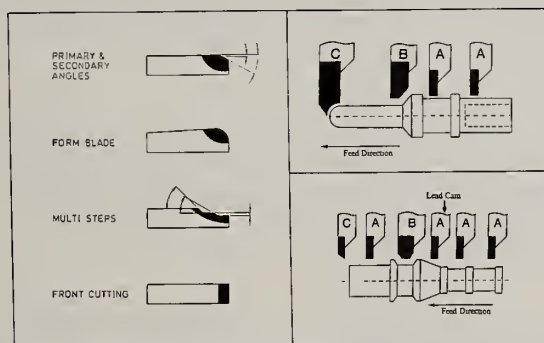
Fig. 3 PCD Cutter Variety

2. Applications

Workpieces featuring sequentially arranged bores with substantial air gaps in-between used to be machined through lineboring, with bushing carriers, or by machining from both sides of the part. Either method is uneconomical and inaccurate. Machining from one side without bushing support in-between or

opposed spindles or table indexing, yields excellent machining results in the most productive way. The tool is guided in the bore through guide pads.
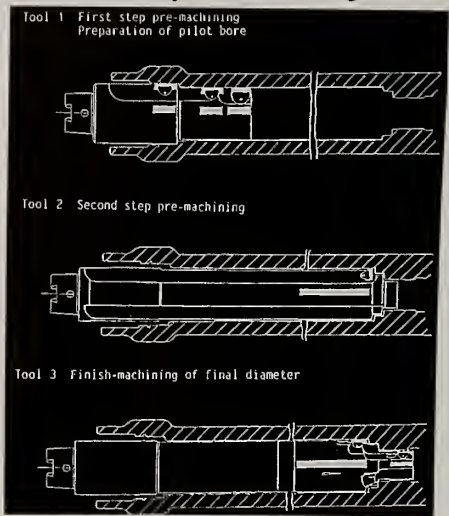
Fig. 4 Steering Housing

High-precision cutting tools designed with peripherally arranged guide pads need clean chemically well-defined coolant to lubricate their frictional contact with the workpiece. Polycrystalline guide pads need less lubrication and allow less well-maintained coolants, thus substantially lowering the cost for cutting fluids. They are an ideal part of the ever more important aspect of "minimum volume" coolant supply.

The machining data of a solid PCD-Endmill are quite impressive and speak for themselves. Possible only because of the meticulously ground PCD cutting edge with a rather unique contour.
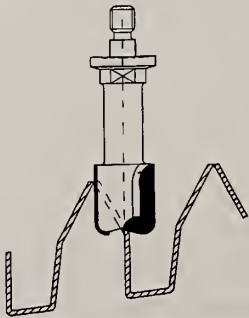
Tool	
Tool Type	PCD End Mill
Drawing #	3 19311-01
Configuration	Cutting Edges = 2, Without Axial Inclination
Dimensions	Diameter = 1 inch
	Length = 1 180 inch
Application	
Workpiece	Automotive Grill
Material	GFK (composite), 35% fiber
Number of Workpieces	600
Specifications	No burrs
Parameters	
Machine	MAKA Machining Center
Spindle Speed	45,000 min⁻¹
Surface Feet	11,780 ft/min
Feed Rate	78 inch/min
Feed per Revolution	0.002 inch/rev
Feed per Cutting Edge	0.001 inch/rev
Coolant	Dry

Fig. 5 Automotive Grill

Polycrystalline diamond tooling, the cutting edge of which are ground with highest precision, can substitute for existing processes. Case in point, an ID/OD-fineboring tool finish-machines the outer and inner diameter of a spool bore in just one pass (operation). This part used to be finished through turning and grinding on two different machines, with two different machining operations. Besides the obvious savings in machine tools, tooling and machining time, this combination PCD-tool guarantees consistent concentricity of outer and inner diameters.
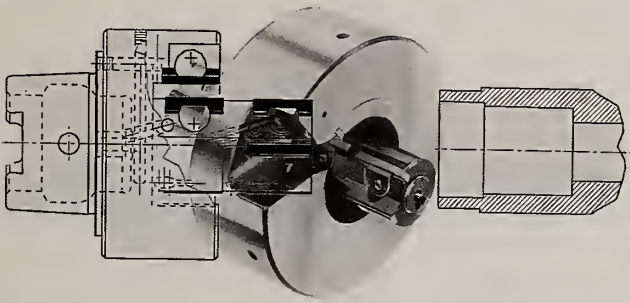
Fig. 6 OD/ID-Machining

3. Summary and Outlook

The importance and acceptance of polycrystalline diamond cutting tools and systems is evident on any modern production floor:

- Nonferrous, lightweight materials, to which diamonds have molecular affinity and no chemical reaction, are gaining in usage at the expense of traditional cast iron and steel materials.
- "Roughing" (e.g. drilling) and "secondary" operations (e.g. honing, roller burnishing), out of cost considerations, have to be kept to a minimum or eliminated entirely.
- The desire for "high-speed machining" to meet shorter cycle times, make even better use of the PCD characteristics. Near-net shape castings allow "one-pass machining" through "combination" tooling.
- Customized tooling design accommodates reliable and efficient use of PCD.
- The price/performance ratio of PCD-tipped tools is very favorable.

Clearly, polycrystalline diamonds have dramatically changed chipmaking machining. While machining parameters, systems and processes undergo perpetual changes, the manufacturing floor will utilize PCD's favorable properties to an even greater extent in years to come.
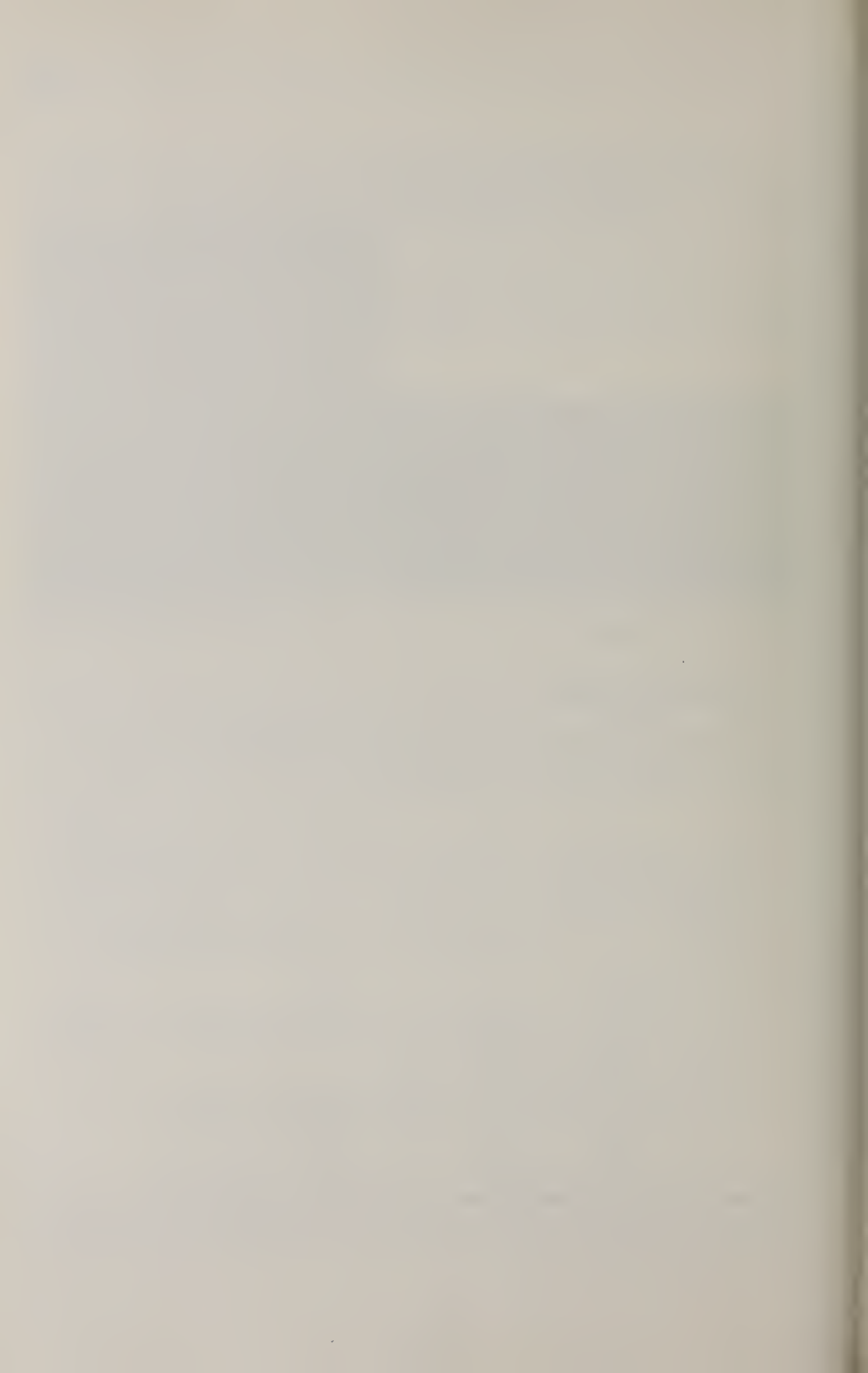
DIAMOND PROCESSING

PROCESSING OF CVD DIAMOND WITH UV AND GREEN LASERS

V.G. Ralchenko, S.M. Pimenov, T.V. Kononenko, K.G. Korotoushenko, A.A. Smolin, E.D. Obraztsova and V.I. Konov

General Physics Institute, ul. Vavilova 38, 117942 Moscow, RUSSIA

Key words: laser processing, polishing, etching, oxidation, cutting tool

Abstract

A review of recent results obtained in GPI on applications of different types of lasers for treatment of CVD diamond is presented. The list of lasers used includes ArF (193 nm wavelength) and KrF (248 nm) excimer lasers, Cu-vapor laser (510 nm), and Ar^+ ion laser (457-514 nm). Fast laser polishing of rough surfaces of as-grown diamond films is described, in particular the finishing of coatings of complex shape (cutting tools). Fine patterning of diamond by laser ablation using an optical projection and direct writing techniques has been developed. The engraving the fine-grained diamond films via localized carbon burning in oxygen using a sharply focused continuous wave Ar^+ laser is demonstrated. Also described are experiments on Ar^+ laser irradiation of seeded substrates to perform selective-area diamond deposition.

2. Introduction

Processing of diamond films often makes a major contribution to the cost of diamond-based devices, that's why new approaches are required in order to increase the processing quality and productivity. The post-growth treatment of diamond films (polishing, patterning, cutting) is not a simple problem because of extreme hardness and chemical inertness of diamond. In particular, polishing of diamond films by a conventional mechanical technique or by ion beams provides relatively low etch rates, although the final surface finish may be high. In this respect the use of lasers for processing of CVD diamond is of great interest. The laser etching of a material is based on rapid heating of the workpiece by a short pulse of photons, which being absorbed in a thin surface layer, cause a local vaporization. The lasers have already demonstrated their high efficiency in surface modification of diamond materials [1-10]. In the present paper we report on the use of several lasers operated in UV and green spectral range for patterning, shaping and smoothing of diamond films.

2. Experimental

The technical parameters of four different lasers used are listed in Table I. These lasers generate short pulses, except of continuous wave Ar^+ laser.

Table I. Laser parameters: wavelength, λ; pulse duration τ; pulse energy E, and maximum pulse repetition rate f.

Laser	λ, nm	τ, ns	E, mJ	f, Hz
ArF	193	20	200	200
KrF	248	15	200	50
Cu	510	20	0.25	10^4
Ar+	514	∞	2 W	--
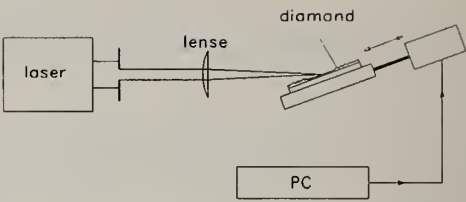
Fig. 1. Optical scheme for laser polishing.

The laser beam was focused at the diamond film surface by a spherical optics for pattern delineation, or by cylindrical optics in case of polishing (Fig. 1). The samples were placed on a computer controlled X-Y table to provide the beam scanning, if necessary, with a step of 1 μm after the action of each successive pulse (or a set of pulses).

3. Results

3.1. Excimer lasers
Due to high optical absorption the ultraviolet excimer lasers are suitable for diamond ablation. In addition, short wavelength light allows to obtain better spatial resolution of the pattern produced. As the diamond absorption edge is at 227 nm, the radiation of only ArF laser (193 nm wavelength) can be effectively absorbed directly in *pure* diamond. However, various defects and amorphous (graphite) inclusions in CVD diamond provide an initial optical absorption at longer wavelengths too. This may cause the formation of an opaque graphitized surface layer under action of a few first laser pulses, the next pulses being absorbed automatically by that self-sustained modified layer.
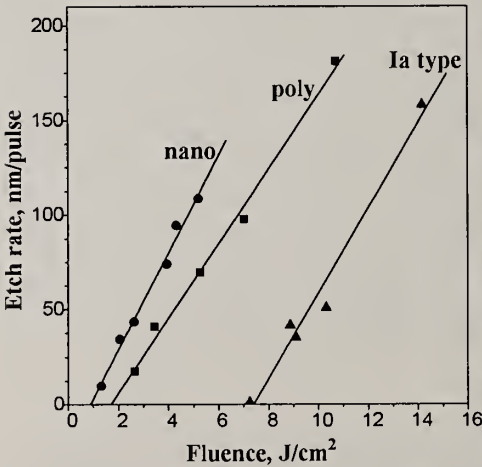
Fig. 2. Etch rate versus fluence of KrF laser for nanocrystalline, polycrystalline and type Ia natural diamond.
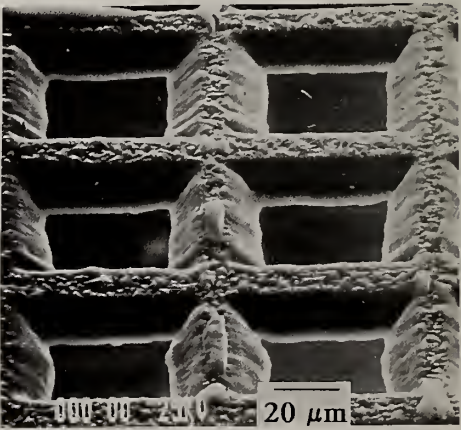
Fig. 3. KrF laser-drilled holes in 20 μm thick free-standing diamond film using a mask projection technique.

The optical absorption and thermal conductivity of the film are important factors, which determine the etch rate, while the hardness of the treated material is not significant parameter. Fig. 2 shows how the etch rate depends on KrF excimer laser fluence (energy density in single pulse) for three diamond materials of different quality. The etch threshold is low (E_{th}=1 J/cm^2) for nanocrystalline films, high (E_{th}=7 J/cm^2) for natural Ia type diamond crystal, and intermediate (E_{th}=2 J/cm^2) one for a polycrystalline diamond film grown in a DC arc plasma. Etch rate increases linearly with fluence, and can easily reach values of ≈100 nm/pulse. The less perfect diamond films the lower laser energies are required to provide the effective ablation. As the excimer lasers usually operate at frequencies of 50-100 Hz, it takes only several seconds to drill a hole or make a deep pattern in diamond film of tens microns thickness. As an example, Fig. 3 shows KrF laser-etched rectangular microholes in a 20 μm thick free-standing diamond film. The film was irradiated through a metal grid with a period of 0.5 mm using the optical projection scheme with X6 demagnification [6].
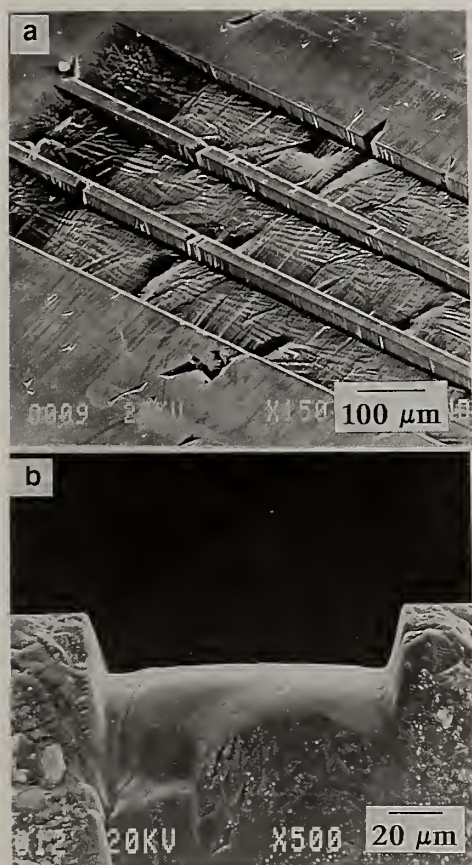
Fig. 4. SEM pictures of grooves etched in polished diamond film by scanning beam of ArF excimer laser: (a) general view, (b) cross-section.
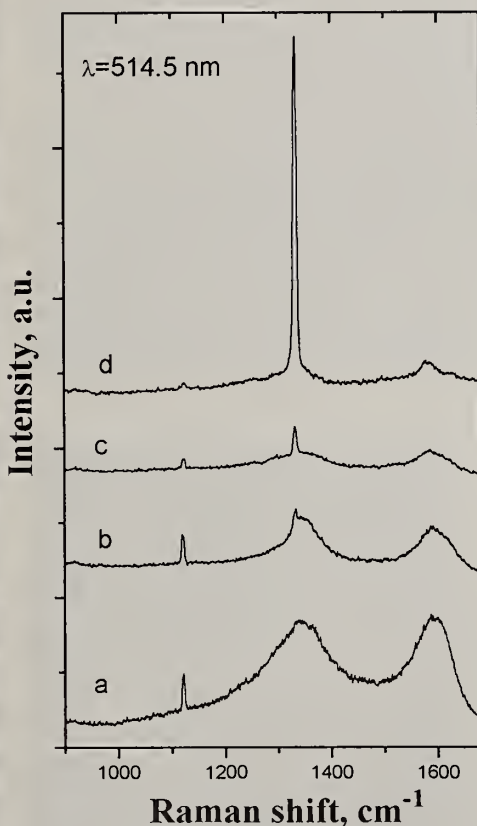
Fig. 5. Raman spectra of diamond film after ArF laser etching (a), after laser cleaning (b), after etching in acid for 1.5 hour (c), and for 3 hours (d).

Fig. 4 shows a series of adjacent 22 μm deep grooves etched with ArF laser on polished side of a diamond film. The sample mounted at a computer-controlled X-Y table was translated by steps of 1 μm, and the laser shot was sent to the surface at every step to illuminate 110 μm x 110 μm area at fluence E=18 J/cm^2. The grooves have nearly vertical side-walls. Surface roughness at the groove bottom was R$_a$=0.1-0.5 μm increasing with diamond grain size.

Usually the etched surface is heavily graphitized as revealed by Raman spectroscopy. However, this graphitic layer can be partially removed by laser cleaning at a reduced fluence, by treatment in hot $H_2SO_4/K_2Cr_2O_7$ acid mixture (see Fig. 5), or nearly completely eliminated by annealing in oxygen at temperature 400°C [7].

Fig. 6 illustrates a little bit more complex structure with triangle teeth cut in diamond by ArF laser in a way similar to that used in fabrication of the trenches in Fig. 4. However, this time the beam scanning was organized in a different manner. First, a single V-shaped groove was produced by moving the rectangular laser spot through distance L=40 μm, equal to the spot width. Then, the sample was translated for the distance L, and irradiation started again to create the new tooth.

Due to high rates of material removal via ablative etching a laser polishing technique is known to be the most fast method for reducing surface roughness of diamond films. The diamond smoothing under excimer laser irradiation has been observed in the pioneer work carried out in General Physics Institute in 1987 [2]. It has been noted that the surface roughness at the laser-ablated area was significantly reduced, the sharp points on surface relief being ablated with higher rate than the valleys. Qualitatively the overheating of a crystal tip can be explained by a vapor screen effect or different heat spread rates from tips and valleys at surface relief. In more detail the laser smoothing effect has been considered in [6-8].
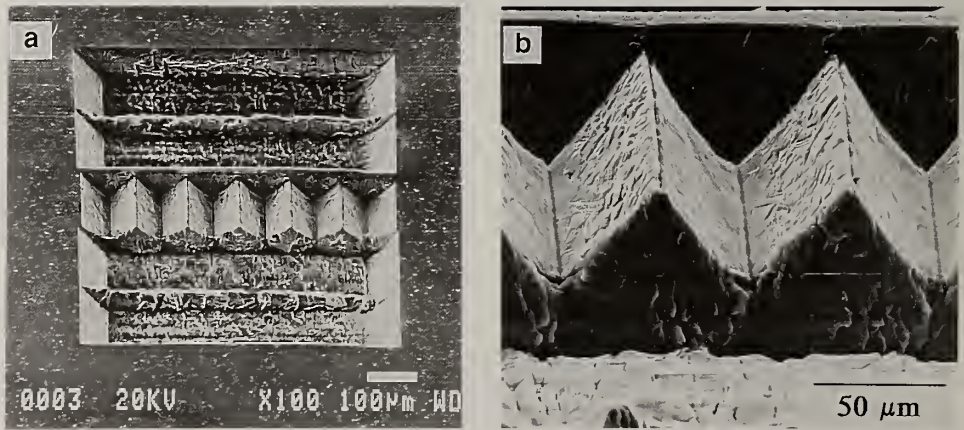
Fig. 6. Triangle teeth-like structure produced in polished diamond film by direct writing technique with ArF laser: (a) general view, (b) at higher magnification.
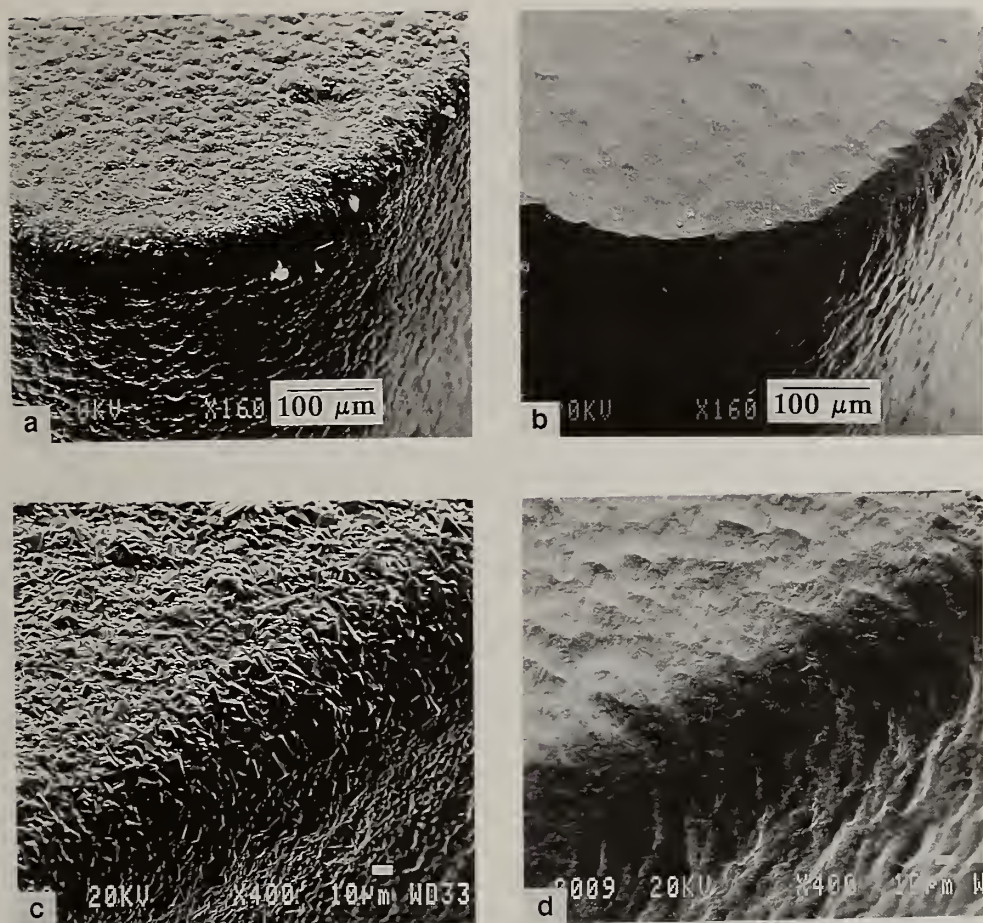
Fig.6a. Diamond coating on WC-Co cutting insert: as-grown (a), after KrF laser polishing (b). The cutting edge taken at higher magnification is shown for as-grown (c) and laser smoothed coatings (d).

The final roughness $R_a \approx 0.1$ μm can be achieved with a grazing laser beam [7]. The polishing procedure is very fast, for instance, an area of 1 cm^2 could be smoothed (ablated by the depth of 10 μm) in less than 10 minutes. The unique feature of laser polishing is the ability to treat curved surfaces of any complex form, (for instance, the cutting edges of CVD diamond tools), which is difficult or inaccessible for other methods. The mechanical or thermochemical polishing of one cutting insert may take hours [11], while the laser polishing can be performed in a few minutes. Fig.6a shows an example of a diamond-coated WC-Co cutting tool smoothed with a KrF laser. It's important that only a small area around the tip nose which actually participates in cutting process can be selectively polished, leaving the rest tool surface as it is.

3.2. Cu-vapor laser

Copper vapor laser has much smaller beam divergency compared to excimer lasers, therefore its beam can be focussed very sharply at the workpiece surface to enhance the incident intensity. In our case the beam spot diameter was about 5 μm, and at pulse energy of 0.25 mJ the fluence reaches values of about 1000 J/cm^2. The high fluence coupled with very high repetition rate (10 kHz) allows to remove up to 200 μm thick diamond layer through one scan of the beam. Fig. 7 shows a 0.8x0.8 mm^2 pit of 200 μm in depth with vertical side-walls etched in 0.4 mm thick diamond film with Cu-vapor laser at scanning velocity 4 mm/s. After one scan over 0.8 mm length the beam was shifted by 2 μm from the previous trace to make new adjacent trace, thus increasing the area treated. It took about 7 min to produce the whole pit. A narrow trench along the left side of pit in Fig. 7 is a trace after single scan. The trench width of about 10 microns promises a possibility to drill deep holes with aspect ratio of 10-20.

This technique allows the precise figured cutting, and could be applied to heat sink applications. For instance, a high power electronic devices can be arranged inside a pit to provide three-dimensional heat spread. The pit of any form can be cut with high accuracy to fit the size and shape of the device.

The surface relief of as-grown film was greatly smoothed with a scanning beam (Fig. 8). The final roughness was further reduced either by multiple beam scanning at normal incidence or by irradiation at grazing angles. In particular, the initial surface roughness of 40-50 μm has been reduced to R_z=1 μm (peak-to-valley amplitude) in direction along the laser scan, and to R_z=3 μm across the scan direction.
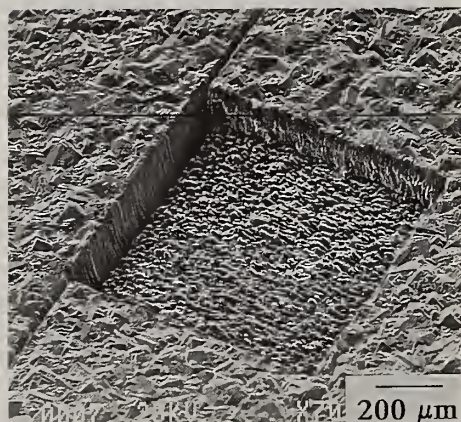
Fig. 7. Square pit 200 μm in depth in diamond film etched with finely focused Cu-vapor laser in scanning mode.
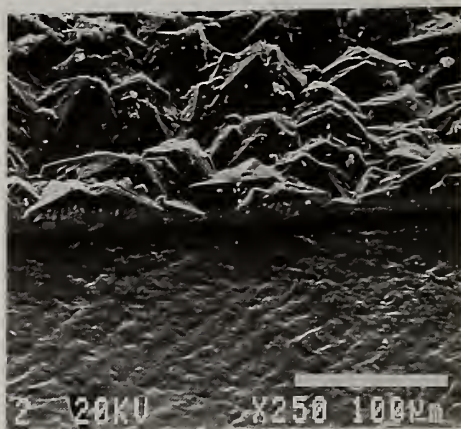
Fig. 8. SEM picture of well-faceted diamond film smoothing with Cu-vapor laser.

3.3. Ar+ ion laser

The nature of ambient gas atmosphere does not influence significantly the etch rate when pulsed lasers are used [2]. However, the laser-induced diamond oxidation can be dominant etching mechanism upon a continuous wave irradiation [10]. Our previous experiments on diamond-like carbon films processing with a c.w. Ar^+ laser have shown, that the fast carbon oxidation localized within the laser spot, can provide the DLC etch rates up to 100 μm/s [5]. We employ a similar approach in attempts to etch nanocrystalline diamond films.

The beam of Ar^+ ion laser was focussed into ≈ 2 μm spot, and scanned over diamond film surface to activate the burning of selected areas. Accurate 10 μm wide grooves have been etched when irradiation was performed in air (Fig. 9a), while no etching has been observed in argon gas. The etch rate of fine-grained diamond, which was assumed to have a low thermal conductivity and relatively enhanced optical absorption, was up to 50 μm/s in spite of the laser power was as low as 1-2 W. Various holes of 1-4 μm in diameter have been also fabricated as shown in Fig. 9b. The direct writing technique is very flexible, the dimensions of grooves can be precisely controlled by laser power, beam scan velocity and by the number of beam passes along the trace.
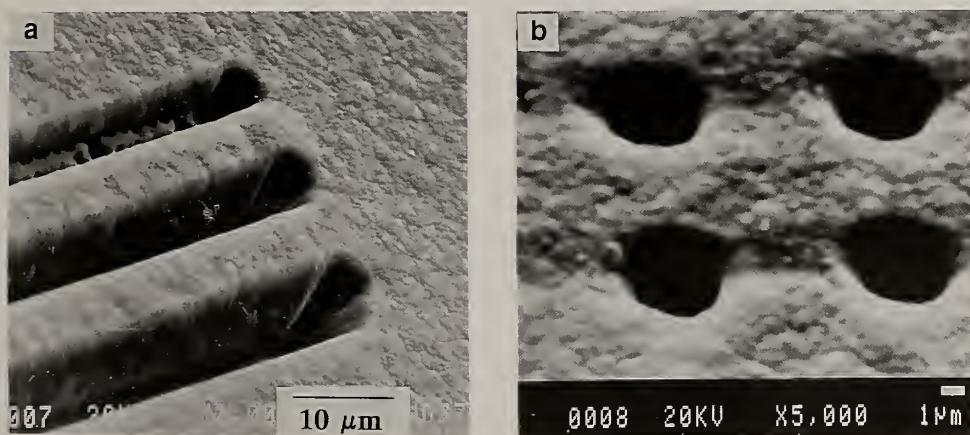
Fig. 9. Channels of 10 μm width (a) and holes of 4 μm diameter (b) burnt off in fine-grained diamond film by oxidation reaction under Ar^+ ion laser irradiation in ambient atmosphere.

An alternative method of diamond pattering is a laser-assisted selective-area deposition (SAD) [4,9,10]. The Ar^+ laser effectively annihilates diamond seeds planted at the substrate, so that the successive diamond growth occurs only at unirradiated area. Fig. 10 illustrates the SAD effect for a 3 μm thick diamond film grown in a DC arc plasma at Si substrate. Some nucleation suppression occurs at low laser power (P=1.0 W). The clear pattern is obtained at higher power (P=1.2 W), the pattern resolution being about 1 μm in this case.
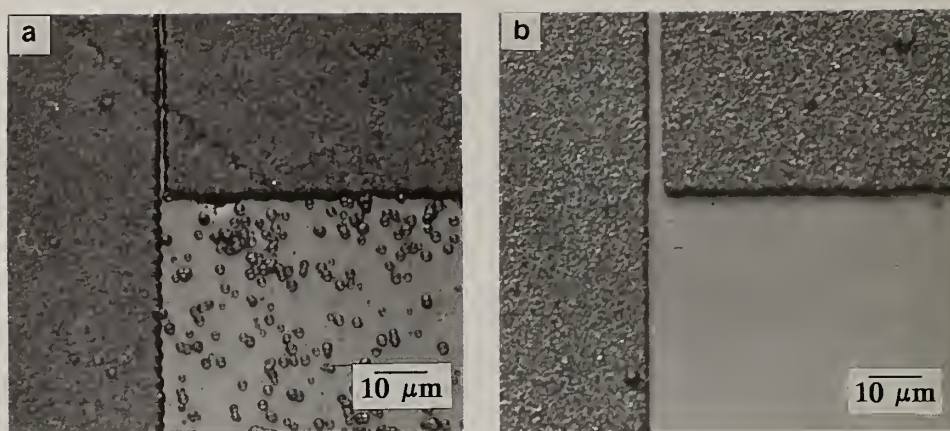
Fig. 10. Selective-area diamond deposition on Si substrate pre-treated with Ar$^+$ ion laser irradiation at low (a) and high (b) laser power. Laser beam size is ≈ 2 μm.

4. Acknowledgements

5. References

1. M. Rothschild, C. Arnone, and D.J. Ehrlich, *J. Vac. Sci. Technol.* B4 (1986) 310.

2. V.P. Ageev, L.L. Bouilov, V.I. Konov, A.V. Kuzmichev, S.M. Pimenov, A.M. Prokhorov, V.G. Ralchenko, B.V. Spitsyn, and N.I. Chapliev: *Soviet Physics-Doklady*, 33 (1988) 840.

3. M. Yoshikawa, in *Diamond Optics III*, SPIE Proc., 1325 (1990) 210.

4. N.I. Chapliev, V.I. Konov, S.M. Pimenov, A.M. Prokhorov, and A.A. Smolin, in *Applications of Diamond Films and Related Materials*, (Elsevier, Amsterdam, 1991) p. 417.

5. V.Yu. Armeev, N.I. Chapliev, E.N. Lubnin, V.I. Mikhailov, V.G. Ralchenko and V.E. Strelnitsky: *Surface Coat. Technol.*, 47 (1991) 279.

6. V.I. Konov, V.G. Ralchenko, S.M. Pimenov, A.A. Smolin and T.V. Kononenko, in *Proc. SPIE*, 2045 (1993) 184.

7. S.M. Pimenov, A.A. Smolin, V.G. Ralchenko, V.I. Konov, S.V. Likhanski, I.A. Veselovski, G.A. Sokolina, S.V. Bantsekov and B.V. Spitsyn, *Diamond and Related Mater.*, 2 (1993) 291.

8. S.M. Pimenov, A.A. Smolin, V.G. Ralchenko and V.I. Konov, *Diamond Films and Technol.*, 2 (1993) 201.

9. V.G. Ralchenko, A.A. Smolin, K.G. Korotoushenko, M.S. Nunuparov, S.M. Pimenov and B.K. Vodolaga, in *Proc. 2nd Int. Conf. on the Applications of Diamond Films and Related Materials*, ed. by M. Yoshikawa et al. (MIU, Tokyo, 1993) p. 475.

10. V.G. Ralchenko, K.G. Korotoushenko, A.A. Smolin and V.I. Konov, in *Advances in New Diamond Science and Technology*, ed. by S. Saito et al. MYU, Tokyo, (1994), p. 493.

11. F. Okuzumi, H. Tokura and M. Yoshikawa, in *Advances in New Diamond Science and Technology*, ed. by S. Saito et al. MYU, Tokyo, (1994), p. 783.

MICROMACHINING OF CVD DIAMOND FILMS USING A FOCUSED ION BEAM

Yoshihiro Mori, Takane Ino, Hitoshi Tokura and Masanori Yoshikawa

Yoshikawa lab., Dept. of Control and Systems Engineering
Tokyo Institute of Technology
2-12-1, O-okayama, Meguro-ku, Tokyo 152, JAPAN

Key words : CVD diamond film, focused ion beam, grooving, ion sputter-machining, resistivity

Abstract

Grooving CVD diamond films using a focused ion beam (FIB) to quarry micro parts is described. The substrate-side surface of a polycrystalline diamond film which is prepared by means of microwave plasma CVD, is able to be grooved by a focused Ga ion beam scanned straight repeatedly. The groove has cross section whose shape is like an inverted Gaussian distribution curve. And the surface roughness of the films before grooved influences that of grooves. Under the same irradiation conditions, deeper, narrower, in short, high aspect ratio grooves are obtained on B-doped semiconducting microwave plasma CVD diamond films. Coating electrical conductive material is also effective method to obtain high aspect ratio grooves. It is supposed that these results are due to the degree of electrification on the surface and that FIB irradiation is a suitable method for micromachining semiconducting diamond films.

1. INTRODUCTION

Diamond shows excellent mechanical and electronic properties, and so it is hopeful material for machine parts, electronic devices, and so on. But, it seems difficult to be applied the etching removal technique like silicon microfabrication technology to making micro parts of diamond because diamond is chemically stable. Therefore, the ion sputter-machining was tried. This machining was applied to the sharpening of diamond styluses[1], and the smoothing of diamond films[2]. If quarrying micro parts of several tens micrometers in size from CVD diamond films is supposed, sputter-machining using a focused ion beam (FIB) is applicable. Less than a FIB of 1 μm in diameter can be obtained by an ion beam gun using a liquid metal ion source. This was applied to preparing the cross-sectional samples for transmission electron microscope

(TEM)[3] and so on, and has the advantage of a maskless micromachining process. This paper describes the grooving of CVD diamond films using a focused Ga ion beam for the application to quarrying micro parts from films.

2. EXPERIMENTAL METHOD

2.1 Focused ion beam irradiation apparatus

Fig. 1 shows a schematic drawing of a FIB irradiation apparatus used in this experiment. This apparatus consists of an ion gun, a chamber for machining, vacuum pumps and power supplies and so on. The gun has a liquid metal (Ga) ion source and lenses to adjust ion beam. There is a stage with a sample holder and a secondary electron detector in the chamber. Accelerating voltage of ion beam is able to be set up to 25 kV. The electrostatic deflector enables the Ga ion beam to be scanned repeatedly in the one-way direction. It is possible to observe a secondary electron image of the sample surface by raster scan. This image gives information of the position of scanning and the focus of the beam.
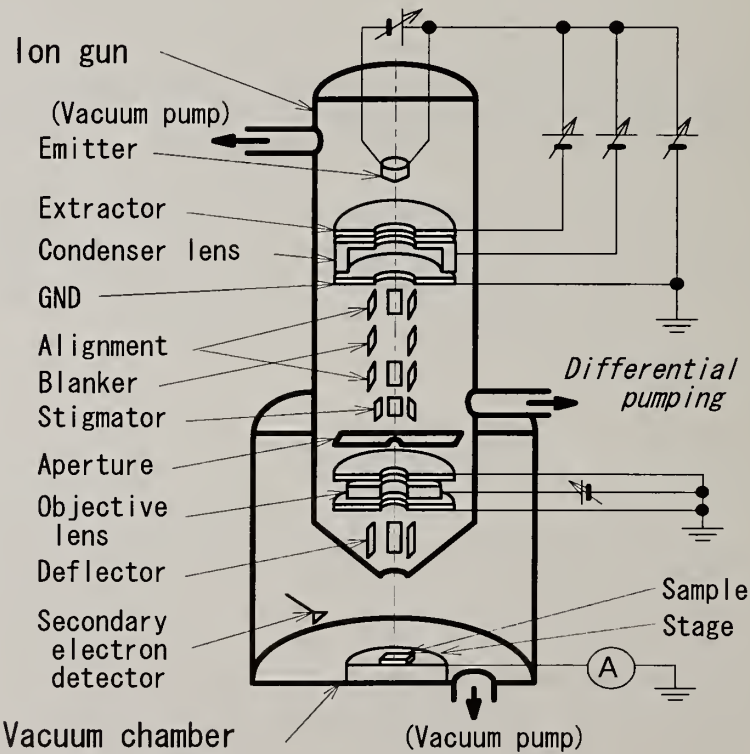
Fig. 1. Schematic diagram of a focused ion beam machine
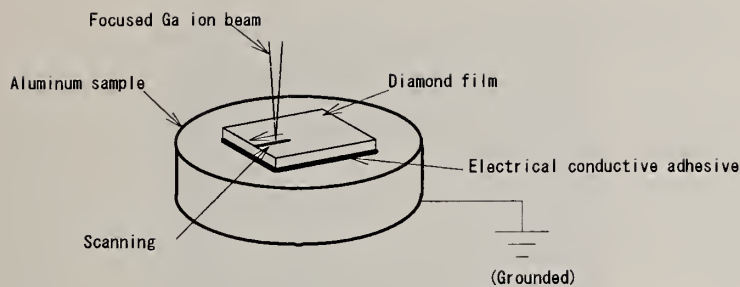
Fig. 2. Sample holder with diamond film and position of ion beam irradiation

2.2 Grooving of CVD diamond films

Grooving on the CVD diamond film using a focused Ga ion beam scanned straight repeatedly was tried.

Three kinds of microwave plasma CVD polycrystalline diamond films were used as samples. One of them was synthesized only from CH_4 and H_2, and others were from CH_4, H_2 and $B(OCH_3)_3$ to dope B in the diamond film. The volume resistibity of the former is 4×10^{13} Ω cm, and ones of the latter are 2×10^{-2} Ω cm, and 8×10^3 Ω cm. They were synthesized on Si substrates, and after that Si was dissolved by HF-HNO$_3$. By this dissolution, the comparatively smooth substrate-side surface was obtained. After cleaned in boiled H_2SO_4-HNO$_3$, films were attached to grounded aluminum sample holders by electrical conductive adhesive with their substrate-side surface outside. After that, a FIB was irradiated at the end of the film (Fig. 2).

A FIB was irradiated with repeated scan for fixed time under the conditions shown in Table Ⅰ. The beam was scanned repeatedly toward outside as in Fig. 2. A beam about 1 μm in diameter is obtained on the surface under these conditions. Current density of the beam is 64 mA/cm^2. Incident angle of the beam was vertical to the surface. The changes of incident angle and scanning velocity by deflection of the beam are able to be ignored, because the distance between deflector and surface of the film is much longer than the scanned length on the film.

Table Ⅰ. Ion beam irradiation conditions

Accelerating voltage	25 kV
Ion beam current	500 pA
Scanned length	47 μm
Scanning velocity	3.4 mm/s
Temperature of samples	Room temperature
Pressure in the chamber	3.3×10^{-3} Pa

3. RESULTS AND DISCUSSION

Fig. 3 shows scanning electron microscope (SEM) photographs of grooves by FIB irradiation. These grooves were obtained by 20 min irradiation. On the pre-irradiation film, there were convex lines which the scratches on the Si substrate were transcribed into. After irradiation, these lines remain on the surface of the grooves shown in Fig. 4. That is to say, the surface roughness of the film before grooved influences that of the groove. The shape of cross section of grooves is like an inverted Gaussian distribution curve. This seems to be because the beam has a Gaussian current density distribution[4].
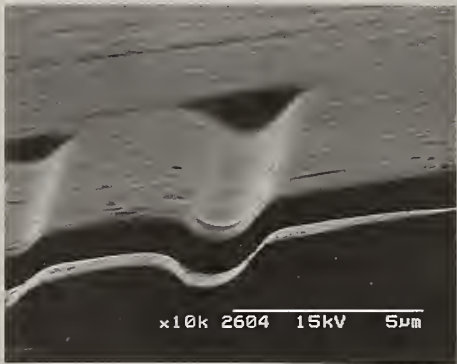
(a) Undoped ; 4×10^{13} Ω cm

(b) B-doped ; 8×10^3 Ω cm
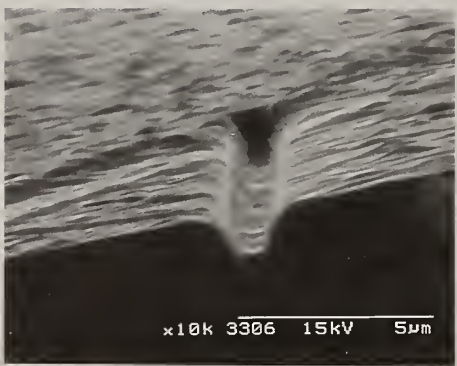
(c) B-doped ; 2×10^{-2} Ω cm

$\overline{5 \ \mu m }$

Fig. 3. SEM photographs of grooves on the CVD diamond films. Films are inclined to make an angle of $85°$.
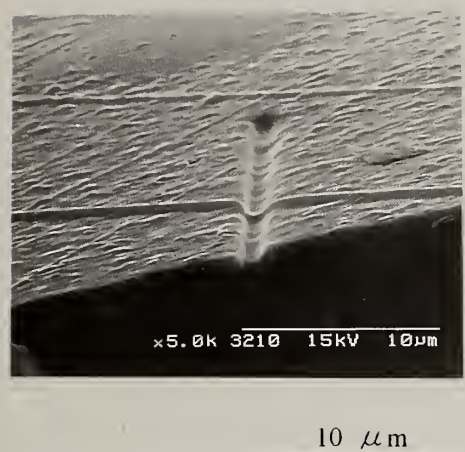
Fig. 4. Influence of convex lines on the surface
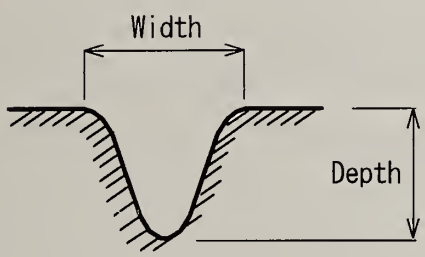
Fig. 5. Definition of the width and the depth of grooves

The depth and the width of grooves are defined as in Fig. 5. Fig. 6 shows the relationships between irradiation time and the width or the depth of grooves on three kinds of films measured with a SEM. As is clear from this figure, the depth is proportional to the irradiation time, but the width saturates as irradiation time goes on. The depth is reflected by ion dose and the width by the diameter of the beam. But the lower the volume resistivity of the film is, the narrower and the deeper the groove is under the same conditions, in short, the higher the aspect ratio is.

The comparison between the undoped thinly Au coated film and uncoated one is presented in Fig. 7. This shows that the aspect ratio of grooves on the coated film is higher than that on the uncoated one.

238
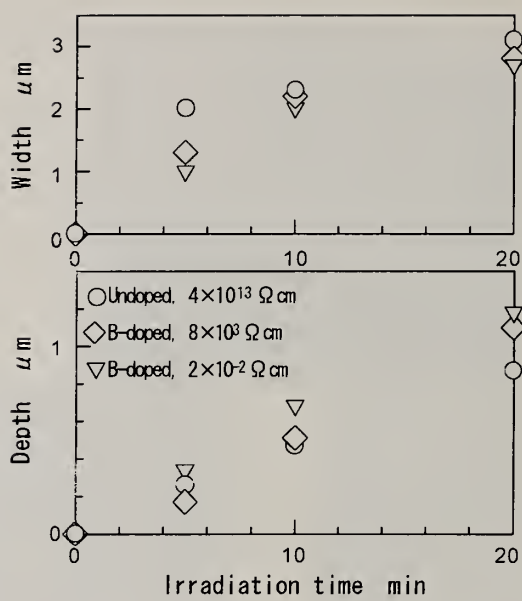
Fig. 6. Relationships between irradiation time of FIB and the width or the depth of grooves on the film of various volume resistivity
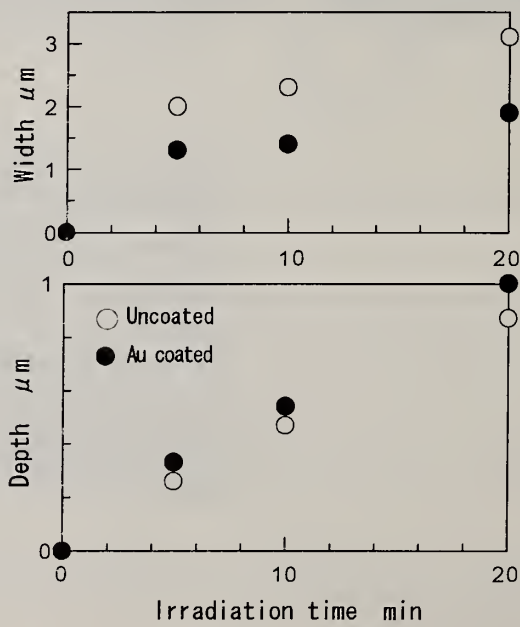
Fig. 7. Relationships between irradiation time of FIB and the width or the depth of grooves on the undoped film coated or uncoated Au
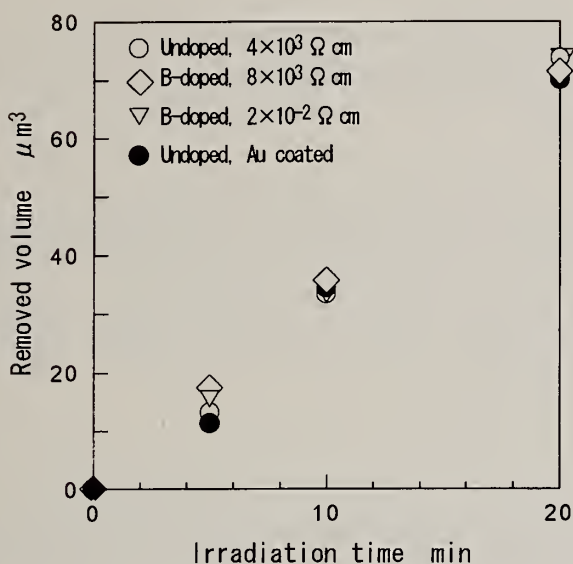
Fig. 8. Irradiation time vs. removed volume

The results in Fig. 6 and Fig. 7 show that the lower the volume or surface resistivity of diamond films are, the higher the aspect ratio of grooves are obtained. It is suggested that these results are due to the degree of electrification. On B-doped films, a FIB is supposed to be less influenced by surface electrification, because low resistivity makes electrons which neutralize positive charge of Ga ion easier to be supplied. But the results shows that in the case of B-doped films, the ion beam is supposed to be deflected slightly, because the width of the grooves is larger than the beam diameter after several minutes irradiation. This suggests that in spite of semiconducting films, neutralization of the ion is not enough.

Fig. 8 shows the relationships between irradiation time of FIB and removed volume. The removed volume of each film is almost the same value under the same condition in spite of the resistivity of films. The sputtering ratio is about 3. The ratio is supposed not to be influenced because of the high ion beam energy which is due to 25 kV in accelerating voltage.

From above, the volume resistivity of the film influences the aspect ratio of grooves. Lower resistivity film is able to be grooved deep in a short time. A FIB technique is considered to be an effective method to micromachine semiconducting diamond film High resistivity films also enable to be grooved in high aspect ratio by coating conductive materials like thin metal film on the surface. Combining several kinds of grooves, it is possible for micro parts to be quarried. Taking the scantiness of removal

volume and the surface roughness of the groove into consideration, thin diamond films with smooth surface are suitable to be quarried.

4. CONCLUSIONS

The grooving of CVD diamond films using a focused Ga ion beam were described. The shape of cross section of the groove is like an inverted Gaussian distribution curve. The depth of groove is proportional to the FIB irradiation time, but the width saturates. The surface roughness of the film before grooved influences that of the groove. And the lower the volume or surface resistivity of the film is, the higher the aspect ratio of the groove is, so a FIB technique is considered to be an effective method to micromachine semiconducting diamond film.

5. REFERENCES

1. I. Miyamoto and N. Taniguchi : J. Jpn. Soc. for Precision. Eng. **46** (1980) 1021.
2. A. Hirata, H. Tokura and M̌ Yoshikawa : J. Jpn. Soc. for Precision. Eng. **58** (1992) 289.
3. M. Tarutani, Y. Takai and R. Shimizu : Jpn. J. Appl. Phys. **31** (1992) L1305.
4. H. Yamaguchi, A. Shimase, S. Hiraichi and T. Miyauchi : J. Vac. Sci. Technol. **B3** (1985) 71.

RAPID POLISHING OF THICK POLYCRYSTALLINE "WHITE" CVD DIAMOND BY LIQUID METAL FILMS

Y. Tzeng, J. Wei, C. Cutshaw, and T. Chein

Department of Electrical Engineering, Auburn University, Auburn, Alabama 36849 USA

Key words: iron, steel, selective melting, smoothing

Abstract

Liquid metal films are selectively formed at the contact points between a solid metal surface and the peaks of diamond grains on a rough CVD diamond because of the lower melting point of the metal carbide than the metal. Diamond grains that form the rough diamond surface dissolve rapidly in the liquid films leading to a smooth surface of the same shape as the solid metal. A flat metal such as iron and stainless steel is used to rapidly planarize a rough CVD diamond.

1. Introduction

The Chemical Vapor Deposition (CVD) techniques have been developed so much in the past ten years that it becomes less expensive to deposit a thick CVD diamond of high optical and thermal quality than to polish the diamond. The cost for polishing a rough CVD diamond rises significantly when the flatness of the as-deposited diamond decreases because a larger volume of CVD diamond must be removed from the surface of a CVD diamond that is not flat to make it flat and smooth. In some applications, rough CVD diamonds of non-planar shapes must be polished to achieve mirror-like surfaces. This requirement makes the polishing process even more complicated.

Diamond is the hardest known material and has been used in many applications for polishing various materials. To polish the hardest material in nature rapidly and economically certainly requires some techniques that do not rely on hard abrasives, especially for polishing large-area and rough CVD diamond. Energetic laser beams and ion beams have been explored with limited success. The energy efficiency of laser is low and the requirement for the time-consuming scan of a laser beam with a constant energy

density in space and time across a large-area diamond surface makes it even more impractical for forming smooth diamond economically. The sputtering yield of carbon is quite low. This makes ion beams unlikely to achieve rapid polishing of rough CVD diamond.

Grigoriev and Kovalsky reported the working of diamond with metal [1]. A metal foil placed on a diamond at a high temperature sinks because carbon atoms can diffuse quickly in a metal and can react with hydrogen to form gas phase products such as methane. Tokura and Yoshikawa rubbed a CVD diamond against a hot and flat iron plate to allow the rough diamond surface to react with iron and become flat and smooth [2]. Processing of diamond by molten metal was reported by Jin, Chen, and Graebner [3] and Wei and Tzeng [4]. Diamond dissolves rapidly in liquid metal. However, because the molten metal reacts with the peaks and the valleys of diamond grains on a rough diamond surface at the same rate, a layer of diamond that is much thicker than that of the surface roughness (peak to valley) must be dissolved before the diamond surface becomes relatively smooth. The local smoothness of the diamond surface does not guarantee the macroscopic smoothness of the diamond film across an area of the size of several diamond grains.

The best way of making use of molten metal for smoothing CVD diamond is to selectively coat the highest peak of diamond grain on the diamond surface with a molten metal film. After this peak reacts with the metal and becomes lower in height, the second highest diamond peak is also selectively coated with the molten metal. This process continues until all the diamond peaks are coated with molten metal films. When the diamond surface becomes smooth, the separated molten metal films join to form a continuous film on the diamond surface. By this means, a rough CVD diamond may be smoothed without needing to remove a thick layer of diamond.

2. Experimental

Rough CVD diamond films are placed on flat and smooth iron or low-carbon steel disks or foils supported by molybdenum disks in a furnace in hydrogen or inert environment. At temperatures between 1150 C and 1250 C, the metal disks or foils remain solid except those contact points between the diamond peaks and the metal surface. Diamond peaks in contact with the metal surface react with metal to form iron carbide, that has a lower melting point than pure iron or a low-carbon steel such as stainless steel. At the processing temperature, therefore, iron in contact with diamond peaks, therefore, selectively forms liquid films on the diamond

peaks leading to the rapid dissolution of diamond peaks and the decrease in the diamond roughness. Figure 1 shows the phase diagram for carbon and iron. At the processing temperature, iron carbide melts to form liquid iron and graphite. The smoothing of diamond is schematically shown in Figure 2.

3. Results and Discussion

Figure 3 shows the surfaces of a 600 um thick CVD diamond before, in the middle of, and after the liquid iron film smoothing process. The time it takes to finish the smoothing process depends on the processing temperature. At around 1250 C, it takes less than 20 minutes to finish. The dissolution of diamond peaks and the smoothing of individual diamond grains during the smoothing process can be clearly seen in this figure. Although the iron surface finally forms a continuous liquid film, the bulk of the iron disk remains solid and provides a reference flat plane for achieving the final flatness of the diamond surface. The final surface roughness is about 2-4 um, which may easily be polished by other means to reach mirror-like finish. There are two major differences between this liquid metal film technique and the simple molten metal technique. The first one is that diamond grains with higher peaks are smoothed first followed by others with lower peaks and then finally the diamond valleys are dissolved in this liquid metal film process. In a simple molten metal process, both diamond peaks and diamond valleys react with molten metal from the beginning of the process. The second one is that the solid metal bulk automatically provides a reference plane, which can be either flat or non-planar in shape, for the final diamond surface. If the diamond is originally not flat or of different thickness in different areas, the thicker area or those areas that touch the metal first will be dissolved first leading to the final diamond surface according to the surface of the metal.

Although the liquid iron film process involves the heating of diamond to temperatures near 1200 C, the high quality of the CVD diamond remains as shown by the FTIR optical absorption spectra (Figure 4) of the diamond before and after the polishing process. These two spectra are practically identical indicating that the diamond did not degrade during the polishing process. The Raman spectrum shown in Figure 5 further indicates that the diamond surface remains high quality after the polishing process.

4. Conclusions

A rapid polishing technique for smoothing rough CVD diamond is reported. This technique uses inexpensive and safe materials such as iron and stainless steel to react with diamond surface. No moving parts are needed. No pressure needs to be applied to the diamond except the weight of the diamond. The process can be scaled up to smooth large-area or non-planar diamond surfaces and can smooth multiple diamond films at the same time.

5. Acknowledgments

6. References

1. A.P. Grigoriev and V.V. Kovalsky, "Working of diamond with metal," INDIAQUA 39, 49, 1984.
2. H. Tokura and M. Yoshikawa, "Polishing of CVD Diamond Film," in Applications of Diamond Films and Related Materials, Y. Tzeng, M. Yoshikawa, M. Murakawa, A. Feldman (eds.), Elsevier Science Publishers B.V., p. 241, 1991.
3. S. Jin, L.H. Chen and J.E. Graebner, "Thinning, shaping and patterning of CVD diamond by diffusional reactions," in Proceedings of the 2nd International Conference on the Applications of Diamond Films and Related Materials, M. Yoshikawa, M. Murakawa, Y. Tzeng, and W.A. Yarbrough (eds.), MYU, Tokyo, p. 189, 1993.
4. J. Wei and Y. Tzeng, "Reaction of CVD diamond with molten iron film," in Proceedings of the 2nd International Conference on the Applications of Diamond Films and Related Materials, M. Yoshikawa, M. Murakawa, Y. Tzeng, and W.A. Yarbrough (eds.) MYU, Tokyo, p. 609, 1993.
5. T.B. Massalski (ed.), Binary Alloy Phase Diagrams, ASM International, p. 843, 1990.
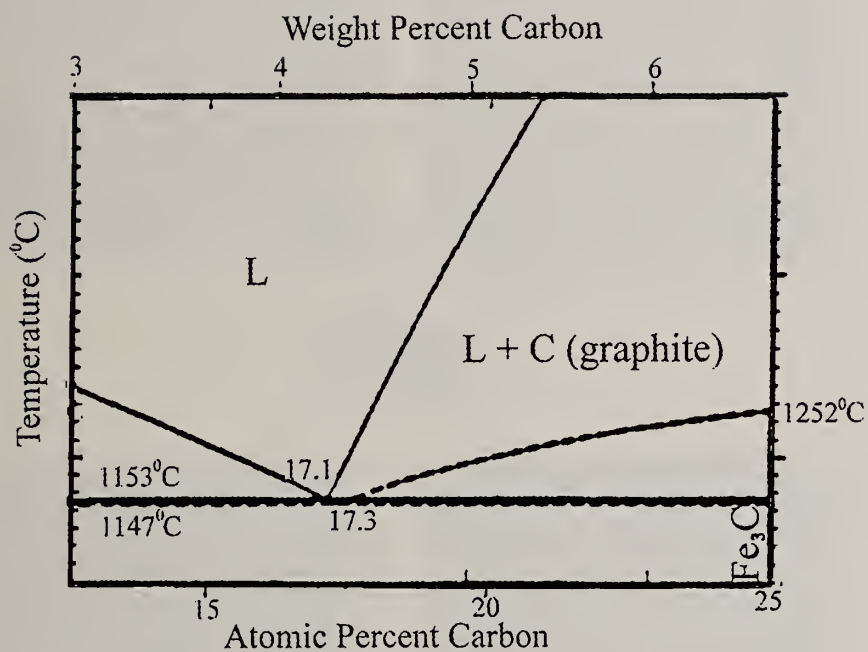
Figure 1. Carbon-iron phase diagram [5].
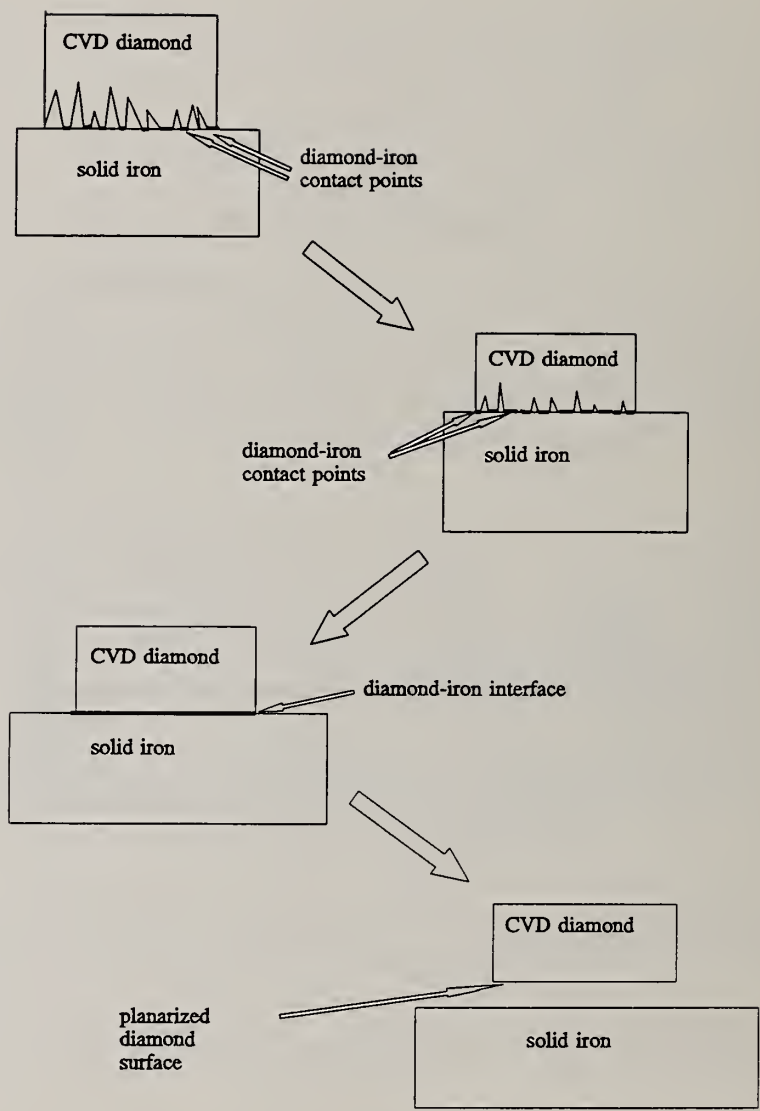
Figure 2. Schematic diagram of a polishing process using liquid iron films.
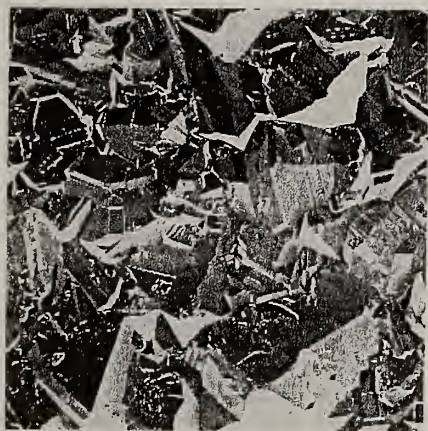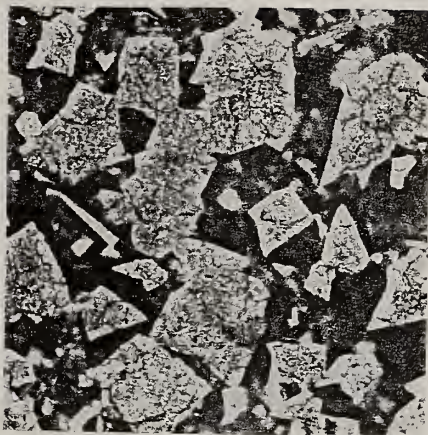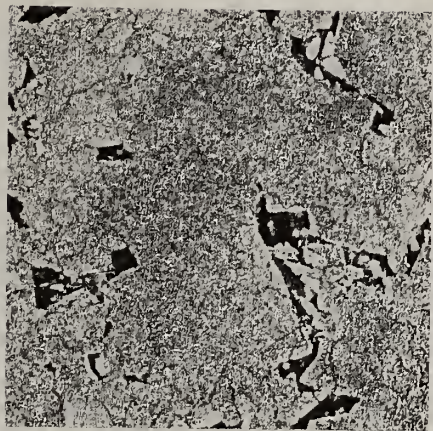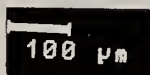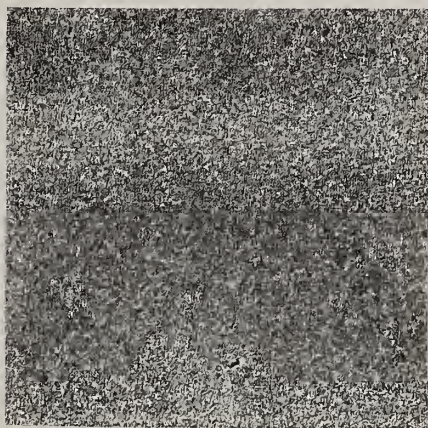
Figure 3. Optical micrographs of diamond surfaces. (a) before polishing; (b) and (c) during the polishing; and (d) after the polishing process.
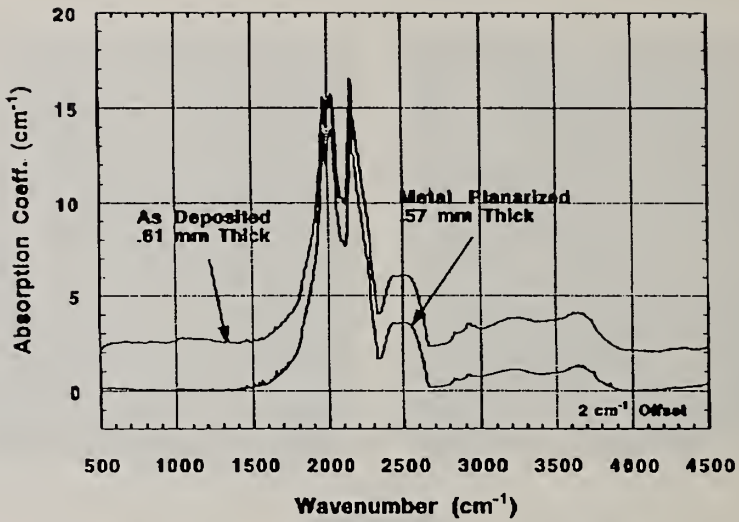
Figure 4. FTIR optical absorption spectra for a CVD diamond before and after the liquid iron film polishing process.
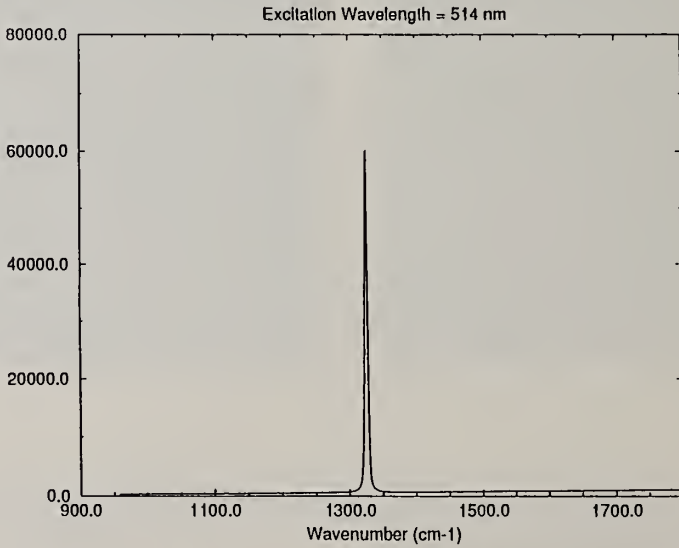
Figure 5. Raman spectrum of a CVD diamond after polishing by the liquid iron film process.

HIGH RATE FINISHING OF POLYCRYSTALLINE DIAMOND FILMS WITH HYPERTHERMAL OXYGEN ATOMS

D. B. Oakes and W. J. Marinelli

Physical Sciences Inc., 20 New England Business Center, Andover, MA 01810, USA

Key Words: Diamond, Finishing, Oxygen Atom, Polishing, Polycrystalline,

Abstract

A novel technique is described which results in high rate, controlled finishing of polycrystalline diamond films. Finishing occurs by directing a beam of hyperthermal (5 to 12 eV) oxygen atoms at glancing incidence upon the diamond sample to preferentially etch surface roughness. The high translational energy of the atoms enables high reaction probabilities (up to 1.0) with diamond and consequently rapid etching rates. Rates up to 1.6 µm/hr were observed. Precise control of the thickness of treated films has been demonstrated by using an in-situ monitor of the process. The monitor is capable of thickness control to ±0.05 µm, enabling finishing to precise specifications.

1. Introduction

The desirable, high growth rate CVD techniques which are used to grow polycrystal-line diamond films (e.g. plasma-jet, oxyacetylene combustion) result in deposits composed of randomly oriented crystallites with surface roughness of the order of 1 to 10 µm. Many present and future applications of these films require that they be finished to precise dimensional specifications and/or that the surface roughness be significantly reduced. Some of these applications include use of diamond as a tool insert for cutting applications, as a protective coatings for precise measuring instruments such as micrometers, in heat sink applications and in optical applications.

Broadly speaking, there are two classes of finishing applications. The first is coarse stock removal, which results in a modest reduction of surface roughness in the as grown polycrystalline diamond film while reducing the film to a desired thickness. This application requires a high etching rate technique which can controllably remove material. The second application is to fine polishing with a resulting surface rough-ness less than 50 nm. Our approach addresses the need for a controlled coarse stock

removal technique and exploits a technology developed and patented by Physical Sciences for generating fast (6 to 12 km/s) atomic beams of O, N, Cl, F and H. The fast oxygen atom beam is directed at a rotating substrate, at glancing incidence. Polishing of the sample is dependent upon two effects: 1) the shadowing of low points on the surface by the high points and therefore the preferential removal of the high points; 2) the low probability of etching from secondary collisions of unreacted oxygen atoms due to first collision energy transfer and the dependence of the reaction rate on incident energy.

2. Experimental

The fast oxygen atom beam is generated from a high temperature (ca. 20,000 K) plasma initiated by a laser-induced pulsed discharge in the throat of a diverging nozzle containing molecular oxygen. The apparatus is shown schematically in Fig. 1. A CO_2 laser is used to initiate the pulsed discharge and is operated at a repetition rate of 3 Hz. Details about this general technique of producing fast atomic beams and the experimental apparatus can be found in the literature [1].
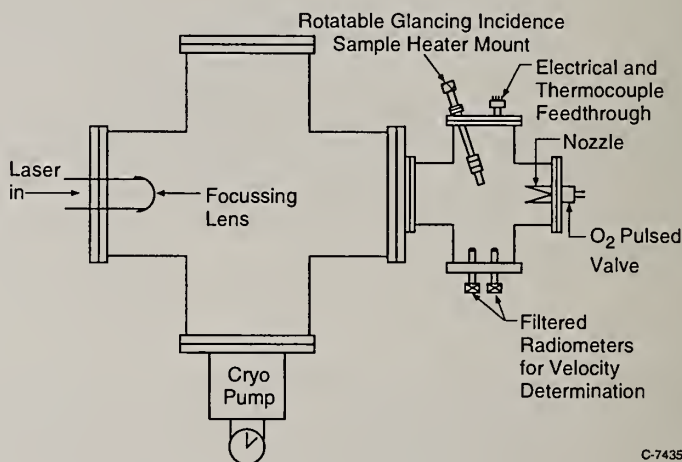
Fig. 1 Schematic of the diamond film finishing apparatus.

The 1 x 1 cm^2 free standing polycrystalline diamond samples were attached to a rotating sample mount capable of holding four samples and heating the specimens to 750 C. Surface roughness of the samples was measured before and after treatment using a Rodenstock RM-600 non-contact optical profilometer. Sample weights were determined with 1 µg resolution using a Cahn microbalance. Etch depths were calculated from the mass loss assuming uniform mass removal (confirmed by SEM). A microcrystalline graphite coated Quartz Crystal Microbalance (QCM) with a sensitivity of 1.254 x 10^{-8} $g/cm^2/Hz$ was used as an in-situ monitor of the oxygen atom flux on the diamond samples. The etch rate of the room temperature graphite was calibrated with respect to the etch rate of the heated diamond.

3. Results and Discussion

The temperature dependence of the etch rate of the diamond samples was determined with oxygen atom beam velocities equal to 8, 10, and 12 km/s and with sample temperatures ranging from 200 to 750 C. At all three velocities the reaction probability of incident oxygen atoms with the diamond sample approached 1.0 near substrate temperatures of 650 C. The temperature dependencies were well described by an Arrhenius dependence and the calculated activation energies were 14.1 ± 1.1, 13.7 ± 1.9, and 8.4 ± 1.4 kcal/mole for beam velocities equal to 8, 10 and 12 km/s respectively.

Experiments were performed to demonstrate the coarse stock removal capabilities of the hypervelocity oxygen atom beam. The goal of coarse stock removal is to improve the surface finish while controllably removing material. Since the technique relies on shadowing of the valleys by the peaks on the diamond surface to improve the finish, experiments were performed with the oxygen beam aligned 70 deg from the sample normals. The finish is expected to be optimized if the reaction probability of the incident oxygen atoms is near unity since rebounding atoms could reach and then etch the diamond in the surface valleys. The sample temperatures were therefore maintained at 720 C to assure high reaction probabilities.

Scanning electron micrographs of a diamond sample before and after treatment are shown in Fig. 2. Before treatment the sample surface is comprised of columnar-like features approximately 2 µm in diameter and approximately 10 µm tall, separated by less than 1 µ. The average surface roughness, Ra, of the sample measured by profilometry was 0.49 µm while the peak-to-valley roughness, Rz, was 3.21 µm.

(a)   (b)
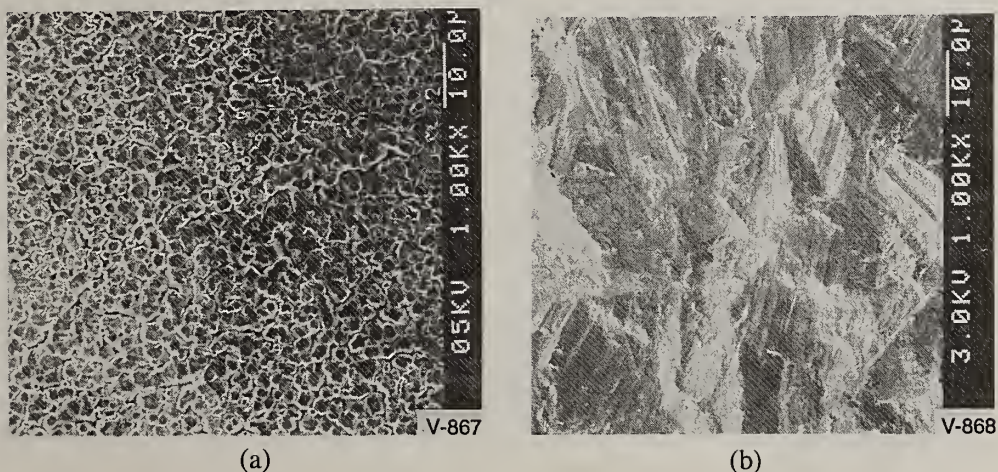
Fig. 2   Polycrystalline diamond film a) before and b) after treatment with the oxygen atom beam.

This sample would be extremely difficult to finish by traditional techniques (eg. abrasive lapping) since these methods remove material very slowly from relatively flat samples. The columnar features were removed by the treatment, exposing the bulk substrate. The Ra and Rz roughness factors were modestly improved to 0.34 and 2.56 µm respectively. A slower fine polishing technique could be applied to this sample to improve the finish further.

An experiment was performed to demonstrate the controllability of the finishing technique. Two samples of differing thickness were processed by the oxygen atom beam with the goal of reducing them to the same thickness. The samples were processed with an angle of incidence of 45 deg, a beam velocity of 10 km/s and at 680 C. The steeper angle of incidence resulted in a higher atom flux on the samples and an increased etch rate of 1.2 µm/h. Both samples were treated for approximately 2 h at which point the thinner sample was removed. Processing was continued on the remaining sample until the QCM monitor indicated that the sample had been exposed to the required dose of oxygen atoms to remove the desired thickness of diamond. The beam was then turned off. The results of the experiment are summarized in Table I. Sample thicknesses were measured to a precision of 2.5 µm with a micro- meter. As indicated, the samples were treated to the same thickness by the technique.

Table I. Summary of the controlled material removal experiment.

Sample	Etch Mass (mg)	Etch Depth (µm)	Pretreatment Thickness (µm)	Post-Treat Thickness (µm)
PSI-1	13.654	38.8	383	340
PSI-2	40.382	114.7	459	340

High rate, controlled etching of polycrystalline diamond films has been demonstrated with the hypervelocity oxygen atom source. Continuing work will include scale-up of the device for large area (300 cm^2) processing with rates up to 12 µm/h.

4. Acknowledgements

5. References

1. Caledonia, G.E., Krech, R.H., and Green, B.D., AIAA Journal 25(1), 59 (1987).

AFFECTED LAYER OF POLISHED SINGLE AND CVD DIAMONDS

Hitoshi Tokura, Atsushi Hirata, Dong Liang and Masanori Yoshikawa

Tokyo Institute of Technology, 2-12-1 O-okayama Meguro-ku, Tokyo 152, Japan

Key words: affected layer, hydrogen plasma etching, mechanical polishing, removal rate

Abstract

Both single and CVD diamonds were mechanically polished by using grinding wheels of #400 or #1500. The polished surfaces were smooth and no cracks could not be observed by a microscope. These surfaces were exposed in hydrogen plasma for 1 hour, cracks appeared on the surface. For the single crystal diamond, the crack shape exhibited the relation with crystallographic orientation of the polished surface and polishing direction. Also on the CVD diamond cracks came out by etching but the size is smaller than those on a single crystal diamond.

1. Introduction

The removal rate of diamond by usual mechanical polishing techniques varies remarkably both with crystallographic orientation and with the polishing direction. The resistivity of diamond to abrasion has been widely studied[1], however the quality of the processed sub-surface has not been studied. Diamond is versatile material and in future it will be applied to optical components or semiconductors, it is necessary to examine the processed sub-surface properties. This paper describes the affected layer of the mechanically polished surface of both single and CVD diamonds.

2. Polishing procedure and etching method

Single crystal diamonds synthesized by HP/HT method and CVD diamond films prepared by arc discharge plasma jet CVD[2] were used, and cube face of a single crystal diamond and a growth surface of CVD diamond were polished. Replacing an cast iron wheel (scaife) with a diamond grinding wheel, a conventional diamond polishing machine was used. A #400 and a #1500 vitrified bonded diamond wheels were selected. After scaife polishing with 0/2μm diamond powder, these samples were polished under the conditions shown in Table 1.

Table I. Polishing conditions

Wheel speed	20m/sec
Applied pressure	600kPa for a single crystal diamond
	1350kPa for a CVD diamond
Polishing time	10-30min
Atmosphere	Air and dry

Hydrogen plasma etching has been known to play an important role to remove non-diamond elements, such as graphite or amorphous carbon, during diamond synthesis from gas phase. In anticipation of mild etching of diamond, microwave hydrogen plasma etching was applied to examine the affected layer, and the etching conditions are listed in Table 2.

Table II. Etching conditions

Microwave power	300W
H_2 flow rate	100cc/min
Gas pressure	30Torr
Temperature	900 °C
Etching time	-60min

3. Results of hydrogen plasma etching

SEM photos before and after etching for 60min of a single crystal diamond polished with a #1500 wheel are shown in Fig.1. As-polished surface looks very smooth and any cracks can not been observed on it. Contradistinctively a lot of cracks appear on the etched surface. The cracks began to come out by etching for 15min. Additional etching made the cracks larger, but etching over 60min did not extend the crack size. From these results, cracks appeared by etching are recognized as the affected layer and hydrogen plasma etching is applicable to evaluate the affected layer of a diamond. Further etching for 60min is found to be optimum.

(a) As-polished　　　　　　　　(b) Etched　　　　　　 50μm

← Polishing direction
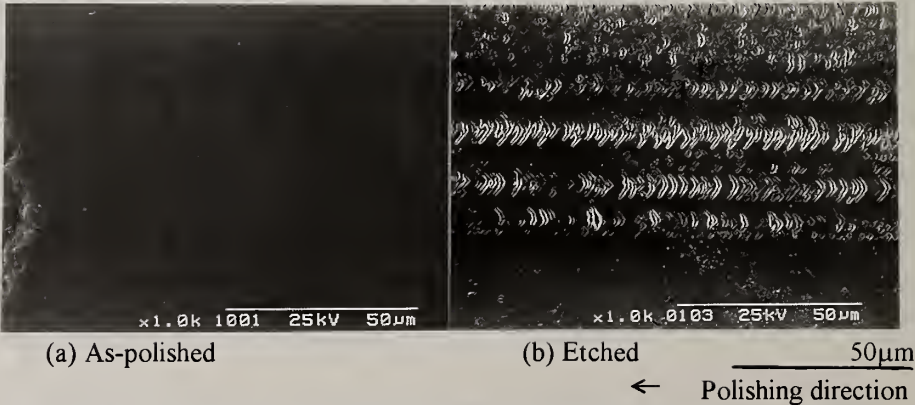
Fig.1 SEM photos of the cube surface polished with a #1500 wheel

4. Affected layers

In order to make clear the influence of grain size of the diamond wheel, cube faces of single crystal diamonds were polished to <100>direction with a #400 or a #1500 wheel. SEM photos of the etched surfaces are shown in Fig.2. In both cases v-shaped cracks line in a polishing direction and ones with a #1500 wheel are smaller than those with a #400 wheel. Average crack lengths are 6μm and 14μm with a #1500 and a #400 wheel, respectively. Removal rate with a #1500 wheel was 1.6μm/min and that with a #400 wheel was 4.3μm/min. Larger grain leads larger affected layer and higher removal rate, and the removal rate has some relation with the clack length.
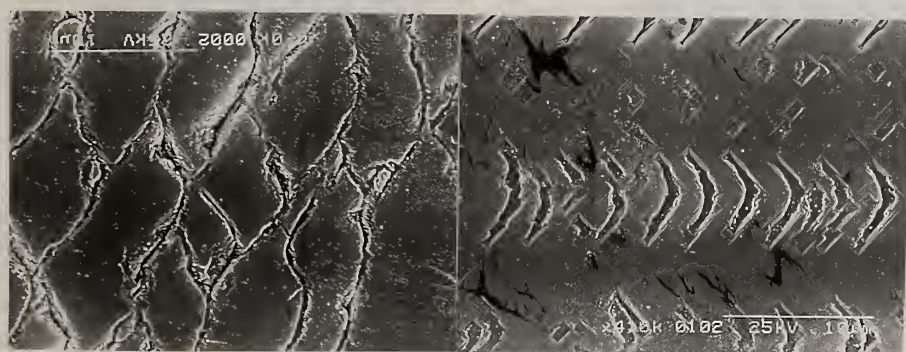
| (a) With a #400 wheel | (b) With a #1500 wheel | 10μm |

← Polishing direction

Fig.2 SEM photos of the etched surface polished with different wheels

To investigate the effect of polishing direction, cube faces were polished to two different directions, such as <100> and <110>, and were etched. As shown in Fig.3, cracks perpendicular to the polishing direction can be observed on the surface polished to <110> direction, while to <100> direction cracks are parallel to the polishing direction. High powered observations derived that {111} cleavage planes along the <110> form the cracks. This suggests the removal proceeds by cleaving and yield affected layers. Removal rate for <100> is 4.3μm/min and 2.7 times larger than for <110> direction. Crack length for <100> was 2 times larger than for<110> direction.

Comparing with a single crystal diamond, CVD diamond films is believed to be harder to polish. Photo of the etched CVD diamonds after polishing with a #1500 wheel is shown in Fig.5. Similar to a single crystal diamond, cracks are observed as well as grain boundary. This means that the affected layer is also formed on the CVD diamond. In spite of heavier polishing pressure, CVD diamond has smaller cracks than single crystal diamond and lower removal rate of 0.5μm/min.

(a) <100> direction   (b) <110> direction   5μm
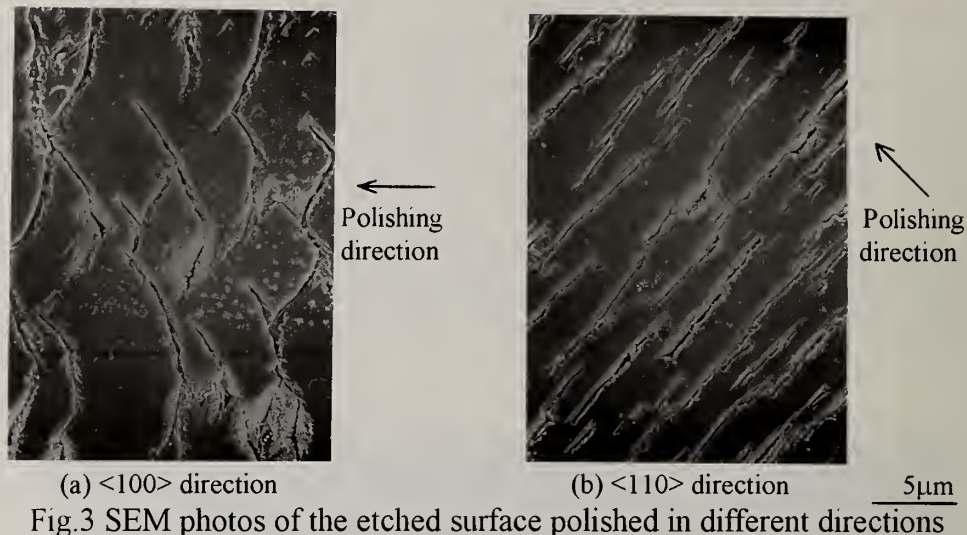
Fig.3 SEM photos of the etched surface polished in different directions

Fig.4 SEM photo of the etched CVD diamond surface polished
        with a #1500 wheel

5. Conclusions

Cracks appear on the mechanically polished diamond surface by hydrogen plasma etching, and the shape are largely dependent on the orientation and polishing direction. The removal rate is related to the crack size and large crack causes high removal rate. Also CVD diamond has similar cracks but the size is much smaller.

References
1.M.Seal: The Abrasion of Diamond, Proc. Roy. Soc., A, 248(1958)379.
2.A.Hirata and M.Yoshikawa: Diamond and Related Materials, 2(1993)1402.

Applications of Diamond Films and Related Materials: Third International Conference, 1995
Editors: A. Feldman, Y. Tzeng, W. A. Yarbrough, M. Yoshikawa, and M. Murakawa

257

POLISHING OF THICK CVD DIAMOND BY AN EXCIMER LASER AND A CAST IRON WHEEL

T. Chein, C. Cutshaw, C. Tanger, and Y. Tzeng

Department of Electrical Engineering, Auburn University, AL 36849 USA

Key words: smoothing, excimer, ablation, polishing

Abstract

Polycrystalline CVD diamond films have been processed using an ArF excimer laser at the incident angles of 0, 30, 45, and 60 degrees from the normal followed by cast iron wheel polishing. The laser was operated at 50 Hz rep-rate with an energy of 150 mJ per pulse and a duration of 15 ns full-width, half-maximum (FWHM). The beam was focused using a cylindrical lens to a cross-sectional area of about 1.25 cm by 50 μm. The CVD diamond samples were mounted on a computer controlled linear translator and scanned at a speed of 2 μm/s. The initially sharp crystallite facets became rounded after two laser scans. The roughness of the 600 μm thick diamond film was reduced from 70 μm to around 15 μm using a Center Line Average (CLA). Rotating cast iron wheel charged with diamond powder was used for achieving final mirror-like surface.

1. Introduction

Diamond is the hardest material in nature. It is frequently used to polish diamond and other materials. Smoothing, or polishing of diamond by diamond powder has been in the history since the 16th century [1]. Diamond abrasive and rotating iron wheel charged with diamond powder are conventional but still the most commonly used methods for polishing diamond. Laser-based methods for polishing diamond [2] are among those newly developed techniques and are capable of smoothing the surface of diamond. The excimer laser ablation is an explosive evaporation process caused by the rapid heating resulting from the UV light absorbed by the ablated material. Solid material can be removed layer by layer as long as the penetration depth of the UV light is short and the average laser power does not cause the bulk temperature of the target to become too high.

2. Experimental

An ArF excimer laser is used for the first part of the process. The laser outputs 193 nm light pulses of 15 ns long at rep-rates ranging from 1 Hz to 200 Hz in a cross-sectional area of 1.25 cm by 2 cm near the laser output window. A cylindrical lens with a focal length of 50 mm is used to focus and reduce the cross-sectional area to about 1.25 cm by 50 μm. Each output pulse of the laser contains photon energy of 150 mJ. The energy density at the diamond surface was calculated to be about 24 J/cm^2,

that is an energy density sufficient for a rapid removal of diamond even if it is greatly reduced due to reflection and absorption by the lens. The CVD diamond sample was mounted on a computer controlled linear translator. The angle of incidence is adjustable by turning the sample holder with respect to the cylindrical lens. The diamond surface with a roughness of 70 μm (CLA) was scanned by the incident beam at a speed of 2 μm/s. Figure 1 is the schematic diagram of the setup for the laser ablation.

After the laser ablation, the diamond sample was loaded on a Sloan surface profilometer to examine its surface roughness. The CVD diamond was then attached to a fixture with the surface to be polished lying against an rotating iron wheel. A weight is applied to the CVD diamond to promote polishing. Diamond particles were inserted into the surface of the iron wheel that rotates at a speed of 500-3000 rpm.

3. Results and Discussion

Figures 2(a)-2(b) show the cross-sectional view of the laser ablated diamond before and after one or two laser scans. After two laser scans, the roughness of the surface was reduced from 70 μm (CLA) to around 15 μm. Sloan profiles show that 40 μm of diamond was removed with an angle of incidence of 30 degrees compared to 30 μm with an angle of incidence of 60 degrees per laser scan. The initially sharp diamond facets were damaged by the photon energy of the laser beam and became rounded as a graphitic and/or disordered diamond surface layer was formed. Figure 3 (a) and (b) shows the Raman spectra of a CVD diamond before and after the excimer laser ablation process. In Figure 3(b), the prominent diamond peak is accompanied by a broad graphite peak and other non-diamond carbon after the laser ablation. At the end of the pulse there is a thin residual graphite layer that must be removed by other means. The diamond surface after being ablated by the excimer laser is not mirror-like. A cast iron wheel charged with diamond powder was used to polish the diamond surface to mirror-like finish as shown in Figure 2(d).

4. Conclusions

Since laser ablation is a line of sight process, the angle of incidence of the laser beam is important to the smoothing of the diamond surface. There is not much selectivity between the removal of diamond peaks and diamond valleys. Laser beam incident at the diamond surface at an angle of 30-60 degrees led to a smoother but still not satisfactory diamond surface. The power density decreases when the angle of incidence increases. Lower power density results in lower etch rate. Laser ablation by continuous scanning can not effectively produce mirror-like surface on thick and initially rough CVD diamond. The hybrid process involving the laser ablation followed by the mechanical polishing technique using a rotating cast iron wheel charged with diamond powder was found sufficient to produce a flat and smooth diamond surface.

5. Acknowledgments

6. References

1. K.E. Spear and J.P. Dismukes (Ed.), Synthetic diamond: emerging CVD science and technology, p. 509, published by John Wiley & Sons, Inc., 1994
2. S.M. Pimenov, A.A. Smolin, V.G. Ralchenko, and V.I. Konov, Diamond Films and Technology, 2 (4), 201, 1993
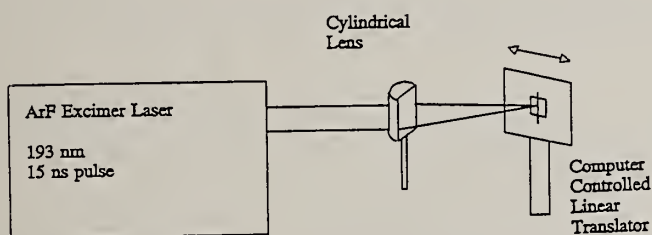
Figure 1. Schematic diagram of a laser ablation system for smoothing CVD diamond.
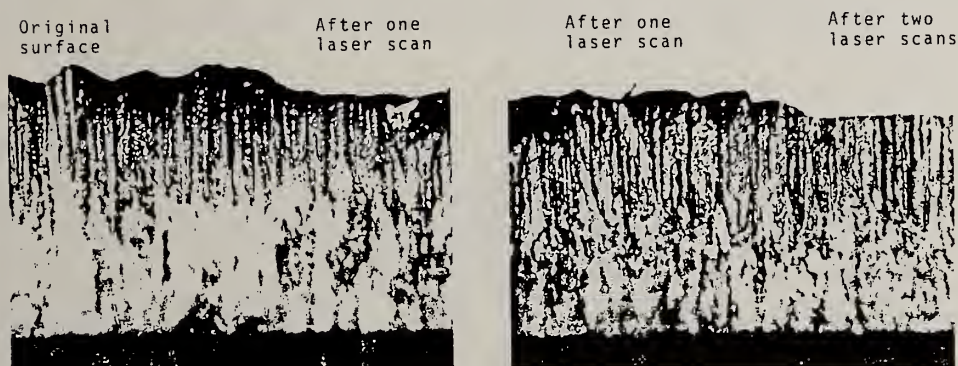
Figure 2. Cross-sectional views of a CVD diamond before and after one or two laser scans by an excimer laser operating at 193 nm. The energy per pulse is 150 mJ and the rep-rate is 50 Hz. The laser is focused to a line of 1.25 cm by 50 μm. The scanning speed is 2 μm/s. The angle of incidence is 60 degrees. The thickness of the diamond film before ablation is 600 μm.
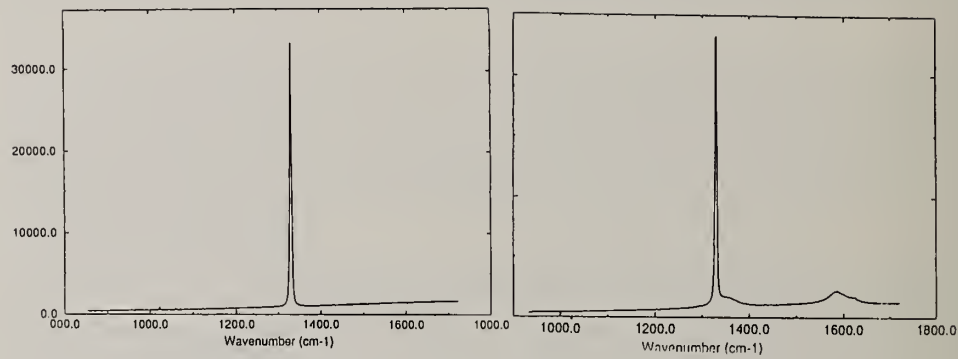
Figure 3. Raman Shifts of the diamond surface (a) before and (b) after being ablated by an excimer laser.

1/4 inch.
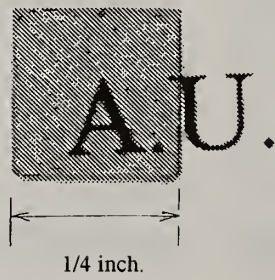
Figure 4. CVD diamond after laser ablation and iron wheel polishing process showing the transparency of the sample.

Applications of Diamond Films and Related Materials: Third International Conference, 1995
Editors: A. Feldman, Y. Tzeng, W. A. Yarbrough, M. Yoshikawa, and M. Murakawa

261

DIAMOND THIN FILM AND SINGLE CRYSTAL ETCHING UNDER CRITICAL ECR PLASMA CONDITIONS

Peiguang Bai[1,2], Jian Liu[1,3], Nalin Parikh[1], G.J. Tessmer[4] and L.S. Plano[4]

[1] Department of Physics and Astronomy, University of North Carolina at Chapel Hill, Chapel Hill, NC 27599-3255, USA.

[2] Present address: Department of Physics, Inner Mongolia Univ. Huhhet, Inner Mongolia, P.R. China.

[3] Present address: March Instruments, Inc., 125-J Mason Circle, Concord, Cal. 94520, USA.

[4] Kobe Steel USA Inc., Electronic Materials Center, P.O. Box 13608, Research Triangle Park, NC 27709, USA.

Key word: diamond, ECR, etching, plasma,

Abstract

Single and polycrystal diamond thin films were etched in a 2.45 GHz microwave plasma system under electron cyclotron resonance (ECR) conditions, in pure oxygen plasma. A very intense (high mode) plasma was observed when the critical ECR field (875 Gauss) was at the microwave window and the magnetic field gradient was increasing away from the window. Because of the flexibility of moving magnetic coils along the length of the chamber, it was possible to establish high mode plasma conditions. Langmuir probe measurements of this high mode plasma showed that the ion current density was more than four times that of the normal mode. Under high mode plasma conditions, reproducible high diamond etching rates were achieved, up to 300 nm/min, for microwave power of 300 Watts and pressures of 3 mTorr of pure oxygen. SEM observations of etched samples revealed smooth surfaces with high uniformity.

1 . Introduction

Diamond-based electronic devices are predicted to be superior to present technology at high frequency and power. Diamonds devices may operate at temperature as high as 1000 K, a temperature that would destroy. devices made from Si and GaAs [1,2]. However, diamond's inert chemical nature and high temperature stability make it difficult to process. Although selective area deposition can accommodate many device structures, other structures require the selective removal of the films [3]. A highly anisotropic dry etching technique compatible with existing diamond process is desirable. Previous work regarding diamond etching via ECR or radio frequency (RF) plasma demonstrated either low rates (less than 10 nm/min) or higher rates that were not reproducible [2].

We have etched single crystal and polycrystalline diamonds under various plasma conditions then (microwave power, magnetic fields, oxygen pressure etc.) and analyzed using Scanning Electron Microscope (SEM) and Raman spectroscopy.

2. Experimental

Diamond etching was performed in a microwave ECR plasma system (Fig. 1) with an ASTeX S-1000 microwave generator, a reducing wave guide and a three-stub tuner installed close to a quarter-wavelength titanium brazed alumina window, which also acted as a vacuum seal. This system can deliver 2.45 GHz microwaves with forward power from 200 to 1000 W. The chamber is cylindrical with dimensions 0.1 m in diameter and 0.8 m long. For these dimensions and the microwave frequency used, it was determined that the electromagnetic wave mode is mainly TE_{01} Two identical coils, M_1 and M_2, can be moved independently along the length of the chamber. A turbomolecular pump combined with the mechanical pump produce base pressure of $\sim 1 \times 10^{-7}$ Torr. A gas mixture of oxygen and argon was introduced into the chamber in front of the microwave window and their flow rate and the chamber pressure were controlled by an MKS mass flow controller and a throttle valve.

Undoped diamond samples of typically 10 μm were grown on Si substrates by microwave plasma CVD which exhibited a strong Raman peak at 1332 cm^{-1}[4]. Following growth, the samples were cleaned in a boiling solution of CrO_3/H_2SO_4 to remove graphite, followed by a standard aqua regia and RCA cleaning. A gold layer of 250 nm was deposited on the diamond film and etch patterns with minimum line width of 2 μm were defined by standard photolithographic process. After plasma etching, the samples were analyzed with SEM to determine etching rates and surface morphology.
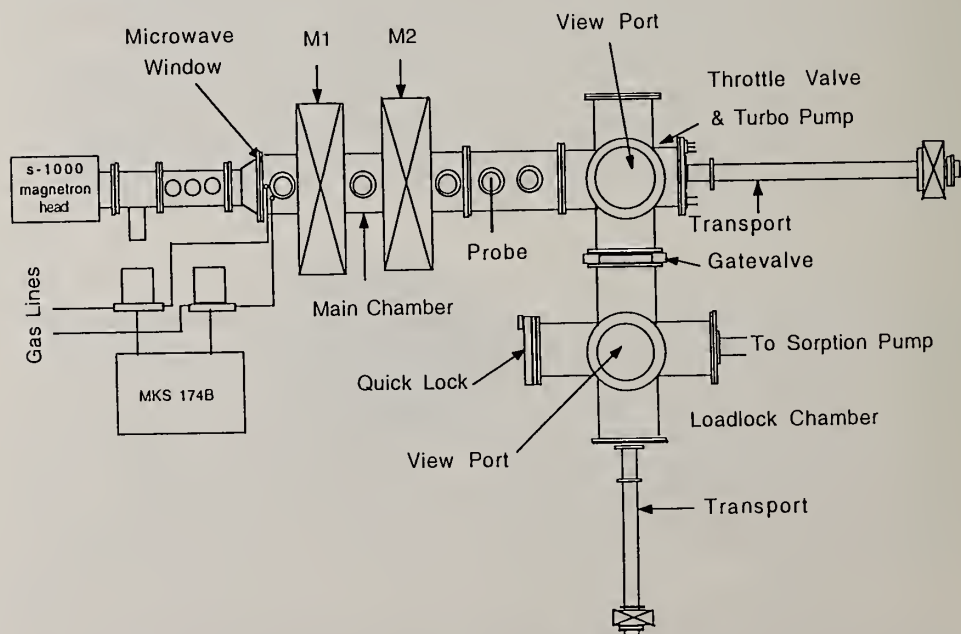
Fig. 1. Schematic of the ECR system, consisting of an ASTeX S-1000 microwave generator, movable magnetic coils (M_1 and M_2), and main and load lock chambers

3. Results and Discussion

A Statistical Experiment Design (SED) was performed to understand the fundamental effects of various process parameters on the etching rate, reproducibility, anisotropy (which determine the line width) and surface morphology of the etched samples. The SED parameters involved in etching and their respective ranges are listed in Table I.

Table I. Parameters and Ranges of Etching Experiments

Process Parameter	Range
Pressure	0.5- 100 mTorr
Microwave Power	200 - 450 W
Magnet M_1 Position	0.15 - 0.25 m from the Microwave Window
Magnet M_2 Position	0.36 - 0.66 m from the Microwave Window
Magnet Current	100 - 140 A (same in both the coils)
Etch time	5 - 60 min.

A large number of etching experiments of both single crystals and polycrystal diamond thin films were carried out. It was observed that at pressures higher than 10 mTorr etching occurred at rates less than 5 nm/min. At these pressures ions are much less energetic, resulting in reduced etching rates. When the pressure was decreased, etching rates increased. For pressures lower than 1 mTorr, the etching rates ranging from 30 nm/min. to 50 nm/min. were obtained. As the pressure was further decreased, the etching rates decreased. At 0.2 mTorr the etching rate was lower than 10 nm/min. again, as a resulting of low plasma density. Severe damage to the gold mask by the plasma and a rough etched surface (Fig. 2 a and 2 b) were observed for etching at pressures lower than 1 mTorr, presumably because of the high ion energies The etching rates at lower pressures were not reproducible. This irreproducibility was also observed by Grot, *et al* [2], but no explanation has been found so far. When combining the requirements of both high etching rate and low surface damage, these SED etching experiments showed that the appropriate pressure range for etching was between 10 mTorr and 1mTorr.
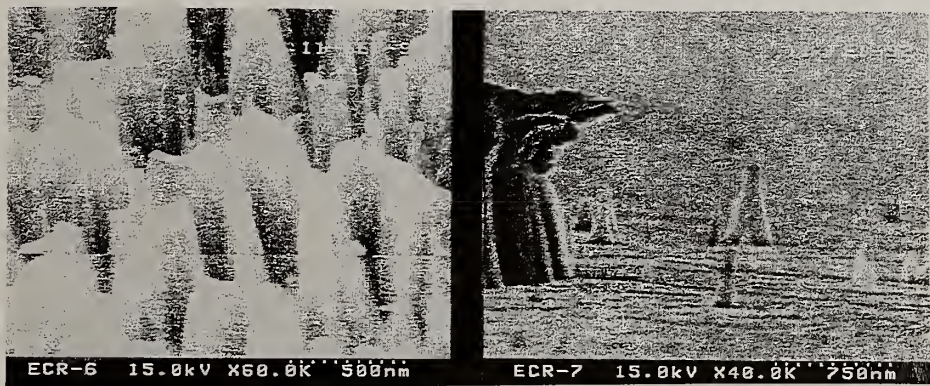
Fig. 2 SEM micrographs of a) damaged gold mask and b) residual diamond cones

Since the etching of diamond occurs by chemical oxygen etching, it is expected that a high atomic oxygen density in the plasma will result in a high etching rate. The atomic oxygen density, on the other hand, depends on the dissociation rate and the recombination rate of oxygen [3]. The dissociation rate is a complicated function of gas density and the collision cross section for oxygen dissociation (which in turn, is a function of the electron energy) and can be determined experimentally [5]. In practice the variation of atomic oxygen intensity with pressure is determined by optical emission spectroscopy (436.8 nm line). These measurements showed that the atomic oxygen density reached maximum for pressure around 2 mTorr, where the highest etching rate was observed, suggesting that, indeed, high atomic oxygen density results in a high etching rates. Another parameter that affects the etching rate is the microwave power because high power results in high atomic oxygen density. The etching rate at 500 W was twice as high as at 300 W. The increase of microwave power increases the atomic oxygen density and results in high etching rate.

The affect of magnetic field on plasma density and hence etching turned out to be dramatic. In our earlier study of plasma characterization using Langmuir probe [6], it was observed that when the coils were placed certain distances from the microwave window and the current through the coils, was adjusted appropriately a critical "high mode" condition was established, named as 'high mode plasma'. In this high mode, the plasma density was more than four times that in the normal mode. The physical basis of the high mode plasma involved placing the ECR critical field (875 G) just in front of the microwave window with a positive magnetic field gradient toward the direction of microwave propagation. These conditions produced a high absorption of microwave power and also prevented charged particles from escaping from the plasma.

In order to study the effect of magnetic field on etching, experiments with different magnetic field configurations were carried out. All these configurations satisfied the high mode plasma conditions. Table II lists the results of the etching experiments using same microwave power and the same pressure but different magnetic field conditions. The table is separated in three different groups corresponding to 3 different magnetic field configurations. The etching was carried out in 100% oxygen plasma. All samples were placed in the center of the M_2 coil where the highest plasma density was observed. The temperature of the sample holder due to plasma heating ranged from 373 - 473 K during the ten to twenty minutes of etching. This variation in temperature depended on the distance from the sample holder to the plasma source.

Table II shows that a reproducible, high etching rate of 100 nm/min was observed, in group 1. No surface damage is seen in the SEM micrograph of Fig. 3. The etching rates under high mode plasma were as high as 300 nm/min. at low microwave power, compared to etching rates of 20 nm/min. in the literature [1,7]. A number of identical experiments at other magnetic field configurations were carried out under the high mode condition, and these experiments confirmed the reproducibility of the etching rate. This reproducible highly anisotropic etching, (a big improvement over the previous results) is result of the high mode plasma, which can be precisely tuned and thus ensure reproducible etching rates.

Table II. Etching Under High Mode Plasma Conditions

Group	Sample No.	M_1(in m)	M_2(in m)	Etching Rate (nm/min)
1	1	0.15	0.48	100
	2	0.15	0.48	100
	3	0.15	0.48	100
2	4	0.20	0.46	280
3	5	0.20	0.43	310

Fig. 3 SEM micrograph of a single crystal diamond after etching in high mode plasma

In Table II, group 1 & 3, it can be seen that a three-fold variation etching rates was observed when only the magnetic field configurations were changed The only parameter varied was the position of coils which determine the magnetic field mirror ratio (difference between the peak value of the magnetic field and the value of the center point in-between the coils). The farther apart the two coils, the larger the mirror ratio. Under the high mode plasma conditions, the electrons will be accelerated near the microwave window where the ECR conditions (875 Gauss) is set. After being accelerated, the electrons travel along the converging magnetic field lines of M_1 and concentrate at the magnetic field peak position of M_1. The electrons move farther to the center of the mirror and reach the peak point where the sample holder is located. In the case of mirror ratios of about 1, as for groups 2 and 3, the magnetic field in the center is about the same as the peak value so that the electrons do not experience a divergent field and can reach the sample holder area. At large mirror ratio, when the magnetic field in the center is significantly less than the peak value of the coils, there will be divergent field from M_1 or M_2 to the center. The low field in the center has less confinement of the electrons than the high field because the Loretz force is proportional to the magnetic field. Therefore, when the high flux of electrons at M_1 move to the M_2 where the sample is located, some electrons are lost to the chamber wall and cannot reach the sample holder area and as a result the plasma density is low and a low etching rates. The marginal higher rate of sample 5 over that of sample 4 is also due to the flatter mirror for sample 5 configuration.

4. Summary

Diamond etching has been studied by varying the parameters such as pressure, microwave power, magnetic field etc. in order to optimize the etching process. It was found that the optimum pressure range is between 1 to 10 mTorr. As expected, high microwave power results in a high etching rate. Under high mode conditions high etching rates upto 300 nm /min., with good morphology and reproducibility were achieved. Higher etching rates were achieved when the magnetic mirror ratio was closer to 1.

5. References

1. M.W. Geis and J.C. Angus, Scientific American, Oct. 1992, 84.
2. S.A. Grot, R.A. Ditizio, G.SH. Gildenblat, A.R. Badzian, and S.J. Fonash, Mat. Res. Soc. Symp. Proc. **242**, 145 (1992).
3. A.J. van Roosmalen, J.A.G. Baggerman, and S.J.H. Brader, *Dry Etching for VLSI* (Plenum Press, New York, 1991).
4. A.J. Tessmar, K. Das and D.L. Dreifus, Diamond and Related Materials, **1**, 89 (1992)
5. F.I. Chen, *Introduction to Plasma Physics*, (Plenum Press, New York, 1974).
6. P.Bai, J. Liu, N.Parikh, M. Swanson, J. Vac. Sci. Technol. A **12**(1), (1994).
7. B.R. Stoner, G.J. Tessmer, and D.L. Dreifus, Appl. Phys. Lett., **62** (15), 1803, (1993).

ELECTROCHEMICAL SURFACE MODIFICATION OF DIAMOND

Pehr E. Pehrsson, Mike Marchywka[1], James P. Long[2], James E. Butler
Code 6174, Chemistry Division, Naval Research Laboratory, Washington, D.C.
20375-5342
[1]Code 7662, E.O. Hulbert Center for Space Sciences, Naval Research Laboratory,
Washington, D.C.
[2]Code 6686, Condensed Matter and Radiation Physics Division, Naval Research
Laboratory, Washington, D.C.

Abstract

An electrochemical etch technique enables separation of large-area diamond films from
diamonds by etching non-crystalline, sub-surface carbon generated by ion
implantation. The same electrochemical treatment selectively oxidizes the surface of
unimplanted semiconducting diamonds, Secondary electron microscopy (SEM),
ultraviolet photoelectron (UPS) and x-ray photoelectron (XPS) spectroscopy reveal
that the surface chemistry creates a region with air-stable, high secondary electron
emission, and possibly negative electron affinity.

1. Introduction

Much uncertainty remains about the link between surface chemistry and/or structure
and electron affinity on diamond. Negative electron affinity has been reported on
(100) and (111) diamond surfaces, and can be controlled by dosing with hydrogen and
heating to reconstruct the surface[1,2]. An electrochemical treatment used to generate
free-standing homoepitaxial diamond films from ion-implanted diamonds[3] also
selectively oxidizes unimplanted semiconducting diamonds. The hydrogenated and
oxidized regions display different secondary electron emission and provide insight into
the role of surface chemistry, especially oxygen and hydrogen, in the generation of
diamond surfaces with negative electron affinity (NEA).

2. Experimental

Natural, type IIB diamonds polished to within 2° of the (100) faces were placed on
edge *between, but not in contact with* two graphite electrodes spaced 2-5 cm apart

and immersed in a beaker of distilled water. The long crystal dimension was parallel to the inter-electrode axis. A 20-500V DC electric field was impressed in the medium by biasing the electrodes for times ranging from 30 to 300 seconds, which produced a current flow of <3 mAmp/cm^2 of electrode area. The samples were transported in air to a monochromatized (0.9 eV FWHM) small-spot XPS and analyzed with 1486 eV AlK$_\alpha$x-rays. Binding energies were referenced to the Au4f$_{7/2}$ peak at 83.93 eV from a piece of sputtered Au. Hydrogenated, plasma-oxidized, and electrochemically etched crystals were analyzed on beam line X24C at the National Synchrotron Light Source (NSLS), Brookhaven National Labs. Samples were biased at -5 V and interrogated with 33 eV photons. Photoelectron spectra were obtained using a double-pass cyclindrical mirror analyzer (CMA). The binding energies were referenced to the Fermi level of a piece of Au foil.

3. Results

The surface of the electrochemically treated diamonds was hydrophilic on the area closest to the cathode (the induced anode (IA)), while the side closest to the anode (the induced cathode (IC)) and the control hydrogenated diamonds were always hydrophobic. Ex-situ XPS confirmed that the O/C ratio on the hydrogenated samples was 1±0.3 atomic % and the C1S binding energy was 283.8±0.1 eV, with 0.9-1.1 eV peak widths. The XPS O/C ratios for all of the oxidized samples except the IA of the EC-treated diamonds were 10±2 atomic % with 284.7±0.1 eV C1S binding energies[4]. The XPS spectra of the IC and IA resembled the plasma hydrogenated and oxidized surfaces, respectively. The transition from the oxidized to the hydrogenated surface occurred largely within a roughly 400 μm region perpendicular to the inter-electrode axis, and corresponding to the border between the different wetting behaviors. The C1S and O/C ratio change from about 4% to 14% on the IC and IA, respectively, with corresponding C1S binding energies of 283.9±0.1 eV and 284.6± 0.1eV. The oxidized, hydrogenated and transition ("stripe") regions on the EC-treated diamonds exhibited comparatively low to comparatively high secondary electron emission intensities, respectively in an SEM (Fig. 1). Ultraviolet photoelectron spectroscopy (UPS) was used to explore the concurrent band structure changes. Spectra from the IC and IA (Fig. 2) resembled those of hydrogen and oxygen-plasma treated crystals, respectively. Oxidation decreased the kinetic energy of the valence band features by 0.7 eV, indicating downwards band-bending, and close to previously reported values for the C1S XPS spectra of oxidized and hydrogenated diamond[4]. The secondary threshold was determined by extrapolating the region of maximum slope to zero intensity. The "stripe" threshold was 0.2±0.1 eV lower in kinetic energy than on the hydrogenated surface, and 0.6±0.1 eV higher than on the fully oxidized surface. The stripe threshold was defined by a sharp (0.2 eV FWHM) peak similar to one attributed by other workers to NEA, specifically the emission of thermalized electrons from the bottom of the conduction band[2].

4. Discussion

The sharp UPS peak after the EC treatment indicates that neither water and other artifacts of the treatment nor air exposure suppressed the NEA property of the surface. While the role of surface contaminants in suppressing NEA on the deuterium plasma treated surface is not specifically addressed here, HREELS of such surfaces show them to be stable and highly resistant to contamination by hydrogen, hydrocarbons or water[5]. UPS showed that only the "stripe" region exhibited the characteristic sharp peak attributed to NEA, while fully hydrogenated surfaces had a much weaker peak or none at all, and the oxidized sides never had any. A surface dipole layer could explain the intense emission from the intermediately oxidized stripe region. Appropriately oriented surface groups, e.g. -OH, with the electronegative oxygen next to the diamond surface and the electropositive hydrogen outermost, could raise the conduction band minimum with respect to the vacuum level and accelerate surface electrons into vacuum. Results by one of the authors (PEP) suggest that the initial oxidation of hydrogenated C(100) surfaces generates hydroxyl groups, while carbonyl groups dominate with continued oxidation[5].

Conclusions

The electrochemical treatment selectively oxidizes semiconducting diamonds, altering the electron emission and inducing possible negative electron affinity . The secondary electron emission properties change depending on whether the surface is terminated with oxygen or hydrogen, with a possible role in the electron affinity played by both a dipole layer and band-bending.

5. Acknowledgements

6. References

1. B.B. Pate, W.E. Spicer, T. Ohta, I. Lindau, J. Vac. Sci. Technol., **17**(5), 1087 (1980)
2. J. van der Weide, R.J. Nemanich, J. Vac. Sci. Technol. B, **12**(4), 2475 (1994)
3. M. Marchywka, P. E. Pehrsson, D.J. Vestyck, Jr., D. Moses, Appl. Phys. Lett., **63**(25), 3521 (1993)
4. P.E. Pehrsson, Proceedings of the 3rd Intl. Symp. on Diamond Materials, V. **93-17**, 668, The Electrochemical Society, Pennington, N.J., 1993
5. Pehr E. Pehrsson, Proc., 187th Mtg. of the Electrochem. Soc., paper 245, Reno, Nev., May 21-26, 1995

Figure 1. A scanning electron micrograph (x20) of a 4 x 4 mm C(100) diamond after electrochemical treatment. The IC (hydrogenated) is on top, the IA (oxidized) is below, separated from the IC by the "stripe" transition region.
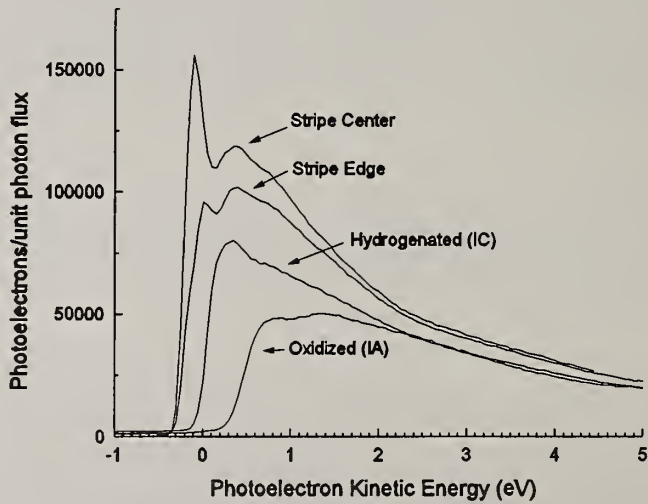
Figure 2. Ultraviolet (33 eV) photoelectron spectroscopy (UPS) from the crystal shown in Fig. 1. The transition region shows the narrow peak attributable to negative electron affinity. Neither the IA nor the IC exibits the NEA peak.

Applications of Diamond Films and Related Materials: Third International Conference, 1995
Editors: A. Feldman, Y. Tzeng, W. A. Yarbrough, M. Yoshikawa, and M. Murakawa

271

LASER POLISHING OF DIAMOND FILMS

P. Tosin, W. Lüthy, and H.P. Weber

Institute of Applied Physics, Sidlerstr. 5, CH-3012 Berne, Switzerland

Key words: absorptance, diamond, laser polishing, ripples

Abstract

We have studied pulsed laser polishing of faceted CVD-diamond films as a function of laser fluence and angle of incidence. A fluence above the ablation threshold leads to polishing by graphitization and subsequent sublimation. The more inclined the laser beam the smoother the surface. Reduction of roughness R_a from 1 μm to below 0.1 μm is achieved. At an angle of incidence α larger than a critical angle α_{crit}, however, a surface instability occurs. This is revealed by the formation of a periodic grating structure which perpetuates itself across the surface irradiated with overlapping pulses. The spacing of the ripples is typically 10 μm. They are oriented parallel to the plane of incidence, irrespective of the laser wavelength or the polarization. Neither diffraction nor interference effects can therefore be the cause for the rippling. Rather, a shadowing effect is shown to initiate the corrugation. The occurrence of permanent ripples poses a limit to the laser polishing of rugged diamond films. However, rippling is avoided and significantly smoother films result (with an average roughness of 33 nm compared to the 0.1 μm mentioned above) by rotation of the diamond film during laser processing.

1. Introduction

Laser polishing of CVD-diamond films is a promising technique in view of thermal, optical, electronic and tribological applications [1]. A processing time of the order of a few minutes per cm^2 is possible [2]. This compares favourably with other polishing techniques mainly due to the high ablation rate of the laser treatment. The higher the angle of incidence the smoother the resulting surface. When the diamond film was reciprocated during ArF laser irradiation incident at 80°, a reduction of roughness R_a from 1 μm to below 0.1 μm was achieved [2].

However, when the laser beam is inclined above a critical angle α_{crit}, ripples

develop which prevent further improvment of the polishing [2,3]. They lie parallel to the plane of incidence, exhibit a spacing of typically 10 µm and propagate over the whole irradiated area upon irradiation with overlapping pulses. Such corrugations often result from an inhomogeneous temperature distribution due to an irradiance modulation imposed by an interference effect. This causes locally different etch rates or liquid flows [e.g. 4,5]. In the case of diamond, interference effects may not dominate the production of the ripples but a two-step mechanism which rests upon shadowing was outlined [3].

Here we discuss the development of the ripples on the basis of locally different angles of incidence inducing varying absorption. We show how the ripples can be avoided and a substantially smoother surface ($R_a = 33$ nm) is accomplished.

2. Experimental details

Synthetic diamond films were deposited on silicon and tungsten substrates employing a dc discharge plasma CVD technique. The films with thicknesses up to 30 µm exhibited a pyramid-like morphology with an average roughness of 0.3 µm. The grain size was a few micrometers.

Laser irradiation was performed using an ArF laser (193 nm) with a pulse duration of 20 ns. The laser beam was focused onto the diamond film with two cylindrical lenses. The sample was displaced normally to the line focus with an overlap of 80% between consecutive laser pulses. The processed area was typically a few mm^2 with a fluence of $1.8 - 30$ J/cm^2. In order to obtain continuous ripples the angle of incidence α was set to 85°.

3. Results and discussion

Fig. 1(c) shows the fully developed corrugations obtained after laser irradiation at an angle $\alpha > \alpha_{crit}$. Interference effects were shown not to initiate rippling because the spacing was independent from wavelength [3]. In addition, if it were the result of an interference effect, one would expect a more regular pattern.

Fig. 1(a) - (c) shows the temporal evolution of the ripples starting with the unirradiated film (a), while (b) represents an intermediate stage. Fig. 1(c) depicts the final pattern. It is seen from micrograph (b) that at first short ridges remain unetched in the shadow of the grains. The inclination of these ridges corresponds to the angle of incidence of the impinging laser beam. In a second step, with further laser irradiation, these randomly distributed ridges join together to form continuous ripples.

(a) unirradiated film   (b) after 150 pulses   (c) after 6350 pulses
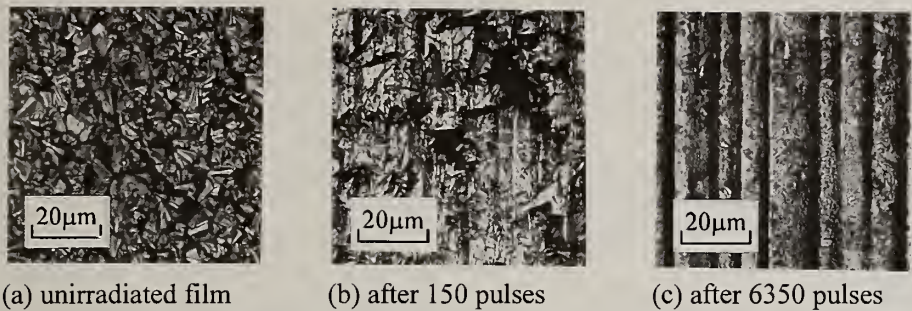
Fig. 1. Temporal evolution of the ripples. The ArF laser fluence was set at 25 J/cm^2. The beam was incident from the bottom at an angle α of 85°.

Fig. 2 shows the cross section of three grains irradiated from the bottom. The shaded areas indicate the material removed upon laser treatment. Basically it is assumed that a certain amount of energy results in the ablation of always the same amount of diamond irrespective of the grain orientation, neglecting a nonzero ablation threshold. This is taken into account by a constant ablation depth d in the direction of the laser beam. In Fig. 2(a) an absorptance of 1 is supposed for all grain faces. The higher the azimuthal angle φ the smaller the ablation depth normal to the surface (see Fig. 3 for the definition of the grain face orientation with respect to the laser beam). In Fig. 2(b) the absorptance A for unpolarized radiation is taken into consideration. It decreases with rising local angle of incidence with the consequence that grain faces with a large φ are even less strongly etched than in (a).

The energy absorptance A in a grain can be calculated from Fresnel's formulas for the amplitude reflection coefficients assuming that the unreflected part of the laser beam is completely absorbed. The result is shown in Fig. 4 for a real part of the refractive index of 3 for diamond at 193 nm. The parameter α is the angle of incidence with
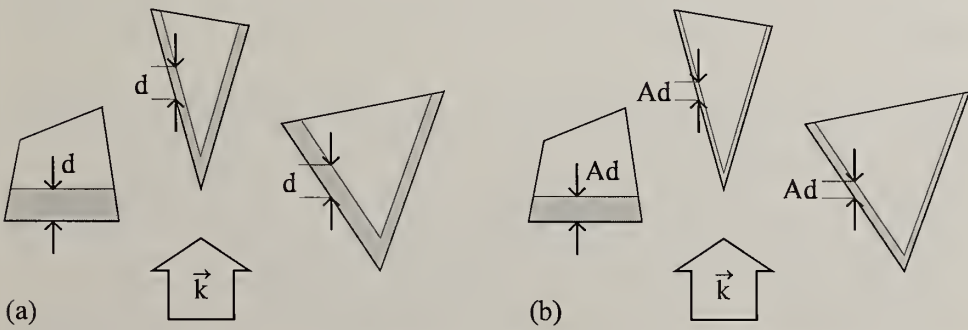
Fig. 2. Laser ablation of diamond grains under the assumption that the absorptance A equals 1 for every grain face (a) or A < 1 for the respective face (b).

274
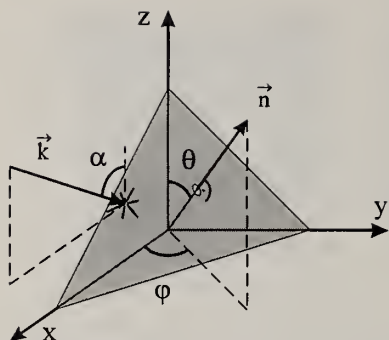
Fig. 3. Geometry.
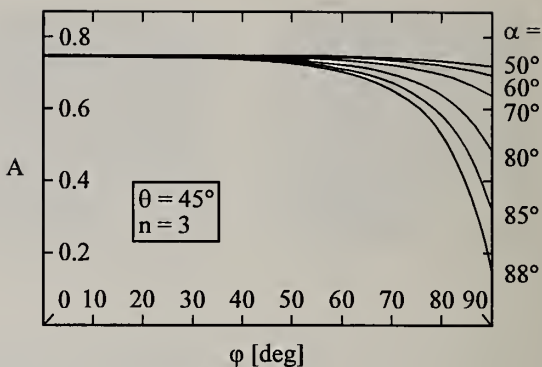
Fig. 4. Absorptance.

respect to the sample normal. It can be seen that grazing incidence above ~85° causes A to drop by a factor of $\gtrsim 2$ when φ is varied from 0 to 90° while this decrease is very moderate for angles of incidence up to 70°. The inclination θ of the grain faces is of minor importance for high α's.

From these calculations we deduce that the generation of ripples is due to (i) shadowing as long as there are asperities raising above the surrounding and (ii) the strong decrease of the absorptance for surfaces oriented with φ nearly 90°, when the angle of incidence is high enough. Surface features with this orientation cannot vanish when the azimuth of the laser beam remains unchanged. When a diamond film is rotated during laser irradiation under 85° ripples do no longer occur, and the roughness R_a drops to only 33 nm [3].

4. References

1. B. Bhushan, V.V. Subramaniam and B.K. Gupta, Diamond Films and Technology 4 (2), 71 (1994)
2. P. Tosin, A. Bächli and A. Blatter, Proc. of 8th Cimtec − World Ceramics Congress and Forum on New Materials 1994 (in print)
3. P. Tosin, A. Blatter and W. Lüthy, (submitted in January 1995)
4. P.E. Dyer and R.J. Farley, Appl. Phys. Lett. 57 (8), 765 (1990)
5. T. Anthony and H. Cline, J. Appl. Phys. 48 (9), 3888 (1977)

Femtosecond Laser Processing of CVD-Diamond

P. A. Molian[1] , Richard Windholz[1],
A. P. Malshe[2], G. J. Salamo[2], H.A. Naseem[2] W.D. Brown[2], and Uwe Stamm[3]

[1]Mechanical Engineering, Iowa State University, Ames, IA 50011
[2]High Density Electronic Center, University of Arkansas, Fayetteville, AR 72701
[3]Lambda Physik, Gottingen, Germany

Keywords: diamond, excimer, femtosecond, laser, machining

Abstract

The feasibility of a 100-femtosecond (fs) pulsed 248-nm UV excimer laser for scribing and blind hole drilling of free-standing diamond was investigated. Raman microprobe analysis, scanning electron microscopy (SEM) and surface profilometer measurement, used to characterize the laser irradiated zones, indicate that fs-laser offered a greater degree of atomization of material removed, reduced thermal component of ablation, absence of clusters and particulates on the machined surfaces, and absence of transformation of diamond to graphite. All these effects are attributed to a new spectrum of fs laser-diamond interactions.

1. Introduction

The state-of-the art CVD-diamond growth technology leads to diamond films with large surface roughness, wavy patterns due to stress-related phenomena, and impurities such as graphite. In wear applications, the surface roughness can cause irreparable damage to the mating part, and in electronics applications, the roughness affects the thermal management characteristics via insufficient resistance and also seriously affects the reproducibility of performance. In optical applications, transmittance of light through the rough side and the smooth side is known to be different. Such examples establish a crucial need for smoothing of CVD-diamond.

Recently, the laser beams have been considered for precision machining of diamond. Among the different lasers, UV-excimer laser appears to be the most appropriate. For example, a study [V.P. Ageeve et al., *Sov Phys Dokl*, v.33, no.11, Nov. 1988, p.840] showed that appreciable material removal (over 300 Å per pulse) occurred with nanosecond (ns) UV-excimer laser as compared to CO_2 laser. In addition, the CO_2 laser generated cracks and linear periodic structures with a period close to that of wavelength. Excimer laser machining of diamond with nanosecond pulses involves two-steps: the transformation of diamond to graphite in the first few laser pulses followed by the sublimation of graphite with the additional laser pulses. Formation of graphite in addition to thermal damage seriously affects the precision and contamination.

Pulse width is a key parameter that affects the length of laser-induced reaction, laser-induced shock wave pattern, characteristics of plasma, and dynamics of ablation products in laser machining. Although ns-pulsed laser effects on diamond machining are fairly known, no work has been reported on the effect of fs-pulsed laser. In this work, laser machining of free-standing diamond films was investigated using a 100 fs-pulsed UV laser (248-nm).

2.   Experimental Details

Free-standing diamond film specimens of nominal thickness 0.5 mm (triangular inserts) and surface roughness of Ra = 0.6 μm were obtained from General Electric Superabrasives Division. A 100-fs pulsed 248-nm laser (Lambda Physik's FAMP system with UV-Amplifier Module) was used for scribing and drilling diamond specimens. The beam was sent through a circular aperture and was focused by a 100-mm focal length lens to a spot diameter of 125 μm. The processing was carried out in ambient with the following parameters: pulse energy 0.2 mJ, and pulse repetition rate 5 Hz. Three blind holes with 10, 50, and 100 pulses and a scribe line of length 0.5 mm at a speed of 1 pulse per μm were made. SEM, microRaman spectroscopy and DekTak II surface profilometer (resolution 3000 Å) were employed to characterize the laser irradiated zones.

3.   Results And Discussion

Figs. 1 and 2 shows the SEM micrographs of fs-laser scribed line and blind-holes. For the scribed line, the depth was 2.3 μm giving a material removal rate of 3×10^{-6} mm^3/pulse. The hole depth, shown in Figure 2, was measured to be 2.36 μm for 100 pulses giving an average etch depth of 236 Å/pulse for an energy fluence of 1.6 J/cm^2. Detailed analysis of features revealed relatively smooth surfaces and absence of particulate formation. There is no evidence of physical degradation such as cracking or surface melting on the processed surface. Fig.3, the Raman spectra for the free-standing diamond film before and after laser processing, indicates that the intensity level of as-received film is stronger than that of laser treated film probably because of the changes in the surface roughness and surface orientation. Further a comparison of the spectra shows that there is absence of amorphous carbon (~ 1550 cm^{-1}) and graphite (~ 1350 cm^{-1} and 1580 cm^{-1}). This strongly suggests that fs-laser , unlike ns-laser, is capable of preventing the formation of non-diamond phases. This is attributed to the extended heating of diamond by the ns-laser and to the resonant transient reaction below threshold energy density by the fs-laser.

The material removal depth per pulse per energy fluence is higher for fs-laser (138 Å/pulse/J/cm^2) compared to the nanosecond (40 Å/pulse/J/cm^2) laser. This is due to extreme intensities (which leads to high rate of coupling energy) and larger absorption depth/thermal diffusion distance ratios offered by the fs-pulses. In fs-

pulse regime heating of diamond, the absorption depth (about 10^{-3} cm for diamond by UV lasers) is much larger than the thermal diffusion distance (about 10^{-6} cm for 100-fs pulse, and 10^{-3} cm for 1-ns pulse). As a result, the heat is deposited in a thin layer and the evaporation temperature can be reached at modest energy fluence. It is important to emphasize that evaporation occurs after the fs-pulse because there simply is not enough time for the atoms to move and to establish a steady-state evaporation regime. With fs-laser irradiation, the energy is supplied to the carriers in a shorter time than the time necessary for the energy exchange with the lattice. Thus, fs-pulses create an extremely hot carrier gas in a cold lattice, and subsequent energy transfer to the phonons results in thermal evaporation that occurs after the fs-pulse. Plasma formation is not expected to occur due to the shorter time frame.

We believe that the following contribute to the observed results: 1. laser interaction time (10^{-15}s) which is much shorter than that of free time between lattice collisions and hence diamond layers are not heated while absorbing laser radiation; 2. laser-induced plasma formation occurs after the photon absorption process is complete; 3. laser-induced absorption is resonant in the lattice and hence process is well controlled and homogeneous; and 4. resonant transient reaction below threshold energy density may not cause diamond transformation as much as in nanosecond laser.

4.   Conclusion

Femtosecond pulsed, UV-excimer laser is capable of providing cleaner and better controlled machining for CVD-diamond in terms of laser-induced mechanical damage, contamination and graphitization.

5.   Acknowledgements
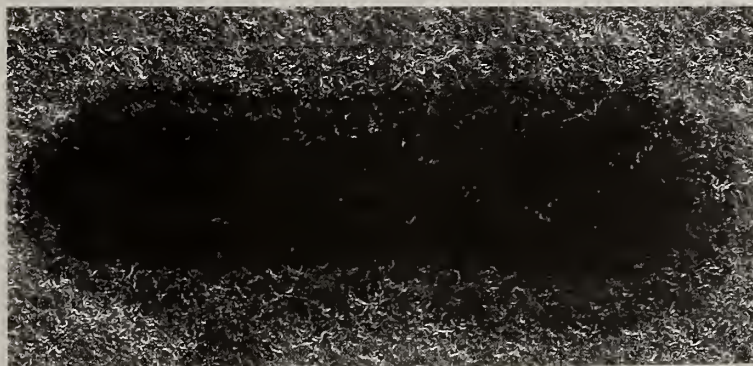
Fig.1. SEM micrograph showing the scribed line, Magnification: 150X

278
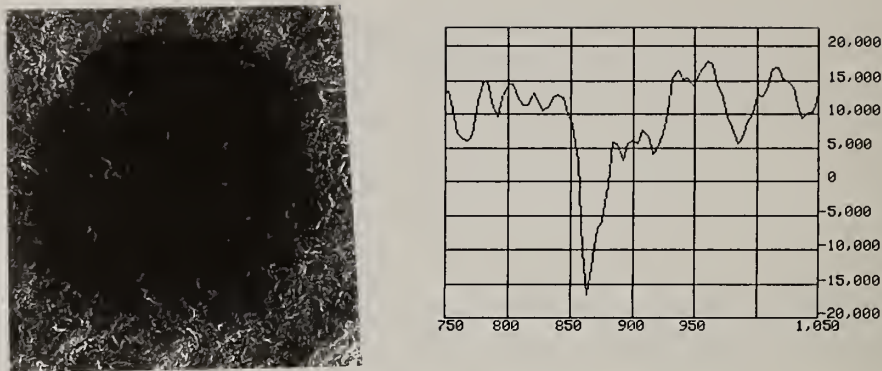
Fig.2　SEM micrograph (300X) and surface profilometer trace of the hole
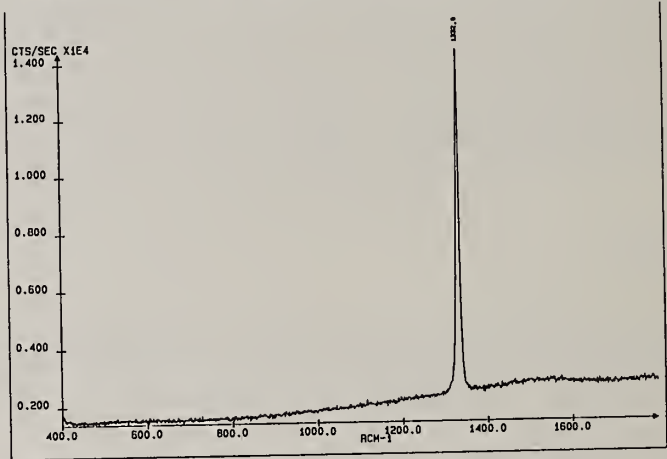
Fig.3.　Raman spectrum of as-received film
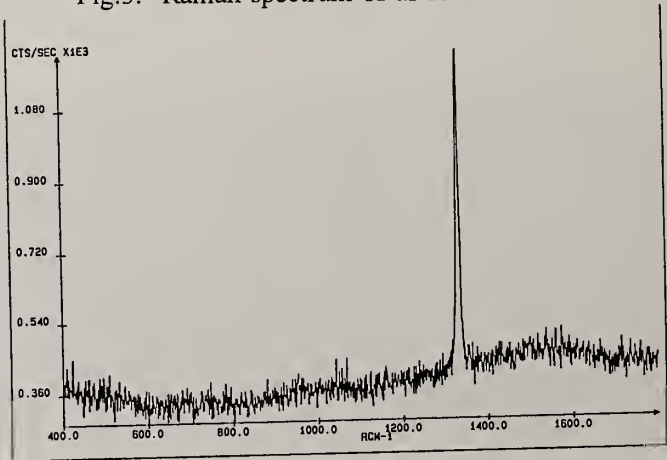
Fig.4.　Raman spectrum of laser irradiated zone

Applications of Diamond Films and Related Materials: Third International Conference, 1995
Editors: A. Feldman, Y. Tzeng, W. A. Yarbrough, M. Yoshikawa, and M. Murakawa

279

LASER PROCESSING OF DIAMOND SUBSTRATES FOR MULTICHIP MODULES: PART I

J. Johnson, A. P. Malshe, E. Callens, S. Jamil, and M. H. Gordon

High Density Electronics Center, University of Arkansas, Fayetteville, Arkansas, USA.

Key words: diamond, MCM, drilling, ablation, numerical simulation, CVD

Abstract

Experimental and numerical data were acquired to study the laser ablation of diamond process for application to multichip modules. Results indicate that plasmas severely limit the thermal efficiency of the process. If the power density exceeds 6.0×10^9 W/cm^2, atmospheric air ionizes and absorbs up to 90% of the beam's energy before it reaches the target. At lower power densities, air breakdown is avoided, but plasmas comprising ablated material hinder the ablation process. As a result, optimal efficiencies obtained with a Nd:Yag Q-switched pulsed laser were limited to 5-10%.

1. Introduction

The trend towards integrated circuit miniaturization has created a need for improved thermal management methods. A potentially viable approach utilizes CVD diamond as a heat spreader. In addition to diamond's high thermal conduction coefficient (5 times that of copper at room temperature), diamond's low coefficient of thermal expansion, high electrical resistivity, and high strength make it an ideal material for backing densely packed, high power circuits.

Three-dimensional multichip modules (MCMs) will dramatically increase computational rates, but their increased power densities will require efficient thermal management. For CVD diamond to meet this requirement in functioning MCMs, additional technologies will need to be developed. For example, fabrication of MCMs will require cutting, polishing, planarizing, drilling, and metalizing the diamond. Our study here concerns the drilling of microvias (~80 μm in diameter) required for interlayer connection in the MCM. Polishing and metalization issues are explored in a companion paper [1]. Experimentally, we drill the microvias with a 10 Hz Nd:Yag laser (10 ns pulse duration) frequency doubled to 532 nm (3-300

mJ/pulse). For all experiments described in this paper, we have focussed the laser beam onto the diamond target with a 100 mm focal length lens. In parallel, we have developed a numerical model of the laser-diamond ablation process. Experimental and numerical data have been used to determine the optimal combination of parameters for quickly drilling defect-free microvias.

2. Numerical Simulation

The numerical code simulates laser drilling with a focused Gaussian beam by solving the two-dimensional (cylindrical) heat diffusion equation with the appropriate boundary and initial conditions [2]. Inputs for the code include: laser power, diamond dimensions, focusing parameters, pulse duration, pulse frequency, temperature dependent properties, duration of incremental time steps, and the number of finite elements. The simulation outputs include: the number of pulses required for drilling the microvia, the isotherms in the remaining material, and the microvia profile.

3. Results and Discussion

Initial results demonstrate the important effect of plasmas on the drilling process. We find that when the power density of the laser exceeds 6×10^9 W/cm^2, air breakdown occurs and reduces the amount of energy reaching the diamond surface. This value is consistent with previously published values [3]. This air breakdown absorbs up to 90% of the incoming energy. Additionally, at any power density sufficiently large to cause material removal, a plume is observed directly above the irradiated diamond. This plume is presumably a carbon plasma which absorbs and/or scatters the incoming laser radiation. To limit the role of the ambient air plasma, and to enable further study of the carbon plasma, we plan to drill in vacuum conditions.

Because of plasma losses for one particular set of data, the fastest drill through times that we experimentally obtain are near 70 s (@ 53 mJ/pulse). We expect faster times in vacuum conditions because we can go to higher powers without losing energy to air breakdown. However, the production of the carbon plasma will likely prevent attaining drill through times which are theoretically predicted by our model (0.4 s). Numerical simulations predict drill-through-times that are one to three orders of magnitude less than those experimentally determined (Fig. 1). Note that the discrepancy is largest at higher pulse energies indicating larger plasma losses with increasing energies. Although numerical simulations predict faster drill through times with increasing energy pulses, experimentally, high energy pulses are not desirable. Even if plasma losses could be eliminated, experimental data show that high energy pulses promote cracks in the diamond substrate which are not observed at lower energies. If these cracks are caused by thermal shock, they likely cannot be suppressed by drilling in a vacuum.

Another important parameter in the drilling process is the location of the focal point with respect to the diamond (Fig. 2). Note the lines representing the top and bottom surfaces of the diamond. The data are plotted at the location of the focal point relative to the diamond sample. Fig. 2 shows that the optimal location of the focal point (relative to the diamond) is a function of the laser beam energy. At higher powers, experimental data indicate that the fastest drill through times are achieved with the laser focused 0.2 mm below the bottom of a 0.83 mm thick diamond substrate. In contrast, at lower powers the fastest drill through time is achieved with the laser focused just below the top surface. This effect is a result of the air plasma. By focusing below the diamond substrate at higher powers, much of the laser energy is absorbed in the diamond sample before reaching the point where air breakdown occurs. However, our model predicts, and the low power data confirm, that the theoretical optimum occurs when the focal point is near the diamond surface.
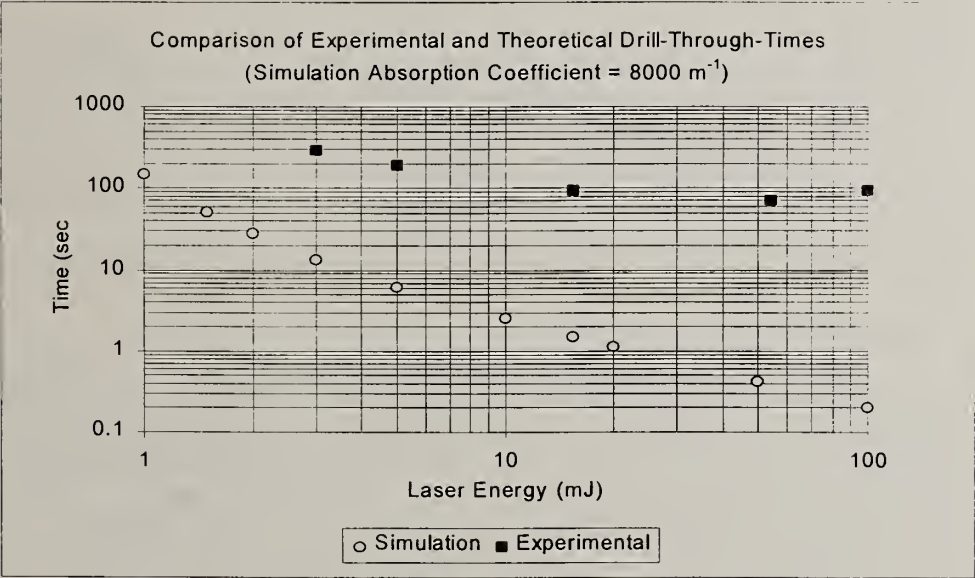
Fig. 1: *Plasma effects on experimental drilling times.*

The thermal efficiency of the drilling process is defined here as the minimum energy required to ablate the empirically determined volume of diamond divided by the energy supplied by the laser source. The maximum thermal efficiency we have achieved in atmospheric air is near 10%. The thermal efficiency predicted by the simulation approaches 100% as the laser beam's power density reaches 10^9 W/cm^2. The predicted efficiencies drop rapidly at laser power densities below 10^8 W/cm^2 because of thermal conduction losses.
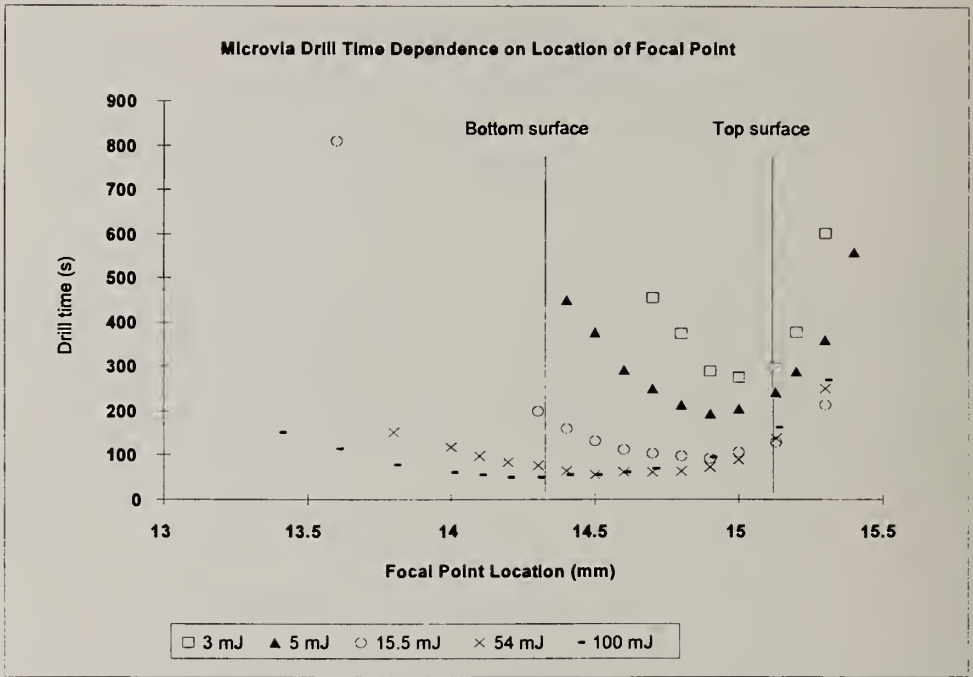
Fig. 2: *Via formation time vs. location of diamond with respect to focal point.*

5. Conclusions

The formation of both air and carbon plasmas during laser ablation of a diamond film is the primary hindrance in developing an efficient drilling process. Computer simulations which do not account for these plasmas predict drilling times which are orders of magnitude faster than experimentally observed. In addition, this discrepancy is found to increase with increasing power densities. The individual roles of the two plasmas will be studied further using experiments in vacuum conditions which should minimize air breakdown.

6. References

1. Jamil, S., M. H. Gordon, G. J. Salamo, H. A. Naseem, W. D. Brown, and Malshe A. P., 1995 NIST Applied Diamond Conference.
2. Gordon, M. H., M. Touzelbaev, M. Xiao, and R.C. Goforth, HTD-Vol. 289, ASME Winter Annual Meeting, 73, (1994).
3. Fowler, M. C. and Smith, D.C., Journal of Applied Physics, 46, 138, (1975).

Applications of Diamond Films and Related Materials: Third International Conference, 1995
Editors: A. Feldman, Y. Tzeng, W. A. Yarbrough, M. Yoshikawa, and M. Murakawa

283

LASER PROCESSING OF DIAMOND SUBSTRATES FOR MULTICHIP MODULES: PART II

Syed Jamil, M.H. Gordon, G.J. Salamo, H.A. Naseem, W.D. Brown and A.P. Malshe

High Density Electronics Center (HiDEC), University of Arkansas, Fayetteville, AR 72701

Key words: diamond, laser, MCM, metallization, polishing

Abstract

The development of new techniques for post-synthesis processing such as polishing and metallization is of intense current interest due to the potential use of diamond as an MCM thermal management substrate. In our laboratory, we have been able to demonstrate chemically clean laser induced coarse polishing and selective laser-assisted metal deposition on diamond substrates. Our technique is based on the use of a liquid ambient as a reactive medium for the laser processing of diamond substrates.

1. Introduction

Rapid changes in the electronic industry are driven by the attractiveness of faster, smaller, and lighter weight electronics. Much of the real estate on a typical semiconductor wafer is occupied by interconnecting electrical lines. The electronic "chips" themselves are so small that a further reduction in chip dimension would not appreciably reduce the size or weight of the electronic package, nor would it result in faster speed of operation. One solution to this obstacle is the concept of the MCM. The term MCM refers to the concept of developing high density electronics by reducing the space taken by interconnects by using multi-layered structures.

For the MCM concept or any high density electronic packaging concept to be successful, thermal management is an essential requirement. High density means high power dissipation. As chips are packed closely together the power density levels are very high. Since CVD diamond has a very high thermal conductivity (1000-1500 W/m°C), and is now available at a reasonable cost, it is now plausible to consider free

standing diamond substrate material for building MCMs [1,2]. Diamond substrates would also bring the benefits of good electrical insulating properties as well as low thermal expansion, (1ppM/°C) compatible with that of silicon, both aspects very important to the development of high density electronics [2].

Probably, the two other more noted attributes of diamond, are its hardness and chemical inertness at room temperature. These attributes mean that the smoothening of CVD-diamond substrates is more difficult than most of the other materials [3]. Another difficulty in working with diamond in high density applications is metallization. For example, it is necessary to pattern conducting lines and coat the inside of via holes with a conductive material [2,4]. This is difficult considering via holes for high density applications will be on the order of 50 to 100 microns. Both of these problems, however, can be addressed using a single technique: Laser-induced reactions in a liquid environment [5].

2. Concept

When laser induced smoothening occurs in air, only a fraction of the energy of the laser pulse goes to the removal of diamond; a significant portion of the energy is absorbed by the plasma which is formed by the ionization of air molecules. Consequently, the system is very inefficient as only a small portion of the laser energy is actually responsible for the removal of diamond. In the case of laser-induced polishing in water, we suspect that the liquid suppresses the plasma (perhaps by providing a physical 'barrier' against the expanding carbon plasma made up of sublimed substrate atoms) . As a result, a significantly higher portion of laser energy is expended in the removal of diamond. The most intriguing outcome is that, we have not observed any graphite formation possibly due to the generation of OH, O and H radicals at diamond : water interface. It is well known that the they selectively etch graphite sp^2 bonded carbon species.

For metallization, the diamond substrate is immersed in a liquid compound containing the conducting material to be deposited. Laser energy is then employed to decompose the compound which leads to the formation of the conducting material. The conducting material is then deposited on the diamond surface. Thus, by scanning the laser beam over the diamond surface, we can deposit an electrical connection from one spatial point to another spatial point on the substrate. Since the laser beam can be focused tightly, the resulting interconnecting lines of a few microns widths would be possible. In addition, one could envision the same technique for coating via holes with conducting material. The schematic of the apparatus is depicted in Fig. 1.

3. Results

In our study, we have found that keeping the diamond sample immersed in liquid leads to high quality coarse polishing of the sample. Preliminary result on coarse polishing is shown in Fig. 2. It shows the SEM micrographs of untreated and laser treated diamond surface in water ambient. Total processing time is 3 seconds on 4 mm² area. We have observed that the laser treated surface in liquid (water) is

chemically cleaner (free of laser-induced graphitic contamination) as confirmed by Raman Spectroscopy than those in air or vacuum. In the manufacturing process, once the coarse material is removed, the sample can be planarized quickly by using a technique developed at HiDEC, University of Arkansas [6]. Much investigation remains to be completed to determine exactly what is happening in order to optimize the parameters.

While the laser can be used to ablate or take away material, it also can be used to add material. That is, the laser can selectively enhance deposition. The SEM picture in Fig. 3 clearly shows a copper line which was deposited on a diamond substrate immersed in a "selected" liquid when a focused laser beam was scanned over its surface. Existence of copper was confirmed by energy dispersive x-ray analysis (EDS). While we have had early success with this technique much work needs to be done to control and to optimize it. For example, here again the choice of the material and laser wavelength are crucial to the concept of the laser enhanced deposition process. The same technique could just as easily be applied to small via holes as to laying down conducting lines.

4. Summary

Although, laser induced polishing has been studied by other researchers, our approach in using a liquid host is unique, and preliminary results on coarse polishing are promising. In addition, we have been successful in using a laser to deposit conducting material from a liquid onto diamond surfaces.

5. Acknowledgement

6. References

1. A.P. Malshe, S. Jamil, M.H. Gordon, H.A. Naseem, W.D. Brown, and L.W. Schaper, *Advanced Packaging* (accepted for publication, 1995)
2. T.J. Moravec, R.C. Eden, and D.A. Schaefer, Proc. of 1993 Int. Conf. and Exhi. on MCMs, 85 (April 1993).
3. H.A. Naseem, A.P. Malshe, R. Beera, W.D. Brown, and L.W. Schaper, Eighth Int. Conf. on VLSI design, New Delhi, India (January 1995).
4. I. Meyÿappan, A.P. Malshe, H.A. Naseem, and W.D. Brown, *Thin Solid Films* (accepted for publication, 1995).
5. S.B. Ogale, A.P. Malshe and S.T. Kshirgar, *Solid State Communications,* <u>84</u>(4), 371(1992).
6. A.P. Malshe, J.G. Glezen, H.A. Naseem, W.D. Brown, and L.W. Schaper, *4th Int. Conference and Exhibition on Multichip Modules*, Denver (Organized by ISHM, IEPS, EIA, IEEE, and CPMT), Denver, CO, April 19-21, 1995 (accepted for presentation).
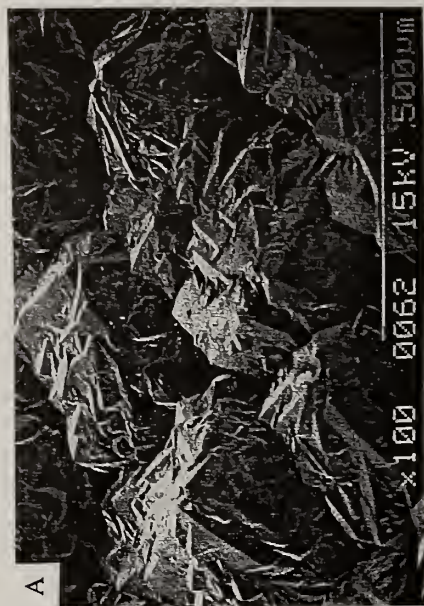
SEM micrograph of diamond films
A) before polishing and B) after polishing
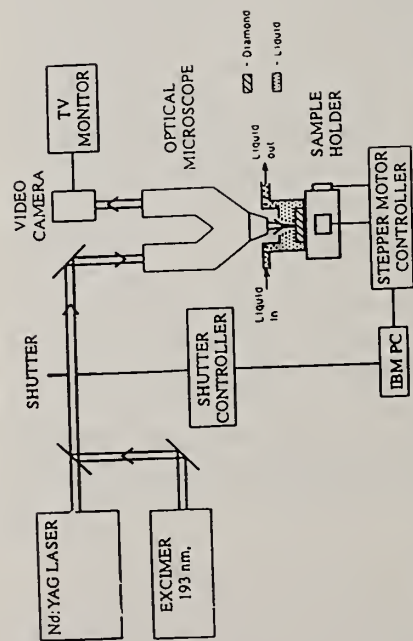
Figure 2

Figure 1: Schematic of the laser porocessing station
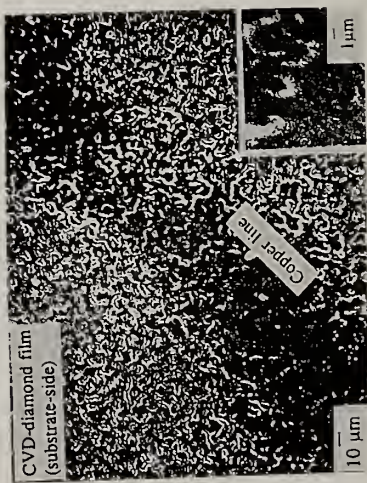
Figure 3: SEM micrograph of laser induced copper
deposited region of diamond film.

DIAMOND GROWTH
AND
GROWTH
CHARACTERIZATION

Applications of Diamond Films and Related Materials: Third International Conference, 1995
Editors: A. Feldman, Y. Tzeng, W. A. Yarbrough, M. Yoshikawa, and M. Murakawa

289

PREPARATION OF HIGHLY ORIENTED DIAMOND THIN FILM BY MICROWAVE PLASMA–ASSISTED CHEMICAL VAPOR DEPOSITION

Hideaki Maeda, Miki Irie, Kyo Ohtsubo, Nobutaka Ohya, Katsuki Kusakabe
and <u>Shigeharu</u> Morooka

Department of Chemical Science and Technology, Kyushu University
6–10–1, Hakozaki, Higashi–ku, Fukuoka 812–81, Japan

Abstract

A highly–oriented diamond thin film was synthesized on a Si (100) wafer by a multi–step microwave plasma chemical vapor deposition (multi–step MPCVD) process. The Si substrate was carburized in a mixture of CH_4 and H_2 without bias and then with a negative bias. The "mesh structure" oriented to the Si (100) was important as an indicator of oriented nucleation. Diamond nuclei were grown to [100] until most of randomly oriented nuclei were buried by {111} faces. The conditions were then switched to those preferred for the [111] growth. This procedure led to a highly [100]–oriented film, but steps between crystallites still remained. Finally $CO2$ was introduced and MPCVD was continued. A remarkably smooth diamond film was thus obtained.

1. Introduction

Formation of large–area single crystalline diamond film is one of the goals of CVD diamond research because of its great potential for application to microelectronic devices. Yugo et al. [1] found that negative biasing was very promising to promote the diamond nucleation on an Si surface. This bias treatment is also effective in controlling the orientation of diamond nuclei on a foreign substrate. Stoner et al. [2], Jiang et al. [3], Wolter et al. [4] and Maeda et al. [5,6] synthesized [100] oriented diamond films on Si or SiC substrates by bias–enhanced MPCVD. In the present study, diamond was synthesized on a Si (100) substrate by a bias–enhanced MPCVD from a gas mixture of CH_4 and H_2. The effects of reaction conditions on nucleation and growth rate of diamond were investigated in detail. Based on these experimental results, reaction conditions were optimized and a highly oriented and smooth diamond film was formed on an Si (100) surface.

2. Experimental

The substrate was a cleaned p–type (100) Si wafer, 5 mm by 10 mm in size, and was placed in a microwave cavity of 2.45 GHz frequency. The substrate temperature was determined optically and was varied by adjusting the microwave power. Gaseous reactants were CH_4, H_2 and CO_2. The substrate holder, made of molybdenum, was usually coated with diamond film prior to the reaction. The upper electrode was molybdenum wire of 2 mm diameter, placed 3 cm above the substrate. The molybdenum wire was used without any coating. Details of the experimental setup was reported elsewhere

[6,7].

Morphology and microstructure of deposits were observed by field–emission scanning electron microscopy (FE–SEM, Hitachi S–900) and field–emission transmission microscopy (FE–TEM, Hitachi HF–2000). Diamond film was characterized by X–ray photoelectron spectroscopy (XPS, Shimadzu ESCA–850) and reflection high–energy electron diffraction (RHEED, Shimadzu μRHEED–2). Film quality was determined by Raman spectroscopy (Laser Raman Spectrophotometer, Jasco NR–1100) using the 514.5 nm line of an Ar ion laser.

3. Results and Discussion

The substrate was first carburized at 830°C without bias. After the carburization, a silicon carbide (Si–C) peak appeared at 100.6 eV in XPS diagram. The carburized surface was very flat, and no change in the surface morphology was detected with the FE–SEM before and after the carburization. The SiC layer, however, was indispensable for deposition of oriented diamond nuclei.

Next, a negative bias was applied and MPCVD was continued. The Si–C peak of XPS rapidly increased, and the morphology of the Si (100) surface was greatly changed as shown in **Figs. 1** (a)–(d). At 1 min after the start of bias treatment, a characteristic pattern on a nanometer scale was formed on the substrate. This pattern tended to orient relative to the (100) face and was observed more clearly after 5 min. This "mesh structure" was important as an indicator for the subsequent formation of oriented diamond film. Results of RHEED and FE–TEM show that the mesh structure was composed of a SiC layer oriented to the Si (100) substrate. Diamond particles are observed as bright

(a) 1 min   (b) 3 min

$[011]$

$[01\bar{1}]$

(c) 5 min   (d) 10 min
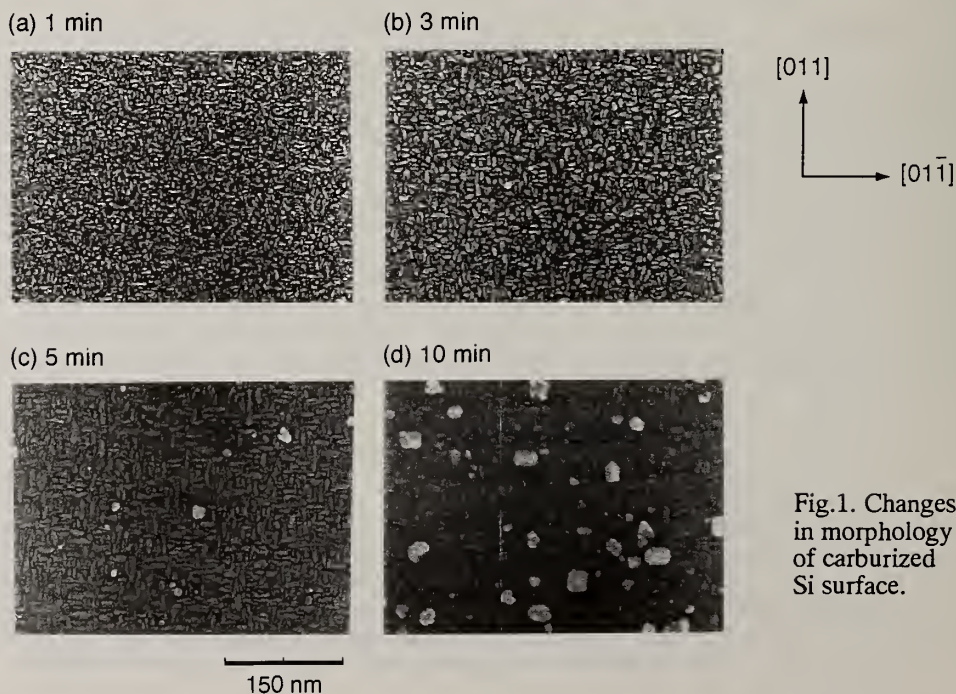
Fig.1. Changes in morphology of carburized Si surface.

150 nm

particles in Figs. 1 (c) and (d). The population density was approximately 10^{10} cm^{-2}, and 30–40% of particles were aligned to the substrate (100). **Fig. 2** illustrates the change in the surface structure, based on TEM image. The morphology of the substrate was very sensitive to the bias treatment conditions, such as biasing voltage, biasing time and substrate temperature.

Even if negative bias voltage was varied, a highly oriented diamond film was hardly formed at all. The negative bias rather obstructed the orientation in the growth stage. **Fig.3** indicates the diamond film formed by continuing the same conditions throughout nucleation and growth. Then, the effects of substrate temperature and CH$_4$ concentration on the growth rate in the [100] and [111] directions were investigated in detail without biasing [6,7]. At substrate temperature lower than 700°C, [100] growth was preferred. The [100] growth was retarded at higher temperature and lower methane concentration. Based on these results, MPCVD conditions in the growth stage were optimized. **Fig. 4** indicates the morphology of the diamond film grown under the optimized conditions on the mesh–structured surface [5,6,7]. **Fig. 5** illustrates the mechanism of the [100] oriented diamond film formation. After [100]–preferred growth, most of the randomly oriented diamond particles are buried by [100]–textured pyramidal diamond particles. The reaction conditions are then switched to those for [111]–preferred growth.

However, steps between {100} facets were still observable on the film surface. Even after the reaction was extended for a longer

Formation of epitaxial β-SiC layer

β-SiC

(100) Si

(a) Carburization stage

Growth of β-SiC

β-SiC

(100) Si

(b) Initial bias treatment stage

Nucleation of diamond on β-SiC

Diamond

β-SiC

(100) Si

(c) Final bias treatment stage
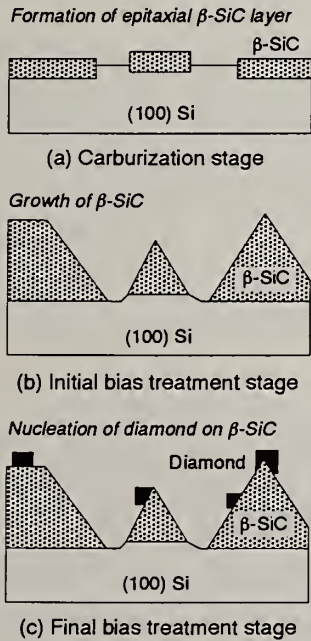
Fig.2. Schematic model for formation of mesh structure.

Fig.3. Diamond film formed without changing growth rate.

[011]

[01$\bar{1}$]

6 μm
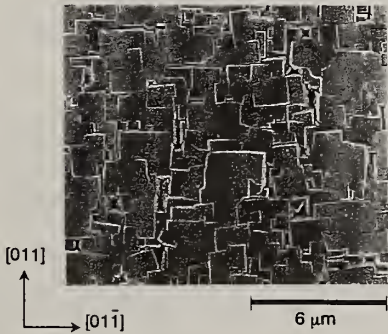
Fig.4. Diamond film formed with changing growth rate.

292

Oriented particle | Randomly oriented particle

[100] [111]

(1) Bias-treated surface

(2) [100] preferred growth

(3) [111] preferred growth
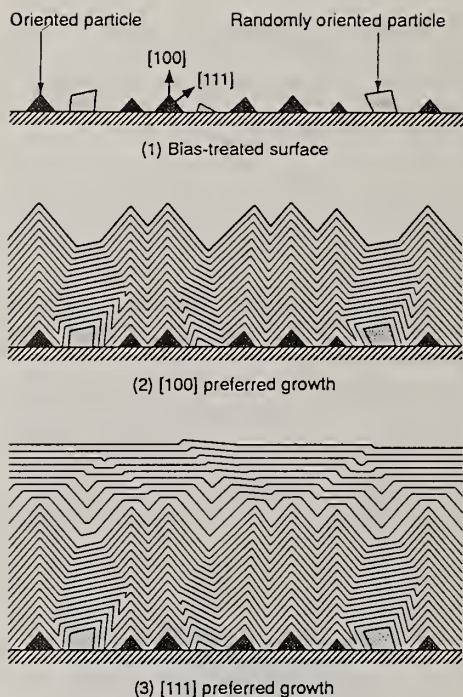
Fig.5. Schematic model for formation of oriented diamond film.

10μm
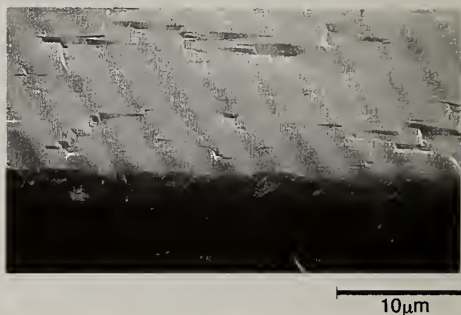
Fig.6. Highly oriented smooth diamond film.

period, secondary nuclei were formed and the quality of the film was not improved. Thus, when the film reached the morphology shown in Fig. 4, CO_2 was introduced to etch steps. After MPCVD for 2–10 h, a smooth [100]–textured film was obtained [7]. Steps on the film surface shown in Fig. 4 essentially disappeared when the film grew to a thickness of 40–50 μm as shown in **Fig. 6** . A sharp peak at 1333 cm^{-1} in the Raman spectrum proved the good crystallinity of the film.

4. Conclusion

A very smooth [100] oriented diamond film of 40–50 μm thickness was formed by controlling nucleation and growth steps precisely.

5. References

1. S. Yugo, T. Kanai, T. Kimura, and T. Muto, *Appl. Phys. Lett.*, **58**, 1036 (1991).
2. B.R. Stoner and J.T. Glass, *Appl. Phys. Lett.*, **60**, 698 (1992).
3. X. Jiang, C.P. Klages, R. Zachai, M. Hartweg and H.J. Fusser, *Appl. Phys. Lett.*, **62**, 3438 (1993).
4. S.D. Wolter, B.R. Stoner, J.T. Glass, P.J.Ellis, D.S. Buhaenko, C.E. Jenkins and P. Southworth, *Appl. Phys. Lett.*, **62**, 1215 (1993).
5. H. Maeda, M. Irie, K. Kusakabe and S. Morooka, Proc. 4th Int. Conf. on New Diamond Sci. Technol., p.153, MYU, Tokyo (1994).
6. H. Maeda, M. Irie, T. Hino, K. Kusakabe and S. Morooka, *J. Mater. Res.*, **10**, 158 (1995).
7. H. Maeda, K. Ohtsubo, M. Irie, N. Ohya, K. Kusakabe and S. Morooka, *J. Mater. Res.*, submitted.

MORPHOLOGY OF DIAMOND PLATE GROWN IN THE C-H-O SYSTEM

M.Nakanose[1] and H.Ichinose[2]

[1]Aerospace Division Space Systems Department Nissan Motor Co.Ltd.
  3-5-1 Momoi Suginami-ku Tokyo 167 Japan

[2]Department of Material Science University of Tokyo
  2-11-16 Yayoi Bunkyo-ku Tokyo 113 Japan

Key words: diamond, plate, high purity, C-H-O system

Abstract

A ECR-CVD system was newly designed and applied on the growth of large scale plate-like single crystal diamond. The diamond plate was grown on the (200) surface of a heated silicon substrate in H_2-CO-O_2 mixing gas. Silicon wafers with (110) and (111) surface were also employed as a substrate. A plate like single crystal ten micro meter in size was grown on the (200) surface at 1123K. Top surface of the platelet crystal was very flat and was parallel to (111) plane, which was parallel to the (200) surface of the silicon substrate. Half peak width of the Raman scattering spectra was 2.6 cm^{-1} showing low impunity content in the platelet crystal less than 1ppm for N and B.

1. Introduction

Diamond crystal has been received considerable interest for various applications such as high quality devises because of wide range transparency ranged from ultraviolet to infrared region, high thermal conductivity, wide electron band gap and excellent chemical stability. However, requested quality of the diamond crystal which is used for the devices is still far beyond the quality level reached at the present stage.

In these days various kinds of techniques such as CVD technique have been developed to produce artificial diamond in bulk and in thin film [1]. But in most cases produced artificial diamond is polycrystalline even if it is thin film or bulk in shape. The biggest shortage of the artificial diamond, especially diamond thin films, is roughens of surface. Smoothness of the surface is quite poorer than it is expected for the use of the electron devices. The roughness of

the diamond thin film is attributed to its polycrystalline structure which consist of small grains around μm in diameter. Most promising way to obtain smooth surface in atomic dimension is that to produce giant diamond plate from vapor. Present authors, therefore, tried to produce the diamond single plate by improved CVD method.

2. Experimental

Polished silicon substrate is heated at the temperature ranged from 1123K to 1173K in H_2-CO-O_2 mixed gas. Three different planes such as (200), (220) and (111) are employed as the growth surface. Diamond plates are grown on a (200) surface of silicon substrate by improved Electro-Cicrotron-Resonance (ECR)-CVD method.

Crystal orientation of the diamond plate is measured by electron channeling pattern of SEM. Roughness of the crystal surface is measured by high resolution SEM equipped with field emission electron gun. Smoothness in atomic dimension of the surface is measured by AFM. Micro Raman spectroscopy is performed and the purity of the produced diamond plate is evaluated by comparing with standard reference specimen.

3. Results and discussion

Morphology of the deposited diamond crystal depended on experimental condition such as substrate temperature, concentration of CO in the mixed gas and growth rate. At certain condition three dimensional large crystal particle which was surrounded by facets was grown as shown in figure 1. Most of particles were symmetrical in morphology. Representative facets were triangular and square in shape. They were parallel to (111) and (200) planes respectively as it is usual. Some of the crystals appeared to be a plate which was hexagonal in shape more than ten micro meter in size and one or two micro meter in thickness. Hexagonal surface was parallel to (111) plane and side surface was parallel to (220) plane. Half peak width of micro Raman spectra obtained from (111) plane was measured to be $\sim$4.5 cm^{-1} and that of (200) was to be 5.5 cm^{-1}. For the hexagonal plate shown in figure 2 the half peak width of the Raman spectra was less than 3.0 cm^{-1} without exception (figure 3, table 1).

The half peak width of hexagonal plate was very close to that of standard high purity specimen which was produced by high pressure method. The result suggests that it was almost free from crystal defects such as dislocation and stacking fault. The small value of the half peak width of the hexagonal plate also shows that quantity of impurity such as hydrogen and nitrogen is quite small in the crystal.

Reference

1. E.S.Etz : Proceedings of First International Conf. on the Application of diamond Films and Related Materials-ADC 91

Figure 1.
Polygonal diamond
particle grown from
vapor.
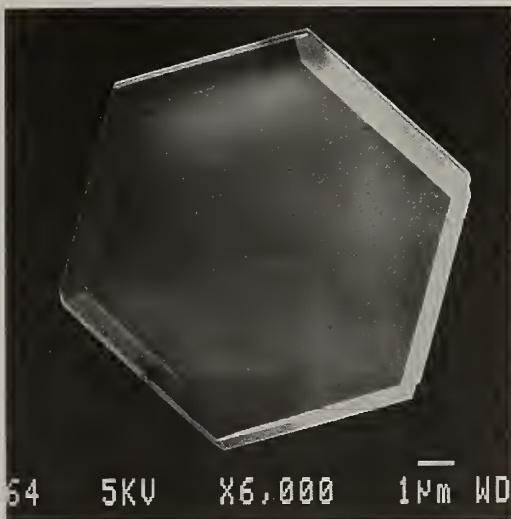
Figure 2.
Hexagonal diamond plate
grown by   ECR method.
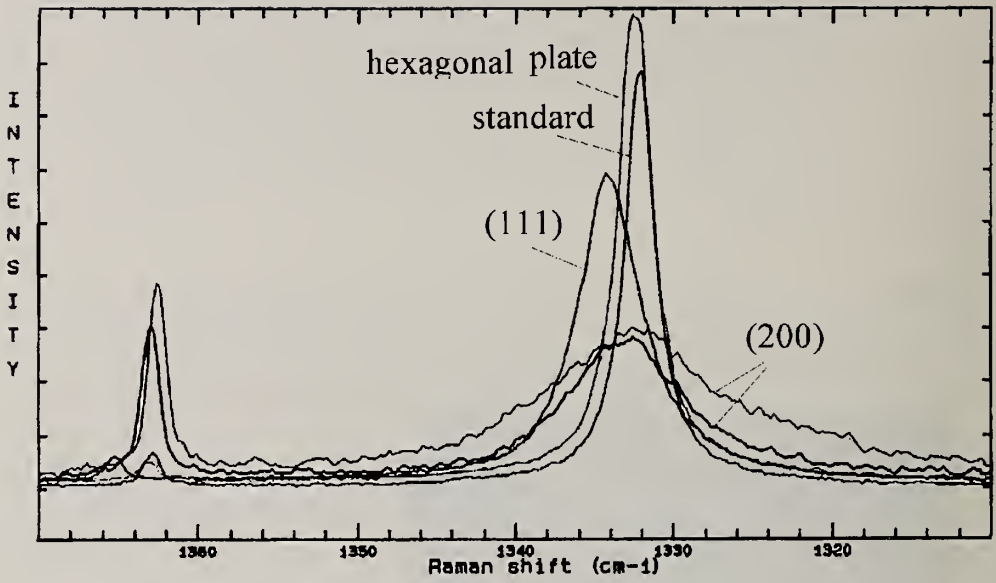
Figure 3. Raman spectrum obtained from   various plane of diamond crystal.

Table 1 (half peak width cm^{-1})

H-Plate	(111)	(200)
3.0	5.4	5.2
2.8	4.0	6.9
2.6	5.0	5.4
	4.4	5.9
	3.6	4.7
	5.2	4.9

Applications of Diamond Films and Related Materials: Third International Conference, 1995
Editors: A. Feldman, Y. Tzeng, W. A. Yarbrough, M. Yoshikawa, and M. Murakawa

297

LOW–TEMPERATURE SYNTHESIS OF DIAMOND FILMS BY PULSE MODULATED MAGNETOACTIVE MICROWAVE PLASMA CVD

Akimitsu Hatta, Hidetoshi Suzuki, Ken-ichi Kadota, Hiroshi Makita, Takuya Yara, Toshimichi Ito, and Akio Hiraki

Department of Electrical Engineering, Osaka University, Suita 565, Japan

Key words: infrared laser absorption spectroscopy, low temperature, magnetoactive microwave plasma, methyl radical, pulse modulation

Abstract

Diamond films were deposited by pulse modulated magnetoactive microwave plasma chemical vapor deposition (CVD). Dependence of the deposition rate on the modulation frequency showed a drastic peaking at 500 Hz. Methyl radical (CH_3) density in the pulse modulated plasma was measured by infrared laser absorption spectroscopy. Optical emission spectroscopy was also carried out to investigate the behavior of atomic hydrogen in the plasma. Time averaged CH_3 density was also enhanced by the pulse modulation, however, the observed behaviors of CH_3 radical density was not sufficient for explanation of the deposition rate.

1. Introduction

Author's group has developed diamond film synthesis in vapor phase by a magneto–active microwave plasma using an almost the same apparatus for the electron cyclotron resonance (ECR) plasma at rather higher pressure than ECR (10 Pa). The goal of diamond film growth over large area at low temperature with high quality has been tried rather successfully. There exist difficulties, however, to improve the growth rate and the film quality for the electronics application.

From a systematic study on low–temperature growth of diamond films, it was revealed that the nucleation time became so long as to decrease the actual growth time with cooling the substrate below 400°C. Nanocrystal seeding is essentially an unique pretreatment for diamond nuclei to improve the film quality and deposition rate at low temperature[1]. Well faceted polycrystalline diamond films have been successfully deposited on low–temperature Si substrates below 200°C by the

magnetoactive microwave plasma CVD. Such high–density and high–quality nuclei due to the seeding with purified nanocrystalline diamond particles can be realized at low temperature neither through scratching nor biasing.

On the other hand, the actual growth rate of the diamond on the steady nuclei decreased with cooling the substrate below 400°C in the continuous discharge plasma, however, it will be enhanced by pulse modulated discharge which enables us to control radical densities in the plasma. The deposition rate of twice as large as one of continuous plasma was achieved at 600°C with the same microwave power of amplitude modulation[2]. Thermal flux to the substrate from the plasma can be reduced with decreasing the duty ratio of the discharge resulting in easily cooling down the substrates for the low temperature deposition.

In a plasma of continuous discharge, the densities of activated species are almost in steady state and it is sometimes difficult to control their ratio as desired. Just after turning on or turning off the discharge, the density of each specie changes drastically due to its production or loss with individual time constants. A repetition of such transitional reaction stages makes it possible to control the generation ratio of radicals. In this work, the effect of pulse modulation of the discharge on the diamond growth was studied.

CH_3 radical is thought to be one of the important species for diamond growth in plasma CVD. It is necessary to know the behavior of CH_3 radicals in actual reactors for diamond film synthesis. The pulse modulated magnetoactive microwave plasma was also investigated by infrared laser absorption spectroscopy (IRLAS) for methyl (CH_3) radical and optical emission spectroscopy (OES).

2. Experimental

The magneto–active microwave plasma CVD system is shown in Figure 1 with a block diagram for the IRLAS system. Continuous or pulse modulated microwave of 2.45 GHz in frequency is generated by a magnetron power unit and is introduced into a cylindrical discharge cavity through a quartz window positioned at the peak of the magnetic field (3.5 kGauss). The modulated forward power rises in 2 μsec followed by overshooting for 50 μsec within 10 % in amplitude. Microwave power was observed to be reflected a little at the increasing phase of the forward power.

In this study, deposition rate of the diamond film by pulse modulated plasma was compared to that of continuous plasma on the scratched Si substrates at conventional temperature, 630°C. The substrates were set on a heated holder positioned at the ECR condition (875 Gauss), positively biased (30V) from the chamber wall. Total gas pressure was 5, 10(typical) or 20 Pa with flowing reaction gases of

CH_4(5sccm) /CO_2(10sccm) /H_2 (85sccm).

The IRLAS measurement unit and the White type multi–reflection cell are mounted on an vibration isolator separated from the plasma chamber. The unit was composed of a infrared diode laser of 14 μm in emission range cooled by liquid He, a monochromator for mode separation, a reference and an absorption signal units. The wavelength of laser was tuned by current modulation. The absorption signal was digitized and stored in a digital oscilloscope. For IRLAS measurements, the substrate holder was removed back and the laser beam passes 24 times through the plasma 1 cm apart from the ECR region to the lower–magnetic field side. An absorption line of CH_3 radical ($\nu_2 = 1 \leftarrow 0$, R(4,0)) at 692.493 cm^{-1} [3] was measured to determined the absolute density by assuming that the methyl radical exist uniformly in only the plasma column and that the rotational temperature is 400K [4], though it has not confirmed in our plasma yet. Optical emission in front of the substrate positioned at ECR condition was monitored during deposition.

3. Results and discussion

Polycrystalline diamond films were fabricated with continuous discharge and also with pulse modulated discharges at all of the experimented conditions. There was no significant difference between the fabricated films in scanning electron microscopy and Raman scattering spectroscopy beside the difference in film thickness and particle size.

The dependence of the deposition rate on the modulation frequency is shown in Fig. 2, where the deposition rate is evaluated from the film thickness grown for 2 hours. The modulated microwave of 5 kW in amplitude and 50 % in duty cycle was applied. The time averaged microwave power evaluated from the difference between the wave forms of forward and reflected microwave powers were 2.5 kW. The deposition rate with the continuous wave (CW) discharge of equivalent microwave power (2.5 kW) was about 0.02 μm/h, as shown by a dotted line in Fig. 2.

Such a great difference between the continuous and pulse modulated plasmas is due to the non–liner increase in deposition rate with increasing the microwave power. The deposition rate of continuous plasma increases dramatically with increasing the microwave power more than 2.5 kW. Because the deposition rate of the continuous plasma reaches 0.3 μm/h at 5 kW, that of pulse plasma of 50 % in duty cycle should become 0.15 μm/h at the modulation slow enough. The pulse modulated plasma CVD shows a great improvement in deposition rate as compared to the continuous plasma of time averaged microwave power, however, it still loses the efficiency as compared to the continuous plasma of the peak microwave power, 5 kW.

Figure 3 shows the time averaged CH_3 radical density in the pulse modulated and continuous plasma. The order of the results at 5 Pa, 10 Pa, and CW(10 Pa) in the CH_3 densities was the same as that in deposition rates. The exceptional result at 20 Pa is possibly due to spatial distribution and/or life time of CH_3 radicals remarkably appeared at higher pressure. CH_3 radical density was actually enhanced by pulse modulation to be about 1.3 times larger than that in the CW plasma, however, it was not observed to depend on the modulation frequency in such the way as the deposition rate was. The enhancement of the deposition rate by pulse modulation cannot be explained only by the CH_3 radical density.

According to the general kinetic theory of molecules, flux of CH_3 radical coming to the surface of the substrate was estimated from the measured density and an assumed gas temperature as 5×10^{16} /s·cm². Supposing that the CH_3 radical is the major specie of carbon source for diamond growth, the probability of CH_3 radical to contribute the diamond growth was only about 1 %.

Figure 4 show the temporal changes in peak intensities of the optical emission spectrum from the pulse modulated magnetoactive microwave plasma. The emission intensity depends on the densities of species to be excited, the density and the energy distribution of the electrons to excite. The electron energy distribution is thought to be in steady state after igniting the discharge. The gradual changes in optical emission intensities means the changes in the electron density and/or the total densities of the species in the lower states and the molecules and radicals to be dissociatively excited.

The emission from H_2 is almost in proportion to the bias current to the substrate (+30 V) meaning the changes in electron density, because the partial pressure of H_2 is thought to be almost stable. The increases in CH, C_2 and H_α emissions means the production of some hydrocarbon radicals to contribute these emissions.

Figure 5 shows the temporal changes in H_α intensity during the pulse after intervals different in length. The transition time to reach the steady state became longer as increased the interval time was. The radicals mainly contributing H_α emission remains more than 0.5 msec after turning off the discharge, resulting in the rapid increase of H_α in the next pulse. On the contrary, it necessary more than 1 msec to become steady state after the interval more than 2 msec. Thus the decay time constant of the radical is estimated about 1 msec. The decrease in deposition rate at lower frequency modulation than 500 Hz is due to such the rapid decay of radicals during the intervals.

4. Conclusion

By the pulse operation of magnetoactive microwave plasma, the deposition rate

of diamond films several times as large as one of the continuous operation was achieved at 500 Hz in frequency with the same microwave power as time averaged one at 630°C in substrate temperature. The optimum frequency is thought to depend on the dissociation rate of the source gases during the discharge and the decay rate of the radicals during the interval. Methyl radical density was observed to be enhanced by the pulse modulation, however, the growth rate was not explained quantitatively by only the methyl radical density. The pulse modulation is expected to reduce the thermal flux to the substrates from the plasma without loss of the deposition rate by decreasing the duty cycle.

Acknowledgements

References

[1] T. Yara, et al., Jpn. J. Appl. Phys., 34(1995)L312.
[2] A. Hatta, et al., Appl. Phys. Lett., 66(1995)1602.
[3] C. Yamada et al., J. Chem. Phys., 75(1981)5256.
[4] S. Naito et al., Rev. Laser Eng., 20(1992)746.
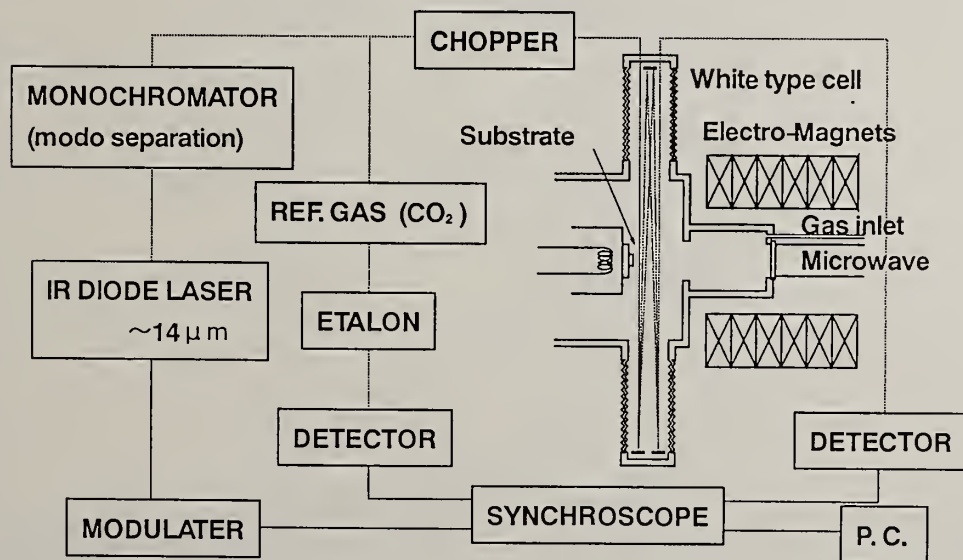
Figure 1: Experimental apparatus for pulse modulated magnetoactive microwave plasma CVD with schematic diagram for infrared laser absorption spectroscopy.
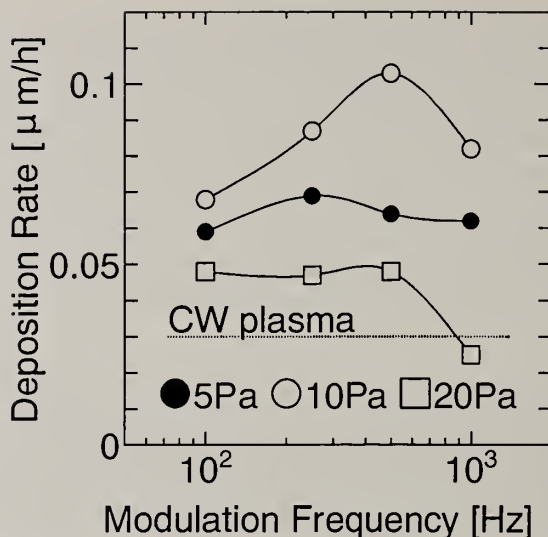
Figure 2: Dependence on the modulation frequency of the deposition rate of fabricated films for square wave amplitude modulation of microwave (50 % in duty cycle and 5 kW in peak power). Total gas pressure was 5, 10 or 20 Pa with flow rate 5sccm of CH_4, 10 sccm of CO_2 and 85sccm of H_2. The dotted line shows the deposition rate by continuous wave plasma of the same microwave power (2.5 kW).
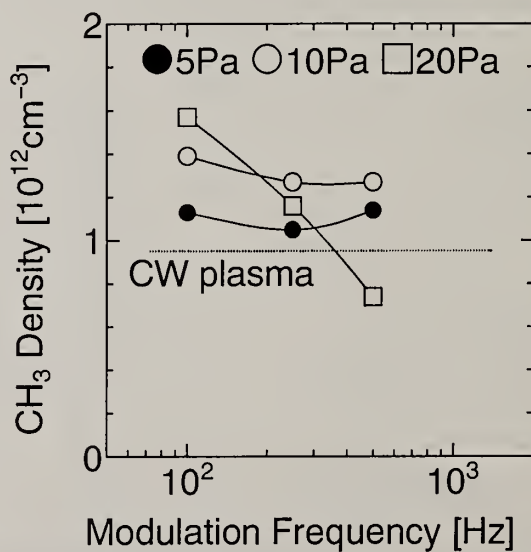
Figure 3: Time averaged CH_3 radical density in the pulse modulated plasma ($CH_4/CO_2/H_2 = 5/10/85$). The dotted line shows the CH_3 density in the continuous wave plasma of the same microwave power (2.5 kW).
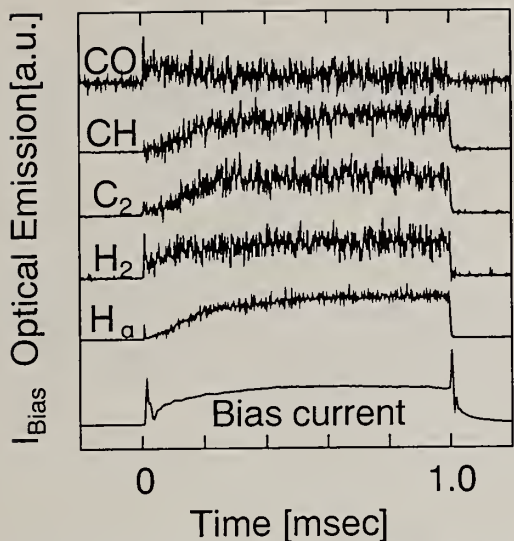
Figure 4: Temporal wave form of each peak intensity in the optical emission spectrum for the pulse modulated magnetoactive microwave plasma (5 kW in peak power, 500 Hz, 50% square wave modulation, 10 Pa, $CH_4/CO_2/H_2 = 5/10/85$). The temporal wave form of substrate bias current in also shown.
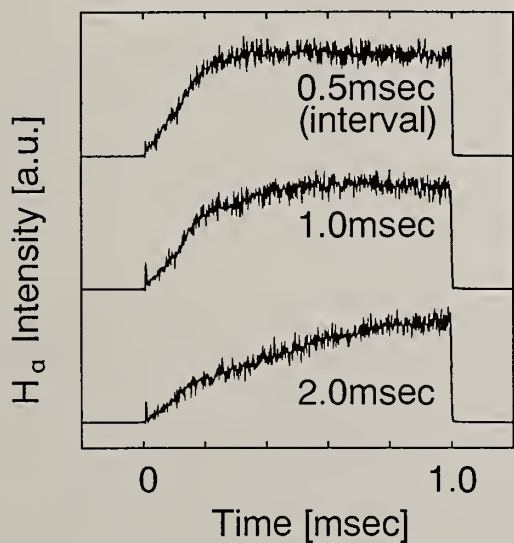
Figure 5: Temporal wave forms of the H_α emission intensity. The microwave was modulated with square wave with 1 msec in pulse width and 0.5, 1 or 2 msec in interval width (5 kW in peak power, 10 Pa, $CH_4/CO_2/H_2 = 5/10/85$).

Applications of Diamond Films and Related Materials: Third International Conference, 1995
Editors: A. Feldman, Y. Tzeng, W. A. Yarbrough, M. Yoshikawa, and M. Murakawa

305

Hydrogen Atom Concentration Measurements by Multiphotonic Excitation LIF Technique - Spatial distribution in a Microwave Bell Jar Reactor.

<u>M. Chenevier</u>[1], A. Gicquel[2] and J.C. Cubertafon[1]

[1]Laboratoire de Spectrométrie Physique, associé au C.N.R.S. U.R.A. 08, Université J. Fourier Grenoble, 140 Avenue de la Physique, B.P. 87 38402 Saint Martin d'Hères, France
[2]Laboratoire d'Ingénierie des Matériaux et des Hautes Pressions, C.N.R.S U.P.R. 1311, Université Paris-Nord, Aveneue J.B. Clément, 93430 Villetaneuse, France.

Key words: actinometry, atomic hydrogen, diamond, laser spectroscopy, microvawe-assisted CVD.

Abstract

Two photons Laser Induced Fluorescence has been carried out in a microwave plasma bell jar diamond deposition reactor in order to obtain spatial distribution of ground state atomic hydrogen and its temperature. Comparison with CARS measurement for the temperature and actinometric ones for the concentration are reported.

1. Introduction

The characterisation of the plasma used for diamond synthesis is essential for a better understanding of the gas phase chemistry of diamond growth. In a microwave-assisted reactor, the plasma is far from the thermodynamic equilibrium and modelling of the growth of vapour deposited diamond is difficult. In order to build a representative model, informations concerning concentration and temperature of chemical species are needed. In low pressure CVD diamond deposition the dominant species is molecular hydrogen and ground state atomic hydrogen is certainly one of the dominant reactive species. So it is important to dispose of data about this specie.

The first excited state of atomic hydrogen lies at 10.2 eV above the ground state, so direct absorption is technically difficult to practice in diamond deposition reactors. Informations on atomic hydrogen can be obtain by optical emission spectroscopy. Despite the fact that this method is easy to use, not too expensive, and that its simplicity is well adapted to such reactors, it is not an absolute method and errors can easily affect this type of measurement. In fact this method provides information about the excited states of the species, and by a very indirect path, about the ground state. So, the OES actinometry needs to be carefully calibrated by a more absolute and direct method. Multiphoton techniques like resonance enhanced multiphoton ionisation (REMPI) [1] or two-photons allowed laser induced fluorescence (TALIF) [2] can be used for this purpose. With the REMPI technique one needs to introduce electrodes in the reactor which is not feasible in a microwave reactor. Therefore, one of the best choice is to use TALIF. However, at pressures such as required in CVD diamond deposition, quenching of the excited state by molecular hydrogen occurs and its effect must be taken into

account. This technique has been used to measure concentration of atomic hydrogen in hot filament reactors [2-5], in RF reactor [6], and only very recently in a microwave reactor by Preppernau et al. [7].

2 Detection and measurement of atomic hydrogen by Two Photons Allowed Laser Induced Fluorescence (TALIF).

In TALIF detection of atomic hydrogen, two 205.14 nm photons are used to excite the n=3 state from the ground state 1s $^2S_{1/2}$. The fine structure of n=3 state leads to 5 sublevels 3s $^2S_{1/2}$, 3p $^2P_{1/2,3/2}$, 3d $^2D_{3/2,5/2}$ which are energy degenerate ($\Delta E=0.144$ cm^{-1}). Due to the selection rule $\Delta l= 0, \pm 2$ for a two photon transition, 3s and 3d sublevels are excited by allowed transition. Depending of the ambient pressure, the desexcitation of these levels occurs after 10 to 20 ns, towards the n=2 levels, giving fluorescence emission of the Balmer α line at 656 nm.

For a given total pressure, the intensity of the fluorescence is proportional to the concentration of atomic hydrogen. The narrow laser linewidth allows to scan over the profile of the excitation transition and to obtain the temperature of atomic hydrogen in its ground state. In the range of pressure of interest, the excitation line profile is dominated by the Doppler effect and is gaussian, and the observed profile results of convolution of laser and Doppler ones. A calibration experiment carried out with an atomic hydrogen source at room temperature was used to obtain the laser width.

3 Experimental details.

1. The reactor

The diamond deposition reactor is a bell jar and C.V.D is assisted by microwave plasma. The plasma is created in a silica bell jar low pressure chamber where standing waves are produced by the microwave antenna (fig 1).
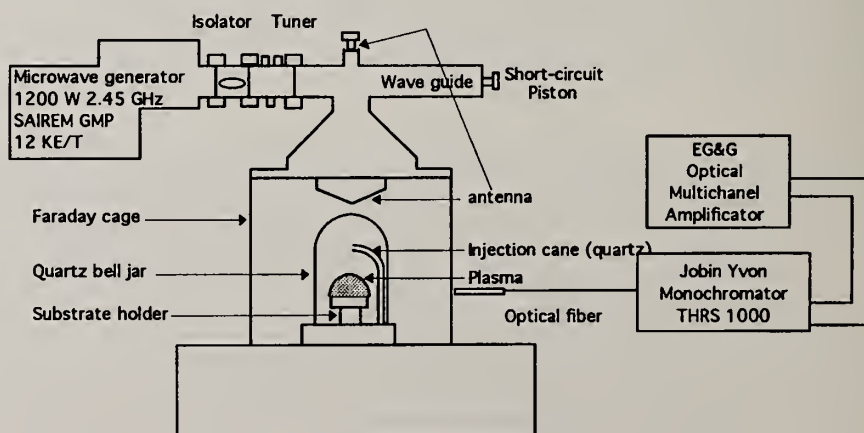
Fig. 1 The bell jarr microwave reactor.

This deposition reactor has been described previously [8]. For the TALIF experiments, two U.V. grade silica windows were added to the bell jar to allow transmission of 205 nm light. The substrate-holder can be placed at various positions in the the plasma ball.

All the experiments were carried out with 50 mm diameter (100)-silicon wafers on which few μm of diamond film were previously deposited in order to study plasma diamond interaction. The whole reactor can be accurately translated vertically and horizontally with respect to the laser beam in order to obtain axial and radial profiles.

The gas flows of H_2, CH_4 and Ar were controlled by three mass flow meters so that the total flow was 100 sccm. The pressure, measured by a capacitance gauge, was regulated by a leak valve, coupled to the gauge, in the pump outlet.

The substrate holder was heated using an AC power supply. Diamond surface temperature was measured by a bichromatic pyrometer.

2. The two photon L.I.F. technique.

The system used to generate light at about 205 nm consists of a pulsed excimer laser (XeCl) emitting at 308 nm. This excimer pumps a dye laser composed of a tunable oscillator and of an amplifier. With Rhodamine B an intense beam is obtained at 615 nm.which is frequency doubled by a KDP crystal to give 307.5 nm. Mixing with the residual 615 nm beam in a BBO crystal, produces the 205 nm beam. This is pulsed at 10 Hz with a pulse duration of about 25 ns, the energy and the linewidth are typically of 50 μJ by pulse and 0,0025 nm respectively. The whole laser system is computer controlled and allows wavelength scanning over a few nm. In our experiment a scan of 0.030 nm is sufficient to cover the line profile with 90 steps. The fluorescence light is collected by two lenses and detected directly by a photomultiplier in front of which an interference filter centered at 656.5 nm is used to eliminate scattered laser light. The resulting signal is treated by a boxcar integrator and sent to a microcomputer. The fluorescence signal is averaged over 20 laser shots for each wavelength step, thus a scan takes about 3 minutes. A block diagram of the experimental set up is shown fig 2. The observed two-photon line profile, its full-width at half-maximum, are directly related to the translational temperature of atoms and the area of the profile to their concentration.

4 Data analysis

The total area of the excitation line profile, obtained by fluorescence observation, is proportional to the number of hydrogen atoms contained in the focal volume. In order to obtain absolute values of the concentration a calibration procedure is necessary [6] but in the present case this was not possible to realize.
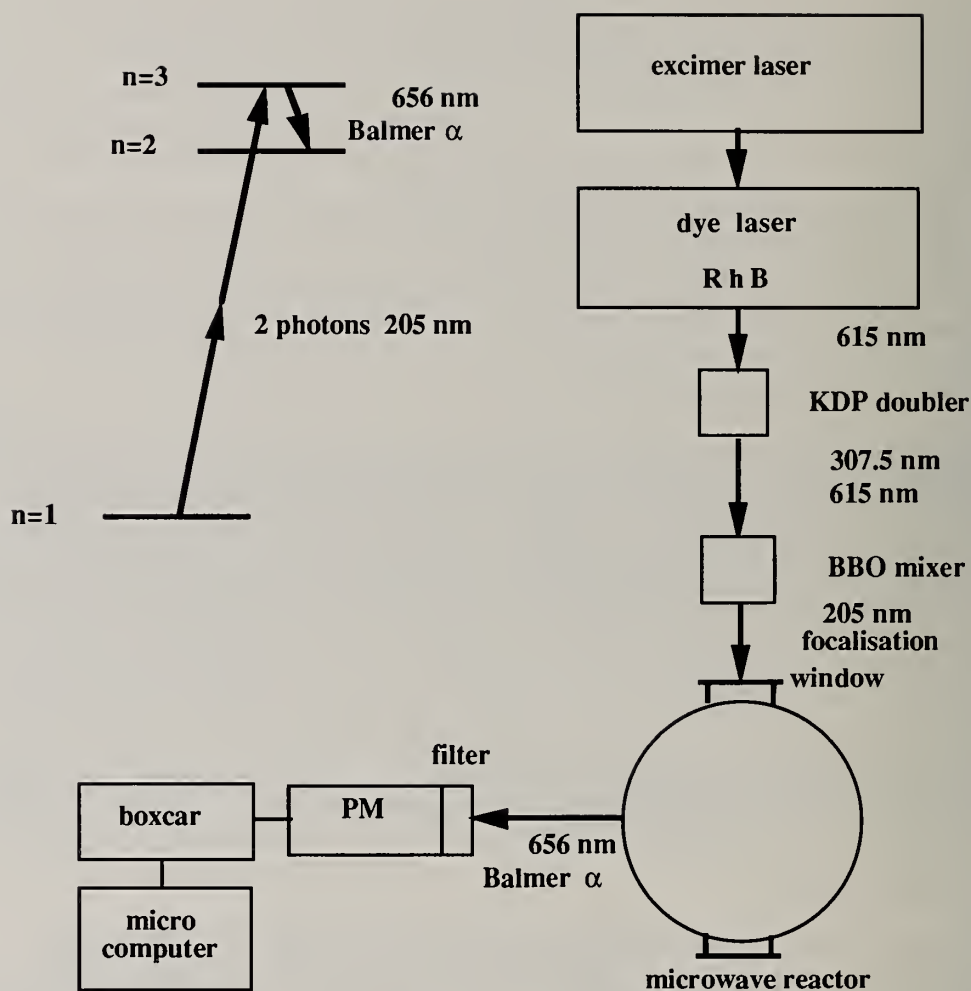
Fig 2 Block diagram of the experimental set-up.

4-1 Width and Temperature.

As atomic hydrogen is the lightest atom, the Doppler broadening line is the largest one, and this is therefore particularly advantageous for temperature measurements from line profiles. By measuring the Doppler linewidth $\Delta\lambda_D$ (full width at half maximum, FWHM) of the fluorescence excitation profile, the H atom temperature can be determined using the formula :

$$\frac{\Delta\lambda_D}{\lambda_0} = \frac{2}{c}\sqrt{\frac{2\,k\,T\,\ln 2}{m}} = 7.16.10^{-7}\sqrt{\frac{T}{M}} \quad (1)$$

where c is the speed of light, k the Boltzmann's constant, m is the mass of the atom, T is the temperature of the atom and M is the mass in amu of the atom.

We can estimate the magnitudes involved by applying Eq.(1) to the H atom at 1500°K for the doubled $1^2S \rightarrow 3^2S\left(^2D\right)$ H atom transition, i.e. for $\lambda_0 = 205.14$ nm, giving a value of 0.0056 nm for $\Delta\lambda_D$.

For our experimental conditions, i.e. pressure of about 25 mbar, the atomic fine structure and the collisional broadening, are of the order of 0.00015 nm for the transition involved, can be neglected. Therefore, the line profile can be considered as a pure gaussian.

By fitting the experimental profile with a gaussian profile :

$$f(\lambda) = a + b \exp\left[-4\ln 2\left(\frac{\lambda - \lambda_0}{\Delta\lambda_R}\right)\right] \qquad (2)$$

we obtain four parameters (a, b, λ, $\Delta\lambda_R$).

Some typical experimental profiles fitted with this profile are presented fig. 3. In this case $\Delta\lambda_R$ is a composition of the Doppler linewidth ($\Delta\lambda_0$) with the laser linewidth ($\Delta\lambda_L$). Thus, by deconvolving $\Delta\lambda_R$, one can obtain $\Delta\lambda_D$ and we can estimate the H atom temperature. For the determination of $\Delta\lambda_L$ we have performed experiments with a room temperature atomic hydrogen source in place of the microwave plasma reactor and a value of 0.0025 nm was obtained.
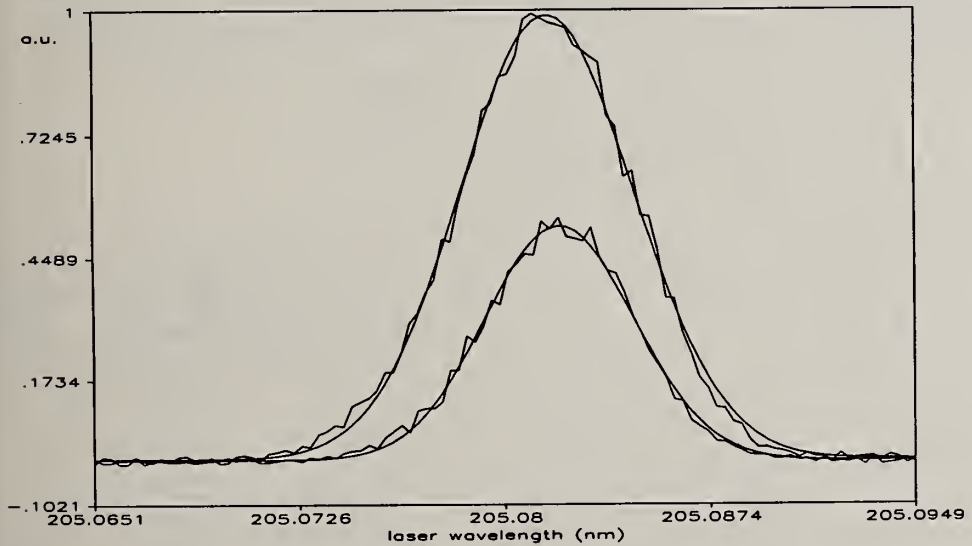
Fig. 3 Two typical fluorescence profiles with fitting curves.

4-2 Total fluorescence, intensity and concentration.

The concentration is proportional to the product of fluorescence amplitude (parameter b of formula 2) by $\Delta\lambda_D$, which must be corrected for the quenching effect. This effect is due to collisional desexcitation of H atom before they fluoresce. According to Meier et al [2] and Preppernau et al [9]the fluorescence yield is given with a very good approximation by

$$F_y = \frac{A_3}{A_3 + Q_3}$$ where A_3 is the rate of spontaneous emission of level $n = 3$ and Q_3 its rate of

quenching. This last quantity can be evaluate by $Q_3 = N_{H2}\, \sigma\, \sqrt{\overline{v}_H^2 + \overline{v}_{H2}^2}$ where N_{H2} is the number densities of the collision partner, here H_2, σ is the quenching cross section and $\overline{v}_H$, $\overline{v}_{H2}$ the mean velocities. Using A_3 and σ values given by Bittner et al [10] the formula

$$F_y = \frac{1}{1 + 0.266\dfrac{p\sigma}{\sqrt{T}}}$$ in which p is in mbar and σ in Å^2, was used to correct our

concentration results. We used for our treatment the value of σ found in [10], i.e. 65 Å^2, however Preppernau et al [9] give a σ value 10% lower.

5 Results
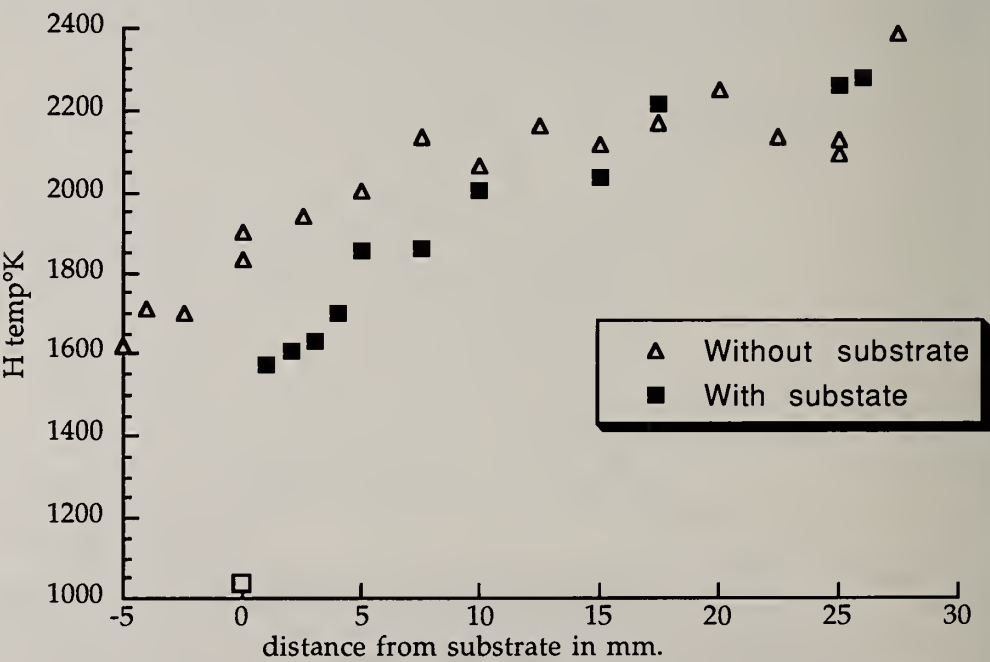
Fig 4 Atomic Hydrogen Temperature measured by TALIF versus distance, with and without substrate.
5-1 Axial and radial distributions of the H atoms temperature and of the H atoms relative concentration have been obtained. For typical discharges condition, microwave power: 600 w, pressure 25 mbar, results of a few runs are presented fig 4 .where axial dependance of H

temperature are shown. In the plasma volume, far from the diamond surface, the influence of the percentage of methane have been studied.

The measurements of the H atoms temperatures have been compared to Coherent AntiStokes Raman Spectroscopy (CARS) measurements, providing ground state molecular hydrogen rotational temperature which have been realised previously in the same reactor [8]. A very good agreement was obtained indicating that atomic hydrogen and molecular hydrogen are in equilibrium. For a substrate temperature of 750 °C, the temperatures measured by TALIF varie from 2200 ± 100 °K for the maximum in the plasma bulk, to 1600 ± 100 °K ay one millimeter of the surface. The corresponding values obtained by CARS are respectively 2150 and 1200 °K [8]. Thorough our experiments, we have also confirmed results obtained by CARS on H_2 showing that the introduction of percentage of methane up to 5% does not change the temperature for the typical discharge conditions described before.

5-2 Comparison with actinometry.
Optical emission spectroscopy has been performed simultaneously to the TALIF measurements with a small amount of argon added to the feed gas (1 %). The variations of the emission intensity ratio of the Hα line over the 750,3 nm line of argon, $I_{H\alpha}/I_{Ar}$, which should be proportional to the H atom molar fraction, have been recorded. A comparison between the H molar fraction provided by the TALIF and the actinometric signal (integrated along the line of sight) has been performed as a function of the methane percentage in the feed gas (see fig 5). The $I_{H\alpha}/I_{Ar}$ is found to be proportional to the H atom molar fraction, as the methane percentage varies. A good agreement between the axial distributions obtained from TALIF and actinometry (OES) [8] is also observed.
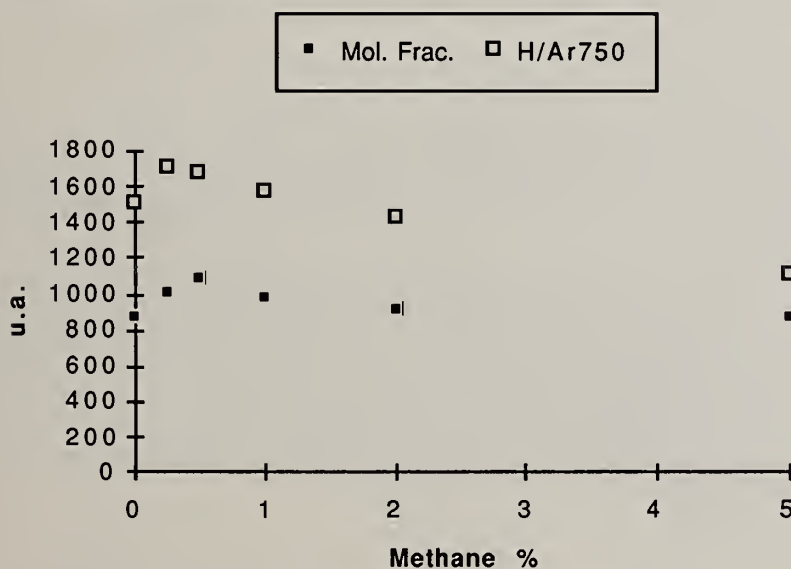
Fig 5 Comparison between actinometry and TALIF

6 Conclusion.

Multiphoton induced fluorescence measurements comport relatively complex experimental

setup, and are not practical for routine monitoring of reacting species in a reactor. We used them here essentially to validate other techniques like actinometry or to give some reference points to model developers.

i - the results show that in the plasma volume atomic hydrogen temperature is very close to that of molecular hydrogen. However at the diamond interface T_H seem to be higher than T_{H_2}.

ii - a good agreement between H concentration variations obtained by TALIF and the ratio $I_{H\alpha}/I_{Ar}$ (actinometry) is found in standard discharge conditions.

iii - comparison with a 1 D diffusional model [11] shows agreement with the spatial distribution of the temperature. This could indicate that of the 600 W injected, roughly 300 W are dissipated in the plasma and 300 W are lost in the wall and the substrate.

Acknowledgements.

1 F.G. Celii and J.E. Butler,
Appl. Phys. Letters **54** (1989) 1031.
2 U. Meier, K. Kohse-Höinghaus, L. Schäfer and C.P. Klages,
Applied Optics **29** (1990) 4994.
3 L. Schäfer, C.P. Klages, U. Meier and K. Kohse-Höinghaus,
Appl. Phys. Letters **58** (1991) 571.
4 J.R. Dunlop, A.D. Tserepi, B.L. Preppernau, T.M. Cerny and T.A. Miller,
Plasma Chem. Plasma Process **12** (1992) 89.
5 M. Chenevier, J.C. Cubertafon, A. Campargue and J.P. Booth
Diamond and Related Materials **3** (1994) 587.
6 D.P. Dowling, T.P. O'Brien, E.M. Davitt, K Donnely, T.C. Kelly, H.F. Dobele, V. Kornas, W.G. Graham, R. Cheshire, M. Higgins and T. Morrow, Diamond and Related Materials 3, (1994), 702.
7 B.L. Preppernau
Communication in Frontier in Cold Plasma Diagnostics LesHouches January 1995
8 A. Gicquel, K. Hassouni, S. Farhat, Y Breton, C.D. Scott, M. Lefevre and M. Pealat,
Diamond and Related Materials **3** (1994) 581.
9 B.L. Preppernau, K. Pearce, A. Tserepi, E. Wurzberg, and T.A. Miller,
to be published in Chemical Physics (1995)
10 J. Bittner, K. Kohse-Höinghaus, U. Meier and Th. Just,
Chem. Phys. Lett. **143** (1988) 571.
11 K. Hassouni, S. Farhat, C.D. Scott, A. Gicquel,
Communication at ADC 95

Applications of Diamond Films and Related Materials: Third International Conference, 1995
Editors: A. Feldman, Y. Tzeng, W. A. Yarbrough, M. Yoshikawa, and M. Murakawa

313

DIAMOND–COATING OF METAL ALLOYS*

M. D. Drory

Crystallume, 3506 Bassett Street, Santa Clara, California 95054 USA

Key words: diamond, metals, adhesion, reliability, steel, titanium

Abstract

Current issues regarding the deposition of diamond on metal is discussed, with an emphasis on mechanical reliability. The very large residual compressive stresses in diamond-coated metals provide a considerable challenge for obtaining useful (adherent) coatings. Encouraging results are reported on the diamond-coating of steel by CVD methods which may be readily extended to the deposition on other common metal alloys.

1. Introduction

Diamond-coating of metals is of profound technological importance and great scientific interest. This stems from the potential broad use of synthetic diamond coatings in abrasion resistant applications on common metal alloys; applications which exploit the extreme hardness of diamond and may also make use of its high stiffness, thermal conductivity and corrosion resistance. Despite the advantages for diamond-coated metals for improving wear resistance, a number of challenges remain for readily depositing diamond layers on widely used metal alloys and performing this at a reasonable cost. The recent efforts in our laboratory in diamond-coating of steel will be described in which encouraging results of broad applicability have been obtained.

Diamond-coating of metal alloys is greatly hindered by the relatively low thermal expansion coefficient of diamond which results in extremely large compression stresses at room temperature. In addition, chemical incapability with common metals, such as steel, promote the formation of graphite at typical diamond deposition conditions by CVD methods. Deleterious effects of the deposition temperature ($\sim$700$\rightarrow$1000°C) also occur for common metal substrates, such as a reduction in hardness and dimensional changes.

The large residual (compressive) stress is estimated for thin diamond coatings by:

$$\sigma = \frac{E \, \Delta\alpha \, \Delta T}{1 - \nu} \qquad (1)$$

where E is the film Young's modulus, ΔT is the processing temperature, $\Delta\alpha$ is the difference in thermal expansion coefficient between the film and substrate, and ν is Poisson's ratio. In the case of diamond, E$\sim$1000 GPa, $\alpha\sim$1.5x10^{-6}°C^{-1}, and $\nu\sim$0.07 [1]. This leads to enormous compressive stresses in the diamond coating upon cooling from typical deposition temperatures (Fig. 1). A more complete analysis of the film stress than given by eqn. (1) accounts for growth or 'intrinsic' stresses, however, the (thermal) elastic stresses have found to be the dominate component in the particularly important case of a diamond-coated titanium alloy [2]. A thorough understanding of the role of intrinsic stresses in synthetic diamond (and it's relationship to microstructure) remains an important topic of research.

The high film stress found in diamond-coated materials is shown schematically in Fig. 1 for a wide range of materials. The sign of the stress determines the failure mechanisms and potential concerns for coating reliability. Films in residual *tension* may exhibit the failure of the coating, interface or substrate, while a *compressive* stress may result in film spalling through a buckling mechanism. The tendency for film failure increases with film thickness and processing temperature, and is greatly dependent on the toughness of the film, interface, and substrate. Details of the mechanics of film reliability are available in the literature [3].

Despite the enormous stress levels expected in the film for diamond-coated metals, tailoring of the process conditions and proper design of

the interface may reduce the tendency for film (and substrate) failure for some applications; an example of which is described below for diamond-coating of steel. In other cases, the residual film stresses may preclude the use of diamond coatings. For example, diamond-coating of quartz may not be practical for erosion protection because of the large tensile stresses which readily promote failure of the film, interface and substrate before a sufficiently thick layer can be obtained. In this application, a different substrate material may be necessary to combine with a thin diamond layer, or the use of an alternative coating on quartz, such as diamond-like carbon.
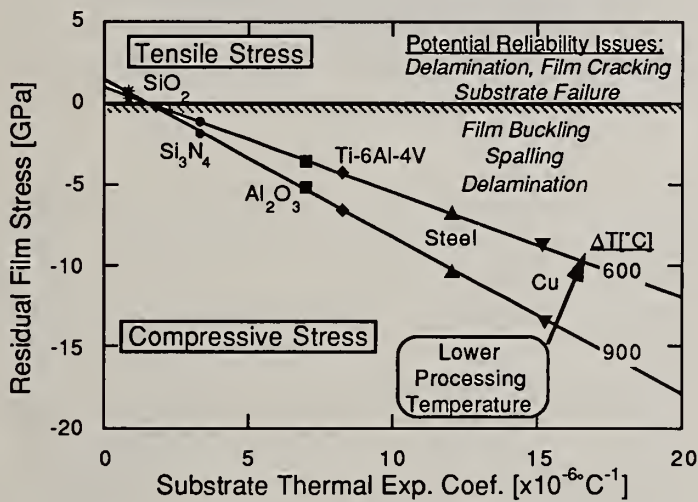
Fig. 1 - Magnitude of residual (thermal) stresses for diamond-coated substrates.

2. Results and Discussion

Diamond-coating of metals is being examined in our laboratory for a number of applications. Previous work on the coating of a common titanium alloy, Ti-6Al-4V, indicates that a very adherent layer was obtained by deposition with a plasma-enhanced CVD (microwave) method[4]. The presence of diamond on the titanium alloy was confirmed by Raman spectroscopy, which also indicated a residual film

stress of ~7GPa (compression) [2]. A measurement of the interface toughness was performed by an indentation technique giving a value of ~40J/m^2*. This result demonstrates the potential for titanium as an interlayer for coating other metal substrates, such as steel.

The need for an interlayer for coating steel is due to the chemical incompatibility with the diamond growth process and the large thermal stresses expected from the difference in thermal expansion coefficient (Fig. 1). This is illustrated by the result of exposing a steel alloy to typical diamond processing conditions (Fig. 2). A 25mm diameter sample of 310 alloy was lightly abraded in a fine diamond powder for nucleation enhancement and placed in a diamond reactor. Typical conditions for growth in a microwave plasma were used, such as 1% CH$_4$ in H$_2$ with an applied power of ~1500W at 2.45GHz excitation. As expected, non-diamond carbon (e.g. graphite) was formed as evidenced by the Raman spectrum (Fig. 2B). The 'soot' appearance of the sample is also consistent with the formation of graphite, emphasizing the need for an interlayer (i.e. barrier) between the substrate and growth environment.

The 310 alloy# was selected for this model study because of its capability of withstanding temperatures of 1150°C, which readily exceeds the deposition temperature [6]. As described below, additional research is needed to lower the deposition temperature in order to access more widely used alloys for contact wear applications, such as bearings. For example, the maximum temperature of 440 alloy should not exceed ~800°C which is a typical deposition temperature for CVD diamond processes. A sample of 310 alloy was prepared for diamond deposition by initially sputtering a thin layer of titanium, and then following the specimen preparation procedure of the previous sample. A direct comparison of the effects of the titanium interlayer are shown in Fig. 3 where the initial deposition experiment (without the interlayer) is provided on the left. Thickness fringes are visible in the right-hand sample in which the presence of an adherent coating is evident.

---

*As discussed elsewhere, adhesion testing is a considerable challenge for diamond-coating substrates due to its extreme hardness and stiffness[4,5].
#Nominal composition of 310 alloy (%): 0.25C, 2.00Mn, 1.50Si, 24.0-26.0Cr, 19.0-22.0Ni, 0.045P, 0.03S [6].

(A)

(B)
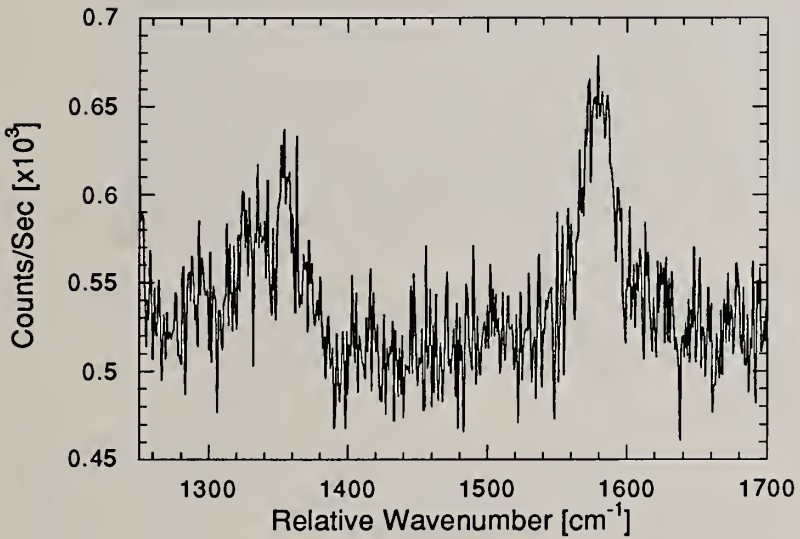
Fig. 2 -   (A) Low-magnification photograph of a steel substrate (3mm thickness) subjected to the CVD diamond process, with (B) the Raman spectrum.

(A)
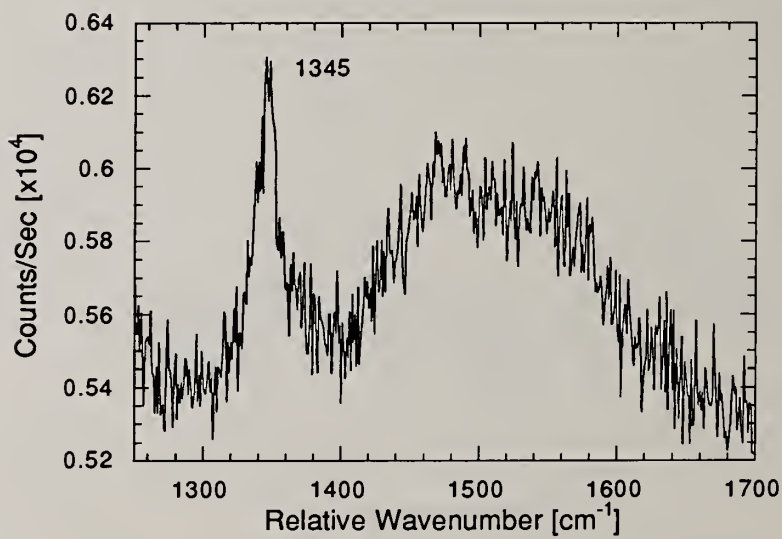
Fig. 3 - (A) Low-magnification photograph of diamond-coating of steel substrate containing a sputtered Ti interlayer(right), with (B) the Raman spectrum.

Raman spectroscopy of the sample containing the titanium interlayer shows that diamond was obtained (Fig. 3B). The large non-diamond carbon peak may indicate a reduction in the hardness and stiffness of the deposited film, relative to diamond, however this does provide an encouraging result for the use of titanium as an appropriate interlayer on steel alloys. The film was further characterized by Raman spectroscopy and scanning electron microscopy (Fig. 4) at the Lawrence Berkeley Laboratory where additional indications of the presence of diamond were found [7].
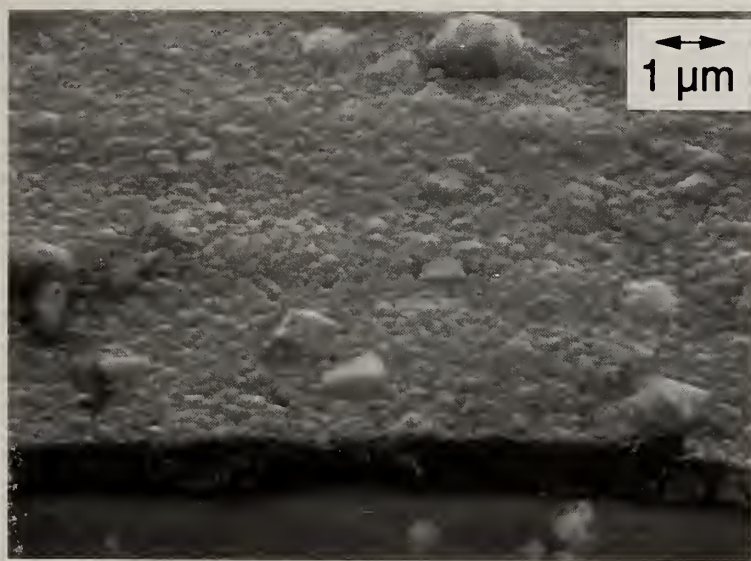
Fig. 4 SEM view of diamond-coated steel sample containing titanium interlayer (Courtesy of J. W. Ager).

Further work is needed to characterize the mechanical properties of the diamond-coated steel sample. The hardness, Young's modulus, and adhesion properties of the diamond film remain to be explored. Possible deleterious effects of the diamond deposition environment (e.g. substrate embrittlement) should also be investigated. Finally, additional understanding is needed for the role of titanium in promoting adhesion to CVD diamond. An initial study of the diamond/titanium interface indicates a complex reaction layer [8].

3. Conclusions

The diamond-coating of metals has been examined with emphasis on the use of a titanium interlayer to obtain an adherent coating on a steel alloy. Further work is needed to fully exploit this encouraging result and obtain useful coatings on common metal alloys. The outstanding issues include:

- mechanical characterization of the diamond-coated steel sample (i.e. measurement of the hardness, Young's modulus, and interface toughness).

- mechanical characterization the substrate and interlayer to determine if any degradation in properties results from the diamond deposition environment.

- interface characterization to understand the role of the titanium interlayer is obtaining exception adhesion.

- reduction of the deposition temperature to access more commonly used metal alloys in commercial applications.

- further development of adhesion testing methods which are appropriate for the extreme hardness and stiffness of diamond.

4. References

1. J. E. Field. *The Properties of Natural and Synthetic Diamond.* Academic Press, 1992.
2. J. W. Ager III, and M. D. Drory, *Phys. Rev. B*, **48** [4] 2601-2607 (1993).
3. J. W. Hutchinson and Z. Suo, *Adv. Appl. Mech.*, **29**, 63 (1991).
4. M. D. Drory and J. W. Hutchinson, *Science*, **263**, 1753-1755 (1994).
5. M. D. Drory and J. W. Hutchinson, unpublished results.
6. *Metals Handbook*, Vol. 1, 10th ed., ASM International, 1990.
7. M. D. Drory and J. W. Ager III, unpublished results.
8. S. S. Perry, J. W. Ager III, G. A. Somorjai, R. J. McClelland and M. D. Drory, *J. Appl. Phys.*, **74** [12] 7542-7550.

Applications of Diamond Films and Related Materials: Third International Conference, 1995
Editors: A. Feldman, Y. Tzeng, W. A. Yarbrough, M. Yoshikawa, and M. Murakawa

321

HETERO-EPITAXY OF DIAMOND FILM ON SILICON

Zhangda Lin, Jie Yang, Kean Feng and Yan Chen

State Key Laboratory of Surface Physics, Institute of Physics,
Chinese Academy of Sciences, Beijing 100080, China.

Key Words: diamond, heteroepitaxy, silicon

Abstract

Local hetero-epitaxial diamond films (100) and (111) on silicon (100) were obtained, results were discussed. Simulation of the hetero-epitaxy process was conducted by a HREELS study of the interactions of activated H_2, CH_4 with silicon covered by C_2H_2.

1. Introduction

By virtue of wide band gap, high mobility, and others, electronic devices made by diamond could work normally in elevated temperatures (above 600°C). Radiation resistance of diamond devices is about 1-2 order of magnitude higher than that of silicon devices, therefore diamond is firmly believed to be an ideal semiconductor material for high temperature, high speed and high power devices. However, natural diamond crystal is rare and expensive, so hetero-epitaxy of diamond is the most realistic approach. Naturally, silicon with diamond structure become the first choice as a substrate for hetero-epitaxy. Due to the high lattice mismatch between silicon and diamond, the possibility of the hetero-epitaxial diamond grown on silicon has been a considerable controversy for a long time.

X. Jiang of Fraunhofer Institute in Hamburg and B.R.Stoner of North Carolina State University have made great effort in overcoming the serious misfit, they used ß-SiC as a buffer layer for diamond epitaxy on silicon. However, our laboratory[1] has got direct evidence of hetero-epitaxial diamond directly formed on mirror-polished silicon wafer observed by high resolution cross-sectional transmission electron microscopy (HREM), only if Si surface had been pretreated properly and growth condition had been controlled appropriately. Further more, epitaxial process of diamond on Si(100) was simulated through interaction of activated H_2 and CH_4 with C_2H_2 adsorbed Si(100).

2. Experiment

A mirror-polished n-type silicon (100) wafer was used as a substrate. The sample had been cleaned carefully with conventional chemical cleaning process. The diamond film was deposited on the clean substrate in a typical hot filament chemical vapor deposition (HF-CVD) device and premixed mixtures of $CH_4 + H_2$ were fed into the chamber. For both D(100)/Si(100) and D(111)/Si(100) the growth parameters were as follows: gas flows H_2/CH_4 SCCM were 100/1.6 and 100/1.0 respectively, pressure in chamber was 20-30torr, the distances of tungsten filament to substrate were 8mm and 6mm respectively, filament temperature was 2000°C, substrate temperature was held at 800°C. The growth time was 4 hours and the total thickness were about 5000Å and 7000Å, respectively. Si substrate has been pretreated. Pretreatment parameters were: DC bias voltage of -40V, time of 30min. A JEOL-2010 electron microscope with point resolution of 1.9Å was used to take HREM image and a Leybold-22 has been used to measure the HREELS spectra.

3. Results and Discussion

As indicated by HREM image in Fig.1, it is clear that the diamond film was grown directly from Si substrate without any intermediate layer. There are about 40 rows of D atoms on 25 rows of Si atoms in the region without amorphous layer. The dislocation and deformation of the D atoms on the interface can be seen. As pointed out in Fig. 1, there is about a 7.3° angle between D(111) and Si(111). From the transmission electron diffraction pattern of this region we can clearly see that the diffraction spots of D (111) rotated with an angle of 10.7° about the Si[110] axis relative to the silicon (111)spots. (Fig.2)

Stoner *et al* explained the tilt angle of 5° between diamond (111) plane and ß-SiC (111) planes in the frame of Hooke law which is valid for elastic mechanics. However, in diamond/Si interface the local array (40 rows/25 rows) on a small epitaxial interface demonstrated that one misfit dislocation relates to an average of 2.67 lattice planes, corresponding to the dislocation density of 0.375, which in much excess of 14% the limitation for elastic deformation of hetero-epitaxial interface[2]. We suggest three components of dislocation formed at the interface: one component [001] of Burgers vector (b1) perpendicular to the boundary plane (001) to accommodate tilt and a second component [110] of the Burger vector(b2) lying in the interface to accommodate interfacial misfit, the third component [110] (b3) azimuthal rotation. Through calculation[3] we obtained the tilting angle of 8.08° and the angle of azimuthal rotation of 11.2° in good agreement with the experiment data of 7.3° and 10.7°, respectively.

Our previous studies[4], demonstated that surface full of CH_3 is in favour of (100) plane growth, while surface full of C_2H_2--(111) plane growth. So we alternated the growth parameter in order to change the ratio of CH_3 to C_2H_2 near the substrate and thus we obtained the D(111) epitaxial layer on Si(100). Its HREM is shown in Fig.3. The diamond(111) also directly grows on Si(100) without any intermediate (like SiC)

existed in between them. The area of epitaxial region is much larger than that we obtained in D(100)/Si(100). From X-Ray diffration, besides the Si (400) peak (substrate contribution), only a sharp and strong D(111) peak exists. A SEM was taken to show the mophology of epitaxial layer. The figure of epitaxial crystal can be seen, its size is about 5-6μm in one dimension.The studies of growth mechanism are in progress. Nevertheless, both D(100)/Si(100) and D(111)/Si(100) local epitaxy show that diamond can grow directly on Si without the need of any buffer layer, also throw light on the posibility of epitaxial diamond on Si with large area.

In order to simulate the epitaxial process of diamond on Si, the interaction of activated hydrogen and methane with silicon preadsorbed by hydrocarbon was strudied using HREELS. A n-type Si(100) wafer with size of 16x8x0.5mm^3 were used as substrate. It was installed into chamber after being cleaned carefully as mentioned above and heated to 1200K for several hours, flashed to 1500K for several cycles and then cooled down slowly to room temperature under 1×10^{-10}torr to obtain 2x1 reconstruction. Oxygen and carbon contaminations were not detected by HREELS and AES. Then the clean Si substrate was exposed to acetylene for 40 seconds at 5×10^{-8} torr, while LEED pattern remained 2x1 reconstruction as that of clean Si(100). HREELS spectrum shown in Fig. 4(a) reveals that the C_2H_2 was adsorbed on Si(100) in molecular form. Later the sample was exposed to atomic hydrogen for 10 min at 5×10^{-7} torr. The LEED pattern gave mainly a domain of (1x1) surface structure while HREELS spectrum shows a series peaks related to loss peaks of CH_2 or CH_3 and 260meV peak belongs to Si-H streching vibration. That means atomic hydroggen opens the Si dimer on the surface and also the carbon double bond of C_2H_2, Further more, the sample was continued to expose to $H_2 + CH_4$ activated by 2200K tungsten filament, the HREELS spectrum (Fig.4(c)) shows greatly weakened Si-H loss peak, the possible reason is due to the abstraction of hydrogen atom adsorbed on surface Si atom and then the replacement of CH_3 (or CH_2), indeed the C-H stretching loss grows a lot. Of course when sample was exposed to activated $H_2 + CH_4$, one possibility is CH_3 (or CH_2) simply adsorbs on Si, another possibity is the CH_3 (or CH_2) catenates each other and form a network. Now we heat the sample and measure the desorption products by QMS we found at 650K much H and a little CH_2 and CH_3 were detected, that means a little CH_2 and CH_3 were indeed adsorbed on Si surface, so they can be desorbed at low temperature, However when the sample was heated continually to 750K, only H was detected, but no CH_2 or CH_3. While the HREELS remains the picture similar to Fig.4(c) shown hydrocarbon still exist on Si surface, only they adsorb on Si surface not in CH_2 (or CH_3) form separately, but catenate each other and form a network, so they can hardly be desorbed, perhaps this is the initial stage of diamond formation. When sample was continued to heat to 900K, C_2H, C_2H_2 and C_2H_3 besides H_2, were detected. It means 900K hydrocarbon redical indeed catenate each other and evolve toward to a diamond structure.

References:
.

1. Jie Yang et al, Appl. Phys. Lett., 65, (1994)3203
2. J.H.Van der Merwe, Appl. Phys, 41, (1970)4725
3. Kean Feng et al, Phys. Rev.B, 51, January (1995)
4. Biwu Sun et al, Phys. Rev. B, 47, (1993)9816
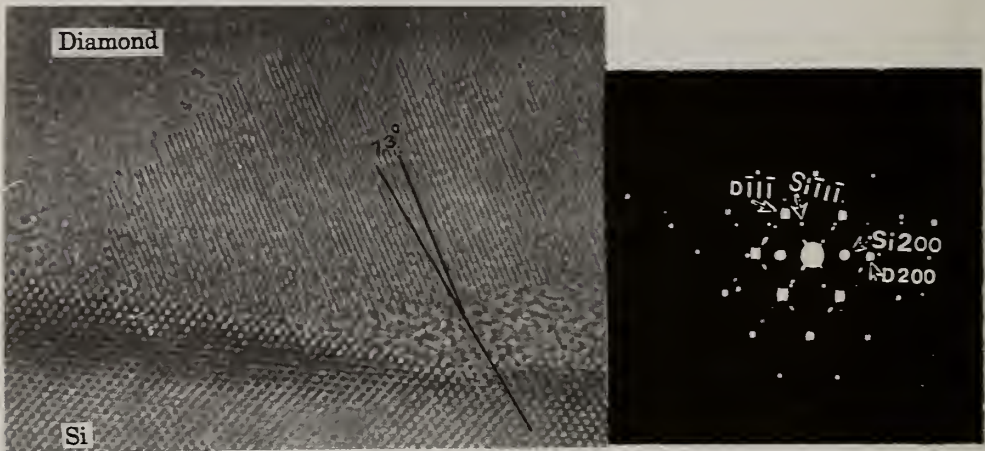
Fig.1. Lattice image of the heteroepitaxial diamond formed on Si(100) wafer. The specimen observed in a <110> direction.

Fig.2. Selected area pattern of TED on the diamond/Si interface.
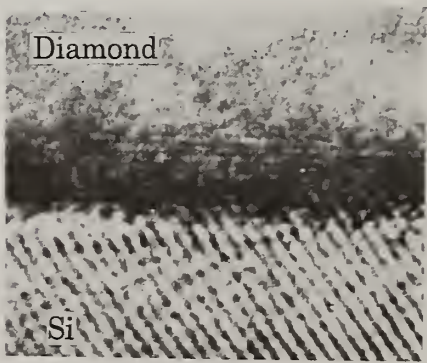
Fig.3. Lattice image of the heteroepitaxial diamond formed on Si(100) wafer. The specimen observed in a <110> direction.
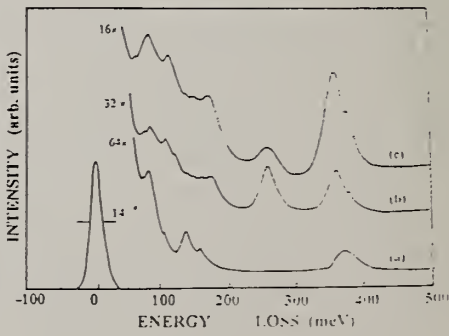
Fig.4. HREELS (a) Si(100) exposed to C_2H_2 40 seconds at 5×10^{-8} torr; (b) preadsorbed Si(100) exposed to atomic H 10min at 5×10^{-7} torr; (c) preadsorbed Si(100) exposed to activated $H_2 + CH_4$ 10min at 5×10^{-7} torr

Applications of Diamond Films and Related Materials: Third International Conference, 1995
Editors: A. Feldman, Y. Tzeng, W. A. Yarbrough, M. Yoshikawa, and M. Murakawa

325

Photoelectron Diffraction Studies of oriented Diamond Nucleation on Silicon (100)

E. Schaller, O. M. Küttel, R. Agostino and L. Schlapbach

Institut de Physique, Université de Fribourg, Pérolles, CH-1700 Fribourg (Switzerland)

Key words: nucleation, SiC, orientation, x-ray photoelectron diffraction

Abstract

(100)-oriented diamond films have been grown on silicon (100) in a microwave plasma assisted CVD tubular deposition system. X-ray photoelectron diffraction (XPD) has been used to study the first minutes of CVD diamond deposition. After 8 minutes of deposition, the diffractogram of the C1s photoemission signal shows an orientation of the SiC interface and of the diamond nuclei. By heating the silicon substrate to 780°C in a pure hydrogen plasma before starting the deposition, any surface damages such as argon bombardment effects are restored and the native oxide layer is removed. Therefore, the silicon surface has a perfect crystalline structure and the (100) orientation can be transmitted to the growing CVD diamond layer through an intermediate, oriented SiC layer.

1. Introduction

While polycrystalline, oriented diamond films are now routinely grown by CVD, no single crystal thin films have been deposited on non-diamond substrate so far. Therefore, it is important to understand the physical and chemical mechanisms which are responsible for the oriented growth on silicon. Various studies on oriented diamond films have been done using scanning and transmission electron microscopy (SEM, TEM)[1], X-ray photoelectron spectroscopy (XPS)[2] or X-ray diffraction (XRD)[3]. Nevertheless, it is not clear, whether orientation already occurs during the first minutes of bias pretreatment or later on during the deposition process.

In this contribution, we report on X-ray induced photoelectron diffraction measurements (XPD) for the characterisation of the very early stage of oriented diamond growth on silicon (100). This technique was used to characterise the surface of silicon substrates before the deposition process and the interface between the diamond film and the silicon substrate.

2. Experimental details

Low pressure diamond growth was performed on silicon (100) substrates via microwave plasma CVD in a tubular deposition system. The substrates were cleaned in acetone and introduced in the plasma system. A first run during 3

fitted Si-C component diffractogram. The detailed structure is weak due to the low coverage by carbon after this short deposition time. However, the four [111] maxima at $\theta = 54.7°$ and the four [011] maxima at $\theta = 45°$ are clearly visible on each diffractogram. The interpretation of these XPD measurements is straightforward: an oriented SiC interface is formed as an intermediate layer on top of which oriented diamond starts to nucleate from the beginning on.
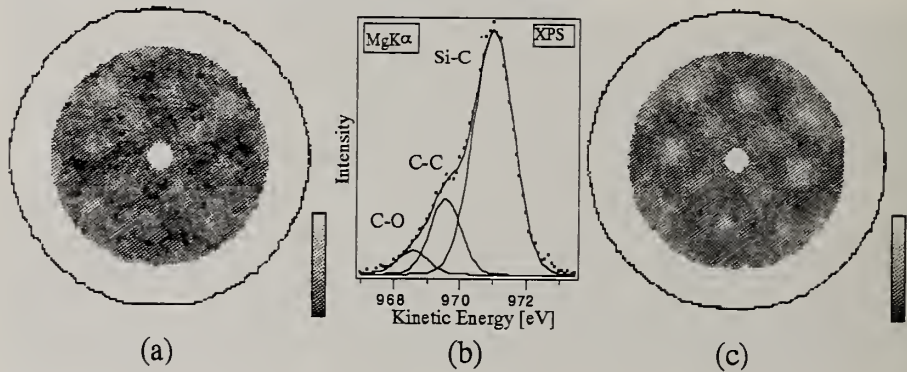
Fig.2: CVD diamond film after 8 minutes of bias pretreatment. **(a)** Stereographic projection of the C-C component of the C1s photoemission signal, **(b)** Fitted C1s photoemission signal, **(c)** Stereographic projection of the Si-C component of the C1s photoemission signal .

The β-phase of silicon carbide shows a zincblende crystalline structure like diamond. As XPD gives structural information which is not sensitive to the lattice constant, a similarity between the two diffractograms in Fig. 2 is observed. It appears that the SiC interface is always oriented with respect to the substrate independent of the parameters used for the pretreatment. At this stage of our study, it is not clear, whether the SiC interface forms an entire layer or just individual islands.

In order to obtain oriented growth of CVD diamond films, a well ordered silicon surface is not necessary before introduction of the substrate in the deposition chamber. We sputtered a silicon substrate with argon ions at 2kV for 20 minutes in order to destroy any crystal structure of the surface. The induced damage has been demonstrated by the absence of any structure in the Si2p photoelectron signal diffractogram. A CVD diamond film was then deposited under similar conditions as described before. After 15 hours of deposition, the SEM image surprisingly shows an (100)-oriented diamond film (Fig. 3a). The crystalline structure of the silicon surface was restored during the first 3 minutes of the deposition when the temperature rises to 780°C. Fig. 3b shows the Si2p diffractogram of the silicon substrate after argon bombardment, followed by 3 minutes of hydrogen plasma. A four-fold symmetry is observed, proving that the silicon surface is well ordered before adding CH4 in the gas mixture. From these measurements we conclude that the silicon substrate transmits in any case the orientation to the growing diamond film via an oriented SiC interface even when the silicon surface is oxidised or partly destroyed before introduction in the deposition chamber. The fact that the substrate plays the dominant role for the orientation of the diamond film can nicely be shown when depositing a CVD

minutes in pure hydrogen was used to adjust the deposition temperature. Nucleation was induced by applying a DC bias of -225 V to the substrate during 8 minutes at 810°C and under 20 mbar of a 2% CH_4/H_2 gas mixture. The parameters for the subsequent deposition were 870°C at 40 mbar with 1% CH_4 in H_2. After 15 hours of deposition, the polycrystalline CVD diamond films show 80% of (100) oriented crystals. The tilting angle of the individual crystals is about 5° as measured by XRD.

XPD is a well-established technique in surface science for studying surface atomic structure of monocrystals[4]. The experiments were performed in a VG ESCALAB Mark II spectrometer modified in order to enable motorised sequential angle-scanning data acquisition[5], equipped with low energy electron diffraction and a $MgK\alpha$ (1253.6 eV) and a $SiK\alpha$ (1740.0 eV) twin anode. The photoelectron emission angle above the substrate is varied by rotating the sample ($0°<\theta<90°$ and $0°<\phi<360°$). The photoelectron diffractograms obtained by this technique reflect a real space projection of the major crystalline directions of the crystal. A stereographic projection is used for the presentation. The surface normal corresponding to the [100] direction, is located in the centre of the plot whereas the outer circle represents an emission angle of 90° off normal.

3. Results

Fig. 1a shows an XPD measurement at 964 eV kinetic energy on an (100) oriented CVD diamond film surface excited with $MgK\alpha$ x-rays. The C1s diffractogram shows four-fold symmetry with the [111] crystallographic directions at $\theta = 54.7°$ and the [011] directions at $\theta = 45°$ as major features. Low index directions are plotted in Fig.1b. The overall fine structure of the CVD diamond film diffractogram is more fuzzy than measurements on a single crystal diamond[6]. This can be explained in terms of a superposition of the diffractograms from different, slightly misaligned microcrystals.
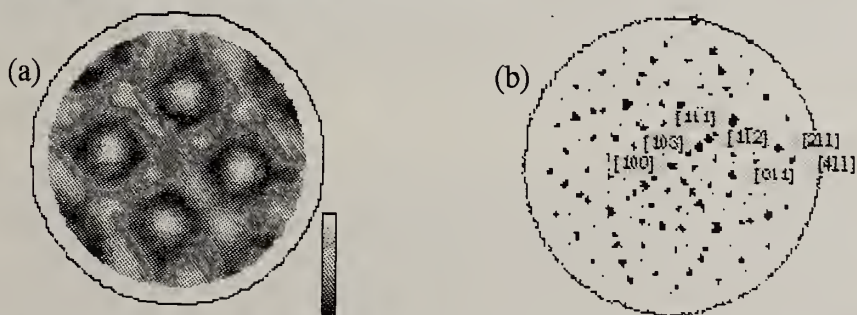
Fig.1: (a) Stereographic projection of the C1s XPD intensities at 964 eV kinetic energy induced by $MgK\alpha$ radiation of a CVD diamond (100) surface after 1 hour of deposition, (b) Plot of the low index directions.

Since XPD is very surface sensitive, investigations have been made after the first minutes of an oriented CVD diamond film deposition. Figure 2a shows the diffractogram of the fitted C-C component of the C1s photoemission signal (Fig. 2b) of a diamond CVD layer after 8 minutes of bias treatment. Fig. 2c shows the

diamond film on a silicon (111) substrate using the same deposition conditions as described above.
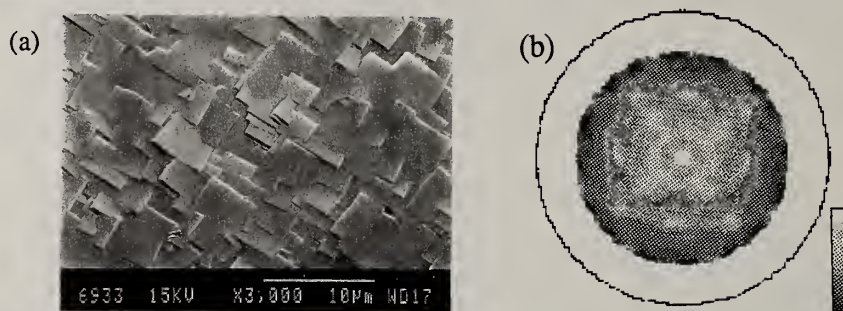
Fig. 3: (a) SEM image of a diamond film deposited for 15 hours on an Ar sputtered silicon substrate, (b) Si2p diffractogram at 1154 eV of a silicon substrate after argon sputtering and heating in hydrogen plasma at 780°C.

An (100) textured film is observed after 15 hours. However, as an (111) silicon surface was used, no (100) orientation can grow, and for the growth of an (111) orientation, the deposition parameters should be changed to get the right α value[7].

4. Conclusions

(100) oriented diamond films have been grown in a microwave plasma assisted CVD tubular deposition system. XPD shows an (100) oriented SiC interface and a preferential orientation of the microscopic crystals after 8 minutes of deposition. A hydrogen plasma treatment for 3 minutes induces a well ordered silicon substrate surface without any native oxide contamination. Therefore, the (100) orientation of the silicon surface can be transmitted to the growing film.

5. References

1. B. R. Stoner, G. H. Ma, S. D. Wolter, W. Zhu., Y. C. Wang, R. F. Davis, and J. T. Glass, Diamond Relat. Mater. **2**, 142 (1993)
2. S. Yugo, T. Kanai, and T. Kimura, Diamond Relat. Mater. **1**, 388 (1992)
3. R. Kohl, C. Wild, N. Herres, P. Koidl, B.R. Stoner, and J.T. Glass, Appl. Phys. Lett. **63**, 1792 (1993)
4. C.S. Fadley, in *Synchrotron Radiation Research: Advances in Surface Science*, edited by R.Z. Bachrach (Plenum, New York, 1990)
5. J. Osterwalder, T.Greber, A. Stuck, and L. Schlapbach, Phys. Rev. B **44**, 13764 (1991)
6. O.M. Küttel, R.G. Agostino, R. Fasel, J. Osterwalder, and L. Schlapbach, Surf. Sci. **312**, 131 (1994)
7. C. Wild, P. Koidl, W. Müller-Sebert, H. Walcher, R. Kohl, N. Herres, R. Locher, R. Brenn, Diamond Relat.Mater., **2**, 158 (1993)

Applications of Diamond Films and Related Materials: Third International Conference, 1995
Editors: A. Feldman, Y. Tzeng, W. A. Yarbrough, M. Yoshikawa, and M. Murakawa

329

Nucleation and Growth of Oriented Diamond Films on Ni Substrates

P.C. Yang[1], T.J. Kistenmacher[2], D.A. Tucker[1], W. Liu[1], F.R.Sivazlian[1]
S.P. Bozeman[1], B.R. Stoner[3], J.T. Prater[4], J.T. Glass[3] and R.F. Davis[1]

[1]Department of Materials Science and Engineering, North Carolina State University,
Raleigh, North Carolina 27695-7919
[2]Milton S. Eisenhower Research Center, Applied Physics Laboratory,
Johns Hopkins University, Laurel, Maryland 20723-6099
[3]Kobe Steel USA , Inc., Electronic Materials Center, RTP, NC 27709
[4]Army Research Office, Research Triangle Park, NC

Key words: oriented diamond, surface melting, X-ray diffraction, H, Ni, Co, Ni4C

Abstract

Oriented (100) and (111) polycrystalline diamond has been achieved without graphite formation. Nucleation is beleived to occur from a Ni-C-H molten surface layer on oriented, metastable, cubic Ni_4C previously nucleated on similarly oriented single crystal Ni substrates. The incorporation of the atomic H lowers the eutectic melting point of the Ni-C system from 1325°C to the 900-1000°C range and also promotes the nucleation of the Ni_4C. X-ray diffraction analysis revealed that the Ni_4C occurs only between the diamond particles and the Ni substrate.

1. Introduction

The growth of highly oriented heteroepitaxial diamond films represents an important step toward the goal of obtaining large area, device quality diamond. Nickel was chosen for investigation as a substrate material in this research initially because of its close lattice match (1.13%) and solvent-catalytic reactivity with diamond [1]. However, more complex, multi-step melt formation, precipitation and nucleation chemistries were discovered. The procedures, results and conclusions of this study are reported below.

2. Experimental

The nucleation and growth were conducted using the three-step sequential process shown in Fig.1. Step 1 involved deoxidization of the diamond seeded surface of [111] and [100] oriented Ni substrates in H_2 at 900°C for 10-30 minutes. In step 2 the Ni temperature was raised to 1100°C where the diamond seeds dissolved rapidly into the Ni. The annealing time varied depending on the degree of seeding and the surface temperature. This allowed sufficient reaction between the nickel, diamond seeds and atomic hydrogen (produced via a hot filament) to form a molten Ni-C-H intermediate layer. In-situ laser reflection interferometry (LRI) revealed large surface reflectivity changes during this multi-step process. This technique monitored the reflection of a He/Ne laser beam from the substrate surface. The intensity of this light depended on the reflection and scattering characteristics on the substrate surface. As shown in Fig. 2, the reflective light intensity during process step 1 was very low, due to the strong scattering by the carbon seeds. This intensity increased rapidly as the temperature was increased. At ≈1100°C a step increase in intensity was observed which was correlated with the formation of a molten surface layer. At this point, the temperature was lowered

to 900°C and the flow of CH_4 was initiated to begin diamond growth (step 3). X-ray diffraction (XRD) and scanning electron microscopy (SEM) were used to study the Ni/C/H interfacial reactions.

Results and Discussion

Figure 3 shows an SEM micrograph of a [111] oriented diamond film; [100] oriented films were also achieved. The representative XRD pattern of the [111] film shown in Fig. 4 consists of a set of strong diffraction spots from the single crystal Ni and weaker diffraction lines from the diamond film. The latter are further divided into a set of closely spaced discrete spots corresponding to diamond crystallites having an average grain size of >5µm and a set of smooth lines corresponding to the normally metastable cubic (NaCl structure) Ni_4C phase having an average grain size of <5µm. These results are summarized in Table I. Additional XRD and SEM studies on surfaces containing only a few diamond particles reveal that the Ni_4C does not occur as a separate phase apart from its association with these particles.

Table I. X-ray diffraction data

d(Å) smooth lines	d(Å) grainy lines	Ni_4C planes	diamond planes
2.03	2.03	{111} 2.04	{111} 2.06
1.75		{200} 1.75	
1.24	1.25	{022} 1.26	{022} 1.26

Based on the above results, a model is proposed to explain the mechanism of oriented diamond nucleation. Specifically, atomic H is incorporated into and lowers the eutectic melting point of the Ni-C system from 1326°C to the 900 - 1000°C range (step 2 in Fig. 1). The reduction in temperature to 900°C (step 3) in tandem with the atomic H in the melt causes the metastable Ni_4C phase to solidify from the melt with the same orientation as the solid Ni on which it nucleates and grows. This carbide phase also solidifies from molten Ni in HPHT diamond processes. The incorporation of atomic H in the Ni-C solution of the present research is believed to play a role analogous to high pressure high temperature in favoring the formation of Ni_4C. It is not known if H is incorporated into the Ni_4C lattice. The Ni_4C provides the sites and template for the subsequent nucleation of the diamond particles as a result of the close lattice matching of the lattice vectors of both phases (see Table I). It is important to note the essential role of atomic H. Neither Ni_4C nor diamond precipitates are produced in an inert ambient at 1 atm. The occurrence of the Ni_4C also contrasts with the formation of an initial graphite layer on solid [100] or [111] oriented Ni prior to the nucleation of diamond in the more common methods of deposition [3].

Conclusions

A multi-step process has been developed to nucleate and grow [111] and [100] oriented diamond films, without graphite deposition, from a molten layer formed via the incorporation of C and atomic H on a solid Ni surface. In-situ LRI was used to study the seeding and multi-step process as a function of temperature. A model involving the initial precipitation on the solid Ni of an oriented metastable cubic Ni_4C phase and the subsequent nucleation of diamond with the same orientation on this essentially lattice matched carbide has been proposed. Atomic H in the melt appears to be analogous to high pressure in the commercial diamond forming process routes.

Acknowledgments

References

1. Y. Sato, H. Fujita, T. Ando, T. Tanaka, and M. Kamo, Philosophical Transactions of the Royal Society of London A **342** (1993) 225.
2. P.C. Yang, W. Zhu, and J.T. Glass, Journal of Materials Research **8** (1993) 1773.
3. D.N Belton and S.J. Schmieg, Journal of Applied Physics **66** (1989) 4223.
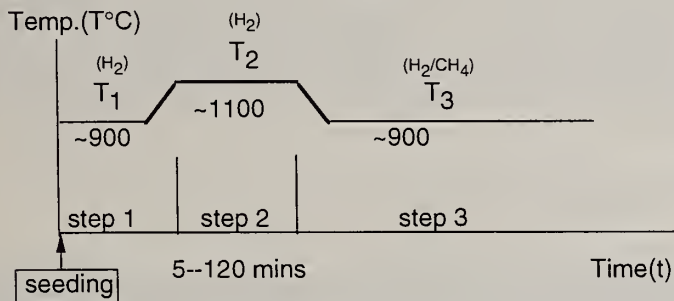
Fig. 1. The schematic diagram of the seeding
and multi-step process.
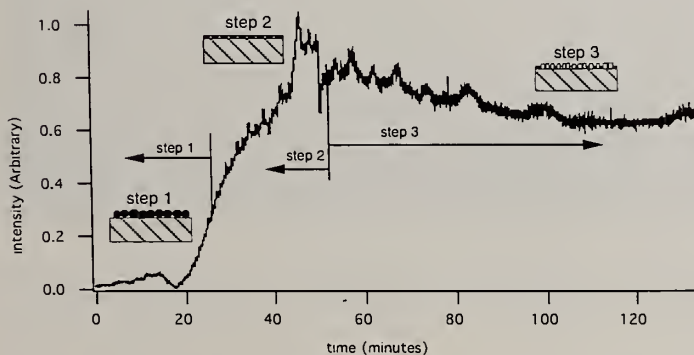
Fig. 2. Laser reflection interferometry spectrun of the seeding
and multi-step process.

332

————10μm
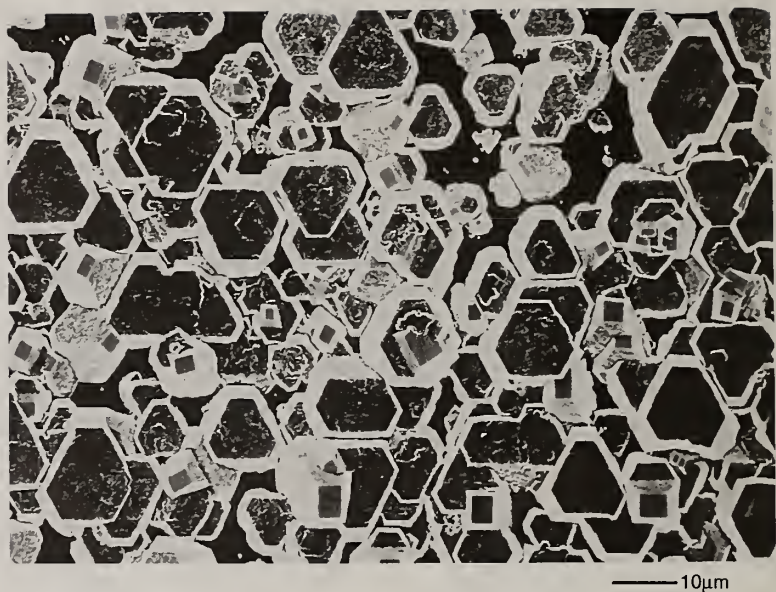
Fig. 3. SEM microstructure of a (111) oriented diamond film on
a Ni(111) substrate grown out by microwave CVD.

| smooth (022) Ni_4C | grainy (220) diamond | smooth (200) Ni_4C | grainy +smooth (111) Ni_4C, (101) graphite (111) diamond |
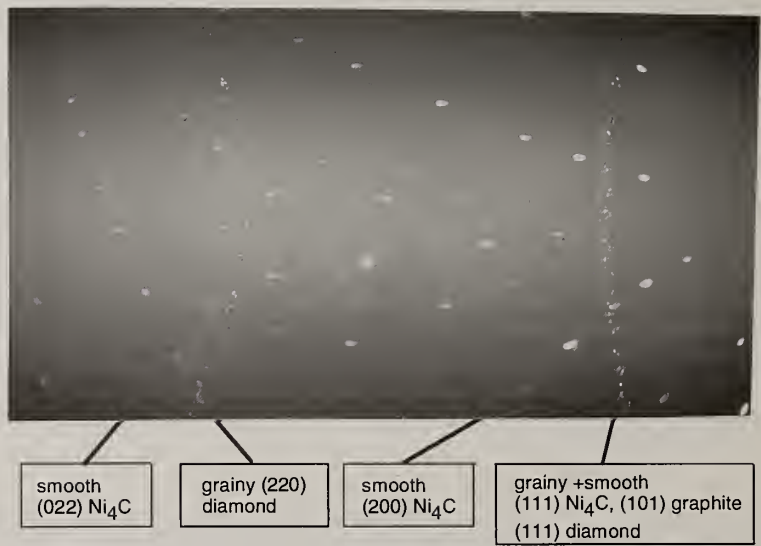
Fig. 4. X-ray diffraction pattern of the (111) oriented diamond film on the (111)
single crystal Ni substrate.

Applications of Diamond Films and Related Materials: Third International Conference, 1995
Editors: A. Feldman, Y. Tzeng, W. A. Yarbrough, M. Yoshikawa, and M. Murakawa

333

SEEDING WITH PURIFIED ULTRAFINE DIAMOND PARTICLES FOR DIAMOND SYNTHESIS BY CVD

H. Makita [1], T. Yara [2], N.Jang [1], K. Nishimura [3], A. Hatta [1], T. Ito [1] and A. Hiraki [1]

[1]Dept. of Electrical Engineering, Osaka Univ., 2-1 Yamada-Oka, Suita,Osaka, 565 JAPAN
[2]Chemical Lab. Sekisui Chemical Co. Ltd., 2-1 Shimamoto, Mishima, Osaka, 618 JAPAN
[3]Kita-Kyushu Polytech Col., 1665-1 Shii, Kokura-minami ku, Kita-Kyushu, Fukuoka, 803 JAPAN

Key words: low temperature fabrication, nanocrystal diamond, pretreatment, seeding

Abstract

Si substrates were seeded with purified nanocrystal diamond particles about 5 nm in diameter synthesized by the implosion process. Ultra high growing particle densities of diamond more than $5 \times 10^{11} cm^{-2}$ achieved and continuous diamond films were formed uniformly in 10 min after deposition started by using conventional microwave plasma chemical vapor deposition (CVD) method. Well-faceted diamond films have been fabricated at 200°C on the Si substrate by the magneto-active microwave plasma CVD method.

1. Introduction

Various methods of substrate pretreatment have been investigated for Chemical Vapor Deposition (CVD) of diamond films aimed at increasing the nucleation density.[1][2][3] Scratching or ultrasonic agitation with diamond powder has been the most useful one. In recent years, bias enhanced nucleation has been improved and some hopeful results for textured growth have been reported.[4] Seeding pretreatment with diamond powder of natural, high-pressure synthesized or implosion synthesized have been also investigated to replace such the damaging process to the substrate. However, its size was too large to increase the particle density, because the minimum size of diamond particles was 38nm.[3]

In this work, we attempted to seed Si substrates with well-defined nanocrystal diamond powder of 5nm average size synthesized by implosion process.[5] The particle diameter is in agreement with the critical nucleus of CVD diamond reported by Yugo *et al.*[6]

It has already been reported that growing particle densities of diamond more than $10^{10}cm^{-2}$ achieved and that the fabricated films showed high adhesiveness on the substrates.[7] It is expected that the quality of fabricated diamond films would be improved and the nucleation time would be dispensable since the film grows directly on purified nanocrystal diamond. Heath *et al*. also attempted to fabricate polycrystalline Si films at low temperatures on nanocrystal seeded SiO_2 substrates.[8]

Unfortunately, the available nanocrystal diamond powder was contaminated heavily and the particles were flocculated. It is necessary to purify the powder and disperse the flocculated powder into individual particles before use for the seeding.

2. Experimental

The commercially supplied nanocrystal diamond powder was dark brown because it was contaminated with unsaturated hydrocarbons, silicates and metals. The diamond powder was characterized using transmission electron microscope (TEM), powder X-ray diffraction (powder XRD) and polarizing microscopy. The contaminants were identified by IR absorption spectrometry, Inductively coupled plasma emission spectroscopy (ICP) and inorganic qualitative analysis. The decontamination process of nanocrystal diamond powder has been previously reported.[7] The purified nanocrystal diamond particle diameter of the TEM images was $30{\sim}60\text{Å}$. The powder was suspended in 50% methyl alcohol mixed with water to create the diamond lyophobic collide. The flocculated diamond particles were removed by centrifugation. This colloidal solution was used to seed Si substrates. Si substrates were dipped into the diamond colloidal solution after removal of the surface oxidized layer in 10% HF acid. Disperse medium and excess diamond particles on the substrate were blown out by air. For comparison, a conventionally pretreated substrate was prepared by scratching the Si substrate surface for 30min with diamond powder of about $40\mu m$ in diameter suspended in ethyl alcohol ultrasonic bath. Both of the seeded and scratched substrates were still mirrorlike.

The seeded and scratched substrates were tested for both high-temperature and low-temperature growth of diamond. A conventional microwave plasma CVD was employed for fabrication of diamond films for the high temperature deposition. For low-temperature deposition, a magneto-active microwave plasma CVD was employed. The details of the magneto-active microwave plasma CVD have been previously reported.[9][10][11] The substrate temperature in the magneto-active microwave plasma CVD was measured by a chromel-alumel thermocouple adhered to the right-side face of the substrate and protected with aluminous gluing agent. The substrate temperature was kept below $200°C$ during CVD by forced cooling from inside of the substrate holder.

3.Results and Discussion

Figures 1 shows scanning electron microscopy (SEM) image of the diamond films formed at 970°C by the conventional microwave plasma CVD. At the high substrate temperature, ultra high growing particle densities of diamond more than $5 \times 10^{11} cm^{-2}$ appeared on the seeded Si substrates. Continuous diamond films were formed in 10 min whereas no recognized particle were remaining in SEM observation before CVD. On the other hand, no growing particles are observed in SEM images on the scratched substrates after 10 min CVD.

Figures 2(a) and 2(b) show SEM images of the diamond films formed for 8 hours at 200°C on the scratched and the seeded substrates, respectively. The film fabricated on the seeded substrate has well-faceted particles. On the other hand, the film fabricated on the scratched substrate has no faceted surface. The nanocrystal seeding is essentially an unique pretreatment for diamond nuclei to improve the film quality fabricated at low temperature, such as 200°C.

4. Conclusions

Diamond nanocrystal seeding has the advantages over the scratching method for ultra high growing particle density resulting in high speed formation of continuous film. Especially, for the fabrication of high-quality diamond film at low temperature, diamond nanocrystal seeding is essential because it is difficult to generate diamond nuclei at low temperature by other methods.

5. Acknowledgment

6. .References

1. S. Yugo, T. Kanai, T. Kimura, and T. Muto, Appl. Phys. Lett. **58**, 1036 (1991)
2. Ewa J. Bienk and Svend S. Eskildsen, Diam. Reat. Matter. **2**, 432 (1993)
3. G. S. Yang and M. Aslam, Appl. Phys. Lett. **66**, 311 (1995)
4. B. R. Stoner, C. T. Kao, D. M. Malta, and R. C. Glass, Appl. Phys. Lett. **62**, 3438 (1993)
5. T. Ikushima, New Diamond **24**, 27 (1992)
6. S. Yugo, A Izumi, T. Kanai, T. Muto and T. Kimura, Proc. 2nd. int. conf. New Diamond Science & Technology (Materials Research Society, Pittsburgh, 1991), pp.385
7. H. Makita, T. Yara, K. Nishimura, A. Hatta, T. Ito and A. Hiraki, Proc. 4th. int. conf. New Diamond Science & Technology (MYU, Tokyo, 1994), pp.191
8. J. R. Heath, S. M. Gates, and C. A. Chess, Appl. Phys. Lett. **64**, 27 (1995)
9. J. Wei, H. Kawarada, J. Suzuki and A. Hiraki, J. Cryst. Growth **99**, 1201 (1990)
10. T. Yara, M. Yuasa, M. Shimizu, H. Makita, A. Hatta, J. Suzuki, T. Ito and A. Hiraki, Jpn. J. Appl. Phys. **33**, 4404 (1994)
11. T. Yara, H. Makita, A. Hatta, T. Ito and A. Hiraki, Jpn. J. Appl. Phys. **34**, L312 (1995)

Table 1. Experimental conditions

	Microwave plasma CVD	Magneto-active microwave plasma CVD
Microwave power	275 W	1.2 kW
Magnetic field	none	87.5 mT
Substrate	Si (100)	Si (100)
Substrate bias	floating	+40 V
Substrate temperature	950~980°C	200°C
Source gas	CO 10 sccm	CH_3OH 15 sccm
Dilution gas	H_2 90 sccm	H_2 85 sccm
Total gas pressure	5 kPa	13.3 Pa
Deposition	10 min	8 hour
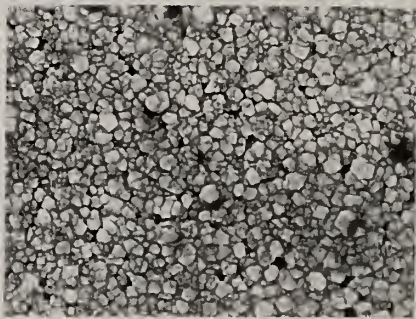
1μm

Fig. 1 SEM image of diamond film fabricated on the seeded substrate at 970°C by the conventional microwave plasma CVD
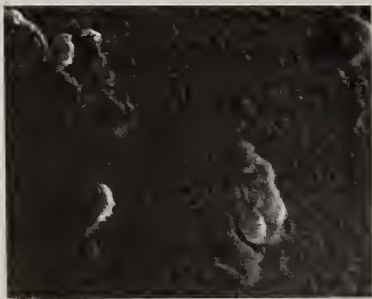
1μm
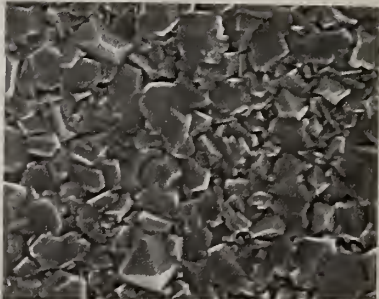
1μm

(a) Scratched substrate   (b) Seeded substrate

Fig. 2 SEM images of diamond films fabricated at 200°C by magneto-active microwave CVD

Applications of Diamond Films and Related Materials: Third International Conference, 1995
Editors: A. Feldman, Y. Tzeng, W. A. Yarbrough, M. Yoshikawa, and M. Murakawa

337

Characterization of Diamond Nucleation Enhancing Layer Formed during Bias Treatment on Silicon

Dae-Whan Kang[1], Bai-Qin LI[2], Ki-Bum Kim[1], and Hwack-Joo Lee[3]

[1]Dept. of Metallurgical Engineering, Seoul National University, Seoul 151-742, Korea
[2]National Laboratory oj Solid State Microstructure and Departmint of Physics, Nanjing University, Nanjing 210093, China
[3]Korea Research Institute of Standards and Science, Taejon 305-600, Korea

Key words: amorphous carbon,BEN,HRTEM,nucleation-enhancing layer, SiC

Abstract

We treated four different Si (100) substrates with dc negative bias for 5, 10, 20 and 60 minutes each. Then, we deposited diamond films with uniform thickness of about 3-4.5 μm onto four Si (100) substrates under the same growth condition. Bias-treated Si surfaces before the deposition of diamond films were analyzed using Raman spectroscopy, HRTEM and AES to investigate the nature of nucleation enhancing layer. The analysis showed that amorphous carbon layer was formed during bias treatment (SiC formation was not identified). We also analyzed bias-treated Si surfaces using conventional TEM. TEM images showed the clear overall procedure of amorphous carbon layer growth as biasing time increased.

1. Introduction

Much attention has been paid to CVD diamond film deposition in order to use it as high-temperature and high-power electronic devices due to its many advantages such as large band gap(5.5eV), thermal stability, high hardness, chemical inertness, etc.[1,2]. The main roadblock in its practical use is the difficulty of growing diamond film heteroepitaxially on nondiamond substrates, especially on Si.

Recent success in growing textured diamond film on Si has presented a possible method of obtaining heteroepitaxial diamond growth[3,4]. This method used BEN(Bias Enhanced Nucleation) technique which is known to be very effective in promoting diamond nucleation on Si[5,6-8]. However, the exact mechanism of this BEN technique is still being debated. Especially, many researchers have argued about the nature of nucleation enhancing layer formed during bias treatment[3-8]. For instance, Sheldon et al.[6] insisted that the nucleation enhancing layer is the amorphous carbon layer from the analysis that used HRTEM and EELS. But their claims cannot explain the results of Wolter[3] and Jiang[4]. Their result showed that the deposited diamond films had a strong orientational relationship with Si substrate, unlike Sheldon's claim of carbon layer having the amorphous structure. On the other hand, Arezzo et al.[7] claimed that the nucleation enhancing layer is SiC from the analysis that used XPS. This claim explains the orientational relationship between diamond particles and Si substrate because the SiC usually forms epitaxially on Si substrate[9]. However, it is

insufficient to explain the Hartnett's result[10], which is difficult to deposit diamond film on crystalline SiC layer without any pretreatment.

The purpose of this paper is to identify the exact nature of nucleation enhancing layer formed at various biasing times by using Raman spectroscopy, cross-sectional high resolution transmission microscopy and Auger electron spectroscopy.

2. Experimental

The diamond deposition was done on 3x3 cm^2 Si (100) from CH_4+H_2 gas mixture by using AsTek microwave plasma CVD system. During bias treatment, the biasing time was varied from 5 to 60 minutes at fixed bias voltage of -260V and the methane fraction of 10%. Detailed processing conditions are summarized in Table I. The thickness and surface morphology of deposited films were investigated by Philips CX 20 scanning electron microscope. Micro-Raman spectroscopy using a 488nm Ar laser of 200 mWatt was used in order to measure the quality of deposited diamond films and to investigate the bonding characteristics of the layer formed during bias treatment. The composition and structure of this layer were investigated by using cross-sectional HRTEM and AES. HRTEM was performed on a Hitachi 9000 NAR electron microscope operated at 300 kV, with a point to point resolution of 1.8Å. In order to clearly identify the layer, the bias-treated samples were also prepared. Especially, polycrystalline Si was deposited on bias-treated samples using SiH_4+H_2 gas mixture by LPCVD to define the interfacial structure in TEM observation.

Table I. Processing conditions

Bias treatment conditions	Diamond growth conditions
microwave power : 800 watt	microwave power : 1200 watt
substrate temperature : 800 °C	substrate temperature : 800 °C
pressure : 15 torr	pressure : 20 torr
bias voltage : -260V, CH_4 : 10%	CH_4 : 0.5%
biasing time : 5, 10, 20, 60 minutes	growth time : 10 hours

3. Results and Discussion

3-1. SEM observation

We have identified that uniform diamond films were deposited on Si substrate irrespective of the biasing times. These films had a similar surface morphology as shown in Fig.1. Many corners of octahedron appeared at growing surface, which means that the growth rate of (100) plane was larger than that of (111) at given growth condition. Cross-sectional views of diamond films are also shown in upper-right region of each figure. While the thickness of grown diamond film with 60 minutes biasing time was 4.5μm, the thickness of other films with shorter biasing time was about 3μm.

3-2. Raman Spectroscopy

Raman spectra of Si after bias treatment at different times were obtained as shown in Fig.2(a). In case of 5 and 10 minutes, no peaks appeared at range of 1100-1700 cm^{-1}. But, 20 and 60 minutes bias-treated samples showed two broad peaks centered at 1350 and 1580 cm^{-1} which are the characteristic peaks of amorphous carbon. Additionally,

there existed a small peak centered at 1160 cm^{-1}, which is associated with amorphous sp^3 bonding character[11]. This result indicates that amorphous carbon layer was formed with considerable thickness above 20 minutes. Two speculations are possible from the results of Raman spectra of 5 and 10 minute samples. First, amorphous carbon layer was still the diamond nucleation enhancing layer although its amount was too small to show its characteristic peak. Second, there must be an additional mechanism about bias enhancing effect, because we were also able to obtain the diamond films in case of 5 and 10 minutes. Further details about these speculations will be discussed in the following sections. Fig.2(b) shows that all grown diamond films had similar Raman spectra consisting of two peaks. One is a sharp diamond characteristic peak at 1332 cm^{-1} and the other is a broad disordered sp^2 peak centered at 1550 cm^{-1}. This result indicates that the change of biasing time did not largely affect the quality of deposited diamond films.

3-3. AES analysis

Auger depth profile analysis was performed to investigate the surface and internal composition of bias-treated samples. The results shown in Fig.3(a) and (b) indicate that Si atoms as well as carbon atoms exist at the uppermost surface of 5 and 10 minutes bias-treated samples. However, an uniform carbon layer was mainly formed during bias treatment of 20 and 60 minutes as shown in Fig.3(c) and (d).

3-4. HRTEM observation

By observing the cross-sectional interface by TEM, interlayers with different structure and thickness were identified in different biasing times. Fig.4 shows that the nucleating interlayer was composed of two different layers. The lower layer was formed just on Si substrate and its thickness slightly decreased from 100Å of 20 minutes to 40Å of 5 minutes. The upper layer was amorphous layer, the morphology and thickness of which were varied with biasing times. In Fig.4(a), the thickness of this amorphous layer was extremely thin of about 30Å. However, 10 minutes bias-treated sample in Fig.4(b) represents amorphous carbon nodules with size of a few hundreds of Å, which was formed on a lower thin amorphous layer. Fig.4(c) shows a thick uniform amorphous layer of about 2000Å. HRTEM observation showed more detailed interfacial structure of bias-treated samples. Fig.5 shows that there was no phase having a different lattice spacing from that of Si at interface, which proves that SiC layer or particle was not formed on Si unlike the results of other researchers[1,3,8]. Fig.5(b) shows HRTEM interfacial image of 20 minutes bias-treated sample. It especially indicates that an upper thick layer was amorphous carbon, as was confirmed by Auger depth profile analysis and Raman spectroscopy in previous sections. Fig.5 also shows that Si surface was remarkably corrugated due to the bombardment of carboneous ions. The extreme roughness of Si brought about the virtual images of lower thin layer observed at low magnification in Fig.4. Above results demonstrate that an amorphous carbon layer, which was formed during bias treatment, is the diamond nucleation enhancing layer as was suggested by Sheldon et al[6].

4. Proposed model about amorphous carbon layer growth

Based on results of surface analyses and discussions, the procedure of amorphous carbon layer growth can be modeled as following. Fig.6 represents the schematic diagrams of this procedure.

Step A : The bombardment of carboneous ions caused Si atom to be sputtered or to be etched away so that Si surface roughness increases. However, such corrugated Si surface is not efficient to form diamond nuclei, which was confirmed by the results of our group's additional experiments.

Step B : Successive ion bombardment breaks carboneous ions or radicals into carbon atoms and they form amorphous carbon layer, which is composed of sp^2 and sp^3 bonded carbon clusters, is deposited on corrugated Si surface.

Step C : After an amorphous carbon layer grows above a critical thickness, arriving carbon atoms tend to form nodules in order to release the high residual stress of amorphous carbon layer.

Step D : As amorphous carbon nodules grow, they meet together and then form a continuous layer. Again, several amorphous carbon nodules form on a lower continuous layer through step C. An amorphous carbon layer thicken through such repeated process. A diagram in step D shows the microstructure of amorphous carbon layer after several repeated processes.

5. Conclusion

We have identified that uniform diamond films were deposited on Si bias-treated for shorter time as well as for 60 minutes. Auger depth profile, Raman spectroscopy and HRTEM indicated that only amorphous carbon layer was formed during bias treatment and that no evidence about SiC formation was identified. Low magnification TEM images showed the clear overall procedure of amorphous carbon layer growth as biasing time increased. The repeated process, including thin amorphous carbon layer formation followed by amorphous carbon nodules formation and growth, formed a thick amorphous carbon layer. Both amorphous carbon layer and nodules formed during bias treatment plays a major role in promoting the diamond nucleation.

6. Reference

1. W.Zhu, B.R.Stoner, B.EWilliams, and J.T.Glass, Proc.of the IEEE, **Vol 79(5)**, 621 (1991)
2. K.Shenai, R.S.Scott, and B.J.Baliga, IEEE Trans. on Electron devices, **Vol.36(9)**, 1811 (1989)
3. S.D.Wolter, B.R.Stoner, and F.T.Glass, Appl.Phys.Lett.,**62(11)**, 1215 (1993)
4. X.Jiang and C.-P.Kalges, Appl.Phys.Lett., **62(26)**, 3438 (1993)
5. S.Yugo, T.Kanai, T.Kimura, and T.Muto, Appl.Phys.Lett.,**58(10)**,1036 (1991)
6. B.W.Shelson, R.Csencsits, J.Rankin, R.E.Boekenhauer, and Y.Shigesato, J.Appl.Phys., **75(10)**, 5001 (1994)
7. F.Arezzo, N.Zacchetti, and W.Zhu, J.Appl.Phys., **75(10)**, 5375 (1994)
8. B.R.Stoner, G.H.M.Ma, S.D.Wolter, and J.T.Galss, Phys.Rev.**B45**, 11 067(1992)
9. H.S.Kong, T.C.Wang, J.T.Glass, and R.F.Davis, J.Mate.Res., **3**, 521 (1988)
10. T.Hartnett, R.Miller, D.Montanari, C.Willingham, and R.Tustinson, J.Vac.Sci. Technol., **A8**, 2129 (1990)
11. R.J.Nemanich, J.T.Glass, G.Lucovsky, and R.E.Shroder, J.Vac.Sci.Technol. **A6**, 1783 (1988)
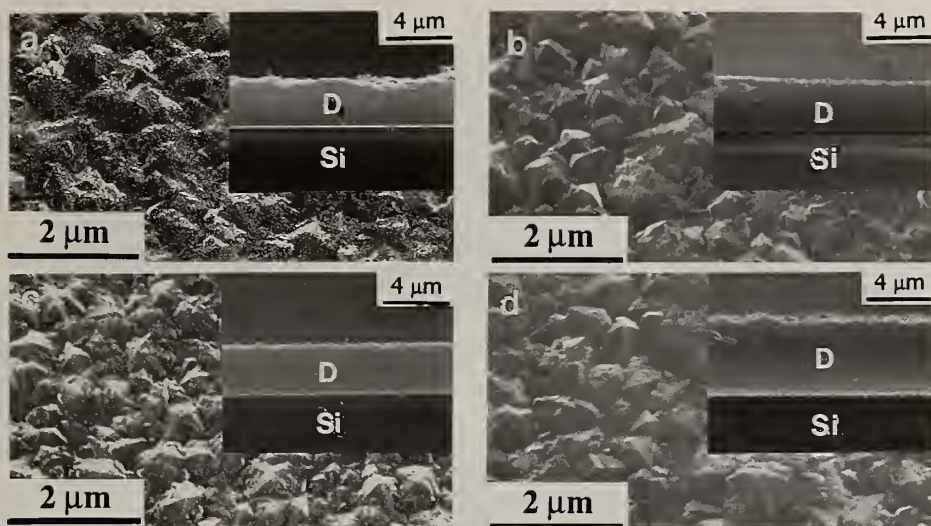
Fig.1 SEM photographs of surface morphology of 10 hour-deposited diamond films
grown on Si bias-treated at -260Vand 10% CH$_4$ for
(a) 5 minutes (b) 10 minutes (c) 20 minutes (d) 60 minutes
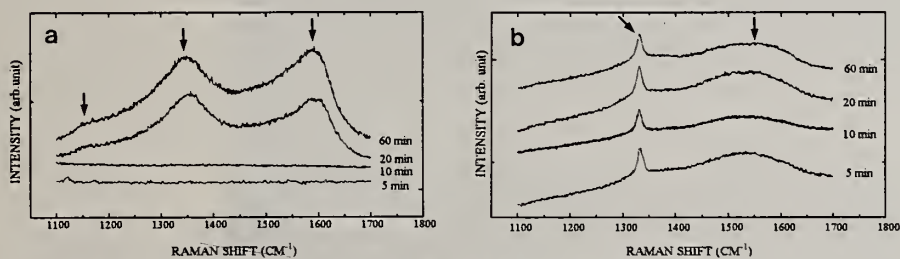
Fig.2 Raman spectra of (a) Si samples bias-treated at -260Vand
10% CH$_4$ for various times (b) its diamond grown films
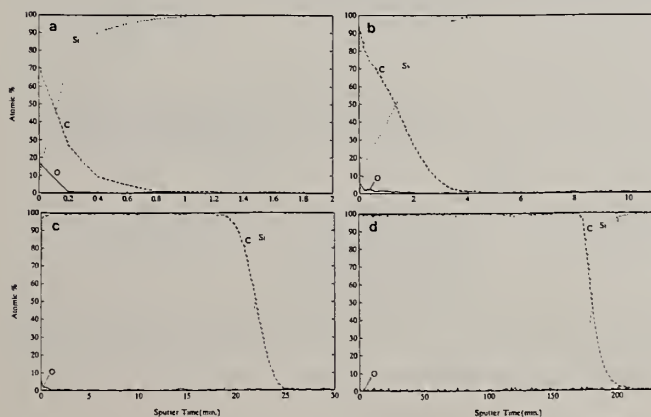
Fig.3 Auger depth
profiles of Si samples
bias-treated at -260V
and10% CH$_4$ for
(a) 5 (b) 10 (c) 20
(d) 60 minutes

342
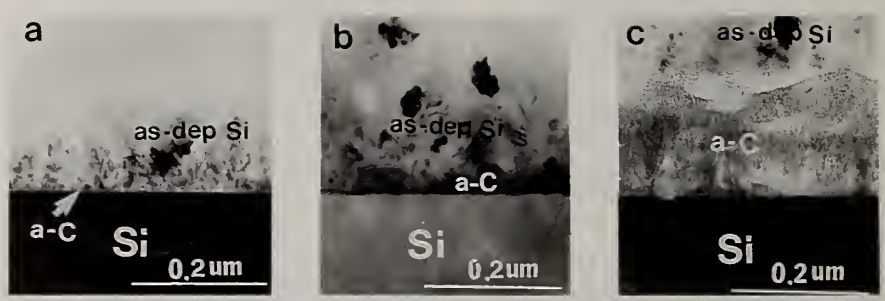
Fig.4 Low magnification images showing the interface formed by
(a) 5 minutes (b) 10 minutes (c) 20 minutes bias treatment
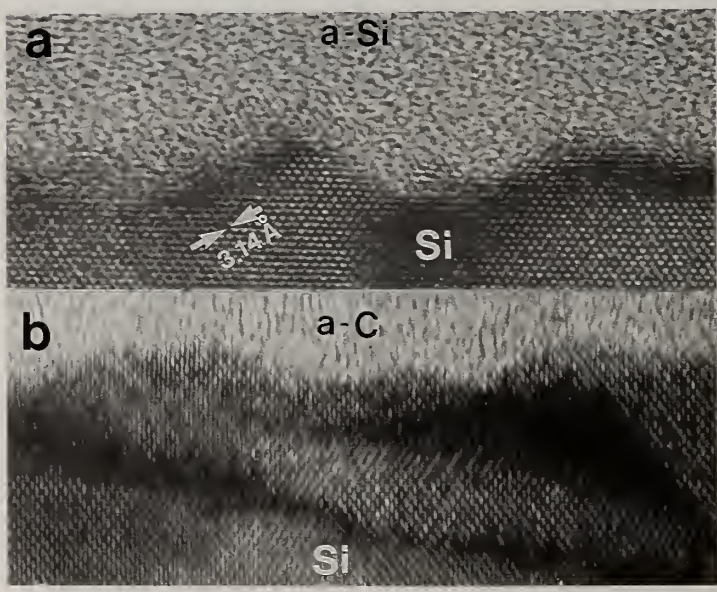
Fig.5 HRTEM images of the interface formed by bias pretreatment for (a) 5 min (b) 20 min
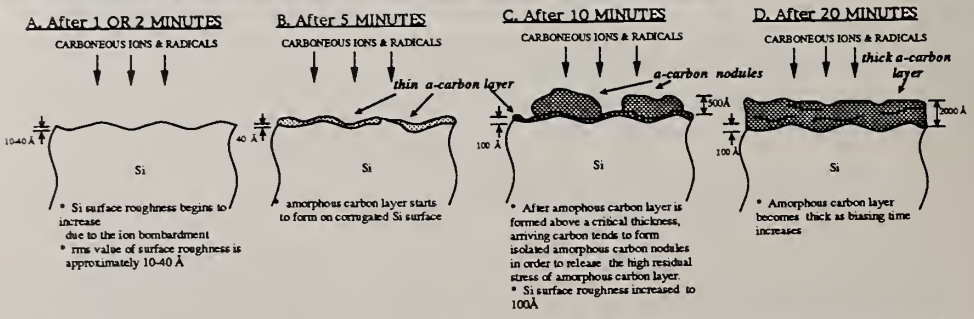
Fig.6 Schematic diagrams of amorphous carbon layer growth during bias pretreatment (based on this experimental results)

DIAMOND NUCLEATION AND GROWTH ON MIRROR-POLISH SILICON WAFER PRETREATED BY SILICON ION IMPLANTATION

Jie YANG[1], Xiaowei SU[2], Qijin CHEN[1], Zhangda LIN[1]

[1]The State Key Lab. of Surface Physics, Inst. of Phys., Chinese Academy of Sciences, Beijing, 100080, P.R.China

[2]National Lab. for Materials Modification by Laser, Ion and Electron Beams, Dalian Univ. of Technology, P.R.China

Key Words: HF-CVD, Ion implantation, Diamond film

Abstract

Diamond films have been obtained by hot-filament chemical vapor deposition (HF-CVD) method on silicon wafer. The substrates were pre-implantated by silicon ion beam (the ion energy is 25keV, implantation dosage is 5×10^{15}, 5×10^{16}, and 2×10^{17} Si^+/cm^2). X-ray diffraction (XRD), scanning electron microscopy (SEM), Cross-sectional transmission electron microscopy (TEM), and Raman spectroscopy were used to characterize the structure of the synthesized films.

1. Introduction

The nucleation of diamond is an essential step for the diamond film synthesis, which depends on the substrate material and is greatly affected by the initial surface conditions of the substrate. From the technological point of view, silicon, as the basic material for present microelectronics, is strongly favored as a substrate material for thin film diamond devices[1]. However, the high lattice mismatch and high surface energy difference between silicon and diamond has caused considerable controversy about possible diamond growth on silicon substrates. In general, owing to the high surface energy of diamond and the relatively low sticking probability of the precursor for diamond nucleation, diamond nuclei grow very poorly on a mirror-polished silicon substrate[2]. Different pretreatment methods have been developed to enhance the diamond nucleation density[3-6] etc. However, In above pretreatment methods many factors affect the nucleation of diamond, for example, residual diamond seeds, carbon precursor, the change of surface stress, and formation of carbide etc. It is not easy to distinguish these different factors from the above pretreatment methods. In this paper, Si^+ ion beam implantation was used to pretreat

the silicon wafer. It is believed that surface stress predominates diamond nucleation. Because ion implantation technique is very mature, the parameters of energy and dosage can be controlled conveniently, so this method has significance not only in theory but also in application.

2. Experimental

Mirror-polished n-type silicon (100) wafers were used as substrates. Si^+ ion implantation was carried out at E=25keV in a MEVVA IV80-10 ion implantation system. The ion current density was about 30 $\mu A/cm^2$. The implantation dosages were
$5x10^{15}$, $5x10^{16}$, and $2x10^{17}$ Si^+/cm^2 respectively. The sample had been cleaned before loading (washing by cleaning lotion, etching in dilute hydrofluoric acid, cleaning with acetone and washing with deionized water). The vacuum during the implantation was better than $3x10^{-4}Pa$. After implantation, the samples were taken out and cleaved into $2x1cm^2$ oblongs. The diamond film was deposited in a typical hot filament chemical vapor deposition (HF-CVD) device. The source gas was diluted CH_4 in hydrogen at the ratio of 0.8% with the total flow rate of 100 sccm (sccm denotes standard cubic centimeter per minute). The distance between the filament and the substrates was fixed at 5mm. Filament temperature was 2100°C; substrate temperature held at 830°C; growth time was 24 hours. X-ray diffraction (XRD) analyses were used to characterize the structure of synthesized film. Scanning electron microscopy (S-450) and transmission electron microscopy were used to study the surface and cross-sectional morphology of the films. The quality of the synthesized films was characterized by Raman spectroscopy (SPEX 1403, 400mW, wavelength 514.5nm).

3. Results and discussions

SEM photographs were shown in Fig.1. it is clear that diamond had been formed on Si wafer. For $5x10^{15}$ samples (show in Fig.1(a)), the diamond film was not continue which indicates the density of nucleation is low, while for $2x10^{17}$ samples (show in Fig.1(b)), well-distributed and continuous polycrystalline diamond film with good crystalline facets has been synthesized and total thickness of diamond film is about $12\mu m$ by cross-sectional observation.

Fig.2 is a Raman spectrum of the as-grown diamond film ($2x10^{17}$ sample) with 488.0nm Ar^+ ion laser excitation. The sharp and strong diamond peak appears at $1332cm^{-1}$, the graphite peak near $1580cm^{-1}$ is very low. It shows that the synthesized diamond film is of good crystallinity. XRD and TEM analyses were also defined that diamond films have been formed on the pre-implanted Si wafer.

The characters of surface implantation were taken into account in the choice of the implantation energy. Because the peak of ion distribution is in the sub-surface of the substrate and the distance between this peak and substrate surface increases with the

increase of the implantation energy, lower energy ion implantation can result in changing the surface stress while keeping the bulk Si wafer's properties. In our experiment, accordingly, the implantation energy was fixed at 25keV, which is the lowest available energy for Si^+ implantation in our ion implantation system.

Ion implantation can increase the surface energy of Si substrate because it involves the process of atomic displacements. This process results from collisional events, radiation-enhanced diffusion, and thermal spikes to different degrees depending on the crystal structure layer and substrate substance[7]. Ion implantation can reduce the difference of surface energy between the Si wafer and the diamond film and enhances the nucleation of diamond on substrate.

Based on previous work[5,8], nanoscale microstructuresare effective nucleation sites for the diamond growth. Ion beam implantation can change the surface structure of Si wafer on the nanoscale level. Two possible factors are related to the changes of surface morphology to affect the diamond nucleation. First, ion implantation favors the formation of precursors of diamond, for example, SiC and amorphous carbon, etc., and second, it increases the sticking probability of these diamond precursors on Si wafer. However, compared with mechanical scratch and chemical etch methods, Si^+ implantation has less effect on the surface morphology of Si wafer. It causes no visible surface damage or roughness viewed with an optical microscopy, while the others usually turn the sample surface rougher. XRD result shows that no SiC has been found. Therefore, we believe that the change of surface stress of Si wafer is the dominant factor for diamond nucleation and growth on Si wafer in our experiments. A very important advantage of this pretreatment method is that it is compatible with other pretreatment methods. It can be used as first step of the combined pretreatment methods.

In summary, Si^+ implantation, a new method without surface mechanical damage of substrate for enhancing diamond nucleation on mirror-polished silicon wafer, has been raised. Well-distributed and continuous polycrystalline diamond film with high quality crystals has been synthesized by HF-CVD method. The surface stress is believed to be one of the most important factors for the diamond nucleation on Si wafer.

References

[1] D.G.Jeng, H.S.Tuan, R.F.Salat, and G.J.Fricano, Appl. Phys. Lett. 56, 1968(1990)
[2] X.Jiang and C.-P.Klages, R.Zachai, M.Hartweg, and H.-J. Fusser, Diamond and Related Materials, 2, 407(1993)
[3] S.Iijima, Y.Aikawa, and K.Baba, Appl. Phys. Lett. 57, 2646(1990)
[4] C.-P.Chang, D.L.Flamm, D.E.Ibbotson, and J.A.Mucha, J. Appl. Phys. 63, 1744(1988)
[5] H.Maeda, S.Ikari, S.Masuda, K.Kusakabe, and S.Morooka, Diamond and Related Materials, 2, 758(1993)
[6] B.R.Stoner, G.-H.M.Ma, S.D.Wolter, and J.T.Glass, Phys. Rev. B, 45, 11067(1992)
[7] X.Jiang, C.-P.Klages, R.Zachai, M.Hartweg, and H.-J.Fusser, Appl. Phys. Lett. 62, 3438(1992)
[8] G.Dearnaley, Ion implantation, Northholland Pulishing Company, Amsterdam (1971)
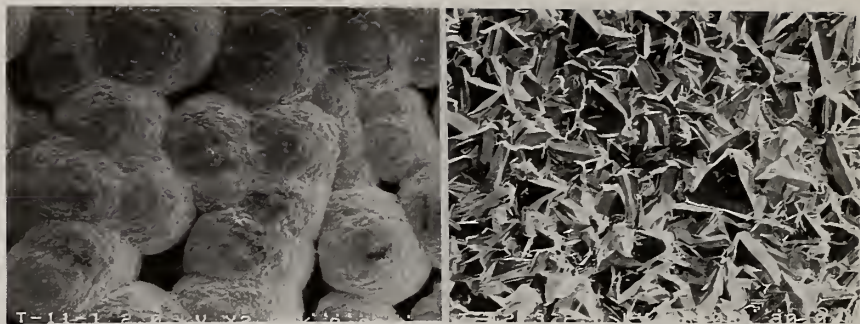
FIG. 1. SEM photographs (a) for 5×10^{15} sample and (b) for 2×10^{17} sample surface morphology of diamond film on Si wafer following Si^+ implantation.
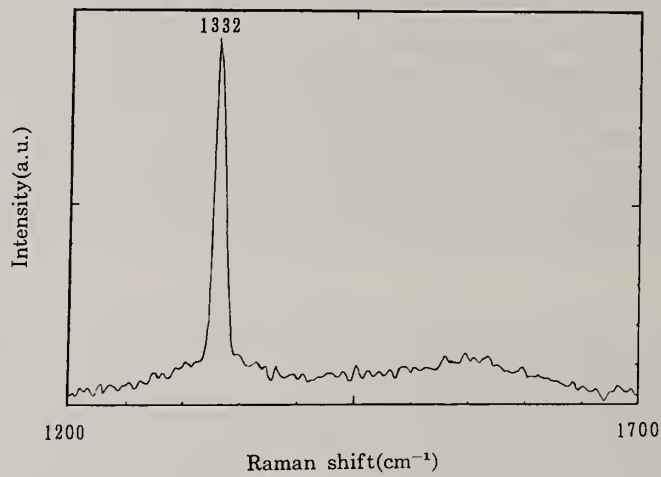
FIG. 2. A Raman spectrum synthesized diamond film on Si wafer following Si^+ implantation.

EFFECT OF ION IMPLANTATION ON THE CVD DIAMOND NUCLEATION DENSITY ON Si SUBSTRATES

C.L. Fritzen, R.P. Livi, J.P. de Souza and J.A.H. da Jornada
Instituto de Física da UFRGS - C.P.: 15051, CEP 91501-970, Porto Alegre - Brasil

Key words: CVD diamond, ion implantation, nucleation

Abstract

Si (100) substrates, scratched with diamond paste (4μm), were implanted in one half of their surface, with $^{40}Ar^+$ (60 keV) and $^{84}Kr^+$ (60, 100 and 300 keV) ions with fluences ranging from 5×10^{13} to 10^{15} ions/cm^2. These samples were placed in a hot filament chemical vapor deposition (HFCVD) equipment and after deposition the diamond nucleation density was analyzed. The nucleation density remained the same as the one for the non implanted area, until a certain critical ion fluence, beyond which decreases rapidly more than three orders of magnitude. This critical fluence depends on the ion mass, energy and on the substrate temperature during the ion implantation. The nucleation density data as a function of ion fluence correlates well with RBS/channeling measurements results that show the amorphisation of the samples at the previously mentioned critical fluences. The results indicate that the atomic motions during the ion induced amorphisation process destroy the small features in the sample surface topography that are responsible for the CVD diamond nucleation.

1. Introduction

The problem of diamond nucleation in CVD synthesis is a very important issue, both for the technological as well as from the scientific side. Many different substrate pre-treatments as well as initial processing conditions are already known to control and enhance nucleation, however a clear microscopic understanding of the process is still lacking. The most common process of enhancing nucleation is scratching the substrate surface, and then, many ideas about the physical process of nucleation were related to strains generated by such processes [1]. As the scratching were efficiently done by diamond powders, some of the ideas were also related to seeding with diamond nanocrystals [2,3]. The picture is however not clear, since nucleation can also be stimulated by scratching with non-diamond materials [4], and also, without scratch, using proper surface treatment [5,6]. In a previous paper [7] we studied the effects of stress generated by a Vickers indentation, were a large stress field is generated, and did not found evidence of nucleation. Also we found a reduction of nucleation in

scratched surfaces subjected to further oxidation [8] indicating that the nucleation is related to fine topological features of the surface, in agreement with previous work [9]. In a recent paper Kobayashi et al. [10] found also a reduction of nucleation after ion implantation with Ar^+ ions at 100 keV. In this paper, we examine with details the effect of ion implantation on suppressing the nucleation on a scratched substrate, in order to have a better understanding of the microscopic mechanisms of diamond nucleation, using different ions, energies, fluences and also substrate temperatures during implantation.

2. Experimental Details

A p-type silicon wafer (100) with 10 cm in diameter was scratched with diamond paste (4µm). After cleaning with acetone, the wafer was cleaved and the samples masked in one half of their area, being then exposed to ion implantation. $^{40}Ar^+$ (60 keV) and $^{84}Kr^+$ (60, 100 and 300 keV) bombarding ions were used with fluences ranging from 5×10^{13} to 10^{15} ions/cm^2, at room temperature (RT). $^{84}Kr^+$ (100 keV) ion implantation were also made at liquid nitrogen temperature (LNT), in the same range of fluences. After these pre-treatments, each half-implanted sample was placed in a hot filament conventional CVD reactor for diamond deposition for 3 hours. During the deposition the reactor chamber pressure was 50 torr; the total gas flow (blown directly over the samples trough the coiled heated tungsten filament) was 200 sccm with 1% methane in hydrogen (99.9 and 99.995% purity respectively). The filament temperature was 1900 °C, and the sample temperature was 750 °C. The filament was negatively biased in relation to the sample, flowing a 5 mA DC current between them.

3. Experimental Results

After the CVD diamond deposition, the samples were analyzed by scanning electron microscopy (SEM) and micro-Raman spectroscopy. Fig.1 shows a SEM micrograph corresponding to a sample implanted with 10^{15} cm^{-2}, $^{84}Kr^+$, 60 keV, in one half of its area. The large nucleation (left hand side) corresponds to the non implanted area. In the implanted area (right hand side) the diamond nucleation is almost completely suppressed by the ion implantation. The SEM micrographs were digitized and statistically analyzed, being determined the nucleation density, n, for the various samples. The ratio n/n_0 of the nucleation density, n, corresponding to each ion implanted scratched sample, to the nucleation density n_0 corresponding to the non implanted scratched area in the sample is shown in fig.2, as function of the ion implantation fluence. For small ion fluences the ratio n/n_0 for the various Ar^+ and Kr^+ implanted samples is equal to one. In this region of ion fluences the beam-substrate interation does not affect the nucleation. After a certain critical ion fluence, that depends on the type of ion, ion energy and substrate temperature during ion implantation, the ratio n/n_0 decreases rapidly, more than three orders of magnitude. Rutherford backscattering/channeling (RBS/channeling) measurements [11] showed

that above the critical ion fluence the substrate surface becomes amorphous. This correlation is in conformity with the results for ion implantation at liquid nitrogen temperature, wich shows a reduction in the ion fluence necessary for nucleation supression, since it is known that amorphisation is facilitated by low substrate temperature.
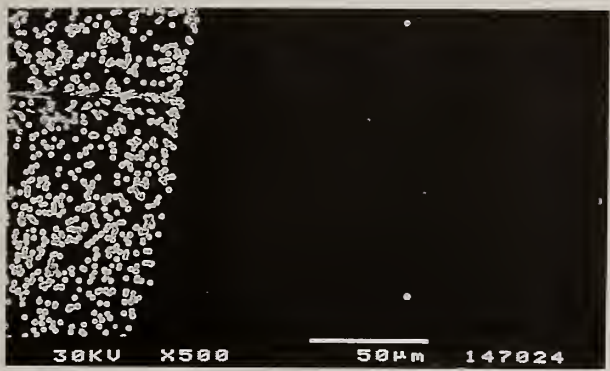
Fig.1. SEM image for the sample implanted with 10^{15} cm^{-2}, ^{84}Kr$^+$, 60 keV, RT, on the right hand side and unimplanted (left).
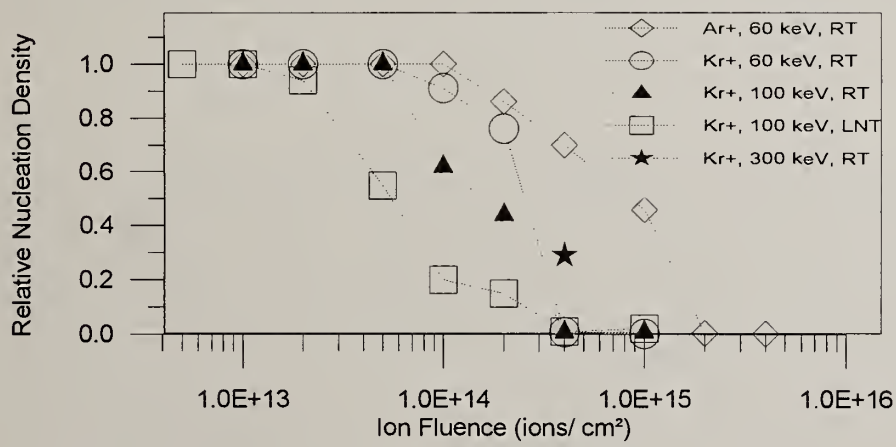
Fig.2. Relative nucleation density n/n_0 as function of ion fluence.

4. Discussion and Conclusions

Our results show clearly a drastic suppression of nucleation, which coincides with amorphisation of the substrate by the ion implantation. However, the amorphisation itself cannot be responsible for this nucleation suppression, since it is known that recrystalization on Si substrate occurs at temperatures below the substrate

temperature used in this experiment for CVD deposition (750 °C). In fact we made a RBS/channeling study of the amorphised substrate after a very short period (2 minutes) at the same condition of CVD deposition, finding a total recristalization of the sample. In view of the previous coments which do not support the idea of stress or seeding as a general explanation for the nucleation, and in view of the above discussed results, we are lead to explain this nucleation suppression to the change in topography of the substrate due to the amorphisation-recristalization process. Therefore, the nature of the nucleation centers should be related to surface topography, in a very small scale, since the depth of the implantation zone is typically of the order of a few tenth of nanomenters. This conclusions is in agreement with our previous study about the suppression of nucleation by oxidation of the surface of Si [8], and also with different studies pointing out the importance of topological aspects of surface [9].

5. Acknowledgments

6. References

[1] S.J. Lin, S.L. Lee, J. Hwang, C.S. Chang and H.Y. Wen, Appl. Phys. Lett., **60**, 1559 (1992).
[2] S. Iijima, Y. Aikawa and K. Baba, J. Mater. Res., **6**, 1491 (1991).
[3] M. Ihara, H. Komiyama and T. Okubo, Appl. Phys. Lett., **65**, 1192 (1994).
[4] H. Maeda, S. Ikari, S. Masuda, K. Kusakabe and S. Morooka, Diamond and Related Materials, **2**, 758 (1993).
[5] S.Yugo, T. Kanai, T. Kimura and T. Muto, Appl. Phys. Lett., **58**, 1036 (1991).
[6] R.A. Rudder, G.C. Hudson, J.B. Posthill, R.E. Thomas and R.J. Markunas, Appl. Phys. Lett., **59**, 791 (1991).
[7] C.L. Fritzen, R.P. Livi, E.H. da Jornada and J.A.H. da Jornada, in Proc. of 10th Brazilian Congress of Engeneering and Materials Science (CBECIMAT), São Paulo, december, 6-9, 1992, p. 88.
[8] C.L. Fritzen, R.P.Livi, E.H. da Jornada and J.A.H. da Jornada, in S. Saito, N. Fujimori, O. Fukunaga, M. Kamo, K. Kobashi and M. Yoshikawa (Editors), Advances in New Diamond Science and Technology, (MYU, Tokyo, 1994), p. 221.
[9] R. Polini, J. Appl. Phys., **72**, 2517 (1992).
[10] K. Kobayashi, M. Kumagai, S. Karasawa, T. Watanabe and F. Togashi, J. Crystal Growth, **128**, 408 (1993).
[11] C.L. Fritzen, R.P. Livi, J.P. de Souza and J.A.H. da Jornada, To be published.

Applications of Diamond Films and Related Materials: Third International Conference, 1995
Editors: A. Feldman, Y. Tzeng, W. A. Yarbrough, M. Yoshikawa, and M. Murakawa

351

EFFECTS OF SOME PHYSICAL PARAMETERS ON DIAMOND CRYSTALLIZATION IN THE NaOH+Ni+C SYSTEM AT 1 ATM.

Kuruvilla A. Cherian, Satyendra Kumar and Rustum Roy

Intercollege Materials Research Laboratory
Pennsylvania State University, University Park, PA 16802, USA

Key words: diamond morphology, liquid-phase, surface recrystallization

Abstract

The NaOH+Ni+C system has been found to lead to diamond surface recrystallization from a liquid phase at atmospheric pressure and about 800C under appropriate experimental conditions. Critical aspects of the process include the following:
a) The simultaneous dissolution of nickel and diamond-carbon in the common solvent.
b) The formation of an intermediate nickel-carbon complex which facilitates the
    availability of sp^3 carbon for subsequent recrystallization on diamond "seeds".
The diamond formation is sensitive to experimental parameters such as pressure, temperature and time, besides nature and concentration of the chemical species involved. Preliminary results of varying some of these parameters are presented. these show variation in the overall growth morphology - from overgrowths of discrete morphology to continuous larger area deposits, under appropriate conditions.

1. INTRODUCTION

It is now becoming clear that in addition to physical and chemical vapour routes for metastable diamond formation, liquid phase routes could also exist. These could involve metal-hydrogen-carbon [1] and metal-oxygen-hydrogen-carbon systems [2]. One of such liquid phase routes is the NaOH-Ni-C system in which diamond surface recrystallization could occur at atmospheric pressure and about 800C under appropriate experimental conditions [3-5]. Critical aspects of the process include a) the simultaneous dissolution of nickel and diamond-carbon in molten NaOH which serves as common solvent for nickel and diamond-carbon, and b) the formation of an intermediate phase which facilitates the availability of sp^3 carbon for subsequent recrystallization on diamond "seeds". These processes could be affected by several factors, and this report deals with the effects of varying some physical parameters such as pressure, temperature and time.

2.EXPERIMENTAL AND RESULTS

Diamond cleavage specimens were subjected to dissolution in molten NaOH together with nickel at temperatures above 800C; the system was then rapidly quenched to room temperature, as has been reported [4]. Several runs were carried out to study the effect

of varying the temperature, period of dissolution and pressure. The diamond specimens were subsequently recovered from the solidified mass adopting suitable acid leaching processes, and examined by optical and electron optical techniques to assess the effect of varying the physical experimental parameters.

2.1 Effect of variation in dissolution period:

Experiments were carried out at 810C with dissolution period being taken as variable. It was observed that the average size of the overgrowths did not vary significantly; while an increase in density of nucleation was apparent. Increased dissolution period apparently leads to increase in local concentration of the carbon atoms. This eventually leads to a change: from isolated crystallites to more denser growth and eventually a continuous deposit. A typical example is shown in Figs.1a&b. Repeats of the experiment with the presence of added graphitic carbon in solution appeared to have a negative effect, but with only diamond-carbon in the system, similar results were obtained.

2.2 Effect of variation in temperature:

Experiments at temperatures <~800C apparently yielded negative results for dissolution periods upto 600 secs. Runs were then carried out at temperatures of 825C, 850C, 875C and 890C, with all other parameters including dissolution period (300 sec.) kept constant. The size distribution of the recrystallized overgrowths formed at these conditions are represented in Figs. 2a-d. Temperature increase apparently leads to increase in the average size of the overgrowths. Repeat of the experiments lead to comparable results and data.

2.3 Effect of pressure

A gas pressurization system, a modified hydrothermal crystal growth system with argon as the pressurizing medium, was used to study the effect of pressure. A pressure of 20,000psi was developed at a temperature of 810C; however, it must be noted that in this case the temperature build up rate and subsequent cooling rates are much different due to the nature of the system employed. Initial results indicate the possibility of larger overgrowths such as that in Fig. 3 being formed under specific conditions; further confirmatory studies would be conducted to confirm this, and subsequently the effect of hydrogen pressure.

3. CONCLUSIONS

Diamond formation by the NaOH+Ni+C liquid phase surface recrystallization process is apparently sensitive to experimental parameters such as pressure, temperature and time, besides nature and concentration of the chemical species involved.

Preliminary results of varying some of these parameters show change in the overall deposition morphology: from discrete overgrowths of discernible triangular and rectangular morphologies to continuous larger area deposits of apparently complex morphology, under appropriate conditions.

4. ACKNOWLEDGEMENT

5. REFERENCES

1.   A.R. Badzian and T. Badzian, in Proc. of the NIRIM International Symp. on Advanced Materials '94, Edited by M. Kamo, H. Kanda, Y. Matsui and T. Sakina, 140-145 (1994)
2.   M.Komath, K.A. Cherian, S.K. Kulkarni and A. Ray, Diamond Relat. Mater., 4, 20 (1994)
3.   A.R. Patel and Kuruvilla A. Cherian, J. Cryst. Growth, 46, 706 (1979)
4.   Kuruvilla A. Cherian, Surf. Coat. Technol., 47, 127 (1991)
5.   E. Pavel, G. Baluta, C.Giurgiu, D. Barb, V. Sandu, M. Morariu and D.P. Lazar, Diamond Relat. Mater., 2, 505 (1993)
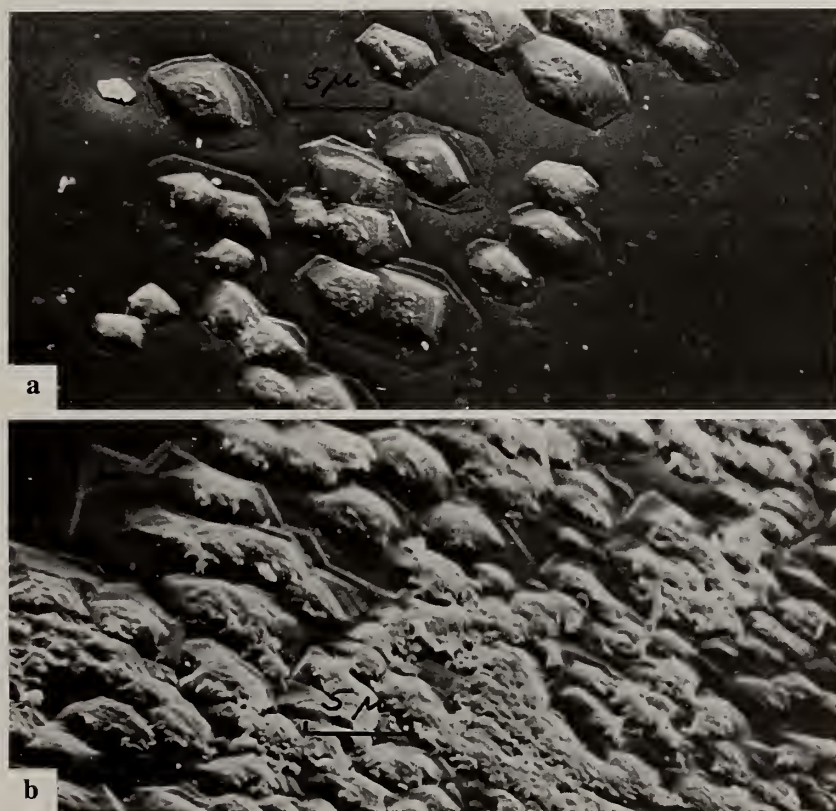
Figure 1 a&b
Effect of increased local concentration of dissolved diamond-carbon, for same temperature. The average size does not show significant change whereas the nucleation density does change.
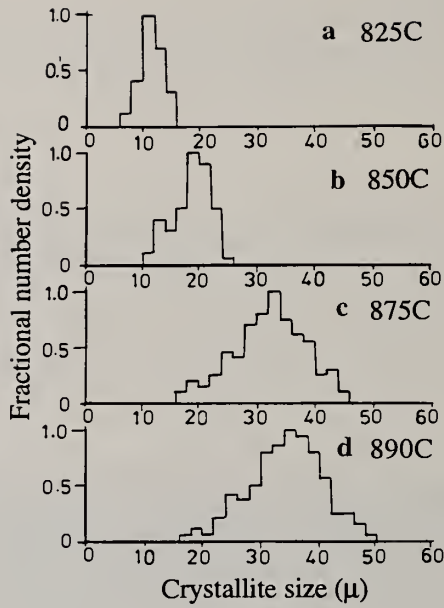
Figure 2 a-c
Size distribution data of the metastable diamond overgrowths at different temperatures,
for the same dissolution period (300 secs.):
Fractional number density vs. Crystallite size for
(a) 825C
(b) 850C
(c) 875C
(d) 890C
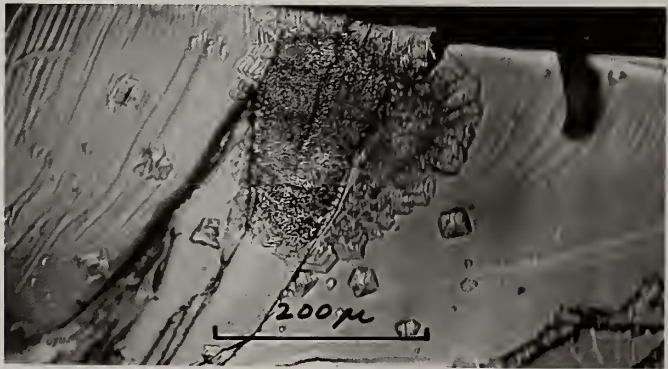
Figure 3.
An example of a larger (~200μ) complex morphologied diamond deposit.

Applications of Diamond Films and Related Materials: Third International Conference, 1995
Editors: A. Feldman, Y. Tzeng, W. A. Yarbrough, M. Yoshikawa, and M. Murakawa

355

DIAMOND SYNTHESIS VIA HYDROTHERMAL PYROLYSIS OF HYDROCARBONS AND HALOGENATED HYDROCARBONS ON DIAMOND SEEDS

Rustum Roy[1], Duraiswamy Ravichandran[1] and Palaniappan Ravindranathan[2]

[1]Intercollege Materials Research Laboratory, The Pennsylvania State University, University Park, PA 16802 , U.S.A.
[2]Harris Ireland, Dundalk Co., Louth, Ireland.

Key Words : Diamonds, Glassy Carbon, Hydrothermal and Halogenated Hydrocarbon.

Abstract

Various hydrocarbons and halogenated hydrocarbons [$CHCl_3$, $CHBr_3$, CHI_3] were subjected to "hydrothermal" reactions in the presence of diamond seeds in the pressure regime 1-5 kbar and at temperatures near 800°C. In many samples the powder X-ray diffraction patterns show substantial increases of the diamond peak. The grown crystals are too small to be observed in the scanning electron microscope. The transmission electron microscope data gives support to the possibility that the grown diamonds are too small to be detected by SEM.

1. Introduction

Bundy et al. [1] in the year 1955 synthesized diamonds presumably based on conditions similar to those found in the nature. It was later hence forward world wide that diamonds could only be made above the Berman - Simon P-T line . 25 years later Spitsyn et al. [2,3] synthesis methods based on ambient pressure synthesis (1 atm.). Later Kamo et al [4] proved by using CVD process that pressure is not a necessary parameter for diamond synthesis.

Starting in 1957, O.F.Tuttle and R.Roy proposed to the Office of Naval Research that they attempt to synthesize diamonds under hydrothermal conditions simulating carbonatite compositions this was unsuccessful. DeVries [5] has pointed out the geological evidence suggesting that diamonds could be possibly grown by hydrothermal processes. Very recently DeVries et al. [6] presented a detailed analysis of our rationale for the potential synthesis of diamonds under hydrothermal p-t conditions.

2. Experimental

A series of hydrothermal experiments has now been made with a wide variety of carbon sources reacted with various fluids sealed in both gold and platinum capsuls. Some two hundred runs have been made over a period of 2 years by two different experimentalists.

(i) Pyrolysis of hydrocarbons

A wide variety of aliphatic and aromatic hydrocarbons were made to react with 5 % diamonds seeds of size < 1μ and subjected to "hydrothermal" conditions at temperatures in the range 700 - 800°C with pressures near 1-1.5 kbars.

(ii) Reaction of glassy carbons with water

The mixture of various glassy carbons (derived from poly vinyl alcohol) with diamond seeds (5 wt %) were subjected to " hydrothermal" conditions at 800 °C for 72 hours at a pressure of 1.4 kbar. Studies have also been made by varying the percentage of water content added in the capsules.

(iii) Pyrolysis of halogenated hydrocarbon :

The goal here was to choose phases which might provide additional catalysis during the "crystallization" of the resulting carbon and easier bond breakage. The following halogenated hydrocarbons ($CHCl_3$, $CHBr_3$, CHI_3) and CCl_4 each mixed with seeds (2 wt. %) and subjected to " hydrothermal" reactions.

We report herein preliminary results of the successful runs in each of these areas.

3. Results and Discussions

Fig. 1 shows the powder X-ray diffraction patterns of before (Fig. 1a) and after (Fig. 1b) for the runs of glassy carbon 500 and diamond seeds reacted at 800°C - 1.4 kbar for 72 hours with 2 drops (33 wt. %, Fig. 1b) and 4 drops of water (72 wt. %, Fig. 1c). In preparing the samples for X-ray diffraction, the same sample area was covered with the same amount of powder so that the peak intensity of diamond should be a reasonably quantitative measure of the concentration of diamonds in the before and after processed samples.

The color of the samples after reaction typically becomes gray from black. Changing the processing temperature to 900°C and even 1,400°C showed less (or the same) amount of growth of diamond. Very significantly, throughout these studies, experiments in Pt capsules did not show the growth of the diamond peak. We attribute this to the fact that hydrogen diffuses through Pt capsules, but not through the Au capsules, and the (H) presence is essential for the growth of diamonds.

The Raman spectrum in all of these samples shows a sharp 1332 cm^{-1} peak,

superimposed on a "graphitic" background as expected. Raman spectra of unreacted samples did not show similar peaks. However, SEM analyses did not show the presence of the typical morphology for diamond growth as observed in the CVD process. In TEM analysis we could not identify individual crystals of diamonds distinctively from that of the seeds. Electron diffraction patterns however show broadened reflections at the "d" values for diamond, that would result from very small crystals.

In the case of the halogenated hydrocarbons, Iodoform (CHI_3) gave the most successful results. Fig. 2 shows powder X-ray diffraction patterns of before (Fig. 2a) and after processed samples (Fig. 2b) of iodoform.

The X-ray diffraction patterns of the before process samples shows well crystallized iodoform reflections dominating, and the diamond peak (2 wt. %) added is barely visible. Whereas the hydrothermal processed samples the X-ray diffraction patterns with "d" values 2.051 and 1.261 peaks are greatly enhanced, with amorphous carbon and I_2 making the rest of the materials balance (same net composition).

4. Acknowledgment

5. References

1. F.P.Bundy, H.T.Hall, H.M Srong, R.H.Wentroff Jr, Nature, 176 (51) 1955.
2 B.V.Spitsyn, L.L.Bouilov and B.V.Deraguin, J.Cryst.Growth, 219 (52) 1981.
3. B.V.Spitsyn, L.L.Bouilov and B.V.Deraguin, Diamond Related Materials, 705 (1) 1992.
4. M.Kamo, Y.Sato, S.Matsumoto and N.Setaka, J.Cryst.Growth , 642 (62) 1983
5. R.C.DeVries, Ann.Rev.Mater.Sci, 161 (17) 1987.
6. R.C.DeVries, R.Roy, S.Somiya and S.Yamada, Proc.IUMRS-ICAMS-Tokyo, Japan August 1993.

358
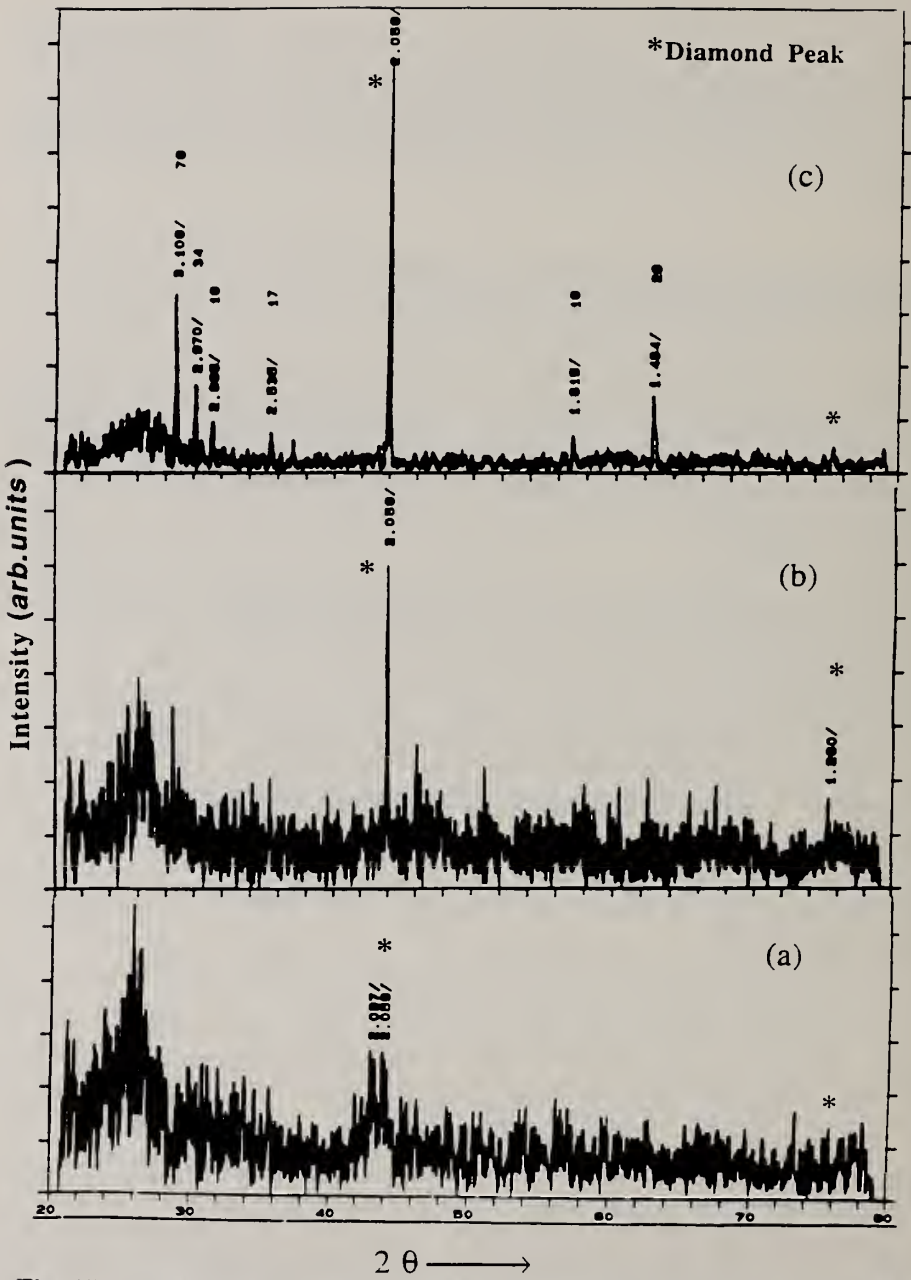
Fig. (1) Powder X-ray diffraction patterns of glassy carbon and diamond seeds before process (1 a) and after process (1 b & 1 c).
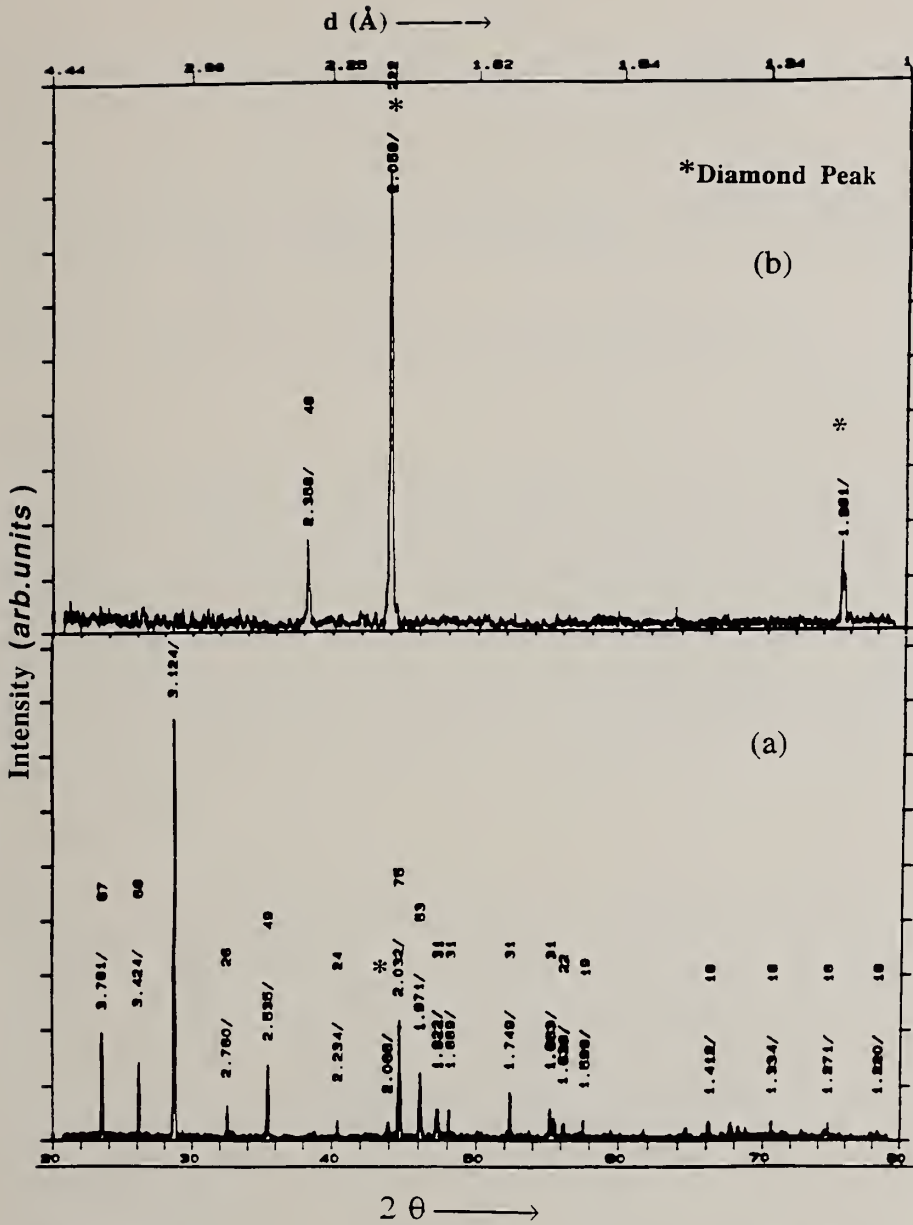
Fig. (2) Powder X-ray diffraction pattern of iodoform and diamond seeds before process (2 a) and after process (2 b).

A CLOSED CVD SYSTEM FOR THE DEPOSITION OF DIAMOND FILMS

E.N. Farabaugh[1], Guan-Ren Lai[2], A. Feldman[1], and L.H. Robins[1]

[1]National Institute of Standards and Technology, Gaithersburg,MD 20899,USA
[2]Precision Instrument Development Center(PIDC), National Science Council, Hsinchu 30077, Taiwan, R.O.C.

Key words: closed CVD system, diamond films, hot filament CVD

Abstract

The results of diamond film depositions based on a closed hot filament chemical vapor deposition (HFCVD) system are given. In this process, no flowing feed gases are used; only a small amount of hydrogen and a solid graphite source are used. Typical deposition conditions are: nominal filament temperature, 1800 °C; nominal substrate temperature, 750 °C; deposition chamber pressure, 1.3 kPa to 10.6 kPa (10 torr to 80 torr); filament-substrate spacing, 4 mm; filament-graphite rod spacing, 7 mm to 20 mm. Growth rates of 0.1 μm/h to 0.3 μm/h were achieved. The presence of the diamond phase was verified by x-ray diffraction (XRD) and Raman spectroscopy.

1. Introduction

In almost all of the different chemical vapor deposition (CVD) processes a constantly flowing feed gas is used [1,2]. The feed gas is a mixture usually consisting of hydrogen, a hydrocarbon (HC) gas and sometimes oxygen. The hydrogen is the source of atomic hydrogen which is critical to the formation of diamond. Atomic hydrogen also attacks the graphitic bond removing graphite that tends to form with the diamond. However, hydrogen is not consumed and is wasted when it is pumped out of the deposition chamber during the diamond deposition process. In the closed process we minimize the amount of hydrogen used in the deposition by admitting only a small amount of hydrogen into the deposition chamber and then closing all chamber access ports.

2. Experimental

Figure 1 shows the closed hot filament CVD reactor. A more detailed discussion of the closed system can be found elsewhere [3]. A fused silica cylinder forms the walls

of the reactor and encloses a substrate heater, a thermocouple for substrate temperature measurement, a filament holder with tungsten filament, a carbon rod source placed parallel to and above the filament, and ports for admitting and removing gases. The filament is a straight tungsten wire held under tension to eliminate filament sag.

The reactor was evacuated to the desired base pressure and then hydrogen was admitted until the chamber pressure for deposition was reached. The chamber was then closed. The substrate and filament were brought to temperature, starting the deposition. The parameter ranges for the closed system deposition were: operating pressure, 1.3 kPa to 10.6 kPa (10 torr to 80 torr); filament temperarture, 1700 °C to 2000 °C; substrate temperature, 750 °C; filament to substrate distance, 2 mm to 4 mm; filament to rod distance, D, 7 mm to 20 mm.

The substrates were polished single crystal silicon wafers and silicon wafers that had been coated previously with diamond. All wafers were 1 cm square. The uncoated wafers were pretreated by rubbing with 0.5 μm diamond paste, washing with ethyl alcohol, and drying in air.

3. Results and discussion

Diamond was grown under a variety of conditions. The diamond phase was verified by x-ray diffraction and Raman spectroscopy [3]. Diamond growth rates were 0.1 μm/h to 0.3 μm/h. The growth rate on bare silicon substrates appeared to be nearly the same as the growth rate on the diamond coated substrates. The growth is envisioned as follows. The hot filament produces atomic hydrogen which serves two functions, to produce gaseous HC species that are precursors to diamond growth and to react with the HC gases at the substrate to produce diamond. All of the transport processes are considered to take place by diffusion although natural convection might occur. The rate of HC gas production is expected to decrease with increasing distance of the graphite rod from the filament. A steady state condition is expected in which the rate of HC production from etching of graphite is balanced by the rate of diamond deposition. The conditions for the steady state have not yet been evaluated.

Analysis of data of the mass gain vs. chamber pressure for diamond grown for 4 h periods with D = 7 mm revealed that there is a maximum mass gain at a chamber deposition pressure of 2.7 kPa (20 torr). It was also noted that when a 5 turn helical filament was used for deposition instead of a straight wire filament, the mass gain was larger by a factor of 2 or 3. The computed length of the helical filament is about 1.4 times the length of the straight filament. Thus, the observed larger growth rate with the helical filament is not strictly proportional to the filament length. This is not surprising in view of previous results that related diamond growth rate with filament turn density[4]. A straight wire filament was prefered because the filament to rod and

filament to substrate distances were better defined.

The diamond mass increase and the graphite rod mass decrease were a function D. For small D, the graphite mass removal is relatively high and as D increases, the graphite mass removal drops off sharply. The diamond mass increase varies only slowly with D; the growth rate gradually decreases as D increases. Figure 2 shows the ratio, in %, of the change in mass of the diamond film to the change in mass of the graphite rod as a function of D. It is clearly seen that the conversion efficiency from graphite to diamond increases with increasing D.

A series of samples was examined by scanning electron microscopy. These samples were grown for 4 h with different D values but the same filament to substrate spacing of 4 mm. No continuous films were formed.. Continuous films could be formed with longer deposition times. The morphology of the diamond varies with D, evolving from unfaceted, poorly defined surface features for D=7 mm, to sharply faceted features on very small particles for D=20 mm. Assuming the best quality diamond corresponds to the sharpest crystal features, the diamond quality improves with increasing D at the expense of growth rate. When the graphite rod etch rate is high (smaller D), it is expected that the HC concentrations in the chamber are high resulting in poor diamond quality. For low etch rate (larger D), lower HC concentrations are expected resulting in better quality diamond. This interpretation is consistent with well-known results in conventional diamond growth; the quality of the diamond decreases with increasing HC fraction in the feed gas when hydrogen/HC mixtures are used. Raman spectra confirmed such a correlation between D and diamond quality.

4. Summary

We have demonstrated that diamond films can be produced in a closed HFCVD system. It was found the quality and growth rate of the diamond is dependent on the filament to graphite rod spacing D. Larger D produced better faceted diamond but at reduced growth rates. Smaller D yielded higher growth rates but poorer quality diamond. Successful diamond deposition in a closed system offers the possibility of reducing CVD diamond production costs.

5. References

1. S. Matsumoto, Y. Sato, M. Kamo, and N. Setka, Jpn. J. Appl. Phys., **17** (1982) L183.
2. A. Swabe and T. Inuzuka, Appl. Phys. Lett., **46** (1985) 146.
3. Guan-Ren Lai, E.N. Farabaugh, A. Feldman, and L.H. Robins, J. Res. Natl. Inst. Stand. Technol., **100** 1 (1995) 43.
4. E.N. Farabaugh, A. Feldman, and L. Robins, in *Applications of Diamond Films and Related Materials*, Proceedings of the First International Conference on the

Applications of Diamond Films and Related Materials, Auburn, AL (Elsevier, Amsterdam 1991) 483.
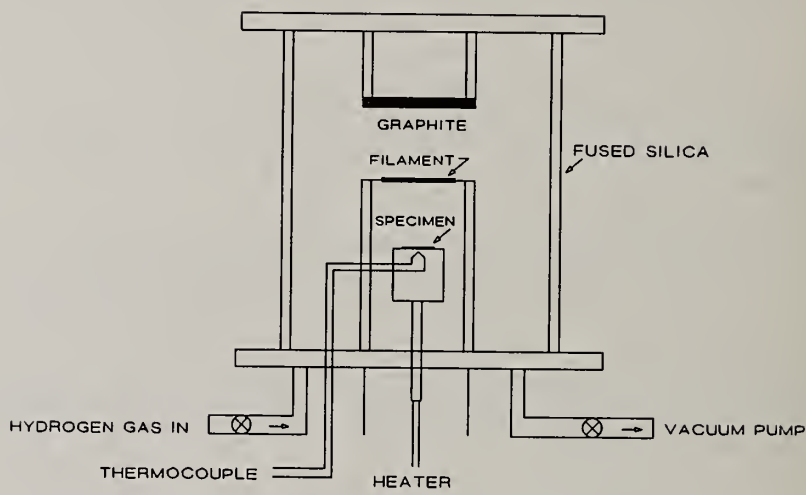
Fig. 1. A drawing of the closed HFCVD system.
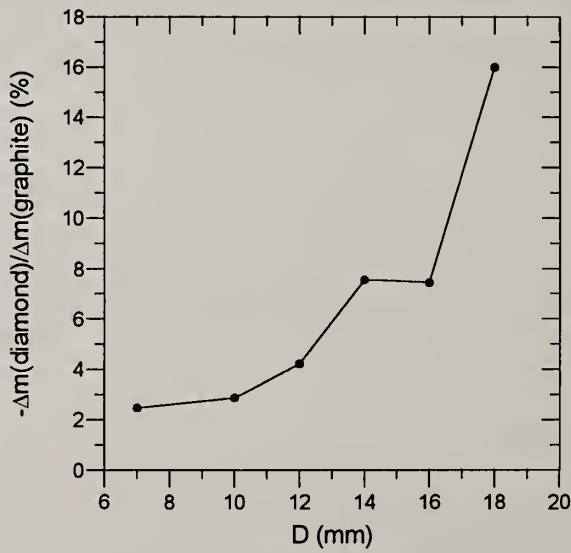
Fig. 2. The ratio, in %, of diamond mass change to graphite rod mass change as a function of D in the closed HFCVD system. The combined standard uncertainty of these measurements is ± 20 %.

ADDITION OF METALS INTO RF PLASMA FOR DIAMOND SYNTHESIS

Masamitsu Nagano, Toshiharu Nagao, Takashi Urasaki, Hiroyuki Mishima, and Hiromichi Ichinose

Department of Applied Chemistry, Faculty of Science and Engineering, Saga University, 1 Honjo, Saga 840, JAPAN

Key words: effects of metals, emission spectra, metals in plasma, plasma CVD, quadrupole mass spectra, rf plasma

Abstract

Metal was introduced to CH_4/H_2 rf plasma. Effects of metals both on the quality of diamond films and on the gas phase reaction were investigated. Most metals depressed the diamond deposition, compared with the case without additive, while Si and Ti did not. Graphitic carbon deposited together with diamond on the addition of Fe, Ni or Mo. Most metals (except for Ti and Pd) deposited in the form of carbide immediately after the introduction into the plasma. The band A cathodoluminescence was observed for all diamond films with and without additive. Si and Ni promoted the conversion of CH_4 to C_2H_x (x = 0 - 6) however they did not facilitate the deposition of diamond.

1. Introduction

The critical role of hydrogen and the affirmative effects of oxygen are widely recognized in the preparation of diamond by plasma CVD. However, effects of metals introduced in plasma were not explored yet although a variety of metals have been employed as the substrates, attempting to improve the deposition rate of diamond, its adhesion to the substrate, and its heteroepitaxial growth. The metals added to plasma is expected to

have influences on the gas phase reaction of carbon sources, on the surface reaction of diamond precursor on the substrate and the characteristic of the diamond. The effects of metals introduced to microwave plasma on diamond synthesis were explored previously[1, 2]. In this experiment, metals were introduced to rf plasma . The metal was introduced into the plasma probably by sputtering, reactive etching or evaporation.

2. Experimental

Diamond was prepared by an inductively coupled rf plasma CVD (Fig. 1), using 1 % or 10 % CH_4/H_2 mixture as a feed gas. The total flow rate was 100 sccm. The reaction pressure was 2 kPa. Si (100) single crystal was used as the substrate. It was abraded with 3 μm diamond slurry before it was mounted on the holder. The substrate was placed in the center of the work coil and was heated to 900 - 950 °C by the plasma. A metal strip (Si, Ti, Fe, Ni, Pd and Mo) was placed in the plasma as shown in Fig. 1. The metal was grounded electrically . Another Si substrate was also placed near the tip of the strip. A discharge took place between the tip of the metal strip and the work coil. The metal was supposed to be introduced into the plasma by sputtering, reactive etching or evaporation. The distance between the strip and the substrate (d) was varied in the range from 30 mm to 200 mm in order to change the rate of introduction of metal into the plasma. When the distance was too short, the plasma was extinguished or the metal melt down.
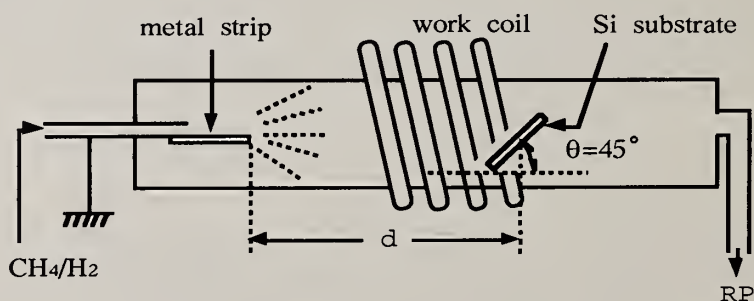
Fig.1 Schematic drawing of rf plasma CVD

The deposits were investigated by X-ray diffraction (XRD), scanning electron microscopy (SEM), X-ray microanalysis (XMA), Raman spectroscopy and cathodoluminescence spectroscopy (CL) with electron beam irradiation of 20 kV. Plasma

emission spectra were measured in ultraviolet-visible range by an optical spectrometer. The resulting gas species were analyzed by a quadrupole mass spectometer.

3. Results and Discussion

3.1 Effects of metals on deposition

When the intensity ratio of the X-ray diffraction peak of the diamond (111) plane to that of Si substrate (400) plane was supposed to be a measure of the deposition rate of diamond, the introduction of most metals into the plasma lowered the deposition rate in comparison with the case without additive, while the introduction of Si or Ti did not. It was found for most metals (except for Ti) that the carbides (SiC, Fe_2C, Ni_3C, MoC) deposited near the tip of the metal strip when the distance between the metal and the substrate (d) was short. The addition of Fe, Ni or Mo also promoted the deposition of graphitic carbon.

3.2 Morphology and quality of diamond films

The mean particle size of diamond was 0.9 μm without additive. Most metals (except for Si) decreased the particle size of diamond as shown in Fig. 2 and the diamond particles became round as the metal was added into the plasma.
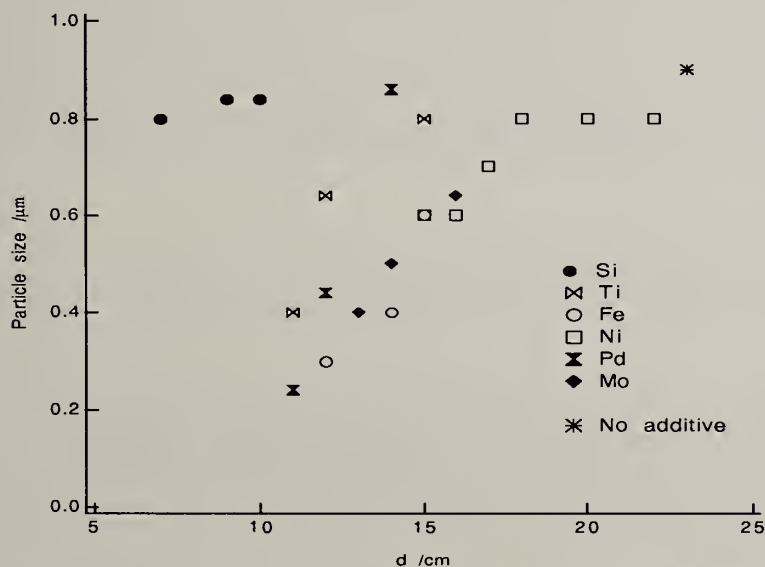
Fig. 2   Change in particle size with the distance between metal strip and substrate (d).

The Raman spectrum of the film with Si had a sharp peak at 1332 cm^{-1} due to the good crystallinity of the diamond. In the cases of other metals, however, the diamond peak was broad and weak, suggesting the degradation of the crystallinity. For all films with and without additive, a cathodoluminescence peak appeared at 430 nm (the band A in natural diamond). Adding Si or Ti, another peak appeared at 740 nm (GR-1 center) as well as the band A. These results suggest the possibility of doping of the metal in the diamond.

3.3 Species in plasma

The emission peaks ascribed to Ti and Pd were found together with those to hydrogen atom and molecule in the plasma emission spectra. Other metals were not detected, probably because their atoms were not stable in the plasma and immediately reacted with CH_4 or its derivatives to form the carbides. The introduction of the metal influenced little on the spectra of hydrogen atom and molecule. Compared with the case without additive, the addition of Ni led to the increase in C_2 concentration while Si did not.

In the plasma, a part of CH_4 is converted to C_2H_x species (x = 0 - 6), which are presumed to play an important role in the diamond deposition[3]. Intending to estimate the ratio of the concentration of CH_y species to that of C_2H_x species, the ratio of ionic current (I_{15}) of M/e = 15 (corresponding to CH_3) to that (I_{26}) of M/e = 26 (corresponding to C_2H_2) was calculated in the case of the addition of Si or Ni. Both Si and Ni promoted the conversion of CH_4 to C_2H_x species up to 10 times of that without additive however they did not promote so much the deposition of diamond.

4. References

1. H. Ichinose, Y. Nibu, H. Katsuki, M. Nagano, Jpn. J. Appl. Phys., 32 (1993) 144-149.
2. M. Nagano, T. Nagao, H. Mishima and H. Ichinose, "Advances in New Diamond Science and Technology" S. Saito et al. ed., p49-52 (1994), MYU, Tokyo.
3. W. Piekarczyk, W.A. Yarbrough, J. Cryst. Growth, 108 (1991) 583-597.

ENHANCEMENT OF DIAMOND GROWTH UNDER UV IRRADIATION

Nobutaka Ohya, Hideaki Maeda, Katsuki Kusakabe and Shigeharu Morooka

Department of Chemical Science and Technology, Kyushu University
6–10–1, Hakozaki, Higashi–ku, Fukuoka 812–81, Japan

Key words: diamond, CVD, growth, morphology, ultraviolet light, catalysis

Abstract

Diamond was grown under ultraviolet (UV) irradiation by the hot filament–assisted chemical vapor deposition method (HFCVD), and the effects of UV irradiation, carbon sources and substrate materials on diamond growth rate were investigated. Diamond growth was promoted by UV irradiation in all reactant systems tested over a temperature range of 400–800°C, and was strongly influenced by gaseous carbon sources. Acetone and ethylene were especially effective in enhancing the diamond growth. Transition metal substrates such as molybdenum and tantalum promoted the growth rate.

1. Introduction

The quality of a CVD diamond film is influenced mostly by removal of non–diamond components with atomic hydrogen. Wood and Wise [1] reported that the removal rate of graphitic carbon was largest at 440–600°C. According to Muranaka et al. [2], 400°C is the lowest temperature for the growth of high quality diamond film and according to the literature diamond growth rate is not practical below 700°C. Thus, a new CVD technique that realizes high growth rate at 400–600°C is needed.

Kamo and co–workers [3] reported that growth of diamond in microwave plasma was promoted by UV irradiation of 230–580 nm. On the other hand, Celii et al. [4] investigated the effect of UV light on growth rate by HFCVD and found that diamond growth was obstructed by UV irradiation. Thus, the role of UV light in diamond growth is still unclear.

In the present study, diamond was grown by HFCVD under UV irradiation and the effects of UV, gaseous carbon sources and substrate materials on diamond growth were investigated.

2. Experimental

Fig. 1 shows a schematic diagram of the reactor system. The deposition chamber was a silica tube of 43 mm i.d. and 100 mm length. The hot filament was a tungsten wire of 0.5 mm in diameter extended in the shape of Λ. The filament temperature was measured by an optical pyrometer assuming an emissivity of 0.25 and was maintained at 2000°C.

Two types of low–pressure mercury lamps (Chiyoda Kohan Co., Japan) were used as

370
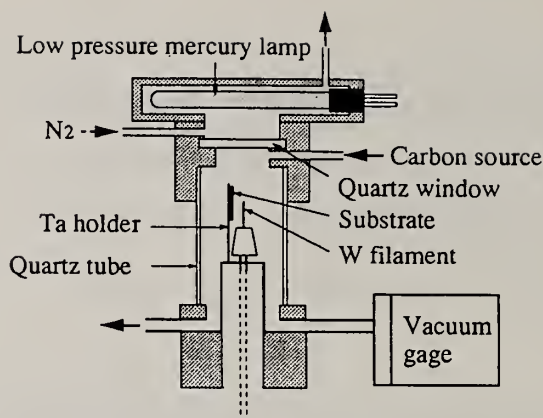
Fig.1 Schematic diagram of reactor used.

UV sources. Type–A lamp (SGL–500 T4u) emitted a 253.7 nm line, and type–B lamp (SGL–500 T4uz) emitted 184.9 and 253.7 nm lines. The type–A lamp was employed, if not otherwise noted. The UV light was usually irradiated parallel to the substrate surface through a high–purity quartz window.

Cubo–octahedral single–crystalline diamond particles of ca. 1.5 μm in size were prepared by MPCVD on an Si (100) substrate of 5 mm by 10 mm. Then five diamond crystals that possessed an (111) face parallel to the substrate (100) were chosen as observation targets. Changes in size of these particles before and after the growth were measured by a field–emission scanning electron microscope (FE–SEM, Hitachi S–900) with no conductive coating, and the growth rate of diamond {100} and {111} faces was calculated. Details of the calculation method were reported elsewhere [5]. In some runs, seed diamond crystals were grown on a molybdenum (Mo) or tantalum (Ta) substrate. The substrate temperature was measured by a thermocouple and was varied between 400°C and 800°C by adjusting the distance between substrate and filament. Carbon sources used were methane (CH_4), ethane (C_2H_6), ethylene (C_2H_4), acetylene (C_2H_2), ethanol (C_2H_5OH) and acetone ((CH_3)$_2$CO). The flow rate of carbon source was 0.5–2.5 cm³/min and that of hydrogen was 50 cm³/min. For comparison, oxygen was added to the CH_4–H_2 system in the same atomic ratio as that of (CH_3)$_2$CO. The total pressure in the reactor was kept at 4 kPa.

3. Results and discussion

Figs. 2 (a) and (b) illustrate changes in size and shape of diamond crystal. Figs. 3 (a) and (b) show the homoepitaxial growth rate of diamond {100} and {111} faces, respectively. The growth rate on each face varied with carbon sources and was in the following order:

$$(CH_3)_2CO > C_2H_4 > C_2H_6 > C_2H_2 > C_2H_5OH > CH_4 \qquad (1)$$
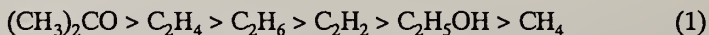
(CH_3)$_2$CO was more effective for growing diamond, compared to CH_4 that is normally used as a carbon source for microwave plasma CVD. Hirose and co–workers [6] reported that organic compounds containing CH_3 groups and oxygen atoms, such as (CH_3)$_2$CO and C_2H_5OH, promoted diamond growth. This acceleration can be explained by the formation of CH_3 radicals at a high concentration and the presence of hydroxyl radicals (OH) which etch non–diamond products rapidly. When O_2 was added to the CH_4–H_2 system in the same atomic ratio as that of (CH_3)$_2$CO, diamond growth was
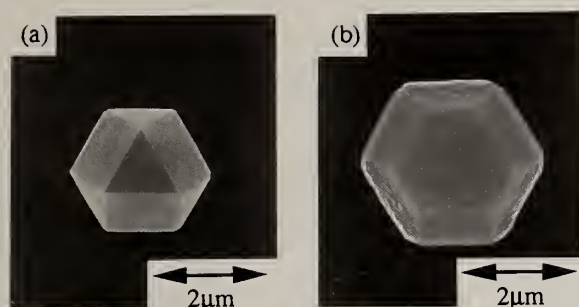
Fig.2 Changes in shape of diamond crystal. (a) Cubo–octahedral crystal before growth; (b) crystal after growth with C_2H_4 under UV irradiation.
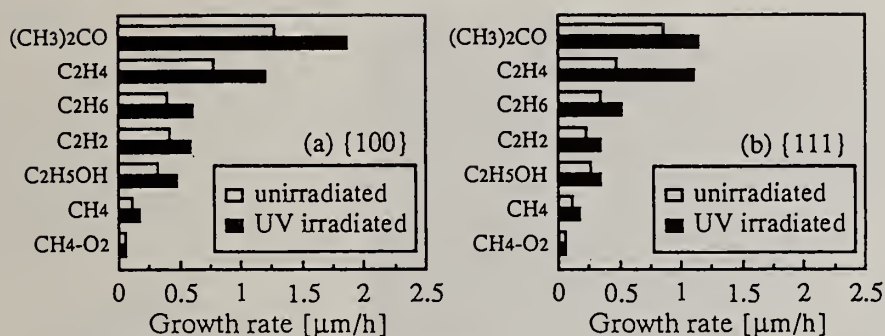
Fig.3 Growth rate of {100} and {111}.

limited as shown in **Figs. 3** (a) and (b). This is due to the difference in dissociation energy of O_2 and $(CH_3)_2CO$.

It was found that C_2H_4 with no oxygen atom was also effective in promoting diamond growth. **Table I** indicates the activation energy for formation of CH_3 and C_2H_5 radicals [7]. The order of activation energy agrees with the order of diamond growth rate. Although CH_3 and C_2H_2 were proposed as gaseous active species for diamond growth [8,9], the results shown in **Figs. 3** (a) and (b) suggest that C_2H_5 radicals are important.

Under UV irradiation, diamond growth was enhanced by a factor of 1.3–2 compared with that without UV irradiation for all carbon sources used. Direct irradiation of UV onto the substrate surface was not required for enhancement of growth, and the difference in the wavelength, 184.9 nm or 253.7 nm, was not essential. This suggests that UV irradiation activated gas phase species and promoted dissociation of them. UV–enhanced diamond growth was observed in the range of 400–800°C, and the surface morphology of diamond was not changed by UV irradiation. As shown in **Fig. 4**, the {111} faces became rough when carbon sources that contained oxygen atoms were employed.

The transition metal substrates of Mo and Ta greatly promoted the diamond growth rate for C_2H_4 and C_2H_6. It is known that Mo is an effective catalyst for hydrogen transfer. Presumably Mo and Ta substrates accelerated the formation of C_2H_5 radicals by catalytic reaction on the substrate surface. This effect was not observed with $(CH_3)_2CO$, due to the oxidation of the substrate surface.

Table 1 Activation energy for fomation of CH3 and C2H5

$C_2H_4 \xrightarrow{+H} C_2H_5$			9 kJ / mol
$C_2H_2 \xrightarrow{+H} C_2H_3 \xrightarrow{+H} C_2H_4 \xrightarrow{+H} C_2H_5$			11 kJ / mol
$C_2H_6 \xrightarrow{+H} C_2H_5$			40 kJ / mol
$CH_4 \xrightarrow{+H} CH_3$			50 kJ / mol
$(CH_3)_2CO \longrightarrow 2\,CH_3 + CO$			197 kJ / mol
$C_2H_5OH \longrightarrow CH_3 + CH_2OH$			350 kJ / mol
$CH_4 \longrightarrow CH_3 + H$			434 kJ / mol
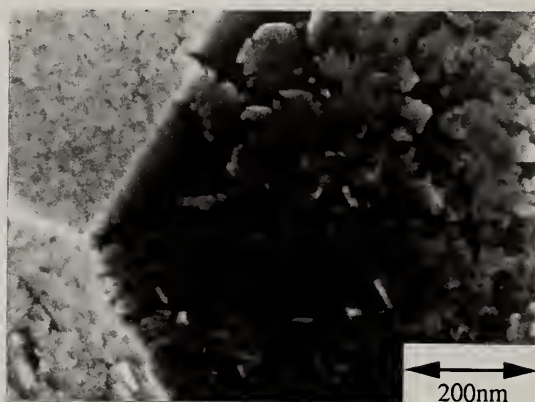
Fig.4 Surface morphology of diamond after growth with C_2H_4 under UV irradiation.

200nm

4. Conclusion

UV irradiation activated vapor–phase species and enhanced the diamond deposition by HFCVD. $(CH_3)_2CO$ and C_2H_4 were effective carbon sources. The catalytic effect of Mo and Ta substrates on diamond growth was also confirmed.

5. References

1. B.J. Wood and H. Wise, *J. Phys. Chem.*, **73**, 1348 (1969).
2. Y. Muranaka, H. Yamashita and H. Miyadera, *Diamond Related Mater.*, **3**, 313 (1993).
3. M. Kamo, T. Ando, Y. Sato, K. Bando and J. Ishikawa, *Diamond Related Mater.*, **1**, 104 (1992).
4. F.G. Celii, H.H. Nelson and P.E. Pehrsson, *J. Mater. Res.*, **5**, 2337 (1990).
5. H. Maeda, K. Ohtsubo, M. Irie, N. Ohya, K. Kusakabe and S. Morooka, *J. Mater. Res.*, in press.
6. Y. Hirose and Y. Terasawa, *Jpn. J. Appl. Phys.*, **25**, L519 (1986).
7. K. Sugawara, K. Okazaki and S. Sato, *Bull. Chem. Soc. Jpn.*, **54**, 2872 (1981).
8. M. Tsuda, M. Nakajima and S. Oikawa, *J. Am. Chem. Soc.*, **108**, 5780 (1986).
9. M. Frenklach and K.E. Spear, *J. Mater. Res.*, **3**, 1633 (1988).

HIGH-RATE DEPOSITION OF DIAMOND FILMS IN $CH_4/O_2/H_2$ MICROWAVE PLASMAS

Tsanheui Chein and Yonhua Tzeng

Department of Electrical Engineering, Auburn University, Auburn, AL 36849 USA

Key words: oxygen, diamond, MPECVD

Abstract

We report diamond films deposited at high rates by microwave plasma enhanced chemical vapor deposition. Diamond films have been deposited on Mo substrates in the temperature range of 900-1620°C in 16% (in vol.) methane diluted by hydrogen at pressures around 130 Torr. Oxygen concentration of 1.6 or 3.2% was added. Raman spectra of the deposited films were taken for comparison. The properties of CVD diamond and the effects of substrate preparation, process start-up conditions, and deposition temperature on the growth rate of diamond films are discussed.

1. Introduction

Diamond is an ideal material for a broad range of applications. In some applications thick and inexpensive diamond is needed. Therefore, high rate of diamond deposition is desirable. Although dc arc jets and combustion flames have been proven to be able to deposit diamond films at high rates, the deposition cost is high as gases are consumed at a very high rate compared to that of microwave plasma enhanced chemical vapor deposition (MPECVD) or hot filament chemical vapor deposition (HFCVD). MPECVD has advantages over other techniques as the process is stable and reproducible results can be obtained. It is, therefore, important that we study high growth rate diamond deposition by the MPECVD method.

The substrate temperature is one of the important parameters in the diamond CVD process. For traditional low power density MPECVD, diamond growth rate decreases when substrate temperature exceeds 1200°C. At substrate temperatures well above 1200°C under low power density microwave plasma conditions, graphitic carbon instead of diamond was deposited. However, it has been found that the growth rate of diamond increased monotonically with increasing substrate temperature up to around 1500° C in a high power density microwave plasma [1].

The concentration of hydrocarbon gas in the gas mixture is another important parameters in diamond CVD. Among various hydrocarbon gases methane is most frequently used by researchers. The typical concentrations of methane in gas mixtures are less than 5% and the growth rates are only several μm per hour at most by means of low power density MPECVD. The diamond growth rate is directly related to the concentration of methane within a limited range. A higher concentration of methane in

the gas mixture increases the deposition rate as well as the graphitic components in the deposit. The challenge in the use of a high concentration of methane in the gas mixture for achieving high diamond growth rate is how to maintain the quality of the diamond.

2. Experimental

Deposition was carried out on molybdenum screws of 1/2 inch in diameter which were polished to a mirror finish. For comparison, some of the substrates were installed without diamond seeding while some were rubbed with 1 μm diamond paste followed by ultrasonic cleaning prior to the insertion in the reactor. In contrast to the typical low concentration of methane (< 5%) in hydrogen, 16% methane concentration diluted by hydrogen was used in this study. Oxygen of 1.6 or 3.2% was introduced to the plasma at different stages of diamond nucleation and growth. Three gas feed processes were adopted to compare the effect on diamond deposition: (i) all reactant gases were fed to the reactor simultaneously, (ii) oxygen was later added to the methane/hydrogen plasma, and (iii) methane was later added to the oxygen/hydrogen plasma. The flow rate in the reactor was 500 sccm and the pressure was maintained at around 130 Torr. Microwave power between 1400 and 1750 W was applied. The deposition temperature was measured by an optical pyrometer. Deposition periods ranged from 45 minutes to 26 hours. The deposited diamond films were characterized by means of Raman spectroscopy and growth rates were determined via optical microscopy.

3. Results and Discussion

We investigated the dependence of the diamond growth rate on the concentration of the oxygen additive and the deposition temperature. Oxygen of 1.6 or 3.2% was added to the mixture of methane and hydrogen. The growth rate of CVD diamond on newly polished, unseeded Mo surface with methane not being fed into the reactor until the substrate had been heated by oxygen/hydrogen plasma to the deposition temperature exceeded 30 μm/h at deposition temperatures ranging from 1300 to 1550°C. With 1.6% O_2 additive, good quality diamond films as shown in Figure 1 have been deposited at a rate up to 35 μm/h at 1550°C on seeded Mo substrate. The growth rate for 3.2% oxygen additive was 50% lower than that for 1.6% oxygen additive.

Raman spectra for diamond films deposited under different conditions are used to examine the crystalline quality of the deposits. An intense first order Raman peak for diamond at 1332 cm^{-1} was observed on the growth side of the films while two broad bands centered at around 1350 and 1580 cm^{-1} in Raman shifts were observed on most of the substrate side of the deposited films. When methane was added at a later stage to the oxygen/hydrogen plasma, the substrate side had a better quality of deposition than that corresponding to other two gas feed sequences. Figure 2 shows the Raman spectrum for the diamond film shown in Figure 1. Figure 3 shows the Raman shifts of samples deposited through three different gas feed processes. Curves (b) and (c) show the characteristics of diamond while curve (a) does not.

4. Conclusions

A high concentration of methane (16% or higher) and a high power density plasma are necessary for obtaining high-rate growth of CVD diamond by MPECVD. Oxygen

additive improves the quality of diamond nucleation and growth in methane/hydrogen plasma at high substrate temperatures. At the substrate temperature of 1500⁰C, the carbon deposits were black and mostly non-diamond when oxygen was not added. Diamond growth rate decreases if a large amount (> 3%) of oxygen additive is included in the feed gases under our experimental conditions. At substrate temperatures exceeding 1600⁰C, individual diamond particles, rather than continuous films, tend to form on unseeded Mo substrates. Diamond grows well at temperatures exceeding 1600⁰C to form smooth (100) surfaces. However, the nucleation density at such high temperatures is either very low or mostly graphitic. The deposition characteristics at substrate temperatures above 1600⁰C thus depend on the sequence in which the reactant gases are introduced. To obtain continuous diamond film at molybdenum substrate temperatures exceeding 1600⁰C, a two-step process to ensure a high nucleation density at a lower substrate temperature followed by a high growth rate of diamond at a high substrate temperature is desirable.

5. Acknowledgments

6. References

1. Y. Tzeng and J. Wei, Program & Abstracts, the Fourth International Conference on New Diamond Science and Technology, p. 63, July 18-22, Kobe, Japan (1994)
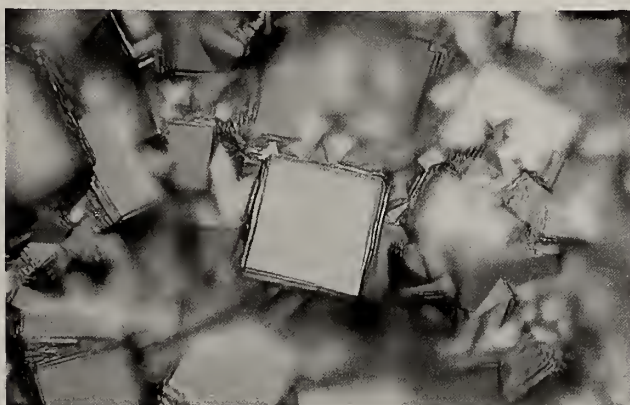
Figure 1. Diamond film deposited at 1550⁰C at around 130 Torr. Methane (16% in vol.) was added to the O_2/H_2 plasma after the molybdenum substrate had been heated to 1550⁰C. The growth rate was about 35 μm/h.
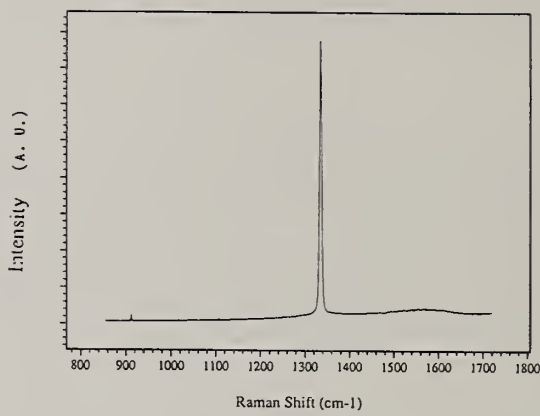
Figure 2. Raman shift for the diamond film shown in Figure 1.
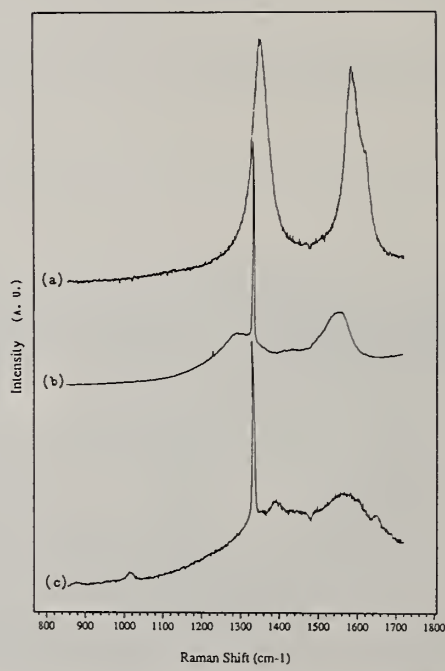
Figure 3. Raman shift for diamond films deposited in different gas feed process: (a) all gases were fed into the reactor simultaneously, (b) O_2 was later added to the CH_4/H_2 plasma, and (c) CH_4 was later added to the O_2/H_2 plasma. The substrate temperature was 1550^0C and pressure was around 130 Torr.

HIGH TEMPERATURE DIAMOND FILM DEPOSITION
ON A NATURAL DIAMOND ANVIL

Thomas S. McCauley, Yogesh K. Vohra

Department of Physics, University of Alabama at Birmingham
Birmingham, AL 35294-1170 U.S.A. Internet: mccauley@phy.uab.edu

Abstract

We report on the growth and characterization of a 100 μm thick by 350 μm diameter diamond layer on the culet of a type Ia brilliant cut natural diamond anvil by microwave plasma-assisted CVD (MPCVD). While our previous work [1] on diamond anvils resulted in homoepitaxial film growth at a rate of approximately 20 μm/hr, the present 100 μm thick diamond layer grew in less than 2 hours. This unprecedented growth rate of ~ 50 μm/hr is believed to be the result of the extremely high substrate temperature (1800°-2100° C) during deposition. The translucent diamond layer was characterized by micro-Raman, low temperature photoluminescence (PL) and PL excitation spectroscopy, as well as atomic force microscopy (AFM). Raman analysis shows the deposit to be of high quality. The PL spectra show numerous features, including prominent emission bands at 575 nm (2.16 eV), 636 nm (1.95 eV), 735 nm (1.68 eV) and 777 nm (1.60 eV).

1. Introduction

Several groups [1-3] have tried to optimize 'high-growth rate' CVD techniques such as DC plasma jet and combustion flame synthesis by operating at high pressures, gas flow rates, carbon concentrations, and substrate temperatures. Snail et al [3] have reported the highest homoepitaxial growth rate (100-200 μm/hr) and substrate temperature (1500° C) during growth on a planar substrate to date. They cite ~ 1900° C as the 'hard vacuum graphitization limit' for diamond, implying that low pressure diamond growth above that temperature should be impossible. In order to test this assertion, and also to explore the effects of extended, non-planar substrates on nucleation and growth, we have carried out a series of deposition experiments on natural diamond anvils by microwave-assisted CVD (MPCVD) in which the substrate temperature was held between 1800°-2100° C, as measure by an infrared pyrometer. As our results show, there is a temperature regime above 1500° C, and possibly above 2000° C, at which 'explosive' growth of diamond is observed at rates of 50-400 μm/hr.

2. Experimental Methods

The substrate for this high temperature deposition experiment was the polished (100) tip of a single-bevel, modified brilliant cut type Ia natural diamond from D. Drukker & Zn. N.V. [1]. The diameters of the central flat and culet were 20 μm and 350 μm respectively, as shown in Fig.1a. The crystal was ultrasonically cleaned in acetone before being placed onto the 1.27 cm diameter molybdenum screw which serves as the substrate stage. We made no attempt to ensure thermal contact between the substrate and the stage by brazing, etc. While the temperature of the stage itself was actively regulated by a heating/refrigeration unit to ~ 1200° C, in the present case the diamond anvil was allowed to equilibrate to the gas-phase temperature of the plasma surrounding it (~ 1800-2100° C). Plasma generation was accomplished using 1200 W of microwave power at 2.45 GHz at a chamber pressure of 90 Torr. Precursor gas flow rates were 500 sccm of H_2 and 10 sccm of CH_4 (i.e. 2% by volume). The substrate temperature rose from 1800-2100° C over the 2 hr. deposition cycle, as measured by our pyrometer using an emissivity of 0.89 for carbon. The presence of the anvil's tip perturbs the electromagnetic field distribution of the plasma ball, resulting in a localized region of high temperature, and therefore higher concentrations of activated gas-phase species such as C_2, around the tip. As the substrate temperature increased toward the end of the deposition cycle, a large (over 5 mm in diameter) of amorphous carbon formed on the tip. This ball was removed by etching in a hydrogen plasma for 30 minutes following deposition, leaving the 100 μm high by 350 μm layer shown in Fig.1b. Plasma etching also resulted in the formation of a hollow region in the center of the layer extending down to the original substrate surface. The micro-Raman and PL spectroscopy system used is described elsewhere [4]. For low temperature PL measurements, samples were cooled to 80-110° K in a Joule-Thomson refrigeration unit manufactured by MMR Technologies. In order to ensure that the observed signals were collected only from the deposited layer, all Raman and PL spectra were acquired in a side-view configuration, with a lateral spatial resolution of ~ 4 μm.

3. Results and Discussion

The surface of the as-grown layer is quite rough and varies in its reflectivity/transmission. AFM analysis of the surface on a sub-micron scale reveals surface features on the order of 0.1-0.5 μm, but no etch pits or evidence of the step-growth mechanism observed in a previous homoepitaxial sample [1]. Raman spectra from the layer show a strong first order diamond mode at 1333 cm^{-1}, with a FWHM of 3.6-4.1 cm^{-1}, comparable to that of the substrate (3 cm^{-1}). The deposit is of very high phase purity, with small amounts of sp^2-bonded amorphous carbon giving rise to the low bands around 1440 and 1550 cm^{-1}. Fig. 2 shows PL spectra taken from the film/substrate interface (upper curve, a) and a region 50 μm above the interface (lower curve, b) at 110-130° K. Both regions show features around 574 nm (2.16 eV), 636 nm (1.95 eV), 737 nm (1.68 eV), and 775 nm (1.60 eV). Note the large increase in the intensity and sharp-

ness of the zero phonon lines (ZPL) at 636, 575, 737 nm, indicating an enhanced incorporation of these defects at the interface. This supports the recent work of Behr et al [4], who observed the same effect with the 575, 560 nm centers in a homoepitaxial film. Note that the intensity of the 775 nm center remains roughly constant with distance from the interface. This may indicate that it is due to an extended defect, rather than a point defect. The PL spectra from the deposit at room temperature shown in Fig.3 for three different excitation wavelengths. Spectra labeled a, b, c, refer to excitation wavelengths of 514.5 nm (green), 457.9 nm (blue), and 632.8 nm (red) respectively. The 737 nm emission is prominent in all three spectra, while the 775 nm band is strongly pumped only with 514.5 nm (green) excitation. Further PL works at low temperature is necessary to study the multiplet structure of this center. At present, the emission appears to be a doublet, 776 and 782 nm, with numerous sidebands at 788 nm and higher wavelengths.

4. Conclusions

In conclusion, we report for the first time the deposition of a high quality diamond layer on a type Ia natural diamond anvil by MPCVD at a substrate temperature between 1800°-2100° C. The growth rate for this process is estimated to be between 50 and 400 μm/hr. We believe that the presence of large concentrations of C_2 are critical to the observed rapid growth. Raman analysis confirms the crystallinity and phase purity of the deposit. Low temperature PL measurements show the enhanced incorporation of optical defect centers with ZPLs at 636, 575 nm due to the unintentional incorporation of nitrogen [1], and 737 nm due to silicon [5] (perhaps from the quartz microwave window). PL excitation studies of the 737 nm band, the origin of which is unknown [6], reveal that it is selectively pumped in the green (~ 500 nm) spectral region. Further investigation of this explosive diamond growth regime at high temperature is in progress, as is the development of further optical and direct methods to measure substrate temperature in-situ.

5. References

1. T.S. McCauley and Y.K. Vohra, App. Phys. Lett. **66** (12), 1486 (1995).
2. K. Ravi, Critical Review in Materials Science and Engineering, B **19**, 203 (1993).
3. K.A. Snail and L.M. Hanssen, J. Crystal Growth **112**, 651 (1991).
4. D. Behr, J. Wagner, C. Wild, and P. Koidl, Appl. Phys. Lett. **63**, 3005 (1993).
5. C.D. Clark, H. Kanda, I. Kiflawi, G. Sittas, Phys. Rev. B Abs. **26** (8) 40 (1995).
6. T.S. McCauley and Y.K. Vohra, Phys. Rev. B **49**, 5046 (1994).

6. Figures
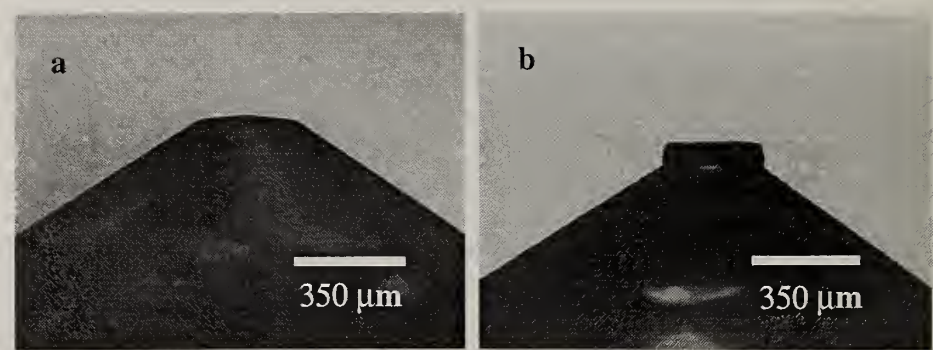
Fig.1. (a) Anvil before deposition, and (b) after deposition and etching.
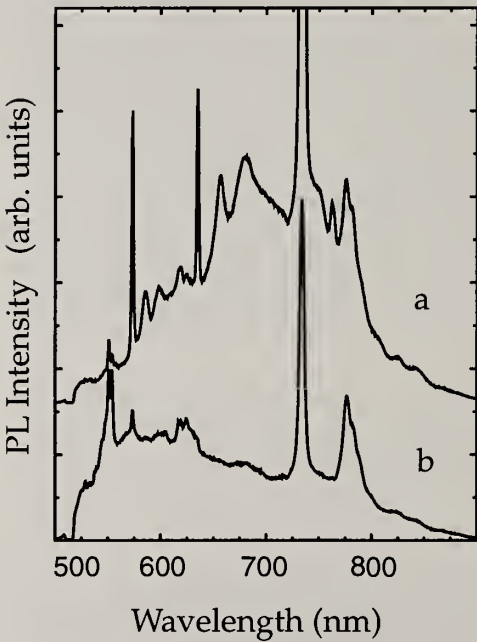
Fig.2. PL of (a) interface, (b) bulk of layer at 110-130° K.
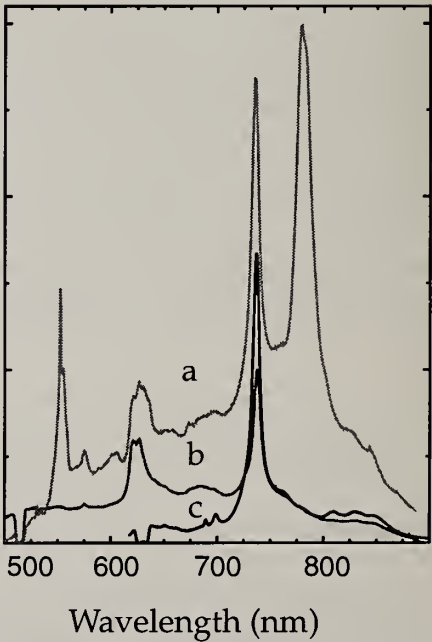
Fig.3. PL at different excitation wavelengths, (a) 514 nm, (b) 458 nm, (c) 633 nm.

IS IT POSSIBLE TO DEPOSIT DIAMOND IN A MICROWAVE PLASMA CVD PROCESS WITHOUT H₂?

Pierre Joeris, Ingo Schmidt, and Carsten Benndorf

Department of Physical Chemistry, University of Hamburg, Bundesstr. 45,
20146 Hamburg, F.R. Germany

Key words: diamond synthesis, equilibrium calculations, gas phase composition, microwave Plasma CVD, Raman spectroscopy, thermodynamic equilibrium

Abstract

We investigated the diamond synthesis in a microwave plasma (MPCVD) using $Ar/CH_4/O_2$, $Ar/C_2H_2/O_2$ and $Ar/CH_4/CO_2$ gas mixtures. These mixtures do not contain molecular hydrogen and are more typical for flame deposition methods in which diamond is deposited, for example, in an ethine/oxygen combustion flame. We focus in the present study to regions of a C/H/O gas composition in the Bachmann „diamond phase diagram" which to our knowledge had not been investigated with MPCVD until now. The ternary C/H/O diagram proposed by Bachmann demonstrates that diamond synthesis takes place only in a limited range of gas compositions. With the commonly used hydrogen/hydrocarbon/oxygen gas mixtures with a hydrogen concentration near 95-99% the experiments are limited to the H-corner of the C/H/O ternary diagram (C/H atomic ratio<0.025). In our experiments, the C/H atomic ratio is kept constant, 1:4 for $Ar/CH_4/O_2$ and 1:1 for $Ar/C_2H_2/O_2$. For each system we determined the range of gas phase composition in which diamond deposition was detected. This was achieved by Raman spectroscopic analysis of the deposited films. The second goal concerned the analysis of the plasma processes by mass spectroscopy, optical emission spectroscopy and model calculations using a program to calculate the thermodynamic equilibrium concentrations. The calculations revealed that a drastic reduction of ethine occurs for carbon mole fractions $X_C=C/(C+O)$ near and above 0.5, this is due to the formation of CO and CO_2 with a high negative ΔG.

1. Introduction

The diamond synthesis in a conventional microwave plasma (MPCVD) or a hot filament (HFCVD) process only takes place with a high hydrogen flow and small amounts of hydrocarbons. The additions of oxygen allows to reduce the concentration of hydrogen but it is still the component with the highest concentration. In the ternary phase diagram of Bachmann et al. [1] including the elements carbon, hydrogen and oxygen these conditions are located in the H-rich corner. Only flame deposition methods were able to reduce the hydrogen content drastically using oxygen/ethine gas mixtures. We report about successful diamond deposition experiments in a microwave

system in which the hydrogen was substituted by argon thus reaching atomic ratios of carbon to oxygen of 0.25 for $Ar/CH_4/O_2$ and 1 for $Ar/C_2H_2/O_2$ gas mixtures.

2. Experimental

The experimental setup is described recently [2]. The microwave plasma system was specially designed for the measuring of optical emission spectra (OES) and quadrupole mass spectroscopy (QMS). We used Si(111) substrates scratched with 0.25 μm diamond grit before the deposition. The substrate temperature was kept constant at 800°C which was measured with a thermocouple placed in the molybdenum substrat holder. Gas flow rates were 100 sccm for argon and 7 sccm for the hydrocarbon while the oxygen flow was varied from 0 to 7 sccm. The pressure was kept constant at 15 torr and the deposition time was two hours. The Raman spectroscopic measurements were performed with an Instruments S.A. U1000 double monochromator using the 488 nm line of an argon ion laser.

3. Results

Raman spectra of the diamond films at various O_2 concentrations in the $Ar/CH_4/O_2$ system are shown in Fig.1. We detect the diamond peak at 1332 cm^{-1} only for high carbon concentrations, $X_C=C/(C+O)$ near 0.5. Higher carbon mole fractions led to the formation of graphitic carbon.
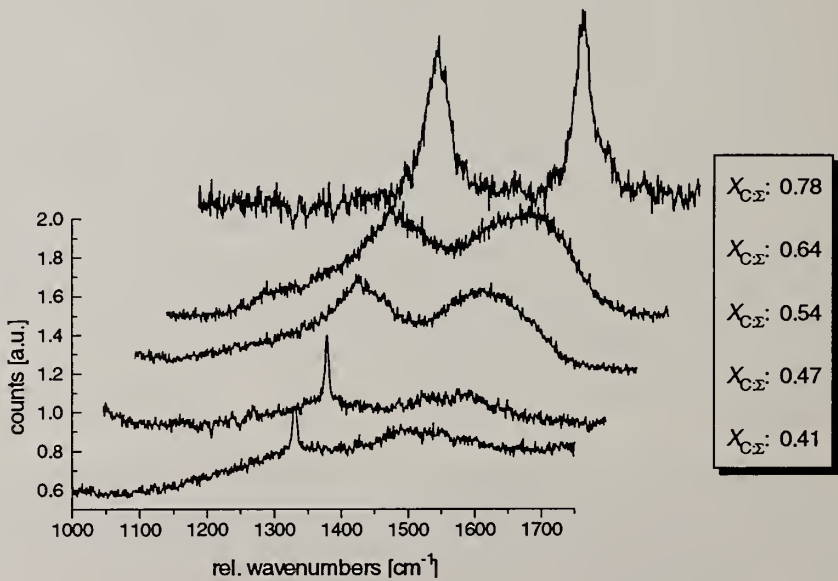
Fig. 1: Raman spectra of films deposited out of $Ar/CH_4/O_2$ plasmas

QMS signal intensities are shown in Fig.2. The methane concentration is nearly independent from the oxygen content. In contrast to this behavior a decrease of the m/e=26 signal from C_2H_2 is observed for increasing O_2 concentration. Without oxygen addition C_2H_2 is by a factor of 5 higher than CH_4. Near $X_C = 0.5$, the C_2H_2 signal drops below the CH_4 signal. We further note a continous increase of the CO signal intensity with increasing O_2 concentration.
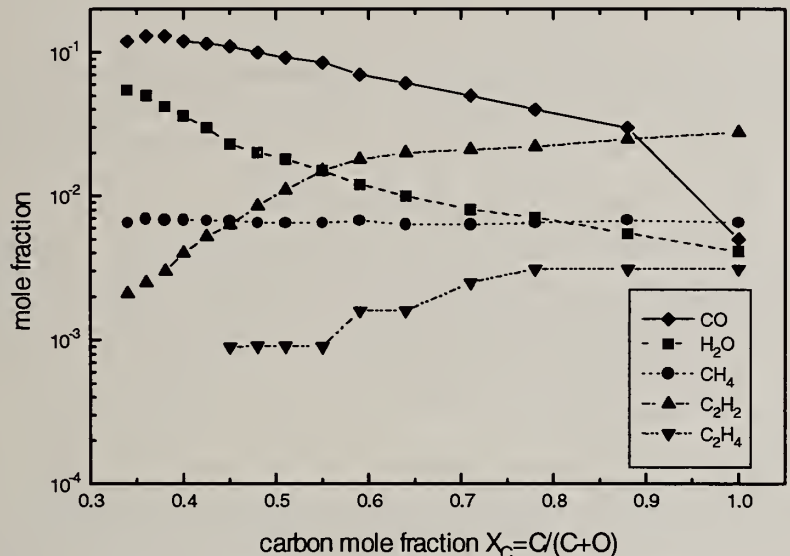
Fig.2: QMS signal intensities in Ar/CH_4/O_2 plasmas
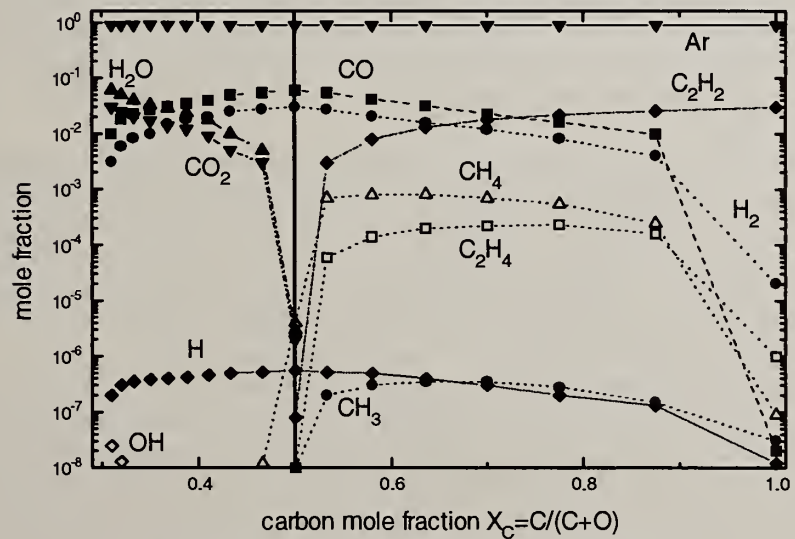
Fig.3: Equilibrium state of the Ar/CH_4/O_2 plasmas

The measured gas phase compositions compare quite well with model calculations using thermodynamic equilibrium conditions. Although a microwave plasma is far away from an equilibrium state our results suggest that most of the gas phase processes can be calculated from thermodynamical equilibrium conditions assuming a gas phase temperature of 1300 K. This assumption results in comparative concentrations between experiments and calculation for the most intense species like CH_4, C_2H_2 and CO. However, in order to reach a H concentration typical for $Ar/CH_4/O_2$ plasmas a much higher gas temperature of 2500 K would be necessary [3]. We created a system of homogenous gas phase reactions and calculated the state of minimized free enthalpie. The results for the $Ar/CH_4/O_2$ system are shown in Fig.3.

We observe a drastic change of gas phase composition in the region of $X_C=C/(C+O)$ near 0.5. For increasing oxygen content there is a drastic decrease of ethine, ethene methane and methyl, while CO_2 and H_2O increases. The variation of the H concentration near $X_C=0.5$ is comparable small. Besides there is a maximum of CO at $X_C=0.5$ at a considerably high mole fraction of approximately 5×10^{-2}. Comparing with the Bachmann diagram and our Raman spectroscopic data this region near 0.5 is the area of diamond growth. No carbon deposition is detected for oxygen mole fractions >0.55, is this concentration lowered to < 0.48 the deposition changes from diamond to graphitic or amorphous carbon.

4. Discussion

We deposited diamond films on Si(111) using gas mixtures of $Ar/CH_4/O_2$, $Ar/C_2H_2/O_2$ and $Ar/CH_4/CO_2$. The diamond content in the films was measured using Raman spectroscopy. Without oxygen we were not able to deposit diamond. The deposition occured only in a limited composition range near the CO line in the Bachmann diagram (C:O atomic ratio 1:1). The composition range given as C/O atomic ratio was determined to be 1-0.7 for the $Ar/CH_4/O_2$ system and 1-0.8 for the $Ar/C_2H_2/O_2$ system. When the carbon concentration was increased above these values, only the deposition of graphitic or amorphous carbon occured. Lower values led to no carbon deposition at all.

In order to change the carbon deposition from graphitic or amorphous to diamond it is necessary to increase the oxygen concentration. QMS and OES indicate that this improvement correlates with the decrease of ethine in the plasma gas. Especially the ratio of methane to ethine is in our opinion critical for the phase purity of the deposited diamond. Oxygen addition reduces the ethine content much more than that of methane. This corresponds very good with our results in a hot-filament reactor [4] showing that this is not only typical for microwave plasma CVD.

The thermodynamic equilibrium calculations revealed that a drastic reduction of ethine occurs for carbon mole fractions $X_C=C/(C+O)$ near 0.5. This is due to the formation of the CO and CO_2 molecules with a high negative ΔG so that the concentration of hydrocarbon species available for carbon deposition decreases. This interpretation is in agreement with experimental results of Beckmann et al. [5] who state that the major role of oxygen addition is to transform active carbon species into CO. Because

of this there is an increase of the H/CH_3 ratio near $X_C=0.5$ which is also important for the diamond deposition.

Comparing experiments in a hot-filament reactor showed that it is not possible to produce diamond films using argon gas mixtures (without additional H_2). This can be explained by the very high oxgen to carbon ratio which is responsible for the destruction of the filaments.

5. Acknowledgements

6. References

[1] P.K.Bachmann, D. Leers, and H. Lydtin, Diamond and Related Materials, 1, 1(1991)

[2] P. Joeris, C. Benndorf, Surface Modification Technologies III, ed. by T.S.Sudarshan and D.G. Bhat, The Minerals, Metals and Materials Society, Warrendale 1990, p.61

[3] N.A. Prijaya, J.C. Angus, and P.K. Bachmann, Diamond and Related Materials, 129, 3(1993)

[4] I. Schmidt, C. Benndorf, and P. Joeris, Diamond and Related Materials, in press

[5] R. Beckmann, B. Sobisch, and W. Kulisch, Proc. of Third International Symp. on Diamond Materials in Honolulu, 183rd Meeting of the Electrochemical Society, Hawaii 1993

THE RANGE OF METALS THAT WORK IN THE LPSSS PROCESS OF DIAMOND SYNTHESIS

H.S. Dewan, D. Ravichandran, J.P. Cheng, W.R. Drawl, K.A. Cherian and R. Roy

Intercollege Material Research Laboratory, The Pennsylvania State University
University Park, PA 16802, USA

Key words: diamond, liquid-phase, LPSSS, metals, $Me_xC_yH_z$, solid-state source

Abstract

In the traditional high pressure, high temperature (HPHT) process for diamond synthesis a great deal of research went into selecting the optimum alloys for diamond growth. By and large combinations of 3d and 4d transition metals proved to be the best. Copper, silver and gold seemed to have been contra-indicated during many decades of HPHT research.

For the LPSSS process in trying to establish the parallelism with HPHT we have now examined many metals, including the noble metals, rare earths, carbide and noncarbide formers, Pb, Sn, Bi, Sb, etc. Very interesting sequences of precipitations of diamond result from Ag and Au, and of course Cu and Ni. Metastable metallic ($Me_xC_yH_z$) liquid droplets (tens of microns in diameter) are formed containing up to 60-70% of C and presumably substantial H^o. These droplets precipitate diamond from the $Me_xC_yH_z$ liquid starting at the surface but going through the body.

1. Introduction

In the LPSSS process of diamond synthesis, solid carbon sources are used, instead of gaseous sources as in the CVD process, for diamond crystal growth. In one embodiment of the LPSSS process, a metal is added as a second phase. The mechanism for the efficacy of the metals, when we announced the LPSSS finding, was unclear. It was not immediately obvious that the process could lead to an intermediate amorphous "liquid" phase with the carbon source in the presence of atomic hydrogen. Next, the C exsolved from the $Me_xC_yH_z$ phase and precipitated as diamond.

There is apparently a parallelism between the HPHT[1] solvent-catalyst process and the LPSSS [2,3] process. In the former, C transforms to diamond which becomes the stable form in a $Me_x+C_y+P_z$ system - here Me represents certain metallic elements or alloys and P, the pressure available - whereas in the latter, the system is $Me_x+C_y+H_z$ with atomic hydrogen playing a role equivalent to that of pressure for diamond formation.

In this paper we summarize the results of investigations regarding the range of metals that work in the LPSSS diamond synthesis process, to try to establish the parallelism with the HPHT process.

2. Experimental

Several metals were investigated. Metal-carbon powder mixtures were prepared by mixing carbon (graphite or glassy carbon powder, Johnson Matthey) with the metal powder (Johnson Matthey, 0.5-1.5μ), and was compacted to 0.25 and 0.5 inch diameter pellets at a pressure of 30 MPa and 120 MPa, respectively. A wave-guided 2.45 GHz microwave tubular reactor setup was used for the processing. In typical runs a pure H_2 plasma was used at 80-100 Torr with the hydrogen flow rate at 80 cc/min. The temperature of the sample was measured by an optical pyrometer and controlled from 750C to 1050C for various runs. The processed samples were characterized by SEM, XRD and Raman spectroscopy.

3. Results and Discussion

The morphological characteristics of the diamond growth in various metal-carbon systems are shown in Fig. 1(a-g). Evidence for the formation of the intermediate "liquid" phases are observed in the case of several non-carbide forming metals. Iron also showed very interesting results. These liquid phases were found to form much below the standard eutectic melting points of the metal-carbon systems - eg. Ag at 750C, Cu at about 800C, and Fe at 1050C. It was observed that the nucleation and growth of diamond occured in association with these "liquid" phases in all cases, rarely on the area of the carbon source. Of course, there is no doubt that these $Me_x + C_y + H_z$ phases are quite volatile and their vapours can move around quite a bit. In some low melting point metal mixture systems, such as Ag-C, Sn-C and Au-C systems, many (metal) spheres of composition $Me_x C_y H_z$ formed, and the precipitation of diamond occurred on or around these spheres. As more and more diamond precipitated from the droplet one is left with a skeleton of molten metal containing polyhedral holes. These experimental evidences therefore suggest that exposure of the metal-carbon mixtures to the atomic hydrogen led to the formation of intermediate $Me_x C_y H_z$ phase during the processing of all these Me+C+H systems. This hydrogenated intermediate phase plays the key role in subsequent diamond precipitation and growth. The Raman spectra of the diamond formed in Ag-C and Fe-C systems are shown in Fig. 2.

Metal carbides were found in some processed samples. With Cr, representative of the carbide formers, abundant euhedral 100 platelets of Cr_3C_2 are formed first, and only later does diamond appear, almost certainly by vapour transport. The XRD results indicated the formation of some iron carbides in the Fe-C system, and lanthanum carbides in the La-C system, but their x-ray diffraction patterns showed that these carbides are different from the ordinary carbides.

In the case of Fe, an intermediate liquid phase which wets diamond appears to have formed. In the case of the other metal carbide formers, however, there appears to be no evidence at present for an intermediate liquid phase; various carbides appear to have formed. Alloys with carbide forming metals which could wet diamond should provide very interesting results.

4. Acknowledgment

5. References

1. R.C. Burns, and A.J.Davis, "Growth of Synthetic Diamond", in The Properties of Natural and Synthetic Diamond, Ed: J.E. Field, Academic Press Ltd. (London), 395-422 (1994)
2. R. Roy, H.S. Dewan, and P. Ravidranathan, Mat. Res. Bull., Vol. 28, 861-866 (1993)
3. R. Roy, H.S. Dewan, and P. Ravidranathan, J. Mater. Chem., 3(6), 685-686 (1993)
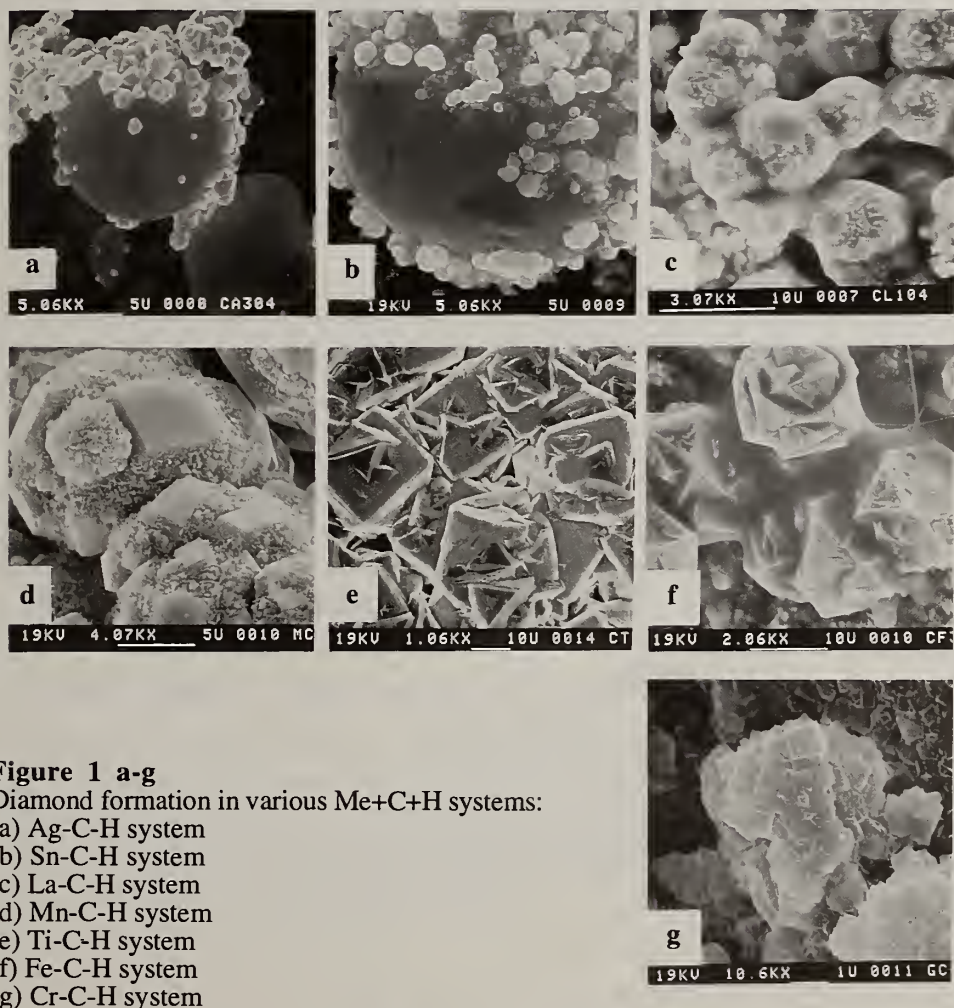
Figure 1 a-g
Diamond formation in various Me+C+H systems:
(a) Ag-C-H system
(b) Sn-C-H system
(c) La-C-H system
(d) Mn-C-H system
(e) Ti-C-H system
(f) Fe-C-H system
(g) Cr-C-H system
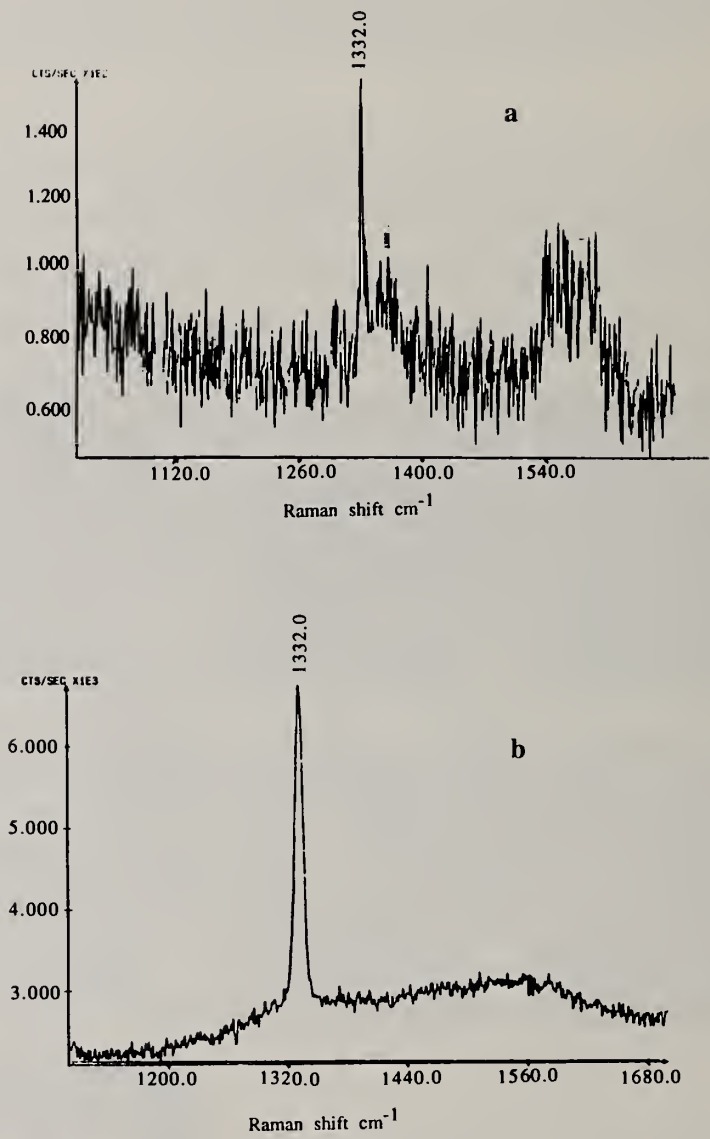
Figure 2 a&b
Raman spectra of diamond formed in:
(a) Ag-C-H system
(b) Fe-C-H system

Applications of Diamond Films and Related Materials: Third International Conference, 1995
Editors: A. Feldman, Y. Tzeng, W. A. Yarbrough, M. Yoshikawa, and M. Murakawa

391

DIAMOND PRECIPITATION AND SINGLE CRYSTAL HOMOEPITAXIAL GROWTH IN THE SYSTEM Ag-C-H

Rustum Roy, Jiping Cheng, William R. Drawl and Kuruvilla A. Cherian
Intercollege Materials Research Laboratory, The Pennsylvania State University, University Park, PA 16802, USA

Key words: diamond, liquid-phase, LPSSS, metals, $Me_xC_yH_z$, solid-state source

Abstract

The sequence of events in the LPSSS process when intimate mixtures of Ag and C are reacted in ~100 Torr of a pure H plasma of 750~950C have been studied in detail. Instead of the equilibrium solubility of ~0.1 % of C in Ag, metastable noncrystalline "liquid" phases with very high concentrations of carbon are formed. These phases, in the form of 10~50 micron "spheres", precipitate euhedral cubo-octahedra of diamonds, leaving metal-rich skeletons. Epitaxial growth on (110) single crystal has also been achieved and its rate is enhanced by this LPSSS arrangement. Possible mechanism for the diamond formation is discussed.

1. Introduction

Since the successful diamond synthesis from carbonaceous vapors below 1 atm. by hot filament CVD and microwave plasma CVD[1,2], various techniques have been developed to deposit diamond films - such as electron beam CVD, laser beam CVD, DC discharge plasma CVD and oxy-acetylene flame CVD[3]. In 1992, Roy and his coworkers reported a new method that can be described as a low-pressure solid state source (LPSSS) method for diamond synthesis[4]. Instead of carbonaceous gaseous sources as in the CVD processes, solid state carbon sources such as graphite, amorphous or glassy carbon powders were used in the LPSSS process. The second phase, usually some metal powder, such as Cu and Ni, was used as a precursor, or as a "catalyst" to nucleate diamond in the LPSSS process. In the present work, the diamond precipitation and single crystal homoepitaxial growth in the system Ag-C-H were investigated to study some key characteristics of the LPSSS process.

2. Experimental

The powder mixture prepared by mixing 70 wt% carbon (graphite powder, Johnson Matthey, <1 μ) and 30 wt% silver (powder, Johnson Matthey, 0.7-1.3μ) was compacted to 0.25 inch diameter pellets at a pressure of 30 MPa. For single crystal homoepitaxial growth, a natural single crystal diamond was implanted in the mixture pellet with a thin layer (~0.1 mm in thickness) of powder mixture of the same composition covering the single crystal.

A wave-guided 2.45 GHz microwave tubular reactor setup was used for the processing. In typical runs a pure H_2 plasma was used at 80-100 Torr with the hydrogen flow rate at 80 cc/min. The temperature of the sample was measured by an optical pyrometer and controlled from 750C to 950C for various runs. The processed samples were characterized by SEM, XRD and Raman spectroscopy.

3. Results and discussion

The sequence of diamond precipitation in the 30 wt% silver mixture system with the processing time is shown in Figs. 1 and 2. A few submicron diamond formed after the first one hour run, and the density and the size of the diamond particles increased with the processing time. It was observed that many metal spheres of composition $Me_xC_yH_z$ formed on the surface of the processed samples, and the precipitation of diamond occurred on or around these spheres (Fig. 2). As more and more diamond precipitated from the droplet one is left with a skeleton of molten metal containing polyhedral holes.

In the absence of external diamond seeds in the silver-carbon mixture, polycrystalline diamond precipitation occurred. When a single crystal diamond substrate was implanted in the mixture, excellent homoepitaxial diamond growth was obtained. Fig. 3 shows the homoepitaxial growth of diamond on a (110) facet of the pre-implanted diamond substrate, and Fig. 4 is the Raman spectra of the sample. The sharp peak at 1332 cm^{-1} associated with diamond crystalline structure, and a flat background signal, indicate that the diamond epilayer is of high quality.

It was reported by Badzian that there is an intermediate Ni-C-H phase formed in the microwave plasma CVD when a nickel foil was put in the reactor, and this intermediate phase facilitates the nucleation of diamond [5]. Recently, evidence for an intermediate phase, involving metal, oxygen and carbon, in a Me+MeOH+C system, facilitating diamond formation from a liquid phase has also been reported [6]. In our experiments, it was found that the silver melted even at temperatures as low as 750C, much below any standard eutectic melting point. It is supposed that the silver was saturated by hydrogen and carbon in the H_2 plasma, and a metastable phase which can be described as $Ag_xC_yH_z$ formed. Evidence has been obtained which show the carbon concentration in $Ag_xC_yH_z$ to be much higher than the equilibrium solubility of C in Ag. Some carbon atoms exsolved from the $Ag_xC_yH_z$ phase in sp^3 state to precipitate diamond. The composition of these $Ag_xC_yH_z$ phases seem to show a value of y = 60-70 atom percent with reference to Ag, and they appear to be noncrystalline.

4. Conclusion

The results of the precipitation of diamonds in the Ag-C-H system show that a "fluid" $Me_xC_yH_z$ phase was formed in the LPSSS processing. The formation of the $Me_xC_yH_z$ phase enhanced the precipitation and growth of the diamond. Epitaxial growth on (110) single diamond crystal has also been achieved in the Ag-C-H system.

5. Acknowledgment

6. References

1. S. Matsumoto, Y. Sato, M. Tsutsuumi, and N. Setaka, J. Mater. Sci., 17, 3106 (1982)
2. M. Kamo, Y. Sato, and S. Matsumoto, J. Cryst, Growth, 42, 642 (1983)
3. P.K. Bachmann, in Thin Film Diamond, edited by A. Lettington, and J. W. Steeds. 31-53 (1993)
4. R. Roy, Press Conference, National Press Club, Washington, DC, Oct. 21,1992
5. A. Badzian, and T. Badzian, in Proc. of the NIRIM Intern. Symp. on Advanced Materials'94, edited by M. Kamo, H. Kanda, Y. Matsui, and T. Sekine, 140-145 (1994)
6. M. Komath, K.A. Cherian, S.K. Kulkarni, and A. Ray, Diam. & Relat. Mater., 4, 20 (1994)
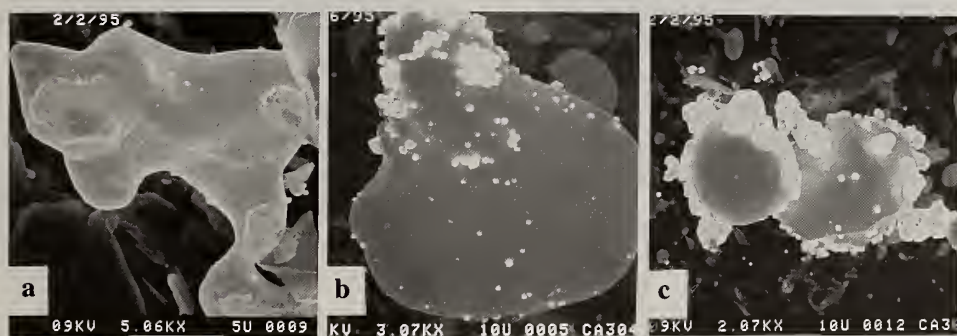
Figure 1 a-c.
$Me_xC_yH_z$ liquid phase formation and diamond precipitation with Ag+C (Ag 30 wt%), processed in pure H_2 plasma at 850C, 100 Torr.

(a) Coalescence of liquid phase and early stage of diamond (subµ size) precipitation (processing time: 1 hour)
(b) Subsequent stage with diamond nucleation becoming more evident (processing time: 4 hours).
(c) Liquid phase ($Me_xC_yH_z$) spheres with associated diamond precipitation (processing time: 8 hours).
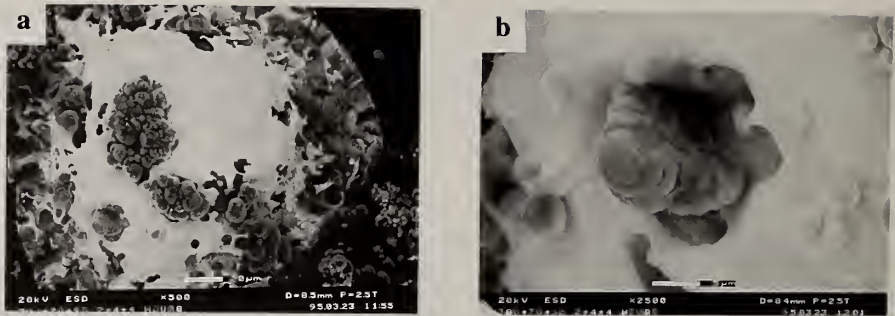
Figure 2 a&b
Diamond precipitation from ($Me_xC_yH_z$)) spheres and associated polyhedral cavity
formation.
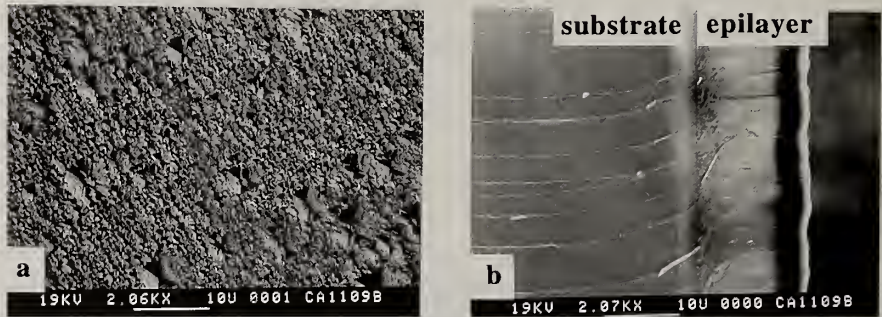
Figure 3a&b
Homoepitaxial growth of diamond on a (110) facet of a diamond substrate
implanted in Ag+C mixture pellets (Ag 30 wt%) processed in pure H_2 plasma at
950C, 80 Torr for 4 hours.
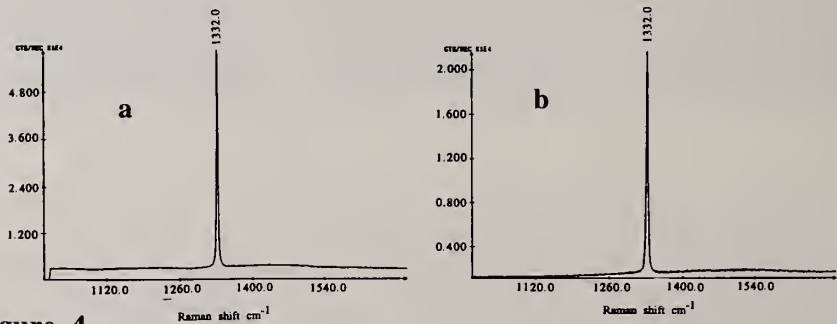
Figure 4.
Raman spectra of the homoepitaxial growth sample:
(a) from the diamond substrate
(b) from the grown layer.

SHOCK-WAVE MICRON-SIZE DIAMOND SYNTHESIS FROM FULLERENES

O.G.Epanchintsev,[1] A.S.Zubchenko,[1] N.N.Kobelev,[1] A.E.Korneyev,[1] A.A.Dityatyev,[2] V.F.Nesterenko,[3] V.A.Simonov[3]

[1] Federal Scientific Center of Russia TSNIITMASH, 4 Sharikopodshipnikovskaya st., Moscow, 109088, Russia
[2] Moscow State University, Moscow, 119899, Russia
[3] Lavrentyev Institute of Hydrodynamics, Russian Academy of Science, Siberian Div., 15 Lavrentyev Avenue, Novosibirsk, 630090, Russia

Key words: diamond, fullerites, high-pressure, shock-induced synthesis

Abstract

Shock-wave synthesis of micron-size diamond is performed from fullerenes C_{60} -- C_{150} powders using the explosive compaction technique with plane shock-wave loading at different pressures in the range of 24-40 GPa. The compacts of different initial compositions consisted of diamond, fcc fullerite C_{60}, graphite and amorphous carbon.

The most coarse diamond grains sized up to 6 μm were formed at the shock pressure of 24 and 40 GPa in the compacts of initial powder mixture copper-5mass.% fullerite and at shock pressure of 40 GPa in the compact of initial powder mixture copper - 10mass.% fullerite. Shock-wave synthesis of diamond is performed without forming intermediate diamondlike phases, such as n-diamond and lonsdaleite (hexagonal diamond) in the final products.

1. Introduction

The structure of the starting carbon materials is a determining factor in direct and catalyzed diamond synthesis [1]. Since the discovery that fullerites, the crystal form of fullerenes - the new family of carbon allotropes - can be obtained in macroscopic quantities [2], it is of great interest to synthesize diamond from these promising carbon structures [3]. The molecules of C_{60}, the most abundant of the fullerene family, have a highly symmetrical pseudospherical structure, which is extremely stable, withstanding hydrostatic pressures of up to 20 GPa [4]. On the application of high pressure exceeding 20 GPa both C_{60} molecules and C_{60} crystals (fullerites) might transform into diamond and diamondlike phases [3-7].

A technique with great potentialities for diamond synthesis appears to be shock-wave compaction of fullerite powders, using explosive systems. The beneficial feature of high - energy explosion treatment of solids is very high concentration of defects generated in crystal lattice and high level of its internal stress which promotes phase transformations and substantially affects the evolution of the material structure. The typical grain size of diamond shock-synthesized from C_{60} or mixed C_{60} / C_{70} fullerites ranges 2 to 100 μm [6,7].

Recently we have succeeded in shock-synthesizing of much coarser diamonds [8]. The dimensions of diamond particles in the recovered compacts reached some microns [9]. In this manuscript we report the experimental results of X-ray structural and TEM analysis of micron-size diamond particles shock-synthesized from fullerites.

2. Experimental

Fullerenes were synthesized under low helium pressure in a carbon arc. Then the fullerenes were extracted by toluene from soot that had been subjected to extraction by chloroform. Mass-spectroscopy indicated the presence of fullerenes from C_{60} to C_{150}, C_{60} being the main fraction . X-ray structural, TEM and light microscopy indicated three crystal phases in this powder: fcc C_{60} a = 14.12 Å, hcp C_{70} (a = 10.66Å, c = 17.20Å) and a small amount of hcp C_{60}. Some difficulties may arise when conducting the experiments because of the necessity to provide intense heat transfer from shock-compressed fullerite particles to the surrounding medium in oder to retain at ambient conditions the high pressure phases formed on shock-loading. To avoid these difficulties we used the initial powder mixture consisting of fullerite (2, 5, and 10 mass %) and copper, fullerite particles being dispersed in a copper matrix as an efficient quenching medium. All compressed samples were investigated by light microscopy, TEM and X-ray structure analysis. Samples for phase determination were prepared by selective dissolution of copper in HNO_3 and separation of carbon phases by centrifugation.

3. Results and discussion

Diamond, graphite and fcc C_{60} were detected in all analyzed specimens, while there was no n-diamond or hexagonal diamond (lonsdaleite): only (111) and (222) diffraction peaks were present, belonging to the diamond space group of Fd3m (Table I). For samples shock-compressed at 24-26 GPa the diamond diffraction lines width depends on the content of the fullerenes in the initial copper-fullerene mixture. The line width of the sample containing 2 and 10 mass % of fullerenes is larger than that of the sample with

5 mass % of fullerenes, which means that the average size of diamond crystallites in the latter is larger.

TABLE I

The indexed X-ray diffraction lines from phases in compacted sample (5% ,38 GPa)

d_{hkl} (Å)	I/I_o	Diamond (hkl) $a = 3.55$Å	fcc C_{60} (hkl) $a = 14.08$Å	Graphite (hkl)
4.96	s		(220)	
4.23	s		(311)	
4.07	m		(222)	
3.41*	s			(002)
3.21	m		(331)	
2.87	m		(422)	
2.71	m		(333),(511)	
2.05	vs	(111)		
1.97	vw		(551),(711)	
1.25	s	(222)		

* Diffuse line
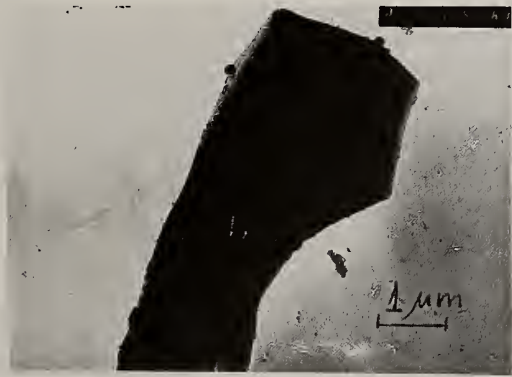
Fig.1 TEM pattern of diamond separated from compacted sample (5%, 38 Gpa)

At a higher pressures (up to 38-40 GPa), the phase composition of the samples does not change, except for a slight increase in the diamond content and a slight decrease in the fcc

398

C_{60} content according to observed changes of diffraction peak intensities. Narrow diffraction lines of diamond are typical for both the 5% sample and the 10% sample. For the 2% sample the diffraction peaks remain diffused as in the case of shock compression at 24 GPa. TEM investigations of the samples after separation confirm that the size of the diamond crystallites is nearly $1\,\mu m$ (Fig. 1).

4. Conclusions

1. Shock-wave synthesis of diamond from fullerene C_{60} - C_{150} powders was performed using the explosive compaction technique with plane shock-wave loading at different pressures in the range of 24-40 GPa. Compared with methods using a gas gun, this technique is very promising for industrial technologies.

2. The compacts of different initial compositions consisted of diamond crystallites, up to 6 μm were formed at shock pressures of 24 and 38 GPa in the compacts of an initial powder mixture copper-5mass% fullerite and at shock pressure of 40 GPa in the powder mixture copper-10mass% fullerite.

3. Shock-wave synthesis of diamond is performed without the formation of intermediate diamondlike phases, such as n-diamond and hexagonal diamond (lonsdaleite) in the final products.

5. References

1. G.Bocquillon, C.Bogicevic,C.Fabre and A.Rassat,J.Phys.Chem.97,12924 ,(1993)
2. W.Kractschmer, L.D.Lamb, K.Fostiropoulos and D.R.Huffman, Nature347,354,(1990)
3. M.Nunez Regueiro,P.Monceau and J.L.Hodeau,Nature,355,237,(1992)
4. S.J.Duclos,K.Brister,R.C.Haddon,et al. Nature351,380,(1991)
5. C.S.Yoo and W.J.Nellis,Science,254,1489,(1991)
6. C.S.Yoo,W.J.Nellis,M.C.Sattler et al. Appl.Phys.Lett.61,273,(1992)
7. T.Sekine,Proc.Japan Acad.,68B,95,(1992)
8. O.G.Epanchintsev,A.E.Korneyev,A.A.Dityatyev et al. Fizika gorenia i vzriva31,N2, (1995).
9. O.G.Epanchintsev,A.S.Zubchenko,Yu.D.Tretyakov et al. Doklady of Russian Academy of Science,340,201,(1995)

CHEMICAL VAPOUR DEPOSITION OF POLYCRYSTALLINE DIAMOND FILMS ON STEEL SUBSTRATES

Lothar Schaefer, Andrea Bluhm, M. Sattler, R. Six, and Claus-Peter Klages

Fraunhofer-Institut für Schicht- und Oberflaechentechnik, Bienroder Weg 54E, D–38108 Braunschweig, Germany

Key words: diamond, steel, tools, hardness, interlayers, diffusion

Abstract

Direct coating of polycrystalline diamond films on steel substrates by conventional activated chemical vapour deposition methods is not possible. Minimum substrate temperatures around 700°C used for diamond deposition cause a decrease in Rockwell and Vickers hardness of more than 35% of the original HRC and HV10 values, respectively. Additionally at temperatures below 500°C, the interaction between the activated hydrogen gas phase and the steel surface leeds to embrittlement, which becomes noticeable by cracks after indentation. Under diamond deposition conditions the interdiffusion between substrate and deposited carbon material also changes the mechanical properties of the substrate and hinders the formation of diamond. To apply highly wear resistent polycrystalline diamond coatings on high speed steel tools we investigated the use of silicon carbide interlayers as well as nitriding pretreatment of the substrate.

1. Introduction

Process technology for the deposition of polycrystalline diamond films is now available in many research institutions and companies all over the world. A variety of processes based on either thermally or electrically activated chemical vapour deposition (CVD) have been developed [1]. Mechanical, optical, thermal and electronic applications have been investigated on a laboratory scale [2]. The use of polycrystalline diamond films as highly wear resistant coating has been demonstrated by a variaty of specific cutting tool applications, where the requirements for adhesion are not extremely severe and temperature resistent substrate materials like tungsten carbide or silicon nitride are applicable.

To utilize the excellent wear properties of diamond coatings for steel parts, which ha-

ve a greater market potential in material machining and mechanical engineering, additional problems caused by diamond deposition conditions and the extremely different material properties of diamond and steel have to be solved. Minimum deposition temperatures around 700°C used for good quality diamond deposition with reasonable deposition rates are not suitable for high speed steel. Together with the interdiffusion between the substrate and deposited carbon the mechanical properties of steel might be changed. The diffusion of deposited carbon into the substrate hinders the deposition process significantly [3]. The difference in thermal expansion causes stress when cooling from deposition temperature to room temperature, thus influencing the adhesion between substrate and coating [4]. For a thin hard diamond coating on a comparably soft steel substrate sufficient load bearing capacity has to be provided.

In this contribution we present results of hardness measurements on two different high speed steel materials exposed to microwave plasma activated gas phases at different temperatures and of diamond CVD on these materials using silicon carbide interlayers and nitriding pretreatment, respectively.

2.   Experimental

Two high speed steels with cobalt content of 8 wt% and below 1 wt%, respectively, used in cutting tool applications were chosen as substrates. The exposure to an activated hydrogen gas phase and the diamond and silicon carbide deposition were performed in an Astex 1.5 kW microwave plasma CVD system at substrate temperatures between 430°C and 760°C. For silicon carbide deposition hydrogen-tetramethylsilane was used [5]. Hardness measurements were performed with standard Rockwell (HRC) and Vickers (HV10) tests. Diamond deposition was verified by Raman spectroscopy. The interdiffusion between coating and substrate was investigated by electron probe microanalyis (EPMA) and secondary ion mass spectrometry (SIMS).

3.   Results and discussion

In order to investigate the influence of activated hydrogen and elevated temperatures on the hardness of high speed steel uncoated ASP 23 (Co < 1 wt%) and ASP 30 (Co ≈ 8 wt%) cutting tool inserts had been exposed to a hydrogen microwave plasma for 20 hours at temperatures up to 760°C. Before exposure the substrates exhibit hardness values of 65 and 66 HRC, respectively. The corresponding Vickers hardness values were 860 and 925. For both substrates the decrease in hardness after plasma treatment was less than 5% for temperatures up to 550°C. At higher temperatures the decrease in hardness exceeded 35% at 700°C and reached nearly 50% at 760°C. Additionally the indentation yielded cracks for both methods, indicating hydrogen embrittlement. The cracks were detected at temperatures as low as 430°C thus demonstrating that hydrogen embrittlement also occurs at temperatures, where no loss in

hardness is found.

Exposing the steel substrates to the above conditions after coating with a 100 nm thick silicon carbide layer did not influence the substrate hardness values. However no cracks could be detected for temperatures up to 560°C. The SiC coating obviously acts as a barrier against the attack of activated hydrogen and avoids hydrogen embrittlement in the temperature region where the loss of hardness of the steel substrates is negligible.

Silicon carbide interlayers on both steel substrates were deposited at temperatures between 510°C and 650°C and characterized with electron probe microanalysis. A subsequent substrate biasing process for diamond nucleation followed by diamond deposition conditions allowed the *in situ* deposition of interlayer and diamond coating in the microwave plasma CVD process. Diamond deposition at 500°C was achieved by reducing pressure and microwave power. However, deposition rates at 500°C were less than 0.1 µm/h. Therefore, diamond deposition on SiC coated steel substrates was performed at higher power leading to substrate temperatures of 710°C, neglecting the loss of hardness of the substrate. The successful deposition of closed, well faceted diamond films with thicknesses of about 0.6 µm after 3.5 hours at this high temperatures clearly demonstrates the diffusion barrier characteristics of the SiC interlayer.

Diamond coating of the steel substrates was also achieved without interlayer deposition. The steel substrates had been pretreated by a plasma nitriding process creating a ferrous nitride containing diffusion zone. After the pretreatment diamond has been successfully deposited at 630°C in a 16 hour process (see Fig. 1). The Raman spectra
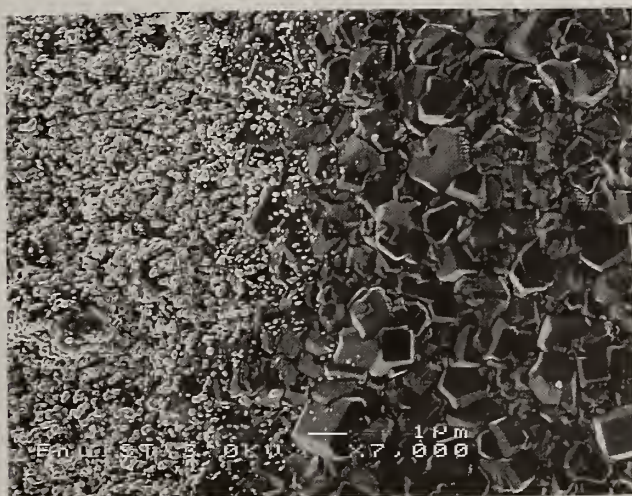
Figure 1: Scanning electron micrograph of a diamond film on nitrided steel

of the faceted areas (right side of Fig. 1) showed a clear diamond peak at 1335 cm^{-1} and only small amounts of non-diamond carbon. However, about 60% of the surface were covered with bright shining particles (left side of Fig. 1) containing up to 7 at% iron detected with EPMA. We conclude from this result, that the saturation of iron by the formation of ferrous nitrides in the diffusion zone significantly reduces the inter-diffusion between the substrate and deposited carbon, so that diamond nucleation and deposition is possible without a prolonged incubation time due to carbon diffusion into the bulk [3]. The diffusion of iron to the diamond surface may be caused by in-complete nitride saturation or by unsufficient barrier properties of the diffusion zone.

4. Summary

Chemical vapour deposition of polycrystalline diamond films has been investigated on two high speed steels with different cobalt content used for cutting tool applications. The difference in cobalt content had no influence on the experimental results. Temperatures above 550°C lead to a decrease of hardness. Embrittlement of the substrate surface, caused by the activated hydrogen atmosphere can be avoided by SiC coating so that diamond deposition on an unaffected substrate can be achieved at temperatures up to 550°C. The SiC coating also acts as a diffusion barrier up to temperatures of more than 700°C as demonstrated by successful diamond deposition. A plasma nitriding pretreatment of the substrates significantly reduces the interdiffusion between substrate and deposited carbon, thus leading to diamond deposition on an uncoated steel substrate.

5. Acknowledgements

5. References

[1] P. K. Bachmann, W. van Enckevort, Diamond and Related Materials, 1 (1992) 1021
[2] ADC ´93, 2nd Int. Conf. on the Application of Diamond Films and Related Materials, M. Yoshikawa, M. Murakawa, Y. Tzeng, and W. A. Yarbrough (Editors), MYU, Tokyo-Japan, 1993
[3] A. Lindlbauer et al., Diamond Films and Technology, 2 (1992) 81
[4] H. C. Shih et al., Surf. Coat. Technol., 57 (1993) 197
[5] X. Jiang and C.-P. Klages, Diamond and Related Materials, 2 (1992) 523

A NEW REGION FOR HFCVD DIAMOND GROWTH AT LOW TEMPERATURE

Z. Li. Tolt[1] L. Heatherly[1], R. E. Clausing[1], and C. S. Feigerle[2]

[1]Oak Ridge National Laboratory, P. O. Box 2008, Oak Ridge, TN 37831-6093
[2]Dept. of Chemistry, University of Tennessee, Knoxville, TN 37996-1600

Key words: growth rate, low temperature, oxygen, HFCVD

Abstract

It has been found that the addition of a small amount of oxygen at the 10^2 - 10^3 ppm level to the mixture of CH_4 and H_2 permits diamond deposition at significantly lower substrate and filament temperatures compared to those in a conventional hot-filament assisted chemical vapor depositon (HFCVD) of diamond. Within a narrow region of feed gas composition, the operable substrate temperature can be extended to as low as 400 °C, and filament temperature to 1350 °C, where no significant amount of H and CH_3 are expected to be produced by the filament. High quality diamond films have been deposited with reasonable growth rates at filament temperatures as low as 1600 °C and substrate temperatures as low as 580 °C. Power consumption is reduced. The filament is subjected to less distortion, and its lifetime is extended indefinitely.

1. Introduction

It has been widely accepted that diamond deposition in a hot filament assisted chemical vapor deposition (HFCVD) reactor requires a filament temperature higher than 1900 °C to activate the gas. Production of atomic hydrogen, along with activated growth species, is considered vital to this technology. [1, 2]. The combined effect of high temperature and carburization of the filament results in frequent breaking and severe distortion of the filament. Under the previously accepted growth conditions, the diamond growth rate reaches a maximum at a substrate temperature around 950 °C, and 700°C is considered to be a lower limit for substrate temperature. Below 700 °C significant amounts of graphitic carbon are co-deposited on the substrate.

In this investigation, it was discovered that by manipulating the composition of the feed gas high quality diamond can be deposited in a HFCVD reactor at significantly lower filament and substrate temperatures. As a result, power consumption is reduced and the filament lifetime is extended indefinitely. Diamond deposition under these low temperature conditions raises questions concerning the growth mechanisms.

2. Experimental Results

Diamond films were grown in a HFCVD reactor with independent substrate and filament temperature control. It was found that within a narrow window of atomic ratio of oxygen to carbon, O/C, the addition of a small amount of oxygen to the mixture of CH_4 and H_2, allows diamond deposition at filament temperatures as low as 1350 °C, and substrate temperatures as low as 400 °C. The optimum O/C ratio is closely related to the CH_4 percentage in the feed gas and is much lower than what has been commonly used in conventional diamond depositions. The width of the applicable O/C window

becomes narrow at low temperatures. Fig. 1 shows a scanning electron microscope (SEM) image of diamonds grown at 1700 °C filament temperature and 580 °C substrate temperature with 0.5% CH4 and 13% O/C ratio (325 ppm O_2). The Raman spectrum shown in Fig. 1 b) has a FWHM of about 6 cm^{-1} indicating a high quality film. Almost no non-diamond carbon was detected. The diamond film shown in Fig. 2 was grown at 1600 °C filament temperature and 580 °C substrate temperature with 1% CH_4 and 19% O/C ratio (950 ppm O_2). The growth rate of both samples was between 0.2 - 0.3 µm/h.

Several interesting phenomena have been observed associated with changes in conditions for growth of these films. First, the diamond growth rate does not monotonically increase with filament temperature. In a certain temperature range, an increase in filament temperature may actually result in a decrease in growth rate. Depending on the specific gas composition used, the growth rate at 1700 °C can be as high as that at 2000 °C, while for intermediate temperatures, the growth rate can decrease. Second, as the substrate temperature decreases, the Raman spectrum reveals that the quality of the films improve dramatically. Third, the growth rate maximizes near 750 °C substrate temperature, about 200 °C lower than what is typically found without oxygen.

3. Discussion

The deposition of diamond at these low filament and substrate temperatures and the unique behavior of the changes in growth rate and film quality with these temperature in this low temperature region are not consistent with previous experience using conventional HFCVD. These observations strongly suggest that the chemistries have changed on both the filament and the substrate. Analysis of the reactor exhaust gas shows that when the filament temperature is significantly lower than 2000 °C, the substrate temperature has an effect on the mole fractions of species in the gas phase. According to thermodynamic calculations, dramatic changes in the gas phase species present should occur at temperatures around 1300 °C for the H, C and O mixture used here. Large differences between the species concentrations near the substrate and those near the filament are to be expected. The mechanisms that enable diamond growth at these low filament and substrate temperatures are not clearly defined at this point, but we suggest that oxygen may be involved in changing: (1) the carbon deposition on the filament, (2) the etching processes for removal of non-diamond carbon from the surface deposit, and (3) the process for hydrogen abstraction from the hydrogenated diamond surface. Additional information on the growth processe are discussed elsewhere [3].

4. Conclusions

High quality diamond can be deposited at significantly lower filament and substrate temperatures than those in conventional HFCVD of diamond while retaining reasonable growth rates. Power consumption by the filament is reduced. The filament is less subject to distortion, and its lifetime is extended indefinitely.

5. Acknowledgments

6. References

1.   J. C. Angus and C. C. Hayman, *Science,* **241**, 877(1988)
2.   F. G. Celii and J. E. Butler, *Annu. Rev. Phys. Chem.*, **42**, 643(1991)
3.   Z. Li Tolt, L. Heatherly, R. E. Clausing, R. W. Shaw and C.S. Feigerle, submitted to the 187th Electrochemical Society Meeting, May, 1995, Reno, NV
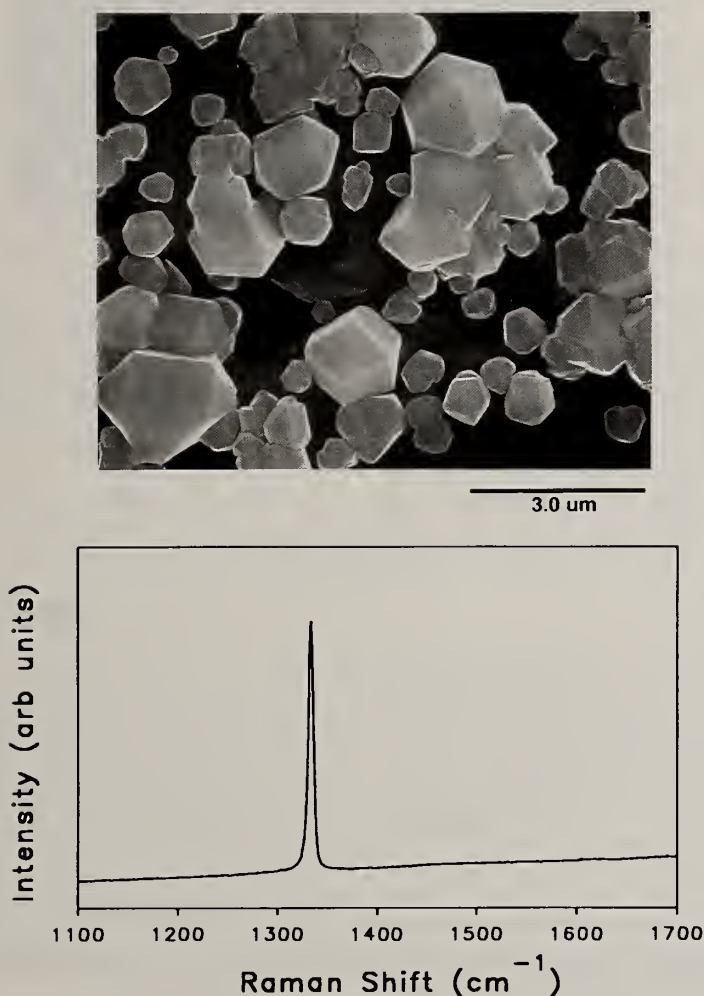
Fig. 1 Scanning electron microscope image of diamond deposite and its Raman spectrum. Growth conditions: T_f=1700 °C, T_s=580 °C, 0.5% CH_4, 13% O/C.
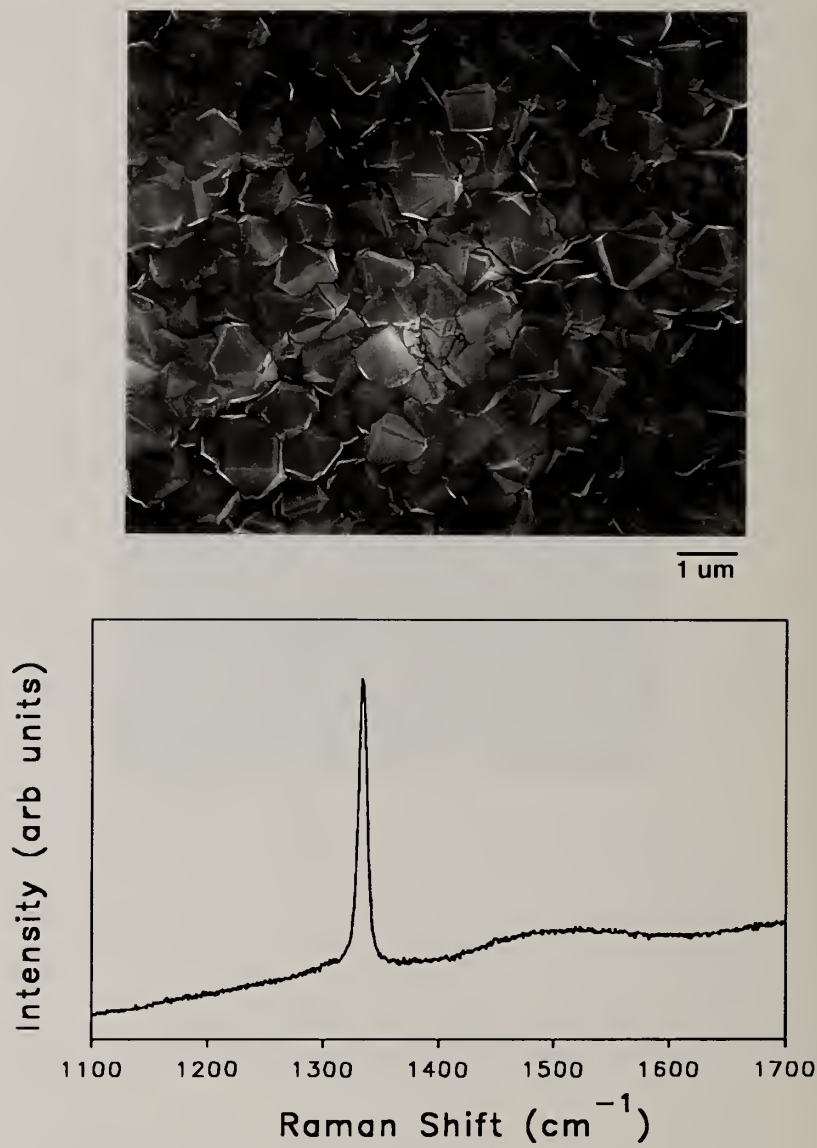
Fig. 2 Scanning electron microscope image of a diamond film and its Raman spectrum.
Growth conditions: T_f=1600 °C, T_s=580 °C, 1% CH_4, 19% O/C.

EFFECT OF PRESSURE ON THE MORPHOLOGY AND GROWTH OF HFCVD DIAMOND AT LOW FILAMENT AND SUBSTRATE TEMPERATURES

Z. L. Tolt[1], L. Heatherly[1], R. E. Clausing[1], and C. Feigerle[2]

[1]Oak Ridge National Laboratory, P. O. Box 2008, Oak Ridge, TN 37831-6093
[2]Dept. of Chemistry, University of Tennessee, Knoxville, TN 37996

Key words: HFCVD, low temperature, morphology, pressure

Abstract

It has been found that diamond can be grown at significantly lower substrate and filament temperatures by adding a small amount of oxygen to the mixture of CH_4 and H_2. In contrast to the insensitivity of the morphology to pressure in conventional HFCVD of diamond, pressure was found to have a significant effect on the diamond morphology in these low temperature deposition processes. At a fixed substrate temperature and CH_4 percentage in the feed gas, the morphology changed from cubo-octahedral to octahedral when the pressure was increased from 10 torr to 90 torr. The particle size also became increasingly non-uniform. The average growth rate saturated at about 20 torr. Changes in the relative concentrations of species such as methane and acetylene in the reactor were found to closely follow the trend of morphology change.

The mechanisms causing pressure to affect the morphology and uniformity under these deposition conditions are discussed in terms of gas phase and surface chemistry as well as growth mechanisms.

1. Introduction

It has been established that the quality of CVD diamond films depends not only on the quality of individual particles but also on the film texture. Texture development results from the competitive growth of randomly oriented crystals. As a result, the morphology of individual crystals can be closely related to the final film texture. A growth parameter, $\alpha=(V_{100}/V_{111})\sqrt{3}$, has been defined to describe the crystallite shape, with cubes corresponding to $\alpha=1$, cubo-octahedrals to $\alpha=1.5$, and octahedrals to $\alpha=3$. Film texture can be predicted from the growth rate ratio with the assumption of infinite surface diffusion. [1, 2] Typically, with cubes, a (111) texture will be developed, with cubo-octahedrals, a (110) texture, and with octahedrals, a (100) texture. Since the (100) textured film with {100} facets is smoother and has less defects, it is usually considered the most desirable film for applications requiring high crystal perfection.

Under the usual activated CVD of diamond using either the hot filament or microwave processes, the growth parameter α has been found to be a strong function of substrate

temperature and the CH_4 percentage in the feed gas. Many studies have shown a common trend that at low substrate temperature and high CH_4 percentage (rich conditions), an α close to 3 (octahedral crystals) is obtained, whereas at high substrate temperatures and low CH_4 percentage (lean conditions), an α close to 1 (cubes) or 1.5 (cubo-octahedrals) is obtained [2, 3]. The same conclusion applies to depositions with oxygen additions. [2, 4] Pressure does not strongly affect the morphology. For this reason, there have not been detailed studies of the effect of pressure on the morphology.

We have reported that the addition of only a small amount of oxygen permits HFCVD of diamond at filament temperatures (T_f) as low as 1400 °C or substrate temperatures (T_s) as low as 450 °C. High quality diamond was deposited with a growth rate of ~ 0.2 µm/h at T_f=1700 °C, T_s=580 °C, 0.5% CH_4, and an oxygen/carbon atomic ratio, O/C, of 13%. [5] One of the many interesting phenomena associated with this low temperature deposition is the unique behavior of growth rate and the morphology changes with the deposition pressure. It has been found that the α value continuously changes with the pressure. Also, particle growth rates and the uniformity of particle size were affected by pressure.

2. Experimental

The deposition was conducted in a conventional quartz tube HFCVD reactor with independent control of the substrate and filament temperatures. The filament temperature was measured by a single-color pyrometer without corrections. The substrate temperature was read through a S-type thermocouple buried in the substrate holder. This reading is estimated to be less than 50 °C lower than the actual surface temperature when the T_f is lower than 1750 °C. The concentrations of stable chemical species in the reactor were measured by residual gas analysis (RGA). For detailed experimental information, one should refer to the reference [5].

3. Results and Discussion

For the present study diamond was deposited at different pressures while holding the other conditions fixed at: T_f=1700 °C, T_s=580 °C, 0.5% CH_4, and O/C=13%. Fig. 1 a) through e) show the scanning electron images of diamonds grown at 12 torr, 24 torr, 40 torr, 65 torr and 90 torr respectively. All the depositions lasted 16 hours. As seen from these images, the particular morphology changed from cubo-octahedral to octahedral as the pressure changed from 12 torr to 90 torr. This indicates that the growth rate ratio of the {100} faces to that of the {111} faces, V_{100}/V_{111}, increases with the deposition pressure. Fig. 2. shows the relationship between the α value and the pressure. At lower pressures (<20 torr) the growth was uniform. As the pressure increased, the particle sizes became more and more uneven. The average growth rate increased for the pressures up to 20 torr. With a further increase in pressure, the growth rate saturated. Accompanying these changes were also changes in the relative concentrations of CH_4 and C_2H_2. Fig. 3. shows the normalized RGA intensities of CH_4, C_2H_2 and CO during these depositions, ($I(CH_4)/I(H_2)$, $I(C_2H_2)/I(H_2)$ and $I(CO)/I(H_2)$). As the pressure was increased, there was more CH_4 present in the gas phase, likely because of the conversion of C_2H_2 to CH_4. The change in the normalized intensity of CH_4 and C_2H_2 closely followed the trend of the change in morphology. Between 12 and 24 torr, the shape of the diamonds hardly changed, nor did the normalized intensity of CH_4 or C_2H_2. For the pressure

range between 40 to 65 torr, in which the morphology changed rapidly with pressure, the percentages of CH_4 and C_2H_2 in the gas also changed rapidly.

In previous morphology studies, the substrate temperature T_S, and the CH_4 percentage of the feed gas have been exclusively correlated to the morphology. In contrast, the morphology change described above was achieved at a constant substrate temperature using a feed gas of constant CH_4 percentage. Kondoh *et al.* studied the effect of gas phase composition on the surface morphology. He correlated the surface morphology to the ratio of the concentration of atomic hydrogen to methyl $[H]/[CH_3]$ [6]. The correlation is consistent with the other empirical observations, *i. e.* the larger $[H]/[CH_3]$ ratio corresponds to the leaner condition and results in (111) surface faces ((110) or (111) texture). The lower $[H]/[CH_3]$ ratio corresponds to the richer condition yielding (100) textured films. Fig. 3 shows that the relative concentration of CH_4 in the gas phase, $[CH_4]/[H_2]$, changed with the pressure even though the CH_4 percentage in the feed gas did not change. With this information, the change of $[H]/[CH_3]$ ratio with the pressure can be estimated. At the typical diamond HFCVD conditions, where the major mechanisms for atomic hydrogen recombination in the gas phase are through trimolecular collisions with molecular hydrogen, (see reaction (1)),

$$H + H + M = H_2 + M \quad (M = H_2) \tag{1}$$
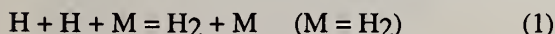
the average lifetime of an atomic hydrogen is inversely proportional to the pressure [7], but the concentration is also, by the universal gas law, proportional to the pressure. The net result would be that the pressure does not affect the absolute atomic hydrogen concentration in the bulk gas. This prediction is consistent with the results of Merier's *et al.* measurements [8]. It is generally accepted that in the bulk gas, $[CH_3]$ is driven by the equilibrium of the fast reaction between H and CH_4 (reaction (2)).

$$CH_4 + H = CH_3 + H_2 \tag{2}$$

A change in $[CH_3]$ would then be caused by the change in the relative concentration of CH_4, $[CH_4]/[H_2]$. (see formula (2.1)).

$$[CH_3]/[H] = K ([CH_4]/[H_2]) \tag{2.1}$$

where K is the equilibrium constant of reaction (2) and is only a function of temperature. Near the substrate, even though the equilibrium of reaction (2) breaks down, we can assume that when the temperature remained the same, the change in $[H]/[CH_3]$ ratio would still be caused only by $[CH_4]/[H_2]$, provided the radical-radical type of recombinations shown by reactions (3) and (4) are not important.

$$CH_3 + CH_3 ---> C_2H_6 \tag{3}$$

$$CH_3 + H ---> CH_4 \tag{4}$$
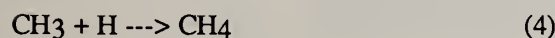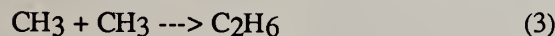
The destruction of CH_3 through reactions (3) and (4) , which have negative active energies, may not be negligible at low substrate temperatures. [9] The rate constants of these two reactions are pressure dependent and larger at higher pressures. According to the RGA measurements shown in Fig. 3, the total increase in the normalized CH_4

intensity, $I(CH_4)/I(H_2)$, was about 25%. The total change in $[H]/[CH_3]$ near the substrate should, therefore, be no more than 25%. Is this change large enough to cause the observed morphology change, or are there other unknown factors that caused the morphology change? The reported morphology studies show that as the substrate temperature is lowered, the α value becomes much more sensitive to the CH_4 percentage in the feed gas. [2, 3] The substrate temperature used here was much lower than any of those already studied. It is not clear though why at lower substrate temperatures, the morphology becomes more sensitive to the gas composition.

It is not known why the particle sizes become less uniform at higher pressures. There may be several factors contributing to the non-uniformity. The bigger particles might nucleate earlier, or the smaller ones might be consumed by the bigger ones during the deposition, or perhaps the surface mobility of growth precursors is limited because of low substrate temperature, or the distribution of active species in the gas phase is not uniform because of low diffusion rates. At this point, it is not clear which one is the dominant factor, or if a combination of factors causes the increasing non-uniformity of size at higher pressures. The very low substrate and gas phase temperatures are, however, the pronounced features of these depositions, and pressure inversely affects the gas phase diffusion coefficient of species, which would aggravate the concentration gradient of active species near the substrate. [9]

4. Conclusions

Diamond has been grown at significantly lower filament and substrate temperatures by adding a small amount of oxygen to the mixture of CH_4 and H_2. The morphology and uniformity of the diamonds grown under these conditions were strongly affected by the deposition pressure. Accompanying the morphology changes with the pressure was a continuous increase in the $[CH_4]/[C_2H_2]$ ratio in the gas phase. It appears that as the substrate temperature is lowered, diamond morphology becomes very sensitive to the CH_4 concentration in the gas phase.

5. Acknowledgments

6. References

1. R. E. Clausing, L. Heatherly, E. D. Specht, and K. L. More, *New Diamond Science and Technology, MRS Int. Conf. Proc.*, ed: R. Messier *et al.*, 575(1991)
2. C. Wild, R. Kohl, N. Herres, W. Müller-Sebert and P. Koidl, *Diamond and Related Materials*, 3, 373(1994)
3. M. A. Tamor and M. P. Everson, *J. Mater. Res.*, 9(7), 1839(1994)
4. Young-Joon Baik and Kwang Yong Eun, *Thin Solid Films*, 212, 156(1992)
5. Z. L. Tolt, L. Heatherly, R. E. Clausing, R. W. Shaw and C. Feigerle*, submitted to the 187th Electro-Chemical Society Meeting, May, 1995, Reno, NV
6. Eiichi Kondoh, Tomohiro Ohta, Tohru Mitomo and Kenichi Ohtsuka, *Diamond and Related Materials,* 3, 270(1994)

7.   Thomas R. Anthony, *Diamond and Diamond-like Films and Coatings*, ed: R. E. Clausing *et al.*, Plenum Press, New York, 1991, pp.555

8.   U. Meier, K. Kohse-Hoinghaus, L. Schäfer, and C. Klages, *Appl. Opt.*, **29**, 4993(1990)

9.   E. J. Corat and D. G. Goodwin, *J. Appl. Phys.* **74**, 2021(1993)
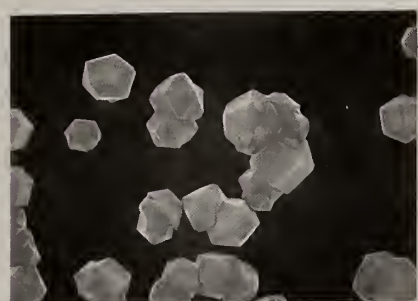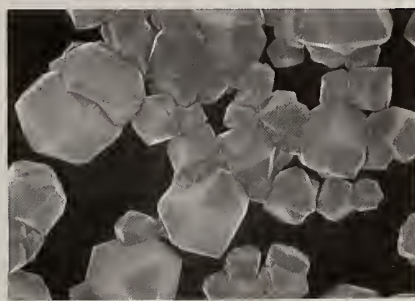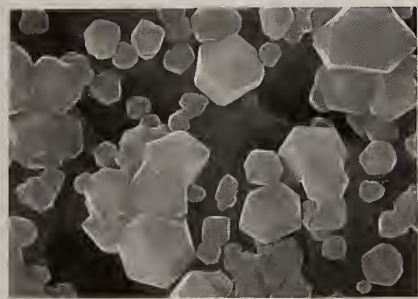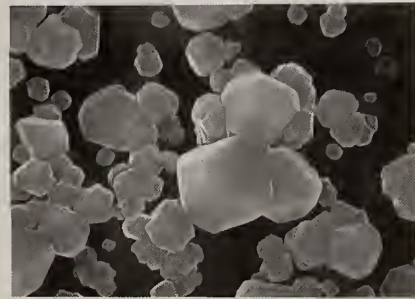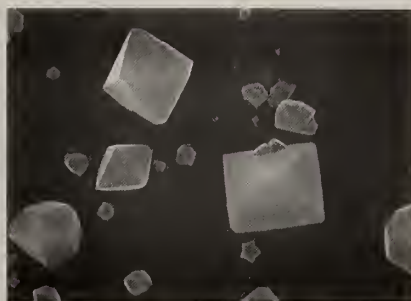
Fig. 1. Scanning electron microscopy images of diamond grown at the conditions: T_f=1700 C, T_S=580 C, 0.5% CH_4, and O/C=13%. a) 12 torr; b) 24 torr; c) 40 torr; d) 65 torr; and e) 90 torr.
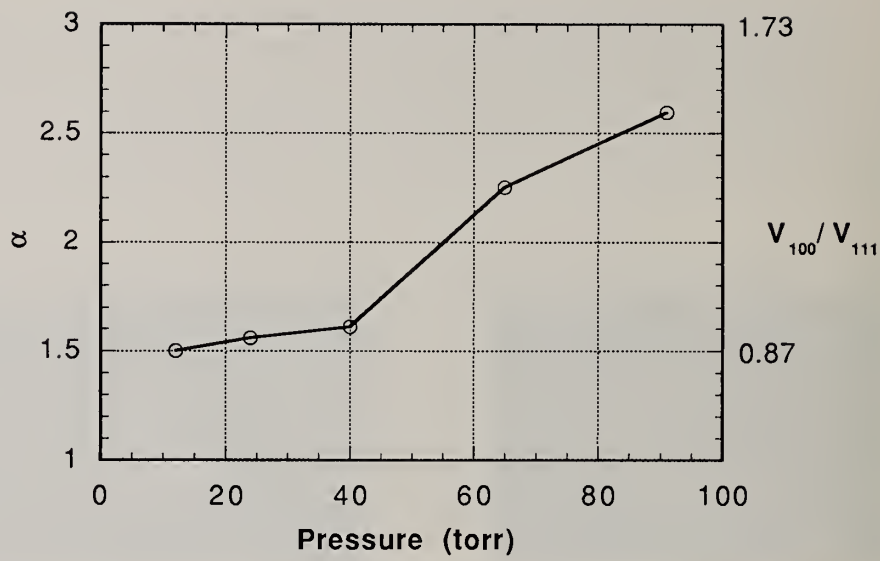
Fig. 2. Change of growth parameter α with the deposition pressure.
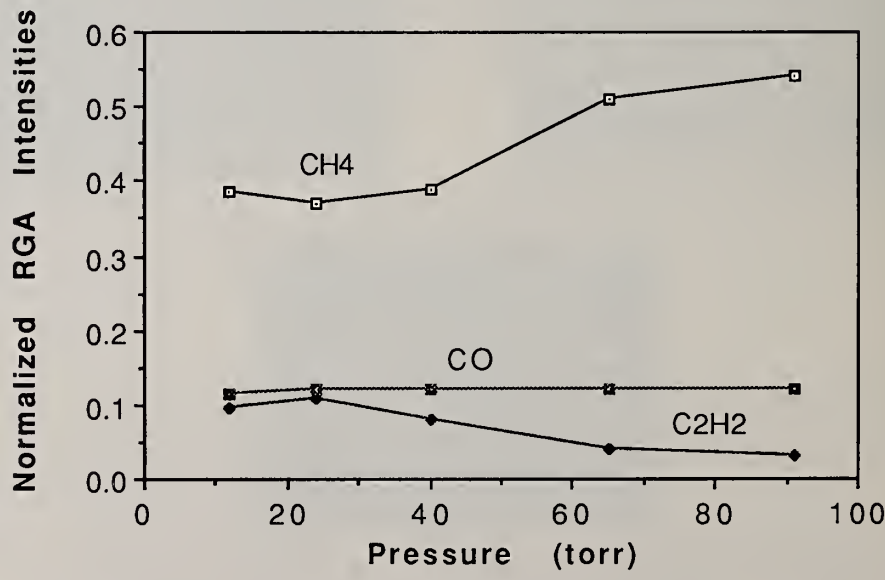
Fig. 3. Normalized RGA intensities of CH_4, C_2H_2 and CO for depositions in Fig. 1.

CORRELATIONS BETWEEN THE DENSITY DISTRIBUTIONS OF C_2, CH AND OH AND THE GROWTH OF DIAMOND IN AN OXY-ACETYLENE FLAME MEASURED BY LIF

R.J.H. Klein-Douwel, J.J.L. Spaanjaars, and J.J. ter Meulen

Dept. of Molecular and Laser Physics, University of Nijmegen, Toernooiveld, 6525 ED Nijmegen, The Netherlands (email: `robertkd@sci.kun.nl`)

Key words: deposition monitoring, deposition optimization, diamond, Laser Induced Fluorescence, oxyacetylene flame

Abstract

Two-dimensional Laser Induced Fluorescence (2D-LIF) measurements are applied to the chemical vapour deposition (CVD) of diamond by an oxyacetylene flame. The fluorescence distributions of C_2, CH and OH are measured for various deposition conditions. The influence of the temperature of the molybdenum substrate and the distance between the substrate and the flame front on the two-dimensional distributions and on the quality and morphology of the deposited diamond is investigated. A clear relation is observed between the C_2 distribution in the flame and the local growth rate and quality of the diamond layer, therefore C_2 is thought to be an important species for diamond growth. Due to lower signal to noise ratios the role of CH as a growth species is less clear. The OH radical is not observed in the boundary layer, so OH seems to be of minor importance. All measurements are performed during diamond deposition.

1 Introduction

In this experiment the 2D-LIF method is applied to the diamond depositing oxyacetylene flame in order to gain insight in the gas phase chemistry and the deposition process. Special attention is given to the boundary layer just above the substrate. Knowledge about the chemistry and dynamics of the dominant precursors is indispensable for the optimization and upscaling of the flame deposition setup. LIF signals of these precursors may also be used to automate the deposition process and allow large scale, stable diamond growth.

2 Experimental

A commercially available welding torch (orifice 1.6 mm ⌀) is used with high purity oxygen and acetylene, see Fig. 1. A molybdenum substrate is positioned at a distance d of typically 1 mm below the tip of the flame front. The substrate is cooled to 1000°C by a pulsed water vaporizer.
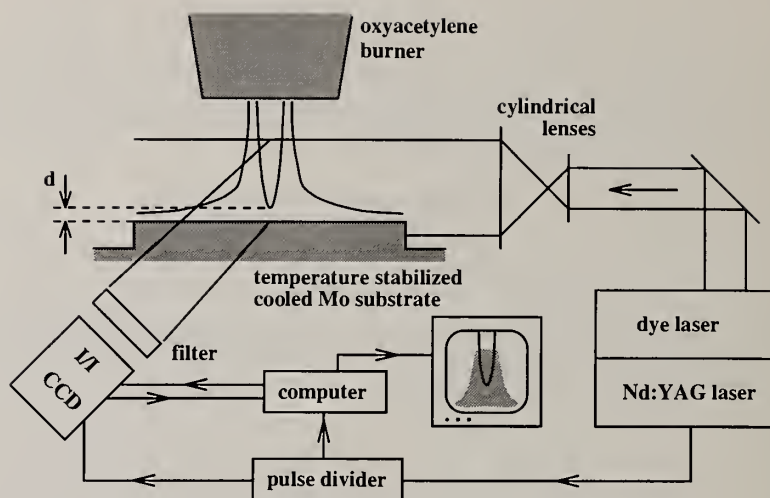
Figure 1: Experimental setup for LIF measurements in the diamond depositing flame

The output of a Nd:YAG pumped dye laser is used to detect several molecular species in the flame. The laser beam is focused in the flame to give a thin laser sheet and the fluorescence is collected using a CCD camera equipped with an image intensifier. The images are further processed with a computer. Emission of the flame itself is suppressed by gating the image intensifier and spectral filtering is applied to minimize scattered laser light and non-resonant fluorescence detection. C_2 is excited at 438 nm and detected at 471 nm (Swan system) and OH is detected at 343 nm after excitation at 308 nm (A-X). CH is excited at 393 nm (B-X) and detected at 431 nm (A-X), where the A state is populated via collisional relaxation from the B state. A spatial resolution of 20 μm is obtained.

The polycrystalline diamond layers are characterized after growth by optical microscopy, Raman spectroscopy and Scanning Electron Microscopy (SEM). A quality factor Q is derived from each Raman spectrum [1] to quantify the quality of the deposited layer.

3 Results

Measurements have been performed at different values for the distance d and the substrate temperature [2]. The C_2 LIF distribution for deposition at d = 0.58 mm is shown in Fig. 2. Maximum signal is found at the flame front, but it can be seen that the entire acetylene feather is filled with C_2. Just above the substrate, in the boundary layer, the C_2 signal has decreased appreciably. The boundary layer, which is important in the deposition process, is typically 100 to 600 μm thick and shows different structures with different deposition distances d. The horizontal distribution of C_2 at the top of the boundary layer is given in Fig. 3.
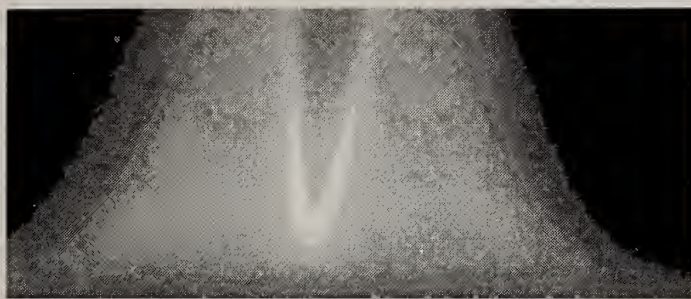
Figure 2: Distribution of C_2 LIF signal during diamond deposition. The substrate is indicated in gray, the burner tip is just outside the image, which is 8 mm wide.

Measurements of CH yield distributions similar to those of C_2, but with a somewhat lower signal to noise ratio. OH is detected only outside the acetylene feather and not in the boundary layer, contradicting optical emission measurements [3].

4 Relation to diamond growth

In Fig. 3 a relation is observed between the Q value at a certain position at the diamond surface and the C_2 density in the boundary layer immediately above it. For d < 1 mm both Q and the C_2 density show a maximum at the centre of the deposited layer and both decrease in moving radially away from the centre. For d > 1 mm, however, Q shows a local minimum at the centre of the deposited layer, similar to the C_2 density distribution.

For two diamond layers the local growth rate variation is determined along the path of the laser beam, see Fig. 4. When compared to the appropriate C_2 profiles in Fig. 3, it is clear that the local growth rate shows a strong relation with the horizontal distribution of C_2 in the boundary layer, except for the small increase near the edge of the diamond layer deposited at d = 0.88 mm.

5 Conclusions

From the observed relation between the C_2 distribution and the local quality and growth rate of a diamond layer, C_2 is expected to play a major role in the diamond deposition process. Indications have also been obtained that CH seems to be important for diamond growth, while OH seems to be of minor importance.

References

[1] J.J. Schermer, J.E.M. Hogenkamp, G.C.J. Otter, G. Janssen, W.J.P. van Enckevort, and L.J. Giling, Diamond Rel. Mat. **2**, 1149-1155 (1993)
[2] R.J.H. Klein-Douwel, J.J.L. Spaanjaars, and J.J. ter Meulen, to appear in J. Appl. Phys. (1995)
[3] K. Okada, S. Komatsu, T. Ishigaki, S. Matsumoto, and Y. Moriyoshi, J. Appl. Phys. **71**, 4920 (1992)
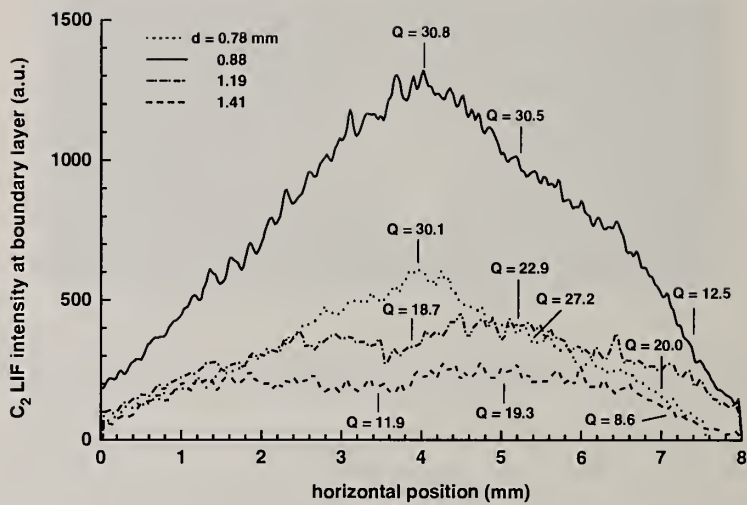
Figure 3: Horizontal intensity profiles of C_2 just above the substrate for different deposition distances d. Q is the quality factor of the diamond deposit at the corresponding position at the substrate.
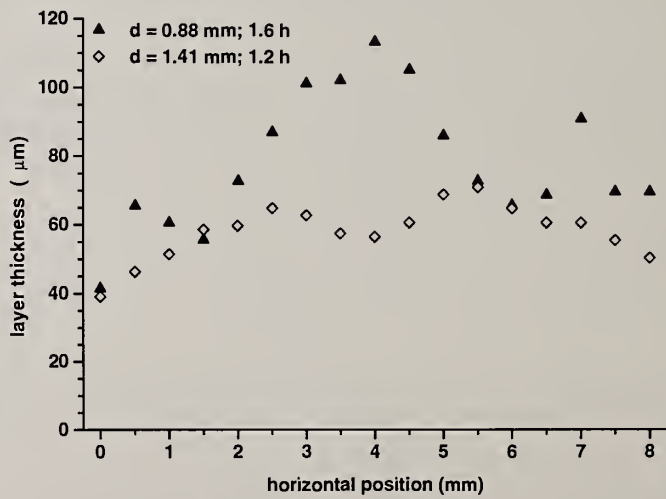
Figure 4: Local growth rate variations along the path of the laser beam for two diamond layers. Deposition times are given also.

EFFECT OF PLASMA FLOW ON DIAMOND GROWTH BY ARC DISCHARGE PLASMA JET CVD

Atsushi Hirata and Masanori Yoshikawa

Tokyo Institute of Technology, 2-12-1, O-okayama, Meguro-ku, Tokyo 152, Japan

Key words: CVD, diamond, flow, growth, plasma jet

Abstract

Effect of plasma flow above a substrate on the growth of diamond has been investigated using a rotating substrate assisted arc discharge plasma jet chemical vapor deposition (CVD). Flow field of a plasma jet has been numerically simulated and variations of velocity above a substrate has been predicted when a substrate is rotated. Morphology and quality of diamonds synthesized under various rotational speeds have been observed using a scanning electron microscope and by Raman spectroscopy, and mass growth rate has been measured.

1. Introduction

Chemical vapor deposited diamond is synthesized on substrates that are mounted in plasma or activated gases. Various diamond CVD techniques such as hot filament CVD, microwave CVD, plasma jet CVD, combustion flame CVD, etc. shows different flow features of plasma or activated gases near substrates according to gas flow rates that are supplied in reactors. Flow field as a function of flow speed and direction is consider to be one of important factor that characterize the growth mode of diamond.

In this paper, effect of plasma flow on the growth of diamond has been investigated by a rotating substrate assisted arc discharge plasma jet CVD apparatus under constant generation conditions of a plasma jet. Moreover, the flow fields of plasma when a rotating substrate is used have been simulated.

2. Experimental set up

A substrate has been rotated up to 2000 rpm to change plasma flow above a substrate surface under the constant generation conditions of the plasma jet . A substrate rotation device was mounted on one-cathode three-anode arc discharge plasma jet CVD apparatus [1]. Magnetic fluid seal assisted bearings have been used for rotating a substrate at high rotational speeds in vacuum with cooling the substrate using water. The axes of substrate rotation and the substrate coincide with the axis of the plasma jet.

Deposition conditions are shown in Table 1. Gas flow rates, electric power, pressure in the reactor and substrate temperature have been set at constant values during deposition of diamond.

Table 1. Deposition conditions

Gas flow rate CH_4	45 cc/min
H_2	1.5 l/min
Ar	4.5 l/min (Cathode) 0.6×3 l/min (Anodes)
Electric power	8.6 kW
Pressure in a reactor	26.7 kPa (200 Torr)
Substrate temperature	970 °C
Substrate Rotation speed	0, 1000, 2000 rpm

3. Numerical simulation of flow field of plasma jet

Flow field of plasma jet when substrate is rotated has been numerically simulated using the software package FLUENT. This calculation is based on steady, axisymmetric, turbulent flow considered with viscosity and compressibility. Local thermodynamic equilibrium is assumed over the entire calculation domain. The renormalization group (RNG) - based κ-ε model [2] has been applied to our turbulence model.

Boundary conditions of temperatures except for the temperature at nozzles have been measured using a thermocouple and the substrate temperature has been set at 1000°C that is a common value for diamond deposition by arc discharge plasma jet CVD. Temperatures of plasma at nozzles have been measured by emission spectrochemical analysis.

Figure 1 shows the prediction of variations of plasma flow at 1.4 mm above a substrate when substrate rotational speeds are 0 rpm and 3000 rpm. At 0 rpm, flow velocity of plasma has radial component only and occurs maximum value of approximately 75 m/s at around the radius distance of 8 mm. When a substrate is rotated at 3000 rpm, circumferential component is added and radial component increases because of viscosity of plasma.

4. Diamond synthesis

Diamond films have been synthesized at the substrate rotational speeds of 0 rpm, 1000 rpm and 2000 rpm. Figure 2 shows SEM photographs of diamond films at the radius distance of 10-15 mm where the increment of the radial component of plasma flow velocity is relatively large. Although grain size increases with increasing of the substrate rotational speed, crystal morphology are unaffected by rotation of a substrate. Raman spectra of diamond films in Fig. 3 show little difference in quality between at 0 rpm and 2000 rpm. Moreover, mass growth rates of diamond films are similar values as shown in Fig. 4. These facts indicate that flow variations of plasma has little effect onthe growth mode of diamond when generation conditions of plasma is fixed.
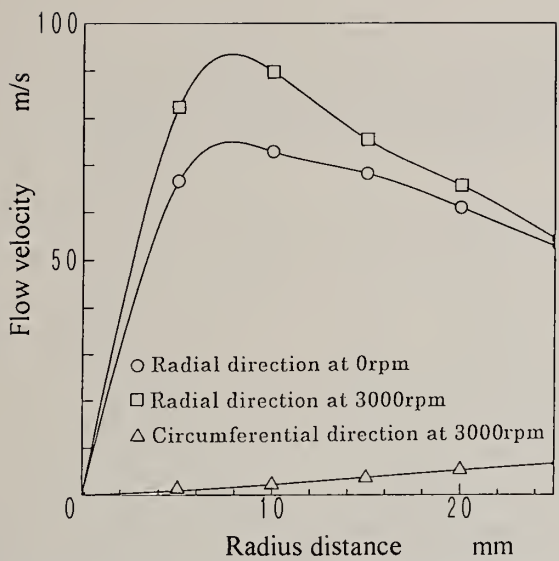
Fig. 1 Variations of flow velocity of plasma at 1.4 mm above a substrate and substrate rotational speeds of 0 and 3000 rpm
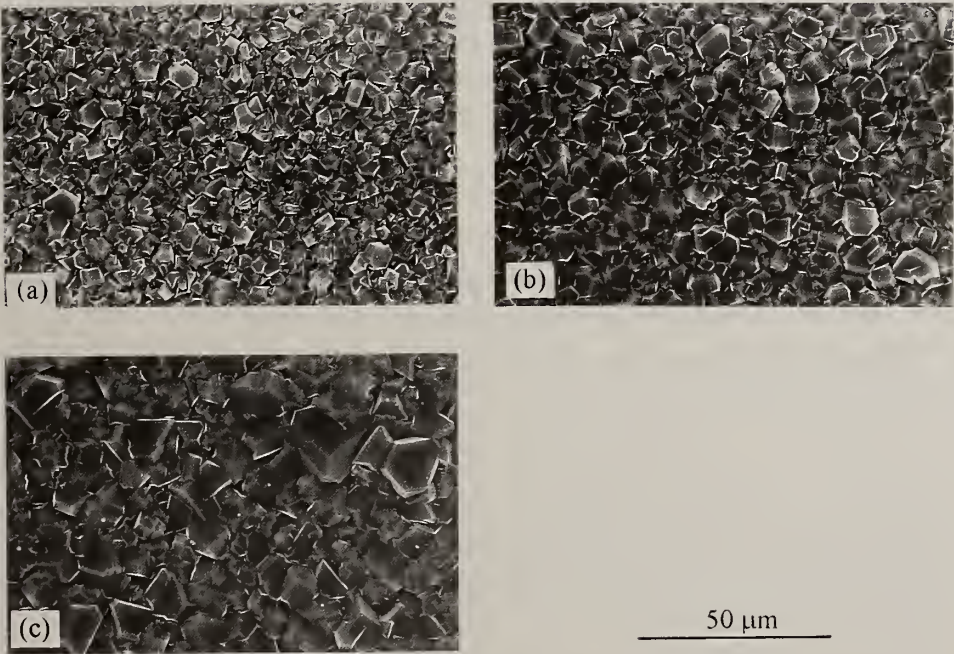
Fig. 2 SEM photographs of diamond films at radius distance of 10-15 mm when rotational speeds are (a) 0, (b) 1000 and (c) 2000 rpm

420
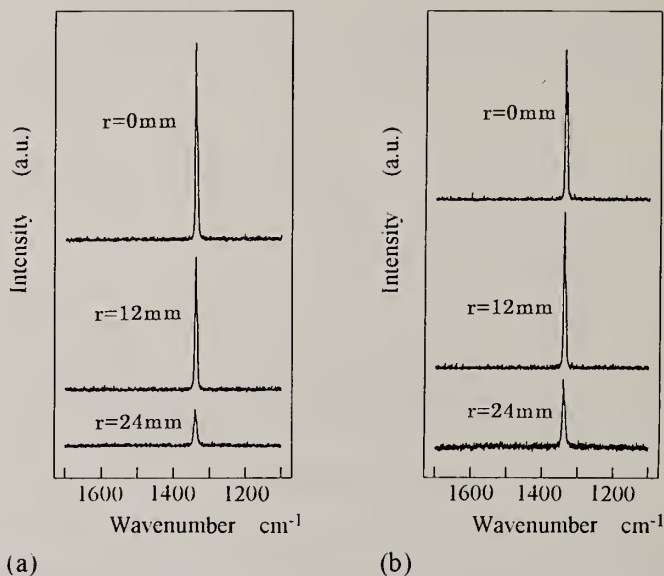
Fig. 3 Raman spectra of diamond films at substrate rotational speeds of (a) 0 and
(b) 2000 rpm. r: radius diatance
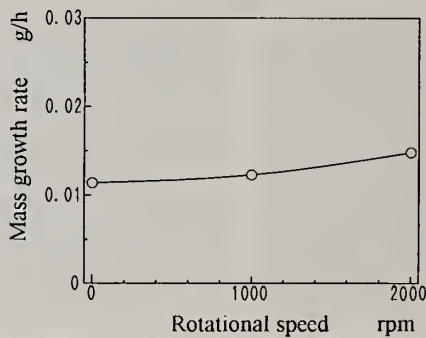
Fig. 4 Relation between mass growth rates of diamond and substrate rotational speeds

5. Conclusions

Diamond films have been synthesized on rotating substrates, and effect of plasma flow
on the growth of diamond has been discussed. Numerical simulation predicts that flow
velocity of plasma increase at higher rotational speeds of a substrate. However,
morphology, quality and mass growth rates of diamond are unaffected by change of the
plasma flow.

References
1. A. Hirata and M. Yoshikawa : Diamond and Related Materials, 2 (1993) 1402.
2. V. Yakhot and S. A. Orszag : J. Scientific Computing, 1 (1986) 3.

EXAMINATION OF DIAMOND GROWTH PRECURSOR DEPENDANCE IN AN ELECTRON CYCLOTRON RESONANCE PLASMA SYSTEM

Donald R. Gilbert and Rajiv Singh

Department of Materials Science and Engineering, University of Florida, Gainesville, Florida 32611

Abstract

We have investigated the deposition of diamond films at relatively low substrate temperatures using an electron cyclotron resonance (ECR) enhanced plasma chemical vapor deposition (CVD) system. Films were separately deposited in a hydrogen ambient from methanol and methane precursor species in the pressure regime of 1.0 Torr. Oxygen was independently added to maintain consistent C/H/O atomic ratios The effect of growth system parameters such as gas composition, temperature, and input microwave power on resultant film morphology was examined using SEM. Structural quality was assessed using X-ray diffraction and Raman spectroscopy. Comparisons were made between growth systems with the same C/H/O atomic ratios for crystalline quality, growth rate, and morphology.

1. Introduction

Chemical vapor deposition (CVD) of diamond thin films at sub-atmospheric pressures has been the subject of a great deal of research in recent years. Diamond deposition has been achieved using many different gas-activating systems, such as hot filament, microwave plasma, oxy-acetylene torch, and DC plasma jet. Although there has been a great deal of success in developing deposition systems, there is still a great deal about low pressure diamond growth that is not thoroughly understood.

Diamond deposition is accomplished almost exclusively using a gas chemistry composed of carbon, hydrogen, and, often, oxygen. The general diamond growth regime has been well established in the C/H/O ternary system [1]. However, the exact roles of the various species in the deposition process are still widely debated. Various hydrocarbon species have been speculated to play primary roles in growth on different crystal planes [2-6]. Hydrogen is speculated to play a number of key roles for diamond growth,

including preferential etching of non-diamond carbon and stabilization of the growing diamond surface. The role of oxygen is more complex [7-12]. Oxygen reacts with gas-phase hydrocarbons to form CO, effectively reducing the concentration of hydrocarbons in the deposition process by forming an extremely stable gaseous compound. As with hydrogen, atomic oxygen (and OH) reacts with the deposited material to etch the non-diamond phases preferentially. It has been reported that oxygen addition to diamond CVD systems results in higher growth rates and better structural quality of deposited films, and also facilitates deposition at lower substrate temperatures. The use of methanol (CH_3OH) as the carbon source for deposition provides several attractive benefits. The inherent C/O ratio is 1:1, placing it within the established "Bachmann triangle" of diamond growth [1]. Because it is a liquid at room temperature, it is easy to handle and can be obtained in very high purity.

2. Experiment

We conducted our experiments in a Plasma-Therm BECR-6 electron cyclotron resonance plasma system, which is shown schematically in Fig. 1. This system uses a series of permanent rare-earth magnets to produce the necessary magnetic field of 875 Gauss in the plasma generation zone that matches the cyclotron-frequency of the free electrons to the 2.45 GHz microwaves. Samples were mounted on a variable-position stage with independent heating capabilities. Substrates consisted of single-crystal silicon thinly seeded with sub-micron diamond particles. Diamond films were deposited for 5 hours at a substrate temperature of approximately 700 °C. Gas mixtures of 1% methanol (CH_3OH) or 1% methane (CH_4) by volume in hydrogen were used, maintaining identical C/H/O ratios for both systems by independent addition of oxygen. The total pressure used for deposition was 1.00 Torr. An input microwave power of either 1000 or 1400 watts was used.
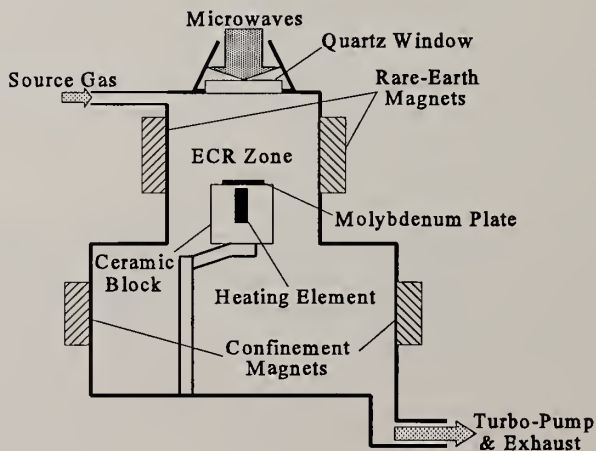
Fig. 1 ECR-CVD system

3. Results

SEM was used to examine morphological variation in films deposited under different conditions. Fig. 2 (a) and (b) shows micrographs of two films deposited at 1.00 Torr and 1400 watts input microwave power from methanol and methane/oxygen, respectively. The methanol-deposited film is continuous and shows regular faceting. The film deposited from the methane/oxygen mixture is not continuous and shows irregular faceting. When deposition was attempted from methane using a C/O ratio of approximately 1.67, a continuous film was formed showing regular faceting similar to the methanol film shown.

(a)   (b)
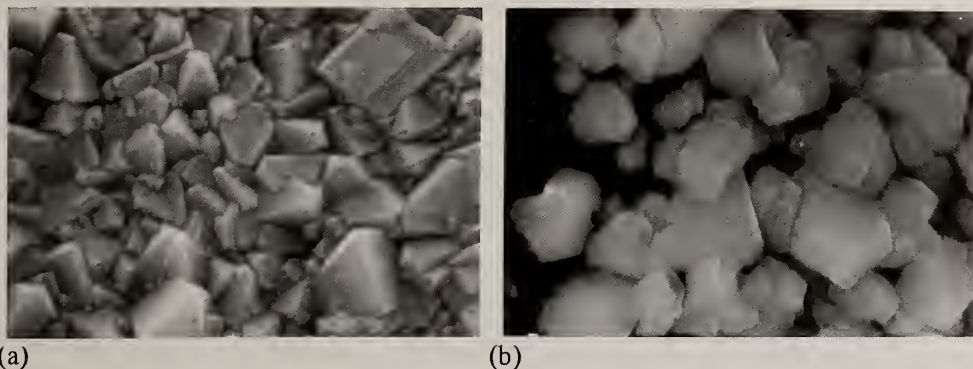
Fig. 2   Films deposited at 700 °C and 1.00 Torr from (a) methanol and (b) methane/oxygen.

Structural evaluation was made using both Raman spectroscopy and XRD. In Fig. 3, a raman spectrum is shown for a film grown from methanol at 1.00 Torr and 1000 watts input microwave power. The characteristic diamond peak is seen near 1333 cm^{-1} with a broad non-diamond (possibly DLC) peak near 1430 cm^{-1}. Although the diamond signal appears weak, the film is very thin, which complicates analysis due to the small sampling volume and the greater scattering efficiency of non-diamond carbon. X-ray spectra for the three films discussed all show the diamond (111) peak at 43.9°.
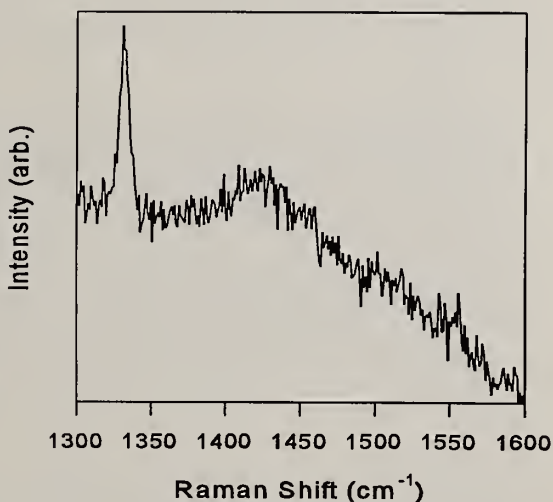
Fig. 3 Raman spectrum of film deposited from methanol.

4. Conclusions

We have shown consistent successful deposition of diamond films in an ECR system from a variety of source gas mixtures. Despite having equivalent C/H/O ratios, films deposited from methanol show very different growth characteristics from films grown from methane/oxygen. Growth in the methane/oxygen system appeared inhibited, probably due to excess oxygen etching. The non-continuous nature of the film made structural characterization difficult, but we speculate that the methane/oxygen deposition contains a smaller percentage of non-diamond carbon than the corresponding methanol-deposited film. This suggests that the source of oxygen in the growth system is an important consideration apart from the C/O atomic ratio.

5. References

1.   P. Bachmann, D. Leers, and H. Lydtin, Diamond and Related Materials **1**, 1 (1991).
2.   C. Wu, M. Tamaor, T. Potter, and E. Kaiser, Materials Research Society Proc. **162**, 133 (1990)
3.   C. Chu, M. D'Evelyn, T. Hauge, and J. Margrave, J. Mater. Res. **5**, 2405 (1990)
4.   M. Frenklach and K. Spear, J. Mater. Res. **3**, 133 (1988)
5.   S. Mehandru and A. Anderson, J. Mater. Res. **5**, 2286 (1990)
6.   S. Harris and L. Martin, J. Mater. Res. **5**, 2313 (1990)
7.   M. Nunotani, M. Komori, M. Yamasawa, Y. Fujiwara, K. Sakuta, T. Kobayashi, S. Nakashima, S. Minomo, M. Taniguchi, and M.Sugiyo, Jpn. J. Appl. Phys. **30**, L1199 (1991)
8.   J. Chang, T. Mantei, R. Vuppuladhadium, and H. Jackson, J. Appl. Phys. **71**, 2918 (1992)
9.   S. Harris and A. Weiner, *Diamond, Silicon Carbide and Related Wide Bandgap Semiconductors*, J. Glass, R. Messier, and N. Fujimori (eds.), MRS Symposia Proceedings **162**, Materials Research Society, Pittsburgh, PA, 103 (1990)
10. Y. Liou, A. Inspektor, R. Weimer, D. Knight, and R. Messier, J. Mater. Res. **50**, 2305 (1990)
11. O. Sanchez, C. Gomez-Aleixandre, F. Agullo, and J. Albella, Diamond and Related Materials **3**, 1183 (1994)
12. W. Weimer, F. Cerio, and C. Johnson, J. Mater. Res **6**, 2134 (1991)

Applications of Diamond Films and Related Materials: Third International Conference, 1995
Editors: A. Feldman, Y. Tzeng, W. A. Yarbrough, M. Yoshikawa, and M. Murakawa

425

MORPHOLOGY EVOLUTION OF DIAMONDS IN COMBUSTION SYNTHESIS

Bi Zhang and Sihua Chen

Department of Mechanical Engineering, Precision Manufacturing Center
University of Connecticut, Storrs, CT 06269, USA

Key words: combustion flame, CVD diamond, morphology, nucleation mechanisms

Abstract

This research investigates morphology evolution of diamonds in combustion synthesis to understand the nucleation mechanisms of diamond phase. Diamond films of various morphologies are deposited on molybdenum substrates in different experimental conditions. These diamond films are studied using scanning electron microscopy, and characterized by μ-Raman spectroscopy at different height levels of a film cross-section. The results show that oxygen affects morphology of the diamond films.

INTRODUCTION

In diamond synthesis from a combustion flame, a mixture of acetylene and oxygen is introduced into a combustion torch and burned in air. Different types of flame can be formed depending on oxygen to acetylene ratio. Diamond can be synthesized when the ratio is slightly less than unity, at which a 'reducing flame' is formed. This flame has three zones: an inner cone, an acetylene feather, and an outer luminous layer. Diamond growth takes place in the acetylene feather. Nucleation mechanisms of diamond phase are not well understood, making the application of this technology very limited. This research investigates morphology evolution of diamond crystals in synthesizing diamond films to understand the nucleation mechanisms of diamond phase.

EXPERIMENTAL SETUP

Connecticut Airgas research grade oxygen with purity level of 99.995% and acetylene with purity level of 99.5% were used as starting materials. Two regulators were used to control the line pressures of the oxygen to 1.4-1.75 kg/cm^2 (20-25 psi) and the acetylene to 0.7 kg/cm^2 (10 psi). The acetylene and oxygen gas flows were then controlled by two flow meters and introduced to a W-300 welding torch that was mounted on a vertically movable stage positioning the torch relative to a substrate surface. A molybdenum disc was polished with diamond pastes and used as substrate. The substrate was mounted on a water-cooled copper block. The substrate temperature was regulated by controlling the flow rate of cooling water and measured by a pyrometer with a repeatability of 2.5 °C. The experiments were conducted at a temperature of 700-1,200 °C; gas flow rates of 1.21-4.07 l/min for oxygen, 1.52-4.03 l/min for acetylene; and a distance of inner cone from substrate of h=1-4 mm.

Scanning electron microscopy and μ-Raman spectroscopy were used to study the morphology evolution of diamonds, and to characterize diamond films. When focused at different height levels of the cross-sections of a diamond film, different morphologies of diamond crystals were observed by SEM, and different spectra by μ-Raman spectroscopy.

RESULTS AND DISCUSSION

Figure 1 is an SEM micrograph showing morphology revolution of a diamond film deposited at an oxygen flow rate of 2.06 l/min, acetylene flow rate of 1.69 l/min, inner cone distance of 1 mm, substrate temperature of 900 °C, deposition time of 0.5 hours. It was observed that a layer of ball-like morphology was in the bottom of the film. These balls were then coated with a layer of deposits of a cauliflower-like and further an octahedral morphologies.
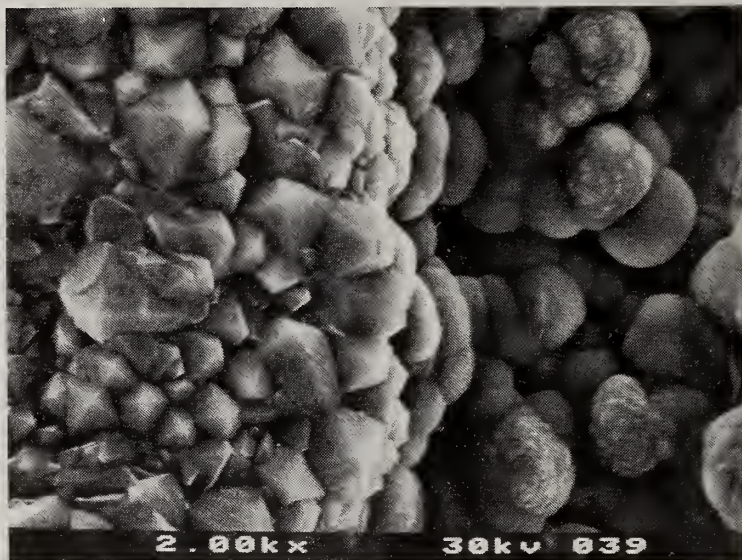
Figure 1   SEM micrograph showing morphology evolution of a diamond film

Ball-like   Cauliflower-like   Octahedral

Figure 2   Evolution of morphological structures in diamond deposition

The deposits of ball-like morphology could be a mixture of graphite and diamond crystallites which formed a rough surface on the ball-like deposits as shown in the SEM micrograph. The diamond crystallites in the ball-like layer grew up to form a cauliflower-like, then octahedral and eventually cubic morphologies. The growth sequence of the diamond film is schematically shown in Figure 2.

The growth of diamond phase from ball-like to cauliflower-like, octahedral and cubic morphologies could be a result of carbon deposition and etching. It has been known that atomic oxygen and hydrogen etch both graphite and diamond at different rates. In a temperature range for diamond to grow, experiments demonstrated that atomic hydrogen etched graphite more rapidly than diamond.

The diamond growth is accomplished when the growth rate is higher than the etching rate, conversely, the graphite etching rate is higher than the growth rate as shown in

Figure 3. An explanation for the difference in growth rates between diamond and graphite may be based on the energy difference in diamond and graphite bondings. For the diamond structure, there are five carbon atoms combined by four single bonds. The single bond energy is 342 kJ/mol [1] which is approximately 5.68×10^{-22} kJ/bond, so the total energy needed to break these bonds is 2.27×10^{-21} kJ/atom. To relieve a carbon atom from graphite, it is necessary to break one double bond (613 kJ/mol) [1] and two single bonds (342 kJ/mol), the total energy is 2.15×10^{-21} kJ/atom. Compared with diamond, less energy is needed to relieve a carbon atom from graphite. With the same amount of energy provided by the formation of a C-etching atom bond, graphite would be more easily etched than diamond.

Diamond　　　　Graphite　　Carbon etching

Carbon deposition
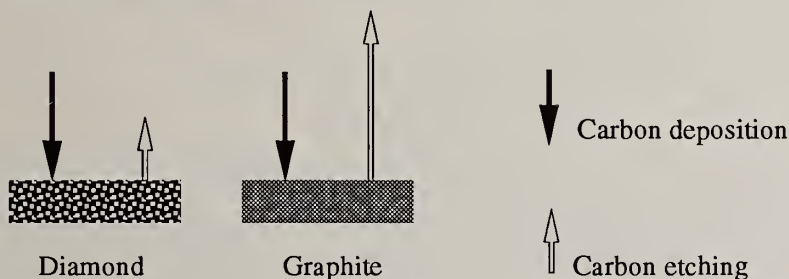
Figure 3　Relative etching rates of diamond and graphite by atomic hydrogen [2]

The μ-Raman spectroscopic studies of diamond films released a similar result. Figure 4 shows Raman spectra of a film deposited at an oxygen flow rate of 3.16 l/min, acetylene flow rate of 3.05 l/min, inner cone distance of 1 mm, substrate temperature of 880 °C, deposition time of 1 hour. The diamond films was measured at different height levels of the cross-sections with the level 1 obtained on the top, and the level 5 in the bottom of a film, while the levels 2-4 were intermediates. Diamond peaks corresponding to 1,333cm^{-1} appeared at all the levels but with different intensities. The level 2 had a strong 1,140cm^{-1} peak which became relatively weak at the level 3, and disappeared at the level 4. Instead, a peak of 1,430 cm^{-1} appeared at the levels 4 and 5. It is believed that the peak of 1,140 cm^{-1} results from nanocrystalline diamonds [3]. However the peak around 1,430 cm^{-1} remains unknown. Yarbrough and Messier [4] described that graphite has two Raman peaks of 1,355 cm^{-1} for disordered graphite and of 1600 cm^{-1} for sp^2 hybridization graphite. The disordered graphite contained both sp^3 and sp^2 hybridization carbon phases. The breadth, position and relative intensity of these peaks can vary significantly. From this statement, it may be assumed that 1,430 cm^{-1} peak represents a form of graphite between disordered and sp^2 structures.

These Raman spectra revealed that diamond growth started from certain form of graphite with a Raman peak at 1,430 cm^{-1}, then followed by the nanocrystalline diamond with a peak at 1,140 cm^{-1}, and finally, the crystalline diamond with a peak at 1,333 cm^{-1}.

CONCLUSIONS

In the combustion synthesis of diamond films, the nucleation of diamond phase started from the ball-like structure that was a mixture of graphite and diamond crystallites. The diamond crystallites grew up to form cauliflower-like, then octahedral, and eventually cubic structures. The growth of diamonds in different structures was a result of carbon deposition and etching. Atomic hydrogen was effective in etching non-sp^3-bonded

428

carbon at a higher rate than etching sp^3-bonded carbon which suppressed the growth of graphite, controlled the growth rate of diamond, and thus affected diamond morphology.
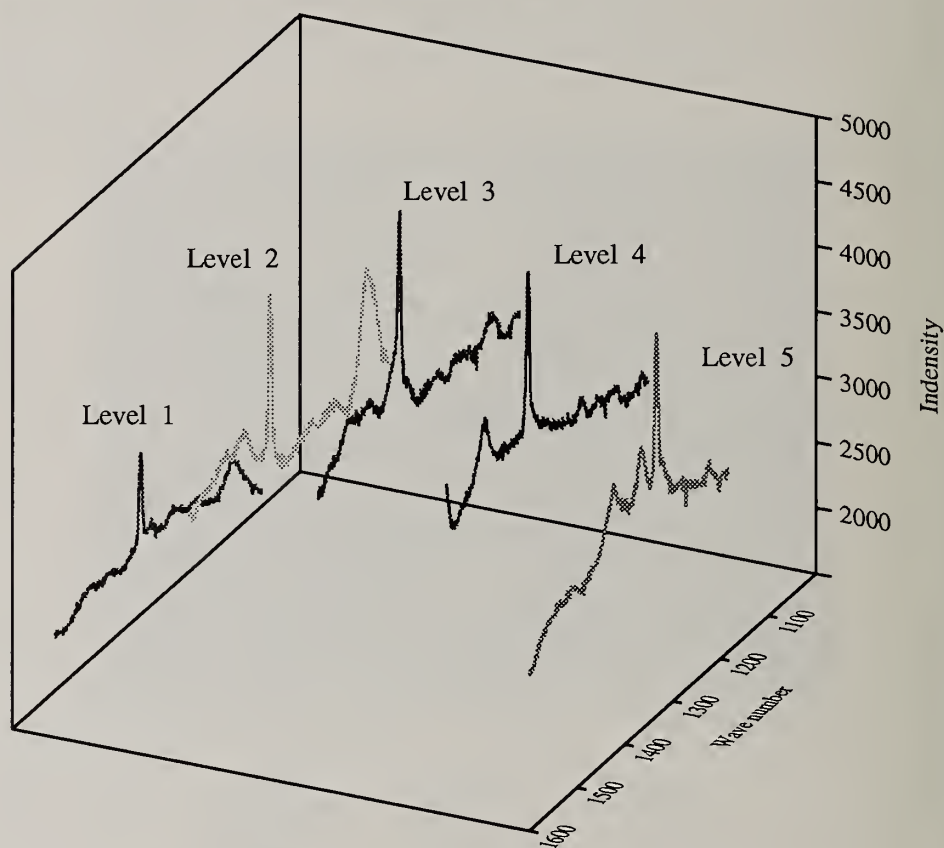
Figure 4 Raman spectra of a diamond film at different height levels

REFERENCES

1. Berry, R. S. *et al.*, Physical Chemistry, Wiley, New York, (1988).
2. Anthony, T. R., MRS Proceedings: Diamond, Silicon Carbide and Related Wide Bandgap Semiconductors, **162** (1990) 61.
3. Nemanich, R. J. *et al.*, J. of Vac. Sci. & Technol., A6(3), (1988) 1783.
4. Yarbrough, W. and Messier, R., Science, **247** (1990) 688.

EVIDENCE FOR SLIP AND DOUBLE SPIRAL GROWTH MECHANISM IN COMBUSTION FLAME SYNTHESIZED DIAMOND

K.A. Cherian*, J. Litster, V. Rudolph and E.T. White

Department of Chemical Engineering, University of Queensland
St. Lucia, Brisbane 4072, Queensland, Australia
*Present Address: Materials Research Laboratory, The Pennsylvania State University, University Park, PA 16802, USA

Key words: diamond growth mechanism, slip, double spiral growth

Abstract

Diamonds have been synthesized by a combustion flame route using $C_2H_2+O_2$. Crystals formed under various conditions were studied in detail for better understanding of the growth mechanisms involved. New evidence has been obtained which show clearly a double spiral crystal growth mechanism operating on some (111) faces of diamond crystals of cubo-octahedral habit. SEM observations suggest that initially formation of a step in a <110> direction pinned at two sites, possibly as a result of high temperature slip, occurs on the (111) face; these two sites become in effect screw dislocation outcrops of opposite sign enabling a double spiral growth mechanism to become operative.

1. Introduction

In spite of the extensive investigations on CVD diamonds, several aspects still await full understanding. For example, the growth mechanisms involved and dependence of crystal morphology on the growth conditions are yet to be understood in full. Both chemical and physical mechanisms of growth determine the final quality of the deposit.

In the case of combustion flame diamonds, not only emission spectra analysis of the combustion flame during synthesis but surface micromorphological studies of the synthesized crystals have also been carried out to understand the growth mechanisms involved [1-4]. While these have provided quite significant insights, the picture is not complete yet. Spiral growth steps together with etch pits on (100) faces have been observed [3], and also two-dimensional step growth mechanism on (110) and (111) faces [4]. This paper reports evidence for a new double spiral growth mechanism operating on (111) faces of cubo-octahedral diamond crystals formed in a combustion flame.

2. Experimental

Diamond deposits were obtained using an oxy-acetylene welding torch with nozzle diameter 1 mm. and using commercial grade acetylene and oxygen gases. Molybdenum

plates 10mmX10mmX0.5mm on a water cooled copper block were used as substrates, on which the torch operating in a fuel rich mode impinged. The flow rates were varied and deposits obtained for various substrate temperatures. The diamond micro crystals thus obtained were subjected to detailed morphological and surface microtopographical examination for evidence of growth mechanisms involved.

3. Observations and results

When nucleation density is low, the individual crystal morphologies become clearly discernible. Cubo-octahedral crystals formed with O_2/C_2H_2 ratio R=0.9 and a combined gas flow rate F=2.1 litres/min., with substrate temperature T at the centre region around 850C; these appeared to have features similar to those already reported. On increasing F, with the value of R kept within the range for diamond synthesis, suitable adjustments of the torch tip to substrate distance had to be made to accommodate the change in length of the inner flame cone. T was also controlled to remain in the 850-900C range. Diamond crystals formed under for a value of F=6.3 with R within the range for diamond synthesis began to show the development of new surface micromorpholoical features; Figs 1-4 reveal these clearly. Initially, a long step or ledge-like feature begins to appear faintly on a (111) face, along a <110> direction, as may be noted in Fig 1. This does not run across the whole face, but appear to be pinned at two points on the (111) face, with the magnitude of the step height apparently larger near the middle, as becomes clear in Fig. 2. This feature seems to have the characterestics of slip, probably due to non-uniform local stresses built up in the growing crystal, with maximum intensity near the central region. With some crystals, the magnitude of the step height appears to be larger; in addition, the points of termination of the step appear as screw dislocations of opposite sign, and lead to a double spiral growth mechanism becoming operative. Figs 2-4 show different stages of development of the double spiral growth mechanism on different combustion flame synthesized diamond crystals. It is known that CVD diamond deposits have a great deal of stress incorporated during growth. The fact that the new observations of step & double spiral growth mechanism were observed for higher growth rates and larger crystal sizes, suggest that what is observed is indeed the result of high temperature activated slip resulting from the stresses accumulated within the growing crystal. Micro Raman studies have provided support for this view, details of which will be published seperately.

4. Acknowledgements

5. References

1.   Y. Matsui, H. Yabe and Y. Hirose, Jap.J. Appl. Phy. 29, 1552 (1990)
2.   T. Abe, M. Suemitsu and N. Miyamoto, J. Cryst. Growth 143, 206 (1994)
3.   K. Okada, S. Komatsu, S. Matsumoto and Y. Moriyoshi, J. Cryst. Growth 108, 416 (1991)
4.   W. Zhu, J. Ahn, H.S. Tan and B.H. Tan, J. Cryst. Growth 125, 649 (1992)
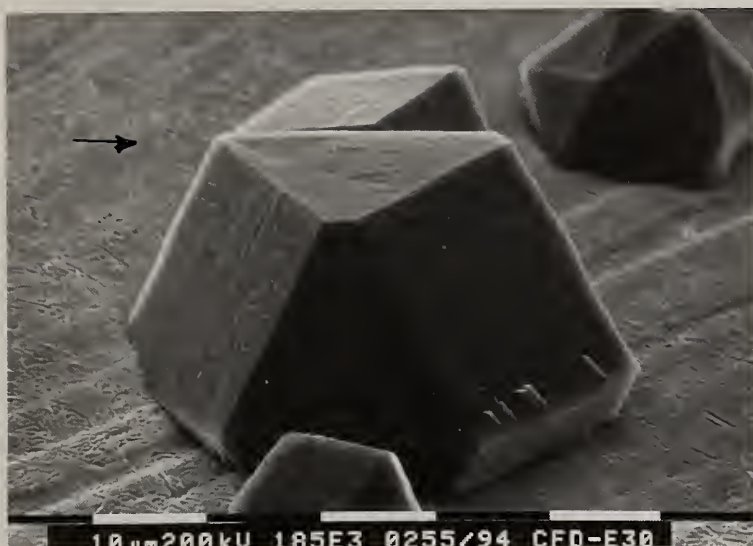
Fig 1.
The faint appearance of a ledge along a <110> direction on the (111) face of a cubo-octahedron.

Fig 2.
The ledge formation is evident, and the magnitude of the step height is apparently larger near the middle.

432
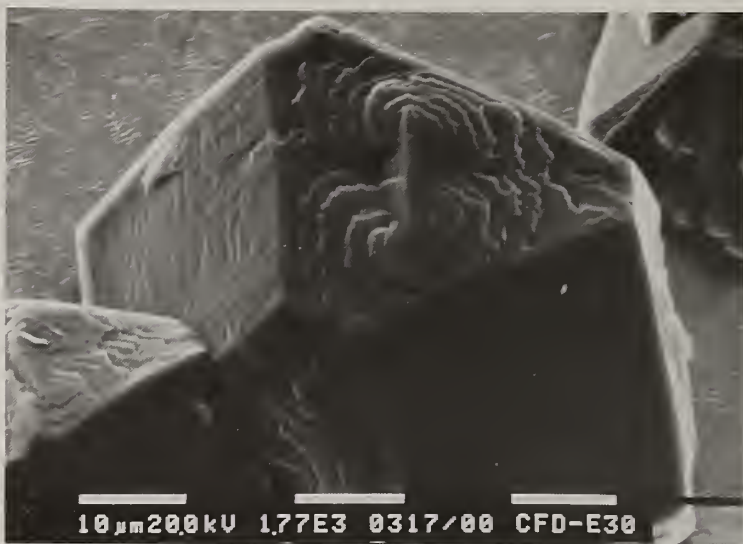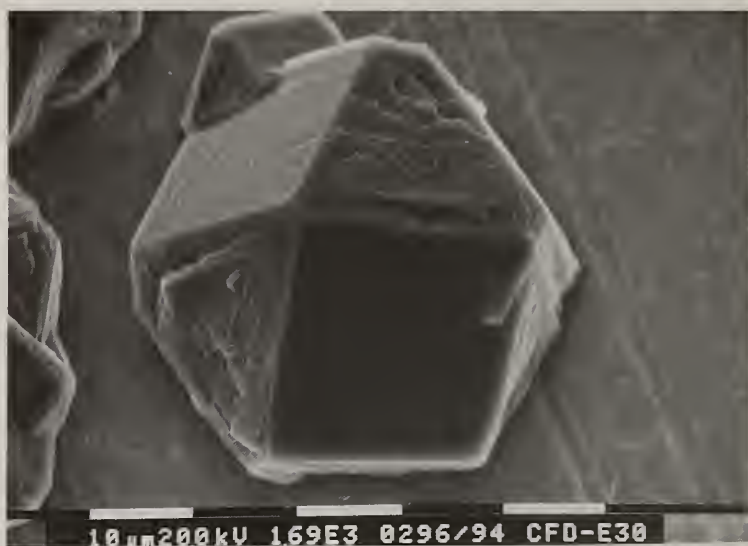
Figs. 3&4.
Different stages of development of the double spiral growth mechanism on different crystals

Applications of Diamond Films and Related Materials: Third International Conference, 1995
Editors: A. Feldman, Y. Tzeng, W. A. Yarbrough, M. Yoshikawa, and M. Murakawa

433

GAS PHASE DIAGNOSTICS FOR CVD DIAMOND GROWTH

L.L. Jones[1], R.W. Shaw[2], C.S.Feigerle[1]

[1]University of Tennessee, Department of Chemistry, Knoxville, TN 37996-1600.
[2]Oak Ridge National Laboratory, Chemical and Analytical Sciences Division, Oak Ridge, TN 37831-6142.

Key words: acetylene, atomic hydrogen, electron impact, methyl radical, REMPI

Abstract

Diamond films have been grown with various morphologies in a hot filament chemical vapor deposition (HFCVD) reactor equipped to monitor the gas phase chemistry. The reactor provided for orifice sampling of gases in the immediate vicinity of the diamond growth surface for introduction into a time-of-flight mass spectrometer. Electron impact ionization was utilized to investigate stable species present during growth. Resonance enhanced multiphoton ionization (REMPI) was employed for the detection of radicals including atomic hydrogen and methyl radical. Measurements have been made of the filament and substrate temperature dependence of the H, CH_3, CH_4, and C_2H_2 relative concentrations.

1. Introduction

The growth rate and quality of diamond films depend directly on the identity and concentration of the species generated in CVD chambers. Most early studies of diamond film growth focused on testing various deposition techniques and characterizing the films produced. A number of chemical mechanisms have been postulated describing CVD of diamond. These mechanisms are under debate and have become an area of increasing research.

Recent studies have started to provide more concrete information necessary for an understanding of the growth process. Methyl radical has been determined to be the dominant growth species under "typical growth conditions" [1-3] . Under other conditions acetylene generates diamond [2] . Mechanisms have been proposed by which both acetylene and methyl radical provide carbon for incorporation into the diamond lattice[4-7] . The atomic hydrogen concentration is also believed to play an important role in diamond deposition. It is required to etch graphite, stabilize the sp3 bonded diamond surface, create radical surface sites and initiate gas phase chemistry.

Hsu introduced the application of molecular beam mass spectrometry to CVD studies, an important breakthrough for measurement of the gaseous composition of the vapor environment in thermal and plasma induced diamond CVD. Hsu provided a detailed explanation of the effects of gas expansion on the observed signals and how to correct for such effects as mass discrimination and scaling due to temperature and pressure [8].

This study employed mass spectrometry techniques similar to Hsu. However, REMPI was used here to measure radical species, as opposed to low energy electron impact ionization. The results show that methane and acetylene concentrations in the near surface gases are dependent on filament temperature and less dependent on substrate temperature. The atomic hydrogen concentration increases dramatically with filament temperature.

2. Experimental

Experiments were performed in a HFCVD reactor designed for gas phase diagnostics. The experimental apparatus is shown schematically in Fig 1. The filament consisted of ~15 cm of 0.5 mm diameter rhenium wire coiled 7 to 9 turns of 3.0 mm diameter. The filament brightness temperature was measured through a side arm glass viewport and the quartz tube using a single color optical pyrometer. The filament was typically 5 to 10 mm from the substrate. The Si wafer substrates were abraded with 6 μm diamond paste on one-half of the top surface. A molybdenum substrate heater/nozzle provided for independent substrate temperature control as well as a uniform lateral temperature. An indication of substrate temperature was obtained from a type S thermocouple located in a well in the heater below the substrate. The sampling orifice was a 200 μm diameter electron microscopy aperture press fitted into the heater. It was elevated slightly to create a post to hold the substrate. The aperture can be replaced easily to change the size in 50 μm increments. The top surface of the substrate and the aperture are flush. Approximately 30% of the inlet gas flows through the hot orifice for the 200 μm aperture under typical growth conditions.

Constant mass flows of CH_4, H_2, and a noble gas mixture of He, Ne, and Ar in H_2 were metered into the chamber with an overall flow rate of 100 sccm. The noble gases were present to provide an internal standard by which systematic effects were eliminated from the results. They were also useful for calibration of the time of flight mass axis for electron impact ionization. The pressure was typically 6 to 10 kPa in the growth portion of the chamber, 0.1 Pa in the expansion region, and 10^{-4} Pa in the mass spectrometer. Diamond deposition was verified using scanning electron microscopy (SEM) and Raman spectroscopy.

The UV beam used for the REMPI measurements of atomic hydrogen and methyl radical was produced by frequency doubling the output of a Nd:YAG pumped pulsed dye laser (Quanta Ray DCR2A/PDL-1) using a β-BaB₂O₄ (BBO) crystal. LD 490 was used to generate 1.5 mJ pulses at
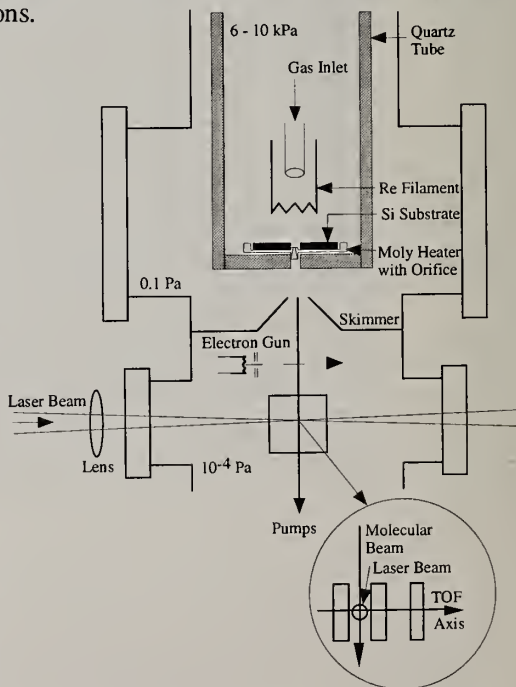
Fig. 1. Schematic of experimental setup. Inset shows the laser beam focused between the time of flight acceleration plates.

243.07 nm, the (2+1) REMPI line for atomic hydrogen. For the (2+1) REMPI line of CH_3 at 333.5 nm, DCM spiked with LDS 698 produced a pulse energy of 2.5 mJ. The beam was focused between the acceleration plates of the mass spectrometer using a 200 mm focal length lens. The time of flight mass spectrometer was commercially available from The R.M. Jordan Co. with a 1 m flight tube and a microchannel plate detector. The signal was amplified and sent to an oscilloscope for digitization. A computer was utilized for further processing.

3. Results and Discussion

Electron impact ionization results for CH_4 and C_2H_2 near the diamond growth surface are shown in Fig 2. The initial feed gas composition was 0.5% CH_4 and 1% each of He, Ne, and Ar in H_2. Data was acquired for m/z=15 and m/z=16 to verify that the signal at mass 16 was methane, and not oxygen. Measurements shown wereperformed with a 1053K indicated substrate temperature, T_s. The actual substrate temperature is estimated to be near 1300K but cannot be directly measured due to restrictions in the setup. Intensities are referred to as "normalized" because the actual signal intensity of the methane and acetylene peaks were divided by the intensity of the neon signal at m/z=22 to correct for mass discrimination and temperature effects. The midpoint temperature for methane concentration reduction and the onset of acetylene production was observed at a filament temperature, T_f, of 1970 K. Only minor differences were obtained when the substrate temperature was allowed to vary with changing filament temperature. Corat and Goodwin reported a similar finding at 2100 K when sampling stable gases near the substrate through a capillary probe [9] . The difference in the emissivity of rhenium and carbon coated tungsten filaments accounts for the deviation in the midpoint temperatures. The relative acetylene concentration was independent of substrate temperature when T_f=2300K. Films were deposited for 18 hours at A, B, and C temperatures (marked on Fig 2) with an indicated substrate temperature of 1053K. SEM and Raman verified diamond growth for $T_f \geq$ 1900K. Growth rates were small for low filament temperatures.
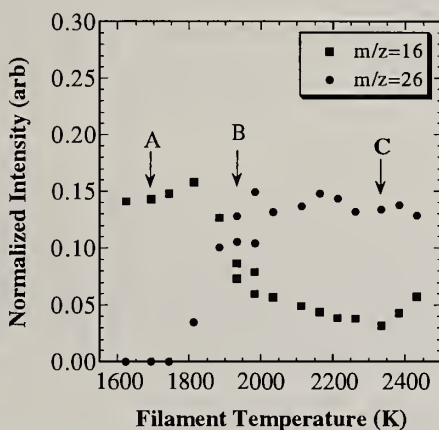
Fig. 2. Electron impact ionization of methane and acetylene verses filament temperature with T_s=1053K. Films were grown at A,B, and C.
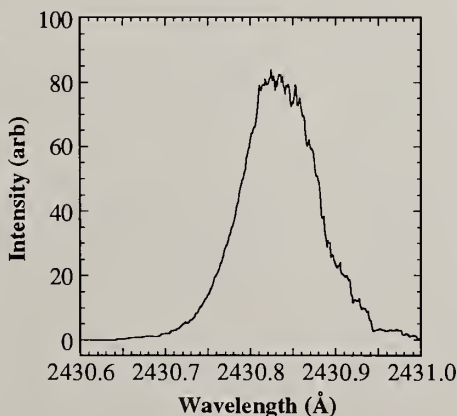
Fig. 3. Wavelength dependence of the (2+1) REMPI signal of atomic hydrogen.

A scan of the atomic hydrogen REMPI signal verses wavelength is presented in Fig 3. The peak results from the $2^2S_{1/2} \leftarrow 1^2S_{1/2}$ transition [10] . The atomic hydrogen signal shows a strong dependence on T_f. The signal becomes detectible at ~1875K and increases dramatically with increasing T_f. These results agree with Celii and Butler's (3+1) REMPI of atomic hydrogen for the bulk gases between the filament and substrate, with an inlet gas composition of 0.5% CH_4 in H_2 [11] .

Scans of methyl radical REMPI signal verses wavelength at 333.5 nm have also been recorded. The peak results from a two photon absorption from the X^2A_2'' electronic ground state of CH_3 to the $3p^2A_2''$ vibrationless state followed by single photon ionization [12] . A preliminary study of CH_3 concentration as a function of filament temperature has been conducted.

4. Summary

Filament and substrate temperature dependencies have been determined for H, CH_3, CH_4, and C_2H_2 for a HFCVD reactor fitted with orifice sampling. REMPI has been utilized to follow the relative concentrations of radical intermediates. There is a strong dependence on the filament temperature for the relative abundances of CH_4, C_2H_2, and H in the near surface gases. These concentrations are much less dependent on the substrate temperature.

Acknowledgements

References

1. Chu, C. J.; D'Evelyn, M. P.; Hauge, R. H.; Margrave, J. L. *Journal of Materials Research* 1990, *5*, 2405.
2. Harris, S. J.; Martin, L. R. *Journal of Materials Research* 1990, *5*, 2313.
3. Martin, L. R.; Hill, M. W. *Journal of Material Science Letters* 1990, *9*, 621.
4. Tsuda, M.; Nakajima, M.; Oikawa, S. *Journal of the American Chemical Society* 1986, *108*, 5780.
5. Harris, S. J. *Applied Physics Letters* 1990, *56*, 2298.
6. Skokov, S.; Weiner, B.; Frenklach, M. *Journal of Physical Chemistry* 1994, *98*, 8.
7. Belton, D. N.; Harris, S. J. *Journal of Chemical Physics* 1992, *96*, 2371.
8. Hsu, W. L.; McMaster, M. C.; Coltrin, M. E.; Dandy, D. S. *Japanese Journal of Applied Physics Part 1* 1994, *33*, 2231 and references there in.
9. Corat, E. J.; Goodwin, D. G. *Journal of Applied Physics* 1993, *74*, 2021.
10. Moore, C. E. *Atomic Energy Levels*; Government Printing Office: Washington, DC, 1949.
11. Celii, F. G.; Butler, J. E. *Applied Physics Letters* 1989, *54*, 1031.
12. Hudgens, J. W.; DiGiuseppe, T. G.; Lin, M. C. *Journal of Chemical Physics* 1983, *79*, 571.

IN SITU OES DIAGNOSIS OF THE DC ARC PLASMA JET IN THE SYSTHESIS OF DIAMOND

Zhen YAN, Zhiwei ZHANG, Hesun ZHU

Research Center of Materials Science, Beijing Institute of Technology, Beijing 100081

Key words: Diamond, OES, Plasma

Abstract

This paper discusses the in situ optical emission spectroscopy system for diagnosis of the DC arc plasma jet used in the synthesis of diamond. The effects of power, the methane flux and the hydrogen flux on the CH, H and C_2 species in the plasma as well as on experimental results are analyzed. The work provides basis for better process control and further theoretic research.

1. Introduction

In recent years there has been a rapid development in low pressure vapor phase technology for the synthesis of diamond. Workers in this field first studied the experimental technology of the process of deposition of diamond. Later they begin to focus their attention on the fundamental physical and chemical processes. It is most meaningful to study the growing process thoroughly in order to accelerate the development of the low pressure vapor phase technology and to provide theoretical guidance to the improvement of the diamond manufacturing technology and the equipment used.

In the diamond deposition process, the inside blaze of the DC arc plasma jet is red in color while the color of the outside blaze changes with the ratio of CH_4 to H_2.. This shows that the process going on in the plasma itself is greatly affected by its

composition. The in situ diagnosis of the deposition process is thus very important and has consequently become a powerful mean used by numerous researchers[1-3].

2. Experimental work

The present authors used an optical emission spectroscopy system to diagnose and study the DC are plasma jet used in the process of making diamond. The advantage of this method is that there exists no direct physical contact with the plasma, so the whole process is comparatively simple.

3. Analyzing the diagnostic results of the DC arc plasma jet

A. The effects of the change in power on the intensity of the spectrum lines.
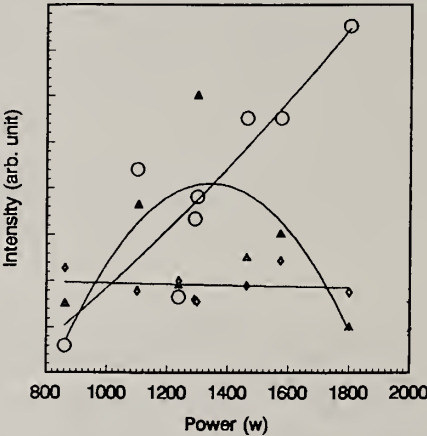
Fig 2. the change of CH/Ar, H_β/Ar, C_2/Ar with the change in power (CH/Ar:Δ; H_β/Ar: O; C_2/Ar:$\lozenge$)

The change in intensity of the spectrum lines with the change in power is determined while keeping the rest of the parameters in the diamond deposition process unchanged. Plot the ratio between the intensity of the emission spectrum lines of CH(431.4 nm), H_β(486.1 nm) and C_2(516.5 nm) against power as in figure 2. From the figure, it can be seen that H_β/Ar tends to increase with power accompanied by a small decrease in C_2/Ar while CH/Ar increases before power reaches 1300W but decreases henceforward. This shows that with the increase in power, the concentration of H atoms tends to increase while C_2 tends to decrease. As for the concentration of CH, it

tends to increase before the power reaches 1300W and then it starts to show a decreasing tendency.

B. The effect of the CH_4 flux

The change of CH/Ar, C_2/Ar, H/Ar with the change in the CH_4 flux while other parameters remain unchanged is shown in Fig. 3. From the figure it is seen that C_2/Ar, and CH/Ar increase rapidly with the CH_4 flux. Although H_β/Ar also has a tendency to increase but the increase is rather small. This shows that with the increase in the proportion of CH_4 the proportions of C_2 and CH in the plasma also increase.
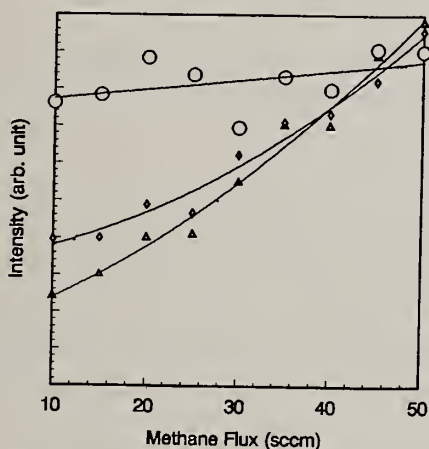
Fig3. the change of CH/Ar, H_β/Ar, C_2/Ar with the change in CH_4 flux. (CH/Ar: Δ; H_β/Ar: O; C_2/Ar: ◊)

C. The effect of the H_2 flux

Fig.4 shows the relation between CH/Ar, H_β/Ar, C_2/Ar and the change in H_2 flux while the rest of the experimental conditions remained unchanged (Ar: 0.24m^3/h; CH_4:20 sccm; current: 75A; voltage: 24V, pressure: 500 Pa). It was found that both CH/Ar and C_2/Ar decrease rapidly with the increase in the H_2 flux. As for H_β/Ar, it increases with H_2 flux, but when it reaches a certain maximum value it begins to remain practically constant. This peak appears when the H_2 flux comes to 140 sccm. This is an indication that with the increase in the H_2 flux, the formation of CH and C_2 is restrained. The concentration of the H atoms in the ground state becomes saturated, when the H_2 flux is 140 sccm.
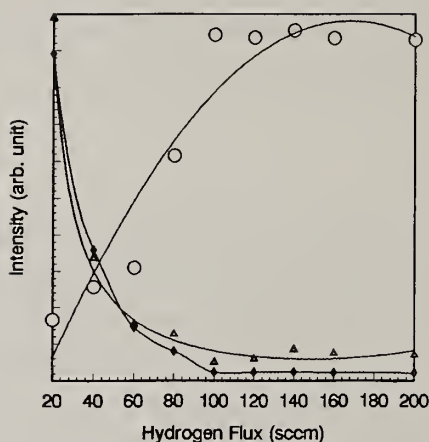
Fig4. the change of CH/Ar, H_β/Ar, C_2/Ar with the change in H_2 flux.
(CH/Ar:$\triangle$; H_β/Ar:O; C_2/Ar:$\Diamond$)

4. Conclusion

A number of useful data was obtained in the experiment on the in situ diagnosis of the DC arc plasma jet in the process of deposition of diamond by using the OES system. This is most significant to the mastery of the technology of synthizing diamond by using the low pressure DC arc plasma jet. It also provides useful information for further study of relevant theories.

Acknowledgment

References

1. O. Matsmuto and T. Katagiri; Thin Solid Films, 146(1987), 283
2. F.G. Celii, P.E. Peherson, H.T. Wang and J.E. Butler, Appl. Phys. Lett., 52 (1988), 2043
3. S.J. Harris, A.M. Weiner, and T.A. Perry; Appl. Phys. Lett., 53   (1988), 1605

Mass and Energy Transport in an H_2 Microwave Plasma Obtained Under Diamond Deposition Discharge Conditions : Role of the Spatial Distribution of the Microwave Power Density.

K. Hassouni[1], S. Farhat[1], C . D. Scott[2] and A. Gicquel[1],

[1] Laboratoire d'Ingénierie des Matériaux et des hautes Pressions (LIMHP)
CNRS-Université Paris XIII, Av. J. B. Clément, Villetaneuse 93430, France
[2] NASA Johnson Space Center, Houston, TX 77058 USA.

Key words : Modeling, Plasma, Microwave

Abstract

The set of transport governing equations of thermochemically non equilibrium H_2 plasma are solved for discharge conditions (power, pressure) corresponding to that of diamond deposition and for a one dimensional diffusive flow. Several reactor simulations corresponding to different axial distributions of the absorbed microwave power density are carried out. The effects of the total absorbed power density and the position of the maximum of the absorbed power density on the axis are studied.

1. Introduction

One of the crucial problems encountered for optimizing and scaling up plasma assisted diamond deposition processes is the understanding of the basic mechanisms involved in the gas phase. This understanding requires the development of satisfactory H_2/CH_4 plasma models. For this purpose, Scott, et al. [1] reported, as a first step, a pure H_2 plasma transport model which may constitute good basis for the investigation of more complex diamond deposition plasmas. In this paper we present some results, obtained using this model, on the effect of the absorbed microwave power density spatial distribution on the plasma chemical composition and temperatures.

2. Model description

In an H_2 plasma operating under moderate pressure conditions, the heavy particle translation-rotation energy, H_2 vibration energy and electron translation energy modes are not in equilibrium and the major chemical species are H_2, H, H^+, H_2^+, H_3^+, H^- and e^- [1]. The transport of these chemical species and energy modes are coupled through the species chemical production rates and energy source terms. As a consequence, the plasma diffusion may be described by 7 species transport equations coupled to three

energy transport equations. The plasma governing equations obtained, under Maxwell-Boltzmann distribution functions assumptions for the three energy modes, were first formulated by Lee [2] and adapted to the case of H_2 plasma and one dimension geometry by Scott, et al. [1]. The details of these equations and the corresponding flux and source terms expressions are explicited in references [1-2].

3. Simulation parameters and boundary conditions

The model described above was used to investigate the diamond deposition microwave plasma bell jar reactor described in reference [3]. In this reactor the plasma volume is spherical in the absence of the substrate holder and almost hemispherical in the presence of this (fig. 1). The radial gradients of the species concentrations and the temperatures vanish at the plasma symetry axis [5]. As a consequence, the plasma transport on this axis may be described by a one dimensional model. The solution of the transport equations requires the boundary conditions for the species and temperatures at the inlet and at the substrate surface. It also requires the knowledge of the microwave power density axial distribution.

3. 1. Boundary conditions

In first approximation, at the inlet of the computation domain, outside of the discharge area, the boundary conditions are choosen by setting the gradients of all the variables to zero. The gas and H_2 vibration temperatures at the substrate surface are given by Coherent Antistokes Raman Spectroscopy (CARS) measurements near the surface [3]. The accommodation of the electron energy at the substrate is very weak [1], and a zero gradient of T_e is assumed at the surface. The species boundary conditions are derived from the surface reactions mechanism reported by Scott [1].

3. 2. Spatial distribution of the microwave power density

The axial profile of the 750.3 nm argon line intensity was determined by optical emission spectroscopy with and without the substrate holder in the plasma. The experiments show that the intensity values, in the plasma bulk far from the substrate, are not affected by the presence of the substrate indicating that the substrate holder is not a microwave reflecting plane. The absorbed microwave power density profiles were derived from these intensity distributions. When the discharge is on without the substrate, the plasma is located in a sphere of radius $\lambda/4$ (λ is the high frequency field wavelength). In this case the axial distribution of the absorbed power is assumed to be the solution of a one dimensional wave equation where the wave is assumed to be injected at the top of the reactor and reflected back at the end of the cavity. The radial profile is assumed to be similar to the axial one. The plasma electrical permittivity is assumed to be constant over all the plasma volume. In the presence of the substrate, the same solution is assumed for the power distribution. The absorbed power distribution is then given by the following relation :

$$PMW(z,r) = P_0 \cdot \cos^2 [2\pi(z-z_0)/\lambda] \cdot \cos^2 [2\pi r/(\lambda^2/16 - z^2)^{1/2}] \qquad (1)$$

where z is the axial coordinate ($z=0$ at the substrate surface) and r is the radial coordinate ($r=0$ at the plasma axis). z_0 is the position of the maximum power density. P_0 is given by the following energy balance :

$$P_{total} = \int_z [\int_r PMW(z,r) \, 2\pi.r.dr] \, dz \qquad (2)$$

4. Results and discussion

The effect of the absorbed microwave power distribution was investigated in terms of P_{total} and z_0 parameters. The transport equations were solved for three discharge conditions : $P_{total} = 300$ W, $z_0=5$ mm and $P=25$ mbar ; $P_{total} = 300$ W, $z_0=10$ mm and $P=25$ mbar ; $P_{total} = 600$ W, $z_0=5$ mm and $P=52$ mbar (fig. 3). The substrate temperature was set equal to 1100 K, the vibration temperature to 1300 K and the recombination coefficient of H-atom to 0.1 [4-5]. For all the cases the computed gas temperature and H_2 vibration temperature are nearly in equilibrium. This is in agreement with CARS measurements carried out on the same device [3].

4.1. Effect of z_0

For a pressure of 25 mbar and P_{total} of 300 W, a small displacement of the maximum of the power density distribution, from 5 mm to 10 mm, leads to an important variation of the gas temperature which increases from 2180 K to 2570 K (fig. 4). As a consequence, the H_2 thermal dissociation rate constant increases leading to a higher H molar fraction ($2.6.10^{-2}$ instead of 10^{-2}, fig. 5). The electron molar fraction in the plasma bulk also increases varying from $5.9.10^{-6}$ to 8.10^{-6} (fig. 6), and the electron temperature increases from 14900 K to 16700 K.

4.2. Effect of the increase of the power density

Deposition experiments have shown that an increase of the averaged power density from 9 W/cm^3 to 18 W/cm^3 has a strong effect on the diamond growth rate and quality [3]. To investigate the effect of this parameter on the plasma properties, the transport equations were solved for two couples (P_{total}, P) corresponding to a constant discharge volume (32.7 cm^3). The results show a strong increase of T_g and H-atom molar fraction which vary from respectively 2180 K to 2800 K and 0.015 to 0.17 (fig. 4 and fig. 5). On the opposite, the increase of the power density leads to a slight decrease of the electron molar fraction (fig. 6), and T_e increases from 14900 K to 15800 K.

5. Conclusion

The results show the strong sensitivity of the plasma behaviour to the microwave power spatial distribution. Especially a small displacement of the maximum position of the power density axial profile leads to an important change of T_g and H-atom molar

fraction. The increase of the power density also strongly increases T_g and consequently the H-atom molar fraction. This may explain the higher quality of the diamond films associated to an higher growth rate obtained at higher power density. The simulation results may be also sensitive to the boundary conditions, which are under study today in our laboratory.
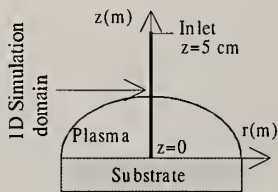
Fig. 1 : Schematic of the investigated discharge
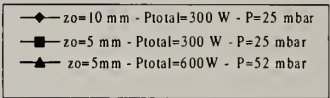
Fig. 2 : Legend of figures
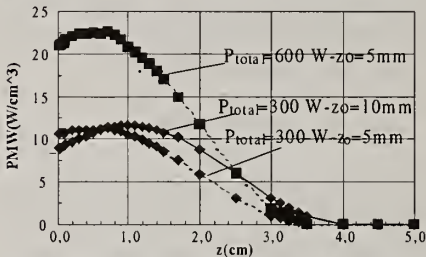
Fig. 3 : Microwave power axial profile
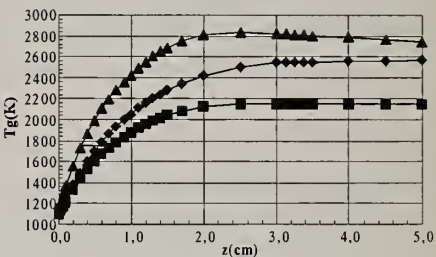
Fig. 4 : Gas temperature axial profile
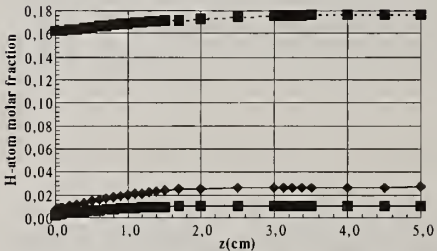
Fig. 5 : H-atom molar fraction axial profiles
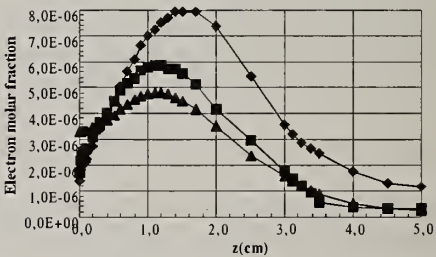
Fig. 6 : Electron molar fraction axial profile

References

[1] C. D. Scott, S. Farhat, A. Gicquel, K. Hassouni, M. Lefebvre, M. Péalat. AIAA 93-3226 (1993)

[2] J. H. Lee, in Thermal Design of Aeroassisted Orbital Transfer Vehicles, Edited by H. F. Nelson, Vol. 96 of Progress in Astronautics and Aeronautics, AIAA, 1985.

[3] A. Gicquel, K. Hassouni, S. Farhat, Y. Breton, C. D. Scott, M. Lefebvre, M. Pealat, Diam. and Rel. Mat. , Vol. 3, n° 4-6, pp 581-586 (1994).

[4] D. G. Goodwin and G. G. Gavillet, J. Appl. Phys. **68**, 6393 (1990)

[5] A. Gicquel, M. Chenevier, K. Hassouni, Y. Breton, J. C. Cubertafon, abstract submitted to 95 Diamond Films Conference, (Barcelona, 1995)

DETERMINATION OF THE PREFERRED CRYSTAL ORIENTATION OF DIAMOND FILMS USING POLARIZED RAMAN SPECTRA

J. Mossbrucker[1] and T. A. Grotjohn[2]

[1]Fachbereich Elektrotechnik, 67663 Universität Kaiserslautern, Germany
[2]Dept. of Electrical Engineering, Michigan State University, East Lansing, MI 48824

Key words: Crystal orientation, Polarization, Polarized Raman, Raman

Abstract

Local and global crystal orientation of various diamond films have been determined by the use of polarized Raman spectra. We present a method for the determination of local (single) crystal orientation on a diamond film within an accuracy of 1.5°. Further, the preferred crystal orientation and the crystal orientation distribution of polycrystalline diamond films have been measured using polarized Raman spectra. In particular, the distribution of the crystal orientation of two different films are presented. The accuracy of this method is approximately 5° for the (100) preferred crystal orientation.

1. Introduction

The analysis of crystal orientation is important for the understanding of the dynamics of crystal growth. Traditionally crystal orientation was measured primarily using x-ray diffraction[1], electron channeling[2], and TEM[3]. Recently, several papers have appeared discussing the determination of the crystal orientation using polarized Raman spectra[4]. Raman scattering determination has several advantages including: It is non-destructive and it needs no special preparation for the sample. However, these papers concentrated on the determination of the crystal orientation of single crystals. These measurements were highly accurate and, hence, an extension to determine the preferred crystal orientation of polycrystalline diamond films is of interest.

In this paper we present a Raman scattering method for the determination of the global crystal orientation of polycrystalline diamond films. Single crystal diamond samples with (100), (110), and (111) orientations are used as test samples and are rotated about the optical axis to verify the accuracy of this method. Polarized Raman spectra of polycrystalline diamond films with preferred crystal orientations have been used to determine the crystal orientation distribution. Specifically, the distribution of the crystal orientation of two diamond films, one mainly (100) and the other mainly (111) oriented, are presented.

2. Polarized Raman Spectra

Raman scattering is a two-photon process and is dependent on the scattering tensor R. Raman intensity depends on the vector of the polarization of the incident and the scattered light relative to the crystal axes. This leads to the determination of the crystal orientation by measuring the anisotropy of the Raman scattering process. Of the 32 crystal classes diamond belongs to the O_h class and the Raman-activity has F_{2g} symmetry[5]. The Raman tensors for this class are represented by:

$$R_x = \begin{bmatrix} 0 & 0 & 0 \\ 0 & 0 & d \\ 0 & d & 0 \end{bmatrix} \qquad R_y = \begin{bmatrix} 0 & 0 & d \\ 0 & 0 & 0 \\ d & 0 & 0 \end{bmatrix} \qquad R_z = \begin{bmatrix} 0 & d & 0 \\ d & 0 & 0 \\ 0 & 0 & 0 \end{bmatrix} \qquad (1)$$

Raman experiments in this paper are performed by using a backscattering rather than a 90^0 geometry Raman set up. In this geometry the direction of propagation vector of the incident and scattered light are perpendicular to the crystal surface. The crystal axis system is described relative to the laboratory coordinate system by using Z-Y-Z Euler angles[7] α, β, and γ as shown in Fig. 1.
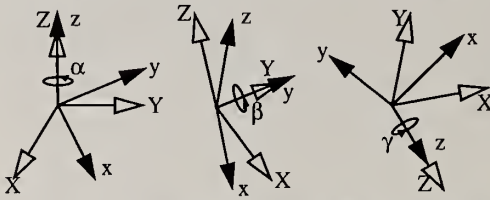
X, Y, Z : laboratory system
x, y, z : crystal axes
α, β, γ : crystal orientation relative to the laboratory system

Fig. 1 : Geometry used to determine crystallographic orientation

Following Placzek[6] the intensity of Raman scattering can be expressed in the form:

$$S_{Raman} = I_e K |e_i R_j e_s|^2 d\Omega \qquad (2)$$

where $K = 4\pi^2 a^2 v^2$, $a = 1/137$ and v is the wavenumber of the scattered light. The scattered energy per unit time into a solid angle $d\Omega$ is given by S_{Raman}, where I_e is the incident energy per unit area per unit time. The unit vectors e_i and e_s define the directions of the electric fields of the exciting and scattered radiation, respectively, and lie in the X-Y-plane of the laboratory system defined by the angles ψ_i and ψ_s as shown in Fig. 2.
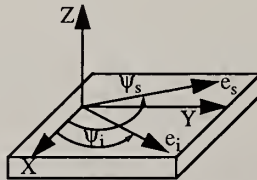
Fig. 2 : Definition of the electric field vector of the incident and scattered light

The Raman intensity can be written as a function of the crystal angles α, β, γ, and the angles of the incident and scattered light ψ_i and ψ_s as follows:

$$I = \frac{1}{d^2}\sum_j (e_i R_j e_s)^2 = C_1(\alpha\beta\gamma\psi_i) + C_2(\alpha\beta\gamma\psi_i)\cos 2\psi_s + C_2(\alpha\beta\gamma\psi_i)\sin 2\psi_s \quad (3)$$

C_1, C_2, and C_3 are non-linear functions containing parameters that can be determined by a best-fit using the least-square-method. These parameters cannot be determined by using only one incident polarization direction. In this paper we have chosen two polarization directions, which are perpendicular to each other. One is parallel to the X-axis and one is parallel to the Y-axis of the laboratory system. Visual observation did not show any lateral beam movement on the sample by rotating the polarization of the incident light. The polarized Raman spectra of a first surface mirror was measured to determine the depolarization of the optics used for the set-up. Although a high aperture microscope objective has been used, only slight depolarization has been detected. All measured Raman spectra have been corrected by this amount of depolarization. Three test samples with (100), (110), and (111) orientations have been used and the data points of the polarized Raman spectra and their best-fit are shown in Fig. 3.
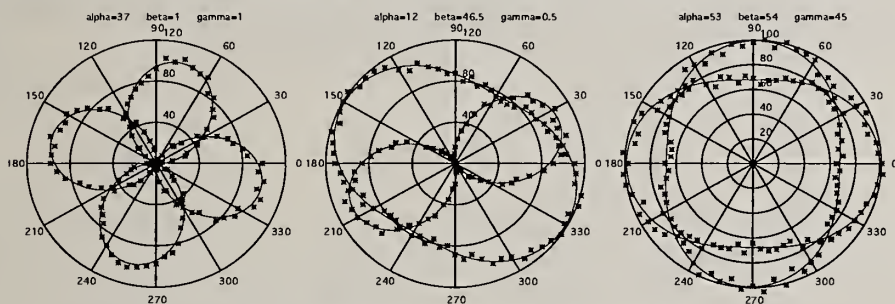
Fig. 3 : Polarized Raman spectra and their best-fit

All three samples were rotated over the Z-axis of the laboratory system. The parameters of the best-fit are then compared with X-ray diffraction measurements:

	(100)		(110)		(111)	
	Raman	X-ray	Raman	X-ray	Raman	X-ray
β	1°	0°	46.5°	45°	54°	55.3°
γ	1°	0°	0.5°	0°	45°	45°
α	37°		12°		28°	

With the knowledge of the accuracy of this method the model can be expanded to more than one single crystal by adding the scatter of all crystals in the viewed patch. Hence, equation (3) can be rewritten as follows:

$$I = \frac{1}{d^2}\sum_{crystals}\sum_j (e_i R_j e_s)^2 \quad (4)$$

It can be shown that if the distribution of the crystal orientation is not known at least approximately, then the parameters of equation (4) cannot be uniquely fit by a best-fit. For example, the polarized Raman spectra of two crystals, one oriented as $\alpha=45°$, $\beta=0°$, $\gamma=0°$ and the other oriented as $\alpha=0°$, $\beta=0°$, $\gamma=0°$, is completely isotropic. Unambiguous fitting requires some initial assumptions or data. With the assumption of a

preferred orientation it is possible to give a best-fit to measured data. Fig. 5 shows polarized Raman spectra of multiple crystals on a polycrystalline film, one mainly (100) and the other mainly (111) textured.
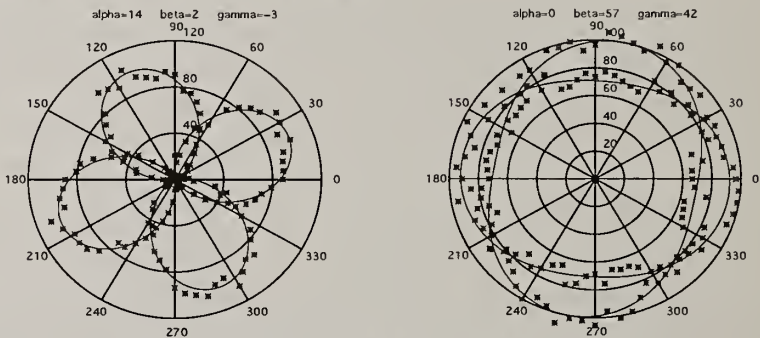
Fig. 4 : Polarized Raman spectra of multiple crystals

Both polarized Raman spectra represent approximately 30 crystals. The distribution of the crystal orientation are nearly Gaussian shaped as shown in Fig. 5.
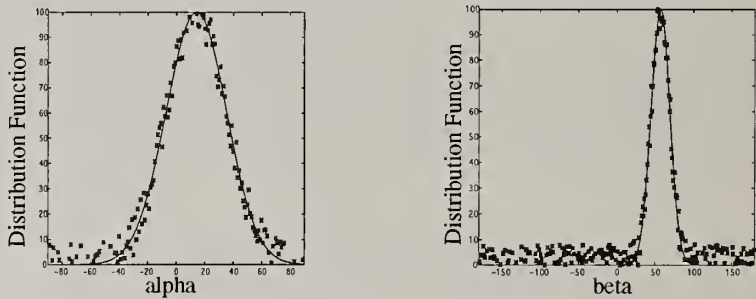
Fig. 5 : Distribution of crystal orientation

Fig. 5 left shows the distribution of the angle α of the (100) textured sample, Fig. 5 right shows the distribution of the angle β of the (111) textured sample. The '*' are data from the best-fit of a Gaussian crystal orientation distribution to the experimental data and do not represent single crystals. The accuracy of the determination of (100) oriented crystals is approximately 5^{0}. Due to noise in the spectra, the distribution does not go to zero. Because the polarized Raman spectrum of (111) oriented crystals is more isotropic as seen above in Fig. 3 and Fig. 4, the accuracy of the determination drops to approximately 10^{0}.

3 References

[1] M.W. Geis, H. I. Smith, B.-Y Tsaur, J. C. C. Fan, D. J. Silversmith, and R. W. Mountain
J. Electrochem. Soc. Solid State Tech. 129, 2812 (1982)
[2] L. Pfeiffer, A. E. Gelman, K. A. Jackson, K. W. West, and J. L. Batstone, Appl. Phys. Lett. 51, 1256 (1987)
[3] M. W. Geis, H. I. Smith and K. Chen, J. Appl. Phys. 60, 1152 (1986)
[4] K. Mizoguchi and S. Nakamisha, J. Appl. Phys. 65, 2584 (1989), J. B. Hopkins and L. Farrow, J. Appl. Phys. 59, 1103 (1986)
[5] D. J. Gardiner and P. R. Graves, Practical Raman Spectroscopy, Springer Verlag Heidelberg, Germany
[6] G. Placzek, Rayleigh-Streuung und Raman-Effekt, Akademischer Verlag Leipzig, Germany
[7] J. J. Craig, Introduction to Robotics Mechanics and Control, Stanford University

Applications of Diamond Films and Related Materials: Third International Conference, 1995
Editors: A. Feldman, Y. Tzeng, W. A. Yarbrough, M. Yoshikawa, and M. Murakawa

449

TIME-RESOLVED AND CW PHOTOLUMINESCENCE SPECTRA OF POLYCRYSTALLINE DIAMOND FILMS

T. Dallas, S. Gangopadhyay, S. Yi, and M. Holtz

Texas Tech University, Lubbock, TX 79409-1051 USA

Key words: diamond films, photoluminescence, time-resolved, tungsten, nitrogen, Si

Abstract

We have studied defect photoluminescence from polycrystalline diamonds grown by two different techniques. Each has a tendency to introduce defects into the diamond lattice. We have used continuous-wave and time-resolved photoluminescence spectroscopy to determine the mid-band gap defect energy levels and their respective lifetimes.

1. Introduction

Growth systems can introduce foreign atoms either intentionally or unintentionally into diamond crystals. This can affect the electronic and optical properties. In this paper, we will discuss the use of photoluminescence in the characterization of diamond films. Continuous-wave photoluminescence (CWPL) has been the preferred method for determining defects. Time-resolved photoluminescence (TRPL) has rarely been used to understand the nature of these defects. The radiative decay rate is a very good indication of the recombination mechanism and can shed some light on the processes involved. Using combined CWPL and TRPL can improve our understanding of basic defect issues in diamonds.

2. Experimental Techniques

We have studied films deposited on molybdenum substrates by arc-jet (Norton) and microwave CVD (Raytheon) methods. The free-standing unpolished samples used in the PL studies were ~ 1 cm^2 in area and 0.1 cm thick. The Raman spectra of both films show a narrow diamond peak at 1332 cm^{-1} and a weak, broad band at ~1600 cm^{-1}. The CWPL and TRPL experiments were carried out at 20 K in a closed cycle refrigeration system. The spectra were excited by an Ar-ion laser (2.41 eV). The PL was analyzed by a double

monochromator and detected by an InGaAs photomultiplier tube. All spectra were corrected for the response of the detection system. The TRPL measurements had a temporal resolution of 100 ps and were done using a N_2-pumped dye laser (500-ps @ 10 Hz) at an excitation energy of 2.48 eV. Detection was accomplished using a two-stage, proximity focused MCP. The PL decays were treated as a superposition of multiexponential decays, after removing the temporal instrument response by deconvolution (see reference 1, for details).

3. Results and Discussion

Figure 1 shows PL spectra for the two diamond films. For the arc-jet grown film (top), the sharp PL peaks appear at 1.681, 1.710, 1.724, 1.734, 1.771, and 2.155 eV. For the microwave CVD deposited film (bottom), the sharp PL peaks were at 1.680, 1.880, 1.945, and 2.155 eV. Both samples exhibit broad backgrounds. The 1.681 eV emission observed in both films is believed to arise from Si impurities.[2,3] This defect persists despite the fact that a Mo substrate was used. However, the 1.681 eV emission is much stronger in the microwave CVD deposited film. The quartz window through which microwaves are injected could be the source of the Si. The peaks labeled with an asterisk in the arc-jet film have also been seen in films produced by the hot-filament CVD technique on Si substrates using a tungsten carbide filament.[4] Since arc-jet and hot filament both use tungsten in the electrode or filament, we speculate that these peaks may originate from tungsten impurities in the film. Further PL studies on well controlled samples should be carried out to achieve a definite identification of these defects. The line at 2.155 eV has been attributed to a nitrogen vacancy center containing a single nitrogen atom and one or two vacancies.[5]
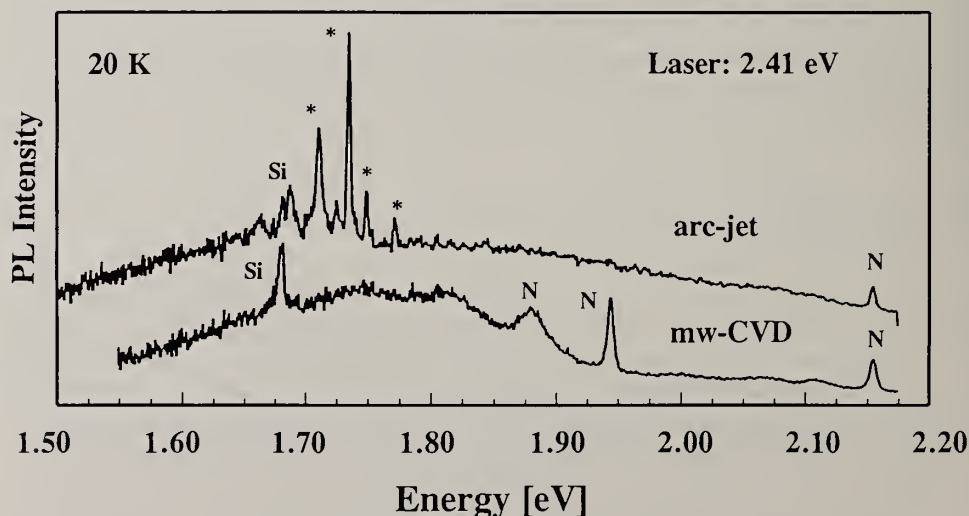
Fig. 1. CWPL results for microwave-CVD (Raytheon) and arc-jet (Norton) films.

Weak phonon sidebands are also observed. The zero-phonon line at 1.945 eV and phonon sidebands at 1.880 eV and lower energies observed in the Raytheon diamond have also been attributed to a nitrogen-vacancy center.[6,7] These peaks have been observed in nitrogen doped films deposited by a microwave CVD system.[7] All the nitrogen related peaks mentioned above have been seen in diamond films deposited by a combustion (oxygen-acetylene torch) process.[8] Since the combustion film is deposited in an open atmosphere, nitrogen incorporation into the film is expected.

The broad PL band observed for both samples is similar to that observed by several groups in undoped and nitrogen doped diamond samples. The origin of this band in undoped films is thought to be from a-Si:C:H[9] or from sp^2-bonded carbon clusters.[5] From the temperature dependence of the broad band PL in nitrogen-doped samples, it was concluded that this band does not originate from a vibronic interaction of the nitrogen centers.[7] In the present study, it was not possible to understand the role of nitrogen in the origin of the broad band PL, just by comparing the shape of the spectra and their temperature dependence. However, the time-resolved studies show that the incorporation of nitrogen modifies the decay times significantly.

Table I. presents the PL decay times for Si and N related centers along with the background luminescence for the microwave CVD diamond film. A comparison of decay times for the broad band PL and the nitrogen-related centers shows that the 0.65 ± 0.1 ns and 9.6 ±1 ns components are from the broad background PL. The nitrogen related sharp phonon lines and side bands had decay times of 29 ± 1 ns (2.155 eV) and 22 ± 1 ns (1.945, 1.880, & 1.776 eV). Our results agree quite well with other groups who have measured lifetimes of 29 ns for the 2.156 eV center, 16.7 ns for the 2.463 eV H_3 center and 40 ns for the 2.985 eV N_3 center.[10] The 1.5 ns decay time for the Si defect is similar to that observed by Sternschulte et al.[3] for the Si center (1.3 ns) in a microwave CVD deposited polycrystalline diamond film. The decay times of the tungsten related centers in the arc-jet film were shorter than the resolution of the system (100 ps). Hence, the decay time analysis for this film at several energies in the 1.5 eV to 2.7 eV range represents the decay time from the broad band PL.

PL Band Sample	2.155 eV (N)	1.945 eV (N)	1.880 eV (N)	1.776 eV	1.680 eV (Si)	1.550 eV broadband PL
Raytheon microwave CVD	0.77 (5%) 10.8 (21%) 28.6 (74%)	0.52 (8%) 8.6 (48%) 23.8 (44%)	0.70 (9%) 9.0 (46%) 21.5 (45%)	0.57 (9%) 9.3 (55%) 20.4 (36%)	1.5 (65%) 9.3 (35%0	0.68 (28%) 10.3 (72%)

Table I. Decay times in nanoseconds (percent contribution).

The broad band PL decay seen in the arc-jet film consists of three components with decay times of 0.58 ± 0.05 ns, 1.6 ± 0.1 ns, and 6.5 ± 1.0 ns and is very similar to the decay times seen for an amorphous carbon film. The amorphous carbon film was deposited by an electron cyclotron resonance plasma system using CH_4/H_2. It is a polymer-like film with a bandgap of 2.7 eV, and contains 40-50% hydrogen. This confirms the presence of sp^2 carbon clusters in the arc-jet diamond sample. It seems that heavy nitrogen doping may produce clusters of amorphous carbon-nitrogen compounds, which are responsible for the broad band PL in the microwave CVD diamond.

4. Conclusions

TRPL is a valuable tool for understanding the origin of defects. Tungsten could be responsible for the unassigned defect peaks seen in diamond films made with tungsten electrodes. The background luminescence in the arc-jet film is very similar to the luminescence found for a carbon polymer. A more detailed report is in preparation.

5. Acknowledgements

6. References

1. C. Palsule, S. Gangopadhyay, A. Kher, W. Borst, U. Schmidt, B. Scher, and B.Schroöder, PRB **47**, 9309 (1993)
2. A. Gorokhovsky, A. Turukhin, R. Alfano, and W. Philips, APL **66**, 43 (1995)
3. H. Sternschulte, K. Thonke, R. Sauer, P. Münzinger, P. Michler, PRB **50**, 14554 (1994)
4. T. Perry & C. Beetz, Raman Scattering, Luminescence, and Spectroscopic Instrumentation in Technology, SPIE Vol. 1055, 152 (1989)
5. L. Robins, E. Farabaugh, A. Feldman, and P. Cook, PRB **43**, 9102 (1991)
6. Y. Yokota, J. S. Ma, T. Ito, A. Hiraki, A. Kurita, T. Kushida, and H. Kawarada, APL **61**, 2138 (1992)
7. L. Bergma, M. McClure, J. Glass, and R. Nemanich, Mat. Res. Soc. Symp. Proc. Vol. 339, 663 (1994)
8. J. Freitas, J. Butler, S. Bishop, W. Carrington, and U. Strom, Mat. Res. Soc. Symp. proc. Vol. 162, 237 (1990)
9. C. Clark and B. Dickerson, J. Phys. Condens. Matter **4**, 869 (1992)
10. G. Davies, in *The Properties of Diamond*, edited by J.E. Field (Academic Press, London, 1979) p. 165

Applications of Diamond Films and Related Materials: Third International Conference, 1995
Editors: A. Feldman, Y. Tzeng, W. A. Yarbrough, M. Yoshikawa, and M. Murakawa

453

Micro-Raman Analysis of Stress State in Diamond Thin Films

Leah Bergman[1], K.F Turner[2], P.W. Morrison[1], and R.J. Nemanich[1]

[1]Department of Physics and Department of Materials Science and Engineering, North Carolina State University, Raleigh, North Carolina 27695-8202.
[2]Naval Research Laboratory, Washington, DC.

Keywords: Raman, diamond, thin film, stress, impurities, defects.

Abstract

We present Raman analyses of the sources of stress in thin diamond films containing different impurity concentrations. The impurities and defects which were detected in the diamonds are the nitrogen, the silicon and the graphitic phase. Our analysis indicates that each of the diamond films exhibits an internal compressive stress. The internal stress was suggested to be due to the various defects and impurities in the samples. The correlation between the internal stress and the graphitic concentration indicates that the graphitic phase is a major contributor to the internal compressive stress in the diamond thin films.

1. Introduction

In this research we analyze the stress in diamond thin films containing different impurity and defect concentrations arising from different growth conditions, and show that the impurities and defects play a very important role as sources of the internal stress. The magnitude of the net stress in these diamonds was inferred from the diamond Raman line shift positions [1]. The Raman analysis of the peak positions indicates that the stress is compressive in each of the diamond films. The deconvolution of the observed net compressive stress into its compressive and tensile components was based on models given in the literature for applicable stress sources in diamond films such as the thermal stress (compressive component) and the stress imposed by grain boundaries (tensile component) [2]. After compensating for these stresses, it was found that the diamond thin films still exhibited internal compressive stress which correlated with the graphitic phase.

2. Experiment

Four diamond samples were investigated and will be referred to as the 20h, HF 0%N, HF 0.2%N and the combustion sample. The 20h sample was grown utilizing the microwave CVD method; the plasma consisted of 1% CH_4 in H_2 at 1000 sccm total flow. The plasma power, pressure, and substrate temperature were maintained at 800 W, 25 Torr and 750^0C, respectively. The growth time was 20 hours and the film was ~ 2 μm thick. The HF 0%N and the HF 0.2%N were prepared utilizing the hot filament

growth method (where %N reflects the N doping level, i.e. the percentage of N_2 to H_2 in the gas phase). The growth time and temperature were 6 hours and 850^0C. The plasma consisted of 1.5% CH_4 in H_2 and the filament temperature was maintained at 2000^0C. The morphology of both samples consists of large diamond grains (~ 70% coverage of the silicon substrate). The combustion sample was grown for a half hour in a controlled combustion chamber. The growth temperature was 1000^0C and the film was ~ 3 μm thick. All the samples were grown on 100 silicon substrates. The room temperature Raman spectra was obtained via the micro mode of spot size ~5 μm. The impurity concentrations were estimated via Secondary Ion Mass Spectroscopy for the Nitrogen impurity, Photoluminescence for the Silicon impurity (via the relative intensity of the 1.681 eV band) and Raman spectroscopy for the graphitic phases.

3. Results and discussion

In this section we present an analysis of the net stress in the diamond samples as predicted from the Raman line shift [1]. Fig. 1a shows the diamond and the graphitic Raman signals for the four samples; Fig. 1b shows the high resolution normalized diamond Raman spectra. From the dependence of the Raman shift Δv on the stress σ

$$\Delta v = v - v_0 = - \alpha\sigma \qquad (1)$$

where v_0 (~ 1332.3) is the Raman peak position of an unstressed diamond and α (~ 1.9 cm-1/GPa) is the pressure coefficient, it was found that all the diamond films exhibit a net compressive stress (σ_{net}). Table I lists the calculated stress values as well as the Raman characteristics of the films obtained from Fig. 1.

Table I The Raman characteristics of the four diamond thin films.

Sample	Diamond Position [cm^{-1}]	$I_{DIAMOND}/ I_{GRAPHITIC}$	Δv [cm^{-1}]	σ_{net} [GPa]
combustion	1333.0	4.6	0.7	-0.37
20h	1334.0	1.8	1.7	-0.90
HF 0%N	1334.5	0.7	2.2	-1.16
HF 0.2%N	1336.5	0.6	4.2	-2.21

We now analyze the sources of stress in the diamond films by identifying the stress components and estimating the contributions to the net stress, σ_{net}, in each of the diamond films. The observable σ_{net} is given by Eq. 2 in terms of the thermal stress, σ_{TH}, and the sum of the internal stresses σ_{IN} :

$$\sigma_{net} = \sigma_{TH} + \Sigma\sigma_{IN} \qquad (2)$$

The thermal stress which arises from the difference in the thermal expansion coefficients of silicon and diamond is expected to be compressive in the growth temperature range of our films [2]. The values of σ_{TH} were obtained from Ref. 2 and are listed in Table II. The total internal stress component $\Sigma\sigma_{IN}$ in the diamond film may be due to various sources such as impurities, structural defects such as dislocation [3], and interactions across grain boundaries. The interactions across grain boundaries, due to atomic attractive forces, has been reported to be the possible origin of the main intrinsic tensile stress, $\sigma_{IN,GB}$, in the diamond films [2]. The $\sigma_{IN,GB}$, has been found to be inversely proportional to the average grain diameter, d, in a film:

$$\sigma_{IN,GB} = [E (1 - v)] (\delta / d) \qquad (3)$$

where δ=0.077 nm is the constrained relaxation of the lattice constant and E(1-v)=1345

GPa is the biaxial Young's modulus of diamond. The average grain size for the combustion, 20h, HF 0%N and HF 0.2%N sample is ~ 3.5, 1, 1.5, and 2.5 µm respectively. The values of $\sigma_{IN,GB}$ as well as the values of the previous stress components found so far are listed in Table II.

Table II The experimental and the calculated stress components of the diamond films.

sample	σ_{net} [GPa]	σ_{TH} [GPa]	$\sigma_{IN,GB}$ [GPa]	$\sigma_{calculated}$ $=\sigma_{TH} + \sigma_{IN,GB}$	Internal Stress[GPa] $=\sigma_{net}- \sigma_{calculated}$
combustion	- 0.37	- 0.155	+ 0.03	- 0.125	- 0.25
20h	- 0.90	- 0.25	+ 0.104	- 0.146	- 0.75
HF 0%N	- 1.16	- 0.23	+ 0.07	- 0.16	- 1.00
HF 0.2%N	- 2.21	- 0.23	+ 0.042	- 0.188	- 2.02

From the results listed in Table II it may be concluded that the thermal stress and the stress due to the grain boundaries are not very significant, and that, after compensating for their contributions ($\sigma_{calculated}$), the samples still exhibit an appreciable excess of internal compressive stress. We suggest that the most probable origins of the internal stress are the various types of impurities and defects present in the diamond thin film. The main impurities and defects in our samples are the presence of silicon, nitrogen, and the graphitic phase. The silicon atom is approximately 40% larger than the carbon atom and accommodation of Si in the diamond matrix would result in a large compressive distortion [4]. The A aggregate, which consists of two nitrogen atoms and is the most common nitrogen form in diamond, is known to induce a relatively small compressive stress distortion [3]. The graphitic phase has been suggested to be the principal defect in diamond films [5], the nature of the stresses arising from the graphitic phase is to date, however, largely undetermined.

To investigate the role of the graphitic phase as a source of internal stress in our thin diamond films, we plotted the relative graphitic concentration versus the internal stress. The graph is shown in Fig. 2, and for each sample the other observed non-graphitic impurities are listed. The correlation shown in Fig. 2 indicates that the graphitic phase may be a major contributor to the internal compressive stress but may not be the sole cause of the stress. The deviation from linearity is attributed to the internal stress exerted by the silicon and nitrogen impurities as well as possibly by structural defects. In conclusion, the diamond thin films exhibit internal compressive stress which correlates well, up to minor deviations arising from other defect stress contributions, with the relative concentration of the graphitic phase.

4. References

1. M.H. Grimsditch, E. Anastassakis, M. Cardona, Phys. Rev. B **18**, 901 (1978).
2. H. Windischmann, G.F. Epps, Y. Cong, R.W. Collins, J. Appl. Phys. **69**, 2231 (1991).
3. Gordon Davies, J. Phys. C: Solid State Phys. **3**, 2474 (1970).
4. A. Mainwood, J. Phys. C: Solid State Phys. **12**, 2543 (1979).
5. Y. Sato and M. Kamo, Surface and Coating Technology **39/40**, 183 (1989).
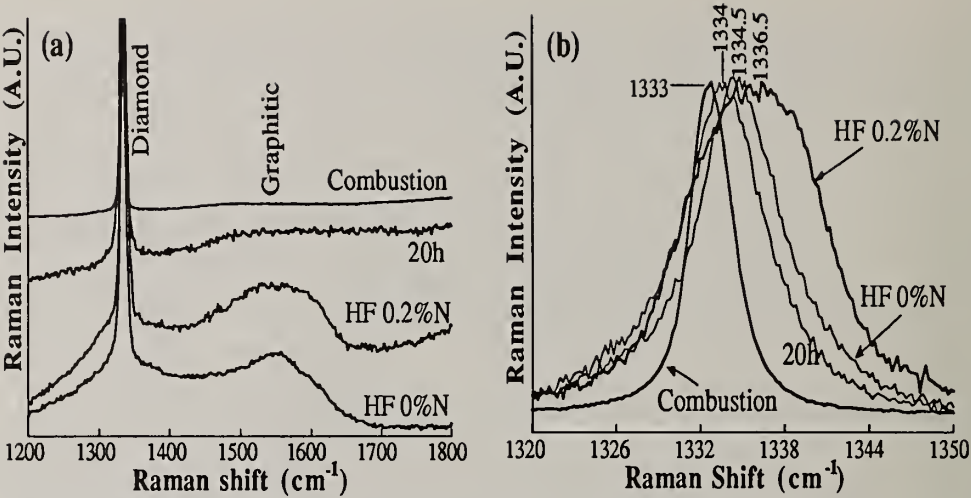
Fig. 1 The Raman spectra of the (a) diamond and graphitic (b) diamond region only.
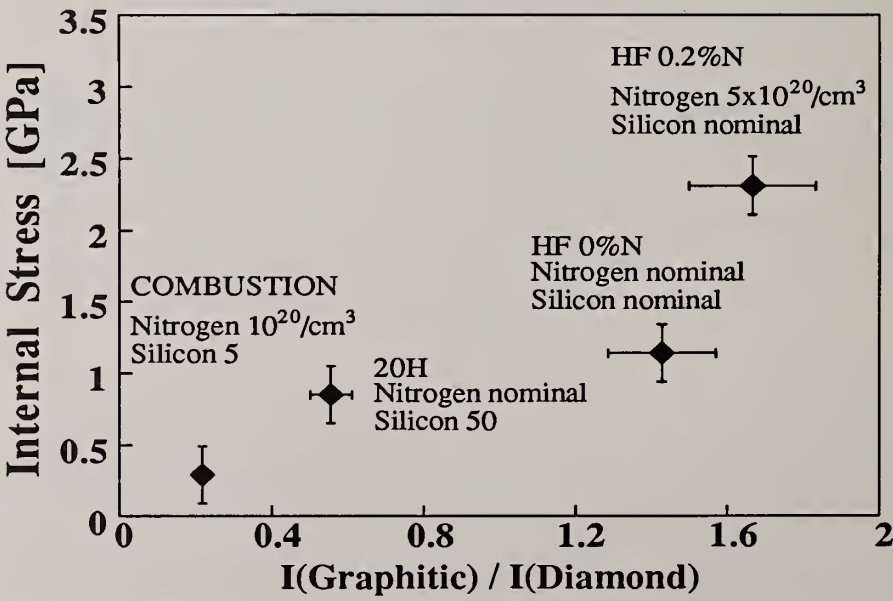
Fig. 2 Correlation of the graphitic phase with the internal stress of the diamond films.

Diamond-Graphite Phase Transition in Ultradispersed Diamond. X-ray and Raman Characterization of Diamond Clusters.

A.Ye.Alexensky, M.L.Baidakova, M.E.Boiko, V.Yu.Davydov, <u>A.Ya.Vul'</u>

Ioffe Physico-Technical Institute, 26 Polytechnicheskaya st., St.Petersburg, 194021 Russia

Key words: cluster, phase transition, Raman scattering, ultradispersed diamonds.

Abstract

The structure and diamond-graphite phase transition in ultradispersed diamond (UDD) have been investigated by X-ray diffraction and Raman spectroscopy. It has been shown that some features of Raman spectrum are an manifestation of the dimensional effect in diamond nanocrystals. The temperature of the phase transition diamond-graphite in UDD is essentially smaller than in bulk diamond single crystals.

1. Introduction

Much effort has lately been made to study a special class of stable structures, known as clusters consisting of several dozens or even hundreds of atoms. Active interest in carbon clusters during the last two or three years was due to the discovery of fullerenes, a new allotropic form of carbon [1,2]. Another carbon material with a cluster structure is ultradispersed diamond (UDD) [3] which can be obtained by detonation directly from carbon of explosives. The characteristic size of UDD clusters, defined as the coherent scattering radius (CSR), is normally within 100 Å. The properties of UDD differ remarkable from those of compact diamonds (heat conductivity, abrasive capacity). However, UDD does not tend to form larger particles, as other ultradispersed materials do, when the ambient conditions are changed. So far, studies have been focused on the production technologies, composite materials and mechanical properties of UDD, while size effects in this nanocluster material have been nearly totally ignored. The present work was aimed at understanding structural characteristics of UDD to reveal its size effects.

2. Methods

UDD samples were obtained in a way described in [4]. Raman spectra were excited by an argon laser ($\lambda = 488$ nm) with the laser radiation power on the sample surface less than 60 Wcm^{-2}. All measurements were made at room temperature in an optical vacuum vessel. A Raman spectrum from a single diamond crystal served as a reference. X-ray diffraction patterns were obtained using a Cu K$_\alpha$ source.

3. Results and Discussion

First-order Raman spectra from a single diamond crystal are known to have active F$_{2g}$ phonons, and the line shape is close to the Lorentzian line [5]. At room temperature, the frequency at which the peak can be observed is $V_0 = 1333.5$ cm^{-1} and the line halfwidth is

$\gamma \cong 1{,}6$ cm^{-1}. One can see in Fig. 1 that the UDD Raman spectrum show a low frequency shift of the line with an asymmetric broadening. The monotonic growth of the scattered light intensity in the longwave region is found to be due to intensive photoluminescence. It is known that the process of one-phonon scattering in bulk single crystals involves, owing to the momentum conservation law, phonons related to the Γ point of the Brillouin zone (q $\cong$ 0, where q is phonon wave vector). For small crystallites, phonons are described by the superposition of plane waves, thus violating the selection rules for the wave vector, so that the spectra may contain phonons with non-zero wave vectors q. A model of phonon dimensional confinement for crystallites of various shape was suggested in [6]. The smaller size was shown to be responsible for the lower fre-

Fig. 1 Unpolarized Raman spectrum of a UDD sample (a) with the Raman spectrum of a diamond crystal shown for comparison (b).

quency and greater asymmetry of one-phonon peak broadening. It seems natural to relate the low-frequency shift in UDD Raman spectrum with an asymmetric broadening to the phonon dimensional confinement in diamond nanocrystals. To check this hypothesis, we have made use of the results of [6] suggesting a model of phonon confinement with the phonon amplitude close to zero at crystallite boundary. In this model, the first-order Raman spectral intensity for sperical crystallites is defined as

$$I(\omega) \cong \int \exp\left(-q^2 L^2 / 4a^2\right) \frac{d^3 q}{\left[\omega - \omega(q)\right]^2 + \left(\Gamma_0 / 2\right)^2} \tag{1}$$

where q is expressed in $2\pi/a$ units and L is the diameter of the nanocrystals, with $a = 3.56$ Å being the lattice constant of diamond, Γ_0 is a natural line width and $\omega(q)$ is the dispersion curve for optical phonons in diamond. To simplify the calculations, the Brillouin zone was taken to be spherical and the phonon dispersion curves to be isotropic. These assumptions are justifiable because only a small region of the Brillouin zone, centered at the Γ point contributes to the scattering. The line shape was calculated using an analytical expression

$$\omega(q) = A - Bq^2 \tag{2}$$

where $A = 1333{,}5$ cm^{-1} and $B = 165$ cm^{-1}. These parameters were determined to describe the neutron scattering data in the [001] direction [7]. With expressions (1) and (2), we have calculated the UDD Raman spectra and estimated the average dimensions of

Fig. 2 Background-subtracted Raman spectrum of a UDD sample (a) and a curve calculated from formula (1) on the assumption of 28 Å spherical UDD nanocrystallites (b).

nanocrystallites in ultradispersed diamond. Fig.2 shows a good agreement between the theoretical and experimental curves for a sphere of 28 Å in size. Data analysis for several UDD samples permits the conclusion to be made that the size distribution of crystallites is relatively narrow and that the sizes of nanocrystalline grains lie between 26 and 29 Å.

X-ray diffraction (XRD) pattern for the UDD samples (Fig.3) contains two main
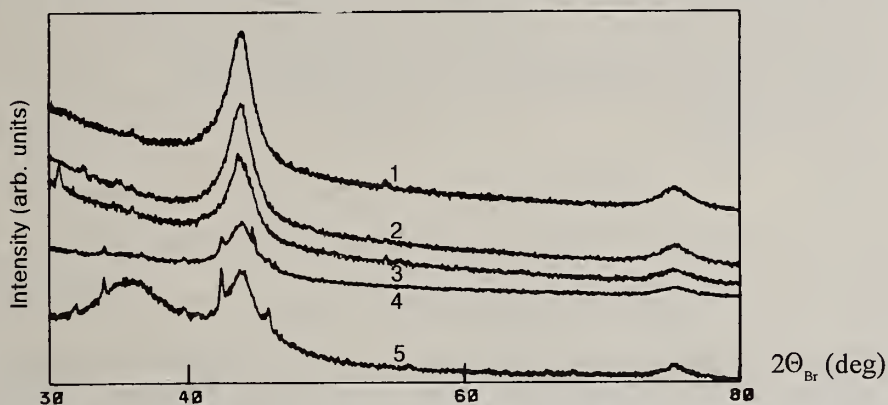
Fig. 3 X-ray diffraction patterns from UDD samples annealed in an argon atmosphere at various temperatures $T^{o}C$: 1 – no annealing, 2 – 700, 3 – 900, 4 – 1000, 5 – 1100.

diffraction peaks at the angles $2\Theta = 43.860$ and 75.320 degrees, all the samples having a typical broadening of the basic (111) reflection. The UDD lattice parameter was found from the position of this peak to be 3.56 Å. The other reflections had a low intensity and a large broadening. CSR defined by Sherer's formula from the diffraction line halfwidth was 36 ± 3 Å, which agrees well with the Raman spectral data analysis. Small-angle scattering measurements were used for an independent estimation of the crystallite sizes (Fig.4). The shape of the crystallites was defined as being spherical by transmission electron microscopy. The characteristic rocking curves contained a peak in the vicinity of 2-3 degrees. The only peak available indicates a dimensional uniformity of the UDD particles. The crystallite sizes determined by Bragg's formula were 32 ± 3 Å. The difference between the particle sizes estimated from the (111) reflection broadening and the small-angle scattering measurements indirectly indicates a certain microporocity (fractal structure) of the object under study.

Analysis of the diffraction patterns from samples annealed isochronically at 700–1100°C in an argon atmosphere for 3 hours (Fig.3) shows that starting from 900°C, there is a structural phase transition of polycrystalline carbon with the diamond structure to carbon with the graphite structure indicated by the appearance of peaks at the angles $2\Theta = 42.380$ degrees. Besides, at the double Bragg angle of 36 degrees, the samples annealed at 1100°C have a very
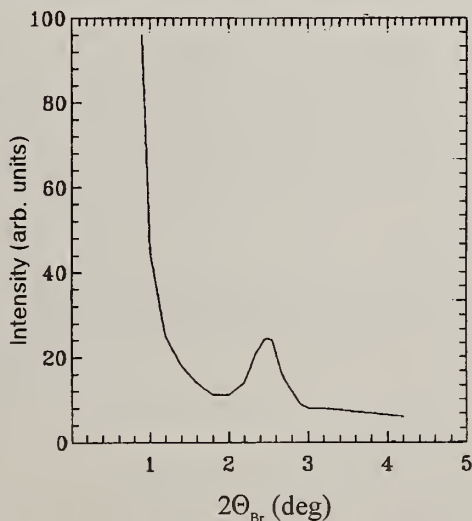
Fig. 4 X-ray diffraction profiles for small-angle scattering of UDD.

broad diffraction peak which can be interpreted as a manifestation of the long range order in the initial matrix. The temperature of the diamond-graphite transition in UDD turns out to be much lower than in bulk diamond single crystals ($T \cong 1600^{\circ}C$). Such a change in the transition temperature could be expected for nanocluster materials. Note that the graphite peaks at 1000 and $1100^{\circ}C$ are accompanied by the diamond peaks in the diffraction patterns. Therefore, one may suggest that graphitization begins at the surface nanocluster particles. During annealing at $1100^{\circ}C$, one assume the formation of polycrystalline graphite particles together with available basic phase.

This work was done within the Russian Programme «Fullerenes and Atomic Clusters» (project №94007).

References

1. H.W.Kroto, J.R.Heath, S.C.O'Brien, R.F.Curl, R.E.Smalley. Nature, v.318, p.162 (1985)
2. W.Krätschmar, L.D.Lamb, K.Fostriropoulos, D.R.Huffman. Nature, v.347, p.354 (1990)
3. A.M.Staver, N.V.Gubareva, A.I.Lyamkin, E.A.Petrov. Fizika goreniya i vzriva, v.20, p.100 (1984)
4. A.I.Lyamkin, E.A.Petrov, A.P.Ershov, G.V.Sakovich, A.M.Staver, V.M.Titov. Dokladi Akademii nauk SSSR, v.302, p.611 (1988)
5. S.A.Solin, A.K.Ramdas. Phys. Rev. B, v.1, p.1687 (1970)
6. I.H.Campbell, P.M.Fauchet. Sol.St.Comm., v.58, p.739 (1986)
7. J.L.Warren, J.L.Yarnell, G.Dolling, R.A.Cowley. Phys.Rev., v.158, p.805 (1967)

CARRIER DIFFUSION LENGTHS IN DIAMOND AND GALLIUM NITRIDE

Craig J. Scott[1], Andre D. Cropper[2], Steve C. Binari[3], Carl White[1], Daniel J. Moore[2]

[1]Morgan State University, Baltimore, Maryland 21239
[2]Virginia Polytechnic Institute and State University, Blacksburg, Virginia 24061
[3]Naval Research Laboratory, Washington, DC. 20375

Key words: diffusion length, electron beam, gallium nitride

ABSTRACT

Electron beam pulses were used as a probe for studying diffusion lengths in diamond and gallium nitride layers. The Laser Electron Beam Induced Currents (L-EBIC) are compared to conventional Thermal Electron Beam Induced Current (T-EBIC) measurements. The diffusion lengths measured in GaN were 7.2 µm and 9.9 µm, with no anneal and a 10 minute anneal at 90°C, respectively. Using the L-EBIC and T-EBIC methods, the measured diffusion lengths were 13.9 µm and 11.6 µm, respectively. The diffusion lengths measured in diamond were 92.0 µm and 83.8 µm for the L-EBIC and T-EBIC measurements, respectively.

1. INTRODUCTION

When device structures are being studied for electronic applications, the diffusion lengths of carriers in the materials are an important indicator of material quality. In this study, diffusion lengths are measured with an electron beam probe. This method is quite useful when examining materials with low dark currents and background doping concentrations because the measured electron and hole currents are dependent on the primary electron beam current injected into to material.

In these experiments, a pulsed electron beam is used to generate free carriers within the sample. In the absence of an electric field, the diffusion current is given by [1]:

$$I_{ph} = [I_0]\exp\left(-\frac{d}{L_n}\right)$$

1

where L_n is diffusion length, d is distance from the collection point to the injection point. The diffusion length is measured from the slope of the ln (I_{ph}) versus distance relationship. Here, the energies used to accelerate the primary electrons in the electron beam probe are sufficient to generate electron hole pairs in the bulk and away from the surface.

2. EXPERIMENT

The set up for this experiment is shown in Fig. 1 The experimental layout is broken into three parts: the electron beam generation section, the modified scanning electron microscope (SEM), and the signal measuring components. The electron beam is pulsed to avoid heating in the material. The pulsed electron beam is created using a conventional tungsten filament thermal source electronically blanked with either a parallel plate field deflector or a laser driven photocathode gun. The lasing system provides a pulse width of 200 femto-seconds at a 76MHz repetition rate.
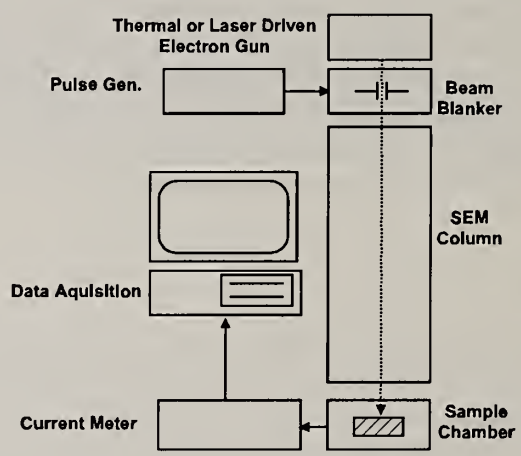
Fig. 1. Electron Beam Test System

Doubling and subsequently tripling the output of a Ti: Sapphire modelocked laser produces UV output between 250-300 nm at up to 30 mW. This wavelength and power are adequate to generate primary electron beam currents for the diffusion measurements[2]. The modified SEM is made up of an interchangeable electron gun and a modified stage for electrical connections to the current meters. The beam spot size was measured to be 0.5 μm at a 10 KeV accelerating voltage.

The GaN samples were 1.3 um thick epitaxial layers on sapphire substrates with various test structures fabricated on them. A structure with a gap size of 25um was

used in the experiments. The electrode metalization was Al/Ti. Details of the material growth and fabrication can be found in [3]. Dark currents were measured on an HP4145 parameter analyzer. At a bias of positive 50 volts, the dark current was measured to be 7.0 pA and the dark resistivity was found to be 1.8×10^{10} ohm-cm. Using the L-EBIC and T-EBIC methods, the electron diffusion lengths were measured to be 13.9 µm and 11.6 µm, respectively. The diffusion lengths measured were 7.2 µm and 9.9 µm, with no anneal and a 10 minute 90°C anneal, respectively. (Fig.2)
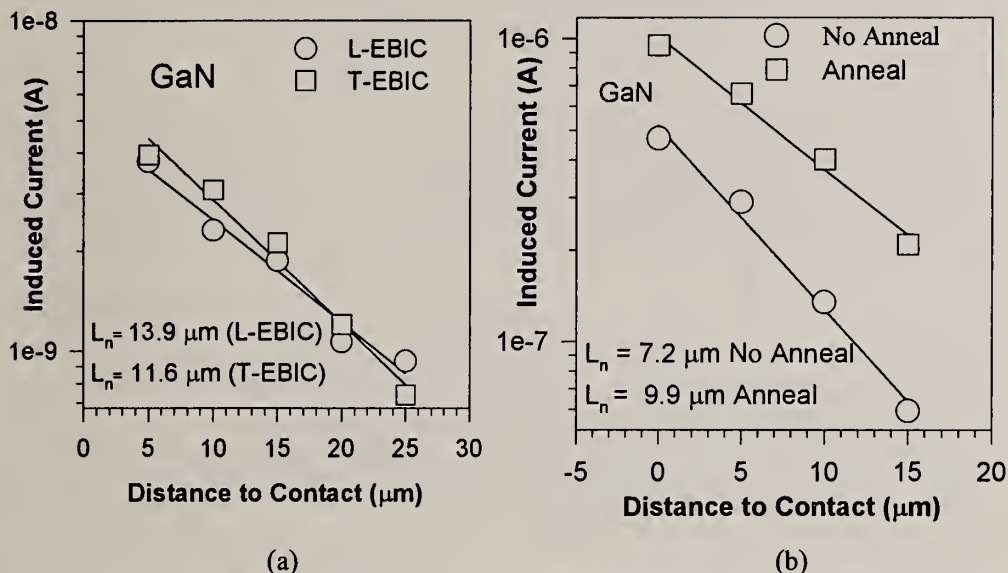
Fig. 2.(a) Comparison of LBIC and EBIC measurements; (b) Electron Beam Induced Currents in Annealed Samples.

The diamond samples were natural type IIA. Here, the layers were much greater than the depth of penetration of electron beam and had a gap size of 350 µm. The electrode metalization was 500 nm of Al. The dark currents were also measured on a HP4145 parameter analyzer. At a bias of positive 100 volts, the dark current was measured to be 5.7 pA and the dark resistivity was found to be 6×10^{11}. The diffusion lengths measured were 92.0 µm and 83.8 µm for the L-EBIC and T-EBIC measurements, respectively. (Fig. 3.)

3. CONCLUSION

Diffusion lengths for electrons in epitaxial GaN and IIA diamond were measured. Larger diffusion lengths were measured for the laser generated electron beam experiments as compared to the thermal electron beam source measurements. Although

the energies and average currents were the same for both L-EBIC and T-EBIC measurements, the duty cycle of the pulsed thermal primary beam currents in our experiments were larger. arises from the results of the annealing experiment. The same sample exhibited a slight reduction in diffusion length after exposure to the electron beam bombardment. After a brief anneal at 90° C the diffusion length showed partial recovery.
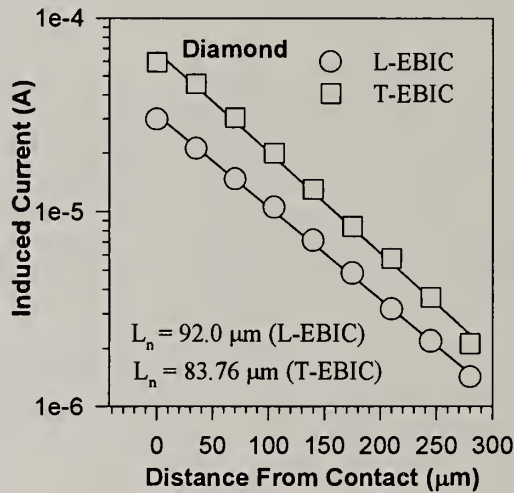
Fig. 3. Electron Beam Induced Currents in Diamond Samples.

4. ACKNOWELEGMENTS

5. REFERENCES

[1] D.E Inoannov and C.A.Dimitriadis, IEEE Trans. Electron Dev., **ED-29**, p.445, (1982).
[2] A.D. Cropper, D.J. Moore, C.J. Scott, and R Green, SPIE Proc. XXVI Annual Symposium on Optical Materials for High Power Lasers, Oct. 24-26, (1994).
[3] S.C. Binari et. al. Electronics Letters, **30**, 11, p.909, (1994).

C-V CHARACTERISTICS OF DIAMOND/SILICON MIS STRUCTURES

T. Nakama, T. Inushima, A. Ogasawara, T. Mizushima, S. Suzuki and T. Shiraishi
Department of Communications Engineering, Tokai University
1117 Kitakaname, Hiratsuka, Kanagawa 259-12 Japan

Key words: deposition, diamond, impurity diffusion, interface, MIS structure,

Abstract

C-V characteristics of diamond/silicon MIS structure were investigated by the use of
the diamond deposited on silicon substrates by the hot-filament method. It is conclud-
ed that a highly resistive layer was formed under the surface of the silicon owing to the
heat damage of the hot filament. This result was confirmed by depositing diamond
with Sb vapor added to the reaction gas.

1. Introduction

When we consider the application of CVD diamond devices, it is important to under-
stand the heat damage which occurs during the diamond deposition. Especially when
impurities are introduced into the reaction gases we have to take into account the impu-
rity diffusion on and into the substrate. In many cases, a silicon wafer is used as a
substrate for the synthesis of diamond. In this paper we investigated the heat damage
and the impurity diffusion in the Si substrate by the C-V measurement of the diamond
/silicon MIS structure. The damage was estimated quantitatively by intentionally intro-
ducing Sb vapor in the reaction gas.

2. Experimental

The diamond films were deposited on a Si wafer by a conventional hot filament CVD
method[1]. The surface of the Si wafer was pre-scratched by diamond powder by
ultra-sonic treatment in methyl-alcohol. The substrates used in this experiment were p-
type of 10 Ωcm and n-type of 4 Ωcm with (100) surfaces. For the Sb vapor effect
measurements, we deposited the diamond, placing the Sb plate near the filament,
where Sb was vaporized by the heat from the hot filament. The thicknesses of the
undoped and the Sb-involved diamond films were about 1.4 and 2.0 μ m respectively.
After rinsing the diamond surface with $CrO_3 + H_2SO_4$ solution, gold dot electrodes (0.5
mm^2) were made on the diamond surface to make an Au/diamond/Si MIS structure.
In order to make clear the impurity diffusion in the substrate, the silicon substrate with
no pre-treatment by the diamond powder was kept in the CVD chamber and underwent
the same deposition process. The C-V characteristics were measured by forming Au
electrodes on them.

3. Results and Discussion

Fig. 1 shows the bias voltage dependence of the dielectric constant (ε_s) of the diamond films which are made by two conditions; without doping and with Sb-vapor involved. The films were removed from the Si substrates and the Au dots were deposited on the rough surface and opposite electrodes were formed on the smooth surface by silver paste. The ε_s of the undoped diamond film is 5.3, which is similar to that reported previously[2]. The ε_s of Sb-involved has strong measurement-frequency and bias-voltage dependence. It is more than 10 times larger than the undoped one. This result indicates that the Sb atoms involved in the diamond film is free and easily moving. The C-V characteristics of MIS structure formed on the n-type Si is shown in Fig. 2. The capacitance shows the measurement-frequency dependence in the high bias-voltage region, which is due to the ε_s of the diamond film. It shows that the interface between Si and the deposited diamond is stable enough to hold the shift of the threshold voltage constant. From the threshold voltage measured from the ideal one and the ε_s obtained in Fig. 1, the surface-state density is calculated to be $7 \cdot 10^{11}/cm^2$, which is a good number when we consider the deposition temperature of the diamond growth. The C-V characteristics of MIS structure depend on the type of the substrate, which is shown in Fig. 3. The capacitances shown in Fig. 3 are obtained at the measurement frequency of 100 kHz and at the same diamond thickness. As is seen in Fig. 3, the threshold voltage of the n-type Si substrate is 20 V and that of the p-type Si is -23 V. Usually there are three mechanisms to explain the shift of the threshold-voltage from the ideal one. One is the trap states in the insulator (diamond) film. However, this is not possible for the result obtained in Fig. 3 because the ε_s of the undoped diamond film has no bias voltage dependence.

Fig. 1. The bias-voltage dependence of the dielectric constant of the diamond film.
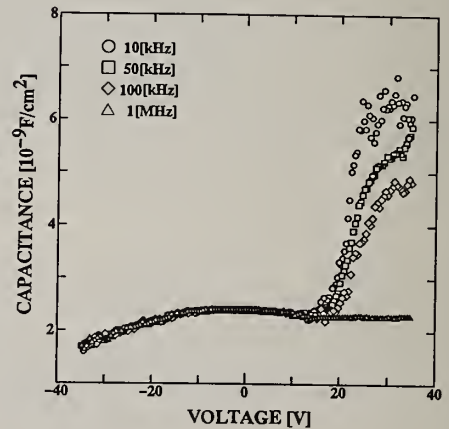
Fig. 2. The C-V characteristics of MIS structure formed on the n-type Si substrate.

The second is the existence of the surface trap-states in the interface. The type of the trap state depends on the deposition process and the deposited material, and it does not depend on the type of the substrate. The third mechanism is the generation of trap states in the substrate. If the substrate gets heat damage or some impurities migrate into the substrate during the diamond deposition, the surface condition changes and we may see the C-V characteristics as shown in Fig. 3. In this case more precise experi-

ments are necessary to explain the substrate dependence.

To make clear the effect of the heat damage or the impurity migration into the substrate, we made an MIS structure with the diamond deposited by adding Sb vapor in the reaction gas. The C-V characteristics of the MIS structure on the p-type Si are shown in Fig. 4. There are two capacitance maxima in Fig. 4 and they have strong frequency dependence. The capacitance becomes almost zero near the zero bias-voltage. The bias-voltages which give the maximum capacitances do not depend on the frequencies and the voltage in the minus bias is 5 V larger than that in the plus bias. This feature is different from what is observed in Fig. 2. The origin of the two maxima in C-V characteristics is in the diffusion of the Sb atoms into the Si substrate. To make clear the diffusion of the Sb atom into the Si substrate during the diamond deposition, C-V measurements of the Si substrates with no diamond film were carried out, and the results are shown in Fig. 5. The substrates used in this experiment were given no diamond-powder treatment and no diamond growth was observed. In Fig. 5 the C-V characteristics obtained using n- and p-type Si substrates are combined. As is seen in Fig. 5, the capacitance has the maximum at -7 V for the p-type and 5 V for the n-type Si substrates and we can see close resemblance between Figs. 4 and 5. It is obvious that the substrate which underwent the deposition process has a highly resistive layer on the surface and it shows MIS characteristics without diamond on it. From the capacitance obtained at large bias-voltage, the thickness of the highly resistive layer is estimated to be 0.8 µm for the n-type and 0.2 µm for the p-type substrates. The double peaks observed in Fig. 4 are explained by the results obtained in Fig. 5; that is, the Sb atoms diffuse into the p-type substrate and produce an n-type high-resistance layer on the surface, whereas the Sb atoms in the n-type substrate produce a high-resistance n-type layer. In this case in the positive bias-voltage region in Fig. 4, the MIS structure is made of the Metal/diamond/n-type Si layer and the C-V characteristics are similar to what is observed
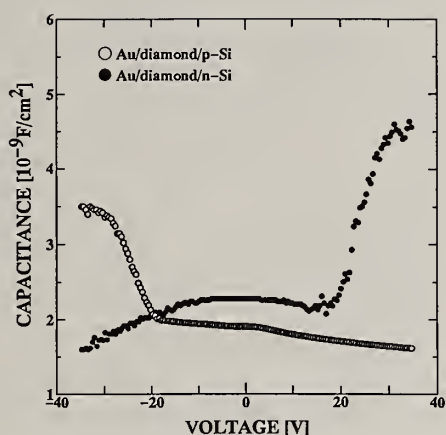
Fig. 3. The substrate-type dependence of the C-V characteristics of the MIS structure formed on Si substrates. Measurement-frequency is 100 kHz.
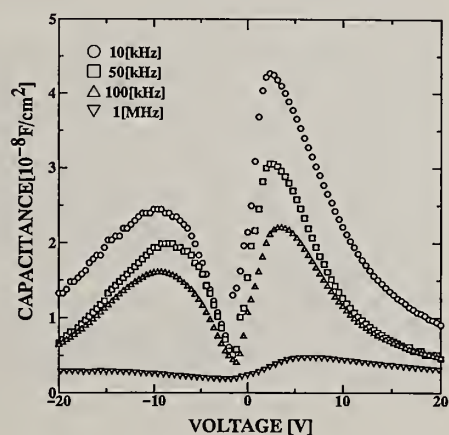
Fig. 4. The C-V characteristics of the MIS structure on the p-type Si with the diamond deposited by adding Sb vapor in the reaction gas.

in Fig. 5. On the contrary in the negative bias-voltage region, the n-type Si layer on the surface of the p-type substrate is in a depletion condition and works as an insulator layer. Therefore the bias-voltage which gives the maximum capacitance should be larger in magnitude in Fig. 4 than that observed in Fig. 5. These features are reproduced in Fig. 6 by the use of the model MIS structures given in the insets of Fig. 6 and the capacitances given in Fig. 5. In the calculation shown in Fig. 6, the shift of the capacitance peak in the negative bias-voltage region is reproduced by assuming the thickness of the n-type layer on the p-type substrate to be 0.2 μm (this corresponds to the -3.4 V shift), which is what we obtained in Fig. 5.

From the above measurements, we concluded as follows:
(a) The interface of diamond/silicon does not suffer the heat damage from the hot filament and the diamond works as a good insulator because the interface-trapped charge is of the order of 10^{11} cm^{-2} and its C-V curve has good reproductivity.
(b) A highly resistive layer is formed under the surface of the silicon. This layer is considered to be made by the heat damage and has less impurity.
(c) When Sb is introduced into the reaction gas, the dielectric constant of diamond increases to be about 30 times larger than that of the natural one and shows strong frequency dependence.
(d) The diffusion of Sb into the silicon substrate is observed. The diffused Sb forms n-type Si under the surface and makes an n-p junction in p-type silicon.

Fig. 5. The C-V characteristics obtained using n- and p-type Si substrates with no diamond-powder treatment.
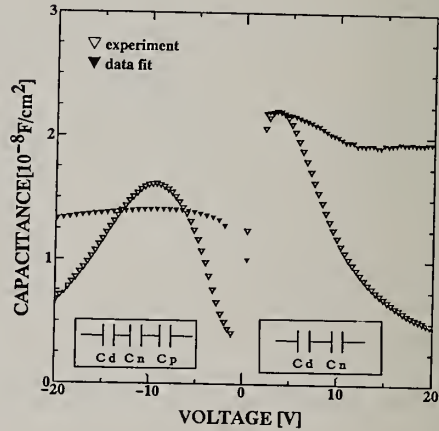
Fig. 6. The comparison with the data obtained in Fig. 4 and the calculation based on the circuits given in the insets of the figure.

4. References

1. S. Matsumoto, Y. Sato, M. Tsutsumi, and N. Setaka, J. Mater. Sci., **17** (1982) 3106.
2. M. W. Geis, Encyclopedia of Applied Physics **5** (1993) 1.

CHARACTERIZATION OF DIAMOND FILMS GROWN ON AlN / SILICON SUBSTRATES AND OF HETEROSTRUCTURES WITH SUCH FILMS.

I.G. Teremetskaya[1], V.P. Varnin[1], V.I. Polyakov[2] , A.V. Khomich[2] , P.I. Perov[2] , N.M.Rossukanyi[2] , A.I.Rukovishnikov[2], A.F.Belyanin[3] and G.Popovici[4]

[1] Institute of Physical Chemistry, RAS,117915 Moscow, RUSSIA
[2] Institute of Radio Engineering & Electronics, RAS, Moscow, RUSSIA
[3] Central Research Technological Institute, 4 Iv.Franko str., 121355 Moscow, RUSSIA
[4] Rockford Diamond Technology, 501 S. Sixth Street, Champain, IL 61820-5579.

Key words: Boron doped diamond films, AlN, photoresponse, optical properties

Abstract

Undoped and boron doped diamond films were grown on AlN coated Si substrates using the HF CVD technique. Optical and electrical characteristics of the films and the structures with such films were measured and analysed.

1. Introduction

The deposition of thin diamond films on foreign substrates is one of the most essential technique for realizing diamond-based electronic and optoelectronic devices. AlN is also a wide gap semiconductor which, unlike diamond, can be doped easily to give an n-type conductivity. That makes the heterostructures comprising of diamond and AlN films to be very interesting for applications in electronics and optoelectronics. However, there are no works, to our knowledge, on growth and characterization of the diamond films on AlN. In this work, AlN films doped with different metals were grown on Si substrates, and undoped or boron doped diamond films were grown on such structures and on Si and W substrates in the same process for independent characterization of the film alone. Optical and electrical characteristics of the diamond films were measured, and photoelectric characteristics of the heterostructures were studied.

2. Experimental

AlN films about 2 μm thick were grown on Si substrates by the magnetron reactive sputtering Al or ceramic AlN+Al targets in an Ar-N_2 gas mixture. Such doping

components as Si, Cu, Zn, Gd, Y were added in the target, or the composite targets were used. The films consisted mainly of a crystalline phase, were highly textured, with <0001> axis normal to the substrate and crystallite sizes around 40-60 nm. At high dopant concentrations (up to 2 at.%), the concentration of the crystalline phase decreased down to 60-90%. Diamond films (undoped and B-doped) were grown on above said substrates by HF CVD from gas mixture of hydrogen with methane, acetone, or both. For optical measurements, windows were etched through the Si substrate and AlN layer for some samples. For electrical and photoelectrical measurements, semitransparent Ti or Ni electrodes were deposited on the film.

3. Results and discussions

Optical properties. To characterize diamond films grown on AlN/Si substrates, UV-VIS and IR spectra have been taken between 190 and 900 nm and between 2.5 and 50 μm, correspondingly. IR spectra of B-doped films (Fig. 1) were characteristic to type II*b* diamonds with a series of relatively sharp zero-phonon lines and the B-induced one-phonon band at 1280 cm^{-1}. These bands appear on the background of a photoionization continuum which extents from the IR into the visible part of the spectrum, producing the characteristic blue coloration of B-doped diamonds. The
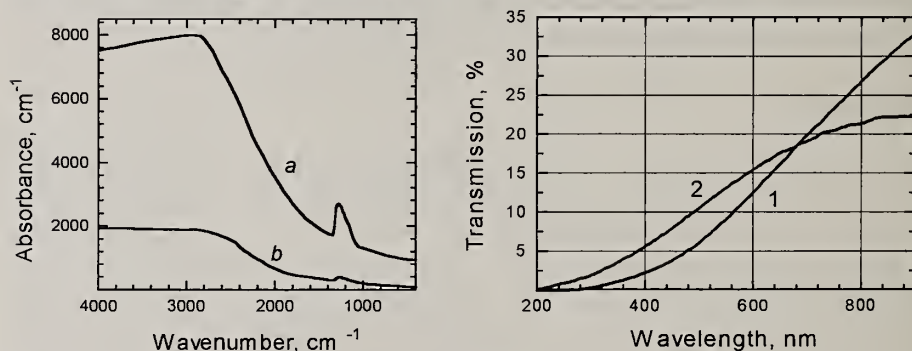
Fig. 1. IR spectra of B-doped diamond films with $N_B = 1.9*10^{20}$ cm^{-3} (*a*) and $2.2*10^{19}$ cm^{-3} (*b*); UV-Vis transmission spectra of undoped 5 μm diamond film (1) and of 1.4 μm boron doped film (2).

first excited state transition of the boron acceptor near 2460 cm^{-1} and the unresolved second and third excited transitions at 2800 cm^{-1} were detected in the IR spectra of our films with low and intermediate uncompensated boron acceptor concentrations (N_B). These bands are broader than the corresponding peaks in single crystals, because of much higher boron doping level in our films than in typical natural semiconductor diamond crystals. It was shown [1], that at high N_B (higher than 10^{19} cm^{-3}), zero-phonon lines had been broadened out into the photoionization continuum due to the wave function overlapping. The value of N_B can be determined quantitatively by measuring the integrated area underneath the peak at 2802 cm^{-1}

[2] or absorption coefficient in the maximum of B-induced one-phonon band around 1280 cm^{-1}[3]. Janssen showed [4], that for homoepitaxial B-doped diamond films at high B concentration, the first method is not valid and the linear relationship between N_B and the area of the above mentioned peak does not hold any longer. Therefore, N_B was estimated in our work from the amplitude of 1280 cm^{-1} band and varied in the film investigated from $5*10^{18}$ to $3*10^{20}$ per cm^{-3}.

The photo-ionization continuum determined the transmittance spectra of B-doped films in the long wavelength part of UV-VIS transmission spectra (Fig. 1), while the indirect diamond bandgap was observed as a sharp increase in the optical density spectra near 224 nm in the UV. The extra near-bandgap absorption in undoped diamond films we attribute mainly to nitrogen impurities, the source of which may be AlN substrate. This assumption is confirmed by the well resolved one-phonon IR band in undoped films, which is characteristic to Ia- and Ib-type diamonds. The surface roughness and the light scattering from the top surface of diamond films grown on AlN was rather weak. The values of surface roughness (derived from the optical spectra) were 1.5-2 times lower for diamond/AlN structures than for diamond films, grown on a preceded silicon substrates in the same growth process.

Electrical properties. The current-voltage (I-V), capacitance-voltage (C-V) characteristics, isothermal Q-DLTS spectra [5], and kinetics of the photoresponse of the Ti (Ni) / diamond / AlN / Si structures were measured. The I-V and C-V characteristics were measured in the frequency range from 1 Hz to 250 kHz and were strongly dependent on the test signal frequency, evidently due to the presence of trapping centers in the bulk of the diamond film and at the interfaces. The noncompensated acceptor concentration N_a-N_d values were estimated from the C-V characteristics measured at frequencies about 1 kHz with the pulse methods which allowed to avoid the bias voltage screening effects. At such frequencies, the bulk resistance influence is excluded [6], so the $1/C^2$ plot gives N_a-N_d. For different samples, the concentrations 10^{16} to $5*10^{17}$ cm^{-3} were obtained. One can see that these values are much smaller than to N_B obtained from the IR spectra. These observations might be understood if one suggests that acceptor recharging does not follow the test signal, either wise smaller N_a-N_d values are probable near the surface of the diamond film. The first reason is excluded taking into account the Q-DLTS results (see below). Smaller concentrations near the surface might be due to the diamond film interaction with the electrode material [7] or some other reason. It should be mentioned that C-V measurement results were related only to the near surface part of the film (depletion layer), while optical measurements give the amount of the noncompensated boron in all the bulk of the film.

Charge-based DLTS spectra [5] were measured at room temperature for the structures M/Diamond/AlN/Si, M/Diamond/Si, and M/Diamond/Tungsten, where M was Ti or Ni. In this technique, the sample was first biased in forward direction during the time

t_1 to charge the deep levels, and after that the discharge of the levels was analyzed to get the deep level parameters. It was found that DLTS spectra in the main peak region were strongly dependent on t_1 for small values but became unchanged at $t_1 > 10^{-3}$ c, as is shown in Fig. 2. One can see that at time intervals 10^{-3} c and larger the most of the centers fully recharged. Therefore the concentration which was obtained from the C-V characteristics measured at 1 kHz, was defined by the recharging of the centers which define the DLTS spectra Fig. 2. These centers are the most probable related to the boron acceptors in the diamond films.
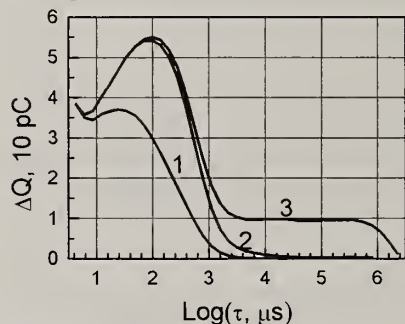
Fig. 2. Q-DLTS spectra of Ti/Diamond/ AlN/Si structure taken at t_1=0.1(1), 1(2), and 10 (3) ms.
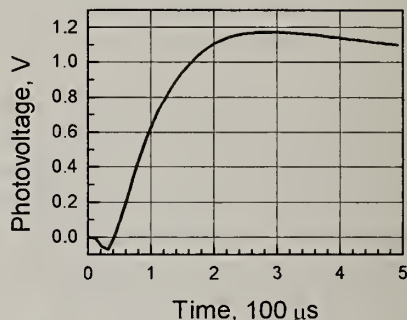
Fig. 3. Photoresponse of the structure as in Fig.2 at a flash lamp illumination.

To estimate the characteristics of the Diamond/AlN/Si heterostructures as possible wide band gap photovoltaics, the open circuit photoresponse was measured at high illumination intensities. It was found that the amplitude of the photovoltage depended on the type and concentration of impurities in AlN and CVD diamond film and, also, from bulk and interface trapping centers. The highest photovoltage exceeding 1.1 V was observed for structures with B-doped diamond films, grown on Zn-doped AlN films with Ti or Ni top electrodes, see Fig 3.

References

1. A.T.Collins, P.J.Dean, E.C.Lightsowlers, W.F.Sherman, *Phys. Rev.* **140** (1965) A4
2. A.T. Collins, A.W.S. Williams, *J. Phys. C: Solid State Phys.*, **4** (1971), p.1789
3. G. Davies, *Chem. Phys. Carbon*, **13** (1977), p.1
4. G.Janssen, W.J.P. van Enckervort, W.Vollenberg, L.J.Gilling, *Diamond and Related Materials*, **1** (1992) p.789
5. V.I.Polyakov, P.I.Perov, A.I.Rukovishnikov, O.N.Ermakova, A.L.Aleksandrov, B.G.Ignatov, Mikroelektronika **16** (1987) p.326 - 333.
6. V.Venkatesan, K.Das, J.A. von Windheim, M.W.Geis, *Appl. Phys. Lett.* **62** (1993), p.1065-1067
7. T.Kobayashi, G.R.Hou, T.Maki, S.Shikama, *Jpn. J.Appl.Phys.* **32** (1993) L 1588

ANALYSIS OF THE SURFACE STRUCTURE OF HFCVD DIAMOND FILMS

Prabhjot Mehta[1], R.E. Clausing[2], L. Heatherly[2], T. Thundat[2], and C.S. Feigerle[1]

[1]Dept. of Chemistry, University of Tennessee, Knoxville, TN 37996-1600
[2]Oak Ridge National Laboratory, PO Box 2008, Oak Ridge, TN 37831-6093

Key words : AFM, diamond, HFCVD, morphology, SEM.

Abstract

Structure analysis was carried out on various surface features of diamond films using scanning electron microscopy (SEM) and atomic force microscopy (AFM). The films were grown via hot filament assisted chemical vapor deposition (HFCVD) in methane and hydrogen gas mixtures. We investigated the surfaces of films grown under parameters selected to produce certain textures or surface features such as penetration twins or hopper shaped faces. The SEM images of these films show that the {100} planes are usually flatter than the {111}. The {111} planes show interesting growth features. The "hopper" shaped structures were imaged in the tapping mode of the AFM, and the angles between planes and their orientations have been determined. These AFM and SEM images are presented with quantitative analyses of the exposed surfaces. Detailed quantitative information will be useful in understanding the growth of these films.

1. Introduction

Diamond has been of great interest due to its extreme properties, which can be exploited for various applications [1]. Chemical vapor deposition of diamond has tremendously increased the applications of diamond films in various fields. The growth mechanisms and the processes of nucleation are quite complex, and ideas about them continue to be developed [2-4]. All mechanisms proposed so far recognize the important link between growth processes and surface morphology, however, relatively little has been done to relate observed morphology and growth features to growth mechanisms.

SEM images reveal the surface, however they do not provide quantitative information such as the identification of planes, etc. Transmission electron microscopy (TEM) is a relatively difficult technique, especially when used on diamond; the hardest material. Recent advances in scanning probe microscopy holds promise, however, that field also has its set of difficulties. Scanning tunneling microscopy (STM) is difficult on diamond due to its insulating properties. Doping the films with boron has made acquiring STM images easier [5]. However, for diamond which is free from impurities, AFM seems to be better suited even though atomic resolution is almost impossible to achieve. Numerous papers have been published on STM and AFM of the surface of diamond films, but they do not include much quantitative analysis.

Everson et al [6] have reported on indexing the faces and orientations of the sloping triangular defects appearing on the {100} surface.

In this paper we report on some of the surface features of diamond films as seen in SEM and further investigated using AFM in the tapping mode. Quantitative analysis was done on the AFM images and their results and implications are presented here.

2. Experiment

The films were grown in a hot filament assisted chemical vapor deposition (HFCVD) chamber at a pressure of ~40 Torr. A carburized tungsten wire filament was used in the quartz growth chamber. The feed gas mixture was composed of 1% methane in hydrogen, and the flow rate was 50 sccm. Films were grown on Si(001) wafers, which were treated first by scratching with diamond paste and next by rinsing with acetone and methanol in an ultrasonic bath. The filament and substrate temperatures used were 2120°C and 1050°C respectively, which were measured using an optical pyrometer without any corrections for the emissivity or reflections. The substrate was positioned ~10mm from the filament. The films were grown for 16 hours.

The films were imaged using a Hitachi S-800 SEM, and the geometry of the various features were analyzed quantitatively using a Digital Instruments Nanoprobe III AFM to identify the orientations of the surface facets. The tapping mode of the AFM was used to obtain images of the surfaces of these films, which were then analyzed using the Nanoscope III software program . All angles were measured from unprocessed images. The AFM was operated in air at room temperature. For the AFM data, commercially available microfabricated silicon cantilevers were used with a spring constant of ~35N/m..

3. Results

Figure 1 shows the representative SEM image of a film containing crystallites with hopper shaped structures. Planes with 3-fold and 4-fold symmetry are easily identified as the {111} and {100} planes, and these planes are oriented such that the polycrystalline film appears to be <110> oriented. The growth rate was ~1.28μ/hr, and the ratio of the growth rate in the <100> to that in the <111> was ~0.87 (α=1.5). The {100} planes appear flatter than the {111} planes. However, in the samples of interest, indented hopper shaped features are present where the {111} planes would normally be. These features indicate that planes with higher indices than the usual {100} and {111} are forming.

AFM images of these and similar samples have been recorded and their surface structure analyzed. The angles between planes were measured, and based on these angles, the planes have been indexed. The identification of these planes, we believe, will be useful in understanding the mechanisms acting during the growth of these films. The angles between a {100} plane and one of the adjacent planes inside the hopper (these planes sharing a common [110] direction) had an average value of 68.6°; and that between {100} and another one of the planes inside the hopper (these also sharing a common [110] direction) was found to be 75.6°. These indicate that the adjacent planes are likely of the families of {221} and {331} respectively. Table I shows a full set of measurements and calculated values. The table is arranged into 3 groups of angles, those between one of the {100} and its adjacent hopper plane, those
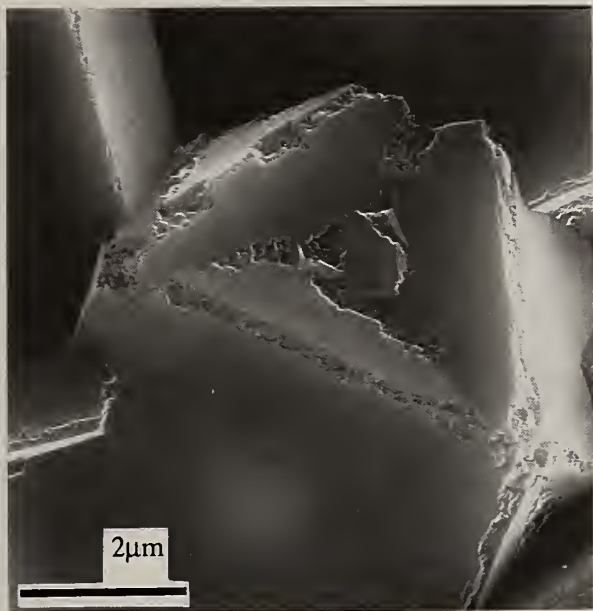
Fig. 1. An electron micrograph of a (111) face. The <110> edges are seen to be broken. (100) faces appear to be flat. The growth rate on these films was ~1.28 μ/hr.

Planes	Calculated angle between the planes (deg.)	Average of measured angles (deg.)	Difference between avg. and calculated (deg.)	Standard Deviation (deg.)
(100)(122)	70.53	68.6	1.9	1.46
(010)(313)	76.74	75.6	1.1	3.89
(001)(221)	70.53	67.5	3.0	1.76
(122)(313)	32.73	29.4	3.3	4.04
(122)(221)	27.26	23.9	3.4	0.95
(221)(313)	32.73	25.5	7.2	2.06
(100)(313)	46.51	42.8	3.7	2.02
(100)(221)	48.19	48.0	0.2	2.88
(010)(122)	48.19	53.1	-4.8	3.31
(010)(221)	48.19	52.0	-3.8	2.22
(001)(122)	48.19	51.3	-3.1	2.28
(001)(313)	46.50	46.6	-0.1	1.88

Table I. The analysis of the data taken for the identification of the planes.
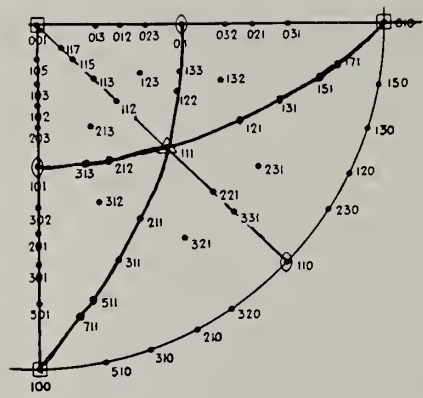
Fig. 2. The standard (001) projection of a cubic crystal. Table I. Shows the analysis of the data taken for the identification of the planes.
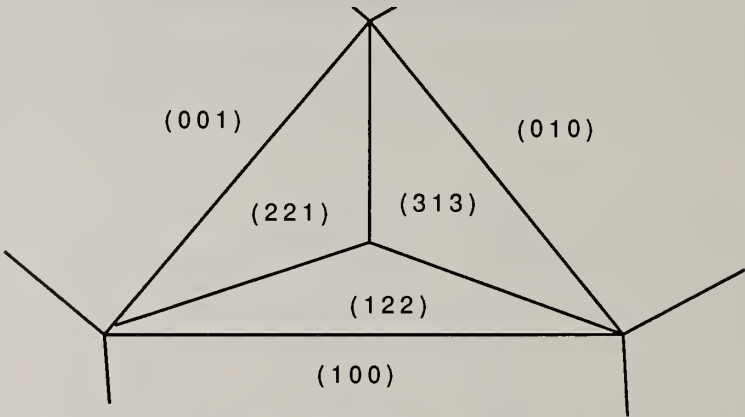
Fig. 3. A schematic of a hopper shaped face. The faces have been indexed as suggested by our calculations and observations of the angles that these faces make with each other are presented in Table 1.

between two adjacent hopper planes, and those between one of the {100} and the other two non-adjacent hopper planes. The angles being reported have been averaged for different sets of same planes seen on the same or on a different image. For each set, the measurements were repeated about ten times. Table I shows the average and the standard deviations of the angles measured as well as the calculated values. The angles between some of the {100} planes were also measured, to check the validity of the measured angles. The average value measured was 90.7°. Sources of error in these measurements could be from the piezo calibration and thermal drift. An error of ~0.5 percent in the z-piezo calibration approximates to ~3° in the angle measurements.

4. Discussion

The planes were indexed by comparison of the measured angles with those obtained from the standard (001) projection with the poles of the hopper facets identified as shown in fig. 2. The angle between the (100) and one of the adjacent planes inside the hopper was measured to have an average value of 68.6° with standard deviation 1.46°. The closest match seems to be the 70.53° for the (122) plane. The 75.6° with standard deviation 3.89° corresponds best with the 76.74° for the angle between (313) and the (010) plane. The additional angles measured between these higher index planes confirm this identification.

The presence of near {221} and {331} faces inside the hopper suggests a growth mechanism involving steps [7] nucleated at an outside edge and proceeding inward into the hopper. Such stepwise growth would lead to planes of the type {221}, {331} etc. depending on the relationships between nucleation of steps and their propagation over the underlying {111} plane. Figure 3 is a diagram showing the relationship of the planes in the hopper to the surrounding {100} planes and corresponds to those shown in fig. 1 and the angles listed in Table I.

We believe quantitative crystallographic information such as that presented here can be used to suggest and test models of growth mechanisms, especially when combined with parametric growth studies.

5. Acknowledgments

6. References

1. J. C. Angus and C. C. Hayman, Science **241**, 913 (1988).
2. M. Frenklach and K. E. Spear, J. Mater. Res. **3,** 133 (1988).
3. S. J. Harris, Appl. Phys. Lett. **56**, 2298 (1990).
4. M. Tsuda, M. Nakajima, and S. Oikawa, J. Am. Chem. Soc. **108**, 5780 (1986).
5. T. J. Kreutz, R. E. Clausing, L. Heatherly,jr., R. J. Warmack, T. Thundat, C. S. Feigerle, and K. Wandelt; J. Phys. B. (in press).
6. M. P. Everson, M. A. Tamor, and D. Scholl, B. R. Stoner, S. R. Sahaida, and J. P. Bade, J. Appl. Phys. 75(1), 169 (1994).
7. W.K. Burton, N. Cabrera, F.C. Frank, Philosoph. Trans. R. Soc. London A **243**, 299 (1951).

Applications of Diamond Films and Related Materials: Third International Conference, 1995
Editors: A. Feldman, Y. Tzeng, W. A. Yarbrough, M. Yoshikawa, and M. Murakawa

479

ELECTRICAL AND PHOTOELECTRICAL PROPERTIES OF HETEROSTRUCTURES BASED ON NANOCRYSTALLINE DIAMOND FILMS

V.I. Polyakov ,N.M.Rossukanyi[1], A.I.Rukovishnikov[1], A.V. Khomich[1], P.I. Perov[1], S.M. Pimenov[2], and V.I.Konov[2]

[1] Institute of Radio Engineering & Electronics, RAS, Moscow, RUSSIA
[2] General Physics Institute, RAS , 117942 Moscow, RUSSIA

Keywords: nanocrystalline diamond films, electrical and photoelectrical properties

Abstract

Nanocrystalline diamond films were grown on Si substrates and their electrical and photoelectrical characteristics were measured as dependent on the technology of the film preparation and post-deposition treatment.

1. Introduction

Thin CVD diamond films are considered as a new prospective material for different applications including optics and electronics. Smooth surface of such films is a well recognized factor for taking advantage of extreme diamond properties in these applications. In particular, for applications in electronics very thin and smooth insulating films are needed capable to widerstand high electric fields and having low trapping center concentrations. Usually, polycrystalline CVD diamond films consist of rather large grains, about 1 mm size, and the surface roughness is also large resulting in some problems when planar devices are fabricated using such films. One of the ways to overcome these drawbacks consists in preparing the diamond films with nanoscale grain sizes (nanocrystalline diamond films). In this work, nanocrystalline diamond films were prepared and their electrical and photoelectrical properties were studied as depended on the technology of the surface treatment and of the contact type and technology.

Experimental results

Nanocrystalline diamond films were grown on Si substrates from methane-hydrogen gas mixture in a DC arc plasma CVD reactor. The films were characterized by 30-50 nm grain size, low surface roughness of down to 10 nm and high microhardness of 75 - 85 GPa.

The parameters of trapping centers on structures prepared were studied by isothermal charge-based deep level transient spectroscopy (Q-DLTS). The Q-DLTS technique, described in details in [1], used cyclic bias pulses to change the charge state of the trapping centers and rate window scanning to measure the parameters of the centers. Fig. 1 shows the Q-DLTS spectra taken at room temperature from the heterostructures comprised of the nanocrystalline diamond film on Si substrate with different metal top electrodes deposited onto diamond film after the surface of the film was modified by the microwave plasma etching in hydrogen gas atmosphere or
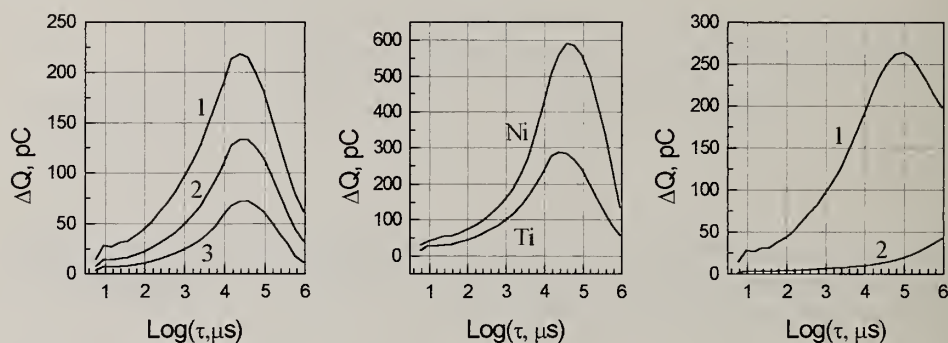
Fig. 1. Q-DLTS spectra of the structure with nanocrystalline diamond film. a (left) - non-etched film, Ti electrode, charging voltage 1 (*1*), .5(*2*) and .25 (*3*) V; b (middle) - non-etched film, charging voltage 1 V; c (right) - Ti electrode, non-etched film (*1*) and etched film (*2*).

without such a treatment. The spectra were measured at different amplitudes and durations of the charging voltage pulses. The analysis of the spectra peculiarities, the main DLTS peak shifting to smaller rate window (τ) values with increasing the pulse amplitude in particular (Fig. 1a), evidences that the trapping centers are localized near the film surface and have a continuos energy spectrum. The choice of the metal electrode and its deposition technology also influences on the interface properties and on trapping center parameters. One can see from Fig. 1 b, that peak amplitudes differs significantly for the Ni thermal evaporated electrodes and Ti ones obtained by magnetron sputtering technique. One of the reasons of such difference could be the interaction of Ni with the diamond film. Energies of the metal particles during the electrode deposition are different for thermal evaporation and magnetron sputtering techniques, so the film surface could be changed during these processes. Such surface treatment as microwave plasma etching in hydrogen atmosphere was specially applied to the film which strongly modified the surface properties. The effect of the etching appeared as a drastical decrease in the trapping center concentrations in the whole rate window range used in this work, as it is seen from Fig. 1 c. The treatment mentioned above proved to be very effective in obtaining

diamond films which showed small leakage currents and low frequency dispersion of C-V characteristics. Fig. 2 demonstrates current-voltage characteristics of the Ti/Diamond/Si and Ni/Diamond/Si structures fabricated with films before (a) and after (b) microwave plasma etching. It is seen that such treatment results in very good insulating properties of the film, especially with Ti electrodes.
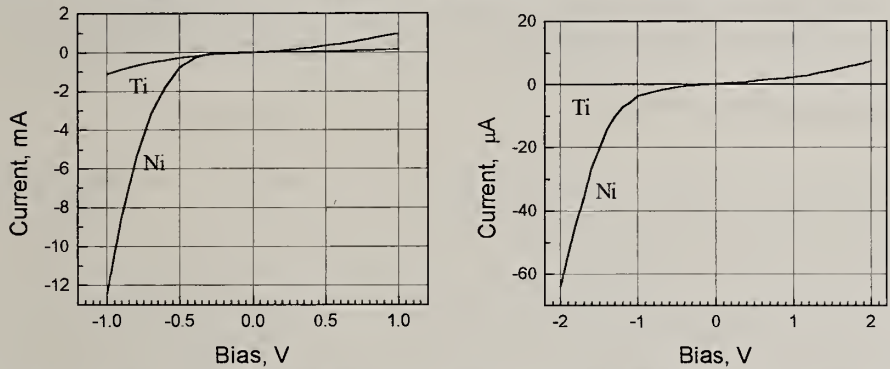
Fig. 2. Current-voltage characteristics of the structures made with non-etched *a* (left) and etched *b* (right) nanocrystalline diamond films.

Photoelectric characteristics of the structures fabricated were measured at different conditions. The open circuit photovoltage was highly dependent on the bias voltage changing its amplitude and even sign at definite biases, see Fig.3. For this sample, the diamond film was grown on the highly doped silicon substrate, so the voltage applied
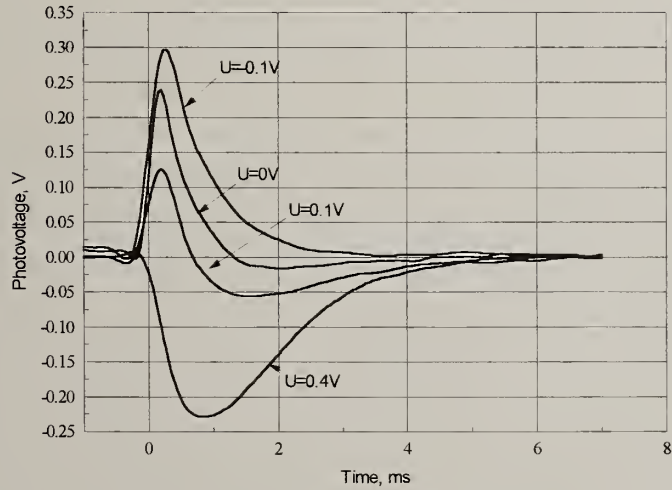
Fig. 3. Photoresponse of the structure with nanocrystalline diamond film with semitransparent Ti top electrode.

to the structure dropped mainly on diamond film. Therefore, the photoresponse observed was connected with the free carrier photogeneration in the diamond film, and the amplitude and sign of the photovoltage was defined by the direction and strength of the electric field in the diamond film. The film treatment in microwave plasma resulted in increased photovoltages. Using the excimer laser (193 nm) excitation, the photovoltage values of .4 V were obtained. These results demonstrate that it is possible to fabricate UV photosensors using nanocrystalline diamond films.

Reference

1. V.I.Polyakov, P.I.Perov, A.I.Rukovishnikov, O.N.Ermakova, A.L.Aleksandrov, B.G.Ignatov, Mikroelektronika **16** (1987) p.326 - 333.

PULSED POWER PROCESSING OF CVD DIAMOND

K. Tsang[1], E. Hyman[1], A. Drobot[1], and B. Lane[2]

[1]Science Applications International Corporation, McLean, Virginia 22102, USA
[2]Plasma Dynamics, Belmont, Massachusetts 20178, USA

Key words: chemical vapor deposition, diamond, plasma, pulsed microwave source

Abstract

The efficiency and cost effectiveness of plasma enhanced CVD has been observed experimentally to scale with microwave power. The microwave energy couples directly to the electron plasma and from the electrons to the background gas. With hydrogen as the background gas the dominant electron processes at typical operating parameters are (1) vibrational excitation, which couples to the translational modes and heats the gas, and (2) electron impact dissociation, which generates the atomic hydrogen needed for the deposition of high quality diamond. Using a first principles Boltzmann solver to determine the electron energy distribution, we find that the primary parameter that determines which process predominates is the electric field strength. By pulsing the microwave field it is possible to substantially enhance hydrogen atom production relative to a cw process of the same average power output, resulting in a more efficient, high quality deposition and lower gas temperature.

1. Introduction

Both the rate of incorporation of carbon into the diamond lattice and the quality of the deposited diamond (absence of defects) increase with the atomic hydrogen density at the substrate surface [1]. We consider a technique to maximize the production of hydrogen atoms in a microwave reactor while maintaining modest power use.

In a microwave plasma enhanced chemical vapor deposition (CVD) diamond reactor the microwave energy couples directly to the plasma electrons and the electron energy is subsequently transferred to the background gas. The electron loss channels include momentum transfer, rotational excitation, vibrational excitation, dissociative attachment, dissociation, electronic excitation, and ionization. At typical operating parameters and with hydrogen as the background gas the dominant loss processes are vibrational excitation, from which energy is gradually transferred to translational modes and results in heating of the gas, and electron impact dissociation, which both heats the gas and produces the hydrogen atoms required for the efficient deposition of diamond on the substrate. The electron energy distribution is highly non thermal with electron dissociation determined by the high energy tail of the electron distribution. In the usual cw mode of operation, the plasma heating, predominately through the vibrational channel, causes the gas to attain a temperature above 3000 K by about 1 ms. At that temperature hydrogen dissociation becomes dominantly a thermal process; dissociation by electrons becomes negligible. Because thermal dissociation is a cooling process the gas reaches a steady state determined by the vibrational heating and the thermal

dissociation cooling. The exact steady state conditions are influenced also by thermal and mass diffusion and hence the geometrical configuration of the reactor and the reactor walls. Thus, in the steady state electron impact dissociation is unimportant as a source of hydrogen atoms although it was critical in initiating the production of chemical radicals.

Numerical results using a first principles Boltzmann solver to determine the electron energy distribution show that the primary parameter that determines which channel is the major loss channel for the electrons is the electric field strength, E. At high field strength the average electron energy is shifted higher and electron impact dissociation is enhanced relative to vibrational excitation and gas heating. However, under cw conditions this represents a very high required microwave power. On the other hand, if the microwave source is pulsed, very high electric fields coupled with low duty factor can access the non thermal electrons to enhance hydrogen dissociation at low average power. Then hydrogen atom production will not require the high gas temperatures that induce thermal dissociation.

2. Electron Energy Distribution

The electron distribution function satisfies the Boltzmann equation. Because at the pressures we are considering, 5×10^3 pascals (40 Torr) and greater, an electron undergoes many collisions as it is heated, the distribution function is nearly isotropic and is well approximated by the zero and first order terms of a spherical expansion. The first order term represents a distortion of the distribution function in the direction of the applied field, oscillating at the microwave frequency. The equation for the spherically symmetric component of the electron distribution function is

$$\frac{1}{3}\left[\left(\frac{eE_0}{m_e}\right)^2 \frac{1}{v^2} \frac{\partial}{\partial v} \left(v^2 \frac{v_m}{v_m^2 + \omega^2} \frac{\partial F_0}{\partial v}\right) + v^2 \nabla \cdot \left(\frac{1}{v_m} \nabla F_0\right) + v \nabla \cdot \left(\mathbf{V} \frac{\partial F_0}{\partial v}\right)\right]$$

$$= L_i + L_x - \frac{2m_e}{M} \frac{1}{v^2} \frac{\partial}{\partial v} (v^3 v_m F_0)$$

where E_0 is the amplitude of the electric field, e, m_e, and v are the electron charge, mass, and velocity respectively, v_m is the electron momentum transfer frequency, F_0 is the zero order approximation to the distribution function, V is the bulk fluid velocity, M is the neutral mass, and L_i and L_x are the inelastic loss terms that affect the distribution function respectively via ionization and excitation of rotational, vibrational, dissociative, and electronic levels. The first term on the left represents the electron velocity diffusion due to the cumulative affect of many small angle scatterings of the electron induced by the oscillating electric field. The next two terms give the affect of the divergence of the diffusive and convective fluxes respectively. In this calculation convective effects have been neglected and a simple approximation for diffusion has been incorporated. The last term on the right gives the energy loss due to elastic collisions. We solve the Boltzmann equation using a finite differencing scheme in velocity and using fitted cross sections for the inelastic loss processes [2]. Note, that because we do not assume a Maxwell-Boltzmann electron distribution we do not determine an electron temperature.

3. Simulation Results

The results we present are from one-pont simulations described in detail in [2] and provide an estimate of the conditions at the center of the plasma. An average power density is used based on the total microwave power of the reactor and the experimentally observed size of the plasma ball. The hydrogen atom density at the substrate will, of course, be lower than its value at the center of the plasma. How much lower will depend on the configuration of the reactor and on wall and substrate conditions but it is reasonable to assume that, other conditions being the same, a higher value produced in the plasma will give rise to a higher value at the substrate.
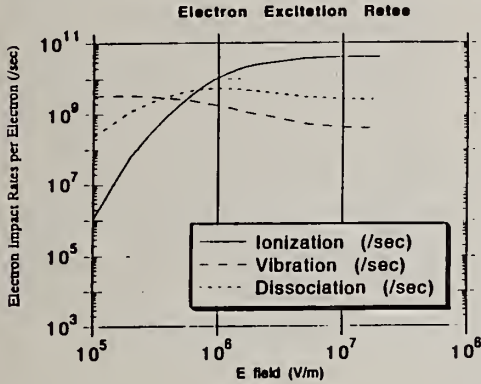
Fig. 1 Electron impact excitation rates at 1.33×10^4 pascals (100 Torr) per electron. Included are ionization, dissociation, and vibration.

Fig. 1 shows the dependence of the electron impact ionization, dissociation, and vibrational excitation rates per electron (s^{-1}) on the electric field at a pressure of 1.33×10^4 pascals (100 Torr). We see that as the E field increases from $\sim 10^5$ V/m to 10^6 V/m and above, the vibrational rate and the dissociation rate exchange their relative positions of dominance. As an example, a cw power density of 5 W/cm^3 at 1.33×10^4 pascals (100 Torr) corresponds to an E field near the center of the plasma of 7×10^4 V/m at 2 ms. Note that as the E field rises above $\sim 10^6$ V/m the rates approach asymptotic values.

Fig. 2 Fractional hydrogen dissociation ([H]/[H$_2$] number density) at 2 ms at a pressure of 1.33×10^4 pascals (100 Torr) as duty factor varies from 1 (cw) to 4×10^{-3}. Pulse length is taken to be 20 μs. Curves show results for three average power densities: 1 W/cm^{-3}, 5W/cm^{-3}, and 15 W/cm^{-3}.

Fig. 2 shows the results of simulations performed at 1.33×10^4 pascals (100 Torr) and run for 2 ms at which point near steady state conditions prevail. A pulse length of 20 μs was used and the duty factor was varied from 4×10^{-3} to 1 (cw). Each curve corresponds to a different average microwave power density: 1 W/cm^3, 5 W/cm^3, and 15 W/cm^3. A duty factor of 0.1, for example, means the microwaves were on for 2 μs out of each 20 μs. The plot shows the fractional dissociation of hydrogen at the end of each run. At 1 W/cm^3 the fractional dissociation increases by more than an order of magnitude as we progress from cw to a duty factor of 4×10^{-3}. At the higher power levels the effect is somewhat less but still impressive. The reduction in the effect is because at the higher power levels the E field at cw is already

larger (Fig. 1) so that the change in the importance of vibration and dissociation as the duty factor is decreased is less pronounced.

We have also investigated the affect of different pressures and the affect of pulse length. At lower pressures the dissociation fraction is higher for a given power density, pulse length, and duty factor. For example, at 8×10^3 pascals (60 Torr) the dissociation fraction is about twice that at 100 Torr. The affect of pulse length is not very great. For example, at 1.33×10^4 pascals (100 Torr) and 5 W/cm^3 changing the pulse length from 20 µs to 100 µs decreases the dissociation fraction at a duty factor of 4×10^{-3} by about 19%.

Finally, consider the affect on the gas temperature in the plasma. Fig. 3 shows the temperature attained and the average power required to achieve a dissociation fraction of 10^{-3} by 2 ms. All cases are for 1.33×10^4 pascals (100 Torr) and a 20 µs pulse length. At cw the power required is ~ 25 W/cm^3 and the gas temperature reached ~ 1050 K. At a duty factor of 4×10^{-3} the power required was less than 3 W/cm^3 and the gas temperature was ~ 630 K.

Fig. 3 Average power required to attain [H]/[H$_2$] number density fraction of 10^{-3} at 2 ms assuming a pressure of 1.33×10^4 pascals (100 Torr) and a 20µs pulse length, for different duty factors, and the resulting gas temperature.

4. References

1. J. E. Butler and R. L. Woodin, "Thin Film Diamond Growth Mechanisms", Phil. Trans. R. Soc. Lond. A **342**, 209 (1993).
2. E. Hyman, K. Tsang, A. Drobot, B. Lane, J. Casey, and R. Post, "One-point Numerical Modeling of Microwave Plasma Chemical Vapor Deposition Reactors", J. Vac. Sci. Technol. A **12**, 1474 (1994).

Epitaxial Growth of B-Doped High Quality Diamond Film on cBN Surface by Chemical Vapor Deposition

G.T. Zou, C.X. Gao, T.C. Zhang, J. Yang, Z.S. Jin
State Key Lab for Superhard Materials, Jilin University
Changchun 130023, P.R.China

Key words: B-doped, cBN, CVD, diamond film, epitaxy

Abstract

B-doped high quality diamond epitaxial films have been obtained on high-pressure synthesized cBN crystals by dc glow discharge chemical vapor deposition (CVD). The deposition conditions and the orientation of cBN crystal are important to diamond oriented nucleation and epitaxial growth. The micro-Raman spectroscopy measurement indicates that the quality of the diamond film grown on cBN {100} surface is close to that of natural diamond. The scanning electron microscopy (SEM) observation shows that the epitaxial film has very smooth surface. The specific resistance of the B-doped epitaxial film is about 0.1 ohm·cm.

1. Introduction

Because of its well-known properties, diamond film has promising applications in high-temperature operating electronic device and wide band-gap laser device. Recently, the epitaxial nucleation and growth of highly oriented diamond (HOD) films on Si and SiC surfaces have been reported. [1,2] The properties of HOD films have been experimentally confirmed to be far superior to those of the traditionally produced polycrystalline diamond films.[3] Due to the large lattice mismatch between the substrate material and diamond, however, the misfit dislocations are produced at the interface between the epitaxial film and the substrate. Diamond grown is thus composed of HOD joined by small-angle grain boundaries.[4]

cBN has almost same lattice parameter and high surface energy as diamond, so it is the best substrate for diamond epitaxial growth. Diamond deposition on cBN surface had successfully achieved in 1990.[5] Recently, many works have been done in this field.[6,7] In1994, a p-n junction of p-type diamond and n-type cBN was reported by a group in japan.[8] This achievement means that the technique of high quality and large area diamond epitaxial film deposition is becoming very important. In this paper, the growth characteristics of B-doped diamond epitaxial film on cBN surface are reported and high quality diamond film is investigated.

2. Experimental

cBN crystal used as a substrate, with well defined surface and in size of ~0.5mm was synthesized by high temperature and high pressure method. It has a zinc blende type structure and its lattice constant is 0.3615nm as confirmed by x-ray diffraction. Diamond was deposited on cBN crystal in a dc glow discharge CVD system which had been reported previously.[9] The mixture of methane and hydrogen was used and the reactive pressure was 4.0kPa. During deposition process, the discharge voltage and current density were maintained at 550V and 2.0A/cm^2 respectively. The temperature of the substrate was maintained at 850°C and measured by a optical pyrometer.

Before deposition, cBN crystals were cleaned by normal chemical cleaning method. Then, they were laid on a Si wafer and put into the deposition system. The pure boron powder was used as a doping source and was put on the Si wafer beside cBN crystals. The surface morphologies of diamond epitaxial film were observed by SEM. The quality of the film was detected by micro-Raman spectroscopy with focusing point of 2.0μm and a Ar$^+$ laser at 514.5nm in wavelength was used. The specific resistance (SP) of the p-type diamond film was measured by a four-probe SP detector.

3. Results and discussion

In the experimental research, it is found that the surface morphologies of diamond on {111} face and {100} face of cBN are quite different. At the early growth stage (1 hour deposition), island-like diamond nuclei are found on cBN {111} face. The density of the island-like nuclei is about 10^{11}/cm^2.

But on cBN {100} face, no island-like nuclei are found. The surface of diamond film on cBN {100} face looks very smooth.

(a) ---- 5μm   (b)
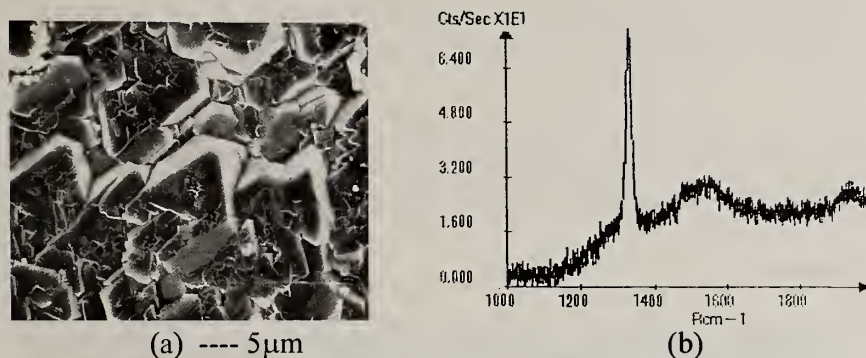
Fig.1 The surface morphology of HOD (a) and its Raman spectrum(b)

After ten hours deposition, diamond films with thickness of 15μm are obtained. On cBN {111} surface, HOD film is formed as shown in Fig.1(a). The micro-Raman spectrum of this sample is shown in Fig.1(b). Diamond peak at 1332.5cm⁻¹ has full width at half maxima (FWHM) ~8.2cm⁻¹. The broad signal at 1560cm⁻¹ and background signal indicate the presence of amorphous carbon. The FWHM and the background intensity at grain boundaries are slightly large than that at surface of diamond grain.

(a)   ---- 5μm   (b)
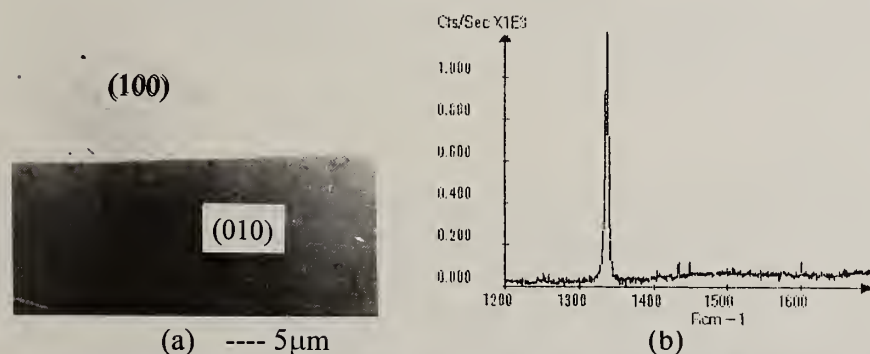
Fig.2 The SEM image of diamond film (a) and its Raman spectrum (b)

On the {100} and {010} surface of cBN, diamond film has very smooth surface and no crystal boundary is seen as shown in Fig.2(a). The micro-Raman spectrum of this sample is shown in Fig.2(b). Diamond peak at 1333.2cm⁻¹ has a FWHM ~6.9cm⁻¹ which is close to that of natural

diamond (5.2cm^{-1}). The broad signal at 1560 is not present in this spectrum. These results indicate that the film grown on cBN {100} or {010} surface is a high quality diamond. Under the suitable deposition conditions, diamond can cover the whole surface of cBN with (100) direction and its largest smooth surface is reached about 0.5mm in diameter.

The doping characteristics of diamond epitaxial growth on cBN surface was same as that of polycrystalline diamond growth on Si surface. The lowest specific resistance of the B-doped diamond epitaxial film is ~0.1ohm·cm.

4. Conclusions

Diamond is preferred to form a highly oriented film on cBN {111} face and to form a continuos epitaxial film on cBN{100} face. The quality of diamond grown on cBN {100} surface is significantly higher than that on cBN {111} surface. The doping property of diamond epitaxial film is same as traditional diamond film. The deposition conditions and the surface orientation of cBN surface are two important factors for preparation of high quality diamond epitaxial film with smooth surface.

5. Acknowledgements

6. References

1. X.Jiang, C.P.Kages and H.J.Fusser, Appl.Phys.Lett., 62(1993)3438
2. B.R.Stoner and J.T.Glass, Appl.Phys.Lett., 60(1992)698
3. B.R.Stoner, D.M.Malta and R.C.Glass, Appl.Phys.Lett., 62(1992)2347
4. W.Zhu, X.H.Wang and J.T.Glass, Phys.Rev.B, 47(1993)6529
5. S.Koizumi, T.Murakami, and T.Inuzuka, Appl.Phys.Lett., 57(1990)562
6. S.koizumi and T.Inuzuka, Jpn.J.Appl.Phys., 32(1993)3920
7. G.Zou and C.Gao, Advances in Diamond Sci.and Technol, (1994)p291
8. T.Tomikawa, et al, Diamond and Related Materials, 3(1994)1389
9. C.Gao, G.Zou and Z.Jin, Chin.Phys.Lett., 11(1994)185

DIAMOND ADHESION, FRICTION, AND WEAR

WEAR-RESISTANT, SELF-LUBRICATING SURFACES OF DIAMOND COATINGS

Kazuhisa Miyoshi

National Aeronautics and Space Administration, Lewis Research Center, 21000 Brookpark Road, MS 23-2, Cleveland, Ohio 44135

Abstract

In humid air and dry nitrogen, as-deposited, fine-grain diamond films and polished, coarse-grain diamond films have low steady-state coefficients of friction (<0.1) and low wear rates ($\leq 10^{-6}$ $mm^3/N \cdot m$). In an ultrahigh vacuum (10^{-7} Pa), however, they have high steady-state coefficients of friction (>0.6) and high wear rates ($\geq 10^{-4}$ $mm^3/N \cdot m$). Therefore, the use of as-deposited, fine-grain and polished, coarse-grain diamond films as wear-resistant, self-lubricating coatings must be limited to normal air or gaseous environments such as dry nitrogen. On the other hand, carbon-ion-implanted, fine-grain diamond films and nitrogen-ion-implanted, coarse-grain diamond films have low steady-state coefficients of friction (<0.1) and low wear rates ($\leq 10^{-6}$ $mm^3/N \cdot m$) in all three environments. These films can be effectively used as wear-resistant, self-lubricating coatings in an ultrahigh vacuum as well as in normal air and dry nitrogen.

1. Introduction

Diamond's excellent tribological properties make it an ideal material for many tribological applications. Its extreme hardness, high abrasion and wear resistance, low coefficient of friction, high seizure and galling resistance, good fatigue strength, high thermal conductivity, good radiation and temperature resistance, chemical and thermal inertness, high corrosion resistance, and environmental compatibility suit it to applications such as the bearings, valves, and engine parts in the harsh environment found in internal-combustion and jet engines [1,2].

However, the applications of natural and high-pressure synthetic diamonds are limited because of their small size and high cost. Also, these crystals have to be bonded to a substrate in a separate operation. This requirement, coupled with their

high cost, limits the general use of diamonds in tribological applications. On the other hand, chemically vapor-deposited (CVD) diamond offers a broader potential because size is, and eventually cost will be, less of a limitation [1]. CVD diamond is available in planar films or sheets. It opens the door to design engineering and tribology technology that can take full advantage of diamond's intrinsic properties in such areas as wear, solid lubrication, erosion, and corrosion applications.

The major drawback of CVD diamond is that its very high surface roughness and high deposition temperature restrict its applications in tribological coatings [1]. These problems must be solved before practical, reliable, and cost-effective diamond coatings become available as wear-resistant, self-lubricating barriers for many types of moving mechanical assemblies. A process must be developed that keeps the deposition temperature below 400 °C for metallic substrates such as steel, smooths the CVD diamond surface to minimize abrasion, and provides satisfactory adhesion to metallic and nonmetallic substrates, including steel and Si_3N_4.

Another drawback to CVD diamond is that its desirable properties are altered during tribological processes. The contaminant surface film adsorbed on diamond film can be removed when it repeatedly slides over the same track of counter-facing material in a vacuum. Then, a fresh, clean diamond surface contacts a clean counterfacing material, and strong bonds form between the two materials [2]. As a result, the coefficients of friction and wear rates of diamond films are considerably higher in a vacuum than in air [3]. Thus, to achieve the best performance for CVD diamond as a wear-resistant, self-lubricating barrier for many moving mechanical assemblies, we must have a good understanding of diamond, of the counterfacing material, and of the type of environment and operation.

The objective of this paper is to provide machine designers, manufacturers, tribologists, lubrication engineers, and end-users with the friction and wear properties of as-deposited, fine-grain; polished, coarse-grain; carbon-ion-implanted, fine-grain; and nitrogen-ion-implanted, coarse-grain CVD diamond films in humid air, dry nitrogen, and ultrahigh vacuum (10^{-7} Pa) environments. These properties can be considered as guides to the tribological applications of CVD diamond films. Some earlier data and experimental details on this research are given in the references [3-8].

2. CVD Diamond

2.1. As-Deposited, Fine-Grain Diamond Films

As-deposited, fine-grain diamond films were produced by microwave-plasma-enhanced CVD (Table I) and were primarily polycrystalline (Table II). Rutherford backscattering spectroscopy revealed that the diamond films consisted of carbon

Table I. Deposition Conditions for Diamond Films

	As-deposited, fine-grain diamond films	Polished, coarse-grain diamond films
Deposition technique	Microwave plasma CVD	Hot-filament CVD
Substrate	Si (100), α-SiC, Si_3N_4	Si_3N_4
Flow rate, cm^3/min		CH_4:H_2 = 1:99
$\quad CH_4$	4	
$\quad H_2$	395	
$\quad O_2$	1	
Pressure, Pa	665	----
Microwave power, kW	0.5	----
Deposition temperature, °C	860 ± 20	900
Deposition time, h	10.5 and 21	----
Thickness, nm	1000 and 800	----

Table II. Comparison of As-Deposited, Fine-Grain Diamond Films and Polished, Coarse-Grain Diamond Films Deposited on Silicon, α-SiC, and Si_3N_4

	As-deposited, fine-grain diamond films	Polished, coarse-grain diamond films
Composition	Essentially carbon, <2.5 at.% hydrogen	Essentially carbon
Microstructure	Polycrystalline	Polycrystalline
Crystal orientation	<110>	<111>
Grain size, nm	20 to 100 nm	10 000
Raman spectrum	Sharp peak centered near 1330 cm^{-1} and broad humps centered near 1320 cm^{-1} and in the 1500 to 1530 cm^{-1} range	Sharp peak centered near 1330 cm^{-1} and broad humps centered near 1320 cm^{-1} and in the 1500 to 1530 cm^{-1} range
Atom-bonding state	sp^3 and sp^2 (variable ratio, very roughly 1:1)	sp^3 and sp^2 (variable ratio)
Surface morphology	Granulated or spherulitic: spherical asperities of different sizes	Flat, polished
Surface roughness, rms, nm	6 to 37	6
X-ray photoelectron spectroscopy (XPS) spectrum	Carbon and oxygen peaks	Carbon and oxygen
C/O ratios in XPS spectrum	8 to 12	-----------------------

and some elements from the substrate material, such as silicon. From the proton recoil detection data, the hydrogen concentration was estimated to be 2.5 at.% in the fine-grain diamond films.

X-ray diffraction data revealed that the crystallites were oriented along the <110> direction. In the smooth, fine-grain diamond films, grain sizes—which were determined from the dark-field images of transmission electron microscopy— ranged from 20 to 100 nm. The lattice constants calculated from the transmission electron diffraction pattern matched well with diamond's known lattice constants [4].

When the Raman spectrum of the as-deposited, fine-grain diamond film was deconvolved, three bands characteristic of CVD diamond films were revealed: (1) a sharp band centered near 1330 cm^{-1}, (2) a broad band centered in the 1500 to 1530 cm^{-1} range, and (3) an even broader band centered near 1320 cm^{-1}. The sharp band centered near 1330 cm^{-1} is characteristic of diamond's sp^3 bonding. The two broad Raman shift bands near 1320 cm^{-1} and in the 1500 to 1530 cm^{-1} range are characteristic of the nondiamond form of carbon. They are referred to as the D band and G band, respectively. The G-band Raman shifts are attributed to the sp^2-bonded carbon, whereas the D-band Raman shifts are attributed to the disorder of the nondiamond carbon present in the diamond films [1]. The as-deposited, fine-grain diamond films contained a considerable amount of nondiamond carbon.

Scanning electron microscopy and surface profilometry revealed that in the as-deposited, smooth, fine-grain diamond films, crystallites had a granulated or spherulitic morphology. The surfaces contained spherical asperities ranging from 6 to 37 nm root mean square (rms) (Table II). X-ray photoelectron spectroscopy (XPS) spectra of the surfaces of the as-deposited, fine-grain diamond films contained oxygen, with C/O ratios ranging between 8 and 12.

2.2. Carbon-Ion-Implanted, Fine-Grain Diamond Films

Carbon ions were implanted into the as-deposited, fine-grain diamond films with an ion implanter operating at an accelerating energy of 60 keV and a current density of 50 μA/cm^2 for approximately 6 min, resulting in a dose of 1.2x10^{17} carbon ions/cm^2 (Table III). The carbon ions penetrated to a calculated mean depth of 88 nm.

XPS spectra of the surfaces of the carbon-ion-implanted, fine-grain diamond films contained oxygen—with C/O ratios ranging between 8 and 12—like those of the as-deposited diamond films. Furthermore, during XPS analysis, the carbon-ion-implanted, fine-grain diamond films were more conductive than the as-deposited diamond films. This increased conductivity indicates that carbon ion implantation

Table III. Carbon-Ion-Implanted, Fine-Grain Diamond Films and Nitrogen-Ion-Implanted, Coarse-Grain Diamond Film

	Carbon-ion-implanted, fine-grain diamond films	Nitrogen-ion-implanted, coarse-grain diamond films
Ion implantation	Carbon ions implanted at 60 keV and 50 μA/cm^2 for 6 min; a dose of 1.2×10^{17} carbon ions/cm^2	Nitrogen ions implanted at 35 keV; a dose of 5×10^{16} nitrogen ions/cm^2
Composition	Essentially carbon	Essentially carbon and nitrogen
Microstructure	Layered structure—amorphous layer on crystalline diamond	Layered structure—amorphous layer on crystalline diamond
Raman spectrum	Broad humps centered near 1320 and in the 1500 to 1530 cm^{-1} range	Broad humps centered near 1320 and in the 1500 to 1530 cm^{-1} range
Surface morphology and roughness	No significant change resulted from carbon ion implantation	No significant change resulted from nitrogen ion implantation

alters the normally insulating diamond surface to an electrically conductive carbon surface and eventually to a graphitic surface.

In the Raman spectra of the carbon-ion-implanted, fine-grain diamond films, a very broad band with a peak centered in the 1500 to 1530 cm^{-1} range and a shoulder near 1320 cm^{-1}, indicative of the amorphous, nondiamond form of carbon, was the prominent feature. The characteristic diamond peak was absent from the Raman spectra of the carbon-ion-implanted diamond films. Furthermore, transmission electron microscopy observation of cross sections of diamond films implanted by carbon ions at 160 keV revealed a layered structure containing an amorphous layer formed on the crystalline diamond layer [6]. No significant changes in surface morphology and roughness resulted from the carbon ion implantation (Table III). The surface features of the carbon-ion-implanted, fine-grain diamond films were almost the same as those of the as-deposited, fine-grain diamond films. The only morphological effect of carbon ion implantation was the rounding of edges. Carbon ion implantation on the fine-grain diamond films with a granulated or spherulitic morphology produced surfaces with somewhat blunt, rounded grains.

2.3. Polished, Coarse-Grain Diamond Films

Polished, coarse-grain diamond films were produced by hot-filament CVD (Table I). They were primarily polycrystalline (Table II), and X-ray diffraction data revealed that the crystallites were primarily oriented along the <111> direction. The grain size was approximately 10 000 nm (10 μm).

When the Raman spectrum of the polished diamond film (surface roughness, 6 nm rms) was deconvolved, three bands were revealed: (1) a sharp band centered near 1330 cm^{-1} (the sp^3 bonding of diamond), (2) a broad band centered in the 1500 to 1530 cm^{-1} range (the sp^2-bonded carbon), and (3) an even broader band centered near 1320 cm^{-1} (the disorder of the nondiamond carbon).

2.4. Nitrogen-Ion-Implanted, Coarse-Grain Diamond Film

Nitrogen ions were implanted into a polished, coarse-grain diamond film with an ion implanter operating at an accelerating energy of 35 keV, resulting in a dose of 5x10^{16} nitrogen ions/cm^2 (Table III). The nitrogen ions penetrated to a calculated mean depth of 47 nm.

The Raman spectrum of the nitrogen-ion-implanted diamond film revealed a very broad band with a peak centered in the 1500 to 1530 cm^{-1} range and a shoulder near 1320 cm^{-1}, indicative of the amorphous, nondiamond form of carbon. The characteristic diamond peak was absent from the Raman spectrum of the nitrogen-ion-implanted diamond film.

No significant changes in surface morphology and roughness resulted from nitrogen ion implantation (Table III). The surface features of the nitrogen-ion-implanted diamond film were almost the same as those of the polished diamond film.

3. Friction and Wear Properties of CVD Diamond

Figure 1 presents steady-state (equilibrium) coefficients of friction and wear rates in humid air (40 percent relative humidity), in dry nitrogen, or in an ultrahigh vacuum (10^{-7} Pa) for the as-deposited, polished, carbon-ion-implanted, and nitrogen-ion-implanted diamond films. Conditions that reduce friction, such as a particular combination of environment and material, usually reduce wear rate as well.

To be an effective wear resistant, self-lubricating material, a material must have a coefficient of friction less than 0.1 and a wear rate of 10^{-6} mm^3/N·m or less.

In humid air and in dry nitrogen, both the steady-state coefficients of friction and wear rates of as-deposited, fine-grain; polished, coarse-grain; and nitrogen-ion-implanted, coarse-grain diamond films were generally low.

In an ultrahigh vacuum, however, both the steady-state coefficients of friction and the wear rates of the as-deposited, fine-grain diamond films and of the polished, coarse-grain diamond film were high. On the other hand, the carbon-ion-implanted, fine-grain diamond films and the nitrogen-ion-implanted, coarse-grain diamond
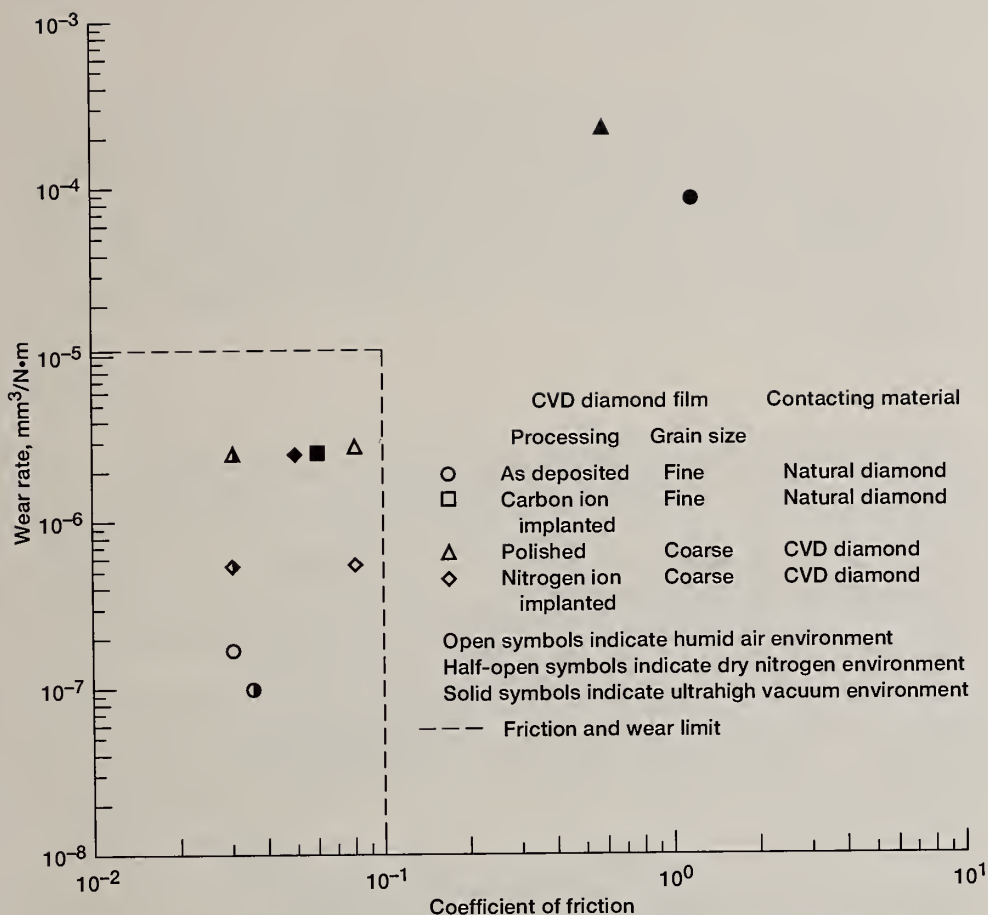
Figure 1.—Relationship between wear rate and coefficient of friction for chemically vapor-deposited (CVD) diamond films.

film had a low steady-state coefficient of friction (<0.1) and a low wear rate ($\leq 10^{-6}$ mm^3/N·m). Thus, the ion-implanted diamond films are effective wear-resistant, self-lubricating films.

4. Concluding Remarks

Both as-deposited, fine-grain diamond films and polished, coarse-grain diamond films can be effective wear-resistant, self-lubricating coatings in humid air and in dry nitrogen, but they are not effective in an ultrahigh vacuum.

Both carbon-ion-implanted, fine-grain diamond films and nitrogen-ion-implanted, coarse-grain diamond films can be effective wear-resistant, self-lubricating coatings in all three environments (i.e., humid air, dry nitrogen, and ultrahigh vacuum).

5. Acknowledgments

6. References

1. Pierson, H.O.: Handbook of Carbon, Graphite, Diamond, and Fullerenes.
Properties, Processing, and Applications. Noyes Publications: Park Ridge,
NJ, 1993.
2. Davies, G., ed.: Properties and Growth of Diamond. Inspec., Institution of
Electrical Engineers, London, UK, 1994.
3. Miyoshi, K., et al.: Friction and Wear of Plasma-Deposited Diamond Films.
J. Appl. Phys., vol. 74, no. 7, Oct. 1993, pp. 4446–4454.
4. Wu, R.L.C., et al.: Synthesis and Characterization of Fine Grain Diamond
Films. J. Appl. Phys., vol. 72, no. 1, July 1, 1992, pp. 110–116.
5. Miyoshi, K.; Wu, R.L.C.; and Garscadden, A.: Friction and Wear of Dia-
mond and Diamondlike Carbon Coatings. Surf. Coat. Technol., vol. 54/55, 1992,
pp. 428–434.
6. Wu, R.L.C., et al.: Ion-Implanted Diamond Films and Their Tribological
Properties. Surf. Coat. Technol., vol. 62, 1993, pp. 589–594.
7. Wu, R.L.C., et al.: Tribological and Physical Properties of Ion-Implanted
Diamond Films. Diamond Films Technol., vol. 3, no. 1, 1993, pp. 17–29.
8. Miyoshi, K., et al.: Physical and Tribological Characteristics of Ion-Implanted
Diamond Films. NASA TM–106682, 1994.

Braze Bonding of Diamond, CBN, Sapphire and Other Non-metallic Hard Materials for Industrial Devices

Alexander <u>Beck</u>, Wabawaska Engineering, CH-8113 Boppelsen, Switzerland

Keyword: Tools

Abstract

The nature of braze bonding by chemical redox reactions causing a diffusion zone on the surface of the nonmetal with the braze alloy is explained briefly. Some technical and economic advantages for tool and device manufacturing are discussed. Samples of monocrystal devices and grinding tools with braze bonded diamond grit demonstrate the potential of this technology particularly for miniaturization. New applications with other hard materials are shown.

Wearing tests have proved that the lifetime of tools with brazed on diamonds is several times as long as of conventional ones with formlocked diamonds. The reason for this is explained.

1. Introduction

Research in alternative fastening methods to replace traditional ones in the production of diamond tools started in the late fourties and led to numerous publications and patents of sometimes rather dubious and by their nature undefined bonding processes. Many of these early publications were reviewed in 1969 by Seal (1). Despite the fact that some brazing methods have been used successfully for the production of gramophone styli with diamond and ruby tips, it is indeed surprising that these technologies have scarcely been further developed for other applications. The main reason for this was probably that too many inter-locked parameters prevented a step by step solution of the problem complex. In addition, there was for years very little sound information available, but much more misjudgment about all kinds of details, - a fact that hampered progress for a long time.

2. The Nature of Brazing

Brazing describes a joining operation for metal parts by which a braze with a melting point considerably lower than that of the work pieces is temporarily melted within the joining gap. During this melting period, by which the braze is melted, a mutual diffusion of atoms between the metal of the work piece and the braze leads to the formation of a thin layer of liquid and solid solutions manifesting the braze joint. If there is no range of mutual solid solubilities between the metals involved no braze joint can be achieved.

It is well known by experience that such purely metallurgical braze joints with hard materials like diamond, alumina etc. cannot be obtained. The way out of this insufficiency, however, was the well-known fact that many metals like Ti, V, Cr, Mn etc. chemically react quite violently with any crucible material when melted. What may be undesirable there is welcome in brazing alloys for diamond etc. where small additions of such metals to otherwise inert brazing alloys provoke chemical redox reactions on the surface of the hard materials, whereby unsaturated chemical compounds are formed. These may remain partially bonded to the lattice of the hard material and in part to the lattice of the braze metal generating a strong diffusion zone. Such chemically reactive brazing alloys are called active brazes. The chemical reaction of an active braze with a transparent material such as sapphire or diamond leads to most evident changes in the braze joint: The contact areas are dark colored, roughened and mat and the total reflection of light is lost.

One of the first active brazes developed was the Ag-Cu eutectic with about 3 to 10% Ti which was obtained by mixing powderized eutectic with finely ground titanium hydride. Amazingly, this was the most successful active braze in the production of gramophone styli. However, for other applications such powder mixtures proved to be largely unsuitable, particularly when brazing tungsten carbide or stainless steel. But exactly these two types of support materials are of special interest in modern tool and device making.

By and by it became evident that case specific active brazes had to be searched for. With their availability, active brazing grew to a very interesting technology offering many respectable advantages to old applications and opening up new solutions to problems.

3. The Advantages of Active Brazing

The major advantages of diamond tools made by the brazing technique are:
- unhindered chipflow over the cutting face
- applicability of much smaller diamonds
- combination with all tungsten carbide shafts for vibration-free machining
- enormously increased lifetime of tools subjected to heat-induced wearing
- miniaturization of tools and devices, e.g. by brazing the diamond on the table for engraving burs, boring rods of small diameters etc.

The unhindered chipflow and the applicability of much smaller stones in comparison with the common mounting methods by vise and braze bed or a mount in sintered bronze are obvious.

The possibility of fixing diamond crystals and thin poly-crystalline platelets to tungsten carbide supports has opened a new era of top quality cutting and milling tools. Tungsten carbide is an outstanding material for its form-stability and its property of vibration absorption. All-carbide tools with a monocrystalline cutting edge find an increasing use in machining plexiglas, plastic lenses, dental devices, jewelry, watch cases and many other products where a mirror finish is requested. Carbide compacts fitted with cutting inserts of monocrystalline diamond or with solid CBN are finding a fastly growing demand because of their obvious advantage to be used on standard tool shafts and millers. Their use with normed tools and shafts also provides a considerable reduction in the price of the tools themselves as well as of the retooling costs on the production line.

Even though the shaping of the insert containment on the tool shaft or the compact and the brazing operation under high vacuum may be somewhat more expensive than the traditional tool fabrication, such higher costs are regularly overcompensated by the much smaller diamond inserts needed and the considerable quality increase of the brazed tools.

The most astounding quality increase stems from the superior heat dissipation from brazed diamonds in all those applications where the interaction of the diamond with the workpiece generates heat. This was first noticed when wearing tests were made with grinding tools for reinforced concrete. The grinding tools fabricated by brazing the diamond grit onto the tool body removed 4,5 to 5 times as much concrete and steel for the same amount of grit wear as the very best tool in the test series with nickel-embedded

diamond grains. A similar observation was made with dressers for grinding wheels: vacuum brazed natural crystals outlasted by nearly two times other dressers fitted with twice as heavy stones that were mounted traditionally in sintered bronze.

The progress in active braze technology, particularly in the formulation of case optimized brazes and the availability of high vacuum furnaces allowing to run fast temperature profiles in both the heating and cooling cycle, opens unconventional solutions for many demands with materials where up to now only marginally satisfying methods were available. Along with techniques permitting highly precise positioning of even very small parts to be brazed together, tool and device production has been opened to miniaturization, as becomes evident on some examples:

- Core drills with brazed on diamond grit are produced for boring holes down to 0,8 mm in diameter into alumina and zirconia substrates up to 3 mm thick.

- Diamond scalpels of 1,2x0,5x0,2 mm are brazed onto syringes of 0,8 mm diameter for microsurgery on eyes.

- Cut-off tool bits with a monocrystal cutting edge of 0,2 mm width are used to section concasted tubes of 18K gold 17 mm OD, 11 mm bore, in the production of wedding ring blanks, thus minimizing chip waste.

- Contour-tracers with ruby balls ∅ 0,5mm brazed onto shafts of 0,3 mm ∅ with a maximum excentricity of 0,01 mm are used in numerical measuring equipment.

- Cutting blades of natural diamond 1,8x0,2x0,5 mm cutting edge are brazed onto supports of steel 18/8 used in cutting devices for optical glass fibres.

Other successfully started applications for active brazing under high vacuum are current leads made by metal-alumina-metal joints for vacuum and pressure vessels; gas detectors with zirconia diaphragm; watch cases of colored zirconia with golden brace latches, ceramic-ceramic joints, polycristalline PVD-diamond platelets to various base metals for tools, heat sinks etc.

With the development of more case specific active brazes the spectrum of applications will, no doubt, expand quickly in the future.

1. Seal, M. "A Review of Methods of Bonding or Making Electrical Contacts to Diamond", Engelhard Technical Bulletin, June 1969.

INVESTIGATIONS ON THE ADHESION INTERFACE OF CVD DIAMOND FILMS

Q.J. Gao[1], Z.D. Lin[2], A.Q. Zhao[2], X.F. Peng[2], H.R. Jiang[1], and X. Xu[1]

[1]Department of Physics, Peking University, Beijing 100871,P.R. China
[2]Beijing Power Metallurgy Institute, Beijing 100078, P.R. China

Key words: adhesion interface, diamond films, strong carbides forming elements

Abstract

We applied the auto hot deformation compensation of straight filament of close arrangement in grid form to synthesize CVD diamond films, and studied systematically the substrates made of ten strong carbides forming elements. We also stepped further to study the WC-Co substrates. The electron diffraction structure analysis showed that carbides grew first on strong carbides forming element substrates. During the nucleation process, we employed the atomic H to extract the carbon in WC on the surface so as to link C in WC to the H atom. The adhesion between the diamond film and the substrate was tested to be quite satisfactory.

1. Introduction

Growing diamond films using low pressure chemical vapour deposition (CVD) has been going on for several decades, and considerable progress has been made in terms of both the deposition techniques and the growth mechanism. Since the first low pressure CVD diamond films were grown with hot filament CVD method, great efforts have been made concerning the investigation on the materials, shapes, arrangement and pretreatments of filaments, the materials and pretreatments of substrates, the distance between filaments and substrates, gas sources, and various influential factors such as the functions, concentration, flow, directions of flow of gases and the pressure in the chamber. It is still not fully clear, however, what the growth mechanism under low pressure is.

2. Results and discussion

We applied the auto hot deformation compensation of straight filament of close arrangement in grid form to synthesizing CVD diamond films, and studied systematically the substrates made of ten strong carbides forming elements, i.e., W, Mo, Ti, Cr, Zr, V, Ta, Nb, Hf, Si. We also stepped further to study the WC-Co substrates.

In our experiment, tungsten filament temperature was about 2000-2200°C; for tantalum filament, about 2500°C. The substrates were mostly placed under the filaments, and sometimes over them. Nine or thirty tungsten filaments in grid form at 2mm intervals rendered heterogeneous growth areas of 2cm x 3cm or 6cm x 9cm. The substrate temperature, adjusted through radiation heating and circulated water cooling, ranged from 900 to 1100°C. The distance between the filament and the substrate was 2-5mm, and at the nearest about 100mm. Other parameters were approximate to regular ones.

We studied the films grown on the substrates of W, Mo, Ti, Cr, Zr, V, Ta, Nb, Hf, Si. The SEM morphology and the exclusive characteristic diamond peak of 1332 cm^{-1} on Raman spectra showed that diamond had been formed. The electron diffraction structure analysis also showed that between the diamond films and the substrates there were WC, Mo_2C, TiC, Cr_7C_3, ZrC, V_2C, Ta_2C, NbC, HfC and b-SiC, respectively. Because of the limited space, only graphs and data regarding Ti are shown here (see Fig. 1-2, and Table 1).

On the basis of investigations on the mechanism of metallization on diamond surface synthesized at high temperature and under high pressure, Lin and Gao proposed in 1989 the regulative inference regarding the structure of the interface between diamond films and substrates: at high temperature of 800-1100°C, corresponding carbides are first formed; the diamond films were grown on these very carbides[1-2]. Experiments have proved this inference.

Among the ten elements, Si is special in that it has both semiconductor property and the crystalline structure of diamond. Therefore, it is one of the best substrate materials for appliances of diamond films in semiconductors and electronics. To grow single-crystal or highly oriented diamond films, men control the nucleation conditions so that diamond can grow directly on a specified facet of Si or first carbonize mirror-finished Si surface, thus forming b-SiC. We also observed that, below 650°C, SiO_2 first grew on the substrate, and we have discussed on this[3]. The above inference concerning the regulation of the adhesion interface of substrates made of strong carbides forming elements, however, is the general regulation suitable for a substrate temperature of 800-1100°C.

Table 1. Electron diffraction data corresponding to Fig. 2

	d(A)			q	
	1	2	3	1-2	1-3
observed	2.176	2.176	1.531	90°	45°
ASTM-TiC	2.179	2.179	1.535	90°	45°
hkl	200	020	220	200-020	200-220

Considering the studies above, we chose YG3, YG5 and YG7 as the growth substrates. In addition to the regular surface treatments, some parts of the substrates were first covered Ti alloy in a vacuum of 10^{-5} Torr as the transitional layer between the diamond film and the substrate. Through our experiments we discovered that as long as we corroded Co off the substrate surface and the content of Co in WC-Co fell in the range from 3% to 7%, Co would exert little influence on the growth of diamond, and neither would Ti alloy transitional layer. The adhesion between the diamond film and the substrate was tested to be quite satisfactory. The reason for this is that during the nucleation process, we employed the atomic H to extract the carbon in WC on the surface so as to link C in WC to the H atom that has reached the substrate surface, thus laying a basis for the connection of C-H precursor and for the formation of sp^3 diamond film thereafter. Here we give several figures as examples. Fig. 3 shows the diamond film grown on YG3; it is the SEM morphology of the diamond film on the edge and lateral side of the substrate. From Fig. 4, it can be observed that the diamond films grew in columns at cross-section views. Fig. 5 and Fig. 6 give the Raman spectra of the diamond film grown on the YG3 substrate, with and without Ti alloy transitional layer, respectively. It can be observed that in the two Raman spectra, no peaks of non-diamond carbon appears. Electron diffraction structure analysis demonstrated that (WC)xH had been formed on the interface.

Further analysis concerning the interface adhesion status and the quantitative measurements of the adhesion strength are still in progress.

It is well known that H atoms play a critical role in growing CVD diamond films under low pressure, and that those H atoms having reached the substrate surface act decisively. According to the formula of the mean free path (l), when the filament temperature is kept a constant, the lower the pressure, the greater the mean free path of H atoms. For p (chamber pressure) equal to $2x10^4$ pa, which is normal for growing diamond films, at 2200°C, l <=34 mm. Obviously, the shorter the distance between the filament and the substrate, the smaller the possibility for the H atoms dissolved by the hot filament to recombine before reaching the substrate surface and the more favorable for the growth of diamond films. In practice, we reduced the distance to 2 mm and the growth rate was accelerated to such a degree that the growth rate of 20mm/h of uniform diamond film could be achieved. As far as

508

techniques are concerned, we realized effectively the auto hot deformation compensation of straight filaments in grid form.

3. Figures

Fig.1 Diamond/Ti   Fig.2 TiC ED patterns   Fig.3 Diamond/YG3   Fig.4 Cross-section
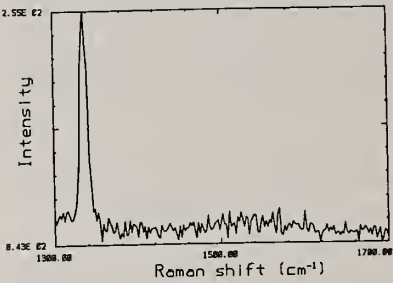
Fig.5 Without Ti alloy transitional layer   Fig.6 With Ti alloy transitional layer
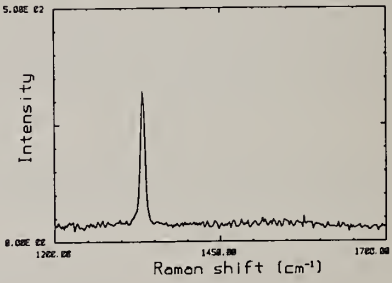
Acknowledgments

References

[1] Z.D. Lin and Q.J. Gao et al., Superhard. Mater.,(P.R. China) No.3(1990)1.
[2] Q.J. Gao and Z.D. Lin et al., Surf. Sci.246(1991)205.
[3] Q.J. Gao, Z.D. Lin and F.X. Lu et al., Thin Solid Films,221(1992)34.

Applications of Diamond Films and Related Materials: Third International Conference, 1995
Editors: A. Feldman, Y. Tzeng, W. A. Yarbrough, M. Yoshikawa, and M. Murakawa

509

TEMPERATURE & STRESS ISSUES IN DEVICES WITH DIAMOND SUBSTRATES DURING MANUFACTURING AND OPERATION

Chandran, B., Schmidt, W.F., and Gordon, M.H
University of Arkansas, High Density Electronics Center (HiDEC) -Department of Mechanical Engineering, Fayetteville, AR 72701.

Key Words: Au-Sn solder, Diamond, GaAs, Stress, Temperature, Voids

Abstract

Finite element thermal and stress analyses were performed on a backside attached GaAs laser diode with a CVD diamond substrate. Two situations were investigated: one corresponding to thermal conditions during manufacture and the other to thermal conditions while operating. The influence of different solder coverage areas and voids in the solder layer on the maximum temperature and stress in the diode were determined. The results show that the stresses in the diode decrease and the maximum temperature increases when the area of the solder layer with respect to the die area decreases from the edges towards the center. It was also found that voids in the solder layer do not significantly increase the maximum temperature in the diode.

1. Introduction

It is well known that the mechanical failure of packaged integrated circuit devices is a major concern for engineers and designers. The high degree of integration, high power level, and high production cost of advanced electronic products, have imposed stringent requirements on packaging designs. Temperature is one of the main factors affecting the performance of integrated circuits. Chip temperatures must be below 80 to a 100°C to ensure proper electrical performance and avoid irreversible degradation of the transistor junction. A graph by Kraus[1] of the thermal acceleration factor which is expressed as the ratio of the failure rate at temperature T over the failure rate at 75°C shows a nearly exponential dependance of the failure rate on the component temperature. In addition to IC devices continuous wave laser diodes with up to 10 Watts of power output and laser diode arrays with up to 20 Watts of power output are now in the market. An excellent candidate for thermal management is diamond. Diamond is an excellent thermal conductor providing an easy path for heat removal. Usually, a solder layer is used to attach the laser diode to the diamond substrate. Eutectic gold-tin is a good choice for the attachment medium given it's excellent

fatigue resistant properties[2]. Also, gold-tin eutectic has the lowest melting temperature of the commonly used hard solders. A major problem with attaching a GaAs laser diode to a diamond substrate using a gold-tin solder is the high thermal stress generated in the die during the bonding operation[3]. One way to reduce the stress is to restrict the solder layer to the central region of the diode. However, incomplete solder coverage reduces the area available for transferring heat to the substrate and can increase the operating temperature of the device.

In this paper, a finite element analysis is used to determine the change in the maximum temperature and stresses in the diode when the bond area is modified due to reduced solder coverage or voids in the solder layer[4]. Voids in the solder layer could increase the thermal resistance between the diode and the diamond substrate and produce a local increase in the temperature in the diode. Solder layer voids also act as stress concentration sites and disrupt the stress field in the diode.

2. Numerical model

The commercial finite element code ANSYS was used to model a 3mm X 3mm X .2032mm thick gallium arsenide laser diode back side bonded to a 0.4064mm CVD diamond substrate or bonded to a GaAs substrate using a 0.0508mm thick Au-Sn solder layer. Two classes of problems were considered. One corresponding to operation of the device, and one simulating manufacture. For operation, the diode was assumed to dissipate 5W of power evenly distributed over the entire top surface. The laser diode was modelled as a homogeneous slab of gallium arsenide. Different ratios of the area of the solder layer to the area of the die were modelled. The effect of solder voids on the maximum temperature and the stress in the diode was also studied numerically. To check the accuracy of the models, the axial and shear stresses obtained were compared with analytically obtained values[3]. Voids were simulated by deleting elements from regions of the solder layer. The steady state thermal analyses for operating conditions were performed by holding the bottom surface of the diamond substrate at 50°C, and applying a heat flux of 0.556W/mm² at the top surface of the die. Simulation of the manufacturing process used a steady state stress analysis performed by applying a temperature differential of 278°C on all the nodes of the model. This would be equivalent to cooling the entire assembly to room temperature from the solder melting temperature of about 280°C. Properties of the gallium arsenide[5],[6], CVD diamond[7] and eutectic gold-tin[8],[9] used in this analysis are: moduli 0.123E6, 1.18E6, 70505 Mpa, CTE 5.58, 2., 16.8 ppm/°C, Poisson's Ratios 0.3, 0.148, 0.41, aand thermal conductivity 0.045, 1.2, 0.057 respectively. Although the properties are temperature dependent, they were held constant in this work.
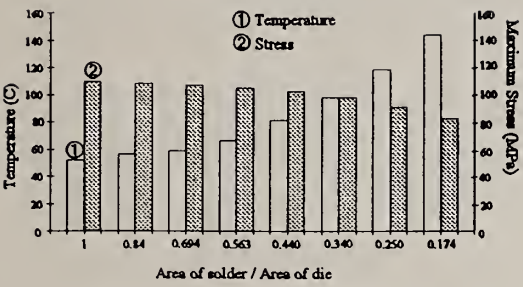
3. Results and discussions

Fig. 1: *Maximum stress and temperature in the diode as a function of the ratio of the solder area to the die area.*
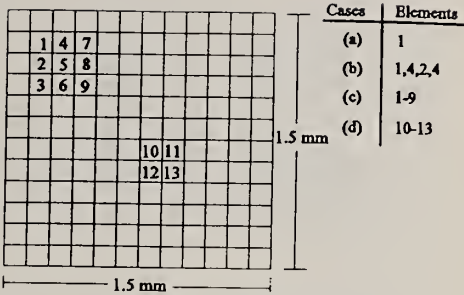
Fig. 2: *Solder layer elements deleted.*

Fig. 1 shows a chart of the maximum temperature in the diode and the maximum stress in the die as the ratio of solder area to die area was decreased from 1 to 0.174. As can be seen from the figure, the maximum temperature in the diode increases and the maximum stress decreases as the solder area decreases. The temperature increase is expected because a smaller solder area would mean a reduced path for heat conduction away from the diode or increased thermal resistance. A smaller solder area with the area reduced at the extreme edges results in a decrease in stress. Note that if the solder area is reduced by removing solder from the center of the package then the stress would be essentially unaffected. The maximum axial stress in the die at the interface between the solder and the die was taken for comparison here because this stress has the maximum magnitude.

Four different type of voids were investigated. Fig. 2 shows the solder layer elements of the FE model and defines the four void geometries considered. Fig. 3 shows the maximum temperature and the stresses obtained for each of the four cases. The diamond substrate was replaced with a lower conductivity GaAs substrate and a thermal analysis was performed. These results are also plotted in Fig. 3. For reference, the temperature and the stress when there is no void present are also shown. The figure shows that the maximum temperature in the diode remains almost the same as when there is no void. Therefore small voids are not important from a thermal standpoint. However, the maximum stress in the diode shows an increase when there is a void, with the peak stresses in all cases directly above the void in the solder layer. As the size of the void increases the stresses decrease. This is because the discontinuity or the stress concentration is not as severe when the void area is larger. Fig. 4 shows the stress distribution along the diagonal length of a square die without a void and for case (a) . The presence of the void in the solder layer produces

512
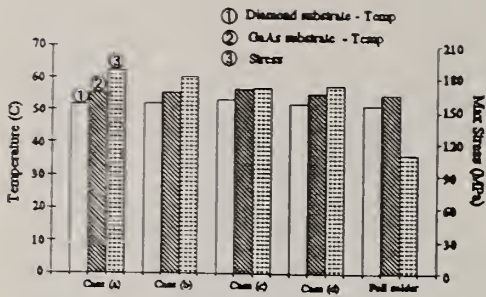
Fig. 3: Max temperature and stress in
the die for different void geometries.
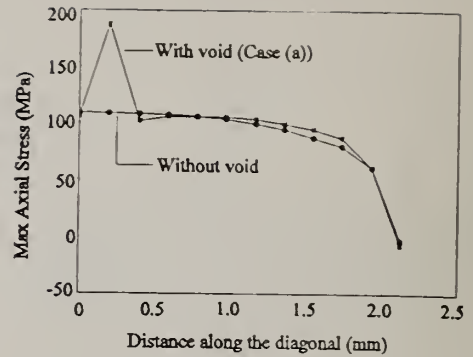
Fig. 4: Stress distribution along the
die in the presence of a void.

in the vicinity of the void a localized increase in the stress as seen in the figure.

4. Conclusion

Decreasing the area of the solder layer with respect to the area of the diode decreases the stresses and increases the maximum temperature in the diode. The results can be used to determine an optimal solder coverage area for device attachment keeping the temperature and stresses below the safe value for the device. It was also found that voids in the solder layer act as stress concentrations which increase the stresses in the diode, but have little effect on the temperature.

5. References

1. Kraus, A.D., and Bar-Cohen, A., Thermal Analysis and Control of Electronic Equipment, McGraw-Hill, 1983.
2. Olsen, D.R., and Berg, H.M., Properties of Die bond alloys relating to thermal fatigue, IEEE Transactions on CHMT, Vol: CHMT-2, No: 2, 1979, pp257-263.
3. Chandran, B., et al., Design parameters for using GaAs dice on synthetic diamond substrates, Proccedings of the ASME-WAM94, AMD-VOL195, pp 29-34.
4. Chiang, S.S., and Shukla, R.K., Failure mechanisms of die cracking due to imperfect die attachment, Proc. 34th IEEE Electronic Components Conferencs, IEEE, New York, 1984, pp 195-202.
5. Hu, J.M., and Pecht, M., Temperature dependence of the mechanical properties of GaAs wafers, Journal of Electronic Packaging, V113, pp 331-336.
6. Eden, R.C., Applicability of diamond substrates to multi-chip modules, Proc. of the International Society of Hybrid Microelectronics, 1991, pp 363-367.
7. Borchelt, E.F., and Lu, G., Application of diamond made by chemical vapor deposition for semiconductor laser submounts, presented at SPIE, Jan 19-20.
8. Yost, F.G., et al., Thermal expansion and elastic properties of high gold-tin alloys, Metallurgical Transactions A, Vol: 21A, July 1990, pp 1885-1889.
9. Product data catalog, Indium Corporation of America, Utica. New York.

ADHESION OF DIAMOND COATINGS SYNTHESIZED BY OXYGEN-ACETYLENE FLAME CVD ON TUNGSTEN CARBIDE

S. Marinković[1], S. Stanković[1] and A. Dekanski[2]

[1]Institute of Nuclear Sciences "Vinča", POB 522, 11001 Belgrade, Yugoslavia
[2]Institute for Electrochemistry ICTM, POB 815, 11001 Belgrade, Yugoslavia

Key words: adhesion; combustion flame CVD; cutting tool

Abstract

The results of a study concerned with chemical vapor deposition of diamond on tungsten carbide cutting tools using an oxygen-acetylene flame in a normal ambient environment are presented. Effects of preparation conditions on the adhesion of the coating have been investigated, including different surface treatment, different position of the flame with respect to the coated surface. effect of an intermediate poorly crystalline diamond layer, etc. In particular, effect of polishing and ultrasonic lapping with diamond powder was compared with that of a corresponding treatment with SiC powder.

1. Introduction

Improvement of cutting tools by hard CVD coatings is widely used today [1]. Although a number of papers has been devoted to the problem of coating cemented cutting tools by diamond layers [1-3 and references therein], the oxygen-acetylene flame CVD has not apparently been used for the purpose. Because of its simplicity and high deposition rate, it was considered interesting to attempt coating tungsten carbide tools by this method.

A capital problem that has to be solved is to achieve a satisfactory adhesion between the diamond coating and the tungsten carbide surface. Several approaches have been suggested in the available literature. In order to remove metallic cobalt from the tool surface because of its detrimental effect on the adhesion, its dissolution in nitric acid using an ultrasound bath has been recommended [2,3]. An ultrasound pretreatment of the carbide surface in a suspension of diamond dust has been reported to cause a cavitation-erosion microflaws, leading to a higher nucleation density and a more uniform continuous film than could be achieved using the conventional polishing

process [3,4]. An intermediate diamond film has been found to increase adhesion [3]. Also, a rough substrate surface was found to result in a better adhesion strength [5].

2. Experimental

Diamond has been deposited on one of the edges of the cutting tool WC/Co (Co content 6 wt%) plate which served as a substrate. By means of a specially designed substrate holder, adjusting the angle between the flame and the substrate and its exact positioning, the edge to be coated was exposed to the flame, the rest of the plate being cooled.

The deposition conditions were chosen so to obtain polycrystalline deposits with well-shaped crystals. Typical deposition conditions were: substrate temperature ~700 °C, except for the very tip of the substrate which, because of the geometry of the substrate, was at a temperature some 100-150 °C higher; total flowrate 270 l/h. The high flowrate was used in order to obtain good crystallinity with a relatively high R value [6,7], that was varied between 1.04 and 1.10.

The samples were treated in water and 1:1 HNO_3 for different time in an ultrasound bath to test their adhesion.

The samples were examined using optical and scanning electron microscopy, X-ray diffraction and Auger electron spectroscopy (AES).

3. Results and discussion

The procedures outlined above were applied to improve adhesion of the coating. The substrate surface was first polished with a diamond paste. Cobalt was removed from the substrate surface by dissolving it in 1:1 HNO_3 in an ultrasonic bath. Since it was found by AES that a slight cobalt content still existed after 10 min treatment, the treatment time was extended to 30 min, thus eliminating the metal or leaving only traces of it in the surface layer. The substrate was then subjected to the action of ultrasound lapping with a suspension of diamond powder in ethanol. In order to compare the effect of surface pretreatment with siliconcarbide powder to that with diamond, the same procedure (polishing and ultrasound lapping) was used with SiC powder on separate substrate samples. Finally, effect of an intermediate film prepared in a separate experiment by using a gas mixture richer in acetylene was examined.

Under these conditions, a small area surrounding the edge was coated by a continuous layer consisting of small (a few micrometers) diamond crystals. Larger crystals were obtained at the very edge of the substrate.

The results of adhesion tests using ultrasonic treatment with water and 1:1 HNO$_3$ acid can be summarized as follows: a) contrary to water, the acid is efficient in removing the diamond coating from the substrate and can be used for comparative adhesion tests; slight damage could be observed already after 5 min; b) by increasing the acid treatment time a progressive removal of the coating takes place, starting with large crystals on the edge and advancing toward the center of the coated area; c) a narrow region, distant from the edge and consisting of small crystals appears to be most stable; it remained on the substrate after prolonged (50 min) exposure to the acid; d) there is no significant difference in adhesion between the coatings deposited on the diamond - and SiC - pretreated substrates, although there are indications that the latter are more adherent.

Deposition of the intermediate layer had no noticeable effect on the adhesion.

Chemical composition of the diamond surface was examined by AES. The elements always found are P, C and O. The phosphorus comes as an impurity from the acetylene gas. In previous diamond deposition experiments on Mo substrates [8] this impurity was responsible for MoP formation as found by the X-ray diffraction.

An analysis of the diamond/substrate interface using AES was attempted. The literature data relative to diamond film AES analysis [4,9,10] generally suggest a careful examination of the carbon KLL line shape, including peak position, line width and fine structure, and comparison of these data with those for cubic diamond, non-diamond carbon and substrate. Our examination showed a difference in fine structure of the carbon KLL line (Fig. 1). The diamond film exhibits two peaks of approximately same height (A and B) at the low-energy side of the main carbon peak, in agreement with the literature data [4,9,10]. The carbon KLL spectrum from the carbide consists of a main peak and a peak on its low-energy side (C), which is at approximately the same position as the lowest-energy peak from the diamond, but considerably stronger than that.

A typical carbon KLL spectrum obtained in the area where the diamond coating was mechanically removed (by scraping) contains, in addition to the main peak, the low-energy peak from the carbide (C') with a shoulder (B') corresponding presumably to the diamond peak B. Although further research is needed before any conclusions concerning the interface could be derived, this result indicates that the diamond coating was not completely removed by scraping. In this connection it seems noteworthy that Perry *et al.* [9], working on diamond deposition on Ti, concluded that delamination occurred within the

516

interfacial reaction layer (Ti/diamond), rather than at the CVD diamond surface.
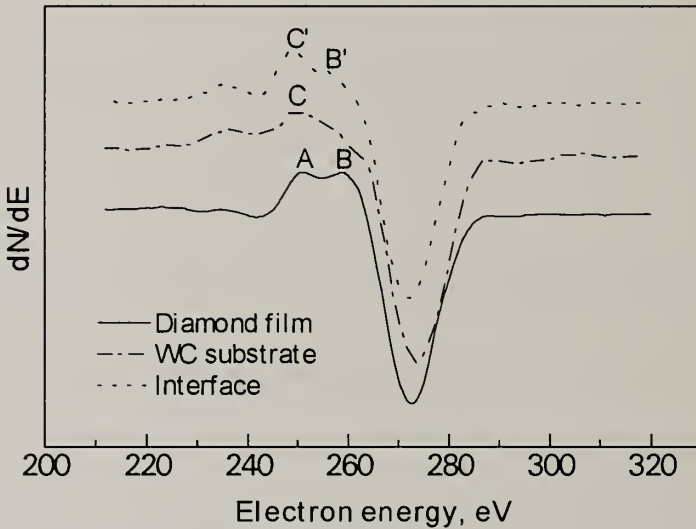
Fig.1. Typical AES spectra of carbon KLL peaks for diamond film, WC substrate and diamond/substrate interface

4. References

1. B. Lux and R. Haubner, Phil. Trans. R. Soc. Lond., A342 (1993) 297.
2. J. Oakes, X.X. Pan, R. Haubner and B. Lux, Surf. Coatings Technol., 47 (1991) 600.
3. H. Itoh, T. Nakamura, H. Iwahara and H. Sakamoto, J. Mater. Sci., 29 (1994) 1404.
4. C.P. Sung and H.C. Shih, J. Mater Res.,7 (1992) 105.
5. X.-L. Peng and Z.P. Gan, Thin Solid Films, 239 (1994) 47.
6. S. Marinković and S. Zec, Diamond and Related Mater. (in press).
7. K.A. Snail and C.J. Craigie, Appl. Phys. Lett., 58 (1991) 1875.
8. S. Marinković and S. Zec, J. Serb. Chem. Soc., 58 (1993) 679.
9. S.S. Perry, J.W.Ager, G.A. Somorjai, R.J. McClelland and M.D. Drory, J.Appl. Phys. 74 (1993) 7542.
10. A. Badzian, T. Badzian and S.-T. Lee, Appl. Phys. Lett., 62 (1993) 3432.

DIAMOND
LARGE AREA/HIGH RATE
GROWTH

Applications of Diamond Films and Related Materials: Third International Conference, 1995
Editors: A. Feldman, Y. Tzeng, W. A. Yarbrough, M. Yoshikawa, and M. Murakawa

519

LOW COST DIAMOND PRODUCTION WITH LARGE PLASMA TORCHES

W. D. Partlow,[1] J. Schreurs[1], R. M. Young[1], I. Martorell[1], S. V. Dighe[1], G. Swartzbeck[1], and J. Burton[2]

[1] Westinghouse Science & Technology Center, 1310 Beulah Rd., Pittsburgh, PA, 15235 USA
[2] SGS Tool Company, 55 South Main St., Munroe Falls, OH 44262 USA

Key words: diamond, economics, manufacturing, production, plasma

Abstract

Using the DC arc deposition technique, we are scaling the diamond deposition process up to high excitation power in order to reduce the manufacturing cost and increase the production rate of polycrystalline diamond. We have operated the process with plasma torches up to 100 kW. A 1/2 MW facility is under construction.

The approach has been guided by a production cost model that takes into account labor, materials, utilities, overhead, depreciation, and cost of capital to project manufacturing costs. The model has identified and quantified the important parameters that are required to achieve low manufacturing cost. Specifically, it has demonstrated the importance of operating at high power and of recycling non-consumed feed gases.

1. Introduction

In order for diamond to penetrate the markets of competitive materials the manufacturing costs must be significantly reduced below present values. We have developed deposition facilities that utilize the high production rates possible with industrial DC plasma torches to reduce manufacturing costs. The approach has been guided by a cost model to project manufacturing costs. The inputs to the model are based as much as possible on experimental data, but also use plasma arc models to projections that guide us into areas that have not yet been reached. We will discuss the model, the diamond deposition facilities used to test the model, and the projections and conclusions about diamond manufacturing that we have been able to draw from our work.

2. Cost Model: DC Plasma Torch Deposition

The model consists of a spreadsheet that takes into account labor, materials, utilities, overhead, depreciation, and cost of capital to determine the volumetric production costs based on empirical or projected production rates for a given grade of diamond. The projections that we have made to higher power operation from low power data are based on the scaling laws [1] derived from heat and mass transfer laws. We have compared our model predictions to those made by the model of Ibis Associates [2], which starts from much more fundamental assumptions, and arrives at some of our inputs, such as deposition rate, from first principles. Our model does not include sample preparation and post-deposition processing. It is specific to volumetric production on a round-the-clock production schedule, assuming 100% yield. Obviously the results are general, and must be adapted to each specific diamond product based on its yield and operational duty cycle.
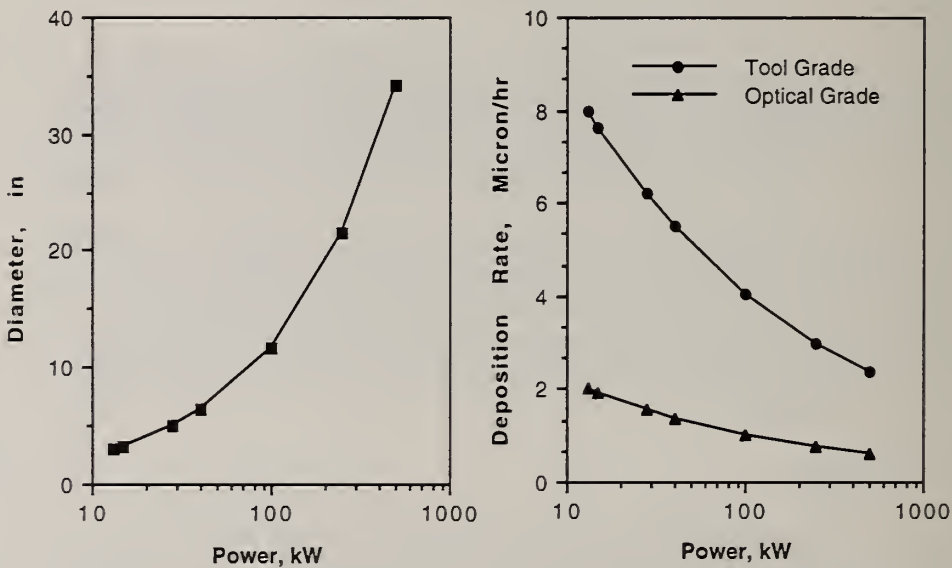
Fig. 1. Scaling laws, based on Ref. 1 used to project deposition characteristics of high power reactors from small reactor data.

Important input parameters to the model included: 8000 operation hours per year; 10 year straight line depreciation; 5.5% annual return on capital; 90% gas recovery when recycling. Labor costs were .048 technician and .024 professional hours per operating hour of the facility. This is based on our experience operating the 13 and 28 kW reactors for diamond production on an unattended round-the-clock basis, and our experience with the larger torches for other applications. The model calculations were run for two grades of diamond: tool grade (dark) and optical grade (clear), the former

having four time higher deposition rate than the latter. The runs for 13 kW and 28 kW are based on experimental data, and the remaining calculations use the scaling law projections.
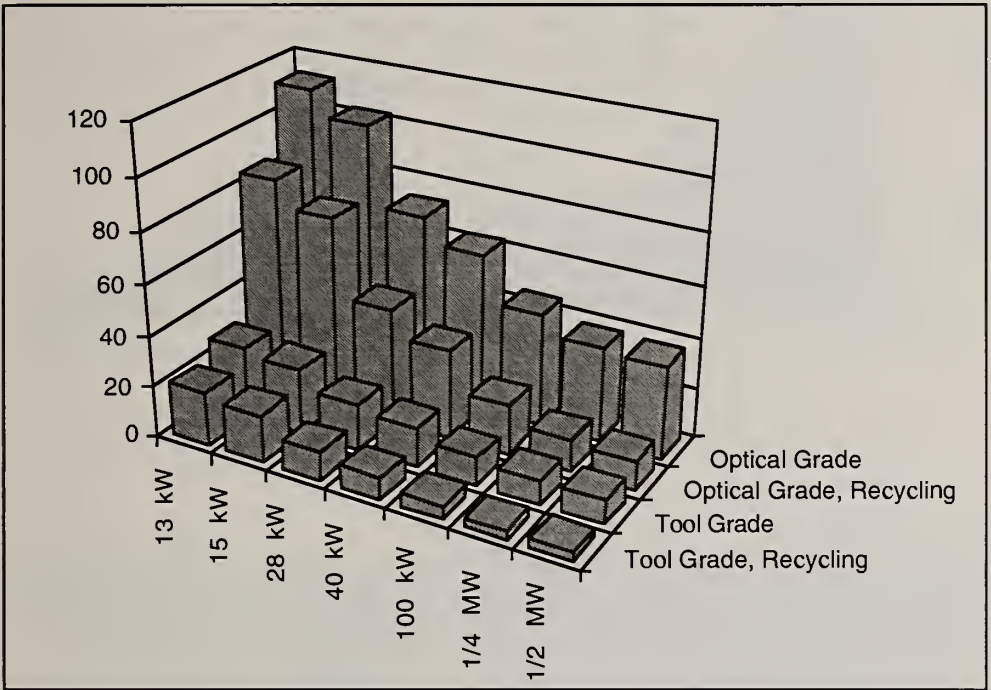
Fig. 2. Summary of the predicted production cost per carat of tool grade and optical grade diamond, with and without gas recycling for several different power plasma torch reactors.

The results of the model are summarized in Fig. 2, which plots cost per carat as a function to plasma torch power for the two grades of diamond, with and without gas recycling. Cost breakdown into four major categories is shown in Fig. 3. For a given grade of diamond, it is seen that increasing power (and therefore volumetric production rate) is the most important factor in reducing costs. This is because labor and fixed costs are a large fraction of total cost at low power operation, and these can be reduced only by production increase. Above about 250 kW, the advantages of power increases are diminished. At high power, production rate is so high that the labor and fixed costs are largely overcome, so that materials and power costs are dominant. In this high power region of operation, the benefits of gas recycling are large. For truly low cost diamond production with plasma torches, high power operation and gas recycling are both necessary.

OPTICAL GRADE NO RECYCLE

OPTICAL GRADE RECYCLE

TOOL GRADE NO RECYCLE

TOOL GRADE RECYCLE
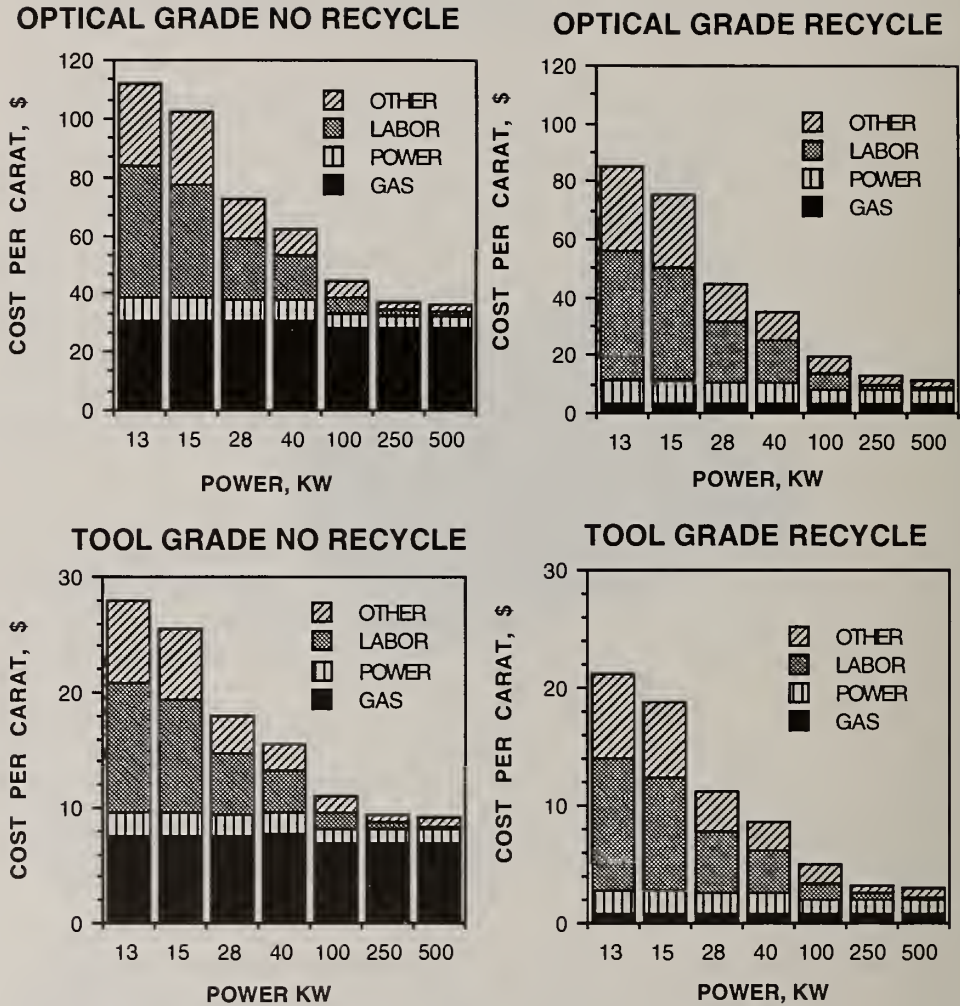
Fig. 3. Bar charts of the production cost predictions of the model, broken down into four categories: gas, power, labor, and "other", which includes maintenance, depreciation, cost of capital, and rent.

3. Description Of The Facilities

Three DC arc-excited diamond deposition reactors are currently in operation at Westinghouse, nominally rated at 15, 40, and 100 kW. A fourth reactor is under construction, to be sized at 1/2 megawatt. The two smallest reactors utilize modified Miller Thermal SG-1B plasma spray torches as the arc-heaters. The 100 kW facility uses a Westinghouse Marc-3 plasma torch, while the 1/2 MW chamber is designed

around the Westinghouse Marc-11 torch. Both of these latter two torches are rugged, industrial arc-heaters capable of hundreds of hours of operation and have found prior use in metallurgy, chemical manufacturing, and waste processing.

All the reactors consist of a water cooled vacuum vessel, sized according to the torch and substrate size. In open-cycle (blow-down) mode, argon and hydrogen gases are brought past the DC arc, heated, and then exhausted into the chamber through a supersonic nozzle of proprietary design. Hydrogen/argon flows are chosen to maximize the diamond deposition rate [3]. Methane, and possibly oxygen, are introduced into the jet. These gases impinge on the target, which is held at a temperature between 800-1100 °C. The chamber pressure is typically 10-50 Torr. The gases are then pulled through a heat exchanger and are pumped back to atmospheric pressure by a series of vacuum pumps. In closed-cycle (recirculated) mode, these gases are brought back around and sent through the arc-heater again, with a small amount of bleed and make-up gases (<10%) being removed or added to the line, respectively.
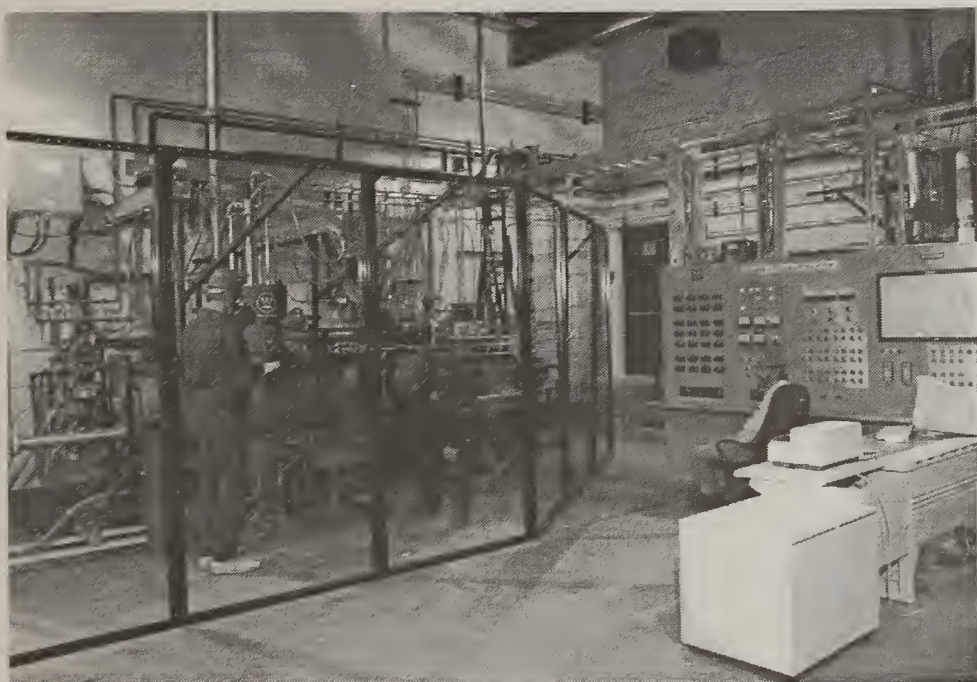

Fig. 4. Photograph of the Westinghouse 100 kW production deposition reactor.

4. Discussion And Conclusions

Of the parameters influencing the production cost of diamond by DC plasma torch, the single most important factor is deposition rate. This is observed in dramatic cost per carat difference, seen in all reactor schemes, between fast depositing diamond (our tool grade) and slower depositing diamond (optical grade). A factor of 4 increase in deposition rate can result in a factor of 4 reduction in cost per carat.

The second most influential parameter is torch size. Here, due to the larger number of carats deposited in larger reactors, an economy of scale is realized. This chiefly comes from reduced labor and capital costs per carat. In absolute terms, however, electrical and especially gas costs rise considerably, and it thus becomes possible to achieve further reductions is cost by recycling the gases. Thus recycling is viewed as the third element required for low cost diamond production. These conclusions rely on the moderately low labor costs that can be achieved via fully-automated, round-the-clock operation of the reactors.

For the very highest power plasma torches, electrical power costs are the largest component. Here it will be necessary to increase the electrical efficiency of the process in order to make major cost reductions. This will require fundamental changes in the process physics or chemistry.

In summary, to decrease the production cost of CVD DC plasma torch diamond to the $5/carat level, it is necessary to use a plasma torch larger than 100 kW in gas recycle mode. To go significantly below this cost level, even larger torches will be necessary.

5. Acknowledgments

6. References

1. R.M. Young, "Deposition Area, Growth Rate, and Arc Power Scaling Laws for Diamond Film Deposition by Arc-Heated Gas Flows," to be published in: Symposium Proceedings, 12th International Symposium on Plasma Chemistry (21-25 Aug. 1995, Minneapolis, MN, USA).
2. Ibis, private communication, Adam T. Singer and Steven M. Riester.
3. R.M. Young, "Hydrogen/rare-gas optimization by simple boundary layer theory for diamond film deposition in arc-heated gas flows," Surface and Coatings Technology, 68/69, 384-387 (1994).

ENGINEERING ASPECTS OF SCALABLE STAGNATION-FLOW REACTORS FOR COMBUSTION SYNTHESIS OF DIAMOND

D.W. Hahn, C.F. Edwards, K.F. McCarty, E. Meeks, M.N. Bui-Pham, and R.J. Kee

Sandia National Laboratories, Livermore, California 94551-0969, USA

Key words: flame stability, heat transfer, Leidenfrost, scalable, stagnation-flow

Abstract

The successful utilization of premixed oxygen-acetylene flames in the chemical vapor deposition (CVD) of diamond has led to an interest in scalable configurations. A stagnation-flow reactor is scalable and can provide the uniform species and heat fluxes necessary for CVD diamond deposition over large surface areas. The present work describes such a scaled-up reactor (2-inch diameter films) along with the relevant engineering considerations, including burner configuration, flame stabilization, and substrate thermal management.

1. Introduction

Synthesis of diamond films using premixed acetylene/oxygen flames has been reported by numerous sources. Among the various approaches which have been demonstrated, use of the atmospheric pressure, stagnation-flow configuration offers the advantages of high deposition rate, inherent film uniformity, and the potential for direct scalability [1,2]. This is typically accomplished by impinging a jet of reactants against the deposition surface to form a highly-strained premixed flame. If the flow field is tailored correctly, the reaction zone realized is a flat flame which supplies uniform fluxes of reactive species and heat over the surface of the substrate.

Achieving uniform nucleation and growth is contingent upon several factors. These include proper conditioning of the approach flow, stabilization of the flame in a flat, uniform mode, and providing for control and extraction of high heat fluxes while maintaining a constant surface temperature.

2. Stagnation-flow reactor

Tailoring of the reactant flow field has been implemented using a unique "trumpet-bell" nozzle geometry as depicted in Fig. 1 [2]. The radially uniform inlet gases enter an axisymmetric, flared nozzle that resembles the bell of a trumpet. To first approximation, the nozzle contour is the ideal stagnation-flow streamline that originates at the inlet throat. The contoured nozzle ensures that the fluid flow behaves as an ideal stagnation flow while eliminating the outer portion of the flow field. By achieving the outer streamline through the nozzle boundary rather than through actual streamlines, reagent use efficiency is greatly enhanced. The design offers the advantages of ideal stagnation flow on a finite scale, optimal use of reactants, and uniform material deposition.

The present stagnation-flow reactor is designed for the synthesis of 5 cm (2") diameter diamond films. The trumpet-bell design has a nozzle throat diameter of 8.3 mm (0.325") and is configured for downward firing against a molybdenum substrate. $C_2H_2/O_2/H_2$ with the molar ratios 1.0/1.03/0.58 flows at a rate 230 slpm, yielding an inlet gas velocity of 72 m/s, and a total heat release of about 100 kW.

3. Flame stabilization

Flame stability may be considered in two parts: establishment of a flat flame, including the roles of flame strain and extinction, and spatial modes in the flame structure. The first item necessitates a flow regime within the limits of flame extinction and flashback. Analytical and experimental analysis of several of these issues have been reported [3,4], including a study of acetylene/oxygen flames in the regimes of interest for diamond synthesis [1].

Spatial modes become important as the reactor is scaled-up. Two particular types of structures observed in the present flame are depicted in Figs. 2 and 3. The nonplanar structure in Fig. 2 has been reported by Ishizuka and Law [4] and may be caused by preferential diffusion coupled with aerodynamic instability. Such an explanation is consistent with the present results, since this feature is often observed when the upper nozzle is not concentric and/or parallel with the lower substrate. Because a substantial radial pressure gradient exists, small differences in alignment between nozzle and substrate can lead to large changes in the flame structure.

A more dramatic flame instability occurs in the outer diffusion portion of the flame (see Fig. 3). The flame displays an angular asymmetry that is manifest in a series of azimuthal structures like the pictured $n = 3$ modes, as well as other higher-order modes ($n = 6$, etc.). Flame stability decreases with mode number, and flame

extinction often occurs when the $n = 3$ mode structure is realized. Because stable operation is achieved with higher numbers of modes, with axisymmetric (i.e. ∞ modes) the most stable, a device was constructed as shown in Fig. 4. The number of vertical pillars may be adjusted to force the outer flame into a particular mode. Typically 12 equally spaced pillars are used, resulting in a marked increase in stability as compared to the unforced configuration.

4. Substrate temperature control

Substrate thermal management entails several aspects, which include consideration of the desired surface temperature range, providing for uniform dissipation of heat fluxes which may approach 1000 W/cm^2, and the ability for real-time control. One approach is the use of spray cooling, which may be divided into two distinct regimes based on the temperature of the sprayed surface. The first is the imposition of an isothermal boundary condition equal to the saturation temperature of the coolant [5]. The alternative method is spray cooling with the surface above the Leidenfrost temperature (where a precipitous drop in heat transfer effectiveness occurs). Because the super-Leidenfrost scheme is not coupled to the saturation temperature, it provides for real time control and tuning of heat extraction to maintain a constant surface temperature [6].

Experiments were performed to validate these cooling strategies for constant heat flux conditions which approximate the present CVD process. For a constant heat flux, the deposition surface temperature scales linearly with the spray-cooled surface temperature. As shown in Fig. 5, the results can be divided into two distinct control regimes. The isothermal boundary segment provides effective cooling but is not optimal for control, having a temperature range of less than 30 K. In contrast, the super-Leidenfrost segment yields a control range of nearly 400 K as the spray flux is varied by a factor of 5. The super-Leidendfrost approach may be readily incorporated into control loop systems and can provide real-time substrate temperature control and radial profiling [6].

5. References

1. M. Murayama and K. Uchida, Comb. Flame, 91:239 (1992).
2. K.F. McCarty, E. Meeks, R.J. Kee, A.E. Lutz, Appl. Phys. Lett.. 63:1498 (1993).
3. W.J. Sheu and G.I. Sivashinsky, Comb. Flame, 84:221 (1991).
4. S. Ishizuka and C.K. Law, Nineteenth Symposium (International) on Combustion, The Combustion Institute, 327 (1982).
5. V.A. Shamamian and H.D. Ladouceur, "Thermal management considerations involved in the design of a substrate mount for large area CVD diamond combustion

deposition," Naval Research Laboratory, unpublished report (1992).

6. C.F. Edwards and D.W. Hahn, Super-Leidenfrost spray cooling, ILASS-95, Institute for Liquid Atomization and Spray Systems, Troy, Michigan, May, 1995.

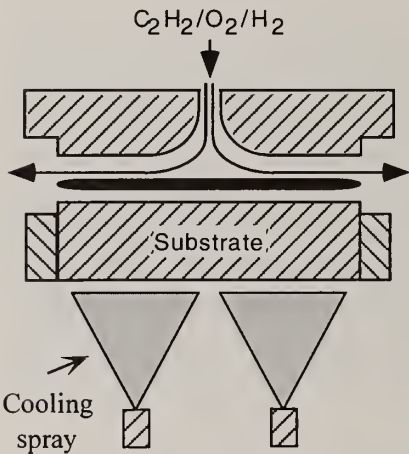Fig. 1. Stagnation-flow reactor.

Fig. 4. Flame stabilizer configured for $n = 6$ modes.

Fig. 2. Side view of nonplanar premixed flame structure.

Fig. 3. Top view of modal structure observed in the outer diffusion flame.

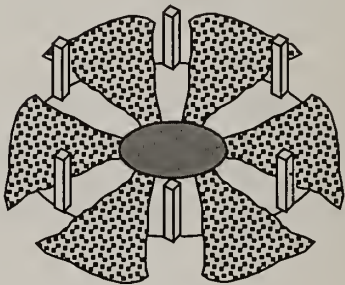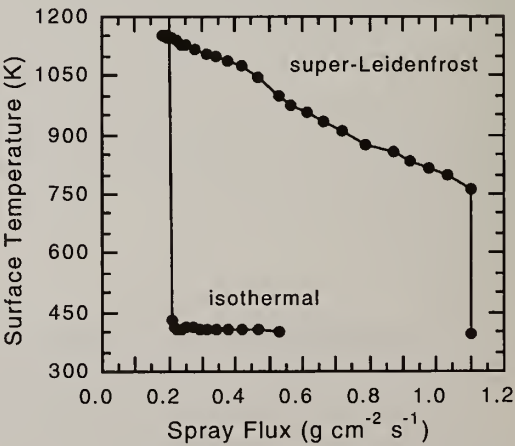Fig. 5. Measured spray-cooling regimes for a constant heat flux of 270 W/cm^2.

Applications of Diamond Films and Related Materials: Third International Conference, 1995
Editors: A. Feldman, Y. Tzeng, W. A. Yarbrough, M. Yoshikawa, and M. Murakawa

529

THE POTENTIAL FOR DIAMOND FIBRE COMPOSITES

MNR Ashfold [1], P W May [1], E D Nicholson [1], P G Partridge [2], G Meaden [2],
A Wisbey [3], M J Wood [3]

[1] School of Chemistry , University of Bristol, BS8 1TS, UK
[2] Interface Analysis Centre, University of Bristol, BS8 1TS, UK
[3] Defence Research Agency Farnborough, GU14 6TD, UK

Key words; composites, costs, diamond, fibres, titanium

Abstract

The manufacture of solid and hollow diamond fibres and of fibre arrays is described.
The effective diamond deposition rate, when defined as mass per unit volume rather
than in $\mu m.h^{-1}$, can be substantially greater for fibre arrays and this could lead to
lower cost CVD diamond. Monofilament diamond fibres have been coated with a
metallic matrix by physical vapour deposition and consolidated by hot pressing to
produce metal matrix composites. Examples of diamond fibres embedded in a Ti-
alloy matrix are presented.

1 Introduction

Both microwave plasma enhanced chemical vapour deposition (MPCVD) and hot
filament CVD (HFCVD) processes have been used to manufacture diamond coated
wires and fibres [1]. In diamond fibre reinforced composites both the physical and
mechanical properties of diamond may be exploited in a single component, thereby
increasing the potential for CVD diamond in engineering. The tensile modulus for
CVD diamond fibre (~900 GPa) is greater, by a factor two or more, than the modulus
of any other fibre except the very high modulus form of graphite fibre [1,2]. The
latter has a similar specific stiffness E/ρ (E = Young's modulus, ρ = relative density)
to that of diamond fibres, and lower modulus graphite fibres are now widely used
both in low cost products (e.g. sports goods) and in aerospace structures. Several
other high strength multiflament fibres (e.g. Nicalon and Tyranno) and monofilament
SiC fibres [2] have superior oxidation resistance to diamond and graphite fibres
above ca. 600 °C. Clearly therefore, quite apart from cost factors , diamond fibres
will need to make maximum use of the advantageous properties of CVD diamond in
order to compete with these commercial fibres.

2 Diamond fibres

Fibres have been made by CVD on to various wire and ceramic cores with diameters in the range 10 -100 μm (Fig.1a) and hollow fibres have been produced by subsequent etching of tungsten or SiC cores (Fig.1b) or by deposition on to helical tungsten coils (Fig.1c) [3]. The hollow fibre dimensions can be selected to give different wall thicknesses and core diameters and hence fibre modulus. Unlike solid fibres, the specific stiffness of hollow diamond fibres is a constant, independent of fibre dimensions and equal to that of CVD diamond [1]. Once incorporated into a composite material, these fibres would not only reduce the composite density, but could also act as cooling channels in for example, thermal management systems [4]. Thin walled fibres may also flex elastically and provide greater transverse strength.

a)

b)

c)
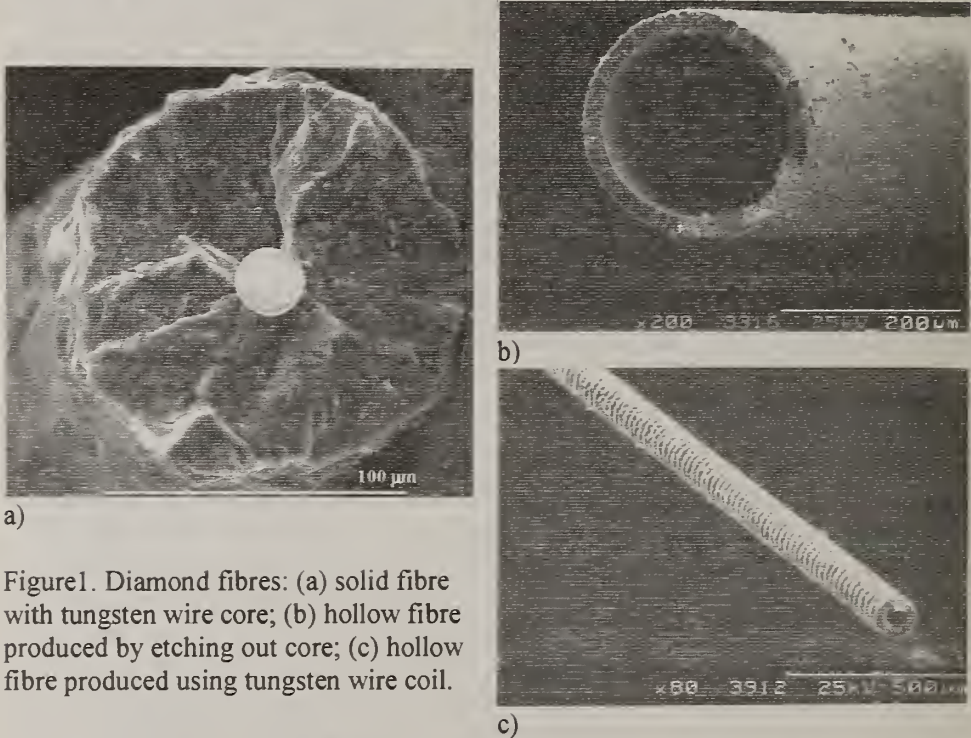
Figure1. Diamond fibres: (a) solid fibre with tungsten wire core; (b) hollow fibre produced by etching out core; (c) hollow fibre produced using tungsten wire coil.

3 Effective diamond deposition rates for fibre arrays

The current high cost of CVD diamond is largely determined by the low deposition rate. However the coating of multiple fibre arrays (Fig.2) may lead to a substantial reduction in the cost of CVD diamond composites.
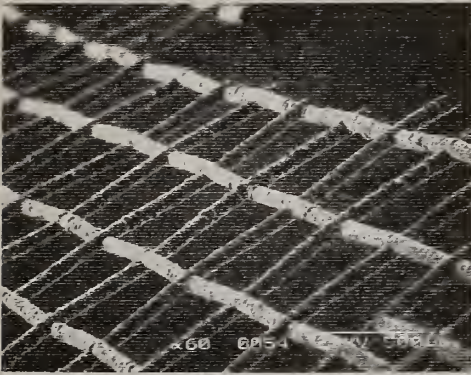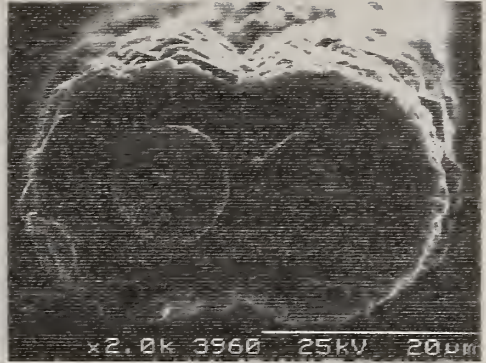
Fig 2 diamond fibre array

Fig 3 Two parallel fibres embedded in diamond

If we define a diamond deposition rate R (μm/h) = x/t , where x is the increase in deposit thickness in a time t, the volume V of diamond deposited per unit time is proportional to the total substrate area and given by, $V_F = x\ L_1L_2N$ on a flat surface (of area L_1xL_2) and by $V_C=\pi(L_1x+x^2)L_2N$ on a long cylindrical surface (diameter L_1, length L_2) where N is the number of surfaces or fibres. For typical values of x/L_1 in the range 0.1-10 the ratio V_C/V_F ~3.5-35. Since parallel fibres may be coated and embedded in diamond (see Fig.3), the mass of diamond deposited per unit time can be an order of magnitude greater for a row of N fibres compared with N flat surfaces with the same projected area. Greater effective deposition rates may be achieved by coating a 3-dimensional square array of fibres. Consider a square array of 100 x 100 fibre cores, each of 20 μm diameter with a spacing between the fibres of 100 μm, which are coated at R = 1 μm/h for 50 h, i.e. until the growing surfaces make contact (Fig.4). A normal section through the fibre diameters will be 12 mm thick, of which 10 mm will be diamond. This corresponds to an effective R = 10 mm / 50 h = 200 μm/h in the diametral direction. Admittedly, the section described would be 21% porous. However these model calculations do suggest that the use of different fibre shapes and spacings can lead to very high effective diamond deposition rates for fibre arrays [5]. With suitable fibre spacings, the arrays may be infiltrated with a polymer or liquid metal to produce diamond fibre reinforced composites.

4 Diamond fibre reinforced Ti-alloy composite

Commercial CVD SiC monofilament fibres about 100 μm diameter with E = 400 GPa are currently used in Ti-alloy metal matrix composites. The use of CVD diamond fibres offers various options. A direct replacement of SiC with CVD diamond could lead to higher composite modulus, or the *same* modulus could be obtained with fewer fibres or the same number of smaller diameter fibres. Compared with SiC fibres, both solid and hollow diamond fibres may lead to substantial increases in the specific stiffness of Ti-alloy composites [1].

532

An example of a Ti-6Al -4V alloy composite containing diamond fibres with a SiC fibre core is shown in Fig.5. After consolidation processing, carbide layers were present at the titanium /diamond interfaces, but the Raman spectrum for the diamond appeared unchanged and no cracks were detected in the diamond deposit. Diamond fibres with ceramic cores are insulators and are less likely to give rise to galvanic corrosion than, for example, graphite fibres in metal matrices.
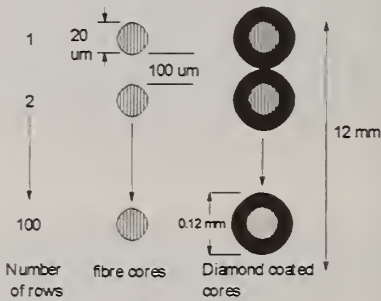
Figure 4 Schematic diagram of through thickness dimensions for cores and diamond coated fibres in a 100 fibre array (see text)
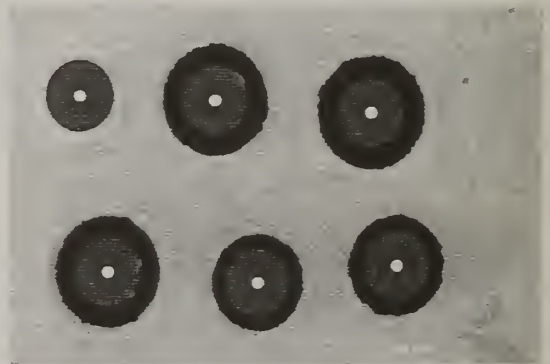
Figure 5, Section through diamond fibre/Ti-6Al-4V alloy composite, showing Sigma SiC fibres coated with various thicknesses of diamond.

5 Conclusions

There is considerable flexibility in the design of both solid and hollow diamond fibres, with different external and internal diameters and tailored elastic modulus values. Composites based on these fibres could have wide application in engineering and there is potential for a substantial cost reduction by coating fibre arrays.

6 References

1 P G Partridge, P W May, C A Rego, M N R Ashfold, Mater. Sci. Tech. 10 (1994) 505
2 A R Bunsell, Fibre Reinforcement for Composite Materials, Elsevier (1988)
3 G H Lu, P G Partridge, P W May, J Mater Sci (1995) In press.
4 P G Partridge, G H Lu, P W May, J W Steeds, Diamond and Related Materials, (1995)
5 P G Partridge, M N R Ashfold, P W May, E D Nicholson, J Mater Sci In press.

Applications of Diamond Films and Related Materials: Third International Conference, 1995
Editors: A. Feldman, Y. Tzeng, W. A. Yarbrough, M. Yoshikawa, and M. Murakawa

533

MULTILAYER DIAMOND COATED WC TOOLS

W.D. Fan, K. Jagannaham, and J. Narayan

Department of Materials Science and Engineering, North Carolina State University, Raleigh, NC 27695-7916

Key words: adhesion, wear resistance, CVD, WC, tools, machining

Abstract

To increase adhesion of diamond coatings, a multilayer structure was developed. The multilayer diamond coating consisted of a first discontinuous diamond layer, an interposing layer, and a top continuous diamond layer. The diamond layer was grown on WC substrates by hot filament chemical vapor deposition and the interposing layer was grown by pulsed laser deposition. Machining tests were used to characterize adhesion properties of the multilayer diamond coatings on WC(Co) substrates. Results indicate that diamond coatings exhibit good adhesion on the WC tool substrates. The wear resistance of the WC tool is improved significantly by the diamond coatings.

Introduction

Diamond coatings on WC tools have been widely used because of the very high wear resistance. Single layer [1,2] and multilayer [3,4] diamond coatings of different design have been investigated. Machining tests are used to investigate the adhesion and tool wear [5,6]. In this work, we describe machining tests that show improvement in wear resistance of WC tools with single layer and multilayer coatings.

Results and Discussion

The multilayer structure is illustrated in Fig. 1. First, the substrate was coated with a discontinuous diamond layer using hot filament CVD [4]. Second, the interposing layer was deposited by pulsed laser physical deposition so that the underlying diamond crystallites were embedded. Finally, a second continuous layer of diamond was grown on the top to form a cutting edge for machining. Before CVD deposition, the tool sample is pretreated to remove cobalt and to improve nucleation of diamond [4]. To expose the structure of the multilayer, angle polishing at $11°$ was used. Fig. 2 is a cross-section of a multilayer coating on WC. The thickness of the TiC layer is about 0.8 µm. The size of diamond crystallites in the discontinuous film is about 0.5 µm and in the top layer about 5 µm. The total thickness of the multilayer diamond film is estimated to be 10 µm.

Diamond (second)
Diamond (first)
Interposing layer
WC(Co)

Fig. 1 Structure of a multilayer diamond coating on WC.

534

Fig. 2 S E M photograph of cross-section of multilayer diamond coating on WC with TiC as an interposing layer.
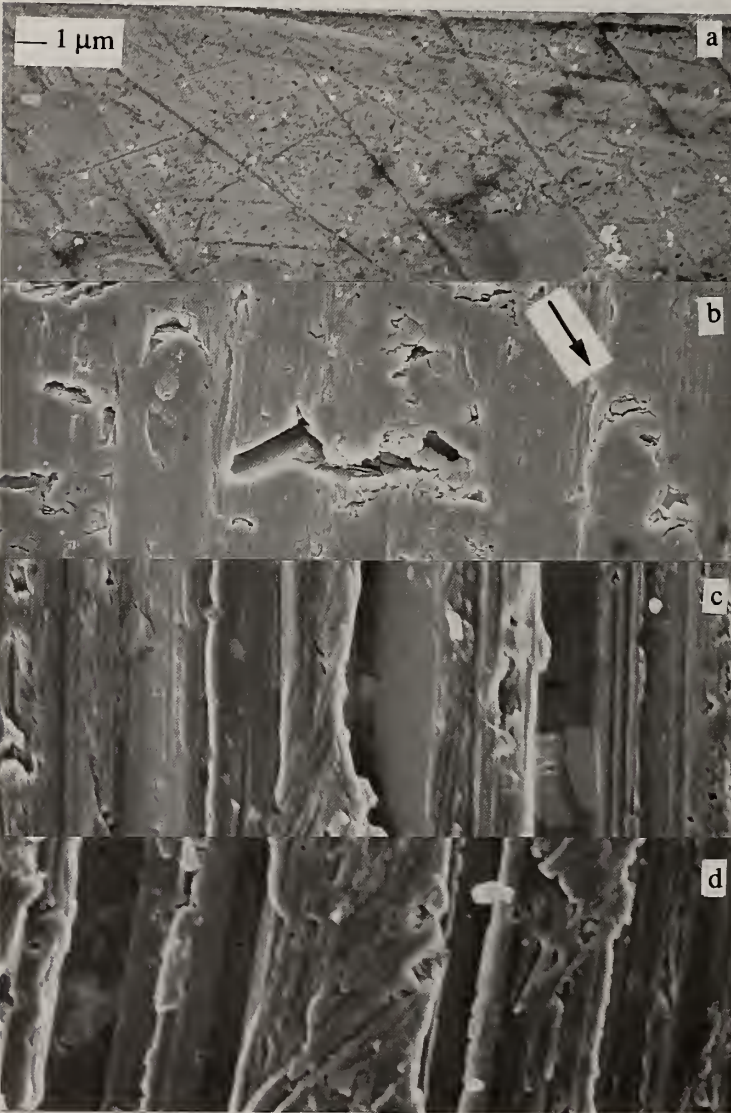

Fig. 3 SEM photographs of surfaces of Al-12.5%Si alloy work pieces before (a) and after dry fly cutting for 5 min. at speed 500 m/min., depth of cut 1 mm, and feed 0.1 mm/rev with (b) WC, (c) WC coated with a single layer of diamond, and (d) WC coated with TiC multilayer diamond.

Work pieces (14x20x52 mm^3) of Al-12.5%Si alloy were polished with 0.3 μm alpha alumina powder before machining tests. The surfaces of Al-Si alloy before and after machining are shown in Fig. 3(a), (b), (c), and (d). Before machining, the surface is smooth. After machining with the WC tool without diamond coating, the surface exhibits tool tracks (Fig. 3(b)). Few deep grooves pointed by an arrow are introduced from the feed step (100 μm). Most of grooves are shallow, and some voids are observed. After machining with the WC tools coated with single layer diamond or multilayer diamond, the surfaces exhibit many deep grooves. The distance between two cutting grooves is about 1-3 μm which is the same order as the distance between cutting edges of diamond particles. The differences in wear patterns between the two work pieces machined with the single layer and multilayer diamond coated tool are small.

It is well known that the cutting force is responsible for plastic flow in the removal of the surface layers. A smaller contact area of a tool tip produces larger shear stresses in a smaller region. When the tip of WC tools without diamond coatings is not sharp, the shear stresses are low, and removal of the surface layer by the plastic flow becomes

Fig. 4 SEM photographs of wear surfaces of WC tool (a), WC tool coated with single layer of diamond (b), and WC tool coated multilayer diamond (c) after dry fly cutting.

difficult because shear stresses are distributed in a large area around the tool tip. When the tool encounters second phase particles, such as Si in Al-Si alloy, it may remove the particle by shear along the interface instead of removal of a surface layer by plastic flow. In Fig. 3(a), the voids indicate that the second phase was removed along the interfaces. When a WC tool is coated with a layer of polycrystalline diamond, the cutting edge of the tool is not smooth in microscopic scale. However, each diamond crystallite exhibits good facets or sharp edges which become a very sharp tool with size 1 to 3 μm. Therefore, this diamond coated tool is a combination of thousands of sharp micro-tools. The grooves in Fig. 3(c) and 3(d) were made by the micro-tools. These sharp tools give rise to plastic flow during machining. Therefore, there are no voids observed in Fig. 3(c) and 3(d).

The life of diamond coated tools is determined by the adhesion characteristics. The WC tool after machining, as shown in Fig. 4(a), exhibits crater wear. The WC tools coated with single layer or multilayer diamond do not exhibit any crater wear (Fig. 4(b) and 4(c)) and there is a continuous diamond film on the both rake and flank faces after machining. Aluminum alloy sticking on the diamond crystallites is observed in Fig. 4(b) and 4(c). The diamond coatings exhibit good adhesion and protect the WC tools from wear. Our previous work [4] showed a better adhesion using a multilayer structure than using a single layer structure. The present machining tests are limited to a short period (5 min.) so that the difference in adhesion and wear resistance of the single layer and multilayer coatings can not be observed. Short life time of diamond coated WC tools and the poor surface finish have been observed in earlier work [5]. This may be due to the larger size of the diamond crystallites.

CONCLUSION

Adhesion and wear resistance of single layer and multilayer diamond coated WC tools were investigated. Results show that these coatings exhibit good adhesion on WC tools and protect the tools from wear during machining. The improvement in wear resistance is due to the small and sharp cutting edges provided by the polycrystalline diamond coatings.

ACKNOWLEDGMENT

Reference

[1] A. Inspektor, C.E. Bauer, and E.J. Oles, Surf. Coat. Technol., 68/69 (1994) P. 359
[2] E.R. Kupp, W.R. Drawl, and K.E. Spear, Surf. Coat. Technol., 68/69 (1994) P.378
[3] C. Tsai, J.C. Nelson, and W.W. Gerberich, Diamond and Related Materials, 2 (1993) P. 617
[4] W.D. Fan, X. Chen, K. Jagannadham, and J. Narayan, J Mater. Res., 9 (1994), P. 2850
[5] K. Shibuki, and K. Sasaki, M. Yagi, T. Suzuki, and Y. Ikuhara, Surf. Coat. Technol., 68/69 (1994) P. 369
[6] C.H. Shen, Transactions of NAMRI/SME, 1994, P. 201

DIAMOND OPTICS

DIAMOND OPTICS: STATUS FOR INFRARED APPLICATIONS

Daniel C. Harris

Chemistry and Materials Branch (Code 474220D), Research and Technology Division, Naval Air Warfare Center Weapons Division, China Lake CA 93555 U.S.A.

Key words: optics, optical properties, infrared optics, window, dome, coating

Abstract

Clear diamond windows with thicknesses up to 1 mm and diameters up to 6 cm have been produced. Several methods have been demonstrated for attaching thin diamond coatings to optical windows. Hemispheric diamond domes with thicknesses up to 1 mm and diameters of 60-75 mm have been grown and optical fabrication is in progress. In the 8-14 μm infrared region, the absorption coefficient is as low as $0.1 - 0.3$ cm^{-1}, optical scatter is below 1%, and emissivity at 500°C is below 3%. Microwave dielectric properties, thermal properties, and most mechanical properties of chemical-vapor-deposited diamond are equivalent to those of Type IIa natural diamond. The mechanical strength of $0.5 - 1$ mm thick chemical-vapor-deposited diamond attained so far is an order of magnitude lower than that of natural diamond.

1. Fabrication of Bulk Optical Diamond

Among optical materials, diamond offers a unique combination of transparency in most of the ultraviolet, visible and infrared regions, low microwave reflection, resistance to thermal shock, chemical inertness, and high durability with respect to waterdrop impact and solid particle abrasion.[1-3] The advent of chemical vapor deposition (CVD)[4,5] makes it possible to fabricate diamond in sizes and shapes that are not available from natural diamond.

Although it is not very difficult to make thin diamond films ($\lesssim 100$ μm) with good infrared transmission, optical-quality bulk material ($\gtrsim 0.5$ mm) is much more difficult to fabricate, and few organizations have demonstrated this capability. Fig. 1 shows progress in fabrication of clear windows at Raytheon. Low quality (black) diamond is produced in some types of reactors at linear growth rates >100 μm/h. However, we are unaware of any success in growing optical quality diamond at rates in excess of ~5 μm/h, regardless of the type of reactor.

Because diamond is the hardest known material, it is extremely difficult to polish. The specimens in Fig. 1 were polished by conventional methods using abrasive diamond grit, which is very inefficient. Other polishing methods include rotation against a hot iron or nickel wheel (called a scaife) under vacuum or hydrogen [6,7], static contact with iron, cerium, lanthanum, or La-Ni eutectic at 600-900°C under Ar [8,9,10], use of ion beams [11,12] and laser ablation [13]. The difficulty with any of these methods is controlling the optical figure (the exact required geometry) of the workpiece.

1993   1994

Centimeters	Centimeters
1 2 3 4 5	1 2 3 4 5

Raytheon Diamond
H157-01
0.35 mm thick

Raytheon Diamond
MP2-54LD
0.75 mm thick
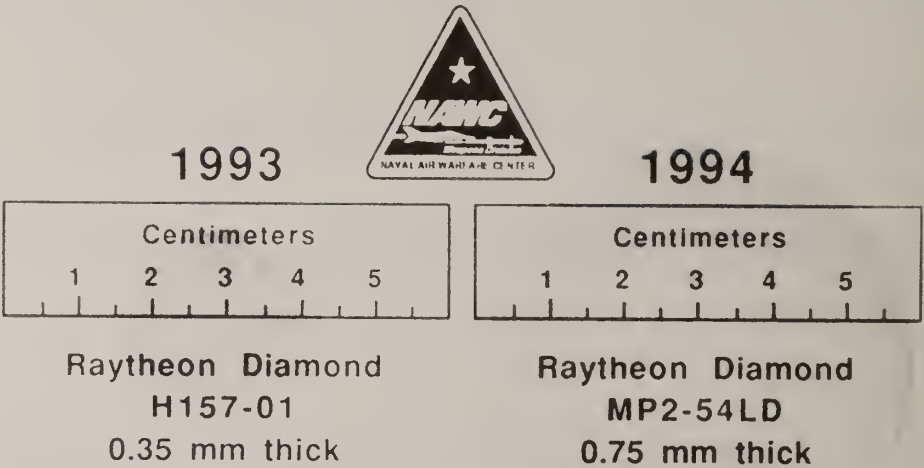
Fig. 1. Polished diamond grown by microwave plasma chemical vapor deposition at
Raytheon Co.

Fig. 2 shows an as-grown CVD diamond dome with a very rough outer surface. Fig.
3 shows a 1-mm-thick dome whose outer surface has been machined to hemispheric
shape with a laser and whose roughness has been reduced by more than an order of
magnitude to <5 μm. Final finishing to remove graphite produced by the laser and to
provide an optical finish still requires abrasive polishing.

Fig. 2.
Raytheon
diamond
dome with
unfinished
surface.

Fig. 3. Diamond dome that has been machined to hemispheric shape with a laser.

2. Diamond Coatings

Bulk diamond windows are required for high thermal shock environments and highly erosive environments in which other materials would fail. However, for many applications, a thin, protective diamond coating would significantly increase the durability of an underlying, softer window material. Growth of diamond directly on most optical materials is prohibited either because the substrate material is attacked by the plasma of the growth chamber or because of the large difference in thermal expansion between diamond and most other materials.

Thin diamond coatings have been grown directly on fused silica, sapphire and a SiO_2-Al_2O_3-ZnO glass ceramic using metal-induced nucleation of diamond (MIND) [14]. In this process, a source of metal is placed in contact with the plasma near the substrate surface on which diamond is to be grown. (The diamond does not grow on the source of metal.) The source can be (1) a thin film of Cr, CrN, Ti, TiN, or Ni; (2) a metal ring containing Cr; or (3) tris(1,1,1-trifluoropentandionato)chromium (III) dissolved in acetone serving as the carbon source for diamond growth. MIND improves the nucleation and adherence of diamond and gives a growth rate of 0.4 μm/h at 650°C. Thick layers cannot be produced because thermal expansion mismatch causes delamination when the diamond thickness exceeds 5 μm.

Alternatively, a sputtered refractory interlayer (SPRINT) such as silica, hafnia, silicon carbide and aluminum nitride can be deposited on the substrate surface and diamond can be grown directly on the interlayer [14, 15]. The interlayer improves adhesion by providing a graded thermal expansion. The interlayer also encapsulates the substrate to protect it from attack by the plasma and creates a diffusion barrier between the diamond and the substrate.
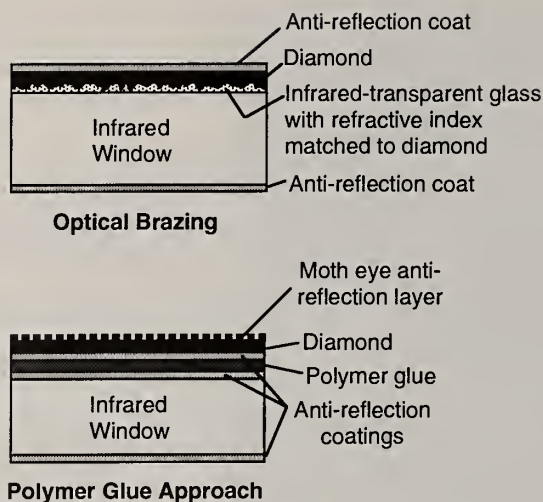
Fig. 4. Two methods for attaching a diamond coating to an optical window.

Instead of depositing diamond directly on a window or an interlayer, diamond can be grown separately and then bonded to the window. Fig. 4 shows two methods that have been demonstrated. In optical brazing [16], the bonding agent is a low-melting, infrared-transparent glass. If As:Se:S chalcogenide glass is used, the index of refraction of the glass is similar enough to that of the diamond that the rough surface of the diamond does not need to be polished to reduce optical scatter. However, the rough points on the diamond surface act as microindentors during raindrop impact. The coated window is more durable if the diamond is polished prior to bonding. The chalcogenide glass softens near 200°C.

In the polymer glue approach in Fig. 4, a polymer that is transparent in the 8-12 μm long wave infrared region (but not in the 3-5 μm midwave region) serves as the bonding layer [17]. Because the index of refraction of the polymer is not matched to that of diamond, antireflection coatings are required at every interface in this structure. The polymer softens near 150°C, but might be useful for short times up to 300°C. Fig. 4 shows a motheye antireflection coating as the outermost layer [18]. This is an all-diamond patterned outer surface that provides optical impedance matching between diamond and air.

3. Optical Properties

Table I summarizes properties that have been achieved for CVD diamond and compares them to properties of Type IIa diamond [19]. The litmus test for "optical-quality" diamond is the transmittance of a thick (>0.3 mm), polished specimen. Fig 5. compares the spectrum of optical-quality CVD diamond to that of natural Type IIa material. Thick diamond is an excellent window for the long wave region, but has significant absorption in the midwave region. CVD diamond with more than a few ppm of hydrogen has sharp C-H absorptions near 3.4 μm and weak, broad absorptions in the 1-phonon diamond region at 8-10 μm. At elevated temperatures where emittance is significant, thin diamond coatings may be useful for the midwave region, but thick diamond is not. Fig. 6 compares the long wave infrared absorption of high-quality

Table I. Summary of Properties of CVD and Type IIa Diamond

|	
Optical absorption coefficient @ 8-12 μm wavelength	
Gem diamond:	0.03-0.05 cm^{-1} @ 10.6 μm @ 20°C
CVD diamond:	0.1 - 0.3 cm^{-1} @ 20°C
	CVD absorption coefficient @ 8-12 μm is ~2x as great at 500°C as at 20°C
Emissivity @ 8-12 μm wavelength	
CVD diamond:	0.02 @ 300°C (sample thicknesses = 0.35 - 0.77 mm)
	0.03 @ 500°C (sample thicknesses = 0.35 mm)
Integrated forward optical scatter	
Gem diamond:	0.2% (@ 0.63 μm integrated from 0.3 to 45°)
(0.3-0.5 mm thick)	0.004% (@ 10.6 μm integrated from 1.1 to 45°)
CVD diamond:	4% (@ 0.63 μm integrated from 2.5 to 70°)
(0.35-0.77 mm thick)	0.2-0.8% (@ 10.6 μm integrated from 2.5 to 70°)
	(There is no significant change in the range 20-500°C)
Refractive index @ 10 μm wavelength	
Gem diamond:	2.376
CVD diamond:	2.38; dn/dT = 15.6 × 10^{-6} K^{-1} (7-12 μm, T = 295-784 K)
Microwave dielectric properties (T = °C)	
Gem diamond:	Dielectric constant (ε) = 5.61 ± 0.05; tan δ = (6±3) × 10^{-4}
(@ 35 GHz) 100Δε/ε$_{18°C}$ =	-0.026 + 0.006886T + 3.831×10^{-7}T^2 + 1.185×10^{-8}T^3 (T = 18-525°C)
CVD diamond:	Dielectric constant = 5.7; tan δ < 4 × 10^{-4} (@ 13.6 GHz)
Thermal conductivity	
Gem diamond:	2300 W/m·K(20°C); 1300 W/m·K (480°C); 500 W/m·K (700°C)
CVD diamond:	2000 W/m·K (20°C); 1200 W/m·K (480°C)
Thermal expansion coefficient	
Gem diamond:	1.0 ppm/K (300 K); 2.7 ppm/K (500 K); 4.4 ppm/K (1000 K)
CVD diamond:	Same as natural diamond
Hardness	
Gem diamond:	76 - 115 GPa (anisotropic)
CVD diamond:	81 ± 18 GPa (decreases by 30% at 800°C)
Fracture toughness	
Gem diamond:	~3.4 MPa√m
CVD diamond:	2-8 MPa√m; 5.3 ± 1.3 MPa√m; 8 ± 2 MPa√m
Young's modulus / Poisson's ratio	
Gem diamond:	1143 GPa / 0.069 (average of anisotropic values)
CVD diamond:	Consistent with gem diamond value
Mechanical strength [19]	
Gem diamond:	~3 GPa (tensile strength)
CVD diamond:	~200 - 400 MPa (No loss of strength at 1000°C)
	(0.5-1 mm thick, polished disks tested by ring-on-ring flexure; load radius = 4.88 mm, support radius = 8.61 mm)
Water jet damage threshold velocity [24]	
(0.8 mm diameter jet; 1-mm-thick, optical-quality diamond on solid backing)	
Gem diamond:	~580 m/s jet velocity
CVD diamond:	200-250 m/s (central crazing); 350-500 m/s (ring fracture)
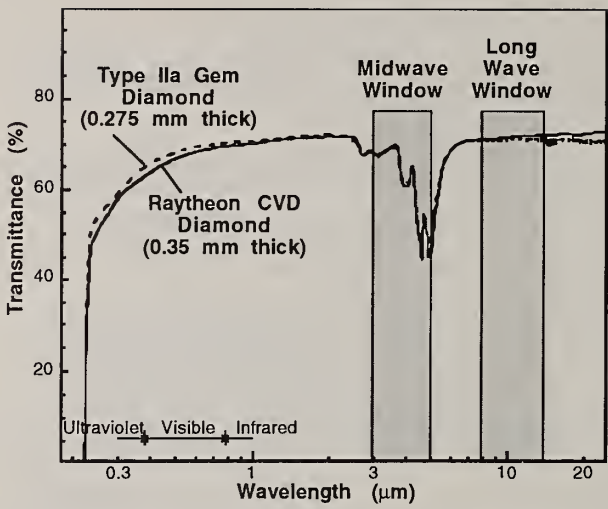
Fig. 5. Comparison of ultraviolet-visible-infra-red transmission of excellent-optical-quality CVD diamond and natural Type IIa diamond. Shaded boxes denote atmospheric infrared transmission windows.
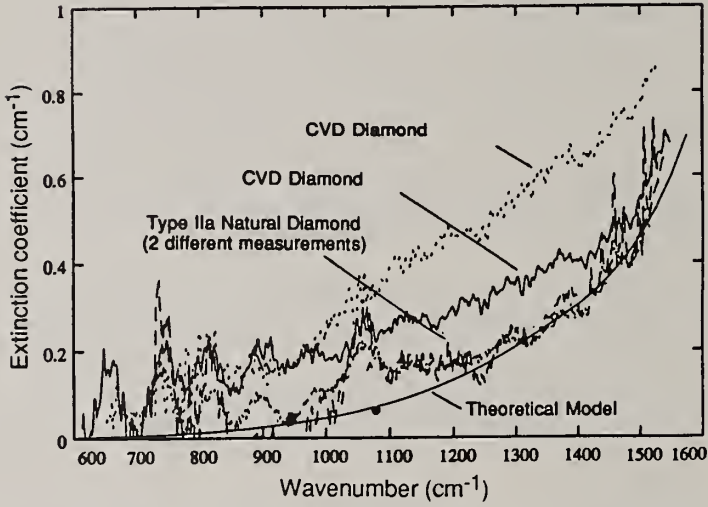
Fig. 6. Long wave infrared transmission of natural Type IIa diamond and two high-quality samples of CVD diamond. Extinction coefficient includes the combined effects of absorption and scatter [20]

CVD diamond to that of Type IIa diamond. Fig. 7 shows long wave infrared emissivity of high-quality CVD diamond measured at 475°C.

4. Mechanical Properties

Table I shows that CVD diamond has attained nearly all qualities of natural diamond except for mechanical strength (and water jet impact resistance that is related to strength). Thin membranes of diamond are 2-4 times stronger than thick disks, but this is because thin membranes cannot have flaws as large as those in thick disks. One investigation of 6 CVD diamond disks with thicknesses in the range 0.18-0.3 mm used gas pressurization to measure bursting strengths of 900 ± 140 MPa [21], which is 2-4 times higher than the values reported for ring-on-ring flexure tests in Table I. It

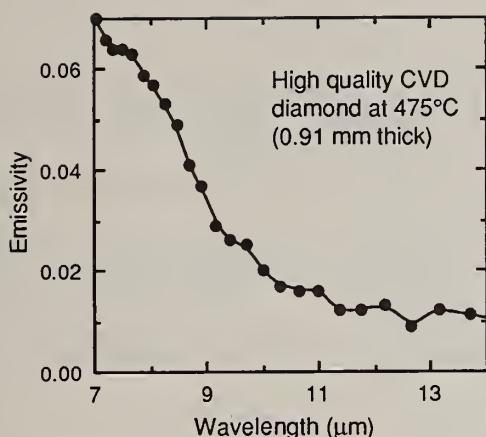Fig. 7. Measured emissivity of excellent-optical-quality CVD diamond in the long wave infrared region. [Data from A. B. Harker, Rockwell Science Center.]

remains to be seen whether thicker disks from the same source tested in ring-on-ring flexure are, indeed, stronger than those reported in Table I. Even with a relatively low mechanical strength, the extremely high thermal conductivity of CVD diamond, coupled with its low thermal expansion, provides a thermal shock resistance that is 2 orders of magnitude greater than that of other optical window materials.

The mechanical strength of CVD diamond is limited by relatively huge flaws in the material that serve as fracture origins. Flaws with a radius of 100-300 μm are found at the fracture origins of disks that are only 800 μm thick. Initial reports of fracture toughness for CVD diamond gave values near 5 and 8 MPa$\sqrt{m}$, which can be compared to the value of 3.4 MPa$\sqrt{m}$ for single-crystal diamond. However, more recent measurements of a wider selection of CVD diamond samples gave fracture toughness values spanning the range 1-8 MPa$\sqrt{m}$ [22]. In the samples that were studied, fracture toughness was not correlated with flaw size and strength was not correlated with thickness. However, there did appear to be a rough correlation of increasing flaw size with increasing thickness. Measurements of residual stress in individual grains within CVD diamond gave values in excess of 1 GPa. [23]. CVD diamond has not performed as well as natural diamond in water jet impact tests [24] or sand erosion tests [25]. Nonetheless, in comparison to most infrared window materials, CVD diamond even in its present state is quite durable.

Progress in fabrication of large specimens of high quality diamond has proceeded at a remarkable pace in the past decade. There is every reason to expect continued progress to provide us with practical diamond optics for applications in which no other material can meet requirements.

5.   References

1.   R. D. Clay and J. P. Clay, "Diamond for Optical Material," *Proc. SPIE* **1984**, *505*, 57-61.
2.   J. Wilks and E. Wilks, *Properties and Applications of Diamond*, Butterworth Heinemann, Oxford, 1991.
3.   J. E. Field, ed., *The Properties of Natural and Synthetic Diamond*, Academic

546

Press, London, 1992.
4. K. E. Spear and M. Frenklach, "High Temperature Chemistry of CVD Diamond Growth," *Pure. Appl. Chem.* **1994**, *66*, 1773.
5. M. N. R. Ashfold, P. W. May, C. A. Rego, and N. M. Everitt, "Thin Film Diamond by Chemical Vapor Deposition Methods," *Chem. Soc. Rev.* **1994**, 21.
6. M. Yoshikawa, "Development and Performance of a Diamond Film Polishing Apparatus with Hot Metals," *Proc. SPIE* **1990**, *1325*, 210.
7. A. B. Harker, J. Flintoff and J. F. DeNatale, "The Polishing of Polycrystalline Diamond Films," *Proc. SPIE* **1990**, *1325*, 222.
8. S. Jin, J. E. Graebner, G. W. Kammlott, T. H. Tiefel, S. G. Kosinski, L. H. Chen and R. A. Fastnacht, "Massive Thinning of Diamond Films by a Diffusion Process," *Appl. Phys. Lett.* **1992**, *60*, 1948.
9. S. Jin, J. E. Graebner, M. McCormack, T. H. Tiefel, A. Katz and W. C. Dautremont-Smith, "Shaping of Diamond Films by Etching with Molten Rare-Earth Metals," *Nature* **1992**, *362*, 822.
10. C. E. Johnson, "Chemical Polishing of Diamond," *Surf. Coat. Tech.* **1994**, *68/69*, 374.
11. A. Hirata, H. Tokura and M. Yoshikawa, "Smoothing of Chemically Vapor Deposited Diamond Films by Ion Beam Irradiation" *Thin Solid Films* **1992**, *212*, 43.
12. B. G. Bovard, T. Zhao and H. A. Macleod, "Oxygen-ion Beam Polishing of a 5-cm-diameter Diamond Film," *Appl. Opt.* **1992**, *31*, 2366.
13. K. V. Ravi and V. G. Zarifis, "Laser Polishing of Diamond," *Proc. 3rd Int. Symp. on Diamond Materials*, Electrochemical Society, Pennington, NJ, 1993, p.861.
14. M. B. Moran, L. F. Johnson and K. A. Klemm, "Method for Growth of CVD Diamond on Thin Film Refractory Coatings and Glass Ceramic Materials,"*Proc. SPIE* **1994**, *2286*, 205.
15. C. J. Brierley, M. C. Costello, M. D. Hudson and T. J. Bettles, "Diamond Coatings for Large Area IR Windows," *Proc. SPIE* **1994**, *2286*, 307.
16. W. D. Partlow, R. E. Witkowski and J. P. McHugh, "CVD Diamond Coatings for the Infrared by Optical Brazing," in *Applications of Diamond Films and Related Materials* (Y. Tzeng, M. Yoshikawa, M. Murakawa and A. Feldman, eds.), Elsevier, Amsterdam, 1991, p 163.
17. A. B. Harker, personal communication.
18. A. B. Harker and J. F. DeNatale, "Diamond Gradient Index 'Moth-Eye' Antireflection Surfaces for LWIR Windows," *Proc. SPIE* **1992**, *1760*, 261.
19. D. C. Harris, "Properties of Diamond for Window and Dome Applications," *Proc. SPIE* **1994**, *2286*, 218; D. C. Harris, *Development of CVD Diamond for Infrared Optical Applications*, Naval Air Warfare Ctr. Weapons Division TP 8210, July 1994.
20. M. E. Thomas and W. J. Tropf, "Optical Properties of Diamond," *Proc. SPIE* **1994**, *2286*, 144.
21. T. J. Valentine, A. J. Whitehead, R. S. Sussmann, C. J. H. Wort and G. A. Scarsbrook, "Mechanical Property Measurement of Bulk Polycrystalline CVD Diamond," *Diamond and Related Mater.* **1994**, *3*, 1168.
22. J. J. Mecholsky, Jr., and L. Hehn, unpublished.
23. A. B. Harker, D. G. Howitt, S. J. Chen., J. F. Flinthoff and M. R. James, "Residual Stress Measurements on Polycrystalline Diamond," *Proc. SPIE* **1994**, *2286*, 254.
24. C. R. Seward, E. J. Coad, C. S. J. Pickles and J. E. Field, "The Rain Erosion Resistance of Diamond and Other Window Materials," *Proc. SPIE* **1994**, *2286*, 285.
25. J. E. Field, Q. Sun and H. Gao, "Solid Particle Erosion of Infrared Materials," *Proc. SPIE* **1994**, *2286*, 301.

PROPERTIES OF CVD DIAMOND FOR OPTICAL APPLICATIONS

Mark P. D'Evelyn,[1] Edward B. Stokes,[1] Peter J. Codella,[1] and Bradley E. Williams[2]

[1] GE Corporate Research & Development, P.O. Box 8, Schenectady, NY 12301 USA

[2] GE Superabrasives, P.O. Box 568, Worthington, OH 43085 USA

Key words: diamond, optics, infrared, UV-visible, Raman spectroscopy

Abstract

The unique multispectral transparency properties of diamond, combined with its chemical inertness, biocompatibility, hardness, and mechanical strength, enable it to serve as a window or optical probe in a variety of aggressive or biomedical environments. We have characterized the optical and mechanical properties of transparent GE CVD diamond using a combination of methods. The optical transmission is nearly equivalent to type IIa natural diamond from the ultraviolet to the far-infrared. Little sp^2 carbon is detectable by FT-Raman spectroscopy with near-infrared excitation for enhanced sensitivity. The Young's and shear modulus, measured by a dynamic resonance method on free-standing disks, have typical values near 1150 and 530 GPa, respectively, in excellent agreement with theoretical values for pure polycrystalline diamond. The fracture strength is typically about 0.8–1 GPa.

1. Introduction

Tremendous progress has been made in the past several years in the routine fabrication of transparent diamond by chemical vapor deposition (CVD) [1-4]. Polycrystalline diamond windows are available commercially at moderate cost in a range of diameters and thicknesses. The present paper briefly describes the optical and mechanical properties of transparent, free-standing GE CVD diamond.

2. Experimental

Transparent diamond was grown to thicknesses between 0.2 and 1 mm using a proprietary chemical vapor deposition process. After growth, the CVD diamond was demounted from the substrate, lapped, and polished on both faces. The thickness of the polished windows was typically constant to within 5–15 µm per cm across the part.

The optical properties of the diamond windows were characterized by transmission spectra between 0.2 and 20 µm (500–50,000 cm^{-1}) and by Raman spectroscopy. UV-visible-near-IR spectra (0.2–2.5 µm) were obtained using a Hitachi 3410 double-beam

spectrometer. Small discontinuity artifacts were sometimes present in the spectra at 0.85 μm where the instrument automatically switches detectors. Fourier-transform infrared spectra were taken using a Nicolet Magna 750 FTIR spectrometer. The reproducibility in the absolute transmission levels in both instruments was ca. 1–3% and was limited by beam-steering effects due to slight deviations from parallelism between the front and back faces of the samples together with the high refractive index of diamond. Rotation of the windows within the sample compartment caused the transmission level at a given wavelength to shift up or down in a periodic way. Raman spectra of the windows were obtained using a Nicolet 950 FT-Raman spectrometer, which uses the fundamental of a YAG laser (1.064 μm; 1.16 eV) as the excitation source. Raman spectroscopy with near-IR excitation has been shown to provide much higher sensitivity to sp^2-bonded carbon [5,6] than with visible excitation, as is typically employed.

The elastic constants of free-standing disks of transparent CVD diamond were determined by a dynamic resonance method described in more detail elsewhere [7]. Briefly, the disks were supported along the nodes of flexural or torsional vibrational modes, and oscillations were induced by a falling ceramic bead. The frequencies of the vibrations were measured using a microphone and signal analyzer, and the Young's and shear modulus were calculated using quasi-analytic formulas [7,8].

The fracture strength was determined by conventional 3-point bend and by pressure-burst measurements, and will be described in detail elsewhere.

3. Results and Discussion

UV-visible-near-IR and mid-IR spectra of selected samples are shown in Fig. 1. The samples included a type IIa natural diamond window, 0.25 mm thick, for reference; a higher-quality CVD diamond window, 0.23 mm thick, and a lower-quality CVD diamond window, 0.26 mm thick. The higher-quality CVD sample is very clear, with small, light-scattering inclusions barely visible. Many more inclusions are present in the lower-quality sample, giving it a slightly brownish tinge, although it is still highly transparent.

The slight discontinuities between spectral regions are due to detector or instrument changes and beam-steering artifacts, as described above. The transparency of the higher-quality sample is seen to closely approximate that of type IIa natural diamond from the ultraviolet through the mid-infrared. The transparency is slightly less at the short-wavelength end of the ultraviolet, presumably due to scattering at internal grain boundaries or inclusions. Notably, absorption within the one-phonon region between 8 and 20 μm is extremely low. Approximately twice as much hydrogen is present in the higher-quality CVD diamond window, ca. 20 ppm, as in the type IIa specimen, based on the integrated intensity of the small C-H stretch features near 2900 cm^{-1}. The lower-quality sample is significantly less transparent, particularly in the visible and ultraviolet. The wavelength dependence of the transmission is indicative of scattering, most likely by grain boundaries or inclusions. Approximately 100 ppm of hydrogen
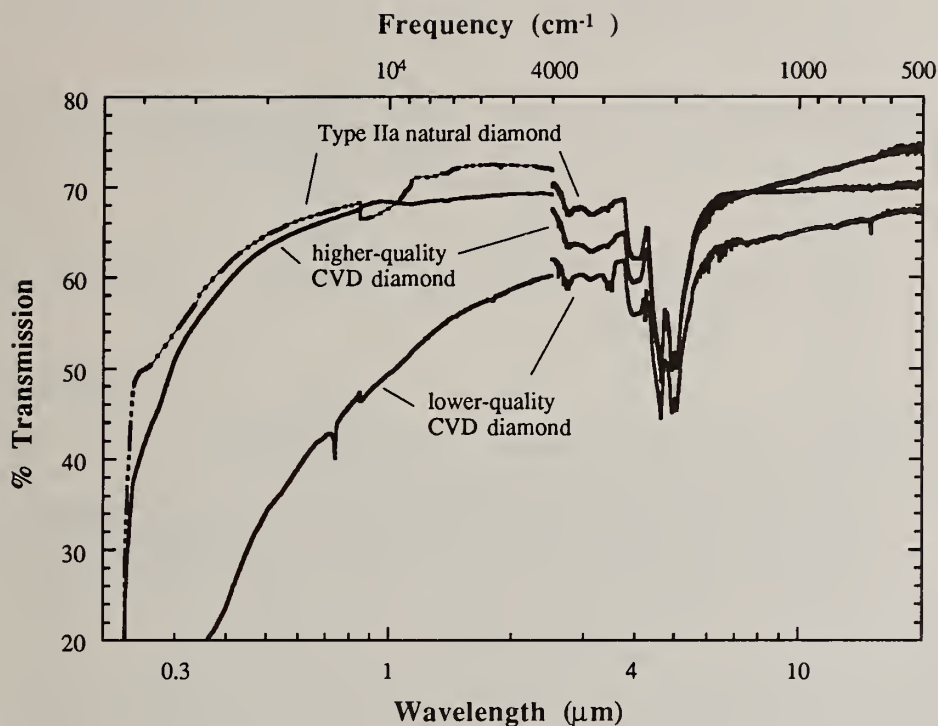
FIG. 1. Combined ultraviolet-visible-near-infrared and mid-infrared spectra of higher-and lower-quality transparent CVD diamond, together with spectra of a type IIa natural diamond for comparison.

was present in this sample, and a weak absorption is also evident in the one-phonon region.

FT-Raman spectra of the same samples shown in Fig. 1 are shown in Fig. 2. The spectra are qualitatively very similar to previous results obtained with near-IR excitation [5,6]. We have found that spectra taken with an excitation energy of 1.16 eV are approximately five times more sensitive to sp^2 carbon than spectra obtained at an energy of 2.41 eV, based on the relative peak height ratios of the 1332 cm^{-1} diamond fundamental and the broad "graphitic" carbon peak. The higher-quality CVD sample is seen to have quite a high "sp^3/sp^2" ratio, although we have measured values as high as 50 in FT-Raman spectra of other CVD diamond samples . There is significantly more sp^2 carbon in the lower-quality sample, suggesting that most of the scattering evident in the transmission spectra (Fig. 1) is due to sp^2 carbon rather than to hydrogen.

The mean values of the Young's and shear modulus obtained on thirteen 10- or 11-mm-diameter transparent CVD diamond disks were 1151 and 531 GPa, respectively, in excellent agreement with theoretical values for pure polycrystalline diamond [9,10].
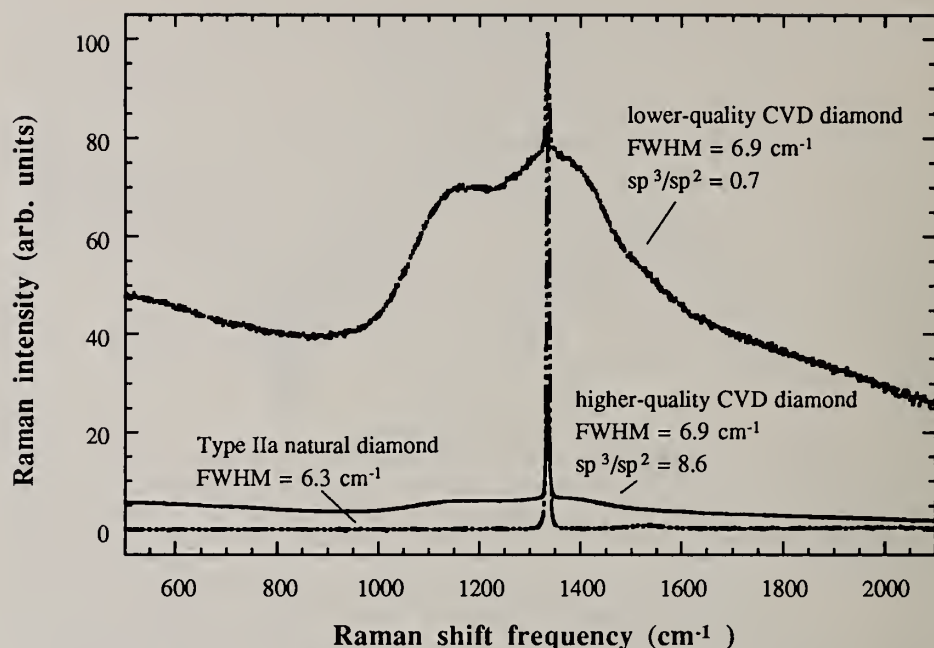
FIG. 2. FT-Raman spectra of the same diamond samples as in Fig. 1. The excitation energy was 1.16 eV (9398 cm^{-1}). The "sp^3/sp^2" ratio is the ratio between the peak heights of the sharp 1332 cm^{-1} peak and the broad underlying peak.

4. References

1. T. R. Anthony and J. F. Fleischer, U. S. Patents 5,110,579 (1992) and 5,273,731 (1993).

2. G. Lu, K. J. Gray, E. F. Borchelt, L. K. Bigelow, and J. E. Graebner, Diamond Relat. Mater. **2**, 1064 (1993).

3. C. J. H. Wort, C. G. Sweeney, M. A. Cooper, G. A. Scarsbrook, and R. S. Sussmann, Diamond Relat. Mater. **3**, 1158 (1993).

4. K. M. McNamara, B. E. Williams, K. K. Gleason, and B. E. Scruggs, J. Appl. Phys. **76**, 2466 (1994).

5. J. Wagner, C. Wild, and P. Koidl, Appl. Phys. Lett. **59**, 779 (1991).

6. E. S. Etz, in *Microbeam Analysis*, ed. J. J. Friel (VCH, New York, 1994) p. 71.

7. M. P. D'Evelyn, D. E. Slutz, and B. E. Williams, "Elastic properties of CVD diamond via dynamic resonance measurements," Mater. Res. Soc. Symp. Proc. **383** (in press); and M. P. D'Evelyn, to be published.

8. J. C. Glandus, Ph.D. Dissertation, University of Limoges (1981, unpublished).

9. C. A. Klein and G. F. Cardinale, Diamond Relat. Mater. **2**, 918 (1993).

10. M. Werner, S. Hein, and E. Obermeier, Diamond Relat. Mater. **2**, 939 (1993).

MICROSTRUCTURAL EVOLUTION AND FLAWS IN CVD DIAMOND

Greg D. Barber[1], W.A. Yarbrough[1], and Kevin Gray[2]

[1]260 Intercollege Materials Research Laboratory, University Park, PA 16803
[2]Norton Diamond Film, Goddard Road, Northboro, MA 01532

Abstract

Regrowth experiments on polished and optically transparent, thick free standing diamond were used to reveal the crystallographic relationships between various grains at the growth surface and show how the microstructure evolves locally. The results show that diamond growth occurs most rapidly on the defect free (110) surface and also suggest that flaw incorporation may occur or be aggravated by twinning during growth. This would imply that varying deposition conditions and methods are not likely, by themselves, to result in much improvement as textured growth with twinning during the growth process are features common to most diamond growth methods. Direct evidence is shown that the dominant growth axis by hot filament assisted CVD is along a <110> direction and that this is not dependent on the presence of defects. This implies that <110>, or near <110>, oriented grains tend to expand laterally (in the plane of the layer) with 2-fold rather than 4-fold symmetry.

Introduction and Experimental

It has been established that during the growth of even the highest quality polycrystalline diamond layers and films, defects and voids of the order of the grain size can and do become incorporated into the diamond microstructure.[1] Such defects and flaws are potentially serious in many applications as they lower the fracture strength, can act to entrain contaminants and can lead to locally discontinuous thermal conduction. In addition it is now well established that stress, including significant micro-stress can exist in the microstructure of CVD diamond. Both of these are likely related to the way in which the microstructure evolves during growth and thus the microstructure and its evolution is being studied.

As polycrystalline diamond is not easily studied using many conventional techniques (e.g., thermal etching) the microstructure of thick free standing diamond, was studied using two different methods. The first was atomic hydrogen etching and the second was the regrowth of diamond on the polished surface. Of these two approaches, the regrowth of diamond on the polished polycrystalline surface proved the most revealing. The samples were thick (>500 µm) free standing, polycrystalline diamond layers where the scale of the microstructure was sufficient to permit the careful study

of relative grain orientations using scanning electron microscopy. Numerous samples of commercially produced, optically polished and transparent material were provided by Norton Diamond Film and small amounts of diamond were regrown to reveal the microstructure and study its evolution. Regrowth was accomplished by tungsten wire hot filament CVD using 1.0 to 1.5 vol % CH_4 in H_2 at 30 Torr. The filament to surface distance was 3.5 mm and this was held constant by spring tensioning of the filaments. The experimental arrangement used was similar to that previously published.[2] The amounts of diamond deposited were sufficiently small to ensure that the observed surface represented the underlying microstructure for each sample.

Results and Discussion

The grains in these layers were strongly <110> oriented as this is the dominant growth axis for most high quality CVD diamond. Individual grains were found to be ~100 µm in size at the polished surface. Some slight surface damage from polishing could be seen in a few samples by scanning electron microscopy (SEM) prior to regrowth, but these were removed entirely during redeposition. Clear evidence was found that some sites grow along a normal to the surface (the thickness direction) at much slower rates than the rest of the surface. Such sites were most commonly found at points where twin boundaries intersect randomly oriented grain boundaries. Sites such as these may lead to the formation of a pit or channel which could lie parallel with or at an angle to the growth direction. Such voids or channels might then become overgrown or encapsulated in the layer at a later stage of growth, thus giving a mechanism by which a flaw could be formed and encapsulated in the growing layer. Upon exposure at the surface by polishing or other finishing operations such voids could clearly serve as strength limiting flaws. This work was pursued in the effort to determine where and how such flaws might first be nucleated, how they might propagate with continued growth, and finally, what process or processes might lead to their termination and incorporation. By this means it was hoped that a means of eliminating flaw formation and incorporation might be found.

An example of the microstructure seen at the polished surface by diamond regrowth is shown in Figure 1. Clearly emergent at the surface are <111> twin boundaries, often related to one another by a 5 fold twin axis approximately normal to the surface or parallel with the layer's growth axis. These became readily visible with very little additional growth, or upon atomic hydrogen etching, as they quickly develop (100) and (111) facets. It has been shown that the dominant texture in much, if not all, optically transparent CVD diamond is along the <110> and it is well known that this results in a dominant (220) x-ray texture for much high quality CVD diamond. It has been suggested that the reason for this is that the growth rate is greatest along <111> twin defect boundaries. However faceting of these single and multiple twin boundaries, as shown in Figure 1, implies that the growth of diamond is indeed greatest on the defect free (110) surface. This also suggests at least one basic mechanism by which extended defects or voids may be initiated and become entrained within the diamond layer, without regard to the specific technology or method used for diamond growth.
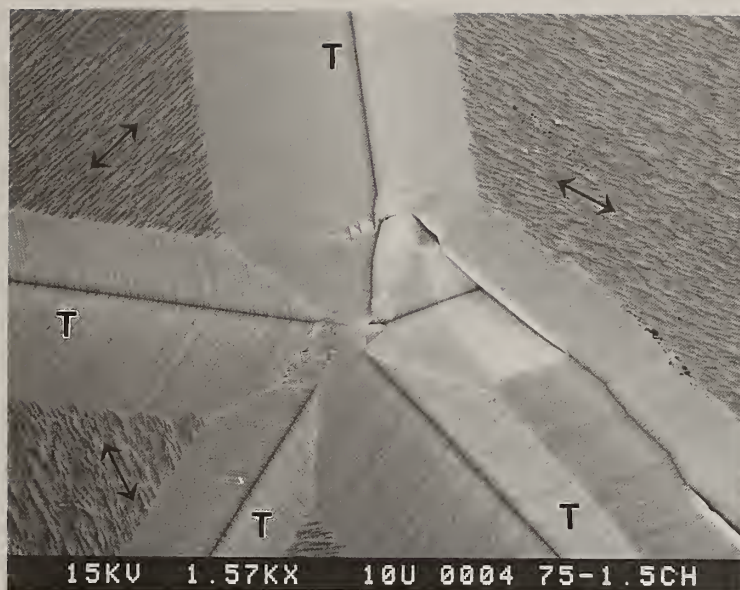
Figure 1

Shown is the regrown surface of a polished, optically transparent, polycrystalline layer. Features revealing the local microstructure include numerous twin boundaries meeting at a five fold twin origin. The twin boundaries are marked with the letter "T". The crystallographic orientation of neighboring grains, or sub-grains, is revealed by the presence of striae or "rows" on the defect free surfaces. These lie parallel with the <011> directions in the plane of the surface along arrows in the above figure.

An oriented micro-facetting of the near (110) polished surface of the grains was also observed as shown in Figure 1 and this facilitated the determination of the relative orientation of each grain or sub-grain as these micro-ledges or "rows" lie approximately parallel with the <110> directions in the plane of the surface. This microfacetting was also observed for atomic hydrogen etched diamond surfaces. This pattern strongly suggests, at least at the low methane concentrations employed in this work, that extension of the lattice is greatest along the <110> directions in the plane of the surface. Consequently the rate of lateral expansion of an individual grain or sub-grain would have 2 fold symmetry for a perfectly <110> textured grain. Thus if one grain is oriented with its surface <110> axis abutting a neighboring grain at an angle to that neighbor's <110> surface axis, one may extend laterally and overgrow the other. Which is most likely to dominate would depend sensitively on the relative misorientation of their dominant <110> growth axes with respect to the growth axis of the layer. More importantly if a surface <110> axis abuts a twin boundary, which does

not propagate as rapidly along the layer's growth axis, the facetted boundary will likely be overgrown by the neighboring grain or sub-grain, entraining a void within the layer. This is illustrated in Figure 2 showing a more fully developed microstructure. Three different sites are marked with arrows where a single or multiple twin boundary appears to be in the process of being overgrown by a third grain whose dominant in-plane growth axis is favorably oriented. This leads to "blind" regions or voids in the surface where the flux of reactive species (e.g., atomic hydrogen and methyl radicals) would be reduced, reducing the local growth rate. Such voids or flaws could then become incorporated into microstructure as the surrounding grains extend vertically and horizontally at greater rates. For an individual site this assumes of course that both grains grow vertically (i.e. along the normal to the surface) at the same rate, and that no further twinning occurs.

Clearly the nucleation and propagation of such voids or "pits" in the diamond surface could, in addition, lead to the incorporation of non-diamond carbon or poorly crystallized material. The basic understanding of diamond CVD requires the presence of atomic hydrogen in sufficient quantities to ensure the absence of sp^2 hybridized carbon at the growth surface. If the partial pressure or flux of atomic hydrogen at a local site is reduced by the formation of pits or a "blinding" process due to twin boundary overgrowth then the quality of deposition will likely be less than optimal.

Shown in Figure 3 is a simple illustration of how twinning, even in the growth of single crystals, can lead to void entrainment and the incorporation of non-diamond carbon. In Figure 3 the crystal structure is projected onto the $(0\bar{1}1)$ plane and the dominant growth axis is taken to be the [011]. Thus growth is taken to occur on the (110) surface and <111> facets are developed as this is a relatively slow growth direction. If twinning occurs on one of these facets then the dominant growth axis, [011], is rotated through an angle of ~70.5° and the [100] direction becomes more nearly aligned with the growth axis of the layer. As this is a slow growth direction, relative to the surrounding crystal, it follows that this twin will likely be overgrown. Along the [111] direction the parent and twin lattices are commensurate with one another. However where the twin crystal meets the parent lattice along the new [111] direction the lattices are incommensurate and it becomes impossible, without significant strain, for the gap between the two to close. Clearly an entrained void, with the possibility of some local stress development can easily result.

Summary and Conclusions

The application of this technique to previously tested samples, where the fracture origins might be identified, could identify the types of relative grain orientation and local microstructure that would have to be avoided to ensure minimum flaw sizes and consistently high strengths for CVD diamond. If the incorporation of voids and defects arises naturally as a result of random in-plane grain orientations coupled with the overgrowth of twin boundaries, and thus is relatively independent of reactor design and the method of gas phase activation used, then void incorporation may likely be relatively difficult to avoid in the growth of well crystallized diamond.

Acknowledgements

References

1. Daniel C. Harris, *Development of Chemical-Vapor-Deposited Diamond for Infrared Optical Applications. Statue Report and Summary of Properties*, Report no. NAWCWPNS TP 8210, Naval Air Warfare Center Weapons Division, China Lake, CA, July, 1994.

2. W. A. Yarbrough, K. Tankala and T. DebRoy, *J. Mater. Res.*, 7 (2), 379 (1992).

Figure 2

Shown is a regrown surface showing how individual grains can overgrow abutting twin boundaries leading to the formation of voids or "pits" in the diamond surface. Marked with arrows are three different sites where, by lateral expansion, a favorably grain appears to be overgrowing a twin boundary between two neighboring sub-grains. Each arrow points approximately Smooth {100} facets, adjoining the twin boundaries and representing the slowest growing faces, are apparent in each case.
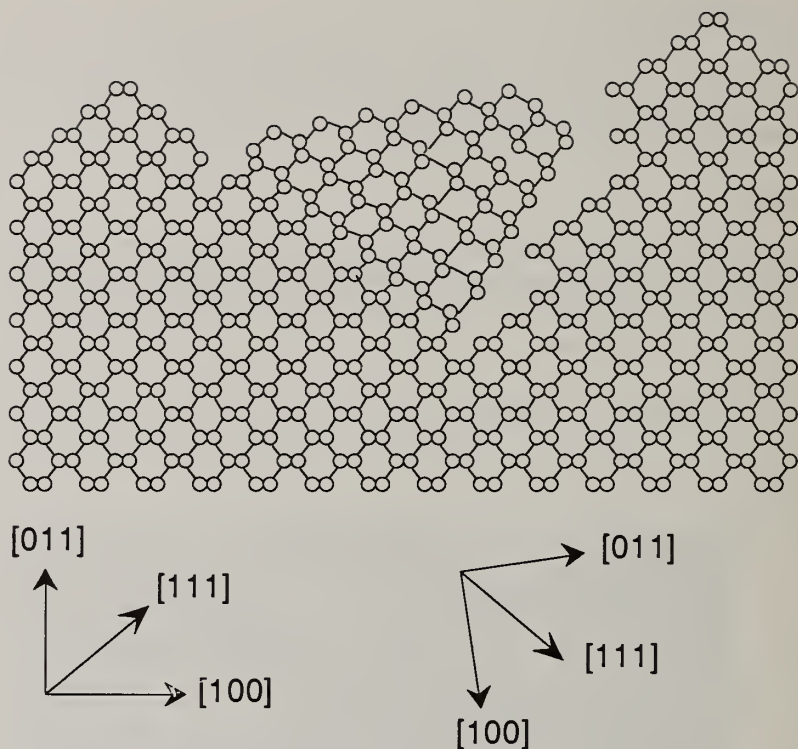
Figure 3

Shown above is a schematic of a twinned diamond crystal projected onto the (011) plane. The arrows on the left designate directions with respect to the parent crystal. The set of arrows to the right show the change in orientation of the directions for the twinned crystal. While these lattices remain commensurate along the twin boundary they are incommensurate along their boundary perpendicular to the twin's [111] direction. This can lead to the incorporation of non-diamond carbon, the development of stress associated with bonding across this surface and/or the encapsulation of void regions.

INEXPENSIVE TECHNIQUE FOR ESTIMATING THE THERMAL CONDUCTIVITY OF CVD DIAMOND FROM THE OPTICAL ABSORPTION

John E. Graebner

AT&T Bell Labs, Murray Hill, NJ 07974, USA

Key words: thermal conductivity, optical absorption, quality control

Abstract

The relationship between thermal conductivity and optical absorption has been investigated for over 60 samples of CVD diamond grown in 10 different laboratories. A simple and inexpensive apparatus is described to enable accurate and quick measurement of the optical absorption coefficient α averaged over the visible spectrum. The thermal conductivities $\kappa_{\parallel}$ and $\kappa_{\perp}$ (with heat flow either parallel or perpendicular to the plane of the sample) were measured by methods described previously -- steady state and laser flash, respectively. The observed correlation between $\kappa_{\parallel}$ or $\kappa_{\perp}$ and α can be used to obtain estimates of $\kappa_{\parallel}$ or $\kappa_{\perp}$ (within uncertainties of $\sim \pm 3$ $Wcm^{-1}K^{-1}$) from a measurement of the optical absorption.

1. Introduction

Measurement of the thermal conductivity of CVD diamond is time-consuming and problematic, with wide variations among measurements made at different laboratories even on the same sample [1]. In many situations such as routine monitoring of production, it would be very convenient to find another property, more easily measured, which scales in some known way with κ. Measuring a wide variety of CVD diamond samples makes it clear that the more transparent samples usually have higher κ than the more opaque ones. We have quantified this observation by measuring the optical absorption coefficient α, averaged over the visible spectrum, for a variety of samples for which $\kappa_{\parallel}$ and/or $\kappa_{\perp}$ have been measured. A clear correlation is observed. The present work is in contrast to several previous reports [2-4] of a correlation between the thermal resistance and the *infrared* absorption, in the 8 μm wavelength range.

2. Measurement Techniques

The parallel thermal conductivity $\kappa_{\parallel}$ for samples of typical dimensions $5 \times 10 \times 0.3$ mm^3 was measured by a steady-state technique [5]. Precautions against errors due to loss of heat by radiation or convection allowed an absolute accuracy of 1-3%, determined mainly by uncertainties in the sample dimensions.

The perpendicular conductivity $\kappa_{\perp}$ was obtained from the diffusivity $D_{\perp} = \kappa_{\perp}/C$, where C is the specific heat per unit volume, assumed to be the same as for single crystal diamond. A high-speed version [5] of the flash diffusivity method was used to measure $D_{\perp}$, thereby determining $\kappa_{\perp}$. Typical uncertainties were $\pm$ 5% for samples less than ~ 400 μm thick and up to $\pm$ 10% for thicker samples.

The wide range of sample thickness t (28 - 950 μm) and sample quality led to a wide range of optical density, α t $= 0.05 - 7$. A large amount of elastic scattering from grain boundaries and from the rough growth surface of unpolished samples made it necessary to take special precautions to collect as much of the unabsorbed light as possible. An integrating sphere with an entrance aperture 5 mm in diameter was used to collect the light, the intensity of which was measured with a silicon photodiode (Fig. 1). The output current from the photodiode was measured with a transimpedance amplifier, providing a voltage output that was linearly related to the light intensity over at least six orders of magnitude. The sample was held in place against the aperture with black masking tape which covered the sample except for a 5-mm-diameter hole directly over the aperture. The amplifier output was observed both with (V) and without (V_o) the sample, and α was calculated from the ratio V/V_o as follows. Allowing for ordinary absorption in the sample, we write $I = 0.706 \ I_o \ e^{-\alpha t}$, where the numerical constant takes into account reflections at the surfaces of the sample. Thus, $\alpha = t^{-1} \log(0.706 \ V_o/V)$. The value of α deduced for any particular sample is found to be very reproducible on repeated measurements. It is also insensitive to whether the light is incident on the rough growth surface or on the smooth substrate side of an as-grown, unpolished sample. Mounting a sample, taking the measurement, and calculating α takes typically less than five minutes. The samples represent several growth techniques, including microwave plasma, hot filament, and arc jet. The unpolished samples were observed visually to have predominantly <110> texture.

3. Results and Discussion

The room-temperature data are plotted as κ_i vs. α in Figs. 2 and 3 for $\kappa_{\parallel}$ and $\kappa_{\perp}$, respectively. In both cases the data follow the generally observed positive correlation between clarity and thermal conductivity. Two samples of (nominally identical) isotopically purified CVD diamond [6] are included to illustrate the higher κ that is possible by removal of the naturally-occurring ~ 1% ^{13}C. The solid lines are a simple function which gives a satisfactory fit to the data:

$$\kappa_i = A_i (\frac{\alpha}{B_i} + 1)^{-1},$$ (1)

with $A_{||} = 20.21$ $Wcm^{-1}K^{-1}$, $B_{||} = 136.7$ cm^{-1}, $A_{\perp} = 22.05$ $Wcm^{-1}K^{-1}$, and $B_{\perp} = 209.0$ cm^{-1}. The data for the isotopically purified samples are not included in the fits. The data lie within $\sim \pm 3$ $Wcm^{-1}K^{-1}$ of the curve for $\kappa_{||}$ and $\sim \pm 4$ $Wcm^{-1}K^{-1}$ for $\kappa_{\perp}$. Part of the greater spread in the case of $\kappa_{\perp}$ may be traced to the higher degree of uncertainty in the $\kappa_{\perp}$ measurement, especially for samples thicker than 0.5 mm.

Equation (1) can be rearranged to obtain a direct correlation between optical absorption and thermal resistivity $W = \kappa^{-1}$:

$$\alpha = B \left[\frac{W}{W_0} - 1 \right] = B \left[\frac{\Delta W}{W_0} \right],$$ (2)

where $W_0 = A^{-1}$ and $\Delta W = W - W_0$. For perfect diamond, one expects $\alpha \rightarrow 0$ as $W \rightarrow W_0$, where W_0 is the thermal resistivity due only to intrinsic phonon-scattering processes such as Umklapp scattering. Equation (2) is intuitively appealing, as one expects at least some types of impurities or defects to give rise to both optical absorption and thermal resistance. It has been suggested [7,8] that the dark color of poor quality CVD diamond is due to light absorption by amorphous carbon, which would also be expected to scatter phonons [5].

4. References

1. A. Feldman, S. Holly, C. A. Klein, and G. Lu, J. Res. Natl. Inst. Stand. Technol. **99,** (1994) 287.
2. E. A. Burgemeister, Physica **93B,** (1978) 165.
3. D. T. Morelli and C. Uher, Appl. Phys. Lett. **63,** (1993) 165.
4. P. K. Bachmann, H. J. Hagemann, H. Lade, D. Leers, D. U. Wiechert, H. Wilson, D. Fournier, and K. Plamann, to appear in Diamond and Related Materials (1995).
5. J. E. Graebner, M. E. Reiss, L. Seibles, T. M. Hartnett, R. P. Miller, and C. J. Robinson, Phys. Rev. **B50,** (1994) 3702.
6. J. E. Graebner, T. M. Hartnett, and R. P. Miller, Appl. Phys. Lett. **64,** (1994) 2549.
7. L. H. Robins, E. N. Farabaugh, and A. Feldman, SPIE Vol. 1534 (Diamond Optics IV, 1991).
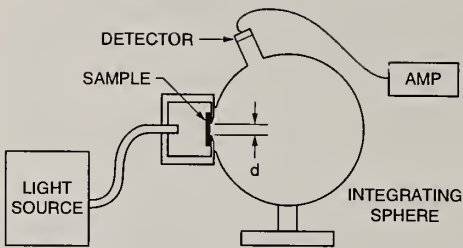8. L. H. Robins, E. N. Farabaugh, and A. Feldman, to appear in Diamond Films and Technology (1995).

Fig. 1. Schematic illustration of a simple apparatus for measuring the optical absorption of a sample. The light source (100W halogen bulb) is connected to the sample chamber by means of an optical fiber bundle. The 15-cm-diameter integrating sphere, coated on the interior surface with highly reflecting material, collects the light for the detector, the output of which is measured by an amplifier with digital readout.
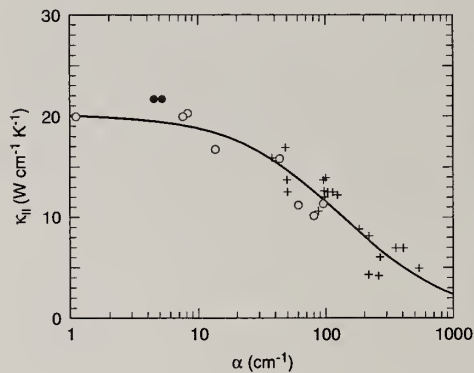

Fig. 2. Parallel thermal conductivity $\kappa_{\parallel}(25\ ^{\circ}C)$ vs. the optical absorption coefficient α for 30 samples of CVD diamond covering a wide range of $\kappa_{\parallel}$ and α. Polished samples are indicated by circles, unpolished by crosses. The two filled circles are data for two nominally identical samples of CVD diamond with isotopic enrichment of ^{12}C. The solid line is a least squares fit of Eq. (1) to the data with fitting parameters given in the text.
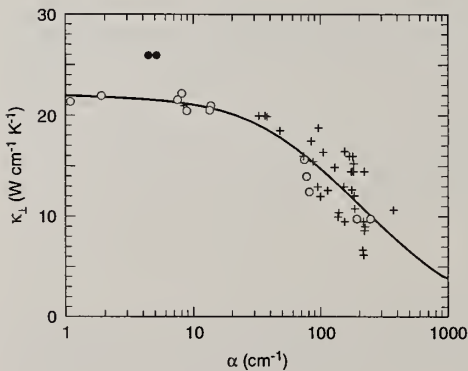

Fig. 3. Perpendicular thermal conductivity at 25 $^{\circ}$C vs. optical absorption for 48 samples of CVD diamond. Fifteen of the samples are also represented in Fig. 2. The meanings of the symbols and the solid line are the same as for Fig. 2.

DIAMOND: AN EROSION RESISTANT AEROSPACE MATERIAL

G H Jilbert, C S J Pickles, E J Coad, and J E Field

PCS Group, Cavendish Laboratory, Cambridge University, CB3 OHE, UK

Key words: diamond, DLC, fracture, erosion, impact

Abstract

Chemical Vapour Deposited (CVD) diamond growth technology has improved
to the point where complete diamond infrared domes are now a possibility.
However there are still considerable barriers to be overcome to ensure that
the erosion resistance of the synthetic material is comparable to that of natural
diamond. The Cavendish laboratory uses two systems to assess the erosion
resistance of materials. The sand erosion rig uses compressed air to
accelerate 300-600 μm sand particles to velocities up to ca. 250 m s^{-1}. The
rain erosion resistance of a sample is evaluated using high velocity jets
designed to simulate the effects of spherical raindrop impact. Both techniques
have revealed the unique erosion characteristics of CVD diamond.

1. Introduction

Diamond is a potentially exceptional infrared transparent window material for
aerospace applications. Existing window systems suffer from low resistance to
sand and rain erosion and thermal shock, all of which diamond with its high
hardness, fracture stress, thermal conductivity and thermal expansion
coefficient would be extremely resistant to. However only the Chemical
Vapour Deposited (CVD) material can be fashioned in the sizes and shapes
required for these windows and domes. At present the strength properties of
the CVD material have not yet been optimised and this is reflected in its
erosion performance.

Extensive data have been obtained at the laboratory on a range of infrared
transparent aerospace materials using both the sand erosion rig (projecting
300-600 μm sand particles) and the Multiple Impact Jet Apparatus (MIJA) for
simulating rain erosion. The sand erosion data can be found in [1, 2] and the
liquid impact data in [3-5]. The sand erosion results are presented in terms of
mass loss per mass of erodent (gravimetric erosion rate) or infrared
transmission loss. MIJA uses up to 300 repeated impacts with highly
reproducible jets of water from a 0.8 mm diameter nozzle on the same site to
determine a damage threshold velocity (the velocity below which the material
remains undamaged regardless of the number of impacts). Full descriptions of
the apparatus can be found in the above references.

2. Damage mechanisms

The extremely high hardness of diamond means that even during high velocity sand erosion there is no evidence of plasticity and the damage sustained is all of a brittle nature. The primary damage mechanism is in the form of a partial or complete ring crack at the edge of the loaded region, introduced by the Rayleigh surface wave. In single crystal diamond the circular symmetry of this crack is destroyed by the tendency to fracture along the {111} cleavage planes [6]. In CVD diamond the crack is diverted by the material's grain boundaries. Secondary damage mechanisms also occur if the specimen is thin. In CVD diamond tensile failure has been observed on the rear surface of the sample in the form of a crazing pattern of cracks and, in the case of liquid impact, a front surface ring of circumferential failure can occur, at a radius far greater than the loaded radius. This is caused by reflected bulk waves reinforcing the Rayleigh wave [7]. The sample's lateral dimensions can also influence the damage mode. CVD and natural diamond samples 6 mm in diameter were impacted in MIJA and damage was observed in the centre of the disc caused by stress waves reflecting off the disc edges and then returning to focus at the centre.

3. Sand Erosion

Natural diamond is one of the most erosion resistant materials. The gravimetric erosion rates for natural diamond, a polycrystalline diamond composite (Syndite), a polycrystalline boron nitride composite (Amborite) and silicon nitride are compared in Table I for a flux of 10.5 kg m^{-2} s^{-1} [6]. The natural diamond and syndite have similar extremely low erosion rates even when compared with silicon nitride, itself a very erosion resistant material.

Table I Gravimetric erosion rates (mg kg^{-1}) as a function of velocity [6].

Material	V = 75 m s^{-1}	V = 140 m s^{-1}	V = 200 m s^{-1}
Diamond	-	0.05	-
Syndite (025)	~0	0.05	0.10
Amborite	1.0	1.2	1.4
Si_3N_4	0.35	-	-

The exposure to sand erosion required to form ring cracks in a sample (again at a flux of 10.5 kg m^{-2} s^{-1}) is plotted for both natural Type I diamond flats [6] and CVD samples (of intermediate quality) in Fig. 1. It is clear that the CVD diamond is considerably weaker than its natural counterpart. Infrared transmission curves from the same experiments detected a decrease in erosion resistance for the growth surface over the nucleation side. The samples were 0.57 mm thick and suffered from the rear surface crazing pattern described above.
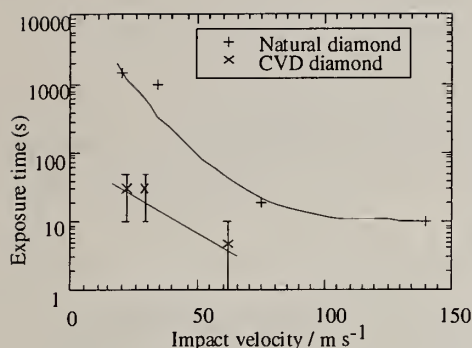
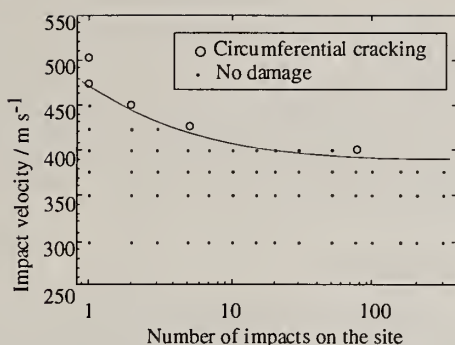Fig. 1 The exposure time required to form ring cracks in natural and CVD diamond.

Fig. 2 The MIJA threshold velocity curve for a 2 mm (poor quality) CVD diamond (growth side).

4. Liquid Impact

Two Type IIa samples of natural single crystal diamond were made available for MIJA assessment. These samples were 6 mm in diameter and 1 mm thick and were susceptible to the stress wave reinforcement mentioned in section 2. This effect will act to reduce the threshold velocity for damage. The threshold velocity for catastrophic failure for a 0.8 mm jet for the two samples was 515 ± 15 m s^{-1} (However fine central cracks were observed on one of the samples at 462 ± 12 m s^{-1}). This agrees well with the value of 525 ± 25 m s^{-1} obtained on a synthetic high temperature, high pressure Type Ia diamond (3.45 mm thick and 9.51 x 8.42 mm across). Since these were the largest natural diamonds that were likely to be tested, CVD samples of the exact same dimensions were also assessed to give a direct comparison between the two materials. The threshold velocities for two samples were 325 ± 25 and 375 ± 25 m s^{-1}, which are considerably lower than those of the single crystal specimens. It has been shown that the liquid impact threshold velocity depends strongly on fracture toughness [5], which can be higher for the CVD material than the natural material [8, 9]. However the strength of the material is severely reduced by large bulk and surface flaws as well as residual stresses [10].

The threshold velocity for circumferential fracture of wider specimens (8 samples, with dimensions in the range 20 to 25 mm in diameter, 0.5 to 1 mm thick) was 420 ± 60 m s^{-1}. The failure was in the form of a ring crack of diameter ~3 to 5 mm, well outside the loaded region (<0.8 mm in diameter) due to the Rayleigh / bulk wave interaction described in section 2 [7]. The large spread in threshold velocities is not a test artefact, since individual samples produced highly repeatable results, but rather it is indicative of the varying quality of samples available from different sources. These samples also exhibited the rear surface tensile failure at threshold velocities of 265 ± 75 m s^{-1}. This emphasises how greatly reducing the thickness (and thus introducing the secondary damage mechanism) has reduced the damage threshold velocity. A full threshold curve was obtained for the growth surface of a single 2 mm thick

CVD sample and this is shown in Fig. 2. This sample is sufficiently thick that stress wave reflections are not a major factor in determining the ring cack position so the ring crack is just outside the loaded zone and there is no rear surface tensile failure. However the threshold velocity (388 ± 12 m s^{-1}) is not as high as might be hoped (since the secondary failure mechanisms have been suppressed). This is because, with current growth technology, the quality of the material decreases as it grows.

5. Conclusions

The results of the study show that the erosion resistance of CVD diamond is considerably lower than that of the natural single crystal material. The strength of the synthetic diamond is reduced by flaws and residual stresses and the quality of samples varies considerably from source to source. This was reflected in the variability of the damage threshold velocities. Most of the samples made available for the study were thin and were susceptible to secondary damage mechanisms, especially rear surface tensile failure. Further erosion data on diamond can be found in Field [11]. Even though there is still a considerable way to go before CVD diamond reaches its full potential, its erosion resistance is already superior to many of the other candidate materials for infrared applications.

6. Acknowledgements

7. References

1. J.E. Field, Q. Sun and H. Gao, SPIE **2286**, 301 (1994)
2. D.R. Andrews, S.M. Walley and J.E. Field, (Proc. Erosion by Liquid and Solid Impact **6**, Cambridge UK, 1983) paper 36
3. C.R. Seward, C.S.J. Pickles and J.E. Field, SPIE **1326**, 280 (1990)
4. C.R. Seward, C.S.J. Pickles, R. Marrah and J.E. Field, SPIE **1760**, 280 (1992)
5. C.R. Seward, E.J. Coad, C.S.J. Pickles and J.E. Field, SPIE **2286**, 285 (1994)
6. Z. Feng and J.E. Field, J. Hard Mater. **1** (4), 273 (1991)
7. C.R. Seward, J.E. Field and E.J. Coad, J. Hard Mater. **5**, 49 (1994)
8. D.C. Harris, SPIE **2286**, 218 (1994)
9. L.P. Hehn, Z. Chen, J.J. Mecholsky, Jr., P. Klocek, J.T. Hoggins and J.M. Trombetta, J. Mater. Res., 9 (6), 1540 (1994)
10. A.B. Harker, D.G. Howitt, S.J. Chen, J.F. Flintoff and M.R. James, SPIE **2286**, 254 (1994)
11. J.E. Field (editor), Properties of Natural and Synthetic Diamond, (Academic Press, 1992)

OPTICAL PROPERTIES OF DIAMOND AT ELEVATED TEMPERATURES

Robin E. Rawles[1] and Mark P. D'Evelyn[2]

[1] Department of Chemistry, Rice University, Houston, TX 77251-1892 USA

[2] GE Corporate Research & Development, P.O. Box 8, Schenectady, NY 12301 USA
and Departments of Materials Engineering and Chemistry, Rensselaer Polytechnic
Institute, Troy, NY 12180-3590 USA

Key words: diamond, refractive index, temperature, interferometry

Abstract

The unique multispectral transparency properties of diamond, combined with its
chemical inertness, hardness, and mechanical strength, enable a variety of optical
applications requiring infrared transparency in aggressive environments. Knowledge
of the optical properties of diamond at elevated temperatures enables the use of Fizeau
interferometry as an *in situ*, non-contact probe of temperature, for homoepitaxial
diamond growth studies, for example, and may be useful for other applications as well.
The temperature dependence of the index of refraction of type IIa natural diamond was
determined by Fizeau interferometry using a HeNe laser. Subtracting the contribution
of thermal expansion to the optical path length, the logarithmic temperature derivative
of the refractive index, $1/n \, dn/dT$, is found to rise from 4×10^{-6} at room temperature to
2.0×10^{-5} at 1200 °C at a wavelength of 633 nm.

1. Introduction

The present investigation of the temperature dependence of the refractive index of
diamond was motivated by several factors. First, we have been investigating the
kinetics of homoepitaxial diamond growth by chemical vapor deposition (CVD) using
in situ Fizeau interferometry [1-3]. Kinetic studies require accurate temperature
measurements, which are nontrivial on single-crystal diamond substrates [4,5], and we
wanted to calibrate the interferometric technique itself as a non-contact temperature
monitor [6]. In addition, certain optical applications of CVD diamond may require
accurate measurements of the temperature dependence of the index of refraction, for
which new measurements would be useful.

The temperature dependence of the index of refraction of natural diamond has been investigated previously by capacitance measurements [7,8], interferometry [9], and theory [10].

2. Experimental

We monitored small variations in the refractive index of diamond using optical Fizeau interferometry [1-3,6]. Three separate, type IIa natural diamond substrates, 1.5×1.5 mm^2 in lateral dimension, were employed. The three samples had (100), (111), or (110) orientations and were 0.246, 0.291, or 0.300 mm thick, respectively. The diamond substrate was held between two slotted mullite rods [1-3,6] which were affixed to a graphite block by Mo foil clips held by Mo threaded rod and nuts. The sample temperature was monitored by a chromel-alumel thermocouple positioned within the graphite block immediately adjacent to the back face of the substrate. The entire assembly was placed in the center of a controlled-atmosphere alumina tubular furnace, approximately 25 mm in diameter and 325 mm long. The ends of the furnace were sealed by water-cooled Conflat flanges, with a glass viewport on one end. The tube was evacuated prior to the start of an experiment, and 1-2% H$_2$ in N$_2$ at 25 Torr pressure was passed through the tube at a flow rate of ca. 300 sccm during the experiment.

Collimated light from a HeNe laser was reflected at near-normal incidence from the front side of the diamond substrate, focused and diverged by a lens, and collected on a CCD video array detector. The existence of a slight wedge angle between the back and front faces of the substrate causes interference in the light reflected from the two faces, producing a spatial fringe pattern. At each lateral position on the substrate, a fringe index $m = 2nt\cos\theta / \lambda$ can be defined, where $n = 2.39$ is the index of refraction of diamond, t is the local thickness, θ is the angle of incidence within the sample ($\approx 0°$), and λ is the wavelength of light (633 nm). The local value of m determines the degree of constructive versus destructive interference between the two reflected beams: the intensity is a minimum if m is an integer and a maximum at half-integer values of m. Changes in t and/or n due to a change in temperature [6] or growth [1-3] alter the local value of m across the substrate, causing the fringe pattern to propagate laterally.

3. Results and Discussion

In these experiments the fringe pattern image was recorded on videotape and displayed on a monitor. The fringe positions at room temperature were recorded, and the sample heated at a rate of 3-5 °C/min up to 1200 °C. Each temperature producing a shift of one fringe (i.e., a pattern identical to the room temperature pattern) was determined. Similar measurements were made as the sample was cooled. The results obtained during the heating ("h") or cooling ("c") cycle in furnace runs on each of the three samples are summarized in Fig. 1. The data were normalized by dividing the number
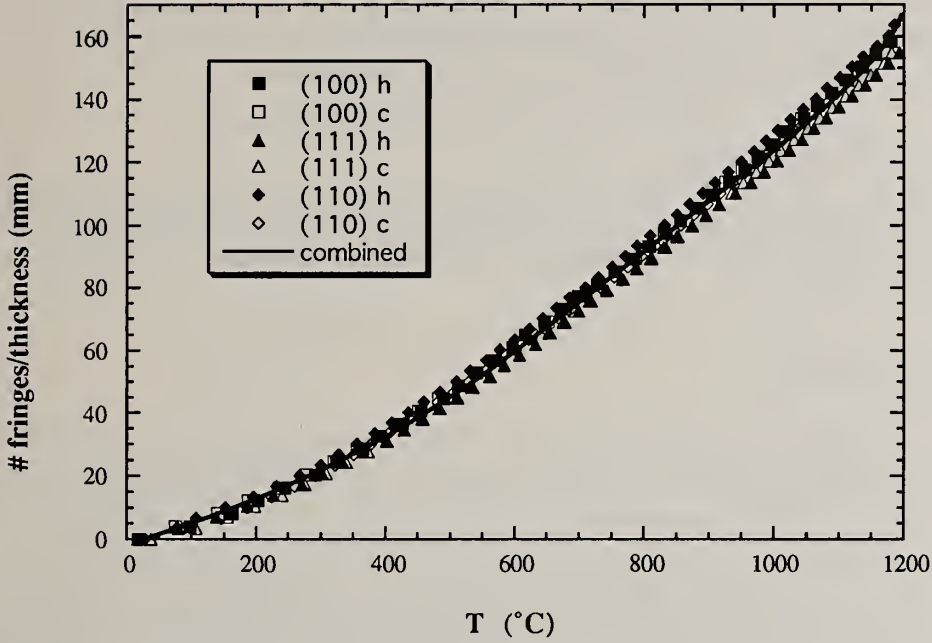
FIG. 1. Summary of fringe movement ($\lambda = 633$ nm) as a function of temperature ("h"–heating; "c"–cooling) of (100), (111) and (110) diamond samples.

of fringe shifts with respect to room temperature, Δm, by the thickness of the sample. Within experimental error, the data lie on a common curve, as expected.

These results can be used to extract the temperature of a diamond window from the number of fringe shifts with respect to room temperature and the known thickness. A polynomial fit to the combined data yields

$$T \text{ (°C)} = 25.6 + 15.42(\Delta m/t) - 0.152(\Delta m/t)^2 + 0.109(\Delta m/t)^3 - 2.9 \times 10^{-6}(\Delta m/t)^4 \qquad (1)$$

The approximate uncertainty in the fit is 5–15 °C.

The rate of fringe movement with temperature is directly related to changes in the thickness and index of refraction: $\lambda/(2nt \cos\theta) \, dm/dT = \alpha + n^{-1}dn/dT$, where α is the thermal expansion coefficient. We determined this quantity by re-fitting the fringe movement data shown in Fig. 1 as a function of temperature (rather than temperature as a function of fringe movement) and differentiating. We then determined $n^{-1}dn/dT$ at a wavelength of 633 nm by subtracting the thermal expansion coefficient, calculated from the thermal linear expansion data recommended by Touloukian [11]. The results can be summarized by

$$n^{-1}dn/dT = 3.2 \times 10^{-6} + 3.76 \times 10^{-8} \, T - 3.78 \times 10^{-11} \, T^2 + 1.50 \times 10^{-14} \, T^3 \qquad (2)$$

where T is the temperature in °C. The present results range from a value of 4×10^{-6} at 25 °C, in good agreement with previous results [7-9], to 2.0×10^{-5} at 1200 °C, a much higher temperature range than had been explored in earlier work.

4. Acknowledgments

5. References

1. R. E. Rawles, C. Kittrell, and M. P. D'Evelyn, in *Diamond Materials*, ed. J. P. Dismukes and K. V. Ravi (The Electrochemical Society, Pennington, New Jersey, 1993), p. 269.
2. R. E. Rawles and M. P. D'Evelyn, Mater. Res. Soc. Symp. Proc. **339**, 279 (1994).
3. M. P. D'Evelyn, R. E. Rawles, T. I. Hukka, and T. A. Pakkanen, in *Advances in New Diamond Science and Technology*, ed. S. Saito, N. Fujimori, O. Fukunaga, M. Kamo, K. Kobashi, and M. Yoshikawa (MYU, Tokyo, 1994), p. 425.
4. Y. L. Yang, L. M. Struck, L. F. Sutcu, and M. P. D'Evelyn, Thin Solid Films **225**, 203 (1993); and Y. L. Yang, Ph.D. Dissertation, Department of Chemistry, Rice University, 1992 (unpublished).
5. V. S. Smentkowski and J. T. Yates, Jr., J. Vac.Sci. Technol. A **11**, 3002 (1993).
6. M. P. D'Evelyn, L. M. Struck, and R. E. Rawles, Mater. Res. Soc. Symp. Proc. **339**, 89 (1994).
7. P. T. Narasimhan, Proc. Phys. Soc. (London) B**68**, 315 (1955).
8. J. Fontanella, R. L. Johnston, J. H. Colwell, and C. Andeen, Appl. Optics **16**, 2949 (1977).
9. G. N. Ramachandran, Proc. Ind. Acad. Sci. **25A**, 266 (1947).
10. P. Y. Yu and M. Cardona, Phys. Rev. B**2**, 3193 (1970).
11. Y. S. Touloukian, *Thermophysical Properties of Matter*, Vol. 13, (IFI/Plenum, New York, 1977) pp. 19-23. The thermal coefficient values calculated using this parameterization are nearly the same as the values recommended by G. A. Slack and S. F. Bartram, J. Appl. Phys. **46**, 89 (1975).

PROPERTIES OF CVD DIAMOND DOMES

CJH Wort, JR Brandon, BSC Dorn, <u>JA Savage</u>*, RS Sussmann and AJ Whitehead
Diamanx Products Ltd, IoM Freeport, P O Box 6, Ballasalla, Isle of Man,
*Defence Research Agency, St Andrews Road, Malvern, Worcs., UK

Key words: CVD, diamond, domes, infrared, properties, strength

Abstract

This paper describes the properties of CVD diamond material, which can be fabricated
as domes up to 70 mm in diameter, by plasma assisted CVD (PACVD). Domes of
"near-net-shape" are reported, showing that good thickness and crystal morphology
uniformity are obtained during the synthesis stage. Preliminary results on the
processing of "as-grown" CVD diamond domes and the tolerances achieved (in the
correct spherical shape) for IR optical applications are presented.

Finally, the characterisation of IR and optical properties and mechanical strength of
CVD diamond planar samples is reported.

1. Introduction

The combination of unsurpassed thermo-mechanical properties and transparency to
long wavelength infrared radiation (LWIR) make pure diamond the ultimate protective
window, or dome, material for heat-seeking missiles that operate in the 8 - 14μm
waveband. The CVD diamond synthesis and processing technologies developed at
Diamanx Products Ltd and its associated research laboratory have already led to the
commercial realisation of high quality, bulk polycrystalline diamond plates [1].
Provided that the crystallites have a low defect density, are not stressed and the grain
boundaries are clean and continuous, polycrystalline diamond exhibits most of the
desirable thermal and optical properties of natural, single crystal Type IIa material [2].

Although the deposition and processing technology is well developed for planar CVD
diamond surfaces, it is not immediately adaptable to curved CVD diamond surfaces. .
To fabricate diamond domes it has been necessary to address and adapt many areas of
the existing CVD diamond technology.

2. Results and Discussion

2.1 Synthesis of CVD diamond domes

PACVD of two trial-dome geometries has been investigated: a shallow dome segment (44.5° segment of a hemisphere of 66mm radius) and a full 70mm diameter hemisphere. Figs. 1 and 2 show a free-standing CVD diamond dome segment and a full-size hemispherical diamond dome, 2.8mm and 0.93mm thick, respectively.
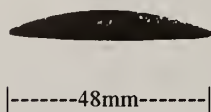

|-------48mm-------|

Fig. 1 Dome segment

Fig. 2 Full hemisphere

Small deviations in the deposition process can result in crystal morphology and growth rate changes, which in turn induced stress, the incorporation of defects (and impurities) and poor thickness uniformity. The thickness uniformity obtained during the synthesis of four dome segments is shown in Fig. 3. The uniformity obtained during the synthesis of thick and thin CVD diamond hemispheres is shown in Fig. 4 below.
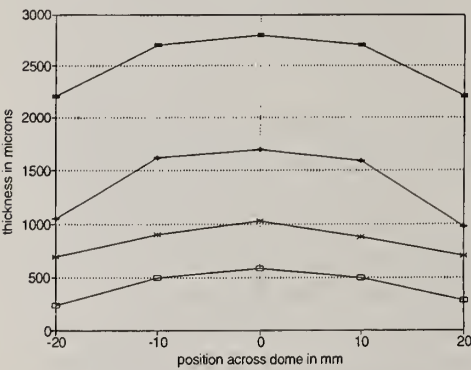
Fig. 3   Dome segment profiles
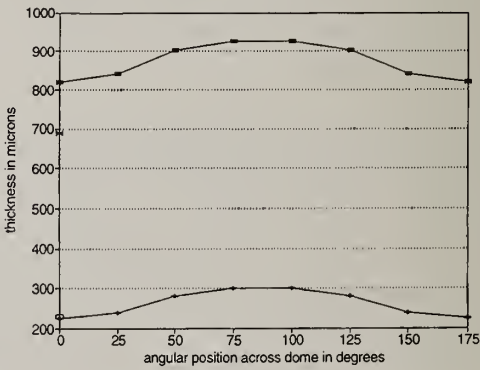
Fig. 4 Full dome profiles

To obtain near-net-shape domes a new PACVD reactor has been developed which incorporates temperature control and gas dynamics configuration to ensure uniform flow of atomic hydrogen and the correct growth species to the non-planar growth surface. Fig. 5 shows the consistency of diamond crystallite morphology as a function of position around a 0.93mm thick full-hemisphere dome of CVD diamond. Raman spectroscopy confirmed the high diamond quality, similar to that shown in Ref. [2].
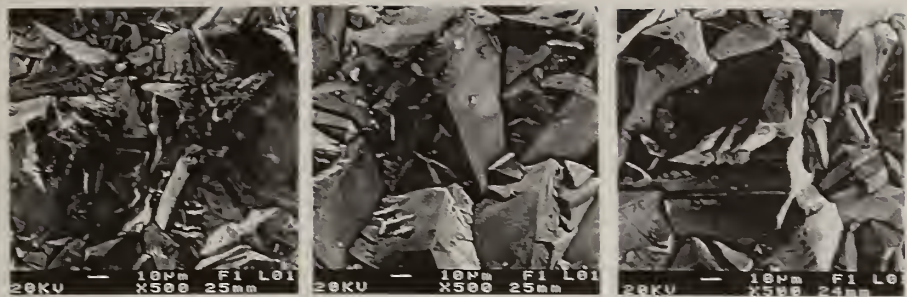
Fig. 5   (a) Dome top (90°)   (b) Dome side (135°)   (c) Dome base (160°)

2.2 Processing of CVD diamond dome segments

An investigation into surface finishing techniques is still underway to determine which combination of processes will provide a suitable surface finish for domed, IR precision optical components. Fig. 6 shows a fracture surface cross-section of a processed dome segment which had an "as grown" thickness maximum of 2.8mm. After preliminary processing the segment had a uniform thickness of 1.938mm with a standard deviation in this value of only 0.025mm. The surface roughness was less than 200nm R_a. Final finishing of curved surfaces, to the economic standard sought, has yet to be achieved; however, work on planar surfaces has shown that final finishing should be relatively fast and should result in a surface roughness of less than 20nm R_a. The fracture surface (Fig. 7) shows the diamond layer to exhibit both trans- and intergranular fracture.
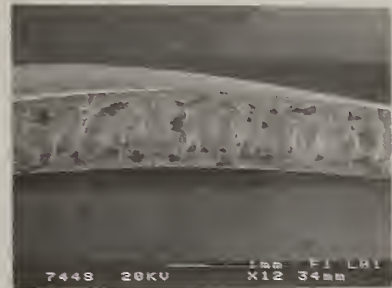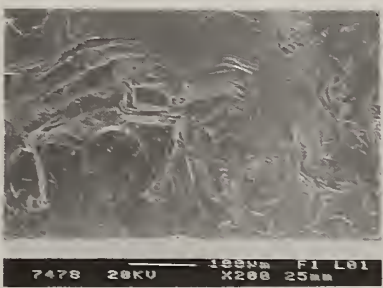

Fig. 6 Processed dome segment

Fig. 7 Fracture surface

2.3 Properties of CVD diamond material

To determine the optical and LWIR transmission properties of CVD diamond it was necessary to cut pieces from a planar sample and process these flat and parallel. The IR transmission through a 0.5nm thick sample was made using a Perkin Elmer 1760X FTIR spectrometer and is shown in Fig. 8. The transmission level in the 8-14μm waveband is at the expected theoretical maximum value of 71.4%. Fig.9 shows the UV/VIS transmission taken through the same sample with a Perkin Elmer

"Lambda 19" spectrometer. There is a reduction in transmission at the shorter wavelengths due to internal scattering and absorption, however in the visible region the sample is colourless and a distinct, far-field image can be resolved.
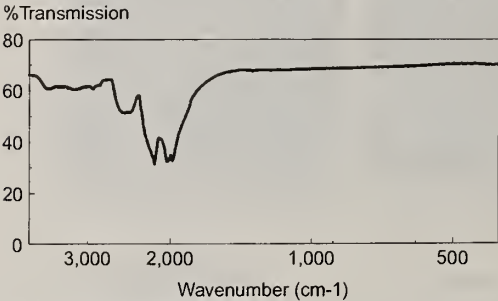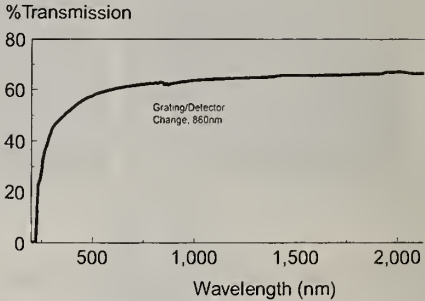

Fig. 8 IR transmission

Fig. 9 UV/VIS transmission

The strength of CVD diamond has been measured using a three point bend test. The test bars were laser cut from different areas of a larger, unprocessed planar disc synthesised in a dome reactor onto a planar substrate and were 2x20x0.8mm in size. Three point bend tests were performed with either the growth (10 samples) or substrate (5 samples) surfaces in tension and the results are shown in Table I.

Sample type	Mean Bend Strength, MPa	Standard Deviation MPa	Weibull Modulus +/- Std. Error
Growth surface in tension	461	29.6	15.6 +/- 1.8
Nucleation surface in tension	987	55.3	17.5 +/- 2.5

Table I. Bend strength of CVD diamond (accounting for surface roughness).

3. Conclusion

Optical quality PACVD diamond domes can be synthesised to near-net-shape; however, final finishing processes still require further development. Analysis of the strength distributions using Weibull statistics [3] indicates that either surface, in tension, has an estimated Weibull modulus in excess of ten, implying greater reproducibility of the mechanical strength than found in most ceramic materials.

4. Acknowledgement

The authors thank the UK Defence Research Agency for its collaboration in this work.

5. References

1. RS Sussmann, *Ind. Diamond Rev.*, 53 (553) (1993) 63.
2. CJH Wort et al., *Diamond and Related Materials*, 3 (1994) 1158-1167.
3. NA Waterman & MF Ashby, *Elsevier Materials Selector*, (1991) 1468-1470.

THIN FILM DIAMOND COATINGS ON GLASS

M. Ulczynski, D. K. Reinhard, M. Prystajko, and J. Asmussen

Electrical Engineering Dept., Michigan State University, East Lansing, MI 48824

Key Words: diamond; glass; optical coatings.

Abstract

Diamond coated glass offers the potential of allowing the use of glass in environments where a hard surface coating or improved chemical resistance is required. This report describes the deposition of diamond films on a variety of glass substrates. Microwave plasma-assisted chemical vapor deposition has been used to deposit continuous and adhering diamond films on borosilicate glasses that exhibit 70% optical transmission. Such films require low substrate temperatures, between 400 C and 500 C, during deposition.

1. Introduction

Diamond has an exceptionally wide optical transmission window, is resistant to chemical attack at ordinary temperatures, and is expected to be highly resistant to abrasion and erosion [1]. Consequently it is of interest as a coating material for other optical materials which are less resilient to hostile environments. The most common optical material is glass, however diamond film deposition on glass can be problematic. Adhesive diamond films deposited by chemical vapor deposition (CVD) have been reported on quartz, which has a low thermal expansion coefficient [2 - 5]. For glasses with lower softening point temperatures and larger thermal expansion coefficients than pure silica, such as borosilicate glasses, adhesion of CVD diamond films has been reported to be a concern [6]. This paper describes the deposition of diamond films on borosilicate glasses and resulting properties of the films.

2. Methods

Diamond was deposited using a low-temperature microwave plasma-assisted CVD method previously described [7]. Corning 7059 glass and [TM]Pyrex were used as substrates. Seeding of the substrates was performed either by a spin-on method as described by Masood et al., [8], or by polishing with fine diamond powder. The substrate temperature during deposition was varied between 440 C and 520 C as mea-

sured by optical pyrometry. Substrates up to 10 cm in diameter have been coated with deposition rates of 1 mg per hour by this method.

4. Results

The resulting films are generally in a state of compression since the thermal expansion coefficient of the glass substrates is approximately twice that of diamond. Many films have shown good long-term adhesion with, for example, diamond films on both Corning 7059 and ^{TM}Pyrex substrates that pass the tape test for adhesion one year after adhesion, and after repeated thermal cycling to 200 C. Other films, however, have shown spontaneous delamination after times ranging from several minutes to several days after removal from the deposition chamber. The most obvious variables affecting adhesion are deposition temperature and film thickness since film stress increases as both of these parameters increase. Long term adhesion is achieved when film thicknesses are less than 3 μm and deposition temperatures are less than 480 C.

The optical properties of the films are highly dependent on the grain size of the polycrystalline film. Larger grain films, with average grain sizes on the order of a micrometer, are translucent, having the appearance of frosted glass. Objects are clearly visible through such films only if they are directly adjacent to the diamond film. In contrast, smaller grain films, with grain sizes on the order of a quarter-micrometer, are transparent. This difference is illustrated in Fig. 1 in which the optical table features are clearly visible through the small grain film, but not the large grain film. Both films however are high quality diamond as indicated by Raman spectroscopy. A Raman spectra, taken with a 30 μm diameter, 514 nm Argon laser, for the transparent film in Fig. 1 is shown in Fig 2.

The optical transmission of the film/substrate combination was measured from the near ultraviolet to the near infrared. For these measurements, a monochromator beam approximately 0.4 cm in diameter was incident on the back of the glass substrate and a 1-cm diameter detector was located 2 cm from the diamond film. Consequently, light reaching the detector is subject to scatter losses in the film.

Fig. 2 shows the optical transmission as a function of wavelength for the transparent film in Fig. 1. The optical interference peak separations indicate a diamond film thickness of approximately 1.18 μm. Transmission values in the red and infrared compare favorably with the ideal value of 75.1% in the absence of interference for a planar, non-absorbing diamond film on the glass substrate, taking the refractive index of diamond as 2.42 and that of the Corning 7059 as 1.53. At smaller wavelengths, the transmission drops, as seen in Fig. 2. Previous studies have indicated that the drop in CVD diamond transmission at smaller wavelengths is due to scattering from grain boundaries [1]. A plot of the transmission loss deduced from Fig. 3 versus the inverse of wavelength shows a fourth-law power dependence, indicative of scattering.

5. Summary

Continuous diamond films which show good long term adhesion have been deposited on borosilicate glasses. Optical properties are strongly dependent on grain size, with larger grain size diamond films appearing translucent and smaller grain size diamond films appearing transparent.

6. Acknowledgments

7. References

1. D. C. Harris, "Properties of Diamond for Window and Dome Applications", Proc. SPIE, vol 2286, pp. 218 - 228, 1994.
2. T. P. Ong and R. P. H. Chang, "Low-Temperature Deposition of Diamond Films for Optical Coatings", Appl. Phys. Lett., vol. 55, pp. 2063 - 2065, 1989.
3. D. J. Pickrell, W. Zhu, A. R. Badzian, R. E. Newnham, and R. Messier, "Near-interface characterization of diamond films on silica and silicon", J. Mater. Res., vol. 6. pp. 1264 - 1276, 1991.
4. Y. Muranaka, H. Yamashita, and H. Miyadera, "Low Temperature (~ 400 C) Growth of Polycrystalline Diamond Films in the Microwave Plasma of CO/H_2 and $CO/H_2/Ar$ Systems", J. Vac. Sci. Technol. A, vol. 9, pp. 76-84, 1991.
5. A. Joseph and Y. Tzeng, "Diamond Coated Quartz and Sapphire Optical Windows", 2nd International Conference on the Applications of Diamond Films and Related Materials, Eds. M. Yoshikawa, M. Murakawa, Y. Tzeng, and W. A. Yarbrough, pp. 429 - 432, MYU, Tokyo, 1993.
6. K. E. Nariman, D. B. Chase, and H. C. Foley, "Growth of Free-Standing Diamond Films on Glass", Chem. Mater., vol 3, pp. 391-394, 1991.
7. M. J. Ulczynski, D. K. Reinhard, M. Prystajko, and J. Asmussen, "Low Temperature Deposition of Thin Film Diamond", Advances in New Diamond Science and Technology, Eds. S. Saito, N. Fujimori, O. Fukunaga, M. Kamo, K Kobashi, and M. Yoshikawa, MYU, Tokyo, 1994.
8. A. Masood, M. Aslam, M. A. Tamor, and T. J. Potter, "Techniques for Patterning of CVD Diamond Films on Non-Diamond Substrates", J. Electrochem. Soc., vol. 138, pp. L67 - L68, 1991.

Fig. 1. Visibility through a large grain-size, translucent film on the left, is compared to visibility through a small grain-size, transparent film on the right.
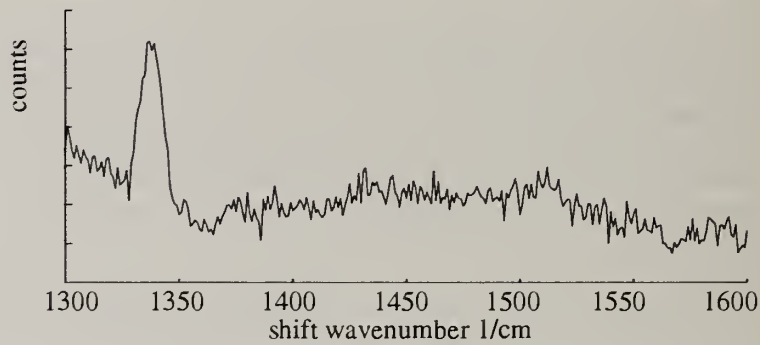

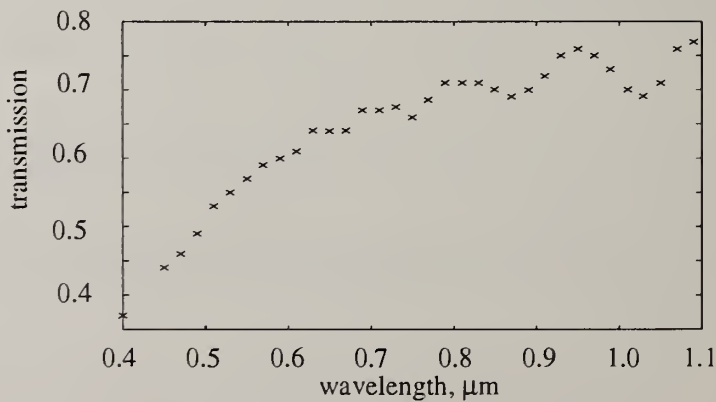Fig. 2. The Raman spectrum for the transparent film in Fig. 1 shows the characteristic diamond peak at 1332 cm^{-1}.

Fig. 3. Optical transmission through the transparent film in Fig. 1.

STUDY ON INFRARED GLASS WINDOW ADHERING TO DIAMND FILM

J. G. Ran   C. Q. Zheng   X. S. Li   P. Fan

Sichuan Union University, Chengdu, Sichuan, 610065.China

Key words: adhesion, diamond film, IR glass window

Abstract

Diamond film (DF) adhered to IR glass to form the IR glass window adhering to DF. First, different DFs were deposited on Si Substrate by MW plasma CVD method. Second, DFs adhered to IR glass. Then, Si substrate was removed with acid. Effects of DF thickness, size and shape of DF grains on IR transparency were studied. The IR transparency of prepared IR glass window adhering to DF was 60% or so at the wavelength of 1.06μm.

1. Introduction

Infrared (IR) glass has been widely used as window and len materials in infrared emmiters and dectectors for its excellent optical properties, easy manufacturing and lower price. But it was limited while being used in harsh environment such as windy with sand or erosive because of its poor wear and corrosion resistances. If it is coated with an anti-wear and anti-corrosion protective layer, IR glass window will overcome its shortcomings and hold its advantages. DF is an ideal protective coating for IR glass window because of its high IR transmittance and good wear and corrosion resistances. However, it is not easy to deposit DF on glasses, and the temperature suitable for DF deposition is so high that IR glass will melt. In the present study IR glass window has been prepared by making DF adhere to IR glass.

2. Experimental

2.1   Preparation of DF

DF has to be of small surface roughness and few internal defects in order to reach

excellent IR transparancy. DF prepared by MPCVD possesses high quality and small surface roughness, so it is more suitable for optical applications. Diamond films having high guality were synthesized on Si substrates under these conditions: microwave power $600-670w$, CH_4 concentration $0.2-0.5\%$, gas pressure $20-50$ Torr[1,2]. The DF SEM is shown in Fig. 1.
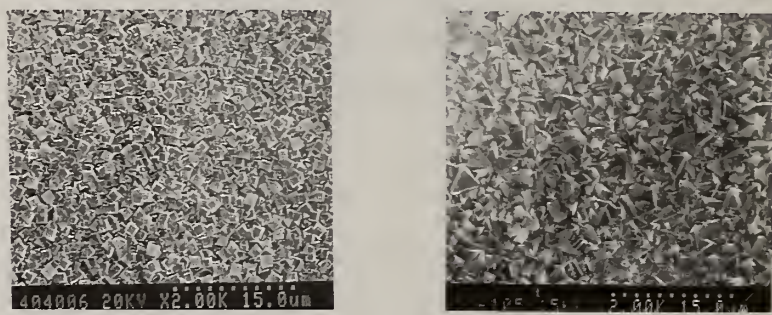

Fig. 1   SEM image of   DF prepared by MPCVD

2. 2   Preparation of IR glass window adhering to DF

First, DF on Si substrate and IR glass window (K9 glass) were cleaned, then DF was glued to K9 glass using GHJ-01 optical glue whose refractive index is 1.55. The Si substrate was etched away by using some corrosive solvent after the glue had been solidified. Thus the K9 glass window adhering to DF was obtained. Effects of DF thickness, diamand grain size and crystalline type on the IR transmittance of the thus prepared K9 glass windows were studied.

3. Results and discussion

3. 1   Effect of DF thickness on IR transmittance

It has been found that the DF thickness has the significant effect on the IR transmittance of the K9 glass adhering to DF. DF having different thickness have been obtained under the the same microwave power, the same CH_4 concentration, the same gas pressure and the different deposition time. The DF thickness and the grain size increase with increasing deposition time. Effects of DF thickness on the IR transmittance are presented in Table I .

Table I .Effect of DF thickness on IR transmittance

DF thickness, μm	2. 2	2. 7	3.2	4. 5
IR trans. , % at 0. 2—2. 5μm	17. 6~66. 2	11. 2~70. 7	9. 8~64. 1	2. 2~43. 7
IR trans. ,% at 1. 06μm	49. 6	47. 7	46. 9	26. 7

Table I shows that the IR transmittance decreases with the increase in DF thickness(and the grain size). There may be two reasons: Firstly, the DF surface roughness increases with the increase in DF thickness, thus it results in an increase in the scattering loss. Secondly, the bulk absorption of IR in DF increases with the increase in DF thickness.

3. 2 Effect of CH₄ concentration on IR transmittance

CH_4 concentration is an important effect parameter on the DF quality. In our study the DF quality was evaluated by using XPS, SEM and Raman spectroscopy[1,3]. It has been shown from SEM of DF that DF deposited at low CH_4 concentration has the better morphology, Clear crystalline grain surface and lower contents of non-diamond. DF deposited at high CH_4 concemtration has worse morphology, many grains are ball-shaped, DF crystalline gains can not be seen and there is an amount of diamond-like carbon (DLC) and graphite. Effects of the DF quality on the IR transmittance are shown in Table I .

Table I . Effects of DF quality on IR transmittance

CH₄ Conc. , %	0. 3	1	2. 5
DF quality (SEM)	better morphology	good morphology	poor morphology
IR tran. , % at 0. 5~2. 5μm	20. 2—72. 9	14. 0~64. 2	2. 1~39. 0
IR tran. ,% at 1. 06μm	57. 3	47. 1	20. 6

3. 3 IR transmittance comparision between K9 glass adhering to DF and that coated with DLCF

Both DF and DLCF are ideal protective coating materials for IR glass windows owing to their high hardness, wear and corrosion resistances and IR transmittance. Comparing IR transmittance of K9 glass adhering to DF with that of K9 glass

coated with DLCF having the same film thickness of $2.2\mu m$, at the same wavelength of $1.06\mu m$ has been shown that the IR transparency of K9 glass with DF is 49.6%, and that of K9 glass with DLCF is 57.3%, larger than that of K9 glass with DF. It is owing to the small surface roughness of DLCF resulting in decrease in the scattering loss.

4. Conclusions

IR glasses including K9 glass has excellent optical properties, but it is limited while being used in harsh enviroment owing to its poor wear and corrosion resistances. It has been found that diamond film or diamondlike carbon film adhered to or coated onto K9 glass can improve wear and corrosion resistances of K9 glass, although there is a certain decrease in IR transmittance. Thus the application field of the K9 glass will enlarge.

5. References

1. J. G. Ran, C. Q. Zheng, J. Huang et al. , Micro-processing Tech. (in Chinese) (2~3)1-7(1990).
2. C. Q. Zheng, J. G. Ran, Z. C. Yuan, Proceeding of 2nd Inter. Conf. on the Appl. of Diamond Films and Related Materials, Aug. 24-27, 1993, Tokyo, Japan, 745-750, Eds. :M.Yoshikawa et al. , MYU K. K. Tokyo(1993).
3. J. G. Ran, C. Q. Zheng, L. H. Liu and C. Xing, Micro-processing Tech. (in Chinese)(2~3)1-7(1990).

Applications of Diamond Films and Related Materials: Third International Conference, 1995
Editors: A. Feldman, Y. Tzeng, W. A. Yarbrough, M. Yoshikawa, and M. Murakawa

581

Anodic Bonding of Diamond to Glass

R. Fuentes[1], L.M. Trolio[2], and J.E. Butler[3]

1) Materials and Technologies Corp., Poughkeepsie, NY
2) Geo-Centers, Inc., Fort Washington, MD
3) Code 6174, Naval Research Laboratory, Washington, DC

key words: adhesion, diamond, membrane, xray lithography

Abstract

A method is described for anodically bonding smooth nanocrystalline diamond films to glass substrates to form extremely flat diamond membranes with the smoothest side available of patterning absorber structures to form masks for proximity focused xray lithography.

1. Introduction

In general, it is desirable to impart or combine the outstanding tribological, mechanical, optical, and electrical properties of diamond onto other materials. One can imagine all sorts of useful structures that can be fabricated this way. Unfortunately, the harsh, high temperature environments where crystalline diamond is grown are oftentimes not compatible with most common materials. Such is the case of glass.

We describe next a method for joining thin films of diamond to glass substrates, thus making structures that share the surface characteristics of diamond and the bulk properties—and ease of manufacture—of glass. As example of one such structure, we have fabricated x-ray mask substrates which consist of a thin (1-2μm thick) diamond film permanently bonded to a glass substrate (7 mm thick). These substrates are flat to better than 300 nm and have a surface roughness of less than 50 nm.

2. Experimental

In order for a bonding method to be truly useful, it has to come close to sharing some of the properties of the materials to be bonded (i.e. polymeric bonds—glues—are not considered adequate for this purpose). Ideally one would like to bond diamond to its substrate without any interfacial or adhesion layer which could prove to be weak, or unstable, chemically or thermally. One such ideal case is provided by the use of Mallory or anodic bonding.[1]

Anodic bonding involves the transfer of ionic species across the interface. Such transfer is facilitated by the simultaneous application of heat and an electrical bias. Typical conditions are 200-650 °C and 1000-5000 VDC. In the case of glasses, the glass substrate is biased negatively with respect to the diamond film.

Unfortunately, diamond (carbon) does not appear to anodically bond directly to glass within the range of experimental conditions stated above (the associated mechanisms will be discussed in the following section). To circumvent this problem, we had to provide an interfacial layer that could be bonded to glass and was also adherent to diamond. Silicon is routinely bonded anodically to glass during the manufacture of conventional x-ray mask substrates and could be easily sputtered onto diamond. Unfortunately, silicon is usually the substrate onto which diamond is deposited and is often removed by wet etching during fabrication of the same structures. During the removal, the Si bond could also be affected. Another material that is now routinely anodically bonded to glass, during the fabrication of x-ray masks, is silicon carbide (SiC).[2] Silicon carbide can also be sputter deposited onto diamond and remain adherent with thicknesses of up to few thousands of angstroms.

For the purposes of this work, crystalline diamond films (0.5—2 μm thick) were grown on silicon substrates by a method described elsewhere.[3] Subsequently, an interfacial layer of SiC, 1000 Å thick, was sputter deposited onto the growth face of the diamond film (as opposed to the Si-diamond interface). The Si-diamond substrate was then assembled onto the glass ring, and biased as illustrated in Figure 1. Time-temperature combinations ranging from 650 °C for 10 min, to 250 °C for 12 hs, at 2000 VDC all proved effective in bonding the structure.

The particular choice of conditions depends on the size of the parts and the maximum acceptable distortion. In cases where flatness is of concern and the parts involved are moderately large—such as in x-ray mask manufacture—the temperature uniformity across the assembly is of critical importance. In our experience, the resulting total warpage can range from a few nanometers to several microns, depending on the temperature uniformity.

Following the above procedures, we fabricated freestanding diamond-on-glass membranes where all the silicon substrate had been removed (by wet etching in a standard ethylenediamine-pyrocatechol etch) and only a drum-like membrane of diamond remained strung across an opening in the glass ring. Such a structure is the basis for a diamond x-ray mask in the so-called "flip" configuration (i.e. the Si wafer has been "flipped over", bonded and removed). Figure 2 depicts a schematic representation of the structure before and after wet removal of the silicon substrate.

An important advantage of these structures is the ability of the Si wafer and diamond film to conform to the shape of the glass substrate. This is particularly important for x-ray mask fabrication with advanced materials like diamond and SiC—which are grown by single sided processes (i.e. the films are deposited on only one side of the wafer). One-sided processes have a tendency to warp the wafer substrate depending on the elastic constants of the deposited material and its thickness. Typical cases result in as-grown un-bonded wafer distortions of a few thousand nanometers. After anodically bonding the substrates and removal of the silicon (see figure 2) we achieved structures that are flat to 10-100 nanometers. This represents an improvement of one to two orders of magnitude over conventional structures that do not remove the Si substrate.

Of considerable importance in the case of diamond and other films with less-than-ideal growth surfaces (i.e. rough) is the fact that in flip structures, such as the above, it is the smoother side that ends up becoming the "working surface". Crystalline films often grow with faceted or rough

surfaces that may present difficulties during its use. Rough surfaces may be difficult to pattern and inspect for defects. These films usually have a significantly smoother surface on the side that interfaces to the silicon substrate. "Flipping" the films then presents this smoother face for processing. Due to its extreme surface energy, diamond is a particularly good example of rough, island-like growth (Volmer-Weber) mechanisms, see Figure 3.

3. Discussion

It is worth to mention that materials that form a stable oxide seems more suitable for anodic bonding to glass. This is the case of silicon and silicon carbide. Conversely, diamond and silicon nitride do not bond to glass by the same procedure. The negative bias on the glass further reinforces the notion that cations may not play an active role at the interface under this conditions (other than contributing to the formation of a space charge region around it). Similarly, metals like chromium and nickel also bond under similar conditions. This indicates that oxidation at the interface plays an important role in anodic bonding under the conditions outlined above.

The fabrication of the structures discussed above illustrates the feasibility to transfer and bond permanently diamond films onto glass substrates. There are three key features of the process that are of significant importance: 1) Allows the transfer of diamond surface properties to inexpensive, easy to fabricate glass substrates; 2) Allows the inheritance of the glass substrate's shape to the diamond film. This is very important for structures that have to be flat, since glass is easily machined and polished flat and the burden of flatness is relieved from single sided growth processes which are common among advanced materials such as diamond; and 3) Allows for the use of the smoother face of the films by "flipping" them during the bonding process. This last aspect has significant consequences in applications requiring sub-micron microlithographic steps to be performed on the surfaces.

4. References

1.   G. Wallis and D.I. Pomerantz, J. Appl. Phys. **40**, 3946 (1969).

2.   One of the authors, R. Fuentes, originally implemented the use of anodic bonding in the fabrication of advanced SiC and diamond x-ray mask structures.

3.   Troilo, L.M., Owens, M.S., Shirey, L., Wells, G., and Butler, J.E., "Nanocrystalline diamond membrane growth by cyclic renucleation", Applied Diamond Conference 1995 proceedings.

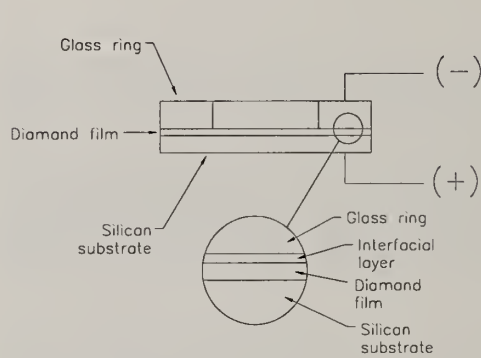584

5. Acknowledgements

Figure 1. Glass ring-diamond film assembly for anodic bonding showing interfacial layer and biasing arrangement.
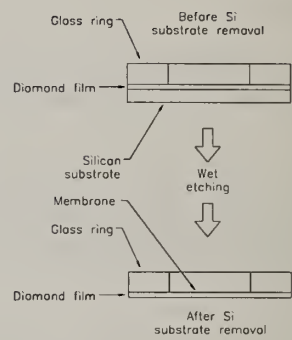

Figure 2. X-ray mask "flip" substrate etching step showing the removal of the silicon wafer and freestanding diamond membrane.
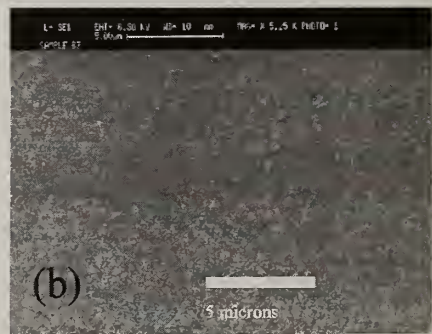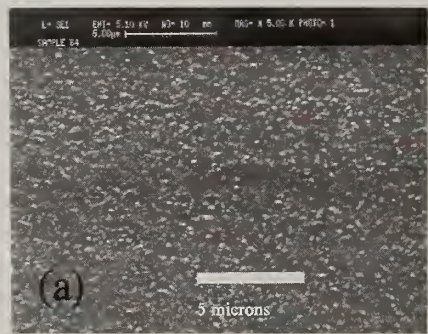

Figure 3. Scanning electron micrographs of (a) the growth surface of a membrane, facing the glass in the 'flip' configuration; and (b) the nucleation side of the membrane, facing away from the glass support in the 'flip' configuration.

Applications of Diamond Films and Related Materials: Third International Conference, 1995
Editors: A. Feldman, Y. Tzeng, W. A. Yarbrough, M. Yoshikawa, and M. Murakawa

585

EXCITON RECOMBINATION RADIATION FROM HIGHLY PURE DIAMOND SYNTHESIZED BY PRESSURIZED COMBUSTION FLAME METHOD

S. Takeuchi[1], M. Suzuki[1], J. Imamura[2], T. Murakami[2], H. Kawarada[2] and M. Murakawa[1]

[1]Nippon Institute of Technology, 4-1 Gakuendai, Miyashiro-machi, Saitama 345, Japan
[2]School of Sci. and Eng., Waseda Univ., 3-4-1 Ohkubo, Shinjuku-ku, Tokyo 169, Japan

Key words: combustion flame, pressure, chamber, free exciton, cathodoluminescence, perfection of diamond

Abstract

We propose a pressurized combustion flame method. Using that system diamond grains were synthesized at process pressures of 400, 760 and 850 torr. Cathodoluminescence analysis shows that the strength of the FE_{TO} peak as well as the F/A ratio increase as the synthesis pressure increases. Therefore, it is concluded that the level of perfection of the diamond crystal is improved by an increased synthesis pressure.

1. INTRODUCTION

Recently, strong exciton recombination radiation has been observed in the cathodoluminescence (CL) spectrum from CVD diamond[1-3]. Generally speaking, in the CL spectrum of diamond, a sharp peak of free-exciton recombination radiation (FE_{TO}) indicating high crystallinity and a broad-band A peak indicating the existence of impurities and crystal defects can be observed. We can evaluate the level of perfection of crystals by means of the intensity ratio (F/A).

In this study, we synthesized diamond at various pressures between 400 and 850 torr, using a system with a chamber installing a torch inside. We measured the CL spectrum of diamond synthesized using the system and obtained the values for FE_{TO} and F/A.

2. EXPERIMENTAL

Figure 1 shows a schematic of the experimental set up developed at our group for synthesizing diamond. Since the present method produces an ideal chemical reaction by reducing the atmospheric concentrations of CO and H_2, a diamond deposition of homogeneous quality without the
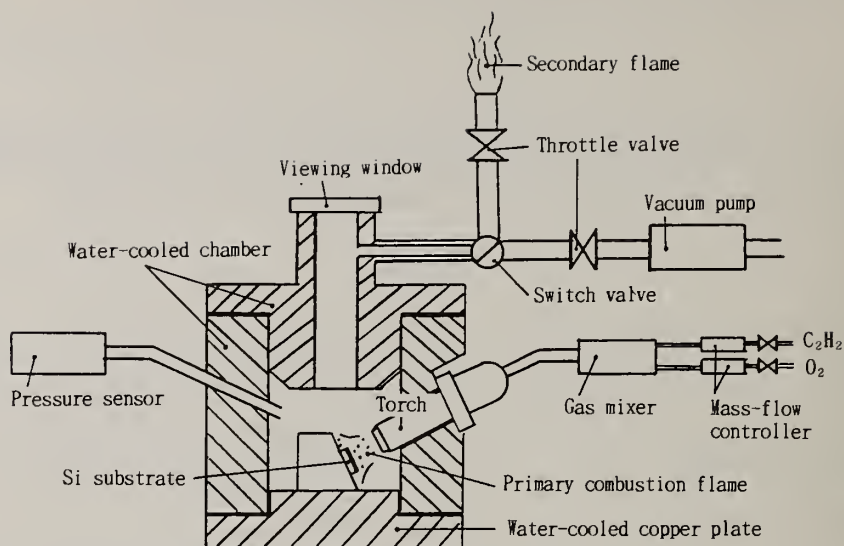
Fig. 1   Schematic view of the experimental set up.

Table 1 Experimental conditions.

Flow rate of C_2H_2	l/min	4.5
Flow rate of O_2	l/min	4.0
Substrate temperature	K	1173
Reaction pressure	torr	400, 760, 850
Torch to substrate distance	mm	7.5 or 3.5

inclusion of atmospheric components can be expected. The primary combustion produces CO and H_2 through a throttle valve. Various reaction pressure for diamond synthesis can be achieved by adjusting the throttle valve openings. In this study, reaction pressure of 400, 760 (atmospheric pressure), and 850 torr were selected. As the substrate for synthesis of diamond, mirror polished Si (100) single crystal plate of 5 mm × 5 mm was used. The conditions of the present experiments are given in Table 1. Furthermore, the distance between substrate and top of the torch was 7.5 mm, in all experiments except one where the distance was 3.5 mm. The deposition time was 1 to 1.5 hours, which produced diamond grains of diameter 10~20 µm.

Cathodoluminescence spectra were measured for the obtained diamond grains and values for FE_{TO} and F/A were calculated. Cathodoluminescence analysis was performed using a scanning electron microscope (Topcon DS-130type) equiped with a liquid-nitrogen cooling stage (Oxford C1001), an ellipsoidal mirror, a monochromator fitted with a 1200 grooves mm⁻¹ grating, and a photo multiplier suitable for

the 2.0 - 6.0 eV photon energy region. The accelerating voltage was 19 kV with a probe current of 2×10^{-8} - 4×10^{-6} A. The temperature during measurement was 80 K.

3. RESULTS AND DISCUSSION

Figure 2 shows typical CL spectra for 15 μm diamond grains synthesized at different process pressures. In each spectra the FE_{TO} peak at 5.27 eV and the broad-band A peak at 2.8 eV can be observed. For comparison, the figure also remarks values of F/A. The value of F/A was 0.1, 2 and 22 for grains synthesized at a pressure of 400, 760 and 850 torr, respectively. Thus, the value of F/A is improved with the increase of synthesis pressure. Furthermore, the strength of the EF_{TO} peak increases from 3 to 780 mV as the synthesis pressure is increased from 400 to 850 torr. Figure 3 shows variations in the value of FE_{TO} from 3 repeated synthesis experiments at each pressure. At 850 torr, the value of FE_{TO} displayed a big scatter (100~780 mV). However, a mean value of FE_{TO} indicates an exceedingly strong peak. The above findings show that the level of perfection of diamond crystal is improved with the increase of synthetis pressure.

In diamond synthesis by the combustion flame method, the distance from torch to substrate surface is also an important factor, since the actual synthesis pressures is related to it. Due to the high gas flow rate and the small nozzle diameter the gas flow velocity is very high. However, the gas flow velocity decreases with increasing distance from the nozzle. Also the flame expands as it comes farther away from the nozzle. The actual synthesis pressure is determined by the chamber pressure and the pressure caused by the flame. Consequently, the
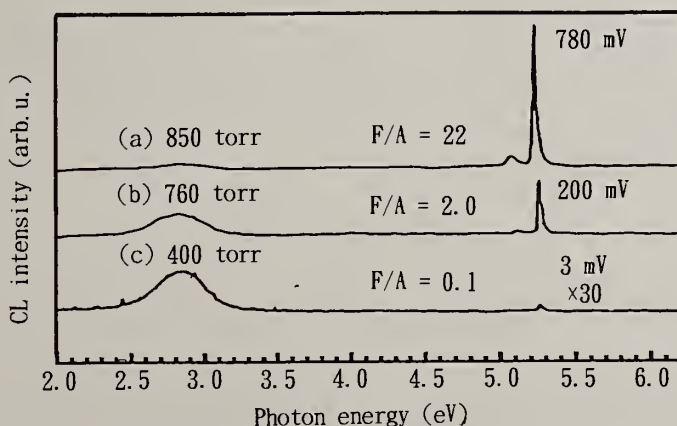

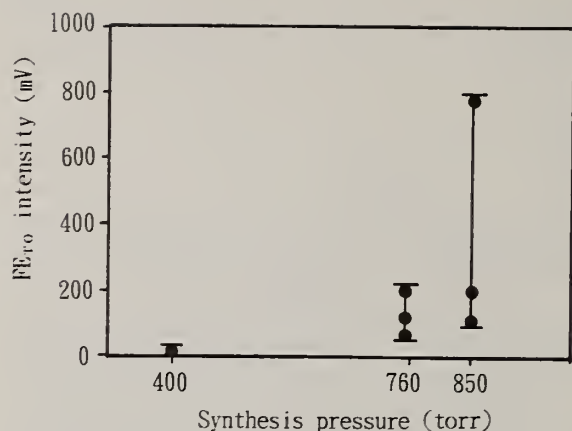Fig. 2 CL spectra of diamond grains synthesized at various pressures

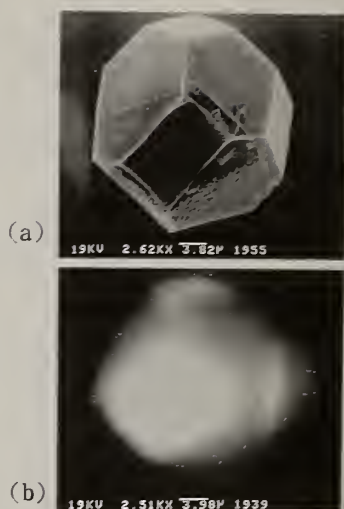Fig. 3 Scatter of FE$_{TO}$ intensity at various pressures.

(a)

(b)

Fig. 4 (a)SEM and (b)CL images of diamond grain at 850 torr and 3.5mm torch to substrate distance.

actual pressure decreases with increasing distance from torch to substrate even though the camber pressure is constant. Thus, an experiment was made at 850 torr and a torch distance of 3.5 mm (compared to 7.5 mm in the other experiments).

In this case CL analysis showed a value of F/A = 20 and a strength of FE$_{TO}$ = 1180 mV. The last value is the highest in this study. This value is comparable to homoepitaxial[4] film grown on single-crystal diamond using the atmospheric chamber flame method[5]. Figure 4 shows an SEM image and corresponding monochromatic (5.27 eV) CL image of a diamond grain. The (100) face is luminescent, which is expected from CL imaging study[2] of isolated particles. In this study all grains displayed comparable strong luminescence. Therefore, it is concluded that the level of perfection of the diamond crystal is improved by an increased synthesis pressure.

4. REFERENCES

1. A.T.Collins, M.Kamo and Y.Sato, J. Phys. Cond. Matt. 1(1989) 4029.
2. H.Kawarada, Y.Yakota and A.Hiraki, Appl. Phys.Lett. 57 (1990) 1889.
3. H.Kawarada, T.Tsutsumi and J.Imamura, Advances in New Diamond Sci. and Tech., MYU, Tokyo (1994) 301.
4. T.Tsutsumi, J.Imamura, S.Takeuchi, M.Murakawa and H.Kawarada, Advances in New Diamond Sci. and Tech., MYU, Tokyo (1994) 363.
5. M.Murakawa and S.Takeuchi, Diamond Films and Tech.,2-4 (1993) 183.

POLYCRYSTALLINE CVD DIAMOND FILMS WITH OPTICAL PROPERTIES CLOSE TO THOSE OF TYPE II DIAMONDS

A.V. Khomich[1], P.I. Perov[1], V.I. Polyakov[1] ,I.G. Teremetskaya[2], V.P. Varnin[2], V.I.Konov[3] , S.M. Pimenov[3] and E.D. Obraztsova[3]

[1] Institute of Radio Engineering & Electronics, RAS, Moscow, RUSSIA
[2] Institute of Physical Chemistry, RAS,117915 Moscow, RUSSIA
[3] General Physics Institute, RAS , 117942 Moscow, RUSSIA

Keywords : diamond films, optical characterization, oxidation behavior

Abstract

The fine-grained diamond films with low absorption in visible and infrared were grown on Si substrates by DC arc discharge and HF CVD. Films with prevailing (111) or (110) orientation of the planes demonstrates high oxidation resistance. The near- and above-bandgap absorption was determined and discussed.

1. Introduction

Diamond transparency from IR to UV combined with excellent abrasive and thermal properties make diamond films a natural choice for optical applications, especially for IR optical protective and antireflecting coatings in high-flying aerodynamic objects. Optical applications require both low absorption and low surface scattering of light in diamond films. A decrease in absorption can be achieved reducing the content of impurities (mainly, nitrogen and non-diamond carbon inclusions), which is controlled by deposition conditions. A way to reduce surface light scattering is to diminish surface roughness by growth of thin fine-grained [1-4] or highly-textured [5] diamond films. Thin CVD diamond films can have some other applications as electronic devices, for example for light-to-electricity conversion [6]. The efficiency of such conversion depends also on surface light scattering and above-bandgap optical properties of CVD diamond films, while usually its absorption coefficient [7] is sufficiently higher than that of single-crystal diamonds. For some of important applications, the diamond film resistance against an oxidation at elevated temperatures is of special interest.

On the basis of these motivations, our study was focused on growth and optical characterization of a few microns thick fine-grained diamond films with low

absorption in visible and infrared. The above-bandgap absorption and oxidation resistance of the films were also investigated.

2. Experimental

The CVD diamond films were grown on silicon substrates with two commonly used techniques - DC arc discharge and HF CVD from mixtures of hydrogen and methane (or acetone). Ultrafine diamond powder of 5 nm grain size was used for Si substrate's pretreatment in ultrasonic bath with the powder suspension in alcohol. This enabled us to increase the diamond nucleation density on the Si surface to more than 10^{10} cm^{-2}.

To produce diamond windows the silicon substrate was partly removed by acid mixture etching. Optical spectroscopy measurements were carried out using an IR and UV-VIS "Specord" spectrometers with a range's 0.185-0.9 µm and 2.5-50 µm. The films were examined also with Raman spectroscopy (488 nm excitation wavelength, 2 µm laser beam spot size). The annealing (oxidation) experiments were performed at 500 -750 C in air or nitrogen atmosphere. The films show good adherence to the substrate and didn't crack or unbound during the annealing with the heating (cooling) rate up to 50 degrees per minute.

3. Results and discussion

a)Optical properties. Optical properties of thin fine-grain diamond films are determined by the crystallite properties itself and the non-diamond carbon content in
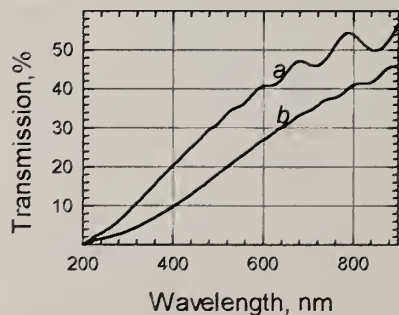
Fig. 1. Transmission spectra of diamond films .95 (*a*) and 2.0 (*b*) µm thick.
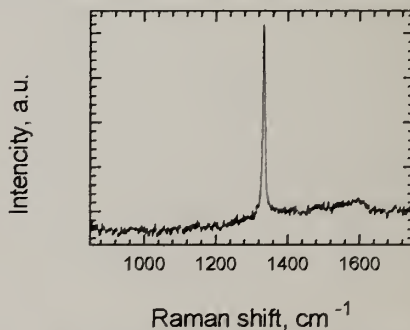
Fig. 2. Raman spectrum of a fine grained diamond film.

the intergrain boundaries. The films investigated showed high transmittance in visible (Fig. 1) and infrared regions modulated by the film interference fringes. The indirect diamond bandgap was observed in all the films as a sharp increase in the optical density spectra near 224 nm. The analysis of the IR and visible transmission spectra showed that the transmission losses were defined mainly by the light scattering from

the growth surface of the film. The surface of the window facing the substrate was as smooth as the starting surface of the silicon wafer. The root mean square surface roughness values of 30 - 70 nm were defined which did not influence significantly on the film IR transparency. By proper optimization of the deposition conditions, we obtained diamond films with negligible absorption in visible caused by non-diamond intergrain boundaries, as confirmed also by the Raman spectroscopy (Fig. 2). The full width at half-maximum of the diamond peak in Raman spectra of these films was among 6 and 7 cm^{-1}, which is only slightly higher than that measured for natural diamond (2.5 cm^{-1}).

Usually, in defect diamond crystals and CVD films some absorption can occur at wavelengths of less than 1350 cm^{-1} due to impurities, imperfections, or disorder that destroy the transitional symmetry and causes the breakdown of the momentum conservation law allowing lattice modes to couple with electromagnetic radiation. The absorption coefficient of our films in the one-phonon band was calculated from the difference between measured transmission and transmission background due to the surface scattering and the tail of the two-phonon absorption. For the 15-25 μm thick films, which were obtained in the same conditions, it was near 5 cm^{-1}. The samples displayed also rather weak absorption in the CH-stretch region, between 2800 - 3000 cm^{-1}, from sp^3-type CH-bonds. The overall content of hydrogen in our films was estimated from integral intensity of C-H band as lower than 0.5%.

b) *Oxidation resistance.* The CVD diamond films are oxidized during the heating in air at elevated temperatures, which decreases their thickness, increase the light scattering and lead to dramatic changes in transmission spectra. The intergrain boundaries and (100) diamond faces are the most sensitive to the oxidation. We examined the transmission spectra and SEM pictures measured in both the etched window and non-etched areas of the silicon-diamond structure. The oxidation rates were determined from the interference fringe shifts.

Some films with prevailing (111) or (110) orientation of the planes at the top surface of the individual crystallites demonstrated an excellent oxidation resistance in air with low oxidation rates. For the diamond windows, the oxidation rate 0.1-0.2 microns per hour at 700 degrees was obtained, which was determined mainly by the bottom surface etching. The heat treatment in nitrogen at such temperatures did not change the film thickness and properties.

c) *above-bandgap absorption* The absorption coefficient spectra at and above the fundamental absorption edge of thin CVD films were calculated from their transmission spectra with the proper correction on surface reflection and scattering. Fig. 3 shows the absorption spectra of CVD diamond films (*a* and *b*) and, for comparison, of a bulk diamond crystal (*c*, [8]). It is seen that the absorption coefficient in this region is higher for the diamond films then for the bulk crystal. The

592

same effect was observed [7] for the films with rather high non-diamond phase content and was attributed to disorder-induced band tail states.
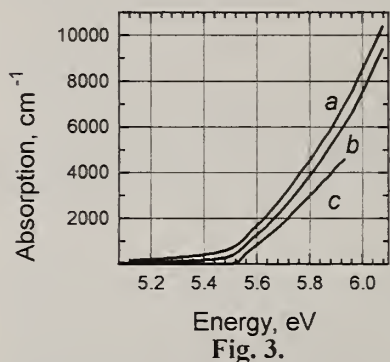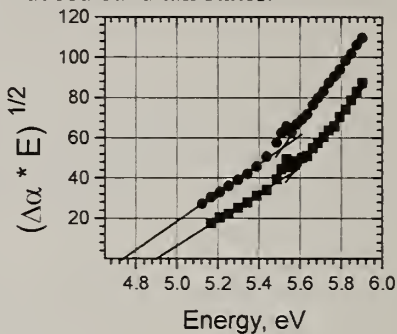

Fig. 3.

Fig. 4.

Fig. 4 shows the dependencies of $(\Delta\alpha E)^{1/2}$ against E, where $\Delta\alpha$ is the difference between the absorption coefficients of the CVD diamond film and type II diamond, and E is the photon energy. Such dependencies are usually used for determination the characteristic energies for interband and impurity optical transitions in indirect band gap semiconductors. There are two distinct parts in each plot that can be fitted by strait lines. These lines crossing point correspond to the diamond indirect gap, and the lower energy parts cross the energy axis at the 4.6 to 5.0 eV energies that are connected with the absorption due to localized states. The breakdown of the selection rules on wave vector k in fine grained diamond films might be one of the main reasons of the higher above band gap absorption in the films comparing to diamond crystals.

References

1. H. Windischmann and G.F. Epps, *J. Appl. Phys.* 68 (1990) 5665-5673

2. R. Erz, W. Dotter, K. Jung and H. Ehrardt, *Diamond and Related Materials*, 2 (1993) 449-453.

3. V.I. Konov, E.D. Obraztsova, S.M. Pimenov, V.G. Ralchenko, A.A. Smolin, A.V. Khomich, V.I. Polyakov, A.I. Rukovishnikov, P.I. Perov and E.N. Loubnin, *SPIE*, Optical materials for high power lasers (1994), to be published.

4. A.V. Khomich, P.I. Perov, V.I. Polyakov, I.G. Teremetskaya and V.P. Varnin, *Diamond Relat. Mater.*, in press.

5. P. Koidl, C. Wild, R. Locher and R. Kohl, Proc. 2nd Int. Conf. on the Applications of Diamond Films and Related Materials, MYU, Tokyo 1993, 87-94.

6. M.A. Prelas, E.J. Charlson, E.M. Charlson, J. Meese, G. Popovici and T.Stacy, Proc. 2nd Int. Conf. on the Applications of Diamond Films and Related Materials, MYU, Tokyo 1993, 329-334.

7. L.H. Robins, E.N. Farabaugh and A. Feldman, *SPIE*, Vol. 1534 (1991) 105-116.

8. C.D. Clark, P.J. Dean and P.V. Harris, *Proc. Royal Society*, 277A (1964) 312-334.

Optical Characterization of Low-Pressure Combustion Growth of Diamond

Elke Jensen, Vasgen A. Shamamian, and James E. Butler
Code 6174, Naval Research Laboratory
Washington, DC 20375

keywords: boundary layer, combustion, diamond, optical emission

Abstract

Reaction chemistry and transport properties play an important role in the chemical vapor deposition
(CVD) of diamond and other materials. We examine the near surface region of species gradients, the
boundary layer, that develops between the bulk gases and the growing diamond surface in a low-pressure
combustion reactor. We present optical emission spectra from low-pressure combustion growth of
diamond when a premixed, flat hydrocarbon flame, (here, an ethylene-oxygen mixture) is lifted and
stabilized on a heated substrate at low pressure (typically below 100 torr). We collect two-dimensional
optical emission spectra from species such as CH, C_2 and OH with an intensified CCD array to
determine species presence and concentrations in the flame and in the boundary layer near the growing
material. These studies provide information to help elucidate the mechanism for diamond growth under
these conditions, as well as analyzing the relationship between the detailed chemical reaction kinetics
and transfer of heat and mass from the activation region.

1. Introduction

There now exist a wide variety of chemical vapor deposition (CVD) methods for growing diamond and
other materials, including microwave plasma, hot filament, dc-arc jet, rf plasma and combustion.[1] Since
the initial experiments that demonstrated the feasibility of diamond thin film synthesis with an
oxyacetylene torch, the method has been widely studied due to its relative simplicity and low capital
cost. Many studies have shown that an atmospheric oxyacetylene flame is an effective environment for
growing diamond, and can produce polycrystalline films at a rate of several tens of microns per hour.[2]
Goodwin and others[3] have shown that diamond can be grown at low-pressure, and have examined effects
such as substrate temperature and gas ratio on the quality of the films so produced.[4]

As for the other CVD methods mentioned above, two of the key factors required for the success of
combustion as a growth technique are the efficient production of the chemical species necessary for
growth, and the physical transport of those species to the reactive surface. In the stagnation point flow
configuration used in these experiments, the directed flow, even at moderately low pressures, favors
development of hydrodynamic (species concentration) and thermal boundary layers. The boundary layer
is, by definition, a region of large gradient in an important property, such as pressure, temperature or
concentration, which arises when the species concentration or bulk gas property is constrained by
interaction with the surface and differs from that present in the bulk gas. In a flat flame where both the
flow speed of the reactant gases and the pressure are experimentally controlled parameters, the boundary
layer thickness can be changed easily. This makes the low-pressure regime a useful and interesting
arena for diagnostics. Here, we present optical emission spectra of a lifted, low-pressure, premixed
ethylene-oxygen flame impinging upon a heated substrate. These studies aim to highlight the importance
of the boundary layer created between the bulk gases and the growth surface in a combustion
environment.

2. Experimental

The low-pressure combustion chamber consists of a pair of 8" diameter stainless steel conflat crosses which allow the torch to feed through from below, and permit optical access from the four sides. The four-way cross on top provides ballast volume to damp acoustical coupling between the pump and the combustion gases. The substrate is introduced from the top, where its gross position in the chamber can be adjusted *via* an o-ring vacuum fitting, and finer adjustments can be made with the micrometers on the X-Y-Z translation stage. Six mini-flange ports are used to pump out the system, and to introduce thermocouple and electrical feedthroughs.

During typical growth runs, the flame does not produce enough heat to bring the 1/4 in. thick molybdenum substrate up to the approximately 900 °C necessary for diamond growth. Therefore, it becomes necessary to actively heat the removable substrate with a 1 in. diameter molybdenum cartridge heater, powered by a voltage-controlled DC power supply. A type C thermocouple measures the substrate temperature through a small hole in the side of the removable stub.

The torch is based on a simple bead burner design discussed in Gaydon and Wolfhard.[5] The 3/4 in. ID water-cooled copper body is filled with 1/8 in. diameter stainless steel beads, held in place with a panel of fine mesh screen. Premixed gases feed the water cooled burner *via* a pair of inlet ports at the bottom of the torch, and the flow is randomized by passing through the interstices between the beads. The beads and screens also provide a large metal surface area for quenching flashback into the gas feed lines, where a commercial flash arrester is installed. The substrate to torch distance, d_s, is approximately 1 torch diameter, or 0.75 in.

Emitted photons are detected with a gated, image-intensified, cryo-cooled CCD detector. The CCD chip consists of a 256 (h) x 1024 (w) array of 27 μm sq. pixels. A UV-grade quartz f/4 lens collects the light, which is imaged onto the blue-enhanced intensifier with a 3 in. focal length, 2 in. diameter lens. Typically, the data are binned together in 5 rows of pixels, so that the final image consists of 50 rows of 1024 pixels.

Figure 1 presents the emission data. Fig. 1(a), presented for reference, shows the total emission intensity from the flame and substrate, integrated over a 100 μs exposure time. The following figures show the filtered emission centered at 560, 430 and 310 nm.[6] Clearly, only the flame itself is visible in these images. The emission is attributed to fluorescence from excited C_2 (d→a), CH (A→X) and OH (A→X), respectively. These images show that the locations of the emitting radicals in the flame differ slightly, as is expected for a premixed hydrocarbon flame.[5]

3. Discussion

The thickness of the thermal or hydrodynamic boundary layer may be estimated by calculating a Nusselt number under the growth conditions. For laminar stagnation-point flow, the dimensionless Nusselt number, Nu_T, is given by the expression $Nu_T = 0.57 \, Re^{1/2} \, Pr^{2/5}$, where Re is the Reynolds number, and Pr is the Prandtl number, v/α, the ratio of the momentum to heat transfer coefficients.[7] The Nusselt number can be related to the thermal boundary layer thickness by $Nu_T \approx l/\delta$, where l is the characteristic length of the system, which in our reactor is approximately 2 cm. Similarly, for the hydrodynamic boundary layer, $Nu_x = 0.57 \, Re^{1/2} \, Sc^{2/5}$ where Sc is the Schmidt number, the ratio v/D, of the momentum versus mass transfer (diffusion) coefficients. At 100 torr, with total flow of about 2.3 slm, the boundary layer thicknesses are calculated to be on the order of 1 mm. In fact, one can, by visual inspection, see a "gap", between the flame front and the substrate surface in the reactor under these conditions. This observation is confirmed by the emission spectra.

At sufficiently low pressures, below about 50 torr, the diffusion lengths of the reactive species become comparable to d_s, the distance between the torch and substrate. Fig. 2 shows a photograph of an ethylene-oxygen flame at 18 torr, where it is clear that the flame sheet has thickened to fill the entire distance between the torch and substrate. There is no longer a well-defined boundary layer, and species transport to the growth surface is diffusion-controlled.[8]

The quality of the diamond may be correlated to the emission from excited state species in the flame under conditions where there is a boundary layer, as there is at atmospheric pressure. This provides a simple indicator of the correct stoichiometry in these fuel-rich mixtures.

4. Conclusions

These studies of the emission from a lifted, premixed ethylene-oxygen flame are of two-fold importance. First, since the emission spectra of the various excited species in the flame change depending upon the conditions of the reactor, this can be used to monitor whether or not one is in the growth domain for quality diamond films. The diamond quality is very sensitive to, for example, small changes in stoichiometry. Errors introduced by the mass flow controllers, or inability to monitor the temperature accurately may take the reactor conditions from diamond growing to non-diamond growing. It is therefore important to have an "absolute" indicator of whether or not one is in the growth regime. Second, the studies presented here lay the groundwork for probing the important boundary layer which the growth species must traverse in order to reach the deposition surface. Future work will include collecting dispersed spectra of various radicals in the flame, and laser-induced fluorescence of the species in the boundary layer.

5. References

1. See review article by F. Celii and J.E. Butler, Annu. Rev. Phys. Chem. 1991, 42:643-684 and references therein.
2. For example, M. Murayama and K. Uchida, Combustion and Flame 91 (1992) 239.
3. N.G. Glumac and D.G. Goodwin, Thin Solid Films 212 (1992) 122; J.S. Kim and M.A. Cappelli, J. Applied Physics 72(11) (1992) 5461.
4. Early studies include those by L.M. Hanssen, K.A. Snail, W.A. Carrington, J.E. Butler, S. Kellogg and D.B. Oakes, Thin Solid Films 196 (1991) 271.
5. A.G. Gaydon and H.G. Wolfhard, Flames: Their Structure, Radiation and Temperature (Wiley and Sons, New York, 1979).
6. These filters are all centered at λ +/- 2 nm, FWHM = 10-12 nm.
7. A.M. Kanury, Introduction to Combustion Phenomena, (Gordon and Breach Science Publishers, NY, 1977), Ch. 3.
8. This photograph shows a different torch than the one described above, but the general arguments concerning boundary layers remain valid.

596

Figure 1: Emission from a low-pressure ethylene-oxygen flat flame. These images were actually collected with a different burner than the one described in the text, but are representative of a lifted flat flame near the appropriate stoichiometry for diamond growth at 60 torr. In Figs. b-d , the white rectangle indicates the position of the substrate, which is not visible through the optical filters. See text for details.

(a) Total emission; 100 μsec exposure.

(b) Emission at 560 nm, 2 ms exposure (C_2).

(c) Emission at 430 nm; 3 ms exposure (CH).

(d) Emission at 310 nm; 3 ms exposure (OH).

Figure 2: Photograph of an ethylene-oxygen flame at 18 torr. One can distinguish the torch nozzle below, and the substrate above the glowing flame.

INFLUENCE OF POST-DEPOSITION ANNEALING AND OXIDATION ON STRUCTURE AND OPTICAL PROPERTIES OF CVD DIAMOND FILMS.

A.V. Khomich[1], P.I. Perov[1], V.I. Polyakov[1], I.G. Teremetskaya[2], V.P. Varnin[2], E.D. Obraztsova[3], S.M. Pimenov[3], and V.G. Balakirev[4]

[1] Institute of Radio Engineering & Electronics, RAS, Moscow,RUSSIA
[2] Institute of Physical Chemistry, RAS,117915 Moscow,RUSSIA
[3] General Physics Institute, RAS , 117942 Moscow,RUSSIA
[4] Institute SMS, 601600 Aleksandrov, Vladimirskaya obl.,RUSSIA

Abstract

UV-VIS and IR absorption and reflection spectroscopy, Raman spectra, photoluminescence measurements and transmission electron microscopy were used in order to investigate the influence of growth conditions on the optical properties and structure of diamond films and to obtain information about the heat treatments effects on their properties.

1. Introduction

The oxidation and annealing of as-grown CVD diamond films at elevated temperatures is a valuable tool for modification of their electrical, optical, and photoelectric properties, for investigating the films' structure, thermal stability and obtaining information about the location of non-diamond carbon phases. The time-dependent oxygen etching behavior of differently prepared diamond films was investigated in details in [1], where transformations of the structure, Raman and photoluminescent spectra were monitored. For oxidation experiments, we choose so called "nanocrystalline" diamond films, because there are only few investigations concerning their internal structure and oxidation resistance.

2. Samples

Diamond films with thickness varied from 0.3 to 30 microns were grown on Si substrates by a DC arc discharge and hot filament CVD from a mixture of hydrogen and methane (or acetone). The annealing (oxidation) experiments were performed at

300 -850 C in air, in hydrogen or nitrogen atmosphere. The same samples were examined by Raman and optical spectroscopy, as by electron microscopic study.

3. Results and discussion

As-deposited films. The Raman spectrum of as-deposited diamond films (Fig. 1) consists of the bands of two carbon phases: sp^3-bonded diamond and sp^2-bonded graphite. The narrow weak band with maximum near 1332 cm^{-1} belongs to well-crystallized diamond phase. A wide band at 1140 cm^{-1} indicates the presence of a ultrafine-grained (or even amorphous) diamond phase, for which all the density of one-phonon states of diamond is displayed. The position of this line coincides with the maximum of TO-like phonon band. The wide bands at 1350 and 1580 cm^{-1} are known for the nanocrystalline (glassy) carbon. The questionable feature is the wide band near 1500 cm^{-1}. This band is usually absent for the micron-size polycrystalline diamond film, so it often called as the "fingerprint" of fine-grained diamond films.

The concentration of carbon-hydrogen groups in our films was of the order of 1.5% as estimated from integral intensity of CH_n stretching mode vibrations in the IR spectra. The sp^3-hybridized CH_2 groups are determined the band intensity, while the absorption due to CH_3 sp^3 groups and due to sp^2-hybridized CH_n groups were rather weak in our as-grown films [2].

The electron microscopic study made using the Pt-C replicas showed that a thin nonstructured layer existed on the surface of the diamond films fabricated, which made the growth relief smoother. The fractographic study of the diamond films showed separate dense, without visible voids and sharp interfaces, 100 - 200 nm size objects which were in some cases the single crystals with 10 - 15 nm blocks, but mainly - the polycrystalline conglomerates, as showed the transmittance electron diffraction study. The stacking faults and twins interfaces were seen in some crystallites.

Oxidation experiments. After oxidation in air at 530 C the morphology of the film becomes more distinct, some particles with sizes of 30 - 50 nm are seen. Internal structure of the films does not suffer any visible changes. Oxidation at 627 C causes the internal structure changes. Polycrystalline conglomerates with the electron diffraction image the same as as-grown films, were transformed into broom-like units consisting from stacks of highly flattened crystallites with maximum linear size about 10 nm. We consider that the visualization of the separate crystallites became possible due to the oxidation removing intercrystallite layers with the same electron-optical properties as for the crystallite ones.

The annealing of diamond films in air leads also to drastic changes in their optical transmission [2] and Raman spectra. At the temperatures higher than 630 C the most

of the non-diamond carbon is removed from samples investigated and the remaining diamond crystallites in the film structure are attacked by the oxygen. During the annealing in air at such temperatures, oxygen removes not only the non-diamond carbon, but the diamond with high density of defects also, which resulted in the significant reducing of the absorption near the band gap edge region . The absorption bands due to CH_n -groups and defect-induced one-phonon band almost disappears during the oxidation at these temperatures.

In the IR spectra of oxidized films the interference fringes are well-observed indicating that the surface of the film is still sufficiently smooth to allow interference between beams reflected internally. Due to the light scattering in the bulk and on the surface of the oxidized films the decline in the UV-VIS and near IR spectra is observed. The mean transmission of free-standing diamond films in the far IR grew from 70% up to 85-92 % [2]. The interference fringes analysis show that such porous films posse the effective refractive indexes up to 1.5-1.7. We used an effective medium approximation to model the optical constants of such oxidized films, in which we assume that the film is composite heterogenous medium consisting of diamond and void components. A calculation of the dielectric functions based on this model showed that the volume fraction of the diamond in such porous films lowered
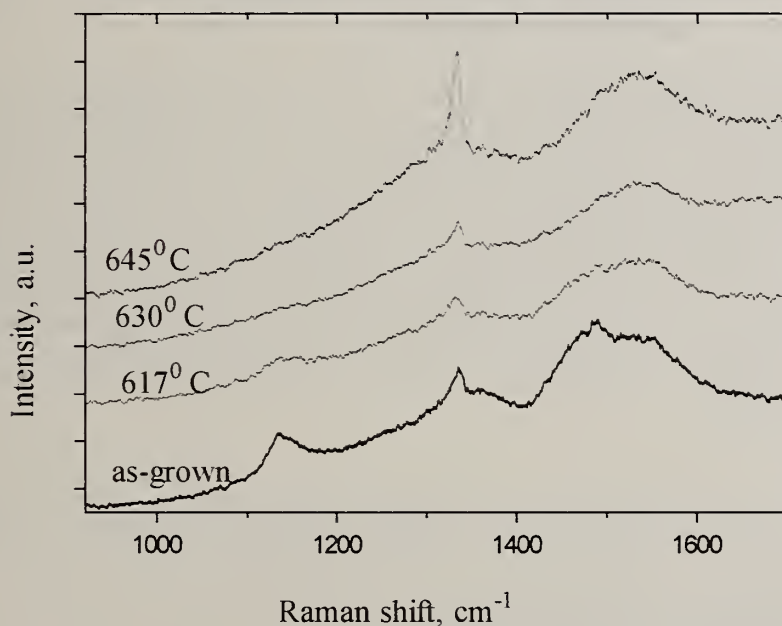
Fig. 1. Raman spectrum transformations due to the sequential oxidation treatments of the nanocrystalline diamond film in air.

down to 60-40 %, in agreement with the estimations from the electron microscopy observations.

We have observed a non-monotonous modification of the Raman spectrum depending on the annealing temperature. For the temperatures lower than 620 C the only change is a minor intensity decrease of all spectral bands. For higher temperatures the trace of a "nanodiamond" phase (at 1140 cm^{-1}) has disappeared abruptly, while the peak of a well-crystallized diamond has become more pronounced and its contribution increased with respect to one's of the graphite bands. Such type of a behavior may be interpreted as removing of the ultrafine-grained diamond phase. Indirectly it may clarify the position of that phase in the bulk of the film. The IR measurements indicate the spreading of the etching process from the surface to the bulk of the sample at temperatures of 620 C. Since the intensity of the signal of a well-crystallized diamond begins to increase at this temperature, it is plausible to suppose that the coarse diamond grains keep unchanged, while the intergrain phase is removed. It corresponds to the disappearance of the amorphous diamond signal in the Raman spectra. It is a weighty argument in favor of situating this phase in the intergrain space. The heat treatment of oxidized porous films in hydrogen at 850 C during 30 min. restores the CH_n stretching bands, while the Raman spectra remained unchanged and the 1140 cm^{-1} Raman band didn't appear. This rule out the possibility, that this band caused by C-H groups.

We observed the long-time processes of the sp^3 CH_n bond concentration growth in such porous samples during their storage in air after the oxidation treatment. Characteristic time of these processes was hundreds of hours, and the CH_n-stretching band shape differed significantly from one for the as-grown films due to higher part of the sp^3 CH_3- groups. The total content of CH_n bonds after some month storage prevailed the content of these bonds in as-grown film films, evidently resulting from the substitution of the C=O (C-O-C) bonds for sp^3 CH_n ones in porous oxidized samples. Heating the sample in air at 180 C during an hour decreased substantially CH_n-bands intensities, and heating up to 250 C was sufficient to remove all the adsorbed hydrogen.

References

[1]. P.K. Bachman, D. Leers and D.U. Wiechert, *Diamond Relat. Mater.*, **2** (1993) 683.
[2]. A.V. Khomich, P.I. Perov, V.I. Polyakov, I.G.Teremetskaya and V.P.Varnin, *Diamond Relat. Mater.*, **4** (1995) in press.

DIAMOND
THERMAL PROPERTIES AND
APPLICATIONS

Thermal Aspects of High Performance Packaging with Synthetic Diamond

P. J. Boudreaux

Laboratory for Physical Sciences
8050 Greenmead Drive, College Park, MD 20740-4000 USA

Key Words: coefficient of thermal expansion (CTE), direct-write metallization, high density interconnect, Multi-Chip Module (MCM), Pin Grid Array (PGA) package, phase change cooling, supercomputer, thermal management, thermal test chip, thick film gold

Abstract

The extraordinary thermal conductivity and dielectric properties of diamond translate into performance and reliability advantages for electronic packaging of high performance semiconductors. Demonstrated diamond substrate Pin Grid Array (PGA) packages and Multi Chip-Modules (MCM) have changed the whole approach to high performance computing. Subnanosecond computer performance is made possible for the first time by a diamond substrate 3-D architecture.

1. Introduction

Diamond is one of nature's most amazing gifts. Everyone knows of its use as a gemstone because of it's "fire" and durability. Yet these are just some of the outstanding physical characteristics that make this crystal unique among naturally occurring elemental minerals. Today we can explain many of diamond's physical properties, and why they are so different from the other allotropic forms:of carbon: amorphous carbon (soot), graphite, and the fullerenes. The extremely strong bonds between the carbon atoms in the diamond structure make it the hardest known
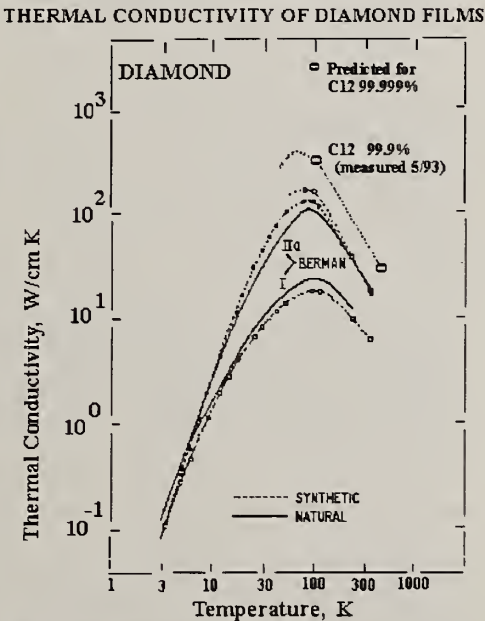
Fig. 1. Thermal conductivity measurements, together with their theoretically predicted values, are plotted vs. absolute temperature for normal and isotopically enhanced diamond films.

material. It is this hardness that explains another superlative property of diamond, it's ability to conduct heat, which at room temperature is again the best of any known material. In fact, as its temperature is lowered to 100 Kelvins (a little above liquid nitrogen temperature) diamond achieves its maximum thermal conductivity. Theory and experiments have shown (**Fig. 1.**) that at this temperature isotopically pure diamond has a thermal conductivity two orders of magnitude greater than at room temperature [1]. Even higher thermal conductivity can be expected through improved isotopic purity. Unlike other good heat conductors, such as copper, diamond is an exceptional electrical insulator. These properties make it an ideal material for advanced semiconductor packaging applications.

Diamond was first grown artificially by high temperature and pressure techniques, but these methods were expensive and produced relatively small single crystal samples. In the early 1980's there were reports of diamond being grown by low pressure plasma methods in the U.S.S.R. These reports were not taken seriously until the Japanese repeated these experiments and proved that the material was indeed diamond. In the United States, other researchers concentrated on developing thick polycrystalline diamond films and plates of substantial diameter.

DIAMOND TEST PACKAGES

Fig. 2. Custom DIP and Pin Grid Array packages contain diamond inserts and heat sinks that match the CTE of silicon chips. Up to 120 watts can be extracted from PGA diamond.

2. Integrated Circuit Packaging

Researchers at the Laboratory for Physical Sciences (LPS) saw opportunities to use diamond to solve problems encountered in high performance computing engines. This did not require high quality material, but could use the polycrystalline material being produced by plasma methods. These polycrystalline plates still had thermal conductivities that were five times better than that of copper and they were very good electrical insulators. The match in the coefficient of thermal expansion (CTE) between diamond and silicon is another excellent feature. This CTE match is far superior to that for silicon and the typical ceramic or metal packaging material used in standard or high performance devices. In addition, the insulating capacity of diamond greatly exceeds that of ceramic. Diamond is a powerful new packaging material with excellent thermal management characteristics for electronic circuits.

Many reliability problems involve the overheating of silicon chips. This is a direct cause of decreased reliability in equipment. Near room temperature, the Arrhenius relationship between the temperature of an integrated circuit and its expected operating lifetime predicts that every reduction of ten Kelvins will double the Mean Time Between Failure (MTBF) of the device. Artificial diamond can be used to extract heat more efficiently, and thereby lower the temperature of high performance or high power integrated circuits. Equipment can now be designed with increased reliability and/or improved performance.

In 1989 LPS scientists began a research program to investigate synthetic diamond applications that would address these issues. Greatly improved thermal management properties were demonstrated using the available plasma-grown polycrystalline diamond material in standard integrated circuit packages [2]. A custom-designed, five watt, silicon thermal test chip highlighted these properties. PGA and dual-in-line packages were modified to use diamond inserts and heat sinks to replace standard ceramic and metal heat sink packages. When diamond is used as a heat spreading insert in integrated circuit packages, it can reduce the thermal gradient to ambient by up to 50% compared to standard ceramic packages. If it is used to transfer heat directly to the ambient environment from the IC, junction temperature gradient reductions greater than 50% are obtainable. These temperature reductions translate directly into improved reliability. Examples of these packages are shown in **Fig. 2**. A second and larger (1 cm^2) test chip (ARSON) is capable of dissipating over 100 watts. **Fig. 3** shows the junction temperature (as measured directly by sensor diodes on the chip) for one of these ARSON test chips in a modified diamond PGA package vs. the power dissipated in the chip. This chip used a solder die attach that we subsequently discovered had a void greater than 50% of the available bond area under the chip. Even with such a devastating failure in die attach, the PGA package with the diamond heat sink maintained a 0.5 degree centigrade per watt thermal resistance. The other curves show data for a delidded package immersed in still fluorinert liquid for pool boiling tests and one where a fluorinert was sprayed as an aerosol directly onto the surface of the powered chip.

3. Hybrids and Multi Chip Modules

Multi Chip Modules are fast becoming a commercial product. Improving their thermal characteristics for high performance circuits is an important reliability issue. Power density has a significant impact on MCM designs. Analytical solutions and finite element analysis modeling indicated that diamond plates substituted for ceramic, metal laminate, and other material substrates in MCMs would significantly improve the thermal performance. For example, it can be shown that in a 7x7 array of identical 1 cm^2 silicon chips, each powered at 40 watts, the temperature rise on the central chip in the

DIAMOND HEAT SINK PGA/ARSON PACKAGE

PF5060 Saturated Fluid
Tsat = 56 deg. C

Direct Spray on Chip

Sprayed Diamond Heat Sink

Pool Boiling

Fig. 3. Plot of chip power vs. junction temperature for a thermal test chip packaged in a diamond PGA. The lower curve represents pool boiling of a delidded PGA in liquid fluorinert. The middle curve plots direct spray cooling of the chip surface. The upper curve is for spray cooling through the diamond with over a 50% void in the solder die attach .

array will be less than 40 degrees centigrade when a 1 mm thick diamond substrate (K=16 w/cm C) is used to conductively extract the heat through only two of the four edges of a 10 centimeter-square substrate [3]. This is a dramatic improvement over what can be done with standard surface cooling techniques.

Designing and testing hybrid circuits was the first step toward achieving these diamond MCM goals. However, metallization that would stick reliably to diamond was another matter. Instead of following the lead of many other researchers who were using a thin film masked Ti-Pt-Au or

Cr-Au based system for fine line lithography [4], a rapid turn-around thick film gold direct write process was used. Without mask steps, it could act as a very quick prototyping development system. The Ohmcraft Micropen Direct Write Machine, Model 400, thick film system was used to directly write gold and dielectric patterns on diamond. After contacting various manufacturers of gold and dielectric inks, a series of tests was conducted to determine the best material to use to write on diamond.

Dupont thick film gold conductive ink type 5725 and Heraeus thick film dielectric ink type IP9118 gave the best test results. These inks match the coefficient of thermal expansion of diamond over the firing temperature range used to cure both the gold and insulating dielectric. Diamond squares 1 cm^2 x 1 mm thick were used as the test substrates. Their "as received" surface roughness (R_a) was 0.5 micron with a surface flatness of 2.5 microns per centimeter. Without any pretreatment of the diamond surface, gold or dielectric adhesion was judged fair to poor with all test inks. Failures were mainly related to gold peeling, and cracking of the ceramic dielectric. The fired gold was often accompanied by gold

Fig. 4. Direct write thick film gold MCMs on ceramic (rectangle) and diamond (4" diameter, 1 mm thick) are shown in visible and IR in 24 C still air at 10 watts. The diamond is isothermal @ 54 C while the ceramic shows hot chips @ 87 C.

"blistering." A ten minute prefiring of the bare diamond surface in ambient air at 850 degrees centigrade yielded a surface that quickly bonded to both the gold metallization and the dielectric coating. Minimal or no gold blistering was observed when a prefired sample was prepared. Tape pull tests, wire bond pull tests, and abrasive grinding proved that there was both a mechanical and an apparent chemical bonding to the diamond. Only a bath of aqua regia or hydrofluoric acid could remove the gold or ceramic dielectric patterns. scanning electron microscope analysis showed that while the first few microns of the original surface were ablated, the polycrystalline grains oxidized along stacking or twinning faults to create a filigree surface that was an ideal surface for adhesion. The intercrystalline boundaries appeared to be filled with a Diamond-Like-Carbon (DLC) material that was more volatile than the diamond crystals. The un-hydrogenated dangling bonds in the DLC are suspected to be the source of the chemical bonding to the matrix components in the thick film gold ink and ceramic dielectric. Large diamond substrates have been repeatedly cycled through this patterning, firing, testing, and pattern removal by acid processes up to seventeen times without apparent degradation to the diamond substrate or to metal and dielectric adhesion.

Once a stable and reproducible direct write gold and dielectric process was developed, nine ARSON chips were assembled into a 900 watt MCM on a 10.16 cm diameter by 1 mm thick diamond substrate. A similar ceramic substrate pattern was also produced for comparison in a series of edge cooling experiments. The ARSON die were attached to the diamond with an unfilled preform thermoplastic. Both *in situ* thermocouples, and on-chip temperature sensor diodes, along with an IR false color imaging analysis thermometer were used to evaluate the design. The MCM was powered to 10 watts on each chip before the ceramic version had to be
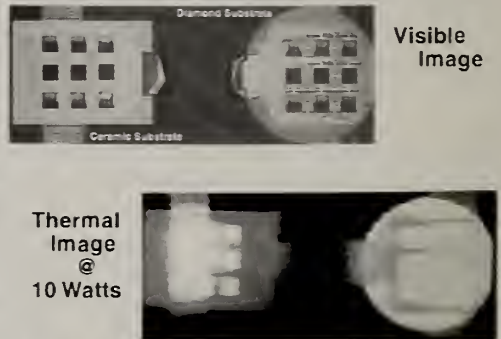
shut down due to overheating in our wind tunnel tests. **Fig. 4** shows an optical photograph of the two MCMs along with a false color IR image of the two devices powered at 10 watts in a still air ambient of 24 C. The diamond MCM is isothermal at 54 C as compared to the ceramic at 87 C and clearly shows the hot spots at the nine chips and the nearby surrounding ceramic substrate.

4. Embedded Resistors and Sensors

All of the substrates used in this work have been cut from larger wafers of polycrystalline diamond with lasers of varying wavelength and power. One constant artifact of this cutting process is the generation of the graphitic phase, sp_2, from the diamond phase, sp_3 , as a residue. This can be readily removed by chemical or oxidizing techniques. However, in our early work in 1989, we observed the negative coefficient of resistance behavior (thermistor) of this graphitic residue embedded in the diamond. Measurements were made of the resistivity and resistance of various laser etched patterns. Initially, a high temperature metal alloy braze was used to form an ohmic contact to the graphitized embedded conductor within the insulating polycrystalline diamond substrate. **Fig. 5** is a plot of one of the very first laser cut samples produced by this method. The sample is 25 mm long by 7 mm wide by 2.5 mm thick diamond. The two long side edges of the rectangle form the parallel resistors. The top and bottom surfaces are polished and insulating. The two ends of the sample are brazed and soldered leads are attached for a four terminal resistance measurement It was repeatedly measured and later calibrated from liquid helium temperatures to well over 700
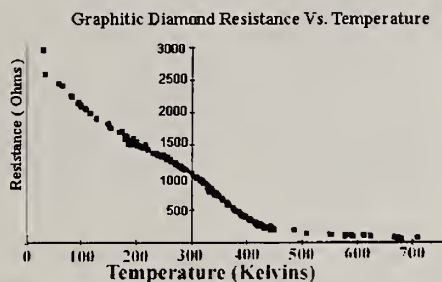
Fig. 5. Embedded graphitic resistor-sensor in diamond substrate shows thermistor behavior from 4.2 Kelvins to over 700 Kelvins.

Kelvins. The two distinct linear regions behave as a thermistor. The "device" was subsequently used as a sensitive thermometer near liquid nitrogen temperatures. It has been stable and repeatable while exposed to ambient and the low temperature environments over the past six years. Recent work has expanded on this effect and we are conducting research, in collaboration with the Naval Research Laboratory, on power resistors and thermistor temperature sensors embedded in the diamond substrate of MCMs. Both use the direct write metal and dielectric capability developed for hybrids and MCMs.

5. A 3-D Diamond Cube Computer

One result of making a silicon chip run faster is that it consumes more power. Increasing the system performance by reducing the latency between chips requires placing the chips closer together, but that increases the power density. These facts affect the design of high performance computing engines in a fundamental way. Three-dimensional electronic interconnect is virtually nonexistent in supercomputers because heat has to be removed from one of the surfaces of the circuit. This *de facto* two-dimensional computer architecture has profound consequences because any signal between circuit boards must travel to the edge

connector, through the back plane, and then to the next board. This over-and-around path is a major source of propagation delay, or latency, in very fast machines. Even at the speed of light, a signal can only travel 30 cm in one nanosecond. In order to construct a computer with a cycle time of less than one nanosecond, the machine must fit inside a fifteen centimeter cube. Based on an analysis of heat extraction from MCMs [5], it was predicted that diamond could reliably handle the extraordinary amount of heat generated in such a cube. The excellent dielectric insulating properties of diamond would also enable the design to utilize laser drilled vertical electrical interconnect vias through the diamond substrate to the MCMs above and below each layer.

Once it was verified that diamond could reliably extract heat using only the edges of the board (and not through the surface area of the board), an architecture was envisioned of stacked vertically interconnected diamond MCMs. By employing diamond as a substrate material in MCMs, the surface area normally devoted to heat removal can now function as the vertical interconnect surface. Elastomeric contacts, miniature conducting springs, or exotic interconnect materials serve as the upper and lower vertical electrical contacts to the MCMs directly above and below. Stacking these vertically interconnected MCMs together like a deck of cards forms the cube shape. Utilizing the six sides of the cube, one could envision using two sides for heat removal, two sides for power input, and two sides for input and output connections. The author was one of those who briefed these ideas to the Materials Research Council which recommended that the Advanced Research Projects Agency (ARPA) begin a diamond cube computer proof-of-principle program. This was made possible by the rapid advances in materials technology and by the cost reductions that were possible through the use of synthetic polycrystalline diamond substrates. Such a concept is shown in **Fig. 6.**

Fig. 6. Vertically stacked 3-D interconnected Multi-Chip Modules form a cube shape as the basis of an advanced supercomputer architecture made possible by the superb thermal conductivity of synthetic diamond. Subnanosecond cycle time supercomputers could be made possible using such a design.

Without diamond, a practical computer like this could not be constructed because of the heat build-up in the silicon chips. The design calls for a 1 mm thick, 10 cm x 10 cm, diamond substrates that have laser-drilled via holes connecting the different boards. The amazing thermal conductivity of diamond allows one to remove 20,000 watts of heat with a temperature rise of only 50 degrees centigrade. This is accomplished by extracting the heat from only two edges of each substrate. These edges act as protruding interdigitated fins into the cooling system. The maximum signal path is the diagonal of the cube which is about 15 cm. This constrains the cycle time to approximately 1.0 nanosecond, which is far above the state of the art in supercomputers today. One manifestation of this concept is shown in the functional proof-of-principle ARPA machine in **Fig.7** for which the author is a technical consultant.

6. Heat Extraction

In the thermal management of microelectronics there are two critical heat paths that must be addressed. The first path is from the logic gate which produces the heat to the boundary of its mounting. This path must rely on thermal conduction and diamond is a new technical solution in this thermal path. This heat must be finally deposited into the environment. Fans and moving fluids have typically been used to convectively remove heat to the environment. However, the interface between the conductive heat mode and the convective heat mode becomes a problem for high heat transfer rates. This barrier represents a high thermal impedance that must be overcome if interior temperatures are to remain low.

One way around this problem is to use a change of phase (i.e., boiling) of the working fluid to help convect away the heat. This works satisfactorily for heat transfer up to 50 watts/cm^2. At or above that rate vapor bubbles begin to cover most of the surface and a vapor "barrier" prevents efficient heat transfer resulting in thermal runaway. Various liquid cooling methods for higher rates have been tried unsuccessfully by others, e.g., jet impingement at IBM, and found to be either unreliable or too complex to incorporate into a commercial system. All of these techniques still require access to the surface area of the integrated circuit package. Recently, however, a new method has led to a breakthrough in this vapor limit. This innovative approach is spray cooling, pioneered and developed by Isothermal Systems Research, Inc.
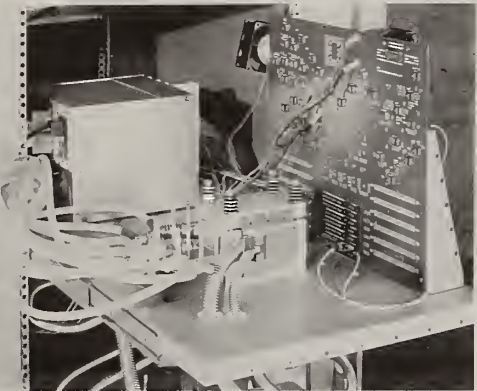
Fig.7. Illustrated is a functioning model of the diamond cube proof-of-principle computer. 1500 Watts of power are supplied by the cables to the left. Spray coolant is supplied to the two sides of the cube via the hoses through the base plate. The large PC board is a lab controller interface. The MCM stack is compressed by the 4 spring assemblies on top of the 4 inch block.

Micro-machined spray heads atomize the liquid into uniform droplets and deliver them as a mass balance to the vapor leaving from the thin liquid film wetting the hot surface. The principle is illustrated in **Fig. 8**. This conformal cooling method does not suffer from the difficulties that have plagued other methods. It is simple, cheap, and reliable to implement in almost any system. This non-cryogenic, hermetically sealed approach to system cooling operates at or near room temperature with only a few ounces of liquid.

The non-ozone-depleting liquid fluorinert is a type that is commonly used in the semiconductor manufacturing industry. It has a well established track record and is

Spray Head Cooling
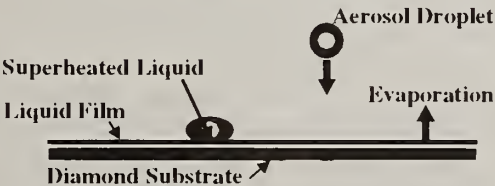
Fig. 8. Aerosol droplet replenishment of the evaporating thin liquid film uses a phase change to remove heat from the diamond substrate.

perfectly compatible with direct contact to the surface of the integrated circuit. When used in this variation, the spray cooled method can totally eliminate the thermal impedance of the package because the chip is cooled directly by the aerosol spray inside the package.

The spray head-to-surface distance, fluid pressure, and flow rate are adjusted to optimize heat extraction. Not only has this method demonstrated a heat removal capacity of more than a 100 watts/cm^2 of aerosol-exposed surface area, but it is one of the most efficient methods possible. The energy cooling cost is only one watt from a wall plug for every 25 watts of heat deposited to the environment. Advanced systems have shown that heat extraction rates up to 250 watts/cm^2 are possible.

7. Conclusions

As an enabling technology, diamond has significantly changed high performance electronics packaging. A low cost direct write thick film gold process has been demonstrated. High power circuits have operated reliably due to this technology and a new 3-D architecture is now available to supercomputer designers. *In situ* graphitic sensors and resistors thermally embedded in diamond offer a new thermal control element over large temperature ranges in harsh environments. The significant manufacturing progress made by the synthetic diamond industry has made this material a commercial reality. This will have an increasing influence on the semiconductor packaging industry, and the computer industry in particular, as more applications reach the cost-to-performance ratio set by the market.

8. Acknowledgments

9. References:

[1] Lanhua Wei, et al., **Thermal Conductivity of Isotopically Modified Single Crystal Diamond,** *Physical Review Letters*, Volume 70, Number 24, pp. 3764-3767, 14 June 1993.

[2] Boudreaux, P. J., et al., **Thermal Benefits of Diamond Inserts and Diamond-Coated Substrates to IC Packages,** *1991 Digest of Papers of the Government Microcircuit Applications Conference,* Volume 27, pp. 251-256, Orlando, FL, November 5-7, 1991, DTIC number GOMAC-91-B160081.

[3] Eden, R. C., **Application of Bulk Synthetic Diamond for High Heat Flux Thermal Management,** *Proceedings of the SPIE Conference on High Heat Flux Engineering II,* Volume 1997, pp.124-135, July 1993, San Diego, CA.

[4] Iacovangelo, C., et al., **Metallizing CVD Diamond For Electronic Applications,** *The International Journal of Microcircuits and Electronic Packaging,* Volume 17, Number 3, Third Quarter 1994, pp.252-258, ISSN 1063-1674.

[5] Leyendecker, A. J., **Thermal Effects in Diamond Substrates,** *Internal Technical Report,* TR-R54-001-91, January 25, 1991.

Recent Advances in Diamond Based Multichip Modules (MCMs)

A.P. Malshe, H.A. Naseem, W.D. Brown, and L.W. Schaper
High Density Electronics Center (HiDEC), University of Arkansas, Fayetteville, AR

Key words : diamond, MCM, processing, thermal, packaging, MCM

Abstract :

Not only due to the unique combination of excellent thermal, electrical, and mechanical properties, but also because of the falling prices, diamond is becoming the material of choice for multichip module (MCM) thermal management. Various economic diamond synthesis and post-synthesis processes are needed to be developed, made perfect and scaled up for the market realization of reliable and affordable diamond MCMs. Major efforts in the past few years have led to the newer technologies and resulted into the fabrication of diamond based prototype 2-D and 3-D MCMs. This paper discusses these recent developments useful not only for MCM but also for other thermal management applications.

1.　　Introduction :

Diamond exhibits an excellent thermal conductivity (k=700-1600 W/m.k for CVD diamond), a low thermal expansion coefficient ($\approx 10^{-6}$), high electrical resistivity (10^{12} ohm.cm), a low dielectric constant (5.5), and high mechanical strength (Young's Modulus $\approx 10^{11}$ Nm^{-2}). These properties of diamond surpass those of all the established substrate materials such as copper, silicon, alumina, aluminum nitride etc. [1, 2]. These properties make it an ideal choice for the heat spreading (thermal management, TM) application for MCMs, laser diodes, single chip packages, GaAs high power amplifiers and numerous such applications. In fact, the thermal conductance of diamond has been recognized since the 1960s and hence single crystal diamond has been used for TM in high power diode applications. However, the cost, availability, and size was prohibitive for its wide application. Due to the recent major developments in the chemical vapor deposition (CVD) of diamond, these substrates are appearing in the market in practically usable sizes at *much* affordable prices [3]. Thus, the combination of unique properties with the affordability makes it a plausible TM substrate for small as well as *relatively* large area electronic packaging applications.

2.　　Diamond for Multichip Module (MCM) Application :

Much of the real estate on a typical electronic system is occupied by interconnecting

electrical lines. The electronic "chips" themselves are so small that a further reduction in chip size would not appreciably reduce the size or weight of the electronic package, nor would it result in improved speed of operation. One solution to this problem is the MCM. In an MCM the interconnection between chips takes place on different layers. Connections between chips can be made on the first floor, second floor, etc. In this approach a reduction in size and an enhancement in speed is accomplished by building vertically with a multi-layered structure. For the MCM concept or any high density electronic packaging concept such as 2-D and 3-D MCMs (Figure 1) to be successful thermal management becomes an essential requirement [4,5]. High density means the correspondingly high power dissipation. As chips are packed closely together the power density levels become very high. Since diamond has a very high thermal conductivity, and is now available at lower cost, it is now plausible to consider free standing diamond substrate material for building MCMs.

3. Thermal considerations and related cost issues for diamond for MCMs :

Diamond has the highest thermal conductivity in the temperature range of typical MCM operation (25-100 °C), and has a lower heat capacity. Thus, it is a good heat spreader and not a heat sink (diamond heat sink is a misnomer). Therefore, for applying diamond in the best configuration it can be placed between a heat source such as a "chip" and a heat sink such as an air cooled surface. Maximum performance benefits of the diamond heat spreaders are obtained when the lowest junction operating temperature of the device generating heat is achieved for a given configuration. Minimum cost is achieved by making the diamond substrate as small as possible, since the cost of CVD diamond directly depends on its volume.

The desired thermal conductivity of diamond is ultimately guided by the power dissipation of the chips on an MCM. As the growth rate (which ultimately decides the cost) of diamond decides its thermal conductivity (through its chemical quality), it also becomes important to find out what is the steady-state or transient power dissipation of the chips such as IC or diode laser. For example, recently it has been shown by ANSYS finite element analysis that for uniform steady-state 10 W/cm^2 power dissipation on 100 cm^2 area of diamond with thermal conductivity of 1500 W/m.K in the edge cooled geometry, the maximum desired thickness of free-standing diamond is only 700 um for the efficient TM (Figure 2) [1].

In another case, when a CVD diamond-coated substrate is used as a heat spreader, the coating is only effective when the heat source radius is similar to the diamond thickness [5]. However, in these situations, the layer of the solder used for die attach to the diamond coating can represent a major thermal impedance, reducing diamond's effectiveness. Typically in a module, the complexity of TM can be addressed either by simplifying MCM power distribution architecture or using various heat sink schemes such as air edge cooling [4], liquid cooling [6] or thermoelectric cooling in combination with diamond heat spreaders.

4.   Diamond synthesis and post-processing for MCM application :

Major developments in the last few decades in chemical vapor deposition (CVD) of diamond phase has resulted into the upgradation of many existing technologies and the realization of many newer ones [7]. Diamond has the unique combination of properties and thus, can be used for umpteen number of applications ranging from tools to optical. Depending upon the product one or more post-synthesis processing steps are essential for the true realization of the product. Due to either one or multiple number of problems in the state-of-the-art CVD diamond such as smaller area, rough surface, "microcavities" in the material, impurities, polycrystalline nature, and the cost, only two large volume products namely CVD diamond tools and CVD diamond thermal spreaders are on their way to the market. Unlike tooling, for heat spreading, particularly for the MCM TM application, thermal quality of the CVD diamond, cutting, polishing, planarization, drilling for vias, via filling using a metal, large area and patterned metallization, die attach, assembly and reliability tests are the essential steps for the product development. Thus, the cost of each step is the prime factor in the market success of such diamond MCM. Following is a brief account of these needs highlighting the cause for the need, the state-of-the-art techniques, typical results, and further demands.

4.a   Diamond synthesis :-

Typically, diamond phase in a CVD reaction is synthesized at higher temperature such as 700-900 °C using a carbon source gas such as methane and a graphite etchant source gas such as hydrogen in the presence of one or more forms of activation agencies such as DC arc, hot filament radiation, and microwaves [8]. The same are the leading deposition activation agencies used in the industries for the production. Further, typically for TM applications, CVD diamond with thermal conductivity more than 1000 W/m.k is essential. Thermal conductivity of diamond is basically controlled by its chemical purity (graphitic nature), its crystallographic orientation, average grain size and microstructure. These can be tailored by the right combination of gas chemistry and substrate temperature. Cost of diamond thermal spreaders drives the market and the synthesis cost is a major share of the product cost. Thus, to reduce the cost one has to increase the power input per unit area for diamond deposition, and/or increase the area of deposition and/or sacrify thermal quality of diamond to a certain extent. Presently, in the market randomly oriented diamond films are available typically with a thermal conductivity equal to or better than 1200 W/m.k for TM application. As a note of caution, presently there is not a *standard* technique for thermal conductivity measurement [9].

4.b   Diamond cutting and drilling :-

The diamond substrates produced using the state-of-the-art CVD techniques have a collar at the outer boundaries which leads to the first need to cut these substrate into a well defined and collarless plane substrate. Further, the need for cutting is raised by the need to have these substrates in the desired shapes guided by the basic design of the MCM and its TM scheme. For the new person in the field, cutting of single crystal gem diamond and

polycrystalline CVD diamond are different in many respects. Hardness of diamond along with its polycrystalline nature offer serious problems in the well defined cutting of diamond substrates using conventional ways. The problem might get complex if one desires to cut thick diamond film deposited on another substrate with different thermal properties. In fact, though diamond cutting is new to CVD diamond industry, it has been developed a few decades before for cutting single crystal diamond slabs (and not gems). Typically, CVD diamond is cut using a pulsed Nd-YAG laser. The wavelength, power and repetition rate of the laser, and the chemical quality of diamond critically decide the definition of the cut, cutting-induced bur / contamination, melting of the material and micro-cracking of the material. Figure 3 shows the SEM micrographs of a good quality laser cut. Also, for some of the applications definition of a cut corner can be well defined by the right choice of the laser wavelength. Laser cutting speed can be enhanced by having right photo-chemistry at the workpiece and introducing the desired gas jet(s).

Though not necessary, drilling of diamond for fabrication of via holes may be important in the fabrication of diamond MCMs, particularly in 3-D MCM application. Via holes are filled with metal for defining metal interconnects through the diamond plane. These vias are typically about 100-150 um in the diameter. Depending upon the size and the design of an MCM the number of the desired vias can vary from few hundreds to few thousands on one diamond MCM plane. The quality of a via-drill is decided by its edge angle, wall contamination, and definition of top surface - hole wall junction. Once again, extreme hardness and chemical inertness of diamond cause serious problems in drilling such fine via holes using conventional techniques. Though drilling of diamond is not new, hardly any published information is available due to the secretive nature of the field. In fact, previously fine diamond drilling has been performed using a laser to clean up the graphitic residues in the natural diamond and thus, to increase its market value. Presently, via drilling for MCM application is being done using a pulsed Nd-YAG laser at 1.06 um. Though not exactly, most of the above discussed parameters and relationships between laser-diamond interaction for cutting hold true for diamond drilling. Recently, successful via drilling has been achieved using laser core-drilling from two sides of the substrate to provide clean, and circular holes [10]. In an another recent attempt, fine laser drilling of diamond has been demonstrated by laser treatment of diamond in a reactive liquid medium [11]. It has been shown that the liquid chemistry plays major role in the machining.

4.c   Diamond polishing and planarization :-

In the-state-of-the-art CVD diamond synthesis, diamond growth in the initial stages of deposition progresses by nucleation either at randomly-seeded sites or at thermally-favored sites. Depending on the growth temperature and pressure conditions favored crystal orientations dominate the competitive growth process. As a result, the grown films have a random polycrystalline structure and a rough surface morphology. Films are also wavy due to nonuniform grain size distribution and stress in the material. Large surface roughness (R_a=2-10 um) and waviness often limit the TM efficiency of diamond substrates because of the large and numerous surface pits. Chemical inertness, hardness, polycrystalline nature, and non-uniform surface chemistry of CVD diamond cause

tremendous problems in applying the established mechanical polishing technique for CVD diamond. To address this problem, various forms of activation agencies such as modified version of mechanical lapping, plasma, hot metal, chemical-assisted mechanical, ion beam and laser beam have been tried and are being developed for economic and contamination-free polishing of diamond films. Polishing process can be further divided into coarse lapping and fine polishing. Typically, lapping is relatively faster and economic. However, polishing is extremely slow, tedious, and is very expensive. Techniques such as mechanical lapping, and laser trimming are advisable for coarse lapping and chemical-assisted mechanical, and ion beam are advisable for fine polishing. Though shown vary promising through publications, in practice hot metal polishing is not advisable due to the rigidity, extremely contaminating and non-uniform polishing nature. Recently, chemical-assisted mechanical polishing and planarization (CAMPP) is shown to be the promising technique for the fine polishing of diamond substrates (Figure 4) [12]. Comparison of the most of these techniques can be found in a recent publication [13]. However, it is very important to note that in a recent investigation it has been shown that due to the "microcavities"-open structures in the CVD diamond films most of them can not be polished *completely* and thus, can not be used for MCM TM application (Figure 5, inset) [14]. In a similar study it has also been shown that only 50% of the diamond surface area needs to be exposed for efficient TM and that "planarization by filling" process can be used to achieve extremely planarized and smooth surface with roughnesses in the range of 20-30 nm measured by AFM on 80x80 um^2 area (figure 5) [15]. This process is very inexpensive and compatible with MCM or any thermal spreader fabrication processing. It contributes in reducing the cost of CVD diamond finishing by about 70%.

4.d   Metallization :-

Diamond MCM requires complex metallization schemes for defining ground and power planes, and X & Y signal lines. Metallization for MCMs can be divided into large area metallization, selective metallization and metal filling of vias [10, 16]. Primarily, gold (Au) or copper (Cu) metals due to their low resistivity are considered for the application. Depending upon the MCM functions the desired metal thickness can range between a few microns to a few tens of microns and desired line width can be few tens of microns. In such situation, plating over thermal evaporation or sputtering is the most simple, economic and production friendly process. In metallization, adhesion of metal to diamond is one of the prime factors in deciding its quality for MCM application. Typically, for improving the adhesion of Au or Cu metallization various adhesion promoter carbide layer forming elements have been used in the metallization [16]. It is important to note that, microcavities described in the above section cause serious blistering problems in such metallization schemes [14] and the "planarization by filling" can efficiently solve such blistering problem [15].

Metal filling of the vias is important for multi-level communication in a 3-D MCM architecture. Typically, for diamond where graphitization temperature is between 700-800 °C, low temperature via filling processes such as metal filled epoxy or plating can be used. Recently in an another approach, via filling has been done with tungsten (W), followed

by sintering and then infusing the W matrix with copper (Cu) [10]. The best mode of filling is decided by the desired function of the vias.

After all the above mentioned processing steps, active "chips" are bonded to the diamond surface by soldering and the chips are further electrically connected to the ground / power / signal layers by wire bonding.

5.   Summary and future directions :

Aggressive efforts in the past few years have resulted in a remarkable success in demonstrating the feasibility of CVD diamond for 2-D and 3-D MCM applications. For making the diamond package production relatively easy and cost effective *intelligent* ways of process control and manufacturing have to be followed. Immediate high volume market application of such diamond substrates for TM exists for single chip, and 2-D multichip module packages for applications ranging from telecommunication to avionics. As a good sign, presently the CVD diamond prices are falling rapidly. As a note to the user one should not only consider the cost of diamond but should consider module performance improvement to cost ratio as a true parameter for the evaluation of upgraded diamond based package. Further, newer 3-D MCM electronics packaging designs, and non-conventional ways for making the diamond substrates should be evaluated for the performance upgradation and cost reduction of existing diamond packages.

References :

1.   A.P. Malshe, S. Jamil, M.H. Gordon, H.A. Naseem, W.D. Brown, and L.W. Schaper, Advanced Packaging , appearing in September / October 1995 issue.
2.   R.J. Connery, C.L. Spiro, C.D. Iacovangelo and J.C. Grande, Proceedings of International Conference on Multichip Modules - ICEMCM '95, 152 (1995).
3.   IBIS-ASTeX data, obtained from Dr. Sevilano at ASTeX, Woburn, MA.
4.   R.C. Eden, SPIE High Heat Flux Engineering II 1997, 124 (1993).
5.   T.J. Moravec and A. Partha, Advanced Packaging, 8 (October 1993).
6.   D.W. Peterson, J.N. Sweet, D.R. Johnson, D.D. Andaleon and R.F. Renzi, The International Journal of Microcircuits and Electronic Packaging 17(4), 383(1994).
7.   Diamond Films and Coatings, R. F. Davis, Editor, p. 147, Noyes Publications, New Jersey (1993).
8.   J.E. Butler and R.L.W. Wooden, Phil. Trans. Roy. Soc. Lond. A 342, 209 (1993).
9.   A. Feldman, 5th Annual Diamond Technology Workshop, Troy, MI, May 18-20, 1994.

10.   W.E. Wesolowski, R.J. DeKenipp, M.P.R. Panicker, Proceedings of International Conference on Multichip Modules - ICEMCM '95, 146 (1995).

11.   S. Jamil, M.H. Gordon, G.J. Salamo, H.A. Naseem, W.D. Brown and A.P. Malshe, appearing in the Proc. of Applied Diamond Conference 1995, Gaithersburg, MD, August 1995.

12.   A.P. Malshe, W.D. Brown, and H.A. Naseem (Unpublished work).

13.   D.G. Bhat, D.G. Johnson, A.P. Malshe, H.A. Naseem, W.D. Brown, L.W. Schaper, C.-H. Shen, Diamond and Related Materials (appearing 1995).

14.   A.P. Malshe, J.H. Glezen, H.A. Naseem and W.D. Brown, appearing in the Proceedings of Electrochemical Society Meetings, Reno, Nevada, May 1995.

15.   A.P. Malshe, J.H. Glezen, H.A. Naseem, W.D. Brown, and L.W. Schaper, Proceedings of International Conference on Multichip Modules - ICEMCM '95, 140 (1995).

16.   W.D. Brown, H.A. Naseem, A.P. Malshe, J.H. Glezen, W.D. Hinshaw, Proceedings of the Spring MRS Conference, San Francisco, CA, April 1995.

Comparison of 2-D and 3-D MCM Signal Interconnect Lengths

Fig. 1

2-D MCM Nearest Neighbor Chips (8)   3-D MCM Chips In Same Distance (116)

Fig. 2

Fig. 3

Unpolished

CAMPP   Fig. 4   ⊢—⊣ 100 μm

"PLANARIZATION *by* FILLING"

X 270

▢⋯ - Partially polished CVD-diamond film

▣ - Filler in CVD-diamond film

Fig. 5

Applications of Diamond Films and Related Materials: Third International Conference, 1995
Editors: A. Feldman, Y. Tzeng, W. A. Yarbrough, M. Yoshikawa, and M. Murakawa

619
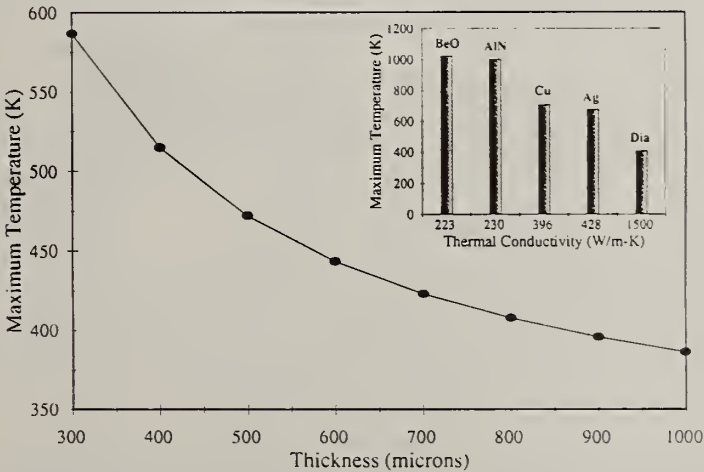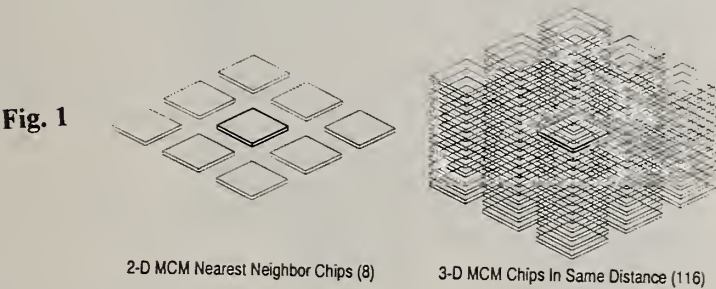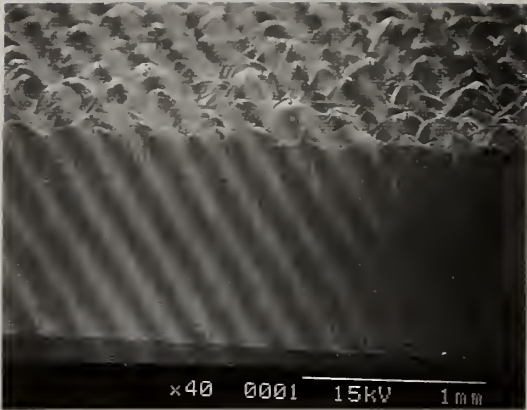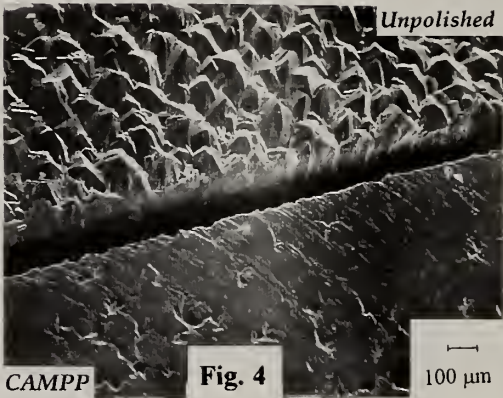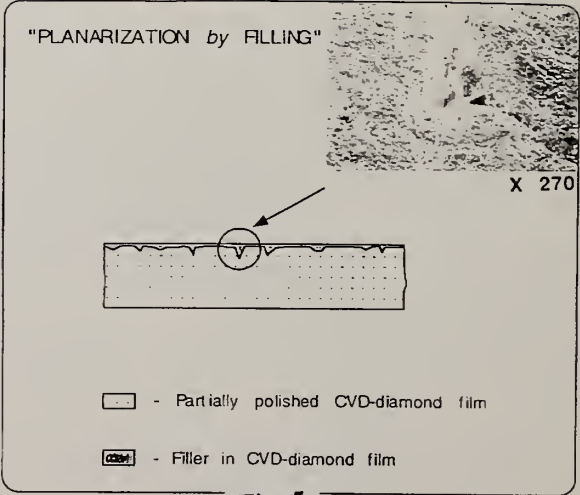
THIN FILM CIRCUIT FABRICATION ON DIAMOND SUBSTRATES FOR HIGH POWER APPLICATIONS

David Norwood[1], Walter Worobey[1], David Peterson[1], Jim Sweet[1], Donald Johnson[1], Doyle Miller[1], David Andaleon[2]

[1] Sandia National Labs, P.O. Box 5800, MS0957, Albuquerque, NM, 87185
[2] Sandia National Labs, P.O. Box 969, MS9103, Livermore, CA, 94551

Key Words: Diamond, Hybrid, Substrates, MCM, Laser, Thin Film, Thermal.

Abstract

Sandia Laboratories has developed a thin film diamond substrate technology to meet the requirements for high power and high density circuits. Processes were developed to metallize, photopattern, laser process, and, package diamond thin film networks which were later assembled into high power multichip modules (MCMs) to test for effectiveness at removing heat. Diamond clearly demonstrated improvement in heat transfer during 20 Watt, strip heating experiments with junction-to-ambient temperature increases of less than 24°C compared to 126°C and 265°C for the aluminum nitride and ceramic versions, respectively.

1. Thin Film Processing on Diamond Substrates

Evaluations were conducted on free standing, polycrystalline, diamond substrates to determine material properties which would influence thin film processes. Physical characteristics such as roughness, camber, thickness, size, etc. will effect both the processes used to define thin film patterns and the circuit elements after completion.

TABLE I. Surface characteristics of diamond vs. alumina substrates.

Substrate Type	R_a Frontside	R_a Backside	Camber
As-Deposited Dia.	4301 Å	> 25 µm	0.320 µm/mm
Polished Diamond	137 Å	1055 Å	0.320 µm/mm
Alumina (As-Fired)	1120 Å	1690 Å	1.800 µm/mm

Bulk characteristics of diamond are well known as a substrate material, but the primary property of high thermal conductivity (~ 1200 W/m·K) is the reason for its
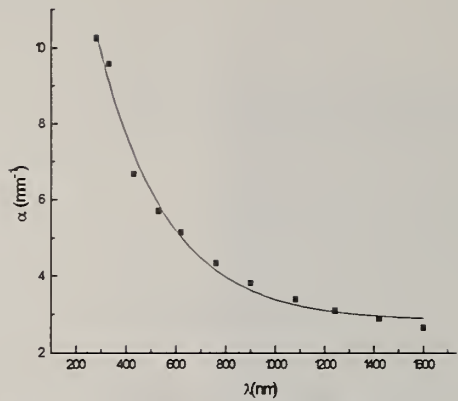
Fig. 1. Absorption Coefficient of
Diamond to Nd:YAG Laser Beam.
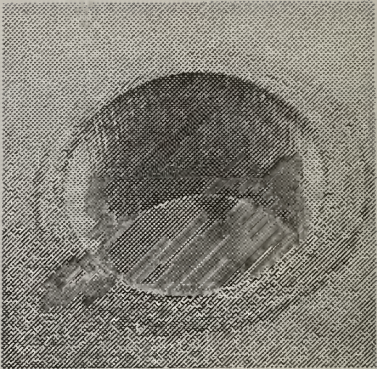
Fig. 2. Hole Drilled (1.5 mm) in
Diamond Using Nd:YAG Laser.

increasing popularity for MCM applications. Past hybrid and MCM work at SNL was accomplished on as-fired alumina substrates with thermal conductivity of ~35.6 W/m·K. Profilometer measurements were made to compare surface smoothness and camber of diamond and alumina substrates. Measurements are shown in Table I.

Thin film processing consists of cleaning, vacuum metallizing, resist processing, etching, and stripping operations. Several tests were conducted to determine whether diamond would withstand these chemicals and operations. Results were positive as diamond remained stable when subjected to TFN etchants. Plasma cleaning and air firing of diamond substrates were the first processes where diamond showed any susceptibility to thin film operations. Oxygen plasma cleaning of diamond for one hour showed a small weight reduction (-0.018%). Air firing diamond at 600°C also produced a small weight reduction. However, air firing at 800°C for 60 minutes destroyed the diamond. Diamond weight was reduced by 69.2% and it was verified that diamond will burn up in the presence of oxygen (air) at temperatures over 600°C.

2. Laser Processing of Diamond

Laser machining and resistor trimming on diamond substrates is essential for many hybrid circuit applications. Work was done to determine if laser processing is feasible on diamond and whether it can be accomplished using a Nd:YAG laser. Research into laser beam absorption [1] showed that diamond has a greater absorption coefficient (α) at shorter wavelengths (Fig. 1). When thin film resistors on diamond substrates were laser trimmed, carbon residue created during trimming was shown to create a conductive path which shorted across the resistor trim region. This problem was resolved by defocusing the beam, reducing power, and precisely controlling the table feed of the laser using the fundamental laser wavelength of 1064 nM. Tantalum oxide was thus formed in the trim area and acted in the same manner as ablating the resistor material. Ta_2N resistors trimmed in this manner were found to be stable with time and temperature [1].

A shorter wavelength (532nm) was attempted for laser machining diamond since it absorbs energy more efficiently in this range. A frequency doubled Nd:YAG laser beam produced the shorter wavelength. Using this beam and a specially built optical trepan assembly, it was demonstrated that through-holes having excellent sidewall morphology were produced in diamond up to 0.25 inch thick (Fig. 2).

3. Thin Film Network Fabrication

Thin film networks (TFNs) were fabricated on diamond substrates by sputter deposition of the Ta_2N, Ti, and Pd metallizations followed by pattern plating of 4 μm gold conductors. Ta_2N resistors were then photoprocessed and temperature stabilized as the final operations. Gold wire and ribbon were used to test the bondability and metallization adhesion of the thin film network. One mil diameter gold wire and 1x3 mil gold ribbons were successfully loop bonded to the diamond circuit pads. Destructive pull testing of wire and ribbon loops showed metallization to be both bondable and adherent.

4. Circuit Assembly and Thermal Testing.

Thin film processes described above were used to fabricate TFNs for an edge-cooled, multichip module test circuit [2]. Test circuits were assembled using diamond, aluminum nitride, and alumina TFNs to make a comparison of the thermal efficiency between these substrate materials. Test circuit details are shown in Fig 3. The characteristics of the ATC03 die assembled on the test circuits and their use as heating elements in MCM thermal resistance studies have been discussed previously [3]. In the data presented here, a one dimensional (1D) model was used for thermal calculations on the three substrate types and these calculations were compared to experimental data. Thermal characteristics of the three substrate types were derived by heating the top row of ATC03 die at 5 Watts per die (20 Watts total) and measuring temperatures at the locations shown in Fig. 3. Thermal performance for the different substrates is shown in Fig. 4. The increase in junction
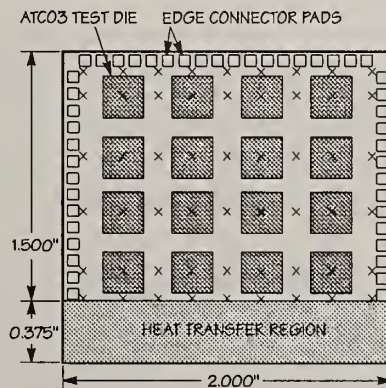
Fig. 3. Edge cooled thermal test circuit for substrate heating tests with fluoroptec temperature measurements taken at X marks.

temperature (ΔT) measured on the heated ATC03 die was 24.3°C for the diamond substrate as compared to 126°C for aluminum nitride and 265°C for alumina. Die junction temperature on the diamond test circuit was significantly lower due to the high thermal conductivity of the diamond substrate. Also, the surrounding substrate temperature remained cooler on the diamond substrate as shown in the thermal images of Fig. 4. A summary of thermal parameter calculations based on experimental measurements of the aluminum nitride and diamond test circuits is shown in Table II. These calculations show the thermal characteristics of diamond as being superior when selecting a TFN and MCM substrate material.
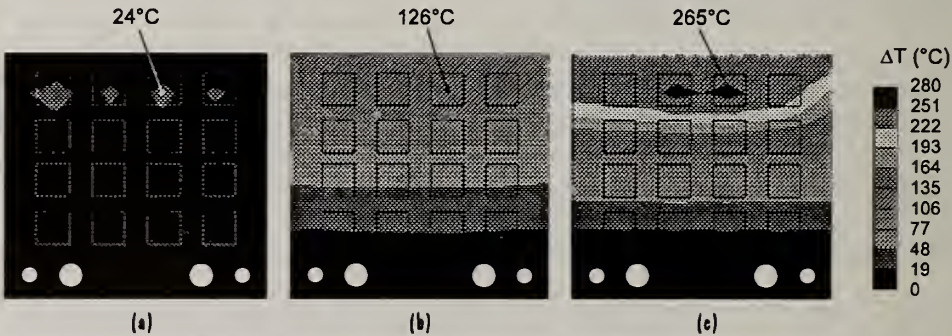
Fig.4. Comparison of thermal performance between (a) 0.0235 in. diamond, (b) 0.0201 in. AlN, and (c) 0.025 in. alumina substrates while heating top row of die with 20 W.

TABLE II. Calculated values of thermal resistance and conductivity of AlN and diamond substrates from measured data.

Substrate Type	Number of Heated Rows	Thermal Resistance (°C/W)	Thermal Conductivity (W/m·K)	Substrate Thickness (mils)
Al Nitride	1	5.79	248	20.1
Diamond	1	0.78	1620	23.5
Diamond	3	0.80	1593	23.5

1. David Norwood, Walter Worobey, David Peterson, and Doyle Miller, "Diamond - A New High Thermal Conductivity Substrate for Multichip Modules and Hybrid Circuits," *Proceedings of the 43rd Electronic Components & Technology Conference*, pp. 910-919, June (1993).

2. D. Peterson, J. Sweet, D. Andaleon, JR. Renzi, and D. Johnson, "Demonstration of a High Heat Removal CVD Diamond Substrate Edge-Cooled Multichip Module," *Int. J. Microcircuits & Electronics Packaging*, 17, 4, pp. 383, (1994).

3. J. N. Sweet, D. W. Peterson, D. Chu, B. L. Bainbridge, R. A. Gassman, C. A. Reber, "Analysis and Measurement of Thermal Resistance in a 3-Dimensional Silicon Multichip Module Populated with Assembly Test Chips," *Proceedings of 1993 Semiconductor Thermal Measurement and Management Symposium.*, pp. 1-7, Feb. (1993).

USING THERMOELECTRIC COOLERS AND DIAMOND FILMS FOR TEMPERATURE CONTROL OF POWER ELECTRONIC CIRCUITS

Jan W. Vandersande[1], Richard Ewell[1], Jean-Pierre Fleurial[1] and Hylan B. Lyon[2]

[1]Jet Propulsion Laboratory/California Institute of Technology, 4800 Oak Grove Drive, M/S 277-212, Pasadena, CA 91109
[2]Marlow Industries Inc., 10451 Vista Park Road, Dallas, TX 75238

Key words: diamond films, thermoelectric coolers, thermal management, power electronics

Abstract

Conventional packaging materials have difficulty dealing with thermal management problems due to high power densities. However, it is possible to combine both active and passive cooling by using thin film thermoelectric coolers and diamond substrates for the temperature control of these high density electronic circuits. The highest power components would be mounted directly onto thin film thermoelectric elements, which would maintain the temperature of these components from a few degrees to tens of degrees below that of the diamond substrate. This allows these components to operate within their required temperature range, effectively manage temperature spikes and junction temperatures, and increase clockspeed. To maximize the efficiency of the thermoelectric cooler, diamond films acting as thermal lenses would be used to spread the heat from the small power device to the larger coolers.

1. Introduction

The need for increased speeds of integrated circuits is accompanied by increased power levels and the need to package IC chips very close together. Combined, these spell very high power densities and severe thermal problems at the package level. Conventional packaging materials have difficulty dealing with these thermal management problems. However, it may be possible to use a combination of active and passive cooling techniques (thermoelectric coolers and very good thermal conductors such as diamond films) for the temperature control of these high density electronic circuits.

We have modeled the case of a typical power amplifier (PA), operating at temperatures substantially above ambient, used in spacecraft applications to determine the advantages and drawbacks of using either thermoelectric coolers or diamond films or both. The results are not surprising but suggest several possible applications for both diamond substrates and thermoelectric coolers.

2. Active and passive cooling above ambient temperature

A 5 watt solid state power amplifier (PA) was used, as a current relevant spacecraft application example, to determine the applicability of thermoelectric coolers and diamonds films relative to temperature control. The PA is 5.4 mm by 3 mm on a 0.10 mm thick gallium-arsenide substrate. The device operates in such a way that 8 watts of thermal power must be conducted away from the PA and that the peak allowable operating temperature of the PA is 110°C. The power producing portion of the PA only occupies about 5% of the total PA area. A simple 2 dimensional finite difference thermal model was used to determine the peak temperature of the PA assuming a uniform temperature on the back surface of the PA. The result was that the peak temperature of the power producing portion of the PA will be about 25°C above the back surface of the PA. The thermoelectric cooler could be used to counteract this temperature differential across the PA substrate.

It was decided to design a thermoelectric cooler which would compensate for only 10°C of the temperature differential across the PA, in order to achieve a high coefficient of performance (COP). This was done to determine the overall impact of the cooler on a system basis. The theoretical maximum COP which can be obtained with current state of the art material is about 3 to 4, depending upon the average temperature of operation [1]. Standard available thermoelectric coolers utilize bismuth telluride alloys for the active material. The smallest leg size for standard coolers is 0.64 x 0.64 mm^2 in cross section. If a cooler, with this size legs, is put over the entire back surface of the PA, only a total of 16 couples will fit. With this leg size, it is will be very difficult to get 8 watts of cooling. This could be obtained only with extremely short legs, 0.2 millimeters or less. It was assumed that each electrode and their associated contact has an electrical contact resistance of 2.5 $\mu\Omega$-cm^2. With this leg length, the electrode and contact resistances become a very significant portion of the total resistance and should be modeled more accurately. At this short leg length, it was estimated that the cooler would require nearly 18 watts of electric power in order to generate 8 watts of cooling power with a 10°C temperature differential. This corresponds to a coefficient of performance of only 0.44.

The major drawback with the microcoolers required for cooling of the PA is the low coefficient of performance. This very poor performance, about 9 times lower than the maximum theoretical COP, is due to the far from optimum values for the length and cross-section of the thermoelectric legs imposed by this design.

This results in two problems: 1) high electrical power requirements, and 2) poor overall cooling of the electronic device to be cooled. The high electrical power requirement, means that more power will be required for the cooler than for the device itself. The second problem is even more troublesome. Because of the low coefficient of performance, now the heat rejection of the PA has increased from 8 watts to 26 watts, as a result of the 18 watts of power needed for the cooler. Since currently there is an even larger temperature gradient going from the back side of the chip to its radiator than there

is across the substrate of the chip, this increase in heat rejection will actually increase the temperature of the PA.

For such an electronic device operating at a temperature above ambient, the solution is thus to improve the thermal conductivity of the board on which the high power components are mounted, rather than use a thermoelectric cooler. The use of high thermal conductivity electrically insulating diamond films will reduce the temperature differential along the board where the chips are mounted [2]. This is typically greater than the temperature differential across the substrate of any chip in the case of the conventional board materials such as alumina or Kovar. Typically, the center of a diamond substrate will not be more than a few degrees higher in temperature than the temperature of the housing. Hence in the case of a diamond board, the power producing part of the PA would now be at about 25°C above the temperature of the back surface of the external frame (compared to at least 20 to 30°C higher in the case of an aluminum board). Thus the use of diamond films (with the highest thermal conductivity known) will set the limit of passive cooling techniques for circuits. Currently, the price of diamond films is still too high for them to be generally used and all the metallization, bonding and contacting problems have not been solved yet. However, diamond films offer a tremendous improvement in passive temperature control of electronic circuits over that of the current materials used.

3. Thermoelectric cooler application

However, two situations where thermoelectric coolers operating at temperatures above ambient would serve a useful purpose were determined. The first of these is where a high power component operates under very transient conditions. If the device only requires high power levels for short periods of time, then a thermoelectric cooler could be useful. It would only be operated when the device needing cooling is operated. It would thus reduce the temperature spikes by more effectively using the heat capacity of the board on which the cooler is mounted.

The second situation where a thermoelectric cooler would be beneficial is if one of two components must be kept at a much lower temperature than all the rest of the electrical components. This could occur with the use of silicon carbide for the majority of components, while a couple of silicon or gallium arsenide components are still being used. Then a thermoelectric cooler could be used just for the low temperature components, allowing the board to run at the higher temperature of the other components.

A third and most interesting situation arises when a device is kept below the ambient board temperature so that substantial increases in performance, clock speed and reliability can be achieved. As an example, a diamond substrate would be at the ambient temperature of 20°C while the device would be operated at -20°C by using a thermoelectric cooler. There is of course a trade off between the measureable improvement in clockspeed and performance, the increase in mean time between failures, the temperature difference through which the heat needs to be pumped and the cost of the

cooling device. It is very likely that there are already electronic devices where operation below ambient would be beneficial and would make sense cost wise. In the near future, a larger number of devices are expected to operate at lower and lower temperatures because of the anticipated substantial increase in power output and the need to increase clockspeed even further.

Since the COP of a thermoelectric cooler increases nearly exponentially with decreasing temperature difference, it is critical that the cooler be as close to the power producing portion of the device as possible. This would mean attaching the thermoelectric cooler directly to the die. In addition, using a diamond film substrate as the heat sink would keep the temperature difference at a minimum by both conducting efficiently the heat and power added to the cooler away without hardly increasing the heat sink temperature. This combination of active and passive cooling allows a device to be kept below ambient with the smallest temperature difference. A diamond film can also be used between the device and the cooler in the case when the area of the device is too small to accommodate the cold side area of the thermoelectric cooler needed to pump the heat produced through the required temperature difference. The diamond film would thus act as a "thermal lens" by effectively spreading the heat over a larger area with only a very small temperature drop across the film. If diamond does not work out because of bonding problems, then another high thermal conductivity material could be used (such as c-BN or SiC).

4. Conclusion

Thermoelectric coolers are not generally useful for the temperature control of high density electronic circuits as our example clearly showed. Passive cooling with high thermal conductivity diamond films will be much more useful for the cooling of circuits above room temperature. However, there are three situations where active cooling with thermoelectric coolers would serve a useful purpose: a component only uses high power for very short periods of time, or a single component must operate at much lower temperatures than the rest of the components in the circuit, or when a device needs to be cooled well below ambient temperature to increase its clock speed

5. Acknowledgments

6. References

1. Goldsmid, H.J., *Electronic Refrigeration*, Pion Limited, London 1986.
2. Olson, J.R., Pohl, R.O., Vandersande, J.W., Zoltan, A., Anthony, T.R., and Banholzer, W.F., Phys. Rev. B., 47, 14850 (1993).

ROUND ROBIN THERMAL CONDUCTIVITY MEASUREMENTS ON CVD DIAMOND

Albert Feldman
National Institute of Standards and Technology
Ceramics Division
Gaithersburg, MD 20899

Key words: diamond, thermal conductivity, thermal diffusivity,

Abstract

A round robin was conducted in which the thermal conductivities of ten specimens of CVD diamond were measured. Four companies supplied the specimens and ten laboratories performed the measurements. The average values of all measurements on a specimen ranged from 420 $W \cdot m^{-1} \cdot K^{-1} \pm 32\%$ for the least conductive specimen to 1660 $W \cdot m^{-1} \cdot K^{-1} \pm 34\%$ for the most conductive specimen. The measured values showed large laboratory to laboratory variations in many instances. Significant specimen inhomogeneity was also found. One laboratory measured thermal conductivity anisotropy which was found to be significant. The large variations observed might be attributable to specimen inhomogeneity and to the manner in which the different techniques sampled the thermal conductivity distribution.

1. Introduction

NIST has brought together people from U.S. industry in a series of workshops for the purpose of discussing the need for standardizing the characterization of chemical vapor deposited (CVD) diamond for various applications [1]. After cutting tools, the largest most immediate use of CVD diamond is expected to be substrates for heat spreading applications. This is because the high thermal conductivity of diamond makes it the most efficient material for heat spreaders. To address this issue, a working group on standardization of thermal conductivity measurement directed toward CVD diamond was established [2]. It was agreed that standardizing the measurement of the thermal conductivity (κ) of CVD diamond was important; however, different laboratories used different methods of measurement. In the absence of a standardized measurement procedure, the group decided to conduct a thermal conductivity round-robin in which several laboratories agreed to perform measurements of κ on a given set of specimens.

2. Specimens

Ten specimens were provided by four companies, Diamonex, General Electric, Norton Diamond Film, and Raytheon. The nominal geometric specifications and nomenclature for the specimens are listed in Table I. Other nominal specifications were, thickness — 300 to 400 μm, thickness uniformity — 1% or less over 5 mm and surface roughness — 0.3 μm Ra or less. The thermal conductivities were targeted to have values of 700, 1000, or > 1300 $W \cdot m^{-1} \cdot K^{-1}$. All specimens having a given suffix were obtained from the same large specimen and, thus, would be expected to have a common thermal conductivity value barring any specimen inhomogeneity.

Table I. Nominal Specimen Dimensions and Nomenclature

Description	Specimen Designations	Nominal Dimensions
Large Disk	LD-X, LD-E	40 mm diameter
Long Bar	LB-X, LB-E, LB-T	4 mm $\times$ 50 mm
Square	SQ-X, SQ-E, SQ-T, SQ-F, SQ-FB	10 mm $\times$ 10 mm

3. Measurement Methods

Several methods of measurement were employed. Table II lists the laboratory participants and the methods employed. All of the methods except for the heated bar method measured the thermal diffusivity D rather than the thermal conductivity κ. Furthermore, most methods measured principally $D_\parallel$ (or $\kappa_\parallel$) which is D (or κ) in the plane of the specimen. The laser flash method was the only one to yield $D_\perp$. Since $D = \kappa/(\rho C)$, where ρ is density (3.515×10^3 $kg \cdot m^{-3}$)

Table II. Laboratory Participants and Measurement Methods Employed

Laboratory	Method and Parameter Measured
Wayne State University (P.K. Kuo)	photothermal beam deflection, $D_\parallel$
AT&T Bell Labs (J.E. Graebner)	heated bar, $\kappa_\parallel$
	laser flash, $D_\perp$.
General Electric (D. Slutz)	modified ÅNGSTROM'S method, $D_\parallel$
Daimler-Benz (O. Käding)	transient grating, $D_\parallel$
Sinku-Riko (R.P. Tye)	modified ÅNGSTROM'S method, $D_\parallel$
	2D laser flash, $D_\parallel$
Norton Diamond Film (G. Lu)	convergent heat pulse, $D_\parallel$
Laboratoire d'Instrumentation (K. Plamann and D. Fournier)	photothermal beam deflection, $D_\parallel$
University of Würtzburg (J. Fricke)	modified ÅNGSTROM'S method, $D_\parallel$
Tsinghua University (Y.Q. Gu)	modified ÅNGSTROM'S method, $D_\parallel$
Nagoya University (I. Hata)	modified ÅNGSTROM'S method, $D_\parallel$

and C is the specific heat (516 $W \cdot s \cdot kg^{-1}K^{-1}$), the conversion factor ρC was taken to be 1.81×10^6 $W \cdot s \cdot m^{-3}K^{-1}$ at room temperature.

4. Results

Table III lists the average of all measured values of the D and κ obtained for each specimen. This includes multiple values measured by an individual laboratory. The error is the standard deviation of the individual measurements and is expressed as a percentage. This average value was calculated in order to assign one parameter value to a specimen and thus may have no physical significance because of many of the specimen variations discussed below.

The large percentage uncertainties are indicative of the considerable variations measured. These variations are due to several causes. In some instances, a single laboratory obtained different values of a parameter at several locations on a specimen indicating a large specimen inhomogeneity over the surface of the specimen. Some measurements, such as the photothermal deflection method and the transient thermal gradient method, had depth selectivity, so that parameters measured on one surface differed from parameters measured on the opposite surface. This indicated a large cross-sectional inhomogeneity. Next, one laboratory found that the thermal conductivity for heat transport parallel to the surface differed from the thermal conductivity for heat transport normal to the surface indicating significant specimen anisotropy. Finally, there are unknown laboratory to laboratory procedural variations. An examination of the uncertainty

Table III. Average of thermal conductivity measurements on each specimen

specimen	# of pts.	mean D (m^2s^{-1})	mean κ ($W \cdot m^{-1}K^{-1}$)	uncertainty
LD-X	8	9.2×10^{-4}	16.6×10^2	$\pm 34\%$
LB-X	10	8.8×10^{-4}	15.9×10^2	$\pm 18\%$
SQ-X	9	8.2×10^{-4}	14.9×10^2	$\pm 35\%$
LD-E	7	2.3×10^{-4}	4.2×10^2	$\pm 32\%$
LB-E	10	2.5×10^{-4}	4.4×10^2	$\pm 14\%$
SQ-E	8	2.6×10^{-4}	4.7×10^2	$\pm 21\%$
LB-T	10	8.0×10^{-4}	14.6×10^2	$\pm 17\%$
SQ-T	8	6.6×10^{-4}	12.0×10^2	$\pm 31\%$
SQ-F	6	6.3×10^{-4}	11.5×10^2	$\pm 30\%$
SQ-FB	7	4.2×10^{-4}	7.6×10^2	$\pm 30\%$

column indicates that the uncertainties for the long bar specimens (LB-X, LB-E and LB-T) are approximately one half the uncertainties in the other specimens. An explanation for this discrepancy is not clear at this time. Figure 1 shows the results reported by the laboratories that performed measurements on LB-T. The error bars are those reported by the measuring laboratories.
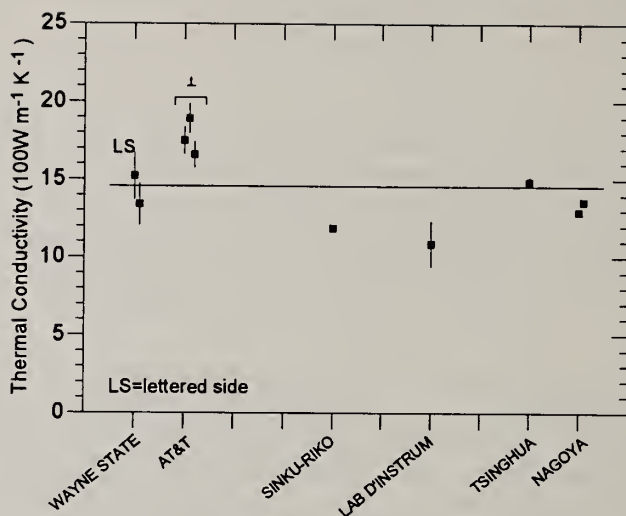
Fig. 1. Values of κ for specimen LB-X. The line is the mean of all values.

Both Wayne State University and AT&T Bell Labs reported values for all specimens. Only AT&T reported the temperature of measurement and the temperature dependence of κ from about 300 K to 390 K. The specimens with the lowest κ showed almost no temperature variation while those with the highest κ showed a significant temperature variation. AT&T was also the only laboratory to measure $D_\perp$ which is found to be larger than $D_\parallel$. The University of Würtzburg measured the specimen densities which deviated significantly from that of diamond. However, for the purposes of this presentation, this variation was not used in the computations.

5. Conclusion

Thermal conductivity measurements have been performed by 10 laboratories on 10 CVD diamond specimens as part of a round robin interlaboratory comparison. Significant variations were found. A full discussion of these measurements is planned for a future publication.

6. References

1. A. Feldman, C. Beetz, M. Drory, and S. Holly, J. Res. Natl. Inst. Stand. Technol. **97**, 387 (1992).
2. A. Feldman, C. Beetz, P. Klocek, and G. Lu, J. Res. Natl. Inst. Stand. Technol. **98**, 375 (1993).

USE OF MODIFIED OF AC CALORIMETRY TO MEASURE THE THERMAL PROPERTIES OF CVD DIAMOND

By

Akikazu Maesono[1] and Ronald P. Tye[2]
[1]ULVAC Sinku Riko, 1-9-19 Hakusan, 226, Yokohama Japan, [2]6 Riverside Drive, Andover MA

Key Words: ac calorimeter, inhomogenity, thermal conductivity, thermal diffusivity

Abstract

Many applications of thin films require that these materials, which are often anisotropic, have a very high thermal conductivity as well as uniform areal properties. For diamond, the combination of a very high thermal conductivity with limited size and form of specimen presents unique measurement challenges.

A modification of the ac calorimeter method has been developed to evaluate the thermal diffusivity of such materials. Details will be provided together with examples of its use to evaluate thermal properties of different CVD diamond films having thickness from 10μm to 600μm. Results using this method will be compared with these obtained by other techniques involved in a recent international comparison.

1. Introduction

Applications in microelectronics packaging, require that generated heat be removed rapidly from smaller, increasingly higher power density components. One means to accomplish this is by utilizing heat spreader designs involving high thermal conductivity materials including more recently CVD diamond.

In using diamond, the combination of limited thickness, anisotropy and very high thermal conductivity provides particular measurement difficulties. Furthermore, since for some applications, the thickness of use can be sufficiently small that the material properties differ from the bulk properties and existing standard methods are not appropriate.

The present paper describes a recently developed method involving a modification of a well known technique for measurement of specific heat which is highly proving to be applicable to thin films. Some examples of its use are included.

2. Method

The ac calorimetric technique is a very sensitive absolute and comparative method for determining specific heat [1,2]. It involves subjecting one coated surface of a specimen to chopped light and measuring the ac temperature response on the opposite surface. The modified technique to measure thermal diffusivity in the inplane direction is also now in wide use and is well documented [3,4]. The principle is again relatively simple but involves subjecting only part of a surface to the chopped light and measuring the ac temperature as a function of the length of exposure due to changing the position of a mask. Since specific heat can also be measured separately, the thermal conductivity can be derived simply. It can also be used for two layer composites [5]. For the normal operating frequency of 0.01 to 30 Hz, the thickness of the specimen is less than 0.4mm. However, for CVD diamond the thickness range can be well in excess of 0.4mm even up to 2mm for films materials having properties similar to natural diamond, 2000 W/m·K. For these, a modification of the technique reducing the area of illumination to a narrow slit to overcome edge reflection effects in required [6]. The following are examples of the use of the modified ac calorimeter (PIT) instrumentation to study thermal properties of CVD diamond.

(i) Effects of Methane Concentration and Thickness

In an early investigation [7] silicon wafers approximately 100μm thick were coated in different methane concentrations with CVD diamond films varying in thickness from 5 to 30μm. The results shown in Fig. 1 indicated that there was an effect of thickness below 20μm but a much greater effect due to methane concentration below 1%.
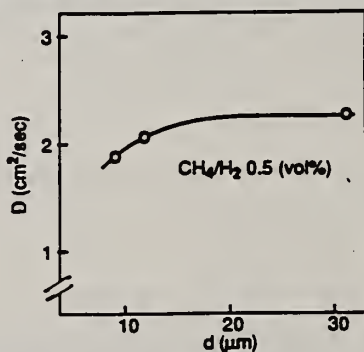
Fig. 1. Effect of methane concentration on the thermal diffusivity of CVD diamond.

(ii) Effects of Crystallite Size

In a study on property enhancement of poly crystalline films [8] 100μm silicon wafers were scratched with diamond to increase nucleation sites and subsequently coated with 10-15μm CVD diamond films in different methane concentrations. The results are shown in Fig. 2. They illustrate not only that the larger crystallite size specimens have much higher values of but also illustrate further the effects of methane concentration below 1%.
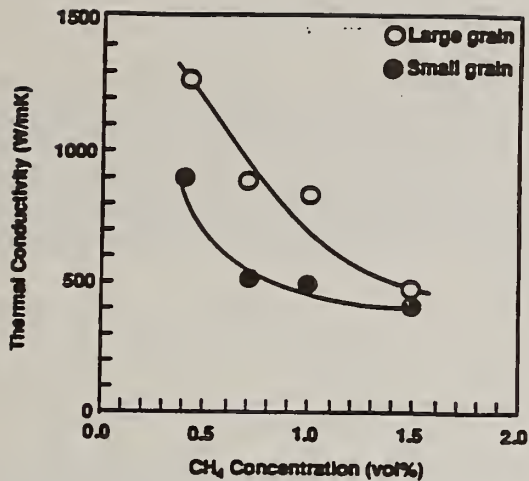
Fig. 2. Thermal conductivity of CVD diamond: effects of crystallite size and methane concentration.

(iii) Thermal Conductivity of a Free Standing Film

As part of an instrument verification measurements were made on three areas of a free standing film and reproducible results of 8.13, 8.08, and 10.12 cm²/s were obtained. The average value corresponded to a thermal conductivity of 1730W/m·K. An independent steady state measurement on the same specimen gave a value of 1700W/m·K.[9]

Due to the apparent inhomogenity, further measurements were made on one area of this specimen but by moving the mask in increments of 20μm instead of the normally used 100μm. The results, as shown in Fig. 3, indicate very local variations due to crystal boundary effects, but also suggest the possibility of using the technique for measurements at the "micro" level [10].
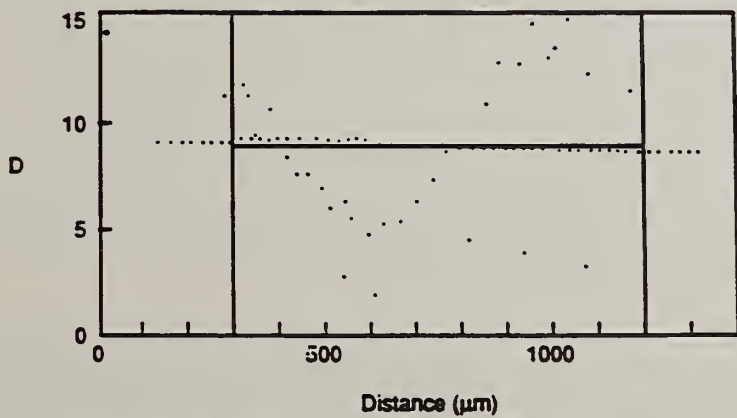
Fig. 3. Thermal diffusivity at 20μm positions on a CVD diamond film.

4. Performance in an International Round Robin

The results of this international study by ten organizations each measuring all or some of a group of specimens of different thermal diffusivity are reported elsewhere at the present conference. The ac calorimeter method was the only one that involved three organizations where the same basic technique was used. The overall results showed an over 80% spread of measured values and existence of some inhomogenities.; However, the results by the present technique as shown in Table 1 illustrate that the uncertainty can be reduced to about 20%.

TABLE 1

Results of Measurements on Three Specimens of CVD Diamond

SPECIMEN	Thermal Diffusivity, cm^2/s		
	LABORATORY 1	LABORATORY 2	LABORATORY 3
LBX (High)	9.97	9.1	8.4
LBE (Low)	2.5	2.4	2.3
LBT (Intermediate)	8.2	7.3	6.6

5. Summary

Examples of the application of the modified ac calorimeter to measure reliable thermal properties of diamond films has been described. It appears that the technique may offer one means to measure thermal properties at the micro-level.

6. References

1. Y.A. Kraftmakher, 1962, Zh. Prikl. Mekh, and Tekh. Fiz5, 176-180
2. P. Sullivan and G. Seidel, 1968, Phys. Rev. 173, 679-685
3. I. Hatta, Y. Gu, R. Kato and A. Maesono, 1994, Proceedings of the 22nd International Thermal Conductivity Conference, Technomic Publishing Co., Lancaster, PA, pp 461-472.
4. A. Maesono, R. Kato, I. Hatta, and R. P. Tye, 1994, Ibid pp 473-484
5. I. Hatta, R. Kato, and A. Maesono, 1987, Japan J. Appl. Phys. 26(3) 475-478
6. Y. Gu and I. Hatta, 1991, Ibid 30(5) 1137-38
7. H. Funamoto, A. Nishikawa, T. Moriya, and K. Sangboni, 1985, Proceedings of Sixth Japan Symposium or Thermophysical Properties, Japanese Society of Thermophysics, Tokyo, pp 177-182.
8. S. Yamashita, Tokyo Gas Co. Ltd., Frontier Research Institute, Yokohama, Japan, 1992 Private Communication. See also Proceedings of Diamond 1992, Conference Organizers in Medicine Science and Technology, Lausanne, Switzerland p 13.101.
9. A. Maesono, R. P. Tye, and R. L. Gardner, 1993, High Temp. - High Press. 25, 329.

Applications of Diamond Films and Related Materials: Third International Conference, 1995
Editors: A. Feldman, Y. Tzeng, W. A. Yarbrough, M. Yoshikawa, and M. Murakawa

635

THERMAL STRESS IN DIAMOND FILMS

V.G. Ralchenko[1], E.D. Obraztsova[1], K.G. Korotoushenko[1], S.M. Pimenov[1],
A.A. Smolin[1], V.G. Pereverzev[1], Yu.V. Lakhotkin[2] and E.N. Loubnin[2]

[1]*Institute of General Physics, ul. Vavilova 38, Moscow 117942, Russia*
[2]*Institute of Physical Chemistry, Leninsky prosp.31, Moscow 117915, Russia*

Key words: thermal stress, Raman spectroscopy, X-ray diffraction

Abstract

Residual stress in polycrystalline diamond films deposited from a DC arc plasma on ten different substrate materials (SiO_2, Si, SiC, Mo, Cu, Ni, Fe-Ni alloy, WC-Co and steel) was measured using micro Raman spectroscopy and X-ray diffraction technique. To improve adhesion some metals were pre-coated with a thin buffer layer of tungsten. The measured stress correlates with expected thermal stress originated from a mismatch in coefficients of thermal expansion (CTE) for diamond and substrate materials. The highest compressive stress at room temperature $\sigma = -11.4$ GPa has been found at Ni substrate, and it increased to -14.3 GPa at T=78 K, while the stress was strongly relaxed at copper because of its plasticity. The stress values determined from Raman spectra using a biaxial stress model are in good agreement with data obtained from X-ray diffraction.

1. Introduction

Thermal stress in diamond films caused by a mismatch in CTE between film and substrate can limit the performance of diamond coatings on cutting tools, sliding parts, optical components, which might be subjected to high mechanical load. Too high residual stress may cause a cracking or delamination of the coating. Therefore, an information about thermal stress is important for many diamond applications. As a rule the thermal stress is compressive due to very low CTE for diamond, $\alpha = 0.8 \times 10^{-6}$ K^{-1} at room temperature. The residual stress as high as ≈ 7 GPa was reported for diamond films deposited on Ti alloy [1] and steel [2]. We used Raman spectroscopy and X-ray diffraction to measure the thermal stress in diamond films on ten different materials.

2. Experimental

The list of substrates used includes silica glass, Si, α-SiC, Mo, steels #60S2 and #R18, WC-Co (6%), Ni, Fe-Ni alloy (Fe-38Ni-1.7V), and Cu. To avoid a

636

graphite formation and/or improve adhesion we used a thin (5-7 μm) buffer layer of CVD tungsten [2] to pre-coat Ni, Fe-Ni alloy, steel, WC-Co and Cu. Diamond films, typically of about 10 μm thickness, were grown in a DC arc discharge using CH_4/H_2 gas mixtures. The substrate temperature T_d was kept between 900-950°C for all samples, except SiO_2 (690°C). For comparison purposes the stress in the films was measured by two methods: Raman spectroscopy and X-ray diffraction. Raman spectra were taken using a Jobin-Yvon S-3000 micro-Raman spectrometer (2 cm^{-1} spectral resolution, excitation wavelength 514.5 nm, laser beam size 2 μm, laser power 40 mW). The sample temperature upon measurements could be varied in the range from 77 K to 600 K. Residual stress was determined also by a low incident beam angle X-ray diffraction technique, similar to the $d\text{-}sin^2\Psi$ method (d is interplanar spacing, Ψ is rotation angle in case of Ψ-goniometer) [3]. The X-ray diffraction measurements were performed with a JDX-10PA diffractometer at Cu-K$_\alpha$ radiation and 0.5x10mm analyzed area. The stresses were calculated with the use of "$1/sin\Theta$ versus $sin^2\Psi$" plots, where Θ is diffraction angle.

3. Results

Fig. 1 shows Raman spectra of diamond films on ten different materials at T=293 K. A negative peak shift (tensile stress) is observed at SiO_2 substrate, and positive peak shifts (compressive stress) at other substrates. A splitting of Raman peak to two lines is clearly seen for Ni and Fe-Ni alloy substrates, for which the peak shifts $\Delta\nu$ exceed 18-20 cm^{-1}. In case of biaxial stress, σ, the Raman peak of *polycrystalline* diamond splits for singlet and doublet shifted from normal position at 1332 cm^{-1} by $\Delta\nu_s$ and $\Delta\nu_d$, respectively [1]:
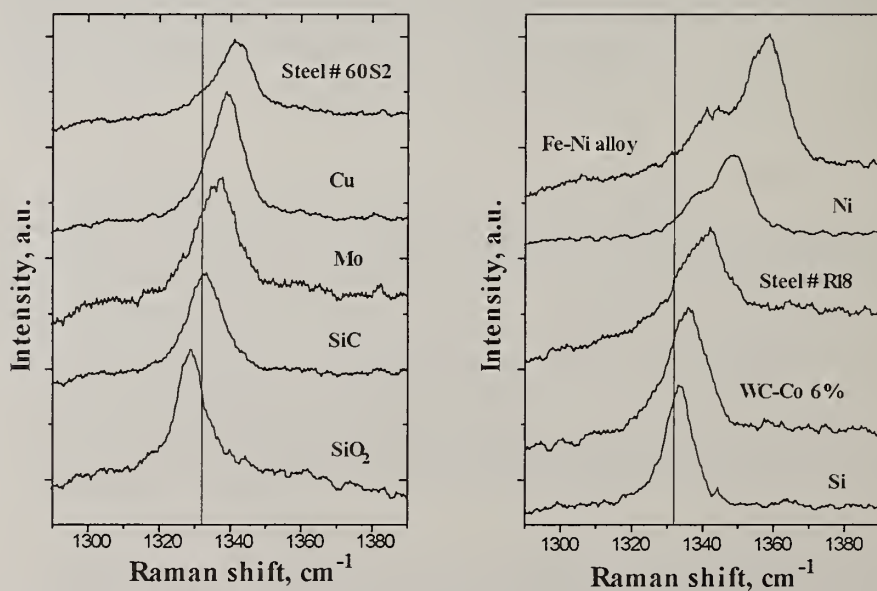
Fig. 1. High-resolution Raman spectra of diamond films on different substrates. The vertical line at 1332 cm^{-1} indicates the peak position for stress-free diamond.

$\Delta\nu_s$ [cm^{-1}] = -0.93 σ [GPa]   for *singlet*   (1)

$\Delta\nu_d$ [cm^{-1}] = -2.60 σ [GPa]   for *doublet*   (2)

At low stress (typically at σ <8 GPa) the peak splitting was not resolved, and a "weighted" shift $\Delta\nu = (1/3)\Delta\nu_s + (2/3)\Delta\nu_d$ was used to calculate the stress:

$\Delta\nu$ [cm^{-1}] = -1.62 σ [GPa]   for *unsplitted peak*   (3)

The Raman peak shift, stress found using eqs. (1-3), and substrate CTE are summarized for different substrate materials in Table I. A dispersion in peak shifts, if existed, was ignored, thus only maximum $\Delta\nu$ and σ values for each sample are shown here. In general, the measured stress increases with substrate CTE value, indicating the thermal nature of residual stress. Tensile stress σ =+2.3 GPa has been found only for SiO_2, which possesses a very low CTE, while other materials generate a compressive stress. For one of the films on Ni the stress as high as σ =-11.4 GPa was measured at T=293 K, and even higher value σ =-14.3 GPa was achieved at T=78 K [4].

The thermal stress σ_{th} was calculated from eq. (4) for all the substrates, assuming the deposition temperature T_d =950ºC (T_d =690ºC for SiO_2):

$$\sigma_{th} = \int_{293K}^{T}(\alpha_f - \alpha_s)dT \qquad (4)$$

where E=1143 GPa and ν =0.07 are Young's modulus and Poisson coefficient for diamond, α_f and α_s are CTE values for film and substrate, respectively.
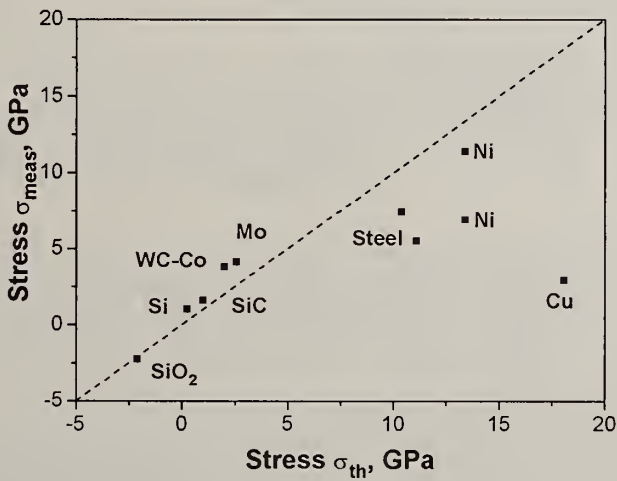
Fig. 2. Comparison of residual stress σ_{meas} determined from Raman spectra with thermal stress σ_{th} calculated from eq. (4) for different substrates. σ_{meas} =σ_{th} along dashed line.

638

Table I. Substrate CTE, α (T=293 K); Raman peak shift $\Delta\nu$, and maximum measured stress σ_{meas} of diamond films at different materials. Doublet shift is marked with (*).

Substrate	SiO$_2$	Si	SiC	WC-Co	Mo	Steel	Ni	Cu
α, 10^{-6} K^{-1}	0.5	2.5	2.8	5.2	5.3	11.2	13	16.7
$\Delta\nu$, cm^{-1}	3.7	1.6	2.6	6.2	6.7	12	29.5*	4.7
σ_{meas}, GPa	+2.3	-1.0	-1.6	-3.8	-4.1	-7.4	-11.4	-2.9

The measured stress is in a reasonable agreement with the calculated thermal stress (Fig. 2), the strong stress relaxation at Cu substrate being ascribed to an easy plastic deformation of copper. Raman peak shift has been found to be proportional to the stress measured by X-ray diffraction technique as shown in Fig. 3. The experimental data were fit with a linear relationship $\Delta\nu$ [cm^{-1}] = a·σ [GPa], with a=1.9±0.2. Also shown for comparison are Raman peak shifts predicted by hydrostatic [5] and biaxial [1] stress models, with coefficients a=2.64 and a=1.62, respectively. Our data seem to be in better agreement with the biaxial stress calculations.
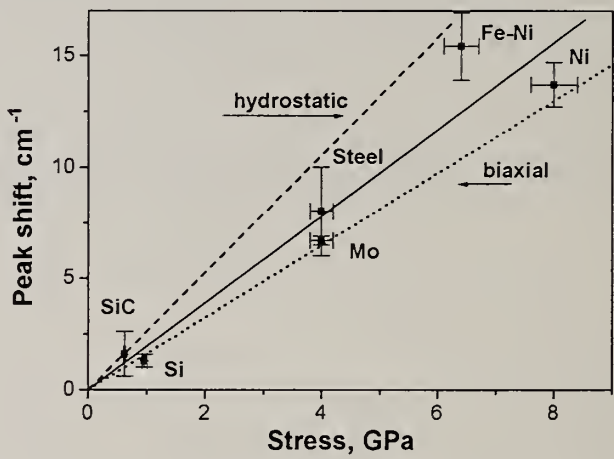
Fig. 3. "Weighted" shift of Raman peak vs stress measured by X-ray diffraction method for diamond films on different substrates. Dashed line is from hydrostatic model with a=2.64 [5], dotted line is biaxial stress model [1], and solid line fits experimental data.

4. References

1. J.W. Ager and M. Drory, *Phys. Rev. B*, **48** (1993) 2601.
2. V.G. Ralchenko, A.A. Smolin, V.G. Pereverzev, E.D. Obraztsova, K.G. Korotoushenko and V.I. Konov, paper presented at *The Diamond Films'95*, Il Ciocco, Italy, 1994.
3. I.C. Noyan and J.B. Cohen, *Residual stress*, Springer, N.Y., 1987.
4. V.G. Ralchenko, E.D. Obraztsova, K.G. Korotoushenko, A.A. Smolin, S.M. Pimenov and V.G. Pereverzev, paper presented at *The MRS Spring Meeting, Symp. I*, San-Francisco, 1995.
5. A. Tardieu, F. Cansell and J.P. Petitet, *J. Appl. Phys.* **68** (1990) 3243.

HIGH TEMPERATURE LIGHT EMITTING DIODES ON INSULATING DIAMONDS.

A. A. Melnikov[1], A. V. Denisenko[1,2], A. M. Zaitsev[1,2], W. R. Fahrner[2] and V. S. Varichenko[1]

[1]Belarussian State University, pr. F. Skoryna 4, Minsk 220050, Belarus
[2]University of Hagen, Haldener Str. 182, Hagen 58084, Germany

Key words: diamond, electroluminescence, ion implantation, pin diode

Abstract

Electrical and optical properties of diamond based light emitting p-i-n diodes have been studied up to 500°C. Bulk and planar structures have been fabricated on natural and synthetic single crystal substrates by ion implantation. Electroluminescence (EL) in blue, green and orange spectral ranges has been observed from the insulating i-layer of the diodes. The EL emission is due to electron-hole recombination through the optical centers in the diamond substrate.

1. Introduction.

Optoelectronic application of diamond has been always of particular interest. By now several types of diamond based light-emitting devices (LEDs) have been demonstrated [1]. In the present report we study operation of diamond based p-i-n LEDs with an emphases to their high temperature properties.

2. Experiment

p-i-n structures were fabricated on polished plates of natural and synthetic high temperature - high pressure diamonds. Concentration of paramagnetic nitrogen in the synthetic crystal was about $2.7 \times 10^{19} \text{cm}^{-3}$. p-type regions were made by ion implantation of boron (25-150 keV, total dose 2×10^{16} cm^{-2}) and subsequent annealing at 1450 °C. n-type regions were fabricated by implantation of lithium (40 keV, 4×10^{16} cm^{-2}) or phosphorous (60 keV, 1.8×10^{16} cm^{-2}) without annealing. The doped regions of the planar structures were separated by 6 μm gap of undoped material. Bulk p-i-n diode was fabricated by the implantation with boron and lithium of two parallel polished surfaces of a natural diamond .

3. Results and Discussion.

Cathodoluminescent (CL) spectrum of the bulk diode's substrate is characterised by the dominant H3 center emission (zero-phonon line at 503 nm) accompanied by the A-band (440 nm maximum) and free exciton recombination (235 nm).

I-V characteristics of the forward biased diode at room temperature (RT) and 400°C are show in Fig. 1 a. The RT characteristics exhibits a region of S-type negative resistance at 25 - 30 V bias. This feature was observed up to 250°C. Vanishing of the negative resistance region at higher temperatures implies intensive interaction of the injected charge carriers with traps located in the undated i-gap [2]. At voltages above 30 V the I-V curve follows the low $I \sim U^3$ indicating limitation of the current space charge and electron-hole recombination in the regime of double injection in insulator [3]. Reduction of the current with the temperature can be explained by a decrease of the carrier life-time and mobility.

EL spectrum of the bulk diode at RT. shows the H3 center emission with a maximum at 520 nm (green colour) (Fig. 1 b). The EL intensity does not change noticeable up to 500°C (Fig. 2 a), though the maximum shifts to the red (529 nm at 400°C). The light emission output of the diode at RT has been measured of 10^{-5} W at electrical power about 0.2 W.

At RT liner dependence of the EL intensity on the electrical current is observed up to 1 mA (Fig. 2 b). At higher currents the dependence comes to a saturation. At 400°C temperature a negative slope of the EL intensity - electrical current dependence is observed at high currents. This effect can be tentatively explained by a shift of the Fermi level of holes at high density of the current and activation thereby of effective nonradiative recombination centers.

CL spectrum of the natural diamond substrate with the planar p-i-n structures reveals the dominating A-band emission (maximum at 440 nm, blue colour) accompanied by the free exciton recombination line.

I-V characteristics of the planar p-i-n structures at RT (both Li^+ and P^+ implanted n-type regions) are shown in Fig. 3 a. Similar to the case of the bulk diode the characteristics exhibit an S-type negative resistance region at about 10 - 25 V applied voltage. However at higher voltages the I-V curves do not follow the cubic low $I \sim U^3$ in the double injection regime. This discrepancy is explained by a short width of the insulating i-gaps of the structures (6 μm). The time of the carrier drift across the i-gap is lower that the carrier life-time in the insulator. The current is not limited any more by the electron-hole recombination (in contrast of the case of the bulk diode where the thickness of the crystal, that is the i-gap, is about 300 μm).

Current flow through the planar structures is accompanied by EL of the A-band (Fig. 3 b). Increase of the current results in an additional luminescence band with a maximum at about 600 nm. The EL intensity of the A-band strongly decreases with temperature and it almost disappears at above 300°C (Fig. 2 b).

CL spectrum of the synthetic diamond substrate prior to the ion implantation reveals only a wide band with a maximum at 520 nm. The implanted regions produce a strong CL of the 575 nm center (orange colour). Both the centers are presented in the EL spectrum of planar p-i-n structures (Fig. 3 b). EL intensity of the 575 nm center proves to be stable up to 500°C temperature (Fig. 2 a). The maximum of the 575 nm center band shifts from 590 nm at RT to 645 nm at 460°C.

4. Conclusions

Electroluminescence in blue, green and orange spectral regions have been excited in diamond based p-i-n structures fabricated by ion implantation. The light emission occurs due to electron-hole recombination through various optical centers initially contained in the substrate. The H3 and 575 nm centers have been shown to be high temperature optical activators of diamond, while the A-band luminescence is quenched rapidly above room temperature.

5. Reference.

1. *Advances in New Diamond Sci. and Technology*, ed. S. Saito. MYU, Tokyo, 1994.
2. V.V Osipov and V.I. Stafeev, Soviet Phys. Semicond., 1 (1967) 1795 - 1804.
3. M. Lampert and P. Mark, *Current Injection in Solids*, Acad. Press, New York 1970.

6. Figures
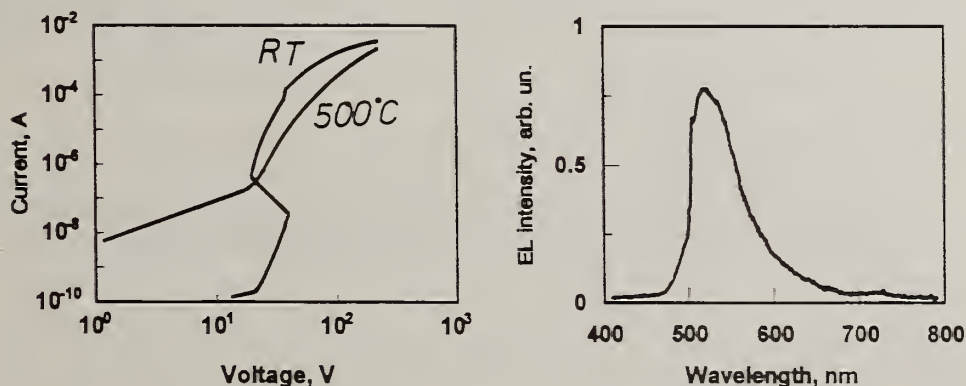
Fig. 1. a. I-V characteristics of bulk p-i-n diode on natural diamond crystal. RT and 500°C. b. EL spectrum of the diode at RT.
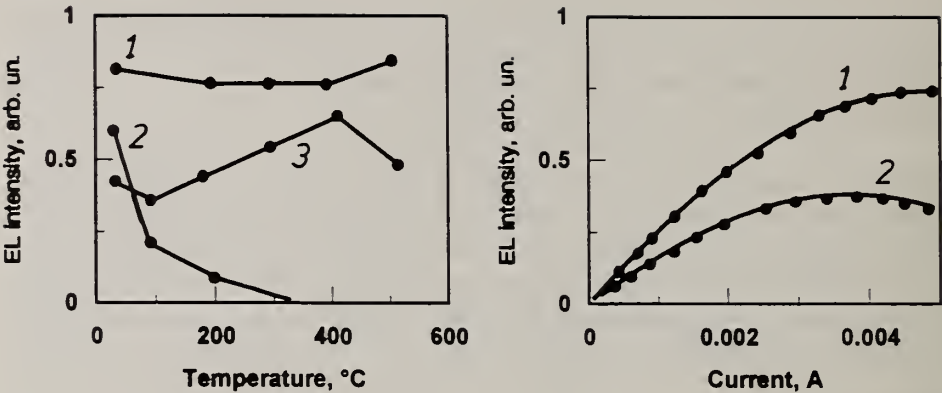
Fig. 2. a). Temperature dependence of EL intensity. 1 - H3 center, bulk p-i-n diode; 2 - A-band, planar p-i-n structure on natural diamond; 3 - 575 nm center, planar p-i-n structure on synthetic diamond.
b). EL intensity of the H3 center vs. electrical current at RT and 400°C. Bulk p-i-n diode on natural diamond.
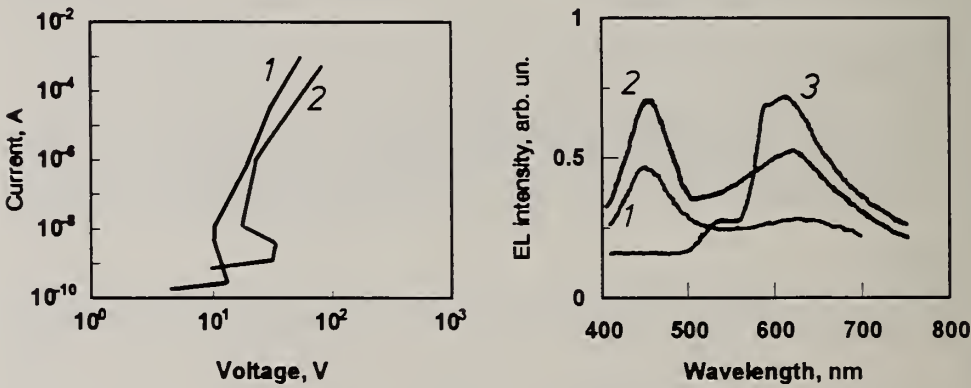
Fig. 3. a. I-V characteristics of a planar p-i-n structure on natural diamond.
1. P$^+$ implanted n-type contact; 2. Li$^+$ implanted n-type contact.
b. EL spectra of planar p-i-n structures. Natural diamond substrate; electrical current: 1) - 0.6 mA, 2) - 2.2 mA. 3) - synthetic diamond substrate.

DIAMOND COATINGS ON INTEGRATED CIRCUITS

D. K. Reinhard, M. Ulczynski, and R. N. Chakraborty

Electrical Engineering Dept., Michigan State University, East Lansing, MI 48824

Key words: diamond; low-temperature deposition; microelectronics; passivation.

Abstract

Diamond over-coatings on substrates which contain microelectronic circuitry may provide a means for reduction of thermal hot-spots, or act as a superior passivation layer. This study reports the results of microwave plasma-assisted chemical vapor deposition of diamond on silicon substrates which contain microelectronic devices. Deposition temperatures are compatible with the aluminum metallization technology commonly used in integrated circuit fabrication. Both passive devices (diffused resistors) and active devices (transistors) were successfully coated.

1. Introduction

Diamond is of interest for electronic packaging because of its combination of thermal, electrical, and mechanical properties. Diamond is already being used as a substrate material onto which heat producing electronic components are attached [1, 2]. In such cases, the high thermal conductivity of diamond combines with its high electrical resistivity and low dielectric constant to provide high-performance heat sinks for microwave integrated circuits, power device modules, and multi-chip modules [3, 4]. However, diamond is also under consideration as an over-coating layer on microelectronic components. It is this potential application that this paper addresses.

2. Background

One potential advantage of diamond films on integrated circuits is as a superior passivation layer. In previous work, for example, hot-filament chemical vapor deposition (CVD) was used to deposit a 2 µm thick diamond film on a silicon wafer containing circuitry including linear amplifiers and resistor elements used for thermal transfer printing devices [5]. It was noted that the resulting devices exhibited superior lifetime in that the diamond coated circuits did not exhibit failure due to abrasion of the resistor elements by the paper. However, the diamond deposition temperature of 850 C for this example is too high for conventional microelectronics which use aluminum metal-

lization. Overlay diamond films have also been proposed for improved thermal management of local hot spots in which, for example, diamond would be used as the dielectric material to fill the gap between source-gate and gate-drain regions of high electron mobility transistors [6]. In order to implement such a device, low temperature deposition of diamond is required.

3. Methods

Silicon integrated circuits consist of a variety of materials including silicon, silicon dioxide, and aluminum based metal layers. These represent a wide variety of thermal expansion coefficients. Diamond deposition on silicon is well established, however deposition on metals and oxides can be problematic. An upper limit on deposition temperature is imposed by the presence of aluminum which has a melting temperature of 660 C. Lower substrate temperatures are advantageous in that differing thermal expansion coefficients can cause considerable intrinsic stress as the substrate and film are cooled from the deposition temperature. Consequently, low-temperature diamond deposition using microwave plasma-assisted chemical vapor deposition was used for this study. The deposition method has been previously described [7].

Silicon substrates with (100) orientation were processed to fabricate resistors and bipolar junction transistors. Boron diffusion through oxide windows was used to form diffused resistors and p-type base regions for the transistors. A subsequent phosphorus diffusion was used to from the n-type emitter regions for the transistors, and ohmic contacts to the n-type collectors. Contact cuts were made to the underlying silicon and aluminum was deposited by thermal evaporation. The aluminum layer was patterned and etched by conventional photolithography to form contact pads for device testing purposes. An oxide passivation layer was not used.

Because abrasive seeding techniques can damage the delicate metallization patterns, a spin-on seeding method was used [8]. Diamond powder, 0.1 μm, was suspended in photoresist as described in reference 8 and spun onto the wafer. During the first few minutes of exposure to the deposition plasma, the photoresist is etched away, allowing the diamond seed particles to be distributed on the wafer.

4. Results

Fig. 1 shows a 100X optical micrograph view of details of the IC structure beneath the transparent diamond film. Higher magnification shows the diamond film to be continuous and polycrystalline. The lightest features in Fig. 1 correspond to aluminum patterns which are 20 μm wide. The other varying patterns correspond to oxide layers of different thickness. Fig. 2 shows cross-sectional drawings through the contact cuts of a resistor and a bipolar transistor. As measured by optical pyrometry, the substrate temperature during deposition was approximately 435 C. Based on before and after weight gain measurements, the diamond film thickness is approximately 0.7 μm.

In order to test the devices after diamond coating, the diamond was selectively removed from the metal contacts pads by plasma etching. Previous reports of the selective etching of diamond have included the use of evaporated aluminum [5] and sputtered silicon dioxide [9] as masking layers. In this investigation, spin-on-glass (SOG) was used as the masking layer. The SOG was patterned by photoresist and wet etching, the photoresist was stripped, and the diamond was etched through to the aluminum test pads. Diamond etching was achieved in an ECR plasma discharge using a mixture of gases including oxygen. Diamond film coated resistors and transistors were tested subsequent to this etching procedure and found to be fully functional. Alternatively, the photoresist may be patterned prior to deposition, as noted in reference 8, such that seeding is not present where the diamond film is not desired.

5. Summary

Diamond over-coatings are of interest for microelectronics because of potential applications for passivation and reduction of local hot spots. In this study, diamond films have been deposited on silicon integrated circuit structures including transistors and resistors. The deposition temperature is sufficiently low so as to not cause damage to the underlying structures, including the aluminum metallization.

6. Acknowledgments

7. References

1. G. Lu, "Applications of CVD Diamond in Thermal Management", pp. 269-274, 2nd International Conference on the Applications of Diamond Films and Related Materials, Eds. M. Yoshikawa, M. Murakawa, Y. Tzeng, and W. A. Yarbrough, MYU, Tokyo, 1993.
2. L. M. Napolitano, Jr., D. D. Andaleon, M. R. Daily, E. Meeks, D. Miller, D. P. Norwood, D. W. Peterson, C. A. Reber, J. E. Robles, and W. Worobey, "Development of Electronic Subsystems on Diamond Substrates", pp. 275-280, ibid.
3. R. C. Eden, "Application of Diamond Substrates for Advanced High Density Packaging", Diamond and Related Materials, Eds. P. K. Bachmann, A. T. Collins, and M. Seal, pp. 1051 - 1058, Elsevier, Lausanne 1, Switzerland, 1992.
4. N. B. Nguyen, "Using Advanced Substrate Materials with Hybrid Packaging Techniques for Ultrahigh-Power IC's, Solid State Technology, pp. 59 - 62, Feb. 1993.
5. F. Jansen and M. A. Machonkin, "Processes for the Preparation of Polycrystalline Diamond Films", U. S. Patent No. 4,925,701, May 15, 1990.
6. S. Rotter, "A Proposed Novel Application of Thin Overlay Diamond Films for Improved Thermal Management of Short Gate High Power Devices", Advances in New Diamond Science and Technology, Eds. S. Saito, N. Fujimori, O. Fukunaga,

646

M. Kamo, K. Kobashi, and M. Yoshikawa, pp. 665 - 668, MYU, Tokyo, 1994.

7. M. J. Ulczynski, D. K. Reinhard, M. Prystajko, and J. Asmussen, "Low Temperature Deposition of Thin Film Diamond", pp. 41 - 44, ibid.

8. A. Masood, M. Aslam, M. A. Tamor, and T. J. Potter, "Techniques for Patterning of CVD Diamond Films on Non-Diamond Substrates", J. Electrochemical Soc., vol 138, pp. L67-L68, 1991.

9. S. A. Grot, G. Sh. Gildenblat, and A. R. Badzian, "Diamond Thin-Film Recessed Gate Field-Effect Transistors Fabricated by Electron Cyclotron Resonance Plasma Etching", IEEE Electron Dev. Letters, vol. 13, pp. 462-464, 1992.

Fig. 1. Optical micrograph of a detail of the diamond film coated IC structure. The lightest colored patterns correspond to aluminum metallization.
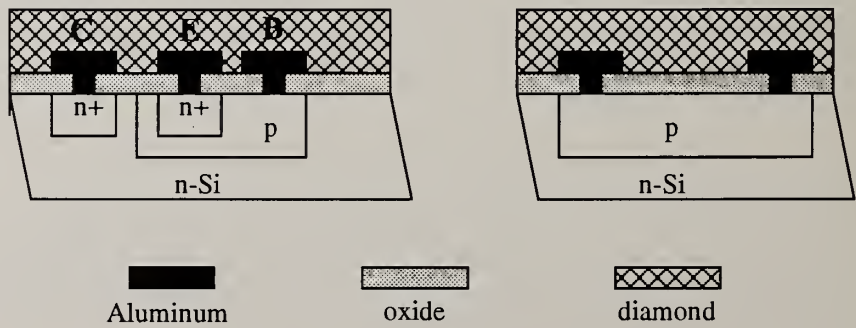
Fig. 2. Cross-sectional drawing of a coated bipolar junction transistor with collector (C), emitter (E), and base (B), and a diffused resistor.

Applications of Diamond Films and Related Materials: Third International Conference, 1995
Editors: A. Feldman, Y. Tzeng, W. A. Yarbrough, M. Yoshikawa, and M. Murakawa

647

THERMAL CONDUCTIVITY OF MW–CVD DIAMOND FILMS SYNTHESIZED WITH VARYING CH₄ CONCENTRATION

Hee-Baik Chae[1], Chang-Yop Lee[1], Yong-Jin Han[1] and Young-Joon Baik[2]

[1] Department of Physics, Soonchunhyang University, Asan P. O. Box 97, 336-600, Republic of Korea
[2] Division of Ceramics, Korea Institute of Science and Technology, Chongryang P. O. Box 131, Seoul, Republic of Korea

Key words: thermal conductivity, MW–CVD diamond film, phonon scatterring, Callaway model, point defect, extended defect, Umklapp process, Normal process

Abstract

Diamond films were synthesized with varying CH₄ concentrations in 2.5 ~ 10 % of the reacting source gases by the microwave plasma assisted chemical vapor deposition. Thermal conductivity was measured on these films by the steady state method in a temperature range 80 ~ 400 K. Higher thermal conductivity was obtained on the diamond film which was synthesized with lower CH₄ concentrations, but thick film synthesized with high CH₄ concentration showed also good thermal conductivity. Phonon scattering processes were considered to analyze thermal conductivity with the Callaway model. Grain size and concentrations of the extended defects and the point defects were used as the fitting parameters. Microstructure of diamond films was investigated with SEM and Raman spectra.

1. Introduction

It has been known that synthesizing with higher CH₄ concentration enhance the defect level in CVD diamond film and caused the reducing thermal conductivity.[1][2] They showed that 1 ~ 5% change of CH₄ concentration in hot filament method significantly effect thermal conductivity on diamond film that thermal conductivity was shown as a hybolic function of CH₄ concentration. It was attributed to the high defect level(such as hydrogen impurity) of the film synthesized with high CH₄ concentration and the point defects scattering with phonons were enhanced in the films. Their measurements were done at room temperature only and on diamond films with thick Si substrate. Their film thickness is thinner than 10 μm that the grain boundary – phonon scattering is also high. Thus, for the full understanding of thermal conductivity in conjunction with synthesizing

condition needs thicker films.

We prepared three CVD diamond films which were synthesized with 2.5 ∼ 10 % concentrations of CH₄ in the gases of Microwave Plasma CVD method. Thermal conductivity of these free-standing films was measured with steady state method in a temperature range 80 ∼ 400 K and analysed.

2. Experiments and Results

Physical characteristics of natural diamond type IIa from ref. 3 and three diamond films which were synthesized with various CH₄ concentration in gases are listed in Table I.

Table I . Physical characteristics and synthesizing conditions for each CVD diamond films. Grain size is the average of top surface on the diamond films. Raman Ib/Id is the ratio of the background to the peak height of diamond.

	MW2	MW3	MW4	type IIa
CH₄ concentration (%)	9.85	7.79	2.46	--
Growth rate (μm/h)	5.7	3.5	0.6	--
Thickness (μm)	160	125	68	--
Grain size, top (μm)	25	20	20	--
Raman FWHM (cm⁻¹)	6.2	4.6	3	--
Raman Ib/Id	0.32	0.16	0.1	--
k(298K) (W/cm K)	10.0	12.6	11.2	24.0
D, Grain size(μm)	4	10	7	1000
c, Point defect level(%)	5	3	3	1.1
c_E, Extended defect (10^{-22}cm³)	13	5	15	0

Measured thermal conductivity is presented in Fig. 1 with fitted curves. The natural diamond thermal conductivity data is taken from ref. 3. We use the full Callaway model to take into account the differences among the longitudinal and transverse phonon modes.[4][5] In this model, the combined mean-free path $l_C{}^{-1}$ is written as the sum of the normal, $l_N{}^{-1}$ and the resistive mean-free path $l_R{}^{-1}$, such as $l_C{}^{-1} = l_N{}^{-1} + l_R{}^{-1}$.

We choose the normal process from Landau and Rumer[6], such as

$$l_N{}^{-1} = A \frac{x}{v} T^5.$$ (1)

where A=0.011 cm, $x = \hbar \omega / k_B T$, v is the sound velocity. In each mode, different values of the Debye temperature and the sound velocity were used. The assumption is made that the resistive scattering rates add, so that

$$l(x) = (l_B{}^{-1} + l_p{}^{-1} + l_U{}^{-1} + l_E{}^{-1})^{-1} + \frac{\lambda}{2} . \tag{2}$$

The individual mean-free paths l_B, l_p, l_U and l_E are associated with the grain boundaries, point defects, umklapp processes and the extended defects[7], respectively. The term $\lambda/2$, half the phonon wave length, is included to avoid the unphysical case where the mean-free path becomes short compared to the phonon wave length. The functional forms of each mean-free paths are chosen to be

$$l_B{}^{-1} = 1/D \tag{3}$$

$$l_p^{-1} = 4\pi^3 V_0 c(1-c)\left(\frac{1}{12+c}\right)^2 \left(\frac{k_B T}{\hbar v}\right)^4 x^4 \tag{4}$$

$$l_U{}^{-1} = B\left(\frac{k_B T}{\hbar v}\right)^2 x^2\, T\, e^{-\frac{C}{T}} \tag{5}$$

$$l_E{}^{-1} = c_E \frac{E}{(2\pi v)^4}\left(\frac{k_B T}{\hbar}\right)^4 x^4 \quad \text{for} \quad x < x_c \tag{6}$$

$$= c_E \frac{E}{(2\pi v)^4}\left(\frac{k_B T}{\hbar}\right)^4 x_c^4 \quad \text{for} \quad x \geq x_c$$

where $x_c = \frac{\hbar v}{k_B T F}$, F is the diameter of the extended object, and V_0 is the volume per atom(5.68×10^{-24} cm^{-3}). We used the parameters $B = 1.5\times10^{-12}$ cm^3, $C = 670 K$, $F = 15.0\times10^{-8}$ cm and $E = 7.19\times10^{15}(\text{cm}^3)\cdot4\pi^5 F^6 = 10^{-22}$ cm^3 to be fixed. Three adjustable parameters D, c and c_E are the grain size, the point defects concentration and the concentration of the extended defects, respectively, which are listed for a good fit in Table I.

Extended defect is a significant effect to have a good fit as Graebner et. al. found in their high quality CVD diamond films.[7] Synthesized in low CH$_4$ concentration film, such as MW3 has low point defect but the extended defect level is higher than MW4 which was synthesized higher CH$_4$ concentration and thus the thermal conductivity is reduced over the measured temperature range. Point defect level for MW3 were fitted as the same level as MW4. Synthesized in the highest CH$_4$ concentration, MW2 film has high level of both defects and thermal conductivity has low values over the temperature range.

3. Conclusions

Film synthesized in lower CH$_4$ concentration has higher thermal conductivity. But increasing the film thickness also enhance thermal conductivity of film synthesized in high CH$_4$ concentration. In the full Callaway model, point defects as well as the extended defects are important in diamond films. Thick film synthesized high CH$_4$ concentration which has low extended defect level showed good thermal conductivity.

650

4. References

[1] K. Baba, Y. Aikawa and N. Shohata, J. Appl. Phys. **69**, 7313-7315 (1991)

[2] C. Gu, C. W. Jin and G. Zou, *2nd International Conference on the Applications of Diamond Films and Related Materials*, ed. by M. Yoshikawa, M. Murakawa, Y. Tzeng and W, A. Yarbrough, Tokyo, 1993

[3] R. Berman., P. R. W. Hudson and M. Martinez, J. Phys. **8**, L430-4 (1975)

[4] J. R. Olson, R. O. Pohl, J. W. Vandersande, A. Zoltan, T. R. Anthony and W. F. Banholzer, Phys. Rev. B **47**, 14850 (1993)

[5] L. Wei, P. K. Kuo, R. L. Thomas, T. R. Anthony and W. F. Banholzer, Phys. Rev. Lett. **70**, 3764 (1993)

[6] L. Landau and G. Rumer, Phys. Z. Sowjetunion **11**, 18 (1937)

[7] J. E. Graebner, M. E. Reiss, L. Seibles, T. M. Hartnett, R P. Miller and C. J. Robinson, Phys. Rev. B **50** 3702 (1994)
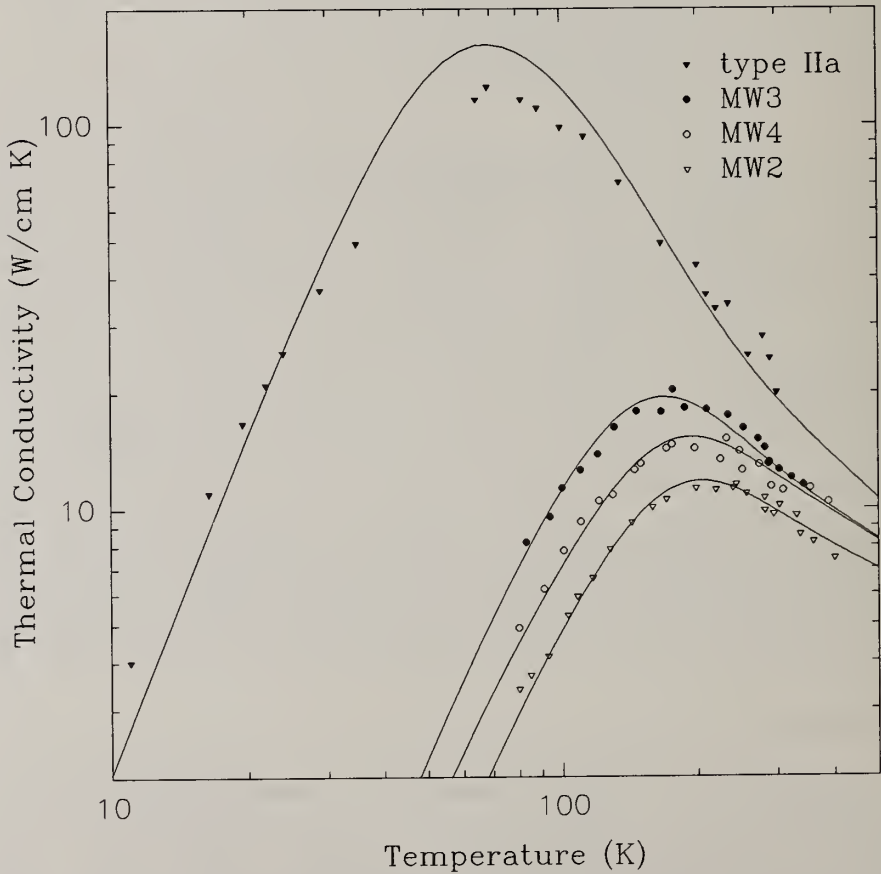
Fig. 1. Thermal conductivity of MW−CVD films and natural diamond type IIa(ref. 3).

STUDY OF THERMAL DIFFUSIVITY MEASUREMENT OF CVD DIAMOND

Yuqin Gu   Lixin Yu

Department of Engineering Mechanics, Tsinghua University, Beijing 100084 China

Key words: ac calorimatric method, CVD Diamond, thermal diffusivity

Abstract

Thermal diffusivity of three free-standing PCVD diamond films have been measured by ac calorimetric method. The thermal diffusivity ranges from 0.28cm²/s to 4.44cm²/s under a variety of the methane concentration from 0.2 to 1.0%(vol).
The systematic errors such as heat loss, non-one-dimensional heat conduction, edge reflection are considered. For the diamond sample, the edge reflection is not able to be negligible and it is analytically corrected.

1. Introduction

CVD diamond becomes one of the most attractive heat spreader material due to its very high thermal conductivity. It is of advantage to use in electronic packaging and heat sink material. The reported thermal conductivity of CVD diamond film ranges over an order of magnitude in relation to the synthetic processing.
Measurements of thermal diffusivities of CVD diamond films with methane concentration from 0.2 to 1.0%(vol) by an ac calorimetric method are presented. The thermal diffusivity is sensitively depended on the methane concentration.
For the sample with high thermal diffusivity such as diamond film the edge reflection of temperature wave at the end of the sample with a finite length should be considered. It is examined and analytically corrected.

2. Theory

An ac calorimetric method has been presented for thermal diffusivity measurement of thin film in the direction parallel to its surface[1]. A modulated light irradiates on the surface of a sample partly shadowed by a mask (shown in Fig.1). A thermocouple with a diameter of $25\mu m$ is attached to the sample with a little silver paste. Moving the mask along with the surface, under the conditions of one-dimensional heat conduction and no heat loss the temperature of the sample is given as,

$$T(x,t)=\frac{Qe^{i\omega t}}{2\omega cd}e^{-kx-i(kx+\frac{\pi}{2})}$$ (1)

where

$$k=\left(\frac{\pi f}{D}\right)^{1/2}$$ (2)

f is the frequency, D is the thermal diffusivity, Q is the amplitude of the heat flux, ω is the angular frequency, c is the heat capacity per unit volume.
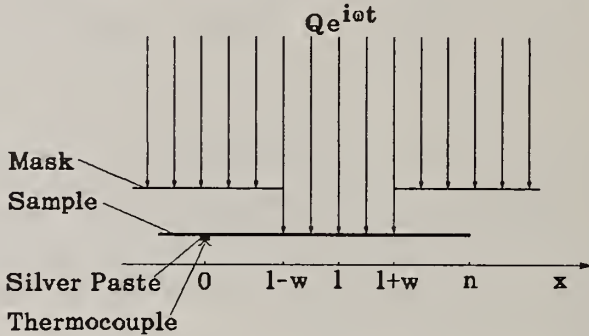
Fig.1 Schematic view of ac calorimetric method

By recording the amplitude of temperature wave in relation to the distance between the middle point of the light and the thermocouple location the decay constant k is obtained and the thermal diffusivity concerned is determined

$$D=\frac{\pi f}{k^2}$$ (3)

For the sample with high thermal diffusivity such as CVD diamond film the temperature wave will reflect at the end of the sample because of the finite length. The thermal diffusivity obtained is an effective value D^*, not real one D. The relation between both values is given as eq.(4)[2][3].

$$\frac{D}{D^*}=\{1-\frac{2e^{-2k(n-l)}[cos2k(n-l)+sin2k(n-l)+e^{-2k(n-l)}]}{1+2e^{-2k(n-l)}cos2k(n-l)+e^{-4k(n-l)}}\}^2$$ (4)

where n is the distance between the thermocouple and the end of the sample in the side with the light spot, l is the average distance from the center of the light spot to the point of the thermocouple location. From eq.(4) it is obtained

$$k(n-l)>\frac{7}{8}\pi, \frac{D}{D^*}\rightarrow 1$$ (5)

When eq.(5) is not satisfied. The measured value D should be obtained with correction in accordance with eq.(4) by an iterative method.

3 Experiment

The rectangular light spot is supplied by an optical system with a halogen lamp as a light source. The sample mounted in a holder locates in a furnace inside of a vacuum chamber. Crosswise thermocouple with the diameter of 25μm attached on the sample to detect the average temperature and the amplitude of the temperature wave through a pre-amplifier and a lock-in amplifier. There is a calculation circuit to evaluate and display the thermal diffusivity and a personal computer to acquire and process the data as well.

The frequency is adjusted to a suitable range to reduce the heat loss, non-one-dimensional effect. The edge reflection effect must have been corrected.

The free-standing diamond film was obtained by removal of the silicon substrate in HF-HNO$_3$ solution from a composite film in which the diamond was grown on the silicon substrate by PCVD. The thickness of the free-standing diamond film ranges from 11.5μm to 28.1μm, the length is about 10mm and the width is 4mm. We corrected the measured values of thermal diffusivity D^* in accordance with eq.(4) and the obtained D which should not be related to frequency.

Experimental results are as follows,

(1)The thermal diffusivity with the edge effect correction D is shown in Fig.3 and ratio of its average value to the measured one D^* at different frequency is shown in Fig.4. These figures indicate that the corrected D at different frequency is quite similar to each other and eq.(4) is proved.

(2)Three samples with different reactive methane concentration from 0.2 to 1.0% CH$_4$(vol) were measured. The thermal diffusivity with correction of edge effect is shown in Fig. 5, it becomes small when the methane content increases. Corresponding to these samples the SEM photos and Raman spectra explained the reason that during increasing of CH$_{4\%}$(vol) the grain size is getting smaller and the content of amorphous/graphitic carbon seems higher.

4. Summary

(1)CVD diamond is a kind of ideal material used as an electronic substrate and heat spreader, its thermal conductivity is related to the processing. Study of thermal diffusivity measurement is very helpful to modify the synthetic processing and to raise the quality of CVD diamond film.

(2)Ac calorimetric method is successfully used to measure the thermal diffusivity of CVD diamond film. Systematic errors such as non-one-dimensional, heat loss can be considered to be negligible with adjusting the frequency at a suitable range. Usually, the edge reflection effect exists due to the finite length of the sample and can be corrected analytically.

(3)Thermal diffusivity of CVD diamond greatly depends on the reactive methane concentration because of the microstructure and amorphous/graphitic carbon.

654
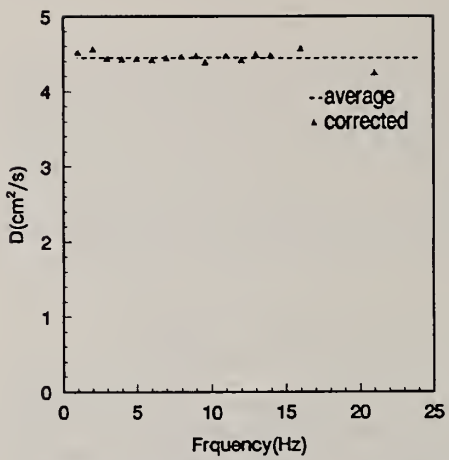
Fig.3 Corrected thermal diffusivity
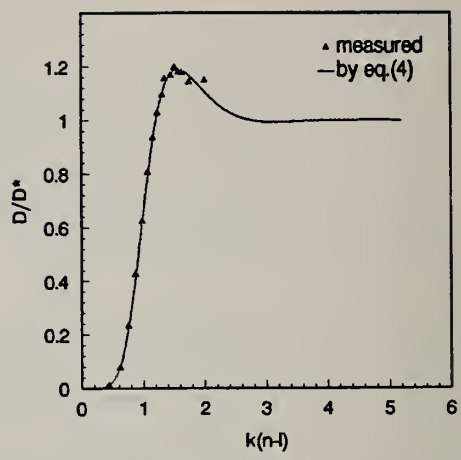
Fig.4 Edge reflection effect
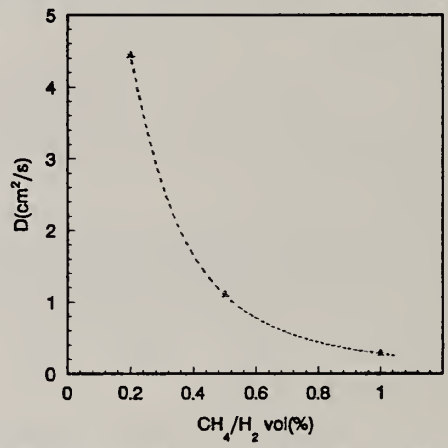
Fig.5 Thermal diffusivity vs methane concentration

5. Acknowledge

6. References

[1]I. Hatta, Y. Sasuga, etal., rev. Sci. Instrum., 56, (1985), 1643
[2]Y.Q. Gu, I.Hatta, Jpn. J. Appl. Phys., 30(5), (1991), 1137
[3]Y.Q. Gu, D.Z. Zhu, etal., High Temp.-High Pres., 25, (1993), 553
[4]Y.Q. Gu, I. Hatta, Jpn. J. Appl. Phys., 30(6), (1991), 1295

MODELLING

CHARGED CLUSTER MODEL IN THE SYNTHESIS OF DIAMOND BY CHEMICAL VAPOR DEPOSITION

Nong M. Hwang[1], Jun H. Hahn[1], and Duk Y. Yoon[2]

[1]Korea Research Institute of Standards and Science, P.O.Box 102, Yusung-gu, Daedok Science Town, Daejon, 305-600, South Korea
[2]Korea Advanced Institute of Science and Technology, 373-1, Kusung-dong, Yusung-gu, Daejon, 305-701, South Korea

Key words: charge, cluster, diamond, graphite, nucleation, soot

Abstract

Charged carbon clusters which are formed by the gas activation are suggested to be responsible for the formation of the metastable diamond film. The number of carbon atoms in the cluster that can reverse the stability between diamond and graphite by the capillary effect increases sensitively with increasing the surface energy ratio of graphite to diamond. The gas activation process produces charges such as electrons and ions, which are energetically the strong heterogeneous nucleation sites for the supersaturated carbon vapor, leading to the formation of the charged clusters. Once the carbon clusters are charged, the surface energy of diamond can be reduced by electrocapillarity while that of graphite cannot because diamond is dielectric and graphite is conducting. Some experimental evidences supporting this charged cluster model will be presented.

1. Introduction

The fundamental question in the low pressure synthesis of diamond [1,2] is how the metastable diamond forms dominantly over the stable graphite in the presence of the gas activation. It should be noted that the dominant formation of the metastable phase over the stable one is also reported in many other systems [3]. In these cases, the phenomena are relatively well understood based on the capillary effect of the small particle especially in the nucleation stage. The capillary effect can be also applied to the low pressure synthesis of diamond. That is, the capillary pressure inside a sufficiently small carbon cluster can be high enough to make a diamond cluster more stable than a graphite cluster. We reported previously that within error of the surface energy of diamond and graphite, the dominance in the nucleation rate between diamond and graphite is reversed [4]. Among the parameters that affect the ratio of the nucleation rate, the surface energy is the only one that can be varied by the processing condition.

The gas activation process is essential to the dominant formation of diamond over graphite. From the point of the capillary effect of the small cluster, the possible role of the gas activation is to modify the surface energy in the way favoring the stability of diamond over that of graphite. The surface energy can be modified by adsorption of either the neutral species or the charged species. Previously, Badziag et al. [5] showed that nanometer-sized diamond can be more stable than

graphite when the atomic hydrogen is adsorbed. When the carbon clusters are charged, the surface energy of diamond can be reduced while that of graphite cannot because diamond is dielectric and graphite is conducting. Both effects of the atomic hydrogen and charges might be additive in favoring the formation of diamond. The purpose of this paper is to suggest the charged cluster model as the possible mechanism for the CVD diamond process. We will show the experimental result implying that the stability between diamond and graphite clusters is directly affected by the presence and the absence of charges.

2. Formation of charged clusters

The typical gas activation is achieved by the hot-filament of the refractory metal and the plasma. The hot-filament of the refractory metal is often used for the source of electrons or an electron gun. The plasma process involves ions and electrons. In both gas activation processes, charges are involved. We notice that in all kinds of the gas activation processes for the diamond synthesis, the charged species can be involved. The thermodynamic analyses [6] of the CVD diamond process predict the driving force for precipitation of graphite or diamond from the gas phase. That is, the carbon in the gas phase is supersaturated for the precipitation of the solid carbon in the presence of charges. Charges are known to be the site that markedly lowers the nucleation barrier. Charge-induced nucleation was manifested by the Wilson's cloud chamber [7] and the bubble chamber [8] experiments, where the charge-induced nucleation is utilized in locating the track of the high energy particles.

When the charge-induced nucleation takes place in the presence of the abundant charges, almost all nuclei will become the charged cluster. They would not coarsen much because the unlimited coarsening of the charged clusters will increase the Coulomb energy. The size of the charged clusters will depend on the relative amount between precipitates and charges. They are presumed to be in the nanometer scale. Another possible effect of the charge would be to make the unbalanced reduction of the surface energy between diamond and graphite because diamond is dielectric and graphite is conducting. The charged clusters are expected to have characteristics similar to that of the colloid suspension.

When the colloid particles sediment, their packing behavior critically depends on whether the force between the charged particles is attraction-dominant or repulsion-dominant. The attraction-dominant flocculated packing of the colloid particles is porous while the repulsion-dominant deflocculated packing is dense [9]. When the charge of the cluster is retained throughout the packing process, the repulsion-dominant dense packing is expected, whereas when the charge is transferred to the substrate during the packing process, the attraction-dominant dense packing is expected. When the charge is lost from the cluster, diamond would be no longer stable with respect to graphite because the electrocapillarity effect disappears. If the cluster still retains the high rotational and vibrational temperature, the transformation from diamond to graphite will take place. The resultant microstructure would be the porous graphitic soot. When the charge is lost after the cluster is thermalized, being in thermal equilibrium with the substrate, the transformation from diamond to graphite would not be activated. The resultant microstructure would be the dense diamond film.

We observed that the porous graphitic soot was evolved on the iron substrate while the diamond film grew on the silicon substrate placed close to the iron substrate. And we noticed a high correlation between the substrate materials

leading to the graphitic soot and the electrode materials having the high charge transfer rate. We can expect that the charge transfer rate of the iron substrate would be affected when the quartz plate is placed beneath the iron substrate. For this, we placed the 3.3 mm thick insulating quartz beneath the 1.5 mm thick iron substrate and compared the resultant microstructural evolution with that on the iron substrates without the quartz plate under the same processing condition of $1\%CH_4$-$99\%H_2$ for 2 hours at the substrate temperature of 1263 K under 2700 MPa. We could make the temperature of both substrates the same by decreasing the filament temperature from 2473 K to 2323 K for the substrate with the quartz. The distance between the filament and the substrate was fixed as 8 mm. The microstructures by scanning electron microscopy are shown in Fig. 1(a) and 1(b) for the substrates without quartz and with quartz, respectively.

In Fig. 1(a), the porous graphitic soot continues to grow even after 2 hours while in Fig. 1(b), the diamond particles begin to grow on the initially formed graphitic soot. The effect of the quartz plate would come from either the thermal insulation or the electrical insulation. We tried to eliminate the effect of the thermal insulation by making the temperature of both substrates the same by decreasing the filament temperature for the substrate with quartz. We were confirmed in the preliminary experiments that the decrease in the filament temperature has the disadvantageous effect on the formation of diamond on the soot. Thus, the difference in Fig. 1(a) and 1(b) is expected to come from the effect of the electrical insulation of quartz. The results imply that the charge might affect not only the stability between diamond and graphite but also the morphological evolution between the dense and the porous structure, supporting our charged cluster model. More detailed treatment of the charged cluster model will be published elsewhere [10].

3. Conclusion

Although it is difficult to confirm experimentally whether the invisible nanometer-sized charged clusters exist in the gas phase in the CVD diamond process, the well-known phenomenon of the ion-induced nucleation predicts the charged clusters. The quartz plate beneath the iron substrate enhances the formation of diamond on soot, indicating the formation of diamond is related to the charge transfer rate.

References

[1] B.V. Spitsyn, L.L. Bouilov, and B.V. Derjaguin, J. Cryst. Growth, 52 (1981) 219.
[2] J.C. Angus and C.C. Hayman, Science, 241 (1988) 913.
[3] K.N. Ishihara, M. Maeda and P.H. Shingu, Acta Metall., 33 (1985) 2113.
[4] N.M. Hwang, G.W. Bahng and D.N. Yoon, Diamond Relat. Mater., 1 (1992) 191.
[5] P. Badziag, W.S. Verwoerd, W.P. Ellis and N.R. Greiner, Nature, 343 (1990) 244.
[6] N.M. Hwang, J. Cryst. Growth, 135 (1994) 165.
[7] J.G. Wilson, The Principles of Cloud-Chamber Technique, pp. 1-17, Cambridge Univ. Press, Cambridge, 1951.
[8] C. Peyrou, Bubble and Spark Chambers, pp. 19-58, Ed. R.P. Shutt, Academic Press, Orlando, 1967.
[9] D.J. Shaw, Introduction to Colloid and Surface Chemistry, 2nd ed. pp. 167-86, Butterworths, London, 1970.
[10] N.M. Hwang, J.H. Hahn and D.Y. Yoon, In preparation.
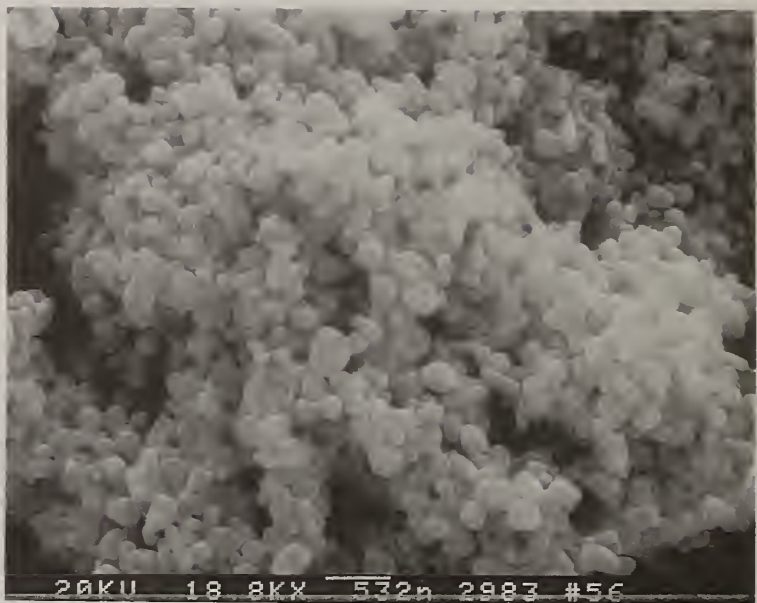
(a)
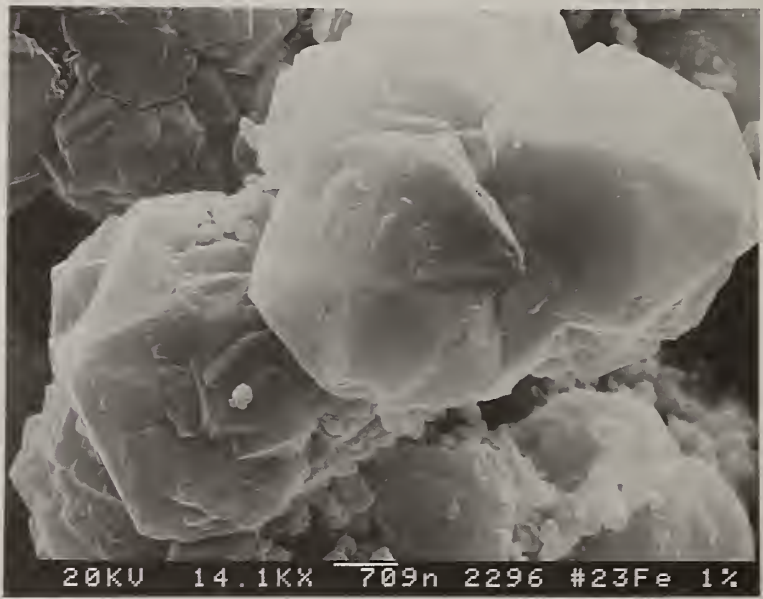
(b)

Fig. 1 Microstructures evolved on the iron substrate (a) without quartz and (b) with quartz below the substrate.

THERMODYNAMIC PARADOX OF DIAMOND DEPOSITION WITH SIMULTANEOUS GRAPHITE ETCHING IN THE LOW PRESSURE SYNTHESIS OF DIAMOND: APPROACH BY CHARGED CLUSTER MODEL

Nong M. Hwang[1] and Duk Y. Yoon[2]

[1]Korea Research Institute of Standards and Science, P.O.Box 102, Yusung-gu, Daedok Science Town, Daejon, 305-600, South Korea
[2]Korea Advanced Institute of Science and Technology, 373-1, Kusung-dong, Yusung-gu, Daejon, 305-701, South Korea

Key words: charge, cluster, diamond, etching, graphite, thermodynamic paradox

Abstract

If diamond deposits and graphite etches simultaneously in the low pressure synthesis of diamond, the chemical potential of carbon in diamond and in graphite would be, respectively, lower and higher than that in the gas phase. The analysis leads to diamond being more stable than graphite, contradicting the well-established stability between diamond and graphite. In the C-H system, the solubility of carbon in the gas phase is minimum at $\approx$ 1500 K and it increases with decreasing temperature. In the charged cluster model, diamond nucleates in the gas phase. The gas phase, being depleted of carbon by the maximum precipitation of the diamond clusters at $\approx$ 1500 K, becomes undersaturated with carbon when super-cooled to the substrate temperature and a portion of the cluster is expected to etch. The unetched portion of the diamond cluster will deposit with simultaneous etching on an atomic scale. Thus, diamond deposition with simultaneous graphite etching can be explained based on the charged cluster model without leading to the thermodynamic paradox.

1. Introduction

Methods for preparing the diamond film by the gas activation process have been relatively well established [1-3]. The underlying principle, however, is not fully understood and there has been much debate as to the mechanism for the chemical vapor deposition (CVD) diamond process [4]. Deryaguin and Fedoseev [1] reported that the activated hydrogen etches graphite at rates orders of magnitude higher than diamond. Similar observations were reported by Angus et al. [5], Setaka [6], and Saito et al. [7]. Further, diamond can be synthesized with graphite as the only source of carbon [8] and diamond deposits with simultaneous etching of graphite [9,10]. These well-confirmed experimental results definitely tell that in the gas activated CVD diamond process diamond deposits and at the same time graphite etches. The atomic hydrogen hypothesis, which was originally suggested by the pioneering Russian scientists [2,11], seems to be no longer a hypothesis but an experimental fact.

However, if diamond deposits and simultaneously graphite etches, the chemical potentials of carbon in diamond and graphite are, respectively, lower and higher than that in the gas phase. And the chemical potential of carbon in diamond becomes lower than that in graphite, which would contradict the well-established stability between diamond and graphite and violate the second law of thermodynamics. In this situation, it is tempting to say that the problem should be approached by kinetics rather than thermodynamics as the atomic hydrogen hypothesis does. To our understanding, however, kinetics should be pursued within thermodynamics; kinetics should never go against thermodynamics. Something must be wrong either in interpreting the experimental observation or in applying thermodynamics.

In the CVD diamond process, there are two problems which are difficult to understand from a thermodynamic point of view: the first is the dominant formation of metastable diamond over stable graphite and the second is the experimental observations [8-10] of the deposition of diamond with simultaneous etching of graphite. Thermodynamically, these are two different problems. Dominant formation of the metastable phase over the stable one is relatively well established [12] by considering the capillary effect of the small particle in the systems such as zirconia [13]. The stability between two phases can be reversed when the size is sufficiently small as in the nucleation stage. Previously Badziag et al. [14]. and Hwang et al. [15] suggested that the nanometer-sized diamond can be more stable than graphite. The first problem can be approached without much difficulty by considering thermodynamics of capillarity. However, the second problem cannot be explained by the capillary effect; the capillary effect of the graphite substrate would be negligible. Only a nanometer-sized graphite particle would be comparable in stability to a diamond particle of the similar size. This second problem seems to favor the atomic hydrogen hypothesis over the models based on capillarity, which are thermodynamically more sound. The purpose of this paper is to examine rigorously the second problem on a thermodynamic basis.

2. Thermodynamic Analysis of the C-H System

We should interpret the experimental observations in a way that does not violate the second law of thermodynamics. First, we need to examine the solubility of carbon in the gas phase in the C-H system. Fig. 1 shows the temperature dependence of the solubility of carbon in the gas phase with respect to diamond (solid line) and graphite (dashed line) at 2700 Pa in the C-H system. The thermodynamic calculations were done using the Thermo-Calc software [16]. For the mixture gas of 1% CH_4-99%H_2, the atomic fraction of carbon is 0.00493. The percentage of CH_4 normally used in the CVD diamond process ranges from 0.5 % to 3 %. And the substrate temperature used in the process ranges from $\approx$ 1000 K to $\approx$ 1300 K. In these ranges of the gas composition and the substrate temperature, carbon in the gas phase is supersaturated with respect to precipitation of the solid carbon; the driving force is for deposition for both diamond and graphite [17]. Neither graphite nor diamond is expected to etch in the processing condition.

From this analysis, it is difficult to understand the experimental observation that graphite etches in the processing condition in which the thermodynamic analysis predicts its deposition. We believe that this difficulty arises because of the implicit assumption that the gas phase nucleation of the solid carbon does not take place. If we assume that the gas phase nucleation of the solid carbon takes place, the

equilibrium amount of the solid carbon precipitation will be maximum at ≈ 1500 K, where the solubility of carbon in the gas phase is minimum. The equilibrium amount of the carbon precipitation with temperatures is calculated in Fig. 2. A part of the carbon clusters having precipitated at ≈ 1500 K will be etched as they move in the gradient of decreasing or increasing temperature. For example, the equilibrium mole fractions of the precipitated graphite at 1500 K and at 1100 K are calculated to be 4.88×10^{-3} and 4.44×10^{-3}, respectively, for the mixture gas of 1%CH_4-99%H_2. Thus, ≈ 9 % of graphite precipitated at 1500 K is expected to etch during cooling to 1100 K. And if the gas phase which is depleted of carbon by the precipitation of the solid carbon at 1500 K is supercooled to the temperature of the substrate, it is expected to etch the graphite substrate.

The possibility of the gas phase nucleation of the solid carbon is dealt in detail by the charged cluster model [18]. The most important point of the charged cluster model is that the charge-induced nucleation of the solid carbon takes place in the gas phase by the presence of abundant charges, which are produced by the gas activation. The resultant nanometer-sized charged carbon clusters are expected to have the diamond structure because of the high capillary effect and the electrocapillary effect by the charges. In the presence of charges, the electrical double layer can be formed on the surface of the clusters. Unbalanced surface energy reduction between the diamond and graphite clusters is expected. The charges are expected to favor the stability of diamond over that of graphite because diamond is dielectric while graphite is conducting. The dense diamond film finally results from the repulsion-dominant packing of the charged diamond clusters, which is analogous to the behavior of the deflocculated colloid suspension.
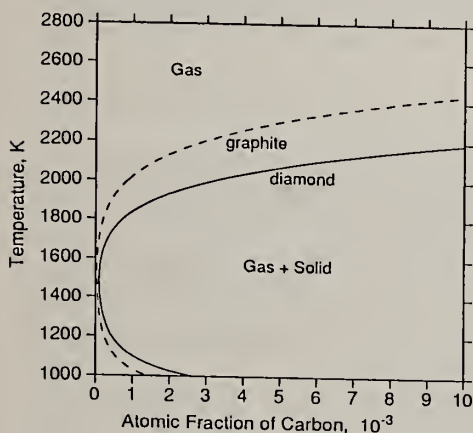
Fig. 1. The calculated temperature dependence of the solubility of carbon in the gas phase with respect to diamond (solid line) and graphite (dashed line) at 2700 Pa in the C-H system.
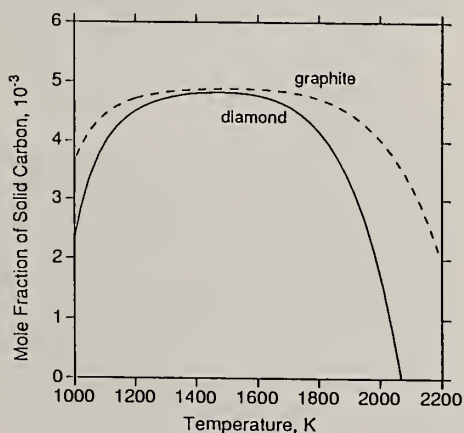
Fig. 2. The calculated temperature dependence of equilibrium mole fraction of the solid carbon at 2700 Pa in the mixture of 1%CH_4-99%H_2 for diamond (solid line) and graphite (dashed line).

When these charged diamond clusters precipitated in the gas phase move toward the substrate, they are expected to etch from the thermodynamic analysis of Fig. 1 and Fig. 2. The unetched portion of the clusters will contribute to making the diamond film. The deposition unit for the diamond film is not an atom but the cluster. The diamond deposits by the cluster unit but at the same time etches by the atomic unit. Thus, on an atomic scale both diamond and graphite are expected to etch at the substrate temperature, satisfying the second law of thermodynamics. But the net result would be the diamond deposition with the simultaneous graphite etching.

3. Conclusion

We could interpret the experimental observation of diamond deposition with simultaneous graphite etching without violating the second law of thermodynamics based on the charged cluster model, which claims that the diamond clusters nucleate in the gas phase and diamond deposits by these clusters.

References

[1] B.V. Derjaguin and D.B. Fedoseev, The Growth of Diamond and Graphite from the Gas Phase (Nauka, Moscow, USSR, 1977) ch. 4.
[2] B.V. Spitsyn, L.L. Bouilov, and B.V. Derjaguin, J. Cryst. Growth, 52 (1981) 219.
[3] S. Matsumoto, Y. Sato, M. Tsutsumi and N. Setaka, J. Mater. Sci., 17 (1982) 3106.
[4] W.A. Yarbrough, J. Am. Ceram. Soc., 75 (1992) 3179.
[5] J.C. Angus, H.A. Will and W.S. Standko, J. Appl. Phys., 39 (1968) 2915.
[6] N. Setaka, in: Chemical Vapor Deposition 1987, Proc. 10th Intern. Conf. on CVD, Eds., G.W. Cullen and J. Blocher, Jr. (Electrochemical Society, Pennington, NJ, 1987) p. 1156.
[7] Y. Saito, K. Sato, H. Tanaka, K. Fujita, and S. Matsuda, J. Mater. Sci., 23 (1986) 188.
[8] H.B. Vakil, presented at First Annual Diamond Technology Workshop Proceedings, Wayne State University, Detroit, MI. Sept. 18, 1989.
[9] A.R. Badzian, T. Badzian, R. Roy, R. Messier and K.E. Spear, Mat. Res. Bull., 23 (1988) 531.
[10] M.C. Salvadori, M.A. Brewer, J.W. Ager III, K.M. Krishnan and I.G. Brown, J. Electrochem. Soc., 139 (1992) 558.
[11] V.O. Varnin, V.V. Derjaguin, D.V. Fedoseev, I.G. Teremetskaya, and A.N. Khodan, Sov. Phys. Crystallogr., 22 (1977) 513.
[12] K.N. Ishihara, M. Maeda and P.H. Shingu, Acta Metall., 33 (1985) 2113.
[13] R.C. Garvie, J. Phys. Chem., 69 (1965) 1238.
[14] P. Badziag, W.S. Verwoerd, W.P. Ellis and N.R. Greiner, Nature, 343 (1990) 244.
[15] N.M. Hwang, G.W. Bahng and D.N. Yoon, Diamond Relat. Mater. 1 (1992) 191.
[16] B. Sundman, B. Jansson and J.O. Andersson, CALPHAD, 9 (1985) 153.
[17] N.M. Hwang, J. Cryst. Growth, 135 (1994) 165.
[18] N.M. Hwang, J.H. Hahn, D.Y. Yoon, To be published in this volume.

THEORETICAL ANALYSIS OF DIAMOND CHEMICAL VAPOR DEPOSITION IN A ROTATING DISK REACTOR

Dean E. Kassmann and Thomas A. Badgwell

Chemical Engineering, Rice University, P.O. Box 1892, Houston, TX 77251, USA

Key words: CVD, diamond, modeling, rotating disk, substrate injection

Abstract

A theoretical model has been developed to investigate transport phenomena and chemical kinetics in a rotating disk diamond chemical vapor deposition (CVD) reactor. The model combines mass, momentum and energy balances for the gas flow with detailed gas and surface kinetics for diamond formation. The model equations were solved numerically to determine gas-phase composition profiles and diamond film growth rates for hot-filament, dc arc-jet and chlorine-activated systems. The model was then used to investigate the benefits of injecting methane through the substrate of a dc arc-jet reactor. This process modification is predicted to increase the diamond growth rate by an order of magnitude.

1. Theoretical Model

A theoretical model for diamond CVD was developed by combining ideas from the work of Coltrin, Kee and Evans [1] and Goodwin and Gavillet [2]. The model is based on mass, momentum and energy balances for a reacting gas flow at steady-state. The similarity transform of Evans and Grief was applied [3] to reduce the model equations to a set of ordinary differential equations. A suitable choice of dimensionless variables leads to the the following model equations:

$$\overline{\rho}\frac{\partial H}{\partial \eta} + H\frac{\partial \overline{\rho}}{\partial \eta} + 2\overline{\rho}F = 0 \qquad \text{(continuity equation)}$$

$$\frac{\partial(\overline{\rho}\omega_j V_j)}{\partial \eta} + \overline{\rho}H\frac{\partial(\omega_j)}{\partial \eta} = M_j\sum_{i=1}^{n^s}\alpha_{ij}^g Da_i^g \gamma_i^g \qquad \text{(species continuity equation)}$$

$$\frac{1}{\overline{\rho}}\frac{\partial}{\partial \eta}\left(\overline{\mu}\frac{\partial F}{\partial \eta}\right) = F^2 - G^2 + H\frac{\partial F}{\partial \eta} + \frac{1}{\overline{\rho}}X \qquad \text{(radial momentum balance)}$$

$$\frac{1}{\overline{\rho}}\frac{\partial}{\partial \eta}\left(\overline{\mu}\frac{\partial G}{\partial \eta}\right) = 2FG + H\frac{\partial G}{\partial \eta} \qquad \text{(circumferential momentum balance)}$$

$$\frac{4}{3}\frac{1}{\overline{\rho}}\frac{\partial}{\partial\eta}\left(\overline{\mu}\left(\frac{\partial H}{\partial\eta}-F\right)\right)=H\frac{\partial H}{\partial\eta}-2\frac{\overline{\mu}}{\overline{\rho}}\frac{\partial F}{\partial\eta}$$ (axial momentum balance)

$$+\frac{1}{\overline{\rho}}\frac{\partial p_a}{\partial\eta}-\frac{1}{\beta}+\frac{1}{Fr}$$

$$\frac{1}{Pr}\frac{\partial}{\partial\eta}\left(\overline{k}\frac{\partial\theta}{\partial\eta}\right)=\overline{\rho}\overline{C}_pH\frac{\partial\theta}{\partial\eta}$$ (energy balance)

$$+\sum_{j=1}^{s}\left[\overline{\rho}\overline{C}_{pj}\omega_jV_j\frac{\partial\theta}{\partial\eta}+\overline{h}_jM_j\sum_{i=1}^{n'}\alpha_{ij}^s Da_i^s\gamma_i^s\right]$$

$$\overline{\rho}=\frac{Mp_a}{\alpha\theta}$$ (ideal gas law)

$$V_j=V_j^c+V_j^T$$ (diffusion velocity sum)

$$V_j^c=\frac{1}{\omega_j}\left(\frac{M_j}{M}\right)\sum_{i\neq j}^{s}\overline{\delta}_{ji}\left[\frac{\partial\omega_i}{\partial\eta}+\omega_i\frac{\partial}{\partial\eta}\ln\left(\frac{M}{M_i}\right)\right]$$ (multicomponent ordinary diffusion equation)

$$V_j^T=-\frac{1}{\overline{\rho}\omega_j}\overline{\delta}_j^T\frac{\partial}{\partial\eta}(\ln\theta)$$ (thermal diffusion velocity equation)

$$\sum_{j=1}^{s}\omega_j=1\qquad\sum_{j=1}^{s}\omega_jV_j=0$$ (mass fraction, diffusion velocityconstraints)

Gas phase and surface reaction kinetics for diamond formation were taken from the dc arc-jet reactor model of Coltrin and Dandy [4]. Additional reactions were added to describe the effects of chlorine on diamond growth. A total of 34 gas phase and 26 surface reactions were included in the model.

2. Simulation Results

The model equations were solved numerically on an IBM RISC/6000 workstation using a modified form of the SPIN code [5] from Sandia National Laboratories. Solutions were obtained for representative hot-filament, dc arc-jet and chlorine-activated systems, with predicted growth rates of 4.9, 37, and 59 μ/hr, respectively.

In the dc arc-jet, hot-filament and chlorine-activated cases, methyl radicals are formed very quickly near the inlet by hydrogen abstraction, but are consumed by subsequent gas phase reactions on their journey towards the substrate. In a recent paper Dandy and Coltrin investigated the possibility of injecting methane into the gas phase near the surface [6], a method referred to here as free-stream injection. They predict that the diamond growth rate in a dc arc-jet reactor may be increased by as much as 75% by injecting the methane into the gas stream just outside the substrate boundary layer. Dandy and Coltrin report a predicted growth rate of about 73 μ/hr for the case described in Fig. 3b of their paper.

While free-stream injection shows great promise for improving growth rates, it may be difficult to implement this concept in a real reactor without disrupting the flow field or introducing other asymmetries that result in a non-uniform deposit.

Another possibility is to inject methane directly through the substrate, with a purely axial flow opposing the bulk fluid motion. This corresponds to the mathematically ideal case of a uniform methane flux emanating from the diamond substrate with a purely axial flow. While uniform substrate injection may also prove difficult to implement in a real system, it is nonetheless instructive to consider the implications of this mathematically ideal case.

Conditions used by Dandy and Coltrin [6] for Fig. 3b of their paper were used to test the implications of substrate injection. Dandy and Coltrin report a predicted growth rate of about 73 μ/hr when the methane is introduced into the free-stream 1 cm above the substrate. Fig. 1 shows the predicted gas phase composition profile when the same amount of methane is introduced through the substrate instead. The predicted methyl radical concentration is extremely high at a mole fraction of 2×10^{-2}, leading to a predicted diamond growth rate of 340 μ/hr. Because the methyl radicals form immediately adjacent to the substrate, carbon incorporation rates are higher than for free-stream injection.

3. Conclusions

From the simulation work performed to date, the following conclusions may be drawn:

- Model predictions for hot-filament and dc arc-jet reactors agree qualitatively with previously published experimental and theoretical work
- The chlorine-activated reactor may be capable of higher growth rates than a dc arc-jet system, while using roughly half the energy
- Model predictions for a dc arc-jet system show that injecting methane through the substrate allows methyl radicals to form immediately above the substrate, resulting in an order of magnitude increase in the predicted diamond growth.

4. References

1. M.E. Coltrin, R.J. Kee, and G.H. Evans, "A Mathematical Model of the Fluid Mechanics and Gas-Phase Chemistry in a Rotating Disk Chemical Vapor Deposition Reactor," *J. Electrochem. Soc.*, **136**, 819-829 (1989).

2. D.G. Goodwin and G.G. Gavillet, "Numerical modeling of the filament-assisted diamond growth environment," *J. Appl. Phys.*, **68**, 6393-6400 (1990).

3. G.H. Evans and R. Greif, "Forced Flow Near a Heated Rotating Disk: A Similarity Solution," *Num. Heat. Trans.*, **14**, 373-387, (1988).

4. M.E. Coltrin and D.S. Dandy, "Analysis of diamond growth in subatmospheric dc plasma-gun reactors," *J. Appl. Phys.* **74**, 9, 5803 (1993).

5. M.E. Coltrin, R.J. Kee, G.H. Evans, E. Meeks, F.M. Rupley and J.F. Grcar, "SPIN (Version 3.83): A Fortran Program for Modeling One-Dimensional Rotating-Disk/Stagnation-Flow Chemical Vapor Deposition Reactors," Sandia National Laboratories Report, SAND 91-8003 (1993).

6. D.S. Dandy and M.E. Coltrin, "Relationship between diamond growth rate and hydrocarbon injector location in direct-current arcjet reactors," *Appl. Phys. Lett.*, **66**, (3), 391-393, (1995).

5. Nomenclature

η	axial coordinate	F	radial velocity	$\overline{C}_{pj}$	species j heat capacity
G	radial velocity	H	axial velocity	$\overline{C}_p$	mixture heat capacity
θ	temperature	P_a	pressure	$\overline{h}_j$	specific enthalpy
V_j	pressure	γ_j^g	gas reaction i rate	$\overline{\delta}_{jm}$	effect. binary diffusivity
γ_j^s	surface reaction i rate	M	mixture molecular wt.	$\overline{\delta}_j^T$	thermal diffusivity
M_j	species j molecular wt.	α	gas constant	$\overline{k}$	thermal conductivity
$\overline{\rho}$	density	$\overline{\mu}$	viscosity	$\overline{\delta}_{ij}$	multicomp. diffusivity
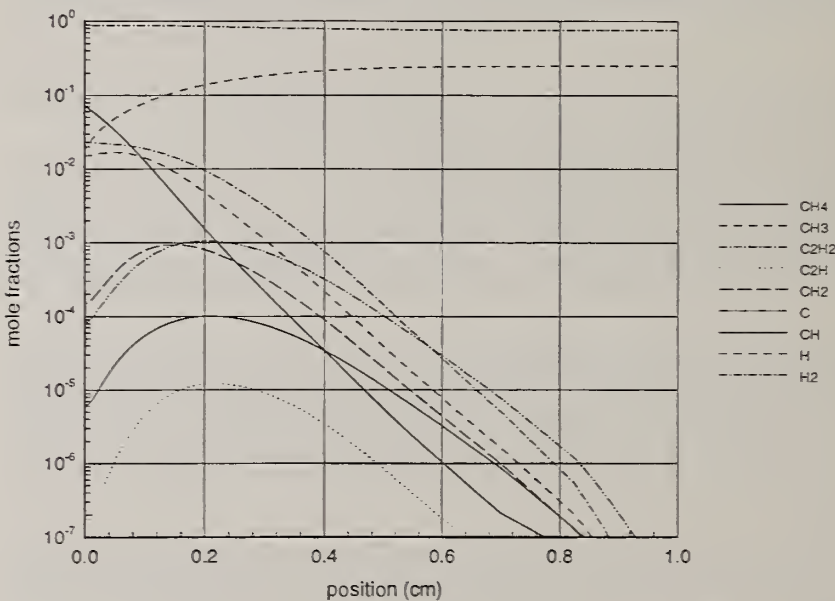
Figure 1 - Gas phase composition profile for a dc arc-jet reactor with substrate injection (substrate is at position 0.0)

MONTE CARLO SIMULATION OF ELECTRON BEHAVIOR IN AN ELECTRON CYCLOTRON RESONANCE MICROWAVE DISCHARGE USING CIRCULAR TM$_{11}$ MODE FIELDS

S. C. Kuo[1], and S. P. Kuo[2]

[1]Brookhaven National Laboratory, Building 815, Upton, New York 11973, USA
[2]Weber Research Institute, Polytechnic University, Farmingdale, New York 11735, USA

Key words: DLC, ECR, EED, sheath, Monte Carlo, TM$_{11}$

Abstract

Electron behavior in an electron cyclotron resonance (ECR) microwave discharge maintained by the TM$_{11}$ mode fields of a plasma-filled cylindrical waveguide has been investigated via a Monte Carlo simulation. Since this discharge has high degree of ionization (>1%), a self-consistent simulation of the plasma dynamics is required. The time averaged, spatially dependent electron energy distribution (EED) is computed self-consistently by integrating electron trajectories subjected to the microwave fields and the space charge field (induced by the ponderomotive and grad-B ($-\mu\nabla_r B$) forces and sheath), and taking into account electron-electron collisions and collisions with hydrogen atoms. At low pressures (~ 0.5 mTorr), the temperature of the tail portion of the EED exceeds 35 eV, and the sheath potential is -177 V. These results, which are about 70% higher than the previous ones (for the TM$_{01}$ mode [1]), suggests that the TM$_{11}$ mode is more effective than the TM$_{01}$ mode for ECR interaction.

1. Introduction

Plasmas generated by electron cyclotron resonance (ECR) interactions have been shown to be particularly suitable for the synthesis of hard diamond-like carbon (DLC) films. This is because the ECR plasmas have low background gas pressure (10^{-5} ~ 10^{-2} Torr at 298 K) but high ionization percentage (~ 10%) and large mean electron energy (up to 10 eV). In the past, numerical simulations of ECR plasmas have assumed either a functional form for the electron energy distribution (EED) or a free space field distribution without considering the plasma effect.

Including the plasma effect, it is shown in our recent work [1] that the microwave field distribution in an ECR plasma is quite different from that in vacuum. First, only TM modes are responsible for maintaining an ECR microwave discharge in a plasma-filled

cylindrical waveguide. Second, the microwave is strongly attenuated by the plasma in its propagation direction. Thus, the effective ECR interaction is confined in a thin layer (~ 1 mm) near the input port of microwave. Consequently, the EED is found to be spatially dependent and has to be evaluated self-consistently. In that work, the lowest waveguide mode, TM_{01} mode, is considered. However, the waveguide dispersion indicates that the TM_{11} mode can also exist in the same frequency range. Moreover, the TM_{11} mode is believed to have a more favorable field distribution for ECR interaction than that of TM_{01} mode. Hence, there is a need to explore the differences between the characteristic features of the ECR plasmas sustained by these two different mode fields. It is the objective of the present work.

2. Simulation Model

A. Particle dynamics
The emphasis in this study is on hydrogen-based plasmas for DLC film deposition [2]. Atomic hydrogen is taken as the background neutral species for the simulation. The steady state plasma density is an input parameter in the simulations. Initially, a sample group of electrons and ions (typically 5000 of each) is randomly seeded throughout the reaction chamber and given a Maxwellian distribution. The trajectory of each charged particle is determined from integration of the equations of motion between collisions. The outcome of the collision at the end of a free flight is determined from the cross-sections for electron-atomic hydrogen and electron-electron interactions, using standard Monte Carlo techniques [3]. Secondary electron-ion pairs generated in ionizing collisions are taken into account. When a charged particle reaches an insulating boundary, it either remains there or bounces back into the plasma, depending on the sticking probability. This probability, which has been assumed to be energy independent, is an input parameter in the simulation.

The simulation is divided into time sections of duration equal to the microwave period. At the end of the section, the mean electron energy, the average momentum exchange frequency, v_m, and the surface charge density, ρ_s, are calculated. These variables are then used to calculate the microwave and space charge fields (in the bulk and sheaths) for the next simulation period. It is in this sense that the simulations are self-consistent. The computation is carried out over a sufficient number of periods to ensure that the final results are not sensitive to the choice of initial conditions.

B. Field analysis
The ECR processing chamber is modeled as a longitudinally magnetized, homogeneous plasma-filled cylindrical waveguide. Under the cyclotron resonance condition, $\omega = \omega_c$ (where ω and ω_c are the wave frequency and electron cyclotron resonance frequency respectively), this waveguide can only support TM mode. Thus, TM_{11} mode is considered for the most effective ECR interaction. Representing the plasma as a lossy, anisotropic dielectric characterized by a dielectric tensor

$$\tilde{\varepsilon}_R(\omega = \omega_c) = \begin{bmatrix} \varepsilon_\perp & \varepsilon_x & 0 \\ -\varepsilon_x & \varepsilon_\perp & 0 \\ 0 & 0 & \varepsilon_{\prime\prime} \end{bmatrix}$$

where,

$$\varepsilon_\perp = 1 - \frac{\omega_p^2}{\upsilon_m^2 + 4\omega^2} + i\frac{\omega_p^2(\upsilon_m^2 + 2\omega^2)}{\omega\upsilon_m(\upsilon_m^2 + 4\omega^2)}$$

$$\varepsilon_x = \frac{2\omega_p^2\omega}{\upsilon_m(\upsilon_m^2 + 4\omega^2)} - i\frac{\omega_p^2}{\upsilon_m^2 + 4\omega^2}$$

$$\varepsilon_{\prime\prime} = 1 - \frac{\omega_p^2}{\upsilon_m^2 + \omega^2} + i\frac{\omega_p^2\upsilon_m}{\omega(\upsilon_m^2 + \omega^2)}$$

and $\omega_p = (n_e e^2/\varepsilon_o m)^{1/2}$ is the electron plasma frequency, the field components of the TM$_{11}$ mode of the waveguide are derived to be

$$E_z = E_0 J_1(pr) \cos\phi \, e^{-\alpha z} \cos(\beta z - \omega t)$$

$$E_r = -(E_0/4p\gamma) \, e^{-\alpha z} \{J_0(pr) [(\varepsilon_{\prime\prime}/\varepsilon_\perp) \, \gamma^2 \cos(\beta z + \phi - \omega t) + p^2 \cos(\beta z - \phi - \omega t)] \\ - J_2(pr) [(\varepsilon_{\prime\prime}/\varepsilon_\perp) \, \gamma^2 \cos(\beta z - \phi - \omega t) + p^2 \cos(\beta z + \phi - \omega t)]\}$$

$$E_\phi = (E_0/4p\gamma) \, e^{-\alpha z} \{J_0(pr) [(\varepsilon_{\prime\prime}/\varepsilon_\perp) \, \gamma^2 \sin(\beta z + \phi - \omega t) - p^2 \sin(\beta z - \phi - \omega t)] \\ - J_2(pr) [(\varepsilon_{\prime\prime}/\varepsilon_\perp) \, \gamma^2 \sin(\beta z - \phi - \omega t) - p^2 \sin(\beta z + \phi - \omega t)]\}$$

$$H_r = E_0 (\omega\varepsilon_0\varepsilon_{\prime\prime}/2p) \, e^{-\alpha z} [J_0(pr) \cos(\beta z + \phi - \omega t) - J_2(pr) \cos(\beta z - \phi - \omega t)]$$

$$H_\phi = -E_0 (\omega\varepsilon_0\varepsilon_{\prime\prime}/2p) \, e^{-\alpha z} [J_0(pr) \sin(\beta z + \phi - \omega t) - J_2(pr) \sin(\beta z - \phi - \omega t)]$$

where E_0 is the field amplitude, $i\gamma = \beta + i\alpha$ is the complex propagation constant, and p is the transverse wavenumber. E_0 is determined from the input microwave power using Poynting's theorem. γ is determined from the dispersion relation, $\gamma^2 = (\varepsilon_\perp / \varepsilon_{\prime\prime}) (p^2 - 2 k_0^2 \, \varepsilon_{\prime\prime})$, where $k_0 = \omega/c$ is the free space wavenumber, with c being the speed of light; and p is determined from the boundary condition that $E_z = 0$ at the transverse boundary, $r = a$ (where a is the radius of the waveguide), i.e. the first root of the equation, $J_1(pa) = 0$, where J_1 is Bessel function of order one.

In addition to the microwave fields, a space charge field, $\mathbf{E}_{sc}$, is also present in the plasma. It is the results of nonuniform distribution of microwave power flux (ponderomotive force) and background magnetic field (grad-B force), and the boundaries (sheaths). $\mathbf{E}_{sc}$ is determined self-consistently in the simulation.

3. Results and Discussion

Consider an ECR reactor having a background pressure P = 0.5 mTorr and a steady state plasma density $n_e = 10^{11}$ cm^{-3}. First, the dispersion relation of the TM$_{11}$ mode is plotted in Fig. 1. It shows that the TM$_{11}$ mode has a cutoff frequency f_{cutoff} = 3.802 GHz. Moreover, due to the plasma, TM$_{11}$ mode can also propagate in the waveguide for $f < f_p$ = 2.846 GHz. For a better input coupling, f = 3.9 GHz is chosen for the simulation. The EED is computed for 300 W input microwave power (same as the previous case using TM$_{01}$ mode [1]) and the result is presented in Fig. 2. The EED is found to be spatially homogeneous in the axial direction due to large electron mean free path. It is, similar to the previous result using TM$_{01}$ mode, also characterized by two temperatures, T_1 = 8.4 eV and T_2 = 35.7 eV. T_2 is increased considerably from the previous result of 21 eV. It confirms that the TM$_{11}$ mode is more effective for electron cyclotron resonance interaction than the TM$_{01}$ mode. The sheath potential in the present case is about -177 V which is also increased proportionally from the previous result of -96 V. Thus, the high energy tail (100 eV < E < 180 eV) which is depleted in the previous case is now confined by the potential barrier of the sheath.
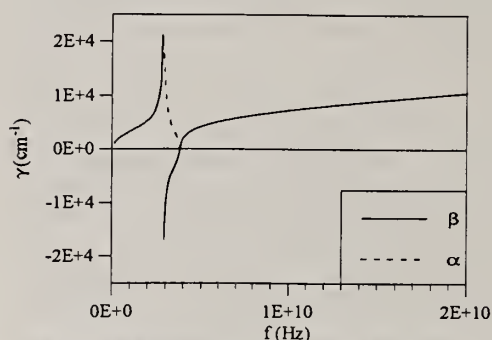
Fig. 1 Dispersion relation for TM$_{11}$ mode. P = 0.5 mTorr. f_{cutoff} = 3.802 GHz
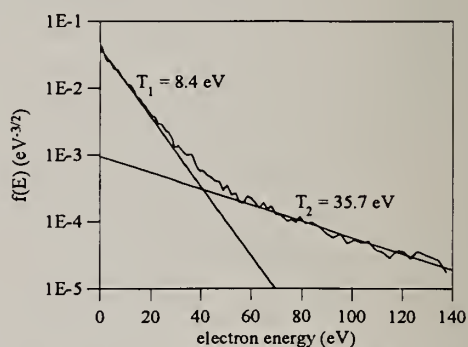
Fig. 2 Electron energy distribution in the ECR reactor for P = 0.5 mTorr. The EED can be characterized by two electron temperatures, T_1=8.4 eV and T_2=35.7 eV.

The present result has demonstrated that the TM$_{11}$ mode is indeed more effective than the TM$_{01}$ mode for electron cyclotron resonance interaction. Plasma produced by TM$_{11}$ mode fields has a larger mean electron energy, and therefore, is more desirable for the application of synthesizing the hard diamond-like carbon films.

Acknowledgments

References

1. S. C. Kuo, E. E. Kunhardt and S. P. Kuo, J. Appl. Phys. **73**, 4197 (1993).
2. S. C. Kuo, E. E. Kunhardt and A. R. Srivatsa, Appl. Phys. Lett., **59**, 2532 (1991).
3. E. E. Kunhardt and Y. Tzeng, J. Comput. Phys. **67**, 279 (1986).

FINITE-ELEMENT MODELING OF A HOT FILAMENT CVD DIAMOND DEPOSITION REACTOR OPTIMIZED FOR LARGE AREA DEPOSITION

Richard Ulrich, Ajay Malshe, Matt Gordon, Jim Palmer and Jun Li

High Density Electronics Center
3202 BEC
University of Arkansas
Fayetteville, AR   72701
(501) 575-5645
FAX: (501) 575-7926
rku@engr.uark.edu

key words: deposition, hot filament, modeling, scale-up, uniformity

Abstract

Gas-phase chemical reactor optimization and scaleup principles are being used to quantify the factors that most affect film deposition extent and uniformity in an HFCVD configuration. This information is being applied to the design and construction of a low-cost reactor to coat two to three inch planar substrates and, later, 3-D tool inserts with better than 10% uniformity. Finite element modeling is being used to evaluate the flow profiles, reactant distribution, and thermal environment for input to the reactor design process. Novel design factors include the use of a recycle stream to increase reactant utilization and effective flowrate, a wide-area filament array for gas dissociation, a substrate-down configuration to avoid convection cells, and a customized gas flow profile to enhance film uniformity.

1. Introduction

Most previous research on hot filament CVD (HFCVD) diamond deposition reactors has centered on the production of high-quality adherent films with less attention paid to process scaleup and commercialization. The purpose of this project is to apply engineering scaleup and optimization principles to this sort of reactor for the purpose of developing the ability to coat large scale 2-D and 3-D substrates with homogeneous adherent diamond coatings. Except for the combustion flame, HFCVD is considered to be the simplest of

all methods and can produce high linear diamond growth rates. Due to its low equipment requirements and operating costs we chose HFCVD as a base system for developing novel methodologies such as gas recycle loops, filament arrays and actively cooled substrates to "intelligently" control the manufacturing process. We are building a HFCVD reactor for this purpose and, during the time that the general layout of the reactor system is under construction, we are conducting finite element modeling of gas velocity, temperature and reactant profiles in order to fine-tune the design specifics.

2. Design Issues

The reactor chamber is stainless steel with a quartz window. The steel construction enables us to operate at much higher pressure (up to 150 torr) than we could in a bell jar since there is a reduced hazard of chamber breakage and the subsequent formation of an explosive gas mixture.

Recycle Loop - to increase both the reactant utilization and the internal flow velocity. The recycle loop is indicated because the reactant conversion is very low per pass and because fluid dynamics modeling and published experimental results show that higher gas velocity results in faster diamond deposition. Both of these issues should benefit from a high-ratio recycle loop. We will also run the reactor on total recycle to study the time-dependent buildup of reactant products and intermediates and to see what effect they have on deposition rate and film composition. In this manner we hope to achieve insights into both the fastest optimization path and the basic reaction chemistry.

Substrate Down Configuration - to minimize the effects of thermally-driven convective cells on internal gas recycle stagnation and to eliminate particulates from the substrate. Finite element modeling is being used to reveal the location and intensity of these cells.

Large Area Filament Array - to provide consistant dissociation of reactant gases over a wide-enough area to provide a uniform coating to a 2" substrate. The filament array must be constructed to provide a wide but flat high-temperature zone in order to dissociate the reactant gases coming out of the entrance nozzle. Since tungsten at 2500 K radiates about 90 W/cm^2, the total surface are of the heater filaments must be kept under about 10 cm^2 in order to keep electrical and cooling demands at a manageable level. Therefore there is a tradeoff between the spatial extent of the heater and the total power that can be provided and removed. We have looked at punched foil, microwire gauze, deposited cross hatch patterns and other heater configurations to arrive at a 2.5 inch square design that will run at less than one kilowatt while providing a high-temperature zone over 36 cm^2.

Cooled Stage - to enable the temperature and temperature distribution of the deposition surface to be controlled instead of having it fixed by radiative heating from the filaments. Active cooling will also be necessary due to the high heat flux from the wide area filament array.

Gas Entry Nozzle - will be either a divergent cone or a novel gas reactant dispersion configuration of our own design. The results of the finite element modeling, described below, are enabling us to first establish the optimal gas flow profile in the vicinity of the substrate, and to then construct a gas dispersion nozzle to give us that profile. Experiments and modeling in our lab indicate that a divergent cone can provide very flat profiles over the 2 - 3 inches we need them, but a flat profile may not be optimal. We have designed a nozzle that can be configured to provide almost any flow velocity profile desired and we will employ this if the modeling shows that such a customized profile is necessary. This nozzle is currently under patent review at the University
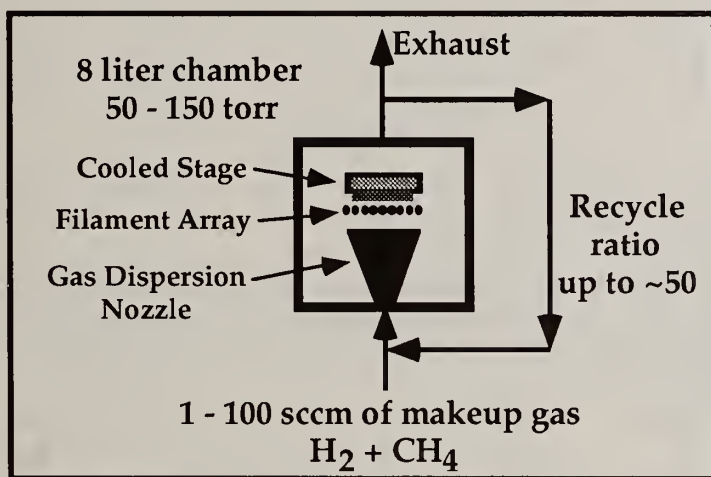
3. Finite Element Modeling

Modeling of gas velocity, reactant concentration and deposition profiles with FLUENT are providing information on the specific requirements of chamber design necessary to achieve wide-area homogeneous films. In the example below a flat velocity profile containing 0.01% reactive species was directed at a 2″ diameter substrate under mass transfer control. The deposition rates are normalized for diamond. As expected, the results show higher deposition rates at the substrate edges than at the middle due to the higher velocities there. Similar modeling has shown that the deposition rate is proportional to reactant concentration, as would be expected for a mass transfer controlled system, and that the total pressure has little effect due to equal and opposite tradeoffs between reactant concentration and gas phase diffusivity.
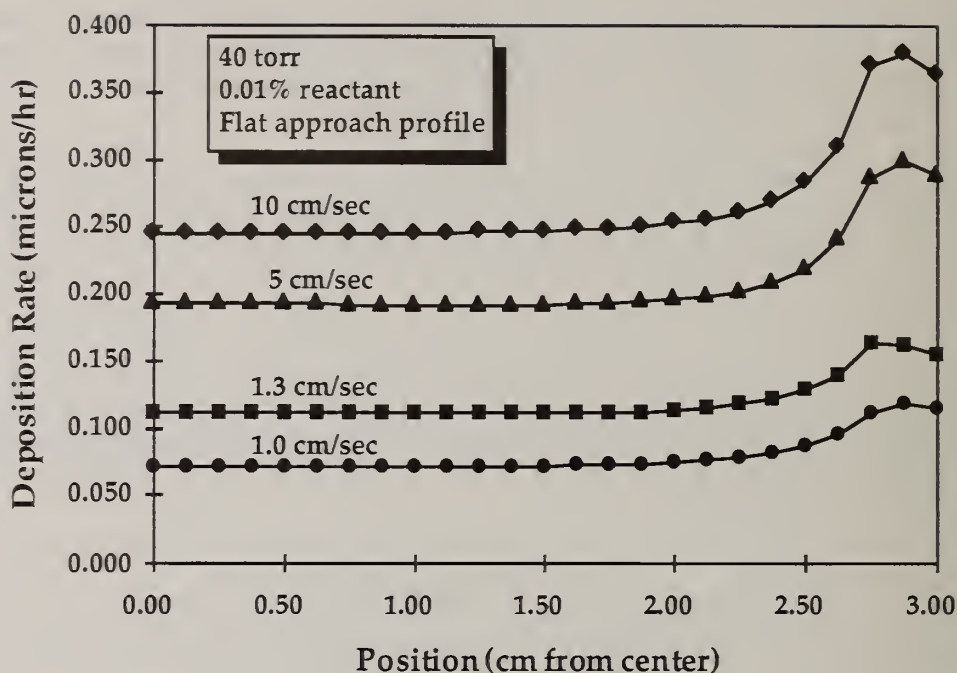
There does not seem to be any single software package capable of fully modeling an HFCVD system. FLUENT does an excellent job of mapping gas flow and temperature profiles but can only handle a total of 10 species and 10 reactions. We are using FLUENT to map out flow and temperature then will combine these results with CHEMKIN and with some of our own in-house software to model the homogeneous and heterogeneous reactions.

4. Future Plans

Reactor design/construction will proceed in parallel with computer modeling to ensure that we arrive at as close to an optimal configuration as possible with our first operational hardware. Initially we will employ a single filament to characterize the uniformity and composition of the resulting film as a function of position away from the filament. Then we'll go to two filaments, varying their separation in order to determine the maximum distance to give film uniformity in between. Finally, these results will be used in conjunction with thermal and flow modeling to implement the filament array and achieve wide-area deposition. Meanwhile, the effects of increased gas velocity and recycled intermediate reaction products will be explored by utilizing the recycle loop at various ratios. Once we are producing high-quality, uniform films over a two or three inch planar substrate we will turn our attention to depositing films over 3-D tool inserts.

CHEMICAL STANDARDIZATION OF THE SURFACE OF DIAMOND

E. Smirnov, V. Gromov, P. Connoly

Technological Institute, Moskovskij pr.26, 198013, St. Petersburg, Russia

Key words: chemical modification, diamond, surface

Abstract

The modern state of the investigation of the chemical transformations with participation of diamond surface centers is considered. The features of the homolytical and heterolytical processes on the diamond surface of with participation of the reagents of different electronic and geometrical structures (oxygen, halogens, hydrogen, ammonia, halogenides of elements) with forming bonds C-E and C-O-E is analyzed. The identification of obtained compounds and their properties determination was carried out by method x-ray photoelectron spectroscopy.

1. Introduction

There is a great interest to the chemical transformations with participation of surface centers of diamond at present time. It is connected with diamond materials perspectives in high temperature electronics, and also in manufacturing of new generation of high quality tools with different types of matrixes. The diamonds with uniform layer of chemically inoculated groups with different electronic and geometrical structure are interesting also in theoretical aspect.

2. The types of reactions on the surface of diamond

The hemosorption transformations with participation of diamonds surface centers can be related to homolytical and heterolytical processes. Among studied reactions with participation of surface functional groups of diamond the reactions with participation of radicals - homolytical processes of combination (A_{dH}) and heterolytical - reactions of nucleophilic and electrophilic substitution (S_N, S_E) were determined. The possible types of these transformations with participation of diamond surface centers may be presented by the following scheme [1]:

$$
\begin{array}{c}
H \quad \overset{\nearrow S_E}{\quad} \quad S_N \quad A_{d_H} \\
O \quad Hal \\
| \quad | \\
\equiv\!\!\!C\!\!\equiv\!\!\!C\!\!\equiv\!\!\!C\!\!\equiv \\
/|\backslash C /|\backslash C /|\backslash \\
/\backslash \quad /\backslash
\end{array}
$$
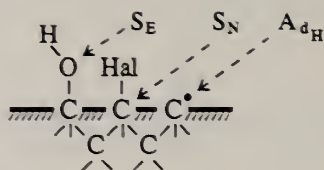
3. Reactions with attacks to carbon atoms
3.1. Homolytical combination (A_{dH})

Real surface of natural and synthetic diamonds (crystals, films) contains oxyfunctional groups identified by method of X-ray photoelectron spectroscopy as C-O, C-OH -COOH [2]. The thermodesorption of these groups in the interval 20-700°C is characterized by giving off CO and CO_2 with maximums at 500-600°C. Under conditions of vacuum and helium current during thermodesorption of CO_2 and CO, the obtaining of surface carbon σ-radicals of diamond (g-factor = 2.0027) was proved by method of ESR [3]. Diamond paramagnetism is changing in accordance with the changing of thermodesorptional spectras, maximum quantity of obtained radicals ($\geq C^{\bullet}$) up to 2.5 $\mu mol/m^2$. The following treatment of the diamond by O_2, Cl_2 or Br_2 leads to ruin of the radicals, resulting in new functional groups (C-O, C-Hal) formation on the surface. The quantity of these combination groups is a function of the synthesis temperature and correlates with the thermodesorption curves and the data of ESR (fig.1)

3.2. Heterolytical nucleophilic substitution (S_N)

The surface compounds containing the groups C-E (E :-H,-CH_3,-OH,-N) were obtained by substitution of the galoid centers of diamond in reactions with H_2,CH_4,H_2O and NH_3. The kinetic isotherms of these reactions are described by equation $\theta = a \ln t + c$ for unhomogeneous surface with activation energy changing in the interval from 29kJ/mol (at $\theta \rightarrow 0$) to 71 kJ/mol (at $\theta=0.5$). The diagram of quantitative substitution of groups versus temperature is shown at fig.2

4. The reactions with attacks to oxygen atom of oxyfunctional groups.

Complex halogenides elements or elementorganic compounds (III-YI groups) synthesis in reactions of electrophilic substitution proton (S_E) in diamond surface layer oxyfunctional groups C-OH, -COOH permits to carry out local modification of the surface. The kinetics of that type reactions is described by equation $-\ln(1-\theta) = kt$ for the model of homogeneous surface. The hemosorption of these reagents takes place under milder conditions starting with room temperature, the activation energy does not exceed 10-20kJ/mol in range of 20-200°C.
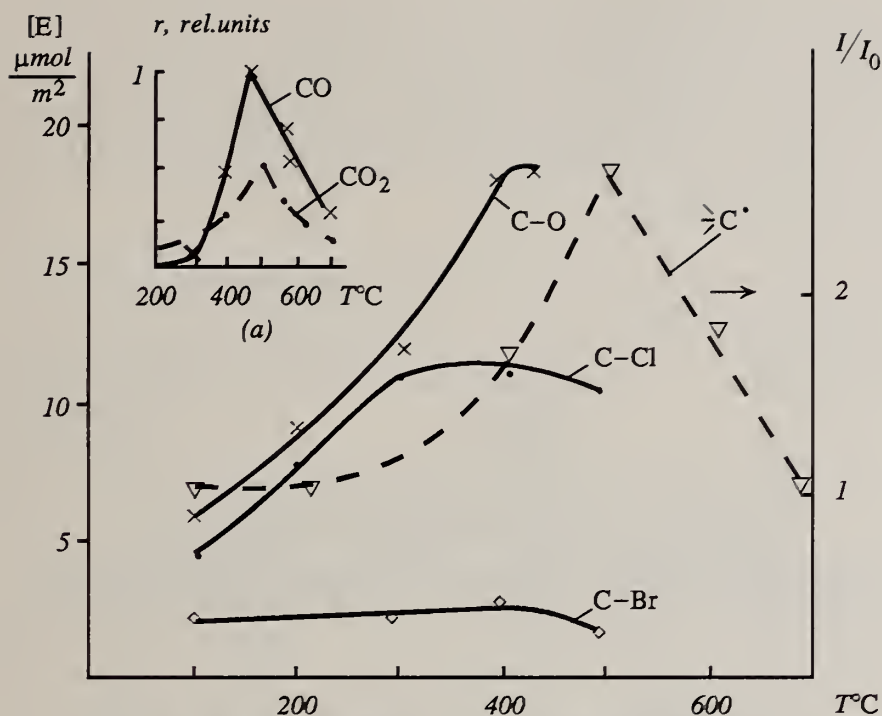
Fig.1. Relative intensity ESR(I/I_0) and concentration [E] of
functional groups, (a) - relative rate of thermodesorbtion.
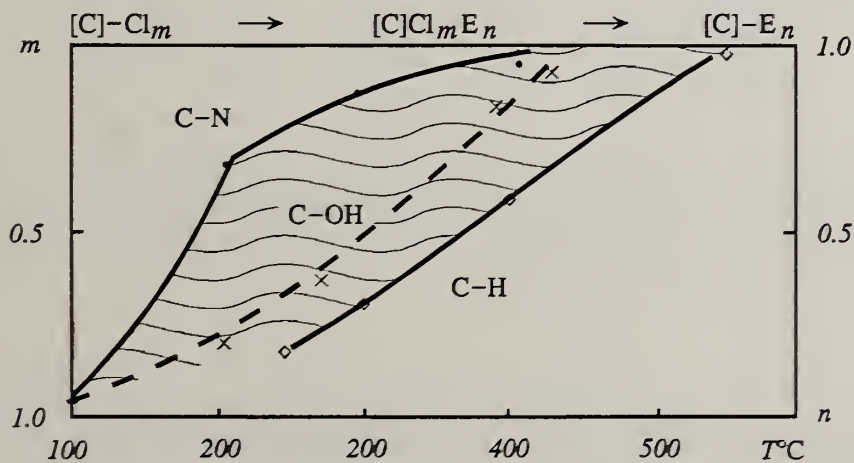
Fig.2. The reaction of substittion (S_N) diagram.

The value of element-haloid group hemosorption depends on the amount of proton containing oxyfunctional groups and changes in the range of 0.1-$5.0\,\mu\text{mol/m}^2$. The calibration and the analysis of basic lines C1s, 01s and elements-modifiers lines were carried out by method of X-ray photoelectron spectroscopy. The composition, nature of bond and energy characteristics of obtained compounds are shown in the table. By means of ellipsometry [4] it was shown that the thickness of the coverings corresponds to one monolayer.

Table. Composition of the monolayer covering after diamond surface modification.

Functional groups	Reacting substance	Product	Max concentration of element, $\mu\text{mol/m}^2$	x-ray photoelectron spectroscopy		
				The line	Bond energy, eV	Relation of atom concentration E/C 10^2
$\geqslant$C$^\bullet$	O_2	C-O	19.0	01s	532.0	10.0
	Cl_2	C-Cl	11.0	Cl2p	199.4	2.5
	Br_2	C-Br	3.0	Br3p	184.8	0.7
$\geqslant$C – Hal	H_2	C-H	11.0		-	-
	H_2O	C-OH	11.0	01s	532.0	3.0
	NH_3	C-N	11.0	N1s	399.0	2.5
C – OH −COOH	Al_2Br_6	C-O-Al	-	Al2p	73.6	1.9
	BCl_3	C-O-B	2.0	B1s	191.6	1.6
	$TiCl_4$	C-O-Ti	2.2	Ti2p$_{3/2}$	458.2	1.9
	PCl_3	C-O-P	1.0	P2p	132.7	0.7
	$VOCl_3$	C-O-V	1.0	V2p$_{3/2}$	516.8	0.7
	CrO_2Cl_2	C-O-Cr	3.5	Cr2p$_{3/2}$	576.5	4.2
	$MoCl_5$	C-O-Mo	-	Mo3d$_{5/2}$	231.9	0.2
	WF_6	C-O-W	1.0	W4d$_{5/2}$	246.7	0.6

The considered processes of diamond surface modification by heteroatoms of different electronic nature opens the perspectives of controlled diamond dopping in synthesis of the semiconductor structures, as well as testing and chemical standartization of diamond surface.

References

1. Smirnov E., Diamonds: preparation, property and application L., LTI, 1984 p.73.
2. Lukjanov I., Smirnov E. et al // J. Theor. and experimental chem., 1989, N4, p.490.
3. Abizov A., Smirnov E. et al // J. Chem. physics, 1992, v.11, N7, p.1002.
4. Gromov V. Introduction to ellipsometry. L. LGU, 1986, p.191.

COMPOSITES AND
DIAMOND-LIKE CARBON

DIAMOND-LIKE CARBON FOR BIOMEDICAL APPLICATIONS

R S Butter and <u>A H Lettington</u>

J J Thomson Physical Laboratory, University of Reading, Whiteknights, P O Box 220, READING RG6 2AF, UK

Keywords: applications, biocompatibility, DLC

Abstract

Early studies involving the implantation of DLC-coated pins into sheep showed good bonding of the tissue to the DLC, indicating its value as a biocompatible coating. During the last few years, interest in this material has been rekindled, with the initiation of a number of *in vitro* and *in vivo* studies. The current state of published work in this area is reviewed, and a wide variety of specific applications for DLC coatings in the field of biomaterials are discussed.

1. Introduction

An implant may be described as a material introduced into the body as a replacment for biological tissue, and which attempts to fulfil the functions of that tissue. Such functions may be mechanical, for example, as in heart valves and artificial joints, or supportive as in orthopaedic plates and pins. The materials used must therefore be carefully tailored to the specific application, to optimise mechanical performance, durability and biocompatibility.

Stainless steel, cobalt-chrome alloys, and titanium and its alloys, particularly with aluminium-vanadium have been used widely used in orthopaedics, where their mechanical properties render them suitable for load-bearing [1,2,3]. In spite of being some of the most corrosion resistant alloys available, all have a finite corrosion rate, and the presence of even small amounts of corrosion products in surrounding tissues can be harmful [4,5], leading to the retraction of soft tissues from the metal, presenting a site for infection [6]. The mismatch in mechanical properties, such as stiffness and modulus, between bone and metal can lead to bone resorption and loosening [3].

The success of polymeric materials in the field of biomedical devices and implants relies on the wide range of properties which can be achieved by manipulation of both

bulk and surface structures [7,8,9]. However, even in the presence of suitable fillers, the mechanical properties render many polymers unsuitable for certain applications. In addition, without surface modification, severe inflammatory reactions can occur, and when used in blood contacting devices require the administration of anticoagulants to prevent blood clotting [10].

Therefore an ideal solution might be to match the bulk material of an implant to the mechanical requirements, and combine this with the superior biocompatibility of carbon in the form of a coating on the implant surface.

As the element at the core of all organic systems, it is likely that carbon should possess good biocompatible properties. Unlike metals, no ions can be leached out, and even particulate carbon can be removed by the lymphatic system without initiation of an autoimmune response [11]. Tissue adheres well to carbon implants, and it appears capable of sustaining a durable interface with living tissue. In the presence of blood, protein is adsorbed onto the carbon surface, rendering it non-thrombogenic, suggesting possible cardiovascular applications [12]. Glassy carbon, a form of pyrolytic carbon, has been used extensively for heart valves [13], and the blood compatibility of pyrolytic carbon coatings has also been promoted in recent years [14,15]. Tubular prostheses produced from fibres coated with carbyne, a polycrystalline carbon with oriented layer structure, have shown excellent thromboresistance in *in vivo* tests [16,17]. Carbon fibre implants promote rapid ingrowth of tissue for ligament repair [18]. Thus carbon, in its various forms, is well established in terms of a biocompatible material.

Diamond-like carbon (DLC) is chemically inert, hard, with good abrasion resistance and low friction. It adheres well to both metals and some plastics, with the aid of an intermediate bonding layer in some cases. These properties, combined with good biocompatibilty would appear to make it suitable as a coating for biomedical implants.

2. In vitro studies of DLC biocompatibility

Preliminary experiments [19,20] with *in vitro* tests using mouse peritoneal macrophages and mouse fibroblasts have shown an encouraging degree of biocompatibility. It was found that there was no difference in levels of lactate dehydrogenase, an enzyme which gives a measure of cell integrity, between cell cultures exposed to DLC coatings, and control specimens, showing that DLC does not adversely affect the cells in culture.

In this work by Thomson et al '91 [19], and subsequent work by Allen et al '94 [21], investigations have been directed towards the use of DLC as a wear-resistant coating on total joint replacements. The cell lines used were chosen as representative of the tissues in this situation; macrophages are actively phagocytic, that is, ingest debris

and foreign material as part of the immune response; fibroblasts are large, irregularly shaped cells which produce the material of connective tissues in the body; and osteoblasts are bone forming cells. The results of cytotoxicity testing using LDH assay for these three cell types showed no statistically significant differences between the DLC-coated and control samples. Optical and scanning electron microscopy revealed normal cellular morphology, and cells were observed to grow faster on the DLC than on the uncoated glass control surfaces. This demonstrates that DLC provides a non-toxic surface on which cells of these three types can attach, grow and divide in a normal manner *in vitro*.

The performance of DLC films on polystyrene and PMMA, produced by a low-temperature plasma-CVD method has also been investigated. These samples showed considerable surface texture on a scale of 0.1 - 1 μm, but were otherwise comparable with harder coatings produced at higher temperatures on steel substrates. Results from Kenacid Blue Cytotoxicity testing with murine fibroblasts showed the cells grew well in both control (uncoated) and DLC-coated culture plates. The attachment of cells to the carbon-coated specimens was considerably enhanced at 24 hours, with comparable values for the subsequent growth rates for the control and DLC-coated samples. Under SEM and atomic force microscopy the cells exhibited normal attachment and growth [22,23].

In order to improve the adhesion of DLC to some substrate materials, an intermediate bonding layer can be used, and is discussed in further detail later. *In vitro* work, using the same cell lines as mentioned above, has shown that DLC films deposited onto glass substrates with an intermediate layer of amorphous hydrogenated silicon also show no evidence of toxicity in the cell culture environment [24].

Other in vitro studies have used human ML-1 haematopoietic myeloblasts, and human embryo kidney (HEK 293) cells. ML-1 cells are immature myeloblasts, which can become differentiated into monocytes or macrophages, as a result of environmental conditions. no cell differentiation was observed, providing a sensitive indication that the DLC has not invoked any toxic response. For both cell types, cell growth studies showed no statistically significant difference in the growth rate between the DLC-coated and uncoated culture dishes [25]. Cell viability studies also showed no adverse effect of the DLC coating, and microscope images revealed normal cellular morphology. The HEK cells require a surface to which they can attach readily, to provide a matrix for cell growth. Neither delayed attachment or cell detachment was observed in this test, confirming that, at least in vitro, DLC provides a biocompatible surface.

3. In vivo studies of DLC biocompatibility

Early studies of the *in vivo* compatiblity of DLC were carried out by a group in Cardiff, and involved the implantation of DLC-coated orthopaedic pins through soft

tissue and into the femurs of sheep. The tissue was observed to bond well to the DLC-coated pins considerably better than to uncoated stainless-steel pins [26], although this work has not been reported in detail.

More recently, a group in Poland has made considerable progress in coating orthopaedic screws with DLC for clinical use, after introducing a relatively high pressure (100 - 300 Pa / 750 - 2000 mtorr) RF plasma technique [27,28]. Initial tests showed the coating was able to withstand repeated screwing into bone. Storage in Tyrod solution at temperatures up to 80°C did not reveal any traces of surface degradation for periods of over 3 months. When DLC coated discs were implanted subcutaneously, intramuscularly and into tibial bone, a thin collagenous capsule was formed, with no evidence of corrosion products or chronic inflammatory reaction over the 52 week test period [29,30]. Clinical trials are ongoing.

4.   Use of DLC in total joint prostheses

The use of DLC as a wear-resistant coating on bearing surfaces of artificial joints is suggested by its hardness and excellent tribological properties, which have been reviewed [31,32]. Properties such as the fracture strength, hardness and coefficient of sliding friction depend on the deposition method and parameters [33], and the coefficient of friction also depends on the environmental conditions of sliding [34,35,36]. Until recently, most DLC friction and wear testing has been carried out in air or gaseous environments, with hard counterface materials such as sapphire, Si_3N_4 and alumina. An exception is the observation of transfer films of PTFE onto DLC for dry sliding contact [37]. Care must be taken that friction and wear testing are representative of the intended application.

The majority of interest regarding DLC has been in coating the femoral head (see Fig 1). The smooth DLC-coated surface would be less susceptible than the relatively soft uncoated metal to third body wear, caused by particles of PMMA bone cement either loose or embedded in the acetabular component. This in turn should reduce the generation of ≤ 1 micron-sized wear debris of polyethylene (PE) which leads to a severe reaction on a cellular level. This smaller PE wear debris is initiated by surface asperities and increased surface roughness of the counterface [38].

Some recent studies [39,40] have addressed the issue of providing a more appropriate environment, conducting wear tests in saline, bovine serum and Ringer's solution. Reciprocating wear tests have been performed on DLC coatings produced by our group at Reading. Testing was carried out at Dept Mechanical Engineering, University of Leeds, with ultra-high molecular weight polyethylene (UHMWPE) pins sliding against DLC-coated stainless steel plates in bovine serum. Results show that the DLC-coated plates fared considerably better than uncoated stainless steel under four separate testing regimes [41,42].

Fig 1. DLC coating of the femoral head of a hip prosthesis

The adhesion of DLC to commonly used implant materials such as stainless steel and Co-Cr alloy is poor, and the inclusion of a suitable intermediate layer between the DLC film and the substrate can have a beneficial effect on coating adhesion [39]. Reactively sputtered silicon carbide has been reported as a successful interlayer for improving adhesion of DLC to Ti-6Al-4V [43], whilst multilayers based on titanium have been succesful for chromium/iron substrates [44]. Amorphous hydrogenated silicon has also been used successfully as a bonding layer for a variety of substrate materials [26]. For DLC coatings on stainless steel substrates with silicon interlayer, some coating degradation has been observed on exposure to biologically relevant fluids [45]. However, whilst damage in a saline solution was significant, a considerably lesser effect was observed for specimens treated in 40% serum in saline. Saline is a more virulent corrosive than serum or other body fluids, and it is possible that the damage was caused by the high proportion of saline in this solution, rather than the serum itself. In addition, the surface roughness of the substrates used for this work was comparable with the film thickness, and perhaps 10^3 greater than that of hip prostheses for clinical use. A decrease in adhesion of DLC has previously been observed on increasing substrate surface roughness [46], and substrate roughness is known to increase stress [39]. Some concern has also been given to the possible release of particulate silicon carbide, should the coating delaminate. It has been shown that in sufficiently high levels, particulate silicon carbide produces a toxic reaction [47], but so do many materials in particulate form which are considered

biocompatible in their bulk forms. Of particular note is the generation of particulate debris of UHMWPE from the acetabular component of prosthetic joints [48,49]. In addition, silicon carbide composites have been used in all-graphite/silicon carbide total hip prostheses [50], and as discussed further below, for blood contacting applications [51]. At present, silicon remains a viable choice of intermediate bonding layer for DLC coatings.

5. Blood-contacting environments

DLC may also be suitable for some blood-contacting situations, such as artificial heart valves. Here, the materials used must be non-thrombogenic, whilst at the same time, must be capable of withstanding turbulent flow conditions, and, literally, a lifetimes' worth of cycles without failure or unacceptable wear. Valves fabricated entirely from glassy carbon have been widely used for the last couple of decades [11], but problems remain with regard to the mechanical properties and durability of these valves. Patients with such devices require pharmocological anticoagulation treatment for life [52].

NiCr18 stainless steel and TC4 alloy satisfy the mechanical requirements for a heart valve, and DLC-coated specimens have been investigated in ex-vivo experiments with whole blood. Haemoglobin concentration and platelet consumption tests showed that the DLC-coated metals compared well with LTI carbon, both of which appeared better than glass or uncoated stainless steel [53]. These initial studies show DLC to be a potential biomaterial for this application.

The associated material, a-Si/C:H has also been advocated as a suitable coating for cardiovascular applications, on the basis of electrochemical considerations. *In vitro* studies, followed by autoradiography as a probe for DNA synsthesis activity showed no difference between the control and a-Si/C:H samples. It was concluded that a tailoring of the electronic properties of a-Si/C:H by altering the deposition parameters can improve haemocompatibility, and render semiconductor materials suitable for the coating of artificial heart valves [51].

The use of DLC as a composite barrier for a glucose enzyme electrode has also been reported [54]. Here, a polycarbonate microporous membrane forms a part of a sensor intended for use in contact with blood. The membrane was coated on one or both sides with DLC to a thickness of up to 50 nm, and were assessed in terms of their porosity, and the permeability coefficients for glucose and oxygen. The permeability coefficient for both glucose was found to progressively decrease as coating thickness increased, allowing tuning of the membrane permeability. In addition to a reduction in biofouling, an extension to the range of linearity of the sensor from glucose concentrations of 5 to > 80 mM was achieved.

6.   Other biomedical applications for DLC

In addition to its potential use as a biocompatible coating on implant materials, DLC also possesses a low coefficient of friction. A potential medical application of this property is the use of DLC coatings as a coating on needles for opthalmic use. Here, the surgeon needs to suture the corneal region, whilst causing a minimum distortion of the eyeball. Experiments involving measuring the force required for a needle to penetrate the cornea of pigs' eyes have shown that a DLC coating reduces the force required for penetration by around 30% [55]. The dark brown/black colour would be of further benefit, by reducing the reflections from operation microscope lights.

References
1   T P Hoar and D C Mears 1966 *Proc Royal Soc A294* 486-510
2   D F Williams 1980 *Phys Med Biol 25(4)* 611-636
3   D F Williams   1987 *J Mat Sci 22*   3421-3445
4   M F Viegas, L M Abrantes & J Lecoeur 1990 *J Mat Sci: Mater in Med 1* 105-109
5   M Therin, A Meunier and P Christel 1991 *J Mat Sci: Mater in Med 2* 1-8
6   A McNamara & D F Williams 1981 *Biomaterials 2* 33-40
7   C R McMillin 1989 *IEEE Eng in Med Biol   June*   30-36
8   A F Tencer 1989 *IEEE Eng in Med Biol   June*   40-45
9   Y Imanishi 1994 *Mat Sci Eng C1* 143-147
10 W G Pitt, K Park & S L Cooper 1986 *J Colloid Interface Sci 111*   343-362
11 G M Jenkins 1980 *Clin Phys Physiol Meas 1(3)* 171-194
12 J C Bokros 1977 *Carbon 15* 355-371
13 G M Jenkins & C J Grigson 1979 *J Biomed Mater Res 13*   371-394
14 A Bertoluzza, C Fagnano et al 1991, In: Spectroscopy of biological molecules,
        Eds R E Hester & R B Girling, Royal Soc Chem, Cambridge, 319-320
15 M D'Addato & T Curti   1994, *Proc 8th CIMTEC* Forum on New Materials,
        Florence, June 28-July 4 1994, to be publ
16 Y P Kudryavtsev, S E Evsyukov, et al 1992 *Carbon 30(2)* 213-221
17 A S Grigorian et al, *Proc 1st Int Conf on Dressing Materials and Polymer
        Implants* Ed V D Fedorov, Russian Academy Medical Sciences, 209-210
18 G M Jenkins and F X De Carvallo 1977 *Carbon 15*   33-37
19 L A Thomson, F C Law, N Rushton and J Franks 1991 *Biomaterials 12*   37-40
20 A C Evans, J Franks & P J Revell 1991 *Surf Ctgs Technol 47*   662-667
21 M J Allen, F Law & N Rushton 1994 *Clin Mater 17* 1-10
22 I R McColl, D M Grant et al 1993 *Diamond & Related Materials 3*   83-87
23 T L Parker, K L Parker et al 1994 *Dia Rel Mater 3* 1120-1123
24 R S Butter, M J Allen et al 1995 *Dia Rel Mater*   in press
25 L Lu, M W Jones & R L C Wu 1993 *Biomed Mater Eng 3(4)* 223-228
26 A H Lettington 1985 *SPIE Conf Proc 590* 100-105
27 S Mitura, Z Has & V Gorokhovsky, 1991 *Surf Ctgs Technol 47* 106
28 S Mitura, E Mitura & A Mitura 1995 *Dia Rel Mater*   in press

29 E Mitura, S Mitura et al 1994 *Dia Rel Mater*, 3, 896-898

30 A Olborska, M Swider et al 1994 *Dia Rel Mater,* 3, 899-901

31 K Miyoshi, J J Pouch & S A Alterovitz 1989 *Mat Sci Forum 52-53* 645-656

32 J F Braza & T S Sudarshan 1992 *Mat Sci Technol 8* 574-581

33 A Raveh, L Martinu et al 1993, *Surf Ctgs Technol*, 58, 45 - 55

34 K Enke, H Dimigen & H Hubsch 1980 *Appl Phys Lett 36(4)* 291-292

35 A Erdemir, M Switala, R Wei & P Wilbur 1991 *Surf Ctgs Technol 50* 17-23

36 K Miyoshi, R L C Wu & A Garscadden 1992 *Surf Ctgs Technol 54/55* 428-434

37 E Yang & J-P Hirvonen 1993 *Thin Solid Films 226* 224-229

38 J Fisher 1994 *Current Orthopaedics 8* 164-169

39 J Lankford et al 1993 *Nuclear Instrum & Methods in Phys Res B80/81* 1441-1445

40 A K Mishra & J A Davidson 1992, in: P J Doherty et al (Eds), *Advances in Biomaterials 10* 111-121

41 J Hailey, J Fisher et al 1995 *J Mat Sci: Mat in Med* submitted for publ

42 R Butter, A H Lettington et al 1995 *Dia Rel Mater* submitted for publ

43 F M Kustas, M S Misra et al 1993 *Tribology Transactions 36(1)* 113-119

44 I R McColl, J V Wood & D M Grant 1994 *Trans I.M.F 72(3)* 120-123

45 L Chandra, M Allen et al 1995 *J Mat Sci: Mater in Med* in press

46 P Wright & W Gray 1978 Rank Taylor Hobson, Private communication

47 M Allen, R Butter et al, 1995 *Bio-Med Mater Eng* in press

48 J R Cooper, D Dowson & J Fisher 1993 *Wear 162-164* 378-384

49 J R Cooper, D Dowson & J Fisher 1993 *Clin Mater 14* 295-302

50 W Huettner, G Keuscher et al 1982 *Adv in Biomater 4* Eds A J C Lee et al, 21-30

51 A Bolz & M Schaldach 1990 *Artificial Organs 14 (4)* 260-269

52 B D Ratner 1993 *Biomed Mater Res 27* 283-287

53 C-q Zheng, J-g Ran et al 1991 *Mat Sci Monogr* Eds Y Tzeng et al, Elsevier, Amsterdam 711-716

54 S P J Higson & P M Vadgama 1993 *Anal Chim Acta 271* 125-133

55 D M Grant, I R McColl, M Golozar & J V Wood 1992 *Dia Rel Mater 1* 727-730

Applications of Diamond Films and Related Materials: Third International Conference, 1995
Editors: A. Feldman, Y. Tzeng, W. A. Yarbrough, M. Yoshikawa, and M. Murakawa

691

SYNTHESIS, PROPERTIES AND APPLICATIONS OF SUPERHARD AMORPHOUS COATINGS

Michael A. Tamor, Research Laboratory, SRL/MD-3439, Ford Motor Company, Dearborn, MI 48121-2053.

Key words: DLC, friction, wear, tribology

Abstract

Low-friction/ultralow-wear coatings allow "surface engineering" for improved performance and durability, and enable use of new light weight or low cost materials. The accepted correlation of wear resistance with hardness suggests use of ceramic carbides and nitrides, with diamond being the ultimate anti-wear coating. While any of these may be deposited by chemical vapor deposition, the high cost (due to low deposition rates and high capital costs) and (usually) high deposition temperatures makes CVD coating impractical for cost-sensitive automotive applications. While rarely as hard as their crystalline counterparts, hard amorphous films exhibit similar (and occasionally superior) tribological properties and may be deposited on virtually any material at low cost. The highly nonequilibrium deposition process - conformal plasma reactive ion plating (CP-RIP) - allows tailoring of film properties and exploration of completely new compositions with no crystalline counterparts. Factors controlling the mechanical and optical properties of amorphous hard coatings, and recent progress in their application will be reviewed.

1. Introduction

Needs for surface engineering of rolling and sliding mechanical components fall into several broad categories: (1) reduction of wear in heavily loaded, lubricated contacts, (2) reduction of both friction and wear in situations where lubrication is limited or even undesirable, (3) reduction of friction and wear of materials that while strong, are tribologically poor, and (4) modification of light weight materials (e.g. Al, Mg) for improved durability in mechanical applications. For this discussion, it is assumed that both contacting members are well finished and sufficiently hard that climbing and ploughing are not relevant. This leaves two dominant wear mechanisms: abrasive wear and adhesive wear. Based in part on traditional descriptions of these, as taught by Rabinowicz[1], the "ideal" tribocoating for automotive applications can be

described. First, it must be at least approximately twice as hard as any prospective wear particle. Above this "2x-hardness" threshold, abrasive wear decreases extremely rapidly.   In our case, this dictates twice the hardness of the hardest components in steel, or roughly 18 GPa. Second, low adhesive friction and wear dictate that the two surfaces, once brought into contact over some microscopic region, always separate with low energy (for low friction) at the original interface (for low wear); i.e. that both are highly cohesive, but not reactive. Solid film lubricants achieve the former, but not the latter. Thus a hard material with a highly stable surface chemistry is desired. Third, the coating must be conformal and very smooth. Fourth, it must not be prone to cleavage. These two virtues are intrinsic to amorphous materials. Fifth, it is helpful, but not essential that the coating be under moderate compressive stress; this tends to close fractures and can actually improve adhesion. Sixth, and most important for large-scale application in price sensitive consumer applications, it must be cheap.

It is important to consider what tribocoatings can and cannot do. Figure 1a represents the stress distribution beneath a Hertzian contact under normal load only. The stress field is almost entirely compressive, with the maximum lying well beneath the surface. Introduction of a suitable coating can reduce both friction and surface wear directly beneath this contact as it slides. However, important effects also occur beneath the surface. As shown in Figure 1b, two changes occur as a lateral force is applied: (1) the compressive zone is moved ahead of the contact, and more importantly, (2) a subsurface tensile zone appears behind the sliding contact.   Most materials are strong even under high cyclic compression, while even mild cyclic
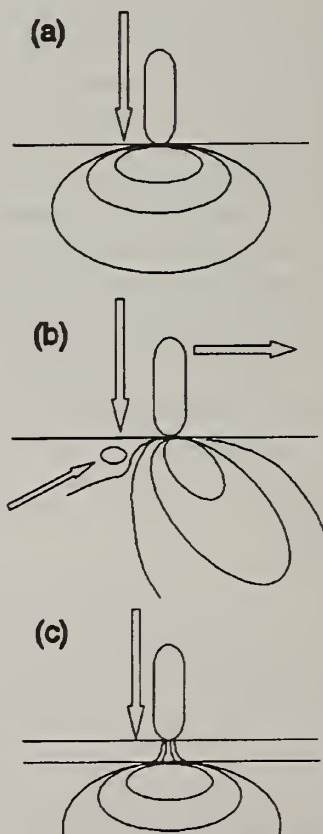
Figure 1 Schematics of the stress distribution beneath a Hertzian contact with normal load only (a), with lateral load (b), and with a thin, hard coating (c).

tension can lead to fatigue and failure. As the magnitude of the subsurface tension is roughly proportional to the coefficient of friction, low friction is key to suppressing subsurface fatigue. Thus a low-friction, low-wear material can suppress a wear mechanism (fatigue and spalling) that is not usually associated with the characteristics of the surface. Obviously, this is important for unlubricated systems. However, even with lubrication, lubricant can occasionally be excluded from small regions of heavily loaded sliding contacts. This occasional unlubricated sliding will not be detected in the measured friction, or even in surface wear, but can lead to rapid subsurface fatigue. Thus coatings can also be used to "back up" the lubricant and prolong system life under higher loads than otherwise possible, or allow use of alternative lubricants with other desirable properties (viscosity, thermal stability, cost, environmental impact, etc.).

In using the term "surface engineering" the unintended implication is that coatings may be used to make an object fabricated of a given material behave entirely (or in large part) as if fabricated from another superior material. This is true so long as the coating is not "probed" electrically, thermally or, as in our case, mechanically to a depth greater than its thickness. Figure 1c shows how the Hertzian stress field is transmitted directly through a thin, hard coating. If it is intended that the coating will prevent deformation of a material that would otherwise be stressed well above its plastic limit - i.e. give the mechanical illusion of the bulk material - the coating must be thick enough to distribute the stress within its own thickness. This is a very thick coating indeed - tens or hundreds of microns. In other words, we cannot rely on thin films to prevent plastic deformation; the substrate must be able to sustain all operating forces even without the film. Thus we look to thin film coatings to <u>enhance</u> performance of already hard materials (e.g. steel, titanium and ceramics) under high loads, and to <u>enable</u> use of softer materials (e.g. aluminum or magnesium) under low normal loads (pure sliding).

2. "Diamondlike" Carbon

Hard amorphous carbon (also known as diamondlike carbon (DLC) and by a variety of tradenames) deposited from energetic (hydro)carbon ions, would appear to satisfy all the criteria for an ideal tribocoating.[2] Indeed, it has been touted for well over a decade as a solution to any number of friction and wear problems. However, DLC suffers from three significant shortcomings which have impeded its application. (1) It is always under very high compressive stress. As shown in Figure 2, this stress increases in proportion to hardness. Even for amorphous hydrogenated carbon (AHC) films near the benchmark hardness of "only" 20 GPa, 2 GPa compressive stress places an unacceptably low limit on film thickness (roughly 1 μm) and makes adhesion unreliable. (2) It is thermally unstable; it begins to convert to graphite and lose its desirable

properties with prolonged exposure to temperatures above roughly 250 C. (3)
The very low friction (coefficient less than 0.1) and wear rate of AHC are
obtained only in very dry conditions which cannot be assured in most
applications. At high humidity, friction and wear of AHC increase so much as to leave it only comparable to a variety of other coatings.

Figure 2 Hardness of various amorphous carbon films as a function of compressive stress.

Self-Stressing of Hard Amorphous Carbon

The origin, or alternatively, the necessity of compressive stress in hard amorphous carbon films has been a topic of interest for some time. Two extreme points of view can be described. First is the quasi-thermodynamic picture used by McKenzie, Muller and Pailthorpe.[3] They refer to the carbon phase diagram and note that at room temperature only 2 GPa of compressive stress will lower the energy of diamond relative to graphite sufficiently that diamond is the stable phase. They propose that "amorphous diamond" is likewise stress stabilized, with the stress, and therefore diamondlike bonding (and in turn hardness) determined by the (hydro)carbon impact energy. Second, is a purely kinetic picture. Lifshitz, Kasi and Rabalais[4] proposed a "subplantation" regime of deposition energy in which graphitically bonded atoms are more readily displaced than those

Figure 3 Compressive stress in AHC as a function of ion energy during deposition. Solid symbols are experimental, while the curve is from theory.

with fourfold diamondlike bonding, so preferentially accumulating the latter. They did not comment on the resulting stress and some of their assumptions were later called into question. More recently, Robertson[5] adjusted a description of the competition between densification by implantation and relaxation by diffusion of defects proposed by Davis for more conventional single-phase materials[6] to reproduce the observed relationship between growth kinetics and stress (Figure 3). While reality comprises elements from both these extremes, the essential question is: what are the prospects for low-stress "diamondlike" coatings. A purely thermodynamic picture holds that compressive stress is essential to the very existence of hard amorphous carbon, while the kinetic picture suggests that stress is merely an accident of the chosen process, and might be avoided. We approach this "chicken-or-egg" question with a *gedanken* experiment. If we imagine that one could somehow generate fully coordinated, all-sp^3 carbon film with no macroscopic stress, we can consider what might happen later. The energy associated with the requisite bond angle and length distortions is quite large (on the order of several eV per atom[7]) and lower coordination arrangements, π-bonded sp^2 pairs, are possible. Having fewer constraints, these can relax more nearly to their undistorted configurations and so lie at significantly lower energy. The barriers to relaxation of the most distorted sites are likely to be small and some relaxation will occur even at low temperature. At low density, the π-bonded pairs occupy roughly the same atomic volume as their sp^3 progenitors. However, the π-orbitals protrude significantly and as pairs accumulate the orbitals will begin to overlap. As they are highly repulsive, some of the energy gain from pairing will go into volume expansion. Thus reconfiguration of two distorted sp^3 sites to a π-bonded pair becomes analogous to inflating a small bubble in the film. This energetically favored process will generate compressive stress even if none was present when the structure was formed. In effect, hard carbon films are "self stressing." Figure 4 is a cartoon of this process. It is not clear what limits this process. Possibilities

Highly Distorted Fourfold Sites

Energetically Favorable

"Relaxed" Paired Threefold Sites

Energetically Unfavorable

Repulsion Impedes relaxation
Relaxation Increases compression
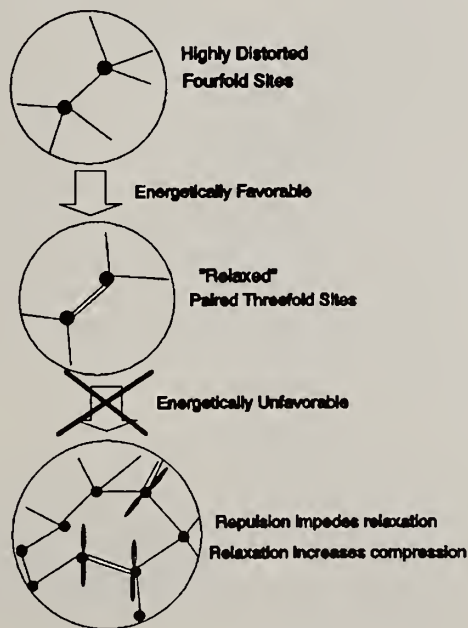
Figure 4 Cartoon of conversion of distorted sp^3-sites to π-bonded pairs.

are: (1) progressively decreasing rate of conversion as the most distorted sites relax first, (2) decrease in the energetic advantage of conversion as the surrounding density of π-orbitals increases, or (3) increase in the energy required for volume expansion against the increasing compressive stress. We can make an order-of-magnitude estimate by assuming (1) a 50% volume increase (as in conversion from diamond to graphite) against a fixed bulk modulus, (2) that hardness is roughly 25% of the bulk modulus (as in diamond and other hard materials) and (3) finally (and arbitrarily) that 5% of the carbon is paired. With these assumptions, hardness is roughly ten times the compressive stress, consistent with the ratio of seven shown in Figure 2. This demonstration that self-induced stress could be sufficient to account for all the observed stress in hard carbon films does not prove that it is actually dominant, but it is at least consistent with the proposition that compressive stress in hard amorphous carbon films is unavoidable.

Self-stressing in hard amorphous carbon would have several important consequences. Obviously, films thickness is strictly limited by the strength of the interface or substrate material. It also means that truly transparent "pure amorphous diamond" cannot exist. The paired sites have an estimated optical gap of 2.5 eV, in good agreement with that measured for the hardest amorphous carbon, and far smaller than that expected for an amorphous analog to diamond. These pairs are likely to be defects within the larger band gap of "amorphous diamond" and so undermine its utility as an electronic material.
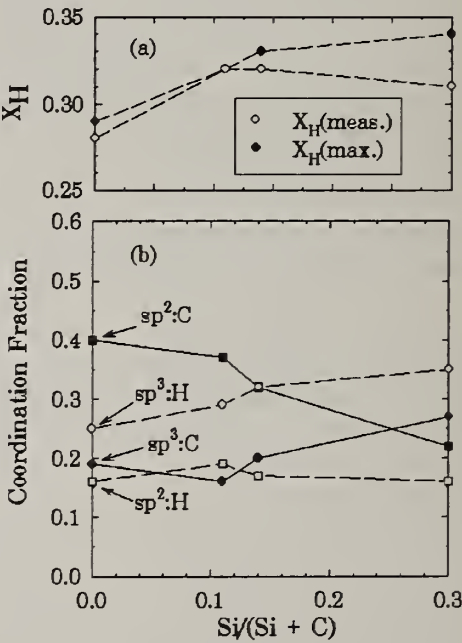
Figure 5 (a) Hydrogen content of Si-AHC as a function of Si content, measured by activation analysis and estimated from NMR results. (b) Breakdown of carbon bonding environments in Si-AHC.

3. Silicon-Stabilized Amorphous Hydrogenated Carbon

One approach to suppressing formation π-bonded pairs is to alloy with a carbiding element. As carbon bonded to the impurity is much more resistant to pairing (carbon in carbides is generally sp^3-bonded) the stress will be reduced accordingly. Assuming that heat has the effect of accelerating the pairing process, the alloyed carbon film should be stable at higher temperature as well. A variety of alloying elements have been tried. All tend to reduce the stress and improve thermal stability with little compromise in hardness. While they tend to make friction insensitive to humidity, the resulting friction coefficient is usually quite high. Silicon was found to be the most effective additive. Inclusion of 5 to 20 atomic percent Si (including H) in AHC reduced compressive stress by roughly 80 %.

Silicon-containing AHC films were studied by nuclear magnetic resonance (NMR) spectroscopy. Figure 5 shows the hydrogen content and a breakdown of carbon bonding environments as a function of silicon content. In Fig. 5a, the hydrogen content as measured by ^{15}N activation at first increased with Si content, and then decreased, while the value determined by NMR agreed at low Si-content, but diverged and continued to increase. This divergence is due to the way the latter was determined. The NMR-derived value is a measure of the hydrogen content of the carbon-hydrogen network only; it is blind to Si-bonded hydrogen. If a lower fraction of Si than C is protonated, the two measures will diverge as the Si-content increases. The lower protonation of Si was qualitatively confirmed by NMR. The breakdown of carbon bonding environments in Fig. 5b shows how increasing Si-content is correlated with increasing fractions of both protonated and unprotonated sp^3 carbon. Interestingly, although the total sp^3 fraction increases, the mean coordination increases only slightly because graphitic carbon is replaced in part protonated sp^3 carbon (also threefold coordinated). Also, the remaining increase in coordination is partially offset by the relative weakness of the increasing population of Si-C bonds. This is consistent with the observation that hardness was almost independent of Si-content.

The NMR results also support the concept of self stressing. Note that the kinetics of the deposition process and the hydrogen content of the films were unchanged, the sp^3-fraction increased considerably while the stress went down. In the kinetic picture, similar kinetics should lead to similar stress, while in the thermodynamic picture, increased sp^3 bonding , should correlate with increased stress. As predicted by the self-stressing proposal, Si simultaneously <u>increases</u> sp^3- bonding while <u>reducing</u> compressive stress.

Silicon addition stabilized the friction coefficient of AHC at roughly 0.08, the same as for AHC dry conditions. Figure 6 compares the friction of AHC without and with Si as a function of humidity. [Note that a COF of 0.05 to 0.1 is typical for lubricated sliding of steel against steel.] Figure 7 shows the weight loss of AHC and Si-AHC following baking in air for one hour at successively higher temperatures. The onset of weight loss was shifted upward roughly 100 C by the addition of silicon. Also, it was observed that partially decomposed AHC films were ineffective tribocoatings while the wear resistance of Si-containing films was only slightly compromised by baking in air at 500 C. While stress reduction and thermal stabilization are readily explained in terms of the increased resistance to π-bonding and oxidation resistance, the role of Si in stabilizing friction against the effects of moisture is not understood at present. In recognition of these two stabilizing effects - against thermal destruction and humidity effects - we refer to this material as "silicon-stabilized" AHC, or simply Si-AHC.
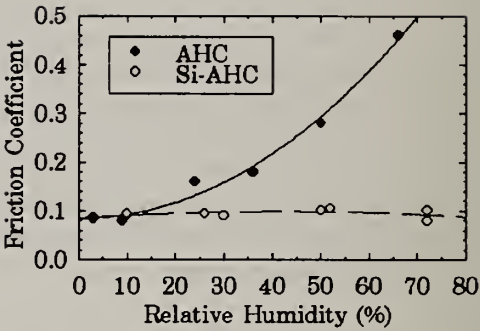
Figure 6 Coefficient of friction for unlubricated sliding of a steel pin against AHC and Si-AHC as a function of ambient humidity.
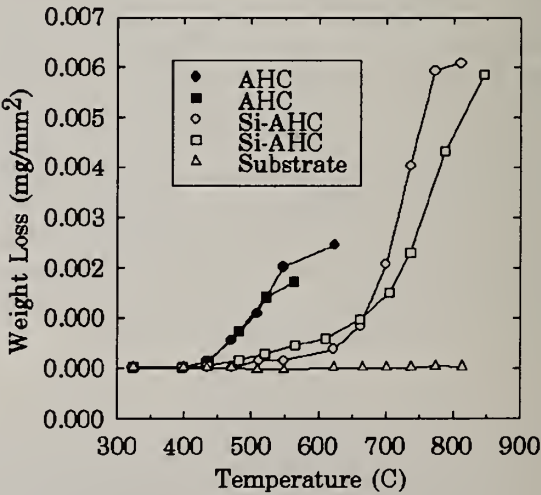
Figure 7 Weight loss of AHC and Si-AHC films after baking in air at successively higher temperatures. The Si-AHC film was roughly three times the thickness of the AHC film.

A typical wear rate of Si-AHC in unlubricated sliding against steel is 3 x 10^{-8} mm^3/N-m. This is nearly two orders of magnitude lower than for competing tribocoatings (TiN, Ti(C,N), B$_4$C) measured under identical conditions and is only slightly higher than the best values reported for diamond. Figure 8 shows the wear rates for a variety of films of roughly comparable hardness in dry sliding against steel. The figure suggests a very rapid increase of film wear with friction, and little, if any correlation with hardness. This is consistent with the introductory description of the "ideal" tribocoating where it was suggested that hardness more than a few times that of prospective wear particles would be of little value. [Wear particles from these amorphous films are extremely small and so do not lead to abrasive self-wear.] Above this threshold, it appears that the surface chemical processes that determine adhesive friction and consequent wear are dominant.
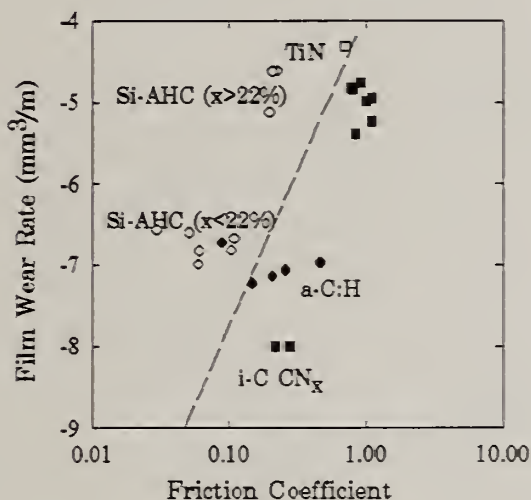
Figure 8 Log-log plot of film wear rate as a function of sliding friction against a 6 mm steel ball under 4.4 N load.

4. Conformal Plasma Reactive Ion Plating

Our process for Si-AHC coating is based on self-biased RF plasma deposition. Radio frequency power is delivered through the components themselves rather than fastening them to a fixed electrode. A plasma envelops each component and the film deposited from ions drawn from that plasma and accelerated by the bias potential. Because the plasma conditions we use produce very little reaction in the plasma - carefully selected carbon- and silicon-containing precursors are accelerated essentially intact - we prefer the term conformal plasma reactive ion plating (CP-RIP). Such processes are most often referred

to as plasma-enhanced chemical vapor deposition (PE-CVD). This is quite misleading because the plasma is not "enhancing" a process that might otherwise occur at a lower rate or a higher temperature, but it is acting as an ion source. Any chemical processes are taking place at or beneath the growth surface.

Cost is major obstacle to introduction of vacuum deposited tribological coatings in consumer products such as automobiles. Components must be washed, loaded into equally clean vacuum systems, those systems pumped down to some required base pressure, the components cleaned again by sputtering, and finally the coating deposited, often at a low rate. Thus the cost of vacuum coatings is very sensitive to the (usually high) capital cost of the system and the time required. Although not cheap by traditional automotive standards, CP-RIP deposited Si-AHC promises to be far cheaper than previous vacuum coatings for a variety of reasons. (1) Although it is really an ion-beam process, the ion source is conformal, meaning it is not a line-of-sight process. (2) It is an all vapor process with no capital or variable expense for solid-vapor conversion by evaporation or sputtering. These are also line-of-sight processes. (3) Large reactors can be loaded more densely than in line-of-sight processes. (4) Energy and reactant are consumed only in proportion to the area to be coated. (5) The deposition rate can be quite high; 4 μm/hr has been demonstrated and higher rates are believed possible. (6) The film composition is similar to that of diffusion pump oil. This allows use of cheap, durable, speed diffusion pumps without fear of contamination by backstreaming. (7) The film properties are unaffected by minor contamination with oxygen or nitrogen. The process is compatible with simple rubber vacuum seals and fast pump-downs. All these characteristics are compatible with simple reactors that are cheap to build, simple and cheap to operate, a fast coating process, and coating properties that are robust against considerable variation in operating conditions.

5. Conclusions

Figure 9 is a somewhat lighthearted illustration of some of the findings of this work. It shows the friction (against steel) of a wide range of materials as a function of their hardness. The square root scale is used to collapse the wide range of hardness and emphasize the trends. The softest materials (tin, lead etc.) exhibit low friction, but because they shear within themselves, they are also high-wear materials. i.e. "bronze age" solid-film lubricants. For sliding of ferrous "iron age" alloys on themselves, friction is high and liquid-film lubrication is usually used. However, for "stone age" ceramics and hard AHC, friction is also low, but unlike for the soft materials, wear is also low. In effect,

the easy shear of the solid film lubricant is achieved, with the shear always occurring at the original contact surface.

Figure 9 also emphasizes the contention that superior hardness does not necessarily translate to superior tribological performance; diamond is well off this hardness scale, yet there would appear to be little room for improvement over AHC. For well engineered tribosystems where substrate materials do not plastically deform under the designed loads and surfaces are smooth enough to prevent abrasive wear, effort should be devoted to understanding and controlling the surface chemistry of the coating, and its interaction with the counterface material, rather than on seeking to increase the coating hardness in the blind faith that hardness alone improves performance. Furthermore, unlike stable crystalline phases, the composition of metastable, kinetically deposited amorphous materials may be modified almost arbitrarily in this effort to master surface chemistry. In conclusion, of the expanding plethora of hard thin-film coatings, silicon-stabilized amorphous hydrogenated carbon best approximates "ideal" tribocoating: it is slippery and wear resistant under a wide range of conditions - with the possibility of further improvement, reasonably stable, smooth, and may be deposited at low temperature at acceptably low cost.
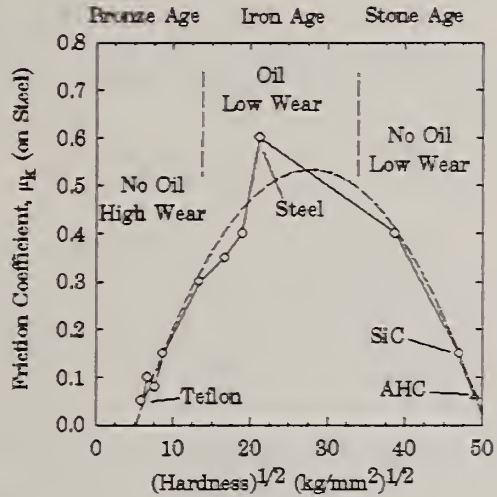
Figure 9 Friction of various materials sliding against steel as a function of hardness. The dashed curve is a parabola fit to the data to emphasize the trends.

6. Acknowledgements

Gangopadhayay for conducting the numerous tribological tests central to this work.

7. References

1)   E. Rabinowicz, <u>Friction and Wear of Materials,</u> (Wiley, NY, 1965); <u>Tribology I: Friction, Wear and Lubrication,</u> (MIT Center for Advanced Engineering Study, Cambridge, 1974).

2)   M. W. Geis and M. A. Tamor, Encyclopedia of Applied Physics, (VCH, New York, 1993), vol. 5, pp. 1-24.

3)   D. R. McKenzie, D. Muller and B. A. Pailthorpe, Phys. Rev. Lett. **67**, 773 (1991).

4)   Y. Lifshitz, S. R. Kasi and J. W. Rabalais, Phys. Rev. Lett. **62**, 1290 (1989).

5)   J. Robertson, Diamond Relat. Mater. **3**, 361 (1994).

6)   C. A. Davis, This Solid Films **226**, 30 (1993).

7)   P. C. Kelires, Phys. Rev. Lett. **68**, 1854 (1992).

AMORPHOUS HYDROGENATED CARBON FILMS FOR TRIBOLOGICAL APPLICATIONS

Arup Gangopadhyay, P.A. Willermet, M. A. Tamor and W. C. Vassell
Ford Research Laboratory, Dearborn, MI 48121, USA

Key words: amorphous hydrogenated carbon, thin films, friction, wear, thermal effects, durability

Abstract

Amorphous hydrogenated carbon (AHC) films show promise in tribological applications. However, the films suffer from two main drawbacks i.e, the films are sensitive to moisture and exhibit high compressive stress which limits the thickness of the films that can be deposited. Modification of film composition by incorporating silicon made AHC films moisture insensitive and also allowed deposition of thick films. Both moisture insensitivity and deposition of thick films were achieved without any compromise with the friction coefficient and the wear of the steel counterface for certain film compositions. The friction and wear test results on films deposited on silicon, aluminum alloys and steel are presented. Also, film durability was evaluated under both unlubricated and lubricated sliding conditions. The tribological and the mechanical properties of the films were also evaluated after heating in air.

1. Introduction

Amorphous hydrogenated carbon (AHC) films possess high hardness (comparable to some of the advanced ceramics), high wear resistance, low wear of a steel counterface, low unlubricated sliding friction coefficients (at low relative humidity) and good resistance to corrosion [1-3]. These properties of AHC films offer some advantages over some of the other thin hard coatings considered for tribological applications. However, AHC films are found to be moisture sensitive i.e., the friction coefficient and the film wear increased with increased relative humidity [4,5]. Also, the films possess high compressive stress which limits film thickness to less than 2 μm. Addition of iron in AHC films reduced the friction coefficient against a steel ball at low relative humidity [6] compared to unmodified AHC films. Addition of tungsten to AHC films reduced the moisture sensitivity but could not eliminate it [6,7]. Our attempts to deposit metal containing films using the procedure described in ref 6 and 7, showed poor film durability. Oguri and Arai [8-10] reported a friction coefficient of 0.04 for silicon containing AHC films against a steel ball at high humidity. Also, the wear rate of the steel ball was reduced by about three orders of magnitude compared to sliding against an uncoated disk. However, their film deposition process used a toxic precursor gas mixture and required heating of the substrate to about 550^0C which is considered too high for most engineering alloys. Meneve et al also reported excellent tribological behavior of silicon containing AHC films deposited from toxic precursor gas mixtures [11]. We have

recently deposited silicon containing AHC films using non-toxic and non-corrosive precursors. These films showed good friction and wear characteristics (12,13). This paper highlights some of the friction and wear characteristics of silicon containing AHC films and presents some new results on heat treated silicon containing AHC films..

2. Experimental Details

A series of AHC films with varying silicon content were deposited by a plasma assisted chemical vapor deposition technique. The substrate bias voltage was either 500 or 1000 V, corresponding to mean ion energies of 150 or 350 eV respectively. The films were deposited on silicon wafers, 2024 and 7075 aluminum alloys and AISI 4340 hardened steels. Films were deposited on aluminum alloys with and without a silicon interlayer. A silicon interlayer was used because AHC films adhered well on silicon substrates. In the case of steel, an interlayer was required for film adhesion which could be either silicon, aluminum or chromium. This paper presents results obtained with a silicon interlayer. The thickness of the silicon interlayer was 0.1 - 2 μm.

Friction and wear tests were conducted using a ball on disk contact geometry. 6.25 mm diameter balls made of 52100 steel were loaded against coated substrates. The tests were generally conducted without a lubricant at a normal load of 4.4 N, a sliding speed of 3.5 cm/s and at relative humidity ranging from 10 to 70 %. A few tests were conducted at sliding speeds up to 250 cm/s to evaluate film durability with and without a lubricant. SAE 5W-20 engine oil was used as a lubricant. At the end of each test, the wear volume of the ball was calculated from the measured wear scar diameter and the wear volume of the film was calculated from three profilometer traces taken across the wear track.

To evaluate the maximum useable temperature, a few films were held in air at 300^0C and 345^0C up to 392 hours. The hardness, elastic modulus, friction coefficient and wear of films were measured following cooling down to room temperature. Hardness and elastic modulus were measured using a microindentation technique using a 5 μm radius spherical diamond indenter at 100 N load. At this load, the depth of indenter penetration in the film was less than 15 % of the film thickness to avoid any contribution from the substrate.

3. Results and Discussions
3.1 Film Characterization
Chemical composition of AHC films - The amount of carbon, hydrogen and silicon in the films deposited on silicon substrates is shown in table I. The amount of silicon and carbon was determined by an electron microprobe technique and the amount of hydrogen was determined by nuclear reaction analysis.

Compressive stress - The compressive stress was calculated from the measurement of the radius of curvature of the substrate using a profilometer trace. The results are shown in table I. It can be seen from the table that incorporation of silicon in the AHC films reduced compressive stress. Deposition of films at higher bias voltage also reduced compressive stress. An AHC film containing 6.7 atomic percent Si and deposited at 1000 V exhibited a compressive stress of only 0.37 GPa, which is a

factor of four less than that of the silicon free AHC films deposited at 500 V bias. These conditions allowed deposition of thick (10 μm) films.

Hardness and elastic modulus - The hardness and elastic modulus of unmodified AHC film were 12 GPa and 115 GPa respectively and these values did not change significantly with the amount of silicon added in the films. These values are lower

Table 1. Chemical composition and compressive stress on AHC films

Bias Voltage V	H Atomic %	C Atomic %	Si Atomic %	Stress, GPa
500	37	61	0	1.6
1000	27.6	72.4	0	0.7
500	31.5	63.1	5.4	1.01
500	32.2	58.46	9.3	1.01
1000	34.3	59	6.7	0.37
500	30.33	47.13	22.53	
500	30.83	46.59	22.58	

than typically reported in the literature (11). This is thought to be related to the indenter geometry. It was observed that the hardness values obtained with a spherical indenter was a factor of two less than that obtained with a triangular pyramidal diamond indenter. Swain and Mencik [14] also reported a similar indenter geometry effect on hardness.

3.2 Friction and wear test results

Films deposited on silicon - The friction coefficients obtained with AHC films deposited at 500 and 1000 V bias are shown in Fig. 1. The films containing up to 9.3 atomic percent silicon exhibited friction coefficients similar to those observed with silicon free films. The films containing about 22 atomic percent silicon showed a large variation in friction coefficients. Most of the silicon in these films is expected to be bonded to carbon. The higher friction coefficient obtained with these films may be related to a more Si-C like surface, which generally exhibits high friction (15). The variation of friction
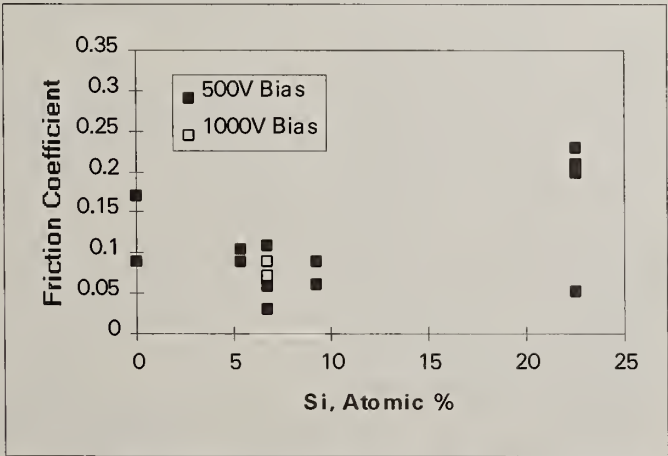
Figure 1. The friction coefficients of AHC films as a function of silicon content.

coefficient with silicon content in the film is in agreement with the observations of Oguri and Arai (9). The wear rates obtained with the films containing up to 9.3 atomic percent silicon are shown in Fig. 2. The wear rates for these films are comparable to those of silicon free AHC films. However, the films containing 22 atomic percent silicon exhibited a large variation in wear rates. There appears to be a correlation between the friction coefficient and the wear rate for the

Figure 2. The wear rates for AHC films as a function of silicon content.

films. The films exhibiting high friction coefficients also tend to show higher wear. The contact area on the balls, tested against films containing up to 9.3 atomic percent silicon, contained a transfer film. The ball wear rate was found to be comparable to that obtained against unmodified AHC films. The high friction coefficients obtained with the films containing 22 atomic percent silicon were associated with high ball wear with the absence of a transfer film on the ball contact area..

These results show that if the silicon content does not exceed 9.3 atomic percent, the friction coefficients and the wear rates of contacting surfaces are comparable to those obtained with unmodified AHC films.

To evaluate the effect of humidity on the friction and wear behavior, AHC films containing 6.7 atomic percent silicon (hereafter referred to as Si-AHC) were deposited on a 7075 aluminum alloy with and without a silicon interlayer. The thickness of the interlayer was 2 microns and that of the Si-AHC film was 10 microns. For comparison, an unmodified AHC film, about 1 micron thick, was also deposited on a silicon substrate. Fig. 3 shows that the friction coefficient increased with relative humidity for the unmodified AHC film but

Figure 3. The effect of relative humidity on friction coefficients of AHC films.

for the Si-AHC film the friction coefficient remained 0.1 or less for the range of

relative humidity studied. It was observed that at low humidity a transfer film formed on the ball contact surface for both unmodified and silicon modified AHC films. At high humidity, the transfer film did not form on the ball surface when slid against the unmodified AHC film but, the transfer film formed when slid against the Si-AHC film. It appears that the presence of silicon in the film facilitates the formation or adhesion of a transfer film on the ball surface at high humidity. Surface analysis is currently being conducted to understand this phenomenon.

Films deposited on aluminum alloys - Initial friction and wear tests on unmodified free AHC films (1.1 micron thick) deposited on an 2024 aluminum alloy showed poor durability. This was believed to be due to either plastic deformation of the substrate or poor adhesion or both. In order to improve film durability, a silicon interlayer, 0.5 micron thick, was deposited. While a thicker coating improved film durability, the friction coefficient was 0.4, which was higher than that observed on a film deposited on a silicon substrate. A deep wear groove was observed on the substrate indicating plastic deformation. The higher friction coefficient was probably due to dissipation of energy to plastically deform the substrate. Therefore, it was believed that reduction of plastic deformation, by increasing coating thickness, would be necessary to reduce the friction coefficient. A series of films were deposited on an Al-11.6 % Si alloy with increasing interlayer thickness since AHC films could not be deposited more than 2 micron thick.

Figure 4. The durability of AHC films on an aluminum alloy as a function of coating thickness.

Fig. 4 shows the durability and friction coefficients obtained with these films. The data points associated with an arrow indicates that the test was terminated before the coating failed. However, examination of the wear track under an optical microscope revealed signs of severe plastic deformation for coatings of 2 micron or less in thickness, indicating that the coating was close to failure. The data shows that the coating durability can be increased from 23 minutes to more than 7 hours by increasing the coating thickness from 0.8 to 2.8 micron. It is interesting to note that friction coefficients also decreased from 0.36 to 0.12 as the coating thickness increased. This is because as the coating thickness increased, the magnitude of stress in the substrate under the contact area decreased and, therefore, less energy was dissipated to plastically deform the aluminum alloy substrate. With Si-AHC films, which could be deposited as thick as 10 microns, a friction coefficient of 0.09 was obtained without an interlayer. However, the optimum coating thickness for any tribological application would depend on the substrate material and test conditions.

Films deposited on steel - Initial experiments with unmodified AHC films, less than 1 micron thick, deposited on an AISI 4340 hardened steel with a silicon interlayer showed a higher friction coefficient (0.27) compared to that observed on silicon substrates. This was also believed to be due to plastic deformation of the substrate. Deposition of a thick Si-AHC film, 6.5 micron, with a 0.86 micron silicon interlayer, reduced the friction coefficient to 0.09.

To evaluate durability, an Si-AHC film, 6.5 micron thick, was deposited on a ground finished (R_a - 0.31 micron) AISI 4340 hardened steel with a 0.9 micron thick silicon interlayer. Friction and wear tests were conducted in two steps; in step one, the test was conducted at a sliding speed of 200 cm/s for 24.5 hours followed by 17.5 hours at 250 cm/s on the same wear track accumulating a total of 5.5 million cycles. The depth of the wear groove was 4.5 micron. The optical micrograph in Fig. 5 shows the smooth wear groove on the film. The unworn region shows the original grinding marks on the steel substrate. The addition of a lubricant significantly improved film wear and ball wear. In the presence of a SAE 5W-20 grade engine oil, very little wear could be observed on the film after 5.5 million cycles as shown in Fig. 6. The original grinding marks on the steel substrate

Figure 5. An optical micrograph of the wear track on Si-AHC film after 5.5 million cycles under unlubricated sliding contact.
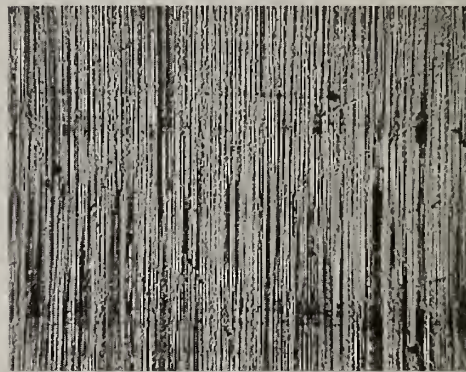
Figure 6. An optical micrograph of the wear track on Si-AHC film after 5.5 million cycles in the presence of a lubricant.

could be seen on the wear track. The ball wear was also reduced by a factor of four in the presence of the lubricant compared to that obtained without any lubricant.

3.3 Thermal effects

Since automotive components largely function in air, it is important to evaluate the tribological characteristics of these films after being exposed to elevated temperatures in air. Si-AHC films were held at 300^0C and 345^0C in air up to 392 hours followed by hardness, elastic modulus and friction and wear measurements. The hardness and elastic modulus of the films after being exposed to 300^0C were comparable to those of the as-deposited film. The friction coefficient and the wear rate for the films are shown in Figs. 7 and 8 respectively. The friction coefficients obtained with the films were comparable to that of the as-deposited film, but the wear rate for the film increased after 248 hours. Although the film wear rate increased, the wear rate still appeared good. A Raman spectrum obtained on the film after 392 hours showed diamond-like characteristics.

The films held at 345^0C became soft after 248 hours and could be easily removed. The film was removed almost immediately during friction and wear testing

4. Conclusions

Incorporation of silicon made AHC films insensitive to moisture while significantly reducing compressive stress allowing deposition of thick films. Both moisture insensitivity and deposition of thick films were achieved without compromising the friction coefficient and wear of the contacting surfaces as long as the silicon content in the films was kept below 9.3 atomic percent.

Figure 7. The friction coefficients of Si-AHC films after heated to 300 C in air.

Increasing the coating thickness increased film durability. In the case of films deposited on an Al-11.6% Si alloy, increasing the coating thickness from 0.8 to 2.8 micron increased coating durability from 23 minutes to more than 7 hours. The friction coefficient decreased from 0.36 to 0.12 under the test conditions used.
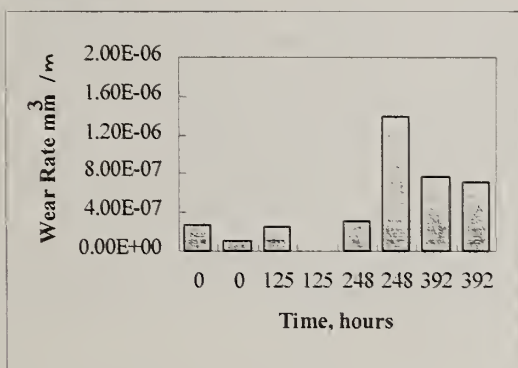
Figure 8. The wear rates for Si-AHC films after heated to 300 C in air.

The presence of a lubricant significantly improved coating durability. After 5.5 million cycles, the depth of the wear groove was only 4.5 micron in an unlubricated test, but in the presence of a lubricant, coating wear could not be measured.

After exposure to 300^0C for 392 hours, the hardness and elastic modulus of the Si-AHC film was comparable to those of as-deposited films. Film wear properties began to degrade somewhat after 248 hours, but good wear behavior was still observed after 392 hours. The mechanical and tribological properties of the film degraded severely when held at 345^0C for 248 hours.

5. References

1. Jansen, F. and Machonkin, M.A., "Wear properties of tetrahedral bonded amorphous thin films," Thin solid films, 140, p227-235, 1986.
2. Zou, J.W., Reichelt, K., Schimidt, K., and Dischler, B., "The deposition and study of hard carbon films," J. Appl. Phys., 65 (10), p3914-18, 1989.

3. Miyoshi, K., Pouch, J.J., and Alterovitz, S.A., "Plasma deposited amorphous hydrogenated carbon films and their tribological properties," Materials Science Forum 52 & 53, p645-656, 1989.

4. Enke, K, Dimigen, H., and Hubsch, H., "Frictional properties of diamondlike carbon layers," Appl. Phys. Lett, 36 (4), p291-292, 1980.

5. Gangopadhyay, A.K., Vassell, W.C., Tamor, M.A., and Willermet, P.A., "Tribological behavior of amorphous hydrogenated carbon films on silicon," J. of Tribology, 116, p454-462, 1994.

6. Dimigen, H., Hubsch, H., and Memming, R., "Tribological and electrical properties of metal containing hydrogenated carbon films," Appl. Phys. Lett., 50 (16), p1056-1058, 1987.

7. Klages, C.P., and Memming, R., "Microstructure and physical properties of metal-containing hydrogenated carbon films," Materials Science Forum, 52 & 53, p609-644, 1989.

8. Oguri, K., and Arai, T., "Low friction coatings of diamond-like carbon with silicon prepared by plasma-assisted chemical vapor deposition," J. Mater. Res., 5 (11), p2567-2571, 1990.

9. Oguri, K., and Arai, T., "Tribological properties and characterization of diamond-like carbon coatings with silicon prepared by plasma-assisted chemical vapor deposition," Surface and Coatings Technology, 47, p 710-721, 1991.

10. Oguri, K., and Arai, T., "Friction coefficient of Si-C, Ti-C and Ge-C coatings with excess carbon formed by plasma-assisted chemical vapor deposition," Thin Solid Films, 208, p158-160, 1992.

11. Meneve, J., Jacobs, R., Eersels, L., Smeets, J and Dekempeneer, E., "Friction and wear behavior of amorphous hydrogenated $Si_{1-x}C_x$ films," Surface and Coatings Technology, 62, p577-582, 1993.

12. Gangopadhyay, A.K., Willermet, P.A., Tamor, M.A., and Vassell, W.C., "Amorphous hydrogenated carbon films for tribological applications I. Development of moisture insensitive films with reduced compressive stress," submitted to Tribology International.

13. Gangopadhyay, A.K., Willermet, P.A., Tamor, M.A., and Vassell, W.C., "Amorphous hydrogenated carbon films for tribological applications II. Films deposited on aluminum alloys and steel," submitted to Tribology International.

14. Swain, M.V., Mencik, J., "Mechanical property characterization of thin films using spherical tipped indenters," Thin Solid Films, 253, p204-211, 1994.

15. Miyoshi, K., and Buckley, D.H., "Friction, deformation and fracture of single crystal silicon carbide," ASLE trans., 22 (1), p79, 1979.

CONTROLLING PROPERTIES OF DLC: EFFECTS OF PRESSURE AND PRECURSOR DILUTION

A.Grill and V.Patel

IBM-Research Division,T.J.Watson Research Center, Yorktown Heights, N.Y.   10598, U.S.A.

Key words: argon, cyclohexane, FTIR, pressure, thermal stability, wear.

Abstract

Diamond-like carbon (DLC) films have been deposited by plasma assisted chemical vapor deposition using a RF excited plasma of cyclohexane. The films have been deposited at different pressures and constant RF power density. For specific combinations of plasma parameters the precursor has been diluted with argon. It has been found that the physical properties and the wear resistance of the DLC films are strongly dependent on the pressure in the reactor and corresponding substrate bias. Films deposited at a pressure above a threshold value had polymer-like characteristics. It was further found that it is possible to enhance diamond-like properties of films deposited above the threshold pressure by diluting the precursor with argon. At sufficiently high dilution of the precursor, DLC films deposited above the threshold pressure had properties similar to those of films deposited below the threshold. The dilution with inert gas also enhanced the thermal stability of the DLC films and films stable at 400 °C have been obtained.

1. Introduction

It is generally believed that, for DLC deposited by the plasma assisted chemical vapor deposition (PACVD) technique, the properties of the film are independent of precursor and deposition condition if the negative substrate bias is larger in absolute value than 100 V to 300 V [1]. Previous studies have shown that the properties of DLC films deposited by a DC excited plasma [2] were dependent on precursor and substrate bias, when deposited at pressures of 100 mtorr to 200 mtorr. It was furthermore found that admixing an inert gas to the DLC precursor in the DC PACVD system, it is possible to lower the threshold bias for obtaining films with DLC properties [3]. By adjusting the substrate bias it was possible to change the properties of the films from soft, polymer-like, to diamond-like.

Manufacturing limitations may often exist with regard to the choice of precursor or plasma conditions achievable with the existing tools. The possibility to adjust the deposition condition for tailoring the right properties of the DLC films could overcome such limitations and enable the preparation of films with properties suitable for the specific applications.

The present paper presents the effects of pressure and dilution of the precursor with argon on the properties of DLC films deposited by RF PACVD from cyclohexane.

2. Experimental

The DLC films have been deposited on Si substrates by a RF PACVD process in a parallel plate reactor described elsewhere.[4] The substrates were heated to 180 °C during deposition. The films have been deposited from cyclohexane or mixtures of cyclohexane with Ar, at a RF power density of 0.144 W.cm^{-2}. The pressure in the reactor was controlled at 100 to 300 mtorr during the deposition from pure cyclohexane and at 200 mtorr during the deposition from the Ar diluted precursor. The substrates were positioned on the RF powered electrode and were at a negative self bias determined by the plasma conditions. The detailed preparation conditions of the studied DLC films are given in Table I.

Table I. Preparation conditions and hydrogen content.

Sample	Precursor	Flow	Pressure	Bias	C_H
		(sccm)	(mtorr)	(-V)	(%)
CY1	C_6H_{12}	10	100	228	44
CY2	C_6H_{12}	10	200	140	44
CY3	C_6H_{12}	10	300	95	47
C2A1	C_6H_{12}+Ar	10+10	200	200	44
C2A2	C_6H_{12}+Ar	6+12	200	200	44
C2A4	C_6H_{12}+Ar	3+12	200	230	38

Infrared absorption in the DLC films was measured using a Fourier transform infrared spectrometer (FTIR) as described in detail elsewhere.[5] The index of refraction of the DLC films was determined by ellipsometry at λ = 6328 Å on films thinner than 1000 Å. The hydrogen content of the DLC films was measured by the forward recoil elastic scattering method (FRES) using a 2.3 MeV ^{4}He beam and fitting the calculated energy distribution of the recoiled atoms to the experimental data, by adjusting the hydrogen concentration in the calculations. The wear resistance of the DLC films was determined using a thin film pin-on-disk type tribotester[6] using polished stainless steel riders (440C ball bearings). The test was performed at loads of 0.029N-0.294N (3-30g) applied to the riders of a diameter of 0.794 cm, corresponding to an initial Hertzian stress of 151MPa-324MPa.

The thermal stability of the DLC films was investigated by annealing the films under vacuum for four hours at temperatures up to 500 °C and and comparing the FTIR spectra and hydrogen content of the annealed films with those of the as-deposited ones.

3. Results and Discussion

The IR absorption bands at 2800-3100 cm^{-1}, obtained from DLC films deposited from pure cyclohexane at the different pressures are shown in Figure 1. The absorption bands correspond to a superposition of C-H stretching vibrations from mainly sp^3 bonded carbon [7, 8]. While the peaks and their deconvolution cannot be used to define the carbon bonding in the DLC films (see reference [7]) the IR peaks can be used for relative comparison of the different films deposited in the same system. In Figure 1 (a) the absorption bands are not normalized, but displayed with the intensity adjusted to full scale, for comparing the shapes of the absorption peaks. In Figure 1 (b) the absorption bands are normalized for identical thickness.

Figure 1 (a) shows that the shape of FTIR peak changes with deposition pressure, the width of the peak increasing with decreasing pressure in the reactor (corresponding to increasing substrate bias). A separate peak becomes visible at 2870 cm^{-1} as the pressure increases. This peak corresponds to a polymeric type sp^3 CH stretching mode [4, 8] and is clearly distinct in the film deposited at 300 mtorr (CY3 in Figure 1 (a)). With decreasing pressure this peak broadens and becomes a shoulder of the main peak. Another polymeric contribution from the olefinic sp^2 CH mode is observed as the shoulder at 2970 cm^{-1}, in film CY3. All peaks have a shoulder at 3050 cm^{-1} corresponding to a contribution from the aromatic sp^2 CH stretching mode .[4] The height of this shoulder is much stronger for film CY1 deposited at 100 mtorr (-228 V DC). The results described above indicate that the films deposited from pure cyclohexane at the higher pressures contain a polymeric fraction in addition to the hard crosslinked DLC. A similar behavior was observed in DLC films deposited by DC PACVD from cyclohexane, however the same variation in the shape of the peaks was observed for films deposited at much larger biases of -400 V DC to -800 V DC [3].

As can be seen in Table I, the variation of the hydrogen content in the discussed films is limited between 44 %, and 47 % hydrogen. However, the intensities of the normalized peaks in Figure 1 (b) indicates a strong decrease in the optically active hydrogen with increasing substrate bias. The intensity of the IR peak of film CY1, deposited at a bias of -238 V DC is less than half that of film CY3 deposited at -95 V DC. This indicates that the DLC film deposited at the lower bias contains much more hydrogen bonded to carbon atoms in C-H bonds than the film deposited at the higher bias. Decreasing the pressure in the plasma and increasing the substrate bias results in enhanced fragmentation of C-H bonds in the plasma species and increasing crosslinking in the DLC film.

The effect of argon dilution of the precursor on the IR absorption in the samples prepared at 200 mtorr is illustrated in Figure 2. Increasing the dilution with argon causes the broadening of the FTIR peak at 2920 cm^{-1} and removes the separation of the peak at 2870 cm^{-1}. The dilution also results in broadening of the peak at the higher wavenumbers and the shape of the peak of sample C2A2 in Figure 2 (a) is almost identical to that of CY1 in Figure 1 (a).
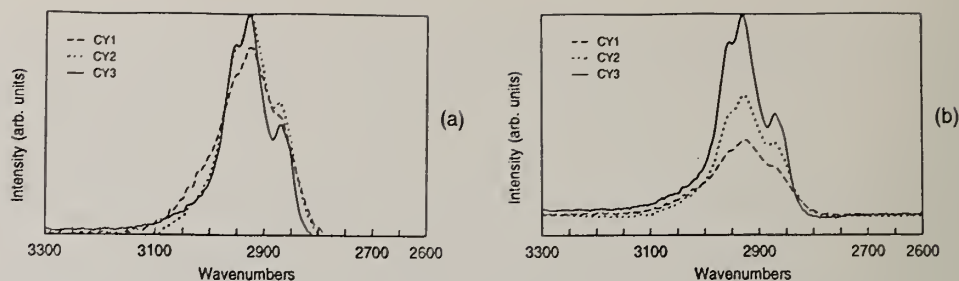
Figure 1.   FTIR peaks obtained from DLC films deposited from pure cyclohexane: (a)
peak heights adjusted to full scale; (b) peaks normalized for identical thickness.

Dilution of the cyclohexane with argon up to a ratio of 1/2 does not change the total hy-
drogen content of the DLC films (44 %), however a dilution of 1/4 decreases the hydrogen
content to 38 % (Table I).   However the bonded hydrogen concentration decreases
monotonously with increasing argon dilution, as indicated by Figure 2 (b), where the in-
tensity of the FTIR peak of sample C2A4 is about half of that of sample CY2. The effect
of argon dilution at constant pressure on hydrogen content and IR absorption in the DLC
films is thus similar to that of increasing bias with decreasing pressure in pure hydrocarbon
plasma.

The effect of the deposition conditions on the index of refraction of the DLC films is pre-
sented in Figure 3. For films prepared from pure cyclohexane, the index of refraction de-
creases with increasing pressure, from 1.84 for the film deposited at 100 mtorr to 1.60 for
the film deposited at 300 mtorr. Dilution of the cyclohexane with argon at a pressure of
200 mtorr results in an increase of the index from 1.67, for the films deposited from pure
cyclohexane, to 2.19, for the film deposited at a dilution of cyclohexane/argon = 1/4.

Both the changes in the FTIR peak, shown in Figure 2, and the changes in the index of
refraction, shown in Figure 3, indicate that dilution of the hydrocarbon precursor with argon
enhances the DLC properties of the films. Increasing argon dilution, at otherwise identical
plasma conditions, induces increased crosslinking in the deposited films as indicated by
broader FTIR peak, less optically active hydrogen, and increased index of refraction.

The variation in the optical properties of the DLC films with the deposition conditions is
reflected in the wear resistance of the films. The wear rates at different normal loads, ex-
pressed in wear track depth per thousand rotations, are presented in Figure 4. The wear rates
are shown on a logarithmic scale and the full-scale bars indicate that the film was worn
through very fast at the specific load. Films CY2 and CY3, deposited at pressures of 200
mtorr and 300 mtorr, were extremely soft and wore through very fast even at a load of 0.029
N (3 g). Film CY1, deposited at 100 mtorr, had a wear rate of 3.7 Å/10^3 rot. at a load of
0.108 N (11 g), but was worn through very fast at a load of 30 g 0.294 N (30 g).

Argon dilution of the precursor resulted in a strong increase in the wear resistance of the
films (Figure 4). While film CY2 had no wear resistance even at a load of 3 g, sample
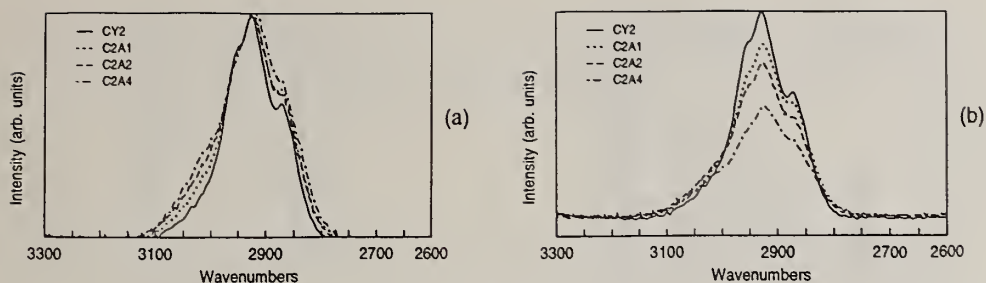
Figure 2. **FTIR peaks obtained from DLC films deposited from cyclohexane+Ar:** (a) peak heights adjusted to full scale; (b) peaks normalized for identical thickness.

C2A2, prepared at a dilution of 1/2 reached a wear rate of only 1.7 $\text{Å}/10^3$ rot. at 30 g. The wear resistance of the films thus correlates with the results of FTIR and index of refraction and shows an enhancement of the diamond-like properties either with decreasing pressure or with increasing dilution with argon, at constant pressure.

The investigation of the thermal stability of the DLC films by FTIR and FRES [9] has shown that for films deposited from pure pure cyclohexane the thermal stability decreases with increasing deposition pressure. While only small changes were observed in the FTIR peak of sample CY1 after annealing at 400 °C, the peak decreased by about 70 % for CY3. A similar behavior was observed for the changes in the total (bonded and unbonded) hydrogen concentration in the films after annealing as well as for the changes in film thickness.

Argon dilution of the precursor had a strong effect on the thermal stability of the DLC films deposited at 200 mtorr. Even a dilution of cyclohexane/argon = 1/1 had a strong effect on the FTIR peak. The FTIR peak obtained from a film deposited at this dilution changed only slightly after annealing at 400 °C, as compared to the strong reduction in its intensity for the sample deposited from undiluted cyclohexane. Increasing the dilution to 1/4 resulted in a DLC film which had a high stability during annealing at 400 °C. No change was observed in the FTIR peak intensity or in hydrogen concentration in the films deposited at this dilution, after annealing at 400 °C. Sample C2A4 was found to be even more stable than sample CY1 which had some hydrogen loss after annealing at 400 °C. After annealing at 500 °C all investigated films undergo much stronger changes and the dilution of the cyclohexane with argon has only a small effect on the behavior of the films at this higher annealing temperature.

The results described above showed that, for deposition of DLC from cyclohexane by RF PACVD at constant power density, there is a pressure threshold for obtaining DLC characteristics. Films deposited at pressures below the threshold display DLC characteristics, such as higher refractive index, shape of FTIR peak, wear resistance, while films deposited above the threshold pressure have polymer-like features. At constant power density decreasing pressure results in increasing substrate bias and the effect of pressure on films properties can be attributed also to the bias effect. Films with polymer-like properties and lower index of refraction were obtained in the present conditions at a bias below 140 V DC, while DLC

716
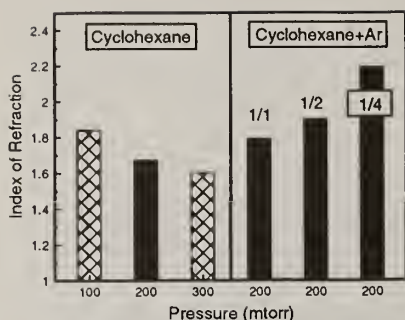
Figure 3. (left) Index of refraction vs pressure in reactor: the numbers indicate the cyclohexane/argon ratio in the plasma gas feed.
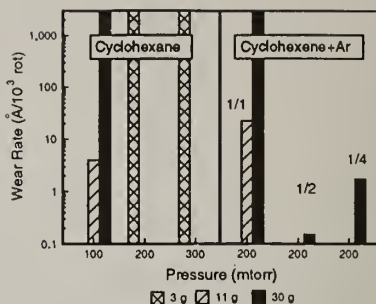
Figure 4. (right) Wear rates of DLC vs pressure in reactor and normal load: the numbers indicate the cyclohexane/argon ratio in the plasma gas feed.

films were obtained at higher bias. Dilution of cyclohexane with argon resulted in improved DLC properties in films deposited at a pressure above the threshold. The improvement increased with increased argon dilution. The dilution of the hydrocarbon with argon also improved the thermal stability of the material at 400 °C.

The effect of pressure, bias, and argon on the properties of the deposited films can be attributed to the effect of ion bombardment of the growing film. Reduced pressure, with corresponding higher negative substrate bias, results in bombardment of the films with ions having higher average energy. Addition of argon to the plasma gas results in higher density of positive ions, from the ionization of the inert gas and from enhanced fragmentation and ionization of the cyclohexane by Penning effects. Even if the argon addition has some effect on increasing the substrate bias, it is most probable that its effect on the properties of the deposited film can be attributed mostly to the increased density of positive ions bombarding the film.

It is thus possible to overcome reactor limitations, such as lowest achievable pressure, or choice of precursor, and yet obtain DLC films by diluting the precursor with the inert gas. One has however to keep in mind that the pressure threshold for obtaining DLC properties is dependent on the system, i.e. reactor geometry, and precursor, and has to be established for the employed system.

4. Summary

Using a RF PACVD process and cyclohexane as a precursor it was possible to prepare hydrogenated carbon films spanning a range of properties. The deposition process could be adjusted to obtain soft, polymer-like films, with relatively low refractive index, or hard wear resistant diamond-like films with higher refractive index. At constant RF power density, the properties of the films could be controlled by the pressure in the reactor, which in turn affects the substrate bias.

Dilution of the cyclohexane with argon enabled the deposition of diamond-like films, at conditions which otherwise produced polymer-like films. The enhancement of the diamond-like properties and the improvement of the thermal stability of the films increased with argon dilution.

5. References

1   P. Koidl, C. Wild, R. Locher and R. E. Sah, in *Diamond and Diamond-like Films and Coatings, NATO-ASI Series B: Physics*, edited by R. E. Clausing, L. L. Horton, J. C. Angus, and P. Koidl (Plenum Publishing Corp., New York, 1991), Vol. 266, p. 243.
2   A. Grill and V. Patel, Diamond Films and Technol. 1 (1992) 219.
3   A. Grill and V. Patel, Diamond and Related Materials 4 (1994) 62.
4   A. Grill and B. S. Meyerson, in *ch.5 of Synthetic Diamond: Emerging CVD Science and Technology*, edited by K. E. Spear and J. P. Dismukes (John Wiley and Sons, New York, 1994), p. 91.
5   A. Grill, V. Patel and B. S. Meyerson, J.Mater.Res. 5 (1990) 2531.
6   A. Grill, B. S. Meyerson and V. V. Patel, *IBM Report RC 13117*, IBM Research Division, Yorktown, NY, 1987.
7   A. Grill and V. Patel, Appl.Phys.Lett. 60 (1992) 2089.
8   B. Dischler, in *Amorphous Hydrogenated Carbon Films Proc. European Mat.Res.Soc.Symp.*, edited by P. Koidl and P. Oelhafen (Les Editions de Physique, Paris, 1987), Vol. 17, p. 219.
9   results to be published elsewhere do to space limitation for the present publication

Hard, Amorphous Carbon Deposited From a Fullerene Discharge

Eric B. Maiken and *Peter Taborek*

Department of Physics, *I.S.I.S.*, University of California, Irvine CA 92717-4575

Key words: fullerenes, hard(a-C), ions, plasma, resistivity, transmittance.

Abstract

Hard, amorphous carbon films were deposited from an ion source using fullerite as carbon feedstock. For fixed ion energies, the film resistivities decreased exponentially with substrate temperature, suggesting activated growth of a conductive phase. Resistivity at 300 K ranged from 10^{-3} to 10^4 Ωm. E_{04} optical gaps of conductive films ranged from 0.1 to 1.1 eV.

1. Carbon-Ion Source

We have constructed a specialized ion source to deposit hard, amorphous carbon (a-C) from a discharge in fullerene vapor. A detailed description of the source has been given elsewhere [1]. An illustration of the carbon-ion gun is shown in Fig. 1. Mixed fullerite powder (C_{60} and C_{70}), was placed in the crucible in the base of source. Fullerenes sublimed into the discharge chamber and fragmented into ionized and neutral carbon clusters in the plasma. Heating the discharge chamber walls was important for preventing condensation of the fullerenes. A beam of molecular carbon ions extracted from the discharge impinged on a sputter-cleaned substrate, and condensed into a film of hard a-C. Depositions have been made under vacuum on C, Si, Ge, Al, W, saphire, and glass at rates of 1 µm per hour. In this work, carbon molecular ion energies were fixed at 300 eV, corresponding to approximately 50 to 150eV per incident atom.
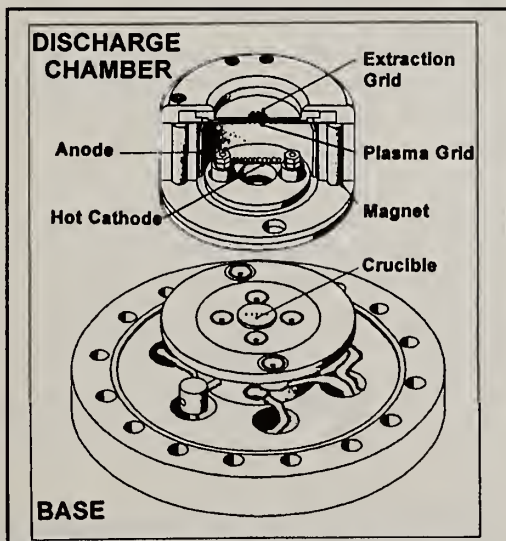
Fig. 1. Section of the carbon-ion source

720

2. Characterization of Hard, a-C Films

Substrate temperature was crucial in determining the optical absorption and the resistivity of the hard a-C films. With other deposition parameters fixed, a narrow temperature range resulted in films with widely ranging resistivities and optical gaps. Fig. 2 illustrates the trend at 300 K for films deposited at different temperatures. The exponential dependence of resistivity on inverse substrate temperature suggests growth of a conductive phase activated at 0.47 eV.
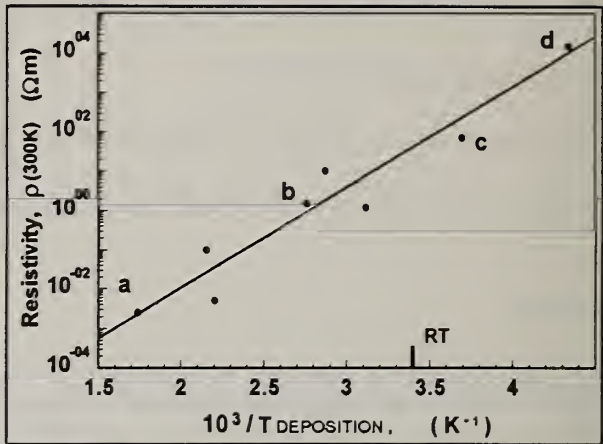
Fig. 2. Resistivities at 300K of eight films deposited at different temperatures. Points a, b, c, d refer to Fig. 3.

Arrhenius plots of dc resistivity of films deposited at four different temperatures are shown in Fig. 3. Measurements were made in situ, with a two point probe consisting of ohmic, aluminum contacts evaporated on a glass substrate. A slight reduction in resistivity occurred upon the initial heating of films above their deposition temperatures. The hysteresis was attributed to growth of the sp^2 bonded regions in the films, though the magnitude of the effect was much less than heating the films during deposition. Subsequent temperature excursions below the annealing temperature gave repeatable data, which is displayed in Fig. 3. We parametricly fit the resistivity data to two activated terms because a single fractional power exponential required nonphysical values for the density of states and carrier localization [1,2].
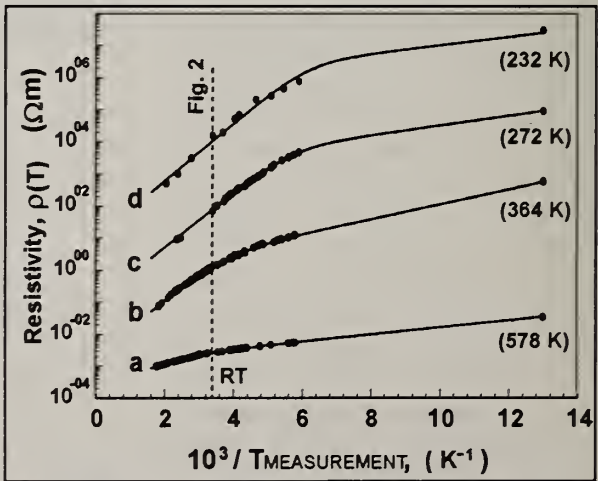
Fig. 3. Resistivity of a-C films deposited at temperatures noted parenthetically. Solid curves are fits to data.

With the resistivity of each film denoted as

$$\rho_i = [\sigma_{1i}\exp(-E_{1i}/k_BT) + \sigma_{2i}\exp(-E_{2i}/k_BT)]^{-1}, \qquad (1)$$

the subscripts (i) represent the four separate data sets in Fig 3, and k_BT the product of the Boltzman constant with absolute temperature. The parameters which provided the best fit to the data sets are listed with deposition temperatures in Table 1.

TABLE I.   Fit Parameters

Sample (i)	T_{DEP}(K)	E_{1i} (eV)	σ_{1i} ($\Omega^{-1}m^{-1}$)	E_{2i} (eV)	σ_{2i} ($\Omega^{-1}m^{-1}$)
a	578	0.11	5.2×10^3	0.022	770
b	364	0.17	450	0.046	1.8
c	272	0.17	10	0.030	10^{-3}
d	232	0.18	1.0	0.026	2×10^{-6}

Parameters fitting equation (1) to the data of Fig. 3.

The activation energies for conduction near room temperature, E_{1i}, were similar to the values found in [2], and close to values expected for excitation of electrons to defect states derived from the presence of non-six fold rings in graphitic clusters [3]. The activation energies E_{2i} are similar to values reported for evaporated carbon films [4].

Infrared transmission spectra of two carbon films of low resistivity, coating silicon substrates, are shown in Fig. 4. The data labeled a and b correspond to depositions under identical conditions to the films a and b in Table I. The curve labeled Si is the transmittance of a polished, uncoated silicon substrate. Curve b, corresponding to a film of intermediate resistivity, shows that the film is transparent in the infrared, and acts as an antireflection coating in the region between
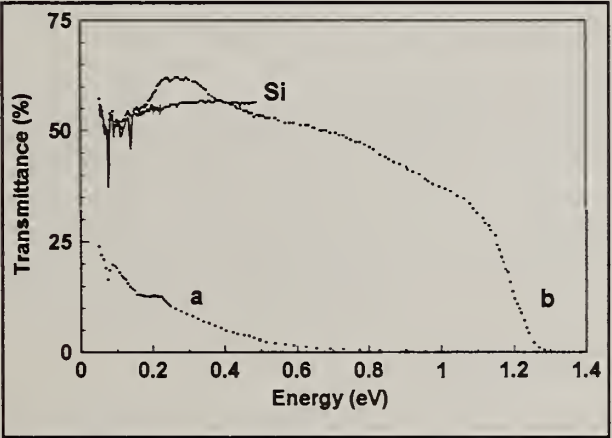
Fig.4 Infrared transmission spectra of conductive films.

0.11 eV and 0.41 eV. Notable in the spectrum are the absence of discrete absorption lines corresponding to infrared activity of intact fullerenes (between 0.1 and 0.18 eV) and hydrocarbons (C-H stretching mode at 0.37 eV), which may have been incorporated into the film during deposition. The gradual decrease in the transmittance

between approximately 0.5 eV and 1.1 eV is characteristic of the broad optical absorption edges found in amorphous carbon [3]. The E_{04} optical gap was 1.1 eV. The rapid decrease in transmittance between 1.1 eV and 1.25 eV was due to the abrupt onset of absorption of photons with energies near the band gap of the silicon substrate. Curve a illustrates the case of a conductive, hard a-C film, approximately 0.5 μm thick, The transmittance of the coated substrate was greatly reduced from the bare silicon. The E_{04} optical gap for this film was less than 0.1 eV.

The electronic and optical properties of heterogenous, amorphous carbon are determined by the proximity of the pi states of the sp^2 bonded phase to the Fermi level. All of the pi states lie within the gap associated with the sp^2 and sp^3 sigma bonds [3]. Graphitic clusters and fullerene fragments were presumably dispersed within the films and distributed over a range of sizes. Additionally, residual five-fold sp^2 bonded rings from fragmented fullerenes and non six-fold ring defects formed during deposition would affect both the density of defect states and the width of the optical absorption edge. The films b of Figs. 2,3 and 4, had moderate resistivity and optical gap. Within the context of the graphitic islands model of [3], the 1.1 eV optical gap arose from the pi bonded cluster size distribution, while the activation energies of conduction E_{1b} and E_{2b} were determined by the density of defects near the Fermi level and the extent of the sp^3 barriers between the pi bonded regions [2]. The conductive films a had small optical gap and conduction activation energies near room temperature (E_{1a}). Both the small values and equivalence of the gap and conduction energies are consistent with broadening of the π and π^* peaks in the density of states with increasing sp^2 bonded cluster size [3].

Mechanical properties of the a-C films were also affected by deposition temperature. Measurements of film stress, made by deflection of silicon cantilevers, indicate that the conductive films displayed lower intrinsic stress than the more insulating films. Representative stresses were: 0.4 GPa for the conductive films (such as a) and 1.5 GPa for the films of intermediate resistivity (such as b). All of the films adhered well to silicon and were highly abrasion resistant, maintaining specular reflectivity after being sanded with silicon carbide sand paper.

Acknowledgements.

References

1. E.B. Maiken and P. Taborek, to be published J Appl. Phys (1995).
2. D. Das Gupta, F. Demichelis, and A. Tagiaferro, Phil. Mag. B **63**, 1255 (1991).
3. J. Robertson and E.P. O'Reilly, Phys. Rev. B **35**, 2946 (1987).
4. A.Deenyi, A. Gheorghiu, A. Belu, and G. Korony, *Conduction in Low-mobility Materials* (Wiley-London, 1971) pps.217-228.

PREPARATION OF DIAMOND-LIKE CARBON AND BORON NITRIDE FILMS BY HIGH-INTENSITY PULSED ION BEAM DEPOSITION*

D. J. Rej[1], G. E. Remnev[2], H. A. Davis[1], I. F. Isakov[2], Yu. F. Ivanov[3],
G. P. Johnston[4], V. M. Matvienko[2], M. Nastasi[1], J. C. Olson[1], A. V. Potyomkin[2],
H. K. Schmidt[5], B. S. Semukhin[6], D. R. Tallant[7], M. O. Thompson[8],
W. J. Waganaar[1], K. C. Walter[1], D. B. Williams[9], and A. N. Zakoutayev[2]

[1]Los Alamos National Laboratory, MS-D434, Los Alamos, NM 87545, USA
[2]Nuclear Physics Institute, Tomsk Polytechnic University, Tomsk 634050, Russia
[3]Institute of Building Engineering, Tomsk Polytechnic Univ., Tomsk 634050, Russia
[4]Chem. Engineering Dept., Univ. New Mexico, Albuquerque, NM 87131, USA
[5]SI Diamond Technology, Inc., 2435 North Blvd., Houston TX 77098, USA
[6]Institute of Strength Physics and Materials Science, Tomsk 634050, Russia
[7]Sandia National Laboratory, P. O. Box 5800, Albuquerque, NM 87185, USA
[8]Materials Science and Eng. Dept., Cornell Univ., Ithaca NY 14853, USA
[9]Materials Science and Eng. Dept., Lehigh Univ., Bethlehem, PA 18015, USA

Key words: boron nitride, diamond, DLC, high-intensity pulsed ion beams

Abstract

Intense ion beams (300-keV C^+, O^+, and H^+, 20-30 kA, 50 to 400-ns pulsewidth, up to 0.3-Hz repetition rate) were used to prepare diamond-like carbon (DLC) and boron nitride (BN) films. Deposition rates of up to 25 ± 5 nm/pulse were obtained with instantaneous rates exceeding 1 mm/s. Most films were uniform, light brown, translucent, and nonporous with some micron-size particulates. Raman and parallel electron energy loss spectroscopy indicated the presence of DLC. The films possessed favorable electron field-emission characteristics desirable for cold-cathode displays. Transmission electron microscopy (TEM) and transmission electron diffraction (TED) revealed that the C films contained diamond crystals with 25 to 125-nm grain size. BN films were composed of hexagonal, cubic and wurtzite phases.

1. Introduction

There has been considerable progress recently in the development of high-intensity pulsed ion beams (HIPIB)[1]. While a primary application driving this development is fusion energy[2], several materials processing applications have emerged. Because of the short range of ions in matter, applications usually involve material surface modification, *e.g.*, implantation, alloying, or deposition. In the high-intensity pulsed ion beam deposition (HIPIBD) process[3-6] (Fig. 1), a beam is propagated into a target, resulting in the significant evaporation and ionization of

target material (*e.g.*, a beam fluence of 100 J/cm^2 deposited over a 0.5 μm range will heat a target surface about 5×10^5 K). Ablated plasma is then condensed at high rates onto an adjacent substrate. HIPIBD is similar to pulsed laser deposition enabling the congruent evaporation and deposition of complex stoichiometric films. There are added benefits since energetic ions penetrate deeper into a target than a laser beam and couple better with surface plasmas and metallic targets. HIPIBD may allow an economical pathway for bulk deposition of advanced coatings. since the efficient HIPIB accelerators cost orders of magnitude less than lasers with comparable output.
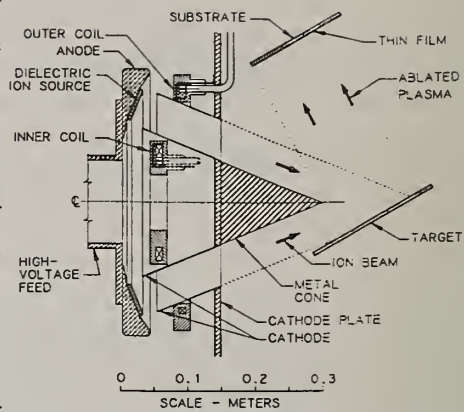
Fig. 1: Experimental arrangement for HIPIBD.

2. Experimental

Experiments were performed on the Los Alamos Anaconda[7] and the Tomsk TEMP accelerators[8]. Beam parameters are listed in Table I. Both accelerators utilized magnetically-insulated ion diodes driven by Marx generators. In Anaconda, an applied-radial magnetic field extraction diode geometry was configured for ballistic focusing of the beam (Fig. 1)[5]. An acrylic dielectric attached to the anode electrode was used as the ion source. The beam converged to a 75-mm-diam focus located approximately 0.30 m from the diode. A $203 \times 152 \times 2.5$ mm graphite target was positioned near the beam focus with its surface 25° from the beam axis. Deposition was performed onto glass, Cr, and Si substrates which were not preconditioned and initially at room temperature. Substrates were placed at either 150 or 225 mm from the target, at angles θ between 0° (Fig. 1) and 90° from target normal. Substrate heating from the condensation of ablated vapor was examined with thin-film Pt thermometers capable of measuring substrate temperature during deposition with nanosecond time resolution[9,10]. Experiments were performed at a base pressure of approximately 1×10^{-6} torr.

Table I: Beam parameters

Device	Energy (keV)	Current (kA)	Pulsewidth (ns)	Species	Power density on target (MW/cm^2)	Repetition Rate
ANACONDA	350	30	400	H,C,O	80	1 pulse/ 3 min
TEMP	300	20	50	H, C	75	0.3 Hz

The TEMP accelerators utilized two innovations that enabled simple and reliable operation at repetition rates of up to 0.3 Hz. First, the magnetic insulation field was generated by a coil connected in series with the diode load. Second, the ions were produced directly from a conducting anode electrode by a preliminary negative prepulse applied before the main positive diode pulse. The beam was focused to a 20-cm^2 cross-section onto a 45-mm-diam C or BN target aligned 45° to the beam axis. Substrates included (100) Si, (100) MgO, and glass, initially at room temperature, and positioned 35 to 50 mm from the target, at $\theta = 0°$.

3. Results

Approximately 10 mg of graphite was ablated with each Anaconda pulse, which was in good agreement with a one-dimensional heat-transport model[11]. From visible framing photography[12], the ablated plume front was observed to expand at approximately 2×10^4 m/s. Deposition rates ranged from 12 to 25 nm/pulse, depending on substrate position relative to the target, while the thin-film Pt resistor calorimeter measurements inferred instantaneous deposition rates of greater than 1 mm/sec. The measured power density incident onto the substrate decreased with increasing angle or target-substrate separation, from 70 kW/cm^2 over approximately a 10 μs period at the 0.15-m separation and $\theta = 0$, to 5 kW/cm^2 over 20 μs at 0.20-m separation and $\theta = 30°$. At the highest heating power, the inferred temperature rise of a glass substrate was about 1500°C, which was above the stability temperature for DLC. The Raman spectra of films deposited at this condition showed a glassy-C characteristic, with DLC characteristics only present at larger target-substrate separations or angles where substrate heating was lower[5]. More complete discussion of the substrate heating measurements may be found elsewhere[10]. Many film properties have already been published[5]. The films were light brown and translucent. A typical stylus profilometry profile is shown in Fig. 2. The films displayed amorphous XRD spectra, while SEM micrographs revealed a uniform, non-porous morphology with feature sizes of ~100 nm, with micron-sized particulates at concentrations of about ten particles per 100 μm^2. Parallel electron energy loss spectroscopy indicated a 25% concentration of sp^3-bonds. Film electrical resistivity ranged from 0.01 to 10 Ω-m. The films possessed favorable electron field-emission characteristics, with good adherence to Fowler-Nordheim theory. Emission was observed at applied electric fields E of 10 V/μm. A reasonably high current was achieved at low applied voltages. This suggests that these films may prove promising for display applications.
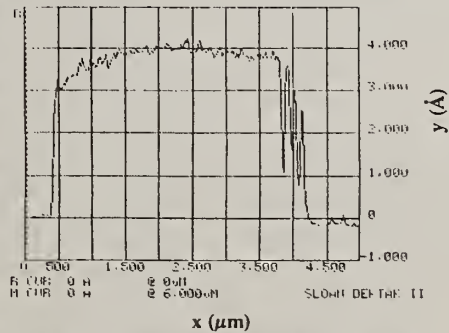
Fig. 2: Profilometry profile of C film, prepared with 20 HIPIB pulses.

Fig. 3: TEM of C film deposited on a MgO substrate.
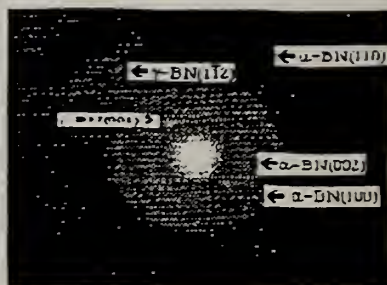
Fig. 4: TED pattern of BN deposited on glass.

Carbon deposition rates on TEMP ranged from 10 to 15 nm/pulse. TEM, TED, and X-ray diffraction indicated the presence of amorphous carbon, crystalline graphite, and diamonds (Fig. 3). Dark field imaging with diffraction analyses showed that the diamonds were 25 to 125 nm in size with a population of up to 10% in the film. The average size of the diamond particles was estimated to be about 63 nm[13].

Boron nitride deposition with the Tomsk beam onto crystalline substrates gave a mixture of hexagonal (α), cubic (β), and wurtzite (γ) phases. Films deposited at room temperature consisted mainly of amorphous α-BN (up to 70%), with tens of percent concentration of β-BN[14]. With glass substrates, TED indicated the presence of amorphous α-BN and single crystalline γ-BN only (Fig. 4). There was no evidence of β-BN formation.

4. References

1. V. M. Bystritskii and A. N. Didenko, *High-Power Ion Beams* (American Institute of Physics, New York, 1989).
2. J. P. VanDevender and D. L. Cook, Science **232**, 831 (1986).
3. Y. Shimotori, M. Yokahama, H. Isobe *et al.*, J. Appl. Phys. **63**, 968 (1988).
4. G. E. Remnev, *et al.*, Laser and Particle Beams **11**, 707 (1990).
5. G. P. Johnston, P. Tiwari, D. J. Rej *et al.*, J. Appl. Phys. **76**, 5949 (1994).
6. G. A. Meli, K. S. Grabowski *et al.*, J. Vac. Sci. Techn. (in press).
7. D. J. Rej, R. R. Bartsch, H. A. Davis *et al.*, Rev. Sci. Instr. **64**, 2753 (1993).
8. I.F.Isakov *et al.*, Vacuum **42**, 159-162 (1991).
9. D. P. Brunco, J. A. Kittl, C. E. Otis *et al.*, Rev. Sci. Instr. **64**, 2753 (1993).
10. J. C. Olson *et al.*, Submitted to Proc. Materials Res. Soc. (1995).
11. H. A. Davis *et al.*, submitted to J. Appl. Phys.(1995).
12. D. J. Rej et al., Proc. 10th Inter. Conf. on High-Power Particle Beams, W. Rix and R. White Eds., (NTIS, Springfield VA, 1994) pp. 222-225.
13. A.N.Zakoutayev, *et al.*, Submitted to Proc. Materials Res. Soc.(1995).
14. A.N.Zakoutayev, G.E.Remnev *et al.*, *op cit.* Ref. 11, pp. 840-843.

Deposition and Characterization of DLC/SiO₂ Nanocomposite Prepared by Ion-Assisted PECVD

Jung H. Lee[1], Dong S. Kim[1], Young H. Lee[1] and Bakhtier Farouk[2]

[1]Department of Chemical Engineering, Drexel University, Philadelphia, PA 19104
[2]Department of Mechanical Engineering, Drexel University, Philadelphia, PA 19104

Key words: adhesion, nanocomposite, optical, PECVD, stress, thin film

Abstract

Various DLC-SiO₂ nanocomposite films were deposited on silicon and quartz substrates maintained at 25 °C in a capacitively coupled, 13.56 MHz powered, asymmetric plasma reactor using styrene and tetraethoxysilane as the source gases, and hydrogen as a carrier gas. High deposition rate (14.3 Å/s) was achieved due to the 8 carbon atoms in styrene. The films have relatively low intrinsic stress, thus it was possible to deposit thicker films (5 μm). The film's Knoop microhardness and optical transparency in the visible region were comparable to those of DLC.

1. Introduction

Diamond-like carbon (DLC) film has attracted considerable attention because of its extreme properties in hardness, thermal conductivity, optical transparency, and chemical resistance. Potential applications include scratch-resistance coating, optical coating, and coating on plastics [1-3]. DLC films have been prepared by a variety of methods including dc or rf plasma-enhanced chemical vapor deposition (PECVD) [4], sputtering [5], and ion beam deposition [6], using a variety of carbon source materials.

During the film formation in rf PECVD, ions play an important role in determining film structure and properties [7]. The structure of deposits can be classified as polymer-like, diamond-like, or graphite-like carbon depending on the ion energy on the substrate. At low ion energy, the film is soft and contains higher concentration of hydrogen, and it is called polymer-like carbon. At medium ion energy, the film contains less hydrogen and more sp³ hybridized carbon. The resulting film is very hard and called diamond-like carbon. At higher range of ion energy, the hydrogen concentration is decreased further and the fraction of sp² coordinated carbon is increased, resulting in graphite rich film.

The most critical problem of DLC films prepared by ion-assisted PECVD is the high intrinsic stress [8]. The stress depends on the ion energy and the film thickness. Therefore, in general, DLC films show very poor adhesion on both metallic and ceramic substrates, and this limits their practical applications. To enhance the adhesion of DLC films, methods such as interfacial layer formation [9], surface cleaning [10], and pulse laser irradiation [11] have been used with limited success. Recently,

functionally graded nanocomposites have received attention for tailoring properties of thin films. Especially, Dorfman et. al. [12-13] have investigated the deposition of diamond-like nanocomposites (a-C:H/a-Si:O) from a plasma discharge of polyphenilmentilsilozane. They found that the deposits are stable.

In this paper, we present a deposition of DLC-SiO$_2$ nanocomposite using a gas mixture of styrene, tetraethoxysilane (TEOS) as the source gas, and hydrogen as the carrier gas in an ion-assisted PECVD system. Film structure, stress, adhesion and optical properties of the films are discussed.

2. Experimental

The details of the experimental set-up are described elsewhere [10]. Briefly, the DLC-SiO$_2$ nanocomposite films were deposited on (100) silicon wafer and quartz substrates maintained at 25 °C in a capacitively coupled, 13.56 MHz powered, asymmetric plasma reactor using styrene (C_8H_8) and TEOS [$Si(OC_2H_5)_4$] as the source gases, and hydrogen as the carrier gas. A self-biased negative voltage (-V_{dc}) is developed at the powered electrode due to the asymmetry of electrode areas. Before the film deposition the substrate surface is cleaned, in-situ, by hydrogen plasma at 45 mTorr, and 60 W for 10 min.

For depositing the films, the hydrogen flow rate was set at 40 sccm, whereas the flow rates of styrene and TEOS were varied to change the chemical composition of the deposited films. Their flow rates ranged 0-3.6 sccm for styrene and 0-3 sccm for TEOS, respectively. The total pressure of the reactor during film deposition varied from 75 mTorr to 300 mTorr. To investigate the effect of interlayer in DLC-SiO$_2$ nanocomposite films, a two-step deposition procedure was employed for some samples by changing the gas flow rates of the source gases. During the first 2 min., the gas flow rate ratio (r), where r is the flow rate of TEOS/(flow rate of TEOS+flow rate of styrene), was maintained at 0.75 until a film thickness of about 40 nm is reached. The applied power and the chamber pressure used in this step were 30 W and 75 mTorr, respectively. In the second step, r was changed to 0.2 at a constant pressure of 77 mTorr. The applied power in the second step was varied to obtain different ion energy at the substrate.

The film thickness was measured using an ellipsometer. The film adhesion on the silicon was evaluated by Scotch tape test. The stress was measured by using a wafer deflection gage for films deposited on 3 inch silicon wafers. Knoop hardness of the film was measured at a load of 0.1 N. The film thickness used for the microhardness test was thicker than 0.5 μm. A UV-VIS spectrometer was used for measure transmission characteristics of the films deposited on quartz.

3. Results and Discussion

Fig. 1 shows the variation of a refractive index (RI) of the film at different gas flow ratio of styrene, and TEOS at a constant power input of 30 W. With increasing r, RI decreased from 2.21 at r=0 to 1.56 at r=1. It can be deduced that the fraction of DLC in the film decreased with increasing r, thus decreasing RI of the film. Also, it appears that the stoichiometry of the nanocomposite can be tailored by adjusting the flow rates of styrene and TEOS.

It is known that the film growth rate is slow when low molecular carbon compound such as methane (CH_4), or acetylene (C_2H_2) is used as the precursor in the rf PECVD. The deposition rate depends mainly upon pressure and bias voltage at a constant substrate temperature, but it is difficult to

obtain over 3 Å/sec from these precursors. Fig. 2 shows the deposition rate of the nanocomposite films as a function of pressure at power input of 30 W and r of 0.2. The deposition rate increases linearly with increasing pressure up to 200 mTorr, then levels off. It was 5.7 Å/sec at 50 mTorr, and increased to 14.3 Å/sec at 250 mTorr. Note that the source of carbon is mainly from styrene. We observed that silicon oxide film prepared from TEOS and H_2 contains negligible C-H concentration (determined by FTIR). Therefore, the high deposition rate obtained is due to styrene which has 8 carbon atoms per molecule.

Fig. 3 shows the film's intrinsic stress as a function of V_{dc} for different types of films: DLC, nanocomposite, and nanocomposite with SiO_2-rich interlayer. The intrinsic stress increases with increasing $-V_{dc}$, and is compressive. The DLC films are shown to have the highest compressive stress. It was 3.7×10^9 dyne/cm^2 at -300 V of V_{dc}, and 7.3×10^9 dyne/cm^2 at -450 V of V_{dc}. Also, the intrinsic stress of films is varied with film thickness. For example, DLC films prepared at -300 V of V_{dc} show that the intrinsic stress was more or less constant up to a thickness of 250 nm, beyond which the stress increased as the thickness increased. The high intrinsic stress of the DLC films affects their adhesion. Thicker DLC films show wrinkling after film deposition, and the threshold film thickness for the adhesion failure decreases with increasing $-V_{dc}$. The nanocomposite film without SiO_2-rich interlayer prepared at the -300 V of V_{dc} showed wrinkling when the film thickness was over about 2 μm, whereas the nanocomposite with SiO_2-rich interlayer was stable up to 5 μm, the thickest film thickness studied in this research. The stability of this film may be due to the combined effects of reduced intrinsic stress (Fig. 3) and chemical locking by SiO_2 molecules at the film-substrate interface.

It is desirable to have good hardness for application in protective layers. We found that the nanocomposite films have greater microhardness than that of DLC film. For example, nanocomposite prepared at -300 V of V_{dc} and 0.2 of r had Knoop microhardness of about 6200 Kg/mm^2, whereas DLC film prepared same V_{dc} showed the Knoop microhardness of about 4500 Kg/mm^2.

Fig. 4 compares the transmittance of the nanocomposite and the DLC films prepared same $-V_{dc}$ of -300 V in UV-VIS region. The nanocomposite is shown to be very transparent in visible region.

4. References

1. J. C. Angus and C. C. Hayman, Science 241, 913 (1988).
2. K. V. Ravi, Mater. Sci. & Eng. B19, 203 (1993).
3. C. V. Deshpandey and R. F. Bunshah, J. Vac. Sci. Technol. A7, 2294 (1989).
4. N. Fourches and G. Turban, Thin Solid Films 240, 28 (1994).
5. F. Richer, K. Bewilogua, K. Kuper, I. Muhling, B. Rau, B. Rother, and D. Schumacher, Thin Solid Films 212, 245 (1992).
6. J. J. Cuomo, D. L. Pappas, J. Bruley, J. P. Doyle, and K. L. Saenger, J. Appl. Phys. 70, 1706 (1991).
7. J. Roberton, Pure & Appl. Chem. 66, 1789 (1994).
8. A. Grill and B. S. Meyerson, in Synthetic Diamond: Emerging CVD Science and Technology, edited by K. E. Spear and J. P. Dismukes (John Wiley & Sons, Inc., New York, 1994), p. 123.
9. A. Grill, B. Meyerson, and V. Patel, J. Mater. Res. 3, 214 (1988).
10. J. H. Lee, D. S. Kim, and Y. H. Lee, Poly. Preprint 35(2), 901 (1994).
11. J. Narayan, V. P. Godbole, G. Matera, and R. K. Singh, J. Appl. Phys. 71, 966 (1992).
12. V. F. Dorfman, Thin Solid Films 212, 267 (1992).

730

13. V. F. Dorfman, A. Bozhko, B. N. Pypkin, R. T. Borra, A. R. Srivasta, H. Zhang, T. A. Skotheim, I. Khan, D. Rodichev, and G. Kirpilenko, Thin Solid Films 212, 274 (1992).
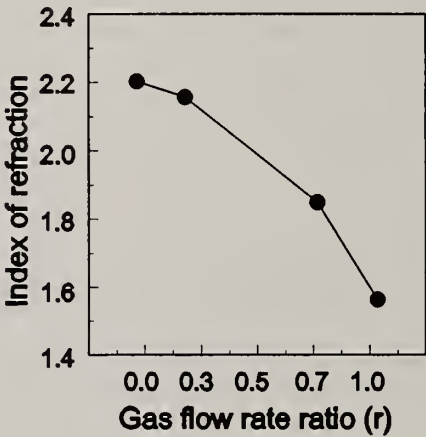
Figure 1. Variation of RI as a function of gas flow rate ratio (r).
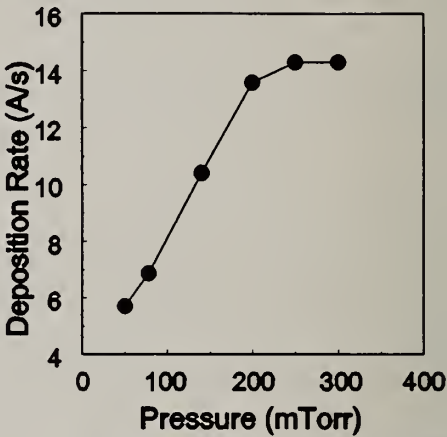
Figure 2. Variation of film deposition rate as a function of pressure.
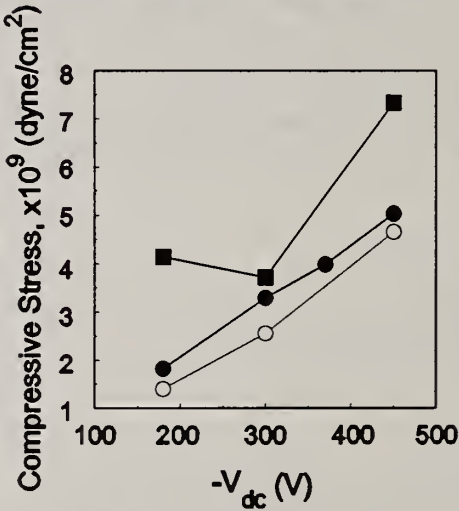
Figure 3. Film stress as a function of -V_{dc}. Filled rectangular:DLC. Filled circle:Nanocomposite. Unfilled circle :Nanocomposite with interlayer.
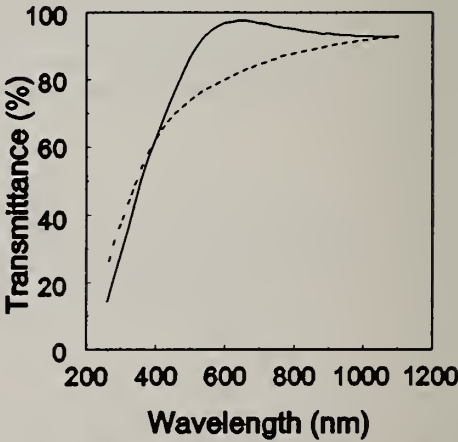
Figure 4. Film transparency in UV-VIS region. Solid line:nanocomposite (124 nm). Dot line:DLC (81 nm).

EFFECT OF DEPOSITION CONDITION AND POST GROWTH IRRADIATION TREATMENT ON THE PHYSICAL PROPERTIES OF DIAMOND-LIKE CARBON FILMS

V.A.Semenovich[1], N.I.Klyui[2],S.I.Frolov[2], V.G.Litovchenko[2], S.N.Dub[1],
B.N.Romanyuk[2]

1 Institute for Superhard Materials Ukr.Nat. Acad.Sci., 254074, Kiev, UKRAINE
2 Institute of Semicond.Physics, Ukr.Nat. Acad.Sci., 252028, Kiev, UKRAINE

Key words: bias voltage, hardness, ion implantation, phase-structure transformation, spectral ellipsometry, Young's modulus

Abstract

Effect of the RF (13.56 MHz) amplitude (Usa) bias voltage on the physical properties of the films has been examined. Relation between the properties of the films and growth conditions were obtained. Bias voltage and gas composition have a marked influence on the properties of prepared films. Nitrogen implantation of diamond-like carbon (DLC) films improves essentially mechanical properties (increasing of the hardness and Young's modulus more than two times), which correlates with changes of the optical properties, namely, decreasing of optical band gap and increasing of refractive index of the implanted layer.

1.Introduction

DLC films possessing a number of unique properties, such as high transparency, chemical and irradiation resistivity, etc., are candidates for modern micro- and opto-electronics. A highly important feature of DLC films is possibility of varying their characteristics under changes of deposition conditions [1]. On the other hand ion implantation offers considerable potentialities of purposeful and controllable modification of DLC film properties. Results of most studies of ion-implanted DLC films have shown that ion implantation leads to the degradation of their optical, mechanical and other properties [2,3]. It is important to note that the most changes of the properties of ion-implanted DLC films have been observed under doses of implantation right up to 10^{16} ions/cm^2 after which with further increasing of dose, changes are not so observed [4]. In resent years special attention has been focused on investigation of DLC films implanted by N$^+$ ions, which is connected with attempts to

synthesize C_3N_4 films [5]. However, the influence of N^+ ions implantation on mechanical and optical properties of DLC films have not been adequately studied. Besides, many workers used only hard DLC films for the N^+ ions implantation. Thus, the purpose of the present work is to verify the possible correlation of the optical constants (n,k) of DLC films and with their synthesis conditions, using concrete method. Another object of the paper is to examine the mechanical properties of DLC films implanted by N^+ ions and search optimal of both implantation parameters and hardness of un-implanted DLC films to improve their physical properties.

2. Experimental details

The synthesis of diamondlike carbon films was carried out in RF parallel plate reactor with watercooling electrodes , using lower pressure (0.1-0.8 torr), constant substrate temperature (about 300 K) and various concentration CH_4 (ranging from 10 to 30%) in CH_4-H_2 gas mixture. The apparatus used for this study has been described in details in ref [6] . The substrate holder was RF (13.56 MHz) biased ($U_s{}^a$) with amplitude ranging in value from 500 to 2000 volts. During the experiment RF bias value was varied under fixation of other deposition parameters. Quartz, silicon and germanium plates were used as substrates. The thicknesses of the films were varied in the region between 100 and 2000 nm.

Spectra of the optical constants of both as-deposited and implanted DLC films in the photon energy range 1.5-6.0 eV were measured by spectral ellipsometry using a rotating analyser [7].

The films obtained have been implanted by N^+ ions with energy of 150 keV and dose of 1×10^{16} ions/cm^2 under current density of ion beam less than 3 μA/cm^2. Implantation has been carried out into cooled substrate through the mask, which was used as shadow for the part of specimen. The mechanical properties of DLC films were studied by Nano Indenter II mechanical properties microprobe (Nano Instrument Inc., Knoxville, TN, USA). This device is capable of high-accuracy recording of the depth of penetration as a function of indenter load. The slope of the unloading curve dP/dh was used to assess the Young's modulus [8]. Tests were performed by Berkovich indenter under loads of some mN and penetration rate of 15 nm/s.

3. Results and discussion

The films obtained, in the main, are characterized near-linear relation between refractive index (n) and $U_s{}^a$ (fig.1). At this takes place extinction coefficient (k) in all three cases does not excess 0.09 and its value correlated with variation of n, depending on $U_s{}^a$. It is seen (fig.1) that increasing of the methane concentration in gas mixture and decreasing $U_s{}^a$ leads to films growth, which have both small value of refractive index (n~1.6) and hardness (H_v~0.6 GPa). The optical gap (E_g) of such films

determined from the spectral dependence of the function $(\alpha \hbar w)^{1/2}$ versus photon energy ($\hbar w$) [1] was about 3.3 eV. At the same time, films obtained under high U_s^a (1500-1700 voltages) from the gas mixture with excess hydrogen was characterized by n~2.0 and H_v~10 GPa. The Eg in this case does not excess 2.0 eV.
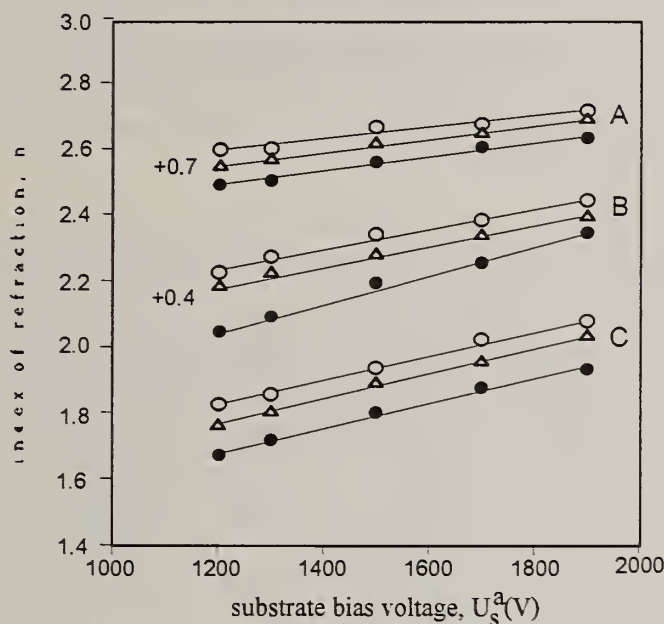
Fig.1. Index of refraction n vs substrate RF (13.56 MHz) bias voltage (U_s^a) for films deposited from gases mixtures: A - CH_4 (20%)/H_2(80%); B - CH_4(25%)/H_2(75%); C - CH_4(30%)/H_2(70%) at different total pressure: ● - 0.8 torr; △ - 0.6 torr; ○ - 0.4 torr.

Further mechanical soft (H_v~0.6 GPa) films have been implanted by N^+ ions. It is seen from Table 1 that after implantation a drastic improvement of mechanical properties of DLC films (modified layer) is observed, i.e. the increase of the hardness and Young's modulus more than two times as against as-deposited DLC films. The last result correlates with a considerable increase of refractive index of the modified layer (from n=1.695 for as-deposited films to n=2.28 for implanted films at λ=6328 Å). Thus, it follows from the above that nitrogen implantation do not induce graphitization of DLC films, but , to our knowledge, results in phase-structure transformations and improves their mechanical properties. It is interesting to point out, as well, that the Eg decreases from 3.3 eV (as-deposited DLC film) to 1.7 eV (implanted DLC film). This is due to hydrogen effusion from the films under ion beam action, that is supported by changes of FTIR spectra in the stretching region of the C-H bonds. Aside from decreasing peak intensity of corresponding C-H vibrations, a small absorption peak has arisen at 2325 cm^{-1} in the FTIR spectra of implanted DLC films. The appearance of the stretched peak at 2325 cm^{-1} cannot be unambiguously assigned either to C≡N

vibrations in implanted film (corresponding peak is about 2200-2240 cm^{-1} [9]) or to C-C vibrations (absorption band corresponding to the stretching vibration of C=C bonds is at 1600 cm^{-1} [9] and C≡C is at 2020 cm^{-1}). In this connection it is difficult to interpret unambiguously the anomalous increasing of hardness, Young's modulus and refractive index of the nitrogen-implanted DLC films. More likely, the above-described effect is due to both factors,i.e. formation of C-N bonds and ion-induced phase-structural transformation in the DLC film. For more complete understanding of the effect revealed, further investigations are required of the effects of as-deposited film structure (different hydrogen concentrations) and doses dependence on physical properties of implanted DLC films.

TABLE 1. Hardness (H) and Young's modulus (E) of DLC films as-deposited and implanted ones by N^{+} ions (E=150 keV, dose=1x10^{16} ions/cm ^{2}). Load depth of indenter=150 nm.

Substrate	Hardness (GPa)		Young's modulus (GPa)		Film thickness (μm)
	As-deposited	Implanted	As-deposited	Implanted	
Si	0.7	2.6	7.7	16.3	1.4
Ge	2.7	6.1	19.6	28.5	1.3
Quartz	1.4	6.4	14.9	46.8	1.3

4. Conclusions

The present paper shows that the optical properties can be controlled by manipulation of the composition of gas mixture and value of RF bias voltage. On the other hand nitrogen implantation of DLC films improves essentially mechanical properties (increasing of the hardness and Young's modulus more than two times), which correlates with changes of the optical properties, namely, decreasing of optical band gap and increasing of refractive index of the implanted layer.

References

1   Hsiao-chu Tsai and D.B.Body, J.Vac.Sci.Technol., A5 (1987) 3287
2   R.Kalish and M.E.Adel, Materials Science Forum, 52&53 (1989) 427
3   J.W.Zou, K.Schmidt, K.Reichelt and B.Stritzker, J.Vac.Sci.Technol., A6 (1988) 3103
4   X.Jiang, J.W.Zou, K.Reichelt and P.Grunberg, J.Appl.Phys., 66 (1989) 4729
5   A.Hoffman, R.Brener, I.Gourman, C.Cytermann, H.Geller and M.Kenny, Abstracts Diamond Films-94 (1994) 3.050
6   A. A. Doroshenko, V. A. Semenovich, S. I. Khandoznko, A.M.Kutsay and M.T.Muinov, J.of Superhard Materials,15 (1993) 15
7   V.G.Litovchenko, S.I.Frolov and N.I.Klyui, Proc. SPIE., 2113 (1994) 86
8   W.C.Oliver and G.M.Pharr, J.Mater. Res., 7 (1992) 1564
9   A.H.Bhuiyan and S.V.Bhoraskar, Thin Solid Films, 162 (1988) 333

STUDY OF DIAMOND LIKE CARBON FILMS PREPARED FROM POLYMER

Z.H.Zheng, Z.Sun, X.J.Wang, Y.Sun, Q.H.Yang

Department of Physics, East China Normal University,
Shanghai 200062, People's Republic of China

Key words: DLC films, friction, heat decomposition, polymer, wear

Abstract

Polymer phenylcarbyne $(PhC)_n$, i.e. $(C_6H_5C)_n$, synthesized by chemical reaction, is a precursor to diamond like carbon. The polymer, when heated from room temperature to 800-1200°C for 1 hr, under 1 atm. of argon or 20 kpa of hydrogen, converted to hard and abrasive solid. The powder of this solid can easily scratch glass and quartz plates. After heat decomposition, the DLC films, obtained by coating $(PhC)_n$ dissolved in organic solvent on various substrates BN, Si_3N_4, and WC had considerably lower coefficient of friction and wear factors than those for BN, Si_3N_4, and WC flats. By SEM, dense diamond crystallites with grain sizes from several tens nanometers to several microns were observed. It proves that under heat decomposition, sp^3 carbon phase has been formed.

1. INTRODUCTION

Diamond and diamond like carbon films are very attractive for wear, lubricating and other uses. To date, various conventional and unconventional methods have been developed to deposit diamond and diamond like carbon films. Among conventional methods, the chemical vapor deposition method [1][2] is most commonly used. In this work, an alternative method for preparing diamond like carbon films is described. The diamond like carbon films were converted from the polymer, which was synthesized by chemical procedures [3]. And wear and friction properties of diamond like carbon films were discussed.

2. EXPERIMENTAL

(a) Preparation of DLC films:

The polymer $(C_6H_5C)_n$ is based on carbon atoms, each carbon atom, bearing one bond to the phenyl substituent, forms three C-C bonds into the randomly constructed three dimensional network as shown in

Fig.1 (given by reference[3]).
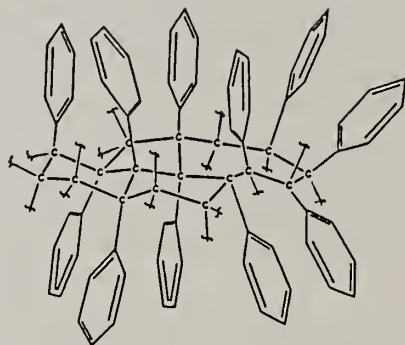
Fig. 1   Schematic representation of 3D network structure

Polymer phenylcarbyne was soluble in organic solvents, and then coated on the surface of various substrates such as Si, Mo, Si_3N_4, BN, WC etc. After heat decomposition at $800-1200^0C$ under 1 atm. of argon or 20 kpa of hydrogen, DLC films with thickness of several microns on the surfaces of substrates can be formed.

(b) Characterization of DLC films:

By SEM, dense crystallites with different grain sizes in DLC films were observed. In Fig.2(a), well faceted crystallites with grain sizes of several microns were formed in some regions of DLC film, while in Fig.2(b) many small ball-shaped crystallites with sizes of several tens to several hundreds nanometers were exhibited in the other regions of the film. It proved that under heat decomposition, sp^3-bonded carbon phase in DLC films was formed [4].
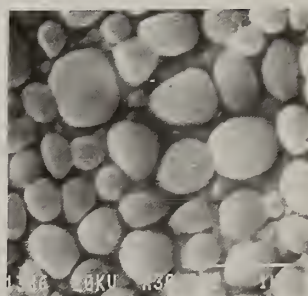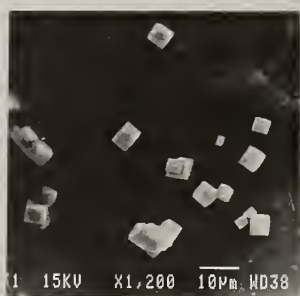
Fig.2 SEM of crystallites with different sizes in DLC films

By XRD measurement of DLC solid powder formed under the similar condition of heat decomposition, (111) peak of diamond is obviously exhibited as shown in Fig. 3.
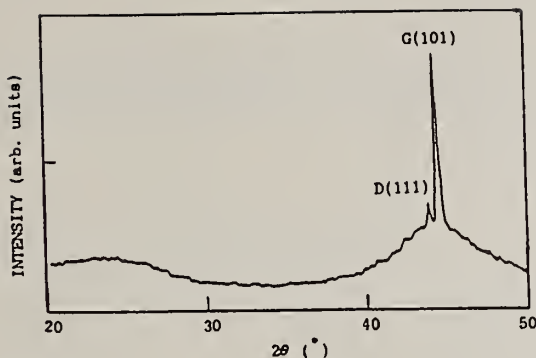
Fig. 3 XRD pattern of DLC films

In Raman spectra of DLC films, as shown in Fig. 4, there exists a broad peak near 1334 cm^{-1}, it was attributed to diamond (1332 cm^{-1}) and nondiamond (1355 cm^{-1}). The peak near 1600 cm^{-1} was assigned as graphite carbon. Besides, there exists an intense peak near 873 cm^{-1}, the assignment of this new peak need further investigation.
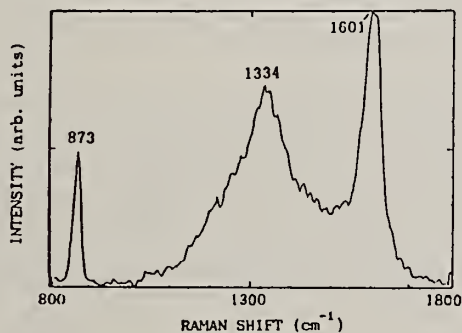
Fig. 4 Raman spectrum of DLC films

(c) Properties of DLC films:

The microhardness of DLC films was measured by indentation hardness test, when the substrate was Si_3N_4, the hardness of DLC films H_v >4000kg/mm^2. The typical coefficient of friction(COF) for DLC films on Si_3N_4 in contact with GCr15 steel ball (ϕ 2mm) was obtained in the dry air. COF is plotted as a function of the number of repeated passes as in Fig. 5.

3. CONCLUSION

Phenylcarbyne is a pyrolytic precursor to diamond like carbon
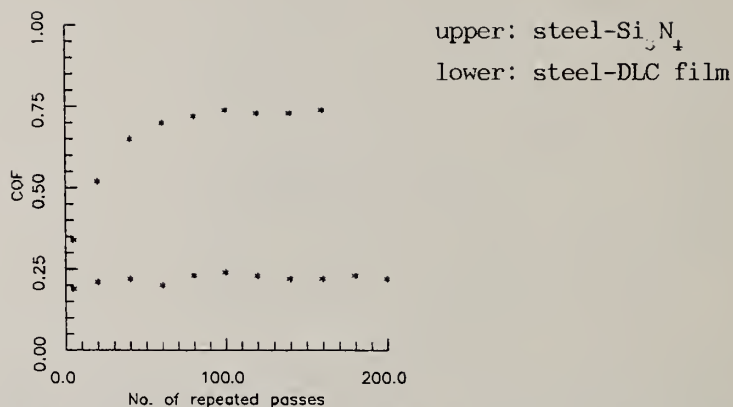
Fig. 5 COF in the function of numbers of repeated passes

films on various substrates. DLC films formed on the surface of WC, Si_3N_4, BN etc, have higher hardness and lower coefficient of friction than that of corresponding substrates. By characteri-zation of SEM, XRD and Raman measurements, the results proved that sp^3-bonded carbon phase structures had been formed in DLC films.

4. REFERENCES

1. B.V.Spitsyn, L.L.Bouilov and B.V.Derjaguin, J.Crystal Growth, Vol.52 (1981) 219
2. S.Matsumoto, Y.Sato, M.Kamo and N.Setaka, J. Mater. Sci., Vol.17 (1982) 3106
3. G.T.Visscher, D.C.Nesting, J.V.Badding and P.A.Bianconi, Science Vol.260 (1993) 1496
4. Z.H.Zheng, Z.Sun, Q.H.Yang and N.Xu, SPIE, Vol.2364 (1994) 566

IN-SITU DLC/TiC COMPOSITE COATING BY PLASMA ENHANCED CHEMICAL VAPOR DEPOSITION

Hsiao Lei Wang and Min Hsiung Hon

Department of Materials Science and Engineering(MAT32),
National Cheng Kung University,Tainan,Taiwan 70101

Key words : composite coating, DLC, PECVD, TiC

Abstract

In-situ DLC/TiC composite film was coated on silicon wafer, steel and glass substrates with titanium chloride, methane, hydrogen and argon gas mixtures by R.F. plasma enhanced chemical vapor deposition. Raman spectra showed the coexistance of DLC and TiC in the films. The growth rate and DLC/TiC ratio of these films were investigated as a function of the inert gas flow rate.

1. INTRODUCTION

Research on amorphous carbon films has captured significant interest for the unique properties[1-3], but the poor adhesion on most of the construction materials has limited the practical use of the coatings. The application of titanium carbide coatings to extend the life and performance of tools has been demonstrated to be successful [4-7]. Composite coating is expected to combine the performance of the two materials, the present study utilizes the good constituent controllability of PECVD to deposit adherent in-situ DLC/TiC composite coating, the structure of the films has been characterized and the influence of Ar is discussed.

2. EXPERIMENTAL

Coatings were prepared in a r.f. plasma enhanced CVD apparatus using capacitively coupled electrodes. The parallel electrodes were 12 cm in diameter with a separation distance of 6 cm. The substrates, including silicon wafer、steel and glass, were placed on the lower electrode which had the rf power applied to it while the upper electrode, used as gas shower, was grounded. $TiCl_4$、H_2、CH_4 and Ar mixtures were used as the feedstocks. The substrate could be heated up to 600 °C by a graphite heater. All of the coatings studied in this paper were formed at 500 °C substrate temperature. Mathane and argon flow rate were the two variables investigated with other coating parameters fixed.

Raman spectra were obtained in a backscattering geometry from the films deposited on the Si wafers with the 514.5 nm Ar$^+$ laser line. The crystallinity of the deposit was analyzed by X-ray diffraction (XRD). Electron spectroscopy for chemical analysis (ESCA) was employed to analyze the composition and chemical shift of the coatings. The film thickness was measured by α-step equipment.

3. RESULTS AND DISCUSSION

The XRD results show the presence of the crystalline TiC phase in the coatings. The characteristic Raman spectra of TiC and diamond like carbon shown in Fig.1 were obtained for all of the coatings . These results indicate that the composite coating of amorphous DLC and crystalline TiC phase was deposited.

As shown in Fig.2 , the deposition rate of coatings increases almost proportionally to Ar gas flow rate. Evidently Ar takes a part in the deposition and enhances the growth of film. This effect, so call Penning effect[8], has been dicussed in some plasma processes[9,10]. The He gas addition produces a similar effect which is not shown here.

The ESCA results provide more information for the influence of Ar addition. Fig.3 shows C1s spectrum for the composite coating. The spectrum is deconvoluted into two components : one is the C_{TiC} peak at 282.3 eV, indicating the combination of carbon and titanium in the coating, and the other is the C_C peak at 285.7 eV, indicating isolated carbon in the composite layer. By curve fitting, the two peaks can be separated and the C_C-to-C_{TiC} ratio is shown in Fig.4. The argon effect on growth enhancement is more obivous for carbon phase than TiC phase. The film density decreases as carbon phase content increases in the coating, as indicated in Fig.5.

5. CONCLUSION

An in-situ DLC/TiC composite coating was deposited by PECVD at 500°C. Amorphous DLC and crystalline TiC phase coexist in the deposited layer. Inert gas addition enhances the coating growth rate and the DLC/TiC ratio is dependent on inert gas flow rate.

6. REFERENCES

1. A. Bhushan, A.J. Kellock, N.H. Cho and J.W. Ager : J. Mater. Res. 7(2) (1992) 404.
2. A. Pastol and Y. Catherine : J. Phys. D 23 (1990) 799.
3. L.H. Chou : J. Appl. Phys. 72 (1992) 2027
4. H.L. Wang, J.L. He and M.H. Hon : Wear 169 (1993) 195.
5. T. Arai, H. Fujita and K. Oguri, Thin Solid Films 165 (1988) 139.
6. N.J. Archer, Thin Solid Films 80 (1981) 221.
7. H.L. Wang, J.L. He and M.H. Hon : Surface Engineering 10(3) (1994) 215.
8. B. Chapman : Glow Discharge Processes (Wiley.New York,1980) p.
9. A. Inspektor-Koren : Surface and Coatings Technology 33 (1987) 31.
10. I. Sugimoto, S. Nakano and H. Kuwano : J. Appl. Phys. 75(12) (1994) 7710.
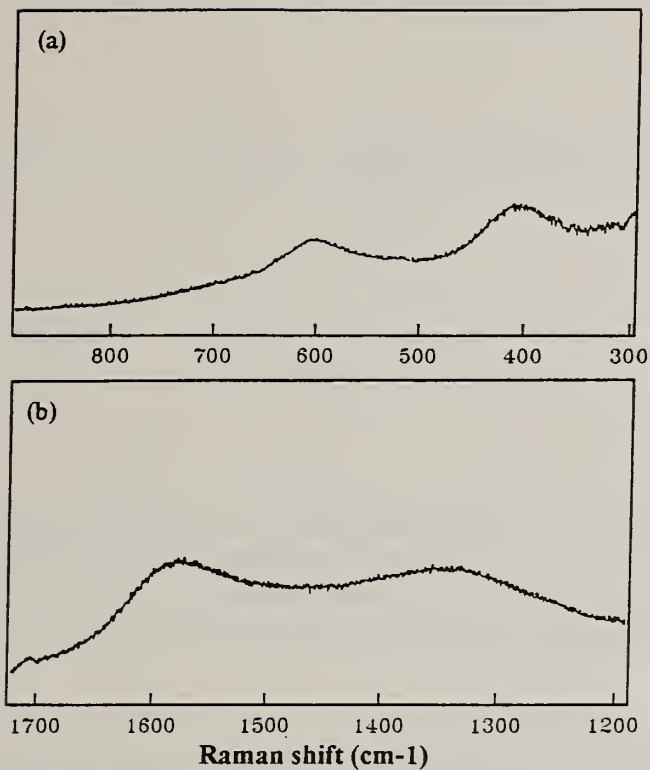
Fig. 1 The Raman spectra of (a)TiC and (b)DLC in the composite coating.
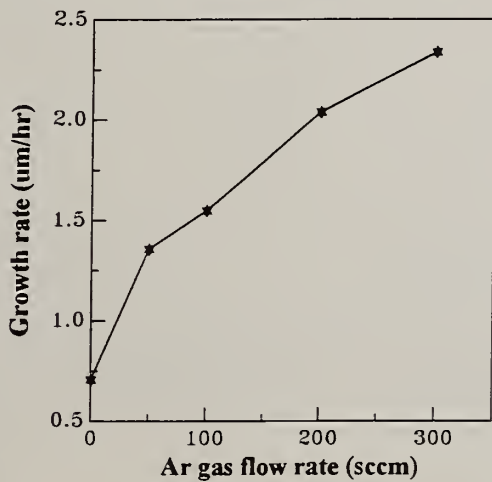
Fig. 2 The dependence of deposition rate of the coatings on the Ar gas flow rate.
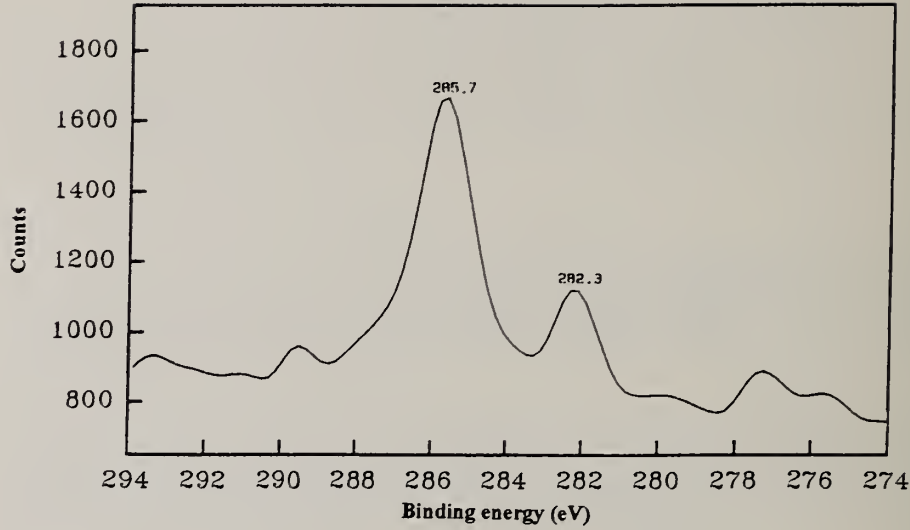
Fig. 3 ESCA spectrum of C1s in the composite coating.
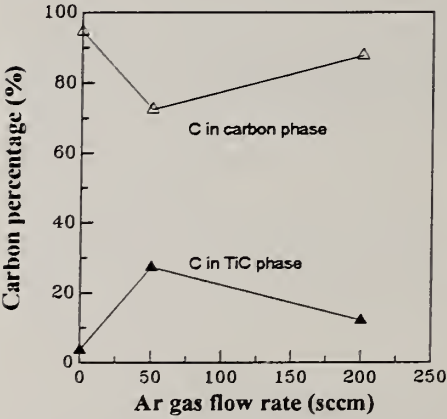
Fig. 4 Relationship between the C_C, C_{TiC} percent and Ar gas flow rate.
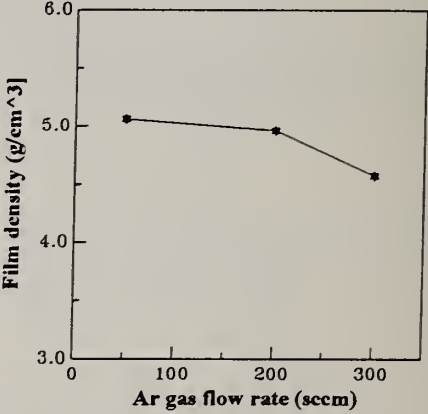
Fig. 5 The dependence of the film density on the Ar gas flow rate.

DIAMOND-LIKE HYDROGENATED AMORPHOUS CARBON PREPARED USING SADDLE-FIELD GLOW-DISCHARGE DECOMPOSITION OF METHANE

F.Gaspari, W.C.W. Chan, P.K. Lim and S. Zukotynski

Department of Electrical and Computer Engineering, University of Toronto, Toronto, Ontario M5S 1A4, Canada

Key words: diamond, DLC, PACVD, saddle field, thin films

Abstract

Diamond-like hydrogenated carbon films were deposited using saddle-field glow-discharge in pure methane. XPS, XAES, Raman and x-ray spectroscopy suggest that the percentage of sp^3/sp^2 bonding was varied over a relatively wide range by adjusting pressure and substrate bias. It was found that a very high percentage of sp^3 bonding could be achieved.

1. Introduction

Several techniques have been developed for the deposition of thin films of diamond-like amorphous carbon [1]. The plasma assisted techniques differ mainly by the form of excitation, dc or rf, and by the deposition pressure. The positive attributes of rf and dc diode discharges are combined in the dc saddle-field glow-discharge. We used the five electrode configuration which consists of the basic saddle field cavity, made of a central wire grid anode that is semitransparent to the passage of electrons, sandwiched between two wire grid cathodes which are semitransparent to the gas phase species. Two heated, coplanar electrodes-substrate holders are placed on the outside of the saddle-field cavity. This electrode arrangement allows for independent biasing of the anode and of the substrate holders. Within the saddle-field cavity, electrons oscillate along the axis of the plasma chamber [2], increasing the effective path lenght for ionizing collisions. This enhances discharge formation at low pressure (over the standard dc discharge) and offers considerable control over the decomposition of precursor species and gas phase reactions. The use of dc accelerating potentials in the saddle-field cavity and at the substrate holders avoids the tuning problems that are encountered with rf techniques, while providing more direct control over the energy, direction of motion and density of ions, which are critical factors in the growth of diamond-like carbon films [3].

2. Experimental

We used the five electrode saddle-field glow-discharge configuration. The central grid was maintained at a DC bias of about +600V. The wire grid cathodes, placed about 5 cm from the central grid were maintained at ground potential. Two solid outer electrodes, about 2 cm past the cathodes, functioned as substrate holders. All electrodes were circular, of 15 cm diameter. The base pressure of the system was about 10^{-9} Torr. All depositions were carried out using undiluted ultra-pure methane at a flow rate of 5 sccm and at an anode current density of 30 $\mu A/cm^2$ on to both glass and high resistivity crystalline silicon substrates. The substrate temperature was 200 °C. The deposition pressure was varied in the range from 30 to 125 mTorr and the substrate holder bias was veried in the range from -75 to +200 V.

Robertson suggests that diamond-like carbon films are best characterized by giving the relative fraction of sp^3 and sp^2 bonding in the films [4]. We used x-ray photoelectron spectroscopy (XPS), electron and x-ray stimulated Auger electron spectroscopy (AES and XAES respectively), and Raman spectroscopy for the characterization of bonding. Experimental details are described elsewhere [5].
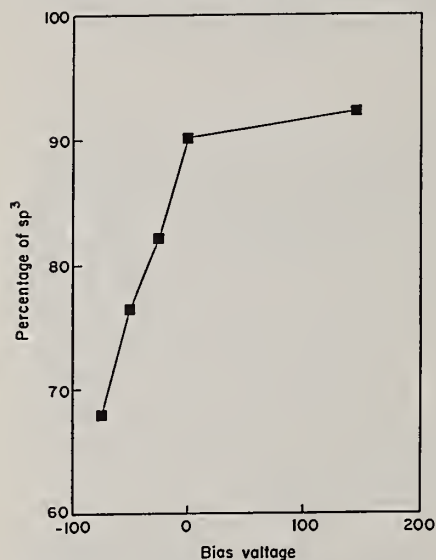
Fig. 1. Percentage of sp^3 bonding in a-C:H grown at 75 mTorr vs. substrate bias.
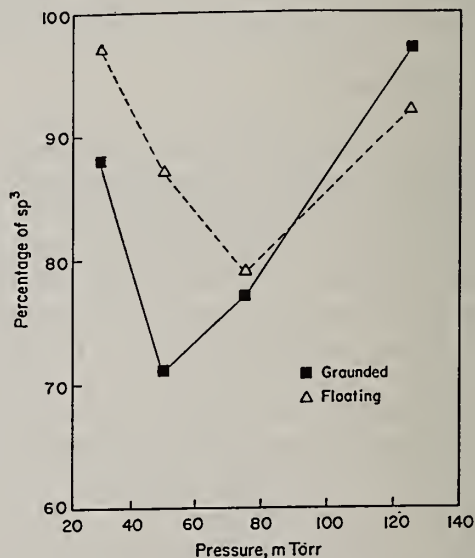
Fig. 2. Percentage of sp^3 bonding vs. pressures.

XAES N(E) and (dN/dE) spectra for a-C:H films deposited with substrate holder biases of
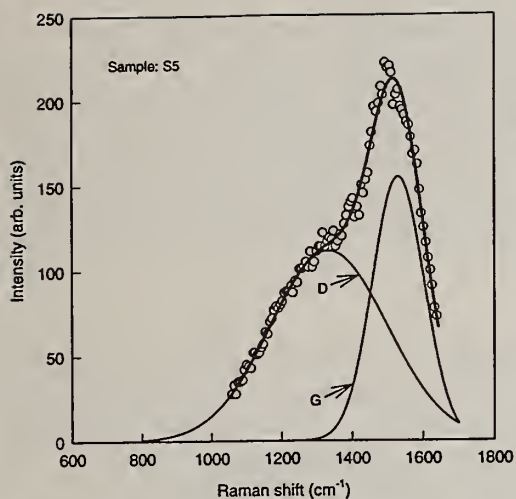
Fig. 3. Raman spectrum of an a-C:H sample. Open circles are experimental data. The thick curve is the fit obtained by summing the gaussians D and G, also shown.
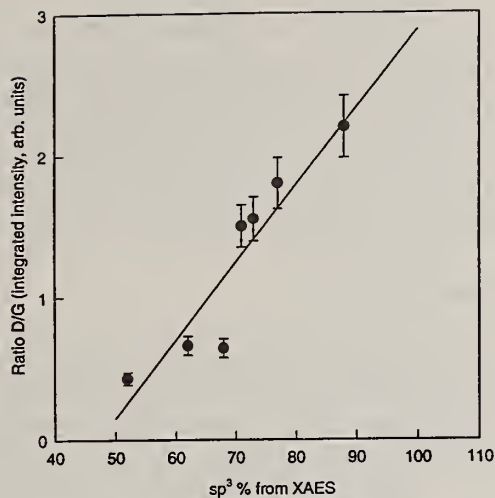
Fig. 4. The ratio of the integrated intensities of the D and G curves vs. the percentage of sp^3 bonding as measured by XAES. The line is a fit to the data.

-75V, -50V, -25V, 0V and +145V were compared with those for diamond and graphite samples indicating a diamond-like nature of the films. The spectra were analyzed using the method proposed by Lascovich et al. [6] to calculate the ratio of the sp^3/sp^2 bonding. The results are shown in Fig. 1. It can be seen that the percentage of sp^3 decreased significantly with increasing negative bias voltage and increased slowly with increasing positive bias voltage for samples deposited at 75 mTorr. The percentage of sp^3 bonding for films deposited at 30, 50, 75 and 125 mTorr are shown in Fig. 2. It can be seen that, in general, floating samples had a higher percentage of sp^3 than grounded samples.

The XPS C 1s peak was measured for graphite, diamond and the a-C:H films. The π loss peak and the plasma loss peak located at 6.5 eV and 27 eV beyond the C 1s peak respectively [7], characteristic of graphite, were seen in the graphite spectrum. However, both were absent in the spectra of the a-C:H films. Furthermore, valence band spectra of our films showed a fairly broad peak located between 16 to 21 eV, a less intense peak located at about 10 to 15 eV and tailed off slowly toward low binding energies. These features confirm the diamond-like nature of the films.

Fig. 3 shows the characteristic Raman spectrum for a typical a-C:H sample. A broad peak at approximately 1500 cm^{-1} and a shoulder at approximately 1300cm^{-1} can be seen. Following

Xu et al. [8], this spectrum was analyzed by fitting two gaussian functions. The two are referred to as G for graphite and D for diamond, respectively. In Fig. 4 we plot the ratio of the integrated intensities of the D and G peaks for samples deposited under various conditions versus the sp^3 concentration as measured by XAES. Our results indicate a strong correlation between the D peak and the percentage of sp^3 bonding, in agreement with the results of Koidl et al. [9]. Recent x-ray diffraction studies further confirm the diamond-like nature of the films and indicate that the sp^3 bonding is associated primarily with tetrahedrally bonded carbon.

Conclusions

Diamond-like hydrogenated carbon films were deposited using saddle-field glow-discharge in pure methane. XPS, XAES and Raman and x-ray spectroscopy suggest that the relative percentage of sp^3/sp^2 bonding can be controlled by adjusting pressure and substrate bias. It was found that a very high percentage of sp^3 bonding could be achieved.

Acknowledgements

References

[1] See, for instance, A. Joshi, S.A. Gangal, and S.K. Kulkarni, *J. Appl. Phys.* **64** (1988) p. 6668, and references therein.

[2] A.H. McILraith, *Nature* **212** (1966) p. 1422.

[3] J. Robertson, *J. Non-Cryst Solids* **164-166** (1993) p. 1115.

[4] J. Robertson, 'Deposition of diamond-like carbon" Chapter 9 in *Thin Film Diamond*, A. Lettington and J.W. Steeds. eds., Chapman and Hall, 1994.

[5] P.K. Lim, F. Gaspari, and S. Zukotynski, *J. Appl. Phys.* to be published.

[6] J.C. Lascovich, R. Giorgi, and S. Scaglione, *Applied Surface Science* **47** (1991) p. 17.

[7] Y. Mizokawa, T. Miyasato, S. Nakamura, K.M. Geib, and C.W. Wilmsen, *J. Vac. Sci. Technol.* A5 1987) p. 2809.

[8] S. Xu, M. Hundausen, J. Ristein, B. Yan, and L. Ley, *J. Non-Cryst. Solids*, **164-166**, 1127 (1993).

[9] P. Koidl, Ch Wild, B. Dischler, J. Wagner, and M. Ramsteiner, *Materials Science Forum* **52-53** 41 (1989).

DIAMOND-LIKE CARBON BIOMEDICAL AND MECHANICAL

BIOCOMPATIBILITY AND SURFACE ANALYSIS OF NITROGEN CONTAINING DLC

R. Hauert[1], G. Spescha[1], B. Keller[1], F. Birchler[2], J. Mayer[2], E. Wintermantel[2]

[1] Swiss Federal Laboratories for Materials Testing and Research (EMPA), CH-8600 Dübendorf (Switzerland).

[2] Inst. for Biocompatible Materials Science and Engineering, ETHZ, (ETH-BWB), Wagistrasse 23, CH-8952 Schlieren (Switzerland).

Keywords: DLC, N-doping, XPS, biocompatibility.

Abstract

Nitrogen doped a-C:N:H films have been deposited by using different mixtures of argon, nitrogen and cyclopentane (C_5H_{10}). With increasing nitrogen content in the film the electrical resistivity, hardness and the wetting angle could been lowered continuously. XPS analysis of the C1s core level revealed the relative contributions of carbon in C-C, C-H and C-N bonds at the surface. Biocompatibility tests (cell culturing with fibroblasts) revealed a good surface biocompatibility by means of proliferation rate and morphological behavior for all nitrogen doped samples.

1. Introduction

Thin films of hard amorphous hydrogenated carbon (a-C:H), also known as "amorphous diamond-like carbon" (DLC), are used for certain applications due to their outstanding properties such as high hardness, chemical inertness, low friction and wear, as well as biocompatibility [1-2]. Specific properties of a-C:H can be modified by introducing additional elements into the PACVD (plasma activated chemical vapor deposition) process. Doping the a-C:H films with nitrogen opens the possibility of continuously tuning, hardness, electrical conductivity and surface energy.

2. Experimental

Film production: The deposition of a-C:H:N films was performed in a stainless steel high vacuum system. Different mixtures of argon, nitrogen and cyclopentane (CPA,

C5H10) where used as feed gases in a RF (13.56 MHz) plasma (for experimental details see [3]). XPS-Analysis: X-ray Photoelectron spectroscopy analysis was performed on a Perkin Elmer PHI 5600ci spectrometer using monochromatized Al Ka X-rays. The atomic concentrations reported here where calculated using PHI sensitivity factors [4]. Biocompatibility: The specimens were sterilized by a threefold washing cycle in a solution of ethanol/ bi-distillated water (70 / 30). 20-30'000 cells (mouse fibroblasts, M3T3 cell line) per sample were incubated in a nutrition medium (DMEM Dulbecco's modified eagle medium, 5% FBS foetal bovine serum, 0.2% Gentamycine) for 2 day at 37°C, 5% CO_2 and 95% rel. humidity. After incubation the specimens were fixated in a 3% glutaraldehyde solution and dehydrated using ethanol / bi-distillated-water solutions (1. 50% EtOH, 2. 75 EtOH, 3. 100 EtOH, 4. 100% EtOH). For the preparation of morphological investigations in the SEM the specimens were critical point dried in CO_2 and sputter coated with platinum [5]. TOF-SIMS: A Physical Electronics model 7200 time-of-flight secondary ion mass spectrometer has been used.

3. Results and Discussion

Composition, XPS and RBS / FRS Analysis: XPS spectra from films #1-#4 resulted in nitrogen concentrations of 0, 4.7, 7.2 and 8.2 at%. The O and Ar concentrations are below 0.5 at% for all four samples. The elemental composition of nitrogen measured by RBS was 0.0, 3.9, 6.6 and 11.5 at% and the hydrogen concentration measured by FRS was 19, 17, 16 and 16 at% for samples #1 to #4 respectively.
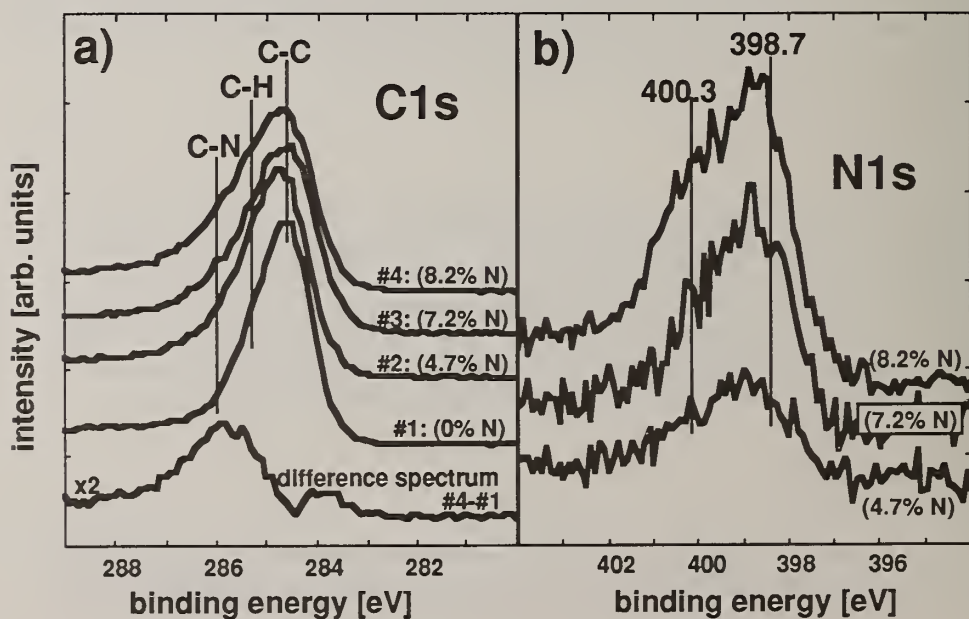
Fig. 1: a) C1s and b) N1s photoelectron spectra of samples #1 to #4. The nitrogen concentrations obtained from the XPS analysis are enclosed.

Chemical analysis: (XPS, IR, TOF-SIMS): The C1s and N1s spectra obtained from sample #1 to #4 are displayed in fig 1a and 1b. In the a-C:H film without nitrogen (sample #1) the slightly asymmetric C1s peak is centered at a binding energy of 284.6±0.2 eV with a FWHM of 1.4 eV which is in agreement with the literature [6,7]. The asymmetry in the C1s peak reveals the presence of an additional contribution at the higher binding energy side (see Fig 1a, sample #1). The main signal around 284.6 eV can be assigned to C-C bonds (graphite has a binding energy of 284.5, [4]) whereas the higher binding energy tail is evidence of C-H bonds, usually located between 284.8 and 285.5 eV [4]. The N-doped samples #2 to #4 reveal, with increasing N content, an increasing C1s intensity around 286.0 eV binding energy (see also fig. 3a difference spectrum) attributed to C-N bonds usually located in the range 285.5 and 287.2 eV [4]. The corresponding N1s spectra of sample #2 to #4 are displayed in fig. 3b. The N1s core level spectra shows at least two different chemical states of nitrogen, one at about 398.7 and the other at 400.3 eV binding energy. Consistent with the literature [4], the main N1s intensity around 398.7 eV can be attributed to nitrogen involved in C-N bonds (-C-NH2, -C-NH-C-, -C-N-C- and -C≡N) [4, 8], whereas the smaller N1s
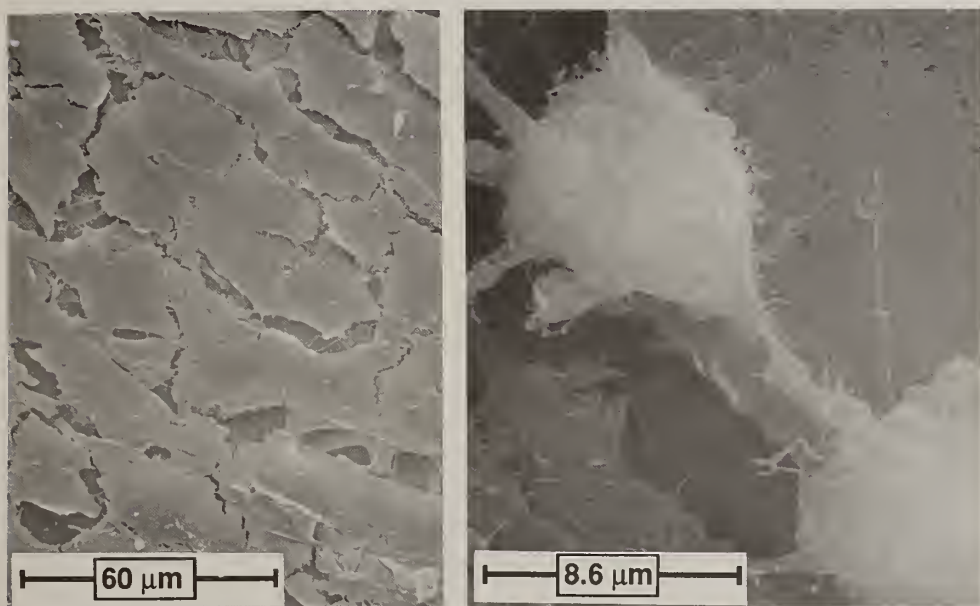
Figure 2: SEM-images of mouse fibroblasts which illustrate the cytocompatibility by cell morphology. Left, Sample #2: Confluent cell layer showing well spread fibroblasts. Space between cells are artifacts due to shrinkage during drying. (magn. 500x). Right, Sample #3: Two fibroblasts just after mitosis which illustrates cell activity. Both cells keep intense contact to the underlying cell layer by their filopodiae. Cell surface shows high density of microvilli on the surface of the cell membranes. (magn. 3500x)

intensity around 400.3 eV is attributed to nitrogen involved in C-N-N bonds [4] or in C=N bonds [8]. IR spectroscopy using photoacoustic detection of the nitrogen containing films showed the presence of additional IR bands for νNH (3358 cm^{-1}), $\nu C\equiv N$ (2224 cm^{-1}), $\nu C=N$ (1622 cm^{-1}), $\nu C-N$ (1272 cm^{-1}) as well as δNH_2 (799 cm^{-1}). By TOF-SIMS analysis of the sample surfaces the following fragments could be detected: C, CH, N and CH_2, NH and CH_3, O, C_2, C_2H, CN and C_2H_2, C_2H_3 and CHN, C_2H_4, C_2H_5, C_3, C_3H, C_3H_2 and C_2N, C_3H_3, C_4, C_4H. At masses higher than 50 it became problematic to distinguish between C_nH_m and $C_{n-1}H_{m-2}N$ ions . An exact determination of the different nitrogen containing species was not achieved by XPS, nor by IR or TOF-SIMS. Further analysis including adequate reference materials will be performed an will be published elsewhere.

Biocompatibility tests (cell culturing with fibroblasts) revealed a good surface cytocompatibility by means of proliferation rate and morphological behavior for all nitrogen doped samples: All cells showed good spreading on the surface, exprimation of philopodiae and a high density of microvilli on the surface of the cell membranes as it is illustrated in figure X. In two days almost confluent cell layers have been observed. No dependence from the nitrogen content in the DLC films could be observed. However, cell morphology and proliferation rate have to be considered as qualitative criteria which are suitable for a preliminary evaluation of cytocompatibility of DLC-coated surfaces. Further cell culture studies investigating mitochondrial activity as an indicator for cell metabolism, protein composition and cell differentiation will allow an improved analysis of the influence of doping elements in DLC on its cytocompatibility.

4. Acknowledgments

5. References

1. J. Robertson, Prog. Solid State Chem. 21 (1991) 199-333
2. Evans. A.C. et al. Surf. Coat. Technol. 47 (1991) 662-667.
3. R. Hauert et al. submitted to Thin Solid Films (1995).
4. J. F. Moulder, W.F. Stickle, P.E. Sobol, K.D. Bomben, *Handbook of X-ray photoelectron spectroscopy*, Ed.: J. Chastain, published by Physical Electronics, Eden Prairie , USA, (1992).
5. M Petitmermet, B. Shah, U. Rösler, J. Mayer, E. Wintermantel, ICM-CTF 24-27 April 1995, San Diego, USA, accepted.
6. S. Schelz and P. Oelhafen, Surf. Sci. **279**, (1992) 137.
7. K.-H. Ernst, J. Patscheider, R. Hauert and M. Tobler Surf. Interf. Anal. **21**, (1994) 32
8. F. Rossi, et al., J. Mater. Res. Vol. **9**, No. 9, (1994) 2440.

Improved Wear of Amorphic Diamond Coated Medical and Dental Implant Substrates

T.L. Jacobs[1], J.H. Spence[1], S.S. Wagal[1], and H.J. Oien[2]

[1]SI Diamond Technology, Inc., 2435 North Blvd., Houston, Texas, 77098, USA
[2]GSEM, Inc., 14657 SW Teal Blvd., Suite 109, Beaverton, Oregon, 97007, USA

Key words: Adhesion, Amorphic Diamond Coating™, Implant, Osseointegration, Wear

Abstract:

Long term implant stability in medical and dental patients has been less than ideal due to wear caused by functional loading. As implant devices wear and suffer mechanical and/or biologic failure of critical components, patients are subjected to replacement surgical procedures. Generation of wear-dependent particles from implant substrates can contribute to both failure modes by increasing wear and eliciting host inflammatory response[1]. Amorphic Diamond Coating™ (ADC™) can be used to minimize or eliminate wear and the generation of wear dependent particles of cobalt chrome, titanium alloys and ultra high molecular weight polyethylene implant substrates used in medical and dental implants. The improved wear properties provided by ADC™ may reduce or obviate the need for replacement surgery for medical and dental implants that fail due to wear and generation of wear-dependent particles.

1. Introduction

Ultra high molecular weight polyethylene (UHMWPE), cobalt chrome, and titanium-6Al-4V are critical substrates used in medical and dental implants. In early clinical trials, prosthetic joints were cemented with cold-cured methyl methacrylate cements which had poor bond strengths. Because this highly allergenic material was placed into marrow spaces of the long bones of the leg, allergic responses were induced in some patients. Mechanical and/or biologic failures of methyl methacrylate cement were a leading cause of implant loss.

Methyl methacrylate has been replaced by the use of titanium alloys and surface coatings that have the biologic property of encouraging bony ingrowth onto implant

shafts placed into bone. This bone-titanium bond has been termed osseointegration and is mechanically stronger, does not illicit an immune response, and is biocompatable as evidenced by healthy hard and soft tissue response in vivo[2]. Osseointegration of implants has eliminated cement failure as one of the most common causes of failure in orthopedic implants.

Eliminating methyl methacrylate cement failures has placed more importance on minimizing implant wear and limiting generation of wear-dependent particles as a cause of mechanical and/or biologic failure of implants. The rate limiting factor for implant function has now focused on material biocompatability and wear in function. Any process that improves wear and biocompatability should favorably affect implant longevity and minimize replacement surgery and its associated morbidity[3].

SI Diamond Technology's Amorphic Diamond Coating™ (ADC™), US Patent # 4,987,007, with hardness greater than 30gpa and coefficient of friction less than 0.1 is ideal for coating implants. Moreover, ADC™ is chemically inert and easily accepted to body chemistry. Because ADC™ is an amorphic material deposited by a high energy coating process, adhesion is satisfactory for these applications. SI Diamond Technology has exclusive rights to the ADC™ process which was developed at the University of Texas at Dallas. This report details the successful application of ADC™ on Co-Cr and Ti-6-4 alloys as a protective layer. SI Diamond Technology and GSEM, Inc. have several patents pending for ADC™ applications.

Fig. 1 Schematic of ADC™ Process

LASER INPUT

Rotation   Rotation

SUBSTRATES

60 Degrees   →   Limit of Useful Deposition

TO +HV ELECTRODE
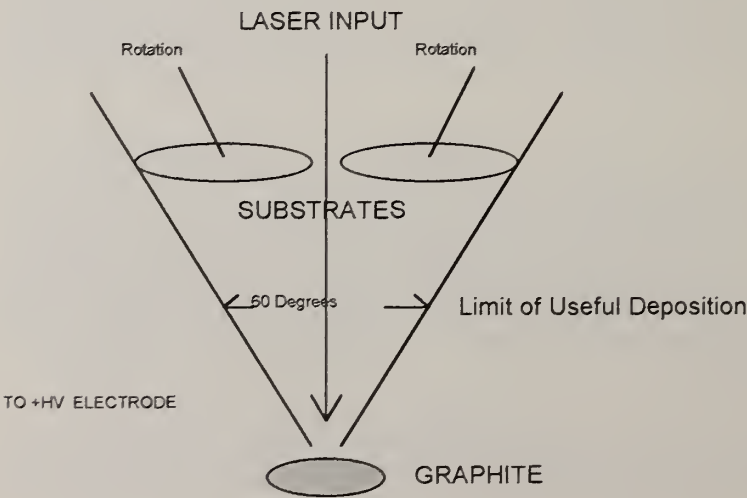
GRAPHITE

ADC™ was applied onto four Co-Cr and four Ti-6Al-4V coupons of 1/2" diameter through a process detailed in Fig. 1. In brief, the output from a high power Q-switched Nd:YAG laser was focused on a graphite rod in a high vacuum chamber to produce a power density of 10^{11} W/cm^2 on the graphite surface. Under those conditions, a highly ionized, energetic carbon plasma was formed. Substrates exposed to ion fluxes emerging from the plasma were coated with ADC™ under certain conditions. The adhesion of the coating was tested by scratch testing and found adequate for this application. Two controls of each type were also tested.

All ADC™ coated coupons were wear tested against UHMWPE substrates using the ASTM F732 wear test protocol. The ADC™ coupon surface and UHMWPE wear substrate were analyzed for wear versus uncoated controls. No appreciable wear was noted and the ADC™ remained intact on all test coupons after testing 1,000,000 wear cycles. There was no delamination or spalling of the ADC™ on any test coupons.

As illustrated in Table I, there was no significant change in UHMWPE wear substrate test mass with ADC™ Co-Cr coupons. All UHMWPE substrates were stored for eight weeks in bovine plasma until absorption equilibrium was reached. During testing each substrate was weighed at 250,000 wear cycle intervals until 1,000,000 cycles had been completed.

Co-Cr ADC™ Coated coupons produced a 73.38% reduction in the average UHMWPE substrate wear associated with control coupons. Improved wear can be totally attributed to ADC™ as the single test parameter.

Table I: Co-Cr ADC™ Coated Coupons at 1,000,000 Wear Cycles

UHMWPE Wear Substrate Mass In Grams

Coupon	Start Avg.	Stop Avg.	Change	% Change
ADC™ Coated	103.000450	103.001450	0.001000	0.000971%
Control	101.884350	101.881750	-0.002600	-0.002552%

Table II: Ti-6-4 ADC™ Coated Coupons at 1,000,000 Wear Cycles

UHMWPE Wear Substrate Mass In Grams

Coupon	Start Avg.	Stop Avg.	Change	% Change
ADC™ Coated	103.001275	103.002800	0.001525	0.001481%
Control	101.881750	101.883950	0.002200	0.002159%

Surface hardness and adhesion of ADC™ on test coupons are presented in Table III. There was no failure of the ADC™ on any of the test coupons and all units were functional after 1,000,000 test cycles.

756

Table III: Surface Harness And Adhesion Of ADC™ Co-Cr and Ti-6-4 Wear Test Coupons

Sample	Pre-Test	Post-Test	% Change
Co-Cr			
ADC™ Thickness (microns)	1.4	NA	
Hardness (Vickers) (Control)	1094 (302)	945	-13.72%
Adhesion (Newton)	17N	15N	-11.77%
Ti-6Al-4V			
ADC™ Thickness (microns)	1.65	NA	
Hardness (Vickers) (Control)	844 (345)	630	-25.36%
Adhesion (Newton)	13N	13N	0%

The decrease in surface hardness of ADC™ Ti-6Al-4V coupons after testing is of considerable interest and is the subject of further research. It should be noted that surface hardness after testing is still 82.6% harder than the control coupon.

Amorphic Diamond Coating™ of implant substrates minimizes implant wear and reduces the generation of wear-dependent particles associated with inflammatory response to medical and dental implants. After 1,000,00 cycles using the ASTM F732 specification, all ADC™ coated coupons remained intact and suffered no appreciable wear.

3. References

1. D. Dowson, M. Diab, B. Gillis, and J. Atkinson, *Polymer Wear And Its Control*, American Chemical Society (1985).
2. Branemark P-I, Zarb GA, Albrektsson T., *Tissue-Integrated Prostheses: Osseiointegration In Clinical Dentistry*, Chicago: Quintessence(11/ 1985)
3. H. Mittelmeier, *The Cementless Fixation Of Hip Endoprostheses*, Springer-Verlag, Berlin (1984).

NEW MEDICAL MATERIAL BASED ON METASTABLE FORM OF CARBON.

V.G.Babaev[1] M.B.Guseva[1], Yu.P.Kudryavtsev[2] A.A.Bondarev,[2]
F.Alexandrov[1], V.V.Khvostov[1], V.M.Babina[1]

1- Department of Physical Electronics, M.V.Lomonosov State University, Moscow 119899 (Russian Federation)

2-.A.N.Nesmeyanov Institute of Organoelement Compounds of Russian Academy of Sciences, Moscow 117813 (Russian Federation).

Key words: Carbyne, protheses, biocompatibility, trombo-resistivity.

Abstract

The experimental data of usage of carbon coated   medical implants and protheses are described. It was   found that the best results are achieved with carbyne   coatings. Carbyne is the linear carbon form based on the   sp-bond. Carbyne covered material are   produced   by specific chemical and physical processes.

From long term experiments an excellent result was   obtained in biocompatibility, thromboresistivity and   flexibility of vascular-, urethra- and endoprostheses.   Application of carbyne coated prostheses increases the   probability of positive operation results by 30% and   widens the operating capabilities especially for small   diameter veins and arteries.

1. Introduction

The development of new materials for application in   surgery remains an important problem. These materials   should possess a set of specific properties and   high   biocompatibility. Carbyne (a linear allotropic form of   carbon [1,2]) was found to be a promising material in   regard to its biomedical properties [3].   The present   paper reports   on the study of biomedical and   thromboresistant properties of Carbylan.

2. Experimental details.

Carbylan (fibers, films and coatings) have been prepared by low temperature dehydrohalogenation reaction [1]. The resonant Raman spectra of Carbylan prepared by dehydrohalogenation of poly(vinylidene halide)s exhibit two lines at $1530 cm^{-1}$ and $2136 cm^{-1}$ which also correspond to the stretching vibrations of cumulated $=C=C=$ bonds in the linear carbon chain (Fig.1).

Fig. 2 shows a distribution curve of the density of electronic states in the valence band of a Carbylan sample prepared by dehydrohalogenation of a poly(vinylidene chloride) film. The curve of the density of states was calculated from the experimental Auger spectrum by self-deconvolution. The electronic terms of linear carbon chains C calculated by the LCAO method for n = 2, 3, ..., 8 atoms are shown in the lower part of the figure (Fig.2). As is seen from the calculated data, the valence band consist of a deep-lying s-subband and a p-subband located above it. The forbidden gap D is observed between these bands. The width of s- and a p-subbands increases with a chain length, while a value of D decreases.

3. Results.

Carbylan has been studied in experiments with animals (white rats and dogs), which were subjected to the implantation of Carbylan samples into liver, pancreas, intestines, stomach etc. followed by macroscopic and histologic sampling by means of autopsy in various periods. Carbylan fibers do not homogenized and fully retain their structure in the animal organism. The fibers have no toxic effect upon the surrounding tissues, they do not cause the edema, plasmo- and hemorrhage, necrosis or alteration of both parenchymatous and muscular cell, suppuration, or pronounced vascular reaction. The fibers possess the natural black color, which does not changes in biological media. That is why it could be easily distinguished on the background of tissue and blood. Starting from the first days of the implantation it was revealed the essentially weak inflammatory reaction of adjacent tissues in the case of carbylan coated implants (Fig 3). Histologic studies show that tissue reaction on carbylan coated implants is due predominantly to operation trauma. It should be emphasized that carbylan coatings can be realized not only on solid surfaces, but also on flexible fibers and thromboresistant knitted vascular prostheses. When subjected to the contact with living body, the epitaxial growth (i.e.

- oriented and adjusted in correspondence with carbyne lattice parameter) of certain kind protein molecules at the surface of carbyne layer can be observed. It was proved by electron diffraction studies of protein layers in vitra experiments in blood. Such oriented growth effect does not take place in the case of other carbon materials: DLC, graphite, diamond. We think it is the fact that predetermines the unique biocompatibility of carbyne to living body. In this manner the program of controlled growth of body tissue is given. This phenomenon was named by us "bioepitaxy" and we consider that it is just the bioepitaxy that is responsible for unique biocompatibility and tromboresistance of carbyne coating.

Acknowledgement

References

1. Yu.P.Kudryavtsev, S.E.Evsyukov, M.B.Guseva, V.G.Babaev, V.V.Khvostov, Russ.Chem.Bull., 42 (1993)399.
2. R.Heimann, Diamond and Related Materials 3(1994)1151.
3. M.B.Guseva et.al., Diamond and Related Materials to be published.

760
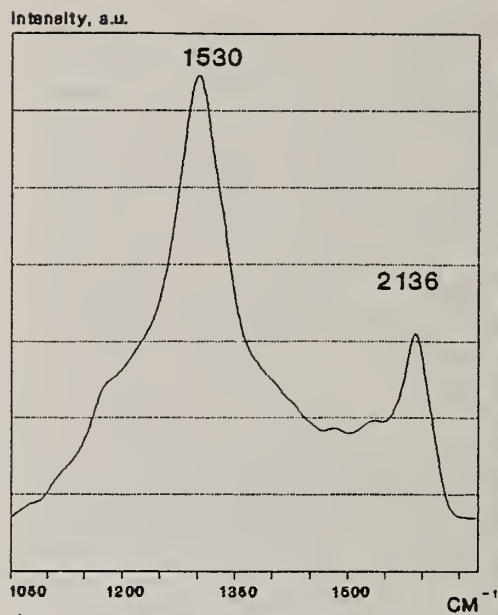
Fig.1 The resonant Raman spectra of Carbylan prepared by dehydrohalogenation of poly(vinylidene halide)s.

Fig.3 Bowels (4 days after implantation of fiber). Inthe interface layer of muscle tissue a thin fibroblast and hyperchrome nuclei are observed (x41).
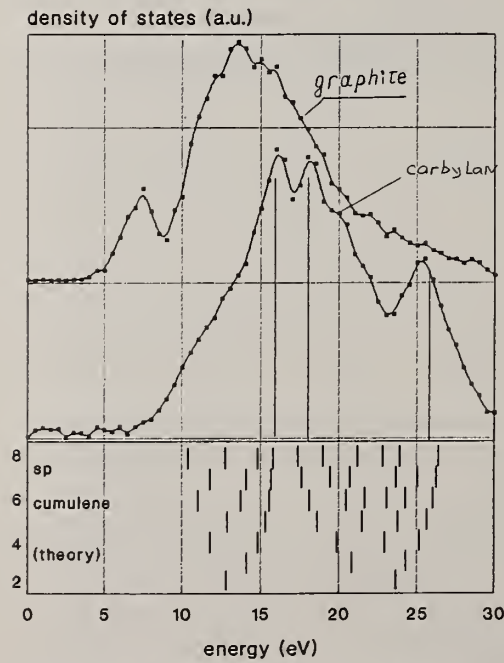
Fig.2 The density of electron states in a valence band of carbyne.

Applications of Diamond Films and Related Materials: Third International Conference, 1995
Editors: A. Feldman, Y. Tzeng, W. A. Yarbrough, M. Yoshikawa, and M. Murakawa

761

DIAMOND-LIKE CARBON FOR HIGH TEMPERATURE SUPERCONDUCTOR ENCAPSULATION

R. A. Beera, W. D. Brown, S. Afonso, F. T. Chan, G. J. Salamo, H. A. Naseem, and A. P. Malshe

High Density Electronics Center (HiDEC),
University of Arkansas, Fayetteville, AR 72701

Key words: DLC, degradation, encapsulation, lonsdaleite, r-f PECVD, YBCO

Abstract

Diamond-like carbon (DLC), a thermodynamically, metastable, amorphous form of carbon, has been a material of recent interest due to its wide range of applications. Depending on the activation agent and deposition conditions, the quality of DLC film varies and can be used for applications ranging from optics to tools. DLC is hard and chemically inert. In the present study, these properties of DLC have been used for the protection of high temperature superconductor (HTSC) thin films. DLC films were deposited on HTSC thin films using an r-f chemical vapor deposition system with methane gas at $30^{\circ}C$. Films were tested for superconducting transition temperature (Tc) and critical current density (Jc) before and after DLC encapsulation. Such encapsulated HTSC films were later exposed to moisture to test the corrosion resistance of DLC:HTSC structures.

1. Introduction

The unique properties of diamond-like carbon films make them suitable materials for electrical, mechanical and optical applications. Among their more attractive properties are extreme hardness, infrared transparency under certain deposition conditions, chemical inertness, good thermal conductivity, and low electrical conductivity [1]. $YBa_2Cu_3O_{7-x}$ is a very interesting material with a high potential for application in electronics and other industrial applications. It has been improved considerably since its discovery to transition temperatures of about 90 K and critical current densities of greater than 10^6 A/cm^2. The fact that the properties of YBCO superconductors degrade with exposure to air or water will limit the use of this material in many potential applications. Applications of these materials, such as electrical interconnects for multichip modules (MCM), magnetic sensors,

SQUIDS etc., will be primarily in the form of thick and thin films where the high surface/volume ratio makes the problem of degradation critical [3]. In this paper, preliminary results of the use of diamond-like carbon films as an encapsulant for YBCO superconductors are reported.

2. Experimental

Diamond-like carbon films were deposited in a parallel plate, capacitively coupled, Reinberg type reactor (Texas Instruments model A24C) operating at 13.56 MHz, using the r-f plasma enhanced chemical vapor deposition technique. Methane (CH_4) gas was used as the carbon precursor gas at a flow rate of 40 sccm. The chamber pressure and r-f power densities were 200 mTorr and 84 mW/cm^2, respectively. All the depositions were performed at room temperature without any external heating and with the substrates mounted on the r-f electrode. A deposition rate of 90 Å/min was obtained for these deposition conditions. DLC films were deposited on both double side polished <100>, p-type, silicon substrates and Corning 7059 glass substrates for the purpose of FTIR and optical bandgap measurements. $YBa_2Cu_3O_{7-x}$ films were deposited on lanthanum aluminate <100> oriented substrates using the in situ pulsed laser deposition technique with a 193 nm ArF excimer laser operated at a repetition rate of 5 Hz and a pulse width of 10 ns with an energy density of 1.5 J/cm^2. The depositions were carried out at a temperature of ~760°C and at an oxygen pressure of 200 mTorr with a bulk stoichiometric YBCO target. All the YBCO films used in this study were c-axis oriented and 2500 Å thick. The critical temperature (Tc) and critical current density (Jc) of the HTSC films were measured using a non-contact measurement system similar to that described in [3]. The HTSC and DLC films were characterized using a Phillips X'pert x-ray diffractometer and a Digital Instruments Nanoscope III Atomic Force Microscope (AFM).

3. Results and Discussion

The diamond-like carbon films exhibited an optical band gap of 3 eV and a refractive index of 2.2. X-ray diffraction analysis of the DLC films revealed the presence of a crystalline form of carbon, with a 2θ peak at 61.66° corresponding to lonsdaleite (hexagonal diamond) [4]. FTIR characterization of the DLC films provided the information on different C-H bonding configurations. FTIR spectrum for a DLC film shows an intense absorption peak associated with a dihydride bonded to sp^3 type carbon is present at 2927 cm^{-1}. A peak at 2876 cm^{-1} is the result of a dihydride bonded with sp^3 type carbon due to symmetry [5]. Peaks around 3500 cm^{-1} and 2200 cm^{-1} are due to residual purge nitrogen bonded to hydrogen and carbon, respectively. The surface morphology of the DLC film was studied using AFM. Figure 1 shows the AFM scan for the surface morphology of a DLC film coated on YBCO film. The film was continuous for a thickness of 400 Å and the

surface was very smooth with an average surface roughness (Ra) of 3 nm.

Diamond-like carbon films of varying thicknesses 400 Å, 800 Å, and 1200 Å were deposited on YBCO superconducting films. The typical critical temperature (Tc) and critical current densities (Jc) of the YBCO films were 89 K and $10^6 A/cm^2$, respectively, with a ΔT of 0.8 K. The Tc and Jc of the HTSC films were measured before and after depositing the DLC film and they remained unchanged with an identical transition temperature (ΔT). The HTSC films were also characterized using an x-ray diffraction technique to identify the different phases before and after encapsulation. Figure 2 shows the x-ray diffraction pattern of YBCO superconducting film after exposure to water and the as deposited film in the inset. The x-ray diffraction pattern after encapsulation essentially exhibited the same peaks as the uncoated superconducting YBCO. AFM scan for the surface morphology of the encapsulated DLC film after water exposure shows a slight change in the average roughness (about 10 nm), which may be due to the fact that the scan was not done exactly at the same place as was done before. The encapsulated YBCO superconducting films have been exposed to water at room temperature in air ambient for 2 hours. The YBCO films were then retested for Tc, Jc, and the transition ΔT, which remained unchanged indicating that there was no degradation in the superconducting films. The intensity of different peaks in the x-ray diffraction pattern after exposure to water vapor clearly indicates that the DLC encapsulation has protected the superconductor from degradation [7].

4. Summary and Conclusions

Diamond-like carbon films were successfully deposited at room temperature on HTSC films for purposes of encapsulation and, hopefully, protection from moisture. The DLC films exhibited good adhesion without any signs of peeling off. The critical temperature transition, ΔT, and the critical current density (Jc) of the YBCO superconductors remained unchanged after deposition of a 1200 Å thick DLC film. The DLC film offered protection to the HTSC film from moisture penetration, and hence, film degradation, which is a major concern in YBCO superconducting film applications.

5. Acknowledgement

6. References

1.   S. S. Ang, G. Sreenivas, W. D. Brown, H. A. Naseem, and R. K. Ulrich, J. Electron. Mater. 22, p. 347 (1993).

2.   E. Saiz and J. S. Moya, Supercond. Sci. Technol. 5, p. 130 (1992).

3.   J. H. Classen, M. E. Reeves, and R. J. Soulen, Rev. Sci. Instrum., 62, p. 996 (1991).

4.   R. A. Beera, W. D. Brown, S. S. Ang, H. A. Naseem, A. P. Malshe, R. K. Ulrich, S. Nasrazadani, and R. C. Goforth, Proc. of International Electronic Packaging Conference, Sep. p. 55 (1994).

5.   J. Robertson, Advances in Physics, 35(4), p. 317 (1986).

6.   M. F. Khan, R. L. Burns, H. M. O'Bryan, Jr., P. K. Gallagher, R. C. Sherwood, and S. Jin, Appl. Phys. Lett. 51(7), p. 532 (1987).
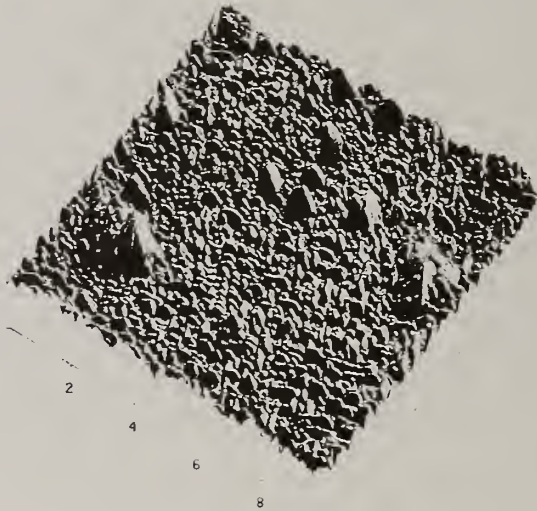
Figure 1. AFM micrograph of DLC film coated on YBCO thin film
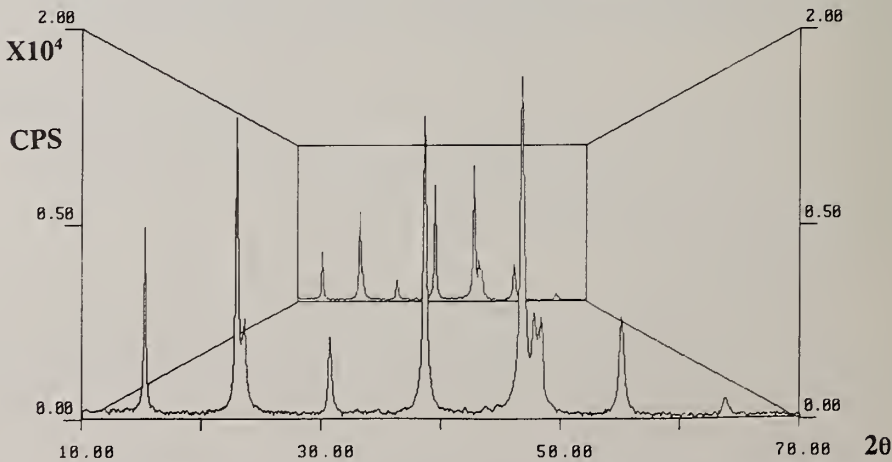
Figure 2. X-ray diffraction pattern of superconducting YBCO film after exposure to water with inset of as deposited film

IMPROVEMENT OF SOLAR CELL EFFICIENCY AND STABILITY BY DEPOSITION OF DLC-FILMS

N.I.Klyui[1], V.G.Litovchenko[1], S.I.Frolov[1], V.A.Semenovich[2], A.P.Gorban`[1], V.P.Kostylyov[1]

1-Institute of Semicond.Physics, Ukr.Nat.Acad.Sci.,252028, Kiev, UKRAINE
2-Institute of Superhard Materials, Ukr.Nat.Acad.Sci.,254074, Kiev, UKRAINE

Key words: solar cell, DLC, implantation, UV treatment

Abstract

Parameters of silicon solar cells (SC) covered by diamond-like carbon (DLC) films have been investigated before and after thermal annealing, ion implantation and ultra-violet irradiation. The significant improvement of SC efficiency was observed for SC with thin (~50-70 nm) antireflecting DLC films. Thick (~1000-1500 nm) DLC films deposited on the working side of the SC allow to increase its stability relating to effect of proton and ultraviolet (UV) irradiation.

1. Introduction

One of the most ways for improvement of solar cell (SC) parameters are the deposition of antireflecting coating on the working surface of SC [1]. It allows to utilize the solar energy more effectively due to decreasing of reflection coefficient (R). For this aim more prospective are diamond-like carbon (DLC) films, structure and properties of its can be varied over a broad range using various deposition parameters [2]. For example, it has been reported recently [2] that the refractive index (n) of DLC films can be varied from 1.6 to 2.3 under changes of the deposition conditions. It is especially important for applications of DLC films as antireflecting coatings for silicon SC, because in order to maximize the Si-SC parameters it is necessary to use a top film with n~1.9-2.3. This is a direct consequence of condition for optimal antireflecting effect $n_{film} = (n_{Si})^{1/2}$. Another importance of DLC feature is their mechanical and radiation resistance, that especially very important for cosmic space apllication of SC. Nevertheless, despite the fact that DLC films are perspective to improve SC parameters, only a few works were devoted to investigations of some aspects of the problem [3]. Thus, the aim of this study is to show that due to deposition of DLC films both the efficiency and stability of silicon solar cells can be improved.

2. Experimental details.

Silicon solar cells with shallow (~1000 nm) combined inversion-diffusion junction were used. To increase photocurrent the isotype barrier was created on the back side of the elements. Front side of some elements was textured by etching in KOH solution. As a result random pyramidal relief was formed. The current-voltage (I-V) relationships for the SC both with and without DLC coating were measured under AM0 illumination conditions. The DLC films used in this study were deposited by decomposition of CH_4 -H_2 gas mixture in a parallel plate reactor. The substrates for deposition were put directly on the cathode of diameter 200 mm, which was cooled by water and capacitively connected to a 13.56 MHz RF generator. The total pressure of the reaction chamber was varied from 0.1 to 0.8 torr. During the plasma decomposition experiments RF bias value was varied from 500 to 2000 volts under fixation of other deposition parameters. Technological parameters and a set-up for deposition of DLC films are defailed in [4]. Optical constants (refractive index n and extinction coefficient k) of DLC films were measured by spectroellipsometry method [5] within spectral range from 1.5 to 5.6 eV. Using dispersion dependencies of n and k the reflection spectra R for SC+DLC films systems were calculated. The optical band gap of DLC films was determined from Tauc equation. SC with and without DLC coating were irradiated by proton of intermediate energies (50-150 keV) at the doses up to $10^{16} cm^{-2}$. The ion beam current density did not exceed $1 \mu A/cm^2$. The ultraviolet irradiation treatments of SC were made by xenon (8.4 eV) and kripton (10 eV) lamps.

3. Results and discussion

Fig.1 shows spectral dependences of optical constants (n,k) for DLC films (d~65nm) used as antireflecting coating for silicon SC. As seen from Fig.1 the refractive index remains roughly constant within spectral range from 1.5 to 4.5 eV (n~2.0) and satisfies the condition for optimal antireflecting effect. The reflection spectra calculated by
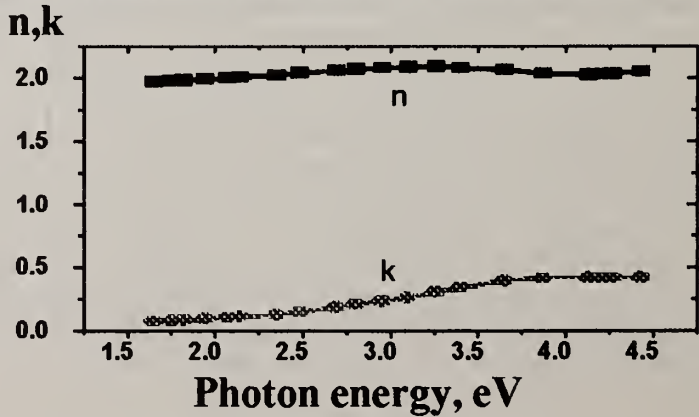
Fig.1. Spectral dependences of optical constants for antireflecting DLC film.

using n(hv) and k(hv) dependences for the SC+DLC film system shows significant decreasing of R value, which attains 1% in the minimum of the reflection band (~600 nm). This, in its turn, leads to a marked improvement of parameters of SC. The increasing of short circuit current J_{sc} attains 25-40%, while the open circuit voltage V_{oc} does not change, but in some cases increases. At the same time the fill factor FF is increased as well. It results in increasing of SC efficiency 1.3 times. The parameters for a typical silicon SC with (sample 1a) and without (sample 1) DLC antireflecting film are presented in Table I. It should be noted that DLC films used as antireflecting coating demonstrated a high thermal stability. Thermal annealing at 350 C for 30 min affected neither the optical constants of DLC films nor the parameters of SC with antireflecting coating (see sample 1b in Table I). It was earlier shown [6] that another way for improving of the SC efficiency was the decreasing of reflectance due to texturing of SC working surface. In Table I the parameters of textured silicon SC without (sample 2) and with (sample 2a) DLC antireflecting film are presented. Taking into account the obtained results (see Table I) and the fact that texturing procedure allows to improve the SC efficiency up to 1.1-1.15 times it may be concluded that due

TABLE I .Parameters of silicon SC with and without DLC antireflecting films

Sample number	DLC film	V_{oc}, mV	J_{sc}, mA/cm^2	FF	η, %
1	-	580	34.2	0.72	10.6
1a	+	590	40.8	0.75	13.4
1b*	+	590	40.7	0.75	13.4
2**	-	555	28.5	0.78	9.0
2a**	+	575	34.0	0.784	11.3

*The sample 1b is the sample 1a after thermal annealing at 350° C for 30 min in N_2.
**The samples 2 and 2a have textured front surface.

to deposition of antireflecting DLC films on textured suface of SC the reflection losses can be practically excluded.

Results of proton implantation effect on silicon SC parameters are presented in Table II. To protect the SC the thick (1300-1500 nm) DLC films with optical band gap ~3.5 eV and refractive index ~1.6 were deposited onto SC working suface. As seen from Table II one-stage (E=50 keV) or multi-energy (50+100 keV) implantation of proton into protected SC practically does not influence its parameters (sample 3a and 3b in Table II, respectively). And only after third stage of implantation (E=150 keV) the SC parameters are slightly deteriorated (sample 3c), while the unprotected SC (sample 4) drastically degraded after this treatments (sample 4a). Some decreasing of the parameters of protected SC is due to penetration of implanted ions throughout top DLC film into SC that results in disordering of silicon subsurface layer. This conclusion is confirmed by results of Monte-Carlo simulation of ion depth distribution as well as by experimental results obtained for SC covered by thicker DLC film

TABLE II . Parameters of silicon SC with and without DLC protective films

Sample number	Thickness of DLC film, nm	Proton implantation		V_{oc}, mV	J_{sc}, mA/cm^2	FF	η, %
		E, keV	D, 10^{15} cm^{-2}				
3	1300	-	-	608	30.8	0.787	10.8
3a	1300	50	3.3	607	30.7	0.787	10.8
3b	1300	50/100	3.3/3.3	606	30.5	0.787	10.7
3c	1300	50/100/150	3.3/3.3/3.3	572	27.2	0.712	8.1
4	-	-	-	524	20.2	0.788	6.1
4a	-	150	3.3	412	15.0	0.578	2.6
5	1500	-	-	580	29.8	0.7	8.9
5a	1500	150	10	565	26.2	0.7	7.6
6	-	-	-	595	37.5	0.66	10.8
6a	-	150	10	350	31.4	0.44	3.5

(d=1500 nm, sample 5) and subjected to implantation of greater ion dose (sample 5a). Indeed, as seen from Table II deterioration of sample 5a parameters is substantially less than for sample 3c inspite of higher ion dose. The unprotected SC (sample 6) subjected to this high dose implantation dramatically degraded (sample 6a).

Irradiation of SC covered by protective DLC films (d~1300-1500 nm) by using UV lamps (xenon-8.4 eV or kripton-10 eV) did not result in any marked change both the SC parameters and optical constants of films. Moreover, improvement of parameters of SC with protective DLC films and previously implanted by proton was observed after UV treatment. At the same time, the UV treatment of unprotected and implanted SC led to further degradation of its parameters.

In summary, the obtained results give evidence to prospective utilizing of DLC films as protective and antireflecting coating for silicon solar cells.

4. References

1. J.Zhao and M.A.Green, IEEE Trans. on Electron Devices, 38(1991) 1925.
2. P.Koidl, Ch.Wild, B.Dischler, J.Wagner and M.Ramshteiner, Materials Science Forum, 52&53(1989) 41.
3. T.J.Moravec and J.C.Lee, J.Vac.Sci.Technol., 20(1982) 338.
4. A.A.Doroshenko, V.A.Semenovich, S.I.Khandoznko, A.M.Kutsay and M.T.Muinov, J. of Superhard Materials, 15(1993) 15.
5. V.G.Litovchenko, S.I.Frolov and N.I.Klyui, Proc.SPIE, 2113(1993) 65.
6. A.Rohatgi and P.Rai-Chondhury, Solar Cells, 17(1986) 119

DIAMOND-LIKE ATOMIC-SCALE COMPOSITE FILMS: SURFACE PROPERTIES AND STABILITY STUDIED BY STM and AFM

B. Dorfman[1], M. Abraizov[1], F.H. Pollak[2], R. Eby[3], Z.-Y. Rong[4], M. Strongin[5] and X.-Q. Yang[5]

[1]Atomic Scale Design, Inc; 90 Lupton Hall; SUNY-Farmingdale; Farmingdale, NY 11735
[2]Physics Department; Brooklyn College of CUNY; Brooklyn, NY 11210
[3]TopoMetrix; One Robertson Drive; Bedminster, NJ 07921-1716
[4]Department of Physics; SUNY-Stony Brook; Stony Brook, NY 11794-3800
[5]Department of Physics; Brookhaven National Laboratory; Upton, NY 11973

Key words: Diamond-like atomic-scale composites, surface morphology, scanning tunneling microscopy, atomic force microscopy

Abstract

Amorphous "diamond-like/quartz-like" composites a-(C:H/Si:O) and metal containing a-(C:H/Si:O/Me) constitute a novel class of diamond-related materials with a number of unique bulk and surface properties. In order to gain a more fundamental understanding of the surface properties and stability of these solids we have performed a scanning tunneling and atomic force microscopy investigation of both a-(C:H/Si:O) and a-(C:H/Si:O/Me) films, including the effects of ion bombardment and annealing.

1. Introduction

One of the most serious impediments to the applications of diamondlike carbon (DLC) materials is the instability due to (a) their amorphous structure and (b) the non-equilibrium nature of the "diamond-like" state. In addition there are problems with substrate adhesion and stress. The electrical properties of DLC also are limited; the available range of electrical resistivity of these films comprises neither the metallic nor common dielectric ranges.

Amorphous "diamond-like/quartz-like" composites a-(C:H/Si:O) and metal containing a-(C:H/Si:O/Me) constitute a novel class of diamond-related materials with a number of unique bulk and surface properties [1,2]: excellent adhesion to virtually any substrate (i.e., metals, crystalline and glass dielectrics, plastics, teflon, etc.), low

stress, variable electrical resistivity over 18 orders of magnitude (10^{14} to 3×10^{-4} ohm-cm) and low temperature superconductivity, controllable optical properties (index of refraction and absorption coefficient), excellent thermal and thermal shock stability of all the major properties (mechanical, electrical and optical). Diamond-Like Atomic-Scale Composites (DLASC) also posses excellent diffusion barrier properties and have an extremely low friction coefficient. Thus this class of materials represents a significant advance over conventional diamondlike films in both stability and in the ability to tailor specific properties over a wide range.

In order to gain a more fundamental understanding of the surface properties and stability of DLASC material and to develop an approach to the controllable nanostructural modification of Me-DLASC we have performed a scanning tunneling (STM) and atomic force (AFM) microscopy investigation. Both a-(C:H/Si:O) and two kinds of a-(C:H/Si:O/Me) films, i.e., with hard-melting (Hf,Cr,W) and noble metals (Pd, Pt) were studied, including the effects of ion bombardment and annealing.

2. Experimental Details

All films were synthesized on $<100>$ Si substrates in an electrical field (DC or RF) from carbon and silicon-containing radicals formed with a plasma discharge from polyorganosiloxane precursors. Metal incorporation was produced by DC magnetron co-sputtering of a metal target. Film thicknesses were ≈ 1 μm (unless otherwise noted). All STM images were taken in the constant current mode, with the set current around 1 nA and the tip bias voltage around -230 mV, with the tip held at negative potential with respect to the sample. The ATM images were obtained in the contact mode with a tracking force < 5 nanonewtons. All experiments were performed in air ambient conditions.

3. Experimental Results

For the STM work several Me-DLASC materials (Me = Cr, W, Pd and Pt) were employed. Shown in Fig. 1 is the STM image of an as-deposited Pt-DLASC sample with a surface resistivity (R_s) of 1000 $\Omega/\square$. On a 100nm scale, it is possible to see that the film exhibits a uniformly distributed bumpy surface, with bump diameters ranging between 150 and 350Å. These bumps have irregular shapes and are in contact with each other. Surface topography on top of these bumps shows structureless amorphous morphology with a roughness of about only 1Å. The surface morphology of a similar as-deposited Pt-DLASC film with $R_s = 1M\Omega/\square$ had a similar appearance.

After annealing in vacuum at 450°C for two hours the STM images of these two films changed dramatically. Figure 2 is a 100x100nm image of film #1 after annealing. The remaining bumps have been separated and are surrounded by rougher
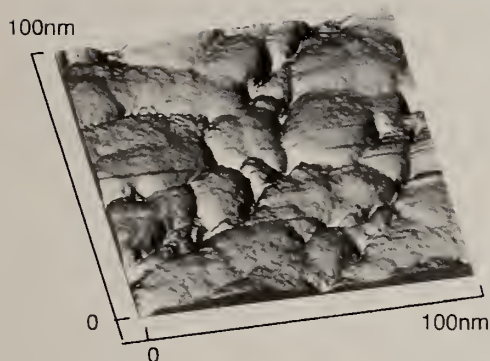
Fig. 1 STM image of an as-deposited Pt-DLASC film.
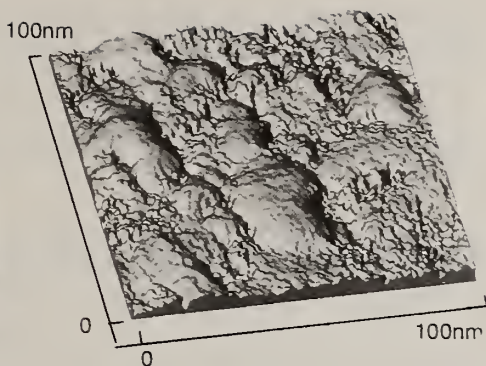
Fig. 2 The Pt-DLASC film of Fig.1 after annealing at 450°C for 2 hours.

regions. This separation was not observed on any of the other as-deposited films. The rougher part of the image represents a higher noise level caused by the strong tip-sample interaction in the poorly conductive regions.

By comparing images taken before and after the samples were annealed at 450°C (for two hours) it was found that (a) the transition-metal containing samples had a high thermal stability while (b) for the Pt-DLASC material, as expected, formation of sp^2-rich regions was observed, indicating that the Pt engenders a "loosening" of the diamond-like matrix with a decrease in the energy barrier. The obtained micro- and nanoscale surface images and observed transformation from sp^3 to sp^2 bonding provides a new understanding of the fundamental structure of the films [3].

Shown in Fig. 3 is a 2000x2000nm AFM image of an as-deposited DLASC film. The overall surface morphology is very smooth. The root-mean-square (RMS) and average (R_a) roughness are 0.74 Å and 0.55 Å, respectively. This smoothness is one of the reasons for the low friction coefficient of this material.

The influence of Ar-ion bombardment (1.5 kV for 10 minutes) on the surface roughness of this DLASC film was investigated using AFM.
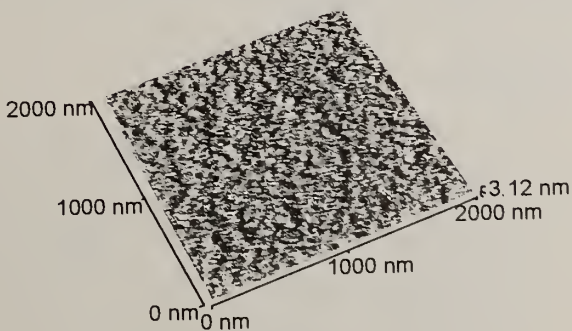
Fig. 3 AFM image of an as-deposited DLASC film.

The surface treatment changed RMS and R_a to only 1.4 Å and 1.1 Å, respectively, which demonstrates the DLASC hardness and wear resistance.

The obtained values of RMS and R_a for the DLASC film (as-depsited and Ar-ion bombarded) in addition to several Me-DLASC films are listed in Table I together with R_s.

TABLE I. Surface properties of some DLASC films

FILM	RMS (Å)	R_a (Å)	R_S ($\Omega/\square$)	COMMENTS
DLASC	0.74	0.55	Insulating	
DLASC[a]	1.4	1.1	Insulating	After Ar-ion bombardment
Hf-DLASC	3.6	2.8	40	
Cu-DLASC	44	31	1000	
Cr-DLASC	39	31	7	3 μm thick
Cr-DLASC[b]	36	27	0.8	
TiN-DLASC	47	36	5000	
Nb-DLASC	57	44	400	

4. Conclusions

Our investigation has shown that DLASC and Hf-DLASC films posses atomic-scale smoothness and that the former material is resistant to wear. The other Me-DLASC composites may require some optimization. The structure and surface of these films are very stable. Noble metals decrease the film thermal stability and controllable nanostructural reconstruction is possible on this basis.

5. References

1.   V.F. Dorfman, Thin Solid Films 212, 267 (1992); V.F. Dorfman, A. Bozhko, B.N. Pypkin, R.T. Borra, A.R. Srivatsa, H. Zhang, T.A. Skotheim, I. Khan, D. Rodichev and G. Kirpilenko, Thin Solid Films 212, 274 (1992).
2.   B. Dorfman, M. Abriazov, B. Pypkin, M. Strongin, X.-Q. Yang, D. Yan, F.H. Pollak, J. Grow and R. Levy, Mat. Res. Soc. Symp. Proc. 351, 43 (1994); B. Dorfman, M. Abriazov, F.H. Pollak, D. Yan, M. Strongin, X.-Q. Yang and Z.-Y. Rong, Mat. Res. Soc. Symp. Proc. 349, 547 (1994).
3.   Z.-Y. Rong, M. Abriazov, B. Dorfman, M. Strongin, X.-Q. Yang, D. Yan and F.H. Pollak, Appl.Phys. Lett. 65, 1379 (1994).

DIAMOND-LIKE CARBON
OPTICS AND ELECTRONICS

ELECTRICAL CHARACTERIZATION OF P-N AND P-I-N DIODE STRUCTURES MADE BY ION BEAM DEPOSITION OF DOPED DIAMOND-LIKE CARBON

H.C. Hofsäss, C. Ronning, U. Griesmeier, M. Gross, A. Cedvall, E. Dreher, J. Biegel

Fakultät f. Physik, Universität Konstanz, Postfach 5560, D-78434 Konstanz, Germany

Key words: doping, diode, Frenkel-Poole, heterojunction

Abstract

We prepared doped diamond-like carbon films (DLC) by alternating deposition of low energy mass separated $^{12}C^+$ and dopant ions on metal and Si substrates. If DLC could be doped n- or p-type, p-n- or p-i-n-like devices should show rectifying behavior. However, the current-voltage (I-V) characteristics of such devices are totally symmetric, indicating that no shift of the Fermi level has occurred. In addition, a compensation effect due to co-doping with N and B was not observed. I-V curves of DLC/Si heterojunctions are discussed. All I-V curves are best described by Frenkel-Poole emission.

1. Introduction

Two types of DLC, hydrogenated amorphous carbon (a-C:H) and H-free tetrahedrally bonded amorphous carbon (ta-C), have attracted attention as material for electronic applications, because of a high resistivity, chemical inertness, and an optical band gap of up to 3 eV. Basic devices such as DLC/Si heterojunctions, exhibiting strongly rectifying I-V characteristics and breakdown voltages well above 100 V, have been fabricated [1,2,3,4]. The forward diode characteristic of DLC/Si diodes was used to determine the resistivity of DLC films [3], and the high breakdown voltages are commonly attributed to the electrical breakdown strength of the DLC [1,3,5,6]. DLC p-n-junctions don't exist yet, and the reports on doping of DLC are contradicting.

Meyerson and Smith first observed a strongly increased conductivity σ for B- and P-doped a-C:H films, which they interpreted as due to n- and p-type doping effects [7]. Recently, Thiele et al. studied the electrical and optical properties of a-C:H, doped with B, N, and P, and found no evidence for a shift of the Fermi level. They concluded, that hopping conduction is increased due to an increased density of states at the Fermi level in the doped material [8]. Also Kalish et al. interpreted the increased conductivity in their N-doped a-C:H films by hopping conduction [9,10].

Doping of vacuum arc deposited ta-C, with N, B and P was first reported by Amaratunga et al. [3], however with little success. Later on, the same group published a series of papers, claiming that (i) undoped ta-C is p-type with the Fermi level at 0.2-0.4 eV above the valence band, (ii) N- and P-doped ta-C is n-type with the Fermi level at about 0.2 eV below the conduction band, (iii) B-doping was unsuccessful and (iv)

the effect of p-and n-type dopants in ta-C and crystalline diamond would be opposite [11,12,13,14]. To our opinion, these conclusions are based on rather weak arguments: The statement, that undoped ta-C is p-type, is based on measured turn-on voltages of ta-C/Si heterojunctions [12]. Fermi level positions in undoped and doped ta-C were derived from the slope of Arrhenius plots of the conductivity σ ($\log(\sigma)$ vs. T^{-1}). However, the data are also in good agreement with a linear relationship between $\log(\sigma)$ and $T^{-1/4}$, characteristic for variable range hopping.

In recent studies we came to opposite conclusions, especially that no shift of the Fermi level occurs upon doping of ion beam deposited ta-C [1]: (i) We have shown, that B doping increases the conductivity more efficient than N doping. (ii) Electrical conduction through ta-C films is best described by Frenkel-Poole emission (field enhanced thermally activated conduction via localized states) and variable range hopping, which also describes the observed temperature dependence of σ very well. (iii) We found a continuous decrease of the resistivity with increasing B and N dopant concentration in the range 0.1 - 5 at.%. We did not observe a maximum in resistivity at a certain dopant concentration. Such an effect was once seen by Veerasamy et al. and interpreted by N atoms compensating p-type ta-C [12]. (iv) The I-V curve of a diode-like N- and P-doped ta-C-device was totally symmetric in voltage [2].

In the following, we discuss the doping effects of DLC by studying the I-V characteristics of p-n- and p-i-n-like DLC devices, as well as DLC/Si heterojunctions.

2. Experimental

DLC (or ta-C) films were prepared by deposition of low energy (100 eV) magnetically mass separated $^{12}C^+$ ions in a UHV-deposition chamber at room temperature and a pressure below 10^{-5} Pa during deposition. Doping was achieved by periodically switching the mass separation magnet between $^{12}C^+$ and the dopant ions $^{11}B^+$, $^{14}N^+$ or $^{31}P^+$, and was controlled via the charge deposited onto the substrate. Details of the deposition system are described in ref. [5]. Diode-like DLC structures were deposited onto mirror-like polished stainless steel substrates, and DLC/Si heterojunctions were prepared using n-type Si (1-10 Ωcm) as well as p-type Si (5-14 Ωcm) substrates. As contacts to the DLC we used either Au or Os pins, or evaporated Al or Au contacts.

3. Results

Our first diode-like device was made by deposition of a 60 nm ^{31}P-doped DLC film on a singly crystalline Ni substrate followed by a 65 nm ^{11}B-doped DLC film [2]. For both layers rather high dopant concentrations of 5 at.% were used. The measured I-V curve was totally symmetric in voltage, indicating that no p-n junction was formed. The strongly non-linear I-V dependence is explained by the Frenkel-Poole conduction mechanism [1]. For the present study we have prepared similar devices on steel substrates, but with lower dopant concentrations. First, a p-n structure was made, consisting of 2 μm 1 at.% ^{14}N doped and 2 μm 1 at.% ^{11}B doped DLC. The I-V curve shown in Fig.1a is totally symmetric in voltage. Again, the non-linear I-V dependence is well explained by Frenkel-Poole emission. The same result was obtained for a p-i-n structure, consisting of 110 nm 0.75 at.% ^{11}B doped DLC, 25 nm undoped DLC and 110 nm 0.75 at.% ^{14}N doped DLC (Fig.1b). We also prepared a device similar to one

studied by McKenzie et al. [14], consisting of 50 nm 0.5 at.% ^{14}N doped DLC on top of a 50 nm undoped DLC layer. This device should show the rectifying behavior of a p-n junction, if we assume that undoped DLC is p-type and changes to n-type conduction upon N doping,. However, the corresponding I-V curve is again totally symmetric (Fig.1c). Finally, in analogy to Veerasamy et al. [12], we tried to find electrical compensation in a DLC sample, co-doped with 3 at.% N and 0.5 at.% B. For the different dopant concentrations the resistivities of DLC are similar [1]. The resistivity of the co-doped DLC film is not significantly increased, showing that an electrical compensation of B and N dopant atoms does not occur.

We have analyzed several DLC/Si heterojunctions with undoped, B-doped, N-doped or P-doped DLC-films of varying thickness between 25 nm and 100 nm. Breakdown voltages V_{br} in excess of 100 V are easily obtained for n-Si as well as p-Si substrates, and also for doped DLC films. Doping reduces V_{br} to some extent [1], however, V_{br} did not depend significantly on the film thickness. We therefore conclude that breakdown occurs in the Si. Also the measured values V_{br} are expected for our Si substrates with carrier concentrations of $\approx 10^{15}$ cm^{-3} [15]. The forward diode characteristic of a DLC/n-Si heterojunction measured at different temperatures is shown in Fig.2. Ohmic conduction or Schottky emission neither explain the voltage dependence nor the temperature dependence of the current. The data are again best explained by Frenkel-Poole emission, where the initial increase of the forward current is due to a voltage-dependent decrease of the resistivity of the DLC film. Eventually, for larger forward bias voltages a resistance limited current may be observed, which is then determined by the resistivity of both the Si substrate and the DLC film.
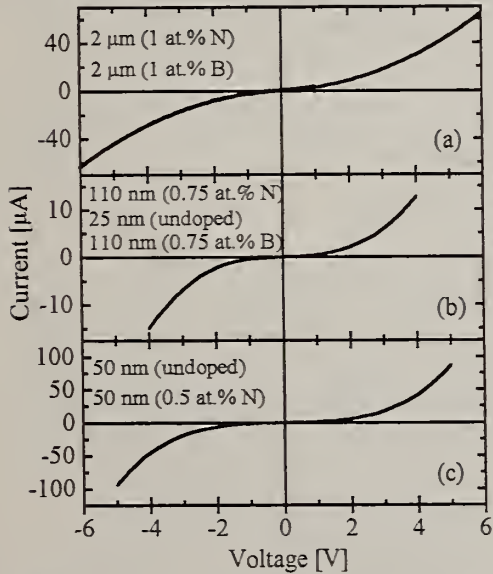
Fig.1: Totally symmetric I-V-curves of differently doped, layered DLC structures deposited on polished stainless steel. The inserts give the layer thickness, dopant species and dopant concentration.
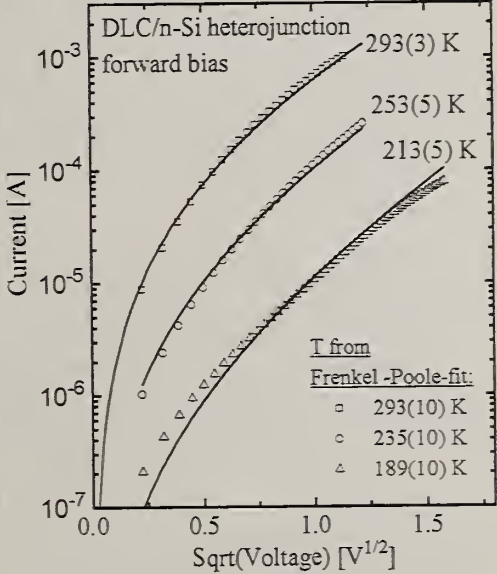
Fig.2: Forward bias characteristic of a DLC/n-Si heterojunction at different temperatures. Solid lines were calculated for Frenkel-Poole conduction. Only T was varied to fit the low temperature data.

4. Conclusions

Several p-n and p-i-n diode-like DLC structures were prepared, which all showed a totally symmetric current-voltage characteristic. The non-linear increase of the current with increasing voltage is described by Frenkel-Poole emission. Electrical compensation in a DLC sample co-doped with N and B was not observed. These results support recent results of our group, that doping of DLC increases the conductivity of the material due to an increased density of localized states in the band tails and at the Fermi level. A shift of the Fermi level upon doping is rather unlikely.

DLC/Si heterojunctions exhibiting high breakdown voltages were fabricated. The forward bias characteristic is dominated by Frenkel-Poole conduction in the DLC, whereas breakdown is believed to occur in the Si material. Breakdown strength and resistivity of the DLC film are difficult or impossible to extract from those I-V curves.

5. Acknowledgments

6. References

1. C. Ronning, U. Griesmeier, M. Gross, H.C. Hofsäss, R.G. Downing and G.P. Lamaze, Diamond and Related Materials 4 (1995), to be published
2. H.C. Hofsäss, J. Biegel, C. Ronning, R.G. Downing and G.P. Lamaze, Mat. Res. Soc. Symp. Proc. 316 (1994) 881
3. G.A. J. Amaratunga, D.E. Seagal, D.R. McKenzie, Appl. Phys. Lett. 59 (1991) 69
4. T. Mandel, M. Frischholz, R. Helbig A. Hammerschmidt, Appl. Phys. Lett. 64 (1994) 3637
5. H. Hofsäss, H. Binder, T. Klumpp and E. Recknagel, Diamond and Related Materials 3 (1994) 137
6. S.B. Hwang, Y.K. Fang, K.H. Chen, C.R. Liu L.C. Kuo, Electr.Lett. (1991) 2043
7. B. Meyerson and F.W. Smith, Solid State Comm. 41 (1982) 23
8. J.U. Thiele, B. Rubarth, P. Hammer, A. Helmbold, B. Kessler, K. Rohwer, D. Meissner, Diamond and Related Materials 3 (1994) 1103
9. R. Kalish, O.Amir, R.Brener, R.A. Spits and T. Derry, Appl.Phys. A52 (1991) 48
10. O. Amir and R. Kalish, J. Appl. Phys. 70 (1991) 4958
11. V.S. Veerasamy, G.A.J. Amaratunga, W.I. Milne, P. Hewitt, P.J. Fallon, D.R. McKenzie, C.A. Davis, Diamond and Related Materials 2 (1993) 782
12. V.S. Veerasamy, J. Juan, G.A.J. Amaratunga, W.I. Milne,, K.W.R. Gilkes, M. Weiler, L.M. Brown, Phys. Rev. B 48 (1993) 17954
13. G.A.J. Amaratunga, V.S. Veerasamy, C.A. Davis, W.I. Milne, D.R. McKenzie, J. Juan, M. Weiler, J. Non-Cryst. Solids 164-166 (1993) 1119
14. D.R. McKenzie, Y. Yin, N.A. Marks, C.A. Davis, E. Kravtchinskaia, B.A. Pailthorpe, G.A.J. Amaratunga, J. Non-Cryst. Solids 164-166 (1993) 1101
15. M.Shur, Physics of Semiconductor Devices (Prentice Hall, Englewood Cliffs, 1990) p. 182 ff.

FORMATION OF CONDUCTIVE NETWORK IN DIAMOND-LIKE CARBON BY INTERCALATION OF COPPER

V.I.Ivanov-Omskii, A.B.Lodygin, S.G.Yastrebov, and V.E.Chelnokov

A.F.Ioffe Physical-Technical Institute, Politechnicheskaya 26, St.Petersburg, 194021, Russia

Key words: DLC, intercalation, cluster, percolation, Mie resonance

Abstract

The electrical conductivity and optical constants were measured in amorphous diamond-like carbon doped with copper. The electrical conductivity is analyzed in terms of percolation theory. The observed specific features of the conductivity as a function of copper content are associated with the formation of two different percolation networks. Analysis of measured optical constants of the material indicates that a nanocomposite structure with two types of clusters several nanometers in size is formed in the material.

We studied thin films (0.2-1.0 μm) of Cu-doped DLC produced by co-sputtering of graphite and copper targets in argon or argonhydrogen (20% H_2) plasma. The DC conductivity, UV, VIS and IR absorption were measured as a function of copper content x in the range $0 < x < 40$ at.%.

The instability of the Cu-C chemical bond gives rise to a nanocomposite structure of the material. As a result, a system of conductive domains, consisting of copper-rich clusters randomly distributed over a dielectric matrix is formed. The conduction through this system is an appropriate object for the percolation theory. Therefore the theory was used to analyze the dependence of the DC conductivity on the copper concentration (Fig.1). The concentration ranges 0-15% and 16-40% are discussed separately.

The rapid growth of conductivity in the range 0-15% can be well explained by the theory based on the model of electrical current percolation through a system of conductive domains randomly distributed over non-zero conducting media [1]. The parameters of percolation system (percolation indices) can be derived from the plot

in Fig.1 by a fitting procedure. The solid curve A in Fig.1 calculated using the equation:

$$\sigma = const \cdot (x_c - x)^{-q}$$

with $q = 6.4$ is seen to fit reasonably the experimental results. This value of the percolation index corresponds to a very rapid growth of conductivity with copper concentration increasing on the left side of the conductivity maximum (by about an order of magnitude per 2% of copper). It is worth noting that the $q = 6.4$ value is unusually high, typical theoretically predicted values for different percolation systems being less than 2 [3]. The values of other critical indices found from the experimental data together with a low value of percolation threshold ($x_c = 14$-16%) can be ascribed to the formation of a percolation net with a relatively low cell density.

Another situation is observed at higher copper contents (above 16 at.%). Dense copper structures (e.g., drops), as it is discussed below, are formed here much more quickly namely before the "freezing" of the carbon matrix. This is believed to cause a drastic decrease in the effective volume fraction of conductive clusters. As a consequence, a reconstruction of the low cell density percolation network takes place and steeply reduces the conductivity (Fig.1).

It is well recognized that the structure of hydrogenated amorphous carbon is a disordered system of graphite-like clusters (GLC) embedded in the sp^3-bonded diamond-like matrix [4]. Domains of copper-intercalated GLC can be considered as one of structural elements of the network. The existence of elements of this kind in the material under investigation was demonstrated in [5]. It is believed that the above-discussed percolation net with a relatively low cell density can be related to such structural elements.

One can expect that decreasing the free energy of the minority component in binary structures with weak interaction between the components leads to a contraction of the corresponding phase surface. This means that the formation of minority component drops embedded in the majority component matrix occurs. The appearance of copper drops or similar formations in the system under study at sufficiently high copper concentrations can be explained in terms of this approach. This process cannot take place at low copper concentrations because the probability of copper-copper coupling is low and the quickly stabilized carbon skeleton retards any further copper atom coalescence. The material with $x > 16\%$ can be also described in terms of the percolation theory with another set of indices estimated in [2] where the value of q was found to be about 2.8. This value is much closer to the theoretical predictions given in [3] as compared with the case of low cell density network at $x < 16\%$. It is possible to detect the dense network consisting of copper

drop-like formations by studying the Mie resonance [6] whose modes are to be observed at the following frequencies:

$$\omega_n = \frac{\omega_p}{\sqrt{1 + \dfrac{n+1}{n}\,\varepsilon_m}}$$

Our measurements (see Fig.2) showed that for the samples with $x > 16\%$ the first resonance absorption peak ($n=1$) is found at about 2 eV [7]. The position of this resonance corresponds to the frequency of surface plasmons excited in spheroid copper drops. The geometrical sizes of the drops can be estimated by using the Drude theory of free electrons with space-limited mean free path. As a result, the following values of the parameters can be evaluated: resonance frequency $\omega_n = 3 \cdot 10^{15}$ s^{-1} (cf. the bulk plasma frequency of copper is $\omega_p = 1.24 \cdot 10^{16}$ s^{-1}), dielectric permittivity of the matrix ε_m is equal to 2.23, electron relaxation time τ is of the order of $7 \cdot 10^{-16}$ s. The parameter τ is related to the electron mean-free path by [8]:

$$\tau = \frac{\tau_0}{1 + L/R}$$

where the relaxation time of bulk copper is $\tau_0 = 7 \cdot 10^{-15}$ s [9], electron mean-free path in copper is $L = 10$ nm [10] and, correspondingly, drop size is estimated at about $R = 1$ nm. The appearance of a low-frequency edge of the second resonance peak at about 3.5-4 eV (Fig.2) was attributed to the formation of one more plasma resonance which corresponds to dense non-spherical low-dimensional copper formations ($n \rightarrow \infty$). It was found that the sizes of these formations coincide with typical GLC sizes [4] being at the same time close to those mentioned above for spheroid drops. Therefore one may assume that the low-dimensional domains have possibly originated from the intercalation of copper into GLC.

Thus, it was shown that different types of copper clusters may be formed in copper-doped DLC depending on the copper content. Therefore DLC doped with copper can be considered as a promising material for conductive cluster engineering.

Acknowledgments

References

1. Efros A.L., Shklovskii B.I.// Phys.Stat.Sol.(b), 1976, v.76, p.475
2. Ivanov-Omskii V.I., Lodygin A.B., Yastrebov S.G.// Solid State Physics, 1995, v.37 (in press)

782

3. Efros A.L., Shklovskii B.I. Electron properties of doped semiconductors. Moscow, "Nauka", 1979 (in russian)
4. Robertson J.// Prog.Solid State Chem., 1991, v.21, p.199
5. Ivanov-Omskii V.I., Frolova G.S.// Tech.Phys., 1995, v.40 (in press)
6. Mie G.// Ann.Phys., 1909, v.25, p.377
7. Ivanov-Omskii V.I., Krivorotov I.N., Yastrebov S.G.// Tech.Phys., 1995, v.40 (in press)
8. Kleeman W.// Ztschr.Phys., 1968, v.214, p.285; ibid. v.215 p.113
9. Johnson P.B., Christy R.W.// Phys.Rev.B, 1972, v.6, N12, p.4370
10. Ruppin R.// J.Appl.Phys. 1986, v.59, N4, p.1355
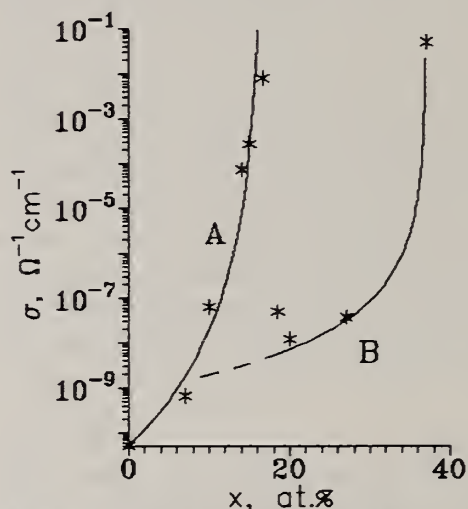
Fig.1. Conductivity of Cu−doped DLC as a function of copper content x
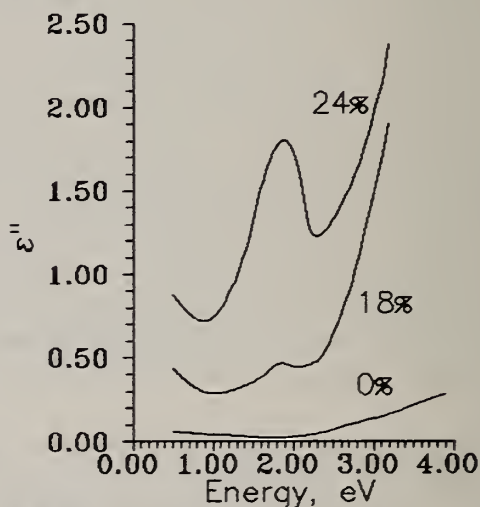
Fig.2. Imaginary part of dielectric function for three copper concentrations

DIAMOND-LIKE CARBON CHARACTERIZATION

DIELECTRIC STRENGTH OF DIAMONDLIKE CARBON (DLC) THIN FILMS FOR ENERGY STORAGE CAPACITORS

M. M. Freeman [1,2], A. L. Barton [2], H. L. Marcus [2]

[1] US Army Armament Research, Development and Engineering Center, Picatinny Arsenal, NJ 07806-5000

[2] Center for Materials Science and Engineering, The University of Texas at Austin, Austin, TX 78712

Key Words: Diamondlike carbon, dielectric strength, DLC, electrical properties

Abstract

The reputation of diamond as the material with the highest dielectric strength of all known insulators has led to interest in its application as a dielectric for high voltage, energy storage capacitors. "Diamondlike" carbon (DLC) films, which exhibit properties very near those of diamond and which can be synthesized routinely on a variety of substrates with uniformity over large areas, may prove to be an equally or even more attractive candidate dielectric for the same high voltage capacitor applications. In this study thin film capacitors were fabricated and voltage conditioned. Then the electrical properties, including dielectric strength, of the DLC films were determined.

1. Introduction

When a voltage is applied to a parallel plate capacitor, the dielectric material acts to retard the flow of current between the electrodes and as an energy storage medium. Since no material is a perfect insulator (a true dielectric), some current will flow; this current is called the *leakage current* of the capacitor. Typically when the applied voltage is increased, the leakage current increases as well although not quite linearly. When the voltage applied is sufficient to cause large numbers of electrons to find their way into the conduction band, the leakage becomes so great that the dielectric acts as a poor resistor and the capacitor is essentially "shorted." This condition - where leakage current runs away - is called *dielectric breakdown*. The voltage at which this happens is referred to as the *breakdown voltage*. And the value of the breakdown voltage divided by the dielectric thickness is the *dielectric strength* of the material.

Breakdown is classified according to the mechanism by which the electrons are able to reach the conduction band. Intrinsic breakdown, which is purely electronic in nature, characteristically takes place in a short time period (0.1 to 0.01 msec), is not dependent on size or shape of the electrodes and does not depend on the rate of rise of the applied voltage. Intrinsic breakdown usually is observed as a whole series of breakdown discharges appearing all over the capacitor at once or in rapid succession. It typically is not a localized effect - it involves either all or large homogeneous

portions of the dielectric. Once it begins, it does not stop until the voltage is lowered or removed and the damage to the capacitor is usually catastrophic. [1, 2]

Thermal breakdown, which relies on the local temperature rise to set up the conditions for electron or ion transport, characteristically takes place over time at a given voltage, is dependent on size and shape of electrodes and is voltage rate dependent. (Shorter pulses make breakdown occur at higher voltages than observed when a dc voltage is applied.) It is observed as a local single point or a few single point discharges which stop before the voltage is removed. Thermal breakdown is not always catastrophic. It is only catastrophic if it induces the conditions for continuous conduction associated with the establishment of a current path. [1, 2]

When test samples are constructed of thin films, the study of breakdown is simplified not only because the voltages required are low for thin dielectric materials, but also because a phenomenon known as "self-healing" will occur. The self-healing process assumes that the current primarily flows through a relatively small portion of the dielectric and that the material in that conducting channel will experience a temperature rise sufficient to vaporize a thin metal electrode. The dielectric material in the region will either melt or vaporize as well leaving the capacitor with a tiny void but otherwise undamaged and able to store energy again. As long as the current from the power supply is limited, this process may take place hundreds of times on a single sample. [3] It is this self-healing property that is the basis for the commercially accepted practice of *voltage conditioning*. By subjecting the sample to successively larger applied voltages, the weaker spots (defects from the manufacturing process) in the dielectric may be removed so that the properties of the dielectric itself may be studied or exploited.

2.   Experimental

The test samples were capacitors constructed of thin aluminum electrodes (nominally 1.5 µm thick) deposited by physical vapor deposition on glass substrates and DLC dielectric deposited by Rf plasma assisted chemical vapor deposition (RFPACVD). The DLC was deposited at low temperature using a gas mixture of 22.5 sccm methane and 50 sccm hydrogen. The authors' preliminary studies verified that this mixture provided a film with an Auger peak characteristic of DLC, good adherence to the aluminum and good insulating properties.

Capacitors with DLC films of several thicknesses, ranging from 0.1 to 1.3 µm, were studied. By utilizing appropriate shadow masking techniques during the deposition of the counter-electrode (the top aluminum layer) a number of capacitors of small area (nominally 38.5 mm^2) were deposited on each substrate. Capacitance was measured with a standard digital multimeter. DLC film thickness was measured using a Tencor Alpha Step 200 profilometer in an area masked during deposition to provide a step. Dielectric constants were calculated from capacitance and thickness data.

Voltage conditioning was performed during which each capacitor was subjected to a slow ramp to 18V in 3V increments with a 1 minute hold after every increment. At the end of each hold period, the dc leakage current was measured with a Keithly 610C electrometer placed in series with the capacitor, a dc power supply and a 1000 Ohm resistor. If the dc leakage current at any point in the test exceeded 1x10^{-4} Amps, the capacitor was subjected to a "clearing pulse" provided by the rapid discharge of a

39000 µF capacitor bank charged to the last "hold" voltage. Leakage current was remeasured and the clearing process repeated at successively higher voltages (not exceeding 18V) until the leakage current was better than 1×10^{-5} Amps. Then the capacitor was re-ramped to 18V to ensure that the leakage current remained low. Only those capacitors which passed this test were subjected to the breakdown study.

Resistivity of the DLC was calculated from the 6V dc leakage current (I) value obtained at the end of the voltage conditioning test based on the thickness (d) of the DLC and the area (A) of the capacitor using the equation $\rho = V A / I d$.

The breakdown test circuit consisted of the electrometer, a current limited dc power supply, a 1000 Ohm resistor and the capacitor. Each test sample was subjected to a slow voltage ramp with a hold at selected voltages of 1 minute duration after which dc leakage current measurements were made. Self-healing events were noted as they occurred during the test, but the ramp test was continued in each case until catastrophic breakdown or shorting (evidenced by a permanent runaway of the current) occurred. The timing and nature of the final breakdown event were also noted. All tests were performed at room temperature under ambient conditions. Dielectric strength was calculated for each sample using the relation Strength = V/d.

3. Results and Conclusions

Thirty test samples were subjected to the voltage conditioning process. Only 25 capacitors passed this acceptance test. Five samples failed because neither capacitance readings nor acceptable dc leakage current readings could be obtained for those devices with DLC films of thickness less than 0.4 µm even after the "clearing" procedure had been attempted to 18V.

Dielectric constants obtained ranged from 5.7-9.3. There was no discernible relationship between DLC thickness and dielectric constant. The average for all 25 samples was 6.8.

The resistivity of the DLC in the best test samples averaged 3.8×10^{13} Ohm-cm. The average over all samples was 8×10^{12} Ohm-cm. The thicker films generally exhibited a slightly lower dc leakage current and, therefore, a slightly higher resistivity.

The highest dielectric strength achieved for any sample was 1.6×10^6 V/cm. The range was 1.8×10^5 to 1.6×10^6. The lower strengths of some samples are probably attributable to defects not removed during voltage conditioning.

During the ramp process, self-healing events occurred in every case at voltages lower than the final breakdown. Often these occurred during the hold period indicating that the local breakdowns were thermal in nature. In general the observable sparks due to the self-healing discharges were randomly located over the capacitor surface. In nearly all cases, catastrophic breakdown occurred after some time at the breakdown voltage and was confined to a local spot or a series of connected spots evidenced by large localized holes or tracking across the surface of the capacitor.

Figs. 1 and 2 show typical curves of dc leakage current v.s. voltage. Breakdown for these samples was 150V and 61V respectively. The cluster of high leakage current

values for sample 21 between 10V and 52V is an indication of the presence of some defect(s) cleared by a self-healing event at 52V.
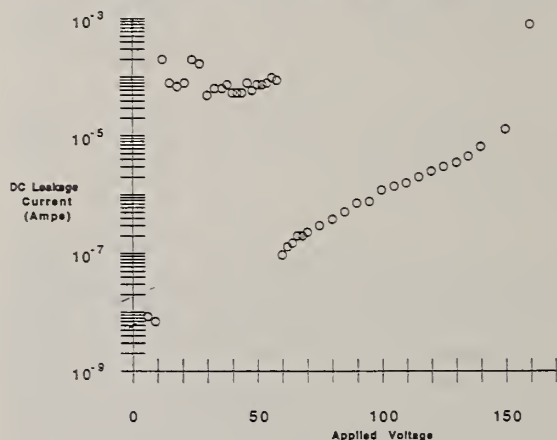
Fig. 1. Sample 21, DLC thickness = 1.26μm   Fig. 2. Sample 2, DLC thickness = 0.49 μm
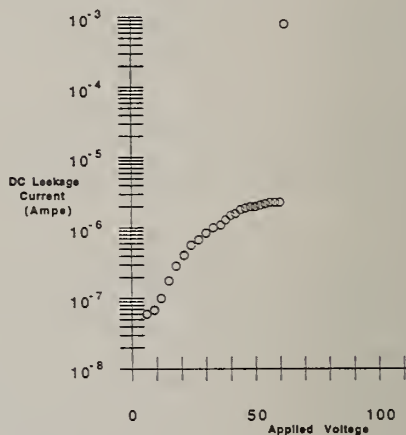
In summary, the DLC films studied exhibited 10^{13} Ohm-cm resistivity, dielectric constants higher than diamond, and dielectric strength of 10^6 V/cm. Breakdown of these DLC films had more of the characteristics of the thermal breakdown mechanism than of the intrinsic mechanism. The presence of defects in the films and the use of dc voltage precluded determination of the intrinsic dielectric strength. In future efforts we will study the pulse breakdown behavior of the DLC films, the structure and composition of this dielectric material and the role defects play in breakdown.

4. Acknowledgments

5. References

1. J.J. O'Dwyer, *The Theory of Dielectric Breakdown in Solids*, Oxford University Press (1964).
2. S. Whitehead, *Dielectric Breakdown of Solids*, Oxford University Press (1951).
3. N. Klein, J. Electrochem. Soc.: Solid State Physics, **116**, 7 (1969).

INFRARED REFLECTANCE AND TRANSMITTANCE OF
DIAMOND LIKE CARBON FILMS
AT NORMAL AS WELL AS GLANCING ANGLES OF INCIDENCE

D. Gupta   and   S.P.Varma

Infrared Radiation Standard Section, National Physical
Laboratory, Dr. K.S.Krishnan Road, New Delhi 110012,INDIA

glancing , infrared, normal, reflectance, transmittance

Abstract

Results of preliminary studies on measurements of specu-
lar reflectance (for angles of incidences: near normal to
60 degrees) and transmittance (for angles of incidences:
normal to 60 degrees) on DLC films on both surfaces
polished germanium as substrate in the spectral region of
400 to 4000 wavenumber are being discussed. The results
of specular reflectance and transmittance measurements
supplement each other and both are useful to characterize
DLC films.

1. Introduction

The hard hydrogenated amorphous carbon (a-C:H) films,
commonly now known as a diamond like carbon (DLC) film,
possesses a unique combination of useful properties [1].
These films are preferably used as an antireflection and
scratch protective coatings on germanium (Ge) and silicon
(Si), generally used for infrared optics.

The results of systematic measurements of specular re-
flectance at near normal incidence and at variable angle
of incidence of 10 to 60 on single as well as double
surface polished Si and Ge in the region of 400 to 4000
cm^{-1} were discussed in our earlier publications [2,3,4].
Recently, transmittance measurements were also carried
out on double surface polished Si and Ge at normal as
well as at variable angle of incidence of 10° to 60° in
this spectral region.

In order to extend the studies further, preliminary
measurements of these parameters were conducted on Ge and

Si blanks coated with DLC film on their both the sur-
faces.In this article, the details of the study and the
salient features of the results have been discussed with
the possibility of utilising these measurements at varia-
ble angle of incidence in the infrared region to charac-
terize these films for their quality and uniformity.

2. Experimental

For the present study DLC films were deposited on both
the surfaces of well polished (mirror like finish) Ge
following the methodology detailed in our earlier publi-
cation [1]. The spectral transmittance and spectral
specular reflectance measurements in the 400 - 4000 cm^{-1}
region were performed on a Perkin Elmer, model 399,
double beam, microprocessor controlled spectrophotometer
based on the optical null method. While the variable
angle specular reflectance measurements were performed on
a commercially available variable angle reflectance
accessory, the variable angle transmittance measurements
were performed on specially designed and custom built
accessory following the methodology discussed in our
earlier publications [2,3,4].

3. Results and Discussions

Although, the specular reflectance and transmittance
measurements at variable angle of incidence between 10° to
60° were performed on a number of DLC films deposited on
similar Ge blanks in different batches of preparation
keeping all the deposition parameters the same, the
results of these measurements on sample I only are shown
in Fig. 1 and Fig. 2 respectively. It is also evident
from Figs. 1,2 that results of specular reflectance and
transmittance are almost complementary to each other.

It is well known that the carbon atoms form bonds with
three different types of hybridization: tetrahedral sp^3 ,
trigonal sp^2 and linear sp^1 .While the vibrational fre-
quencies typical for tetrahedrally bonded carbon (sp^3)
bonding in hydrocarbon appear around 2900 cm^{-1}, the fre-
quencies typical for trigonal (sp^2) carbon bonding
appear around 3000 cm^{-1} . These frequencies corresponding-
ly show up in the transmittance/ specular reflectance
spectra of our study also. As a matter of fact, the peak
at 2900- 3000 cm^{-1} (Figs. 1,2) is the combined intensity
of (i) the characteristic absorption of carbon bonding in
hydrocarbon, and (ii) the minima/maxima of interference
in the DLC films. The peak around 1000 cm^{-1} has been,

naturally,tailor made to obtain the desired transmittance through the DLC film coated Ge blank.

The position of peak around 3000 cm^{-1} shows considerable shift due to variation in the angle of incidence whereas the shift in 1000 cm^{-1} peak is only marginal (Figs.1,2). Similar trend has been observed in the peak intensities of these two peaks also. The results obtained from reflectance spectral studies are found to be supplemented by those obtained from the transmittance spectral studies at variable angle of incidence (Figs. 1,2).

A plot (Fig. 3) of angle of incidence versus position of peak minima around 3000 cm^{-1} (curve A) predicts a linear relationship and indicates that a variation of 10 degrees in the angle of incidence shifts the peak position by 100 cm^{-1}. Fig. 3 also shows the relationship between reflectance values (intensities) at peak minima and the angle of incidence (curve B). Though, Fig. 3 pertains to the data of sample I (Fig.1) but the similar results have been derived for other samples also.

These are only the results of our preliminary studies on these samples and detail studies are in progress. As indicated in our earlier publications [2,3,4], these variations in reflectance/transmittance values with the angle of incidence will reveal the structure of the film. However, the variation in the absorption and the contribution due to interference both at various angle of incidence would be useful for characterization of quality and uniformity of DLC films.

Acknowledgements

References

1. P.N.Dixit, S.P. Varma, O.S. Panwar, T.Seth,D.Gupta and R. Bhattacharyya,Infrared Phys. Technol.35,617 (1994).
2. D. Gupta and S.P. Varma, Appl. Opt. 29,1872(1990).
3. D. Gupta and S.P. Varma,Infrared Phys.34,55 (1993)
4. D. Gupta and S.P. Varma, Metrologia 30, 433(1993).

Fig. 1

Fig. 2

Fig. 3
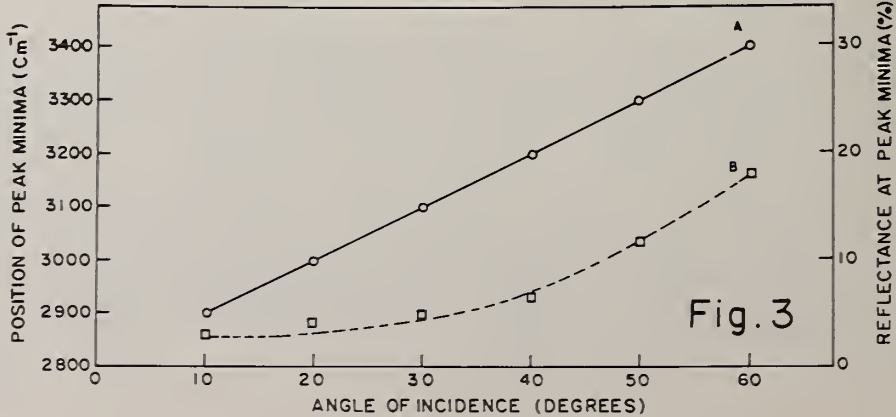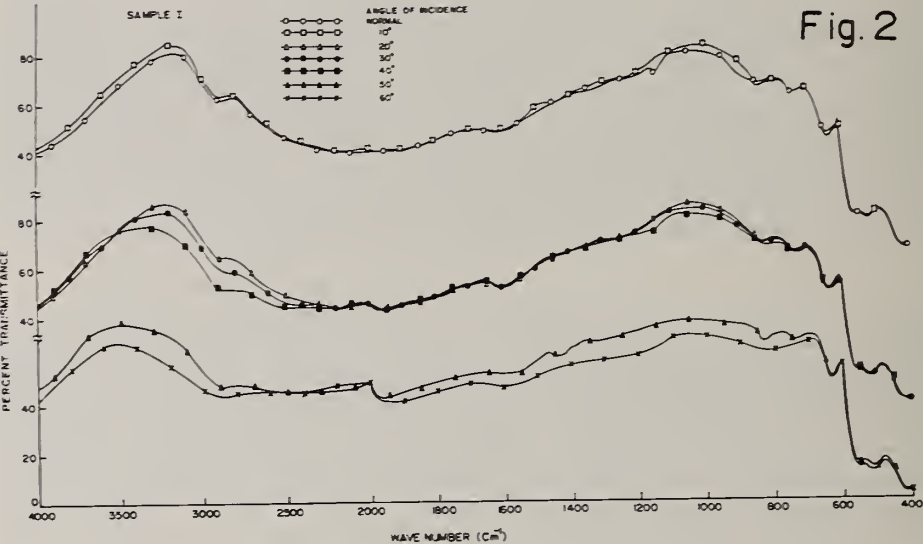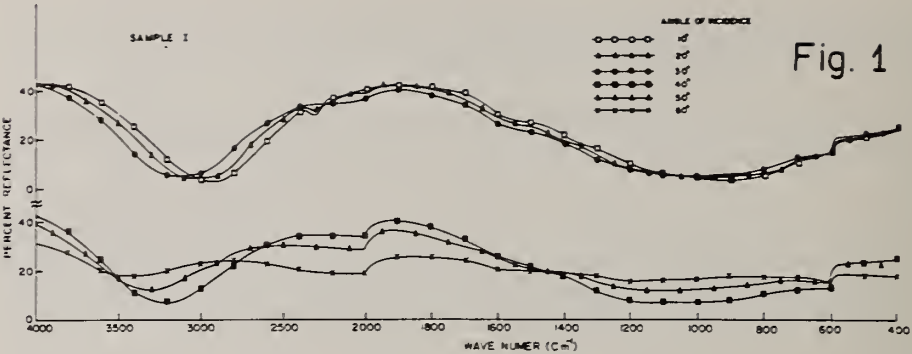
Diamond-Like Carbon Film on ZnSe
by AC-Sputtering and MPCVD Hybrid Method
for Infrared Window Applications

Vittaya Amornkitbamrung and Noppadon Suttisiri
Department of Physics, Faculty of Science, Khon Kaen University, Khon Kaen 40002,
Thailand

Key words: AC-Sputtering, DLC, infrared windows, MPCVD, zincselenide

Abstract

The diamond-like carbon films have been deposited on zincselenide by
hybrid method. In the first stage, the deposition was used by the dual graphite target
sputtering method, AC current 65-70 mA, voltage of 540-840 V in the pressure of 300
mTorr, high purified argon atmosphere, this process taking one hour. Secondly, chemical
vapor deposition (CVD) was performed using 500 W of microwave power at frequency
2450 MHz, in the mixed gas pressure about 2000 mTorr (Ar : 350 mTorr, H_2:1400 mTorr,
methanol vapour :250 mTorr) for times of 5, 15, 30, 45 hours. The samples were
examined by optical microscope (magnification 100 or 400 times) and by infrared
absorption (4000-200 cm^{-1}) which showed absorption peaks from C-H stretching mode
vibrations at 2860, 2880, 2920 and 2960 cm^{-1} . The adhesion test is using the tunsten tip
scratching on the DLC surface by spring load strength 122.9 gram in weight.

1. Introduction

Diamond windows are a natural for applications as leading optical elements
on missiles with exceptional resistance to rain and dust erosion. If we can directly a CVD
diamond film onto a ZnSe or ZnS infrared optic, fame and fortune await.
Direct deposition of CVD diamond on ZnSe or ZnS does not look
promising at this point. The basic problem is that the atomic hydrogen environment
necessary for diamond deposition eats up the ZnSe or ZnS quite rapidly.
In 1991, V. Amornkitbamrung and N. Suttisiri succeeded in deposition DLC
on various substrates by AC-sputtering [1]. In this work, we combined the AC-sputtering
and microwave plasma CVD of hydrogen+methanol into the hybrid method for coating
DLC on ZnSe windows to solve the etching problem of ZnSe in plasma.

2. Figures

The AC-sputtering and MPCVD hybrid system have been shown in Fig. 1. In the first step, the sputtering in argon atmosphere process was performed in the lower part for forming the carbide on ZnSe,may be zinccarbide.The next step, ZnSe substrate was transferred into the microwave chamber for the MPCVD of mixed gases; argon, hydrogen and methanol vapour.
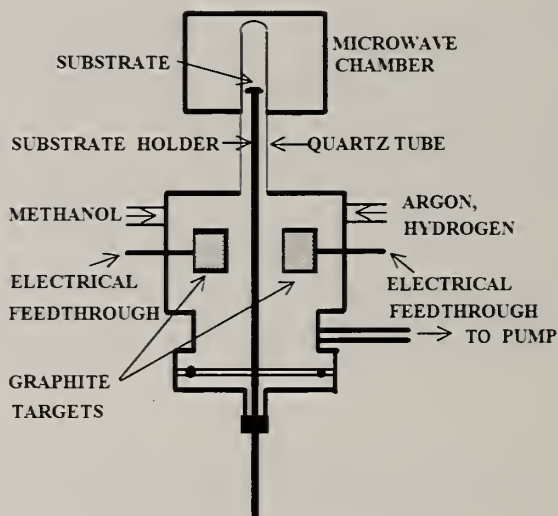
Fig. 1 AC-Sputtering and Microwave Plasma CVD Hybrid System.

The infrared absorption have been shown in Fig. 2, it showed absorption peaks from C-H streching mode vibrations at 2860, 2880, 2920 and 2960 cm^{-1}

Fig. 2 Infrared Absorption Spectroscopy for 1 Hour Sputtering and 30 Hours MPCVD.

The adhesion test by spring load strength 122.9 gram in weight was showed the crack surface as shown in Fig. 3.
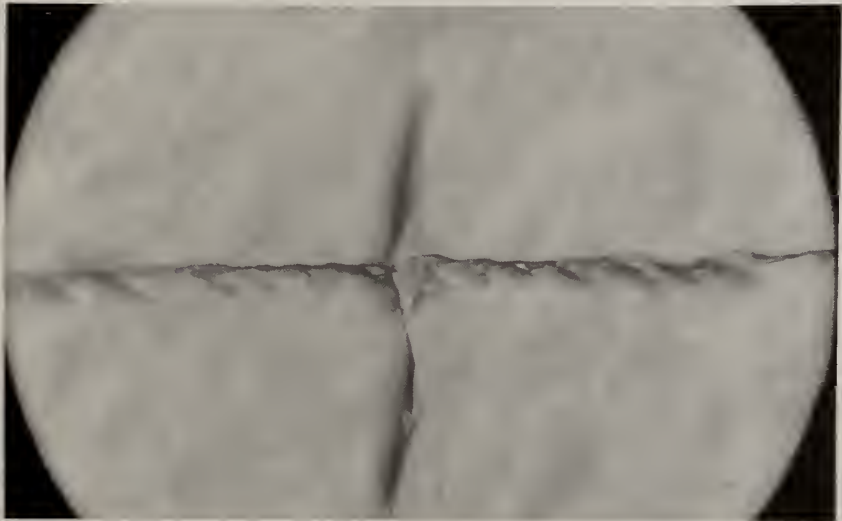
Fig. 3 Optical Microscopic Image 400X of The Same Sample for IR Absorption Test.

3. Reference

1. V. Amornkitbamrung and N. Suttisiri,"Formation of Diamond-Like Carbon Films by 50 Hz Sputtering from Dual Graphite Targets"; Surface and Coating Technology, vol.47,pp.533-537(1991).

STM AND PHOTOCONDUCTIVITY STUDIES OF a:DLC FILMS

I. Rusman[1], L. Klibanov[1], E. Ben-Jacob[2], and N. Croitoru[2]

Department of Physics and Astronomy, Department of Electrical Engineering and Physical Electronics, Tel-Aviv University, POB 39040, Ramat-Aviv 69978, Israel

Key words: a:DLC, graphite phase, photoconductivity, STM

Abstract

Scanning Tunneling Microscopy and Spectroscopy (STM and STS) were applied for obtaining nano scale information on morphological and electronic properties of Amorphous Diamond Like Carbon (a:DLC) and Indium Tin Oxide (ITO) films (usually used as contact material to a:DLC). The a:DLC films have shown smooth topographic relief; their electronic band gap is estimated as of about 1 eV. I-V characterization of the ITO grown on the a:DLC has revealed nano-clusters of non-degenerate semiconductor within the matrix of degenerate semiconductor. It is presumed that I-V characterization of the ITO/a:DLC can yield the map of the graphite-like clusters' location over the a:DLC surface. It is assumed also that the graphite phase is responsible for the high recombination rate of photocarriers in a:DLC, reducing mobility-lifetime ($\mu\tau$) product value.

1. Introduction

Usually amorphous Diamond Like Carbon (a:DLC) consists of sp^3-bonded (diamond-like) matrix around sp^2-bonded (graphite-like) clusters [1]. The relative fraction of such clusters determines the optical and electrical properties of the a:DLC. For this reason it is crucial to develop a reliable method to examine the a:DLC film for presence of the graphite phase.

STM analyses provide accurate nano-scale topographic images and I-V curves of a:DLC due to its high inertness. Atomically resolved images of locally ordered areas were obtained in [2,3,4,5,6-10]. I-V characterization on DLC was performed in [4].

Here we present an additional approach to graphite-like clusters' mapping. We describe the STM experiments with a:DLC/metallic layer, ITO/a:DLC, ITO/graphite, ITO/Corning glass and discuss some qualitative aspects of our observations.

Recently, photoconductivity in a:C films was investigated [11]. We present results of our measurements of the photoconductivity in the a:DLC films prepared by rf plasma decomposition of methane CH$_4$ [12].

2. Experimental results and discussion

<u>a:DLC/metallic layer</u>. Reproducible STM images were obtained on the 150 Å a:DLC/metallic layer, using sample voltage of 2.0 V with demanded tunneling current of about 1 nA. Large flat regions were observed with nano-scale features (Fig. 1). Atomic resolution was not observed. We assume that this is reasonable result, because the probability to observe a basal plane of the graphite-like inclusions is rather low. The identification of the graphite-like inclusions with other orientations and, moreover, distorted is complicated. Fig. 2 shows typical I-V curve using STS for a sample voltage of 1 V and a demanded current of 0.5 nA. This I-V was selected out of a large set of I-V that were taken for a series of demanded currents, corresponding to I-V taken with different tip-sample separations (analogous experimental procedure was performed for all I-V characterizations described below). The set of I-V has shown similar features. Qualitatively, the electronic gap between band tails can be estimated as of about 1 eV. I-V curves without gap were not observed.

<u>ITO/a:DLC/C.g., ITO/a:DLC/Si(100), ITO/C.g., and ITO/Si(100)</u>. Images obtained on the 750 Å ITO films, grown on the different substrates, have shown considerable differences between their topographic features. In particular, ITO/a:DLC/C.g. has demonstrated much stronger roughness than ITO/a:DLC/Si. We assume that there is some correlation between 3000 Å a:DLC film quality and the roughness of the ITO overlayer. This assumption is in agree with our experience of growing a:DLC on the Si and Corning glass. a:DLC films deposited on the Si exhibit the best quality.

Fig. 3 shows I-V obtained on ITO/a:DLC/C.g. for a sample voltage of 10 mV and a demanded current of 0.5 nA. Fig. 3(a) shows I-V with metallic behavior typical for a degenerate semiconductor. The metallic I-V were obtained over about 80 % of the analyzed surface. However, I-V with gap of up to about 3 eV (Fig. 3(b)) typical for a non-degenerate semiconductor were obtained over about 20 % of the analyzed surface. On the ITO/a:DLC/Si(100) I-V with gap were observed over about 10 % of the analyzed surface. On the ITO/C.g. and ITO/Si I-V with gap were observed over less than 1 % of the analyzed surface.

<u>ITO/graphite</u>. Fig. 4 shows typical I-V for the ITO film grown on pyrolytic graphite. We have used graphite substrates with two preferential orientations: parallel and perpendicular to basal plane. In the latter case we have observed the disappearance of the degeneration in the ITO overlayer much more frequently.

<u>Photoconductivity</u>. Fig. 5 shows the current vs temperature in the a:DLC for the bias of 5V under the dark and light conditions. The Au/a:DLC/Al device was exposed to an incident He-Ne laser light of 80 mW/cm^2 power at a temperature in the range of 20^{0}C÷-130^{0}C. Measured photocurrent was of about two orders of magnitude

higher than the dark current in the range of $-120^\circ C \div -130^\circ C$. This behavior of the photocurrent with temperature is typical for amorphous materials [13].

As expected, the measured photocurrent was proportional to G^γ, where G is a volume generation of carries and γ is a constant. For the a:DLC thin films we have obtained $\gamma=0.8$. This value of γ corresponds to high density of states (DOS) in the band gap [13]. A major effect of high DOS in the band gap is to make the observed decay time τ of photocurrent, after the excitation has ceased, longer than the carrier lifetime. Our measurements of τ after rectangular pulse of light have given values of 10^{-3} sec, whereas lifetime in amorphous semiconductors is of about 10^{-9} sec [13].
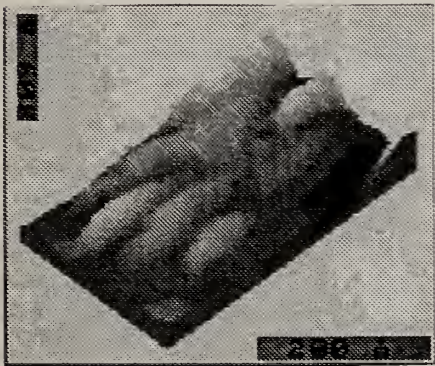
Fig. 1. Nano-scale feature observed on 150 Å a:DLC film. The image extend over lateral area of about $225*360\text{Å}^2$.
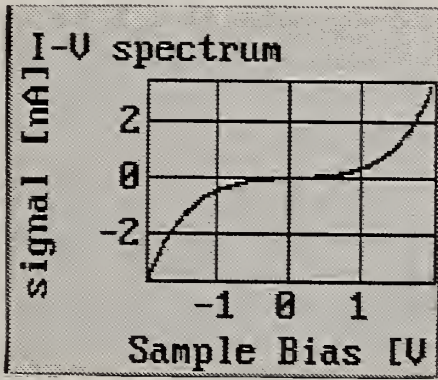
Fig. 2. Typical I-V curve with electronic band gap obtained for a:DLC. Sample voltage $-2V<V_s<2V$.
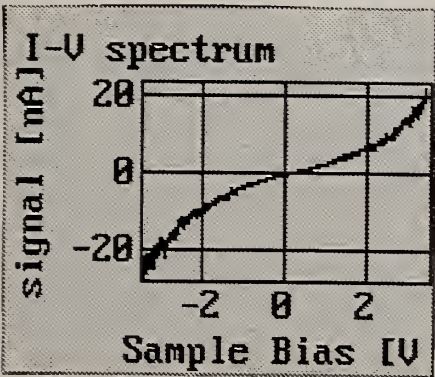
Fig. 3(a). I-V curve with metallic behavior obtained for ITO/a:DLC film. Sample voltage $-3.5V<V_s<3.5V$.
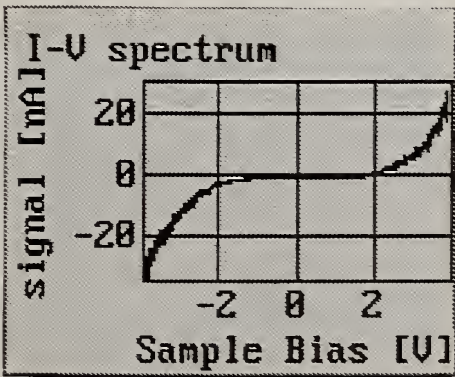
Fig. 3(b). I-V curve with band gap obtained for ITO/a:DLC film. Sample voltage $-4V<V_s<4V$.
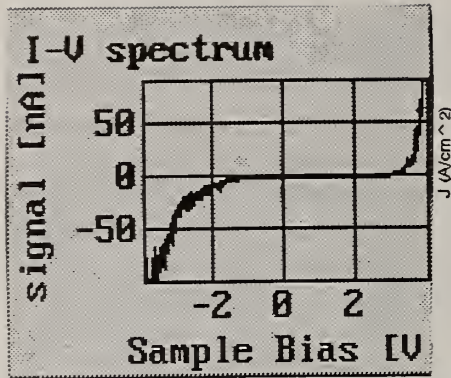
Fig. 4. I-V curve of ITO/graphite. Sample voltage $-4V<V_s<4V$.
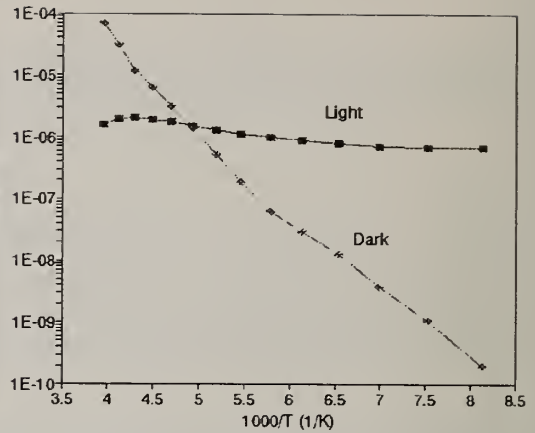
Fig. 5. Photocurrent and dark current versus temperature for a:DLC film.

3. Conclusions

We have obtained I-V data on the ITO/a:DLC, which have demonstrated existence of nano-clusters of non-degenerate semiconductor within the matrix of degenerate semiconductor. Our I-V data, obtained on the ITO/graphite, have shown that poorly ordered graphite can cause growth of the ITO as a non degenerate semiconductor. We presume that it is graphite phase on the a:DLC surface that leads to the local disappearance of the degeneration of the ITO/a:DLC. We suggest, furthermore, that improvement of the photoconductivity in the a:DLC films can be obtained by the reducing of relative fraction of the graphite phase.

4. References

1. C. Jager, J.J. Titman, and R.J. Newport, *Thin Solid Films*, 227 (1993) 3.
2. B. Marchon *et al*, *IEEE Transactions on Magnetics*, **27** (6) (1991) 5067.
3. S. Bhargava *et al*, *Solid State Com.*, **90** (3) (1994) 205.
4. L. Vazquez *et al*, *J. Vac. Sci. Technol. B*, **10** (2) (1992) 566.
5. J.A. Martin *et al*, *Appl. Phys. Lett.*, **57** (17) (1990) 1742.
6. R. Hiesgen, L. Eng, and D. Meissner, *Proc. of the Third International Symposium on Diamond Materials*, **93** (17) (1993) 654.
7. G.J. Vandentop *et al*, *J. Vac. Sci. Technol. A*, **9** (4) (1991) 2273.
8. B. Marchon, M. Salmeron, and W. Siekhaus, *Phys. Rev. B*, **39** (7) (1989) 12907.
9. S. Ferrer *et al*, *Surf. Sci.*, 251/252 (1991) 960.
10. N.H. Cho *et al*, *J. Appl. Phys.*, **71** (5) (1992) 2243.
11. D. McKenzie *et al*, *J. Non-Cryst. Solids*, 164-166 (1993) 1101.
12. L. Klibanov, M. Alaluf, S. Velkin, I. Rusman, and N. Croitoru, *Proc. of the 7th Israel Materials Engineering Conference*, November 1994, Haifa, Israel.
13. A. Madam, M. Shaw, *The Physics and Application of Amorphous Semiconductors*, Academic Press, London (1988).

801

Detection of Graphite-Like Clusters in DLC by Intercalation of Copper

V.I.Ivanov-Omskii and G.S.Frolova

A.F.Ioffe Physical-Technical Inst., St. Petersburg, 194021, Russia

Key words: annealing, cluster, copper, DLC, graphite, intercalation

Abstract

We report on a study of copper-induced IR absorption bands associated with intercalation of copper into graphite-like clusters (GLC) in DLC. A collection of spectral data is presented to illustrate the phenomenology of the copper-carbon interaction. Thermal annealing in vacuum reduces initially the intensity of the copper-born bands, which then exhibits a tendency for the starting value to be restored at room temperature if the copper concentration does not exceed 15%. The changes are reversible to a lesser extent at higher annealing temperatures and concentrations of copper.

1. Introduction

The much used cluster model of DLC is based on the assumption that carbon atoms in the sp2 and sp3 sites grouped into sp2-bonded graphite-like clusters (GLC) embedded in a sp3-bonded matrix [1]. However, various estimations of the degree of sp2 clustering are still contradicting. A study of the interaction of non-carbide-forming metals with GLC seems to offer an additional approach to the detection of GLC. It has recently been shown that incorporation of copper into DLC activates in the optical absorption the otherwise silent vibrational modes of the GLC carbon skeleton, labeled G (1580 icm) and D (1355 icm) which are well-known to be only Raman-active in copper-free DLC [2]. This suggests that copper intercalates into GLC, reducing the symmetry of carbon skeleton vibrations and making them IR active. Thus, IR absorption measurements permit detection of copper-intercalated GLC .

2. Experimental results

DLC films were produced by magnetron co-sputtering of graphite and copper targets in argon-hydrogen plasma onto silicon and KBr substrates. The pressure was held within 0.1 - 1.0 mTorr range during the film growth. The magnetron power was controlled in the range 0.4 to 0.5 kW. It was possible to produce 0.5 to 1.5 μm thick

films. The IR transmission was measured at room temperature as a function of copper concentration x (0<x<40%) within the vibration frequency range (1000 - 4000 icm). We failed to find any spectral evidence of the existence of copper-carbon bonds. This result correlates well with the fact that copper is not a carbide-forming metal. However, the copper-carbon interaction manifests itself in the activation of vibrational modes of the GLC carbon skeleton, which are otherwise silent in the optical absorption [2]. This is illustrated in Fig.1, where fragments of IR transmission spectra of copper-free and copper doped DLC films are presented the frequency region in question. It is apparent that copper excites absorption bands which are practically invisible in copper-free DLC. With increasing copper concentration, the intensity of the copper-induced IR bands first increases and then saturates at about 15 % [2]. This behavior has been observed for the set of samples with a proportion of sp2 sites about 60 % [2]. The saturation is assumed to correspond to the full occupation of sites available for intercalation. Suppression of the GLC phase by reducing the gas pressure during the film growth increases the film hardness and diminishes the intensity of copper-born bands. The latter effect is illustrated in Fig.2 and attributed to a rise of the sp3 to sp2 sites ratio as would be expected from the subplantation model of DLC growth [3] if one takes into account an enhancement of carbon atoms velocity with reducing pressure. The IR absorption of samples annealed at various temperatures in a vacuum 0.1 mTorr was measured in an effort to examine the interaction of copper intercalant with GLC. Figure 3 shows the intensity of copper-born band G as a function of the duration of isothermal annealing. By assuming that the intensity is proportional to the number of copper atoms intercalated into GLC, the equilibration time is found to be rather fast for intercalation at the annealing temperatures, being well within one hour. The temperatures at which the absorption under discussion disappears are approximately between 280 and 350 K, which corresponds to the values expected for the actual binding energy. The thermal stability of the intercalated copper states decreases with copper content. increasing Figure 4 displays the G band absorption as a function of temperature of isochronous anneal immediately after the treatment and 15 days later. A well pronounced tendency for restoration of the initial level of intercalation is clearly observed at room temperature. This is indicative of the proximity of the reservoir of removed copper to the intercalant sites. In any case the intercalation of copper into GLC appears as a fairly reversible process. The room-temperature relaxation of G band absorption of the 9 % Cu sample is shown in the insert on the left under side of Fig.4. The solid line represents exponential decay with a time constant of the order of 70 hours. At higher annealing temperatures and copper concentrations the observed phenomena lose their reversibility.

3. Acknowledgments

4. References

1. J.Robertson, 1986, Adv.Phys. 35, 317
2. V.I.Ivanov-Omskii and G.S.Frolova, 1995, Tech.Phys.40 (in press)
3. J.Robertson, 1993, Phil.Trans.R.Soc.Lond.A, 342, 277

5. Figure captions

Fig.1. Fragments of transmission spectra of DLC in a vicinity of the G and D bands for the various copper concentrations: 1 - 0%; 2 - 3%; 3 - 15%; 4 - 24%.

Fig.2. Fragments of transmission spectra of DLC in a vicinity of the G and D bands for the two different growth pressures: 1 - 1 mTorr; 2 - 6 mTorr.

Fig.3. The intensity of G band of DLC: Cu after the isothermal anneal for 9% of Cu at: 1 - T=500K; 2 - T=550K; 3 - T=620K; 4 - for 14% Cu at 500K.

Fig.4. The intensity of G band of DLC: Cu after the isochronal anneal for 9% Cu during 1 hour: 1 - after 1 hour; 2 - after 15 days.

The insert: room-temperature relaxation of the intensity.

Fig.1

Fig.2

Fig.3

Fig.4

Applications of Diamond Films and Related Materials: Third International Conference, 1995
Editors: A. Feldman, Y. Tzeng, W. A. Yarbrough, M. Yoshikawa, and M. Murakawa

805
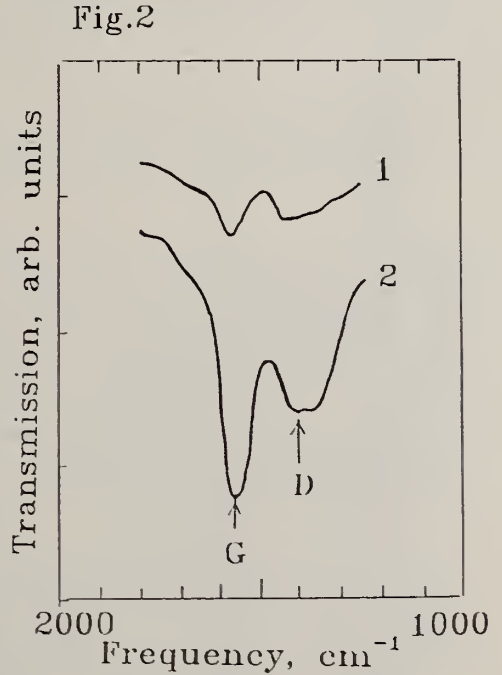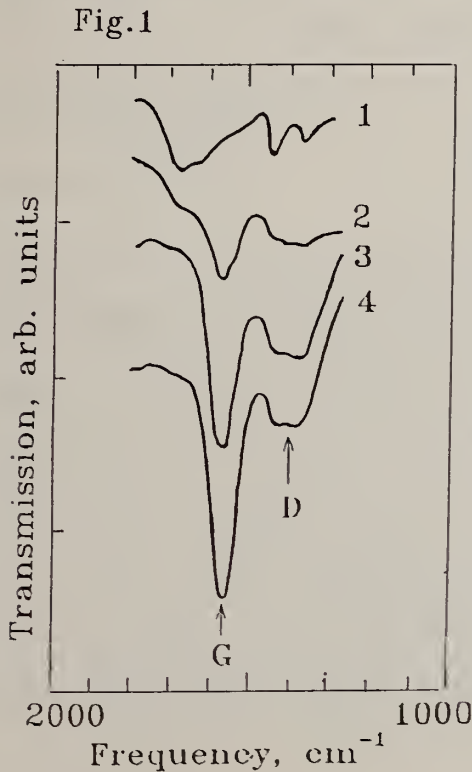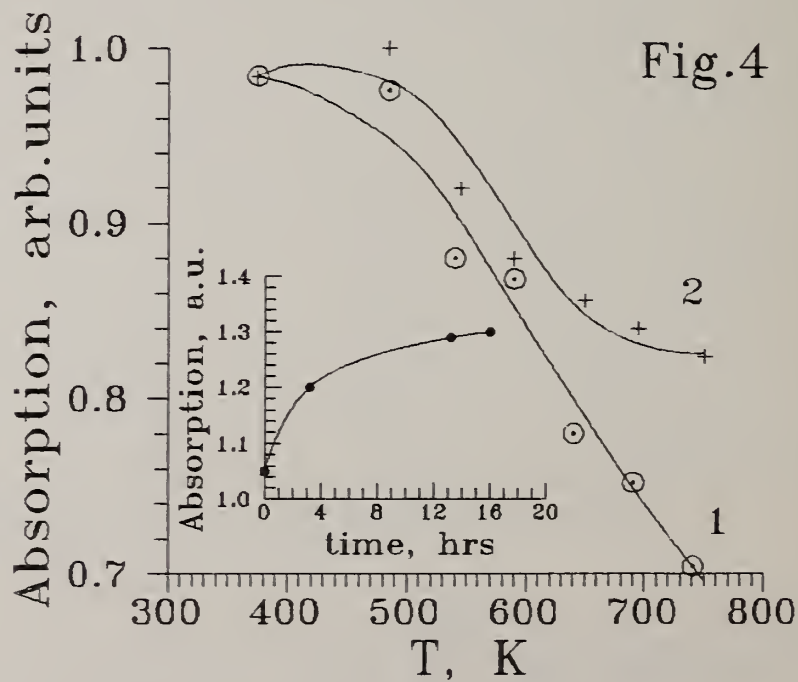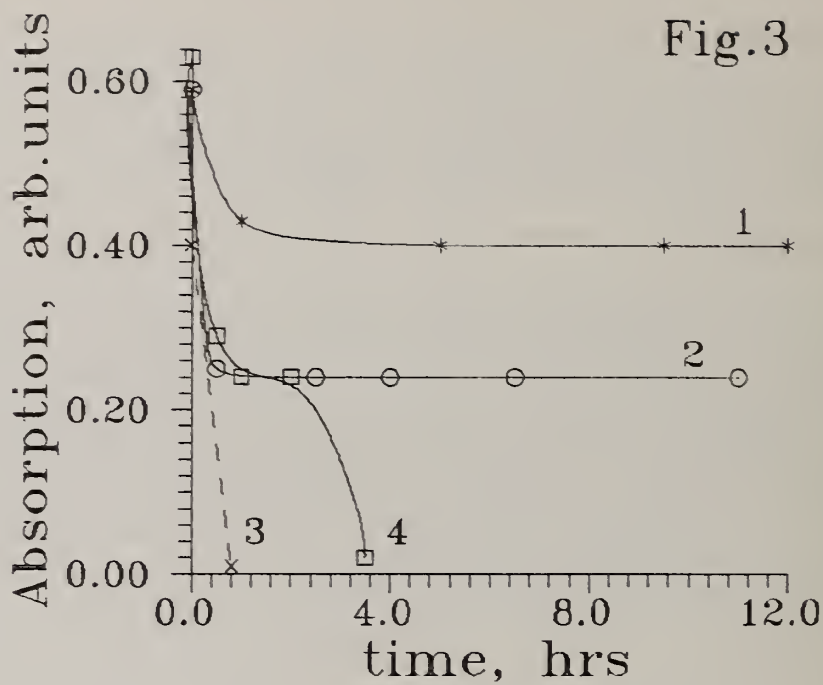
Characteristics of Si-containing diamond-like carbon film deposited at low temperature

Weng-Jin Wu and Min-Hsiung Hon

Department of Materials Science and Engineering MAT32, National Cheng Kung University, Tainan, Taiwan 70101

Abstract

Si-containing diamond-like carbon film was deposited by rf plasma CVD at 300 °C with gases of CH_4, Ar and SiH_4. The coatings were characterized using Raman spectroscopy, scanning electron microscopy (SEM), X-ray photoelectron spectroscopy (XPS), and micro Vickers indentor. The smooth coatings the C/C+Si above 78 at.% and the knoop hardness $1500kg/mm^2$ measured with a load of 50gf were obtained.

Key words: DLC, Raman, XPS

1. INTRODUCTION

Diamond-like carbon (DLC) films are promising hard coatings because they exhibit high hardness, chemical inertness and a low coefficient of friction. However, their internal stress and poor adhesion on many substrates limit their practical applications. To improve these problems other elements such as Ti, Ta and W was introduced in the coatings to form so called Me-C:H [1-2]. It has been reported by several authors [3-5] that the addition of a small mount of silicon to DLC will improve the adhesion and other properties such as friction coefficient.

Although the studies proposed that the silicon-containing diamond-like carbon coatings has excellent properties the deposition temperature in some processes was higher than 500 °C [5]. In this study a low temperature (under 300 °C) process developed and the growth behavior and the structure in the coatings were discussed.

2. EXPERIMENTAL

The Si-containing diamond like carbon film was deposited using a parallel-plate, capacitively coupled 13.56 MHz r.f. plasma system. Electrodes of 8 cm spacing with the grounded gas distributor were used for deposition. The feed gases consisting of CH_4, SiH_4 and Ar were introduced into the system in which the gas flow was measured by mass flow controllers and the reaction pressure was moinitored by a capacitance manometer. The substrates of silicon wafer and Corning 7059 glass were placed on a charged, negatively self-biased internal electrode for deposition and allowed the positive ion bombardment to take place on the substrate surface during the film growth.The parameters of the experiment were as follows: substrate temperature: 50-300°C, CH_4 flow rate: 17 sccm, SiH_4 flow rate: 0-2.5 sccm, Ar flow rate: 20 sccm.

The growth rate was determined by α -step surface profile measurement system. Film composition and structure were analyzed by Raman spectroscopy and XPS respectively. Surface morphology was observed by SEM. The hardness was measured by Vickers with a load of 50 gf on the coatings about 1.2 um thick deposited on Si(100).

3. RESULTS AND DISCUSSION

Film growth rate shown in Fig.1(a) indicates a negative dependence on temperature. It is similar to the report of a-SiC:H deposition [6], which is a result of the plasma polymerization process with different reaction rate constant at different deposition temperature as indicated by Yasuda [7]. With the increasing of silane flow rate, the growth rate of the coatings increases due to the increasing of introduced silicon in the coatings .

Fig.2 shows that the carbon content decreases from C/C+Si=90at.% to 78at.% as silane flow rate increases from 0.5 sccm to 2.5 sccm.

As the silicon content was increased in the coating, SiC phonon vibration frequency at 770-790 cm^{-1} [8] is still not detected from Raman spectrum but the characteristics of diamond-like peak at 1540 ± 20 cm^{-1} [8,9] is observed, as shown in Fig.3. It is shown that a slight increase in silane flow rate will reduce the graphite content in the coatings in Fig.4 because the disorder broaden peak at 1580cm^{-1} disappears, the peak at

$1350cm^{-1}$ is weakened whereas the diamond-like carbon phase becomes the main structure in the coatings.

For the hardness of the coatings only 1500 kg/mm^2 was obtained with a load of 50gf on the coatings about 1.2um due to the soft Si substrate. The actual hardness of the coatings should be higher.

4. CONCULSIONS

The growth behavior of Si-containing diamond-like carbon film depending on substrate temperature and silane flow rate is discussed. SiC phonon vibration frequency is not observed in Raman spectrum for the coating and the characteristics of diamond-like carbon phase in the coatings is obvious. Slight increase in silicon content will decrease graphite content in the coatings.

5. ACKNOWLEDGMENTS

6.REFERENCES

1. H. Dimigen, H. Hubsch and R. Memming, Appl. Phys. Lett. 50, 1056, (1987)

2.M. Wang, K. Shmidt snd K. Reichelt, J. Mater. Res. V7, No.6, (1992) 1465

3.K. Oguri and T. Arai, Surf. Coat. Technol., 47 (1991) 710

4.J. Meneve, E. Dekempeneer, R. Jacobs and J. Smeets, Diamond Relat. Mater., 1 (1992) 553

5.K. Oguri and T. Arai, J. Mater. Res. V5, No.11, (1990) 2567

6. J.L.He, L.C.Chang and M.H.Hon, 2nd International Conference on the Applications of Diamond Films and Related Materials, Japan, August 25-27, (1993) 413

7.H. Yasuda: Plasma Polymerization (Academic Press, Inc., New York, 1985) 198

8.P. V. Huong, Diamond Relat. Mater. 1 (1991) 33

9.P. V. Huong, J. Molecul. Struct. 292 (1993) 81
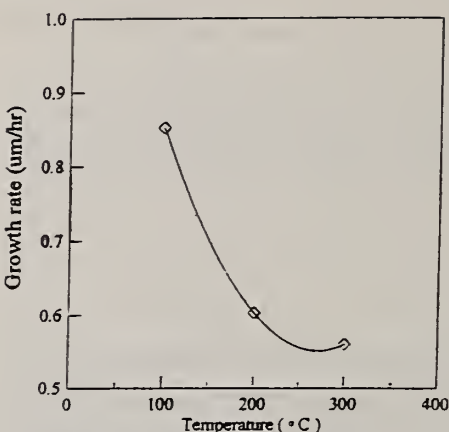
Fig. 1   Dependence of Si containing DLC deposition rate on substrate temperature.
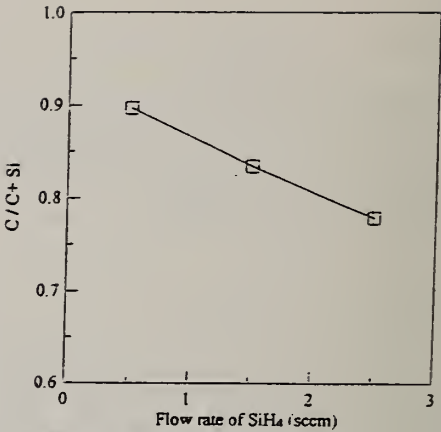
Fig. 2 Dependence of Si containing DLC composition (at.%) on SiH₄ flow rate.
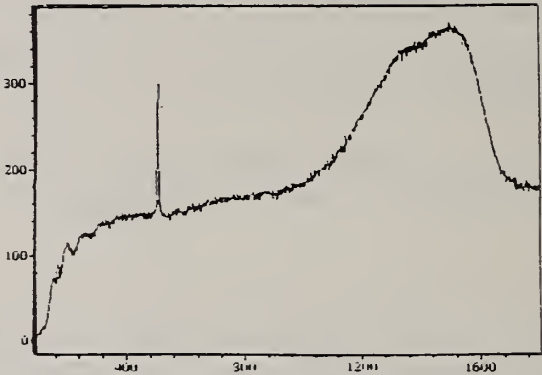
Fig. 3 Raman shift of Si-containing DLC.
SiH₄=1.5 sccm, Ts=260°C
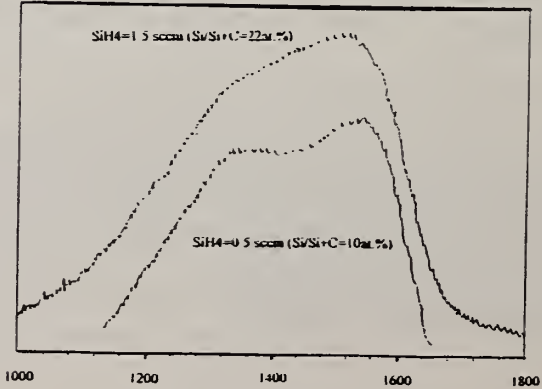
Fig. 4 Raman shift of Si-containing DLC.
Ts=260°C

Applications of Diamond Films and Related Materials: Third International Conference, 1995
Editors: A. Feldman, Y. Tzeng, W. A. Yarbrough, M. Yoshikawa, and M. Murakawa

809

PROPERTIES OF VACUUM ARC DEPOSITED AMORPHOUS HARD CARBON FILMS

Simone Anders[1], André Anders[1], C. Singh Bhatia[2], Sébastien Raoux[1],
Dieter Schneider[3], Joel W. Ager III[1], and Ian G. Brown[1]

[1]Lawrence Berkeley Laboratory, University of California, Berkeley, CA 94720
[2]SSD/IBM, 5600 Cottle Road, San Jose, CA 95193
[3]Fraunhofer-Institut für Werkstoffphysik und Schichttechnologie,
  Helmholtzstr. 20, D-01171 Dresden, Germany

Key words: Cathodic arc deposition, amorphous hard carbon, elastic modulus, optical gap

Abstract

Amorphous hard carbon films formed by vacuum arc deposition are hydrogen-free, dense, and very hard. The properties of amorphous hard carbon films depend strongly on the energy of the incident ions. A technique which is called Plasma Immersion Ion Implantation can be applied to vacuum arc deposition of amorphous hard carbon films to influence the ion energy. We have studied the influence of the ion energy on the elastic modulus determined by an ultrasonic method, and have measured the optical gap for films with the highest sp^3 content we have obtained so far with this deposition technique. The results show an elastic modulus close to that of diamond, and an optical gap of 2.1 eV which is much greater than for amorphous hard carbon films deposited by other techniques.

1. Introduction

Vacuum arc deposition is an efficient and clean method for forming amorphous hard carbon films [1-4]. If a graphite cathode is used in a vacuum arc plasma source a fully ionized carbon plasma is produced with a kinetic energy of the ions of about 20 eV. When the plasma condenses on a substrate an amorphous hard carbon film is formed. It has been found that the properties of amorphous hard carbon films depend strongly on the energy of the incident ions [1, 4, 5-7]. A technique called Plasma Immersion Ion Implantation can be applied to vacuum arc deposition to tailor the film and interface properties [8, 9]. In this method the substrate is immersed in a plasma (a carbon plasma in this case) and a pulsed negative bias is applied to the substrate. An electric sheath is formed during the bias pulse and ions from the plasma are accelerated toward the substrate. The ion energy is given by the applied voltage and the ion charge state which is one for a cathodic arc produced carbon plasma. During the bias pulses ions are implanted into the substrate whereas between the pulses low-energy deposition takes place. In the early stage of the film deposition intermixing occurs between the substrate and the newly formed film. This leads to excellent interface properties regarding

adhesion. In the later stage of the deposition the film itself is bombarded by the ions which modifies the film. In earlier investigations we have measured film properties such as hardness and elastic modulus [5, 12, 13], mass density [5, 12], coefficient of friction [5], stress [7], Raman spectra [5, 7], sp^3 content [12], and structure [12]. In this paper we describe measurements of the optical properties by ellipsometry and of the elastic modulus using an ultrasonic technique.

2. Deposition

A cathodic arc plasma source with macroparticle filter was used to deposit amorphous hard carbon films on silicon substrates [10, 11]. The graphite cathode of 6 mm diameter was surrounded by a cylindrical anode. The discharge current was 300 A, the duration 5 ms, and the repetition rate 1 Hz. A negative pulsed bias voltage in the range of 0 to - 2000 V was applied to the substrate during immersion in the plasma. The bias pulses had a duration of 2 μs and the pulse off-time was 6 μs. The Si (100) substrates were mounted on a water-cooled holder to keep them at room temperature during the deposition. The base pressure was 10^{-4} Pa.

3. Elastic modulus

The elastic modulus was determined by an ultrasonic surface wave technique [14-16]. In this method surface wave pulses with a broad bandwidth are generated by a nitrogen pulse laser with a wavelength of 337 nm. The ultrasonic signal, which is influenced by the structure of the surface film, was measured by a piezoelectric transducer in the frequency range of 50-250 MHz. The surface wave phase velocity as a function of frequency was determined using a Fourier transform technique. To calculate the elastic modulus of the films the inverse problem of surface wave dispersion in coated materials was solved.

The elastic modulus was measured for a series of amorphous hard carbon films with thickness 100 nm. The films were deposited at various pulsed bias voltages in the range 0 to -2000 V. Fig. 1 shows the elastic modulus as a function of the bias voltage.
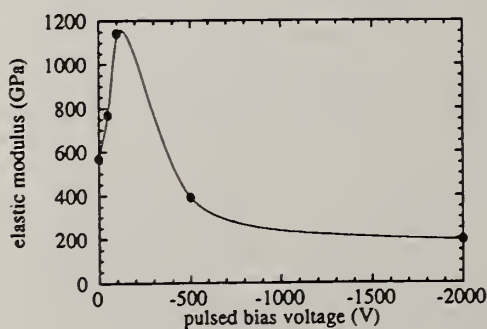
Fig. 1: Elastic modulus of amorphous hard carbon films as a function of the pulsed bias voltage applied during deposition.
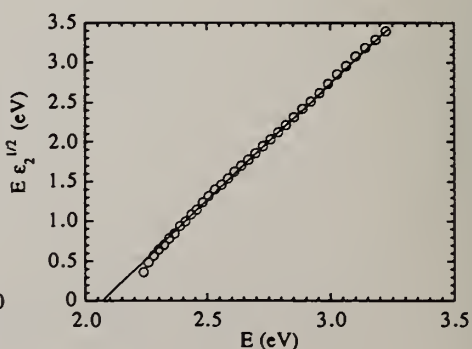
Fig. 2: The optical gap is the intersection with the x-axis of a plot of $E\,\varepsilon_2^{1/2}$ vs. the photon energy E.

4. Ellipsometry

For determining the optical properties of cathodic arc deposited amorphous hard carbon films, we used a spectroscopic ellipsometer. The ellipsometric experimental data $\Psi(hv)$ and $\Delta(hv)$ have been measured from 1.5 to 4.1 eV for a film deposited at a pulsed bias voltage of -100 V with a thickness of 80 nm on silicon. The measured parameters are defined as $\rho_p/\rho_s = \tan\Psi\exp(i\Delta)$, where ρ_p and ρ_s are the complex reflection coefficients for light polarized parallel and perpendicular to the plane of incidence, respectively. A model assuming three media (ambient/film/substrate) was used to analyze the data with the assumption of film properties interpolating between the properties of graphite and diamond. The best fit of the model to the experimentally determined data was obtained assuming a ratio of 90% diamond to 10% graphite in the film (with an accuracy of ±5%). From the optical constants $n(hv)$ and $k(hv)$ determined by ellipsometry where n and k are the real refractive index and the extinction coefficient we have calculated the dielectric constants $\varepsilon_1(hv)$ and $\varepsilon_2(hv)$ using $\varepsilon_1 = n^2 - k^2$ and $\varepsilon_2 = 2nk$. The optical gap was determined from

$$E\,\varepsilon_2^{1/2} = B(E - E_0)$$

which is based on the assumption that in amorphous semiconductors the density of states beyond the mobility edge has a square root dependence on energy, and that the centers of the valence and conduction band are parabolic [17, 18]. E is the photon energy, E_0 is the optical gap, and the constant B is proportional to the joint density of states. Fig. 2 shows $E\,\varepsilon_2^{1/2}$ as a function of the photon energy E. Following the analysis method described in [3] the optical gap was determined from this graph to be about about 2.1 eV.

5. Discussion and Conclusions

The elastic modulus determined by the ultrasonic method reaches the highest values for films deposited at - 100 V bias voltage. These results can be compared to the elastic modulus of diamond of about 1140 GPa [14]. This indicates a very high percentage of sp³ bonds in these films. It has been found that the hardness and the elastic modulus of amorphous hard carbon films are linearly related with a proportionality factor is of order 10 [16]. This also indicates a very high hardness of the films. A comparison to the elastic modulus of these films determined by nanoindentation [12, 13] shows that the data obtained by the ultrasonic method are about a factor of two larger. This might be due to the fact that nanoindentation measures the elastic modulus perpendicular to the films whereas the ultrasonic method determines the elastic modulus parallel to the film.

The optical gap determined by ellipsometry is much larger than for hydrogen-free amorphous hard carbon films deposited by other methods such as laser ablation or sputtering with typical values of 0.5 - 1.5 eV [19]. Only films deposited by cathodic arc deposition have been reported having an optical gap larger than 2 eV [3]. A large optical gap is also an indication of a high sp³ content (the optical gap of diamond is 5.5 eV).

The maximum of the elastic modulus at - 100 V bias is in agreement with all other measurements we have performed with different methods and for different

812

parameters, all showing the most "diamond-like" character of the films at this bias voltage.

Acknowledgments

References

1. D. R. McKenzie, D. Muller, B. A. Pailthorpe, Z. H. Wang, E. Kravtchinskaia, D. Segal, P. B. Lukins, P. J. Martin, G. Amaratunga, P. H. Gaskell, and A. Saeed, Diamond Relat. Mater. 1, 51 (1991).
2. I. I. Aksenov and V. E. Strel'nitskii, Surf. Coat. Technol. 47, 98 (1991).
3. R. Lossy, D. L. Pappas, R. A. Roy, J. J. Cuomo, and V. M. Sura, Appl. Phys. Lett. 61, 171 (1992).
4. P. J. Fallon, V. S. Veerasamy, C. A. Davis, J. Robertson, G. A. J. Amaratunga, W. I. Milne, and J. Koskinen, Phys. Rev. B 48, 4777 (1993).
5. S. Anders, A. Anders, I. G. Brown, B. Wei, K. Komvopoulos, J. W. Ager III, and K. M. Yu, Surf. Coat. Technol. 68/69, 388 (1994).
6. J. J. Cuomo, D. L. Pappas, J. Bruley, J. P. Doyle, and K. L. Saenger, J. Appl. Phys. 70, 1706 (1991).
7. J. W. Ager III, S. Anders, A. Anders, and I. G. Brown, Appl. Phys. Lett., to be published.
8. A. Anders, S. Anders, I. G. Brown, M. R. Dickinson, and R. A. MacGill, J. Vac. Sci. Technol. B 12, 815 (1994).
9. A. Anders, S. Anders, I. G. Brown, and I. C. Ivanov, Mat. Res. Soc. Symp. Proc. 316, 833 (1994).
10. S. Anders, A. Anders, and I. G. Brown, J. Appl. Phys. 74, 4239 (1993).
11. A. Anders, S. Anders, and I. G. Brown, Plasma Sources Sci. Technol. 4, 1 (1995).
12. G. M. Pharr, D. L. Callahan, S. D. McAdams, T. Y. Tsui, S. Anders, A. Anders, J. W. Ager III, and I. G. Brown, Appl. Phys. Lett., to be published.
13. S. Anders, A. Anders, J. W. Ager III, Z. Wang, G. M. Pharr, T. Y. Tsui, I. G. Brown, and C. S. Bhatia, Spring Meeting of the Materials Research Society, 1995, San Francisco, to be published.
14. D. Schneider, H.-J. Scheibe, Th. Schwarz, and P. Hess, Diamond Relat. Mater. 2, 1396 (1993).
15. D. Schneider, T. Schwarz, and B. Schultrich, Thin Solid Films 219, 92 (1992).
16. B. Schultrich, H.-J. Scheibe, G. Grandremy, D. Schneider, and P. Siemroth, Thin Solid Films 253, 125 (1994).
17. G. A. N. Connell, Amorphous Semiconductors, ed. by M. H. Brodsky, Topics in Applied Physics (Springer, Berlin, 1966), Vol. 36, p. 73.
18. J. Tauc, R. Grigorovic, and A. Vancu, Phys. Status Solidi 15, 627 (1966).
19. D. L. Pappas, K. L. Saenger, J. Bruley, W. Krakow, and J. J. Cuomo, J. Appl. Phys. 71, 5675 (1992).

PROPERTIES ANALYSIS OF DIAMOND LIKE THIN FILMS BY IN-SITU X-RAY DIFFRACTION.

Baranov A.M.[1], Sleptsov V.V.[1], Tereshin S.A.[1], Mikhailov I.F.[2], Pinegin V.I.[2]

[1]Institute of Vacuum Technique, 7 Nagorny Proezd, Moscow 113105, Russia.
[2]Kharkov Polytechnic University, 21 Frunze St., Kharkov 310002, Ukraine.

Key words: DLC, *in-situ* X-ray analysis, growth mechanism, density

Abstract

For the first time *in-situ* X-ray monitoring was applied for superthin DLC films investigation. The objects of *in-situ* investigations were DLC films obtained by RF-method on silicon substrates. The density, thickness and root-mean-square roughness of DLC films were controlled during the process of the film growth. The results of an investigation revealed that the roughness and density of DLC films were varied at the early stage. It was shown that obtained results can be explained by island mechanism of DLC films growth.

1. Introduction

DLC films have attracted considerable attention because of their potential utilization in electronics and soft x-ray optics [1-3]. It is important to note that for creation high quality structures necessary to have parameters control DLC layers during deposition process. However up to the present time the methods of *in situ* investigation of diamond-like layers properties have not been elaborated. In this report we presented results DLC films investigations by *in-situ* x-ray monitoring system.

2. Experimental details

The diamond-like carbon films have been deposited in RF plasma (13.56 MHz). The mixture of C_6H_{12} with Ar have been used as the working gas. The pressure in the chamber has been changed from 0.1 Torr up to 0.5 Torr.

The deposition has been carried out at the temperature at 300 K on the silicon wafers having the roughness of the surface 4 A .

The scheme of the vacuum system is shown in the Fig. 1. The X-ray beam has been introduced inside the vacuum chamber through beryllium window. The ray incidence angle with the silicon surface has been 1°. The experimental date of the reflected ray intensity have been subjected to the computer treatment directly in the process of deposition for the purpose of getting the dependence $V(t)$; $\rho(t)$ and $\sigma(t)$. The count rate was varied from 1000 photon/sec. to 2500 photon/sec. in depend on power of X-ray source.
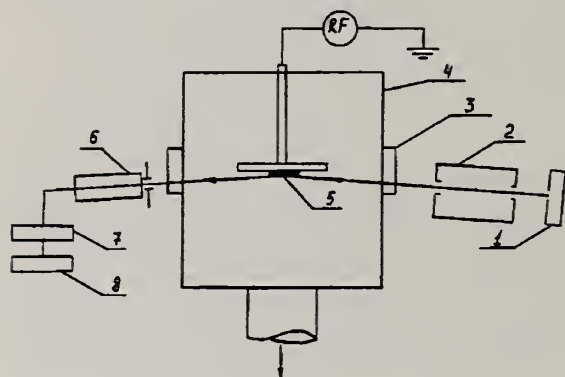
Fig.1. Schematic drawing of the deposition system with in situ monitoring.
1-x-ray tube; 2-collimating system; 3-Be-window; 4-vacuum chamber; 5-sample; 6-x-ray counter; 7-registration block; 8-computer.

3. Theory

In general case the equitation for reflected coefficient amplitude from the system film-substrate can be represented by:

$$r_{os} = \frac{r_{0f}D_f + r_{fs}D_s\,exp(-2id\chi)}{1 + r_{0f}r_{fs}D_sD_f\,exp(-2id\chi)} \qquad [1]$$

where r_{0f} and r_{fs} are the Fresnel coefficients; D_f and D_s -Debye-Waller factors taking into account the film surface and silicon wafers roughness [4], d- thickness, $\chi = (2\pi/\lambda)(\varepsilon - cos^2\theta)^{1/2}$.

During the experiment we use the grazing angles $\Theta \gg \Theta_c$, where $r_{fs}r_{0f} \ll 1$. Thus, for simplification of analytic consideration we use the asymptotic :

$$r_{ij} \approx |\varepsilon_i - \varepsilon_j|/4sin^2\Theta \qquad [2]$$
$$\varepsilon = 1 - \delta + \iota\gamma \qquad [3]$$

where δ-refraction decrement; γ-absorption coefficient.

For the diamond-like films it could be considered to be of $\gamma=0$. Thus the reflected ray intensity $R=|r_{0f}|^2$ is determined by film thickness (d), refraction decrement (δ_f) and root-mean squire roughness (σ). Then

$$R=1/16\sin^4\Theta\{\delta_s^2D_f^2+D_s^2(\delta_s-\delta_f)^2-2\delta_fD_fD_s(\delta_s-\delta_f)\cos2\chi d\} \quad [4]$$

Supposing δ_f and D_f slow varying function of thickness d, we consider them constant in the range L/2 (where L=44 A -period of oscillation) and write the expression for the average reflectivity $M^2=<R>/R_s$ and the contrast $K=(R_{max}-R_{min})/(R_{max}+R_{min})$. From this system we obtained that:

$$\delta_f = \delta_s(1-M/\sqrt{2}(1-\sqrt{1-K^2})^{1/2})$$
$$D_f = D_s\frac{M\delta_s}{\sqrt{2}\delta_f}(1+\sqrt{1-K^2})^{1/2} \quad [5]$$

4. Result and discuss

In Fig. 2 (curve 1) the dependence of the reflected ray intensity from the film deposition time is shown. The first minimum observation shows that the film refraction decrement $\delta_f < \delta_s$. In accordance with Bragg condition one could conclude that the total grown film thickness is about 70 A.
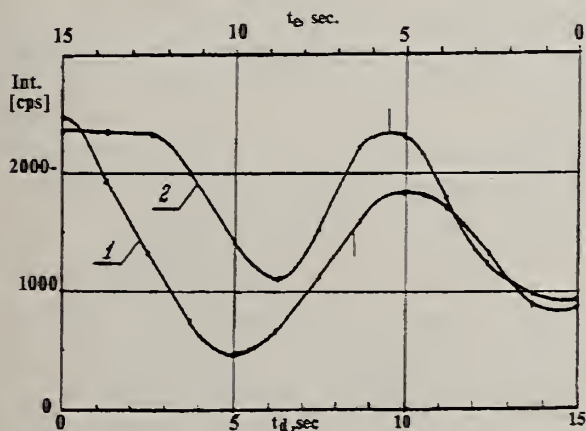
Fig.2. Time dependencies of spectral reflection intensity during deposition (1) and etching (2) of DLC film.

The dependence of intensity of the reflected beam from the system silicon - DLC film in the process of etching is shown in Fig. 2, curve 2. The etching has been carried out in RF discharge. Oxygen

has been used as working gas. It is obvious that the etching curve repeats curve in the process of deposition. However the deposited film etching is carried out more rapidly. Going out of the I (t) dependence to the constant value approximately equal to the ray intensity from the clean silicon wafer before the deposition process carrying out indicates that the etching process stoppage. The obtained σ_f, δ_f and V values during deposition and etching are presented in table 1. The film density is calculated using the equitation from ref. [4]. It is seen from table 1 that density and roughness increase steeply while thickness increase in the range 0-L/2. At late time values of σ_f and δ_f are essentially unchanged. On the contrary values of σ_f and δ_f are not varied during etching process and have had values corresponding ones in the range of thickness from L-3/2L during deposition process. That means that at the early stage of growth the DLC film grows by the island mechanism. However when the thickness exceeds 22 A the film becomes continuous. Therefore we have not seen varying of σ_f and δ_f values during all etching process.

Table 1.

	Deposition			Etching		
	V, A/sec	σ, A	ρ,g/cm^3	V, A/sec	σ, A	ρ,g/cm^3
0÷L/2	4.4	4	1.72	6.3	4	2
L/2÷L	4.4	6.1	1.9	6.3	4	2.0
L÷3/2L	4.7	5.9	2.05	4.4	4	1.98

5. Conclusion

The first we demonstrated a feasibility of the study of diamond-like film's growth kinetics by the use of *in-situ* X-ray monitoring. *In-situ* method has given us the opportunity to obtain the values of the growth rate, density and roughness as well as find out growth mechanism of DLC film in the beginning stage of film growth.

6. References

1.Polykov V.I.,et. al., Diamond and Related Mat., 1992, 1, 626-629.
2.K.K. Chan, S.R.P. Silva and G.A.J. Amaratunga, Thin Solid Films, 212 (1992) 232.
3.P.E. Kondrashov, I.S. Smirnov, V.V. Sleptsov, A.M. Baranov, V.M. Elinson, Diamond and Related Materials, 1995, v. 4, 109-112.
4. T. Barbee " Multilayer for x-ray optics", Opt.Eng., vol.25, No8, pp.898.

MULTILAYER INTERFERENCE STRUCTURES FOR X-RAY MIRRORS BASED ON CARBON FILMS .

P.E.Kondrashov[1], I.S.Smirnov[1], E.G. Novoselova[1], A.M. Baranov[2], V.V. Sleptsov[2].

[1]Inst. of Electronics and Mathematics, B.Vuzovskiy per.,3/12,Moscow, Russia.
[2]Institute of Vacuum Technique, 7 Nagorny Proezd, Moscow 113105, Russia.

Key words: DLC, multilayer structures, x-ray mirrors, carbon film

Abstract

The properties of diamond-like multilayer interference structures in x-ray range were investigated. The structures with periods upto 33 A were obtained by ion-plasma methods. The difference between experimental and theoretical results were discussed.

1. Introduction

The multilayer interference structure (MIS), which is an analog for multilayer mirrors of visible region is the most important X-ray optical element. At present the MISs having the layers of highly absorbing atoms of heavy metals (W, Re etc.), which alternate with the layers of light atoms (B, Be, C) have got the most spreading [1,2].

In this paper we investigate the potentiality of production of purely carbon MIS based on diamond-like films. The possibility of diamond-like layer production with various densities and with minor $\Delta\varepsilon$ permits to obtain the structure with high resolution; and slight absorption of carbon layers allows to attain the wanted value of reflection coefficient at the expense of increasing the number of periods. The main advantage of such MIS is the low absorption of carbon in X-ray range. All these facilities permits to create broad band mirrors for soft X-ray optics.

2. Experimental details

The carbon layers were obtained by DC magnetron sputtering of graphite target in argon (a-C) and by plasma-ion beam deposition in C_6H_{12} (a-C:H) from sources that mounted in vacuum chamber. The optical characteristics were tested on experimental multilayer structures consisting of upto 45 coupled layers of carbon with different properties. The numerical computations of

reflecting ability of multilayer carbon structures were carried out by recurrence relation which is based on the Fresnel equations [3,4]. The depositions have been carried out at the temperature at 300 K on the quartz wafers having the roughness of the surface 6 A. For the study of multilayer structures was used x-ray reflectometer with copper anode (λ=1.54 A).

3. Results and discussion

The experimental dependencies of the reflection coefficient versus the incidence angle (Θ) of the beam for some multilayer structures are presented at fig.1. The multilayer structures consist of 50 layers with equal thickness. The period of structures (d) varied from 33 A to 68 A according to Bragg condition $2d\sin(\Theta)=\lambda$. It is obvious that a decrease of period leads to decrease of Bragg reflection coefficient. It is a result of that the reflection coefficient from interface of layers decreases with angle as $R \sim 1/\sin^4\Theta$.
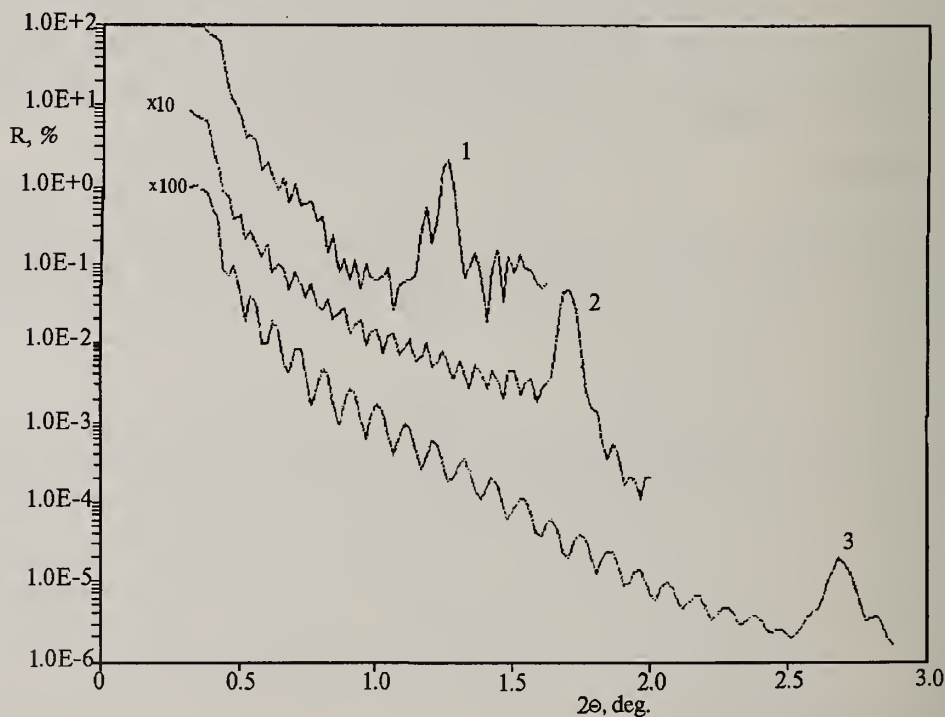
Fig.1. The dependencies R(Θ) for multilayer structures with different periods: 1-d= 68 A; 2-d=51 A, 3-d=33 A.

The Fig.2 shows the experimental dependencies of R=f(Θ) for multilayer structures consisting of 50 layers (fig.2,curve 1), 90 layers (fig.2, curve 2) and the theoretical dependence of R=f(Θ) (fig.2, curve 3) for the structure as presented on fig.2,curve 1. The theoretical curve was calculated taking into account roughness o f the quartz substrate. Besides we use the following

suppose. In the X-ray range for carbon we can suppose that absorption $\gamma=0$.
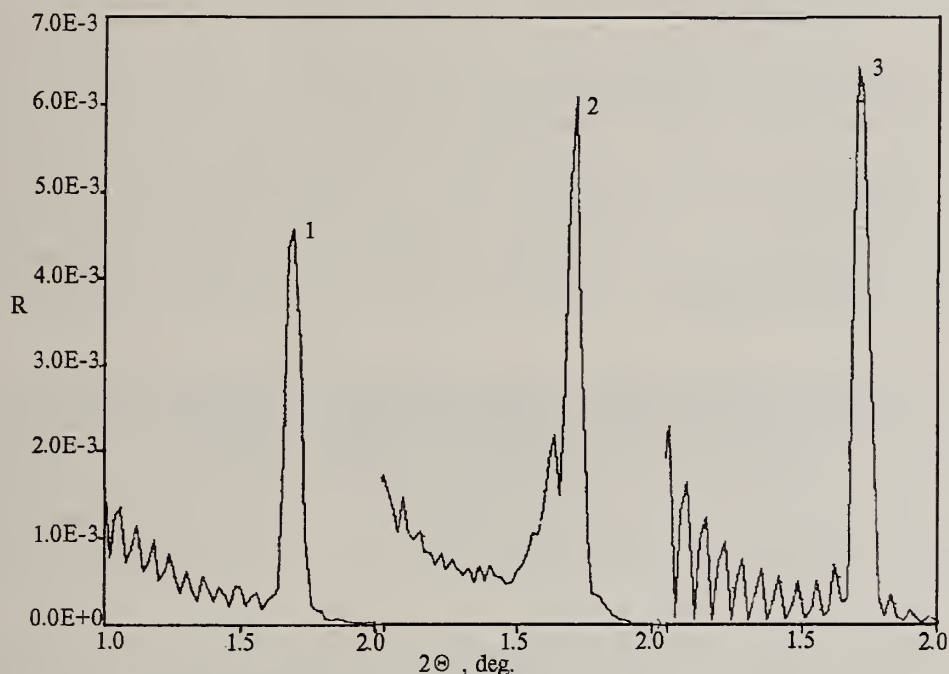
Fig.2. Experimental (curve 1,2) and theoretical (curve3) dependencies of $R=f(\Theta)$ for the structure with period 51 A.

Therefore the reflection coefficient of multilayer structure depends on the difference between refraction decrement (δ) of alternating carbon layers. In our case $\Delta\delta=1*10^{-6}$. It is clear that the reflection coefficient R^{max} for theoretical dependence is 0.7 %. This value is about 1.5 time higher than for the experimental one. Also, the peak full width at half-maximum is equal to 0.03° and 0.035° for theoretical and experimental dependencies, respectively.

The difference like this between the theory and the experiment could be connected with the roughness of the interfaces as well as with the accidental dispersion in the thickness of the layers, forming the multilayer structure.

Using Eq.1 and Bragg condition we can evaluate the influence of the accidental dispersion in the layers thickness on the reflection coefficient and the resolution of the formed MIS as follows.

The resolution of the X-ray mirror could be found from the equitation [2]:

$$\frac{\lambda}{\Delta\lambda}=\frac{1}{tg(90-\Theta)\Delta\Theta}$$

(1)

where Θ is the angular position of the first Bragg peak and $\Delta\Theta$ is the width of peak at the half-maximum.

If the average quadratic dispersion in the period of the structure is equal to Δl, the resolution of the structure could not be more then $\lambda/\Delta\lambda \leq l/\Delta l$. Hence, one could evaluate the average quadratic dispersion Δl of the structure under investigation. Substituting the experimental values $\Theta=0.87°$ and $\Delta\Theta=0.035°$ into the expression (1) we shall find $\lambda/\Delta\lambda=25$. Taking into account that $l=52$ A we shall get that $\Delta l= 2$ A that is approximately equal to 4 % of the structure period. This value says about the high quality of the structure. It is important to note that the calculated value ($\lambda/\Delta\lambda=18$) for C/Ni multilayer structure is less then for DLC MIS .

Supposing that Δl decreases the reflection ability of the mirror due to the same law ($R \sim R^{max}\exp\{-\Delta l/l\}$), that roughness we could not explain the difference between the theoretical and the experimental values of R^{max} by the presence of the accidental dispersion in the periods of structure. It could be made if it is supposed that there is a roughness of interfaces $\sigma=2$ A. In the present study in order to consider roughness (σ) influence we have used the expressions for the Debye-Waller factors [2].

Fig.2, curve 2 shows experimental dependence for MIS consisting of 90 layers. It is seen the reflection ability of such structure is higher then of the structure with 50 layers (curve 1)However there is a satellite peak near a Bragg peak. From the Bragg condition we found that the satellite peak corresponds to $d=52.8$ A. It means that the growth rates of carbon layers increases during deposition process. In consequence of this the reflection ability of formed structure of less then theoretical one.

4. Conclusion

We have shown the possibility forming of a high quality diamond-like carbon MIS with a very small period. It was found that intensity of the calculated first Bragg peak was higher than one in compared the experiment. That is the consequence of both factors the interface roughness and random fluctuation in layers' thicknesses. We are sure that these MIS will be able to find wide application in the field of soft X-ray optics.

5. References

1.T.W.Barbee, Optical Engineering, v.25 N8 (1986) p.899.

2.A.V.Vinogradov and I.V.Kogevnikov,Proc.FIAN, v.196 (1989) p.63 (in Russian).

3.L.G.Parrat Phys.Rev.,v.95 N2 (1954) p.359.

4.P.E. Kondrashov, I.S. Smirnov, V.V. Sleptsov, A.M. Baranov, V.M. Elinson, Diamond and Related Materials, 1995, v. 4, 109-112.

CUBIC BORON NITRIDE

TRIBOLOGICAL PROPERTIES OF C-BN FILMS FABRICATED BY THE REACTIVE ION PLATING METHOD AND MODIFIED BY ION IMPLANTATION

Masao Murakawa, Shuichi Watanabe and Shojiro Miyake

Nippon Institute of Technology, 4-1 Gakuendai, Miyashiro-machi, Minamisaitama-gun, Saitama 345, Japan

Key words: c-BN, ion plating, ion implantation, tribology, wear, adhesion

Abstract

Tribological properties in narrow and broad senses were measured for cubic boron nitride films made by ion plating with or without subsequent ion implantation to increase adhesion of the films. First, a pure tribological property, such as the frictional coefficient, against stainless steel and diamond indenters was investigated for a c-BN film made with graded composition control through a titanium interlayer in air (for both indenters) and vacuum (for diamond indenter). The film showed a very good value (about 0.025-0.03) in both environments. We then report on the trial application of our c-BN film, believed to have a good tribological property, to a more practical tribological use, i.e., as a protective coating for drills. The tested WC-Co alloy drills had a c-BN coating or film made by ion plating and modified with the post-treatment of ion implantation to improve adhesion. The modification substantially increased the adhesion and the frictional property as well, resulting in substantial decrease of the thrust compared with the conventional TiCN coating.

1. Introduction

Cubic boron nitride (c-BN) film, as is well known, has many excellent properties such as high chemical stability, high hardness, and low friction, and thus is suitable for use with iron-based materials. In particular, c-BN film is suitable for coating surfaces that come into contact with iron-based materials, where diamond cannot be used because of its high chemical affinity for iron.

Films of cubic boron nitride can be formed by magnetically enhanced plasma ion plating (MEP-IP) [1] developed by us, which is a reactive ion plating method using a hot-cathode plasma discharge in a parallel magnetic field.

2. Experimental details

2.1. Preparation of c-BN film

The c-BN film was deposited either onto a silicon substrate for use in the basic tribology test or onto a WC-Co alloy drill substrate for use in the cutting performance test (drilling test) using JIS SCM440 (Cr-Mo steel). Details of the equipment and basic characteristics of the c-BN film deposited have been described in a previous paper [1].

The c-BN film samples used for the experiment were deposited onto the substrate by the graded composition controlling technique [2] with a titanium interlayer between the gradient layer and the substrate to improve the adhesion of the film. The thickness of each layer was as follows: about 100-200 nm for the Ti interlayer, 150-250 nm for the graded composition layer and 200-300 nm for the top c-BN layer.

2.2. Ion implantation treatment

In the cutting performance test of c-BN-coated drills, attempts to increase adhesion have been pursued by the adoption of a post-treatment of ion implantation without or with annealing to stabilize the interface layer, thereby realizing adequate interfacial ion mixing. Two implant species of nitrogen and/or carbon were used in an ion implantation apparatus provided with a mass separating unit [3]. The post-treatment conditions are shown in Table I.

2.3. Friction and wear test

(1) Comparison of basic tribological properties between c-BN coating and other conventional hard coatings

A reciprocal sliding testing machine [4] was used to compare the tribological performance of the c-BN film described in 2.1. and other conventional hard films such as TiN, TiC and TiCN coated onto a polished WC-Co alloy plate at thicknesses of about 0.5, 4-5, 2-3 and 2-3 μm, respectively. The latter three conventional hard coatings were all deposited using a conventional ion plating apparatus. The indentation load of a stainless steel ball was applied perpendicular to the surface of the specimen while the specimen holder was moved back and forth. The friction test was performed at room temperature in air with 40-50 % relative humidity with the friction distance of one stroke of 10 mm, the contact friction speed of 10 mm per 6 s, and the indentation load of 0.98 N.

(2) Basic tribological properties of c-BN coating against diamond in atmosphere and vacuum

A swinging-type sliding testing machine [5] was used in a friction test in which an indenter made of natural diamond with ground finishing surfaces of approximately 0.1μm roughness, and the tip radius of 0.5 mm was slid against the c-BN film in air atmosphere (without lubricants) at ambient temperature with 40-50 % relative humidity in a semiclean room.

In a friction test of c-BN film against the diamond indenter in vacuum, the same swinging-type sliding testing machine was used in a vacuum environment of 2-3x10^{-4} Pa, instead of in ambient atmosphere. The test was conducted at ambient temperature.

2.4. Evaluation of cutting performance of c-BN coated drills

In this paper, the cutting performance of drills with c-BN coatings of type I or type II listed in **Table I**, and with a diameter of 6.0 mm is described, because a ϕ 6.0 mm drill is usually standard in performance tests.

The performance of a coated drill was investigated through boring operation using a

conventional machining center. Our evaluation test was conducted in such a way that the boring operation was continued for 1000 hits, and cutting forces of thrust and torque were measured during operation. The wear condition of the drill was also observed as required using a SEM. The work material was Cr-Mo steel alloy available commercially (JIS SCM440). The boring operation conditions are shown in **Table II**.

Table I Post-treatment conditions of c-BN coating used for drilling test.

Type	Ion implantation	Annealing
I (N⁺)	Ion energy: 135keV and 35keV Dosage: 1×10^{16} ions/cm² (at 135keV) 6×10^{15} ions/cm² (at 35keV)	Pressure: $1\sim5\times10^{-3}$ Pa Temp.: 760°C Time: 3 h
II (N⁺, C⁺)	Ion energy: 135keV(for N⁺) and 90keV(for C⁺) Dosage: 1×10^{16} ions/cm² (at 135keV) 8×10^{15} ions/cm² (at 90keV)	

Table II Boring operation conditions

Revolution	3000 rpm
Max. cutting speed	57 m/min
Feed rate	0.1 ~ 0.25 mm/rev.
Boring depth	10 mm
Lubricant	None (dry)
Work material	SCM440 (Hv $_{(5000)}$ =164)

3. Results and discussion of basic tribological properties of c-BN film

3.1. Comparison of basic tribological properties between c-BN coating and other conventional hard coatings

Figure 1 shows the result of the comparison described above which corresponds to the case of a relatively low pv (pressure x velocity) value. As clearly shown in this figure, the frictional coefficient of c-BN film against a stainless steel ball indenter is not only low but also stable compared with those of other conventional hard coatings, thus indicating that c-BN coating may be feasible in various other practical tribological applications such as cutting inserts, drills or the like.

However, it should be noted here that when the c-BN film deposited onto the WC-Co alloy plate was subjected to a frictional wear test under a higher pv value, the film showed premature damage on its surface compared with TiCN film, thereby indicating the necessity of a means of increasing the adhesion.

3.2. Basic tribological properties of c-BN coating against diamond indenter in atmosphere and vacuum

Since the above-mentioned results shown in Fig.1 showed that c-BN coatings could possibly possess good frictional properties against other materials as well, we concieved of applying c-BN coatings to the construction of a "zero wear system" by choosing diamond as the counterpart to c-BN, because both materials can form a wear system wherein both low friction and low wear can be achieved at the same time.

Figure 2 shows a plot of the frictional coefficient between c-BN coating deposited onto a silicon substrate using the graded composition controlling technique with a
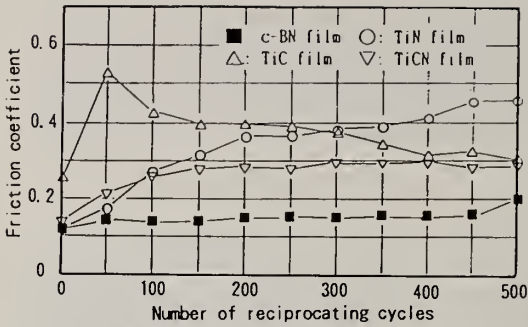
Fig. 1 Comparison of frictional property between c-BN film and various conventional hard films. [Substrate: WC-Co alloy, Load: 0.98 N, Stainless ball indenter: φ6.35mm]
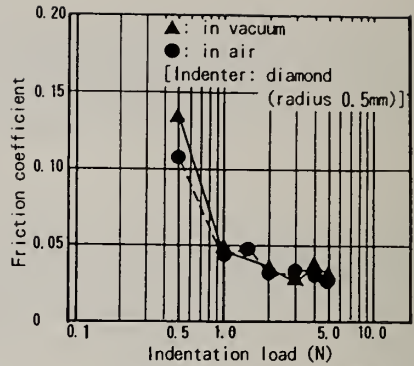
Fig. 2 Friction coefficient between c-BN coating and diamond indenter versus indentation load.

titanium interlayer [2] and a diamond indenter versus indentation load varied from 0.5 N to 4.9 N; the test was performed in air and vacuum using the testing devices, as mentioned above. The frictional coefficient values are plotted in the figure as those at the 20th stroke or swinging movement, taking into consideration the exclusion of the influence of instability during the initial sliding period. As shown, it was unexpectedly found that the frictional coefficients in question at room temperature and under dry conditions can be as low as 0.03, the general trend being that the coefficient shows a gradual decrease as the vertical indentation load increases.

Figure 3 shows variations in the frictional coefficients of c-BN film shown in Fig.2 under air or vacuum conditions, with the number of reciprocating or swinging cycles. The results clearly show that the frictional coefficient of the c-BN coating can be very low and stable as well for an increasing number of sliding cycles irrespective of the test environment. Although not shown, both c-BN coatings were observed as to their worn surfaces using SEM, resulting in the unexpected finding that there was no trace of wear at all on the sliding surfaces, irrespective of the surrounding atmosphere.

On the basis of these findings, it appears that a tribological system consisting of c-BN and diamond is very promising for use in severe environments where the use of lubricants is impossible, for example, in space.

4. Results and discussion of tribological properties of c-BN film when applied to cutting tools

The above-mentioned results, i.e., excellence of c-BN films in termes of basic tribological properties, prompted us to apply c-BN film to a severer use in terms of pressure, sliding velocity and temperature, i.e., as cutting tools such as drills.

4.1. Problems of the drills coated with our previously tested c-BN film

We have already reported [6] on the trial fabrication of a c-BN-coated drill following type I post-treatment in Table I, and its basic performance test. Although the drills showed some utility in that they can perform better than noncoated WC-Co alloy drills,
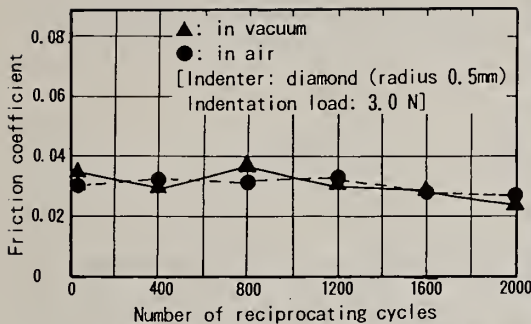
Fig. 3 Variations in friction coefficients of c-BN coating against diamond indenter in air and vacuum with the number of reciprocating cycles.
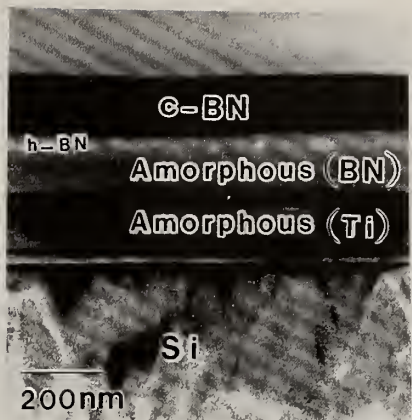
Fig. 4 Cross-sectional transmission electron micrograph of the c-BN film.

they also presented some problems which required further investigation and/or countermeasures: unexpectedly high values of torque and thrust compared with those of commercially available TiCN-coated WC-Co alloy drills (although the values in question were lower than those of noncoated drills). This was unexpected considering the general superiority of c-BN over TiCN, as shown in Fig. 1. Accordingly, we subjected the tip of the drill with type 1 post-treatment to AES observation after 500 hits.

Based on the results (not shown) it was speculated that the c-BN film on the convex portion adjacent to the tip edge ground area prematurely peeled off the substrate due to the severe cutting forces involved, resulting in the higher values of torque and thrust during boring. This indicated that the c-BN film modified by type 1 ion implantation post-treatment had insufficient durability, although the c-BN film even without this post-treatment shows good performance when applied to tribological operation where a lower value of pv prevailed compared with the cutting operation.

4.2. HREM observation of c-BN films deposited on Si and modified by the type I ion implantation post-treatment [7]

In the following, we will report briefly on the most important HREM (high-resolution electron microscopy) observations of the c-BN film, which has the same composition as the one applied to the cutting tools mentioned above, to investigate why the c-BN layer broke rather unexpectedly, as mentioned above.

Figure 4 shows a cross-sectional transmission electron micrograph of the c-BN film in question. It is noted that h-BN, with thickness of about 20-50 nm, is seen between c-BN films and amorphous BN layers. This indicates that a h-BN layer still exists in the c-BN coating subjected to ion implantation with nitrogen species, as in the other c-BN film [8] made by IBAD (ion beam assisted deposition) but without any post-treatment of ion implantation.

This seems to suggest strongly that h-BN is formed before c-BN formation can be initiated. Thus, we conclude that this very thin h-BN layer beneath the pure c-BN layer can be very detrimental when the coating is used in an environment or operation where a high pv value is involved, as in cutting operations.

4.3. Means of increasing the adhesion of our c-BN coating further

To render the h-BN layer included in the as-deposited c-BN coating harmless, we concieved the type II post-treatment shown in Table I. The basic idea of this post-treatment is to use not only nitrogen ion for the purpose of achieving intermixing along the interface between the substrate and Ti interlayer thereby increasing the adhesion, but also carbon ion for the additional purpose of transforming the h-BN layer into an amorphous BN phase in order to increase the adhesion along the interfaces of the h-BN layer. Although not shown, this countermeasure has proved to be very effective, as judged from the tribology test using the swinging-type tester.

4.4. Performance test of the improved c-BN coating applied to drills

(1) Use of c-BN film for single coating onto the WC-Co alloy drills

Two kinds of drill, i.e., <1> drills with c-BN films subjected to the type I post-treatment (referred to as c-BN(N)/WC-Co drill hereafter) and <2> drills with c-BN films subjected to the type II post-treatment (referred to as c-BN(C)/WC-Co drill hereafter), were compared with <3> noncoated WC-Co alloy drill under the test conditions shown in Table II.

Figure 5(a) shows the test results for these drills in terms of their torque and thrust values versus the feed rate. It is clear that (1) both c-BN-coated drills have lower values of torque and thrust than those of the noncoated drill, and (2) the thrust values of the c-BN(C)/WC-Co drill are obviously lower than those of the c-BN(N)/WC-Co drill, although there is no difference in the torque values between the two c-BN-coated drills.

(2) Use of c-BN film for double coatings onto the WC-Co alloy drills

Although not shown, even the c-BN-coated drills with adhesion improved by means of nitrogen-plus-carbon ion implantation could not surpass the commercially available TiCN-coated drills with respect to torque and thrust when the c-BN film was used as a single coating, most likely due to too small a thickness (about $0.5 \mu m$) compared with that of TiCN coating ($3-5 \mu m$).

Thus, we applied c-BN coatings as the outermost protective coatings on top of TiCN coatings in an attempt to improve the overall antiwear performance of the TiCN-coated drills due to the excellent thermal property of c-BN.

Accordingly, two additional kinds of drill, i.e., <4> drills with c-BN films subjected to the type II post-treatment on the TiCN coating (referred to as c-BN(C)/TiCN/WC-Co drill hereafter), and <5> drills with TiCN films (referred to as TiCN/WC-Co drill hereafter) were prepared for the drilling performance test carried out under the conditions shown in Table II.

(a) single coating

(b) double coating

⟨4⟩ c-BN(C)/TiCN/WC-Co after 1st hit
⟨4⟩ c-BN(C)/TiCN/WC-Co after 1000 hits

⟨1⟩ c-BN(N)/WC-Co drill
⟨2⟩ c-BN(C)/WC-Co drill
⟨3⟩ noncoated WC-Co drill

⟨5⟩ TiCN/WC-Co after 1st hit
⟨5⟩ TiCN/WC-Co after 1000 hits
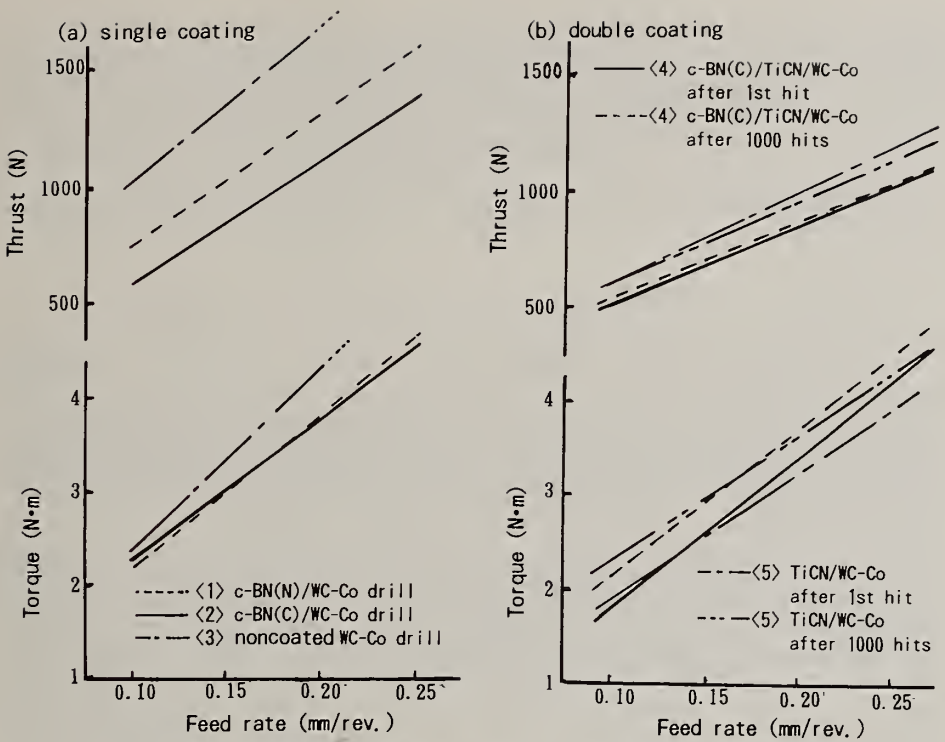
Fig. 5 Variations in torque and thrust forces with feed rate during boring boring test (work material: SCM440, boring depth: 10mm, lubrication: dry).

Each of the drills was subjected to up to 1000 hits of boring, and the torque and thrust values were measured during the test. In **Figure 5(b)**, which shows a plot of the relevant values for the first and 1000th hits, it can be seen that drill ⟨4⟩ (c-BN(C)/TiCN/WC-Co) exhibits a lower thrust value after 1000 hits than that of drill ⟨5⟩ (TiCN/WC-Co) irrespective of the feed rate. As for the torque value, it is generally seen that the c-BN(C)/TiCN/WC-Co drill has lower values than those of the TiCN/WC-Co drill within a feed range below 0.15 mm/rev., while the reverse trend can be seen beyond a feed rate of 0.20 mm/rev.

At present it cannot be stated definitively whether these comparative results on torque for drills ⟨4⟩ and ⟨5⟩ indicate generalized characteristics or not, since the torque measurement values generally have large scatter, and accordingly the two curves for the torque in question may merely overlap with each other within the range of error.

Lastly, tested drills ⟨3⟩, ⟨4⟩ and ⟨5⟩ were observed using SEM to determine the amount of wear after 500 hits and 1000 hits. Although not shown, drill ⟨3⟩ (noncoated WC-Co drill) was found to have reached the end of its life, defined as the time at which wear amounting to 0.08 - 0.1 mm on the front flank is reached and regrinding is required, after only 500 hits of boring. In contrast to this, both drills ⟨4⟩ and ⟨5⟩

showed significantly improved antiwear properties since the amount of wear for each drill was still on the order of 0.08 mm even after 1000 hits of boring. However, as far as the amount of wear along the flank face is concerned, neither of them showed any significant difference, probably because the c-BN film was still too thin to function adequately as a protective layer immediately adjacent to the tip edge where stresses are very severe. It is noted here that drill <4> (c-BN(C)/TiCN/WC-Co) retained c-BN film along its cutting edges both after the 1st and 1000 hits, as determined by micro-IR measurement.

5. Conclusions

Basic friction and wear properties of c-BN films prepared by the magnetically enhanced plasma ion plating (MEP-IP) method were examined at applied vertical loads representing macroscopic (0.5 - 4.9 N) sliding conditions. Subsequently, more practical friction and wear properties of c-BN films were examined by performing the drill boring test on films prepared first by MEP-IP deposition followed by modification by single or double ion implantation of nitrogen or nitrogen and carbon species to increase the adhesion.

The results are summarized as follows. (1) c-BN films generally show surprisingly good tribological properties such as low friction coefficient or low wear rate when a stainless-steel ball indenter is slid on the film in air, or a diamond indenter is slid on the film either in air or in vacuum of $2-3x10^{-4}$ Pa. (2) c-BN films subjected to a post-treatment of nitrogen and carbon ion implantation to transform the inherent h-BN layer into a harmless amorphous BN (a-BN) layer, thereby increasing the adhesion and/or the integrity of the film itself, showed a significant improvement in the wear rate, examined by the sliding wear test or by an actual drilling test, over the previous c-BN films without this post-treatment.

References

1. M. Murakawa and S. Watanabe: Surface and Coatings Technology, 43/44 (1990) 128.
2. M. Murakawa and S. Watanabe: ibid, 43/44 (1990) 145.
3. M. Hirano and S. Miyake: Trans. ASME, J. Tribol., 110 (1988) 64.
4. S. Watanabe, S. Miyake and M. Murakawa: Surface and Coatings Tech., 62 (1993) 558.
5. I. Sugimoto and S. Miyake: J. Appl. Phys., 64 (1988) 2700.
6. M. Murakawa, S. Watanabe and S. Miyake: Proc. 2nd Int. Conf. on the Applications of Diamond Films and Related Materials, MYU, Tokyo, (1993) 597.
7. S. Watanabe, S. Miyake, W. Zhou, Y. Ikuhara, T. Suzuki and M. Murakawa: Appl. Phys. Lett., 66 (1995) 1478.
8. D. J. Kester, K. S. Ailey, R. F. Davis and K. L. More: J. Mater. Res., 8 (1993) 1213.

SPUTTER DEPOSITION OF CUBIC BORON NITRIDE FILMS

K.Bewilogua, A.Schütze, S.Kouptsidis and H.Lüthje

Fraunhofer-Institut für Schicht- und Oberflächentechnik, Bienroder Weg 54 E,
D-38108 Braunschweig (F.R.G.)

Key words: adhesion, c-BN, film growth, hardness, sputtering

Abstract

Cubic boron nitride (c-BN) films can be prepared by sputter deposition. Targets,
mostly hexagonal boron nitride (h-BN) or boron, which have low electrical conduc-
tivities, will be used. For the application of effective and reliable d.c. magnetron
sputter techniques, conducting target materials are necessary. Boron carbide (B_4C)
was proven to be a suitable candidate. A d.c. magnetron sputter process was devel-
oped in three phases. At first a r.f. diode sputter process was optimized for a h-BN
target and transferred to a B_4C target, followed by d.c. magnetron sputtering exper-
iments with the boron carbide target. Correlations between process parameters and
film properties as well as some structural features of the sputter deposited films will
be reported.

1. Introduction

Like diamond, cubic boron nitride (c-BN) is extremely hard, electrically insulating,
transparent in the visible spectral range and chemically inert. The application of di-
amond as a tool coating is limited because of the insufficient thermal stability under
normal atmosphere and the pronounced reactivity with ferrous metals. Cubic boron
nitride is an alternative to overcome these problems. Therefore, c-BN coatings are
very promising in view of wear reduction of tools for steel machining. Moreover,
owing to its electrical, optical and chemical properties other applications of c-BN
coatings will be expected.

In the last few years several research groups have prepared c-BN films using differ-
ent methods, e.g. plasma assisted CVD [1] or electron cyclotron resonance plasma
processes [2] and various PVD techniques like ion plating [3], ion beam assisted
deposition (IBAD) [4,5] and sputtering [6,7].

In the present paper the sputter deposition of c-BN films, especially with electrical-
ly conducting targets, as well as the film structure and some essential properties
will be discussed.

2. Target materials

Most of the sputter deposition experiments known so far were performed using ei-
ther hexagonal boron nitride (h-BN) or boron (B) targets. Tanabe et al. [8,9] pre-

pared BN films combining ion beam sputtering of B or h-BN targets with an simultaneous ion bombardment of the substrate. They concluded that B is much more suitable for the deposition of c-BN than h-BN. Due to the low electrical conductivities of h-BN and B, the sputter deposition of c-BN films requires radio frequency (r.f.) power at the target electrodes, both in diode [6,7] or magnetron [10] arrangements.

With respect to effective high rate and large area deposition, d.c. magnetron sputtering seems to be very promising. However, for the application of this technique, conducting target materials are to use. Possible candidates are boron rich metal borides, e.g. ZrB_{12}. Mitterer et al. [11] prepared decorative coatings by reactive sputtering of this material, but no BN phases were observed.

We have chosen boron carbide (B_4C, $\rho < 10^2$ Ωcm at room temperature) as the target material for our sputter experiments. The first results were recently published [12]. The development of a d.c. magnetron sputter process was subdivided in different phases. First a r.f. diode sputter process was optimized for a h-BN target and transferred to a B_4C target, followed by d.c. magnetron sputtering experiments with the boron carbide target. Boron carbide was preferred because it could be expected that the only "impurity" of carbon, at least partially, can be removed by a reaction with nitrogen, e.g. towards the stable molecule C_2N_2.

According to a large amount of experimental data Hackenberger et al. [13] concluded that stoichiometric or nearly stoichiometric BN films contained the highest amount of the cubic phase. In most reported cases of sputtering with h-BN targets, atomic ratios B:N $\approx$ 1 in the films could be realized only if the sputter gas consisted of a Ar/N_2 mixture [7,14,15] because h-BN targets dissociate during sputtering with pure argon [16]. As an example, Fig.1 shows the B:N ratios in films deposited by r.f. sputtering of two different targets. For h-BN the ratio B:N $\approx$ 1 was reached at nitrogen flows > 1 %, while for B_4C at least 10 % were necessary. It should be noted that this critical flow seems to depend on the target surface conditions which can be different for new and old targets. However, to clarify this problem, further ex-
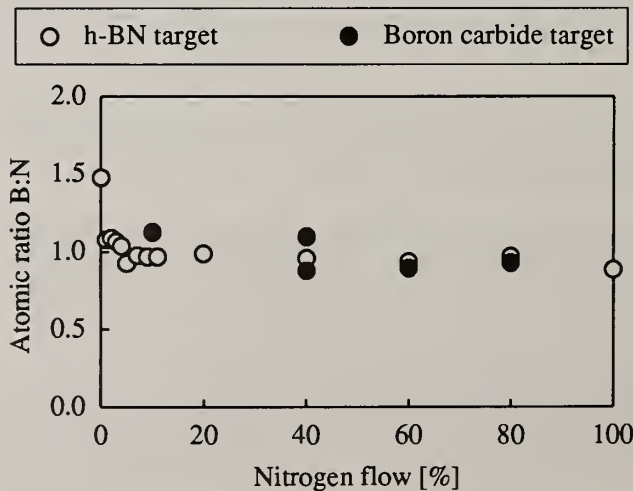
Fig.1:
Atomic ratios B:N for films sputter deposited with h-BN and B_4C targets. Nitrogen flow: (N_2/Ar+N_2)

periments are necessary. In contrast to the mentioned findings, Mieno and Yoshida [6] prepared nearly stoichiometric c-BN films in pure Ar. The reason for this obvious difference is not clear.

3. Experimental details

The experimental conditions for the sputter deposition of c-BN films by r.f. (13.56 MHz) diode sputtering with h-BN [7] and B_4C targets [12,17], as well as by d.c. magnetron sputtering with B_4C targets [17], were reported in detail elsewhere. In both configurations the ionization was enhanced by additional magnetic coils positioned around the substrate holder. The substrate electrodes were operated either with a d.c. potential or with r.f. power. In the r.f. mode the d.c. self bias, or the power, could be kept constant during the deposition process. Some import parameters will be summarized as follows:

r.f. diode sputtering:

- Target diameter: 150 mm
- Target - substrate distance: 70 mm
- Target power: 750 to 1000 W
- Substrate potential: -50 to -500 V (d.c. or d.c. self bias)
- Substrate temperature: up to 350°C
- Nitrogen flow ($N_2/Ar+N_2$):   0 to 100 %
- Deposition rate: about 0.5 μm/h

d.c. magnetron sputtering:

- Target dimensions: 254 mm x 127 mm
- Target - substrate distance: 80 mm
- Target power: 750 to 1500 W
- Negative substrate potential: up to -550 V (d.c. or d.c. self bias)
- Substrate temperature: up to 500°C
- Nitrogen flow: up to 50 %
- Deposition rate: about 0.5 μm/h

It shall be noted that in the d.c. magnetron mode at higher nitrogen flows the danger of target poisoning and arcing increased.

The structure and composition of our c-BN films were mainly characterized by transmission infrared(IR) spectroscopy and by electron probe micro analysis (EPMA), respectively. Further structural information was obtained from transmission electron microscopy (TEM) [12]. The hardness was determined from nanometer indentation measurements (see e.g. [18]).

The content of c-BN in mixed films was estimated from the IR absorption intensities I_h (at a wave number near $v = 1400cm^{-1}$ (h-BN)) and I_c (near $v = 1100cm^{-1}$ (c-BN)). The ratio of the fractions f_c and f_h of both phases can be calculated as $f_c/f_h = 0.6\ \alpha_c/\alpha_h$ [19]. Using the rough approximation $I_i \sim \alpha_i$ (i: h,c) [17], where α_i are the absorption coefficients, it follows that $f_c/f_h \approx 0.6\ I_c/I_h$.

It should be mentioned that in the literature, different calibration factors were used (see [19]) and therefore a comparison of published data is rather problematic. Fur-

thermore, the IR spectra provide only averaged values and do not take into account the structural changes through the film thickness which occur typically from amorphous BN (a-BN) next to the substrate followed by turbostratic BN (t-BN) and finally c-BN (see below).

4. Results and discussion

4.1. r.f. sputter deposition

Fig. 2 shows the dependence of the c-BN content on the nitrogen gas flow for both target materials h-BN and B_4C. In contrast to Mieno and Yoshida [6] we could not prepare any cubic phase sputtering with pure Ar. However, already at 2 % N_2 flow high c-BN contents were reached. For the boron carbide target a similar depen-
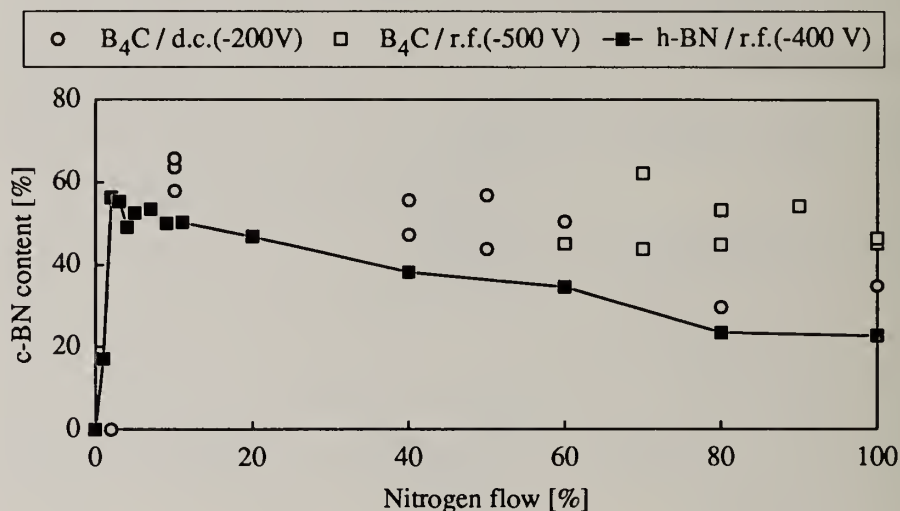
Fig. 2: c-BN contents vs. relative nitrogen flow for boron carbide and h-BN targets and for different operation modes of the substrate electrode (d.c. or r.f., the corresponding bias values are given in the legend)

dence was found, but c-BN growth was not observed until there was 10 % N_2 in the sputter gas. For both target materials there exists a clear correlation between c-BN content and B:N ratios (Fig. 1). With further increasing N_2 flows, the content of the cubic phase decreased in both cases, but even films deposited with pure nitrogen contained considerable amounts of c-BN. Our films with thicknesses of a few 100 nm could be deposited with d.c. potentials at the substrate. However, due to the low electrical conductivity of BN this will be problematic sputtering thicker films. In the d.c. mode the substrate ion current densities could be estimated. At substrate voltages of -200 V (conditions for high c-BN contents) the ratio of ions to deposited boron atoms was calculated as about $F_i/F_B \approx 10$. At -50 V bias and a nitrogen flow of 10 %, F_i/F_B was about 5 and the films consisted only of h-BN. Both values are in good agreement to the data published by Reinke et al. [20] for c-BN growth.

Films deposited with a boron carbide target obviously contained carbon. However,

the C:B ratio (1:4 in B_4C) could be reduced from 1:4 in films sputtered at low nitrogen flows to about 1:8 in films prepared at nitrogen flows > 50%. A possible explanation for this reduction was given in section 2. The BN films deposited with the two different targets contained a few percent of oxygen.

Cross section TEM investigations [12] revealed that our sputter deposited films also show the phase evolution well known for c-BN films (see e.g. [21]). The growth starts with an amorphous BN (a-BN) phase of a few nm in thickness followed by a highly oriented turbostratic (t-BN) layer with the c-axis parallel to the surface with a thickness of about 10nm. Then a nanocrystalline (crystallite dimensions ~ 10 nm), almost single-phase c-BN film with preferred orientation, grows.

Even if the growing films are bombarded only with low energy ions, leading to h-BN growth, the t-BN phase grows highly oriented. A change, e.g. of the bias voltage, during the film growth causes immediate c-BN generation. This suggestion was concluded from the results shown in Fig. 3. The deposition was started with a substrate voltage of -50 V (h-BN deposition). After some minutes the voltage was changed to -200 V (c-BN growth conditions). The IR spectrum (a) is that of a mixed phase film, (b) that only of the first h-BN film. Measuring the mixed film (a)
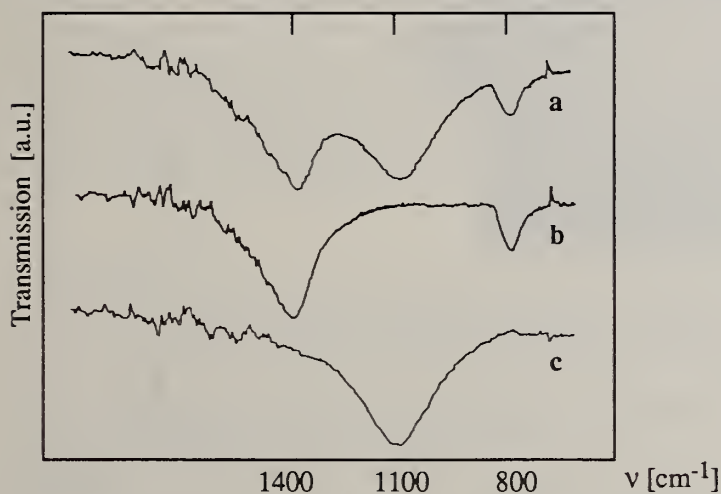
Fig. 3: IR spectra of a two layer BN film (a), a pure h-BN film (b) and of the top layer of the two phase film (c); Substrate: Si, -200 V d.c., target: B_4C,

against reference (b), the result is a spectrum of a pure c-BN layer (c). TEM investigations supported this interpretation. Although such c-BN films in many cases delaminated from the substrates after several hours or days, some films had a good adhesion for a long time. The hardness of the nearly pure c-BN films was determined to be up to 50 - 60 GPa. These hardness values are in the range of those reported in the literature for polycrystalline c-BN (e.g. [22]).

The above mentioned preferred orientation of the c-BN crystallites can be revealed from the electron diffraction patterns of our films both on silicon as well as on steel substrates. Fig. 4a shows the diffraction diagram which is an accessory to the re-

cently presented cross section TEM image [12] of a film deposited with a boron carbide target. The reflections indicate that the c-axis ($[0002]_t$ direction) of the turbostratic (t-BN) phase and the $\langle 111\rangle_c$ direction (c-BN) are perpendicular to the substrate normal direction. Furthermore the $\langle 110\rangle_c$ direction is parallel with the substrate normal. A preferred orientation of the c-BN crystallites was revealed only by a few groups so far, whilst in most cases no indications for a preferred c-BN growth were reported [5,21]. Ballal et al. [23] found the same orientation as in our films ($\langle 110\rangle$ of c-BN parallel with the substrate normal). Their films were prepared by an ion assisted pulsed laser technique. Hofsäss et al. [24] used mass separated ion beam deposition and observed a non-uniformity of the c-BN diffraction rings, but a crystallographic relation between the BN phases and the substrate was not derived.
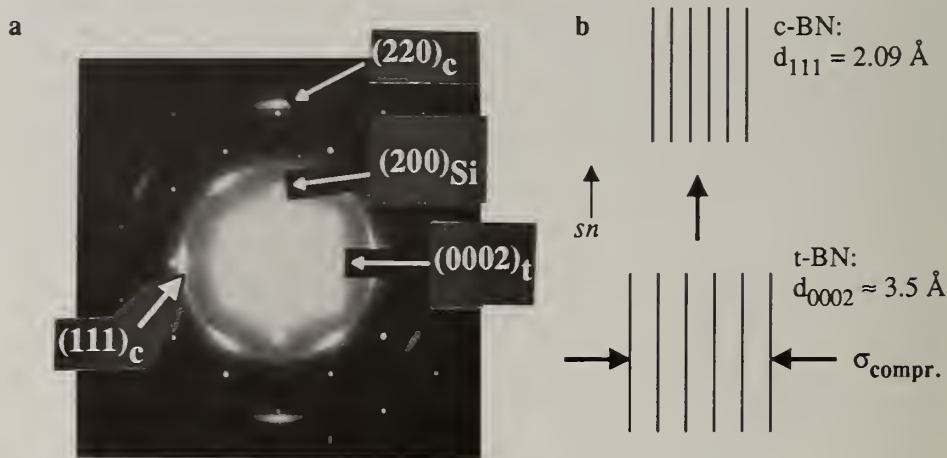
Fig.4: Electron diffraction pattern of a sputter deposited c-BN film (B_4C target) [12] (a); Model for the transformation from t-BN ($\rho_m \leq 2.2$ g/cm^3) to c-BN ($\rho_m = 3.48$ g/cm^3), sn: substrate normal (b)

A simple model, schematically shown in Fig. 4b, can explain the parallelism of the directions $\langle 0002\rangle_t$ and $\langle 111\rangle_c$. The preferred orientation of the t-BN phase obviously will be caused by high compressive stresses which are generated by the intensive ion bombardment during the c-BN film growth [25]. A further effect of the high compressive stresses could be that due to the high compressibility of h-BN in the c-axis direction [26], accompanied by a puckering of the hexagonal planes, a transformation from $\langle 0002\rangle_t$ to $\langle 111\rangle_c$ occurs. A similar mechanism also has been discussed for the high pressure and high temperature synthesis of diamond.

Reasons why the preferred c-BN orientation occurs in some films and not in others or any correlation to the used deposition method, are still not clear.

The adhesion of our sputtered c-BN films (thicknesses some 100 nm) on Si, steel, hard metal or other substrates is in many cases insufficient. Starting the deposition with a h-BN layer (see Fig. 3) seems to be a way of improving the adhesion and to increase the film thickness. However, to clarify this question, intensive experimental work must be performed.

4.2. d.c. magnetron deposition

The d.c. magnetron sputter deposition of BN films was performed with a boron carbide target. To realize sufficiently high ion current densities at the substrate, the magnetron was operated in the unbalanced mode and additionally an electromagnetic coil around the substrate electrode was used. Using this arrangement at a d.c. potential of -300 V at the substrate, up to about 0.5 μm thick films with c-BN contents between 60 and 70 % could be prepared. As in the case of r.f. sputter deposition, a good reproducibility of the cubic phase content was reached. Also with respect to adhesion behaviour and mechanical properties no essential differences between the two applied sputter techniques were found. At present the films are still rather inhomogeneous over substrate areas of ≈ 1 cm^2.

5. Summary and conclusions

Both by r.f. diode and d.c. magnetron sputtering with boron carbide targets, BN films with high contents of the cubic phase could be prepared. Properties and behaviour of the films obtained by the two discussed methods are similar. However, the d.c. magnetron sputter technique should have a great potential with respect to higher deposition rates. Using the r.f. sputter method, for h-BN and B$_4$C targets a similar dependence between c-BN content and reactive gas flow was derived. Our films, sputter deposited on Si and steel substrates, exhibited a preferred orientation of the c-BN crystallites which can be explained by a simple model which considers the effect of high compressive stresses. In many cases the deposited, some 100 nm thick, films delaminated from the substrates after short times. At present the adhesion of c-BN films seems to be a general problem for all applied deposition methods.

Acknowledgements

References

[1]   W.Dworschak, K.Jung and H.Ehrhardt, Diamond and Related Materials 3 (1994) 337.
[2]   A.Weber, U.Bringmann, R.Nikulski and C.-P.Klages, Surf.Coat.Technol. 60 (1993) 493.
[3]   M.Murakawa and S.Watanabe, Surf.Coat.Technol. 43/44 (1990) 128.
[4]   D.J.Kester and R.Messier, J.Appl.Phys. 72 (1992) 504.
[5]   D.L.Medlin, T.A.Friedmann, P.B.Mirkarimi, P.Rez, M.J.Mills and K.F.McCarthy, J.Appl.Phys. 76 (1994) 295.
[6]   M.Mieno and T.Yoshida, Jpn. J. Appl. Phys. 29 (1990) L1175.
[7]   K.Bewilogua, J.Buth, H.Hübsch and M.Grischke, Diamond and Related Materials 2 (1993) 1206.
[8]   N.Tanabe, T.Hayashi and M.Iwaki, Diamond and Related Materials 1 (1992) 883.

[9]   N.Tanabe and M.Iwaki, Diamond and Related Materials **2** (1993) 512.
[10]   D.G.Rickerby, P.N.Gibson, W.Gissler and J.Haupt, Thin Solid Films **209** (1992) 155.
[11]   C.Mitterer, P.Losbichler, W.S.M.Werner, H.Störi and J.Barounig, Surf.Coat.Technol. **54/55** (1992) 329.
[12]   H.Lüthje, K.Bewilogua, S.Daaud, M.Johansson and L.Hultman, Thin Solid Films **257** (1995) 40.
[13]   L.B.Hackenberger, L.J.Pilione, R.Messier and G.P.Lamaze, J. Vac. Sci. Technol. A **12** (1994) 1569.
[14]   M.D.Wiggins and C.R.Aita, J. Vac. Sci. Technol. A **2** (1984) 322.
[15]   K.H.Seidel, K.Reichelt, U.Schaal and H.Dimigen, Thin Solid Films **151** (1987) 243.
[16]   C.R.Aita, Materials Science Forum **54/55** (1990) 1.
[17]   A.Schütze, K.Bewilogua, H.Lüthje, S.Kouptsidis and S.Jäger, Surf.Coat.Technol. (in press).
[18]   M.Fryda, K.Taube and C.-P.Klages, Vacuum **41** (1990) 1291.
[19]   S.Jäger, K.Bewilogua and C.-P.Klages, Thin Solid Films **245** (1994) 50.
[20]   S.Reinke, M.Kuhr and W.Kulisch, Surf.Coat.Technol. (in press).
[21]   D.J.Kester, K.S.Ailey, R.F.Davis and K.L.More, J.Mater.Res. **8** (1993) 1213.
[22]   N.V.Novikov, Yu.V.Sirota, V.I.Malnev and I.A.Petrusha, Diamond and Related Materials **2** (1993) 1253.
[23]   A.K.Ballal, L.Salamanca-Riba, C.A.Taylor II and G.L.Doll, Thin Solid Films **224** (1993) 46.
[24]   H.Hofsäss, C.Ronning, U.Griesmeier, M.Gross, S.Reinke, M.Kuhr, J.Zweck and R.Fischer, submitted to Nucl. Instr. and Meth. B.
[25]   D.R.McKenzie, W.D.McFall, W.G.Sainty, C.A.Davis and R.E.Collins, Diamond and Related Materials **2** (1993) 970.
[26]   R.W.Lynch and H.G.Drickamer, J. Chem. Phys. **44** (1966) 181.

SYNTHESIS OF NITRIDES FROM MICROWAVE NITROGEN PLASMA

Andrzej Badzian, Teresa Badzian, and William Drawl

Materials Research Laboratory, The Pennsylvania State University, University Park, PA 16802, United States

Key words: carbon-nitrogen compounds, nitrides, nitrogen plasma, Si-N-C system

Abstract

We have undertaken a study on ternary nitrides as wide band gap materials for prospective electron emitters. A nitrogen plasma ignited inside a tuned 2.45GHz microwave cavity is chemically reactive. Both diamond and graphite are etched by this plasma. Disordered diamond crystals have been synthesized from mixtures of CH_4 and N_2. Attempts to make C_3N_4 have failed. Instead, disordered diamond particles embodied in amorphous para-cyanogen were obtained. It creates doubt that such a compound exist. However, these facts demonstrate the valuable chemical reactivity of nitrogen plasmas and point to novel synthesis of nitrides. A crystalline phase within the Si-N-C system was obtained when the surface of a silicon wafer was exposed to species created by etching graphite immersed in a nitrogen plasma. Crystals with square shape 3-5μm in size having a distinct x-ray diffraction pattern were produced.

1. Introduction

Among a variety of approaches to nitrides synthesis, one is accomplished by direct interaction of elements with nitrogen. The nitrogen molecule has a high dissociation energy of 225 kcal/mole [1]. This paper considers formation of nitrogen plasmas in a microwave cavity as a means for activation of molecular and possibly atomic nitrogen. The chemical reactivity of a nitrogen plasma depends on the excited states of N_2, N_2^+ and the formation of atomic nitrogen. Active nitrogen is a useful research tool to study nitrides formation. This paper reports on the synthesis of phases in the C-N and Si-N-C systems.

2. Synthesis of Nitrides

Prospective applications for nitrides has renewed interest in the synthesis and properties of these materials [2,3]. Materials such as hexagonal and cubic BN, Si_3N_4, TiN and Ti(C,N) have become useful materials throughout the world.

A review of nitride properties and methods of synthesis was performed by Samsonov in 1969 [1]. Since this time nitrides have faced new challenges. Expectations were and are high for low pressure synthesis of cubic BN but not much progress has been

made to increase the grain size from the nanometers range as documented in the early seventies. Issues of doping of diamond with nitrogen and existence of a β-C_3N_4 phase which is predicted to be harder than diamond have introduced confusion with no clear conclusion reached.

The discovery of negative electron affinity of AlN supports focus on wide band gap nitrides as electron emitters [4]. We believe that experiments with active nitrogen can contribute to the synthesis of new ternary phases as a prospective electron emitters.

3. Active Nitrogen

The term "active nitrogen" has been taken to refer to any excited form of nitrogen, molecular or atomic [5]. Active nitrogen has a limited number of excited species, for example: excited nitrogen atoms and molecules, as well as other species such as N_2 and results of their recombination. Molecular nitrogen can be thermally activated by a tungsten filament above 2000K as it was demonstrated in 1966 [6,7]. Dissociation of molecular nitrogen on or near the filament appears to be followed by partial desorption into the gas phase as N atoms. In a similar fashion a microwave cavity was used to obtain a nitrogen discharge over the range 0.01 to 100 Torr [8].

4. Carbon Nitride

No reliable evidence exists at this moment for a crystalline phase in the binary C-N system. The only known solid compound is paracyanogen, a polymer which may have a condensed polycyclic structure. Trace amounts of impurities have been shown to facilitate polymerization of cyanogen $(CN)_2$ to a dark solid at 300-500°C [9,10].

In our experiments with a microwave plasma C-H-N and C-N gas systems have been studied. Deposition from CH_4+N_2 mixtures resulted in diamond films in which the atomic structure has been disturbed and displays ABCABC cubic stacking [11]. Although deposits obtained from $CH_4+N_2+H_2$ do not contain nitrogen. Analysis by Auger electron spectroscopy and by x-ray photoelectron spectroscopy revealed only carbon in the films. The sensitivity for nitrogen detection by these methods is about 0.5 atomic %. No nitrogen was found according to cold neutron depth profiling performed at the National Institute of Standards and Technology. The detection limit for nitrogen is $4.5 \cdot 10^{15}$ at/cm^2 which is ~250 atom ppm for 1μm thick layer [12]. We believe that formation of HCN takes place during the process. The abstraction of hydrogen can be done by CN radicals and vice versa. However, nitrogen was not incorporated into the diamond lattice because it does not dwell on the diamond surface.

Etching-deposition experiments were performed on a strip of graphite [13]. The top of the strip was heated to 1100°C by N_2-H_2 plasma. Deposition appeared on cooler region ~600°C. The deposit was composed of soft material with hard inclusions. The hard inclusions were found to be particles of disordered diamond. The soft material was composed of graphite fibers. The microstructure of these fibers were distinctly different from fibers grown with a metal catalyst. The stacking of graphite planes was perpendicular to the axis of the fiber in contrast to the parallel orientation in the metal catalyst grown fibers. These results were obtained by dark field TEM images.

In summary the experiments with the C-H-N gas system did not give any clue to formation of a C-N crystalline phase. However, they did demonstrate the influence of N on the growth processes.

Study of C-N gas system was conducted using solid carbon (diamond) and a nitrogen plasma. A ball shaped plasma was formed when nitrogen gas was passed through a tuned microwave cavity as shown in Fig. 1. No hydrogen was added. The plasma ball was formed at pressures higher than 25Torr. At lower pressures the luminous plasma trends to locate near the silica tube wall. At 80Torr, the plasma appears to have a pink color, while at other conditions it appears yellow or green in color.
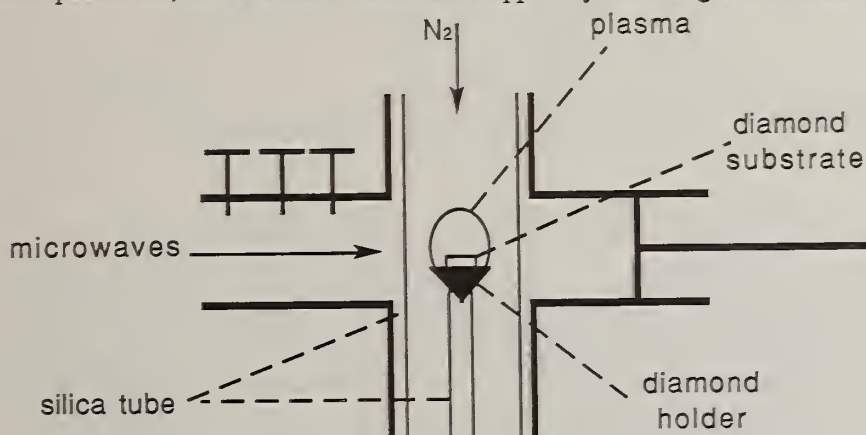
Fig. 1. Etching of diamond in microwave reactor

A natural diamond crystal placed in the reactor (Fig. 1) undergoes etching at 1000°C and 80Torr. Deep pores are formed on the (001) surface and the microfacets (111) are etched much faster. As a result a soft, black material was deposited onto the cold silica wall. Raman spectra taken from this material does not show any signature. We believe that CN radicals are formed during the etching of diamond and that they condense on the wall as paracyanogen.

A different interaction with the plasma was observed for a CVD diamond film grown on a natural diamond substrate. A black deposit was formed when the crystal was heated up to 1150°C for 15 minutes at 80Torr in a nitrogen plasma. This deposit was formed on the top of the CVD diamond film. It was composed of a soft material and hard microcrystal agglomerates. The Raman spectra does not indicate graphite for the soft material. Auger electron spectroscopy indicates C and N. Preliminary data from electron diffraction taken from microcrystal agglomerates does not show any similarity to β-C_3N_4 structure which has been previously described [14-17].

5. Preparation of a Si-N-C Phase

Experiments dealing with the formation of a ternary phase Si-N-C were conducted in the apparatus shown in Fig. 2. It is proposed that CN radicals are created during etching of graphite by nitrogen. The graphite temperature was 1150°C and the deposition took place on mirror polished (001) silicon wafer at 1020°C. The nitrogen
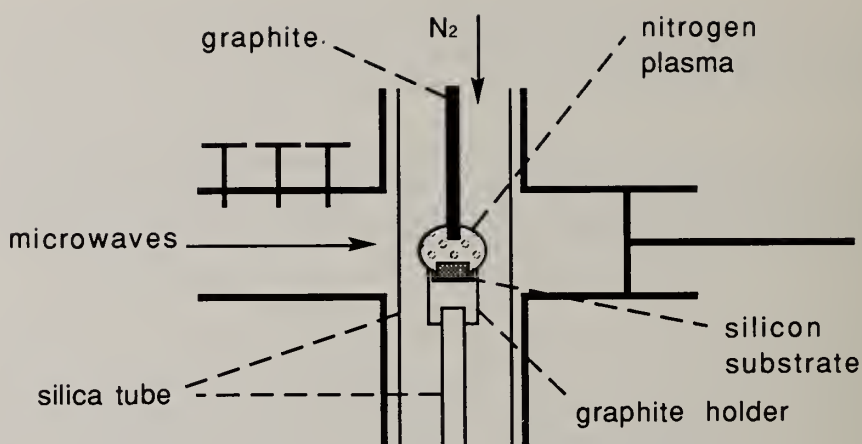
Fig. 2. Synthesis of a Si-N-C phase in microwave reactor.

pressure was 50Torr and the distance between graphite and Si was 6mm. Microcrystals shown in Fig. 3 are grown during an 18 hour exposure. Qualitative chemical analysis by electron microprobe indicates elements of Si, N and C are present. The ratio of Si to N is close to one and content of carbon is at a few atomic percent. The analysis was conducted at a low acceleration potential for electrons so the Si substrate did not interact with electrons. The areas between crystals shown in Fig. 3 did not show the presence of nitrogen, only Si and C were detected. The corresponding x-ray diffraction pattern does not fit to α- and β-Si_3N_4 phases. The Si-N-C phase is not listed in the x-ray power diffraction files.
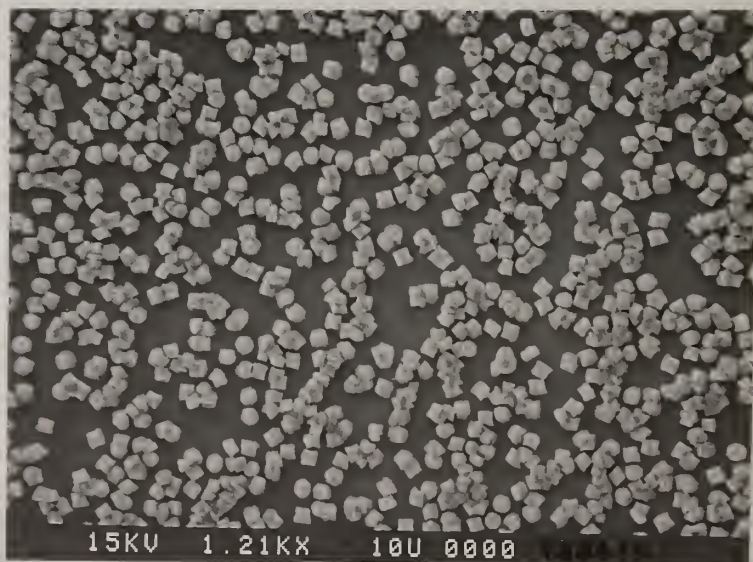
Fig. 3. Secondary electron image of Si-N-C crytals. Bar 10μm.

6. Conclusion

The chemical reactivity of microwave nitrogen plasma was demonstrated in experiments on the etching of diamond surfaces and the formation of C-N and Si-N-C phases.

The hypothetical β-Ci_3N_4 phase was not found in our experiments. Active nitrogen has attracted a lot of attention in the past but the role of nitrogen in the growth processes of diamond, graphite and the influence of atomic nitrogen on phase equilibria of nitrides requires a new inquiry.

7. Acknowledgments

8. References

1. G.V. Samsonov, Nitrides, Kiyev, Naukova Dumka (1969), English translation FTD-MT-24-62-70.
2. S. Strite and H. Morkoc, J. Vac. Sci. Technol. B10 (1992) 1237.
3. R.F. Davis, Proceedings of the IEEE 79 (1991) 702.
4. M.N. Yoder, SPIE, Diamond-Film Semiconductors 2151 (1994) 72.
5. A.N. Wright and C.A. Winkler, Active Nitrogen, Academic Press, New York (1968).
6. S.B. Nornes and E.E. Donaldson, J. Chem. Phys. 44 (1966) 2968.
7. V.J. Mimeault and R.S. Hansen, J. Phys. Chem. 70 (1966) 3001.
8. A.D. MacDonald, D.V. Garskell and H.N. Getterman, Phys. Rev. 130 (1963) 1841.
9. N.V. Sidgwick, "The Organic Chemistry of Nitrogen," Oxford at the Claredon Press (1942) pp. 300-302.
10. N.N. Greenwood and A. Earnshaw, "Chemistry of Elements," Pergamon Press, Oxford (1993) p. 336.
11. A. Badzian, T. Badzian and S.-Tong Lee, Appl. Phys. Lett. 62 (1993) 3432.
12. G.P. Lamaze, A. Badzian, T. Badzian, R.G. Downing and L. Pilione, Advances in New Diamond Science and Technology, S. Saito et al. (eds.), MYU, Tokyo (1994) p. 341.
13. A. Badzian and T. Badzian, SDIO/IST-ONR Diamond Technology Initiative Symposium 11-13 July 1989, Crystal City, Virginia, Abstract W5.
14. A.Y. Liu and M.L. Cohen, Science 245 (1989) 841.
15. K.M. Yu, M.L. Cohen, E.E. Haller, W.L. Hansen, A.Y. Liu and I.C.. Wu, Phys. Rev. B 79 (1994) 5034.
16. C. Niu, Y.Z. Lu and Ch.M. Lieber, Science 261 (1993) 334.
17. M.Y. Chen, X. Lin, V.P. Dravid, Y.W. Chung, M.S. Wong and W.D. Sproul, Surf. Coat. Technol. 54, 55 (1992) 360.

845

EXCIMER LASER INDUCED CHEMICAL VAPOR DEPOSITION OF BORON NITRIDE FILMS.

V.P.Ageev, V.I.Konov, M.V.Ugarov

General Physics Institute, 38 Vavilov str., 117942 Moscow, Russia

Key words: CVD, boron nitride, excimer laser

Abstract

The radiation of KrF pulsed excimer laser was used for the deposition of thin BN films from the vapor phase containing borazine ($B_3N_3H_6$). The dependencies of the film deposition rate upon borazine pressure, laser fluence and substrate were obtained. The composition and the structure of the deposited boron nitride was analysed by means of Raman scattering spectroscopy and Auger electron spectroscopy, which showed that stoichiometric hexagonal boron nitride is the main component of the deposited films. A simple deposition model is proposed, which takes into account chemisorption and partial decomposition of borazine molecules on the substrate surface between laser pulses and final decomposition of the intermediate product during the laser pulse.

1. Introduction

Boron nitride is one of the most interesting III-V group compounds. The "boron-nitrogen" atomic system is isoelectronic with a couple of carbon atoms, so boron nitride and carbon exist in the same allotropes (hexagonal and cubic BN are analogues of graphite and diamond, respectively). This similarity provides similar material properties [1]. In some aspects c-BN even has some advantages as compared to diamond, since it is more stable with respect to the cubic-to-hexagonal transition, to oxidation in the air, and some others. Besides, the BN-films can be easily doped during the growth by variety of impurity atoms supplying either n- or p-type of electrical conductivity, that expands significantly the area of BN-applications in a wide band semiconductor electronics.

At the present time various methods of chemical vapor deposition (CVD) and physical vapor deposition (PVD) of BN films stimulated by various external energy sources are known [2-7]. Interesting results has been obtained in experiments [8] on plasma CVD of BN coating with the parallel enhancement of c-BN nucleation by excimer laser radiation, which creates new possibilities for selective area BN film deposition with high space resolution.

By the present work we extend the area of laser applications for the BN deposition. The results of thermal induced CVD process by the direct action of multi-pulsed UV laser radiation on solid surface in borazine atmosphere are reported.

In experiments the KrF excimer laser was used emitting 17-ns pulses of the 248-nm radiation with pulse repetition rate up to 50 Hz. A projection optical scheme was applied to provide an uniform illumination of substrate surface over the area of $0.6 \times 1.2 \text{mm}^2$. Irradiation was performed in a stainless steel vacuum chamber equipped with a system of sample heating (in the temperature range of $T = 20\text{-}400°C$) being pumped out to the base pressure of 10^{-8} Torr. Electronic quality c-Si wafers with surface orientation <100> were used as substrates. Before experiments substrates were developed by the 40% water solution of NH_4F to remove the natural oxide. Borazine $(B_3N_3H_6)$ was used as a monocomponent gaseous precursor.

2. Experimental results and discussion

In the experiments it is important to avoid laser-induced substrate melting, i.e. the pulsed laser fluence (E) is to be confined by the melting threshold of c-Si ($E_m \approx 0.5 \text{ J/cm}^2$ for KrF laser radiation with $t_{FWHM} = 17$ ns). Otherwise, a capillary instability of a liquid surface layer results in the significant surface corrugation of the film [9].

It was experimentally demonstrated that during the initial period of laser irradiation the reflectance from the substrate (R) diminishes gradually from the initial value of $R = 0.6$ typical of a clean c-Si surface to the value of $R = 0.15$. Thus the positive feedback in the radiation supplies the additional fluence restriction and the upper limit of laser fluence should be twice lower than the c-Si surface melting threshold. Let us note, that a deposition restriction via a laser evaporation effect is out of question here, since the laser ablation threshold of BN-film ($E \sim 0.5 \text{ J/cm}^2$) appeared to be far above this limit.

A deposition kinetics in our experiments was studied in terms of dependencies of film growth rates on pulsed laser fluence, substrate temperature and vapor pressure, where pulsed average rate (V) was derived from film thickness (H) and number of laser shots (N) $V = H/N$. It was demonstrated that the deposited film thickness was proportional to the number of pulses. Some typical data of the deposition kinetics are presented in Fig.1 and Fig.2. As seen from the first one all dependencies of deposition rates on laser fluence have well-distinguished maxima at a certain optimum fluence value of $E \sim 0.15 \text{ J/cm}^2$, these "optimum" rates being dependent of substrate temperature in a non-trivial manner, as shown in Fig.2. Under optimum conditions BN film deposition rate of the order of 1A per pulse was realised.

Experiments carried out at various values of vapor pressure in the range of $P = 0.1\text{-}5$ Torr showed the deposition rate to have linear dependence on pressure for all substrate temperatures.
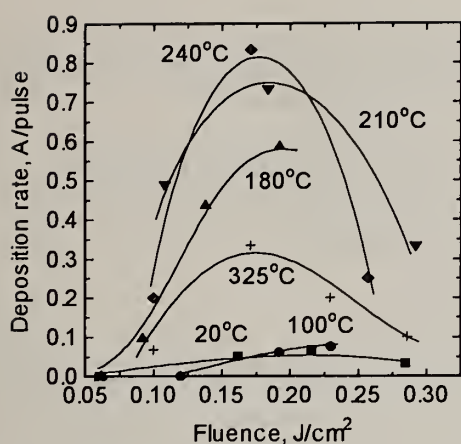
Fig.1. Dependencies of film deposition rate upon laser fluence at various substrate temperatures.

Fig.2. Dependence of deposition rate upon substrate temperature.
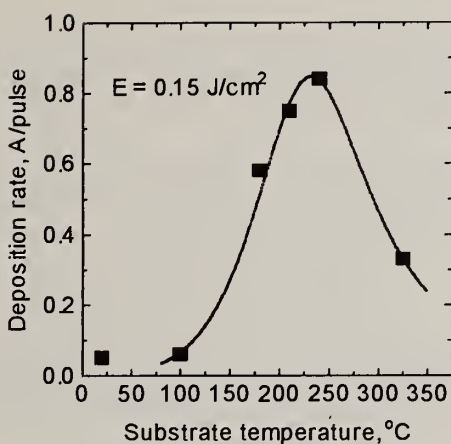
Auger electron spectroscopy (AES) analysis showed the BN film chemical content to be close to stoichiometric practically through the whole film thickness. An interesting side result, demonstrated by profile AES analysis, consisted in the fact that film atoms penetrated into the c-Si substrate surface layer even at laser intensities below the melting. It provides the possibility of laser induced surface doping of c-Si substrate parallel to the laser induced CVD of BN film.

The film crystallinity was analysed by Raman spectroscopy in the vicinity of active vibrational modes in h-BN and c-BN [10]. Comparison of deposited film spectra, which demonstrated the evident peak near 1365 cm^{-1}, with known reference ones showed that under near to optimum conditions the film structure approached that of h-BN rather than a-BN or c-BN. It was also demonstrated that the films with the best structure were grown under the same conditions that were characteristic of the highest deposition rate.

The presented results ensure us that the pulsed laser CVD of BN-film proceeds, mainly, in the following way: the deposition is going due to the pulsed thermally induced adlayer decomposition, the adlayer being formed at the surface during the time interval between laser shots. From this standpoint many features of deposition kinetics become qualitatively transparent. Nevertheless, it appears to be impossible to understand some of them (such as the deposition rate dependence on the substrate temperature shown in Fig.2) without additional information on the adlayer structure.

Certain information concerning it may be taken from the experimental results of TPD of $B_3N_3H_6$ from the surfaces of mono crystalline Si and a-BN [11]. It was shown that two

molecular phases are present in the adsorbed layer - multilayer physisorbed (Φ) and weakly chemisorbed (A). To explain the obtained experimental results we suppose the existence of another one, more strongly bonded borazine phase (Γ).

The deposition process may be considered consisting of two independent stages:
1. Processes of adsorption and decomposition of borazine molecules on the surface in the intervals between laser pulses. These are the main reactions:

Borazine (vapor) $\Leftrightarrow$ Borazine (A-phase),

Borazine (A-phase) $\Leftrightarrow$ Borazine (Γ-phase).

2. Processes occurring during thermal pulse generated by a laser pulse. The thermal decomposition of Γ-phase generated on the surface during the first stage plays the main role in the formation of the final deposit.

In this terms the curve of Fig.2 represents the dependence of the equilibrium surface concentration θ_Γ upon surface temperature. Its shape is determined by the competition of two reversible reactions taking place at the first stage. The curved line is an approximation of the experimental points based on the kinetic equations written for these reactions.

The initial increase of the deposition rate as the pulse fluence rises (Fig.1) should be attributed to the thermal activation of Γ-phase decomposition reaction obeying the Arrhenius-type activation law. The existence of maxima in all V(E)-curves and subsequent decrease in deposition rate values must be connected with the process limitation by thermal desorption of adlayer particles of the same phase.

A more detailed mathematical description of all the processes will be reported elsewhere.

3. References

1. R.C.DeVries, in R.E.Clausing (ed.), Diamond and Diamond-like Coatings, Plenum press, N.Y., 151 (1991).
2. T.Takahashi, H.Itoh, and M.Kuroda, J. Cryst. Growth **53**, 418 (1981).
3. O.Gafri, A.Grill, D.T.Itzhak, A.Inspektor, and R.Avni, Thin Solid Films **72**, 523 (1980).
4. M.Sokolowski, A.Sokolowska, A.Ruzek, Z.Romanowski, B.Gokieli, and M.Gajewska, J. Cryst. Growth **52**, 165 (1981).
5. M.Satou and F.Fujimoto, Jpn. J. Appl. Phys. **22**, L171 (1983).
6. G.Kessler, H.-D.Bauer, W.Pompe, and H.-J.Sheibe, Thin Solid Films **147**, L45 (1987).
7. G.L.Doll, J.A.Sell, C.A.Tailor II, and R.Klarke, Phys. Rev. B **43**, 6816 (1991).
8. S.Komatsu, Y.Moriyoshi, M.Kasamatsu, and K.Yamada, J. Appl. Phys. **70**, 7078 (1991).
9. I.Ursu, I.N.Mihailescu, Al.Popa, A.M.Prokhorov, V.P.Ageev, A.A.Gorbunov and V.I.Konov, J. Appl. Phys **58**, 3909 (1985).
10. D.M.Hoffman, G.L.Doll, and P.C.Eklund, Phys. Rev. B **30**, 6051 (1984).
11. C.Chiang, S.M.Gates, D.Beach, Surf. Sci. **261**, 88 (1992).

Effect of the Growth Process on Boron Nitride Thin Films Electrical Properties.

N. Badi, A.Bousetta [a)], M. Lu, and A.Bensaoula

Space Vacuum Epitaxy Center, University of Houston, Houston, Texas 77204-5507

Key words: ECR, c-BN, conductivity, ions, neutrals

Abstract

Boron nitride thin films were grown on Si substrates using electron cyclotron resonance (ECR) plasma-, ion beam (IBD), and neutral beam- (NBD) assisted vapor depositions. The electrical properties of the BN films were investigated using Hall measurements. It was found that the films grown by NBD technique where p-type, those grown by ECR technique where n-type, whereas those grown by IBD where either n- to p-type depending on the ion energy. The composition of the films was investigated using EPMA, and it was found that most films were off-Stoichiometric (B/N ≤ 1 for ECR and B/N> 1 for NBD and IBD). The B/N ratio was higher for IBD BN films (up to 22 %). A model based on native defects centers (nitrogen vacancy and boron anti-site) is presented to account for the conductivity of the BN films.

[a)] corresponding author:

1. Introduction

Cubic boron nitride(c-BN), because of its very wide bandgap (> 6.1 eV) and the possibilities of both p- and n-type doping, is a very attractive material for high temperature electronic devices. Although there is increasing effort in synthesizing c-BN at low pressure, very little information are given on the electrical properties of as-grown, and n- or p-type doped BN material.

Introducing c-BN into electronic devices requires materials with adequate quality and the fabrication of p- and n-type conductivity regions with controlled impurity. Up to date the only cBN p-n diodes were produced under high pressure and high temperature conditions. In fact Mishima et al [1] have fabricated p-n junctions using Be for p-type and Si for n-type doping. Preliminary attempts on the effect of doping boron nitride thin films with aluminum and zinc impurities did not yield significant results [2]. Recently Bar-Yam *et al.* [3] examined theoretically the conduction type in as-deposited BN films in relation with the growth conditions and stoichiometry.

The challenge encountered in making reliable and high performance BN electronic devices is the difficulty to grow BN films with a high cubic phase content. Stabilizing this material in its cubic phase will allow a better control of the doping concentration. A number of different techniques have been described for the growth of BN films using a variety of deposition process [4-10]. Most of these techniques use an energetic plasma to enhance the growth of c-BN. The arrival rate of atoms at the surface is kept low enough to ensure that these atoms can migrate along the surface to a surface step and be incorporated. In general the c-BN formation requires a hybridization change from sp^2 to sp^3 accompanied by a reduction of the interplanar spacing which cannot be accomplished without both a bond breaking and a change in the chemical nature of the bond. It is clear that without energetic species, the BN films will stabilize in the hexagonal structure. The role of the energetic ions is to break the bonds of surface atoms and provide the kinetic necessary for cBN formation.

In this work we have used three different techniques to grow cubic (>80 %), mixed cubic/hexagonal (10-20 %) and hexagonal BN thin films. We have recently reported the successful growth of Stoichiometric BN films on Si(100) with a cubic phase content >80 % using neutralized nitrogen ion bombardment [11].

The aim of the present work is to understand the effect of the growth techniques on the structural and electrical properties of BN thin films. A model based on native defects centers (nitrogen vacancy and boron anti-site) is presented to account for the conductivity of the BN films.

2. Experiment

Fig. 1 shows a schematic diagram of the experimental apparatus. The latter consist of a neutralizer atomic beam source (NABS) adapted to a 3 cm diameter Kaufman-type ion source to deliver nitrogen species (the neutralizer can be easily removed to allow for direct ion bombardment), an electron cyclotron resonance (ECR) and electron beam evaporators for boron and carbon. Prior to deposition, silicon substrates were degreased using standard solvents, etched in a 10 % HF solution, rinsed in DI water and dried with nitrogen. The substrates were thermally cleaned in situ at 850 °C for 15 min. The substrate temperature was maintained at 450 °C during film deposition. Bombardment of the sample was done using either pure nitrogen gas (ECR) or nitrogen mixed with argon (IBD or NBD) by changing the mixed ratio of nitrogen to argon gas fed into the ion source, while keeping a constant pressure of 3×10^{-4} Torr in the ion source chamber. The background gas pressure in the growth chamber was 4×10^{-8} Torr which rose to 10^{-5} - 10^{-4} Torr during deposition.
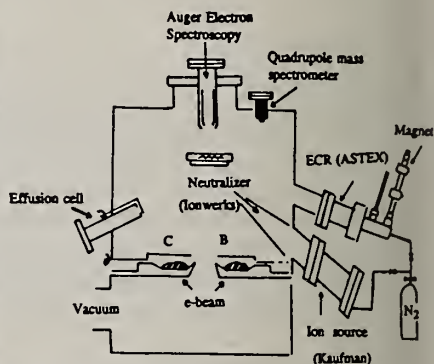
Fig. 1 schematic diagram of the experimental apparatus. The neutralizer beam source is shown fitted to a Kaufman source.

Boron (99.9%) was evaporated from an electron beam evaporator at a rate maintained at 0.2 Å/s. All the results presented were achieved using identical growth conditions (T_S = 450 °C, B rate = 0.2 Å/s, 50:50 N_2/Ar for neutral and ion assisted growth and pure N_2 for ECR-assisted growth). The boron flux was controlled using quartz thickness monitor located above the substrate. The fraction of cubic BN in the films was analyzed by Fourier Transform Infrared Spectroscopy (FTIR) which is the most commonly used technique to quantitatively characterize the cBN content of thin films. The film thickness and stoichiometry (B/N ratio) were determined using electron probe microanalysis (EPMA). The film resistivity and conductivity-type of the c-BN films were investigated by Hall measurements.

3. Results

FTIR spectra of BN films deposited using the three above mentioned growth techniques are shown in Fig. 2 (a to c). The measurements indicated that the BN films deposited using the neutralized nitrogen beam have a very high percentage of cubic phase (80 %), those deposited with ions are mixed hexagonal-cubic with only 10-20 % cubic, and those deposited using ECR-assisted growth were pure hexagonal. In Table 1 are reported the electrical properties of BN films as measured by Van der Pauw technique. The results show that the NABS and most of the ions-assisted deposited BN films are p-type. However, the NABS assisted deposited BN films, although more cubic, have lower resistivities than those deposited by ion-assisted technique. On the other hand the films deposited by ECR-assisted technique were n-type with a much lower resistivity.

Table 1: Electrical properties vs. growth techniques

Technique	ECR	NBD	IBD
Phase	hexagonal	80% cubic	20 % cubic
Type	n	p	n or p
$\rho(\Omega\text{-cm})$	0.01 - 0.1	0.1 - 1.0	1 - 24
N (cm^{-3})	10^{17}-10^{18}	10^{16}-10^{17}	10^{14}-10^{15}
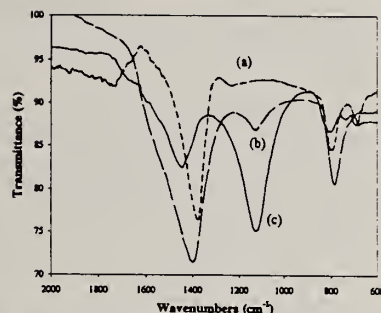
Fig. 2 Infrared transmission spectrum of BN films deposited at 500 °C with different nitrogen sources (a) ECR (b) Kaufman and (c) Kaufman/Neutralizer.

In order to understand the above results, it is worth mentioning the different features of the techniques used in this work. ECR is a known technique which generate species (ions and neutrals) with energies in the range 20 to 30 eV and the Kaufman source produces more energetic species (100-1000 eV). Note that the ion beam energy used in this paper was in the range of 300 to 600 eV. On the other hand the neutralizer is a tool which not only neutralizes the ions produced by the Kaufman source but also decreases their energy (50 to 100 eV). It also increases and focuses the nitrogen beam.

As we mentioned earlier the BN films deposited by ECR-assisted technique were: hexagonal, n-type, and have low resistivity. The B/N ratio as estimated by EPMA was in the range of 0.97 -1.00. In the ECR process, boron is evaporated towards the substrate and at the same time nitrogen gas is squinted through a radio-frequency discharge spark. The plasma condition develops a negative dc bias at the substrate and the potential difference between the plasma and the substrate accelerate the ions toward the latter. The fact that no cubic phase was found in the films suggests that the ions involved in the ECR process did not provide enough energy to destabilize the hexagonal structure and allow a cubic phase formation.

The appearance of the cubic phase (10-20%) in the BN films grown using the Kaufman source confirm the effect of ion energy on the kinetic of the c-BN formation. Although our growth conditions (energy, substrate temperature etc...) were similar to that of Kester and Messier [12], the cubic content in our films was much lower. Most of the BN films obtained using this technique were p-type and have a B/N ratio in the range of 1.11- 1.12. Note that when low energy ion   (300 eV) was used, the B/N was up to 1.22 and the BN films obtained were n-type. The films are much more resistive (1 to 24 Ωcm) as compared to those obtained by the ECR process (0.1 to 0.01 Ωcm).

Using the neutralized beam technique, the cubic phase of the films was higher (80 %) and the B/N was in the range 1.04-1.05. The latter is smaller than that obtained using ions suggested that more nitrogen is incorporated into the film.

2. Discussion and proposed model

It is common knowledge that the most probable point defect in cubic boron nitride is a Schottky defect i.e., a vacancy in the cation or anion sublattices. This mechanism has been theoretically analyzed in the framework of a quasichemical approximation in which point defects of non-stoichiometric origin in c-BN are also predicted [13]. The presence of interstitial defects is not excluded when boron nitride films contain a mixed amorphous-hexagonal-cubic. These defects are accommodated within the amorphous and/or hexagonal

regions of the film. This is possible because of the wide spacing between sp²-hybridized layers and the weak interlayer π bonds.

The n-type conductivity of the pure hexagonal films grown by ECR techniques is mainly related to native defects more probably nitrogen vacancies which behave like an intrinsic donor centers. An electron trapped in one donor state can move over to another state in its spacial neighborhood provided that the latter is not occupied. However the B/N ratio was in the range 0.97- 1.00 suggesting that there is more nitrogen into the film. To explain why nitrogen vacancies are present, one might suggest that the nitrogen species migrate to either interstitial sites or to some amorphous regions present in the film as shown in Fig. 3-a. We have also investigated the incorporation of C during growth using e-beam evaporated graphite. The BN films were hexagonal but p-type. The change in conductivity from n to p-type can be due to the reduction of the electronic delocalization on B neighbors. The presence of carbon doping or cluster of carbon atoms stabilize the electron in a nitrogen vacancy due to fast electron exchange possibility. In this way the carbon atom behaves like an acceptor and leads to p-type conductivity.

In ion-assisted growth process, especially at low energy (300 eV), the penetration depth of nitrogen ions is very shallow. Hence, the irradiated region of the target condenses to a nitrogen deficient material resulting in non-stoichiometric, boron-rich films. This behavior leads to nitrogen vacancies in our films and obviously intrinsic donor centers and could explain why IBD deposited BN films were n-type.

One way of limiting the nitrogen out diffusion is to increase the ion energy. In fact the BN films grown at much higher energy (500-600 eV) have a much lower B/N ratio. However the conductivity of the films was p-type suggesting that mechanisms other than N vacancies is taking place. We suggest that, with these energetic species, damage and defect formation would occur. This not only impedes the formation of the cubic phase but also changes the local composition of the films. Recoiled atoms leave the surface (sputtered) or are deposited at sites different from their original one (antisites). The more likely site to be occupied by B is nitrogen vacancies. The resulting B (N) antisite will be ionized by an electron moving from a N vacancy to another (see Fig. 3-b). The ionized boron antisite B⁻(N) will possess an effective negative charge which makes it an acceptor center and explains the p-type conductivity of BN films.
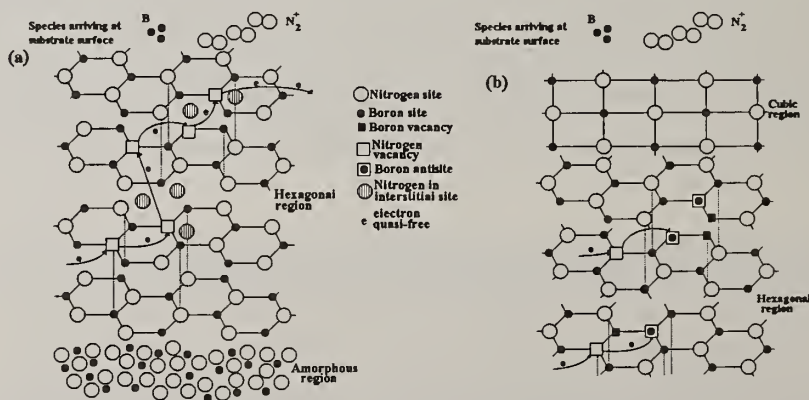
FIG.3 N vacancies and B antisites mechanism in ECR (a) and IBD deposition process (b).

The BN films deposited by NBD were all p-type and have resistivities lower than those deposited using IBD. We have reported [11] that the neutralizer atomic beam source is capable of delivering a high flux, low energy, and focused nitrogen beam. This technique will increase the amount of nitrogen arriving at the target and compensate for nitrogen out diffusion. The low energy regime will reduce sputtering and defect formation. In fact B/N ratios near unity (1.04-1.05) suggest that the films are stoichiometric with few N vacancies and B antisites. Hence the p-type conductivity measured in the NBD BN films could be more explained by the presence of contaminants into the films than B anitsites. In fact SIMS result did show the presence of low levels of Fe, Ni, and Cr contaminants which may have been due to the deposition process using stainless steel neutralizer. Several modifications of the neutralizer cone which would eliminate this contamination are being made by Ionwerks.

4. Conclusion

Three techniques: ECR, IBD, and NBD were used in this project to deposit BN thin films on Si(100). The use of these techniques allowed for both nitrogen ions and neutrals to be used. It was found that BN films deposited with NBD were p-type, those deposited using ECR were n-type and those deposited using IBD were either n- or p-type depending on the ion energy. A model suggesting nitrogen vacancies for n-type films and boron antisite or impurities for p-type is proposed.

Acknowledgment

References

1. O. Mishima, K. Era, J. Tanaka, and S. Yamoka, Appl. Phys. Lett. **53**, 962 (1988)
2. N. Ahmad and D.Lichtman, Sensors and Actuators.18,397 (1989)
3. Y. Bar-Yam, T. Lei, T.D. Moustakas, D.C. Allan and M. P. Tejer, Mat. Res. Soc. Symp. Proc. **242**, 335 (1992)
4. M.Mieno,T.Yoshida, and K.Akashi, J.Jpn.Inst.Metals **52**, 199 (1988)
5. M.Mieno,T.Yoshida, surf.coatings technol. **52**, 87 (1992)
6. T.Wada and N.Yama Shita, J.Vac,Sci.Technol. A**10**, 515 (1992)
7. N.Tanabe, T.Hayashi, and M.Iwaki, Diamond and Related Materials **1**, 883 (1992)
8. A.K.Ballal, L.Salamanca-Riba, G.L.Doll, C.A.Taylor,and R.Clarke, J.Mater.Res.**7**, 1618 (1992)
9. D.J.Kester, K.S.Ailey, R.F.Davis, and K.L.More, J.Mater.Res **8**,1213 (1993)
10. A.Weber *et al.*, J.Phys. III (Paris) **2**,1931(1992)
11. Ming Lu, A. Bousetta, R. Sukach, A. Bensaoula, K. Walters, and J. A. Schultz Appl. Phys. Lett. **64**, 1514 (1994)
12. D. Kester and R. Messier, J. Appl. Phys. **72**, 504 (1992)
13. A.P.Garshin and V.E.Shvaĭko-Shvaĭkovsii, Phys.Solid.State. **36**, 159 (1994)

THEORY OF IMPURITY VIBRATIONS IN CUBIC BORON NITRIDE AND BORON PHOSPHIDE

D. N. Talwar

Department of Physics, Indiana University of Pennsylvania, Indiana PA 15705-1087

Abstract

Using a phenomenological lattice dynamical scheme in the Greens function framework we have studied the phonon modes in both perfect and imperfect cubic boron nitride and boron phosphide. A novel optimization procedure is considered for determining the eleven force constant parameters of a second-nearest neighbor Rigid-ion model. Simple perturbation models are used for describing the impurity vibrations of isolated defects. Good agreement with the experimental data is obtained, whenever a comparison is possible: in fact most of the results are predictions.

Key words: Lattice dynamics, Green's function, Infrared absorption, Raman scattering, impurity modes

1. Introduction

Cubic boron nitride (cBN) and boron phosphide (BP) have received considerable attention in recent years for applications in opto-electronic devices [1]. Both of these III-V compound semiconductors are mechanically strong and belong to the family of hard materials such as diamond and gallium nitride. Although, cBN has been used in the past as polishing and grinding material, it has other potential applications for use in electronic devices in situations involving high temperatures or pressures. The amount of theoretical knowledge on these materials is, unfortunately, limited to a handful of studies and, in particular, the data on phonon spectra and vibrational properties of defects are rather scarce.

This paper is concerned with the prediction of phonons of cBN and BP by using a novel optimization procedure for determining force constant parameters of a second-nearest neighbor Rigid-ion-model (RIM). By incorporating lattice phonons in the Greens function formalism and using simple perturbation models, we have reported for the first time the vibrational behavior of isolated {Li(a^{2-}), Be(a^-), C(a^-), Al(i), Si(d^+) and Si(a^-)} defects in cBN and BP. For the perfect materials, our theoretical results for optical phonons at the center of the Brillouin zone are in reasonably good agreement with the existing infrared absorption and Raman scattering data. In the case of BP, our calculations of lattice vibrations along high symmetry directions compare favorably well with the first principle calculations reported recently by Alves and Kunc [2]. In the absence of experimental data on impurity modes, we will discuss the results of force variation correlation with covalence for charged impurities in cBN and BP with several III-V and II-VI compound semiconductors.

2. Theoretical Method

The phonon frequencies and the respective eigenvectors of the vibrations at high symmetry points in the Brillouin zone are calculated by using an optimized eleven parameter RIM for cBN and BP. The model parameters are obtained to the available phonon frequencies and elastic constants by using a nonlinear least-square fitting technique with constrained parameters and weighting. In Fig. (1), we have displayed the calculated one-phonon density of states for cBN (upper panel) and BP (lower panel).

The phonon values are incorporated in the phenomenological Greens function theory for studying the impurity vibrations [3]. The advantage of our technique over an *ab initio* method is that it allows the coupling of the vibrations of the defect to the bulk crystal. It also provides a simple way to visualize which type of vibrational modes remain localized around the defect.

For a substitutional defect in BP (say), the point group symmetry is T_d and the displacement combinations can be chosen that transform as a particular row of one of the irreducible representations of the point group. To simulate infrared (IR) active modes, for example, we need to consider only those displacement responses which transform as the vector irreducible representations of the applied electric field. For the T_d point group, this is the F_2 representation. In defining the impurity perturbation, we have considered only the changes in the atomic mass at the impurity site as well as the changes in the nearest-neighbor impurity-host force constants. Thus, in the Green's function theory, the F_2-type impurity modes will appear at frequencies ω_{imp} when the real part of the determinant vanishes 1.e.,

$$\text{Re} \mid I + G.P \mid = 0 \quad . \tag{1}$$

In Eq. 1, G is the Greens function matrix of the host lattice and P is the perturbation matrix in the impurity space. For isolated light defects occupying B or N(P) sites in BN and BP, we have displayed our theoretical results of localized vibrational modes in Figs. 2 and 3, respectively as a function of nearest neighbor force constant change parameter t or u. Similar calculations for the gap modes in BP are shown in Fig. 4.
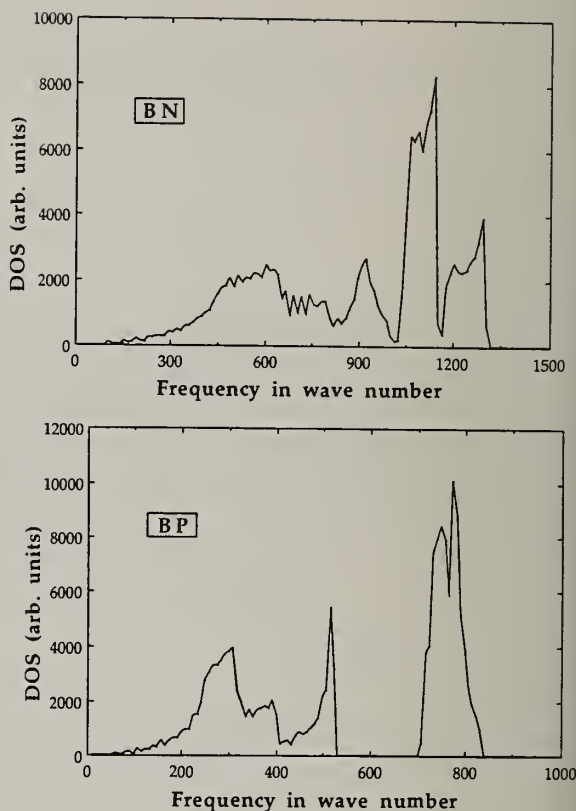
Fig. 1 Calculated one phonon density of states for cBN (upper panel) and BP (lower panel) on the basis of an eleven parameter Rigid-ion-model.

3. Results

Lattice Dynamics: To the best of our knowledge, there exist no data on phonon dispersions from the inelastic neutron scattering experiments. However, a few Raman scattering and IR absorption measurements have been reported in recent years. For BP, a lattice dynamical study based on local density functional theory, has also appeared in the literature. The results of our RIM11 calculations for phonon dispersions are found to be in reasonably good agreement with both the experimental and theoretical data [1-2].

Impurity modes: Since the masses of B and N atoms are not significantly different, there exists no gap between the acoustical and optical branches of cBN. In BP, however, our calculations suggest a wide phonon gap in the frequency range of 533-707 cm^{-1}. This means that in both cBN and BP, we expect high frequency localized vibrational modes (LVMs) for light impurity atoms occupying either the B and/or N(P) (see Figs. 2-3) sites. In BP, on the other hand, one expects gap modes to emerge from the minimum of the optical band for heavier impurity atoms occupying the B-site. For lighter impurities on the P-site, besides high frequency LVMs, one also expects gap-modes to emerge from the top of the acoustical band (see Fig. 3). Clearly, the impurity-mode frequencies are strongly affected by the variation of the impurity-host interaction parameter (t or u). between the acoustical and optical branches.
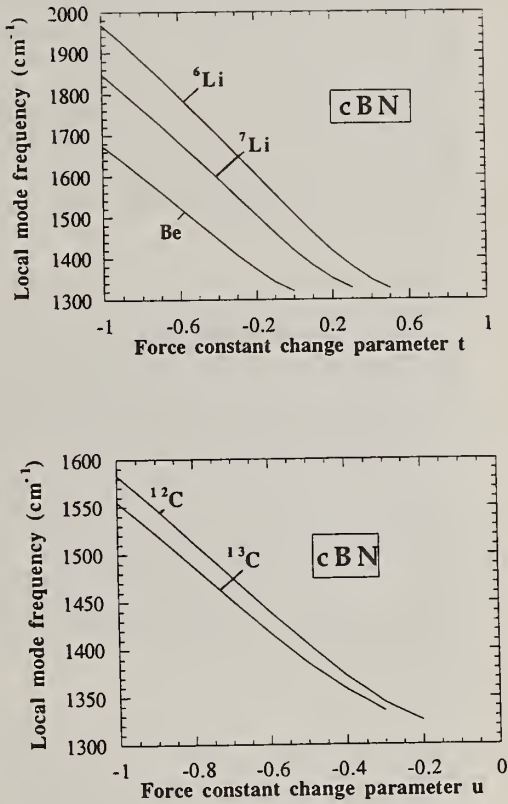
Fig. 2 Calculated Localized vibrational modes due isolated defects in cBN: upper panel for impurities occupying the B-site lower panel for impurities occupying the N-site.

4. Discussion and Conclusion

The perusal of Fig. 2-3 reveals that only light impurities such as Li_B (double acceptor), Be_B (single acceptor) and $C_{N(P)}$ (single acceptor)in cBN and BP can give rise to high frequency localized vibrational modes. In BP, on the other hand, heavier impurities occupying the B-site (e.g., Al_B, Si_B, and Ga_B) can give rise to gap modes between 533- 707 cm^{-1}. Our recent comprehensive study of impurity modes due to charged defects in III-V compounds has shown that acceptor defects occupying the III-site cause softening in the nearest neighbor interaction between impurity and the host lattice atoms, whereas acceptors occupying the V-site cause strong stiffening in the impurity-host interactions. We expect same trend to exist between the force variations and the charged impurities in BP and cBN.

858

In conclusion, we have reported for the first time the results of our comprehensive theoretical calculations for the vibrational behavior of isolated point defects in cBN and BP. Although, very simple simple perturbation models are used in describing the impurity potentials, the results have clearly demonstrated the usefulness of the Greens function approach in discriminating the site selectivity of defects.

Silicon behaves like amphoteric defect in GaAs i.e, it can act like a donor if occupies the Ga -site and an acceptor if sits on the As-site. This has been clearly demonstrated by the observation of the high frequency localized vibrational modes [3]. In BP, we only expect to see the gap mode if Si-behaves like an acceptor impurity. Carbon acceptor in BP can cause both localized as well as gap modes. These predictions can be easily checked by the high resolution Fourier transform infrared absorption and Raman scattering experiments.
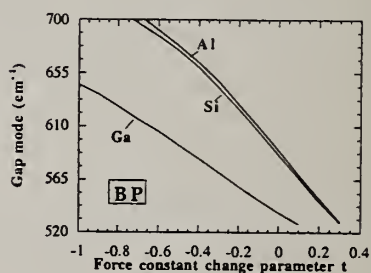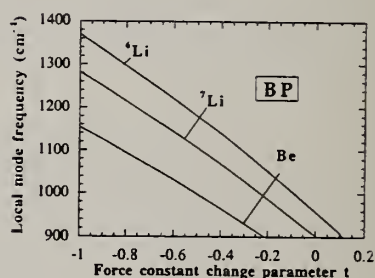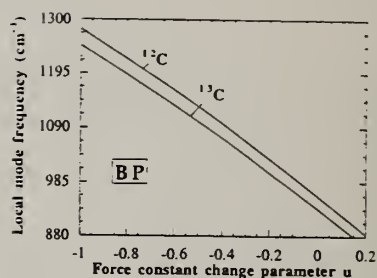
Fig. 3 Calculated localized vibrational and gap modes due to isolated defects in BP: Local mode for defects occupying the P site (upper panel), local mode for defects occupying the B-site (middle panel and gap mode for defects occupying the-Bsite in BP.

References

1. Y. Kumashiro, *J. Mater. Res.* **5**, 2933 (1990).
2. H. W. Leite Alves and K. Kunc, J. Phys. Condens. Matter 4, 6603 (1992).
3. D. N. Talwar, K. S. Suh and C. S. Ting, *Philos. Mag.* **B54**, 93 (1987); K. S. Suh, Ph. D. thesis, *University of Houston*, 1988 (unpublished).

ENERGETIC STATES OF ISOLATED NATIVE DEFECTS IN CUBIC BORON PNICTIDES

D. N. Talwar[1], N. Badi[2] , A. Bousetta[2] and A. Bensaoula[2]

[1]Department of Physics, Indiana University of Pennsylvania, Indiana PA 15705-1087
[2]Space Vacuum Epitaxy Center, University of Houston, Houston Texas 77204

Abstract

The major chemical trends in the deep-energy levels of isolated sp^3- bonded substitutional native defects are reported for the first time in boron pnictides. Band structure calculations, based on a second-neighbor tight-binding theory, are presented for BN, BP, and BAs and the results are obtained for the electronic energy states of substitutional (isolated) defects in the Green's-function framework. For sp^3- bonded impurities, a perturbation potential in the modified central-cell atomic like configuration is considered in which the off-diagonal elements in the perturbation matrix are systematically incorporated. Calculated results for the bound electronic states of isolated vacancies in BN are compared and discussed with the experimental data.

Key words: Band structure, tight-binding, Green's function, electronic states

1. Introduction

In recent years, the commercial realization of light emitting diodes and lasers using III-V compound semiconductors has generated considerable theoretical and experimental interests in studying their electronic and phonon properties. For boron pnictides (BX, with X = P, As, Sb and N), however, very little information is known despite of their potential use in optoelectronic and microelectronic devices under extreme environmental conditions.

As the interest in these compounds shifts towards energetic and kinetic characteristics of charge carrier trapping and recombination centers, the knowledge of band structure and electronic properties of defects become important. To the best of our knowledge, there are no results available on the electronic energy bands from angle-resolved photo emission spectroscopy. However, some data exist from soft x-ray, and uv absorption spectroscopy yielding bandgaps and occupied bandwidths. Results from few optical studies on cBN, BP, and BAs have also been known, however, the existing values for the bandgaps are surprisingly scarce. The earlier result on the calculated indirect gap for BN was reported to be in the range from 3.5 to 10.5 eV, whereas the soft x-ray and uv absorption studies found the gap to be 6.0 and 6.4 eV, respectively. Recent calculations of cBN in the local-density approximation (LDA) has provided much better and consistent results. For BP and BAs, the calculated band gaps still fall between 1.2-4.2 eV and 1.1-1.6 eV, respectively.

The inconsistencies in the existing data for the electronic band structure and the need for energetic positions of the intrinsic localized defect-levels in boron pnictides have motivated us to undertake the present study. Electronic band structures of BN, BP, and BAs are studied by using an empirical tight-binding (TB) theory and the results are compared to the recent *first-principles* LDA calculations. For sp^3-bonded impurities, we have considered a perturbation potential in the modified central-cell atomic like configuration. For cBN, the bound electronic (acceptor and donor) states for intrinsic defects are studied by using a TB Greens function theory and the results are compared and discussed with the recent experimental data.

2. Theoretical Method

Model Hamiltonian: Empirical tight-binding model is used here to describe the electronic behavior of both perfect- and imperfect crystals with isolated defects. We begin first by describing the perfect crystal Hamiltonian $\mathbf{H}^o$ and then discuss the perturbation potential $\mathbf{P}$ due to isolated intrinsic defects in boron pnictides. A second-neighbor TB Hamiltonian $\mathbf{H}^o$ was constructed for the perfect zinc-blende crystals following Koster and Slater:

Fig. 1 Calculated electronic energy bands (upper panel) and the electronic density of states based on an a second-neighbor tight-binding scheme.

$$\underline{\mathbf{H}}^o = \sum_{n\,\mathbf{R}} |n,a,\mathbf{R}\rangle \, E_{n,a} \, \langle n,a,\mathbf{R}| \;+\; \sum_{n\,\mathbf{R}} |n,c,\mathbf{R}+\tau\rangle \, E_{n,c} \, \langle n,c,\mathbf{R}+\tau| \;+$$
$$\sum_{n\,n'\,\mathbf{R}\,\mathbf{R}'} \{\, |n,a,\mathbf{R}\rangle \, E_{nn'}(\mathbf{R},\mathbf{R}') \, \langle n',c,\mathbf{R}'| + \text{H.c.}\}. \tag{1}$$

Here H.c. means Hermitian conjugate, $\mathbf{R}$ specifies the face-centered-cubic lattice positions of the anions; the quantum numbers n run over the basis orbitals s, p_x, p_y, p_z; the site index a and c represent the anion and cation, respectively. The terms $E_{n,a}$ and and $E_{n,a}$ are respectively the diagonal elements of $\mathbf{H}^o$ in the basis $|n,a,\mathbf{R}\rangle$ and $|n,c,\mathbf{R}+\tau\rangle$, whereas the transfer-matrix elements $E_{nn'}$ are considered non-zero only between nearest-and second-nearest-neighbor atoms namely between $|\mathbf{R}-\mathbf{R}'| = \sqrt{3}\,a_0/4$ and $\sqrt{2}a_0/2$, respectively. The states $|n,a,\mathbf{R}\rangle$ and $|n,c,\mathbf{R}\rangle$ are localized basis orbitals centered on the anion at $\mathbf{R}$ and the cation at $\mathbf{R}+\tau$ with $\tau = a_0/4)\,(1,1,1)$, with a_0 being

the lattice constant. In this representation, the Hamiltonian H^o is an 8x8 matrix with 23 interaction integrals. These interaction integrals for BN, BP, and BAs are obtained by an empirical fit to the recent experimental and/or reliable theoretical band structures at the Γ, X, and L critical points. As a representative case, the results of our calculation for the band structure and the density of states of cBN are displayed in Fig. 1. The advantage of the TB scheme is that besides its good fitting to the energy bands of the perfect systems, the explicit dependence of the two-center integrals on inter atomic distance enables us to construct reasonably accurate perturbation potentials for studying the electronic properties of defects.

Deep-level theory: To treat the deep levels associated with isolated defects in boron pnictides, a perturbation potential **P** is constructed in the modified central-cell atomic like configuration. In other words, the on-site matrix elements of this potential are obtained from the atomic-energy differences of the impurity and the host (see below for the discussion of treating the case of an ideal vacancy) lattice atoms. To account for the off-diagonal elements in the perturbation matrix, the effects of lattice relaxations are systematically included following the procedure of Talwar *et al.* Long-ranged Coulombic tail of the potential (for a non-isoelectronic defect) is neglected because the energies of the deep levels are controlled mainly by the central-cell part of the potential. The effects of long-ranged, dielectrically screened Coulomb interaction, if desired, can be incorporated *a posteriori* into the theory.

Since, the defect potential **P** is local in the TB basis, the Koster-Slater theory is a convenient method for determining the bound state energies E of the defect. Assuming **P** to be the impurity potential, the Hamiltonian H^o will be modified to H $(= H^o + P)$ for the perturbed crystal. The calculation of the bound electronic states of isolated defects in the gap can be achieved by solving the Fredholm determinantal equation

$$\det[\ I - (EI - H^o)^{-1}P] = 0 ,\qquad(2)$$

where $G^o = (EI - H^o)^{-1}$ is the Greens function of the host crystal. By considering appropriate symmetry (T_d) of the single isolated defect and using Group theoretical arguments, the secular equation (2) can be factored into smaller size determinants. That is, for the states of symmetry l where $l = a_1$ (s-like) or t_2 (p-like) may be taken at the site κ of either cation or anion, the partial Greens function can be written in terms of the Hilbert transform of the local spectral density $D_{l\kappa}(E)$ function as

$$G_{l\kappa}^o(E) = \sum_n \int_{-\infty}^{\infty} dk^3 \frac{(<l'\kappa|k,n> <l'\kappa|k,n>)}{(E - E_n(k))} = \int_{-\infty}^{\infty} dE' \frac{D_{l\kappa}(E')}{(E - E')} = \frac{1}{P_{l\kappa}} .\qquad(3)$$

Here $E_n(k)$ is the n-th eigenvalue and $<l\kappa|k,n>$ is the n-th eigenfunction at the wavevector **k**. By considering appropriate **P** and by incorporating the band structure of the perfect crystals obtained from the tight-binding theory, we can solve Eqs. (2) and (3) in the appropriate irreducible representations of the impurity point group. In actual numerical calculations, a standard (Lehman-Taut) tetrahedron numerical technique was used and for the energies E within the band gap the integral Eq.(3) was solved by using a special-point method.

3. Results and Discussion

Deep levels: Since the experimental results for the energetic states due to impurities in boron pnictides are sparse, our discussion here is limited only to native (ideal vacancy) defect centers in BN. To calculate the bound electron states due to isolated defects, we first obtained the spectral density of states by incorporating the band structure of the host systems. Appropriate Green's functions and the perturbation potentials are used in Eqs. (2-3) for estimating the electronic states of impurities occupying either B and/or N site in BN. If one of the two lattice sites in BN is converted to an ideal vacancy, we assume the on-site matrix elements of $\underline{P}$ to be infinite $[P_{l\kappa} \to \pm \infty]$ in magnitude and set a zero value for the off-diagonal matrix elements. By setting the impurity's orbital energy equal to infinity, allows the impurity atom to be decoupled from the host lattice. If we consider l to be either s- or p-orbital state, then Eq. (3) corresponds to the bound states of a_1- or t_2-symmetry associated with site κ. The results for ideal vacancy levels in cBN are reported in Table I. Our calculations suggest that the energies of the bound states (t_2-symmetry) of B (V_B) and N (V_N) vacancies are near $E_v + 0.28$ eV and $E_v + 4.03$ eV, respectively. In other words the B- and N-vacancies in cBN behave as acceptors and donors. The prevailing affect of defects on luminescence and conduction in graphite like BN due to native acceptors and donors has been suggested [7-8]. The nature of defects which create shallow levels is believed to be the impurity atoms that are segregated on the crystallite surface. Carbon atoms play an essential role in creating such defects and can stablize B- and N-vacancies. Interstitial carbon atoms on the other hand can produce deep traps. The energetic positions of such local levels are being investigated and the detailed results will be reported elsewhere.

Table I. Calculated bound electronic states of native defects in cBN. All energies are measured from the top of the valence band.

Impurity center	Energy level $E_v + eV$
V_B	0.28 (t_2)
V_N	4.03 (t_2)

References

1. Y. Kumashiro, *J. Mater. Res.* **5**, 2933 (1990).
2. R. M. Wentzcovitch, M. L. Cohen, and P. K. Lam, *Phys. Rev.* **B36**, 6058 (1987); R. M. Wentzcovitch, S. Fahy, M. L. Cohen, and S. G. Louie, *Phys. Rev.* **B38**, 6191 (1988).
3. M. P. Surh, S. G. Louie and M. L. Cohen, *Phys. Rev.* **B43**, 9126 (1991)
4. Y-N. Xu and W. Y. Ching, *Phys. Rev.* **B44**, 7787 (1991).
5. D. N. Talwar, K. S. Suh and C. S. Ting, *Philos. Mag.* **B54**, 93 (1987); K. S. Suh, Ph. D. thesis, *University of Houston*, 1988 (unpublished).
6. G. F. Koster and J. C. Slater, *Phys. Rev.* **95**, 1167 (1956).
7. E. J. Andrey, A. Katzir, and J. T. Suss, *Phys. Rev.* **B13**, 2831 (1976); ibid *Phys. Rev.* **B11**, 2370 (1975).
8. M. B. Khusidman, V. S. Neshpor, and L. I. Feldgun, *Isv. AN SSSR, Neorgan Mater.* **22**, 696 (1986).

CARBON-NITROGEN FILMS

ION BEAM ASSISTED SPUTTERED CARBON NITRIDE FILMS

K.G. Kreider, M.J. Tarlov, L.H. Robins, R.B. Marinenko, and D.T. Smith

NIST, Gaithersburg, MD 20899

Key words: amorphous, carbon nitride, hard films, ion beam, sputtered

Abstract

We have produced amorphous carbon nitride coatings containing up to 40% nitrogen using ion assisted planar magnetron RF sputtering in a nitrogen atmosphere. Both WDX and XPS indicate this composition. Coatings up to 2 μm thick were produced on alumina, silicon, SiO_2, and glass substrates using a graphite target. Films with 95% transparency in the visible wavelengths and harder than silicon have been produced. XPS studies confirm the stability of a carbon nitrogen phase up to 630 °C. The Raman spectra are compared with those of carbon and carbon nitride films prepared by other methods.

1. Introduction

Theoretical predictions of some of the outstanding properties of carbon nitride have been made by Liu and Cohen[1] in 1989. Recent efforts using sputter deposition [2-3], and pulsed laser deposition in the presence of an RF plasma [4], have produced small fractions of the desirable C_3N_4 structure. Amorphous films of carbon nitrogen have also been produced in a capacitively coupled rf plasma reactor [5] and by rf sputtering in nitrogen [6-9]. Li et al. [8] have reported sputtered carbon nitride films with high hardness values and Chen et al. [9] have reported Raman studies on similar films. Amorphous carbon nitride may have outstanding hardness and thermal conductivity like crystalline C_3N_4. To achieve the excellent properties resulting from the high energy, sp^3 diamond-like CN bond the sputter deposition process we use employs two techniques that enable nitrogen atoms to impact the growing film at high energies. First, the deposition process takes place at lower pressures; 0.3 Pa versus 2.5 Pa to 1300 Pa more commonly used [2-6]. Second, a beam of ionized nitrogen is directed on the substrate to provide the necessary kinetic energy to generate the high energy diamond-like tetrahedral bond between the carbon and nitrogen.

2. Experimental

Carbon nitride film sets were sputter deposited from a graphite target (99.9% purity)

on silicon, aluminum oxide, fused quartz, copper, and nickel alloy substrates. The substrate temperatures ranged from 40 °C to 325 °C and the carbon target to substrate distance was 6-8 cm. The arrangement for magnetron sputtering with ion beam bombardment employed a 3 cm Kaufmann ion source at 10 cm from the substrate. The nitrogen pressures during sputtering ranged from 0.2-0.3 Pa and beam voltages were 50-500 V. The resistivity of all films was determined with a four point probe, and all were examined optically for flaws, buckling, adhesion, and transparency.

3. Results

The deposition variables investigated to obtain high quality films included: background nitrogen pressure, magnetron power, ion beam voltage and current, substrate material, substrate temperature, target to film distance, and film thickness. The most useful substrates were silicon wafers, glass, and alumina although adherence was more of a problem on glass. Most films were made with 150-200 W rf with the 5 cm magnetron; and 50-100 V and 5-10 mA were the best ion beam parameters. Higher ion beam powers removed the film. Since the ion beam covered only a 3 cm diameter spot, we were able to examine the film in areas impacted by the ion beam ($\sim 0.1\mu m$ thick) and the unimpacted areas adjacent to the spot ($\sim 1\ \mu m$). Initial tests to determine suitable substrate temperatures and nitrogen sputter deposition pressures indicated much better adhesion and uniformity at lower temperatures and pressures. Most of the films had electrical resistances greater than 10^6 ohms, however, a few had a 4 point resistance as low as 10^4 ohms in 1 μm thickness ($\rho = 1$ ohm cm).

High nitrogen pressures (> 3 Pa) without the ion beam did not lead to higher nitrogen contents in the films and led to soft, poor quality films. We therefore concentrated on using the lowest pressures our planar magnetrons permitted (0.2-0.3 Pa). All films were produced in nitrogen (99.999%) after a pump down to $1\text{-}1.5 \times 10^{-4}$ Pa. Electron probe microanalysis with x-ray wavelength dispersive spectrometry (WDX), was used to analyze the approximate composition of the films. The C:N ratio, which was determined using a Bastin-PROZA [10] routine for the atomic percentage values, varied from 65:35 to 70:30 ($\pm 20\%$) for films produced by magnetron sputtering in 0.3 Pa N_2 over a substrate temperature range of 50 °C to 170 °C. An ion beam impacted film had less nitrogen (31%). Films that were heated in N_2 to 730 °C for 2 h were depleted in nitrogen (C:N=85:15). Hardness of the films was measured using an ultra-low-load; instrumented indenter. . A Berkovich three-sided diamond pyramid indenter tip was used over a range of indentation loads. With the thinner films, it was not possible to determine accurately the film hardness due to film-substrate interactions. Several of the unimpacted thicker films, however, were significantly harder (10-12 GPa) than their substrates which agrees with data from Li et al. (10) obtained on similiar films. The film regions impacted by the ion beam were much thinner (40 nm) than the surrounding film of carbon nitride formed from

the sputtered carbon target alone. Although they appeared to have compositions similar to the thicker regions, as measured by XPS, and display a similar Raman signature as discussed below, they appeared visually transparent. In order to quantify their optical properties a spectrometer was used in the comparative mode for transmittance measurements. The results of this scan indicate that less than 5% of the incident light was lost due to reflection and absorption in the visible wavelengths (1.8-3.0 eV) for an ion beam impacted 40 nm thick film. The transmittance decreased rapidly with decreasing wavelength in the UV region, possibly due to the onset of the inter-band optical absorption of the CN_x film.

Six representative films were examined by Raman spectroscopy using 514.5 nm radiation. The carbon nitride films on glass and silicon all showed an amorphous broad band signal in the 1300-1700 wave number region, which is similar to the broad band of amorphous carbon. The results presented in Figure 1 were typical. Here the middle curve shows the response of the clear film and the upper curve represents the response of thicker and darker partially transparent films on silicon. The bottom curve is the spectrum of the bare silicon substrate. These spectra are similar to those reported for carbon nitride [8] and nitrogen-implanted, diamond-like carbon films [9] with the graphite band, 1590 cm^{-1}, more pronounced than the disorder band and shifted to lower frequencies. The Raman spectra demonstrate the sensitivity of the technique for detecting the presence of the very thin films.

XPS was also used to ascertain the surface composition of the sputter-deposited carbon nitride films. In the spectrum of the as-deposited film, only features attributable to carbon, nitrogen, and oxygen were detected. Using standard XPS atomic sensitivity factors for the C 1s (0.31) and N 1s (0.49) photoelectron lines, a carbon:nitrogen atomic ratio of 62:38 was determined from peak height measurements. Following annealing to 630 °C, essentially no oxygen was detected from the film surface region. The calculated carbon:nitrogen ratio changes slightly to 64:36, which agrees well with the bulk film compositional measurements using WDX. Apparently the surface of carbon nitride films incorporated oxygen upon exposure to the ambient. The carbon nitride film is thermally stable up to 630 °C and the surface composition after annealing is similar to that of the bulk.

4. Conclusions

Sputtered carbon nitride films were produced using magnetron sputtering of graphite with a nitrogen ion beam. The smoothest and most defect-free films were produced at low (50-175 °C) temperatures and low nitrogen pressures (<0.3 Pa). Ultrathin ion beam impacted films (30-100 nm thick) appeared transparent. They had similar composition to the thicker films (30-40% N) and had greater than 95% transparency in the visible range. The films lost nitrogen in a nitrogen atmosphere at 720 °C, however, no change of the carbon nitrogen ratio was observed after heating to 630 °C in vacuum. This indicates the decomposition temperature lies between 600

and 700 °C. The hardness of these films was greater than silicon or fused silicon dioxide.

5. References

1.   A.Y. Lui and M.L. Cohen, Science, 245, 841 (1989).
2.   E.E. Haller, M.L. Cohen, and W.L. Hansen, "Hard Carbon Nitride and Method for Preparing Same," May 5, 1992, U.S. Patent 5,110,679.
3.   D. Marton, K.J. Boyd, A.H. Al-Bayati, S.S. Todorov, and J.W. Rabalais, Phys. Rev. Lett Vol. 73-1, 118 (1994)
4.   C. Niu, Y.Z. Lu, and C.M. Leiber, Science, 261, 334, 16 July 1993.
5.   H. Han and B.J. Feldman, Solid State Com., Vol. 65-9 921   (1988).
6.   J.J. Cuomo, P.A. Leary, D. Yu, W. Reuter, and M. Frisch, J. Vac. Sci. Tech. 16(2), 299 (1979)
7.   C.S. Torng, J.M. Sivertsen, J.H. Judy, and C. Chang, J. Mat. Res V5-11, 2490 (1990) p 2490.
8.   D. Li, Y-W Chung, and W.D. Sproul, J. Appl. Phys. 74 219   (1993)
9.   M.Y. Chen, D. Li, X. Lin, V.P. Dravid, Y-W. Chung, M-S. Wong, and W.D. Sproul. J. Vac. Sci. Tech. A11 (3) 521 (1993)
10.   J.L. Poucher, R. Poucher "Electron Probe Quantitation," Plenum Press (1991) p 31-75.
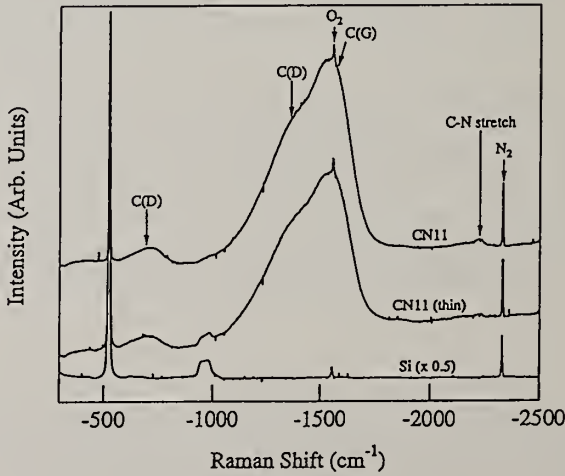
Figure 1. Raman spectra of transparent (middle) and darker (top) ion beam impacted carbon nitride films and of uncoated silicon substrate (bottom).

COVALENT CARBON NITRIDE FILMS SYNTHESIZED BY ABLATED GRAPHITE PLASMA UNDER ION BEAM CO-PROCESSING

Zhong-Min Ren, Yuan-Cheng Du, Zhi-Feng Ying, Mao-Qi He, and Fu-Ming Li

Fudan University, Department of Physics, State key joint laboratory for material modification by laser, ion and electron beams, Shanghai, 200433, China

Keywords: carbon nitride, ion beam, laser ablation, optical emission spectrum

Abstract

Carbon nitride thin films, with N-concentration about 41% have been synthesized by pulsed laser ablation of graphite under a low-energy nitrogen ion beam bombardment. Electron diffraction and X-ray photoelectron spectra measurements have shown the existence of polycrystallite covalent beta-C_3N_4 structure in the films. During the syntheses, YAG laser ablation was used with different laser wavelengths: 355, 532 nm and 1,06 μm individually. The analyses of the optical emission spectra (OES) of the ablated plasma indicated that the use of 532 nm laser is more proposed for the purpose of synthesis of good carbon nitride films.

I.Introduction

Covalent carbon nitride, beta-C_3N_4, was predicted by Liu and Cohen[1,2] to be a good candidate for extreme hardness. Many groups[3-7] have tried to synthesize carbon nitride materials. It's not until now, Niu[8] deposited covalent solid carbon nitride using atomic-beam-assisted laser ablation, and the experimental evidence supported the beta-C_3N_4 structure. This led to detailed investigations of this tetrahedral solid both at theoretical and experimental aspects[9,10].

In our experiment, we synthesize carbon nitride films using laser ablation of graphite under low-energy nitrogen ion beam bombardment. XPS, HEBS, Raman, and electron diffraction measurements are used to characterize obtained films. In our experiment, in order to select an appropriate laser, we study the optical emission spectra OES of the plasma produced by the laser ablation of graphite at different wavelengths: 355, 532 nm and 1.06 μm.

II.Experimental

In our experimental set up, as described in a previous paper[11], a YAG laser with base wavelength 1.06μm is used to generate a laser beam to ablate graphite. A kaufman broad-beam source is used to generate a nitrogen ion beam. The YAG laser provides 80 ns with energy 50 mJ per pulse. The plasma OES of the portion 4-6 mm away from the graphite target is sampled by a 4400 Boxcar for signal processing.

III.Results and discussion

HEBS measurements show that the N-content the 532 nm laser deposited film is about 41%. The film deposited by 355 laser ablation contents less N species. In the TEM and diffraction measurements, the deposited films by 532 or 355 nm laser ablation appear to be predominantly amorphous with a certain volume fraction of polycrystallites. In the electron diffraction pattern[11,12], obvious diffraction rings corresponding to beta-C_3N_4 structure could be seen, suggesting the existence of polycrystal beta-C_3N_4 materials. According to rough estimation, the ratio of polycrystal structures in the film by 532 nm ablation is higher than that by 355 nm.

The chemical states of carbon and nitrogen species in the films are studied by XPS analyses[12]. The N 1s peak is found to be composed of two peaks at 399.1 eV and 397.4 eV. The peak at 399.1 eV is thought to be characteristic of C-N covalent bonds with almost no charge transfer between C an N. The C 1s peak is composited of three peaks at 283.7, 284.5 and 286.9 eV respectively. The peak at 286.9 eV is probably related to covalent C-N structures. The XPS results provide strong suggestion of the existence of beta-C_3N_4 embedded in amorphous matrix in the films.

Fig.1 gives two OES of the ablated graphite plasma by the 532 and 355 nm laser respectively. As for the 532 nm ablated plasma similar to that by 1.06 'm laser , atomic carbon line CII [13] at about 3921, 4075, and 4267 Å etc. could be seen, implying excited atomic carbon species in the ablated plasma. Energetic carbon species such as C atoms are thought to be critical to the synthesis of carbon nitride materials. Some CN red and violet peaks could also be been such as 3883(0-0) and 4200(0-1) Å etc.. These CN radicals are resulted from combination between the sputtered C atoms and energetic N atoms produced by the nitrogen ion source which generates a mixed N_2^+/N^+ beam. Such CN radicals in the ablated plasma near the surface of graphite target will probably lead to high ratio of CN structures in the deposited carbon nitride films, just as demonstrated by previous experiments[11,12]. Some C_2 swan bands such as 5165(0-0), 4730(1-0), 4383(2-0) etc. could also be seen. Many optical analyses of ablated/sputtered carbon plasma have shown these C_2 swan bands[14]. As for the 355 nm ablated plasma, strong and asymmetric C_2 swan bands could be seen, implying a large concentration of excited C_2 radicals in the plasma,
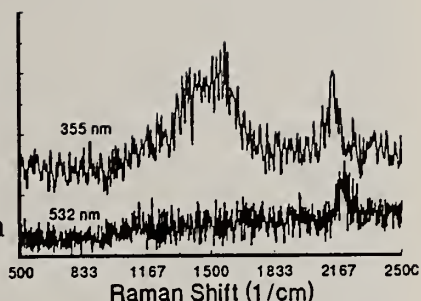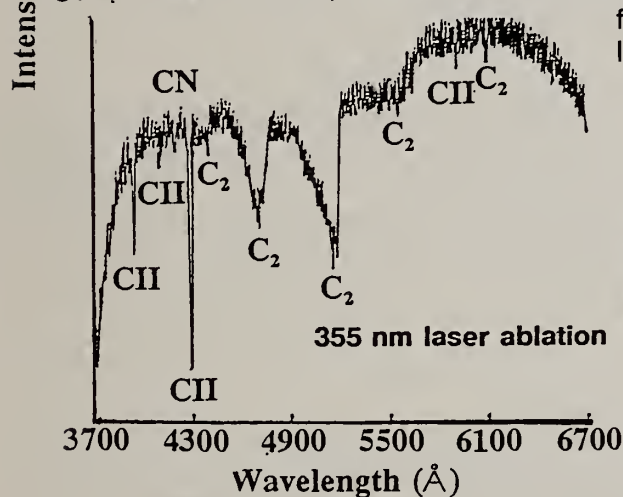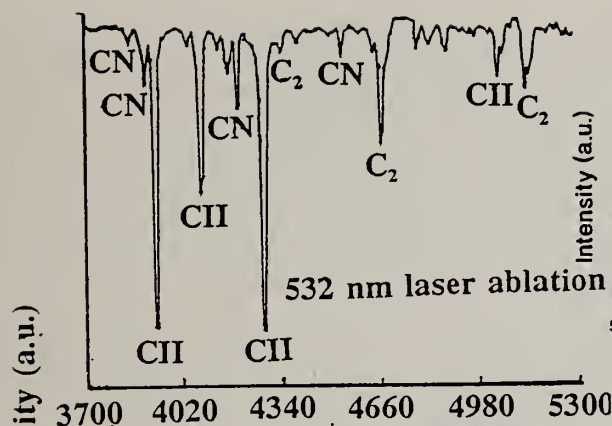
Figure 2. Raman spectra of deposited carbon nitride films by 355 nm and 532 nm laser ablation.

Figure 1. Optical emission spectrum of the ablated graphite plasma by 355 nm and 532 nm laser.

although some CN peaks and atomic C peaks could also be seen. A large concentration of excited C_2 in the plasma will probably lead to high ratio of amorphous carbide structures in the deposited carbon nitride films. We could conclude that the plasma by the 355 nm laser ablation contains a large concentration of excited C_2 radicals, while the plasma by 532 nm laser ablation contains a large concentration of excited atomic carbon. The active carbon species sputtered by laser are thought to be critical for the chemical combination and polycrystallites formation. We would propose the adoption of 532 nm laser used for graphite ablation.

Figure 2 illustrates Raman spectra of deposited films by 355 and 532 nm laser. The spectrum of the film by 355 nm ablation shows a broad and asymmetric peak in the region from 1100 to 1700 cm^{-1} representing amorphous carbon structures resulted from a large concentration of excited C_2 radicals in the laser-ablated plasma, and a peak at about 2140 cm^{-1} corresponding to CN triple bonds probably resulted from some excited CN radicals in the plasma. In the Raman spectrum of the film by 532 nm ablation, only one obvious peak at about 2190 cm^{-1} could be been, suggesting that the deposited film is mainly composed of C-N triple bonded structures resulted from CN radicals in the precursor plasma. The large concentration of excited atomic carbon in the 532 nm ablated plasma could possibly react with energetic nitrogen species in the nitrogen ion beam to form CN radicals before arriving on the substrate. Therefore, such excited atomic carbon radicals also contribute to the C-N triple bonded structures in the deposited films.

IV.Conclusion

Carbon nitrode films with N-content about 41% have been synthesized by ion-beam-assisted laser ablation of graphite. Experimental analyses strongly suggest the formation of covalent carbon nitride beta-C_3N_4 in obtained films. The adoption of 532 nm laser used for ablation of graphite is much more proposed than others such as 355 nm laser for the purpose of produce of good carbon nitride films.

References

1. A.Y.Liu and M.L.Cohen, Science, **245** 841 1989
2. M.L.Cohen, Science, **261** 307 1993
3. J.J.Cuomo, et al., J.Vac.Sci.Technol. **16(2)** 299 1979
4. M.Y.Chen, et al., J.Vac.Sci.Technol. A**11(3)** 521 1993
5. H.X.Han and B.J.Feldman, Solid State Commun., **65(9)** 921 1988
6. M.R.Wixom, J.Am.Ceram.Soc., **73** 1973 1990
7. F.Fujimoto and K.Ogata: Jpn.J.Appl.Phys. **32** 420 1993
8. C.Niu, Y.Z.Lu, and C.M.Lieber, Science, **261** 334 1993
9. W.Schnick: Angew.Chem.Int.Ed.Engl. **32(11)** 1580 1993
10. J.L.Corkill and M.L.Cohen: Phys.Rev.B**48(23)** 17622 1993
11. Z.M.Ren, et al., Appl.Phys.Lett. **65(11)** 1361 1994
12. Z.M.Ren, et al., Phys.Rev.B, **51** Feb15 1995 to be published
13. J.Reader et al., in the "Wavelengths and Transition Probabilities for Atoms and Atomic Ions" NSRDS-NBS 68 U.S.Government Printing Office 1980
14. G.Herzberg, in the "Molecular spectra and molecular structure I. Spectra of diatomic molecules", 2nd Ed. Van Nostrand Reinhold, New York,1950

Applications of Diamond Films and Related Materials: Third International Conference, 1995
Editors: A. Feldman, Y. Tzeng, W. A. Yarbrough, M. Yoshikawa, and M. Murakawa

873

A STUDY OF MAGNETRON SPUTTERED CN_x FILMS

D.G. Chen, F.X. Lu, R. Yang, D.W. Liu, W.X. Yu, Q.B. Sun and B. Song

University of Science and Technology Beijing, Beijing 100083, P.R.China

Key words: CN_x FILMS, magnetron sputtering, characterization

Abstract

C_3N_4 was predicted to have a crystal structure of β–Si_3N_4, and a hardness superior to that of diamond, and hence become a target attracting scientists all over the world. In the present paper CN_x films were successfully prepared by DC magnetron sputtering of pure graphite target in pure nitrogen atmosphere. N/C ratio and the nature of the chemical binding of C-N atoms were analyzed by SEM, TEM, XPS spectroscopy, IR spectroscopy and MPM and was found to be strongly process related.

1. Introduction

Liu and Cohen [1,2] predicted theoretically that a new compound of C and N may exist which may possibly have the same crystal structure of β–Si_3N_4, and have a inter-atomic bond length shorter than that of diamond. and should have a bulk modulus (and so a hardness value) superior to that of diamond.

Encouraged by this prediction many scientist all over the world are trying to prepare this new super-hard material. For example, Han et al. [3] obtained C-N films by decomposing of a CH_4-N_2 mixture in a plasma; Maya et al. [4] reported that C-N films could be prepared by pyrolysis of organic compounds; Toring et al. [5] had obtained C-N films by r.f sputtering of graphite target in Ar-N_2 atmosphere. Besides, C-N films were also claimed to be prepared by DC magnetron sputtering [6-10], and ion beam assisted deposition [11]. However, up to now , all those films were basically amorphous, and the C/N ratio was generally low (less than 40%), and so were named as CN_x film. Recently, Niu et al. [12] claimed to have prepared C-N films having 40% nitrogen by laser ablation of graphite target, and they were able to show electron diffraction rings which could be interpreted by the crystal structure as predicted. Nevertheless, they were not able to show the structure by X-ray diffraction, and the hardness of the CN_x films were not reported.

In the present investigation, CN_x films were prepared by DC magnetron sputtering of pure graphite target in pure N_2 atmosphere, the structure and properties of the resultant CN_x

films were characterized by XPS. TEM. SEM . IR spectroscopy and Mechanical Properties Microprobe (MPM).

Experimental

CN_x films were prepared by DC magnetron sputtering of pure graphite target in pure nitrogen atmosphere. Single crystal Si ([100] orientation) and KCl were used as substrate material. Si substrate were used for preparation of samples for hardness measurement and SEM. XPS and XRD analysis. whilst the KCl substrate were used for studies of IR properties.

Single crystal Si substrate were thoroughly cleaned in ultrasonic bath in acetone and methanol. and was further cleaned by ion bombardment prior to deposition. No heating was applied. the estimated temperature rise during sputtering was no higher than $100^\circ C$. Film thickness were controlled to be within 500 - 1000 nm. The process parameters used are: target-substrate distance 60 mm; magnetron power 300 W; sputtering power. 300-1500 W; pressure. 0.4-10 Pa: bias voltage. -50 ~ -400 V.

Results and Discussions

It was shown by SEM that all the C-N films obtained were extremely smooth and featureless. indicating the amorphous nature of those films. From the intensities of C_{1S} and N_{1S} peaks in XPS spectra of the CNx films , N/C ratio in the C-N films were calculated and is shown in Table I . where it can be seen that a N/C ratio as high as o.42 was obtained.

However. we were not able to show the distinct relationship between N/C ratio and the process parameters from the limited data shown in Table I . Nevertheless. a general trend was obvious that the N/C ratio was strongly related to the bias voltage. that is. the higher the bias. the less the N/C ratio. The effect of sputtering power seemed to be more complicated. By comparing samples CN-1, CN-2 and CN-3, one may come to the conclusion that there was no linear relationship between the N/C ratio and the sputtering power. With increasing power. the N/C ratio first increased. and then decreased.

Table I. N/C ratio (x) of the CNx films

Sample	CN-1	CN-2	CN-3	CN-4
Gas pressure (Pa)	0.4	10	0.4	0.4
Bias voltage (V)	-50	-50	-50	-400
Sputtering power (kW)	310	100	1000	1500
x	0.42	0.38	0.33	0.21

The position of C_{1S} and N_{1S} peaks were found shifted from the peak position for carbon (graphite. 284.7 eV) and atomic nitrogen (409.9 eV). The C_{1S} peaks were shifted toward the higher binding energy side. whereas the binding energy for N_{1S} peaks were significantly less than that of atomic nitrogen and NH_3 (405.6 eV) [13]. but very close to that of the non-polarimetric nitrogen (399.0 eV) [11,12].

The present results coincides well with that of Niu et al. [12] and Fijimoto et al. [11], and also coincides with that predicted by Cohen [14]. Since there is little chance for the non-polarimetric nitrogen atoms to be present independently in the films, one can infer that those non-polarimetric nitrogen must be present in certain forms of chemical compound of C and N.

The nature of the C-N bonding can also be depicted by infrared spectroscopy. The IR spectra of CN1 (having the highest N/C ratio) and CN4 (having the lowest N/C ratio) are shown in
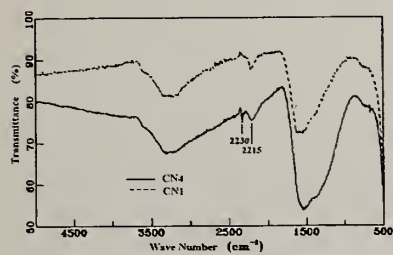
Figure 1   Typical IR spectra of CN$_x$ films

Fig.1. The sharp peaks located approximately at 2215 cm^{-1} and 2230 cm^{-1} are of particular interests. The former is related to C=N double bond, whereas the later is related to C≡N triple bond. It can be seen that for sample CN1, only the 2215 cm^{-1} peak is discernible, whereas the 2215 cm^{-1} and 2230 cm^{-1} peaks are all present in the CN4 sample. This indicates that appreciable amount of C≡N triple bonding did exist in sample CN4 but not (or negligible) in CN1. Apparently, higher bias and sputtering power is more beneficial for the formation of C≡N triple bonding. TEM observations (Fig.2) showed that, although both of the samples CN1 and CN4 were amorphous in nature as depicted by their electron diffraction patterns, but certain very small particles (white dots) was discernible in CN4 (see Fig.2(b)), but not for CN1. However it was not possible to show any details of these particles.
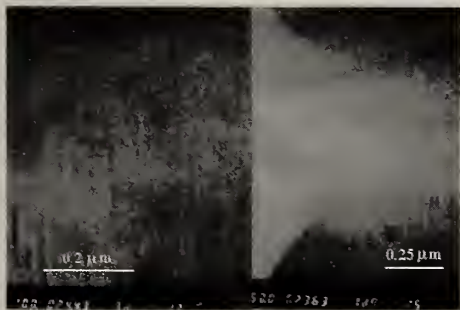
Figure 2   TEM bright field image of CN1 (left) and CN4 (right)

Mechanical Properties Micro-probe (MPM) was carried out using the NANO-INDENTER-II instrument which has an accuracy in displacement measurement of ± 0.04 nm, and an accuracy of load of ± 75 nN. In the present investigation the load was set to 4 mN. The results are listed in Table II, where it can be seen that the sample CN4 showed the highest value of hardness and modulus as compared to other samples. Apparently this is related to the structure (and the nature of bonding) of the CN$_x$ films. Again this shows the beneficial effect of higher bias and sputtering power. The hardness of 31.3 GPa and modulus of 220 GPa is much higher than that reported in the literature [9] for CN$_x$ films prepared by the same method. However, these value are far below that predicted theoretically. This is because our films were basically amorphous, and the structure of these films were a mixture of double

and triple C≡N bonds. Apparently, more work needs to be done for preparation of CN_x films having even higher hardness and modulus.

Table II. Micro hardness and bulk modulus of CN_x films

sample	x	hardness (GPa)	modulus (GPa)
CN1	0.42	5.0	52.7
CN2	0.38	1.8	48.2
CN3	0.33	10.8	114
CN4	0.21	31.3	220

Conclusions

CN_x films having C≡N triple bonds can be prepared by DC magnetron sputtering of graphite in pure nitrogen atmosphere. N/C ratio is strongly correlated with sputtering power and the bias voltage. N/C ratio is not directly related to the hardness and modulus. What is important is the formation and the amount of C≡N triple bonds in the CN_x films. Higher bias voltage and high sputtering power are beneficial to the increase of C≡N triple bonds, and so are helpful to increase the hardness and bulk modulus.

Acknowledgment

References

1. A. Y. Liu and M. L. Cohen, *Science*, 245(1989)841.
2. A. Y. Liu and M. L. Cohen, *Phys. Rev.*, **B, 41**(1990)10727.
3. H. X. Han and B. J. Feldman, *Solid State Comun.*, 65(1988)921.
4. L. Maya, D. R. Cole and E. W. Hagaman, *J. Amer. Ceram. Soc.*, **74**(1991)1686.
5. C. J. Toring, J.M. Sivertsen, J. H. Judy and C. Chang, *J. Mater. Res.*, **5**(1990) 2490.
6. J. J . Cuomo, P. A. Leary, D. Yu, W. Reuter, and M. Frisch, *J. Vac. Sci. and Technol.*, **16(2)** (1979)299.
7. M. Y. Chen, X. Lin, V. P. Dravid and Y. W. Chung, M. S. Wong, and W.D. Sproul, *J. Vac. Sci. and Technol.*, **A11 (3)** (1993) 521.
8. M. Y. Chen, X. Lin, V. P. Dravid and Y. W. Chung, M. S. Wong, and W.D. Sproul, *Surf. and Coat. Technol.*, **54/55** (1992)360.
9. D. Li, Y. W. Chung, M. S. Wong, and W. D. Sproul, *J. Appl. Phys.*, **74(1)** (1993) 219.
10. M.Y. Chung, X. Lin, V. P. Dravid, Y. W. Chung, M. S. Wong, and W. D. Sproul, *Tribology Transaction*, **36** (1993) 491.
11. F. Fijimoto and K. Ogata, *Jpn. J. Appl. Phys.*, **32**(1993)L420.
12. C. Niu, Y.Z. Lu, C. M. Lieber, *Science*, **261** (1993) 334.
13. J. H. Lu and C.Y. Chen in : *Techniques for Surface Analysis*, Electron Industry Press (1987)213. (in Chinese).
14. M. L. Cohen, *Science*, **261** (1993) 307.

Synthesis and Characterization of Co-Deposited Carbon Nitride and Boron Materials.

A.Bousetta, N. Badi, A. Bensaoula and M. Lu
Space Vacuum Epitaxy Center, University of Houston, Houston, Texas 77204-5507

Key words: ECR, CBN, coating ,composition, low temperature, nitride

Abstract

Carbon boron nitride (CBN) thin films were grown on Si and NaCl at temperatures in the range of 100-400 °C using electron-beam evaporation of graphite and boron assisted with electron cyclotron resonance (ECR) plasma generated nitrogen species. The effect of varying the boron flux on the compositional, structural, and electrical properties of the films was investigated using electron probe microanalysis (EPMA), Auger depth profiling (ADP), X-ray photoelectron spectroscopy (XPS), Fourier transform infrared spectroscopy (FTIR), and Hall measurements. The films were either carbon rich with B/N<1 and C/N>1 or boron rich B/N>1 and C/N>1. Although the nitrogen flux was kept constant for all deposition, the nitrogen content in the film varied with the B concentration in the film. In fact lower nitrogen content was found in films with higher B concentration and vice-virsa. The CBN films synthesized were either graphitic-like whose composition was $C_{0.59}B_{0.10}N_{0.31}$ or more insulating- BN like whose composition was $C_{0.33}B_{0.42}N_{0.25}$.

1. Introduction:

The structural similarity between hexagonal boron nitride and graphite suggests the possibility to produce a range of carbon-boron-nitride compounds. The importance of synthesizing this material stems from the fact that the combination of the semi-metal quality of the graphite with the insulator quality of hexagonal boron nitride could lead to a range of novel materials with interesting adjustable electrical properties.

Co-deposition of carbon, boron and nitrogen was first reported by Badzian et al.[1], using chemical vapor deposition technique. In their experiment, the C-B-N material, whose composition was not mentioned, was synthesized through the reaction of a BCl_3-CCl_4-H_2-N_2 mixture with a carbon rod maintained at 1950 °C. The authors observed that below this temperature a ternary phase would be difficult to form. Later Chen et al.[2], deposited CBN solid solution with composition $(BN)_xC_{1-2x}$ and assumed that their C-BN material was a substitution of B and N atoms for a pair of carbon atoms in the graphite hexagonal lattice. Another finding was that their compounds decomposed to B_4C and C when heated to 2200 °C or higher. The preparation of boron-substituted graphite by the high temperature reaction of B_4C and graphite was studied by Lowell [3], who determined that boron substitution in graphite does not exceed 2.35 % at 2350 °C and a solid phase C-B-N could only be a metastable one. Most of the CVD work published before 1987 revealed a two phase BN-C mixtures.

The first evidence of a $C_x(BN)_{1-x}$ type material was published by Kouvetakis et al.[4,5]. In fact XPS measurements showed the existence of bonding between the three elements C, B, and N and chemical analysis determined two compositions x= 0.03 and 0.3. Other techniques such as plasma-assisted CVD [6] and pyrolisis [7] were used to prepare such materials but their composition was of $C_xB_yN_{1-x-y}$ type far from the usual $(BN)_xC_{1-2x}$.

The possibility of preparing C-B-N materials over a range of compositions, with a corresponding range of properties, allows some unique fundamental and technological opportunities. These materials, if properly investigated and synthesized, will have useful applications in the field of hard coatings, electronic devices, and optics.

In this paper we present a new method for depositing C-B-N materials. It consists of electron-beam evaporation of graphite and boron assisted with electron cyclotron resonance (ECR) plasma generated nitrogen species. The major advantages of ECR over other techniques (i.e. CVD) are its low temperature (100-400 °C) and low pressure $< 10^{-4}$ Torr operation. All experiments were performed at a constant C rate while the B rate was varied in order to obtained different film compositions. Our preliminary results showed that the films where of $C_xB_yN_{1-x-y}$ type. Two compositions were determined by EPMA: $C_{0.59}B_{0.10}N_{0.31}$ and $C_{0.33}B_{0.42}N_{0.25}$. The present study was undertaken to determine the suitability of our technique to synthesize a ternary C-B-N compounds. The effect of boron introduction into CN materials was investigated using Auger depth profiling, Fourier transform infrared spectroscopy (FTIR), Raman spectroscopy, and electrical resistivity. X-ray photoelectron spectroscopy (XPS) data for $C_{0.33}B_{0.42}N_{0.25}$ film on Si are also presented.

2. Experimental

Carbon boron nitride films were deposited on 1-in.-diam (100)-oriented n-type doped silicon (0.5 Ωcm) and NaCl substrates. The silicon substrates were cleaned using standard solvent , then stripped of the oxide using HF for 1 min.; followed by rinsing in dionized water. NaCl was cleaned with methanol. The substrates were dried with nitrogen before loading into the vacuum chamber. An *in-situ* direct heating to 900 °C and 300 °C for 5 min. was performed for Si and NaCl respectively and the substrate temperature was lowered to an appropriate growth temperature. The base pressure of the system was 3×10^{-8} Torr and rose to 1×10^{-4} Torr during deposition. Carbon and boron were obtained by electron beam evaporation of pure graphite (99.999%) and pure boron (99.999%) respectively. The carbon deposition rate was kept constant (0.2 Å/sec) for all experiments while the boron rate was varied in the range of 0.02 to 0.1Å/sec. The deposition rate was constantly measured and checked during deposition using a quartz crystal microbalance monitor located in the vicinity of the substrate. Research grade nitrogen was fed to the ECR source (ASTEX) with a flow of 4 sccm. The growth rate was about 150 nm/hr and films with thicknesses in the range of 300-5000Å were obtained.

3. Results and Discussion

As mentioned earlier the composition of CBN film deposited on Si and NaCl was checked using EPMA. $C_{0.59}B_{0.10}N_{0.31}$ was determined for films deposited on Si using a low boron rate (0.02 Å/sec) and $C_{0.33}B_{0.42}N_{0.25}$ and $C_{0.31}B_{0.40}N_{0.29}$ were determined for films deposited on Si and NaCl substrates respectively using a higher boron rate (0.1 Å/sec). Note that no trace of oxygen was detected into the films.

The uniformity and composition of the CBN films was also checked by Auger depth profiling (Fig.1) however the amount of nitrogen detected was lower than that detected by EPMA. This lower level detection can be related to a sputtering process (electron induced surface modification) rather than to the film composition.
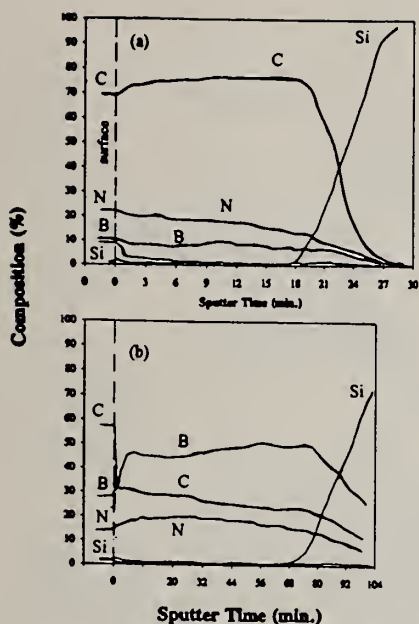
Fig. 1 Auger depth composition profile of (a) $C_{0.59}B_{0.10}N_{0.31}$ and (b) $C_{0.33}B_{0.42}N_{0.25}$ films deposited at 400 °C on Si (100).
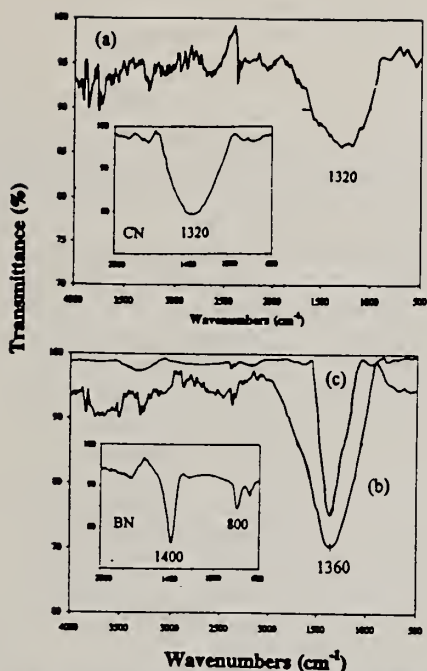
Fig. 2 Infrared transmission spectrum of BN films deposited at 500 °C with different nitrogen sources (a) ECR (b) Kaufman and (c) Kaufman/Neutralizer.

1000-1600 cm^{-1} and centered at 1320 cm^{-1}. This peak is very similar to that of pure CN although it is much wider. From this wide peak it is very difficult to determine the molecular structure of the film and we can only suppose that B-N, C-N, B-C groups are contain in this range. However there is no significant trace of O-H, N-H, and B-H modes since there no apparent peaks at 3400, 3200, and 2500 cm^{-1} respectively. The results show that there is no significant amount of oxygen and hydrogen into the film. For films deposited a higher boron rate and whose composition was $C_{0.33}B_{0.42}N_{0.25}$, the FTIR spectrum (Fig. 2-b) shows a much narrower peak (1220-1690 cm^{-1}). The peak is also shifted to higher wavenumber and it is centered at 1360 cm^{-1}. This peak is closer to that of a pure hexagonal BN film (see inset). Fig. 2-c shows the FTIR spectra of CBN with similar composition than that of Fig. 2-b but deposited on NaCl substrate. The peak is very narrow(1200-1460 cm^{-1}) but it is located at the same position (1360 cm^{-1}) than that of (b). The results show a direct relationship between the introduction of B (reduction of C) and the width and the shift of the main FTIR peak. Note that small amount of oxygen and hydrogen are detected in (c).

In order to determine the type of chemical bonding involving C, B, and N, we have performed XPS analysis. This was done only on B rich CBN films and Fig. 3 show the B, C, and N spectra of a $C_{0.33}B_{0.42}N_{0.25}$ type deposit. Each spectrum shows a composite peak which is an indication that the film does not consist of a two-phase mixture of carbon and boron nitride but rather of a CBN composition. Using C (284.6 eV), B(189.8 eV), and N (398 eV) as reference peaks, we have identified peaks such as BCN, BN, and CN as shown in Fig. 3.

Preliminary electrical measurements at 300 K were obtained using Hall measurement. The resistivity values for C rich films were in the range 0.1 to 0.8 Ωcm whereas the CBN films whose composition was $C_{0.33}B_{0.42}N_{0.25}$ have a much higher resistivity (20 to 400 Ωcm).

880

The results reflect the change in the electrical properties of the CBN composite as the boron content changes the material from a semi-metallic graphitic material to a BN-like insulating material.

Finally in Fig. 4 (a & b) show the Raman spectra for both metallic and insulating CBN films respectively. The spectrum in Fig. 4-a is characteristic of a disordered graphitic CN film having a high frequency peak or graphitic peak (G) at 1580 cm^{-1} and a disorder peak (D) at lower frequency (1388 cm^{-1}). The CBN film with higher B content shows a much wider Raman peak. This peak can be separated into two peaks at 1350 and 1530 cm^{-1}. It is difficult to estimate the structural quality from these spectra. The fact that the D and G peaks are well defined in Fig. 4-a suggests that the C-rich CBN films could have a better crystalline quality.

Fig. 4 Raman spectrum for an (a) $C_{0.59}B_{0.10}N_{0.31}$ and (b) $C_{0.33}B_{0.42}N_{0.25}$ films deposited at 400 °C on Si (100).

Fig. 3 XPS spectrum of the main elements C,B, and N in $C_{0.33}B_{0.42}N_{0.25}$ film deposited on Si at 400 °C.

4. Conclusion

We have presented preliminary results of C-B-N compounds deposited at low temperature (100-400 C) using ECR-assisted vapor deposition. The CBN films were either C rich or B rich depending on the initial B rate. At low boron rate the films have a composition $C_{0.59}B_{0.10}N_{0.31}$ and were semi-metallic and at high B rate the films have a composition $C_{0.33}B_{0.42}N_{0.25}$ and insulating type. The XPS measurement showed the existence of bonding between the main elements C, B, and N and suggest that a single-phase CBN may be present in the film with higher B content.

References

[1]- A.R. Badzian, S. Appenheimer, T. Niemyski, and E. Olkusnik, *in Proceedings of the 3rd International Conference on Chemical Vapor deposition*, edited by F.A. Glaski (American Nuclear Society, Hinsdale, IL, p.747 (1972)
[2]- S.H. Chen and R.J. Diefendorf , *in Proceedings of the 3rd international Carbon Conference*,Baden-Baden, Germany 1980.
[3]- C.E. Lowell, J. Am. Ceram. Soc. 50(3), 142 (1967)
[4]- J. Kouvetakis, R.B. Kaner, M.L. Sattler, and N. Bartlett, J. Chem. Soc.Chem. Com., 1758 (1986)
[5]- J. Kouvetakis, T. Sasaki, C. Shen, R. Hagiwara, M. Lerner, K.M. Krishnan, and N. Bartlett, Synth. Metals 34, 1 (1989)
[6]- M. Yamada, M. Nakaishi, and K. Sigishima, J. Electrochem. Soc. 137(7), 2242 (1990)
[7]- L. Maya, and L.A. Harris, J. Am. Ceram. Soc. 73(7), 1912 (1980)

EXELFS STUDIES OF CN$_x$ THIN FILMS

R. Räty[1], S. Csillag[1], H. Sjöström[2], J-E Sundgren[2]

[1]University of Stockholm, Dept. of Physics, Box 6730, S-113 85 Stockholm, Sweden
[2]University of Linköping, Thin Film Division, Dept. of Physics, S-581 83 Linköping, Sweden

Key words: CN$_x$, EELS, EXELFS

Abstract

Electron energy loss spectroscopy is used to analyse the structure of a CN$_x$ thin film deposited on a Si (001) substrate, held at 500°C, by reactive magnetron sputtering. The elemental composition is determined to ~20 at% nitrogen. From the near edge spectra of the carbon K edge a sp^2 contents of ~53 % could be estimated. In the Extended Energy Loss Fine Structure analysis an unusually broad and intense peak was found in the RDF at ~8.8 Å. This peak is regarded as evidence of some large scale spherical structures also seen in the High Resolution Electron Microscopy micrographs.

1. Introduction

Carbon nitrites has been the object for intense studies after the theoretical predictions of the ultra hard β-C$_3$N$_4$ phase. It has turned out that this specific compound is difficult to synthesise, but a large number of other materials with interesting properties have been discovered during these attempts. In this paper an EELS analysis is performed on a CN thin film with a N content of ~20 at%, which previously have been found using nanoindentation to have a hardness of 40 to 60 GPa and a elastic recovery as high as 85 % [1]. HREM images of the film display strongly bent and curved "graphite-like" planes, which can be formed by introducing pentagons into a graphite structure. In such a structure the nitrogen atoms are substitutionally incorporated in the graphite structure. The curved planes causes bonding between the basal planes an thus a three dimensional network. Similar structures of three dimensionally bonded carbon have been predicted to have a bulk moduli as high as 362 GPa [2] which should be compared with that of diamond 433 GPa.

2. Experimental details

The 300 nm thick carbon nitride films were deposited onto Si(001) substrates held at a temperature Ts of 500 °C by reactive d.c. magnetron sputtering of pure carbon in

nitrogen discharges. The details of the deposition system and process have been described in more detail elsewhere [1]. The HREM analyses of the films were performed using a Philips CM 20 UT transmission electron microscope (TEM) having a point resolution of 1.9 Å. EELS measurements was performed on an ion milled sample with a 100 keV STEM electron microscope (VG, HB501) with a Gatan PEELS spectrometer. The low loss spectra together with C K and N K edge and near edge spectra were recorded.

3. Analysis and results

The plasmon energy is found to be 24.7 eV, which means the free electron density is comparable to those of graphite, 26-27 eV [3],[4], amorphous carbon, 23-24 eV [3], [4] and substances like CBN, 25 eV [5] and C_{60}, 26 eV [6]. An quantitative elemental analysis of the ionisation edge intensities gave a nitrogen concentration of 17-20 at% compared to carbon, which is consistent with the RBS results. Traces of oxygen and silicon could also be identified by the weak presence their ionisation edges.

The C K and N K near edge spectra are shown in Fig 2. The carbon spectra shows much less detail than the nitrogen edge, this is probably due to an amorphous carbon layer on the film, a remnant from the ion milling.

The π^* peak reveals the presence of sp^2 bonds i.e. trigonally bound atoms [7]. Following the procedure Berger et al [3] uses for carbon the sp^2 fraction, f, was calculated. Due to lack of symmetry the electrons in the sp^2 bonds are split in energy, into the π^* and σ^* peaks, no splitting is present in the symmetrical sp^3 bonds where consequently the π^* peak is missing. By comparing the π^*/σ^* ratio of an unknown compound to one that is 100 % sp^2 one is able to estimate the amount of sp^2 bonds in the unknown

$$f_{CN_x}\left(sp^2\right) = \frac{I_{\pi^*g}}{I_{\pi^*CNx}} \frac{I_{\sigma^*CNx}}{I_{\sigma^*g}} \approx 53 \pm 10\%$$

sample, with the reservation for other types of bonds present. The ratio was normalised to that of graphite, which is a pure sp^2 compound. The π^*/σ^* ratio is strongly

Fig. 2 The C K and N K near edge spectra after background subtraction. The carbon ionisation energy is 285 eV and the edge has been shifted to overlap with the nitrogen edge at 401 eV. The edges are essentially the same i.e. they mirror the same chemical environment.

Fig. 1 The lowloss spectra of the CNx film

orientation dependent so the spectra has to be an average of all possible beam directions in relation to the planes, this should however not be a problem since the bent planes suggested for the film structure automatically yield an average for the material.

An EXELFS analysis was performed of the N K edge in order to determine the radial distribution function (RDF). Unfortunately a weak oxygen edge at 532 eV, most probably surface contamination, limited the energy range that could be used in the analysis. EXELFS analysis [8] extracts structural information from the modulations in the ionisation edge originating from interference between the outgoing electron wave with the back scattered wave from the atoms in the neighbourhood. These modulations are typically found from ~20 eV behind the edge up to a few hundred eV. Assuming that the ejected electron wave can be approximated with a plane wave the modulations can be described by

$$\chi(k) = \sum_j \frac{N_j}{r_j^2} \cdot \frac{f_j(k)}{k} \cdot e^{-2\sigma^2 \cdot k^2} \cdot e^{-2r_j/\lambda} \cdot sin\left(2kr_j + \Phi(k)\right)$$

where k is the wave number for the electron wave, N is the number of atoms in the shell, r the distance from the central atom, f(k) the back scattering amplitude which is differs for different atoms, σ is the Debye-Waller factor describing the disorder in the material, λ is the inelastic mean free path and $\Phi(k)$ is the phase change in the wave as it is back scattered.

After background and plural scattering removal from the N K edge a Fourier transform of the modulations yield the RDF which is shown in Fig 3. Since the energy range is limited the determination of the short inter atomic distances is not very accurate. These peaks correspond to the long wavelengths in the modulations, which are most affected by the limited energy interval. So the in plane inter atomic distances can unfortunately not be determined, they are all smeared out to one peak. The next peak at 3.5 ±0.2 Å corresponds to the distance between the planes obtained also with diffraction, see Fig. 4. The most significant feature is however the broad peak at ~8.8Å .The broadness of the peak shows that there is a distribution in the distances either in the individual shells and/or that
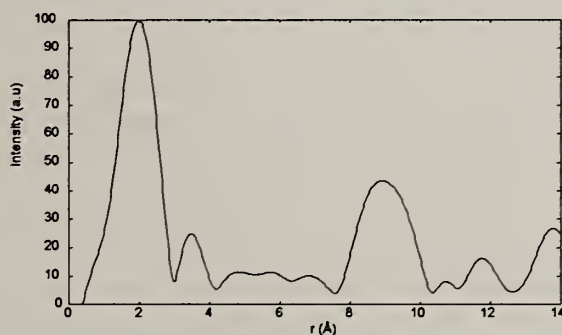
Fig. 3 The RDF of the N K edge. A phase correction of 0.36 Å has been added to the peaks, the average of the phase correction for carbon (0.35) [9] and that of nitrogen (0.37) [9] is used since there is no way to distinguish between the different back scattering atoms. In this case the difference between the back scattering phase corrections is so small that this doesn't affect the results. Notice the broad peak at ~8.8 Å which indicates that there are some large scale spherical structures in the CN_x film. The peak is unaffected by different analysis procedures and a similar peak although not as intense is also found in the carbon spectra.

884

there are different sized shells. In a "normal" RDF, from light atom backscatterers, there are no strong peaks that far out. The intensity of a peak in a RDF depends on the factors in front of the sine term in the expression above. That is the intensity for a given number of atoms at distance r is essentially inversely proportional to r^2, since the Debye-Waller factor is small and the inelastic mean free path comparably long (at least 100 Å). Geometrical factors may however also influence the intensity, spherical symmetry for example may introduce some focusing effects of the back scattered electron wave thereby increasing the intensity. To account for the high intensity of the peak a relatively high concentration of atoms is needed at this distance and a comparably low concentration of atoms within this shell, otherwise the intensity of the electron wave will be reduced by the atoms in between. The simplest assumption satisfying these requirements is a spherical shell. However looking at the formula above and normalising it with regards to the intensity of the first peak one can see that 35-60 atoms are sufficient to produce this peak. Spreading these atoms on a 8.8 Å radius sphere gives approximately 50-80 $Å^2$ per atom, a very airy structure, so a part of a sphere or possibly a ring of atoms, sections through bent planes or tubes, is more reasonable. This would confirm the existence of large scale semi spherical structures that are seen in the HREM pictures, there are also additional peaks seen at 11.5 and 13 Å.
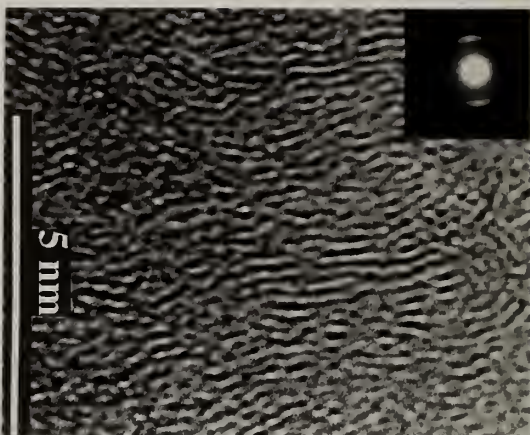
Fig. 4 shows a HREM micrograph from the investigated carbon nitride film. The microstructure can be described as graphite-like where the basal planes are bent into a wavy structure. The curved structures were found to have radii in the range 8-18 Å. The diffractograms obtained from this structure (the inset in Fig. 4) show a clear effect of deviation around a preferential orientation and the average plane distance between the basal planes as determined from both diffraction patterns and HREM micrographs was 3.47 Å

1. H. Sjöström et al, submitted to PRB.
2. A.Y. Liu and M.L. Cohen, Phys. Rev. B 45 (1992) 4579.
3. S.D.Berger and D.R.McKenzie, Phil. Mag. Lett. 57 (1988) 285.
4. H.Tsai and D.B.Bogy, J. Vac. Sci. Tech. A 5 (1987) 3287.
5. O. Stephan et al, Science 266 (1994) 1683.
6. Y. Saito, Jap. J. Appl. Phys. 30 (1991) 1068.
7. R. Brydson et al, Microsc. Microanal. Microstruct. 2 (1991) 159.
8. M.A. Tafreshi et al, Microsc. Microanal. Microstruct. 1 (1990) 199.
9. B.K Teo and P.A. Lee, J. Am. Chem. Soc. 101 (1979) 2815.

THE INVESTIGATIONS OF C:N SINGLE CRYSTALS GROWTH AND ITS PROPERTIES.

V.G.Babaev, M.B.Guseva, V.V.Khvostov, V.M.Babina, A.M.Moryashov.

Department of Physical Electronics, M.V.Lomonosov State University, Moscow 119899 (Russian Federation).

Key words: nitrogen, sputter assisted plasma enhanced deposition.

Abstract

We present the results of a study on atomic and electron structure of C:N single crystals prepared by sputter assisted plasma enhanced deposition in Ar/N ambient. The samples were characterized by high energy electron diffraction, TEM, Auger Electron and Raman Spectroscopy. The investigations show that at temperature of T=-100 ^{0}C C:N films were amorphous, but at higher temperatures they contain many microcrystallites some micrometer in size. The nitrogen content in the films depends on temperature. It was 36% at low temperatures and decreased slightly at higher temperatures. Raman spectrum possesses two broad peaks with maxima $v=1350 cm^{-1}$ and $v=1580 cm^{-1}$. The first is due to =C=N- and thesecond C=C vibrational modes. No C-H vibration modeswere observed in C:N films.

1.Introduction.

Hard C:N films have been attracting a great deal of interest due to their vast potential for a wide variety of application - extreme mechanical strength, chemical inertness, high thermal conductivity, tunable optical properties and IR transparency. Several attempts have been made to synthesize C:N compounds, using physical vapor deposition such as reactive d.c. magnetron sputtering [1], r.f. sputtering [2], chemical vapor deposition (CVD) [3-6] and laser ablation [7].

2.Experimental details.

Films were deposited using a sputter assisted plasma enhanced deposition system. A graphite target (purity 99,999%) 30 cm in diameter was used. Argon and nitrogen were mixed outside the chamber. The substrates (c-Si, NaCl) were placed on a heated, cooled and biased holder. The holder could be heated up to 200 ^{0}C or cooled
down to -100 ^{0}C. A typical deposition process was as fallows: the vacuum chamber was evacuated to 10 Torr by turbomolecular pumper , the desired gas mixture was introduced into chamber at pressure of 10^{-4}. -10^{-2} torr . The bias voltage was varied from 0 to -200 V. The Raman spectra of the C:N films were measured at atmospheric room temperature by a backscattering method using U1000 device. The Ar+ ion laser with a wavelength of 514.5 nm was used. Wave number resolution was 4 cm^{-1} . The measuring was performed with a step 2 cm^{-1} .

To study the surface of films both electron microscopy and Auger electron spectroscopy with self-deconvolution of KVV Auger line were used. Both methods were described in detail in [8].

3.Results and discussion.

3.1 Chemical Composition
The experimental results obtained by Auger spectroscopy are presented in Fig.1, where nitrogen concentration of the films is shows as a function of deposition temperature. Ar partial pressure was constant during the
deposition and was equal to $1*10^{-3}$ Torr. To obtain a high nitrogen concentration in the films it was necessary to decrease the deposition temperature up to T=-100 ^{0}C.

3.2 Transmission electron microscopy
The diffraction patterns from TEM observation of as-deposited samples at low temperatures are amorphous. At room temperature deposition (Fig 2) it was observed six first order point reflections corresponding to d=4.60 A interplane distance. This structure corresponds to a closely packed carbon-nitrogen chains with cylindrical symmetry. The calculated inter chain distance is a=5.30 A. At T>180 ^{0}C single crystals (Fig 3a) was observed. The diffraction pattern shows a hexagonal (hk.0) reflections with d_{100} =4.60 A This yields the hexagonal lattice constant a = 5.30 A.

3.3 Auger electron spectroscopy study of valence band
High resolution KVV Auger spectrum of carbon was recorded from room temperature C:N films with chemical composition C - 80% , N - 20% .

(DOVS) as a function of electron binding energies E in this C:N film is shown in the Fig.4. The DOVS n(E) shows two sharp maxima at E=19 and E=26 eV corresponding to the top and the bottom of one dimensional σ band structure of cumulene chains. The electron states below then E=19 eV correspond to π band. Calculated binding energies of cumulene and polyyne chains are shown for comparison in Fig.5.

3.4 Raman Spectroscopy
Raman spectra of C:N films with different nitrogen concentration are shown in fig.6.Raman spectra shows two
broad maxima at $\nu_1 = 1550^{-1}$ cm and $\nu_2 = 1350$ cm^{-1} . The first maximum ν_1 correspond to vibration frequencies of carbon =C=C= chains and the maximum ν_2 correspond to =C=N-vibration frequency. From Fig.6 we can conclude, that the intensity of =C=N- vibration maximum increases with the increasing of nitrogen content in C:N films.

4.CONCLUSIONS

The lattice constant a=5.30 A is in the range of lattice constants of a different hydrocarbon single crystals.The formation of C:N polymer can be described as follows. First stage is formation of -C≡N clusters by graphite sputtering in Ar/N gas mixture. Second stage is polycondensation: (-C ≡ N) - (=C=N-) and formation of poly(cian). In this stage we obtain oriented polymer chains. In third stage at higher temperatures the crosslinkage between poly(cian)chains: / (=C=N-)$_n$ → (≡C -N-)$_n$ and formation of single poly(cian) crystal take place.

5.REFERENCES
1. M.Y.Chen, X Lin, V.P.Dravid, Y.W.Chung, M.S.Wong and W.D.Sproul, Surf.Coat.Technol.,54-55 (1992),360.
2. C.J.Torng, J.M.Siversten, J.H.Judy and C.Chang, J. Mater.Res.. 5 1990242490. .
3. M.Ricci, M.Trinquecoste, P.Delhaes, Surf.Coat.Technol., 47(1991)2299.
4. M.Ricci, M.Trinquecoste, F.Auguste, R.Canet, P.Delhaes, C.Guimon, G. Pfister-Guilljuzo, B.Nysten and J.P.Issi, J.Mater.Res.,8 (1993) 480.
5. H.X.Han and B.J.Feldman, Solid State Commun.,65 (1988) 921.
6. J.H.Kaufman and S.Metin. Phys.Revs.B., 39 (1989) 13053.
7. C.Nui, Y.Z.Lu and C.M.Leiber, Science, 261, (1993) 334.
8. M.B.Guseva, V.G.Babaev, V.V.Khvostov et all, Diamond and Related Materials, 3 (1994), 328-331.
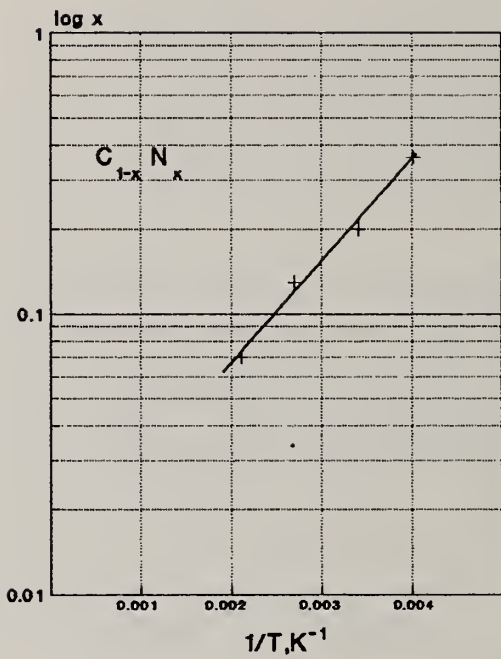
Fig.1 Evolution of N content with
deposition temperature

Fig.2 Diffraction pattern from C:N film
(T=20 °C).

Fig.3a Electron micrograph of C:N single
crystal (x20000)

Fig.3b Diffraction pattern from C:N film
(T=180 °C).
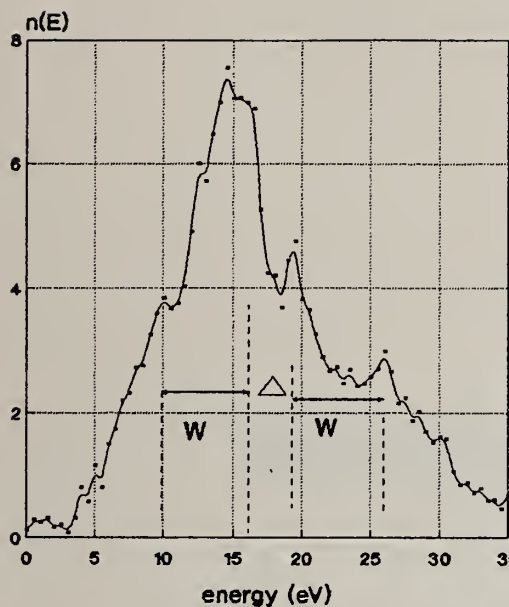
Fig.4 Density of states in the valence band of C:N film.
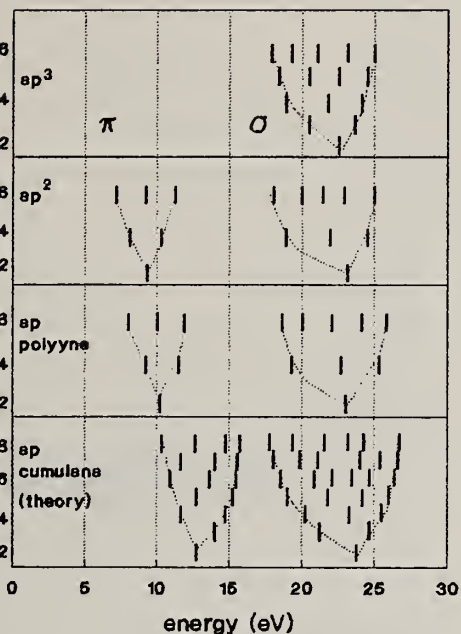
Fig.5 Calculated electronic terms of linear carbon chains.
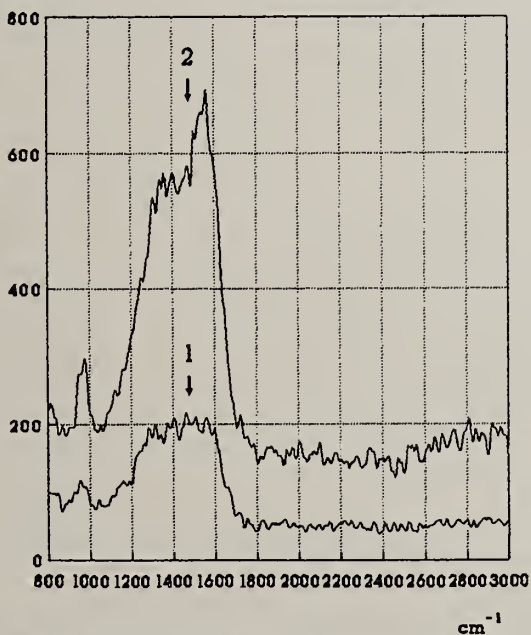
Fig.6 Raman spectra of C:N films: 1- 17at% , 2 - 23at% of nitrogen.

MISCELLANEOUS

PREPARATION AND CHARACTERIZATION OF SIC NANOFIBRILS

Chunming Niu, and David Moy

Hyperion Catalysis International Inc., 38 Smith Place, Cambridge, MA 02138

Key words: silicon carbide, nanofibrils, nanowires, nanorods, nanocomposites

Abstract

SiC nanofibrils have been prepared by direct reaction of carbon nanotubes with vapor phase SiO. The carbon nanotubes which are characterized by having substantially uniform diameters between 70-120 Å, multiple graphitic carbon layers arranged concentriclly around the tube axis, and a hollow core, were prepared by catalytic decomposition of hydrocarbons. Electron microscope studies of SiC nanofibrils as prepared revealed that the reaction was a pseudo-topotactic transformation since the product inherited macroscopic features of the starting carbon nanotubes. The diameters of the SiC are substantially uniform, and average about 150 Å. The crystallographic structure of the product was characterized with X-ray and electron diffraction. Both XRD and ED patterns can be indexed as β-silicon carbide with a cell parameter of $a = 4.36$ Å. Furthermore, the select area electron diffraction studies of individual SiC fibrils suggest that they are multi-twinned single crystals.

1. Introduction

Recently, nanostructured materials have attracted considerable experimental and theoretical interest. The study in this area has led to various new materials[1], such as high temperature ceramics exhibiting superplasticity or porous silicon with novel optical properties. SiC nanofibrils are interesting for their potential in the development of supertough, superstrong ceramic and metal matrix nanocomposites. Because of high surface area and high temperature properties, SiC nanofibrils are also interesting for use as a support for the development of new catalysts[2]. In addition, SiC is a wide band gap semiconductor. It has high electron mobility, thermal conductivity, hardness and stability at high temperature. Interesting electronic and optical properties may result from its nanofibril structure.

Although several methods are available for the preparation of SiC fibers with large diameters[3], the synthesis of SiC nanofibrils has remained a challenge. Herein, we report

our studies of the preparation and characterization of SiC nanofibrils. We have found that catalytically grown carbon nanotubes can be totally converted to SiC nanofibrils by direct reaction of the nanotubes with gas phase SiO. As prepared SiC nanofibrils are characterized by narrow diameter distribution in the range of 100 - 200 Å and unique macroscopic morphologies of interwined bird's nest-like clusters or semiparallel bundles, which are inherited from the starting carbon nanotubes. The individual SiC nanofibrils are multi-twinned single crystal β-SiC nanorods.

2. Experimental

The SiC nanofibrils were prepared by direct reaction of carbon nanotubes with vapor phase SiO (Johnson Matthey) at high temperature between 1200-1400 °C. The carbon nanotubes were manufactured by a continuous commercial catalytic process[4]. X-ray diffraction patterns were recorded using a Phillips diffractometer at a 2θ rate of 1°/min from 20° to 80°. SEM studies were carried out with a JEOL JSM-640 microscopy. TEM studies were performed on a Phillips EM 420 microscopy.

3. Results and Discussion

Fig. 1 shows TEM and SEM micrographs of the starting carbon nanotubes. The
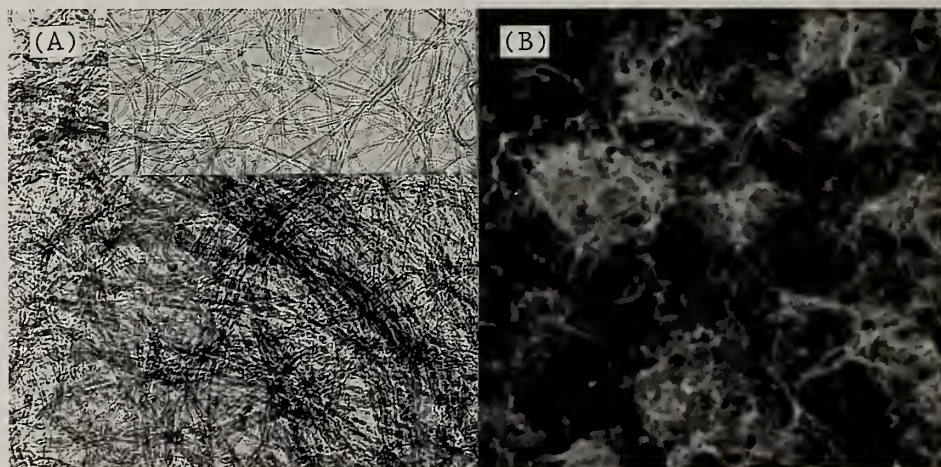
Fig. 1. Electron micrographs of the carbon nanotubes: (A) TEM micrograph of dispersed nanotube bundles, x100000. The diameters of the tubes are ~ 80 Å. The inset shows highly dispersed carbon nanotubes; (B) SEM micrograph of as prepared carbon nanotubes, x20000. The tubes are interpenetrating to form a bird's nest like texture. The diameter of the nests are ≤ 1 μm.

microstructure (Fig. 1A) of the starting carbon nanotubes are similar to that reported

for buckytubes[5]. As prepared tubes are substantially free of amorphous carbon coating, and are characterized by a narrow diameter distribution of 70-120 Å, aspect ratios of 500-1000, and a hollow core. The macroscopic morphologies of the tubes depend on the design of the catalysts. In Fig. 1B, the aggregates are made up of tubules that are highly interwined, resembling bird's nests.

After reaction with SiO, The black color of the carbon nanotubes was changed to dark green. Fig. 2 shows electron micrographs of the greenish product. The TEM photo (Fig. 2A) revealed that the hollow carbon nanotubes were converted to solid needle-
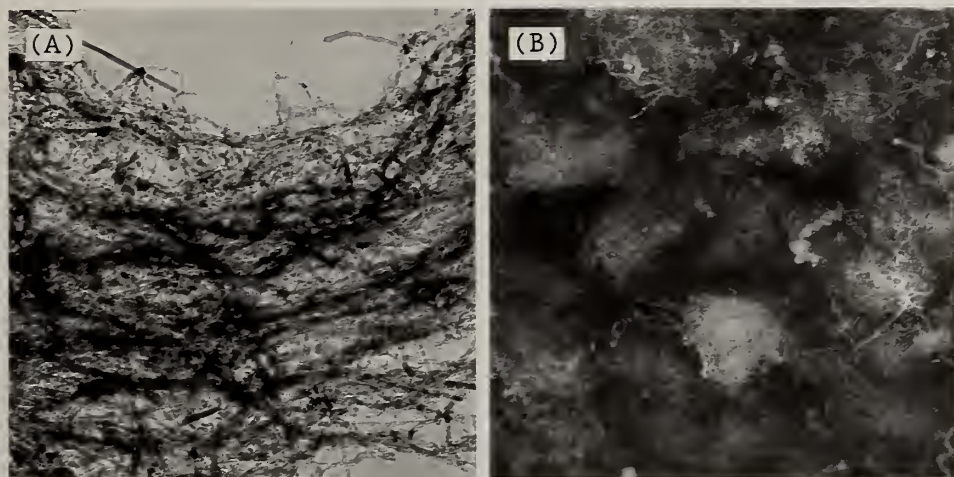
Fig. 2. Electron micrographs of the SiC nanofibrils: (A) TEM micrograph of the SiC nanofibrils, x62500; The diameters of the fibrils are ~ 150 Å; (B) SEM micrograph of as prepared SiC nanofibrils, x10000. The aggregates resemble that of the starting carbon nanotubes.

like fibrils. No hollow carbon nanotubes were observed. The absence of hollow tubules indicated that a complete conversion of the carbon nanotube was achieved. The examination of as prepared sample with SEM (Fig. 2B) revealed that the macroscopic morphologies of the product remain almost unchanged in comparison with that of the starting materials (Fig. 1B). As shown in Fig. 2A, the diameters of needle-like fibrils are remarkably uniform. The average diameter is about 150 Å, which is about 50% bigger than that of the starting carbon nanotubes. The crystallographic structure of the product was characterized by X-ray and electron diffraction. The results in comparison with the β-SiC standard of JCPD 29-1129 are tabulated in Table 1. All reflections of XRD pattern recorded from 2θ of 20°-80° and the ED ring pattern recorded from multiple nanofibrils can be indexed as β-SiC with a cell parameter of $a = 4.36$ Å. Furthermore, electron diffraction studies of single fibrils suggested that individual fibrils are multi-twinned single crystals.

Table 1. XRD and ED Results of SiC Nanofibrils

| d-Space (Å) | | | Intensity | | | h k l |
XRD	ED	29-1129*	XRD	ED	29-1129	
2.53	2.54	2.5200	100	vs	100	1 1 1
2.19	2.20	2.1800	6	w	20	2 0 0
1.55	1.54	1.5411	30	s	35	2 2 0
1.32	1.31	1.3140	21	s	25	3 1 1
1.26	1.25	1.2583	3	w	5	2 2 2
---	1.10	1.0893	---	w	5	4 0 0
---	1.00	0.9999	---	w	10	3 3 1
---	0.97	0.9748	---	w	5	4 2 0
---	0.89	0.8895	---	w	5	4 2 2
---	0.83	0.8387	---	w	5	5 1 1
---	0.74	---	---	w	---	---
---	0.45	---	---	w	---	---

* JCPD card: 29-1129, β–SiC, Cubic/F-43m, a=4.3589 Å
vs: very strong, s: strong, w: weak

Although the mechanism of reaction is not clear at this point, it appears that diffusion of Si and C atoms during the reaction is very much confined within individual carbon nanotubes in the direction perpendicular to the tube axis, and that the reaction of the carbon nanotubes with vapor phase SiO is a pseudo-topotactic transformation since the macroscopic characteristics of the starting carbon nanotubes remain almost unchanged in the SiC products. A complete conversion of the carbon nanotubes to the SiC nanofibrils is easily achieved. It has been reported[3] that a similar reaction for the preparation high surface area SiC powder using carbon black as the starting carbon material never proceeded to completion. We believe that the unique structure of the carbon nanotubes, such as nanometer diameters (small diffusion length)and looseness (easy diffusion for SiO) of the aggregates (Fig. 1) are key factors allowing a total conversion.

4. References

1. G. Whitesides, et al, Science, 252, 1312(1991); H. Gleiter, Adv. Mater., 7/8, 474(1992); C. T. Canham, Appl. Phys. Lett., 57, 1046(1990); T. K. Sham, et al, Nature, 363, 331(1993).
2. W. Habel, et al, J. Organometallic Chem., 486,267(1995); R. V. Krishnarao, et al, J. Mater. Sci., 29, 2741(1995); D. Zhou, et al, Chem. Phys. Lett., 222, 233(1994); R. S. Wagner, et al, Appl. Phys. Lett., 4, 89(1964); K. Okada, et al, J. Amer. Ceramic Soc., 77, 1691(1994).
3. M. Benaissa, et al, J. Mater. Sic., 29, 4700(1994); J. Crystal Growth, 131, 5(1993).
4. H. Tennent, et al, US Patents 4,663,230(1987); 5, 165, 909(1992).
5. S. Iijima, Nature, 354, 56(1991).
6. We thank Y-Z. Lu at Harvard MRL for his assitance in microscopic work.

HIGH PRECISION MACHINING OF CARBON PRODUCTS

Toshiaki Furusawa, Hiroshi Hino, Susumu Norose and Simesu Nakamura

School of Science and Engineering,Teikyo University
1-1 Toyosatodai,Utsunomiya-shi,Tochigi,JAPAN

Key words: high-precision machining,carbon fibrous composite,glass-like carbon,single-crystalline diamond,CBN

Abstract

The purpose of this study is to obtain the optimum conditions to form high precision finished surface of carbon fibrous composites and glass-like carbon. The accuracy of finished surface and tool failure are investigated. The states of diamond tools have singular wears which are different from usual abrasive wear owing to isotolopy of carbon. As the surface textures, in the case of composite surface textures of finished surface are different in matrix, reinforcing material itself and boundary. In the case of glass-like carbon, surface textures depend on the sharpness of cutting edge.

1.Introduction

The carbon materials are attempting to be used toward the high technological fields because of high strength, anti-wear and electrical conductivity, etc. Regarding the machining of these materials,it is extremely difficult to finish a smooth and high-precision surface with few surface defects because of the brittle property of these. Moreover,the problem of tool wear is also seriously[1].
The purpose of this study is to obtain a minimally rugged and homogeneous finish surface of carbon fibrous composites and glass-like carbon,while paying attention to tool life. This report is a summary of a test machining by changing the tools and varying cutting conditions machined on an ultra-precision lathe.

2.Testing methods

The composites used were as shown in Table Ⅰ. Pitch based and mesophase pitch based carbon fibers were used as the reinforcing materials. Then we call these PCFRM and MCFRM. It's possible to say that both fibers fracture without yielding, because the value of breaking elongation are almost equal to the value calculated from the tensile strength and the Young's modules. The fiber orientation was nearly two-dimensional random. The glass-like carbon used was shown in Table Ⅱ.
Table Ⅲ showed the tools used. The crystal orientation of the single-crystalline diamond tool was almost (100) on the cutting face. Since the high-precision cuttings are aimed in this study,tests were carried out by paying special attentions to testing machine and environmental conditions. The machine was an ultra-precision disk lathe built with air spindle and granite bed. The environmental conditions were room temperature of $20\pm1°$ and humidity of $55\pm2\%$.

3.Test results and discussions

(a) Carbon fibrous composites
In the high-precision cutting of aluminum based composites the finished surface have the different textures on the reinforcing materials and the matrix, because these materials which have the different strength are deformed and fractured by a same tool[1]. Therefore, the surface textures of the finished surfaces are classified into matrix, fibers themselves on which the surface defects are formed, and the boundary between fiber and matrix.
Shown in Fig.1 are these surface parameters, an acceptable results are obtained with the MCFRM. In the case of PCFRM, the projecting height of fibers is larger than the

Table I Carbon fibrous composites

Carbon fiber/AC7A		
Material constants of fibers		
	Pitch based	Mesophase pitch based
Diameter of fiber	12.5μm	7-16μm
Length of fiber	0.22-1.5mm	0.22-1.5mm
Tensile strength	686MPa	1960MPa
Young's modulus	33.3GPa	441GPa
Elongation	2.1%	0.5%
Density	1.63×10³kg/m³	2.08×10³kg/m³
Processing method	High pressure casting	
AC7A		
Young's modulus	71.0GPa	
Tensile strength	267MPa	

Table II Glass-like carbon

Bending strength	225MPa
Young's modulus	29.4GPa
Density	1.55×10³kg/m³
Shore hardness	130

Table III Tools used

Single-crystalline diamond tool	
Rake angle	0°
Clearance angle	5°
Approach angle	30°
Rounded radius	0.4mm
Cubic boron nitride(CBN) tool	
0°, 0°, 11°, 11°, 45°, 45°, 0.4mm	
Grade	BN200
Cemented carbide tool	
-5°, -6°, 5°, 6°, 15°, 15°, 0.4mm	
Grade	K10
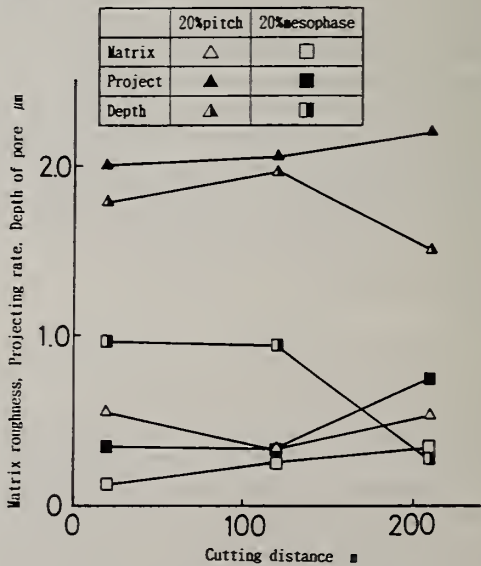
Fig. 1 Variation of cutting distance and surface parameters in the case of PCFRM and MCFRM (Single-crystalline diamond, N=1000rpm, V=145-393m/min, f=0.01mm/rev, d=10μm)

depth of pores. On the contrary, the depth of pores caused by falling-off of fibers is larger in the case of MCFRM. Moreover, there is a tendency for the depth of pore to decrease with the both composites. It's possible to say that mesophase pitch based fiber is brittle because of the larger Young's modules and the smaller elongation in comparison to the mechanical properties of both fibers. Thus, when finished surface is generated by diamond cutting, the pores caused by fracture and falling-off of fibers are formed.

On the other hand, in the case of pitch-based fiber as the Young's modules of fiber is smaller than that of matrix and the tensile strength of fiber is 2.6 times as larger as that of matrix, therefore the fibers are not easy to fracture even if the matrix suffers severe strain. Subsequently the fibers are not fractured but tend to project in the process of elastic recovery after the passage of tool edge, since the cutting direction is parallel to the fiber orientation. The fibers tend to remain on the finished surface so that the pores relatively decrease.

Fig.2 shows the scanning electron microscopy (SEM) photographs of the outline of the damaged tools used in the test of carbon fibrous composites. In comparison to the alumina fiber composites[1], the states of tool damage are singular. Exactly the tool damage used in the test of alumina fiber composites is abrasive wear, but in the case of PCFRM that isn't uniform with the pit and in the case of MCFRM that is irregular with the groove parallel to the friction direction.

(a) 20% PCFRM(Cutting distance:245m)   (b) 20% MCFRM(Cutting distance:245m)

Fig. 2 SEM photographs of damaged tools(Cutting conditions : Fig. 1)

(b) Glass-like carbon

Shown in Fig.3 are the SEM photographs of the finished surface cut by the single-crystalline diamond, the CBN and the cemented carbide tool. Besides, the photograph of the surface polished with the sand paper of #4000 is shown in this figure. In the case of the diamond tools, the textures of the finished surface are formed by the brittle fracture. On the other hand, in the case of the CBN tool and the cemented carbide there are locally flat portions on the surface, but the pore formed by the brittle fracture are remained. As for the polished surface there is not the surface cracks on the surface.

Shown in Fig.4 are the SEM photographs of worn tools. The amounts of the tool wear are large. From Fig.3 and Fig.4, it is considered that the reason for an improvement of the surface roughness with the CBN tool and the cemented carbide should be to the rubbing between tool flank and workpiece because of the severity of tool wear. It seems to consider that the wear type of these tool are mainly abrasive. But in the case of the single-crystalline diamond tool shown in Fig.4, the tool wear isn't uniform with the pit, the state of tool wear is similar to the case of carbon fibrous composites. This phenomenon seems to be caused by the isotolopy of carbon.

(a) Single-crystalline diamond

(b) CBN

(c) Cemented carbide

(d)#4000 polishing
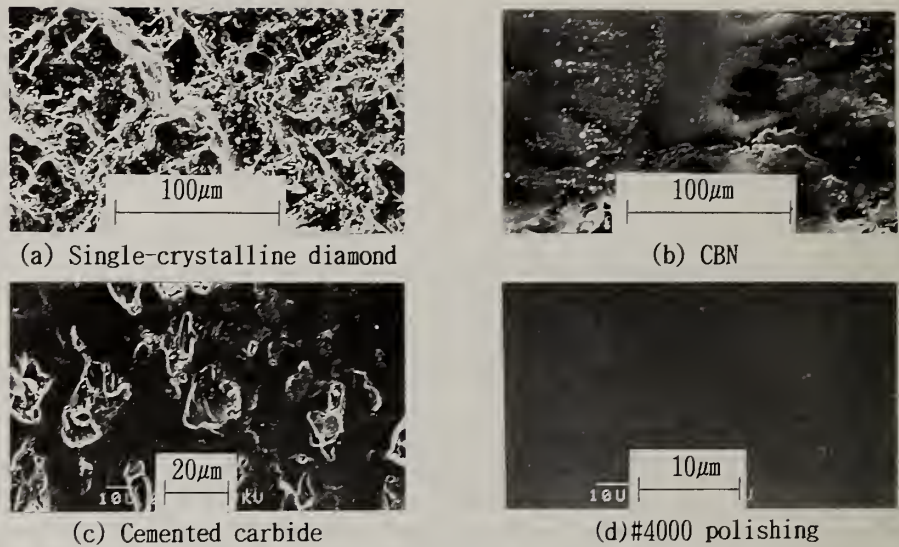
Fig. 3   SEM photographs of finished surfaces(N=1000rpm, V=314-393m/min, f=0.12μm/rev, d=0.5μm, 20times cut)

(a) Single-crystalline diamond   (b) CBN   (c) Cemented carbide
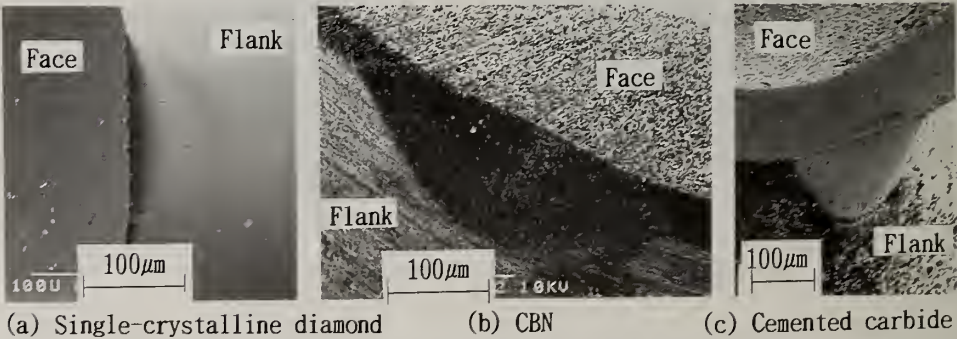
Fig. 4   SEM photographs of worn tools(Cutting conditions : Fig. 3)

4.Conclusion

By making machining finish of carbon fibrous composites or glass-like carbon using an ultra-precision lathe, the followings are revealed.

(1) The finished surfaces of the composites are divided into three portions,that is,the matrix,the reinforcing materials themselves,and the boundary between the reinforcing material and matrix.

(2) The states of diamond tools have singular wears which are different from usual abrasive wear owing to isotolopy of carbon.

5.References

1.T.Furusawa,H.Hino,S.Norose,T.Isogai,S.Nakamura,K.Yamada,K.Kishi:J.of JSPE,58,4(1992)641.

THE EFFECT OF SUBSTRATE BIAS ON SELECTED PROPERTIES OF Ta-C FILMS DEPOSITED BY FCVA TECHNIQUE

Tay B K, Shi Xu, Tan H S , Li Zhong and Tu Yuqiang
School of Electrical and Electronic Engineering, Nanyang Technological University,
Singapore 2263

Key words : filtered cathodic vacuum arc, substrate bias, tetrahedral amorphous carbon, thin film deposition

Abstract

Substrate bias is known to be an important parameter in the determination of properties of films deposited by Filtered Cathodic Vacuum Arc (FCVA) technique. The bias affects the ion energies reaching the substrate during the film growth process. In this paper, substrate bias was varied keeping other deposition conditions constant to study the effect of the bias on the properties of the film. The films were characterized by their optical and mechanical parameters using the ellipsometer, profilometer, spectrometer and nanoindentor.

1. Introduction

FCVA technique has been reported to be an efficient method of producing at relatively low temperature ($< 60°C$) high quality films virtually free of macroparticles [2-3]. Extensive study has shown that 80% of the carbon atoms in the film produced by such a technique form a random tetrahedral (sp^3) network, hence the name Tetrahedral-Amorphous Carbon (Ta-C) film. Studies of the Ta-C film properties correlated to the sp^3 bonding has been carried out extensively by Martin, McKenzie, Fallon, Veerasamy, and their co-workers [2-7]. In particular, the determination of the optimal deposition ion energy to obtain high sp^3 content was important for developing practical film deposition processes. A range of films were therefore grown under different substrate bias voltage to vary the energy distribution of the carbon ions incident on the substrate. In this paper, we shall present the measurement results for some properties of the films and compared these results with those reported by other research groups.

2. Experimental Details

2.1   Deposition Setup

The system allows the deposition of several films at two different substrate dc bias voltages in a single run. The substrate can be left floating or negatively biased from 0 to -120V. The system base pressure was below 2.6×10^{-4} Pa but rises to 2.6×10^{-3} Pa

during deposition due to the gas released from the carbon target at room temperature. The arc current was set to 60 A and the toroidal magnetic field was fixed at 40mT. Deposition was carried out at room temperature.

2.2   Preparation of substrates

The substrates used were <100> oriented n-type silicon wafers of average thickness 0.28µm and Vitreosil quartz of average thickness 0.49mm. Both the silicon and glass surfaces were precleaned using acetone, trichloroethane, and de-ionized water treatment in an ultrasonic bath. Hydrofluroic acid was also used to remove the native oxide layer on the silicon surface. The properties of the deposited films were analysed in the following ways. The refractive index and thickness of the films were measured by using a ellipsometer producing an elliptically polarised incident narrow beam at a wavelength of 632.8 nm. The technique was used together with a Dektak 3030 profilometer step measurement to determine the stress. The optical properties of the films were also assessed over the range 250 - 900 nm on a Perkin Elmer uv-vis spectrometer. The surface roughness of films were also studied using the Atomic Force Microscopy (AFM) from Park Scientific Instruments. The hardness properties of the films were investigated using a nanoidenter from Nano Instruments.

3. Experimental Results

3.1   Thickness / Deposition Rate / Surface Roughness Measurement

The deposited film thickness was about 60 nm. Under the conditions described herein, the deposition rate at the substrate was estimated to be 0.3 nm/sec over an area of 20 cm^2. The AFM surface topography showed that the film surface were very smooth and the average root mean square (RMS) surface roughness of a 1µm x 1µm ta-C film deposited on silicon was 0.2nm. Few macroparticles and surface defects were observed.

3.2   Compressive Stress Measurement

The stress of the deposited film is always found to be compressive due to the generation of sp^3 bonds. The stress was determined by measuring the curvatures of the silicon substrates before and after deposition. Fig. 1 shows the dependence of compressive stress on substrate bias voltage. For each film examined by the profilometer, several separate areas of the film were measured and the variation of the results gives an indication of the error (as shown by the error bars). This uncertainty is due to the nonuniformity of the substrate curvature. The figure shows that the film stress peaked at a bias of about -100V compared to -120V found by Fallon [5].

3.3   Hardness Measurement

The hardness of the 60 nm Ta-C films deposited on silicon substrates was assessed from the loading-unloading curves measured by a nanoindentor. The nanoidenter technique allows indentation depth as thin as 10 nm to assess the film characteristics. The hardness, calculated from the plastic indentation depth of the indentation curve, is high in the surface layer and decreases as the indenter tip approaches the softer silicon substrates. As shown in Fig. 2, for an indentation depth of about 10% of the film

thickness, hardness values ranging from 34 - 42 GPa were obtained for the various conditions. To avoid the effect of substrate, a thicker film (~100 nm) was deposited under 0V bias and its hardness was found to increase from 36 GPa to 51 GPa.

3.4 Refractive Index Measurement

Fig. 3 shows the refractive index as a function of substrate bias. The refractive index and the absorption coefficient of the films at 633nm were found to be about 2.5 and 0.04 respectively compared to the values of 2.4 and 0.7 found by Martin [6].

3.5 Optical Energy Bandgap Measurement

Films produced from the cathodic arc are highly transparent in the visible spectrum. The film transmittance and reflectance were measured and the data were converted to optical constants n and k and then to the dielectric function $\varepsilon_1 + i\varepsilon_2$. A plot of ε_2 as a function of E (where E was the photon energy) were drawn from which the optical gap was determined by the intercept of the linear portion of the plot on the energy axis. Fig. 4 shows the optical gap as a function of substrate bias, ranging from 1.7 - 2.2 eV which were close to the values found by Veerasamy. [7]

4. Conclusion

The properties of amorphous diamond have been studied in terms of the substrate bias. The compressive stress and energy bandgap reached a maximum at around -100V bias whereas the hardness peaked at around -60V bias. The refractive index varies little over the range of the substrate bias. The technique of FCVA promises to be a viable method of depositing hard carbon films onto a variety of substrates at room temperature.

5. Acknowledgements

6. References

1. I I Aksenov, S I Vakula, V G Padalka, V E Strelnitskii and V M Khoroshikh, Sov. Phys. Tech. Phys. 25, 1164, 1980
2. P J Martin, S W Filipczuk, R P Neterfield, J S Field, D F Whitnall, D r McKenzie, J. Mater.Sci Lett, 7, 410, 1988
3. D R McKenzie, D Muller and B A Pailthorpe, Phys Rev. Letter, 67, 773, 1991
4. D R McKenzie, D Muller and B A Pailthorpe, Z H Wang, E Kratvchinskaia, D Segal, P B Lukins, P D Swift, P J Martin, G Amaratunga, P H Gaskell and A Saeed, Diamond Relat. Mater. 1, 51, 1991.
5. P J Fallon, V S Veerasamy, C A Davis, J Roberston, G A J Amaratunga, W I Milne, J Koskinen, Phys Rev B, 48, 7, 1993
6. P J Martin, Surface Engineering, 9, 1, 1993
7. V S Veerasamy, G A J Amaratunga, W I Milne , Diamond Relat.Mater.,2, 782, 1993

904
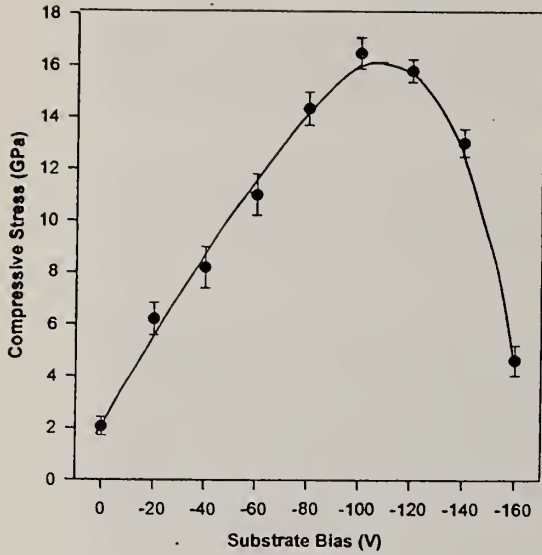
Fig 1 : Graph of Compressive Stress as a function of Substrate Bias
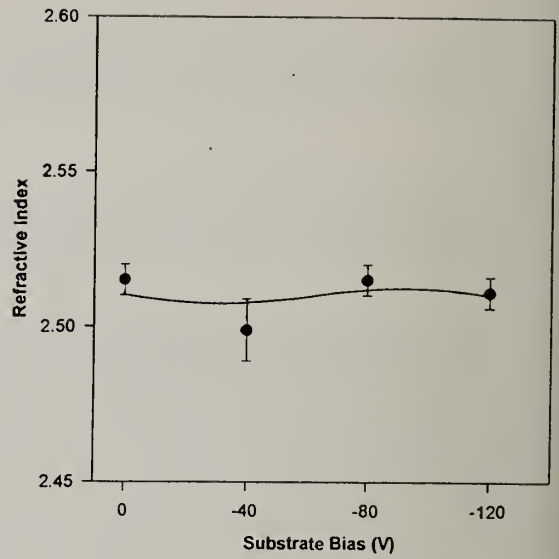
Fig 3 : Graph of Refractive Index as a function of Substrate Bias
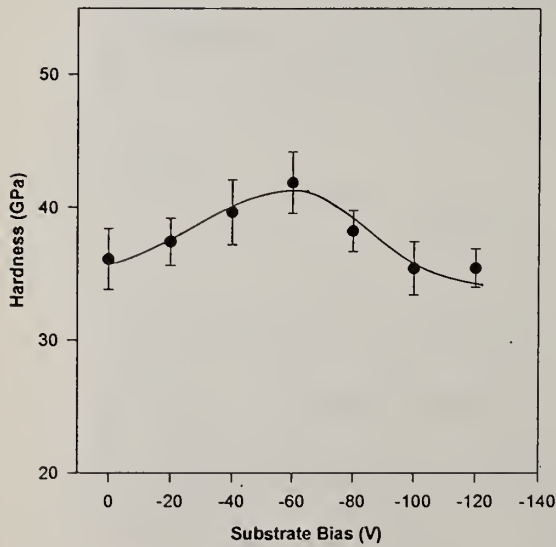
Fig 2 : Graph of Hardness as a function of Substrate Bias
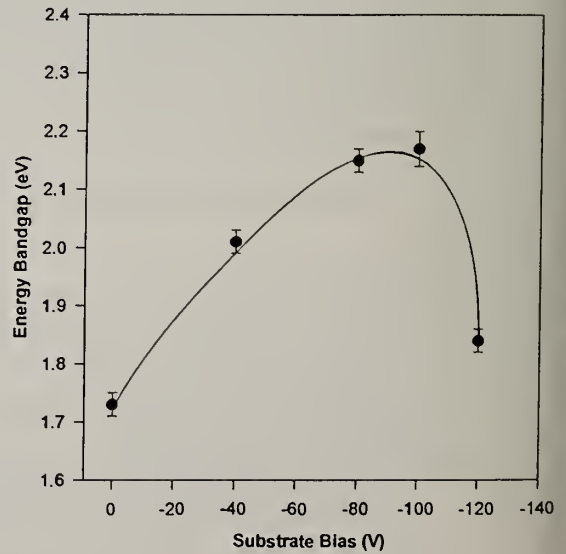
Fig 4 Graph of Energy Bandgap as a function of Substrate Bias

SURFACE MODIFICATION OF GLASS MICROSPHERES BY CARBON

E.Ivanova and M.Tsvetkova

St.Petersburg Technological Institute, Moscovsky Pr.26
St.Petersburg, 198013, Russia

Key words: carbon, low temperature synthesis, microspheres, surface

Abstract

Atom-molecular constructing of glass microspheres surface has been carried out at
450 °C from the gaseous mixture of tetrachloromethane and methane. It has been
shown, using chemical qualitative analysis, UV- and vibrational spectroscopy, that
the aromatic structures have been constructed on the glass surfaces. The present
investigation has resulted from the necessity to improve thromboresistance of glass
microspheres used for medical purposes.

1. Experimental data

Hollow microspheres of high silica content (86%) with the the mean particle
diameter 50 mcm were taken for investigation. Samples of microspheres were put
into the quartz reactor and treated with a gas mixture of methane and
tetrachloromethane vapour at 450 C. Gaseous products of the reaction were caught
by 0.2 n alkali solution. The selection of dynamic conditions for the synthesis
provided constant concentrations of tetrachloromethane and methane in the
reaction zone. After the reaction was complete and gaseous reaction products were
removed by the methane flow, there was formed a layer of carbon on the glass
microspheres surface. This carbon layer was investigated by combustion analysis.
The nature of layers has been studied using the technique of optical electronic
spectroscopy, Raman and FTIR spectroscopy.

2. Results

When considering the mechanism of the interaction of the gaseous mixture
tetrachloromethane-methane and glass microspheres surface,it is necessary to pay
attention to the surface structure of the microspheres. The surface structure of the
glasses of high silica content is characterized by the presence of silane and
siloxane groups. Dehydratation of silicate surface produces "stressed syloxane

surface" as a result of intramolecular condensation of OH-groups. Such a surface is known to have an increased chemisorbtion activity. There first occurs the process of interaction of active dehydrated sytes of the silicate surface, which were formed under the action of reaction temperature (450 C), and the components of the gaseous mixture. Parallel to that, hydroxyl groups, formed by the process of intramolecular hydrolysis, can also take part in the reactions. So as a result of the interaction of glass surface and gaseous mixture, functional groups of Si-O-C(CH3)3 type are formed on the surface. When reacting with tetrachloromethane, these groups take part in the formation of condensed aromatic fragments which are linked into a spatially polymeric structure. The thickness of the carbon layer being applied, is regulated by the time of the synthesis.

3. Practical applications

Carbon-coated microspheres found medical application in examining blood microcirculation in human organs. To reduce the extent of mechanical clogging of blood vessels, the injection of small amounts of spherically-shaped microparticles made of biologically inert material is suggested. The particles now in use (of proteins,protacryl and also glass balls) when introduced into blood vessels cause a change in the blood microcirculation because of the secondary aggregation of blood elements. Glass carbon-coated microspheres demonstrated eleven-times increase in thromboresistance (from 34% to 3%) and are successfully used to study blood microcirculation in different organs.

SILICON-CONTAINING DIAMOND LIKE-CARBON COATINGS FORMED BY ION BEAM ASSISTED DEPOSITION (IBAD): PROCESSING AND PROPERTIES OF A NEW CATEGORY OF HARD, WEAR RESISTANT THIN FILMS.

C.G.Fountzoulas[1], T.Z.Kattamis[2], J.D.Demaree[1] and J.K.Hirvonen[1]

[1]U. S. Army Research Laboratory, Materials Directorate, Watertown, MA 02172-0001
[2]Institute of Materials Science, University of Connecticut, Storrs, CT 06269-3136

Amorphous silicon-containing diamond like-carbon (Si-DLC) coatings were formed by thermal evaporation of a tetraphenyl-tetramethyl-trisiloxane (($C_6H_5)_4(CH_3)_4Si_3O_2$) diffusion pump oil (Dow Corning 704) onto silicon and steel substrates with simultaneous bombardment of the growing film with 40 keV Ar^+ ions to decompose the $(C_6H_5)_4(CH_3)_4Si_3O_2$ molecules. Both the current density of the ion beam and the oil arrival rate were varied to produce hard, adhesive films on room temperature substrates, with densities ranging from 1.4 to 2.3 g/cm^3 and Knoop microhardness values (at 15 g load) from 1000 to 2100 MPa. Unlubricated friction coefficients against an AISI 52100 alloy high chromium steel ball with a 100 g load ranged from 0.03 to 0.40, depending on deposition conditions. All films were more wear-resistant than the substrate materials. The properties of the coatings deposited on AISI alloy 4130, 17-7 PH, 440-C and 4340 (bare and Ti/Cr nitride precoated) steel substrates were extensively studied. Measured microhardness values (about 2,040 MPa) were substantially higher for the coatings on the nitride precoated 4340 steel due to precoating effects. The film cohesion and adhesion failure loads for these coatings increased with increasing hardness of the underlying (nitride) layer.

1. Introduction

The friction coefficients of unlubricated conventional DLC films in dry gases can be as low as 0.01, but they increase considerably with increasing humidity, reaching values of 0.10 to 0.20 with a 10% relative humidity, whereas conventional DLC films doped with other species such as Si and Ti, exhibited low friction coefficients in humid environments [1]. Films of many materials, including Si-DLC, have previously been successfully deposited by IBAD at liquid nitrogen temperatures using a variety of species (e.g. Ti) and are highly promising for tribological applications because of their high hardness and low friction coefficients. Various methods for producing Si-DLC films have been reported elsewhere [1, 2]. In the present work the IBAD process was carried out on silicon and steel substrates held at room temperature, using deposition parameters judged amenable to process scale-up for larger components of interest to the Army.

2. Experimental Details

Silicon wafers and various (polished down to 0.05 μm alumina) alloy steel specimens consisting of AISI 4130, 17-7 PH, 440-C and 4340 were coated with Si-DLC films, using the IBAD process. Similar coatings were subsequently deposited on Cr-preplated 4340 steel specimens (average chromium thickness = 18.1 μm), as well as on TiN-precoated -Cr-preplated 4340 steel. The 3.2 μm thick TiN coating on that specimen was deposited by steered cathodic arc plasma PVD. A Zymet-100 non-mass analyzed ion implanter was used for the preparation of the specimens, as previously described [2,3], using energetic Ar^+ ion bombardment of a vapor deposited precursor material: tetraphenyl-tetramethyl-trisiloxane (704 Dow-Corning diffusion pump oil). The precursor material was vapor deposited through a 3 mm diameter nozzle from a heated reservoir. The oil temperature was maintained at about 140 °C and was monitored by a thermocouple. The substrate was inclined at 45° with respect to both the horizontal ion beam and the vertical flow direction of the vaporized oil. A shutter was placed above the oil container to start and stop the oil deposition. The growing film surface was continuously bombarded by a slowly oscillating (1 Hz) ribbon (0.02 m x 0.20 m) Ar^+ ion beam at 40 keV, for a total bombardment time of 240 min. The peak ion current density in the ribbon beam was varied from 31 μA cm^{-2} to 140 μA cm^{-2} (Table I) as read by a Faraday cup.

3. Results and Discussion

3.1 Compositional Analysis

The average stoichiometry of the films was $C_{67}Si_9O_6H_{15}Ar_3$, as measured by RBS. The relative amounts of C, Si, and O are almost identical to those found in the precursor, and the main effect of the ion beam was to drive off hydrogen and to add trace amounts of Ar.

3.2 Coating Thickness

Measurements of the average coating thickness are exhibited in Table I. For a given steel, such as AISI 17-7 PH or 440-C, the coating thickness increases with increasing beam current density. Thickness appears also to depend on the chemical composition of the substrate.

3.3 Hardness

The Knoop microhardness of the coatings, uncorrected for any substrate hardness effects, was measured at a 15 g load and ranged between 1,017 KHN (kg mm^{-2}) for a Cr-preplated 4340 low alloy steel substrate to 1,320 KHN for a 440C steel substrate (Table I). Even at this low load the maximum indentor penetration exceeded by far the value of 1/10 of the coating thickness, thus the effect substrate hardness had to be considered. Nanoindentation was, therefore, used for three specimens (#1 to #3), Table I. The microhardness value was (KHN 1825) substantially higher for the TiN-precoated-Cr-preplated 4340 steel specimen #8, most likely because the underlying

TiN has a measured hardness of about 2,094 KHN, compared with 825 KHN for 4340 steel.

Table I. Average Si-DLC Film Thicknesses, Microhardness and Nanohardness for Various Ion Beam Current Densities

#	SUBSTRATE	Current Density, J ($\mu A /cm^2$)	Thick-ness (μm)	Micro hardness (KHN)	Nano hardness (GPa)
1	4130 steel	90	1.80	1150	11.10
2	17-7 PH steel	31	2.03	1189	11.31
3	17-7 PH steel	56	3.01	1230	12.13
4	440-C steel	104	2.94	1235	-
5	440-C steel	140	4.31	1320	-
6	4340 steel	120	2.21	1113	-
7	Cr-preplated 4340 steel	120	2.41	1017	-
8	TiN-precoated-Cr-preplated steel	120	2.38	1825	-

3.4 Cohesion and Adhesion Failure Load

Using a CSEM-Revetest automatic scratch apparatus the measured average values of cohesion failure load, L_C, and adhesion failure load, L_A, are shown in Table II. As expected, for a given substrate both L_C and L_A are higher for thicker coatings. Also, as expected for a given coating thickness [4], the two failure loads increase with increasing substrate hardness. (Compare specimens #7 and #8.) In both specimens the Si-DLC coating thickness is about the same. It should be noted here that specimen # 8 exhibits two well defined adhesion failure loads: $L_{A1(Si-DLC/TiN)} = 24.29$ N, between the Si-DLC and TiN layer; and $L_{A2(TiN/Cr)} = 36.27$ N, between the TiN and Cr-coating. The latter is very close to that measured on TiN-precoated-Cr-preplated substrates in absence of a Si-DLC coating [5].

Adhesion between the chromium (preplate) and 4340 steel appears to be strong without delamination, as previously reported [5] with no interfacial failure nor any cracks propagating between the chromium layer and the steel substrate. There is no delamination observed between chromium layer and the 4340 steel.

3.5 Friction Coefficient

Unlubricated friction coefficients of the coatings deposited on silicon wafers against a 52100 High Chromium steel ball with a 200 g load ranged from 0.03 to 0.4, depending on the deposition parameters. Table II shows average values of μ^* corresponding to four scratches per specimen. The coefficient thus measured is in fact a scratching coefficient defined as $\mu^* = \mu_a + \mu_p$, where μ_a is the adhesion component and μ_p the ploughing component. Average measurements are summarized in Table II. Again, all specimens have about the same friction coefficient with the exception of the TiN-

precoated specimen which has the lowest value [$\mu^* = 0.09$], presumably because then μ_p virtually vanishes due to the hardness and rigidity of the TiN subcoating.

3.6 Abrasive Wear Resistance

Measured specific wear rates are reported in Table II for specimens #1 to #3. Each point represents an average of two tests of equal duration. The wear rate of the three specimens is about the same, within experimental errors. This is understandable, because all three coatings have approximately the same hardness, friction coefficient and adhesion failure load.

Table II. Average Cohesion Failure Load, L_C, Average Adhesion Failure Load, L_A, Friction Coefficient m^* between 0-60 N, Friction Coefficient m^{**} at 1 N, and Specific Wear Rate, W_s, $(mm^3\ N^{-1}m^{-1})$ for Si-DLC Films.

#	SUBSTRATE	L_C(N)	L_A(N)	μ^* (0-60 N)	μ^{**} (1N)	W_s x10^6
1	4130 steel	8.04	11.13	0.211	0.100	3.16
2	17-7 PH steel	6.13	12.13	0.231	0.133	2.95
3	17-7 PH steel	6.71	13.31	0.220	0.112	8.60
4	440-C steel	10.83	21.34	0.222	0.182	-
5	440-C steel	15.17	24.07	0.180	0.113	-
6	4340 steel	8.71	14.21	0.190	0.131	-
7	Cr-preplated 4340 steel	7.25	20.81	0.155	0.120	-
8	TiN-precoated-Cr-preplated steel	9.19	*L_{A1}=24.3 L_{A2}=36.3	0.120	0.090	-

*$L_{A1}=L_{A(Si-DLC/TiN)}$, $L_{A2}=L_{A(TiN/Cr)}$

4. Conclusions

The room temperature IBAD method described above yields smooth, amorphous Si-DLC films with growth rates varying from 0.1 to 0.3 μm/hr. The microhardness, friction coefficients, and wear resistance of the films were comparable to the the DLC films produced by other means, some of which require more demanding conditions, e.g., liquid nitrogen substrate temperatures. The cohesion and adhesion failure loads increase with increasing coating thickness and underlying layer hardness.

References

1. T. Hioki, Y. Itoh, A. Itoh, S. Hibi and J. Kawamoto, Surf. Coat. Technol. 46, 233 (1991).
2. C. G. Fountzoulas, J. D. Demaree, W. E. Kosik, W. Franzen and J. K. Hirvonen, J. Vac. Sci. Technol. B Vol. 12, No. 2, p. 977, Mar/Apr 1994.
3. C. G. Fountzoulas, J. D. Demaree, W. E. Kosik, W. Franzen, W. Croft and J. K. Hirvonen, MRS, 279, Beam-Solid Interactions (1993).
4. P. A. Steinmann, Y. Tardy and H. E. Hintermann, Thin Solid Films, 154, 333 (1987).
5. K. J. Bhansali and T. Z. Kattamis, Wear, 141, 59 (1990).

SIMULATION OF PLASMA FLOW IN TOROIDAL SOLENOID FILTERS

Shi Xu, Tu Yu Qiang, Tan Hong Siang and Tay Beng Kang
School of Electric and Electronic Engineering, Nanyang Technological University, Singapore 2263

Key words: simulation, filtered cathodic vacuum arc, plasma, tetrahedral amorphous carbon

Abstract

An improved drift approximation model with an added radial electrostatic field has been successfully developed to quantitatively describe the plasma motion in the toroidal solenoid in a FCVA system. It is found that the additional radial electric field mainly confines the z-directional drift of the ions. A perfect quantitative fit is obtained for our simulation results to the Storer's experimental data. Our model also provides the value of the plasma density and the electron-ion collision frequency as a function of the B field strength and they agree perfectly with the experimental data cited in the literature. The potential difference between the duct wall and the plasma centre which gives the radial electric field can also be determined from the simulation, and the results are in the same order as measured.

1.   Introduction

The Filtered Cathodic Vacuum Arc (FCVA) technique has proven to be one of the promising methods of producing a wide range of high quality hard coating materials [1-5]. Recent investigations [2,3,6,7] have indicated that FCVA produced ta-C may be useful for electronic, optical and mechanical applications. The main feature of the FCVA technique is to guide the plasma generated from the cathodic vacuum arc through a toroidal solenoid and thus prevents the passage of neutral atoms, macroparticles and other unwanted ions. In order to design an efficient magnetic filter, it is desirable to have a mathematical model to simulate the plasma motion in a toroidal solenoid. Two different models, namely the Flux-tube model [8-10] and the Drift model [11-14], have been developed to describe the plasma motion in a torus. The former is, in principle, a single particle model and ignores the coupling effect between electrons and ions which is crucial to the plasma transportation in this case. The later includes the coupling effect between electrons and ions. However, the radial electrostatic field between the centre of the plasma and the torus duct wall, which is a very important parameter influencing the plasma behavior [9,10], has not been taken into account.

A model, based on the drift approximation with an added radial electrostatic field, is proposed to describe the influence of the radial electrostatic and axial magnetic fields on the behavior of plasmas in a torus. The experimental results of Storer *et al* [15] are

fitted by our computer simulation to verify the applicability of our model in describing the plasma flow in a toroidal magnetic solenoid.

2. The Model

A schematic configuration of a quarter torus solenoid and the coordinate system used in the model are shown in Figure 1. The same set of assumptions in [11]are used in our derivation. The equation of electron motion in an electromagnetic field, with collisions between electrons and ions and the radial electric field being taken into account, is [11,14]

$$m\frac{d}{dt}\mathbf{v}_e = -q(\mathbf{E}+\mathbf{v}_e\times\mathbf{B})+m\nu_{ei}(\mathbf{v}_i-\mathbf{v}_e)-q\mathbf{E}_\varphi \tag{1}$$

$$M\frac{d}{dt}\mathbf{v}_i = q(\mathbf{E}+\mathbf{v}_i\times\mathbf{B})+M\nu_{ie}(\mathbf{v}_e-\mathbf{v}_i)+q\mathbf{E}_\varphi \tag{2}$$

In the above equations $\mathbf{v}_e$ and $\mathbf{v}_i$ are electron and ion velocity, respectively, ν_{ei} is defined as the collision frequency of an electron with ions and ν_{ie} is frequency of collisions of an ion with electrons. $\mathbf{E}$ is the polarization electric field and $\mathbf{B}$ is the curvilinear magnetic field in the torus, while m and M are the electron and ion mass, respectively. The radial electric field $\mathbf{E}_\varphi$ is [16-19]:

$$\mathbf{E}_\varphi = -q\nabla U = -q\nabla\left(\phi_0 r_\varphi^2\right) = -2q\phi_0 r_\varphi \tag{3}$$

where r_φ, r_d have their usual meanings expressed in figure 1, and the duct dc bias potential is $\varphi_0 = \phi_0 r_d^2$. Solving equations 1 and 2, we obtain a set of two differential equations

$$\frac{\sigma_\perp B_0^2}{Mn}\left(1+\frac{1}{\Omega^2}\right)r_0^2\frac{dr}{dt} - \frac{2\phi_0 q z r^2}{M\Omega\left(1+\Omega^2\right)} - r\left(V_\parallel^2+\frac{V_\perp^2}{2}\right) = 0 \tag{4}$$

$$\frac{dz}{dt} + \frac{2\phi_0 r^2}{B_0 r_0\left(1+\Omega^2\right)} + \frac{2\phi_0 r}{B_0\left(1+\Omega^2\right)} - \frac{M}{qB_0 r_0}\left(V_\parallel^2+\frac{V_\perp^2}{2}\right) = 0 \tag{5}$$

These ordinary differential equations were solved using fourth and fifth order Runge-Kutta formulae. The simulation program consists of three parts, namely, the input ion generator, the ion motion in the torus and a check to test whether the ion will pass to the next point in the torus. To simulate the experiment done by Storer et al [15,20] a well-collimated plasma beam is generated from a source whose exit has a 1.27 cm radius and is located 2.2 cm inside the entrance of the torus [10,15]. The torus radius $r_0 = 14$cm and the duct radius $r_d = 1.525$cm. The energy of the ejected ions is assumed to have Gaussian distribution with a centre energy $E_0 = 30$ eV and thermal energy $E_T = 10$ eV [10,15]. The Fe mass was used for the ion mass and ion's average charge was taken as 1.5 [10,15].

3. Simulation Results and Discussions

It is shown in our model that the plasma motion in a toroidal solenoid is a function of the $\mathbf{B}$ field, the radial $\mathbf{E}$ field, the plasma density, the collision frequency between ions and electrons, and the ion input energy. The symbols in Figure 2 show experimentally

measured currents in the toroidal solenoid for several different magnetic field strength carried out by Storer *et al* [15]. The lines in Figure 2 are our simulation fit. It is seen that when the magnetic field strength is relatively high (B $\geq$ 0.041 T) the fitting is very good. The ion current decreases exponentially along the torus. For B = 0.027 T, however, our simulation curve shows an 'elbow' shape. It is thought due to the disturbance of the −70V biased current measuring plate to the relatively low density plasma beam when the **B** field strength is weak. Figure 3 shows the wall current measured [15] when B=0.027T (solid circles) and our simulation result (solid curve). They show a generally good agreement although the experimental wall current is a bit lower than that from our simulation, which is understandable if we take into account the disturbance introduced to the plasma beam by the measuring plate as explained above. The attenuation length of a plasma beam inside a toroidal solenoid for various different **B** filed strength is determined and plotted in Figure 4. A good quantitative fit is seen in the figure. However, the simulation results are sensitive to a number of fitting parameters, namely, the plasma density, the electron-ion collision frequency and the radial electric field. All these parameters are functions of the magnetic field. Figure 5 shows the change of the plasma density n with the magnetic field strength. It shows a perfect match between the measured data ($\sim 10^{20}$ m^{-3} [11]) and our simulation results. Figure 6 shows the electron-ion collision frequency v_{ie} as a function of the magnetic field strength. When B increases from 0.027 T to 0.065 T v_{ie} increases from 7.9×10^8 to 1.45×10^9 s^{-1}, which is also an excellent fit to the experimental results $10^8 - 10^9$ s^{-1} [11].

The radial electric field has a significant effect on the plasma guiding centre drift along the z-direction. In our model there exists a best potential value φ_0 which gives the highest throughput with a given set of parameters of B, n, and v_{ie}. We take this value as the duct wall potential at the given set of parameters of B, n, and v_{ie}. The solid line in Figure 7 shows, when we fit the Storer's experimental data, the potential difference used between the duct wall and the plasma centre as a function of the magnetic field. The corresponding fitting parameters of n, and v_{ie} are shown in Figure 5 and 6. It is found that when the magnetic field increases from 0.027T to 0.065T the potential difference increases from 3.3V to 9.0V. The value is in the same order as measured by Prasad *et al* at B = 0.1T [19] and fits very well to our duct wall potential measurement shown by the open squares in the figure.

4.   Conclusion

The guiding centre drift approximation has been successfully improved by adding a radial electrostatic field into the equations of the plasma motion in the toroidal solenoid. With the addition the plasma motion in a FCVA system can be quantitatively described.

The Storer's experimental results have been successfully simulated by our model. Good quantitative fits are obtained for our simulation results to the measured values, such as ion currents versus distance along the torus for various B field strengths, the ion current attenuation length, and the wall current. Our model also provides the value of

the plasma density and the electron-ion collision frequency as a function of the B field strength and they also agree perfectly with the experimental data cited in the literature. The potential difference between the duct wall and the plasma centre which gives the radial electric field can also be determined from the simulation, and the results are in the same order as measured by Prasad *et al* [19] and fit well to our own measurements.

References

[1]   I. I. Aksenov, V. A. Belous, *et al*, *Sov. J. Plasma Phys.*, **4**, 428 (1978).
[2]   P. J. Martin, S. W. Filipczuk, *et al*, *J. Mat. Sci. Lett.*, **7**, 410 (1988).
[3]   D. R. McKenzie, D. Muller, *et al*, *Diamond and Related Materials,* **1**, 51 (1991).
[4]   P. J. Fallon, V. S. Veerasamy, C. A. Davis, J. Robertson, G. A. J. Amaratunga, W. I. Wilne and J. Koskinen, *Phys. Rev. B*, **48** (7), 4777 (1993).
[5]   P. J. Martin, R. P. Netterfield, *et al*, *Surface and Coating Technology*, 49, 239 (1991).
[6]   V. S. Veerasamy, G. A. J. Amaratunga, W. 1. Wilne, P. Hewitt, P. J. Fallon, D. R. McKenzie and C. A. Davis, *Diamond and Related Materials*, **2**, 782 (1993).
[7]   V. S. Veerasamy, G. A. J. Amaratunga, J. S. Park, W. I. Wilne, H. S. MacKenzie and D. R. McKenzie, *J. Appl. Phys. Lett.*, **64** (17), 2297 (1994).
[8]   A. I. Morozov, *Sov. Phys. Dokla.*, **10**, 775 (1966).
[9]   I. I. Aksenov, V. G. Padalka, *et al*, *Sov. J. Plasma Phys.*, **6**, 504 (1980).
[10]   D. B. Boercker, D. M. Sanders, J. Storer and S. Falabella, *J. Appl. Phys.*, **69** (1), 115 (1991).
[11]   V. S. Veerasamy, G. A. J. Amaratunga and W. 1. Wilne, *IEEE Transactions on Plasma Science*, **21** (3), 322 (1993).
[12]   G. Schmidt, *Phys. Fluids*, **3**, 961 (1960).
[13]   N. Khizhnyak, *Soviet Phys. - Tech. Phys.*, **10** (5), 655 (1965).
[14]   V. S. Voitsenya, A. G. Gorbanyuk, I. N. Onishchenko, B. G. Safronov, N. A. Khizhnyak and V. V. Shkoda, *Soviet Phys. - Tech. Phys.*, **12** (2), 185 (1967).
[15]   J. Storer, J. E. Galvin and 1. G. Brown, *J. Appl. Phys.*, **66** (11), 5245 (1989).
[16]   1. I. Aksenov, V. A. Belous, *et al*, *Sov. J. Plasma Phys.*, **4**, 758 (1978).
[17]   R. C. Davidson, *Phys. Fluids*, **19** (8), 1189 (1976).
[18]   D. B. Batchelor and R. C. Davidson, *J. Plasma Phys.*, **14** (1), 77 (1975).
[19]   R. R. Prasad and M. Krishnan, *J. Appl. Phys.*, **61** (1), 113 (1987).
[20]   1. G. Brown *et al*, *Appl. Phys. Lett.*, **47** (4), 358 (1985)
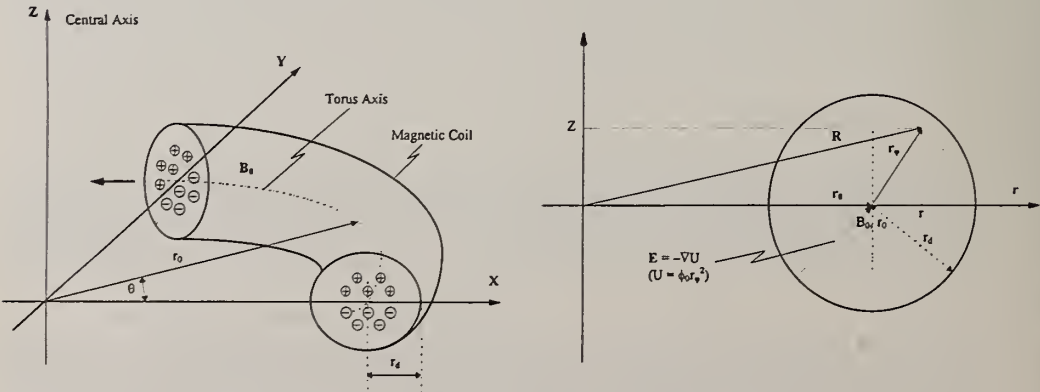
Figure 1.   Schematics of the toroidal solenoid and the coordinate.
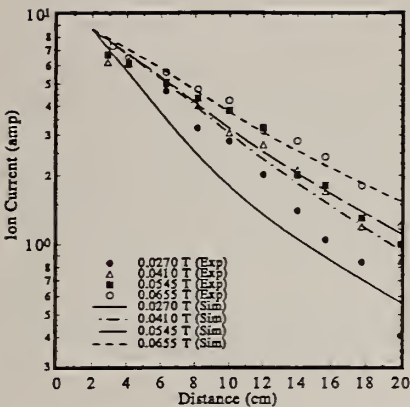
Figure 2. The ion currents in the torus for various magnetic field strengths. Symbols are the experimental data [15] and lines are our simulation fit.

Figure 5. The change of the plasma density n with the magnetic field strength B. The solid line is the quadratic fit.

Figure 3. The wall current measured [15] (solid circles) and our simulation result at B=0.027T
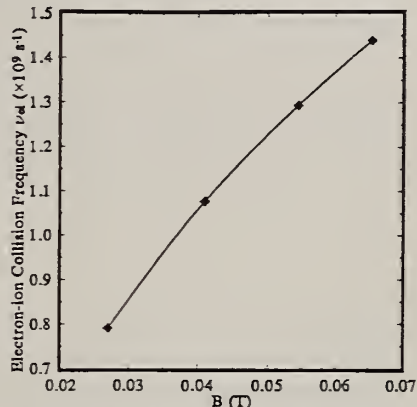
Figure 6. The electron-ion collision frequency ν_{ie} as a function of the magnetic field strength B. The solid line is the quadratic fit.

Figure 4. The attenuation length of a plasma beam inside the torus for various **B** filed strength. (Open circles are Storer's results and solid line is our simulation).
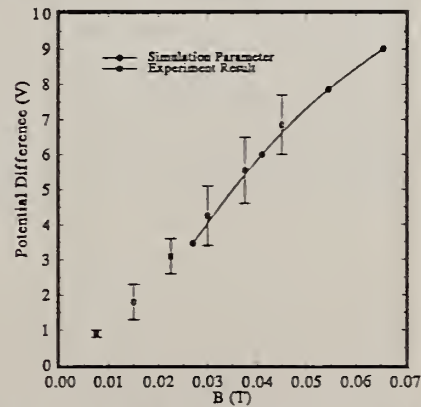
Figure 7. The potential difference as a function of the magnetic field strength B. Our experimental data are also shown as open squares. The solid line is the quadratic fit.

A LOCAL FILM DEPOSITION FOR MICROWAVE DEVICES

Alexander V. Chenakin, Vladimir I. Skachko

TOR, Building 17, Radioengineering Faculty, Kiev Polytechnic Institute,
Pr. Pobedi-37, Kiev-252056, Ukraine

Key words: amplifier, deposition, integrated circuits, plate, transistor

Abstract

This paper presents the results of investigations of microwave and millimeter wave integrated circuits for low noise transistor amplifiers. We propose a technology of local film deposition for production of low loss integrated circuits. This technology gives the opportunity to realize the high potential parameters of modern field-effect transistors better than fin-line, microstrip and other known microwave circuits give. An original construction of low noise transistor amplifier is described. It is achieved extremely low noise figure due to concentration of electromagnetic field in that region, where lossy dielectric is absent.

1. Introduction

At present the major problem in development of low noise microwave and millimeter wave transistor amplifiers is to decrease the noise figure. The problem may be mainly solved by two ways: creation of transistors with high potential opportunities, and realization of these opportunities in various models of amplifiers.

Microstrip designs of low noise amplifiers, having shown themselves to advantage in the microwave band, are now used, and not without success, in the millimeter band. However, despite the great opportunities of the advanced technology in production of microstrip integrated circuits, some common inherent disadvantages should be pointed out. First, it is high losses, especially in a short-wave part of the millimeter band, in the microstrip lines as well as in the circuits of matching them with input and output waveguides. Besides, increasing frequency causes increasing technological difficulties in production of microstrip integrated circuits and their matching with the waveguide.

To some extent, the above mentioned disadvantages are eliminated or attenuated in designs of amplifiers on fin-lines unifying the advantages of waveguides and technology of planar high frequency integrated circuit's production. At the same time, use of fin-lines faces the problem of matching the field-effect transistors, especially in the millimeter band. This is because the increasing frequency causes the decreasing output and, especially, input impedance of transistors, requiring matching of sections of the transmission lines with the wave impedance of a few tens of Ohm. Realization of such wave impedance values using fin-lines faces serious technological difficulties and increases the losses. Besides, the fin-lines suffer high losses due to presence of lossy dielectric. These factors result in increase of the noise figure of the amplifiers.

In this connection a development of new technologies for production of microwave and millimeter wave low loss integrated circuits is urgent currently.

2. Low noise amplifier

A new technology of local film deposition was developed for original construction of low noise amplifier. The use of proposed design of low noise transistor amplifier allows to eliminate the above mentioned disadvantages, inherent to microstrip and fin-line integrated circuits. Let us consider the basic construction of one-cascade amplifier shown in Fig. 1. The amplifier consists of rectangular waveguide section.
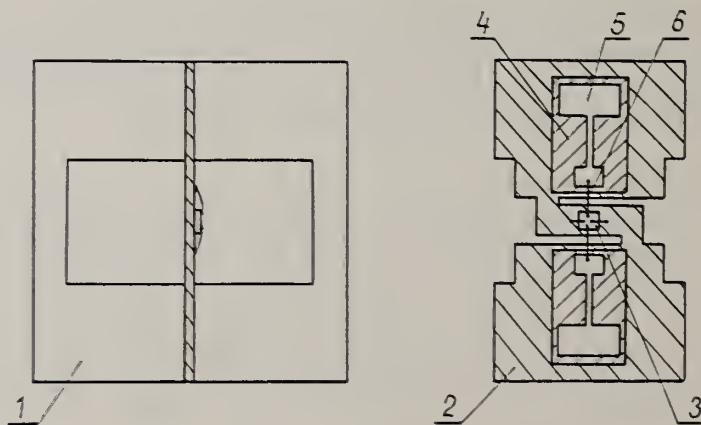
Fig. 1 Basic construction
(1-Waveguide, 2-Metal plate, 3-Transistor, 4-Dielectric layer, 5-Feed circuit, 6-Wire conductor)

Inside it a metal plate is mounted in parallel to narrow wall of the waveguide. In this plate the slots are cut off in such a way, that being inserted into waveguide the plate

forms the ridges of input and output sections of H-waveguide. On a lateral side of the plate a hybrid integrated circuit is performed using the mentioned technology of local film deposition. This technology allows to perform previous deposition of local areas of thin (near 5 micrometers) dielectric layer on a surface of metal plate with following deposition of capacitors, resistors and conductor elements. The field-effect transistor is mounted on the plate and connected with input and output section of H-waveguide by thin wire conductors. The gate and drain of transistor are connected with corresponding feed circuits. The sources of transistor are grounded. The matching of active component of input and output transistor impedance performed using stepwise H-waveguide junction. Changing the distances between ridges of H-waveguide by appropriate choice of slot width in the metal plate, the necessary value of H-waveguide impedance can be easily obtained. The wave impedance is calculated using the closed-form expressions presented in [1]. The reactive component of transistor impedance is compensated by appropriate selection of length of short-circuit stub. The technique for design of stepwise H-waveguide junction was developed with the help of exact methods of electromagnetic field theory. Besides, the simplified technique of analysis and design of the amplifier and same active microwave devices based on this technology was also developed.

The major advantage of proposed low noise amplifier design is an absence of lossy dielectric in zone of main electromagnetic field concentration and direct matching on input and output waveguides. Due to these features the proposed integrated circuit has extremely low losses and allows to make use of high potential parameters of modern transistors in order to obtain very low values of noise figure. One of additional advantages of the amplifier is also an effective heat removal from transistor, which mounted on the relatively thick metal plate. That does not exclude the operation of the amplifier at deep cooling. The disadvantage of proposed amplifier is its low power gain. The gain may be increased using additional cascades on the common plate.

3. Technology

The proposed technology for production of microwave low loss integrated circuits includes the following stages:

1. Preparation of metal plate: A cooper plate is used. A mechanical polish and chemical clearing for necessary adhesion is made.

2. Deposition of dielectric layer: Local deposition of film dielectric layer is made with the help of additional thin metal plate with special windows. We have investigated various chemical compositions for achievement a good adhesion and high electrical parameters. A dielectric composition based on SiO_2 is used. The thickness of dielectric layer is about 5 micrometers.

3. Deposition of film conductors: Deposition of thin film cooper conductors on the dielectric layer with following gold coating of the plate and the conductors is made.

4. Deposition of film capacitors: A square elements of the conductor surfaces for the capacitors of feed circuits are used.

5. Deposition of film resistors: Deposition of thin film nickel resistors is performed. The resistors are connected with corresponding conductors of feed circuits.

6. Cut of slots in the plate: In the plate the slots are cut off. Their width dictates the clearance between the ridges of H-waveguide. Since realization of the calculated configuration usually presents some difficulties, it is approximated with the straight-line segments.

7. Installation of field-effect transistors: The transistors are mounted on the plate by soldering or bonding. The transistor electrodes are connected with corresponding feed circuits by gold wire conductors with the help of ultrasonic welding.

4. Conclusion

The described original construction of low noise transistor amplifier was developed and investigated in different frequency ranges. It was indicate that proposed construction of amplifier practically does not increase a noise figure of used transistor. The analysis and experimental investigations show the high potential opportunities of proposed technology for microwave and millimeter wave devices, such as low noise transistor amplifiers, mixers, converters, which require the extremely low noise figure.

5. Reference

1. Wolfang J. R. Hoefer, Miles N. Burtn "Closed-form expressions for the parameters of finned and ridged wave-guides", IEEE Transactions on Microwave Theory and Techniques, Vol. MTT-30, December 1982, pp. 2184-2190.

Applications of Diamond Films and Related Materials: Third International Conference, 1995
Editors: A. Feldman, Y. Tzeng, W. A. Yarbrough, M. Yoshikawa, and M. Murakawa

921

PRODUCTION OF CARBON-METAL AND GRAPHITE-METAL COMPOSITES FROM OXIDIZED GRAPHITES

N.I.Kovtyukhova, A.A.Chuiko

Institute for Surface Chemistry, National Academy of Sciences of Ukraine, 31 Prospect Nauky, 252022 Kiev, Ukraine

Key words:carbon metal composite, oxidized graphite, transition metal

Abstract

New carbon composites containing nanometer-sized Cu and Ni particles distributed in layer carbon matrix have been produced by the thermal decomposition of $Cu(2+)$ and $Ni(2+)$ amino complexes embedded into the graphite oxide matrix, and the chemical metallization of the highly dispersed oxidized graphite modified with $Cu(2+)$ and $Ag(+)$ amino complexes.

1. Introduction.

Carbon composites containing ultrafine metal or metal oxide particles are of great interest not only as catalysts but also as electric and magnetic devices, anti-bacterial agents etc. Due to the layer structure and high content of oxygen-containing groups embedded in carbon layers, oxidized graphites offer promise as effective adsorbents for metal ions and, hence, as carbon precursors of various metal-containing composites.

This work deals with the preparation and structure of oxidized graphites modified and intercalated with $Cu(2+)$, $Ni(2+)$ and $Ag(+)$ amino complexes and the composites production through their thermal decomposition and chemical metallization. Oxidized graphites of two different oxidation degrees have been investigated: the graphite oxide (GO), in which every carbon layer has oxygen-containing groups in its structure, and the highly dispersed oxidized graphite (HDOG), in which only 2-3 near-surface carbon layers are of the approximate composition of the graphite oxide carbon layers.

2. Experimental.

The GO was prepared by oxidation of graphite with $KMnO_4$ in concentrated H_2SO_4 [1]. The HDOG was prepared by the mechanical dispergation of graphite bisulphate followed by the hydrolysis. The HDOG particle thickness was about 100 nm. The GO and HDOG were used as their aqueous dispersions containing 2% of the dry substance.

The modification of the oxidized graphites with metal ions was carried out as follows. The dispersion sample was diluted with aqueos ammonia solution followed by the addition of metal ammoniate solution. The GO and HDOG content in the reaction mixture was 1 g/l, the concentration of metal ions was 0.02 M. After stirring for 2 h the mixture was filtered off, and the residue was washed with water and dried under vacuum.

The thermal decomposition of the resultant GO-metal complexes [GO-M] was studied by derivatography method (Q-1500D instrument). The samples were heated in air up to 300 C and in Ar flow up to 800 C. The decomposition products are indicated in the paper as [C-M-3] and [C-M-8], respectively. The structural change due to heat-treatment was analyzed with X-ray difractometer DRON-1 (CuKα - radiation). The microscopic features of the samples were observed with a scanning electron microscope SCAN-SEAM.

The HDOG modified with metalions [HDOG-M] was subjected to chemical plating with Ni by stirring the mixture of the [HDOG-M] and aqueous solution containing 50g/l $NiSO_4$, 20g/l NaH_2PO_2, 50g/l NH_4Cl, 70g/l NaCit, 85 ml/l 25% NH_3 for 15 h at 80 C.

3. Results and discussion.

The quantity of Cu(2+), Ni(2+) and Ag(+) amino complexes adsorbed on the GO and HDOG depends on pH of the medium. The maximum number of bound ions is observed in pH range of 10-11 for GO and 12-13 for HDOG, and equals 3.6 mmol/g of Cu(2+) and 2.6 mmol/g of Ni(2+) for GO and 0.76 mmol/g of Cu(2+) and 0.34 mmol/g of Ag(+) for HDOG. The interaction of the metal ions with the GO and HDOG results in a pH decrease of the reaction mixture, which indicates that the metal ions are bound by acidic functional groups on the oxidized graphites surface. The interaction also leads to an increase of GO interlayer spacings by 0.7-0.8A (Fig.1). This fact can be explained by intercalation of the metal ammoniates into GO.

The comparative study of the IR spectra of pure GO and [GO-M] indicates shifts of the bands due to γ(O-H) and γ(C-O) to the low-frequency side and the appearence

of new bands that may be assigned to the stretching vibrations of carboxylic groups coordinated to metal ions. The comparative study of the electronic spectra of the [GO-M] and initial solutions of Cu(2+) and Ni(2+) amino complexes shows that metal ammine ions lose one or two ammonia molecules when fix in GO phase. These results allow us to suggest that GO forms complexes with metal amino complexes due to the replacement of ammonia molecules in the coordination sphere of a metal ion by oxygen-containing groups of GO carbon layers.

Thus two different kinds of oxidized graphites modified with metal amino complexes have been obtained. The first one is [GO-M], where metal ions are situated both on the external surface of the GO particles and in the interlayer space. The second one is [HDOG-M], where only 2-3 near-surface layers contain the metal amino complexes. Taking into account the difference in the metal content and structure of the graphites metal derivatives, we have tried two different metods of composites production. 1- Thermal decomposition of the [GO-M]is expected to give carbon-metal composites with the metal particles evenly distributed in carbon matrix. 2-Chemical plating of the [HDOG-M] with Ni, which allows to obtain graphite-metal composites where the metal particles distribution along C-axis is determined by the HDOG lamellae thickness (~100 nm).

The XRD patterns of the heat-treated GO-metal complexes are illustrated in Fig.1. In the [C-M-3] samples, the sharp peak of the original GO shifts toward lower angle, which indicates the increase of C-spacing in carbon residue by 0.6-1.0 A in comparison with that of the initial GO - metal complexes. The same heat-treatment of the pure GO [2] results in a decrease of the interlayer spacings to the value of 3.5 A characteristic of graphite. This fact indicates that metal species in the [C-M-3] as well as in [GO-M] are situated both on the external surface of the composite particles and in the interlayer space. XRD patterns of the heat treated samples indicate that Cu species are present as crystallized CuO essentially , while Ni species are in amorphous state or dispersed at atomic level. The further heat of the samples in Ar flow up to 800 C leads to the
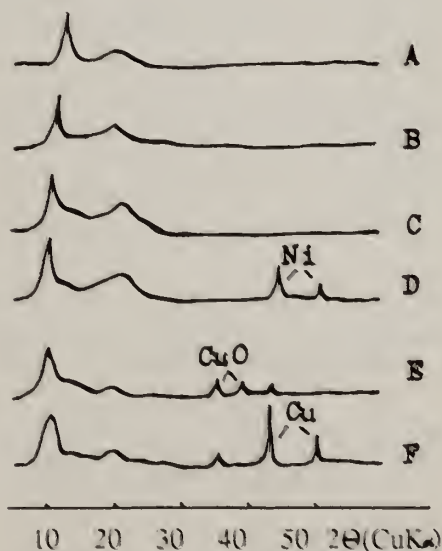
Fig.1. The effect of heat- treatment on XRD patterns of [GO-M]: A-GO; B-[GO-Ni]; C-[C-Ni-3]; D-[C-Ni-8]; E-[C-Cu-3]; F-[C-Cu-8]

carbon composites containing clusters of Cu and Ni, which have an average sise of 150 A and 100 A, respectively.

The heat of the [GO-M] as well as pure GO in air up to 300 C results in removal of water and oxygen-containing groups of GO carbon layers. For [GO-M], the beginning temperature of the oxygen-containing groups removal is 35^0 lower than that for the pure GO. This can be explained by catalytic effect of the metal ions on the reaction of carbon oxidation with oxygen releasing from the GO layers. The decomposition of the amino complexes occurs in temperature range of 170-240 C, the reduction of CuO with the carbon of matrix begins at 295 C. The obtained [C-M-8] have 52.3% of Cu and 38.4% of Ni.

The SEM photographs of the [C-M-8] have shown a lot of particles with the size of 200-3000 nm evenly distributed on the surface. Since the average size of the metal particles is 10-15 nm, we suggest that the most of the metal clusters with a size lower than 10 nm are distributed inside the carbon matrix. The conductivity of the Ni-composite is four times more than that of the carbon matrix. The composite is able to be magnetized.

The chemical metallization of the [HDOG-M] results in the precipitation of 1.17g/g and 1.45 g/g metallic Ni on the surface of [HDOG-Cu] and [HDOG-Ag], respectively. No Ni precipitation is observed on the surface of the initial HDOG. So chemosorption of the metal ions can be used for the HDOG surface activation instead of the expensive two-step method of graphite impregnation with solutions of $Sn(2+;4+)$ and $Pd(2+)$ salts, which is commonly used prior to the chemical plating of graphite powders with Ni. Though the quantity of $Ag(+)$ ions fixed on the HDOG surface is 2.24 times lower than that of $Cu(2+)$ ions, the quantity of Ni precipitated on the [HDOG-Ag] is 1.24 times higher than that precipitated on the [HDOG-Cu]. This fact indicates that $Ag(+)$ ions have the higher catalytic activity in the $Ni(2+)$ reduction than $Cu(2+)$ ions.

The SEM photographs of the metallized HDOG show the relatively even distribution of the Ni particles with the size about 900 nm over the HDOG surface. These samples are also able to be magnetized.

Thus the described above methods offer a new route for preparing a variety of composites containing ultrafine metal and metal oxide particles in layer carbon matrix.

4. References

1.Hummers W., Offeman R. // J.Amer.Chem.Soc.-1958.-8O,N6.-P.1339.
2.Rodriguez A.M.,Timenez P.V.//Thermochimica Acta.-1984.-78,N1-3.-
   P.113-122.

ADDITIONAL PAPERS

DIAMOND COATED INSERTS, DRILLS AND END MILLS

T.Suzuki,T.Hattori, A.Endo, M.Yagi, K.Shibuki and M.Kobayashi
Materials Development Division, Toshiba Tungaloy Co., Ltd.
1-7 Tsukagoshi, Saiwai-ku, Kawasaki 210, Japan

Key words : diamond coating, inserts, drills, end mills, cutting tools

Abstract

Current status of CVD diamond for the application to cutting tools was briefly summarized, focused on microstructures, adhesion strength and cutting performance. Diamond-coated cemented carbide inserts, drills and end mills were tested against Al-Si alloys and problems for expanding tool market were also discussed. Further, the potential use of thick diamond films for replacing with PCD was described.

1. INTRODUCTION

Since the success of synthesizing diamond from gases at low pressure [1], diamond-coated cutting tools have been considered as the first main product in the CVD diamond field. However, it has been prevented for the last decade because of the weak adhesion strength with most substrates and availability only for non-ferrous materials such as Al-Si alloys, carbon and Cu etc. Most companies first targeted to coat CVD diamond on cemented carbide inserts, but few companies have succeeded to commercialize diamond-coated drills and end mills so far.

Automotive industries are now trying to change into light-weight nonferrous materials such as Al-Si alloys for fuel efficiency[2,3]. One of the obstacles preventing the development of CVD diamond lies in its high cost, compared with hard ceramics films such as TiN, TiC and (Ti,Al)N. To reduce costs, cell volume needs to increase and increasing cell volume is now technical challenges. Therefore, the development of an advanced reactor may play a key role in driving down production costs. In this paper, we will show that the adhesion of diamond films with cemented carbide inserts, drills and end mills is strong enough to use for Al-Si alloys. Further, recent status and problems for commercializing CVD diamond cutting tools are briefly

discussed.

2.MICROSTRUCTURE OF DIAMOND FILM

The cutting performance of diamond-coated tools should depend not only on adhesion strength but also on the microscructure of diamond films. In fact, the bending strength of thick diamond films(> 0.5 mm) is lower than that of PCD. This is because that the bonding strength of grain boundaries is weak or films do not consist of well-crystallized diamond. Few reports have analyzed grain boundaries of CVD diamond in terms of mechanical properties of films.

Figure 1(a) shows a transmission electron micrograph of diamond films deposited by the microwave plasma CVD method [4]. As far as we know, there is no significant difference in microstructure of films deposited by various synthetic methods. The grain size is generally small, 0.2-1 μm, and randomly oriented. It is not clear whether oriented- or randomly oriented-particles show better cutting performance. Electron diffraction pattern was taken from the <110> direction where multiple twins were seen, together with streaks in the <111> directions. Figure 1(b) is an enlarged view of Fig.1(a), showing many twins intersecting by 70.5 and 109.5°. In some area, Moire patterns were seen as indicated by arrows. These are caused by the superposition of two coherent grain boundaries and called $\Sigma 9$ boundaries. The coherent boundaries such as the twin boundary($\Sigma 3$ boundary) would not induce a detrimental effect on cutting performance, but not certain for incoherent boundaries.

3. ADHESION STRENGTH WITH CEMENTED CARBIDE

The difficulties associated with poor adhesion strength with cemented carbide have prevented activities of CVD diamond researches so far [5]. It is well known that Co atoms in cemented carbide can move around grain boundaries even at low temperature(< 500°C) and react with diamond at the initial stage of deposition. By our experience and discussions with many researchers, the following factors should dominate the adhesion strength between diamond films and cemented carbide substrates.

a) surface treatment before deposition
b) Co content

c) kinds of cemented carbide substrates(grain size. impurities etc.)
d) synthetic condition

The (a) is the most important factor and each company has developed own techniques so far. We also investigated effects of surface roughness on the adhesion strength of WC-Co, compared to that of WC without Co [6,7]. Figure 2 shows schematic illustration of decarburization process which roughens the surface and improves the adhesion strength.   First, the sintered-WC inserts were placed under O_2 or H_2 plasma circumstance to etch carbon atoms around the surface. The tungsten atoms left on the surface were recrystallized while carbon atoms were etched away and resulted in the formation of small particles with the size of 10-100 nm. The tungsten layer was carburized at the initial stage of the diamond deposition. During this process, small WC grains were formed and the surface roughness was enhanced.   The results of cutting performance will be shown in section 4.1. It is well accepted that Co atoms around surface preferentially deposits graphitic phase and results into poor adhesion strength with substrates. On the other hand, the (c) and (d) have not been well recognized [8].

4. CUTTING PERFORMANCE

4.1 Inserts

As far as we know, many companies use microwave reactors to coat diamond on cemented carbide inserts. The problem is that cell volume of a microwave reactor is still small and needs to increase to reduce the cost. The number of inserts which are uniformly coated in a microwave reactor is at most 30-40. Further, it takes several hours to coat films by 10-20 μm in thickness. In the future, scaling up a microwave reactor should be key issue for further development of diamond-coated inserts.

Diamond-coated cemented carbide was tested in milling and turning with Al-Si alloy and compared to the results of diamond-coated WC as shown in Fig.3(a). The nose wear of diamond-coated WC-Co was kept within 0.1 mm up to 100 passes which was closed to that of diamond-coated WC. Similar to the results of the milling test, the results from the turning tests with diamond-coated WC-Co showed great performance as in Fig.3(b). The rapid increase in flank wear was observed in diamond-coated WC-Co inserts after ~40 min, although diamond-coated WC retained its performance up to 1 h.

4.2 Drills

Most researchers now accept by experience that the hot-filament method is better than the microwave for coating diamond on twist drills. Here, since each company has own techniques for coating diamond, no one knows accurate information on the synthetic methods.

Diamond-coated drills with ~10 μm in thickness were tested using A390 by making holes to investigate wear resistance. Figure 4(a) shows a scanning electron micrograph of diamond-coated twist drills after making holes by 7000. The microstructure in Fig.4(b) showed well faceted particles and indicated no wear even after severe cutting tests. Thus. once CVD diamond films are strongly adhered with cemented carbide drills, the tool life against A390 is long enough to make holes by tens of thousands.

4.3 End mills

Higher precision cutting performance is required for diamond-coated end mills than that in diamond-coated twist drills, so surface roughness of CVD diamond becomes serious problems. Further, the coating area of CVD diamond is much longer that that of drills, which have prevented the development and commercialization of diamond-coated end mills.

Figure 5 shows schematic illustration of cutting tests by diamond-coated end mills. Figure 6(a) shows a scanning electron micrograph of diamond-coated end mills after cutting A390 by 20 m. The arrows indicate workpiece which is often left around the surface after cutting tests. The microstructure of diamond particles, shown in Fig.6(b), indicates no wear even after severe cutting tests. Thus, when the workpiece is A390, diamond-coated end mills shows great cutting performance unless the films peel off the cemented carbide.

5. POTENTIAL USE OF THICK DIAMOND FILM

Recently, thick CVD diamond films(>0.5 mm) have been intensively studied for the practical purposes with the development of a microwave reactor. The purpose of R & D of thick films is to replace them with PCD for cutting tool applications. The scale-up of a reactor has been lowering the cost of CVD diamond films per carat and it gradually approaches PCD value. Since CVD diamond films do not contain Co or Ni, the wear resistance should be

greater than that of PCD.

One of the applications of thick diamond films with large market is for oil drilling by blazing them on cemented carbide bits. At present. a large number of PCD is used for oil drilling, mainly for digging soft stones. In the U.S. and Russia, some oil companies are now trying to use thick CVD diamond films for this purpose. The problems in the PCD lie in the lack of fracture toughness. During oil drilling, some of them are often tipped by the shock with stones, which shortens total life time of diamond bits. There is not sufficient data and even proper method for estimating fracture toughness of thick diamond films. In the future, researches on thick diamond films will be more important with the development of a reactor.

6. REMARKS

Diamond-coated inserts, drills and end mills now show great cutting performance for Al-Si alloys which will be used for automotive engines in the near future. In particular, diamond-coated inserts and drills have been already commercially available. although they have not been widely used in the automotive factories. The high cost and difficulties of mass production have been preventing the development of CVD diamond market In the future, several companies in the U.S. and Japan will have to cooperate each other in order to get into automotive industries and constantly provide CVD diamond cutting tools.

ACKNOWLEDGEMENT

7. REFERENCES

1. S.Matsumoto, Y.Sato, M.Kamo and N.Setaka. Jpn. J. Appl. Phys. **21** (1982) L183.
2. B.Lux and B.Haubner. Phil. Trans. R. Soc. London A **342** (1993) 297
3. N.Kikuchi and H.Yoshimura. New Diamond (1988) 42.
4. K.Shibuki, K.Sasaki, M.Yagi and T.Suzuki, Surface Coating and Technology **68/69** (1994) 369.
5. K.Kanda, S.Takehara. S.Yoshida and F.Shimakura. 2nd International Conference on the Applications of Diamond Films and Related Materials.

MYU. Tokyo (1993) p.565.
6. K.Saijo, M.Yagi, K.Shibuki and S.Takatsu, Proc. 1st Japanese Int. SAMPE Symposium (1989) p.1436.
7. K.Shibuki, M.Yagi and T.Suzuki, Diamond Films and Technology **3** (1993) 31.
8. Dr. J. Herb, private communication.
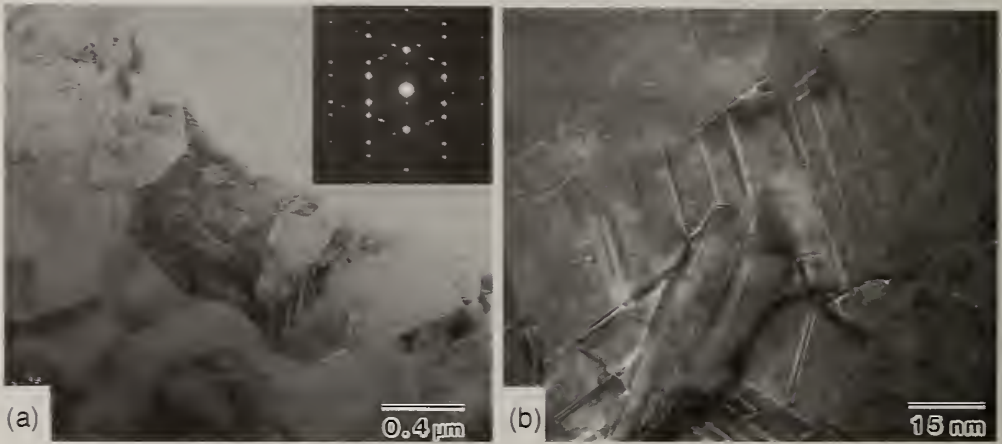
Fig.1. Transmission electron micrographs of diamond films deposited by the microwave plasma method : (a) Twin patterns are seen as extra spots, (b) Enlarged view of (a), showing $\Sigma 9$ boundaries as indicated by the arrows, together with many $\Sigma 3$ boundaries
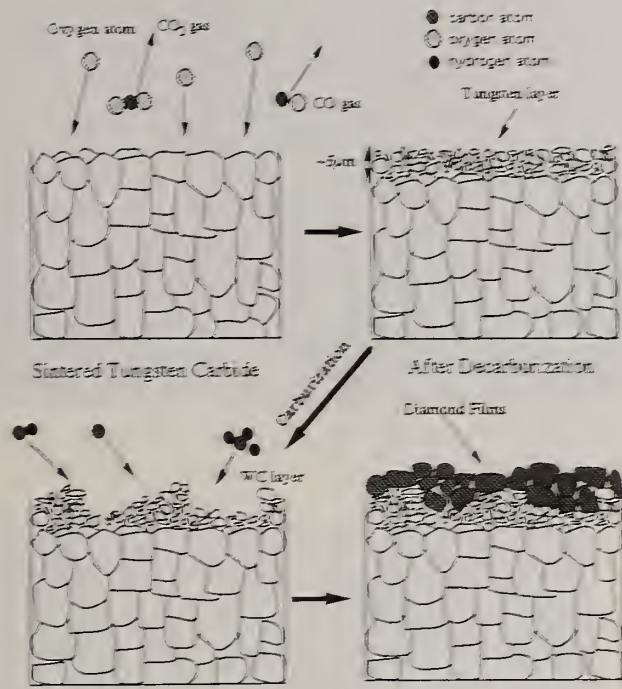
Fig 2. Schematic illustration of decarburization process [4]

(a)

(b)
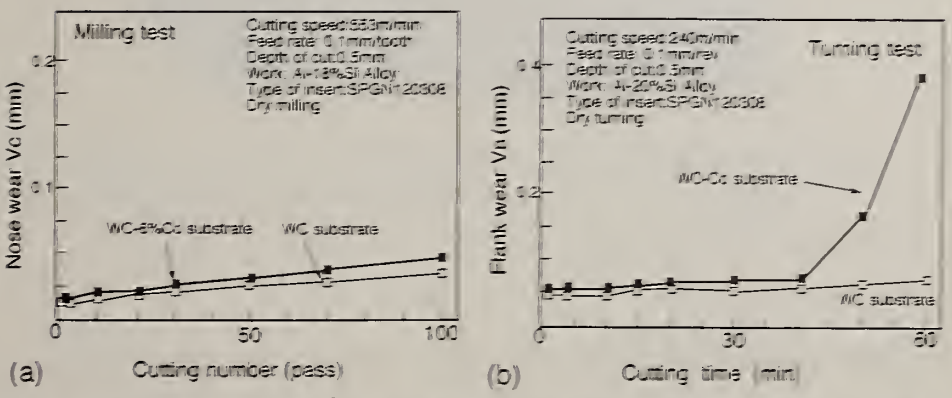
Fig.3. Comparison in flank wear between diamond-coated WC-6%Co and
diamond-coated WC with decarburization.
(a) milling test. (b) turning test
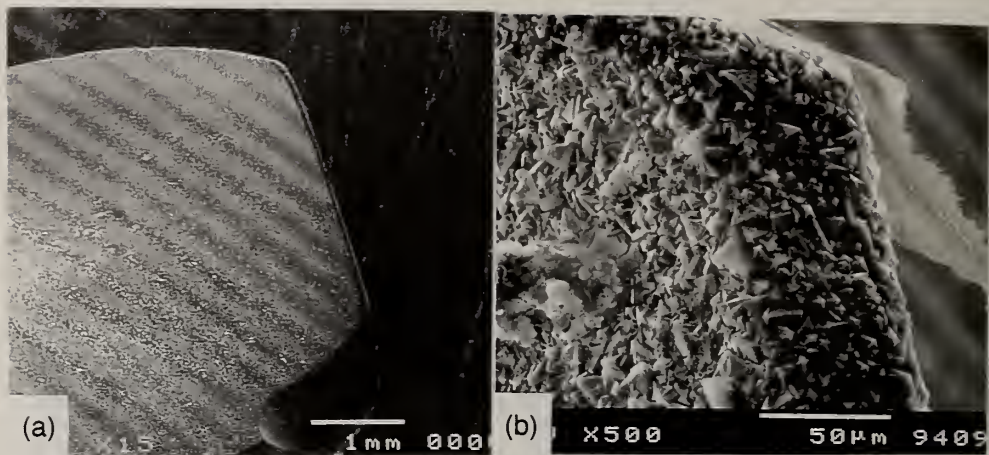
Fig.4. Scanning electron micrographs of diamond-coated twist drills after making 7000 holes : (a) Low magnification, (b) Enlarged view showing no wear.
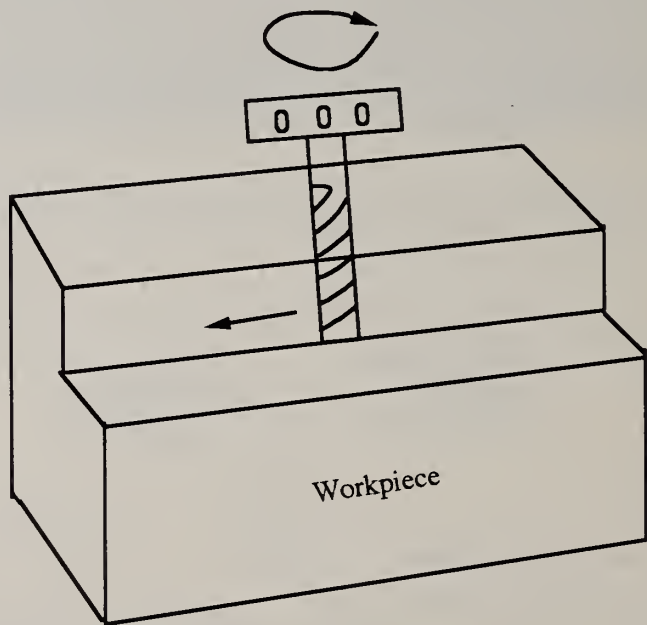
Fig.5. Schematic illustration of cutting tests by diamond-coated end mills.
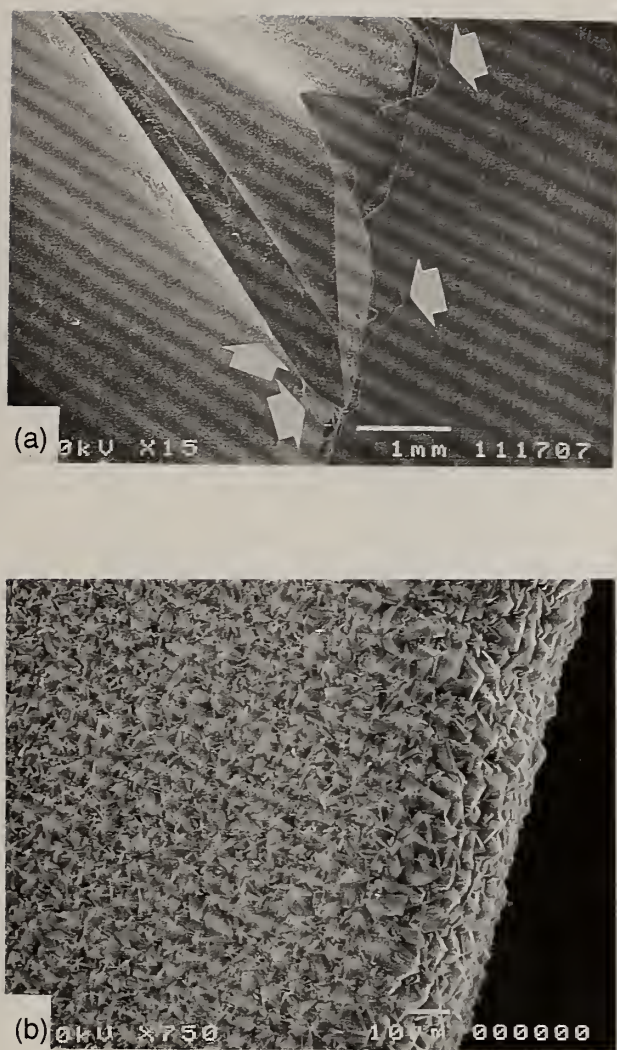
Fig.6. Scanning electron micrographs of diamond-coated end mills after
cutting tests with A390 : (a) The arrows indicate workpiece,
(b) Enlarged view of edge after washing with acid, showing no wear.

AUTHOR INDEX

SUBJECT INDEX

948